Macromolecules

Perspective

pubs.acs.org/Macromolecules

o-Nitrobenzyl Alcohol Derivatives: Opportunities in Polymer and Materials Science

Hui Zhao,[†,⊥] Elizabeth S. Sterner,[‡] E. Bryan Coughlin,*[,‡] and Patrick Theato*[,†,§,⊥]

[†]Institute for Technical and Macromolecular Chemistry, University of Hamburg, Bundesstrasse 45, D-20146 Hamburg, Germany

[‡]Department of Polymer Science & Engineering, University of Massachusetts, 120 Governors Drive, Amherst, Massachusetts 01003-4530, United States

[§]World Class University (WCU) program of Chemical Convergence for Energy & Environment (C_2E_2), School of Chemical and Biological Engineering, College of Engineering, Seoul National University (SNU), Seoul, Korea

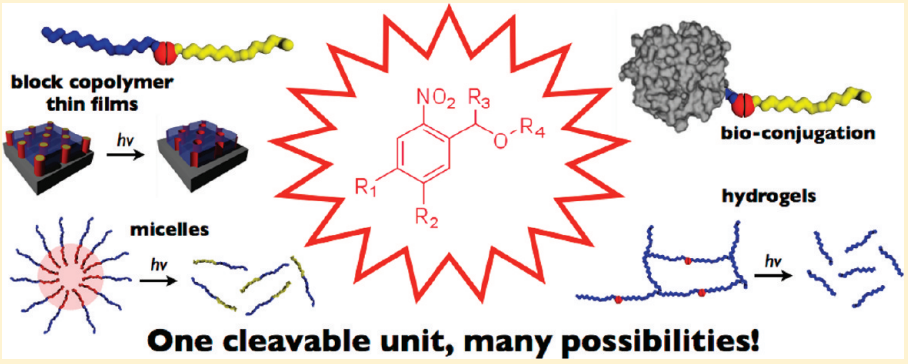

ABSTRACT: Polymers featuring photolabile groups are the subject of intense research because they allow the alteration of polymer properties simply by irradiation. In particular, the *o*-nitrobenzyl group (*o*-NB) is utilized frequently in polymer and materials science. This Perspective pays particular attention to the increasing utilization of this chemical group in polymer chemistry. It covers the use of (i) *o*-NB-based cross-linkers for photodegradable hydrogels, (ii) *o*-NB side chain functionalization in (block) copolymers, (iii) *o*-NB side chain functionalization for thin film patterning, (iv) *o*-NB for self-assembled monolayers, (v) photocleavable block copolymers, and (vi) photocleavable bioconjugates. We conclude with an outlook on new research directions in this rapidly expanding area.

1. INTRODUCTION

Photolabile groups have been used extensively in synthetic organic chemistry and have found numerous applications in academia and industry. While organic synthesis engaged the use of photolabile protecting groups as a tool for orthogonal deprotection, the development of photoacid generators, which act as H^+ sources upon irradiation, and acid-sensitive photoresists have enabled the production of photosensitive materials employed in the microelectronic[1] and coatings industries.[2] Bochet has previously summarized the various photolabile groups that find intensive application in synthetic chemistry.[3]

Among the many photolabile groups that have been studied, *o*-nitrobenzyl (*o*-NB) alcohol derivatives have gained tremendous attention in the area of synthetic organic chemistry and beyond. First described by Schofield and co-workers,[4] the chemistry was not widely recognized until Woodward and co-workers utilized what has become one of the most popular photolabile protecting groups.[5] It is based on the photoisomerization of an *o*-nitrobenzyl alcohol derivative into a corresponding *o*-nitrosobenzaldehyde upon irraditation with UV light (Scheme 1), simultaneously releasing a free carboxylic acid. This mechanism has been investigated in detail, most recently by Wirz and co-workers.[6,7]

The photodeprotection of *o*-NB esters usually yields carboxylic acids, accompanied by an *o*-nitrosobenzaldehyde.[10] Fréchet and co-workers demonstrated that the concept could be expanded to yielding organic bases by employing *o*-nitrobenzyl carbamates of amines and diamines, which then result in the release of the respective alkylamines.[11] Logically, this chemistry was extended to *o*-NB variants used for alcohol deprotection[12] and peptide deprotection.[13] 2-Nitrobenzylidene acetals have also been utilized, releasing 1,2-dihydroxy compounds after photolysis and subsequent ester hydrolysis.[14] This chemistry has recently been extended to an *o*-nitrobenzyl triazole linker, prepared by the [2 + 3] Huisgen cycloaddition or "click" reaction of alkynes and azides, releasing a free 1,2,3-triazole leaving group.[15] Recent developments have focused on the design of *o*-NB-based protecting groups with a red-shifted absorption to allow photolysis to occur using two-photon excitation techniques.[16]

Linkers and protecting groups based on *o*-NB chemistry can usually be cleaved in minutes when exposed to 300−365 nm

Received: September 9, 2011
Revised: December 9, 2011
Published: January 26, 2012

   dx.doi.org/10.1021/ma201924h | *Macromolecules* 2012, 45, 1723−1736

Scheme 1. Photoisomerization Mechanism of *o*-Nitrobenzyl Alcohol Derivatives into an *o*-Nitrosobenzaldehyde, Releasing a Carboxylic Acid[3,8,9]

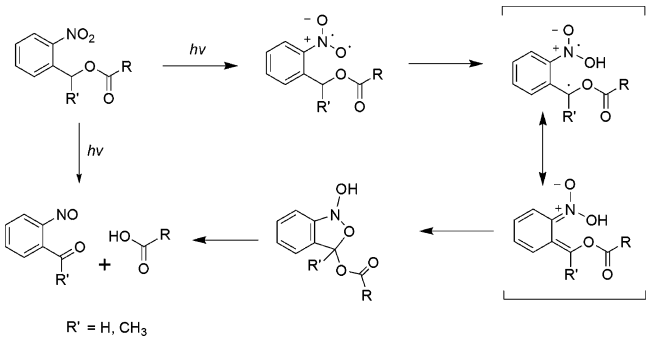

light, with times varying from several hours with a low-intensity 1.3 mW/cm^2 365 nm source[15] to 5 min or less when applying light intensities of 20−40 mW/cm.[2,17] Photocleavage efficiency tends to improve when wavelengths near 300 nm are used, as the *o*-NB linker itself displays an absorption maximum at or near this wavelength.[6] Studies have also shown that including substitutents on the aromatic ring or at the benzyl position of the linker can shift the photocleavage wavelength[18] or prevent the formation of photodimerized byproducts.[19]

Other advances in photocleavable junction structure and application include *o*-NB thioxanthone derivatives, which act as intramolecular sensitizers,[20] and the 2-(2-nitrophenyl)-propoxycarbonyl (NPPOC) photolabile protecting group, which was developed to address possible issues with photocleavage byproduct photodimerization.[21−24] Its photocleavage proceeds via a β-elimination mechanism, resulting in a styrenic product that protects against the formation of the expected *o*-nitrosobenzaldehyde. Other studies focused on the integration of an orthogonal photolysis of different photoprotecting groups, e.g., 3′,5′-dimethoxybenzoin, in conjunction with *o*-NB derivatives.[3,25,26]

The application of photolabile molecules, especially *o*-NB derivatives, is not limited to organic synthesis as can be seen by recent developments in biological applications of such photolabile compounds.[27] Photoactivated bioagents, so-called "caged compounds", are an important tool for studying cell signaling events.[7] Consequently, reversible photoswitches have also been investigated. As an example, Chang and co-workers presented a "caged peroxide generator" based on photolysis of an *o*-NB-protected 1,2,4-trihydroxybenzene. This linker can be triggered on demand and was shown to produce H_2O_2 by reducing molecular oxygen via a superoxide intermediate.[28] Reviews by Heckel, Xing, Zhang, and their respective co-workers have summarized the various applications of caged and light-switchable small molecules (e.g., neuroactive amino acids, steroid hormones, lipids, and cellular signaling molecules), proteins, and nucleic acids.[29−31]

Recently, Katz and Burdick have reviewed developments in the area of light-responsive biomaterials, which include the use of the *o*-NB functionality.[32] Besides its focus on biological complexes, it represents the first summary of synthetic polymers that contain *o*-NB moieties. Even though *o*-NB esters have been investigated in polymer science since 1977,[33,34] it has not been until very recently that studies appeared that take full advantage of this photolabile group in polymer and materials science applications.

Within this Perspective, we focus on the incorporation of *o*-NB-based photolabile groups in polymer materials. We pay particular attention to the increasing utilization of this chemical group in polymer chemistry in the past few years. We cover the use of (i) *o*-NB-based cross-linkers for photodegradable hydrogels, (ii) *o*-NB side chain functionalization in (block) copolymers, (iii) *o*-NB side chain functionalization for thin film patterning, (iv) *o*-NB for self-assembled monolayers, (v) photocleavable block copolymers, and (vi) photocleavable bioconjugates, and we conclude with an outlook on this rapidly expanding area.

2. *O*-NB-BASED CROSS-LINKERS FOR PHOTODEGRADABLE HYDROGELS AND NETWORKS

While research directions in biochemistry and biomaterials have focused on "caged compounds",[31] the first breakthrough applications of *o*-NB-based photolabile linkers in polymer science have been achieved in the preparation of cross-linked networks.[35] Motivated by biological applications, the scientific community has found these photodegradable hydrogels to be of great interest. For example, *o*-NB-based cross-linkers have been used in the cross-linking of hydrophilic poly(ethylene gylcol) chains, resulting in hydrogels which are commonly used as scaffolds in tissue engineering and drug delivery. Torro and co-workers reported a first example of model cross-linked networks based on *o*-NB linkers in 2007.[36] Their synthesis can be summarized in two steps: First, a four-armed star polymer containing *o*-NB linkers and terminal azides was prepared by atom transfer radical polymerization (ATRP) of *tert*-butyl acrylate followed by a simple postmodification of the terminal bromide into azide. In the second step, cross-linking was achieved by adding a bifunctional alkyne under copper(I) catalysis conditions, resulting in the CuAAC formation of 1,2,3-triazole linkages. An alternative route used a bifunctional *o*-NB linker and a tetrafunctional unit for the CuAAC cross-linking reaction (Scheme 2). Further, they demonstrated that a photodegradable four-arm star polymer with terminal azides can be prepared by a one-pot CuAAC/ATRP reaction. The insoluble network could be degraded to linear polymers with a defined molecular weight by exposure to UV light.

Similarly, Kasko and co-workers also used a cross-linking system based on *o*-NB (Figure 1, upper).[17] However, they combined the efficient light degradable property of *o*-NB esters with the biocompatibility of PEO, resulting in a photocleavable hydrogel.[37−39] This laid the foundation to trap living cells in the hydrogels, which may be released upon irradiation with light in a highly controlled manner (Figure 1a). Using two-photon photolithography, 3D channels for the migration of cells can successfully be obtained (Figure 1b). This "smart hydrogel" takes advantage of *o*-NB-based cross-links and thus opens an exciting application area for hydrogels.[40,41] More recently, Kasko and co-workers have extended the application of photodegradable hydrogels based on *o*-NB cross-links to negative and positive patterning strategies. Furthermore, conjugating the *o*-NB unit to a coumarin dye in the photodegradable macromer enabled the two-photon degradation of the *o*-NB group as well as fluorescence visualization of the hydrogel.[42]

Similarly, Kros and co-workers prepared photodegradable hydrogels based on dextran.[43] By utilizing the acrylate−thiol Michael addition of dithiolated PEG to dextran functionalized with acrylate-modified *o*-NB moieties, they were able to form

dx.doi.org/10.1021/ma201924h | *Macromolecules* 2012, 45, 1723−1736

Scheme 2. Cross-Linking Network Based on *o*-NB Linker (Reprinted with Permission from Ref 36. Copyright 2007 American Chemical Society)

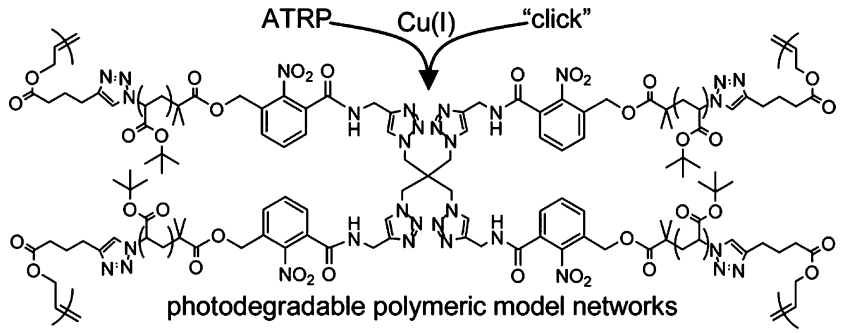

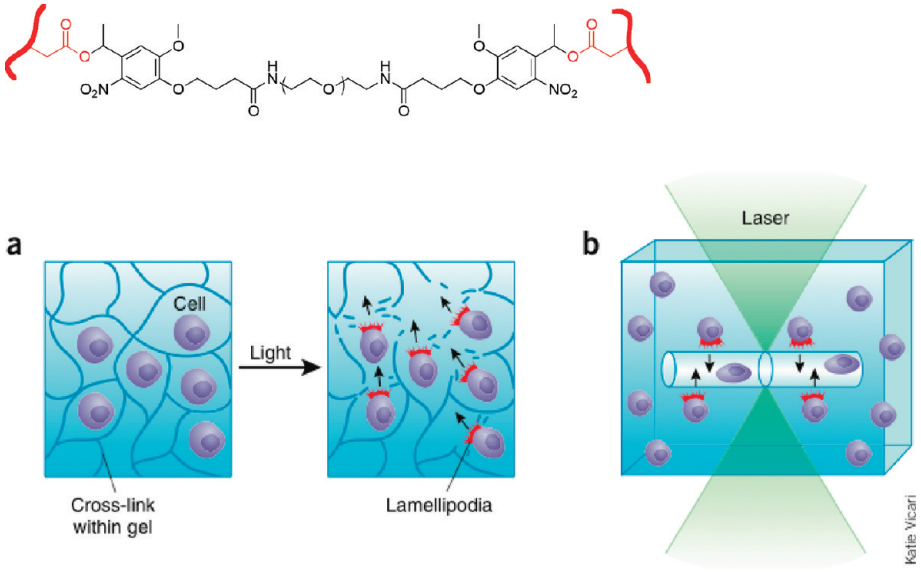

Figure 1. Chemical structure of a photodegradable hydrogel based on an *o*-NB linker (upper) (redrawn after ref 17) and light-induced migration of entrapped cells (lower).[37]

biocompatible hydrogels. Photodegradation of the hydrogels was achieved by UV irradiation at 365 nm for 72 h, releasing green fluorescent protein from the hydrogel. They also demonstrated that the photodegradation was possible via a two-photon excitation using a pulsed near-infrared laser. Shoichet and co-workers have extended these photolabile chemistries to agarose- and hyaluronan-based materials,[44] producing three-dimensional structured materials with applications to tissue scaffolding[45] and using the unmasking of photolabile moieties to anchor biomolecules to hydrogel surfaces to allow these materials to control cell growth and mobility.[46] Recently, Anseth and co-worker showed that thiol–ene click chemistry as well as strain-promoted azide–alkyne cycloaddition in combination with *o*-NB-based localized degradation allows fabrication of 3D cytocompatible hydrogels.[47] Kasko and co-workers could also demonstrate that *o*-nitrobenzyl ether linkers allows the photorelease of potential drugs within hydrogels.[48]

Further, Burdick and co-workers showed that thin film poly(hydroxyethyl methacrylate)-based hydrogels could be spatially altered when copolymerized with *o*-NB acrylate and subsequently irradiated, resulting in dramatic swelling in the irradiated areas,[49] thereby controlling spatially and temporally material properties and cellular interactions. The spatial and temporal manipulation of mechanical properties of hydrogels plays an important factor in cell growth, which was investigated by Wang and co-worker, who studied the photoinduced softening of *o*-NB cross-linked polyacrylamide hydrogels.[50]

Besides macroscopic gels and networks, Landfester and Klinger recently demonstrated the successful use of *o*-NB-based cross-linkers for the fabrication of photodegradable PMMA microgels. Utilizing miniemulsion techniques, particles in the range of 140–200 nm were prepared. Of particular note is the wavelength-controlled selective degradation of these hydrogels, achieved by using carbonate and carbamate *o*-NB cross-linkers.[51]

3. *O*-NB SIDE CHAIN FUNCTIONALIZATION IN POLYMERS AND BLOCK COPOLYMERS TO PHOTOTRIGGER MICELLE DISRUPTION

Responsive micelles formed from environmentally (pH, redox, light, temperature, etc.) sensitive block copolymers in solution have attracted great attention since they find potential applications in targeted drug delivery, cosmetics, and many other fields.[52] In particular, light is an intriguing external stimulus because it is efficient and convenient and can be applied in a targeted and specific manner via a variety of focusing or lithographic techniques. Consequently, light responsive block copolymer micelles have been explored for entrapping dyes and drugs with the intention of releasing them at a defined time

dx.doi.org/10.1021/ma201924h | *Macromolecules* 2012, 45, 1723–1736

and location. For recent reviews on photoresponsive block copolymers, see publications by Gohy and co-workers and Zhao.[53,54] *o*-NB esters are a good candidate for constructing light responsive materials since they are efficiently cleavable upon UV exposure. Early works by Zhao and co-workers explored the use of pyrenylmethyl esters, which can be cleaved upon UV irradiation to yield 1-pyrenylmethanol and the corresponding carboxylic acid.[55] Later, Zhao and co-workers turned their focus to *o*-NB and nicely demonstrated its use as a side chain functionality within amphiphilic block copolymers to prepare light responsive micelles (Figure 2).[56] In this aspect, Gohy and co-workers conducted a fundamental study on the possibilities of polymerizing 2-nitrobenzyl methacrylate under various controlled radical polymerization conditions.[57] It was discovered that 2-nitrobenzyl acrylate cannot be polymerized under conditions suitable for ATRP, nitroxide-mediated polymerization (NMP), or reversible addition−fragmentation chain transfer (RAFT) polymerization. In contrast, 2-nitrobenzyl methacrylate can be polymerized under RAFT conditions with some degree of control and under ATRP with better control as long as conversions are kept below 30%.

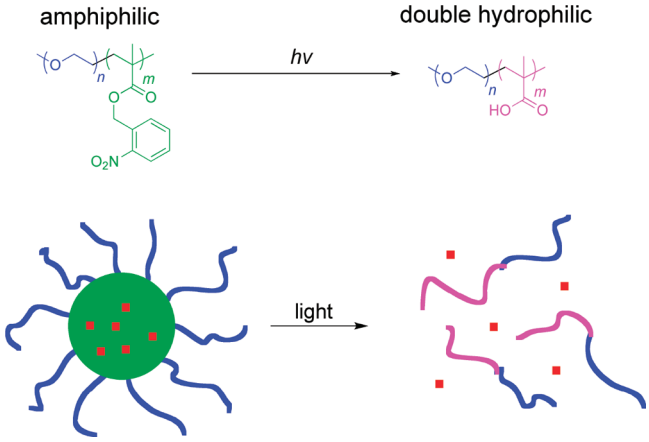

Figure 2. Chemical structure and photolysis of *o*-NB-containing amphiphilic block copolymers and their use for photocontrolled drug release (redrawn after ref 56).

Accordingly, Zhao and co-workers synthesized an amphiphilic block copolymer composed of poly(ethylene oxide) (PEO) and poly(2-nitrobenzyl methacrylate) (PNBM) by ATRP starting from a PEO macroinitiator. Because of the *o*-NB group, this amphiphilic block copolymer can be turned into a double hydrophilic block copolymer upon irradiation, i.e., photocleavage of the ONB ester yielding essentially a poly(methacrylic acid) block. Consequently, Zhao and co-workers demonstrated that this results in the destruction of the micelles, as demonstrated by the controlled release of Nile Red—previously trapped inside the hydrophobic core of the micelle—upon irradiation (Figure 2). Thus, it is one of the first examples showing the potential application of *o*-NB linkers in drug delivery and phototherapeutics.

Zhao and co-workers extended this concept by adding a thermosensitive material, yielding multiresponsive (temperature and light) micelles based on *o*-NB.[58] They synthesized a thermal- and light-sensitive diblock copolymer composed of a hydrophilic poly(ethylene oxide) (PEO) block and a temperature- and light-sensitive poly(ethoxytri(ethylene glycol)-acrylate-*co*-*o*-nitrobenzyl acrylate) (P(TEGEA-*co*-NBA)) block by ATRP (Figure 3). Above the lower critical solution temperature (LCST) of the thermosensitive poly(ethoxytri(ethylene glycol)) block, the block copolymer is amphiphilic and self-assembles into micelles. After UV irradiation, the LCST of the block copolymers shifted from 25 to 36 °C due to the change of hydrophilicity from the deprotection of the *o*-nitrobenzyl acrylate comonomer to acrylic acid (Figure 3). Nile Red is known to fluoresce in hydrophobic environments, but this fluorescence is negligible in aqueous solution and was used to probe the micelle formation. Before irradiation, micelles were formed of the photoprotected block copolymer that had Nile Red in their core, resulting in high fluorescence. After irradiation, the fluorescence dropped sharply, indicating release of the dye and disintegration of the micelles. Raising the temperature further caused the now-deprotected copolymer to again form micelles, sequestering the Red Nile and restoring the system's fluorescence (Figure 3).

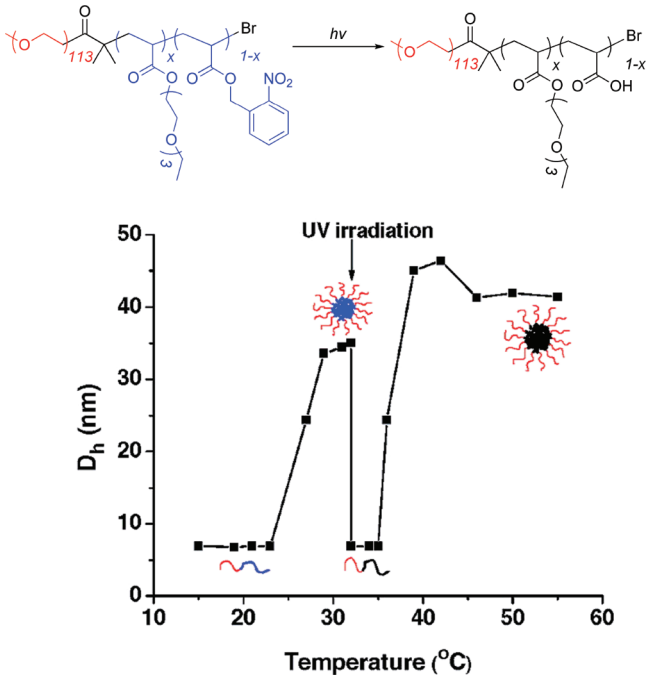

Figure 3. Thermo- and light-sensitive micelles based on *o*-NB-containing copolymer and their hydrodynamic diameter (D_h) response to temperature changes and UV irradiation. (Reprinted with permission from ref 58. Copyright 2008 American Chemical Society.)

It was later shown that a 20 wt % solution of PEO-*b*-P(TEGEA-*co*-NBA) forms micelles upon heating above the LCST, resulting in a optically isotropic gel that can withstand finite yield stress. Upon UV irradiation the *o*-NB ester is cleaved resulting in dissociated micelles, leading to a transformation from a gel to a free-flowing liquid.[59] Similar effects have been observed for the thermo- and light-sensitive triblock copolymer P(TEGEA-*co*-NBA)-*b*-PEO-*b*-P(TEGEA-*co*-NBA), in which the temperature-induced sol−gel transition originates from the formation of a 3D network of hydrophobic cores of dehydrated P(TEGEA-*co*-NBA) blocks bridged by hydrophilic PEO chains.[60]

In efforts to accelerate the degradation time, Zhao and co-workers designed an amphiphilic triblock copolymer with multiple photocleavable moieties positioned repeatedly along the hydrophobic middle block.[61] PEO chains were attached as hydrophilic blocks to a hydrophobic polyurethane containing *o*-NB groups. The block copolymer micelles showed fast

dx.doi.org/10.1021/ma201924h | *Macromolecules* 2012, 45, 1723−1736

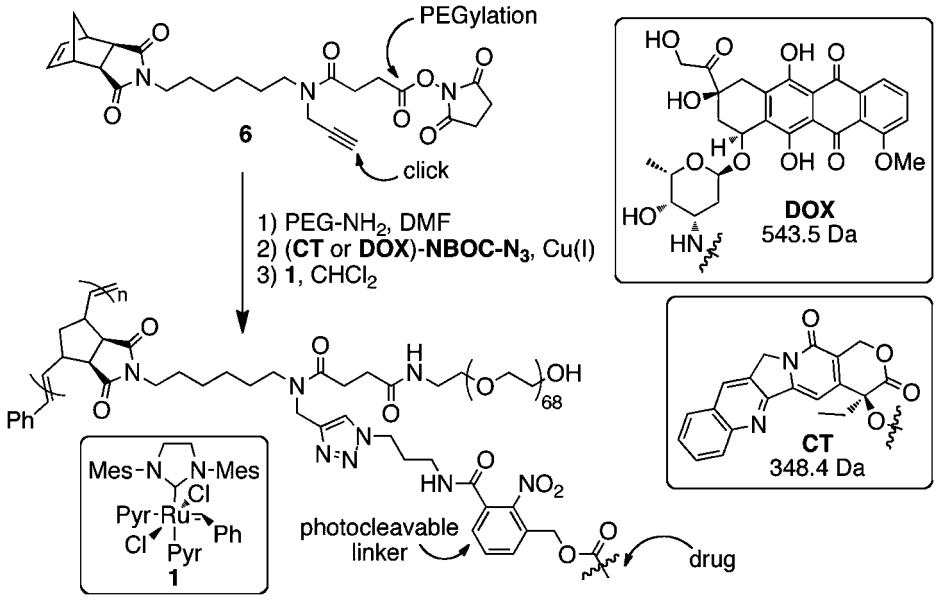

Figure 4. Synthesis and structure of polynorbornene-*g*-PEO polymers. (Reprinted with permission from ref 65. Copyright 2010 American Chemical Society.)

photocleavage of the micelle core within 180 s, and as a result a burst release of hydrophobic guests was achieved. An alternative approach was reported by Thayumanavan and co-workers, who synthesized photocleavable facially amphiphilic dendrimers that form micelles in water.[62] Upon irradiation with UV light (365 nm, 200 s) photocleavage of the *o*-NB esters occurred and resulted in a slight change of the hydrophilic−lipophilic balance, which was sufficient to cause dissociation of the micelles and subsequent release of hydrophobic guest molecules. Noteworthy, the cleavage of *o*-NB groups from polymeric side chains results in the release of nitrosaldehyde, which may be toxic or cause other side effects in vivo.

While most approaches focused on micellization in water, Gohy and co-workers synthesized poly(dimethoxynitrobenzyl acrylate)-*block*-polystyrene as a block copolymer with photocleavable side groups in one block.[63] Upon UV irradiation in chloroform the resulting hydrophilic poly(acrylic acid) block becomes insoluble, and the block copolymer self-assembles in micelles, which were used to trap dyes into the micelle core. Rather than utilizing *o*-NB esters to alter the solubility properties of a polymer chain, Grubbs, Tirrell, and their respective co-workers have used *o*-NB esters for the photoinduced release of covalently bound drugs from bottle-brush polynorbornene-*g*-PEO polymers (Figure 4).[64] UV irradiation released the drug molecules (doxorubicin or camptothecin) from the brush core. Viability tests of MCF-7 human breast cancer cells mixed with the micelles showed at least a 12-fold increase in toxicity after irradiation-induced drug release.[65]

Meijer and co-workers showed that particle aggregation can also be controlled via an intramolecular collapse of a single polymer chain. They designed and synthesized a poly(norbornene) with 2-ureidopyrimidone (UPy) groups in the side chain, which were protected at the terminal carbonyl site with an *o*-NB ether. As a result, this effectively decreased the strong association of UPy groups. Photodeprotection of the *o*-NB group released the UPy groups, permitting their intramolecular dimerization and resulted in a decrease in hydrodynamic volume. AFM analysis of spin-cast films of these solutions revealed single chain nanoparticles.[66] In an elegant approach, Almutairi and co-workers designed light-sensitive polymers based on a self-immolative quinone−methide system.[67] Photocleavage was possible via one- and two-photon processes. They were able to encapsulate Nile Red as a model guest molecule within polymeric nanoparticles and release the guest upon irradiation. In contrast, Wei and co-workers utilized third-, fourth-, and fifth-generation poly(imidoamine) (PAMAM) dendrimers as nanocarriers and peripherally modified these dendrimers with photocleavable *o*-NB groups.[68] Salicylic acid and adriamycin could be encapsulated in the core of the dendrimers and released upon UV irradiation (365 nm). They found that the fourth generation dendrimer was best suited to hosting the guest molecules.

4. *O*-NB SIDE CHAIN FUNCTIONALIZATION FOR THIN FILM PATTERNING

There has been one early report on including *o*-NB ethers in the main chain of polyethers, which were prepared by polycondensation of 2-nitro-1,3-xylylenedibromide with 4,4′-isopropylidenediphenol.[69] It was demonstrated that these polymers decomposed upon UV irradiation and thus suggested these materials for positive-type photoresists. Similar work was conducted by Lee and co-workers, who synthesized a polyimide precursor with *o*-NB ester functionalities in the side chains. They could show that this polyimide became soluble in basic solution after UV irradiation and thus can be used as positive photoresist.[70] Doh and Irvine designed a terpolymer poly(*o*-nitrobenzyl methacrylate-*co*-methyl methacrylate-*co*-(ethylene glycol) methacrylate) (P(*o*-NBMA-*co*-MMA-*co*-EGMA)) to prepare thin film patterns on the micrometer scale. They demonstrated that for a terpolymer composition of 43 wt % *o*-NBMA, 38 wt % MMA, and 19 wt % EGMA the exposed areas of a thin film could be dissolved by phosphate-buffered saline after UV irradiation (see Figure 5). Conjugation of biotin to the hydroxyl end groups of PEGMA units allowed selective immobilization of streptavidin on the surface and led to multicomponent protein patterning.[71] In follow-up work, Doh and co-workers used an optimized photosensitive terpolymer to pattern arrays composed of several proteins by utilizing

dx.doi.org/10.1021/ma201924h | *Macromolecules* 2012, 45, 1723−1736

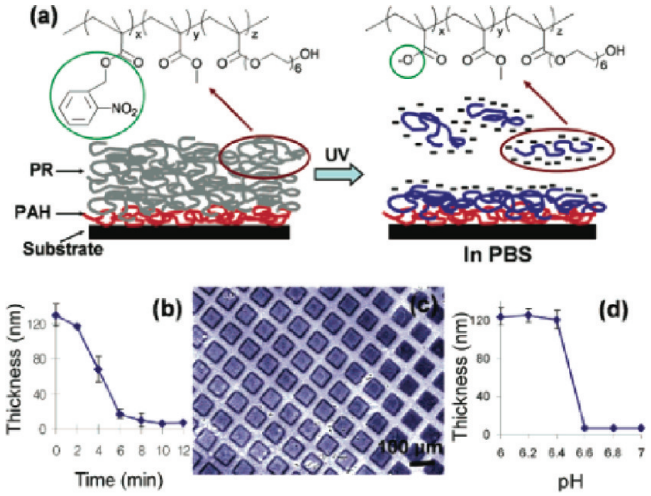

Figure 5. Chemical structure of a photosensitive terpolymer and its mechanism for patterning. (Reprinted with permission from ref 71. Copyright 2004 American Chemical Society.)

microscope projection lithography. They could also extend this approach to the photopatterning of immune cells.[72]

Batt and co-workers undertook a similar approach. They prepared a photosensitive hydrogel surface composed of acrylamide, methylenebis(acrylamide) and functional group-containing methacrylate (FGM). This FGM could either be 2-nitrobenzyl methacrylate or 2-aminoethyl methacrylate hydrochloride, which after polymerization was used to form the 2-nitrobenzyl-derived carbamate. UV irradiation resulted in cleavage of the *o*-NB group and allowed for local protein immobilization through primary amines available on lysine residues by bis(sulfosuccinimidyl)-suberate or carbodiimide coupling chemistry.[73]

Another exciting approach was taken by Ionov and Diez, who utilized the combination of thermoresponsive and photoresponsive characteristics for the patterning of thin polymer films. They synthesized a series of copolymers composed of *N*-isopropylacrylamide and *o*-nitrobenzyl acrylate and could show that the LCST of these polymers differed by almost 50 °C before and after UV irradiation. This temperature-dependent solubility behavior was used to pattern spin-coated thin films by patterned UV irradiation. Sequential removal of irradiated and nonirradiated areas could be achieved by washing steps at different temperatures, allowing the patterning of proteins.[74]

o-NB-based photoresists can be employed in the patterning of organic electronics, which was shown by Ober and co-workers. They synthesized a copolymer composed of 3,3,4,4,5,5,6,6,7,-7,8,8,9,9,10,10,10-heptadecafluorodecyl methacrylate and *o*-nitrobenzyl methacrylate and observed that it was soluble in hydrofluoroethers before irradiation and insoluble after irradiation with UV light at 365 nm (Figure 6). Thus, they could demonstrate that this copolymer represents a nonchemically amplified acid-stable resist for submicrometer patterning of PEDOT:PSS.[75]

5. *O*-NB FOR SELF-ASSEMBLED MONOLAYERS (SAMS) TO CONTROL SURFACE PROPERTIES

While applications of photopatternable polymer thin films on the basis of *o*-NB are continuously growing, there have also been studies presented on photocleavable self-assembled monolayers (SAMs). SAMs in general have proven powerful tools to control surface energy, which influences a variety of properties, e.g., adhesion, wetting and flow profiles, or etch resistance. Moore and co-workers have utilized photopatternable SAMs using *o*-NB chemistry to direct liquid flow inside microchannels (Figure 7).[76] Essentially, the *o*-NB-based SAM was employed in a photolithographic—and thereby contact free—method resulting in patterns of differing surface free energies inside microchannels. This difference in the surface free energies confined aqueous solutions to the irradiated, and thus hydrophilic, regions resulting in control of the flow patterns, as shown in Figure 7.

Rather than merely taking advantage of a change in surface hydrophilicity after UV irradiation of an *o*-NB-derived SAM, several studies have concentrated on utilizing the distinct surface chemistry obtained after photocleavage. Evans and co-workers first studied a SAM containing *o*-NB as a protecting group for COOH and NH_2 groups on gold surfaces. In comparison to photodeprotection by UV irradiation in solution, on gold surfaces a lower chemical yield (<50%) was achieved. This might presumably be due the quenching of excited molecules by the gold or an imine formation in case of protected amines.[77] However, for *o*-NB-protected carboxylic groups on SAMs, the yield during UV irradiation could be dramatically improved in the presence of acids.[78] Using HCl/methanol as a catalyst resulted in formation of the methyl ester.

Kikuchi and co-workers prepared a SAM on a glass substrate featuring an *o*-NB group as well as an activated ester group, 1-[3-methoxy-6-nitro-4-(3-trimethoxysilylpropyloxy)phenyl]ethyl

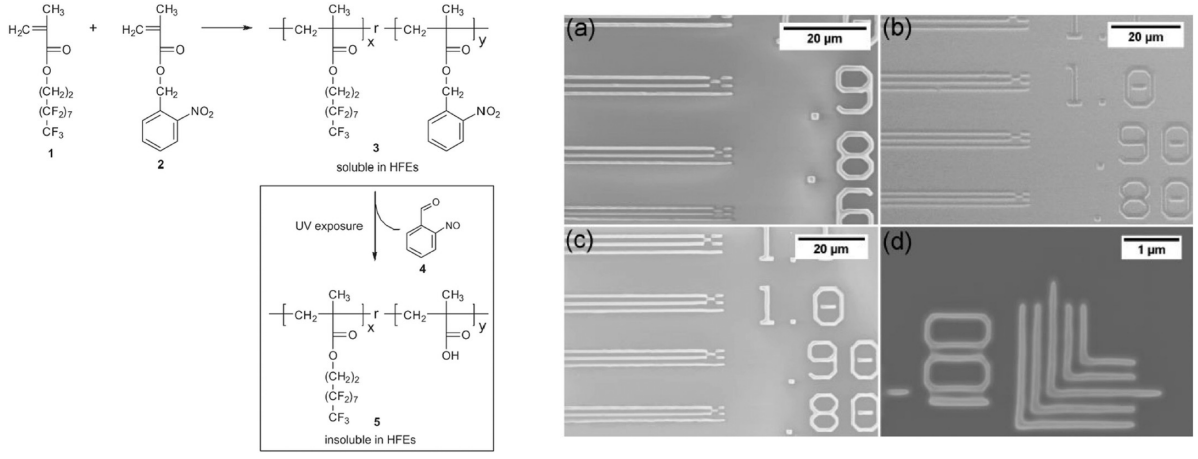

Figure 6. Synthesis of the UV-sensitive acid-stable polymer resist and patterned photoresist SEM images.[75]

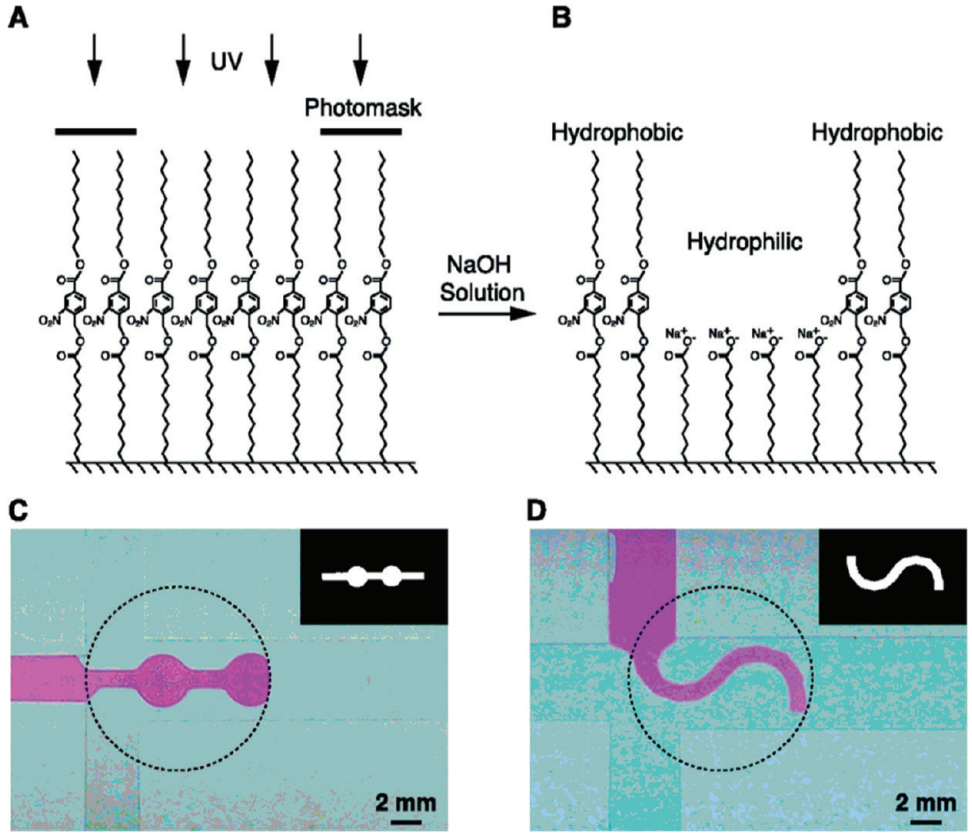

Figure 7. (A, B) Photopatterning by UV light to induce hydrophilic and hydrophobic surface patterns inside microchannels. (C, D) Flow profiles of dilute Rhodamine B aqueous solution inside the surface patterned microchannels.[76]

N-succinimidyl carbonate, that allowed for the attachment of amino-terminated poly(ethylene glycol) (PEG-NH_2), resulting in photopatternable PEG-SAMs.[79] Upon UV irradiation, it was possible to detach PEG and thus change from a cell nonadhesive to a cell adhesive substrate. In combination with illumination through a photomask, cellular patterns were created.

Jonas and co-workers demonstrated that surface modification based on *o*-NB groups is orthogonal to a benzoin-based photoprotection group. They showed that mixed SAMs of both photocleavable groups can be selectively cleaved by choosing the appropriate irradiation wavelength. The benzoin group is almost quantitatively cleaved by irradiation at 254 nm, while the *o*-NB group remained fully intact under these conditions. Irradiation at 365 nm resulted in the cleavage of not only the *o*-NB but also the benzoin group, likely due to its weak absorbance band at 380 nm. However, irradiation at 411 nm leads to cleavage of the *o*-NB with the benzoin group being stable.[80] In further studies, they described an optimized *o*-NB-based photodeprotection for carboxylic acid groups to be utilized within SAMs on quartz slides, 1-(4,5-dimethoxy-2-nitrophenyl)ethyl 4-(triethoxysilyl)butanoate. Standard deprotection by a single-photon process (UV irradiation at 365 nm) was confirmed in solution and in a monolayer. Additionally, a two-photon deprotection could be achieved with a 780 nm laser, which provided access to near-field induced patterning.[81] They could also induce the photodeprotection by localized two-photon induced activation through neighboring enhanced electromagnetic near-fields around metallic nanostructures.[82]

Zhao and co-workers prepared gold nanoparticles functionalized on the surface with *o*-NB alcohol as well as gold nanoparticles with benzylamine on the surface (Figure 8).[83] Taking advantage of the light-triggered "click" reaction of *o*-nitrobenzyl alcohol with benzylamine, which results in the formation of 2-(*N*-benzyl)indazolone, they were able to assemble the gold nanoparticles upon irradiation with UV light. The length of the formed nanochains increased with increasing irradiation time.

Such surface-immobilized photocleavable groups based on coumarin have recently been used by Zhu and co-workers, who presented a mesoporous silica nanoparticle-based drug delivery system.[84] Bowman and co-workers immobilized *o*-NB acrylate on silica nanoparticles and used those to grow linear polymer grafts by a thiol−acrylate polyaddition reaction.[85] Upon exposure to UV light, the grafted polymers were released and analyzed and were found to be similar to polymers formed in bulk.

6. *O*-NB JUNCTIONS TO CLEAVE BLOCK COPOLYMERS

Block copolymers (BCPs) have been studied extensively due to their ability to self-assemble into a range of well-defined, well-ordered structures. Most common are the spherical, cylindrical, gyroidal, and lamellar morphologies found in bulk.[86] In recent years the interest in block copolymers serving as nanotechnological templates has resulted in a multitude of research efforts. Block copolymer thin films with a morphology oriented perpendicular to the substrate are the current focus of many research groups, with a particular aim of preparing well-ordered, nanoporous thin polymer films. Currently, several challenges have to be addressed to overcome the limitations still present in thin block copolymer films. The first is achieving high lateral order in the morphology, and the second is facile, selective removal of one phase.

dx.doi.org/10.1021/ma201924h | *Macromolecules* 2012, 45, 1723−1736

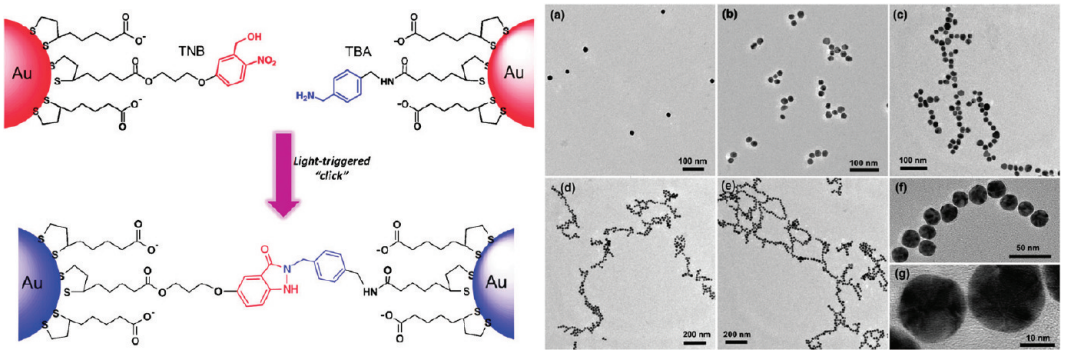

Figure 8. (left) Light-triggered covalent assembly of gold nanoparticles. (right) TEM micrographs of the Au NPs after UV irradiation of increasing time: (a) 0, (b) 5, (c) 10, (d) 15, and (e) 30 min. Images (f) and (g) are the high-resolution TEM characterizations of an obtained Au NPs nanochain.[83]

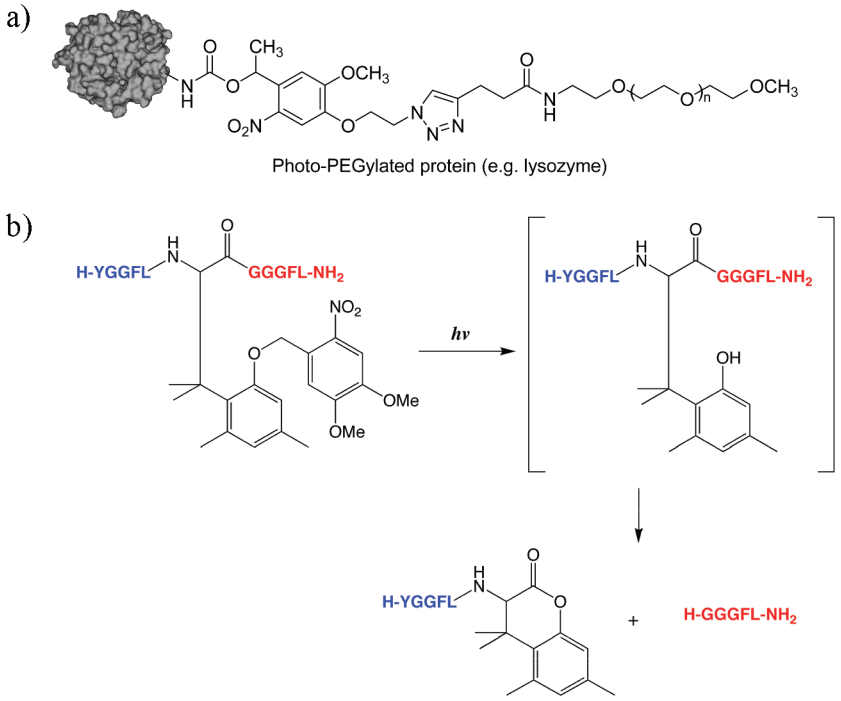

Figure 9. (a) Photocleavable PEGylated lysozyme[105] and (b) schematics of a photoinduced peptide bond cleavage (redrawn after ref 106).

Several methods that allow for selective removal of one domain have been presented in the literature, such as chemical etching, ozonolysis, pH induced hydrolysis, and UV degradation. In particular, block copolymers with a cleavable junction are interesting since they can be used as precursors for generating hollow structures after cleavage and selective removal of one of the blocks. This can have an impact on the formation of hollow micelles and nanoporous polymeric materials.[87,88]

As *o*-NB is a well-known photocleavable junction, photocleavable block copolymers can be prepared based on this structure. In early work, Penelle and co-workers explored the synthesis of a photolabile initiator for ATRP on the basis of *o*-NB. The polymer obtained by ATRP was then coupled to amine-terminated polystyrene to yield the photocleavable block copolymer, whose photolability was demonstrated by GPC analysis.[89] However, no thin film characterization was performed, even though the same group presented an alternative approach that utilizes an anthracene dimer as a photocleavable junction point which resulted in PS-*b*-PMMA that showed a cylindrical microdomain morphology.[90,91] The anthracene dimer approach suffered from the fact that symmetric dimers as well as nonreacted homopolymer had to be removed by selective solubilization.

Kang and Moon adopted the original idea of Penelle, becoming the first to prepare and characterize photocleavable block copolymer thin films based on *o*-NB.[92] They prepared the photocleavable diblock copolymer polystyrene-*block*-poly(ethylene oxide) (PS-*hν*-PEO) by ATRP using an *o*-NB-functionalized PEO macroinitiator (Figure 10). The photolysis of PEO-*hν*-PS has been studied by GPC, which showed that the molecular weight of the block copolymer decreased with increasing time of UV exposure. Since PEO-*b*-PS is a well-known block polymer for the generation of well-ordered films, they also used the PEO-*hν*-PS to get ordered nanoporous films by spin-coating. Compared to other cleavable block copolymers (i.e., the acid-cleavable trityl ether junction),[93] the *o*-NB-based block copolymer can be cleaved into two blocks under mild conditions. As a result, they demonstrated that a porous polystyrene film can be obtained after irradiating the block

dx.doi.org/10.1021/ma201924h | *Macromolecules* 2012, 45, 1723–1736

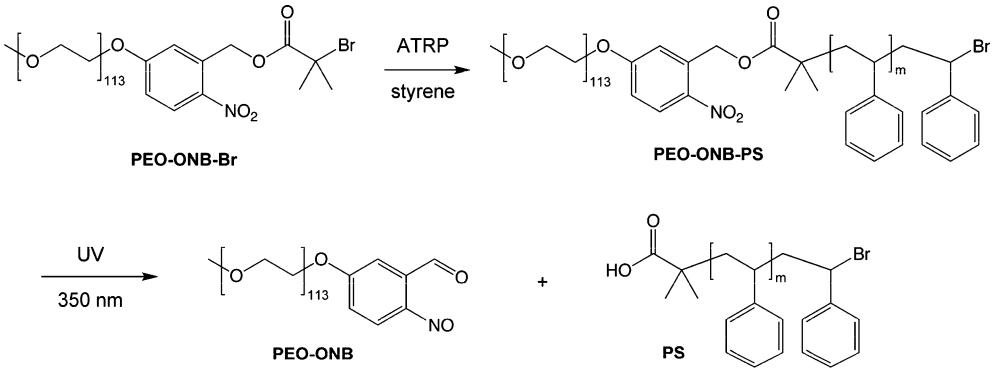

Figure 10. Synthesis and photolysis of PEO-*hν*-PS by ATRP (redrawn after ref 92).

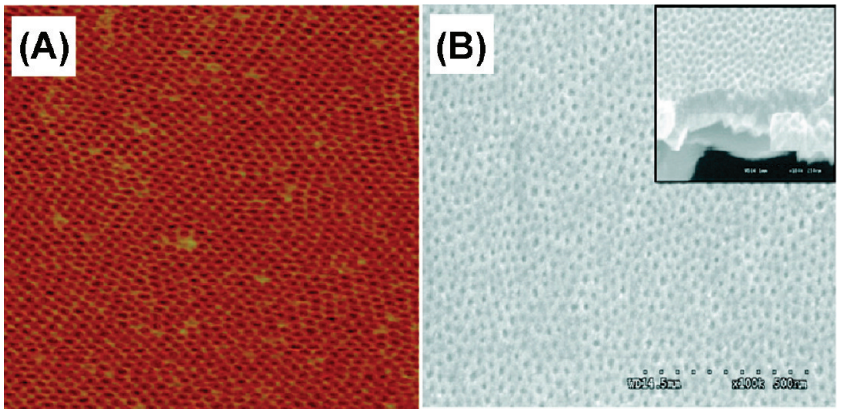

Figure 11. (A) AFM image (1 × 1 μm^2) of PS-*hν*-PEO (23.7-*b*-5.0 K) films (thickness = 43 nm) spin-coated onto silicon wafers and solvent annealed for 2 h (benzene/water). (B) SEM image of the nanoporous PS thin film resulting from photocleavage and selective solvent removal (methanol/water) of PEO phase. A side view (45°) is shown in the inset image. (Reprinted with permission from ref 92. Copyright 2009 American Chemical Society.)

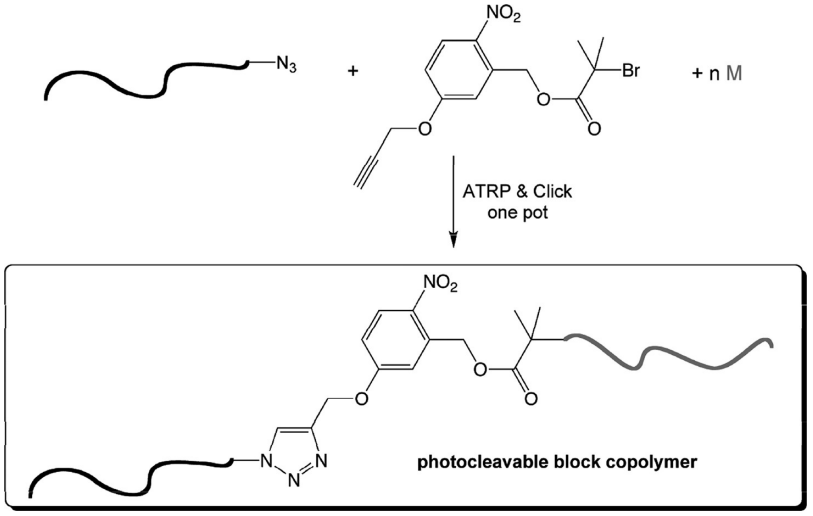

Figure 12. Synthesis of PEO-*hν*-PS by ATRP–CuAAC click reaction (redrawn after ref 95).

copolymer thin film with UV light followed by washing with a water/methanol mixture (Figure 11).

A bifunctional *o*-NB-based ATRP initiator can also be prepared for the synthesis of symmetric homopolymers that can be degraded upon UV irradiation.[94] Recently, Fustin and co-workers developed a more versatile synthetic route toward photocleavable block copolymers on the basis of an *o*-NB junction.[95] As copper(I) is known to be a catalyst for both ATRP and azide–alkyne cycloaddition (CuAAC) click reaction, they performed ATRP and click chemistry in a one-pot synthetic strategy using an ONB ester featuring dual functionality to synthesize several photocleavable block copolymers including PS-*hν*-PEO, which was used in the work of Kang and Moon (Figure 12). An advantage of their work is that their synthesis avoids the preparation of a macroinitiator, (PEO-*o*-NB-Br in Figure 10), which are often more difficult to synthesize than small molecule initiators (Figure 12). Theato, Coughlin, and co-workers extended this approach by combining

dx.doi.org/10.1021/ma201924h | *Macromolecules* 2012, 45, 1723–1736

RAFT polymerization and a subsequent intermacromolecular azide–alkyne click reaction, providing more flexibility in the synthesis of photocleavable block copolymers.[96] Highly ordered thin films were prepared, and after photoetching the resulting nanoporous films were used to prepare the first examples of nanostructures from a photocleavable polymer template.

Besides well-ordered nanoporous thin film applications, amphiphilic block copolymers with an *o*-NB junction also find use in the encapsulation/release of objects through, for example, a polymersome–micelle transition. Meier and co-workers synthesized an amphiphilic poly(γ-methyl-ε-caprolactone)-*block*-poly(acrylic acid) (P*m*CL-*o*-NB-PAA) with *o*-NB junction by ring-opening polymerization and ATRP (Figure 13). A dual

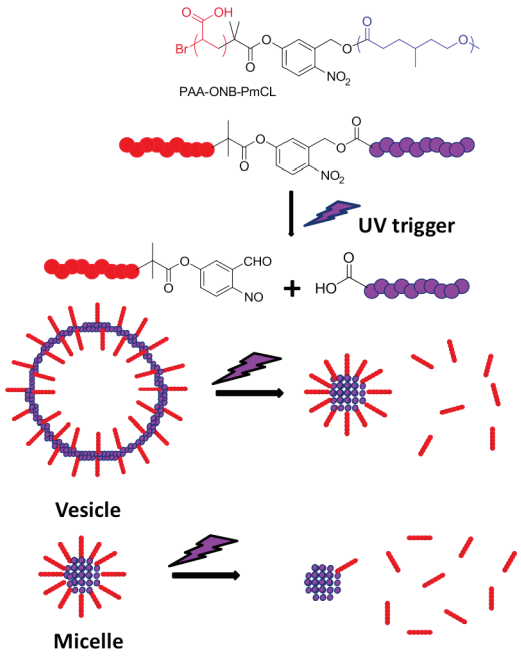

Figure 13. The concept of photocleavable nanocarriers based on amphiphilic block copolymers with *o*-NB junctions (redrawn based on ref 97) .

initiator based on *o*-NB was synthesized and used for the sequential ring-opening polymerization of *m*CL and ATRP of *tert*-butyl acrylate (*t*BA).[97] Afterward, the P*t*BA block was hydrolyzed, resulting in the amphiphilic diblock copolymer P*m*CL-*o*-NB-PAA, which forms aggregates in aqueous solution. Those aggregates—proposed to be micelles or polymersomes—can be degraded by light, demonstrated by a decrease in the size of the aggregates after UV irradiation.

An alternative approach was presented by Zhao et al., who utilized a photodegradable polyurethane block (PUNB) in their synthesis of an amphiphilic triblock copolymer, PEO-*b*-PUNB-*b*-PEO. The short polyurethane middle block was composed of multiple *o*-NB units that allowed a fast photodegradation of the micelles in solution.[61]

Poly(ε-caprolactone)-based block copolymers that feature an *o*-NB photocleavable junction have also been investigated by Nojima and co-workers. They have prepared a polystyrene-*block*-poly(ε-caprolactone) diblock copolymer with an *o*-NB-based junction. They demonstrated that this block copolymer possesses a cylindrical morphology and the crystallization behavior of the PCL chains behaves very differently before and after irradiation with light, as a result of the cleavage of the PCL chains.[98]

Klán and co-workers extended the use of photocleavable junctions based on *o*-NB to an orthogonal photocleavable linker, which functionalized the benzylic and phenacyl positions with leaving groups.[99] The detachment of the groups can be achieved selectively and orthogonally upon irradiation. A very promising alternative to the *o*-NB-based photocleavable junction was reported by Keller and co-workers, who prepared photolabile diblock copolymers with a truxillic acid junction.[100]

7. PHOTOCLEAVABLE BIOCONJUGATES

Applications of *o*-NB linkers in conjugating biological and synthetic molecules have increased over the past few years. Hydrophilic *o*-NB-based photocleavable linkers can be cleaved using small UV diodes, which combine several advantages (small, no heat release, narrow emission profile). Such linkers have been described as suitable for supports in chemical proteomics.[101] Similarly, biotinylated photocleavable polyethylenimine has been synthesized and investigated for the controlled release of nucleic acids from solid supports.[102] Nagamune and co-workers have presented a biotinylated photocleavable caging agent on the basis of the 6-bromo-7-hydroxycoumarine-4-ylmethyl group that can be used for site-selective caging of plasmids.[103] Burke and co-workers demonstrated a mulitpurpose *o*-NB linker that featured two orthogonal functional groups, *N*-hydroxysuccinimidyl and sulfhydryl, allowing for the selective binding of peptides or other amine-terminated groups and oligonucleotides, which can then be used for nucleic acid selections.[104]

The idea of selective removal of polymers has also inspired protein scientists. While PEGylation is a common technique to enhance the pharmacokinetic properties of proteins, it abrogates protein activity in many other applications. Deiters and co-workers have taken advantage of this fact and conjugated a photocleavable PEG to lysozyme. This resulted in a completely inactive enzyme whose activity could be recovered after irradiation with UV light (λ = 365 nm) for 30 min, due to removal of the PEG unmasking the protein (Figure 9a).[105] The concept of alteration of peptides by light was taken further by Shigenaga and co-workers, who designed a photocleavable amino acid that could induce a peptide bond cleavage at the C-terminal position based on the integration of an *o*-nitrobenzyl ether group that triggers a cascade of reactions upon irradiation with either single-photon UV or two-photon near-IR light (Figure 9b).[106]

8. OUTLOOK AND CHALLENGES OF PHOTOLABILE GROUPS IN POLYMER CHEMISTRY

We have highlighted active research areas in polymer and materials science that utilize the photolysis of *o*-nitrobenzyl groups. This field is rapidly developing and new reports are published frequently. We have paid particular attention to research achievements in polymer chemistry. Photodegradable hydrogels with *o*-NB-based cross-linkers are being used to construct tailored hydrogels that can be further elaborated by selective photodegradation. These hydrogels are currently studied as three-dimensional matrices to entrap and guide cells, and future applications may include adjustable feature size and novel geometries. Side chain functionalization in block copolymers uses *o*-NB to produce smart materials with tunable hydrophobicity–hydrophilicity and LCST properties, with an overall goal of producing micelles with tunable assembly and

dx.doi.org/10.1021/ma201924h | *Macromolecules* 2012, 45, 1723–1736

disassembly behavior. Further investigation of these materials may include micelles designed to host guest molecules for photoinduced delivery. Thin film patterning with side chain functionalized *o*-NB materials and *o*-NB-based self-assembled monolayers allows for the tailoring of surface energies and chemistries through photocleavage. Side chain functionalized *o*-NB materials may provide new methods of photolithographic patterning of microscale thin polymer films, while photocleavable self-assembled monolayers may allow the modification of surfaces on the nanoscale, such as those in microfluidic channels or on nanoparticles. This is particular interesting, as it could be foreseen to use such surface modification techniques to guide liquid flows between two plates without the need for static side walls. Technologically exciting is the utilization of *o*-NB junctions to cleave block copolymers upon irradiation, accessing feature sizes that are difficult to achieve with current lithographic techniques. Herein, the distinct synthetic placement of the photocleavable moiety becomes important. Selective solvent removal of one component generates nanoporous membranes, which can further serve as nanoscopic templates. Finally, bioconjugates based on *o*-NB chemistry lend researchers the ability to use photolysis to trigger the unmasking or release of a biologically active compound, causing a cascade of reactions. The possibility to trigger the photolysis of *o*-NB moieties by one- and two-photon inducted absorption have already been applied in a few examples, and further investigations of these chemistries are expected to lead to exciting developments when it comes to localized release of biological moieties. More fundamental investigations to enhance photolysis, via increased kinetics or alteration of photolysis wavelength, will permit faster dynamics and system responses.

While this Perspective has highlighted some of the current developments, there are certainly untold opportunities to combine the orthogonality of photolability with other chemical transformations and techniques for material manipulation. In this respect, the utilization of *o*-NB photocleavable moiety can be regarded as the counterpart to "click chemistry" in polymer science. "Unclicking" chemical bonds selectively and precisely presents a new and rising research area in polymer science and *o*-NB groups will surely play a dominant part in this area.[107−109] Thus, the synthetic combination of click methods to prepare macromolecules with phototriggered "unclicking" based on *o*-NB groups will result in advancements in macromolecular engineering with high fidelity. Undoubtedly, the careful application of *o*-NB cleavage strategies will continue to facilitate the preparation of macromolecular materials with unprecedented structural control.

Further, insight regarding the limits of the photocleavage reaction of *o*-NB groups is needed. The fact that a nitrosoaldehyde is released after cleavage may be problematic for certain biological applications. However, aldehydes are also suitable candidates to be used in a "reclicking" chemistry with amines, hydrazines, or hydroxyamines.[110] This may be utilized to cleave and re-form polymer and block copolymer chains on the molecular level.

All in all, it is fascinating to see that the precise positioning of a single functional group within a polymer chain allows the delicate control of a variety of polymer properties,[111] ranging from the controlled folding of polymer chains to synthetic routes that may eventually facilitate the synthesis of macromolecules with controlled primary structures.[112−114] The opportunity to combine this controlled synthesis of macromolecules with the cleaving polymer chains in a controlled way by utilizing *o*-NB groups provides myriads of possibilities.

AUTHOR INFORMATION

Corresponding Author

*E-mail: coughlin@mail.pse.umass.edu (E.B.C.); theato@chemie.uni-hamburg.de (P.T.).

Present Address

[⊥]Institute for Technical and Macromolecular Chemistry, University of Hamburg, Bundesstr. 45, D-20146 Hamburg, Germany.

Biographies

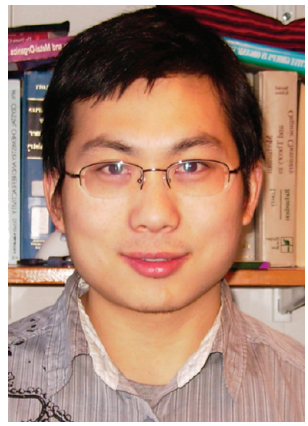

Hui Zhao received his B.S. in Material Chemistry from Shandong Polytechnic University, China, in 2006. He received a Master's degree in Polymer Chemistry from Zhejiang University, China, in 2010, under the guidance of Prof. J. Z. Sun and Prof. B. Z. Tang. He then joined the group of Prof. P. Theato to pursue a PhD degree in Chemistry. As a visiting student, he spent 6 months in the group of Prof. E. B. Coughlin at the University of Massachusetts, Amherst. His research interest includes synthesis of photocleavable polymers and block copolymers based on *o*-nitrobenzyl derivatives and their application as nanoporous materials.

Elizabeth S. Sterner was born in 1985 in Minneapolis, MN. In 2007, she received her B.S. in chemistry with Honors from Creighton University, where she did undergraduate research with Dr. Stephen S. Gross preparing ionic liquid-polymer composites. She is currently working toward her doctorate in polymer science and engineering at UMass Amherst under the supervision of Prof. E. Bryan Coughlin. Her current research projects focus on applications of photocleavable junctions to complex polymer architectures.

E. Bryan Coughlin studied chemistry at Grinnell College and received his B.A. in 1988. Upon the completion of his Doctorate in Chemistry at the California Institute of Technology in 1993 under the direction of John Bercaw, he joined the Central Research and Development Department of the DuPont Company. He was on the technical staff for nearly 6 years. He is a coinventor of DuPont's Versipol Polyolefin Technology Platform and has over 25 patents to his name. Since 1999, Dr. Coughlin has been on the Faculty of the Polymer Science and Engineering Department at the University of Massachusetts, Amherst, where he is currently a Full Professor. He has won a number of research awards: NSF CAREER award, 3M nontenured faculty award, DuPont Young Faculty award, among others. He has been actively involved in the governance of the Polymer Materials: Science and Engineering Division of the American Chemical Society. His research interests are broad and cover aspects of synthetic polymer chemistry and material characterization studies of polymers for use in fuel cells, lithium ion batteries, light harvesting polymer for organic photovoltaics, functional hybrid materials, and fire-safe polymers.

Patrick Theato studied chemistry at the University of Mainz and the University of Massachusetts, Amherst, and obtained his Ph.D. degree under the supervision of Prof. R. Zentel at the University of Mainz in 2001. Shortly after, he was awarded a Feodor Lynen Postdoctoral Research Fellowship from the Humboldt Foundation and joined the group of Prof. D. Y. Yoon at Seoul National University (Korea), where he worked as a postdoctoral fellow, followed by a short research stay at Stanford University with Prof. C. W. Frank. In 2003, he joined the University of Mainz as a young faculty and completed his Habilitation in 2007. From 2009 to 2011 he held a joint appointment with the School of Chemical and Biological Engineering at Seoul National University within the WCU program. In 2011, he accepted a prize senior lectureship at the University of Sheffield, UK. Shortly after he moved to University of Hamburg, Germany, where he is currently an associate professor for polymer chemistry. His current research interests include the defined synthesis of reactive polymers, design of multi-stimuli-responsive polymers, versatile functionalization of interfaces, hybrid polymers, polymers for electronics, templating of polymers, and light responsive polymers.

■ ACKNOWLEDGMENTS

Financial support from the German Science Foundation (DFG) under Grant TH 1104/4-1 and an International Collaboration in Chemistry award from the National Science Foundation (CHE 0924435) is gratefully acknowledged. Acknowledgment is also made to the Donors of the American Chemical Society Petroleum Research Fund for partial support of this research under Award 49892-ND7. This research was partly supported by the WCU (World Class University) program through the National Research Foundation of Korea funded by the Ministry of Education, Science and Technology (R31-10013).

■ REFERENCES

(1) Thompson, L. F.; Willson, C. G.; Bowden, M. J. *Introduction to Microlithography*; American Chemical Society: Washington, DC, 1983; Vol. *219*.
(2) Reiser, A. *Photoreactive Polymers*; John Wiley and Sons: New York, 1989.
(3) Bochet, C. G. *J. Chem. Soc., Perkin Trans. 1* **2002**, *2*, 125−142.
(4) Barltrop, J. A.; Plant, J.; Schofield, P. *Chem. Commun.* **1966**, *22*, 822−823.
(5) Patchornik, A.; Amit, B.; Woodward, R. B. *J. Am. Chem. Soc.* **1970**, *92*, 6333−6335.
(6) Il'ichev, Y. V.; Schworer, M. A.; Wirz, J. *J. Am. Chem. Soc.* **2004**, *126* (14), 4581−4595.
(7) Pelliccioli, A. P.; Wirz, J. *Photochem. Photobiol. Sci.* **2002**, *1*, 441−458.
(8) Gaplovsky, M.; Il'ichev, Y. V.; Kamdzhilov, Y.; Kombarova, S. V.; Mac, M.; Schworer, M. A.; Wirz, J. *Photochem. Photobiol. Sci.* **2005**, *4*, 33−42.
(9) Corrie, J. E. T.; Barth, A.; Munasinghe, V. R. N.; Trentham, D. R.; Hutter, M. C. *J. Am. Chem. Soc.* **2003**, *125*, 8546−8554.
(10) Holmes, C. P.; Jones, D. G. *J. Org. Chem.* **1995**, *60* (8), 2318−2319.
(11) Cameron, J. F.; Frechet, J. M. J. *J. Am. Chem. Soc.* **1991**, *113*, 4303−4313.
(12) Specht, A.; Goeldner, M. *Angew. Chem., Int. Ed.* **2004**, *43* (15), 2008−2012.
(13) Marinzi, C.; Offerc, J.; Longhia, R.; Dawson, P. E. *Bioorg. Med. Chem.* **2004**, *12*, 2749−2757.
(14) Sebej, P.; Solomek, T.; Hroudna, L.; Brancova, P.; Klan, P. *J. Org. Chem.* **2009**, *74*, 8647−8658.
(15) Sterner, E. S.; Tsai, T.; Coughlin, E. B. Unclicking the "click": a photo-releasable 1,2,3-triazole in block copolymers. In *Abstracts of Papers, 240th ACS National Meeting*, Boston, MA, 2010; p PMSE-363.
(16) Aujard, I.; Benbrahim, C.; Gouget, M.; Ruel, O.; Baudin, J.-B.; Neveu, P.; Jullien, L. *Chem.—Eur. J.* **2006**, *12* (26), 6865−6879.
(17) Kloxin, A. M.; Kasko, A. M.; Salinas, C. N.; Anseth, K. S. *Science* **2009**, *324* (5923), 59−63.
(18) Holmes, C. P. *J. Org. Chem.* **1997**, *62*, 2370−2380.
(19) Guillier, F.; Orain, D.; Bradley, M. *Chem. Rev.* **2000**, *100*, 2091−2157.
(20) Woell, D.; Laimgruber, S.; Galetskaya, M.; Smirnova, J.; Pfleiderer, W.; Heinz, B.; Gilch, P.; Steiner, U. E. *J. Am. Chem. Soc.* **2007**, *129* (40), 12148−12158.
(21) Woell, D.; Smirnova, J.; Galetskaya, M.; Prykota, T.; Buehler, J.; Stengele, K.-P.; Pfleiderer, W.; Steiner, U. E. *Chem.—Eur. J.* **2008**, *14* (21), 6490−6497.

(22) Hasan, A.; Stengele, K.-P.; Geigrich, H.; Cornwell, P.; Isham, K. R.; Sachleben, R. A.; Pfleiderer, W.; Foote, R. S. *Tetrahedron* **1997**, *53* (12), 4247−4264.
(23) Giegrich, H.; Eisele-Buhler, S.; Hermann, C.; Kvasyuk, E.; Charubala, R.; Pfleiderer, W. *Nucleosides Nucleotides* **1998**, *17*, 1987−1996.
(24) Buhler, S.; Lagoja, I.; Giegrich, H.; Stengele, K.-P.; Pfleiderer, W. *Helv. Chim. Acta* **2004**, *87* (3), 620−659.
(25) Blanc, A.; Bochet, C. G. *J. Org. Chem.* **2002**, *67* (16), 5567−5577.
(26) Bochet, C. G. *Tetrahedron Lett.* **2000**, *41* (33), 6341−6346.
(27) Zhao, Y.; Zheng, Q.; Dakin, K.; Xu, K.; Martinez, M. L.; Li, W.-H. *J. Am. Chem. Soc.* **2004**, *126*, 4653−4663.
(28) Miller, E. W.; Taulet, N.; Onak, C. S.; New, E. J.; Lanselle, J. K.; Smelick, G. S.; Chang, C. J. *J. Am. Chem. Soc.* **2010**, *132*, 17071−17073.
(29) Mayer, G.; Heckel, A. *Angew. Chem., Int. Ed.* **2006**, *45*, 4900−4921.
(30) Shao, Q.; Xing, B. *Chem. Soc. Rev.* **2010**, *39*, 2835−2846.
(31) Yu, H.; Li, J.; Wu, D.; Qiu, Z.; Zhang, Y. *Chem. Soc. Rev.* **2010**, *39*, 464−473.
(32) Katz, J. S.; Burdick, J. A. *Macromol. Biosci.* **2010**, *10* (4), 339−348.
(33) Barzynski, H.; Jun, M.-J.; Saenger, D.; Volkert, O. *Lithographic Printing Plates and Photoresists Comprising a Photosensitive Polymer*, U.S. Patent 3,849,137. November 19, 1974.
(34) Petropoulos, C. C. *J. Polym. Sci., Part A :Polym. Chem.* **1977**, *15* (7), 1637−1644.
(35) Johnson, J. A.; Turro, N. J.; Koberstein, J. T.; Mark, J. E. *Prog. Polym. Sci.* **2010**, *35*, 332−337.
(36) Johnson, J. A.; Finn, M. G.; Koberstein, J. T.; Turro, N. J. *Macromolecules* **2007**, *40* (10), 3589−3598.
(37) Jay, S. M.; Saltzman, W. M. *Nature Biotechnol.* **2009**, *27* (6), 543−544.
(38) Lutolf, M. P. *Nature Mater.* **2009**, *8* (6), 451−453.
(39) Blow, N. *Nature Methods* **2009**, *6*, 619−622.
(40) Tibbitt, M. W.; Kloxin, A. M.; Dyamenahalli, K. U.; Anseth, K. S. *Soft Matter* **2010**, *6*, 5100−5108.
(41) Kloxin, A. M.; Tibbitt, M. W.; Anseth, K. S. *Nature Protoc.* **2010**, *5* (12), 1867−1887.
(42) Wong, D. Y.; Griffin, D. R.; Reed, J.; Kasko, A. M. *Macromolecules* **2010**, *43*, 2824−2831.
(43) Peng, K.; Tomatsu, I.; van den Broek, B.; Cui, C.; Korobko, A. V.; van Noort, J.; Meijer, A. H.; Spaink, H. P.; Kros, A. *Soft Matter* **2011**, *7*, 4881−4887.
(44) Musoke-Zawedde, P.; Shoichet, M. S. *Biomed. Mater.* **2006**, *1*, 162−169.
(45) Luo, Y.; Shoichet, M. S. *Nature Mater.* **2004**, *3*, 249−253.
(46) Luo, Y.; Shoichet, M. S. *Biomacromoecules* **2004**, *5*, 2315−2323.
(47) DeForest, C. A.; Anseth, K. S. *Nature Chem.* **2011**, *3*, 925−931.
(48) Griffin, D. R.; Patterson, J. T.; Kasko, A. M. *Biotechnol. Bioeng.* **2010**, *107* (6), 1012−1019.
(49) Ramanan, V. V.; Katz, J. S.; Guvendiren, M.; Cohen, E., R.; Marklein, R. A.; Burdick, J. A. *J. Mater. Chem.* **2010**, *20*, 8920−8926.
(50) Frey, M. T.; Wang, Y.-l. *Soft Matter* **2009**, *5*, 1918−1924.
(51) Klinger, D.; Landfester, K. *Soft Matter* **2011**, *7*, 1426−1440.
(52) Rijcken, C. J. F.; Soga, O.; Hennick, W. E.; van Nostrum, C. F. *J. Controlled Release* **2007**, *120* (3), 131−148.
(53) Schumers, J.-M.; Fustin, C.-A.; Gohy, J.-F. *Macromol. Rapid Commun.* **2010**, *31* (18), 1588−1607.
(54) Zhao, Y. *J. Mater. Chem.* **2009**, *28*, 4887−4895.
(55) Jiang, J.; Tong, X.; Zhao, Y. *J. Am. Chem. Soc.* **2005**, *127* (23), 8290−8291.
(56) Jiang, J.; Tong, X.; Morris, D.; Zhao, Y. *Macromolecules* **2006**, *39* (13), 4633−4640.
(57) Schumers, J.-M.; Fustin, C.-A.; Can, A.; Hoogenboom, R. *J. Polym. Sci., Part A: Polym. Chem.* **2009**, *47* (23), 6504−6513.
(58) Jiang, X.; Lavender, C. A.; Woodcock, J. W.; Zhao, B. *Macromolecules* **2008**, *41* (7), 2632−2643.
(59) Jiang, X.; Jin, S.; Zhong, Q.; Dadmun, M. D.; Zhao, B. *Macromolecules* **2009**, *42* (21), 8468−8476.
(60) Woodcock, J. W.; Wright, R. A. E.; Jiang, X.; O'Lenick, T. G.; Zhao, B. *Soft Matter* **2010**, *6*, 3325−3336.
(61) Han, D.; Tong, X.; Zhao, Y. *Macromolecules* **2011**, *44*, 437−439.
(62) Yesilyurt, V.; Ramireddy, R.; Thayumanavan, S. *Angew. Chem., Int. Ed.* **2011**, *50*, 3038−3042.
(63) Bertrand, O.; Schumers, J.-M.; Kuppan, C.; Marchand-Brynaert, J.; Fustin, C.-A.; Gohy, J.-F. *Soft Matter* **2011**, *7*, 6891−6896.
(64) Johnson, J. A.; Lu, Y. Y.; Burts, A. O.; Lim, Y.-H.; Finn, M. G.; Koberstein, J. T.; Turro, N. J.; Tirrell, D. A.; Grubbs, R. H. *J. Am. Chem. Soc.* **2011**, *133*, 559−566.
(65) Johnson, J. A.; Lu, Y. Y.; Burts, A. O.; Xia, Y.; Durrell, A. C.; Tirrell, D. A.; Grubbs, R. H. *Macromolecules* **2010**, *43*, 10326−10335.
(66) Foster, E. J.; Berda, E. B.; Meijer, E. W. *J. Am. Chem. Soc.* **2009**, *131*, 6964−6966.
(67) Fomina, N.; McFearin, C.; Sermskadi, M.; Edigin, O.; Almutairi, A. *J. Am. Chem. Soc.* **2010**, *132*, 9540−9542.
(68) Li, Y.; Jia, X.; Gao, M.; He, H.; Kuang, G.; Wei, Y. *J. Polym. Sci., Part A: Polym. Chem.* **2010**, *48*, 551−557.
(69) Iizawa, T.; Kudou, H.; Nishikubo, T. *J. Polym. Sci., Part A: Polym. Chem.* **1991**, *29* (13), 1875−1882.
(70) Choi, O. J.; Chung, M. K.; Ryu, Y.; Lee, M.-H. *Polymer (Korea)* **2002**, *6*, 701−709.
(71) Doh, J.; Irvine, D. J. *J. Am. Chem. Soc.* **2004**, *126* (30), 9170−9171.
(72) Kim, M.; Choi, J.-C.; Jun, H.-R.; Katz, J. S.; Kim, M.-G. *Langmuir* **2010**, *26* (14), 12112−12118.
(73) Bhatnagar, P.; Malliaras, G. G.; Kim, I.; Batt, C. A. *Adv. Mater.* **2010**, *22*, 1242−1246.
(74) Ionov, L.; Diez, S. *J. Am. Chem. Soc.* **2009**, *131*, 13315−13319.
(75) Taylor, P. G.; Lee, J.-K.; Zakhidov, A. A.; Chatzichristidi, M.; Fong, H. H.; DeFranco, J. A.; Malliaras, G. G.; Ober, C. K. *Adv. Mater.* **2009**, *21* (22), 2314−2317.
(76) Zhao, B.; Moore, J. S.; Beebe, D. J. *Science* **2001**, *291*, 1023−1026.
(77) Chritchley, K.; Zhang, L.; Fukushima, H.; Ishida, M.; Shimoda, T. *J. Phys. Chem. B* **2006**, *110*, 17167−17174.
(78) Prompinit, P.; Achalkumar, A. S.; Han, X.; Bushby, R. J.; Walti, C.; Evans, S. D. *J. Phys. Chem. C* **2009**, *113* (52), 21642−21647.
(79) Kikuchi, Y.; Nakanishi, J.; Nakayama, H.; Shimizu, T.; Yoshino, Y.; Yamaguchi, K.; Yoshida, Y.; Horiike, Y. *Chem. Lett.* **2008**, *37* (10), 1062−1063.
(80) Del Campo, A.; Boos, D.; Spiess, H. W.; Jonas, U. *Angew. Chem., Int. Ed.* **2005**, *30*, 4707−4712.
(81) Alvarez, M.; Best, A.; Pradhan-Kadam, S.; Koynov, K.; Jonas, U.; Kreiter, M. *Adv. Mater.* **2008**, *23*, 4563−4567.
(82) Alvarez, M.; Best, A.; Unger, A.; Alonso, J. M.; del Campo, A.; Schmelzeisen, M.; Koynov, K.; Kreiter, M. *Adv. Funct. Mater.* **2010**, *20*, 4265−4272.
(83) Lai, J.; Xu, Y.; Mu, X.; Wu, X.; Li, C.; Zheng, J.; Wu, C.; Chen, J.; Zhao, Y. *Chem. Commun.* **2011**, *47*, 3822−3824.
(84) Lin, Q.; Huang, Q.; Li, C.; Bao, C.; Liu, Z.; Li, F.; Zhu, L. *J. Am. Chem. Soc.* **2010**, *132* (31), 10645−10647.
(85) Khire, V. S.; Kloxin, A. M.; Couch, C. L.; Anseth, K. S.; Bowman, C. N. *J. Polym. Sci., Part A: Polym. Chem.* **2008**, *46*, 6896−6906.
(86) Kim, H.-C.; Park, S.-M.; Hinsberg, W. D. *Chem. Rev.* **2010**, *110* (1), 146−177.
(87) Chen, D.; Jiang, M. *Acc. Chem. Res.* **2005**, *38* (6), 494−502.
(88) Bang, J.; Jeong, U.; Ryu, D. Y.; Russell, T. P.; Hawker, C. J. *Adv. Mater.* **2009**, *21* (47), 4769−4792.
(89) Goldbach, J. T.; Russell, T. P.; Penelle, J. Synthesis and characterization of poly(styrene-block-methyl methacrylate) containing a nitrobenzyl alcohol derivative as a photoclavable junction point. In *Abstracts of Papers, 224th ACS National Meeting*, Boston, MA, 2002; p POLY-572.
(90) Goldbach, J. T.; Russell, T. P.; Penelle, J. *Macromolecules* **2002**, *35* (11), 4271−4276.

(91) Goldbach, J. T.; Lavery, K. A.; Penelle, J.; Russell, T. P. *Macromolecules* **2004**, *37* (25), 9639−9645.
(92) Kang, M.; Moon, B. *Macromolecules* **2009**, *42* (1), 455−458.
(93) Yurt, S.; Anyanwu, U. K.; Scheintaub, J. R.; Coughlin, E. B.; Venkataraman, D. *Macromolecules* **2006**, *39* (5), 1670−1672.
(94) Cerqua, S.; Sterner, E.; Theato, P.; Coughlin, E. B. Photocleavable polymers with an *ortho*-nitrobenzyl alcohol linker. In *Abstracts of Papers, 238th ACS National Meeting*, Washington, DC, 2009; p PMSE-128.
(95) Schumers, J.-M.; Gohy, J.-F.; Fustin, C.-A. *Polym. Chem.* **2010**, *1*, 161−163.
(96) Zhao, H.; Gu, W.; Sterner, E.; Russell, T. P.; Coughlin, E. B.; Theato, P. *Macromolecules* **2011**, *44* (16), 6433−6440.
(97) Cabane, E.; Malinova, V.; Meier, W. *Macromol. Chem. Phys.* **2010**, *211*, 1847−1856.
(98) Nojima, S.; Ohguma, Y.; Kadena, K.-i.; Ishizone, T.; Iwasaki, Y.; Yamaguchi, K. *Macromolecules* **2010**, *43*, 3916−3923.
(99) Kammari, L.; Solomek, T.; Ngoy, B. P.; Heger, D.; KLan, P. *J. Am. Chem. Soc.* **2010**, *132*, 11431−11433.
(100) Yang, H.; Jia, L.; Wang, Z.; Di-Cicco, A.; Levy, D.; Keller, P. *Macromolecules* **2011**, *44*, 159−165.
(101) Piggott, A. M.; Karuso, P. *Tetrahedron Lett.* **2005**, *46* (47), 8241−8244.
(102) Handwerger, R. G.; Diamond, S. L. *Bioconjugate Chem.* **2007**, *18* (3), 717−723.
(103) Yamaguchi, S.; Chen, Y.; Nakajima, S.; Furuta, T.; Nagamune, T. *Chem. Commun.* **2010**, *46*, 2244−2246.
(104) Saran, D.; Burke, D. H. *Bioconjugate Chem.* **2007**, *18*, 275−279.
(105) Georgianna, W. E.; Lusic, H.; McIver, A. L.; Deiters, A. *Bioconjugate Chem.* **2010**, *21* (8), 1404−1407.
(106) Shigenaga, A.; Yamamoto, J.; Sumikawa, Y.; Furuta, T.; Otaka, A. *Tetrahedron Lett.* **2010**, *51*, 2868−2871.
(107) Brantley, J. N.; Wiggins, K. M.; Bielawski, C. W. *Science* **2011**, *333* (6049), 1606−1609.
(108) Roth, P. J.; Kessler, D.; Zentel, R.; Theato, P. *J. Polym. Sci., Part A: Polym. Chem.* **2009**, *47* (12), 3118−3130.
(109) Sumerlin, B. S.; Vogt, A. P. *Macromolecules* **2010**, *43* (1), 1−13.
(110) Kolb, H. C.; Finn, M. G.; Sharpless, K. B. *Angew. Chem., Int. Ed.* **2001**, *40* (11), 2004−2021.
(111) Theato, P. *Angew. Chem., Int. Ed.* **2011**, *50* (26), 5804−5806.
(112) Schmidt, B. V. K. J.; Fechler, N.; Falkenhagen, J.; Lutz, J.-F. *Nature Chem.* **2011**, *3* (3), 234−238.
(113) Lutz, J.-F. *Nature Chem.* **2010**, *2* (2), 84−85.
(114) Ouchi, M.; Badi, N.; Lutz, J.-F.; Sawamoto, M. *Nature Chem.* **2011**, *3*, 917−924.

Macromolecules

Article

pubs.acs.org/Macromolecules

Photoinitiators with β-Phenylogous Cleavage: An Evaluation of Reaction Mechanisms and Performance

Markus Griesser,[†] Claudia Dworak,[‡] Sigrid Jauk,[‡] Michael Höfer,[‡] Arnulf Rosspeintner,[†] Gottfried Grabner,[§] Robert Liska,*[,‡] and Georg Gescheidt*[,†]

[†]Institute of Physical and Theoretical Chemistry, Graz University of Technology, Stremayrgasse 9, 8010 Graz, Austria

[‡]Institute of Applied Synthetic Chemistry, Vienna University of Technology, Getreidemarkt 9/163/MC, 1060 Vienna, Austria

[§]Max F. Perutz Laboratories, University of Vienna, Campus-Vienna-Biocenter 5, 1030 Vienna, Austria

Supporting Information

ABSTRACT: Bimolecular photoinitiators based on benzophenone and *N*-phenylglycine ideally overcome limitations of classical two-component systems, such as the possibility of deactivation by a back electron transfer or the solvent cage effect. Furthermore, if they are covalently linked, loss of reactivity by diffusion limitation could be reduced. Here we show that such an initiator displays unusually high photoreactivity. This is established by photo-DSC experiments and mechanistic investigations based on laser flash photolysis, TR-EPR, and photo-CIDNP. The β-phenylogous scission of the C−N bond is highly efficient and leads to the production of reactive initiating radicals at a short time scale.

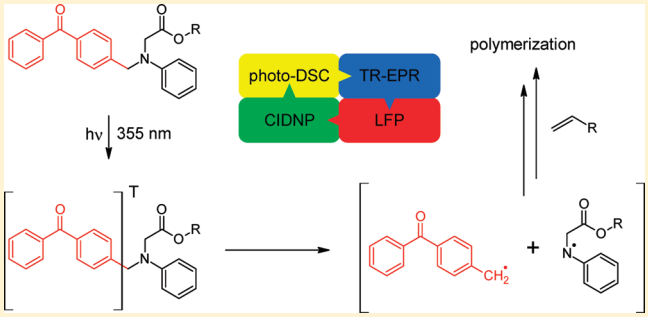

INTRODUCTION

Radical photopolymerization is the key technique for the curing of decorative and protecting films and coatings within a fraction of a second.[1] In this process, the photoinitiators (PIs) play an important role as they have a great impact on the curing rate, double bond conversion (DBC), and the resulting polymer properties. Standard bimolecular photoinitiating systems generally consist of a ketone-based initiator such as benzophenone (BP) combined with tertiary amines as co-initiators. After excitation, BP is able to accept an electron from the co-initiator, followed by the slower and rate-determining proton transfer. However, the efficiency of such systems is usually reduced by the much faster back electron transfer (BET), resulting in a deactivation of the process. To avoid this problem, *N*-phenylglycine (NPG) is used as co-initiating species due to its ability for spontaneous decarboxylation after electron transfer to the excited ketone, thus preventing the BET (Scheme 1).[2,3]

Another limitation of the well-known type II photoinitiators is the bimolecularity, especially in formulations of higher viscosity or at a higher degree of conversion, where diffusion is hampered. To circumvent this problem, we have bound the NPG co-initiator covalently to the chromophore unit, thus keeping the co-initiator in close vicinity of the PI.[4] Additionally, as the solvent cage effect is avoided, substantially enhanced photoreactivity could be observed, especially in water-based systems.[5] Generally, the photochemical and photophysical properties of such a PI chromophore are influenced by the type of linker, usually heteroatoms. Various covalently bound BP−amine systems have been investigated, revealing an optimum in photoreaction quantum yield by using an aliphatic linker between the moieties.[6−8] For our research we employed a methylene spacer to covalently bind phenylglycine derivatives to the PI chromophore as in [(4-benzoylbenzyl)phenylamino]-acetic acid (**1**; Scheme 1). Recent studies compared the reactivity of such covalently bound systems to the physical mixtures of the single components (4-methylbenzophenone, MBP, with **3** or **4**, respectively) and BP/triethanolamine (TEA), a widely used mixture in industry. Surprisingly, **1** showed a polymerization rate 3 times higher than the reference PIs.[4] Further experiments with **2**, the ethyl ester of compound **1**, revealed also remarkable photoreactivity, thus indicating that additional mechanisms besides decarboxylation might be responsible for the high efficiency. By steady-state photolysis experiments photoproducts could be identified that indicated a β-phenylogous cleavage.[4]

The promising reactivity of compounds **1** and **2** motivated us to carry out an in-depth investigation presented here. A basis for the understanding of the photochemical processes can be provided by the reference PIs (4-benzoylbenzyl)-*N*-methyl-*N*-phenylamine (**5**) and (4-benzoylbenzyl)-*S*-phenyl sulfide (**6**), the latter being an established model compound for the β-phenylogous cleavage mechanism.[9] Sulfide **6** is another candidate for a comparable reaction mechanism.

Received: January 4, 2012
Revised: January 19, 2012
Published: February 3, 2012

Scheme 1. Combined Electron and Proton Transfer from NPG to the Excited BP Followed by Spontaneous Decarboxylation of NPG

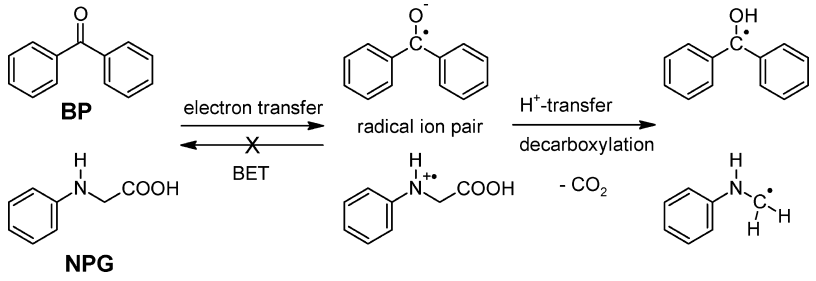

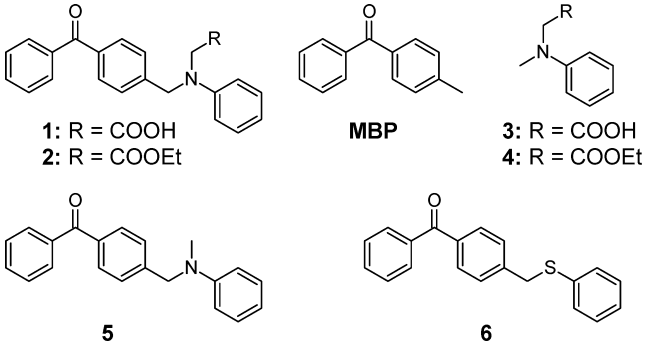

Figure 1. Structures of the investigated PIs.

Herein we present our investigations on the photoreactivity and photochemistry of the investigated PIs. Moreover, we tested the influence of oxygen inhibition in comparison to commercially available PI systems.

The mechanism was examined by laser flash photolysis (LFP), time-resolved electron paramagnetic resonance (TR-EPR), and photochemically induced dynamic nuclear polarization (photo-CIDNP).

EXPERIMENTAL SECTION

Materials. All reagents were purchased from Sigma-Aldrich and were used without further purification. The solvents were dried and purified according to standard laboratory procedures.

[(4-Benzoylbenzyl)phenylamino]acetic acid (**1**),[4] [(4-benzoylbenzyl)phenylamino]acetic acid ethyl ester (**2**),[4] *N*-methyl-*N*-phenylaminoacetic acid (**3**),[10] *N*-methyl-*N*-phenylaminoacetic acid ethyl ester (**4**),[11] (4-benzoylbenzyl)-*N*-methyl-*N*-phenylamine (**5**),[12] and (4-benzoylbenzyl)-*S*-phenyl sulfide (**6**)[13] were synthesized according to procedures described in the literature. All spectroscopic data were in agreement with the reported data.

Characterization. ^{1}H and ^{13}C NMR spectra were recorded on a Bruker AC-200 FT-NMR spectrometer with $CDCl_3$ as solvent. ATR-FTIR spectra were recorded on a Biorad FTS 135 spectrophotometer with Golden Gate MkII diamond ATR equipment (L.O.T.). TLC was performed on silica gel 60 F_{254} aluminum sheets from Merck. UV absorption was measured using a Hitachi U-2001 spectrometer with spectrophotometric grade methanol (MeOH), acetonitrile (MeCN), and cyclohexane as solvent. HPLC measurements were carried out on a reversed-phase HP-1100 HPLC system with a DAD detector. All separations were carried out on a Waters Xterra MS C_{18} column, particle size 5 μm, 150 × 3.9 mm^2 i.d. A linear gradient with flow 0.8 mL/min was formed from 97% water to 97% MeCN over a period of 30 min. Gas chromatography/mass spectrometry was performed on a Hewlett-Packard 5890/5970 B system using a fused silica capillary column (SPB-5, 60 m × 0.25 mm). MS spectra were recorded using EI ionization (70 eV) and a quadrupole analyzer.

Photo-DSC was conducted with a Netzsch DSC 204 F1 Phoenix with autosampler.[14] The compounds were irradiated with filtered UV-light (EXFO Omnicure 2001, 280−450 nm) by a wave guide attached to the photo-DSC unit. The light intensity at the surface level of the cured samples was measured with an EIT Uvicure high energy integrating radiometer to be 13 mW/cm^2. The default light intensity at the tip of the light guide was 1000 mW/cm^2. All measurements were carried out in an isocratic mode at room temperature under a nitrogen atmosphere. To permit an oxygen free irradiation of the samples, a nitrogen purge (~50 mL/min) was used for at least 5 min prior to the measurements.

Nanosecond transient absorption spectroscopy was carried out using the third harmonic (355 nm) of a Q-switched Nd:YAG laser (Spectra-Physics LAB-150) with a pulse duration of 8 ns. Transient absorbances were measured in a right-angle setup using a cell holder with incorporated rectangular apertures defining a reaction volume of dimensions 0.17 cm (height), 0.32 cm (width), and 0.13 cm (depth) within the cell. Pulse energies between 0.1 and 4 mJ/pulse were used, the typical value for the measurement of transient spectra being 2 mJ/pulse. Pulse energies were measured using a ballistic calorimeter (Raycon-WEC 730). Solutions were deoxygenated by bubbling them with argon. Further details of experimental procedures have been published previously.[15]

Time-resolved continuous-wave electron paramagnetic resonance (cw TR-EPR) experiments were performed using a frequency-tripled Continuum Surelite II Nd:YAG laser (20 Hz repetition rate; 355 nm; ca. 10 mJ/pulse; ca. 10 ns), a Bruker ESP 300E X-band spectrometer (unmodulated static magnetic field), and a LeCroy 9400 dual 125 MHz digital oscilloscope. In the course of a TR-EPR experiment, the desired magnetic field range is scanned by recording the accumulated (usually 50−100 accumulations) EPR time responses to the incident laser pulses at a given static magnetic field. The system is controlled using a program developed, kindly provided and maintained by Dr. J. T. Toerring (Berlin, Germany). Argon-saturated solutions were pumped through a quartz tube (i.d. 2 mm, flow ca. 2−3 mL/min) in the reactangular cavity of the EPR spectrometer. The solutions were 5−20 mM of PI concentration in acetonitrile.

The hyperfine coupling constants (hfcs) of the free radicals were calculated using the Gaussian03 package.[16] All calculations (geometry optimizations and single point calculations) were conducted at the B3LYP[17,18] level of theory with the basis set TZVP.[19]

Photo-CIDNP experiments were performed on a 200 MHz Bruker AVANCE DPX spectrometer. Irradiation was carried out using a frequency-tripled Spectra-Physics Nd:YAG INDI laser (355 nm, ca. 40 mJ/pulse, ca. 10 ns) and a Hamamatsu (Japan) Hg−Xe lamp (L8252, 150 W, 300 ms). The following pulse sequence was used: presaturation−laser/lamp flash−30° rf detection pulse (2.2 μs)−free induction decay. The concentrations of the initiators were typically 0.01 M in d_3-acetonitrile, deaerated by bubbling argon through the solution.

RESULTS AND DISCUSSION

Laser Flash Photolysis. Nanosecond transient absorption spectroscopy of solutions of the ethyl ester **2** at concentrations between 2 × 10^{-4} and 3 × 10^{-3} M was used to gain information on the early photochemical steps. The irradiation wavelength (355 nm) excites **2** into the n, π^* state of the benzophenone

dx.doi.org/10.1021/ma3000225 | Macromolecules 2012, 45, 1737−1745

moiety; the π, π^* transitions of the benzophenone and the aniline moieties both lie at higher energies (λ < 320 nm). It was therefore expected that the first transient appearing on the nanosecond time scale would be the characteristic benzophenone triplet−triplet absorption around 520 nm.[3] The expected absorption band was indeed observed in the apolar solvent 2,2,4-trimethylpentane, but not in more polar solvents, in which case the first measured transients indicated an entirely different excited-state structure. The corresponding photophysics was analyzed in detail; these data, which have no direct bearing on the mechanism of photopolymerization initiation, will be published elsewhere.

In deaerated MeCN, the excited-state transients decayed within a time interval of 200 ns. On a longer time scale, two absorption bands remained. The microsecond-range lifetimes of these transients suggested that they originated from radical photoproduct species. Figure 2 shows the temporal absorbance

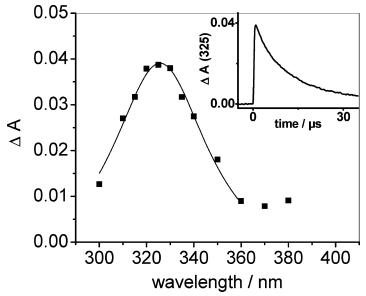

Figure 2. Transient absorption spectrum obtained at 200 ns upon 355 nm laser flash photolysis of the ethyl ester **2** (6×10^{-4} M) in MeCN. Inset: temporal absorbance change at 325 nm at 1.4 mJ/pulse.

change as well as the spectrum of a transient **7**, exhibiting a narrow absorption band with a maximum at 325 nm, resembling the absorption of the *p*-benzoylbenzyl radical obtained by photolysis of *p*-benzoylbenzylphenyl sulfide.[9]

The decay of the transient **7**, as shown in the inset of Figure 2, proceeded by a superposition of first- and second-order components with rates $k_1 = 10^5$ s^{-1} and $2k_2/\varepsilon = 6 \times 10^5$ cm s^{-1}, respectively. While the second-order component is probably caused by radical dimerization, the first-order component may be due either to a reaction of the radical with the substrate or to the influence of residual O_2. In an oxygen-saturated solution, the lifetime of the radical is indeed reduced and the decay purely first-order, corresponding to a rate constant with O_2 of 1.6×10^9 M^{-1} s^{-1}; this is in excellent agreement with published values for the reaction of substituted benzyl radicals with O_2, which is known to generate benzylperoxyl radicals.[20]

A second transient **8** present 200 ns after the laser pulse displayed a spectrum with maximum absorption at 410 nm. The spectrum as well as the decay of **8** is shown in Figure 3. With reference to a combined pulse radiolysis and pulsed laser photolysis study of *N*-phenylglycine,[21] **8** can unambiguously be assigned to the neutral aminyl radical derived from the *N*-phenylglycine ethyl ester moiety of **2**. **8** was found to decay in a clean second-order reaction, the rate constant of which was determined as $2k_2 = 1.2 \times 10^9$ M^{-1} s^{-1} based on the extinction coefficient, ε = 1650 M^{-1} cm^{-1}, given for the *N*-phenylglycine aminyl radical in aqueous solution at pH 10.[21]

In MeCN as solvent, the formation of both **7** and **8** was completed within 200 ns after the laser pulse, but the kinetics of their formation could not be measured because of overlapping

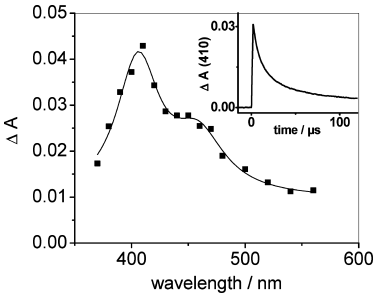

Figure 3. Transient absorption spectrum obtained at 200 ns upon 355 nm laser flash photolysis of the ethyl ester **2** (3×10^{-3} M) in MeCN. Inset: temporal absorbance change at 410 nm at 1.6 mJ/pulse.

excited-state absorptions. Using 2,2,4-trimethylpentane as an apolar solvent, the radical transient spectra were similar to those in MeCN and could again be assigned to **7** and **8**. The excited state spectrum, on the other hand, was different and corresponded to the triplet−triplet band of benzophenone with a maximum at 530 nm, as mentioned above. The decay of the triplet at 530 nm ($\mathbf{2}^T$) and the buildup of the absorption of **8** at 410 nm are shown in Figure 4. The kinetic congruence between

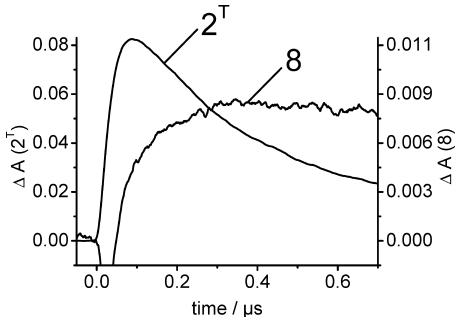

Figure 4. Temporal absorbance change of $\mathbf{2}^T$ at 530 nm and **8** at 410 nm upon 355 nm laser flash photolysis of the ethyl ester **2** (1×10^{-3} M) in 2,2,4-trimethylpentane.

both traces is a strong indication that the local benzophenone triplet is the precursor of the aminyl radical **8**.

An important question was whether the formation of the radicals **7** and **8** was due to a unimolecular bond cleavage process or to a bimolecular interaction between a triplet-excited molecule $\mathbf{2}^T$ with another molecule **2** in its ground state. Remarkably, the transient spectra gave no indication of the formation of benzophenone ketyl radicals, as would be expected for an H-abstraction reaction by the triplet. Any other bimolecular reaction that might lead to bond cleavage in **2**, caused either by ground-state complex formation or by a diffusion-influenced excited-state process, would depend on the concentration of **2**. We therefore measured the yield of the aminyl radicals **8** at [**2**] ranging from 2×10^{-4} to 3×10^{-3} M. The results are shown in Figure 5 in the form of the absorbance of **8** at 410 nm, normalized to the same optical density at the laser wavelength (A = 1 at λ = 355 nm), versus the energy of the laser pulse. The dependence found is linear, with all data points lying on the same straight line. Two conclusions can be drawn from this experiment: (1) there is no influence of the concentration of **2**, and (2) the formation process is purely monophotonic.

The photodegradation of **2** is thus a unimolecular as well as monophotonic process. On the basis of the chemical

dx.doi.org/10.1021/ma3000225 | *Macromolecules* 2012, 45, 1737−1745

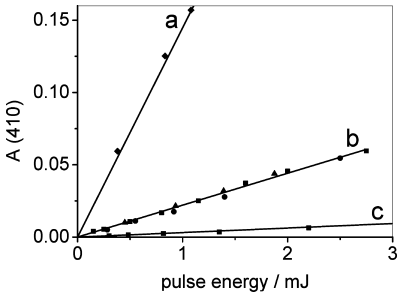

Figure 5. Absorption of **8** at 410 nm obtained 200 ns after 355 nm laser flash photolysis of the ethyl ester **2** (■, 3×10^{-3} M; ◆, 1×10^{-3} M; ●, 6×10^{-4} M; ▲, 2×10^{-4} M) in (a) 2,2,4-trimethylpentane, (b) MeCN, and (c) oxygen-saturated MeCN as a function of laser pulse energy.

assignment of the observed radicals, it must be assumed that photolysis of **2** proceeds by a direct, β-phenylogous cleavage of the C–N bond (Scheme 2).

A further result shown in Figure 5 concerns the influence of O_2 saturation on the yield of **8** in MeCN, which was found to be reduced by a factor of 7 compared to a deoxygenated solution. A similar reduction was observed for the formation of **7**, which further strengthens the conclusion that both **7** and **8** originate from the same photochemical step. The radical yield will moreover merely be reduced by a factor of about 1.4 in an air-equilibrated solution, in good agreement with the polymerization data (Figure 3).

Finally, the yield of radical **8** was found to be strongly dependent on the solvent (Figure 5). The value of the product $\varepsilon_{410} \times \Phi(\mathbf{8})$ was found to be 640 M^{-1} cm^{-1} in MeCN and 3820 M^{-1} cm^{-1} in 2,2,4-trimethylpentane. Because of lack of knowledge concerning the extinction coefficient of the aminyl radical and its possible solvent dependence, a serious estimation of the quantum yield is not possible. Interestingly, assuming a solvent-independent extinction coefficient and a quantum yield of unity in 2,2,4-trimethylpentane, we obtain $\Phi(\mathbf{8})$ = 0.17 in MeCN.

Magnetic Resonance: General. Insight into the early stages of the polymerizations was obtained by continuous-wave TR-EPR and ^{1}H CIDNP. Whereas EPR is able to establish radicals formed within the first 50 ns after irradiation,[22,23] the CIDNP technique provides insight into the products formed via the primary radical pair.[24,25] As a model for the reactivity of phenylglycin-derived photoinitiators, we have, as a paradigm, investigated ethyl ester **2**. Moreover, we present CIDNP investigations of **6**, which should display similar reactivity.

TR-EPR. Laser flash photolysis of the ester **2** inside a microwave cavity of an EPR spectrometer leads to the time-resolved EPR spectrum displayed in Figure 6a. Slices of the spectrum taken at consecutive time frames (boxcar-type) indicate that, within the detection period of the experiment (ca. 5 μs), the EPR signal remains constant in terms of its splitting pattern (see Supporting Information). The almost matching signal intensities at the low- and high-field portion of the spectrum indicate that the triplet mechanism is dominating.[26] The EPR spectrum is composed of (at least) two components (Figure 6b) with the dominating component stemming from radical **7** originating from the MBP moiety. This is borne out by comparison with published data[27] and DFT calculations (Figure 7). Accordingly, the biggest ^{1}H hfc is attributed to the α-protons at the exocyclic methylene group carrying the highest spin population; the smaller ^{1}H hfcs of 0.50 and 0.173 mT are assigned to the *ortho* and the *meta* protons of the adjacent phenyl group, respectively. The phenyl group carries a spin population that is too small to lead to discernible splittings. At closer inspection of the EPR signal, it can be anticipated that the EPR signal is composed of at least two components (see arrows in Figure 6b), which have a somewhat bigger *g*-factor as the spectrum of **7**. Owing to the dominance of the spectrum of **7**, the hyperfine structure of these weaker

Scheme 2. Reaction Products Generated by Photolysis of 2 Determined by LFP, TR-EPR, and ^{1}H CIDNP (See Color Code for Assignments)

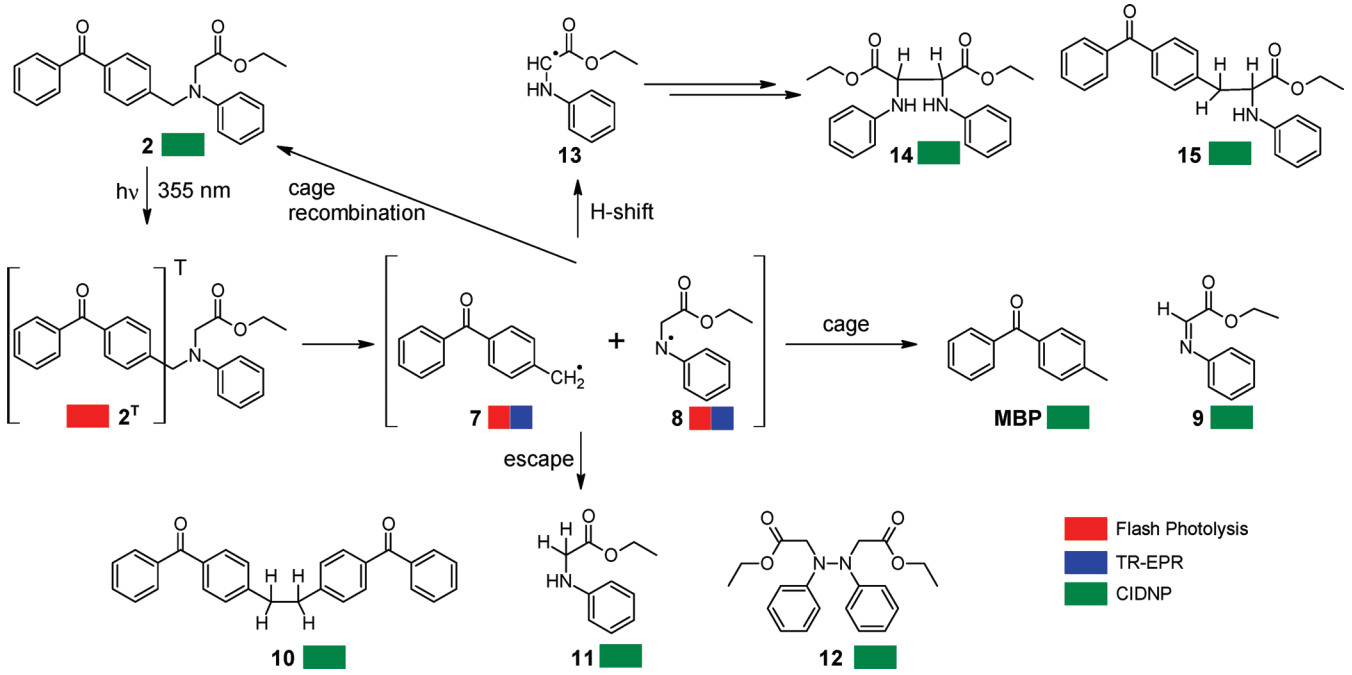

dx.doi.org/10.1021/ma3000225 | *Macromolecules* 2012, 45, 1737–1745

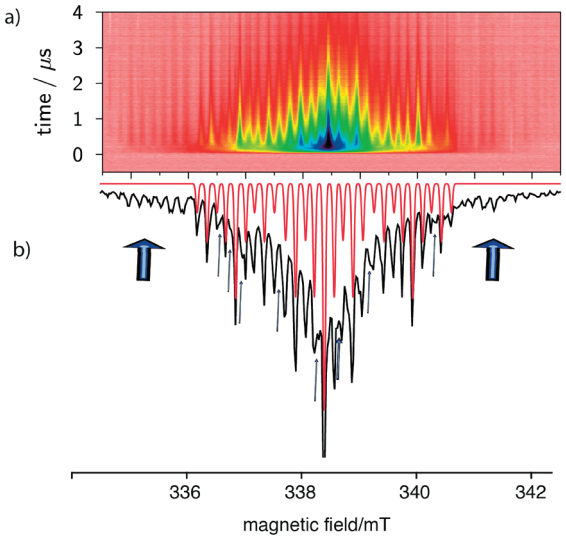

Figure 6. (a) TR-EPR spectrum obtained upon photolysis of **2**. (b) Boxcar-type slice between 1 and 1.5 μs and simulation of the EPR spectrum comprising radical **7** (red).

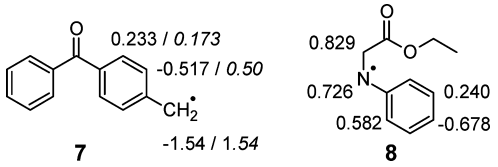

Figure 7. Calculated hyperfine coupling constants (B3LYP/TZVP) of **7** and **8** in mT (the numbers in italics at **7** indicate the experimental data used for the simulation of the EPR spectrum).

spectra cannot be unambiguously determined. Nevertheless, it can be provisionally attributed to the aminyl radical **8** and its follow-up products. The theoretical predictions for **8** are in excellent agreement with published data of comparable radicals, and several line distances in the weaker EPR components can be connected with these hfcs.[28,29]

Accordingly, we were able to establish the primary radicals formed directly upon photolysis of **2** by TR-EPR. The occurrence of more than two spectra suggests that particularly the aminyl radical **8** presumably forms paramagnetic follow-up products on a time scale that is shorter than 0.5 μs.

^{1}H CIDNP. The NMR signals (Figure 8a) of **2** can be assigned in the following way: The aromatic region can be divided into two parts: one from δ = 7.40 to 7.80 ppm comprising the ^{1}H resonances of the benzophenone moiety and the second one attributed to the phenyl hydrogens of the glycine moiety with two multiplets at δ = 6.65 and 7.17 ppm. The two singlets at δ = 4.72 and 4.22 ppm are assigned to the methylene protons adjacent to the nitrogen atom. The quadruplet at δ = 4.17 ppm and the triplet at δ = 1.24 ppm (^3J = 7.1 Hz) stem from the terminal ethyl group (see the color-coded assignment in Figure 8a).

The CIDNP spectrum (Figure 8b) recorded immediately after the laser pulse shows a new signal in absorption at δ = 2.44 ppm. This singlet can be assigned to the methyl group of MBP (reference NMR spectrum, see Supporting Information). Another prominent signal in this region is an emissive singlet at δ = 3.08 ppm. It can be assigned to the methylene protons of **10**, an "escape" product of two radicals **7** (see Scheme 2). The different polarization compared to the MBP peak adds to this assignment because these products have to be formed via "escape" and "cage" processes, respectively, causing differing polarizations according to Kaptein's rules.[30] The polarized singlets at δ = 4.72 and 4.22 ppm stem from the recombination of the initial radical pair (**7** and **8**) leading to parent **2** in the singlet state. In the aromatic region, various polarization patterns occur. They can be connected to **2**, but significantly,

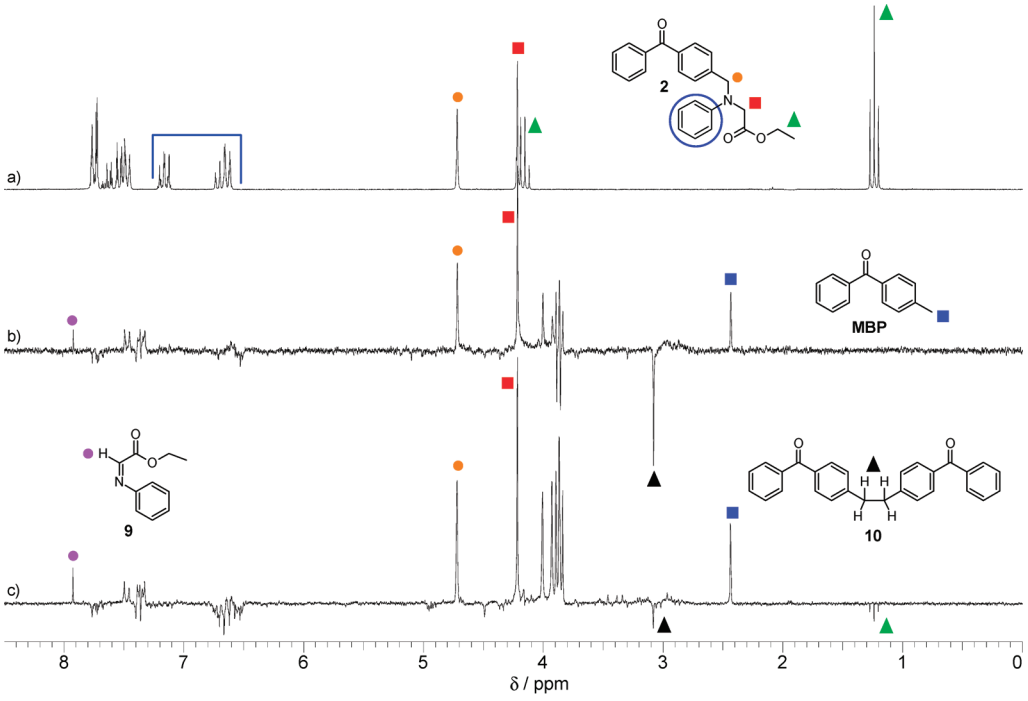

Figure 8. (a) ^{1}H NMR spectrum of **2**. (b) ^{1}H CIDNP spectrum obtained immediately after the laser pulse. (c) ^{1}H CIDNP spectrum obtained after irradiation using a Hg–Xe high-pressure lamp (300 ms).

dx.doi.org/10.1021/ma3000225 | *Macromolecules* 2012, 45, 1737–1745

the absorptive peaks around δ = 7.35 ppm can be straightforwardly assigned to the meta-protons next to the aliphatic bridge of dimer **10**.

The remaining resonances are attributable to the aromatic protons of the diverse disproportionation products shown in Scheme 2. The signal with the highest shift lies at δ = 7.92 ppm in absorption. It can be assigned to the imine hydrogen of disproportionation product **9**.

The remaining signals are a singlet at δ = 4.01 ppm and a multiplet around δ = 3.85 ppm. The multiplet is probably composed of at least two overlapping signals. Their multiplicities are not distinct, and they can therefore not be explicitly assigned to reaction products. An indication of their origin can be deduced from time-resolved CIDNP. In Figure 9, it can be seen that the two emission peaks increase in intensity when the time delay between laser and rf pulse is increased to 10 and 100 μs, respectively. This suggests that the products are formed via a relatively long-lived radical species, presumably aminyl radical **8.** Thus, the peaks can be provisionally assigned to products formed via **8** (see Scheme 2). Another possible reaction pathway is a hydrogen shift, which generates radical **13** by transferring the radical center from N to the neighboring C atom. This would finally lead to products **14** and **15**, and the corresponding methylene protons should be detected in the δ = 4 ppm region.

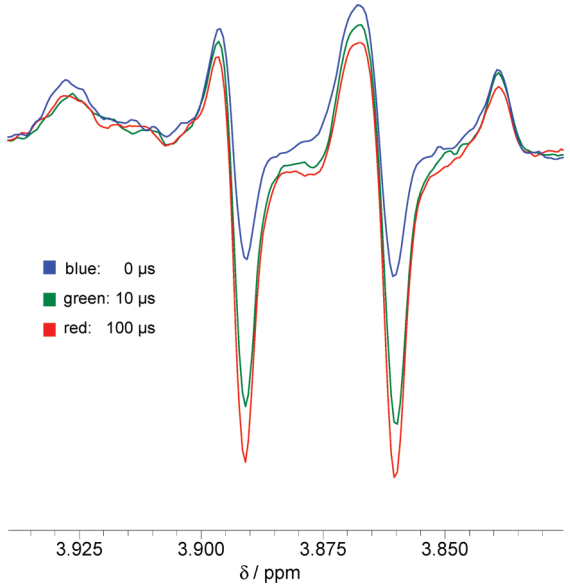

Figure 9. Zoom into the CIDNP spectrum of **2** recorded using the Nd:YAG laser with different time delays between laser and rf pulse (0–100 μs).

The use of a Hg–Xe high-pressure UV lamp provides the possibility of observing additional follow-up products owing to the substantially longer irradiation time (millisecond range). The corresponding ^{1}H CIDNP spectrum (Figure 8c), however, is essentially similar to the one obtained by laser irradiation. One difference is that the peak group around δ = 3.85 ppm shows no emissive components. This is very likely the consequence of the longer evolution time for the products in the case of the lamp experiment causing a different polarization pattern.

To investigate if the same principle of β-phenylogous cleavage is also observed at the same time regime as for **2**, when the amino group is replaced by S–Ph, we have additionally investigated compound **6**. In the aromatic region, the NMR spectrum (Figure 10a) of **6** shows resonances between δ = 7.15 and 7.80 ppm with the high-field signal attributable to the S–Ph protons and the methylene proton singlet at δ = 4.25 ppm. After laser irradiation the CIDNP spectrum (acquisition without delay) shows two distinctive polarized signals (Figure 10b). The first is visible in absorption at δ = 4.25 ppm, indicating the regeneration of the parent compound via the radical pair (geminate recombination). The second peak appears in emission at δ = 3.08 ppm and is attributed to **10** formed by the "escape" recombination of two radicals **7**. Although the peaks in the aromatic region show polarizations in absorption and emission, their individual assignment is hindered by massive overlap. An expected product, only containing aromatic protons is the S–S product **17**, which should form concurrent to dimer **10**. Further CIDNP spectra were recorded using the Hg–Xe UV lamp (Figure 10c). For **6**, in contrast with **2**, products are found, which do not originate from the primarily formed species. Whereas the signals at δ = 4.25 and 3.08 ppm (the latter showing different polarization because of signal evolution over time) and those in the aromatic region remain (although with a more pronounced polarization pattern), a new emission peak of MBP can be found at δ = 2.43 ppm. Here, MBP cannot be formed directly from the primary radical pair because no source for easily abstractable hydrogens is present. Consequently, a second molecule of **6** or **10** can serve as a hydrogen donor; therefore, this process does not occur at the short time scale of the laser experiment, but the longer irradiation period of the lamp allows for such secondary reactions. The reaction mechanism derived for **6** is shown in Scheme 3.

Photoreactivity and Influence of Oxygen Inhibition. The PI concentration of a given formulation generally varies between 1 and 7 wt % for industrial applications and has a high impact on reactivity and curing depth. To analyze the influence of concentration of the covalently bound PIs on their reactivity, photo-DSC experiments with PIs **1** and **2** and the reference PI systems MBP/**3** and MBP/**4** were performed. The PI concentration varied from 1 to 50 mM (0.03–1.7 wt % of **1**) in 2-ethoxyethoxyethyl acrylate (EEEA) as monomer. Monofunctional EEEA was selected because of its low viscosity, and it is significantly more susceptible to oxygen inhibition compared to highly viscous, multifunctional monomers.

The double-bond conversion (DBC), the time until maximum polymerization rate (t_{max}) is achieved and the rate of polymerization (R_P) itself are the parameters to characterize the reactivity of a PI.[14] As presented in Figure 11, the DBC was quite high and above 75% for all PI systems. Especially with acid **1**, a high level (85%) of conversion was reached already with a concentration of about 3 mM (0.1 wt %), which might result from the decarboxylation step. The value for t_{max} remained also steady until a concentration of 6 mM and increased at lower concentrations. The highest impact of concentration could be seen for the R_p. The acid **1** and ethyl ester **2** exhibited both very high rates of polymerization at higher concentrations compared to the physical mixtures of MBP and **3** and **4**, respectively. The sudden decrease of R_p at lower concentrations might be rationalized by the fact that in formulations containing the covalently bound PIs **1** and **2** electron and proton transfers occur not only on an intramolecular but also on an intermolecular level, whereas the

dx.doi.org/10.1021/ma3000225 | *Macromolecules* 2012, 45, 1737–1745

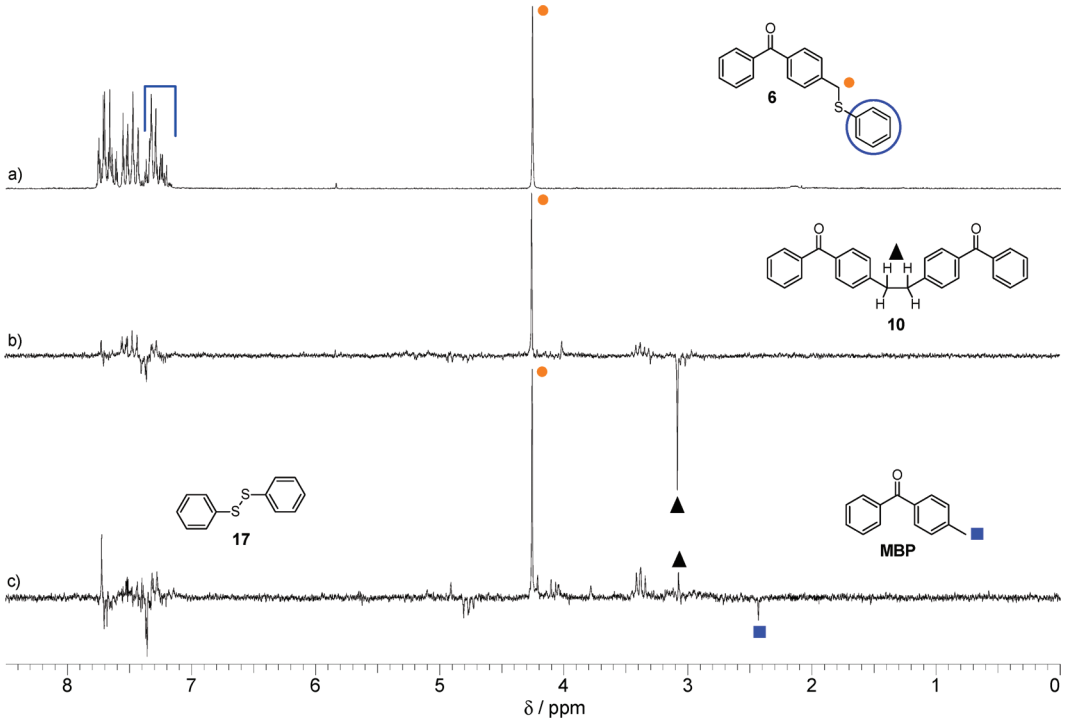

Figure 10. (a) ^{1}H NMR spectrum of **6**. (b) ^{1}H CIDNP spectrum obtained immediately after the laser pulse. (c) ^{1}H CIDNP spectrum obtained after irradiation using a Hg–Xe high-pressure lamp (300 ms).

Scheme 3. Reaction Products Generated by Photolysis of 6, Determined by ^{1}H CIDNP

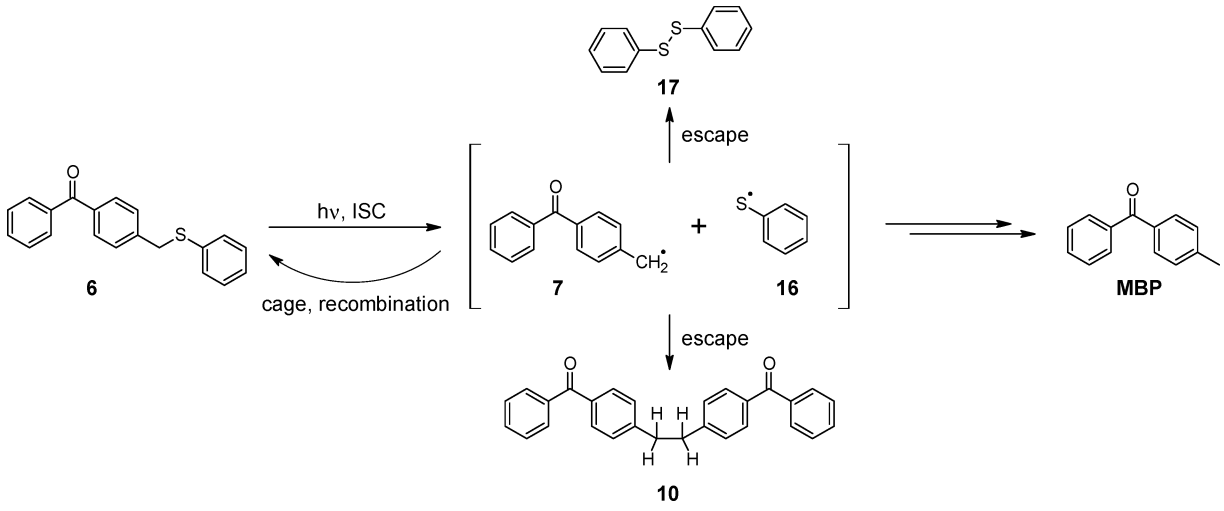

intermolecular processes are reduced by far at lower concentrations.

Comparison of PI Reactivity under Nitrogen Atmosphere and Air. For economic reasons, the use of nitrogen atmosphere for industrial applications of photocuring should be avoided, being an additional cost factor. Therefore, PI systems should be developed, which are unperturbed by oxygen inhibition. Using NPG as co-initiator, the decarboxylation step delivers enough CO_2 to entirely displace the dissolved oxygen and hinders the permeation of additional oxygen into the coating.[31] To investigate the behavior of the BP-NPG PI **1** during photopolymerization under different conditions, comparative experiments under N_2 atmosphere (50 mL min^{-1}) and under air were carried out. The formulation consisted of a mixture of three different acrylates (56% Genomer 4312, 21% Miramer M220, and 21% Miramer M320) and the PI (2 wt %). We investigated benzophenone methylamine **5**, which cannot undergo a decarboxylation reaction, and the physical mixtures of MBP and NPG and *N,N*-dimethylaminoethyl benzoate (DMAB) as reference PI systems. Generally, the effect of oxygen inhibition in MBP/amine systems is less pronounced than in monomolecular type I PIs like 2-hydroxy-2-methyl-1-phenyl-propan-1-one (Darocur 1173), as recent studies have shown.[32] This can be easily explained by the role of the amine, which acts as effective hydrogen donor for the peroxy radicals. Therewith a highly reactive radical in the α-position of the amine is generated, which is able to restart the polymerization process. Additionally, it is well-known that excited state BPs are able to decompose peroxides, giving new oxygen-centered

dx.doi.org/10.1021/ma3000225 | *Macromolecules* 2012, 45, 1737–1745

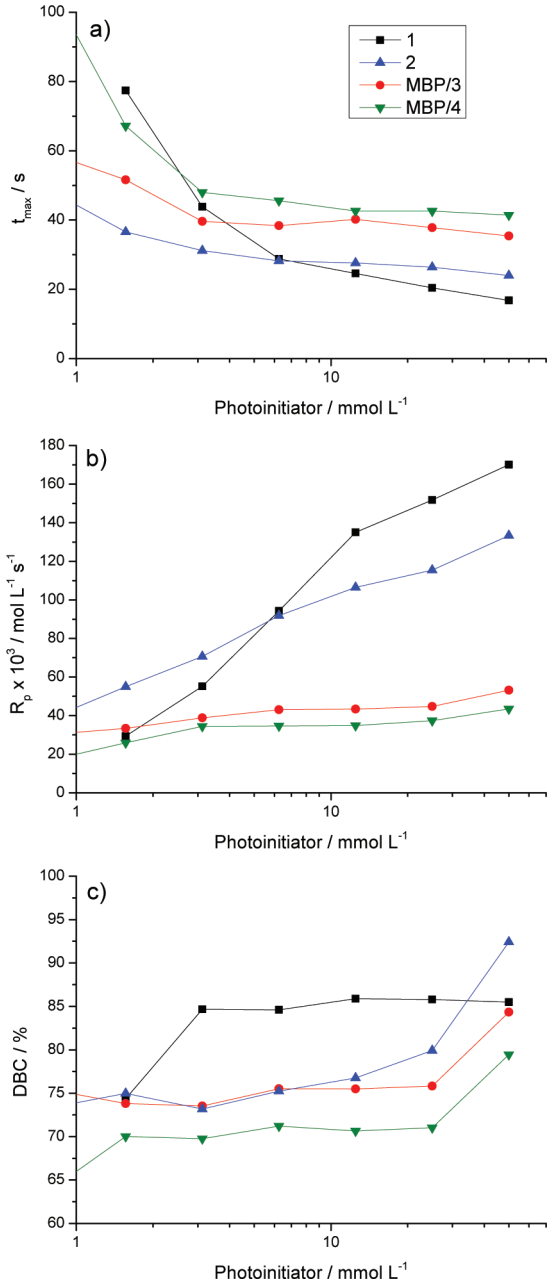

Figure 11. Dependence of PI reactivity on PI concentration (in EEEA) expressed by (a) t_{max}, (b) R_p, and (c) DBC.

radicals which are also able to initiate the polymerization process.[33,34]

Figure 12 displays, that covalently bound BP-NPG **1** exhibited the highest photoreactivity (short t_{max}), which was only slightly decreased (longer t_{max}) by curing under air. More interesting were the results for the DBC and R_p. For the PI systems containing the NPG moiety, **1**, and MBP/NPG, DBC and R_p did not change significantly when switching from nitrogen to air atmosphere due to formation of the CO_2 layer. Thus, the covalently bound PI **1** showed a better reactivity under air than the industrially used PI system MBP/DMAB and the structure analogous benzophenone methylamine **5**, which possesses no acid group for decarboxylation.

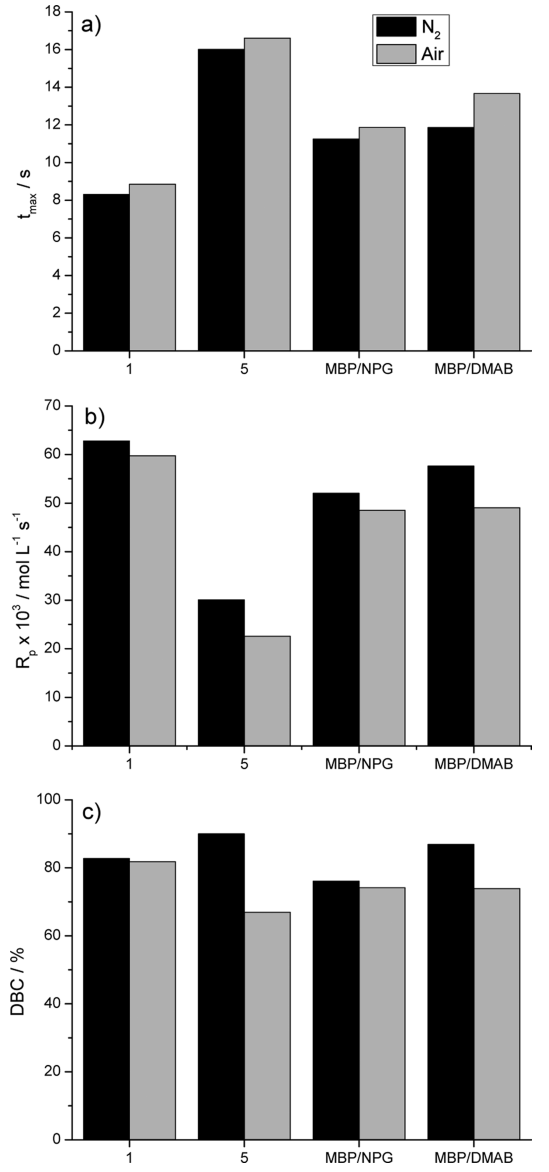

Figure 12. Data for photo-DSC experiments of PI **1** in comparison to **5**, MBP/NPG, and MBP/DMAB: (a) t_{max}, (b) R_p, and (c) DBC.

SUMMARY

The aim of our studies was to investigate the photochemical and photophysical behavior of a covalently bound BP *N*-phenylglycine PI system. Particularly the principle that the BET process is avoided by spontaneous decarboxylation from *N*-phenylglycine after electron transfer to the excited ketone leads to a high efficiency. The reactivity of the new PI was tested by photo-DSC experiments, determining values for t_{max}, DBC, and R_p at different PI concentrations. The values for the rate of polymerization exceeded the R_p of the physical mixtures of MBP/NPG and MBP/NPG ethyl ester by far, showing the high impact of the covalently bound co-initiator group on the efficiency. Thus, the properties of the primary radicals formed from the photoinitiator are decisive for the polymerization. In this context, it will be challenging to determine in which manner these primary radicals can be established in the growing polymer chain.[35,36] Comparing our new covalently bound PI **1** to PI systems used in industry, our compound exhibited improved performance in the presence of oxygen outperform-

dx.doi.org/10.1021/ma3000225 | *Macromolecules* 2012, 45, 1737−1745

ing typically used bimolecular PIs. During the curing process a protecting CO_2 layer on the polymer surface was formed from the decarboxylation step, thus preventing the oxygen inhibition.

Scheme 2 indicates the decisive intermediates, which were established by optical spectroscopy (LFP), TR-EPR, and photo-CIDNP. These methods provided the quantum yield and the time regime of the initial processes. In addition to the structure of the primary radicals, their follow-up products could be characterized. Thus, the mechanism of the β-phenylogous cleavage was established.

Our investigations also underpin the substantial efficiency of the MBP-moiety for β-cleavage reactions.[37]

■ ASSOCIATED CONTENT

Supporting Information

TR-EPR spectra of **2** (time slices); NMR spectrum of MBP. This material is available free of charge via the Internet at http://pubs.acs.org.

■ AUTHOR INFORMATION

Corresponding Author

*E-mail: rliska@ioc.tuwien.ac.at (R.L.); g.gescheidt-demner@TUGraz.at (G.G.).

Notes

The authors declare no competing financial interest.

■ ACKNOWLEDGMENTS

Financial support by the Austrian Science Fund (FWF) for this project, P19769-N14, and an Omnicure 2000 unit from EXFO are gratefully acknowledged.

■ REFERENCES

(1) Yagci, Y.; Jockusch, S.; Turro, N. J. *Macromolecules* **2010**, *43*, 6245−6260.

(2) Brimage, D. R. G.; Davidson, R. S. *J. Chem. Soc., Perkin Trans. 1* **1973**, *5*, 496−499.

(3) Bensasson, R. V.; Gramain, J.-C. *J. Chem. Soc., Faraday Trans.1* **1980**, *76*, 1801−1810.

(4) Jauk, S.; Liska, R. *Macromol. Rapid Commun.* **2005**, *26*, 1687−1692.

(5) Ullrich, G.; Burtscher, P.; Salz, U.; Moszner, N.; Liska, R. *J. Polym. Sci., Part A: Polym. Chem.* **2006**, *44*, 115−125.

(6) Allen, N. S.; Lam, E.; Howells, E. M. *Eur. Polym. J.* **1990**, *26*, 1345−1353.

(7) Allen, N. S.; Lam, E.; Kotecha, J. L.; Green, W. A.; Timms, A.; Navaratnam, S.; Parsons, B. J. *J. Photochem. Photobiol., A* **1990**, *54*, 367−388.

(8) Mateo, J. L.; Bosch, P.; Catalina, F.; Sastre, R. *J. Polym. Sci., Part A: Polym. Chem.* **1992**, *30*, 829−834.

(9) Yamaji, M.; Inomata, S.; Nakajima, S.; Akijama, K.; Tobita, S.; Marciniak, B. *J. Phys. Chem. A* **2005**, *109*, 3843−3848.

(10) Murahashi, S. I.; Komiya, N.; Terai, H.; Nakae, T. *J. Am. Chem. Soc.* **2003**, *125*, 15312−15313.

(11) Tanaka, N.; Tamai, T.; Mukaiyama, H.; Hirabayashi, A.; Muranaka, H.; Akahane, S.; Miyata, H.; Akahane, M. *J. Med. Chem.* **2001**, *44*, 1436−1445.

(12) Gaertzen, O.; Buchwald, S. L. *J. Org. Chem.* **2002**, *67*, 465−475.

(13) Heine, H. G.; Rosenkranz, H. J.; Rudolph, H.; (Bayer, A.-G.). DE 2155000, 1973; 12 pp.

(14) Dworak, C.; Kopeinig, S.; Hoffmann, H.; Liska, R. *J. Polym. Sci., Part A: Polym. Chem.* **2009**, *47*, 392−403.

(15) Baranyai, P.; Gangl, S.; Grabner, G.; Knapp, M.; Köhler, G.; Vidóczy, T. *Langmuir* **1999**, *15*, 7577−7584.

(16) Frisch, M. J.; Trucks, G. W.; Schlegel, H. B.; Scuseria, G. E.; Robb, M. A.; Cheeseman, J. R.; Montgomery, J. A.; Jr.; Vreven, T.; Kudin, K. N.; Burant, J. C.; Millam, J. M.; Iyengar, S. S.; Tomasi, J.; Barone, V.; Mennucci, B.; Cossi, M.; Scalmani, G.; Rega, N.; Petersson, G. A.; Nakatsuji, H.; Hada, M.; Ehara, M.; Toyota, K.; Fukuda, R.; Hasegawa, J.; Ishida, M.; Nakajima, T.; Honda, Y.; Kitao, O.; Nakai, H.; Klene, M.; Li, X.; Knox, J. E.; Hratchian, H. P.; Cross, J. B.; Bakken, V.; Adamo, C.; Jaramillo, J.; Gomperts, R.; Stratmann, R. E.; Yazyev, O.; Austin, A. J.; Cammi, R.; Pomelli, C.; Ochterski, J. W.; Ayala, P. Y.; Morokuma, K.; Voth, G. A.; Salvador, P.; Dannenberg, J. J.; Zakrzewski, V. G.; Dapprich, S.; Daniels, A. D.; Strain, M. C.; Farkas, O.; Malick, D. K.; Rabuck, A. D.; Raghavachari, K.; Foresman, J. B.; Ortiz, J. V.; Cui, Q.; Baboul, A. G.; Clifford, S.; Cioslowski, J.; Stefanov, B. B.; Liu, G.; Liashenko, A.; Piskorz, P.; Komaromi, I.; Martin, R. L.; Fox, D. J.; Keith, T.; Al-Laham, M. A.; Peng, C. Y.; Nanayakkara, A.; Challacombe, M.; Gill, P. M. W.; Johnson, B.; Chen, W.; Wong, M. W.; Gonzalez, C.; Pople, J. A. *Gaussian 03, Revision E.01*; Gaussian, Inc.: Wallingford, CT, 2004.

(17) Becke, A. D. *J. Chem. Phys.* **1993**, *98*, 5648−5652.

(18) Stephens, P. J.; Devlin, F. J.; Chabalowski, C. F.; Frisch, M. J. *J. Phys. Chem.* **1994**, *98*, 11623−11627.

(19) Schaefer, A.; Huber, C.; Ahlrichs, R. *J. Chem. Phys.* **1994**, *100*, 5829−5835.

(20) Tokamura, K.; Ozaki, T.; Nosaka, H.; Saigusa, Y.; Itoh, M. *J. Am. Chem. Soc.* **1991**, *113*, 4974−4980.

(21) Canle, M.; Santabella, J. A.; Steenken, S. *Chem.—Eur. J.* **1999**, *5*, 1192−1201.

(22) Gatlik, I.; Rzadek, P.; Gescheidt, G.; Rist, G.; Hellrung, B.; Wirz, J.; Dietliker, K.; Hug, G.; Kunz, M.; Wolf, J.-P. *J. Am. Chem. Soc.* **1999**, *121*, 8332−8336.

(23) Hristova, D.; Gatlik, I.; Rist, G.; Dietliker, K.; Wolf, J.-P.; Birbaum, J.-L.; Savitsky, A.; Moebius, K.; Gescheidt, G. *Macromolecules* **2005**, *38*, 7714−7720.

(24) Griesser, M.; Neshchadin, D.; Dietliker, K.; Moszner, N.; Liska, R.; Gescheidt, G. *Angew. Chem., Int. Ed.* **2009**, *48*, 9359−9361.

(25) Gescheidt, G.; Neshchadin, D.; Rist, G.; Borer, A.; Dietliker, K.; Misteli, K. *Phys. Chem. Chem. Phys.* **2003**, *5*, 1071−1077.

(26) Adrian, F. J. *Res. Chem. Intermed.* **1991**, *16*, 99−125.

(27) Yamaji, M.; Inomata, S.; Nakajima, S.; Akiyama, K.; Tobita, S.; Marciniak, B. *J. Phys. Chem. A* **2005**, *109*, 3843−3848.

(28) Beckert, D.; Fessenden, R. W. *J. Phys. Chem.* **1996**, *100*, 1622−1629.

(29) Roberts, B. P.; Vazquez-Persaud, A. R. *J. Chem. Soc., Perkin Trans. 2* **1995**, 1087−1095.

(30) Kaptein, R. *Chem. Commun.* **1971**, 732−733.

(31) Koshima, H.; Ding, K.; Miura, T.; Matsuura, T. *J. Photochem. Photobiol., A* **1997**, *104*, 105−112.

(32) Dworak, C.; Liska, R. *J. Polym. Sci., Part A: Polym. Chem.* **2010**, *48*, 5865−5871.

(33) Walling, C.; Gibian, M. J. *J. Am. Chem. Soc.* **1965**, *87*, 3413−3416.

(34) Ingold, K. U.; Johnston, L. J.; Lusztyk, J.; Scaiano, J. C. *Chem. Phys. Lett.* **1984**, *110*, 433−436.

(35) Guenzler, F.; Wong, E. H. H.; Koo, S. P. S.; Junkers, T.; Barner-Kowollik, C. *Macromolecules* **2009**, *42*, 1488−1493.

(36) Voll, D.; Junkers, T.; Barner-Kowollik, C. *Macromolecules* **2011**, *44*, 2542−2551.

(37) Zhang, W.; Feng, K.; Wu, X.; Martin, D.; Neckers, D. C. *J. Org. Chem.* **1999**, *64*, 458−463.

Macromolecules

Article

pubs.acs.org/Macromolecules

Tunable Organophotocatalysts for Polymerization Reactions Under Visible Lights.

Mohamad-Ali Tehfe,[†] Jacques Lalevée,*[,†] Fabrice Morlet-Savary,[†] Bernadette Graff,[†] Nicolas Blanchard,[‡] and Jean-Pierre Fouassier[§]

[†]Institut de Science des Matériaux de Mulhouse IS2M, LRC CNRS 7228, ENSCMu-UHA, 15 rue Jean Starcky, 68057 Mulhouse Cedex, France

[‡]Ecole Nationale Supérieure de Chimie de Mulhouse, Laboratoire de Chimie Organique et Bioorganique EA 4566, Université de Haute Alsace, 3 rue Alfred Werner, 68093 Mulhouse Cedex, France

[§]UHA-ENSCMu, 3 rue Alfred Werner, 68093 Mulhouse Cedex, France

Supporting Information

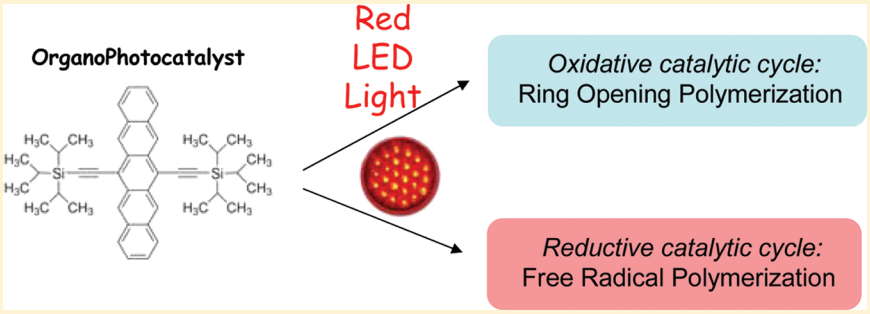

ABSTRACT: New organic photocatalysts derived from pyrene, anthracene, naphthacene, and pentacene are presented here for the formation of free radicals through a photoredox catalysis. These OPCs can work according to *an oxidative cycle* in a three component system in combination with diphenyl iodonium salt and a silane or in *a reductive cycle* in combination with amine and alkyl halide. This OPC behavior is highlighted through an investigation of the associated excited state and redox properties. The free radicals generated are characterized by ESR or photolysis experiments. Upon household LED bulb or Xe lamp exposure, the oxidative three-component system is able to promote the ring-opening polymerization ROP of an epoxide whereas the reductive three-component system is very efficient to initiate the free radical photopolymerization FRP of an acrylate. This ability of OPCs to initiate different polymerization reactions (ROP and FRP) is clearly an outstanding property.

INTRODUCTION

Recently, photoredox catalysis using ruthenium or iridium complexes has emerged in organic synthesis as a unique approach for the formation of free radicals or ions under very soft irradiation conditions: sunlight, fluorescent bulb, or LED bulb.[1] However, these metal complexes are very expensive and must be often prepared. The development of organic photocatalysts **OPC** for the photoredox catalysis is very important: the advantages could be a lower cost, commercial availability, lower toxicity, better stability and solubility, easier extractability. Very recently, **OPC** based on different dyes (e.g., eosin-Y) were proposed but the reversibility of the redox process that governs the **OPC** regeneration remains an open question.[2]

Metal based photocatalysts PC were recently proposed in different photoinitiating systems for polymerization reactions under very soft irradiation conditions.[3,4] In this area, the PCs play the role of a photoinitiator (PI) that would be recovered during the initiation step. In an oxidative cycle, the three component system (PC/iodonium salt (Ph_2I^+)/silane where PC = e.g. Ru, Ir, anthracene derivatives - Scheme 1) generates silyliums that can initiate the ring-opening polymerization ROP of an epoxy.[3] In a reductive cycle associated with a different three component system (PC/amine/alkyl halide where PC = e.g. Ru or Ir derivatives—Scheme 1), free radicals can also be

Scheme 1

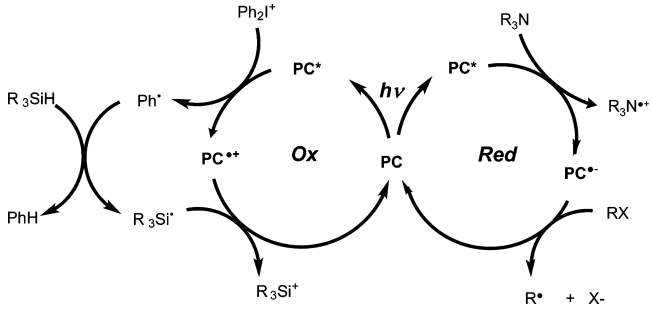

Received: January 7, 2012
Revised: February 3, 2012
Published: February 9, 2012

Scheme 2

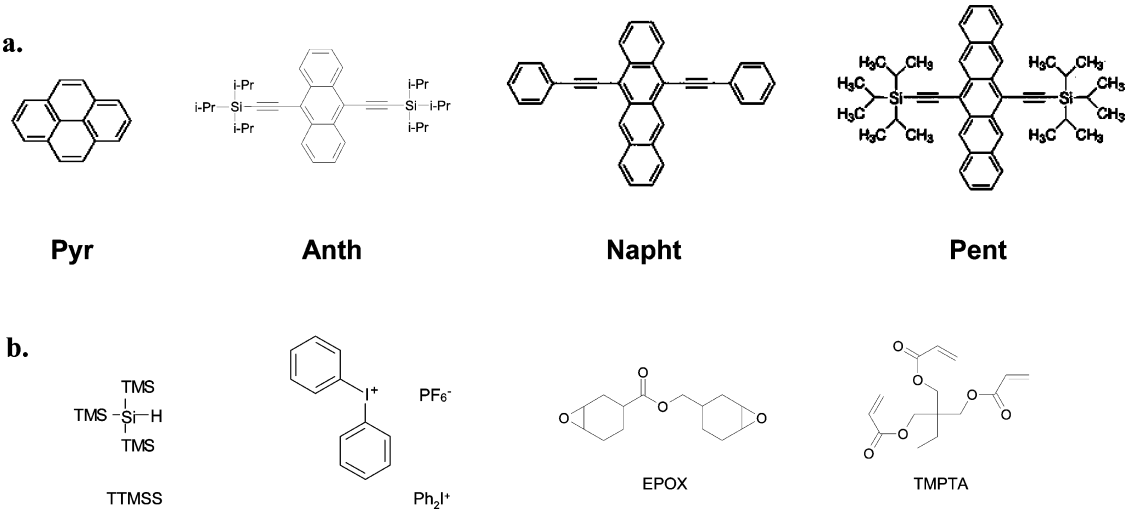

generated to initiate the free radical polymerization FRP of acrylates.[3a,4,5]

The development of **OPC**s for polymerization under very soft irradiation conditions (sunlight, LED, or fluorescence bulbs...) remains a huge challenge. In the present paper, new **OPC**s working according to the oxidative and reductive cycles shown in Scheme 1 will be proposed. These **OPC**s are based on polycyclic aromatic hydrocarbons (PAHs): pyrene, anthracene, naphthacene, and pentacene derivatives (Scheme 2a). Interestingly, they exhibit different light absorption properties that can be tuned from the UV to the red wavelength range through an appropriate selection of the PAHs. **OPC**s usable upon different excitation wavelengths (blue, green, yellow, and red) have never been reported before for ROP and FRP[6a−c] (see a first review on PCs in ref 6d). The use of **Anth** as PC in a oxidation cycle has been already presented in ref 5; this compound will be used here as reference.

The proposed **OPC**s will be used in conjunction with a silane (tris(trimethylsilyl)silane, TTMSS, $(TMS)_3SiH$) and an iodonium salt (Ph_2I^+) in an oxidative cycle for the photopolymerization of an epoxide ((3,4-epoxycyclohexane)methyl 3,4-epoxycyclohexylcarboxylate, EPOX) or in conjunction with an amine (ethyldimethylaminobenzoate) and an alkyl halide (phenacyl bromide) in the reductive cycle for the photopolymerization of an acrylate (trimethylol propane triacrylate, TMPTA) (Scheme 2b). Photopolymerization profiles will be recorded; the excited state processes, the redox properties as well as the free radicals generation will be discussed in detail.

EXPERIMENTAL PART

1. Compounds. The compounds investigated here are presented in Scheme 2 and used with the best purity available (>98%). Pyrene (**Pyr**), 9,10-bis[(triisopropylsilyl)ethynyl]anthracene (**Anth**), 5,12-Bis(phenylethynyl)naphthacene (**Napht**), 6,13-Bis(triisopropylsilylethynyl)-pentacene (**Pent**), tris(trimethylsilyl)silane ($(TMS)_3SiH$), diphenyliodonium hexafluorophosphate (Ph_2I^+), ethyldimethylaminobenzoate (EDB) and phenacyl bromide were obtained from Aldrich.

2. Irradiation Sources. Several lights were used: (i) LED bulbs (I_0 = 15 mW cm^{-2} at a distance of 4 cm) centered at 462; 514; 591 or 630 nm for blue, green, yellow and red light, respectively - the emission spectra for these LED bulbs are given below in Figure 1; (ii) polychromatic light from a Xe−Hg lamp (I_0 = 56 mW cm^{-2}).

3. Free Radical Photopolymerization (FRP) Experiments. Trimethylol propane triacrylate (TMPTA from Cytec) was used as a low viscosity monomer. The film polymerization experiments were carried out in laminate. The three-component photoinitiating systems are based on **OPC**/EDB/phenacyl bromide (0.5%/4.5%/3% w/w). The films (20 μm thick; the thickness of the sample was determined from the IR spectrum of the formulation[7]) deposited on a BaF_2 pellet were irradiated (see the irradiation sources above). The evolution of the double bond content was continuously followed by real time FTIR spectroscopy (JASCO FTIR 4100) at about 1630 cm^{-1}.[7]

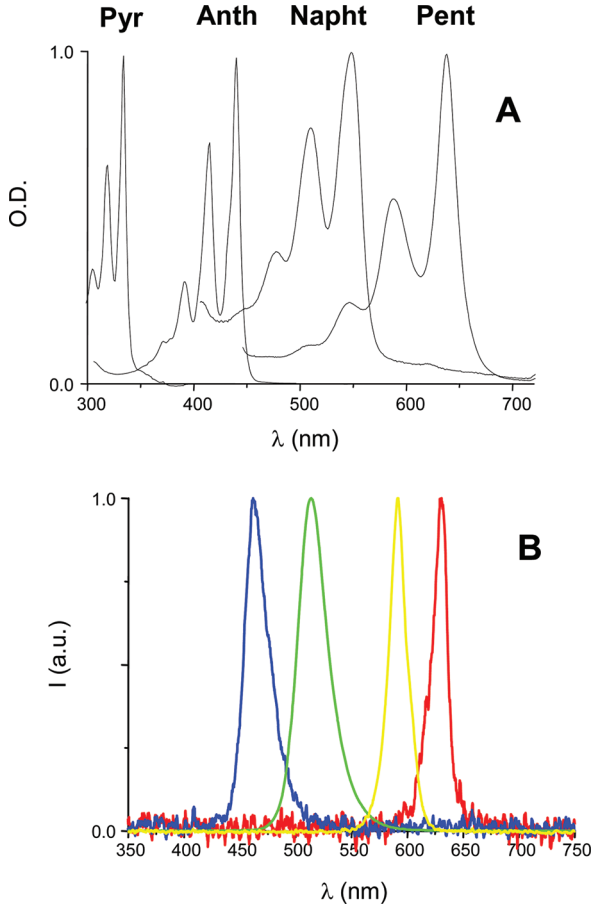

Figure 1. (A) UV−visible absorption spectra for the investigated **OPC**s. (B) Emission spectra of the used LED bulbs.

4. Free Radical Promoted Cationic Polymerization (FRPCP). The two- and three-component photoinitiating systems are based on

dx.doi.org/10.1021/ma300050n | Macromolecules 2012, 45, 1746−1752

Table 1. Parameters Characterizing the Photochemical Properties of the Photocatalysts[a]

	λ_{max} (nm)/ε (M^{-1} cm^{-1})	E_{ox} (V/SCE)	E_{red} (V/SCE)	E_{S1} (eV)	τ (ns)[b]	$k_{ox}(Ph_2I^+)$ in M^{-1} s^{-1} [ΔG_{ox} (eV)]	k_{red}(EDB) in M^{-1} s^{-1} [ΔG_{red} (eV)]
Pyr	334/54000	1.33	−2.2	3.44	14.7	1.7×10^{10} [−1.91]	7.3×10^{8} [−0.24]
Anth	440/40600	0.97	−1.47	2.78	5.5	4×10^{9} [−1.61]	6.6×10^{9} [−0.31]
Napht	548/23600	0.87	−1.1	2.23	7.97	2.8×10^{10} [−1.16]	8.1×10^{9} [−0.13]
Pent	638/23800	0.83	−0.93	1.90	6.78	4.1×10^{9} [−0.87]	1.6×10^{8} [+0.03]

[a]Light absorption and redox properties (in acetonitrile), singlet state energy level (E_{S1}) and lifetime (τ), and rate constants of interaction with Ph_2I^+ and EDB in acetonitrile are given. The free energy changes for the oxidation ^{1}**OPC**/Ph_2I^+ (ΔG_{ox}) or reduction of ^{1}**OPC**/EDB (ΔG_{red}) were calculated by eq 1 using E_{ox}(EDB) = 1 V and E_{red} (Ph_2I^+)= −0.2 V.[12] [b]Under air. [c]For methyldiethanolamine.

PC/Ph_2I^+ (0.5%/2% w/w) and **PC**/$(TMS)_3SiH$/Ph_2I^+ (0.5%/3%/2% w/w), respectively. The residual weight content is related to the monomer. The experimental conditions are given in the figure captions. The monomer (3,4-epoxycyclohexane)methyl 3,4-epoxycyclohexylcarboxylate (EPOX or UVACURE 1500) was obtained from Cytec.

The photosensitive formulations were deposited on a BaF_2 pellet (25 μm thick). The evolution of the epoxy group content is continuously followed by real time FTIR spectroscopy (JASCO FTIR 4100).[8] The absorbance of the epoxy group was monitored at about 790 cm^{-1}. The Si−H conversion for $(TMS)_3SiH$ is followed at about 2050 cm^{-1}.

5. ESR Spin Trapping (ESR-ST) Experiments. ESR-ST experiments were carried out using a X-Band spectrometer (MS 400 Magnettech). The radicals were produced at RT under LED bulb exposure (except otherwise noted) and trapped by phenyl-*N*-*tert*-butylnitrone (PBN).[9]

6. Fluorescence Experiments. The fluorescence properties of the different photocatalysts were determined using a JASCO FP-750 spectrometer. The fluorescence lifetimes of the different **OPC**s were determined from time-resolved experiments (Jobin-Yvon Fluoromax 4). The interaction rate constants kq were extracted from a classical Stern−Volmer treatment:[6b] $1/\tau = 1/\tau_0 + kq[Q]$ where τ and τ_0 stand for the lifetime of the photocatalyst in the presence and absence of quencher Q, respectively.

7. Redox Potentials. The redox potentials were measured in acetonitrile by cyclic voltammetry with tetrabutylammonium hexafluorophosphate 0.1 M as a supporting electrolyte (Voltalab 06-Radiometer; the working electrode was a platinium disk and the reference a saturated calomel electrode-SCE). Ferrocene was used as a standard and the potentials determined from the half peak potential were referred to the reversible formal potential of this compound. The free energy change ΔG_{et} for an electron transfer reaction is calculated from the classical Rehm−Weller equation (eq 1)[10] where E_{ox}, E_{red}, E_T, and C are the oxidation potential of the donor, the reduction potential of the acceptor, the excited state energy and the Coulombic term for the initially formed ion pair, respectively. C is neglected as usually done in polar solvents.[11]

$$\Delta G_{et} = E_{ox} - E_{red} - E_T + C \quad (1)$$

RESULTS AND DISCUSSION

1. Photochemical Properties of the Studied Organophotocatalysts. The absorption spectra of the different **OPC**s depicted in Figure 1A allow a large and efficient covering of the emission spectra of (i) the different LED bulbs in the visible wavelength range (blue, λ_{max} = 462 nm; green, 514 nm: yellow, 591 nm; and red, 630 nm; Figure 1B) or (ii) the Xe−Hg lamp that delivers a UV−visible light. **Pent** is well adapted for red and yellow lights, **Napht** for green light, **Anth** for blue light, and **Pyr** for UV light (Figure 1).

The redox properties of the compounds investigated are gathered in Table 1. The oxidation potentials decrease in the series **Pyr** > **Anth** > **Napht** > **Pent**. The cyclic voltammetry investigation of the **OPC**s investigated reveals that the oxidation process is partly reversible: in Figure 2A, it can be observed that the ratio of the anodic/cathodic peak currents

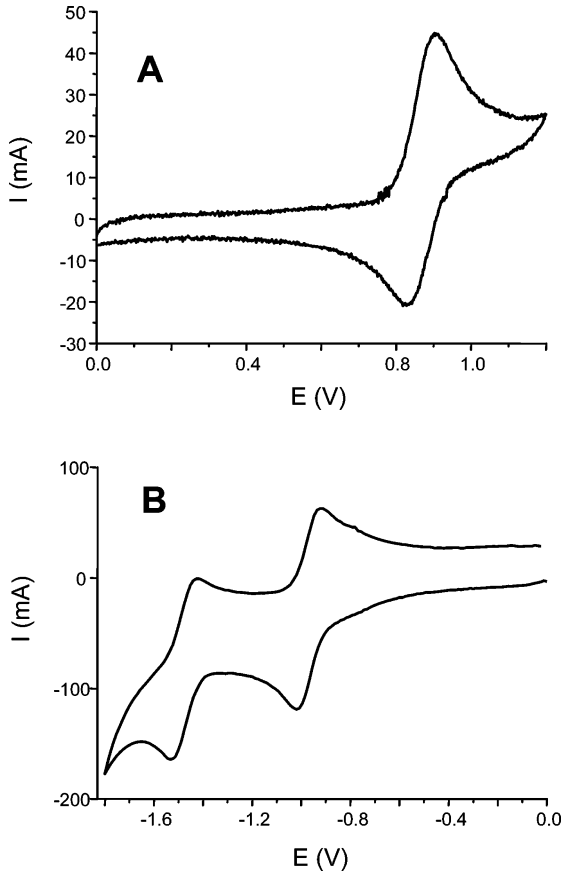

Figure 2. Examples of cyclic voltammograms: (A) oxidation and (B) reduction of **Pent**.

i_a/i_c is <1. The reversibility for **Napht** and **Pent** is rather good ($i_a/i_c \sim 0.8$): better than that found for **Anth** ($i_a/i_c \sim 0.4$) in ref 5. The reduction potentials are also strongly affected by the selected **OPC** and decrease in the series: **Pent** > **Napht** > **Anth** > **Pyr**. The reversibility of these reduction processes is rather good, e.g., the ratio of the anodic/cathodic peak currents i_a/i_c close to 1 for **Napht** and **Pent** (Figure 2B).

The excited state energy levels decrease in the series **Pyr** > **Anth** > **Napht** > **Pent** in agreement with the red-shifted transitions when going from **Pyr** to **Pent**. The S_1 lifetimes of the selected compounds are rather long: this ensures that these excited states can easily react with the quenchers to start the catalytic cycles.

2. The Oxidative Cycle to Initiate ROP. *2.1. Reaction Mechanisms.* From fluorescence quenching experiments

(Figure 1 in the Supproting Information), very high ^{1}**OPC**/Ph_2I^+ interaction rate constants are determined (e.g., $k = 4.1 \times 10^9$ M^{-1} s^{-1} for **Pent** and 2.8×10^{10} M^{-1} s^{-1} for **Napht**; Table 1). This process promotes the decomposition of the iodonium salt (1) by electron transfer: for all the investigated **OPCs**, this reaction is favorable according to the highly negative free energy change (from $\Delta G = -0.87$ eV for **Pent** to -1.61 eV for **Pyr**).

$$^1\mathbf{OPC} + Ph_2I^+ \rightarrow \mathbf{OPC}^{\bullet+} + Ph^{\bullet} + Ph - I \quad (1)$$

$$Ph^{\bullet} + (TMS)_3Si{-}H \rightarrow Ph - H + (TMS)_3Si^{\bullet} \quad (2)$$

$$(TMS)_3Si^{\bullet} + \mathbf{OPC}^{\bullet+} \rightarrow (TMS)_3Si^+ + \mathbf{OPC} \quad (3)$$

$$(TMS)_3Si^+ + M \rightarrow (TMS)_3Si{-}M^+ \quad (4)$$

The formation of phenyl radicals ($Ph^{\bullet}$) is well supported by ESR-ST experiments for all the investigated **OPCs**, e.g., upon irradiation of a **Pent**/Ph_2I^+ solution with a red LED bulb, the PBN radical adduct (characterized by $a_N = 14.3$ and $a_H = 2.2$ G; reference values in[3,13]) is easily observed (Figure 3A).[3,13]

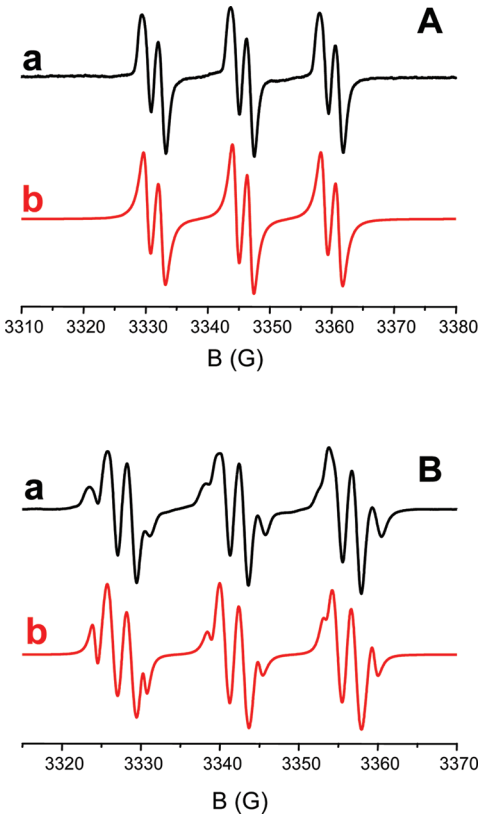

Figure 3. ESR spectra obtained after red LED bulb irradiation of: (A) a **Pent**/Ph_2I^+ solution (in *tert*-butylbenzene/acetonitrile), $[Ph_2I^+]$ = 0.01 M: experimental (a) and simulated (b) spectra; (B) a **Pent**/Ph_2I^+/$(TMS)_3SiH$ solution (in *tert*-butylbenzene/acetonitrile), $[Ph_2I^+]$ = 0.01 M: experimental (a) and simulated (b) spectra. Phenyl-*N*-*tert*-butylnitrone (PBN) is used as spin-trap.

In presence of silane, these $Ph^{\bullet}$ radicals are converted into silyl radicals $R_3Si^{\bullet}$ by a hydrogen abstraction reaction 2. This is also well supported by the observation of $R_3Si^{\bullet}$ in the irradiated three component system (**OPC**/Ph_2I^+/R_3SiH) in ESR-ST experiments: the irradiation of a **Pent**/Ph_2I^+/$(TMS)_3SiH$ solution with a red LED bulb leads to two PBN radical adducts corresponding to $Ph^{\bullet}$ and $(TMS)_3Si^{\bullet}$ (Figure 3B). For the silyl radical, the PBN radical adduct is characterized by $a_N = 14.8$ G and $a_H = 5.7$ G (see reference values in refs 3 and 13). Free radicals are not observed for the irradiation of Ph_2I^+/$(TMS)_3SiH$ solution with red light clearly indicating that **OPC** is required.

The photolysis of the **OPC** in the three component systems (**OPC**/Ph_2I^+/$(TMS)_3SiH$) is much slower than in the two-component systems (**OPC**/Ph_2I^+) as shown in Figure 4. For example using **Pyr** as **OPC**, the oxidation photoproducts (pyrene-1,6quinone and pyrene-1,8 quinone) characterized by a strong absorption at about 450−460 nm[14] are only observed in the absence of $(TMS)_3SiH$ (Figure 4A). In the presence of the silane, these photoproducts do not appear anymore (Figure 4B). These results highlight a regeneration of the **OPC** in the presence of $(TMS)_3SiH$. Such a behavior was previously observed in metal photocatalysts (iridium or ruthenium based)[3] and can be ascribed to the oxidation of the silyl radicals by $\mathbf{PC}^{\bullet+}$ (Scheme 1) leading to the formation of silylium ions $(TMS)_3Si^+$, known to easily initiate a ROP process (4).[3,8] The ability of these three-component systems to initiate the ROP of epoxides is in full agreement with the mechanism given in Scheme 1. This polymerization initiating ability will be discussed below (see in part 2.2 below).

The reduction potentials of $\mathbf{OPC}^{\bullet+}$ (0.83 V for $\mathbf{Pent}^{\bullet+}$ to 1.33 V for $\mathbf{Pyr}^{\bullet+}$) are quite close to that of $Ru(bpy)_3^{3+}$ (1.2 V) or $Ir(ppy)_3^+$ (0.77 V); the oxidation of $(TMS)_3Si^{\bullet}$ by $Ru(bpy)_3^{3+}$ or $Ir(ppy)_3^+$ was already evidenced.[3] Therefore, these redox properties of **OPCs** quite well support (3) and the associated photocatalyst behavior (i.e., the regeneration of **OPC** in the three component systems). However, the lack of a complete reversibility of the oxidation process (see above) suggests that the cation radical $\mathbf{OPC}^{\bullet+}$ can lead to side reactions. This is a nonperfect photocatalyst behavior in line with a partial recovery of the **OPC** in the photolysis of the three-component systems.

2.2. OPC/Iodonium Salt/Silane: An Initiating System for ROP. The ring-opening photopolymerization of (3,4-epoxycyclohexane)methyl 3,4-epoxycyclohexylcarboxylate EPOX under air in the presence of **OPC**/Ph_2I^+ is quite slow for the different selected irradiation conditions, e.g., Xe−Hg lamp for **Pyr**/Ph_2I^+ or red LED bulb for **Pent**/Ph_2I^+ (Figure 5). Rather low final conversions are reached, e.g., <20% using **Pent**/Ph_2I^+. This highlights the low ability of $\mathbf{OPC}^{\bullet+}$ (generated from the ^{1}**OPC**/Ph_2I^+) as an initiating species of ROP. In absence of Ph_2I^+, the polymerization process is not observed.

Interestingly, in the presence of the silane, excellent polymerization profiles are obtained: the different three-component systems (**OPC**/Ph_2I^+/$(TMS)_3SiH$) can be considered as excellent initiating systems (Figure 5A curve 1 vs curve 2 and Figure 5B curve 1 vs curve 2). Upon red or green light exposure, the **Pent** and **Napht** based systems exhibit higher polymerization initiating abilities than that found for previously proposed systems involving violanthrone derivatives.[15] The conversion limits for these systems can be partly ascribed to significant increases in viscosity lowering diffusion rates; the consumption of the OPC is also involved.

3. The Reductive Cycle to Initiate FRP. *3.1. Reaction Mechanisms.* Fluorescence quenching experiments (Figure 2 in the Supporting Information) lead to high ^{1}**OPC**/EDB interaction rate constants k (from $k = 1.6 \times 10^8$ M^{-1} s^{-1} for **Pent** to 8.1×10^9 M^{-1} s^{-1} for **Napht**; Table 1). The electron transfer reaction 5 is favorable for **Pyr**, **Anth** and **Napht** as

dx.doi.org/10.1021/ma300050n | *Macromolecules* 2012, 45, 1746−1752

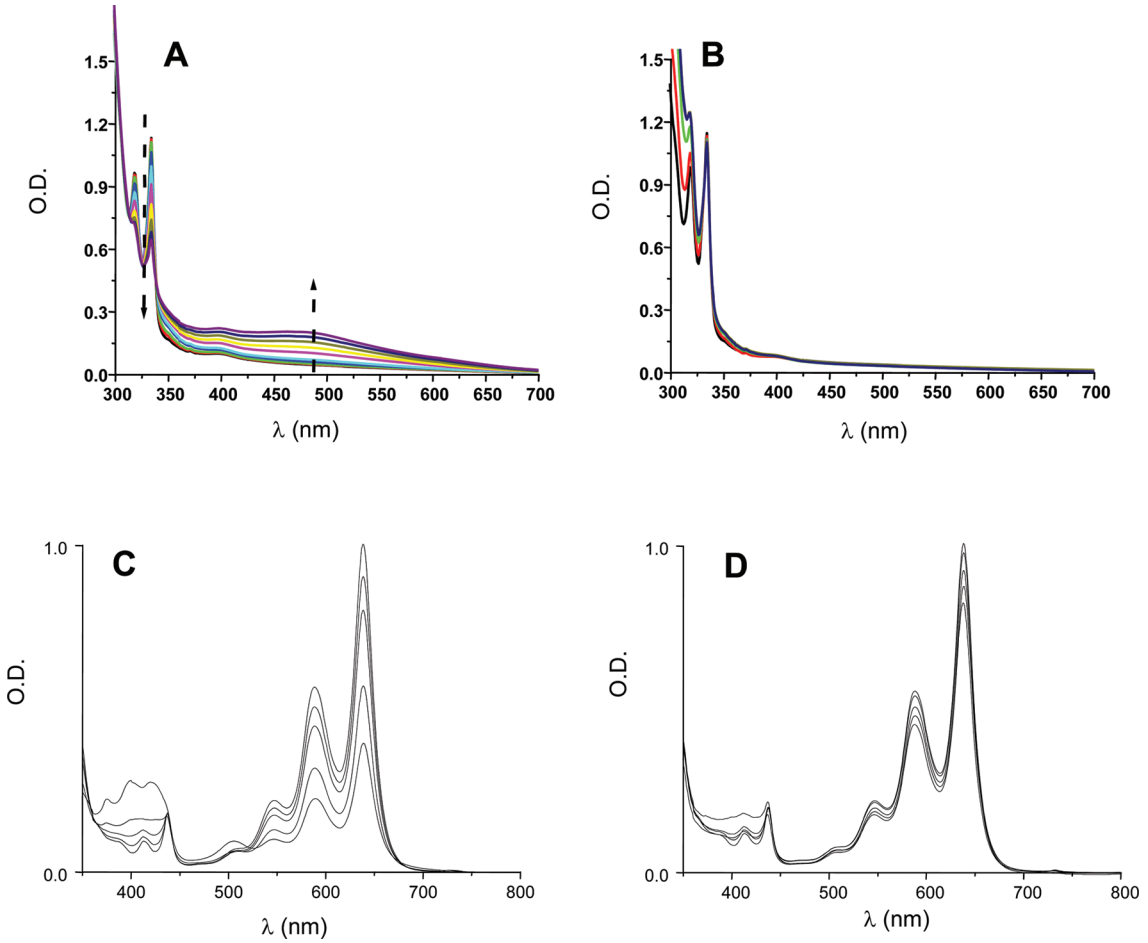

Figure 4. UV−visible spectra at different irradiation times. Photolysis of **Pyr**/Ph_2I^+ (1.75×10^{-5} M/8.6×10^{-3} M) (A) and **Pyr**/Ph_2I^+/$(TMS)_3SiH$ (1.75×10^{-5} M/8.6×10^{-3} M/2×10^{-2} M) (B); from t = 0 to 60 s; in acetonitrile; Xe−Hg lamp exposure. Photolysis of **Pent**/Ph_2I^+ (1.75×10^{-5} M/8.6×10^{-4} M) (C) and **Pent**/Ph_2I^+/$(TMS)_3SiH$ (1.75×10^{-5} M/8.6×10^{-4} M/2×10^{-2} M) (D); from t = 0 to 240 s; in acetonitrile/*tert*-butylbenzene; red LED bulb exposure.

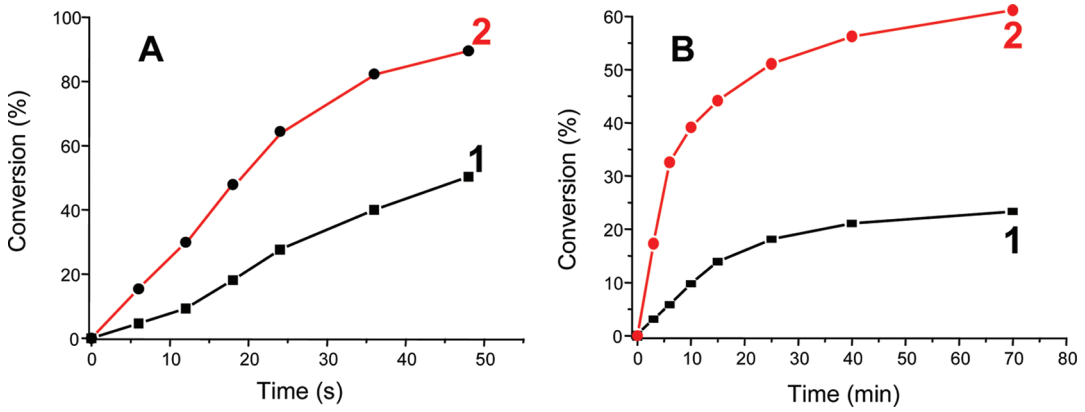

Figure 5. Compared polymerization profiles of **EPOX** under air upon: (A) a Xe−Hg lamp exposure in the presence of (**1**) **Pyr**/Ph_2I^+ (0.5%/ 2% w/w) and (**2**) **Pyr**/$(TMS)_3Si$−H/Ph_2I^+ (0.5%/3%/ 2% w/w) under air. (B) a red LED bulb irradiation in the presence of (**1**) **Pent**/Ph_2I^+ (0.5%/ 2% w/w) and (**2**) **Pent**/$(TMS)_3Si$−H/Ph_2I^+ (0.5%/3%/ 2% w/w).

revealed by the calculated negative free energy change ΔG (Table 1). For **Pent**, the process is not exergonic (ΔG = +0.03 eV): this is in agreement with the lower ^{1}**Pent**/EDB interaction rate constant compared to those found for the other **OPC**s.

$$^1\mathbf{OPC} + \mathrm{EDB} \rightarrow \mathrm{OPC}^{\bullet -} + \mathrm{EDB}^{\bullet +} \quad (5)$$

$$\mathbf{OPC}^{\bullet -} + \mathrm{R-Br} \rightarrow \mathbf{OPC} + \mathbf{R}^{\bullet} + \mathrm{Br}^{-} \quad (6)$$

In the presence of phenacyl bromide, phenacyl radicals are generated according to eq 6, i.e., for the irradiation of a **Napht**/EDB/phenacyl bromide solution with a green LED bulb, the PBN adduct of the $PhC(=O)CH_2^{\bullet}$ radical is observed (a_N = 14.8 G; a_H = 4.6 G, in agreement with ref 13) (Figure 6). For the two component system (**Napht**/phenacyl bromide), free radicals are not observed thereby demonstrating that the amine

dx.doi.org/10.1021/ma300050n | *Macromolecules* 2012, 45, 1746−1752

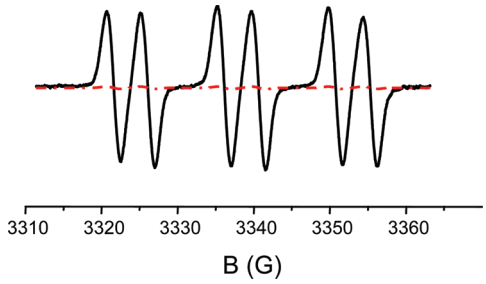

Figure 6. ESR spectra obtained after a green LED bulb irradiation (30 s) of **Napht**/phenacyl bromide (dot line) and **Napht**/EDB/phenacyl bromide (full line) in *tert*-butylbenzene/acetonitrile. Phenyl-*N*-*tert*-butylnitrone (PBN) is used as spin-trap.

is necessary in eq 5 and in the catalytic cycle. The reduction potential of phenacyl bromide (−0.78 V vs SCE)[16] is higher than the oxidation potentials of the different OPC$^{\bullet-}$ (−2.2, −1.47, −1.1, and −0.93 V for **Pyr**, **Anth**, **Napht**, and **Pent**, respectively; see Table 1): reaction 6 is therefore thermodynamically favorable. These results show that the reductive cycle presented in Scheme 2 is still valid for the new **OPC**s proposed here.

3.2. OPC/Amine/Alkyl Halide: An Initiating System for FRP. The free radical polymerization of trimethylol propane triacrylate (TMPTA) in laminate in the presence of **OPC**/EDB/phenacyl bromide is rather efficient under visible lights (Table 2 and Figure 7: curve 3) ∼ 67% conversion within 400s

Table 2. Polymerization Rates (R_p) and Final Conversion for the Polymerization of TMPTA in Laminate[a]

OPC	$R_p/[M_0] \times 100^b$ (s^{-1})	nonversion (%) for t = 400s
Pyr[a]	8	77
Anth	0.4	55
Napht	1	67
Pent	<0.4	∼40

[a]Initiating system: **OPC**/EDB/Phenacylbromide (0.5%/4.5%/3% w/w). Xe−Hg lamp irradiation (λ > 390 nm) except for OPC = **Pyr**. For **Pyr**, no filter is used to ensure a UV light irradiation. [b]$[M_0]$: the initial monomer concentration.

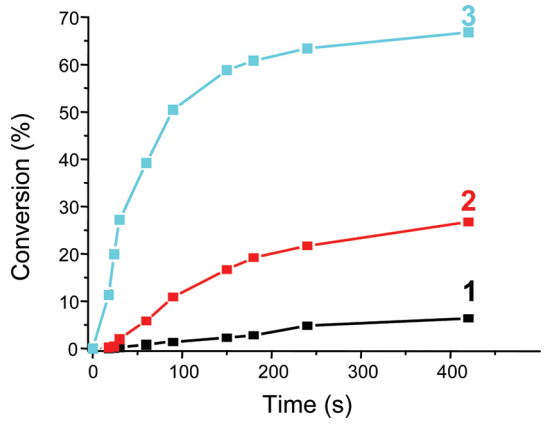

Figure 7. Polymerization profiles of TMPTA upon a Xe−Hg lamp irradiation (λ > 390 nm) in laminate in the presence of (1) **Napht** (0.5% w/w); (2) **Napht**/EDB (0.5%/4.5% w/w); (3) **Napht**/EDB/phenacyl bromide (0.5%/4.5%/3% w/w).

under the Xe−Hg lamp exposure. In the absence of phenacyl bromide (Figure 7, curve 2) or EDB, the efficiency drastically drops down. This clearly highlights the role of the three-component combination in the formation of the polymerization initiating radicals i.e. the phenacyl radicals (as observed by ESR). The relative efficiency of the different **OPC**s to initiate the polymerization can be ascribed to (i) their different light absorption properties (Figure 1A) and (ii) the ^{1}**OPC**/EDB interaction rate constants which are strongly affected by the selected **OPC** (see Table 1).

CONCLUSION

In the present paper, new colored organophotocatalysts that can work according to oxidative (in the presence of a silane and iodonium salt) or reductive (in the presence of an amine and alkyl halide) catalytic cycles are presented. Through the oxidative cycle, silylium ions are easily generated and start a ring-opening polymerization under very soft irradiation conditions and under air. Using the reductive cycle, phenacyl radicals are formed and initiate the FRP. This OPC series allows a tunable character (from blue to red) for the excitation. The use of these **OPC**s for applications in organic chemistry deserves to be investigated in forthcoming papers.

ASSOCIATED CONTENT

Supporting Information

Fluorescence quenching and Stern−Volmer treatments for the OPC/Ph_2I^+ interaction. This material is available free of charge via the Internet at http://pubs.acs.org/.

AUTHOR INFORMATION

Corresponding Author

*E-mail: j.lalevee@uha.fr.

Notes

The authors declare no competing financial interest.

ACKNOWLEDGMENTS

The authors thank the Agence Nationale de la Recherche (ANR BLAN-0802; ANR SILICIUM); J.L. thanks the Institut Universitaire de France for the support. Thanks are due to Dr. J. P. Malval (IS2M) for his help in the fluorescence lifetime determination.

REFERENCES

(1) (a) Nicewicz, D. A.; MacMillan, D. W. C. *Science* **2008**, *322*, 77−80. (b) Shih, H.-W.; Vander Wal, M. N.; Grange, R. L.; MacMillan, D. W. C. *J. Am. Chem. Soc.* **2010**, *132*, 13600−13603. (c) Zeitler, K. *Angew. Chem., Int. Ed.* **2009**, *48*, 9785−9789. (d) Narayanam, J. M. R.; Stephenson, C. R. J. *Chem. Soc. Rev.* **2011**, *40*, 102−113. (e) Dai, C.; Narayanam, J. M. R.; Stephenson, C. R. J. *Nature Chem.* **2011**, *3*, 140−145. (f) Ischay, M. A.; Lu, Z.; Yoon, T. P. *J. Am. Chem. Soc.* **2010**, *132*, 8572−8574. (g) Yoon, T. P.; Ischay, M. A.; Du, J. *Nature Chem.* **2010**, *2*, 527−532. (h) Larraufie, M. H.; Pellet, R.; Fensterbank, L.; Goddard, J. P.; Lacôte, E.; Malacria, M.; Ollivier, C. *Angew. Chem., Int. Ed.* **2011**, *50*, 4463−4466. (i) Courant, T.; Masson, G. *Chem.—Eur. J.* **2011**, DOI: 10.1002/chem.201103062.

(2) (a) Neumann, M.; Fuldner, S.; Konig, B.; Zeitler, K. *Angew. Chem., Int. Ed.* **2011**, *50*, 951−954. (b) Liu, Q.; Li, Y.-N.; Zhang, H.-H.; Chen, B.; Tung, C.-H.; Wu, L.-Z. *Chem.—Eur. J.* **2011**, DOI: 10.1002/chem.201102299. (c) Fagnoni, M.; Dondi, D.; Ravelli, D.; Albini, A. *Chem. Rev.* **2007**, *107*, 2725−2756.

(3) (a) Lalevée, J.; Blanchard, N.; Tehfe, M.-A.; Morlet-Savary, F.; Fouassier, J. P. *Macromolecules* **2010**, *43*, 10191−10195. (b) Lalevée, J.; Blanchard, N.; Tehfe, M. A.; Peter, M.; Morlet-Savary, F.; Gigmes, D.; Fouassier, J. P. *Polym. Chem.* **2011**, *2*, 1986−1991. (c) Lalevée, J.; Blanchard, N.; Tehfe, M. A.; Peter, M.; Morlet-Savary, F.; Fouassier, J. P.

Macromol. Rapid Commun. **2011**, *32*, 917−920. (d) Lalevée, J.; Blanchard, N.; Tehfe, M. A.; Peter, M.; Morlet-Savary, F.; Fouassier, J. P. *Polym. Bull.* **2011**, *68*, 341−347. (e) Lalevée, J.; Peter, M.; Dumur, F.; Gigmes, D.; Blanchard, N.; Tehfe, M. A.; Morlet-Savary, F.; Fouassier, J. P. *Chem.—Eur. J.* **2011**, *17*, 15027−15031.

(4) Zhang, G.; Song, I. Y.; Ahn, K. H.; Park, T.; Choi, W. *Macromolecules* **2011**, *44*, 7594−7599.

(5) Tehfe, M.-A.; Lalevée, J.; Morlet-Savary, F.; Graff, B.; Blanchard, N.; Fouassier, J.-P. *ACS Macro Lett.* **2012**, *1*, 198−203.

(6) (a) Crivello, J. V. *Photoinitiators for Free Radical, Cationic and Anionic Photopolymerization*, 2nd ed.; Bradley, G., Ed.; John Wiley and Sons: New York, 1998. (b) Fouassier, J. P. *Photoinitiation, Photopolymerization and Photocuring: Fundamental and Applications*; Hanser Publishers: New York, 1995. (c) *Photoinitiated polymerization*; Belfield, K. D., Crivello, J. V., Eds.; ACS Symposium Series 847; American Chemical Society: Washington, DC, 2003. (d) Fouassier, J. P.; Lalevée, J. *Photoinitiators for Polymer Synthesis: Scope, Reactivity and Efficiency*; Wiley-VCH: Weinheim, Germany, to appear in 2012. (e) *Handbook of radical vinyl polymerization*; Mishra, M., Yagci, Y., Eds.; M. Dekker, Inc: New York, 1998.

(7) (a) Lalevée, J.; Alloas, X.; Jradi, S.; Fouassier, J. P. *Macromolecules* **2006**, *39*, 1872−1879. (b) Lalevée, J.; Zadoina, L.; Alloas, X.; Fouassier, J. P. *J. Polym. Sci. Part A: Chem* **2007**, *45*, 2494−2502. (c) Fouassier, J. P.; Allonas, X.; Lalevée, J.; Visconti, M. *J. Polym. Sci., Part A: Polym. Chem.* **2000**, *38*, 4531−4541.

(8) (a) Tehfe, M.-A.; Lalevée, J.; Gigmes, D.; Fouassier, J. P. *Macromolecules* **2010**, *43*, 1364−1370. (b) Tehfe, M.-A.; Lalevée, J.; Gigmes, D.; Fouassier, J. P. *J. Polym. Sci., Part A: Polym. Chem.* **2010**, *48*, 1830−1837.

(9) Tordo, P. In *Spin-trapping: recent developments and applications*, Atherton, N. M., Davies, M. J., Gilbert, B. C., Eds.; Electron Spin Resonance 16; The Royal Society Of Chemistry: Cambridge, U.K., 1998.

(10) Rehm, D.; Weller, A. *Isr. J. Chem.* **1970**, *8*, 259−271.

(11) Lalevée, J.; Dirani, A.; El-Roz, M.; Allonas, X.; Fouassier, J. P. *Macromolecules* **2008**, *41*, 2003−2010.

(12) Fouassier, J. P.; Burr, D.; Crivello, J. V. *J. Photochem. Photobiol. A: Chem.* **1989**, *49*, 317−324.

(13) (a) *Landolt Bornstein: Magnetic Properties of Free Radicals*; Fischer, H., Ed.; Springer Verlag: Berlin, 2005; Vol. 26d. (b) Chandra, H.; Davidson, I. M. T.; Symons, M. C. R. *J. Chem. Soc. Faraday Trans. 1* **1983**, *79*, 2705−2711. (c) Alberti, A.; Leardini, R.; Pedulli, G. F.; Tundo, A.; Zanardi, G. *Gazz. Chim. Ital.* **1983**, *113*, 869−871. (d) Lalevée, J.; Blanchard, N.; El-Roz, M.; Graff, B.; Allonas, X.; Fouassier, J. P. *Macromolecules* **2008**, *41*, 4180−4186.

(14) (a) Pierce, R. C.; Katz, M. *Environ. Sci. Technol.* **1976**, *10*, 45−51. (b) Sigman, M.; Schuler, P. F.; Gosh, M.; Dabestani, R. T. *Environ. Sci. Technol.* **1998**, *32*, 3980−3985.

(15) (a) Tehfe, M.-A.; Lalevée, J.; Morlet-Savary, F.; Graff, B.; Fouassier, J.-P. *Macromolecules* **2011**, *44*, 8374−8379. (b) Tehfe, M.-A.; Gigmes, D.; Dumur, F.; Bertin, D.; Morlet-Savary, F.; Graff, B.; Lalevée, J.; Fouassier, J.-P. *Polym. Chem.* **2012**, DOI: 10.1039/C1PY00460C.

(16) Renaud, J.; Scaiano, J. C. *Can. J. Chem.* **1996**, *74*, 1724−1730.

Macromolecules

Article

pubs.acs.org/Macromolecules

Superstructures of Double Functionalized Host–Guest Acrylmonomers Containing Chiral Phenylalanine-*click*-cyclodextrin and Polymers

S. Gingter, B. Mondrzik, and H. Ritter*

Institute of Organic Chemistry and Macromolecular Chemistry, Heinrich-Heine-University Duesseldorf, Universitaetsstraße 1, D-40225 Duesseldorf, Germany

Supporting Information

ABSTRACT: We report the preparation of acrylic monomers D- or L-mono-(6-phenylalanine-acrylamido-6-deoxy)-β-cyclodextrin $\mathbf{3_D}/\mathbf{3_L}$ and their corresponding copolymers $\mathbf{4_D}/\mathbf{4_L}$ bearing NIPAAm and D- or L-phenylalanine as guest and β-cyclodextrin as host moieties. To implement the cyclodextrin resin (CD) into the monomer, microwave accelerated cycloaddition (click-reaction) was performed. For the new design of polymers having both host and guest species in the polymer side chain, inter- and intramolecular interactions could be observed. The resulting supramolecular structures were characterized by NMR, DLS, TEM, and LCST measurements.

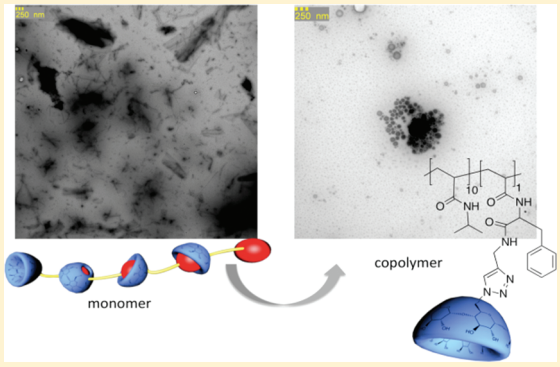

INTRODUCTION

Supramolecular structures are ubiquitous in nature particularly in biological systems, the most common are DNA, microtubuli, or microfilaments which are built out of proteins.[1] Scientist have been inspired by nature and have investigated various systems mimicking biomolecules by synthetic supramolecular structures with interesting properties and functions.[2−6] Superstructures formed by hydrogen bonds were reported for the first time by Lehn et al.[7] Many contributions about the formation of supramolecular polymers formed by hydrogen bonding can be found in literature.[8−12] However there have been few works dealing with the self-assembly into supramolecular polymeric structures via host–guest interaction.[13,14] For example Harada et al. reported about the formation of supramolecular helical polymers, recently.[15] The self-assembly behavior of phenyl modified β-cyclodextrins has been investigated by Liu et al.[16]

Also self-assembly of gels through shape selective molecular recognition with CD for linear and cyclic guest molecules was investigated on a macroscopic scale very recently.[17] Furthermore there have been few works dealing with self-assembly of chiral compounds. For example a monomer end-capped with a cholesteryl group was threaded with CD to form a helical polymer.[18] Star polymers and polymer brushes were synthesized from amphiphilic chiral monomers and their self-assembly investigated.[19,20]

However there have been few works dealing with supramolecular structures based on host–guest interaction from chiral monomers.[21] Monomers based on macrocyclic hosts comprising both host and guest moiety offer a wide range of opportunities for new supramolecular materials and applications.[22] Next to calixarenes and cucurbiturils particularly cyclodextrins (CDs) are important macrocyclic hosts, because they are water-soluble, natural products suitable for medical applications.[23,24] Although cyclodextrins are frequently used for chiral separation of racemates in column chromatography, the phenomena of chiral recognition of synthetic polymers has not yet been extensively investigated.[25−29] Thus, we want to report about the preparation and properties of a new typ of polymerizable acrylic monomer containing chiral β-CD as host and phenylalanine as guest moiety in the same molecule. We chose CD as a host and phenylalanine as a guest compound because the aromatic moiety builds stable complexes with CD and phenylalanine is an important, chiral biomolecule.

MATERIALS AND EXPERIMENTAL SECTION

All reagents used were commercially available (Sigma-Aldrich, Acros Organics) and were used without further purification. β-cyclodextrin was obtained from Wacker Chemie GmbH, Burghausen, Germany, and used after drying overnight at a vacuum oil pump over P_4O_{10}. D- and L-Phenylalanine (98.5%) were purchased from Alfa Aesar GmbH & CoKG, Germany. Acryloylchloride (97%) and *N*-isopropylacrylamide (NIPAAm, 97%) were obtained from Sigma-Aldrich, Germany, and used as received. Azoisobutyronitrile (AIBN) (96%) and *N*,*N*-dimethylformamide (DMF) were purchased from Fluka, Germany. Dimethyl sulfoxide-d_6 (99.9 atom % D) and deuterium oxide, D_2O, were obtained from Deutero GmbH, Germany.

^{1}H NMR was performed using a Bruker Advance DRX 200 spectrometer operating at 200.13 or 500 MHz for protons using

Received: January 30, 2012
Revised: February 2, 2012
Published: February 14, 2012

   dx.doi.org/10.1021/ma3002164 | *Macromolecules* 2012, 45, 1753–1757

Scheme 1. Synthesis of Monomers 3_D, 3_L and Copolymers 4_D, 4_L

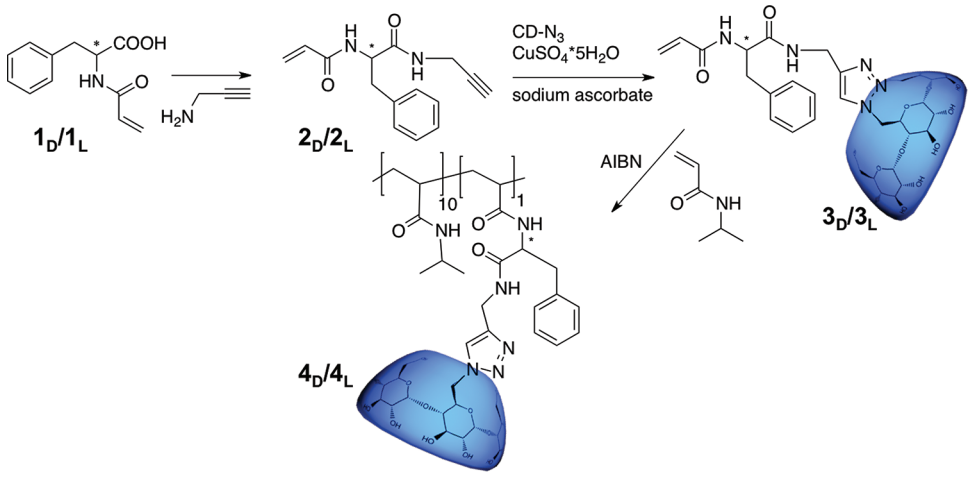

DMSO-d_6 or Deuteriumoxide 99.9% as solvents. The chemical shifts (δ) are given in ppm using the solvent peak as an internal standard. FT-IR spectra were recorded on a Nicolet 6700 FT-IR spectrometer equipped with an ATR unit. MALDI–TOF mass spectrometry (MALDI–TOF MS) was performed on a Bruker Ultraflex TOF time-of-flight mass spectrometer using a 337 nm nitogen laser. The samples were dissolved in acetonitrile/water and mixed with dithranol matrix. Molecular weights and molecular weight distributions were measured by size exclusion chromatography (SEC) using a Viscotek GPCmax VE2001 system that contained a column set with one Viscotek TSK guard column HHR-H 6.0 mm (ID) × 4 cm (L) and two Viscotek TSK GMHHR-M 7.8 mm (ID) × 30 cm (L) columns at 60 °C. *N*,*N*-Dimethylformamide (DMF, 0.1 M LiCl) was used as eluent at a flow rate of 1 mL × min^{-1}. A Viscotek VE 3500 RI detector and a Viscotek Viscometer model 250 were used. The system was calibrated with polystyrene standards with a molecular range from 580 D to 1 186 kD.

Turbidity experiments were performed on a Tepper cloud point photometer TP1. Relative transmission of a laser beam with a wavelength of 670 nm was recorded for each experiment. The measurements were performed at a temperature range between 5 and 70 °C and a heating rate of 1 °C min^{-1} using Hellma Suprasil precision cells 110 Q-S. Critical solution temperatures derived from these experiments were determined at 50% relative transmission. Dynamic Light Scattering (DLS) experiments were carried out with a Malvern Zetasizer Nano; ZS ZEN 3600 at a temperature of 20 °C. The particle size distribution is derived from a deconvolution of the measured intensity autocorrelation function of the sample by a General Purpose Methode (non-negative least squares) algorithm included in the DTS software. Each experiment was performed at least five times. Polarimetric measurements were performed at T = 20 °C in dimethyl sulfoxide or water (λ = 590 nm). Microwave-assisted synthesis was performed using a CEM Discover synthesis unit (monomode system). The temperature was measured by infrared detection with continuous feedback temperature control and maintained at a constant value by power modulation. Reactions were performed in closed vessels under controlled pressure. Transmission electron microscopy (TEM) images were recorded on a Zeiss EM902 A microscope at 80 kV.

- The *N*-acrylated aminoacid $\mathbf{1}_D/\mathbf{1}_L$ was prepared according to the method described before.[30]
- Mono(6-azido-6-desoxy)-β-CD was synthesized according to the method described before.[31]

D- or L-*N*-(1-Oxo-3-phenyl-1-(prop-2-yn-1-ylamino)propan-2-yl)acrylamide, $2_D/2_L$. The respective *N*-acrylated amino acids $\mathbf{1}_D/\mathbf{1}_L$ (10 mmol, 2.19 g) were solubilized in THF (100 mL) at room temperature. *N*-Methylmorpholine (1.01 g, 10 mmol) was then added to the amino acid solution, followed by further addition of isobutyl chloroformiate (10 mmol, 1.37 g). During the addition of the isobutyl chloroformiate, a white precipitate of *N*-methylmorpholine hydrochloride was formed. Propargylamine (10 mmol, 0.55 g) was then added to the reaction mixture. A slight formation of CO_2 could be observed. The mixture was further stirred for 1 h at room temperature. The hydrochloride salt was then filtered, and the clear solution evaporated to dryness. The product was further dried at a high vacuum pump to yield 1.3 g (47%) of white solid. Polarimetric measurement (DMSO) $\mathbf{2}_L$ α_D^{20} = 30°; $\mathbf{2}_D$ α_D^{20} = −28°. ^{1}H NMR (200 MHz, DMSO-d_6) δ (ppm): 8.60 (s, 1H), 8.43 (d, J = 8.7, 1H), 7.36 − 7.07 (m, 5H), 6.36 − 6.18 (m, 1H), 6.02 (dd, J = 2.4, 17.1, 1H), 5.57 (dd, J = 2.4, 10.0, 1H), 3.94–3.78 (m, 2H), 3.16 (t, J = 2.5, 1H), 3.00 (dd, J = 4.8, 13.7, 1H), 2.79 (dd, J = 9.7, 13.6, 2H). FT- IR (diamond) ν(cm^{-1}): 3273.3 (ν NH), 3069.6, 2961.5, 1645.7 (amide I), 1622.4 (C═C), 1547.2 (amide II), 1496.1 (Ar), 1436.2, 1382.4, 1325.0, 1241.4, 1224.6, 1192.7, 990.8. Anal. Calcd: C, 69.7; H, 5.43; N, 11.61. Found for $\mathbf{2}_L$: C, 69.7; H, 6.6; N, 10.6. Found for $\mathbf{2}_D$: C, 70.02; H, 6.4; N, 10.59.

D- or L-Mono(6-phenylalanine-acrylamido-6-deoxy)-β-cyclodextrin, $3_D/3_L$. We approached microwave-assisted cycloaddition by giving $\mathbf{2}_D/\mathbf{2}_L$ (0.2 g, 0.82 mmol) to a solution of mono-(6-azido-6-desoxy)-β-CD (1.42 g, 1.23 mmol) in 2 mL DMF in a pressure-resistant test tube. To the clear solution were added sodium ascorbate (25 mg, 0.1 mmol) and copper(II) sulfate pentahydrate (40 mg, 0.2 mmol). The tube was sealed and placed in the CEM monomode microwave and irradiated at 85 °C and 140 W for 60 min. After precipitating with acetone (50 mL) the products were collected by filtration to yield 1.5 g (80%) product. FT-IR (diamond) ν (cm^{-1}): 3356.4 (ν OH), 2927.2, 2102.7, 1652.1, 1497.1, 1437.5, 1385.8, 1254.9, 1082.1, 1029.1, 1003.0, 936.0, 863.9. MALDI TOF MS m/z = 1416 $[M + Na]^+$.

Copolymer $4_D/4_L$. A 0.5 g sample of $\mathbf{3}_D/\mathbf{3}_L$ (0.18 mmol) was solved with 0.24 g (1.8 mmol) *N*-Isopropylacrylamide in 10 mL DMF. The solution was flushed with argon for 15 min, and then 7.4 mg (1 wt %) AIBN in DMF was added to the solution. The mixture was further stirred at 80 °C for 24 h. The product was obtained by precipitation in diethylether and afterward purificated by dialysis in a MWCO 3500 and lyophilized to yield 0.6 g. ^{1}H NMR (200 MHz, D_2O): δ = 7.93–7.83 (m), 7.44–7.06 (m), 5.31–4.82 (m), 3.86 (s), 3.14–2.69 (m), 1.10 (s). FT-IR (diamond) ν (cm^{-1}): 3295.3 (OH), 2971.1, 2931.4, 1640.5 (amide I), 1536.8 (amide II), 1459.2 (Ar), 1387.1, 1367.1, 1240.5, 1153.7, 1130.7, 1080.7, 1032.0, 1004.3. $\mathbf{4}_L$ α_D^{20} = 14° $\mathbf{4}_D$ α_D^{20} = 18°, SEC measurement: $\mathbf{4}_D$, M_n = 45 000, P_D 1.3; $\mathbf{4}_L$, M_n = 42 000, P_D 1.3.

RESULTS AND DISCUSSION

Monomers *N*-acryloyl-D-phenylalanine ($\mathbf{1}_D$) and *N*-acryloyl-L-phenylalanine ($\mathbf{1}_L$) were prepared according to the method described before. Further modification of monomers **1** was

dx.doi.org/10.1021/ma3002164 | *Macromolecules* 2012, 45, 1753–1757

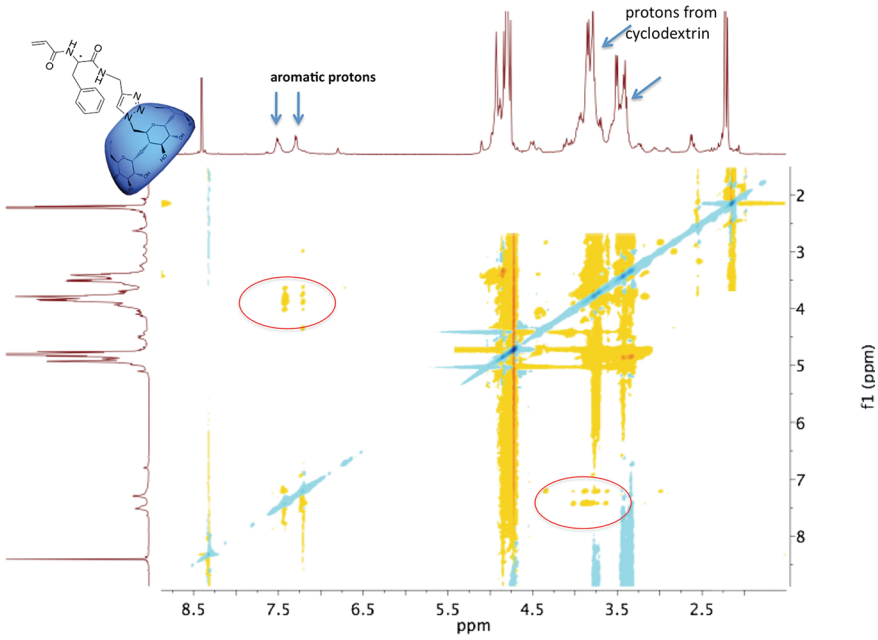

Figure 1. 2D ROESY NMR experiment of $\mathbf{3}_D$ showing the correlation between protons of the phenyl ring and protons of the inner cavity of CD.

carried out by condensation of the carboxylic group with propargylamine to obtain the corresponding alkin moiety *N*-(1-oxo-3-phenyl-1-(prop-2-yn-1-ylamino)propan-2-yl)acrylamide, $\mathbf{2}_D/\mathbf{2}_L$. The microwave accelerated click-reaction employing Cu(I) catalysis with sodium-ascorbate lead to the desired monomers mono-(6-phenylalanine-acrylamido-6-deoxy)-*β*-cyclodextrin, $\mathbf{3}_D$ and $\mathbf{3}_L$. To confirm that the monomers did not racemize significantly during the synthesis, polarimetric measurements were performed in dimethyl sulfoxide as solvent, $\mathbf{3}_D$ exhibited $\alpha_D^{20} = -28°$ and $\mathbf{3}_L$ $\alpha_D^{20} = +30°$, respectively. Copolymers $\mathbf{4}_D$ and $\mathbf{4}_L$ comprising *N*-isopropylacrylamide (NIPAAm), D-mono-(6-phenylalanine-acrylamido-6-deoxy)-*β*-cyclodextrin ($\mathbf{3}_D$) and L-mono(6-phenylalanine-acrylamido-6-deoxy)-*β*-cyclodextrin ($\mathbf{3}_L$), respectively, were obtained by free radical polymerization with AIBN as initiator (Scheme 1). The structures of all synthesized polymeric compounds have been characterized by spectroscopic methods, elemental analysis and polarimetric measurements. The molecular weights and molar weight distribution of polymers $\mathbf{4}_D$ and $\mathbf{4}_L$ were determined by size exclusion chromatography (SEC) showing similar results.

To confirm the formation of the proposed intermolecular interaction between the hydrophilic and hydrophobic moieties in case of the monomers $\mathbf{3}_D$ and $\mathbf{3}_L$ 2D ROESY-NMR-spectroscopy was carried out to show the expected correlation between the inner cavity protons of *β*-CD and the protons of the phenyl ring. Figure 1, as an example for a 2D ROESY NMR spectrum of $\mathbf{3}_D$, illustrates clearly interactions of protons from the phenyl group with protons of the CD cavity (for ROESY of $\mathbf{3}_L$, see Supporting Informations).

In addition the ^{1}H NMR spectra of the monomer exhibits clear peak shifts compared to the ^{1}H NMR spectra of *β*-CD which can be assigned to the complexation of the monomer $\mathbf{3}_D$ (Supporting Information).

The formation of large supramolecular structures formed by intramolecular interactions were found in DLS measurements of the monomers $\mathbf{3}_D$ and $\mathbf{3}_L$ exhibiting hydrodynamic diameters with a mean coil size of about 100 nm (Figure 2 as an example for $\mathbf{3}_D$). The structure can then be disassembled by addition of adamantylcarboxylate (ad-COO$^-$ K$^+$)in slight excess, which is a

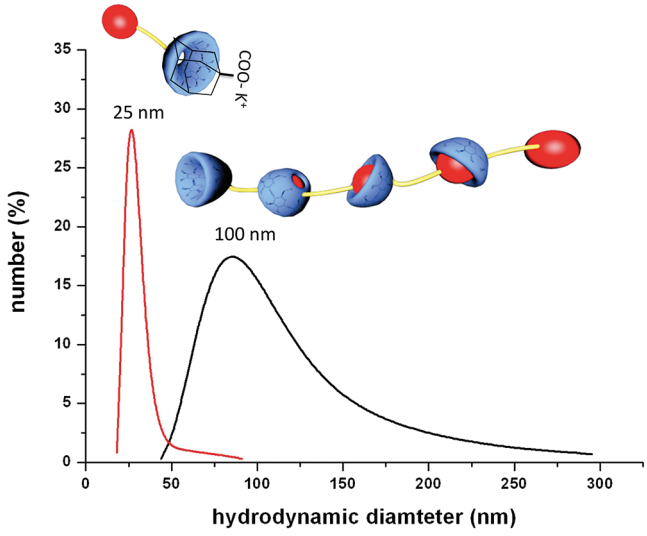

Figure 2. DLS measurement of monomers $\mathbf{3}_D$ (2 mg/mL) and $\mathbf{3}_D$ complexed with potassium adamantylcarboxylate (1 mg) and schematic illustration of complexes.

suitable competing guest molecule with a higher complex stability with *β*-CD than the phenylring of $\mathbf{3}_D$. After addition of ad-COO$^-$ K$^+$ to the aggregate of $\mathbf{3}_D$ the hydrodynamic diameter decreases as mentioned above down to 25 nm, as the *β*-CD moieties have the tendency to aggregate, the diameter does not further decrease even after addition of ad-COO$^-$ K$^+$ in great excess.

Furthermore, we were able to show that the supramolecular aggregates of **3** can also be disassembled by increasing the temperature of the solution and that the formation of the supramolecular structure can be monitored over time (Supporting Information).

In order to qualify the structure and nature of the supramolecular inclusion complexes, TEM (Transmission Electron Mikroscopy) was conducted. The microscope image (Figure 3) shows the formation of large linear structures for the

dx.doi.org/10.1021/ma3002164 | *Macromolecules* 2012, 45, 1753−1757

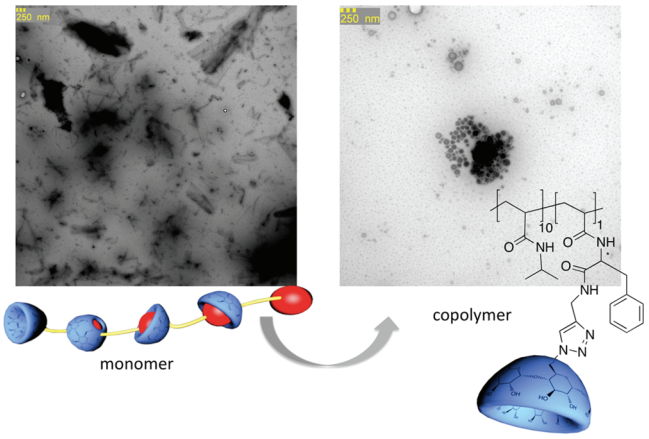

Figure 3. TEM measurement of 3_D exhibiting tube-like superstructures.

supramolecular structure formed from the monomers. In comparison the picture of the copolymers **4** exhibits round vesicles with a higher order than the aggregates of **3**. Both samples exhibit aggregation induced by the intermolecular host–guest interaction.

Furthermore, the solution properties of copolymers 4_D and 4_L were investigated. As expected, copolymers 4_D, 4_L (1:10) are soluble in cold water below the critical solution temperature (LCST). However, due to the presence of incorporated hydrophilic comonomers 3_D, 3_L a significant affect on the cloud point value of pure Poly-(NIPAAm) is shifted from 32 to 39.0 °C (3_L) and to 40.5 °C (3_D) respectively. The cloud point shift difference of 1.5 °C regarding the D- or L-enantiomer is a strong hint to different stereoinduced interactions (Figure 4).

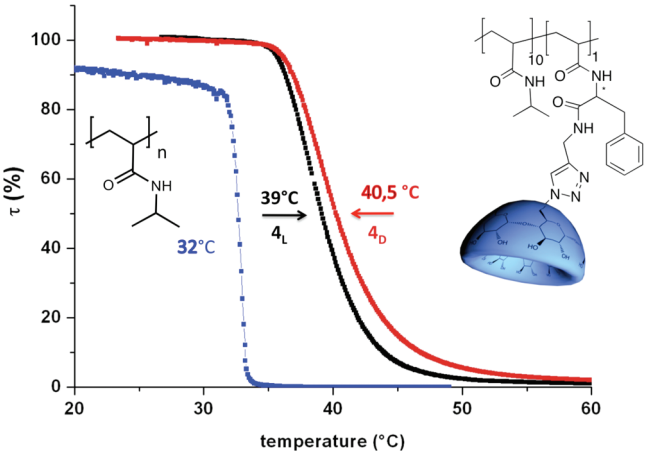

Figure 4. LCST measurements of 4_D and 4_L in comparison to Poly(NIPAAm) (10 mg/mL).

To confirm the supposed diastereomeric effects, DLS measurements of the copolymers were carried out. Surprisingly, in contrast to the small difference in cloud points copolymers exhibited strong differences of hydrodynamic diameters of 16 nm for the 4_L and 63 nm for the 4_D, respectively (Figure 5).

Since SEC measurements of 4_D and 4_L confirm nearly identical masses and mass distributions; the big difference of supramolecular aggregates in aqueous solution is a result of the phe chirality.

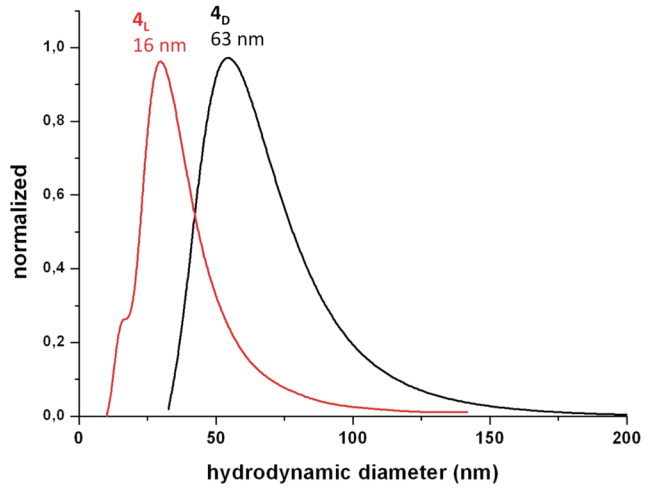

Figure 5. Hydrodynamic diameters of polymers 4_D and 4_L (1 mg/mL).

CONCLUSION

We have investigated the formation of a new cyclodextrin- and phenylalanine-based monomer and the resulting supramolecule. The intermolecular interaction was proven by 2D ROESY NMR experiments. The quality of the supramolecule was investigated via TEM and DLS, exhibiting large formations of 100 nm in diameter, which could be disassembled by addition of potassium adamantylcarboxylate. Thus we conclude that we have succeeded in synthesizing a new type of monomer bearing both host and guest moiety forming supramolecular structures. Furthermore we were able to show enantioselective recognition of copolymers containing D- or L-phenylalanine moieties by use of DLS and LCST measurement. The results clearly indicate that enantioselective recognition of the polymeric attached chiral amino acid takes place due to host–guest interaction with *β*-CD. The D-enantiomer of polymeric attached phe shows a much stronger increase in hydrodynamic diameter than the L-enantiomer due to CD-interaction.

ASSOCIATED CONTENT

Supporting Information

DLS measurements, ^{1}H NMR spectra, FT-IR spectra, and 2D ROESY NMR. This information is available free of charge via the Internet at http://pubs.acs.org/.

AUTHOR INFORMATION

Corresponding Author

*E-mail: h.ritter@uni-duesseldorf.de.

Notes

The authors declare no competing financial interest.

REFERENCES

(1) Wolf, S. L. *Molecular Cell Biology*; Wardwoorth: Belmont, CA, 1996.
(2) Hasegawa, Y.; Miyauchi, M.; Takashima, Y.; Yamaguchi, H; Harada, A. *Macromolecules* **2005**, *38* (9), 3724–3730.
(3) Tsai, C.-C; Leng, S.; Jeong, K.-U.; Van Horn, R. M.; Wang, C.-L.; Zhang, B. W.; Graham, M. J.; Huang, J.; Ho, R.-M.; Chen, Y.; Lotz, B.; Cheng, S. Z. D. *Macromolecules* **2010**, *43* (22), 9454–9461.
(4) Song, J.; Malathong, V.; Bertozzi, C. R. *J. Am. Chem. Soc.* **2005**, *127* (10), 3366–3372.
(5) Nakano, T.; Okamoto, Y. *Chem. Rev.* **2001**, *101*, 4013–4038.

(6) Mitchell, J. C.; Harris, J. R.; Malo, J.; Bath, J.; Turberfield, A. J. *J. Am. Chem. Soc.* **2004**, *126* (50), 16342−16343.
(7) (a) Lehn, J.-M. *Adv. Mater.* **1990**, *2*, 254−257. (b) Gulik-Krzywicki, T.; Fouquey, C.; Lehn, J.-M. *Proc. Natl. Acad. Sci. U.S.A.* **1993**, *90*, 163−167. (c) Lehn, J.-M. *Makromol. Chem. Macromol. Symp.* **1993**, *69*, 1−17.
(8) Kraus, T.; Budesinsky, M.; Cisarova, I.; Zavada, J. *Angew. Chem., Int. Ed.* **2002**, *41* (10), 1715−1717.
(9) Kraus, T.; Budesinsky, M.; Cisarova, I.; Zavada, J. *Eur. J. Org. Chem.* **2004**, 4060−4069.
(10) Wilson, D.; Perlson, L.; Breslow, R. *Bioorg. Med. Chem.* **2003**, *11*, 2649−2653.
(11) Liu, Y.; Fan, Z.; Zhang, H.-Y.; Yang, Y.-W.; Ding, F.; Liu, S.-X.; Wu, X.; Wada, T.; Inoue, Y. *J. Org. Chem.* **2003**, *68*, 8345−8352.
(12) Miyauchi, M.; Takashima, Y.; Yamaguchi, H.; Harada, A. *J. Am. Chem. Soc.* **2005**, *127*, 2984−2989.
(13) Tomatsu, I.; Hashidzume, A; Harada, A. *Macromolecules* **2005**, *38*, 5223−5227.
(14) Harada, A.; Kobayashi, R.; Takashima, Y.; Hashiduzme, A.; Yamaguchi, H. *Nature Chem.* **2011**, *3*, DOI: 10.1028/NCHEM.893.
(15) Takashima, Y.; Osaki, M.; Harada, A. *J. Am. Chem. Soc.* **2004**, *126*, 42.
(16) Zhao, Y.; Liu, Y. *Sci China: Ser. B Chem.* **2006**, *49* (3), 230−237.
(17) Yamaguchi, H.; Kobayashi, R.; Takashima, Y.; Hashiduzme, A.; Harada, A. *Macromolecules* **2011**, *44*, 2395−2399.
(18) Liu, J.-H.; Chiu, Y-H; Chiu, T.-H. *Macromolecules* **2009**, *42*, 3715−3720.
(19) Skey, J.; Willcock, H.; Lammens, M.; Du Prez, F.; ÒReilly, R. K. *Macromolecules* **2010**, *43*, 5949.
(20) Ding, L.; Huang, Y.; Zhang, Y.; Deng, J.; Yang, W. *Macromolecules* **2010**, *44*, 736−743.
(21) Takashima, Y.; Osaki, M.; Harada, A. *J. Am. Chem. Soc.* **2004**, *126*, 42.
(22) Amajjahe, S.; Choi, S. W.; Munteanu, M.; Ritter, H. *Angew. Chem., Int. Ed.* **2008**, *47*, 3435−3437.
(23) Wenz, G. *Adv. Polym. Sci.* **2009**, *222*, 1−54.
(24) Schurig, V. *J.Chromatogr. A* **2001**, *906*, 275−299.
(25) Quin, L.; He, X.; Li, W.; Zhang, Y. *J. Chromatogr. A* **2008**, *1187*, 94−102.
(26) Lu, J.; Coffey, H.; Detlefson, D. J.; Li, Y.; Lee, M. S. *J. Chromatogr. A* **1997**, 76.
(27) Chiari, M.; Desparti, V.; Cretich, M.; Crini, G.; Janus, L.; Morcellet, M. *Electrophoresis* **1999**, *28*, 2614−2618.
(28)
(29) Gingter, S.; Bezdushna, E.; Ritter, H. *Macromolecules* **2010**, *43* (7), 3128−3131.
(30) Gingter, S.; Bezdushna, E.; Ritter, H. *BJOC* **2011**, 204−209.
(31) Choi, S. W.; Munteanu, M.; Ritter, H. *J. Polym. Res.* **2009**, *16*, 389−394.

Macromolecules

Article

pubs.acs.org/Macromolecules

Catalytic Activities for Olefin Polymerization: Titanium(III), Titanium(IV), Zirconium(IV), and Hafnium(IV) β-Diketiminato, 1-Aza-1,3-butadienyl−Imido, and 1-Aza-2-butenyl−Imido Complexes Bearing an Extremely Bulky Substituent, the Tbt Group (Tbt = 2,4,6-$[(Me_3Si)_2CH]_3C_6H_2$)

Hirofumi Hamaki,[†,§] Nobuhiro Takeda,[†,∥] Masaaki Nabika,*[,‡] and Norihiro Tokitoh*[,†]

[†]Institute for Chemical Research, Kyoto University, Gokasho, Uji, Kyoto 611-0011, Japan

[‡]Petrochemicals Research Laboratory, Sumitomo Chemical Co., Ltd., 2−1 Kitasode, Sodegaura, Chiba 299-0295, Japan

Supporting Information

ABSTRACT: β-Diketiminato and 1-aza-1,3-butadienyl−imido complexes $[MCl_3\{TbtNC(Me)CHC(Me)NMes\}(thf)_n]$ (**1a**, **1b**, **1c**) and $[M(=NTbt)Cl_2\{C(Me)CHC(Me)NMes\}Li(tmeda)]$ (**3a**, **3b**, **3c**) (M = Ti, Zr, Hf) bearing an extremely bulky substituent, Tbt group (Tbt = 2,4,6-$[(Me_3Si)_2CH]_3C_6H_2$) showed high activities for ethylene polymerization and ethylene/1-hexene copolymerization (up to 1.1×10^7 g of polymer·mol M^{-1} h^{-1}). Complexes **1a**, **1b**, **3a**, **3b**, and **3c** could produce ultrahigh molecular weight ethylene/1-hexene copolymers ($M_w > 4 \times 10^6$) that were hardly soluble in *o*-dichlorobenzene under the molecular weight measurement conditions.

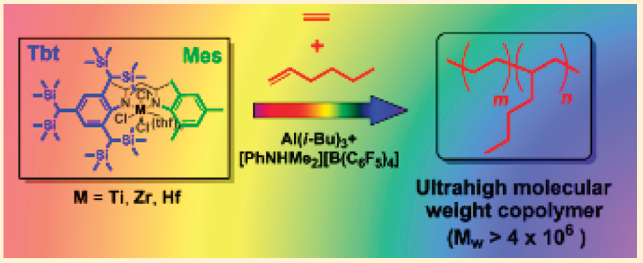

INTRODUCTION

In recent years, there has been immense research interest in preparing catalysts to produce linear low-density polyethylene (LLDPE) such as ethylene/α-olefin copolymers. This is due to the following significant rheological and mechanical properties of LLDPE compared to the conventional polymers of ethylene: high tensile strength, higher impact and puncture resistance, superior toughness, good organoleptics and low blocking, excellent clarity and gloss, and easy blending with other polyolefins.[1]

On the other hand, ultrahigh molecular-weight polyethylenes (UHMW−PEs: $M_w = 10^6$−10^7) are an example of engineering plastics. Although polyethylenes (PEs) with molecular weights on the order of 10^5 are easily accessible with a variety of metallocene catalysts, UHMW−PEs with molecular weights on the order of 10^6 are difficult to obtain. Catalysts that display ultrahigh selectivity for chain growth (propagation) are required for the production of UHMW−PEs. Such catalysts have to perform 35 000 to 350 000 insertions without any "errors" (e.g., β-hydride elimination or chain transfer reaction). UHMW−PEs possess excellent abrasion resistance and impact strength, very low coefficient friction, good self-lubricants properties, as well as good resistance at low temperature.[2−7] Heterogeneous Ziegler−Natta catalysts are capable of producing ultrahigh molecular-weight copolymers, however, they have broad distributions of molecular weight and chemical composition.[8] With regard to homogeneous catalysts, Aida and co-workers reported that crystalline nanofibers of linear PEs with an ultrahigh molecular-weight ($M_w = 6.2 \times 10^6$) and a diameter of 3 to 5 Å were formed by the polymerization of ethylene with mesoporous silica fiber-supported titanocene, using MAO as a cocatalyst.[9] Starzewski and co-workers reported on simple structural variations based on the donor−acceptor metallocene which unexpectedly resulted in high efficiency as polymerization catalysts for the synthesis of UHMW−PEs ($M_\eta = 3.9 \times 10^6$).[10] Recently, Huang and Ma's groups reported that bis(β-diketiminato)Zr complexes bearing two different substituents on the *N*-terminals show moderate catalytic activity for ethylene polymerization and formation of UHMW−PE ($M_\eta = 1.2 \times 10^6$).[11]

As for ethylene/propylene copolymerization, Fujita and co-workers reported the synthesis of ultrahigh-molecular-weight amorphous ethylene/propylene copolymers with M_w of 1.0×10^7 using a bis(salicylaldimine)Zr complex.[12] As for 1-hexene polymerization, Kakugo, Miyatake, and co-workers reported the formation of ultrahigh-molecular-weight 1-hexene homopolymers with M_w of 5.7×10^6 using a thiobis(phenoxy)titanium complex.[13] As for ethylene/1-hexene copolymerization, Jordan and co-workers achieved the formation of ultrahigh-molecular-weight ethylene/1-hexene copolymers with M_w of 1.6×10^6 using a sterically crowded tris(pyrazolyl)borate complex.[14]

While much attention has focused on the modification of cyclopentadienyl ligands to provide stereoselective catalysts,[15] other efforts have sought new catalyst systems by the inclusion

Received: October 30, 2011
Revised: January 21, 2012
Published: February 6, 2012

   dx.doi.org/10.1021/ma2024107 | *Macromolecules* 2012, 45, 1758−1769

Chart 1. Representative Post-Metallocene Catalysts for Olefin Polymerization

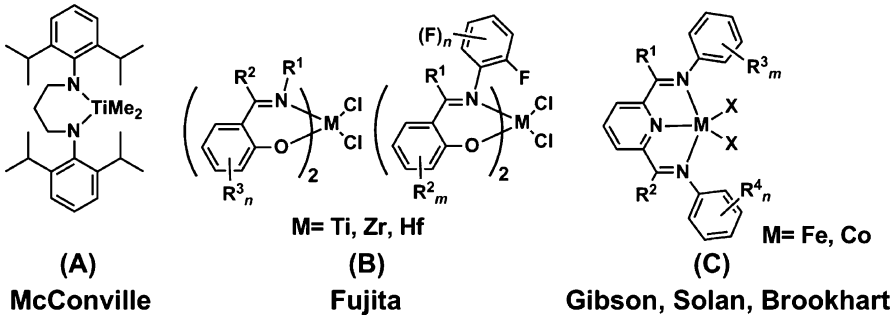

Chart 2. β-Diketiminato Complexes and 1-Aza-1,3-Butadienyl−Imido Complexes

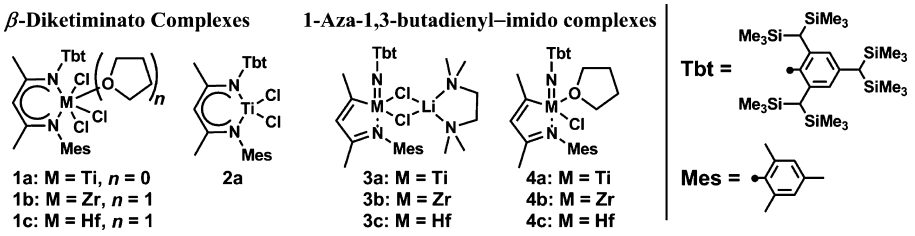

of non-cyclopentadienyl ancillary ligands about the transition metals not limited to group 4 metal (so-called post-metallocene catalysts).[16] Especially, the olefin polymerization catalysts bearing the nitrogen ligands have been developed because various substituents could be introduced on *N*-terminals near to the metal center.

For example, in 1996, McConville and co-workers repor ted a non-metallocene living higher α−olefin polymerization catalyst based on a bulky chelating diamido complex [DipN-$(CH_2)_3$NDip]$TiMe_2$ (Dip = 2,6-diisopropylphenyl) (**A**, Chart 1) although this catalyst (**A**) did not show high catalytic activity (up to 7.6×10^5 g of [poly(1-octene)] mol $Ti^{-1}h^{-1}$).[17] Fujita and co-workers at Mitsui Chemicals have developed the so-called "FI catalysts", which are salicylaldimine complexes of group 4 metals (**B**).[18] These catalysts (**B**) display very high ethylene polymerization activity (up to 6.6×10^9 g of PE mol Zr^{-1} h^{-1}). Since 1998, Gibson, Solan and Brookhart groups reported that the cobalt and iron complexes bearing the bis(arylimino)pyridine ligands (**C**) show very high (unprecedented for these metals) catalytic activities for ethylene polymerization (up to 1.1×10^8 g of PE mol Fe^{-1} h^{-1}), in some cases as high as those of the most efficient group 4 metallocenes.[19]

On the other hand, the chemistry of β-diketiminato complexes is of much current interest.[20] β-Diketiminato ligands are bidentate ligands bearing two nitrogen atoms. β-Diketiminato ligands attract considerable attention due to their isoelectronic relationship with cyclopentadienyl anion. β-Diketiminato ligands play important roles as monoanionic spectrator ligands by the virtue of their strong binding ability to metals, their tunable steric and electronic demands, and their diversity of bonding modes. β-Diketiminato complexes of trivalent titanium and tetravalent group 4 metals have already been reported by Lappert,[21] Theopold,[22] Budzelaar,[23] Smith,[24] Mindiola,[25] Huang,[11] and so forth.

In 2006, we have already reported the preparation of unsymmetric β-diketiminato complexes of Ti(III), Ti(IV), Zr(IV), and Hf(IV) bearing two different *N*-aryl groups, an extremely bulky substituent [Tbt = 2,4,6-$[(Me_3Si)_2CH]_3C_6H_2$] and a moderately bulky substituent [Mes = 2,4,6-$(CH_3)_3C_6H_2$] (Chart 2).[22a] Furthermore, we reported that the reductions of these β-diketiminato complexes gave the ring-contracted 1-aza-1,3-butadienyl−imido complexes of Ti(IV), Zr(IV), and Hf(IV) (Chart 2).[26a]

Here, we report the catalytic activities of these β-diketiminato, 1-aza-1,3-butadienyl−imido, and 1-aza-2-butenyl−imido[26b] complexes and the formation of an ethylene/1-hexene copolymer having unprecedentedly ultrahigh molecular-weight using extremely bulky catalyst systems.

RESULTS AND DISCUSSION

Catalytic Activities of β-Diketiminato and 1-Aza-1,3-butadienyl−Imido Complexes by Using a High-Throughput Screening System. Ethylene polymerization and ethylene/1-hexene copolymerization catalyzed by several complexes (**1a**, **1b**, **1c**, **2a**, **3a**, **3b**, **3c**, **4a**, **4b**, and **4c**) with several cocatalysts [modified-methylalumoxane (MMAO), $Al(i\text{-}Bu)_3/B(C_6F_5)_3$, $Al(i\text{-}Bu)_3/[PhNHMe_2][B(C_6F_5)_4]$ and $Al(i\text{-}Bu)_3/Ph_3C[B(C_6F_5)_4]$ were systematically investigated. Polymerization conditions were as follows: 40 °C, ethylene = 0.6 MPa, 1-hexene = 60 μL (in the case of copolymerization), toluene (total) = 5 mL, MMAO/complex = 1000/1, $Al(i\text{-}Bu)_3$/complex/B-compound = 400/1/3, complex = 0.1 μmol, 20 min (Figure 1, Figure 2 and Table 1).

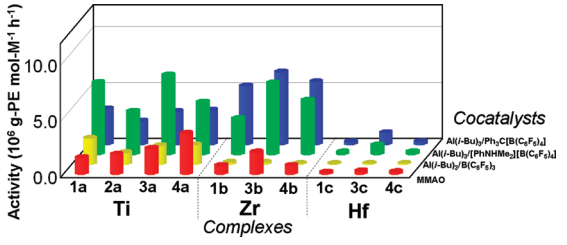

Figure 1. Ethylene homopolymerization catalyzed by several complexes and several cocatalysts (red, MMAO; yellow, $Al(i\text{-}Bu)_3/B(C_6F_5)_3$; green, $Al(i\text{-}Bu)_3/[PhNHMe_2][B(C_6F_5)_4]$; blue, $Al(i\text{-}Bu)_3/Ph_3CB(C_6F_5)_4$; ethylene pressure, 0.6 MPa).

dx.doi.org/10.1021/ma2024107 | *Macromolecules* 2012, 45, 1758−1769

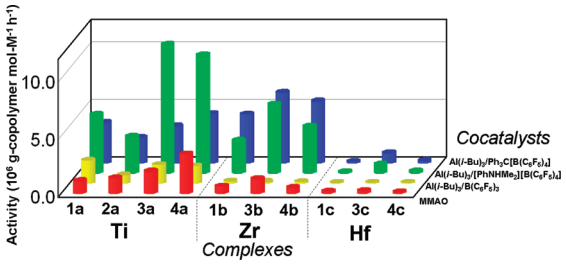

Figure 2. Ethylene/1-hexene copolymerization catalyzed by several complexes and several cocatalysts (red, MMAO; yellow, Al(*i*-Bu)$_3$/B(C$_6$F$_5$)$_3$; green, Al(*i*-Bu)$_3$/[PhNHMe$_2$][B(C$_6$F$_5$)$_4$]; blue, Al(*i*-Bu)$_3$/Ph$_3$CB(C$_6$F$_5$)$_4$; ethylene pressure, 0.6 MPa).

Table 1. Ethylene Homopolymerization and Ethylene/1-Hexene Copolymerization Catalyzed by Several Complexes with Cocatalyst (Al(*i*-Bu)$_3$/[PhNHMe$_2$][B(C$_6$F$_5$)$_4$]) by Using a High-Throughput Screening System for 20 min[a]

		activity	
entry	complex	homopolymerization, 10^6 g of PE mol M^{-1} h^{-1}	copolymerization, 10^6 g of copolymer mol M^{-1} h^{-1}
1	**1a**	6.5	5.1
2	**2a**	3.9	3.3
3	**3a**	7.2	11.3
4	**4a**	4.7	10.4
5	**1b**	3.3	2.9
6	**3b**	6.4	6.4
7	**4b**	4.9	4.9
8	**1c**	0.2	0.2
9	**3c**	0.9	0.9
10	**4c**	0.2	0.3

[a]Conditions: polymerization temperature 40 °C, polymerization time 20 min, ethylene pressure 0.6 MPa, (in the case of copolymerization: 60 μL 1-hexene added), toluene (total) 5 mL, Al(*i*-Bu)$_3$/complex/[PhNHMe$_2$][B(C$_6$F$_5$)$_4$] = 400/1/3, and complex = 0.1 μmol.

The results indicate that a combination of Al(*i*-Bu)$_3$ and [PhNHMe$_2$][B(C$_6$F$_5$)$_4$] is the best cocatalyst for both ethylene polymerization (activity: 7.2 × 10^6 g of PE mol Ti^{-1} h^{-1} using **3a**, Figure 1) and ethylene/1-hexene copolymerization (activity: 1.1 × 10^7 g of copolymer mol Ti^{-1} h^{-1} using **3a**, Figure 2). The activities for the copolymerization of ethylene and 1-hexene using 1-aza-1,3-butadienyl−imido titanium complexes (**3a**, **4a**) were higher than those for ethylene homopolymerization. This phenomenon, so-called "comonomer effect" is often observed in metallocene catalysts.[27] These results indicate that the catalytic activities of titanium, zirconium and hafnium complexes decrease in this order, and in the same metal systems, the catalytic activities also decrease in the order of LiCl(tmeda)-coordinated 1-aza-1,3-butadienyl−imido complexes (**3a**, **3b**, **3c**), THF-coordinated 1-aza-1,3-butadienyl−imido complexes (**4a**, **4b**, **4c**), tetravalent metal β-diketiminates (**1a**, **1b**, **1c**) and trivalent titanium β-diketimiate **2a** (Chart 3).

The β-diketiminato and imido complexes bearing a Tbt group showed good activity (Table 1, up to 1.1 × 10^7 g of copolymer mol Ti^{-1} h^{-1}) for synthesis of polyolefins using a non-metallocene system. A number of examples of active catalysts for ethylene polymerization with early transition metals bearing β-diketiminato ligands have been reported, but their activities in olefin polymerization are generally moderate to low.[12,28,29] High catalytic activity for ethylene polymerization catalyzed by β-diketiminato complexes has been reported by

Chart 3. Tendency of Catalytic Activities

Ti Complexes > Zr Complexes >> Hf Complexes

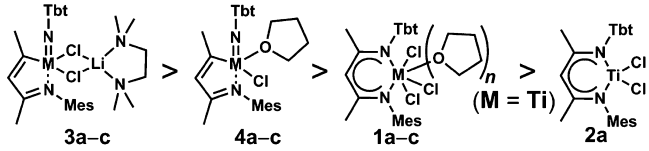

Collins and co-workers.[30] They synthesized mono-, bis(β-diketiminato) complexes and monocyclopentadienyl β-diketiminato mixed complexes of group 4 metals, and found that monocyclopentadienyl β-diketiminato zirconium complexes having an electron-withdrawing group in the *N*-aryl moiety showed the highest catalytic activity for ethylene polymerization (up to 1.1 × 10^7 g of PE mol Zr^{-1} h^{-1}).

As for ethylene polymerization, terminal imido complexes of group 4 metal usually show low activity[31−33] except for some examples such as tris(pyrazolyl)methane-supported terminal imido complexes of titanium, which show a dramatically different activities depending on the imino groups on the *N*-terminal.[34] The most active catalysts (5.0 × 10^7 g of PE mol Ti^{-1} h^{-1}) are found for bulky, electron-donating alkyl *N*-substituents (adamantyl, *t*-Bu and 1,1,3,3-tetramethylbutyl groups).

On the other hand, the 1-aza-1,3-butadienyl−imido complexes of Ti(IV), Zr(IV), V(III) and Nb(V) were recently reported by Mindiola,[35] Stephan,[36] Tsai,[37] and Bergman group.[38] However, they did not mention the catalytic activity for olefin polymerization. Thus, the high catalytic activities of the β-diketiminato and 1-aza-1,3-butadienyl−imido complexes of group 4 metals bearing a Tbt group for olefin polymerization are very interesting.

Formation of Ultrahigh Molecular-Weight Ethylene/1-Hexene Copolymer. We carried out the ethylene/1-hexene copolymerization catalyzed by the new complexes by stirring for a long time (60 min) at 2.5 MPa of ethylene pressure, and compared their activities with those using **Zr−Dip2** [zirconium β-diketiminate bearing two bulky Dip (2,6-diisopropylphenyl) groups on the *N*-terminals],[29] **CGC−Ti**,[39] and **PHENICS** (Table 2, Chart 4).[40]

CGC−Ti (developed by Dow and Exxon) and **PHENICS** (developed by Sumitomo Chemical) catalysts exhibited an excellent catalytic performance of producing high molecular weight ethylene/1-hexene copolymers with high 1-hexene contents due to the open nature of the catalyst active site that allowed them to incorporate sterically large monomers into a growing polymer chain.

The copolymerization were examined by using the complexes (**1a**, **1b**, **2a**, **3a**, **3b**, **3c**, and **4a**) combined with cocatalysts of Al(*i*-Bu)$_3$ and [PhNHMe$_2$][B(C$_6$F$_5$)$_4$]. This copolymerization became to take place violently after stirring for 40 min. The titanium 1-aza-1,3-butadienyl−imido complex **3a** produced ultrahigh molecular-weight copolymer with M_w 3.5 × 10^6 (M_w/M_n 5.5) determined by gel permeation chromatography (GPC). Much high molecular weight copolymers were obtained using the complexes (**1a**, **1b**, **3b**, **3c**, and **4a**). However, we were not able to determine either their M_w using GPC or their viscosity-average molecular weight (M_η) based on [η] due to their extremely low solubility in *o*-dichlorobenzene, which is indicative of their exceptionally ultrahigh molecular-weight. The copolymers was also insoluble in 1,2,4-trichlorobenzene at 152 °C. The general technique for studying the microstructure and evaluating α-olefin incorporation is ^{13}C NMR spectrum. However, we could not determine

dx.doi.org/10.1021/ma2024107 | *Macromolecules* 2012, 45, 1758−1769

Table 2. Ethylene and 1-Hexene Copolymerization Using Several Metal Complexes

entry	complex	activity, kg of copolymer mol M^{-1} h^{-1}	T_m (DSC), °C	M_w[c] × 10^4	M_w/M_n[c]	short chain branches[b]
1[a]	**1a**	580	136	*d*	*d*	12
2[a]	**2a**	trace				
3[a]	**3a**	1600	115	347	5.5	18
4[a]	**4a**	640	118	*d*	*d*	18
5[a]	**1b**	2240	128	*d*	*d*	11
6[a]	**3b**	3880	132	*d*	*d*	13
7[a]	**3c**	12	121	*d*	*d*	19
ref 1[a]	**Zr−Dip2**	420	131	450	4.5	0.0
ref 2[e]	**PHENICS**	140 000	108	188	4.3	20
ref 3[f]	**CGC−Ti**	130 000	108	111	3.8	20

[a]Reactor: 0.4 L autoclave. Conditions: polymerization temperature 40 °C, polymerization time 60 min, ethylene 2.5 MPa, 1-hexene 10 mL, toluene 190 mL, complex 2.5 μmol, Al(*i*-Bu)$_3$ 0.25 mmol, and [PhNHMe$_2$][B(C$_6$F$_5$)$_4$] 7.5 μmol. [b]Number of short chain branches per 1000 carbons determined by FT−IR. [c]Determined by GPC with polystyrene standard (conversion as PE: $M_w = 17.7 \times A_w$). [d]Cannot be determined because of less solubility. [e]The polymerization condition is similar to that of condition a except 1-hexene 4 mL, toluene 196 mL, complex 0.005 μmol, and [PhNHMe$_2$][B(C$_6$F$_5$)$_4$] 1.5 μmol. [f]The polymerization condition is similar to that of condition a except 1-hexene 8 mL, toluene 192 mL, complex 0.001 μmol, and [PhNHMe$_2$][B(C$_6$F$_5$)$_4$] 1.5 μmol.

Chart 4. Reference Complexes of Group 4 Metal

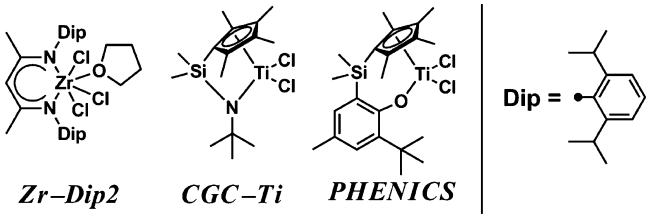

Zr−Dip2 *CGC−Ti* *PHENICS*

comonomer sequence distributions in ethylene/1-hexene copolymers due to less solubility in *o*-dichlorobenzene at 135 °C.

These ultrahigh-molecular weight ethylene/1-hexene copolymers represent the highest molecular weight hitherto known. The 1-hexene contents of copolymers in the use of the titanium complexes (**3a** and **4a**) and the hafnium complex (**3c**) are higher than those of copolymers in the use of the titanium complex (**1a**) and the zirconium complexes (**1b** and **3b**). We examined catalytic activity for ethylene/1-hexene copolymerization using 1-hexene amount as follow (**1a**, **1b**, **2a**, **3a**, **3b**, **3c**, **4a**, and **Zr−Dip2** (10 mL), **CGC−Ti** (8 mL), and **PHENICS** (4 mL)) because we wanted to obtain ethylene/1-hexene copolymers with the almost same 1-hexene content. The comonomer (1-hexene) reactivity decreases as follow: **PHENICS** > **CGC−Ti** > **3a**, **3c**, **4a** > **1a**, **1b**, **3b** ≫ **Zr−Dip2**. The ethylene/1-hexene copolymer obtained by **1a** showed a high melting point (T_m = 136 °C) and contained 12 short chain branches carbons per 1000 of polymer chain calculated from FT−IR spectrum.[41]

Chain termination pathway is governed by several factors such as temperature, solvent, and counteranion. Scheme 1 shows some chain termination reactions such as (a) direct β-hydride transfer from the propagating chain end to the coordinating monomer (Scheme 1a), (b) β-hydrogen elimination giving metal hydride (Scheme 1b) and transfer to aluminum compounds (Scheme 1c).[42]

The reason for the formation of an ultrahigh molecular-weight copolymer might be interpreted in terms of the inhibition of chain termination by β-hydride transfer or β-hydrogen elimination due to the steric protection afforded by the Tbt group. This effect has also been observed by Brookhart and co-workers for Ni^{II} and Pd^{II} α-diiminato complexes on various *N*-terminals,[43] and is consistent with the calculations by Ziegler and co-workers,[44] which show that steric pressure promotes olefin insertion and disfavors β-hydrogen elimination.

Furthermore, ethylene/1-hexene copolymerization by the use of zirconium β-diketiminate (**Zr−Dip2**) bearing two 2,6-diisopropylphenyl (Dip) groups on the *N*-terminals afforded only UHMW−PE.[29] Novak and co-workers have already reported the preparation of zirconium β-diketiminate bearing on *N*-terminals of various R-groups (Me, Ph, *o*-tolyl, 2,6-dimethylphenyl, and Dip) and catalytic activities for ethylene polymerization.[29] However, the molecular weight of PEs have not been described by Novak and co-workers. Collins and co-workers reported the molecular weight of PEs were low ($M_n \sim 8 \times 10^4$) catalyzed by the zirconium β-diketiminates bearing two Ph and *p*-CF$_3$C$_6$H$_4$ groups on *N*-terminals.[30]

Scheme 1. Representative Chain Termination Pathways in Polymerization Catalyzed by Group 4 Metal Complexes

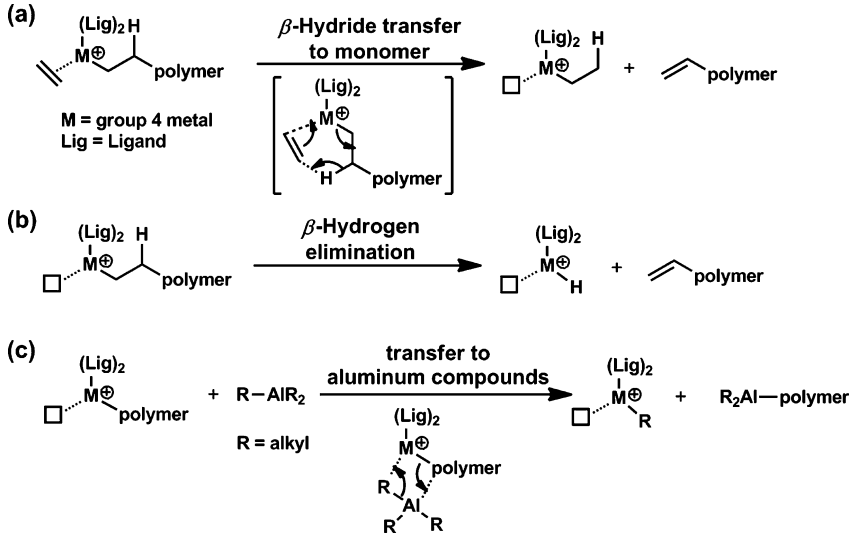

dx.doi.org/10.1021/ma2024107 | *Macromolecules* 2012, 45, 1758−1769

This phenomenon is most likely explained by supposing that, in the case of **Zr−Dip2**, two bulky Dip groups on the *N*-terminals prevented a 1-hexene molecule from approaching to the zirconium center, whereas, in the case of **1b**, a 1-hexene molecule is able to approach to the zirconium center from the side of less bulky Mes group (Scheme 2).

Scheme 2. View Showing a Frame Format for Ethylene and 1-Hexene Approach to Zirconium Center [(a) Zr−Dip2 (b) 1b]

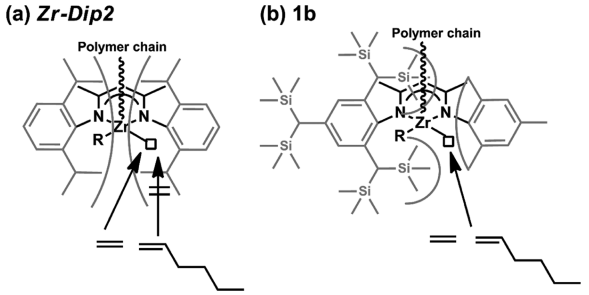

In fact, judging from the space-filing model representations (X-ray analysis) of **1b** and **3b**, there seems to be enough space around the zirconium centers of **1b** and **3b** relative to that of **Zr−Dip2** because of the cavity afforded by the combination of the Tbt and Mes groups (Figure 3).[26a]

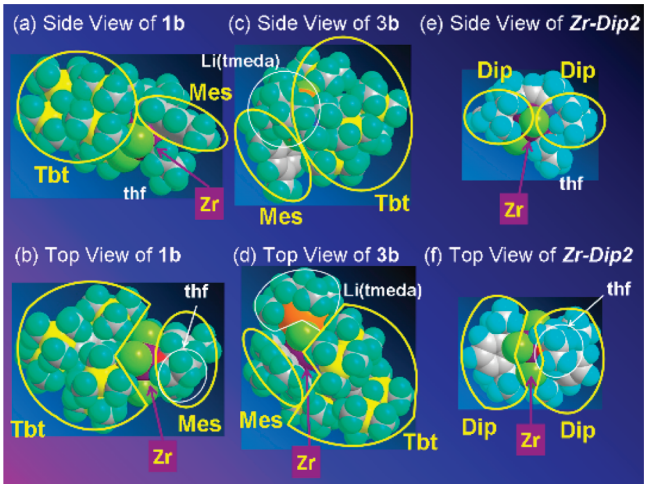

Figure 3. Space-filling model representations of zirconium complexes **1b**, **3b**, and **Zr−Dip2** (gray, C; light green, H; orange, Li; blue, N; red, O; yellow, Si; greenish yellow, Cl; purple, Zr).

Effect on the Polymerization Temperature. The temperature effect (from 40 to 180 °C) on the ethylene/1-hexene copolymerization was examined (Table 3, Figure 4).

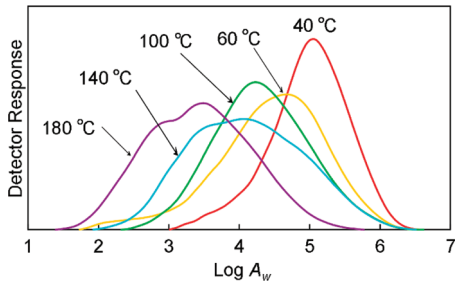

Figure 4. GPC traces of ethylene/1-hexene copolymers obtained by **3a**/Al(i-Bu)$_3$/[PhNHMe$_2$][B(C$_6$F$_5$)$_4$] under several polymerization temperature (red, 40 °C; yellow, 60 °C; green, 100 °C; blue, 140 °C; purple, 180 °C).

On increasing polymerization temperature from 40 to 180 °C, the catalytic activity for **3a** was found to remarkably decrease. The reduction of catalyst activity in the polymerization performed at higher temperature could be attributed to a catalyst irreversible deactivation rather than increase of chain propagation rate. A very high molecular weight with M_w = 1.1 × 10^6 was achieved even for the copolymer formed at 140 °C. The GPC trace at 40 °C is not symmetric and bears a shoulder toward low molecular weight, which is indicative of more than one active species. As a matter of course, the number of active species at 60, 100, 140, and 180 °C is more than that of active species at 40 °C.

The M_w/M_n values correlating with the molecular-weight distribution exhibit a substantial increase from 5.5 to 24.2 when the temperature increases from 40 to 60 °C, and then decrease to 9.7 at 100 °C and increase again to 19.9 at 140 °C. Although there appears no clear reason at this moment why the M_w/M_n values display this irregular change, the separations of broad peaks in GPC curves into normal curves (the Flory component) may provide an explanation for this phenomenon (Figure 5).

The model of multiple active sites on this catalyst may be described as follows: each type of active center produces a polymer characterized by a most probable distribution curve. The GPC traces of the whole polymer sample would be formed by adding together the most probable distribution curves of different active centers.[45] The mathematical expression of the most probable distribution is shown in the following eq 1:

$$W(\ln M) = ky^2M^2 \exp(-yM) \quad (1)$$

where $W(\ln M)$ is the nongeneralized weight fraction, as the function of ln M; y is a parameter defining the average molecular weight; and k is a parameter that defines the peak area. Through several regression calculations, the parameters (k and y) of a suitable number of Flory curves were determined and the sum of these curves was determined to fit the experimental data of

Table 3. Temperature Effect of Ethylene/1-Hexene Copolymerization[a]

entry	complex	polymerization temperature, °C	activity, kg of copolymer mol Ti^{-1} h^{-1}	T_m (DSC), °C	[η], dLg^{-1}	M_w[c] × 10^4	M_w/M_n[c]	short chain branches[b]
1	**3a**	40	1600	115	*d*	347	5.5	18
2	**3a**	60	1400	121	11.6	166	24.2	17
3	**3a**	100	1280	125	9.1	122	9.7	17
4	**3a**	140	600	129	6.9	112	19.9	14
5	**3a**	180	200	131	2.8	19	13.7	6

[a]Reactor: 0.4 L autoclave. Conditions: polymerization time 60 min, ethylene 2.5 MPa, 1-hexene 10 mL, toluene 190 mL, complex 2.5 μmol, Al(*i*-Bu)$_3$ 0.25 mmol, and [PhNHMe$_2$][B(C$_6$F$_5$)$_4$] 7.5 μmol. [b]Number of short chain branches per 1000 carbons determined by FT−IR. [c]Determined by GPC with polystyrene standard (conversion as PE: M_w = 17.7 × A_w). [d]Cannot be determined because of less solubility.

dx.doi.org/10.1021/ma2024107 | *Macromolecules* 2012, 45, 1758−1769

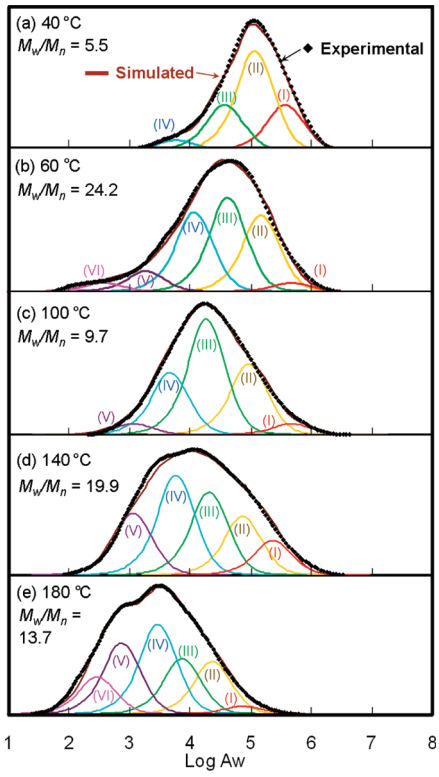

Figure 5. Segmentation of GPC curves into from 4 to 6 normal distribution curves [(a) polymerization temperature, 40 °C; (b) polymerization temperature, 60 °C; (c) polymerization temperature, 100 °C; (d) polymerization temperature, 140 °C; (e) polymerization temperature: 180 °C; black, experimental GPC traces; brown, simulated GPC traces (the sum of the Flory components); red, yellow, green, blue, violet, and pink, the Flory components].

catalysts (Figure 5). It is found that all the GPC traces can be deconvoluted into from four to six Flory components. Each Flory component should correspond to polymers produced on a certain type of active center. Therefore, it is possible to deduce the distribution of active centers and its changes by tracing the position and relative peak intensity of each deconvoluted Flory component. The six most-probable peaks were named as peaks I, II, III, IV, V, and VI, respectively.

The separation of GPC curve at 40 °C shows that the copolymers produced by the active species II are predominant at this temperature. The GPC curve at 60 °C is separated to six normal curves, derived from three predominant active species (II, III, and IV) and minor two active species (V and VI), which provide the lower molecular-weight copolymers. Since the existence of many active species results in the wide distribution of the molecular weight of copolymers, these separations may explain the increase of the M_w/M_n values from 5.5 to 24.2 with the temperature increase from 40 to 60 °C. The separation of GPC curve at 100 °C suggests that active species III is predominant relative to active species II and IV. The smaller number of active species at 100 °C than that at 60 °C may explain the smaller M_w/M_n value at 100 °C (9.7) than that at 60 °C (24.2). Because of the similar reason, the M_w/M_n value at 140 °C (19.9) is larger than that at 100 °C (9.7).

The Table 3 showed that the higher polymerization temperature resulted in the increase in the T_m values despite the decrease in the M_w values with keeping almost the same short chain branches. Although there is no clear reason for these phenomena, a possible explanation is as follows. The copolymer at 40 °C bears long chain branches and the copolymers at 60 and 100 °C do not almost have them. Therefore, the T_m value at 40 °C is lower than those at 60 and 100 °C.

Effect on the Ethylene Pressure. The ethylene pressure effect (from 0.4 to 4.0 MPa) on the ethylene/1-hexene copolymerization was examined at 40 °C using **3a**/Al(*i*-Bu)$_3$/[PhNHMe$_2$][B(C$_6$F$_5$)$_4$] catalyst system compared with **CGC−Ti** as a reference. (Table 4, Figure 6).

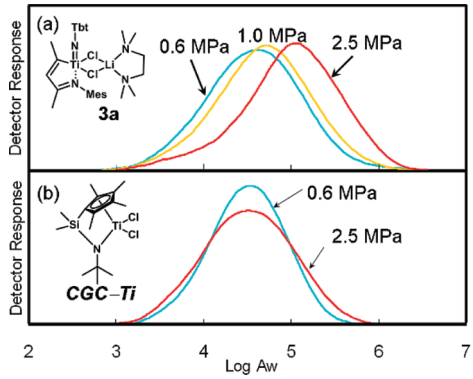

Figure 6. GPC traces of ethylene/1-hexene copolymers obtained by **3a** and **CGC−Ti** using cocatalysts of Al(*i*-Bu)$_3$ and [PhNHMe$_2$][B(C$_6$F$_5$)$_4$] under several ethylene pressure [(a) **3a**; (b) **CGC−Ti**; blue, 0.6 MPa; yellow, 1.0 MPa; red, 2.5 MPa].

The catalytic activity of **3a** was found to increase as the ethylene pressure increases from 0.6 to 2.5 MPa, giving higher molecular weight for the resulting copolymer (Figure 7). Higher ethylene pressure means the enhancement of ethylene concentration in toluene, which should be the main reason for the increase in the catalytic activity. The detailed analyses on the

Table 4. Ethylene Pressure Effect of Ethylene/1-Hexene Copolymerization

entry	complex	ethylene pressure, MPa	activity, kg of copolymer mol Ti^{-1} h^{-1}	T_m (DSC), °C	M_w[c] × 10^4	M_w/M_n[c]	short chain branches[b]
1[a]	**3a**	0.6	880	78	145	4.7	35
2[a]	**3a**	1.0	1200	92	177	4.7	22
3[a]	**3a**	2.5	1600	115	347	5.5	18
4[a]	**3a**	4.0	1120	123	*d*	*d*	18
ref 1[e]	**CGC−Ti**	0.6	100 000	71	89	2.7	34
ref 2[e]	**CGC−Ti**	2.5	130 000	108	111	3.8	20

[a]Reactor 0.4 L autoclave, conditions: polymerization temperature 40 °C, polymerization time 60 min, 1-hexene 10 mL, toluene 190 mL, complex 2.5 μmol, Al(*i*-Bu)$_3$ 0.25 mmol, [PhNHMe$_2$][B(C$_6$F$_5$)$_4$] 7.5 μmol. [b]Number of short chain branches per 1000 carbons determined by FT−IR. [c]Determined by GPC with polystyrene standard (conversion as PE: M_w = 17.7 × A_w). [d]Cannot be determined because of less solubility. [e]The polymerization condition is similar to that the condition a except 1-hexene 8 mL, toluene 192 mL, complex 0.001 μmol and [PhNHMe$_2$][B(C$_6$F$_5$)$_4$] 1.5 μmol.

dx.doi.org/10.1021/ma2024107 | *Macromolecules* 2012, 45, 1758−1769

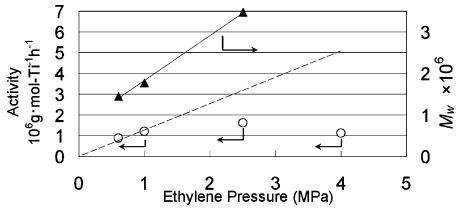

Figure 7. Catalytic activity and molecular weight of for ethylene/1-hexene copolymer obtained by **3a**/Al(i-Bu)$_3$/[PhNHMe$_2$][B(C$_6$F$_5$)$_4$] under several ethylene pressure (○, activity; ▲, molecular weight of copolymer (M_w); broken line, linear approximation from 0.6 to 1.0 MPa of ethylene pressure).

increase in the catalytic activity turned out that increasing ethylene pressure from 1.0 to 2.5 MPa caused a considerable growth in the catalytic activity, but the growth was not linear. Similar relations were also noted for polymerization with the use of other catalytic systems.[46] In contrast, the catalytic activity of **3a** was found to decrease as the ethylene pressure increases from 2.5 to 4.0 MPa (Figure 7). This behavior might be explained by the insufficient diffusion of the monomer caused by high-viscosity of polymerization solution and/or polymer precipitation, resultant from less soluble ultrahigh molecular weight of copolymer.

The molecular weight of the copolymers for **3a** received a considerable effect by changing the ethylene pressure from 0.6 to 2.5 MPa compared with the molecular-weight of the copolymers for **CGC−Ti**. In the case of **3a**, the nearly linear relation of the M_w values with ethylene pressure was found within the pressure range of 0.6−2.5 MPa (Figure 7). Olefin reactivities mostly depended on the structure of alkyl groups R attached to the double bond in α-olefin (CH_2=CH_2−R) molecules [relative olefin reactivities with Ziegler−Natta catalysts: 80 (R = H) and 1 (R = *n*-hexyl)].[47] The insertion of ethylene to the active center is predominant to the insertion of 1-hexene in the case of both **CGC−Ti** and **3a**. The rate of the chain termination reaction in the case of **3a** is slower than that in the case of **CGC−Ti** due to steric hindrance by an extremely bulky substituent, Tbt group. Therefore, the ultrahigh molecular weight copolymer ($M_w > 4 \times 10^6$) can be formed by using **3a** when the ethylene pressure is 4.0 MPa.

The DSC analysis indicated that the T_m values of copolymers increased gradually along with ethylene pressure from 0.6 to 4.0 MPa. The introduction of 1-hexene produces butyl branches which result in lower melting points than those of the linear PEs. The short chain branches decreased along with the increase in ethylene pressure from 0.6 to 2.5 MPa and the T_m value increased gradually. The reason for increasing the T_m value at 4.0 MPa of ethylene pressure relative to the T_m value at 2.5 MPa might be formation of ultrahigh molecular-weight ethylene/1-hexene copolymer although the values of the short chain branches were same in the both case of 2.5 and 4.0 MPa of ethylene pressure.

Catalytic Activities of β-Diketiminato Complexes of Titanium and Zirconium Bearing Cp and Cp* Ligands. Group 4 metal complexes bearing β-diketiminato and cyclopentadienyl ligands [M(C$_5$R$_5$)Cl$_2${TbtNC(Me)CHC(Me)NMes}] (**5a**: *M* = Ti, *R* = H, **5b**: *M* = Ti, *R* = Me, **6a**: *M* = Zr, *R* = H, **6b**: *M* = Zr, *R* = Me) is prepared by the reaction of a lithium β-diketimiante [Li{TbtNC(Me)CHC(Me)NMes}] with MCl$_3$(C$_5$R$_5$) (Scheme 3).

The copolymerization of ethylene and 1-hexene was examined by using complexes (**5a**, **5b**, **6a**, and **6b**) in the

Scheme 3. Preparation of Titanium and Zirconium β-Diketiminates Bearing Cp and Cp* Ligands

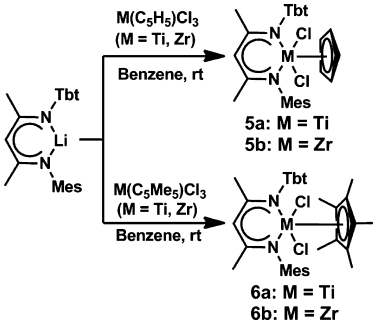

presence of cocatalysts of Al(*i*-Bu)$_3$ and [PhNHMe$_2$][B(C$_6$F$_5$)$_4$] (Table 5). These results indicated that Cp*-supported titanium

Table 5. Ethylene and 1-Hexene Copolymerization Catalyzed with Complexes/Al(*i*-Bu)$_3$/[PhNHMe$_2$][B(C$_6$F$_5$)$_4$]

entry	complex	activity, kg of copolymer mol M^{-1} h^{-1}	T_m (DSC), °C	M_w[c] × 10^4	M_w/M_n[c]	short chain branches[b]
1[a]	**5a**	9600	128	38	9.3	11
2[a]	**6a**	33 600	108/118	78	9.2	18
3[a]	**5b**	18 400	134	52	3.9	11
4[a]	**6b**	30 800	130	153	3.2	14
ref 1[e]	**1a**	576	136	*d*	*d*	12
ref 2[e]	**1b**	2240	128	*d*	*d*	11
ref 3[f]	**CGC−Ti**	130 000	108	111	3.8	20

[a]Reactor: 0.4 L autoclave. Conditions: polymerization temperature 40 °C, polymerization time 60 min, ethylene pressure 2.5 MPa, 1-hexene 10 mL, toluene 190 mL, complex 0.25 μmol, Al(*i*-Bu)$_3$ 0.25 mmol, and [PhNHMe$_2$][B(C$_6$F$_5$)$_4$] 1.0 μmol. [b]Number of short chain branches per 1000 carbons determined by FT−IR. [c]Determined by GPC with polystyrene standard (conversion as PE: M_w = 17.7 × A_w). [d]Cannot be determined because of less solubility. [e]The polymerization condition is similar to that the condition a except complex 2.5 μmol and [PhNHMe$_2$][B(C$_6$F$_5$)$_4$] 7.5 μmol. [f]The polymerization condition is similar to that the condition a except 1-hexene 8 mL, toluene 192 mL, complex 0.001 μmol, and [PhNHMe$_2$][B(C$_6$F$_5$)$_4$] 1.5 μmol.

β-diketiminate **6b** show almost 14 times higher catalytic activity for ethylene/1-hexene copolymerization (activity: 3.1 × 10^7 g of copolymer mol Zr^{-1} h^{-1}) than **1b**.

Such high activity may suggest the η^5-coordination mode of the β-diketiminato ligand in **5a**, **5b**, **6a**, and **6b** as in the case of [TiCl$_2$(η^5-Cp){η^5-[DipNC(Me)]$_2$CH}].[30] The η^5-coordination mode of the β-diketiminato ligand in **5a**, **5b**, **6a**, and **6b** might lead to the less steric protection of the Tbt groups, and hence **5a**, **5b**, **6a** and **6b** could produce the relatively lower molecular-weight copolymer ($M_w < 1.5 \times 10^6$) compared with **1a** and **1b** ($M_w > 4 \times 10^6$).

Catalytic Activities of 1-Aza-2-butenyl−Imido Complexes Bearing Phosphonium Ylide. We have successfully transformed the 1-aza-2-buteneyl complexes [Ti(=NTbt)Cl{C(Me)(PMe$_3$)CHC(Me)NMes}] (**7a**) and [Ti(=NTbt)Cl{C(Me)(PMe$_2$CH$_2$CH$_2$PMe$_2$)CHC(Me)NMes}] (**8a**) bearing a phosphonium ylide moiety from the 1-aza-1,3-butadienyl complex (**3a**) just by adding PMe$_3$ and Me$_2$PCH$_2$CH$_2$PMe$_2$, respectively (Scheme 4).[26b] The copolymerization of ethylene

dx.doi.org/10.1021/ma2024107 | *Macromolecules* 2012, 45, 1758−1769

Scheme 4. Preparation of Titanium Complexes Bearing 1-Aza-2-butenyl−Imido and Phosphonium Ylide

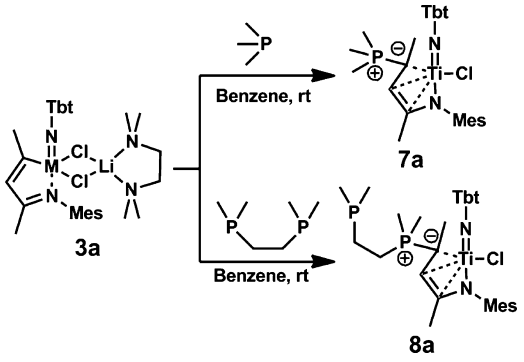

and 1-hexene was also examined by using the 1-aza-2-butenyl-imido titanium complexes (**7a** and **8a**) in the presence of cocatalyst Al(*i*-Bu)$_3$ and [PhNHMe$_2$][B(C$_6$F$_5$)$_4$] (Table 6).

These results indicated that the catalytic activity for ethylene/1-hexene copolymerization of the 1-aza-2-butenyl complex **7a** (activity: 2.2 × 10^6 g of copolymer mol Ti^{-1} h^{-1}) is higher than that of the 1-aza-1,3-butadienyl complex **3a** (activity: 1.6 × 10^6 g of copolymer mol Ti^{-1} h^{-1}) at 2.5 MPa of ethylene pressure, whereas the catalytic activity of **8a** for ethylene/1-hexene copolymerization is lower than those of **3a** and **7a**. The reason for the high activity in the case of **7a** relative to **3a** and **4a** is interpreted by changing electron density of the C$_3$N moiety which of **7a** is more negative than that of **3a** determined by the DFT calculations.[26b] On the other hand, the reason for the low activity in the case of **8a** is most likely interpreted in terms of the coordination of phosphorus atom (not ylide part) of Me$_2$PCH$_2$CH$_2$P$^+$Me$_2$ to cationic titanium center during the chain propagation. The catalytic activities and M_w of ethylene/1-hexene copolymers using **7a** and **8a** were found to increase as the ethylene pressure increases from 0.6 to 2.5 MPa. The complexes **7a** and **8a** can also afford ultrahigh molecular-weight ethylene/1-hexene copolymer at 2.5 MPa. However, 1-hexene incorporation in the copolymer obtained by the use of **7a** and **8a** are less than that in the case of **3a** under the same conditions.

CONCLUSION

(1) *β*-Diketiminato, 1-aza-1,3-butadienyl, and 1-aza-2-butenyl complexes of group 4 metals bearing an extremely bulky substituent (Tbt) showed high catalytic activity for making polyolefins (up to 1.1 × 10^7 g of PE mol Zr^{-1} h^{-1}). (2) Ultrahigh molecular-weight ethylene/1-hexene copolymers (M_w > 4 × 10^6, short chain branches C/1000C up to 19.0) were obtained by using the complexes (**1a**, **1b**, **3a**, **3b**, **3c**, **4a**, **7a**, and **8a**). The ethylene/1-hexene copolymer obtained by **1a** showed a high melting point (T_m 136 °C) and contained 12 short chain branches carbons per 1000 of polymer chain calculated from FT−IR spectrum. (3) The molecular-weight of copolymers increased as the ethylene pressure increased from 0.6 to 4.0 MPa in the case of **3a**. (4) The catalytic activities decreased and the molecular weight distribution irregularly changed but tended to broaden as the polymerization temperature increased from 40 °C to higher temperature in the case of **3a**. Even the copolymer formed at 140 °C was found to have a very high molecular weight of M_w = 1.1 × 10^6, although the catalytic activity showed remarkable decrease at the higher temperature. (5) The 1-hexene contents in copolymers obtained by the use of titanium complexes (**1a** and **3a**) were higher than those in the case of zirconium complexes (**1b** and **3b**). (6) The tendency of catalytic activities of various complexes for ethylene/1-hexene copolymerization and molecular weight of ethylene/1-hexene copolymer are shown in Chart 5.

The physical properties such as tensile strength impact and puncture resistance of ultrahigh molecular-weight ethylene/1-hexene copolymers are under investigation.

EXPERIMENTAL SECTION

Materials. Unless otherwise described, all operations were performed in an MBRAUN Labmaster glovebox under an atmosphere of purified argon. Celite was activated at 200 °C under vacuum for 1 day. Cyclopentadienyltitanium trichloride, cyclopentadienylzirconium trichloride, pentamethylcyclopentadienyltitanium trichloride, pentamethylcyclopentadienylzirconium trichloride were purchased from AZmax. Co. Ltd. Isobutylmethylaluminoxane (MMAO; MMAO−3A 5.7 wt % Al in toluene) and triisobutylaluminum (1 M solution in toluene) were purchased from Tosoh Finechem. Co. Ltd. Tris(pentafluorophenyl)borane, Trityl tetrakis(pentafluorophenyl)borate and *N*,*N*-dimethylanilinium tetrakis(pentafluorophenyl)borate were purchased from Asahi Glass Co. Ltd. and used as 5.0 mM and 1.0 mM toluene solutions. [TiCl$_3$\{TbtNC(Me)CHC(Me)NMes\}] (**1a**), [TiCl$_2$\{TbtNC(Me)CHC(Me)NMes\}] (**2a**), [Ti(=NTbt)Cl$_2$\{C(Me)CHC(Me)NMes\}Li(Me$_2$NCH$_2$CH$_2$NMe$_2$)] (**3a**), [Ti(=NTbt)Cl\{C(Me)CHC(Me)NMes\}(thf)] (**4a**), [ZrCl$_3$\{TbtNC(Me)CHC(Me)NMes\}(thf)] (**1b**), [Zr(=NTbt)Cl$_2$\{C(Me)CHC(Me)NMes\}Li(Me$_2$NCH$_2$CH$_2$NMe$_2$)] (**3b**), [Zr(=NTbt)Cl\{C(Me)CHC(Me)NMes\}(thf)] (**4b**), [HfCl$_3$\{TbtNC(Me)CHC(Me)NMes\}(thf)] (**1c**), [Hf(=NTbt)Cl$_2$\{C(Me)CHC(Me)NMes\}Li(Me$_2$NCH$_2$CH$_2$NMe$_2$)] (**3c**), and [Hf(=NTbt)Cl\{C(Me)CHC(Me)NMes\}(thf)] (**4c**) were prepared according to the methods in the literature.[26a] [Ti(=NTbt)Cl\{C(Me)(PMe$_3$)CHC(Me)NMes\}] (**7a**), and [Ti(=NTbt)Cl\{C(Me)(PMe$_2$CH$_2$CH$_2$PMe$_2$)CHC(Me)NMes\}] (**8a**) were prepared according to the methods in the literature.[26b] Li\{TbtNC(Me)CHC(Me)NMes\}],[48] [ZrCl$_3$\{[DipNC(Me)]$_2$CH\}(thf)] (**Zr−Dip2**),[29] **CGC−Ti**,[39] and **PHENICS**,[40] were prepared according to the methods in the literatures, respectively. ^{1}H NMR (300 MHz) and ^{13}C NMR (75 MHz) spectra were recorded on a

Table 6. Ethylene and 1-Hexene Copolymerization Catalyzed with Complexes/Al(*i*-Bu)$_3$/[PhNHMe$_2$][B(C$_6$F$_5$)$_4$][a]

entry	complex	ethylene pressure, MPa	activity, kg of copolymer mol Ti^{-1} h^{-1}	T_m (DSC), °C	M_w[c] × 10^4	M_w/M_n[c]	short chain branches[b]
1	**7a**	0.6	720	82/104	228	4.2	14
2	**7a**	2.5	2240	120	446	5.4	3
3	**8a**	0.6	180	77/115	191	13	25
4	**8a**	2.5	920	122	423	9.2	3
ref 1	**3a**	0.6	880	78/116	145	4.7	35
ref 2	**3a**	2.5	1600	115	347	5.5	18
ref 3	**4a**	2.5	640	118	*d*	*d*	18

[a]Reactor: 0.4 L autoclave. Conditions: polymerization temperature 40 °C, polymerization time 60 min, 1-hexene 10 mL, toluene 190 mL, complex 0.25 μmol, Al(*i*-Bu)$_3$ 0.25 mmol, and [PhNHMe$_2$][B(C$_6$F$_5$)$_4$] 1.0 μmol. [b]Number of short chain branches per 1000 carbons determined by FT−IR. [c]Determined by GPC with polystyrene standard (conversion as PE: M_w = 17.7 × A_w). [d]Cannot be determined because of less solubility.

dx.doi.org/10.1021/ma2024107 | *Macromolecules* 2012, 45, 1758−1769

Chart 5. Tendency of Catalytic Activities and Molecular Weight of Ethylene/1-Hexene Copolymer Using β-Diketiminato, 1-Aza-1,3-butadienyl−Imido, and 1-Aza-2-butenyl−Imido Titanium Complexes

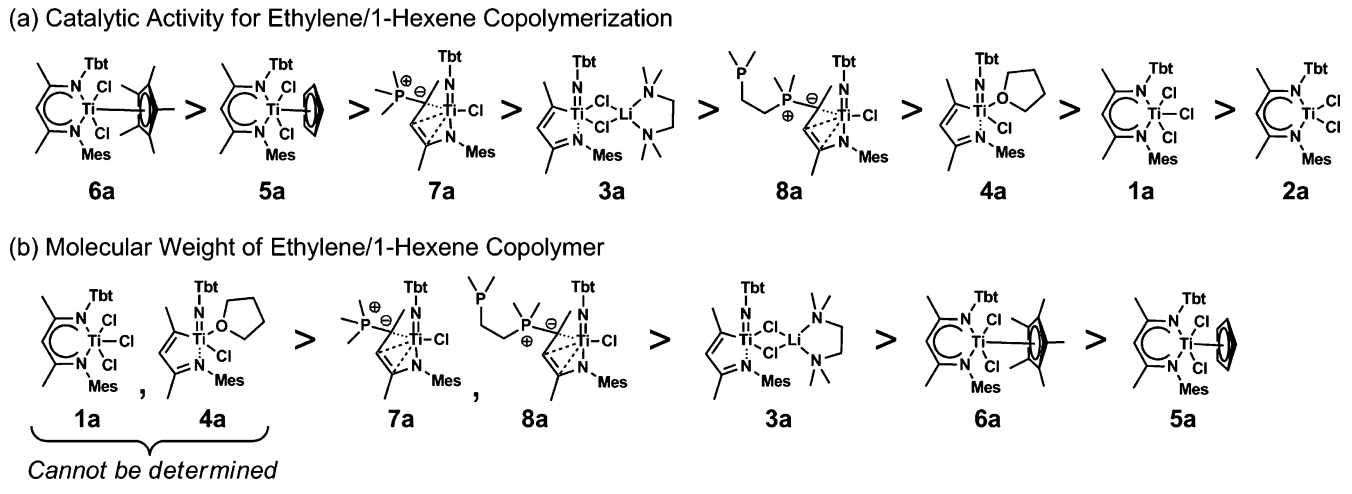

JEOL JNM AL-300 spectrometer. The ^{1}H NMR chemical shifts were reported with reference to the internal residual C_6D_5H (7.15 ppm). The ^{13}C NMR chemical shifts were reported with reference to the carbon-13 signal of C_6D_6 (128.0 ppm). Multiplicity of signals in ^{13}C NMR spectra was determined by DEPT techniques. Melting points were determined on a Yanaco micro melting point apparatus and are uncorrected. Elemental analyses were carried out at the Microanalytical Laboratory of the Institute for Chemical Research, Kyoto University.

Synthesis of [TiCpCl$_2${TbtNC(Me)CHC(Me)NMes}] (5a). A solution of [Li{TbtNC(Me)CHC(Me)NMes}] (40.0 mg, 51.7 μmol) in benzene (1 mL) was added to a slurry of pentamethylcyclopentadienyltitanium trichloride (13.6 mg, 62.0 μmol) in benzene (1 mL), and the reaction mixture turned dark red. After stirring for 1 d, the solvent was removed under reduced pressure. Toluene was added to the red residue, and the filtration through Celite gave a dark red solution. The solution was concentrated by evaporation and recrystallized from *n*-hexane/toluene at −40 °C, yielding dark red crystals. [TiCpCl$_2${TbtNC(Me)CHC(Me)NMes}] (**5a**, 28.1 mg, 57%): mp 158−161 °C (dec). ^{1}H NMR (300 MHz, C_6D_6, 25 °C): δ 0.22 (s, 18H, Si*Me*$_3$), 0.24 (s, 18H, Si*Me*$_3$), 0.37 (s, 18H, Si*Me*$_3$), 1.48 (s, 1H, Tbt *p*-benzyl), 1.83 (s, 2H, Tbt *o*-benzyl), 2.04 (s, 6H, Mes *o*-*Me*), 2.06 (s, 3H, *Me*), 2.07 (s, 3H, *Me*), 2.44 (s, 3H, *Me*), 6.14 (s, 5H, C_5H_5), 6.22 (s, 1H, 3−C*H*), 6.63 (s, 2H, Mes *m*-*H*), 6.66 (br s, 2H, Tbt *m*-*H*). ^{13}C NMR (75 MHz, C_6D_6, 25 °C): δ 2.2 (q, Si*Me*$_3$), 2.9 (q, Si*Me*$_3$), 18.3 (q, *Me*), 19.0 (q, *Me*), 20.4 (q, Mes *o*-*Me*), 21.2 (d, Tbt *o*-benzyl), 22.5 (d, Tbt *o*-benzyl), 25.4 (q, *Me*), 29.3 (d, Tbt *p*-benzyl), 119.0 (s, C_5H_5), 127.9 (d, Tbt C_m), 128.9 (d, 3-CH), 129.2 (d, Tbt C_m), 129.9 (d, Mes C_m), 130.1 (s), 131.3 (s), 132.2 (s), 135.2 (s), 137.5 (s), 145.7 (s), 146.5 (s), 157.8 (s, *C*(N)), 167.1 (s, *C*(N)). Anal. Calcd for $C_{46}H_{82}N_2Si_6Cl_2Ti$: C, 58.13; H, 8.70; N, 2.95. Found: C, 58.00; H, 8.92; N, 2.93.

Synthesis of [ZrCpCl$_2${TbtNC(Me)CHC(Me)NMes}] (5b). A solution of [Li{TbtNC(Me)CHC(Me)NMes}] (40.1 mg, 51.7 μmol) in benzene (1 mL) was added to pentamethylcyclopentadienylzirconium trichloride (16.3 mg, 62.0 μmol), and the reaction mixture turned yellow. The procedure similar to that in the preparation of **5a** afforded the product as yellow crystals. [ZrCpCl$_2${TbtNC(Me)CHC(Me)NMes}] (**5b**, 38.2 mg, 74%): mp 182−184 °C (dec). ^{1}H NMR (300 MHz, C_6D_6, 25 °C): δ 0.22 (s, 18H, Si*Me*$_3$), 0.27 (s, 18H, Si*Me*$_3$), 0.29 (s, 18H, Si*Me*$_3$), 1.49 (s, 1H, Tbt *p*-benzyl), 1.91 (s, 6H, Mes *o*-*Me*), 1.96 (s, 2H, Tbt *o*-benzyl), 2.10 (s, 3H, *Me*), 2.20 (s, 3H, *Me*), 2.40 (s, 3H, *Me*), 5.93 (s, 1H, 3−C*H*), 6.02 (s, 5H, C_5H_5), 6.62 (br s, 2H, Tbt *m*-*H*), 6.66 (s, 2H, Mes *m*-*H*). ^{13}C NMR (75 MHz, C_6D_6, 25 °C): δ 1.8 (q, Si*Me*$_3$), 2.5 (q, Si*Me*$_3$), 18.6 (q, *Me*), 19.1 (q, *Me*), 20.8 (q, Mes *o*-*Me*), 21.2 (d, Tbt *o*-benzyl), 22.8 (d, Tbt *o*-benzyl), 25.8 (q, *Me*), 29.8 (d, Tbt *p*-benzyl), 119.2 (s, C_5H_5), 127.4 (d, Tbt C_m), 128.6 (d, 3-CH), 129.7 (d, Tbt C_m), 130.6 (d, Mes C_m), 130.9 (s), 131.5 (s), 132.5 (s), 135.9 (s), 137.9 (s), 145.6 (s), 145.9 (s), 158.9 (s, *C*(N)), 168.1 (s, *C*(N)). Anal. Calcd for $C_{46}H_{82}N_2Si_6Cl_2Zr$: C, 55.59; H, 8.32; N, 2.82. Found: C, 55.78; H, 8.38; N, 2.90.

Synthesis of [TiCp*Cl$_2${TbtNC(Me)CHC(Me)NMes}] (6a). A solution of [Li{TbtNC(Me)CHC(Me)NMes}] (80.1 mg, 103 μmol) in benzene (1 mL) was added to pentamethylcyclopentadienyltitanium trichloride (36.0 mg, 128 μmol), and the reaction mixture turned dark red. The procedure similar to that in the preparation of **5a** afforded the product as dark red crystals. [TiCp*Cl$_2${TbtNC(Me)CHC(Me)NMes}] (**6a**, 84.4 mg, 80%): mp 198−201 °C (dec). ^{1}H NMR (300 MHz, C_6D_6): δ 0.18 (s, 18H, Si*Me*$_3$), 0.20 (s, 18H, Si*Me*$_3$), 0.21 (s, 18H, Si*Me*$_3$), 1.39 (s, 1H, Tbt *p*-benzyl), 1.82 (s, 3H, *Me*), 1.89 (s, 3H, *Me*), 1.91 (s, 6H, C_5Me_5), 2.00 (s, 3H, *Me*), 2.05 (s, 2H, Tbt *o*-benzyl), 2.11 (s, 9H, C_5Me_5), 2.40 (s, 6H, Mes *o*-Me), 6.18 (s, 1H, 3−C*H*), 6.62 (br s, 2H, Tbt *m*-*H*), 6.72 (br, 2H, Mes *m*-*H*). ^{13}C NMR (75 MHz, C_6D_6, 25 °C): δ 1.0 (q, Si*Me*$_3$), 1.8 (q, Si*Me*$_3$), 14.0 (q, C_5Me_5), 14.2 (q, C_5Me_5), 18.0 (q, *Me*), 18.8 (q, *Me*), 20.4 (q, Mes *o*-*Me*), 20.8 (d, Tbt *o*-benzyl), 22.3 (d, Tbt *o*-benzyl), 25.2 (q, *Me*), 29.6 (d, Tbt *p*-benzyl), 120.8 (s, C_5Me_5), 127.1 (d, Tbt C_m), 128.3 (d, 3-CH), 129.1 (d, Tbt C_m), 130.2 (d, Mes C_m), 130.3 (s), 131.7 (s), 132.7 (s), 135.4 (s), 137.2 (s), 144.5 (s), 144.6 (s), 156.9 (s, *C*(N)), 165.1 (s, *C*(N)). Anal. Calcd for $C_{51}H_{92}N_2Si_6Cl_2Ti$: C, 60.02; H, 9.09; N, 2.74. Found: C, 60.32; H, 8.82; N, 2.77.

Synthesis of [ZrCp*Cl$_2${TbtNC(Me)CHC(Me)NMes}] (6b). A solution of [Li{TbtNC(Me)CHC(Me)NMes}] (79.8 mg, 103 μmol) in benzene (1 mL) was added to pentamethylcyclopentadienylzirconium trichloride (42.6 mg, 128 μmol), and the reaction mixture turned yellow. The procedure similar to that in the preparation of **5a** afforded the product as yellow crystals. [ZrCp*Cl$_2${TbtNC(Me)CHC(Me)NMes}] (**6b**, 81.7 mg, 60%): mp 230−233 °C (dec). ^{1}H NMR (300 MHz, C_6D_6): δ 0.23 (s, 18H, Si*Me*$_3$), 0.26 (s, 18H, Si*Me*$_3$), 0.30 (s, 18H, Si*Me*$_3$), 1.44 (s, 1H, Tbt *p*-benzyl), 1.78 (s, 3H, *Me*), 1.82 (s, 6H, *Me*), 1.88 (s, 3H, *Me*), 2.00 (s, 3H, *Me*), 2.06 (s, 6H, *Me*), 2.11 (s, 2H, Tbt *o*-benzyl), 2.13 (s, 6H, *Me*), 2.32 (s, 3H, *Me*), 5.26 (s, 1H, 3−C*H*), 6.64 (br s, 2H, Tbt *m*-*H*), 6.70 (s, 2H, Mes *m*-*H*). ^{13}C NMR (75 MHz, C_6D_6, 25 °C): δ 1.7 (q, Si*Me*$_3$), 1.9 (q, Si*Me*$_3$), 14.8 (q, C_5Me_5), 15.1 (q, C_5Me_5), 18.3 (q, *Me*), 18.8 (q, *Me*), 20.7 (q, Mes *o*-*Me*), 21.1 (d, Tbt *o*-benzyl), 22.6 (d, Tbt *o*-benzyl), 25.8 (q, *Me*), 30.3 (d, Tbt *p*-benzyl), 120.9 (s, C_5Me_5), 127.2 (d, Tbt C_m), 128.4 (d, 3-CH), 129.4 (d, Tbt C_m), 130.4 (d, Mes C_m), 130.7 (s), 132.5 (s), 133.4 (s), 135.6 (s), 137.8 (s), 144.9 (s), 145.5 (s), 157.8 (s, *C*(N)), 165.4 (s, *C*(N)). Anal. Calcd for $C_{51}H_{92}N_2Si_6Cl_2Zr$: C, 57.57; H, 8.72; N, 2.63. Found: C, 57.80; H, 8.54; N, 2.69.

Polymerization Characterization. The copolymer samples were prepared in sample tubes (10 mm in diameter) by dissolving 250 mg of the copolymers in 3.0 mL of *o*-dichlorobenzene containing 0.3 mL of *o*-dichlorobenzene-d_4.[49] As short chain branches (1-hexene content) of ethylene/1-hexene copolymers were measured using a JASCO

dx.doi.org/10.1021/ma2024107 | *Macromolecules* 2012, 45, 1758−1769

IR−810 spectrometer with an estimated error of ±0.5 mol %.[40] Molecular weights (M_w and M_n) and molecular weight distributions (M_w/M_n) were determined by high-temperature gel permeation chromatography (GPC) and calibrated using polystyrene standards. GPC analysis was performed with a HLC−8121GPC/HT liquid chromatograph at 152 °C in *o*-dichlorobenzene using a TSK−GEL GMHHR−H(20)HT column. Differential scanning calorimetry (DSC) melting curves were recorded at a rate of 5 °C/min using a Seiko SSC-5200 instrument. The melting point (T_m) of copolymers was measured from the second heating.

Polymerization by Screening System. A Symyx PPR system was used for primary screening experiments. A preweighed glass vial insert and disposable stirring paddle were fitted to each reaction vessel of the reactor. The reactor was then closed, and 0.25 M Al(*i*-Bu)$_3$ (160 μL, 40 μmol) and toluene were injected into each reaction vessel through a valve. The total volume of reaction mixture (in the case of copolymerization: 60 μL 1-hexene added) was adjusted to 5 mL with toluene. The temperature was then set to 40 °C, the stirring speed was set to 800 rpm, and the mixture was pressurized to 0.6 MPa. A toluene solution of precatalyst (a 0.1 μmol, 1 mM toluene solution) and a toluene solution of a boron compound [B(C_6F_5)$_3$, [PhNHMe$_2$]-[B(C_6F_5)$_4$] or $Ph_3CB(C_6F_5)_4$] (a 0.3 μmol, 1 mM toluene solution) was successively added. When MMAO was used as a cocatalyst, MMAO (a 100 μmol, 0.25 M toluene solution) and a catalyst precursor (a 0.1 μmol, 1 mM toluene solution) were added. Ethylene pressure in the cell and the temperature setting were maintained by computer control until the end of the polymerization experiment. The polymerization reactions were allowed to continue for 20 min unless consumption of ethylene reached preset levels. After polymerization reaction, the temperature was allowed to drop to room temperature and the ethylene pressure in the cell was slowly vented. The glass vial insert was then removed from the pressure cell and the volatile components were removed using a centrifuge vacuum evaporator to give a polymer product.

Typical Procedure of Ethylene/1-Hexene Copolymerization in the Case of β-Diketiminato, 1-Aza-1,3-butadienyl−Imido and 1-Aza-2-butenyl−Imido Complexes of Group 4 Metals. An autoclave having an inner volume of 0.4 L was dried under vacuum at 130 °C, and purged with argon. Then, 1-hexene (10 mL) and toluene (190 mL) were charged, and the vessel was heated to 40 °C. After ethylene was introduced (2.5 MPa), Al(*i*-Bu)$_3$ (a 0.25 mmol, 1.0 M toluene solution) was added. Subsequently, the complex (a 2.5 μmol, 0.10 mM toluene solution) and [PhNHMe$_2$][B(C_6F_5)$_4$] (a 7.5 μmol, 5.0 mM toluene solution) were added. Polymerization was carried out at 40 °C for 1 h, and the reaction was quenched by adding methanol (5 mL). A few minutes later, the reaction mixture was poured into acidic methanol (400 mL with 5 mL of 1 M HCl). The polymer was collected by filtration and washed with methanol and dried in a high vacuum oven at 80 °C for 8 h to constant weight.

Procedure of Ethylene/1-Hexene Copolymerization in the Case of PHENICS. The polymerization procedure is similar to that in the case of other complexes as shown above except for the use of toluene 196 mL, 1-hexene 4 mL, the complex (**PHENICS**, 0.005 μmol) and [PhNHMe$_2$][B(C_6F_5)$_4$] (a 1.5 μmol, 5.0 mM toluene solution).

Procedure of Ethylene/1-Hexene Copolymerization in the Case of CGC−Ti. The polymerization procedure is similar to that in the case of other complexes as shown above except for the use of toluene 192 mL, 1-hexene 8 mL, the complex (**CGC−Ti**, 0.001 μmol) and [PhNHMe$_2$][B(C_6F_5)$_4$] (a 1.5 μmol, 5.0 mM toluene solution).

Effect on Polymerization Temperature for Ethylene/1-Hexene Copolymerization. The polymerization procedure is similar to other copolymerization procedures as shown above except that the polymerization temperatures are 60, 100, 140, and 180 °C instead of 40 °C.

Effect on Ethylene Pressure for Ethylene/1-Hexene Copolymerization. The polymerization procedure is similar to other copolymerization procedures as shown above except that the ethylene pressures are 0.6, 1.0, and 4.0 MPa instead of 2.5 MPa.

Procedure of Ethylene/1-Hexene Copolymerization in the Case of PHENICS. The polymerization procedure is similar to that the above one except toluene 196 mL, 1-hexene 4 mL, the complex (**PHENICS**, 0.005 μmol) and [PhNHMe$_2$][B(C_6F_5)$_4$] (a 1.5 μmol, 5.0 mM toluene solution).

Procedure of Ethylene/1-Hexene Copolymerization in the Case of CGC−Ti. The polymerization procedure is similar to that the above one except toluene 192 mL, 1-hexene 8 mL, the complex (**CGC−Ti**, 0.001 μmol) and [PhNHMe$_2$][B(C_6F_5)$_4$] (a 1.5 μmol, 5.0 mM toluene solution).

Effect on Polymerization Temperature for Ethylene/1-Hexene Copolymerization Using 3a. The polymerization procedure is similar to that the above one except that the polymerization temperatures are 60, 100, 140, and 180 °C instead of 40 °C.

Effect on Ethylene Pressure for Ethylene/1-Hexene Copolymerization Using 3a. The polymerization procedure is similar to that the above one except that the ethylene pressure are 0.6, 1.0, and 4.0 MPa instead of 2.5 MPa.

■ ASSOCIATED CONTENT

Ⓢ Supporting Information

Experimental data for polymerization using high-throughput screening system, GPC and DSC data, and a picture of the polymer dissolving in *o*-dichlorobenzene. This material is available free of charge via the Internet at http://pubs.acs.org.

■ AUTHOR INFORMATION

Corresponding Author

*E-mail: tokitoh@boc.kuicr.kyoto-u.ac.jp (N.T.); nabikam@sc.sumitomo-chem.co.jp (M.N.).

Present Addresses

[§]Petrochemicals Research Laboratory, Sumitomo Chemical Co., Ltd., 2−1 Kitasode, Sodegaura, Chiba 299−0295, Japan.

[∥]Department of Chemistry and Chemical Biology and International Education and Research Center for Silicon Science, Graduate School of Engineering, Gunma University, 1−5−1 Tenjin-cho, Kiryu, Gunma 376−8515, Japan.

Notes

The authors declare no competing financial interest.

■ ACKNOWLEDGMENTS

This work was partially supported by Grants-in-Aid for Scientific Research [Nos. 12CE2005, 17GS0207, 14078213, and 15750031] and the 21 COE Program on Kyoto University Alliance for Chemistry from the Ministry of Education, Culture, Sports, Science, and Technology, Japan. We thank Mr. Seiki Kiuchi for experimental assistance, Mr. Takashi Kohara for NMR analysis and Ms. Hiroko Hirahata and Mr. Yoshio Yagi for GPC analysis, and Mr. Takahiro Hino and Mr. Shohei Matsushita for primary high-throughput screening experiments. We express also our sincere gratitude to Mr. Tatsuya Miyatake for their helpful discussions throughout this research project.

■ REFERENCES

(1) (a) Niaounakis, M.; Kontou, E. *J. Polym. Sci., Polym. Phys.* **2005**, *43*, 1712−1727. (b) James, D. E. In *Encyclopedia of Polymer Science and Engineering*; Mark, H. F., Bikales, N. M., Overberger, C. G., Menges, G., Eds.; Wiley-Interscience: New York, 1985; Vol. *6*, pp 429−454. (c) Kulshrestha, A. K.; Talapatra, S. In *Handbook of Polyolefins*; Vasile, C., Ed.; Marcel Dekker: New York, 2000; pp 1−70. (d) Cran, M. J.; Bigger, S. W. *J. Plast. Film Sheeting* **2006**, *22*, 121−132. (e) Jin, H.-J.; Kim, S.; Yoon, J.-S. *J. Appl. Polym. Sci.* **2002**, *84*, 1566−1571. (f) Starck, P.; Malmberg, A.; Lofgren, B. *J. Appl. Polym. Sci.* **2002**, *83*, 1140−1156. (g) Quijada, R.; Narvaez, A.; Rojas, R.; Rabagliati, F. M.; Galland, G. B.; Maules, R. S.; Benabente, R.; Perez, E.; Perena, J.; Bello, A. *Macromol. Chem. Phys.* **1999**, *200*, 1306−1310. (h) Galland, G. B.; Seferin, M.; Mauler, R. S.; Dos, S.; Joao, H. Z. *Polym. Int.* **1999**, *48*, 660−664. (i) Quijada, R.; Scipioni, R.; Mauler, R.; Galland, G.;

Miranda, M. S. *Polym. Bull.* **1995**, *35*, 299−306. (j) Quijada, R.; Dupont, J.; Lacerda, M.; Scipione, R.; Galland, G. *Macromol. Chem. Phys.* **1995**, *196*, 3991−4000.
(2) Wang, L. C.; Harvey, M. K.; Ng, J. C.; Scheunemann, U. *J. Power Sources* **1998**, *73*, 74−77.
(3) (a) Liu, J.-C. US Patent 6,635,728, 2003. (b) Rastogi, S.; Lemstra, P. WO Patent 9835818, 1998. (c) Knuuttila, H.; Sormnnenm, P. WO Patent 9507305, 1995.
(4) Brant, P.; Canich, J. US Patent 5,444,145, 1995.
(5) Weiser, M.-S.; Wesolek, M.; Mülhaupt, R. *J. Organomet. Chem.* **2006**, *691*, 2945−2952.
(6) Chen, Y.-X.; Marks, T. J. *Organometallics* **1997**, *16*, 3649−3657.
(7) Bluhm, M. E.; Folli, C.; Pufky, D.; Kröger, M.; Walter, O.; Döring, M. *Organometallics* **2005**, *24*, 4139−4152.
(8) Kashiwa, N.; Imuta, J.; Tsutsui, T.; Hama, S.; Kojoh, S. *Macromol. Symp.* **2000**, *159*, 19−26.
(9) Kageyama, K.; Tamazawa, J.; Aida, T. *Science* **1999**, *285*, 2113−2115.
(10) Starzewski, K. A. O.; Xin, B. S.; Steinhauser, N.; Schweer, J.; Benet-Buchholz, J. *Angew. Chem., Int. Ed. Engl.* **2006**, *45*, 1799−1803.
(11) Gong, S.; Ma, H.; Huang, J. *J. Organomet. Chem.* **2008**, *693*, 3509−3518.
(12) Ishii, S.; Saito, J.; Matsuura, S.; Suzuki, Y.; Furuyama, R.; Mitani, M.; Nakano, T.; Kashiwa, N.; Fujita, T. *Macromol. Rapid Commun.* **2002**, *23*, 693−697.
(13) (a) Fujita, M.; Seki, Y.; Miyatake, T. *J. Polym. Sci., A: Polym. Chem.* **2004**, *42*, 1107−1111. (b) Miyatake, T.; Mizunuma, K.; Seki, Y.; Kakugo, M. *Makromol. Chem. Rapid Commun.* **1989**, *10*, 349−352.
(14) Michiue, K.; Jordan, R. F. *Organometallics* **2004**, *23*, 460−470.
(15) (a) Kaminsky, W.; Kulper, K.; Brintzinger, H. H.; Wild, F. R. W. P. *Angew. Chem., Int. Ed. Engl.* **1985**, *24*, 507−508. (b) Ewen, J. A.; Jones, R. L.; Razavi, A. *J. Am. Chem. Soc.* **1988**, *110*, 6255−6258. (c) Coates, G. W. *Chem. Rev.* **2000**, *100*, 1223−1252.
(16) (a) Britovsek, G. J. P.; Gibson, V. C.; Wass, D. F. *Angew. Chem., Int. Ed. Engl.* **1999**, *38*, 428−447. (b) Gibson, V. C.; Spitzmesser, S. K. *Chem. Rev.* **2003**, *103*, 283−315. (c) Gibson, V. C.; Redshaw, C.; Solan, G. A. *Chem. Rev.* **2007**, *107*, 1745−1776. (d) Suzuki, Y.; Terao, H.; Fujita, T. *Bull. Chem. Soc. Jpn.* **2003**, *76*, 1493−1517. (e) Makio, H.; Terao, H.; Iwashita, A.; Fujita, T. *Chem. Rev.* **2011**, *111*, 2363−2449. (f) Matsugi, T.; Fujita, T. *Chem. Soc. Rev.* **2008**, *37*, 1264−1277. (g) Camacho, D. H.; Guan, Z. *Chem. Commun.* **2010**, *46*, 7879−7893. (h) Wasilke, J.-C.; Obrey, S. J.; Baker, R. T.; Bazan, G. C. *Chem. Rev.* **2005**, *105*, 1001−1020. (i) Stephan, D. W. *Organometallics* **2005**, *24*, 2548−2560. (j) Delferro, M.; Marks, T. J. *Chem. Rev.* **2011**, *111*, 2450−2485. (k) Nomura, K.; Zhang, S. *Chem. Rev.* **2011**, *111*, 2342−2362. (l) Zeimentz, P. M.; Arndt, S.; Elvidge, B. R.; Okuda, J. *Chem. Rev.* **2006**, *106*, 2404−2433. (n) Hou, H.; Luo, Y.; Li, X. *J. Organomet. Chem.* **2006**, *691*, 3114−3121. (o) McGuinness, D. S. *Chem. Rev.* **2011**, *111*, 2321−2341.
(17) Scollard, J. D.; McConville, D. H. *J. Am. Chem. Soc.* **1996**, *118*, 10008−10009.
(18) (a) Makio, H.; Kashiwa, N.; Fujita, T. *Adv. Synth. Catal.* **2002**, *344*, 477−493. (b) Mitani, M.; Saito, J.; Ishi, S.; Nakayama, Y.; Makio, H.; Matsukawa, N.; Matsui, S.; Mohri, J.; Furuyama, R.; Terao, H.; Bando, H.; Tanaka, H.; Fujita, T. *Chem. Record* **2004**, *4*, 137−158.
(19) (a) Britovsek, G. J. P.; Gibson, V. C.; Kimberley, B. S.; Maddox, P. J.; McTavish, S. J.; Solan, G. A.; White, A. J. P.; Williams, D. J. *Chem. Commun.* **1998**, 849−850. (b) Small, B. L.; Brookhart, M.; Bennett, A. M. A. *J. Am. Chem. Soc.* **1998**, *120*, 4049−4050.
(20) Bourget-Merle, L.; Lappert, M. F.; Severn, J. R. *Chem. Rev.* **2002**, *102*, 3031−3065.
(21) (a) Hitchcock, P. B.; Lappert, M. F.; Liu, D.-S. *J. Chem. Soc., Chem. Commun.* **1994**, 2637−2638. (b) Deelman, B.-J.; Hitchcock, P. B.; Lappert, M. F.; Leung, W.-P.; Lee, H.-K.; Mak, T. C. W. *Organometallics* **1999**, *18*, 1444−1452.
(22) Kim, W.-K.; Fevola, M. J.; Liable-Sands, L. M.; Rheingold, A. L.; Theopold, K. H. *Organometallics* **1998**, *17*, 4541−4543.
(23) Budzelaar, P. H. M.; van Oort, A. B.; Orpen, A. G. *Eur. J. Inorg. Chem.* **1998**, 1485−1494.
(24) Kakaliou, L.; Scanlon, W. J. IV; Qian, B.; Baek, S. W.; Smith, M. R., III; Motry, D. H. *Inorg. Chem.* **1999**, *38*, 5964−5977.
(25) (a) Basuli, F.; Bailey, B. C.; Huffman, J. C.; Mindiola, D. J. *Chem. Commun.* **2003**, 1554−1555. (b) Basuli, F.; Bailey, B. C.; Tomaszewski, J.; Huffman, J. C.; Mindiola, D. J. *J. Am. Chem. Soc.* **2003**, *125*, 6052−6053. (c) Mindiola, D. J.; Scott, S. *Nature Chem.* **2011**, *3*, 15−17. (d) Basuli, F.; Tomaszewski, J.; Huffman, J. C.; Mindiola, D. J. *J. Am. Chem. Soc.* **2003**, *125*, 10170−10171. (e) Fout, A. R.; Kilgore, U. J.; Mindiola, D. J. *Chem.—Eur. J.* **2007**, *13*, 9428−9440.
(26) (a) Hamaki, H.; Takeda, N.; Tokitoh, N. *Organometallics* **2006**, *25*, 2457−2464. (b) Hamaki, H.; Takeda, N.; Tokitoh, N. *Inorg. Chem.* **2007**, *46*, 1795−1802.
(27) Chien, J. C. W.; Nozaki, T. *J. Polym. Sci., Part A: Polym. Chem.* **1993**, *31*, 227−237.
(28) Shaviv, E.; Botoshansky, M.; Eisen, M. S. *J. Organomet. Chem.* **2003**, *683*, 165−180.
(29) Jin, X.; Novak, B. M. *Macromolecules* **2000**, *33*, 6205−6207.
(30) (a) Vollmerhaus, R.; Rahim, M.; Tomaszewski, R.; Xin, S.; Taylor, N. J.; Collins., S. *Organometallics* **2000**, *19*, 2161−2169. (b) Resconi, L.; Chadwick, J. C.: Cavallo, L. In *Comprehensive Organometallic Chemistry III*; Bochmann, M.., Ed.; Elsevier: Oxford, U.K., 2007; pp 1092−1094.
(31) (a) Krishnamurti, R.; Nagy, S.; Tyrell, J.; Etherton, B. P. WO Patent 0007725, 2000. (b) Etherton, B. P.; Krishnamurti, R.; Nagy, S. WO Patent 0007726, 2000.
(32) Ikai, S.; Kai, Y.; Murakami, M.; Nakazawa., H. (Ube kosan) JP Patent 1999−228614, 1999.
(33) Nielson, A. J.; Glenny, M. W.; Rickard, C. E. F. *J. Chem. Soc., Dalton Trans.* **2001**, 232−239.
(34) Adams, N.; Arts, H. J.; Bolton, P. D.; Cowell, D.; Dubberley, S. R.; Friederichs, N.; Grant, C. M.; Kranenburg, M.; Sealey, A. J.; Wang, B.; Wilson, P. J.; Cowley, A. R.; Mountford, P.; Schröder, M. *Chem. Commun.* **2004**, 434−435.
(35) (a) Basuli, F.; Kilgore, U. J.; Brown, D.; Huffman, J. C.; Mindiola, D. J. *Organometallics* **2004**, *23*, 6166−6175. (b) Basuli, F.; Huffman, J. C.; Mindiola, D. J. *Inorg. Chim. Acta* **2007**, *360*, 246−254.
(36) Bai, G.; Wei, P.; Stephan, D. W. *Organometallics* **2006**, *25*, 2649−2655.
(37) Chang, K.-C.; Lu, C.-F.; Wang, P.-Y.; Lu, D.-Y.; Chen, H.-Z.; Kuob, T.-S.; Tsai, Y.-C. *Dalton Trans.* **2011**, *40*, 2324−2331.
(38) Tomson, N. C.; Arnold, J.; Bergman, R. G. *Organometallics* **2010**, *29*, 5010−5025.
(39) (a) Canich, J. A. M. (Exxon) U.S. Patent 5,026,798, 1991. (b) Devore, D. D.; Timmers, F. J.; Hasha, D. L.; Rosen, R. K.; Marks, T. J.; Deck, P. A.; Stern, C. L. *Organometallics* **1995**, *14*, 3132−3134. (c) Stevens, J. C.; Timmers, F. J.; Wilson, D. R.; Schmidt, G. F.; Nickias, P. N.; Rosen, R. K.; Knight, G. W.; Lai, S.-y. (Dow Chemical Company) *Eur. Pat. Appl.* 0416 815 A2, 1990.
(40) (a) Katayama, H.; Nabika, M.; Imai, A.; Miyashita, A.; Watanabe, T.; Johoji, H.; Oda, Y.; Hanaoka, H. JP Patent H9−87313, 1997. (b) Nabika, M.; Miyatake, T. *Kobunshi Ronbunshu* **2002**, *59*, 382−387. (c) Hanaoka, H.; Hino, T.; Souda, H.; Yanagi, K.; Oda, Y.; Imai, A. *J. Organomet. Chem.* **2007**, *692*, 4059−4066. (d) Hanaoka, H.; Hino, T.; Nabika, M.; Kohno, T.; Yanagi, K.; Oda, Y.; Imai, A.; Mashima, K. *J. Organomet. Chem.* **2007**, *692*, 4717−4724. (e) Nabika, M.; Katayama, H.; Watanabe, T.; Kawamura-Kuribayashi, H.; Yanagi, K.; Imai, A. *Organometallics* **2009**, *28*, 3785−3792. (f) Senda, T.; Hanaoka, H.; Hino, T.; Oda, Y.; Tsurugi, H.; Mashima, K. *Macromolecules* **2009**, *42*, 8006−8009. (g) Senda, T.; Hanaoka, H.; Okado, Y.; Oda, Y.; Tsurugi, H.; Mashima, K. *Organometallics* **2009**, *28*, 6915−6926. (h) Senda, T.; Hanaoka, H.; Nakahara, S.; Oda, Y.; Tsurugi, H.; Mashima, K. *Macromolecules* **2010**, *43*, 2299−2306.
(41) Blitz, J. P.; McFaddin, D. C. *J. Appl. Polym. Sci.* **1994**, *51*, 13−20.
(42) (a) Rappé, A. K.; Skiff, W. M.; Casewit, C. J. *Chem. Rev.* **2000**, *100*, 1435−1456. (b) Kaminsky, W.; Ahlers, A.; Möller-Lindenhof, N. *Angew. Chem., Int. Ed. Engl.* **1989**, *28*, 1216−1218. (c) Tsutsui, T.; Ishimaru, N.; Mizuno, A.; Toyota, A.; Kashiwa, N. *Polymer* **1989**, *30*,

1350−1356. (d) Yoshida, T.; Koga, N.; Morokuma, K. *Organometallics* **1995**, *14*, 746−758.
(43) (a) Killian, C. M.; Tempel, D. J.; Johnson, L. K.; Brookhart, M. J. *J. Am. Chem. Soc.* **1996**, *118*, 11664−11665. (b) Rix, F. C.; Brookhart, M. L.; White, P. S. *J. Am. Chem. Soc.* **1996**, *118*, 4746−4764.
(44) Margl, P.; Deng, L.; Zieger, T. *Organometallics* **1999**, *18*, 5701−5708.
(45) (a) Kissin, Y. V. *J. Polym. Sci., Part A: Polym. Chem.* **1995**, *33*, 227−237. (b) Jiang, X.; Wang, H.; Tian, X.; Yang, Y.; Fan, Z. *Ind. Eng. Chem. Res.* **2011**, *50*, 259−266. (c) Soares, J. B. P. *Chem. Chem. Eng. Sci.* **2001**, *56*, 4131−4153.
(46) (a) Zuo, W.; Zhang, M.; Sun, W.-H. *J. Polym. Sci., Part A: Polym. Chem.* **2009**, *47*, 357−372. (b) Pietruszka, A.; Białek, M.; Czaja, K. *J. Appl. Polym. Sci.* **2012**, *123*, 1848−1852.
(47) Krentsel, N. A.; Kissin, Y. V.; Kleniner, V. I.; Stotskaya, L. L. *Polymers and Copoymers of Higher α-Olefins*; Hanser Publichers: Munich, Germany, 1997; pp 243−335.
(48) (a) Takeda, N.; Hamaki, H.; Tokitoh, N. *Chem. Lett.* **2004**, *33*, 134−135. (b) Hamaki, H.; Takeda, N.; Yamasaki, T.; Sasamori, T.; Tokitoh, N. *J. Organomet. Chem.* **2007**, *692*, 44−54.
(49) de Pooter, M.; Smith, P. B.; Dohrer, K. K.; Bennet, K. F.; Meadows, M. D.; Smith, C. G.; Schouwenaars, H. P.; Geerards, R. A. *J. Appl. Polym. Sci.* **1991**, *42*, 399−408.

Macromolecules

Article

pubs.acs.org/Macromolecules

Alternating Ring-Opening Polymerization of Cyclohexene Oxide and Anhydrides: Effect of Catalyst, Cocatalyst, and Anhydride Structure

Elham Hosseini Nejad, Carlo G. W. van Melis, Tim J. Vermeer, Cor E. Koning, and Rob Duchateau*

Laboratory of Polymer Chemistry, Eindhoven University of Technology, P.O. Box 513, 5600 MB, Eindhoven, The Netherlands

Supporting Information

ABSTRACT: Ring-opening copolymerization of cyclohexene oxide with alicyclic anhydrides containing different ring strain (succinic anhydride, cyclopropane-1,2-dicarboxylic acid anhydride, and phthalic anhydride) was performed applying metal salen chloride complexes, (salen)MCl (M = Al, Cr, Co; salen = *N*,*N*-bis(3,5-di-*tert*-butylsalicylidene)diimine) with different metals and ligand−diimine backbones. While some of the bulk copolymerizations afforded poly(ester-*co*-ether)s, all solution polymerizations produced perfect alternating copolymers. The chromium catalysts performed best while the aluminum catalysts were the least active ones. For each metal, the salophen complexes yielded the best performing catalyst. A variety of cocatalysts have been employed: bis(triphenylphosphoranylidene)ammonium chloride, *N*-heterocyclic nucleophiles including 4-(dimethylamino)pyridine, *N*-methylimidazole, and 1,5,7-triazabicyclododecene and the phosphines trimesitylphosphine, tris(2,4,6-trimethoxyphenyl)phosphine, tricyclohexylphosphine to triphenylphsophine. Of all cocatalysts, bis(triphenylphosphoranylidene)ammonium chloride was found to be the most efficient cocatalyst in combination with salophenCrCl for the copolymerization of cyclohexene oxide with phthalic anhydride, and 1 equiv was enough to reach optimum activity. *N*-Heterocyclic nucleophiles showed the lowest activity. Of the three anhydrides used, phthalic anhydride is the most reactive giving the highest conversions and the highest molecular weight products.

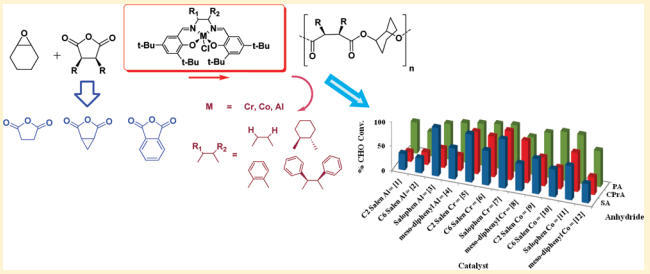

INTRODUCTION

Approximately 40 years ago, Inoue and co-workers reported for the first time the copolymerization of oxiranes with carbon dioxide and anhydrides using organometallic compounds.[1] The design of efficient metal-based catalysts for the selective coupling of carbon dioxide and various epoxides to obtain polycarbonates has made significant improvement over the past decades.[2−9] In the meanwhile, copolymerization of epoxides and anhydrides has received much less attention.[10,11] The earlier studies by Inoue[12] and Maeda[13] on the anhydride−oxirane copolymerization with aluminum porphyrinato and magnesium diethoxide catalysts were promising, but the difficulty of obtaining high molecular weight polymers along with the undesirable side reaction of oxirane homopolymerization prevented its development as a general pathway for quite some time. Recent reports on the copolymerization of several alicylic oxiranes and anhydrides using a zinc 2-cyano-β-diketiminate[11,14] and chromium salophen and porphyrinato[10] catalysts renewed the attention to this scientific area. Like for the corresponding oxirane−CO_2 copolymerization,[1,15−17] the metal salen and porphyrinato-catalyzed oxirane−anhydride copolymerizations generally require a cocatalyst to obtain good yields and selectivity.[10] For example, mainly oligoethers and low activities were observed when aluminum and chromium tetraphenylporphyrinato and chromium salophen complexes were employed without cocatalysts. Adding nucleophilic cocatalysts considerably improved the catalyst's performance and ester content of the poly(ester-*co*-ether)s obtained. Interestingly, recently Coates and co-workers reported the alternating epoxide−maleic anhydride copolymerization using a salen chromium chloride catalyst *without* a cocatalyst.[18]

Here we describe the alternating ring-opening copolymerization of cyclohexene oxide with anhydrides containing different ring strain; succinic anhydride (SA), cyclopropane-1,2-dicarboxylic acid anhydride (CPrA), and phthalic anhydride (PA, Figure 1) using metal−salen complexes, (salen)MCl (M = Al, Cr, Co; salen = *N*,*N*-bis(3,5-di-*tert*-butylsalicylidene)-diimine), with different metals and ligand−diimine backbones (Figure 2) as catalysts. Regarding the important role of a cocatalyst for the metal salen-catalyzed epoxide−CO_2 copolymerizations[10,15−17] and concerning the limited amount of data on the related epoxide−anhydride copolymerizations, we have also investigated the effect of various cocatalysts and solvents in the ring-opening copolymerization of cyclohexene oxide and alicyclic anhydrides.

EXPERIMENTAL SECTION

Reagents. Succinic anhydride, cyclopropane-1,2-dicarboxylic acid anhydride, phthalic anhydride, 4-(dimethylamino)pyridine, *N*-methyl-

Received: November 27, 2011
Revised: January 25, 2012
Published: February 7, 2012

dx.doi.org/10.1021/ma2025804 | *Macromolecules* 2012, 45, 1770−1776

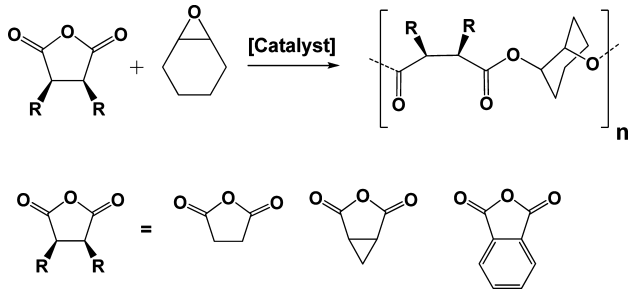

Figure 1. Synthesis of polyesters from cyclohexene oxide and dicarboxylic acid anhydrides (succinic anhydride, cyclopropane-1,2-dicarboxylic acid anhydride, and phthalic anhydride).

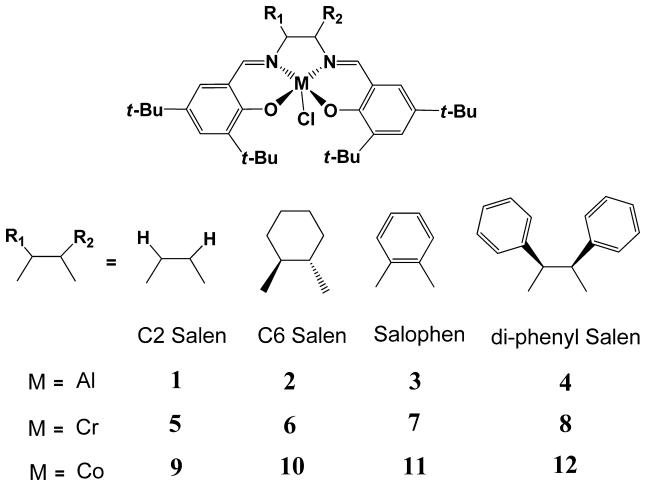

Figure 2. General structure of (salen)MCl catalysts utilized for the copolymerization reactions.

imidazole, 1,5,7-triazabicyclododecene (TBD), and bis(triphenylphosphorylidine)ammonium chloride were purchased from Aldrich and used as received. Trimesitylphosphine, tris(2,4,6-trimethoxyphenyl)phosphine, and tricyclohexylphosphine were purchased from Strem Chemicals. Triphenylphosphine was bought from Fluka. All phosphine cocatalysts were used as received. Cyclohexene oxide was purchased from Aldrich, dried over CaH_2, then distilled, and stored under argon. Succinic anhydride and cyclopropane-1,2-dicarboxylic acid anhydride were sublimed prior to use. Phthalic anhydride was recrystallized from chloroform. The salen complexes were prepared according to the procedure found in the literature.[19] Toluene (Aldrich), petroleum ether (60−80 fraction, Aldrich), and Isopar E (ExxonMobil), a solvent which consisits predominantly of C8−C9 isoparaffinic haydrocarbons with the boiling point of 118−140 °C, were dried over an alumina column and stored on 4 Å molecular sieves under argon. All manipulations were performed under an inert atmosphere or in a nitrogen-filled MBraun glovebox unless stated otherwise. The catalysts **1**−**12** have been synthesized according to literature procedures.[2,20−27]

Copolymerizations of Anhydrides and CHO. The copolymerizations were performed at 110 °C in both bulk (150 min) and in toluene (300 min) with an oxirane:anhydride:catalyst(:cocatalyst) ratio of 250:250:1(:1).

Bulk. A mixture of anhydride (2.5 mmol), CHO (2.5 mmol), and catalyst (10 μmol) was reacted in a 2 mL crimp cap vial equipped with a stirring bar placed in an aluminum heating block mounted on top of a stirrer/heating plate. The polymerization was conducted at 110 °C for 150 min unless stated otherwise. All analyses were performed on crude samples.

Solution. A 2 mL crimp lid vial equipped with a stirring bar was charged with a mixture of anhydride (2.5 mmol), CHO (2.5 mmol), and catalyst (10 μmol) in toluene (1 mL) and was placed in an aluminum heating block mounted on top of a stirrer/heating plate. The polymerization was conducted at 110 °C for 300 min. All analyses were performed on crude samples.

Methods. NMR spectra were recorded on a Varian Mercury Vx (400 MHz) spectrometer at 25 °C in chloroform-d_1, and ^{1}H NMR spectra were referenced internally using residual solvent proton signals. SEC analysis was carried out using a Waters 2695 separations module, a model 2414 refractive index detector (at 40 °C), and a model 486 UV detector (at 254 nm) in series. Injections were done by a Waters model WISP 712 autoinjector, using an injection volume of 50 μL. The columns used were a PLgel guard (5 μm particles) 50 × 7.5 mm column, followed by two PLgel mixed-C (5 μm particles) 300 × 7.5 mm columns at 40 °C in series. THF was used as eluent at a flow rate of 1.0 mL min^{-1}. Samples were filtered through a 0.2 μm PTFE filter (13 mm, PP housing, Alltech). For calibration polystyrene standards were used (Polymer Laboratories, M_n = 580−7.1 × 10^6 g mol^{-1}). Data acquisition and processing were performed using Waters Millennium 32 (v4.0) software. MALDI-ToF-MS analysis was performed on a Voyager DE-STR from Applied Biosystems equipped with a 337 nm nitrogen laser. An accelerating voltage of 25 kV was applied. Mass spectra of 1000 shots were accumulated. The polymer samples were dissolved in THF at a concentration of 1 mg mL^{-1}. The cationization agent used was potassium trifluoroacetate (Fluka, >99%) dissolved in THF at a concentration of 5 mg mL^{-1}. The matrix used was *trans*-2-[3-(4-*tert*-butylphenyl)-2-methyl-2-propenylidene]malononitrile (DCTB) (Fluka) and was dissolved in THF at a concentration of 40 mg mL^{-1}. Solutions of matrix, salt and polymer were mixed in a volume ratio of 4:1:4, respectively. The mixed solution was hand-spotted on a stainless steel MALDI target and left to dry. The spectra were recorded in the reflectron mode. All MALDI-ToF-MS spectra were recorded from the crude products. In-house developed software was used to characterize the polymers in detail and allowed us to elucidate the individual chain structures, the copolymer's chemical composition, and topology (see Supporting Information for more details).[28,29]

RESULTS AND DISCUSSION

Effect of Catalyst Structure on Catalytic Behavior. To study the effect of the steric and electronic environment of the catalyst on the catalytic performance, we decided to vary both the salen−diimine backbone and the metal in the catalysts (salen)MCl (**1**−**12**, Figure 2). The copolymerizations were carried out in bulk and toluene with DMAP as cocatalyst.

As expected, the bulk polymerizations showed higher conversion rates compared to the solution polymerizations, but the effect of the metal and ligand structure on the catalytic behavior was very similar as for the solution polymerizations. Whereas some of the bulk polymerizations afforded poly(ester-*co*-ether)s, all solution polymerizations produced perfect alternating copolymers (Figures 3 and 4). The results of the

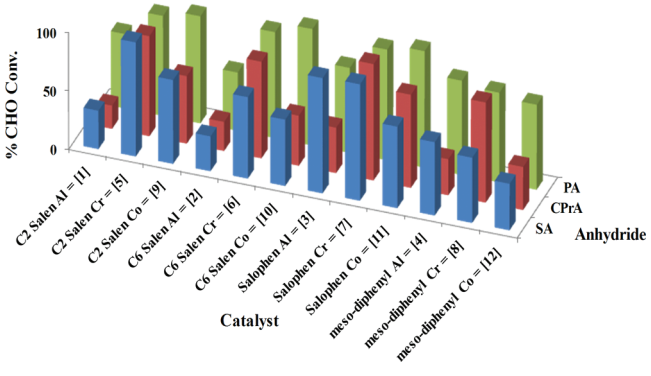

Figure 3. CHO conversion for the copolymerization of CHO and anhydrides catalyzed by (salen)MCl catalysts.

dx.doi.org/10.1021/ma2025804 | *Macromolecules* 2012, 45, 1770−1776

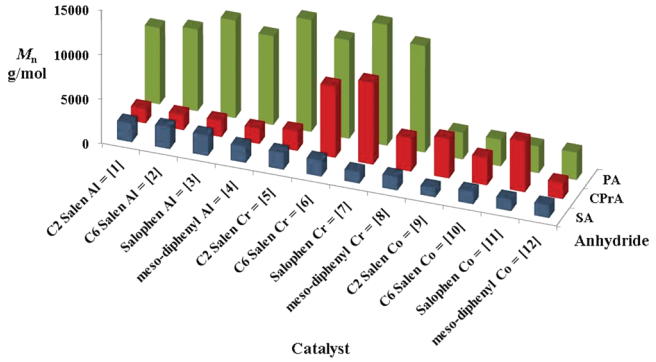

Figure 4. M_n values for the copolymerization of CHO and anhydrides catalyzed by (salen)MCl catalysts.

bulk and solution polymerizations are tabulated in the Supporting Information as Tables S1 and S2, respectively. From Figure 3 it is clear that overall the chromium catalysts performed best while the aluminum catalysts were the least active ones. When looking at the CHO–SA copolymerization, it is clear that the salophen complexes (**3**, **7**, **11**) gave the highest activity, followed by the ethylene-bridged chromium (**5**) and cobalt (**9**) complexes and the aluminum *meso*-diphenyl complex **4**. The corresponding *meso*-diphenyl salen chromium (**8**) and cobalt (**12**) complexes proved to be the least active for CHO–SA copolymerization. Summarizing, for each metal the salophen complexes yielded the best performing catalysts, and chromium clearly outperformed the other two metals, making chromium salophen **7** the most active catalyst of all tested. Sterically encumbering substituents such as two diphenyl groups on the diimine backbone had a negative effect on the catalytic activity. The catalytic behavior of catalysts containing sterically less demanding ethylenediimine and cyclohexylene-diimine backbones was almost identical. Darensbourg et al.[19] reported a similar trend in catalytic activity for the copolymerization of cyclohexene oxide and CO_2 catalyzed by chromium salen systems: **8** showed the lowest reactivity while **5** and **6** exhibited similar activities.

It was assumed that increasing the ring strain in the anhydride backbone would also lead to higher reactivity and possibly also to higher molecular weight products.[10] To investigate the effect of anhydride ring strain in this type of copolymerization, the aliphatic succinic anhydride (SA) monomer was replaced by the alicyclic anhydrides: phthalic anhydride (PA) and cyclopropane anhydride (CPrA). PA indeed showed higher reactivities than SA. For CPrA the situation was less clear as aluminum and cobalt catalysts gave slightly higher conversions for SA-based copolymers while chromium clearly yielded higher conversions for CPrA-based copolymers. The polymer molecular weight seemed to be related to the reactivity of the anhydride. Polymers obtained from PA and CHO copolymerizations showed quite high M_n values (Figure 4). CPrA- and SA-based copolymers generally exhibited lower molecular weights. In all cases though, the observed molecular weights were lower than the theoretical values for a living system. This is attributed to the presence of small amounts of hydrolyzed anhydrides that can function as chain transfer agents (CTAs).[30–32] To verify this, the copolymerizations of PA and CHO without and with a small amount (0.5%) of isophthalic acid in addition to PA and CHO were compared. The results obtained confirm that presence of hydrolyzed anhydrides can indeed act as CTA lowering the polymer molecular weight (CHO + PA: 86% conversion, M_n = 16 200 g/mol, PDI = 1.2; CHO + PA + diacids: 90% conversion, M_n = 12 100 g/mol, PDI = 1.3). The differences in molecular weight for the CHO–anhydride copolymers at comparable CHO conversion (e.g., see the runs with **7** in Figures 3 and 4) indicate the presenc of varying amounts of diacids depending on the anhydride. Atempts to purify the anhydrides by double sublimation or crystallization did not result in a significant improvement of the molecular weight, which indicates that removal of the traces of diacids is difficult or that the water responsible for the diacid formation is introduced during the sample preparation or polymerization.

All polymers exhibited narrow molecular weight distributions and the M_n values displayed a linear relationship with the % CHO conversion, which is consistent with a living or, taking the unintended presence of CTAs into account, immortal polymerization process (Figure 5).

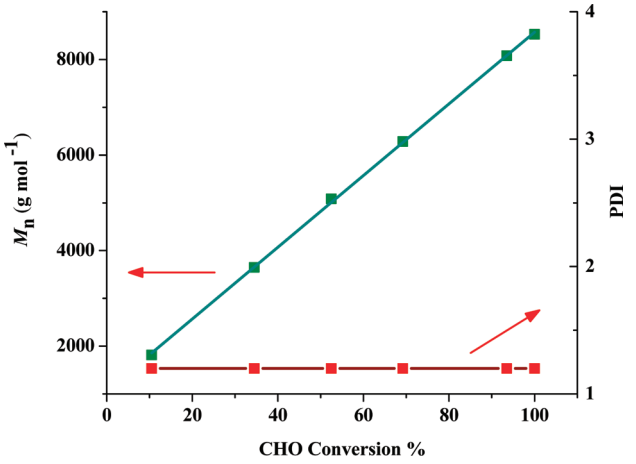

Figure 5. Development of M_n (green) and PDI (red) versus CHO conversion for the **7**/DMAP catalyzed CHO–PA copolymerization.

Effect of Cocatalysts on Catalytic Behavior. While there have been numerous studies on epoxide–CO_2 copolymerization involving metal salen or porphyrinato catalysts in combination with nucleophilic cocatalysts,[4,15,17,19,23,25,33,34] thus far there have only been few reports on the copolymerization of epoxides and anhydrides utilizing these catalyst systems. A recent report on the chromium porphyrinato, TTPCrCl, and salophen (**7**) catalyzed copolymerization of CHO and anhydrides (e.g., SA, CPrA, PA) clearly showed that the presence of a cocatalyst dramatically improved the catalytic activity and ester content of the obtained polymers.[10] Conversely, a recent study demonstrated that the copolymerization of propylene oxide and maleic anhydride (MA) catalyzed by **6** proceeds smoothly in petroleum ether without the need of a cocatalyst.[18]

Herein we have studied and compared the effect of different types of cocatalysts including *N*-heterocyclic nucleophiles, phosphines, and PPN^+Cl^- in ring-opening copolymerization of cyclohexene oxide and phthalic anhydride. Since **6** is an effective epoxide–CO_2 copolymerization catalyst in combination with the above-mentioned cocatalysts and both **6** and **7** proved to be effective catalysts for the copolymerization of CHO and anhydrides, these two catalysts were chosen to study the effect of different cocatalysts on the catalytic behavior.

dx.doi.org/10.1021/ma2025804 | *Macromolecules* 2012, 45, 1770–1776

Cocatalyst-Free. First we investigated whether the recent finding of Coates, that the copolymerization of propylene oxide and MA catalyzed by **6** proceeds smoothly in petroleum ether at 45 °C in the *absence* of a cocatalyst, is a general feature.[18] Thus, the copolymerization of maleic anhydride (MA) and CHO were carried out in toluene and petroleum ether, in both the presence and absence of DMAP as cocatalyst and using **6** and **7** as catalysts. After 24 h at 45 °C in toluene in the presence of DMAP as cocatalyst, no conversion of CHO and MA could be observed. This is in agreement with previous results that copolymerization of CHO and anhydrides (e.g., SA, PA, CPrA) catalyzed by **7**/DMAP in toluene were only found to proceed with good catalytic activity at elevated temperatures (110 °C).[10] Copolymerizations in toluene without cocatalyst resulted in low conversions and produced poly(ester−ether)s with mainly (>85%) ether functionalities. In petroleum ether and in the presence of DMAP an insoluble lump of probably cross-linked material was produced. Only in petroleum ether in the *absence* of DMAP a tractable soluble polymer was formed. The obtained polymer was found to be a poly(ester−ether), poly[$(C_6H_{10}O)_x(C(=O)CH=CHC(=O)-OCH_6H_{10}O)_y$], with 58% and 30% ester functionalities for **6** (conversion 89%; M_n = 5800 g/mol, PDI = 4.4) and **7** (conversion 99%; M_n = 3400 g/mol, PDI = 2.5), respectively. Because of the low solubility of SA, CPrA, and PA in petroleum ether at room temperature, the copolymerization of CHO and SA, CPrA, or PA in petroleum ether could not be performed as a comparison. The copolymerization of SA, the saturated congener of MA, in Isopar E at 110 °C using **6**/DMAP as catalyst system after 5 h resulted in a perfect alternating copolymer with 98% conversion of CHO and SA. The same copolymerization carried out *without* a cocatalyst resulted in low conversion (27%) after 5 h. Extending the polymerization time to 24 h increased the conversion up to 73%. Interestingly, also in this case pure alternating copolymers were obtained. Using **7**/DMAP resulted in full conversion and formation of pure alternating CHO−SA copolymers after 5 h. In the *absence* of cocatalyst only 50% conversion was observed, but again a pure polyester was formed. These results indicate that the double bonds of MA moieties in the CHO−MA copolymers are most probably cross-linked in the presence of DMAP. Furthermore, it can be concluded that aliphatic hydrocarbons are suitable solvents for the CHO−anhydride copolymerization and seem to have a positive effect on the selectivity of the catalyst, while without cocatalyst in toluene poly(ester-*co*-ether)s were obtained, in aliphatic hydrocarbons pure polyesters were formed. For the CHO−SA/PA/CPrA copolymerizations, the presence of a cocatalyst clearly enhances the catalytic activity of the catalyst. However, DMAP has no influence on the selectivity as pure polyesters were also obtained in the absence of cocatalyst.

N-Heterocyclic Nucleophiles. DMAP, *N*-MeIm (*N*-methylimidazole), and TBD (1,5,7-triazabicyclododecene) were selected as *N*-heterocyclic nucleophilic cocatalysts. DMAP has proven to be one of the more effective cocatalysts in epoxide−CO_2 copolymerizations, while *N*-MeIm and TBD have shown lower reactivities in epoxide−CO_2 copolymerizations catalyzed by **6**.[17,19] Studies by Darensbourg et al. demonstrated that DMAP showed 5 times higher reactivity than *N*-MeIm at 1 equiv loading during epoxide−CO_2 copolymerization using **6**.[17] The same trend as found for the epoxide−CO_2 copolymerization was also observed for the epoxide−anhydride copolymerizations. Of the three cocatalysts, TBD was clearly the least effective one (Table 1). In line with the results displayed in Figure 3 (Table S1), complex **7** shows for all three cocatalysts a slightly higher activity than **6**.

Table 1. CHO−PA Solution Copolymerization Catalyzed by 6 and 7 with Different *N*-Heterocyclic Nucleophiles as Cocatalysts[a]

entry	catalyst	cocatalyst	CHO conv[b] (%)	M_n[c] (g/mol)	PDI[c]
1	**6**	DMAP	62	5200	1.2
2	**7**	DMAP	91	9300	1.2
3	**7**	DMAP (3)	90	7800	1.2
4	**7**	DMAP[d]	70	11600	1.3
5	**7**	DMAP[d] (3)	80	8800	1.2
6	**6**	*N*-MeIm	56	5700	1.2
7	**7**	*N*-MeIm	78	6900	1.2
8	**6**	TBD	17	2100	1.3
9	**7**	TBD	43	4300	1.2

[a]Reaction condition = toluene, temperature = 110 °C, time = 60 min, [anhydride]:[CHO]:[cat]:[cocat.] = 250:250:1:1. [b]Determined by ^{1}H NMR. [c]Determined by SEC. [d]Recrystallized DMAP.

Next, the effect of variation in the cocatalyst:catalyst ratio was studied using **7** as catalyst and four different cocatalyst:catalyst ratios (Figure 6). Whereas for DMAP

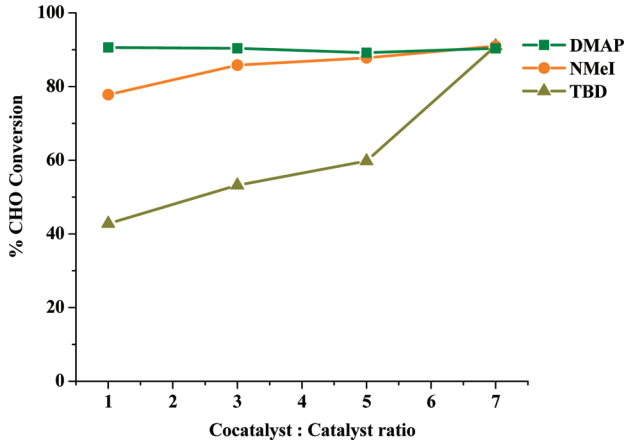

Figure 6. Effect of cocatalyst:catalyst ratio on CHO−PA copolymerization using **7** and *N*-heterocyclic Lewis bases as cocatalyst.

variation in the cocatalyst concentration had no effect on the catalytic activity of the system, for *N*-MeIm and especially TBD there was a significant increase in catalytic activity with increasing cocatalyst:catalyst ratio. The same enhancement of the catalytic activity by increasing the *N*-MeIm:catalyst ratio was reported earlier for the epoxide−CO_2 copolymerization.[23] This suggests that the catalyst−cocatalyst interaction is reversible and the strength of the binding interaction is in the order DMAP > *N*-MeIm > TBD. Interestingly, the polymer molecular weight decreased with increasing amount of DMAP and to a lesser extent for *N*-MeIm, whereas the opposite effect was observed for TBD (Table S6, Supporting Information). Although the observed effect of the cocatalyst:catalyst ratio on the molecular weight of the polymer is significant and not an inaccuracy of the SEC measurement, its explanation is not straightforward. The increase of the polymer molecular weight with increasing TBD concentration can be explained by the increase in conversion, keeping in mind that we are dealing with an intrinsically living system. The decrease of the polymer molecular weight with increasing DMAP (or *N*-MeIm) clearly has another origin. Introduction of water by increasing the

dx.doi.org/10.1021/ma2025804 | *Macromolecules* 2012, 45, 1770−1776

concentration of the cocatalyst seems plausible since recrystallized (diethyl ether) DMAP produced somewhat higher molecular weight polymers than unpurified DMAP under the same conditions (Table 1). Nevertheless, comparing the polymers produced with dried DMAP show a drop in molecular weight with increasing DMAP:Cr ratio. MALDI-ToF-MS spectra of the polymers obtained with **6** or **7** and DMAP as cocatalyst mainly showed DMAP end-functionalized charged chains. Although MALDI-ToF-MS is a qualitative technique, it is clear that at least some of the polymers are initiated by DMAP, indicating that DMAP functions as a chain transfer agent. Therefore, increasing the DMAP concentration is believed to result in more chains of lower molecular weight for the same conversion. Alternatively, since the thus obtained chains are zwitterionic, $DMAP^{+}\text{-}C_6H_{10}O\text{-}[C(=O)\text{-}R\text{-}C(=O)O\text{-}C_6H_{10}\text{-}O]_n^{-}$, it is not unlikely that backbiting occurs resulting in low molecular weight cyclic polymer structures.[35,36] Unfortunately, since the charged DMAP-end-capped polymers obscured the MALDI-ToF-MS spectra, it was impossible to make a reliable statement about the relative concentration of cyclic structures and water-initiated polymers as a function of DMAP concentration.

Phosphines. Four sterically and electronically different phosphines have been selected to be used as cocatalysts in combination with **6** and **7** for the copolymerization of CHO and PA: trimesitylphosphine ($PMes_3$), tris(2,4,6-trimethoxyphenyl)phosphine (TMPP), tricyclohexylphosphine (PCy_3), and triphenylphsophine (PPh_3). The copolymerization results are given in Table 2. The negligible activity for $PMes_3$ can be attributed to the large cone angle of the phosphine considerably lowering its nucleophilicity.[37] The other phosphines showed comparable results and there was no clear trend in activity with respect to steric bulk or electron-donating ability of the phosphines. Kinetic studies of the CHO–PA copolymerization catalyzed by **7** in the presence of PCy_3 as cocatalyst showed a linear relationship between CHO conversion and molecular weight, characteristic for a living behavior (Figure 7).

Table 2. Copolymerization of CHO and PA Catalyzed by 6 and 7 with Different Phosphine Cocatalysts[a]

entry	catalyst	phosphine	cone angle (deg)	CHO conv[b] (%)	M_n[c] (g/mol)	PDI[c]
1	**6**	$PMes_3$	212	3	800	1.2
2	**7**	$PMes_3$	212	0	800	1.2
3	**6**	TMPP	185	76	6900	1.4
4	**7**	TMPP	185	85	8200	1.3
5	**6**	PCy_3	170	76	6100	1.2
6	**7**	PCy_3	170	91	7000	1.2
7	**6**	PPh_3	145	6	5600	1.3
8	**7**	PPh_3	145	71	5400	1.3

[a]Reaction condition = solution, temperature = 110 °C, time = 60 min, [anhydride]:[CHO]:[cat.]:[phosphine] = 250:250:1:1. [b]Determined by ^{1}H NMR. [c]determined by SEC.

Complex **7** shows the best activity in combination with PCy_3, followed by TMPP and PPh_3. We therefore investigated the effect of the cocatalyst:catalyst ratio for these phosphines on the catalytic activity of **7** in the CHO–PA copolymerization

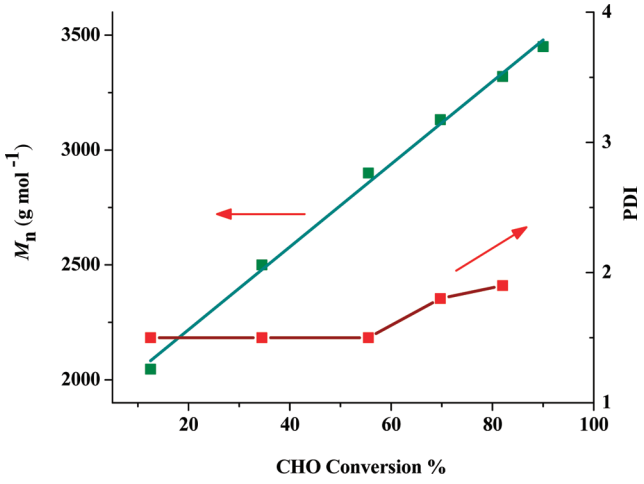

Figure 7. Development of M_n (green) and PDI (red) vs CHO conversion % of CHO–PA copolymers with PCy_3 as the cocatalyst catalyzed by complex **7**.

(Figure 8, Table S7 in the Supporting Information). For all three phosphines, the catalytic activity increased with increasing

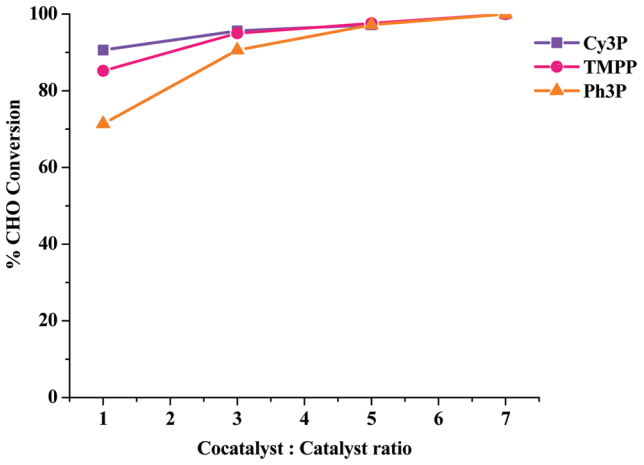

Figure 8. Effect of cocatalyst:catalyst ratio on CHO–PA copolymerization using **7** and phosphines as cocatalyst.

cocatalyst:catalyst ratio and differences between the phosphines were only small. For a cocatalyst:catalyst ratio of ≥5 all three phosphines gave the same activity. Whereas for DMAP and TBD a significant dependence of the polymer molecular weight on the cocatalyst:catalyst ratio was observed, for the phosphines no clear trend was found.

Bis(triphenylphosphoranylidene)ammonium Chloride ($PPN^{+}Cl^{-}$). Ultimately, we focused on bis(triphenylphosphoranylidene)ammonium chloride as cocatalyst. As this type of cocatalyst produced one of the most active (salen)MCl catalysts for epoxide–CO_2 copolymerization,[15,17,38] and on the basis of similarities between the epoxide–CO_2 and epoxide–anhydride copolymerization observed in this study, we expected similar good results. Indeed, $PPN^{+}Cl^{-}$ proved to be an efficient cocatalyst, and 1 equiv was enough to reach optimum activity. Comparing complexes **6** and **7** with $PPN^{+}Cl^{-}$ showed a very similar activity for **6** and **7** (**6**: 90% CHO conversion, M_n = 13 100, PDI = 1.2; **7**: 92% CHO conversion, M_n = 14 000, PDI = 1.2). Increasing the cocatalyst:catalyst ratio had no effect on the activity (Table 3).[15,17,34,39] The linear

dx.doi.org/10.1021/ma2025804 | *Macromolecules* 2012, 45, 1770–1776

Table 3. Copolymerization of CHO and PA Catalyzed by 7 with Different PPN^+Cl^-:7 Ratios[a]

entry	cocat. (equiv)	CHO conv[b] (%)	M_n[c]	PDI[c]
1	PPN^+Cl^- (1)	98	8100	1.2
2	PPN^+Cl^- (3)	99	4600	1.2
3	PPN^+Cl^- (5)	99	4000	1.2
4	PPN^+Cl^- (7)	99	3000	1.1
5	PPN^+Cl^- [d] (1)	84	15000	1.2
6	PPN^+Cl^- [d] (3)	93	9600	1.2

[a]Reaction condition = solution, temperature = 110 °C, time = 60 min, catalyst = 7, [anhydride]:[CHO]:[cat.]:[PPNCl] = 250:250:1:1. [b]Determined by ^1H NMR. [c]Determined by SEC. [d]Double recrystallized PPN^+Cl^-.

relationship between CHO conversion and molecular weight and the low PDI even at high conversions confirmed the living nature of this copolymerization in the presence of PPN^+Cl^- as cocatalyst (Figure 9).

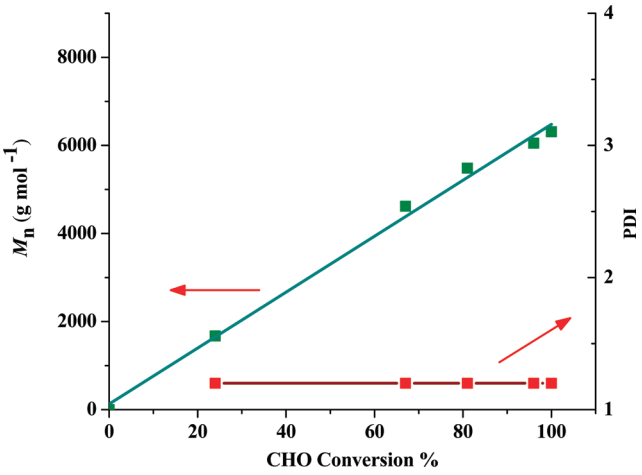

Figure 9. Development of M_n (green) and PDI (red) vs CHO conversion % of CHO–PA copolymers with PPN^+Cl^- as the cocatalyst catalyzed by complex 7.

Worth mentioning is the gradual decrease of the polymer molecular weight with increasing PPN^+Cl^-:7 ratio. The SEC shows a bimodal distribution in which two distributions differ by approximately a factor of 2 in molecular weight (Figure 10). As reported earlier, this is most likely due to the presence of traces of hydrolyzed anhydrides, leading to bimetallic catalytically active species. Increasing the PPN^+Cl^- concentration leads to an overall reduction of the molecular weight, suggesting that either water present in PPN^+Cl^- or PPN^+Cl^- itself functions as a chain transfer agent, resulting in more polymer chains with lower molecular weight upon increasing cocatalyst:catalyst ratio. Independent experiments using dried PPN^+Cl^- (double recrystallization from diethyl ether and acetone) confirmed that drying this particular cocatalyst significantly affects the molecular weight (9600 g/mol vs 4600 g/mol for dried and undried PPN^+Cl^- (3 equiv), respectively). However, comparing runs with differet amounts of double recrystallized PPN^+Cl^- and nonrecrystallized PPN^+Cl^- revealed that also for dried PPN^+Cl^- a clear drop of molecular weight was observed which is attributed to PPN^+Cl^- functioning as chain transfer agent.

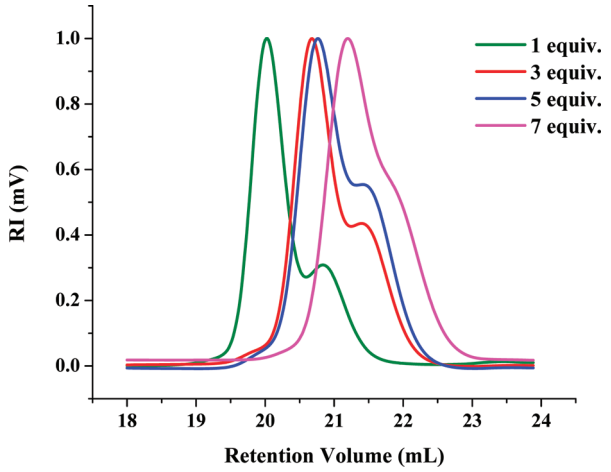

Figure 10. Development of M_n in GPC of CHO–PA copolymers obtained at various PPN^+Cl^-:7 ratios.

CONCLUSIONS

Variation of salen backbone, the metal, and the type of cocatalyst and cocatalyst:catalyst ratio all affect the epoxide–anhydride copolymerizations in a similar way as was found for the corresponding CHO–CO_2 copolymerization.[40] The chromium salophen complex 7 proved to be the most effective catalyst for the epoxide–anhydride copolymerization. Of all cocatalysts tested, PPN^+Cl^- exhibited the highest activity, and only 1 equiv was sufficient to reach the optimum activity. Phosphines and *N*-hetrocyclic nucleophiles were less effective cocatalysts, and higher than equimolar amounts of cocatalyst were necessary to reach the optimum activity. Worth mentioning is the fact that several cocatalysts (e.g., DMAP, PPN^+Cl^-) function as chain transfer agents, and increasing the cocatalyst:catalyst ratio results in a reduction of the molecular weight of the produced polymer, while the catalytic activity is not affected. It has to be said though that the absolute molecular weights cannot be compared as variable traces of water in monomer and cocatalyst can result in effective chain transfer and therefore has a significant effect on the polymer molecular weight as well.

ASSOCIATED CONTENT

Supporting Information

Tables and figures of the bulk copolymerization of CHO with anhydrides (SA, CPrA, and PA) catalyzed by **1–12** in the presence of DMAP as cocatalyst. This material is available free of charge via the Internet at http://pubs.acs.org.

AUTHOR INFORMATION

Corresponding Author

*Phone: +31 40 247 4918; Fax: +31 40 246 3966; e-mail: r.duchateau@tue.nl.

Notes

The authors declare no competing financial interest.

ACKNOWLEDGMENTS

We thank DSM Research for financial support and the Foundation of Emulsion Polymerization (SEP) for the use of the MALDI-ToF-MS machinery.

REFERENCES

(1) Tsurutat, T. M. K.; Inoue, S. *Makromol. Chem.* **1964**, *75*, 211−214.
(2) Paddock, R. L.; Nguyen, S. T. *J. Am. Chem. Soc.* **2001**, *123*, 11498−11499.
(3) Lu, X.-B.; Feng, X.-J.; He, R. *Appl. Catal., A* **2002**, *234*, 25−33.
(4) Eberhardt, R.; Allmendinger, M.; Rieger, B. *Macromol. Rapid Commun.* **2003**, *24*, 194−196.
(5) Cohen, C. T.; Thomas, C. M.; Peretti, K. L.; Lobkovsky, E. B.; Coates, G. W. *Dalton Trans.* **2006**, 237−249.
(6) Meléndez, J.; North, M.; Pasquale, R. *Eur. J. Inorg. Chem.* **2007**, 3323−3326.
(7) Sugimoto, H.; Kuroda, K. *Macromolecules* **2008**, *41*, 312−317.
(8) Ren, W.-M.; Zhang, X.; Liu, Y.; Li, J.-F.; Wang, H.; Lu, X.-B. *Macromolecules* **2010**, *43*, 1396−1402.
(9) Niu, Y.; Zhang, W.; Li, H.; Chen, X.; Sun, J.; Zhuang, X.; Jing, X. *Polymer* **2009**, *50*, 441−446.
(10) Huijser, S.; HosseiniNejad, E.; Sablong, R. l.; de Jong, C.; Koning, C. E.; Duchateau, R. *Macromolecules* **2011**, *44*, 1132−1139.
(11) Jeske, R.; Rowley, J.; Coates, G. *Angew. Chem., Int. Ed.* **2008**, *47*, 6041−6044.
(12) Aida, T.; Inoue, S. *J. Am. Chem. Soc.* **1985**, *107*, 1358−1364.
(13) Maeda, Y.; Nakayama, A.; Kawasaki, N.; Hayashi, K.; Aiba, S.; Yamamoto, N. *Polymer* **1997**, *38*, 4719−4725.
(14) Jeske, R. C.; DiCiccio, A. M.; Coates, G. W. *J. Am. Chem. Soc.* **2007**, *129*, 11330−11331.
(15) Darensbourg, D. J.; Mackiewicz, R. M.; Rodgers, J. L.; Phelps, A. L. *Inorg. Chem.* **2004**, *43*, 1831−1833.
(16) Darensbourg, D. J.; Mackiewicz, R. M.; Rodgers, J. L. *J. Am. Chem. Soc.* **2005**, *127*, 17565−17565.
(17) Darensbourg, D. J.; Mackiewicz, R. M. *J. Am. Chem. Soc.* **2005**, *127*, 14026−14038.
(18) DiCiccio, A. M.; Coates, G. W. *J. Am. Chem. Soc.* **2011**, *133*, 10724−10727.
(19) Darensbourg, D. J.; Mackiewicz, R. M.; Rodgers, J. L.; Fang, C. C.; Billodeaux, D. R.; Reibenspies, J. H. *Inorg. Chem.* **2004**, *43*, 6024−6034.
(20) Niu, Y.; Zhang, W.; Pang, X.; Chen, X.; Zhuang, X.; Jing, X. *J. Polym. Sci., Part A: Polym. Chem.* **2007**, *45*, 5050−5056.
(21) Martinez, L. E.; Leighton, J. L.; Carsten, D. H.; Jacobsen, E. N. *J. Am. Chem. Soc.* **1995**, *117*, 5897−5898.
(22) Wöltinger, J.; Bäckvall, J.-E.; Zsigmond, Á. *Chem.—Eur. J.* **1999**, *5*, 1460−1467.
(23) Darensbourg, D. J.; Yarbrough, J. C. *J. Am. Chem. Soc.* **2002**, *124*, 6335−6342.
(24) Darensbourg, D. J.; Yarbrough, J. C.; Ortiz, C.; Fang, C. C. *J. Am. Chem. Soc.* **2003**, *125*, 7586−7591.
(25) Darensbourg, D. J.; Mackiewicz, R. M.; Phelps, A. L.; Billodeaux, D. R. *Acc. Chem. Res.* **2004**, *37*, 836−844.
(26) Chisholm, M. H.; Gallucci, J. C.; Quisenberry, K. T.; Zhou, Z. *Inorg. Chem.* **2008**, *47*, 2613−2624.
(27) Dzugan, S. J. *Inorg. Chem.* **1986**, *25*, 2858−2864.
(28) Huijser, S.; Staal, B. B. P.; Huang, J.; Duchateau, R.; Koning, C. E. *Angew. Chem., Int. Ed.* **2006**, *45*, 4104−4108.
(29) Huijser, S.; Staal, B. B. P.; Huang, J.; Duchateau, R.; Koning, C. E. *Biomacromolecules* **2006**, *7*, 2465−2469.
(30) Aida, T.; Inoue, S. *Acc. Chem. Res.* **1996**, *29*, 39−48.
(31) van Meerendonk, W. J.; Duchateau, R.; Koning, C. E.; Gruter, G.-J. M. *Macromolecules* **2005**, *38*, 7306−7313.
(32) Nomura, N.; Taira, A.; Nakase, A.; Tomioka, T.; Okada, M. *Tetrahedron* **2007**, *63*, 8478−8484.
(33) Darensbourg, D. J.; Moncada, A. I. *Macromolecules* **2009**, *42*, 4063−4070.
(34) Darensbourg, D. J.; Ulusoy, M.; Karroonnirum, O.; Poland, R. R.; Reibenspies, J. H.; Çetinkaya, B. *Macromolecules* **2009**, *42*, 6992−6998.
(35) Jeong, W.; Hedrick, J. L.; Waymouth, R. M. *J. Am. Chem. Soc.* **2007**, *129*, 8414−8415.
(36) Jeong, W.; Shin, E. J.; Culkin, D. A.; Hedrick, J. L.; Waymouth, R. M. *J. Am. Chem. Soc.* **2009**, *131*, 4884−4891.
(37) Tolman, C. A. *Chem. Rev.* **1977**, *77*, 313−348.
(38) Cohen, C. T.; Chu, T.; Coates, G. W. *J. Am. Chem. Soc.* **2005**, *127*, 10869−10878.
(39) Darensbourg, D. J.; Moncada, A. I. *Inorg. Chem.* **2008**, *47*, 10000−10008.
(40) Darensbourg, D. J. *Chem. Rev.* **2007**, *107*, 2388−2410.

Macromolecules

Article

pubs.acs.org/Macromolecules

Ethylene Homopolymerization Kinetics with a Constrained Geometry Catalyst in a Solution Reactor

Saeid Mehdiabadi and João B. P. Soares*

Department of Chemical Engineering, University of Waterloo, Waterloo, Ontario, Canada N2L 3G2

Supporting Information

ABSTRACT: The solution polymerization of ethylene was studied in a semibatch reactor using a constrained geometry catalyst (CGC) and methylaluminumoxane (MAO). The influence of ethylene concentration, temperature, MAO, and catalyst concentrations on ethylene polymerization kinetics was investigated systematically. The deactivation of the CGC/MAO system during ethylene polymerization was described with a first order thermal deactivation mechanism that included reversible activation and deactivation with MAO. Interestingly, the polymerization order with respect to ethylene varied with ethylene concentration from first to second order. The trigger mechanism was shown to describe well the effect of ethylene concentration on polymer yield and polymerization kinetics. Low MAO concentration favored formation of polymer chains with unsaturated chain ends that in turn led to the production of polymers with higher long chain branch densities. It was also observed that CGC did not behave as a true single site catalyst at low MAO concentrations.

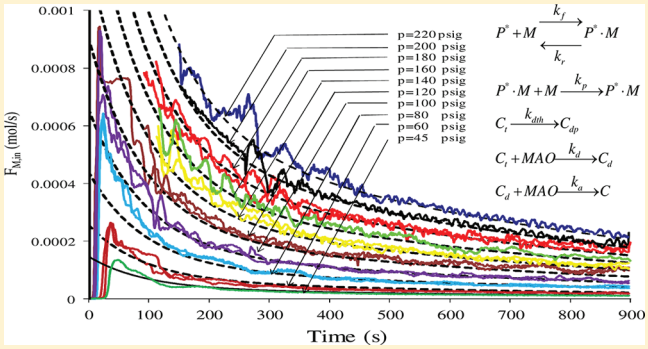

INTRODUCTION

Constrained geometry catalysts (CGC) are transition metal complexes bearing linked amido ligands that have found wide interest both in academia and industry since 1990.[1] This type of catalyst retains one of the cyclopetadienyl rings of metallocenes, but replaces the other ring with a nitrogen substituent that coordinates with the metal center, usually a group 4 metal (Zr or Ti).[2] Figure 1 depicts the structure of an exemplary CGC. These complexes are also known as half-sandwich catalysts.

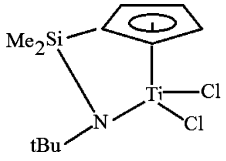

Figure 1. Structure of a constrained geometry catalyst.

When activated with MAO or borates, CGC can produce polyolefins with long chain branches (LCB) by the reinsertion of chains terminated with reactive double bonds (macromonomers). In the case of ethylene polymerization, vinyl-terminated chains are created by chain transfer to ethylene or β-hydride elimination.

The amide donor ligand of the complex depicted in Figure 1 stabilizes the electrophilic metal center, while the short Me_2Si< bridging group creates a more open environment at the metal site compared to conventional metallocenes.[3] Consequently, these catalysts allow the facile incorporation of bulky monomers, including 1-alkenes, cycloalkenes, and styrene[4] into random ethylene copolymers that are characterized by narrow molecular weight and chemical composition distributions.

Although several experimental studies on olefin homo- and copolymerization with CGC have been published,[5−11] only a few investigations have dealt with polymerization kinetic studies. In one such study, ethylene was polymerized with CGC and the authors concluded that as monomer concentration increased, the polymer yield also increased, but that the MAO/CGC ratio had no effect on polymer yield; unfortunately, no information was reported on catalyst decay, which has a marked influence on polymer yield.[12] In another study,[13] the CGC $TiMe_2$/tris(pentafluorophenyl)boron/MMAO system was used in a continuous stirred-tank reactor (CSTR) for ethylene homopolymerization. Ten polymerization runs were performed to investigate the effect of reactor average residence time, temperature, ethylene and hydrogen concentrations on polymerization kinetics. Polyethylene samples with LCB frequencies varying from 0.07 to 0.16 were made and the CGC appeared to behave as a single site catalyst. The authors concluded that a first order catalyst decay model was not appropriate to explain the observed results, but did not propose an alternative theoretical model to describe their data. They assumed a first order propagation step with respect to ethylene

Received: November 28, 2011
Revised: January 31, 2012
Published: February 13, 2012

   dx.doi.org/10.1021/ma202577n | *Macromolecules* 2012, 45, 1777−1791

concentration and based on this assumption estimated some reaction rate constants.

In the present investigation, ethylene was polymerized with CGC/MAO in a semibatch solution reactor. The polymerization of ethylene was studied systematically by changing ethylene, catalyst, and MAO concentrations. A kinetic model, based on the trigger mechanism,[14] was proposed, tested, and then refined based on monomer uptake curves and polymer yield data. First order thermal decay of the catalyst along with reversible and irreversible deactivation of the catalyst sites by MAO were satisfactory to explain the effect of catalyst and ethylene concentration, as well as polymerization time, on ethylene uptake curves. Polymers produced at low MAO concentrations had higher unsaturated chain end density and long chain branch frequencies.

EXPERIMENTAL SECTION

Materials. Methylaluminoxane (MAO, 10 wt % in toluene, Sigma-Aldrich) was used as received. Ethylene and nitrogen (Praxair) were purified by passing through molecular sieves (3 and 4 Å) and copper(II) oxide packed beds. Toluene (EMD) was purified by distillation over a *n*-butyllithium/styrene/sodium system and then passed through two packed columns in series filled with molecular sieves (3, 4, and 5 Å) and Selexorb for further purification. All air-sensitive compounds were handled under inert atmosphere in a glovebox.

The catalyst, dimethylsilyl(*N*-*tert*-butylamido)(tetramethylcyclopentadienyl)titanium dichloride (CGC−Ti), was purchased as a powder from Boulder Scientific and dissolved in toluene, which was first distilled over metallic sodium and then passed through a molecular sieve bed before polymerization.

Polymer Synthesis. All polymerizations were performed in a 500 mL Parr autoclave reactor operated in semibatch mode. The polymerization temperature was controlled using an electrical band heater and internal cooling coils. The reaction medium was mixed using a pitched-blade impeller connected to a magneto-driver stirrer, rotating at 2000 rpm. This stirring speed was selected to ensure that mass and heat transfer limitations did not influence the flow rate of ethylene to the reactor. Prior to use, the reactor was heated to 125 °C, evacuated, and refilled with nitrogen six times to reduce the oxygen concentration in the reactor; then, 250 mL of toluene and 0.5 g of triisobuthyl aluminum (as impurity scavenger) were charged to the reactor. The reactor temperature was increased to 120 °C and kept constant for 20 min for stabilization. Finally, the reactor contents were blown out under nitrogen pressure. This procedure ensured the removal of impurities from the reactor walls.

In a typical polymerization run, 200 mL of toluene was charged into the reactor, followed by an appropriate amount of MAO (10 wt % toluene solution), introduced via a 5 mL tube and a 20 mL sampling cylinder connected in series with an ethylene pressure differential of 40 psig. A specified volume of toluene was placed in the sampling cylinder before injection to wash the tube wall from any residual MAO solution. Then, the band heater was powered on to commence heating of the reactor up to 120 °C. Ethylene was introduced to the reactor until the solvent was saturated with ethylene. After approximately 10 min, when the reactor temperature was stabilized, catalyst solution was injected using the same method for MAO injection, but with a lower pressure differential to ensure a minimum pressure increase in the reactor at the start of the polymerization, but still enough to transfer the catalyst solution completely to the reactor. Ethylene was supplied on demand to maintain a constant reactor pressure and monitored with a mass flow meter. With the exception of a 1−2 °C exotherm upon catalyst injection, the temperature was kept at 120 °C ± 0.15 °C throughout polymerization. After 15 min, the polymerization was stopped by closing the ethylene valve and immediately blowing out the reactor contents into a 2-L beaker filled with 400 mL of ethanol. The polymer produced was then kept overnight, filtered, washed with ethanol, dried in air, and further dried under vacuum.

Polymer Characterization. Polymer molecular weight distribution (MWD) and averages were measured at 145 °C with a Polymer Char high-temperature gel permeation chromatographer (GPC), under a trichlorobenzene (TCB) flow rate of 1 mL/min. A column bank of three PLgel Olexis 13 μm mixed pore type 300 × 7.5 mm columns were used for GPC separations. The GPC was equipped with three detectors in series (infrared, 15° angle light scattering and differential viscometer) and calibrated with polystyrene narrow standards.

The ^{13}C NMR spectrum was taken on a Bruker 500 MHz system with 5 mm tube. The probe temperature was set at 120 °C. Acquisition parameters were 14 μs 90° pulse, inverse gated proton decoupling and 10 s delay time between pulses. 10,000 scans were used for data averaging. The highest intensity peak was referenced to 30.0 ppm. Deuterated *o*-dichlorobenzene was used to obtain the field-frequency lock.

Fourier transform−infrared spectroscopy was used to quantify the vinyl groups in the polymer chains.[15] The spectra were recorded from 400 to 4000 cm^{-1}, after 32 scans, with a resolution of 2 cm^{-1}. The absorption band at 908 cm^{-1}, representative of vinyl groups, was used to measure the amount of vinyl groups in the polymer.

RESULTS AND DISCUSSION

Effect of Ethylene Concentration. The effect of ethylene concentration on polymerization kinetics was investigated by varying the total reactor pressure from 35 to 220 psig at a constant temperature of 120 °C. A complete randomized design, with 11 monomer concentration levels and at least two replicates at each level, was adopted. All polymerizations were performed at a catalyst concentration of 0.547 μmol/L, 222.8 mL of solvent, and 2.0 g of MAO solution. Polymer yields and molecular weight measurements are summarized in Table 1.

Table 1. Polymerization Run Results (Monomer Concentration Effect)

run	reactor pressure (psig)	M_w	M_n	PDI	polymer yield (g)	activity (kg PE/(mol Ti·h))
120A	120	188 600	91 500	2.06	5.59	40 900
60A	60	121 000	52 600	2.30	1.70	12 400
100A	100	166 600	74 100	2.25	4.39	32 100
80A	80	142 800	69 900	2.04	3.01	22 000
120B	120	174 900	80 600	2.17	6.01	44 000
80B	80	150 700	68 600	2.20	2.80	20 500
60B	60	115 600	55 300	2.09	1.75	12 800
100B	100	163 100	78 100	2.09	4.10	30 000
120C	120	173 700	75 800	2.29	5.51	40 300
100C	100	167 300	74 400	2.25	4.10	30 000
45A	45	95 600	40 800	2.34	1.01	7 300
140A	140	202 600	96 500	2.10	6.70	49 000
140B	140	212 600	99 000	2.15	7.80	57 000
45B	45	110 500	48 900	2.26	0.90	6 600
140C	140	206 100	99 000	2.08	7.78	56 900
180A	180	237 300	109 600	2.17	10.40	76 100
35A	35	73 800	32 200	2.29	0.50	3 700
160A	160	216 600	105 000	2.06	8.60	62 900
160B	160	227 200	102 000	2.23	9.13	66 800
180B	180	240 400	106 900	2.25	10.44	76 300
220A	220	261 300	115 500	2.26	13.23	96 700
200A	200	247 900	102 000	2.43	12.20	89 200
220B	220	253 900	112 000	2.27	14.40	105 300
200B	200	250 700	110 200	2.27	11.69	85 500

Polymerization Order with Respect to Ethylene Concentration. Polymer yield versus ethylene concentration in the reactor liquid phase is shown in Figure 2. (The experimental data by Lee et al.[16] were used to calculate ethylene

dx.doi.org/10.1021/ma202577n | *Macromolecules* 2012, 45, 1777−1791

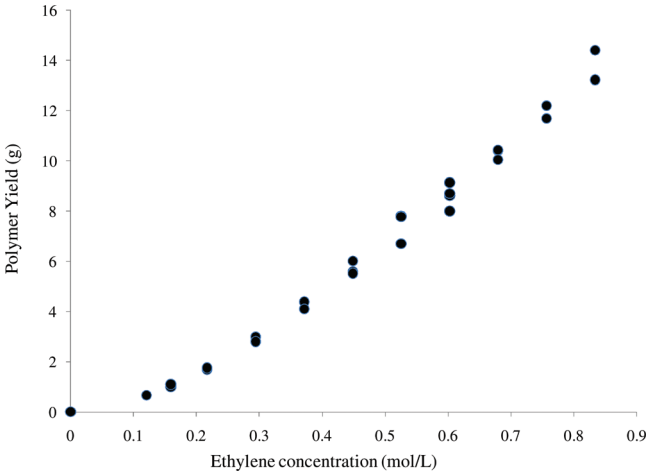

Figure 2. Polymer yield versus ethylene concentration in the reactor liquid phase.

concentration in the liquid phase corresponding to total reactor pressure.) As expected, the curve passes through the origin, but a curvature is seen at low ethylene concentrations which clearly points out to a nonfirst order dependence of the polymerization rate on ethylene concentration. When the polymer yield is plotted versus the square of ethylene concentration in the reactor liquid phase for the low concentration range (Figure 3),

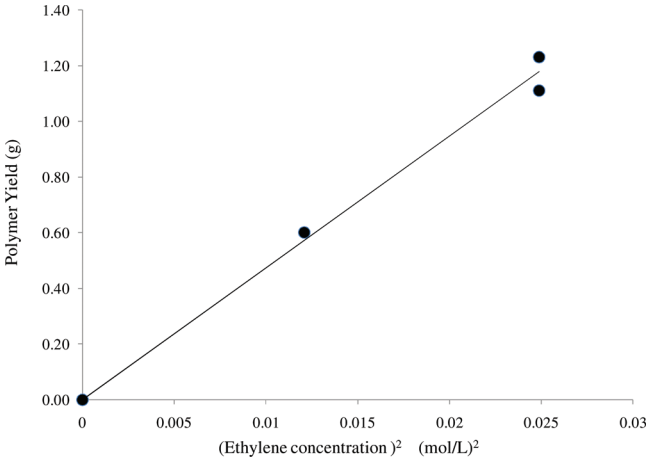

Figure 3. Polymer yield versus the square of ethylene concentration in the reactor liquid phase (low ethylene concentration range).

a linear relation is observed, suggesting a second order dependency at low ethylene concentrations. Contrarily, Figure 2 shows that polymer yield depends linearly on ethylene concentration for values higher than approximately 0.4 mol/L. This indicates that the propagation order with respect to ethylene concentration changes from two to one when the ethylene pressure is increased. Ethylene polymerization orders higher than one were also reported by other investigators.[17−22] We propose the mechanism described in eqs 1 and 2 as a possible explanation for the observed change in propagation order.

$$\mathrm{P^*} + \mathrm{M} \underset{k_r}{\overset{k_f}{\rightleftarrows}} \mathrm{P^*{\cdot}M} \tag{1}$$

$$\mathrm{P^*{\cdot}M} + \mathrm{M} \xrightarrow{k_p} \mathrm{P^*{\cdot}M} \tag{2}$$

The formulation of eqs 1 and 2 is consistent with the main assumptions of the trigger mechanism,[14,23] according to which a monomer molecule first forms a complex with the active site and insertion into the growing polymer chain only takes place if a second monomer unit approaches the active site, "triggering" the insertion. In the above mechanism P* is the uncomplexed active site with a growing polymer chain of any length, while P*·M is a growing polymer chain complexed with a monomer molecule. Reversible complex formation between active site with one monomer molecule is also accepted.[24−26]

Assuming that the reaction described in eq 1 is at fast equilibrium, one can write,

$$[\mathrm{P^*{\cdot}M}] = \frac{k_f[\mathrm{M}][\mathrm{P^*}]}{k_r} \tag{3}$$

The total concentration of active sites, C_t, in the reactor at a given time is given by the sum of complexed and uncomplexed active sites

$$C_t = [\mathrm{P^*{\cdot}M}] + [\mathrm{P^*}] \tag{4}$$

Substituting eq 3 in eq 4 and solving for [P*] yields,

$$[\mathrm{P^*}] = \frac{k_r}{k_r + k_f[M]} C_t \tag{5}$$

Finally, combining eqs 5 and 3 gives the concentration of complexed sites in the reactor at a given time,

$$[\mathrm{P^*{\cdot}M}] = \frac{k_f[\mathrm{M}]C_t}{k_r + k_f[\mathrm{M}]} \tag{6}$$

According to eq 2, the polymerization rate is given by the expression,

$$R_p = k_p[\mathrm{P^*{\cdot}M}][\mathrm{M}] \tag{7}$$

which can be combined with eq 6 to find the final expression for the polymerization rate governed by the mechanism expressed in eqs 1 and 2,

$$R_p = \frac{k_p C_t k_f [\mathrm{M}]^2}{k_r + k_f[\mathrm{M}]} \tag{8}$$

or,

$$R_p = \frac{k_p C_t K [\mathrm{M}]^2}{1 + K[\mathrm{M}]} \tag{9}$$

where

$$K = \frac{k_f}{k_r} \tag{10}$$

Consequently, at low ethylene pressures $K[M] \ll 1$, and eq 9 simplifies to

$$R_p = k_p C_t K [\mathrm{M}]^2 \tag{11}$$

and the polymerization order with respect to ethylene concentration approaches two. Inspection of eq 9 will also demonstrate that the polymerization rate becomes first order with respect to ethylene concentration as [M] increases and $K[\mathrm{M}] \gg 1$. Therefore, eq 9 seems adequate to describe the change in polymerization order depicted in Figure 2.

dx.doi.org/10.1021/ma202577n | Macromolecules 2012, 45, 1777−1791

Catalyst Deactivation. The activation of coordination catalysts, such as CGC, by MAO involves fast reduction and alkylation reactions yielding the catalytically active sites. After achieving a maximum polymerization activity, most coordination catalysts deactivate following a profile that depends on catalyst type, polymerization temperature, and impurity level in the reactor. Figure 4 shows the ethylene consumption rates as a function of polymerization time for several ethylene pressures. Since the catalyst solution is injected using an ethylene pressure differential, as described in the Polymer Synthesis section, the ethylene pressure inside the reactor after catalyst injection is momentarily increased above the pressure regulator set point, generating an apparent lag in ethylene flow rate depicted in Figure 4 for the first few seconds of polymerization. In addition,

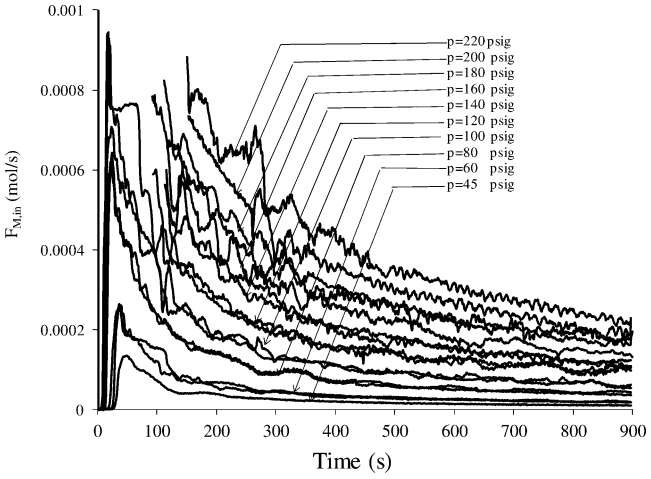

Figure 4. Ethylene reactor feed flow rate versus time at different total reactor pressures.

for the few runs performed at very high ethylene pressures, the ethylene flow meter was deliberately bypassed during the first couple of minutes because the ethylene flow rates at the beginning of those runs were beyond the flow meter measuring range. Finally, when the catalyst solution is injected, the temperature inside the reactor is disturbed by a few tenths of a degree during the first one or 2 min of polymerization. These experimental limitations decrease the reliability of the ethylene flow rate measurements during the first 2 min of polymerization; therefore, this data will not be used during model fitting below.

The first order catalyst decay model requires a linear relationship between the logarithm of monomer consumption rate and time. However, this model fails to describe the polymerization data with CGC adequately, as shown in Figure 5 for a typical polymerization run.

As an alternative to the first order catalyst decay model commonly assumed for coordination catalysts, a second order model could be proposed to describe the data presented in Figure 4,

$$\frac{dC_t}{dt} = -k_d {C_t}^2 \tag{12}$$

In eq 12, it is assumed that the catalyst activation is instantaneous: as soon as the catalyst is injected in the reactor and comes in contact with MAO, all the catalyst sites are activated. Starting with eq 12, the following expression for

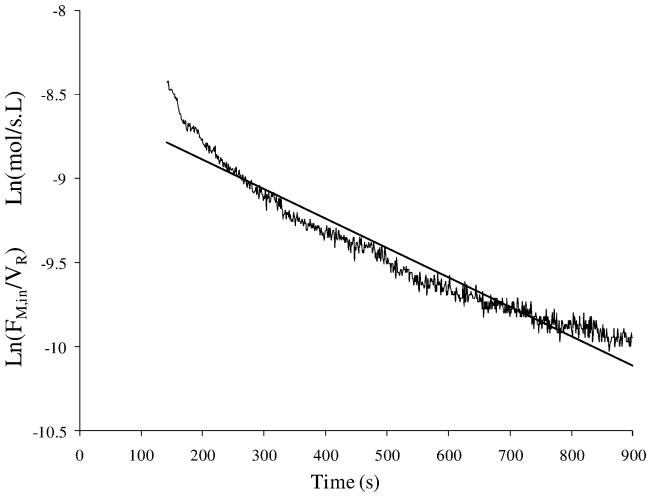

Figure 5. Experimental ethylene uptake curve and first order catalyst deactivation model for ethylene polymerization with CGC at total reactor pressure of 120 psig (run 120 B in Table 1).

monomer consumption rate can be derived (derivation details are given in Appendix A, Supporting Information):

$$F_{M,in} = \frac{k_p K V_R C_0 [\mathrm{M}]^2}{(1 + K[\mathrm{M}])(1 + k_d C_0 t)} \tag{13}$$

Rearranging eq 13 gives

$$\frac{V_R}{F_{M,in}} = \frac{(1 + K[\mathrm{M}])}{k_p K C_0 [\mathrm{M}]^2} + \frac{(1 + K[\mathrm{M}]) k_d C_0}{k_p K C_0 [\mathrm{M}]^2} t \tag{14}$$

Equation 14 shows that, for second order catalyst decay kinetics, the plot of the reciprocal of the monomer consumption rate versus time is linear. Figure 6 illustrates this behavior

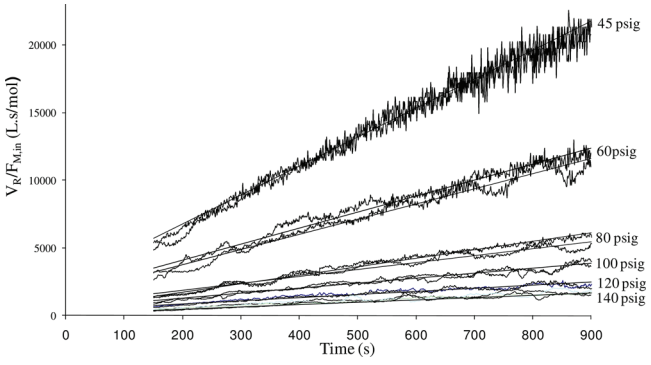

Figure 6. Second order decay model for CGC deactivation at several ethylene partial pressures.

for some typical polymerization runs performed at different ethylene partial pressures. As explained above, the reliability of the ethylene flow rate measurements during the first minutes of polymerization is not high; therefore, short polymerization time data was omitted during data fitting.

Equation 13 can be integrated to derive an expression for the total number of moles of polymer, *n*, made in the reactor after a given polymerization time,

$$n = \frac{k_p K V_R [\mathrm{M}]^2}{(1 + K[\mathrm{M}]) k_d} \ln(1 + k_d C_0 t) \tag{15}$$

dx.doi.org/10.1021/ma202577n | *Macromolecules* 2012, 45, 1777–1791

Although the polymerization curves presented in Figure 6 seem to be well described with a second order decay model, eq 15 reveals that the polymer yield is not a linear function of the initial catalyst concentration (C_0). However, the additional experimental results that will be reported below show that the polymer yield is indeed linearly related to catalyst concentration, which contradicts the dependency predicted by eq 15. Consequently, a simple second order catalyst decay law is not adequate to describe the system under consideration. Before proposing a modification for this deactivation mechanism, results for the effect of catalyst concentration on the polymerization rate will be discussed.

Effect of Catalyst Concentration at High MAO Concentration. *Effect of Catalyst Concentration on Polymer Yield.* Six polymerizations were performed at a constant MAO concentration (the same MAO concentration at which the previous set of polymerization runs, given in Table 1, were performed), but different catalyst concentrations and two polymerization temperatures, to investigate the effect of catalyst concentration on polymer yield at high MAO concentration. The polymerization conditions are summarized in Table 2. Runs 160A, 160B, 180A, and 180B have already been reported in Table 1 and are reproduced in Table 2 for easy comparison. Polymer yield and molecular weight measurements using GPC are shown in Table 3.

Table 2. Polymerization Conditions (Catalyst Concentration Effect)

run	temperature (°C)	pressure (psig)	catalyst concentration (μmol/L)
C-3	140	120	2.55
C-2	140	120	1.89
C-1	140	120	1.22
160A	120	160	0.547
160B	120	160	0.547
160C	120	160	0.274
160D	120	160	0.274
180A	120	180	0.547
180B	120	180	0.547
180C	120	180	0.274

Table 3. Polymer Yield and Molecular Weight Results (Catalyst Concentration Effect)

run	M_n	M_w	PDI	polymer yield (g)
C-1	35 500	93 400	2.63	5.68
C-2	33 900	94 400	2.79	3.95
C-3	34 000	91 400	2.68	2.78
160A	105 000	216 600	2.06	8.6
160B	102 000	227 200	2.23	9.13
160C	101 700	225 400	2.22	4
160D	99 700	232 200	2.33	4.35
180A	109 600	237 300	2.17	10.4
180B	106 900	240 400	2.25	10.44
180C	105 800	247 900	2.34	5.03

The first three polymerization runs in Table 2 (runs C-1, C-2, and C-3) have the same polymerization conditions, except for the catalyst concentration. Figure 7 plots polymer yield versus catalyst concentration for these three runs, showing a clear linear relationship. Moreover, a linear extrapolation shows

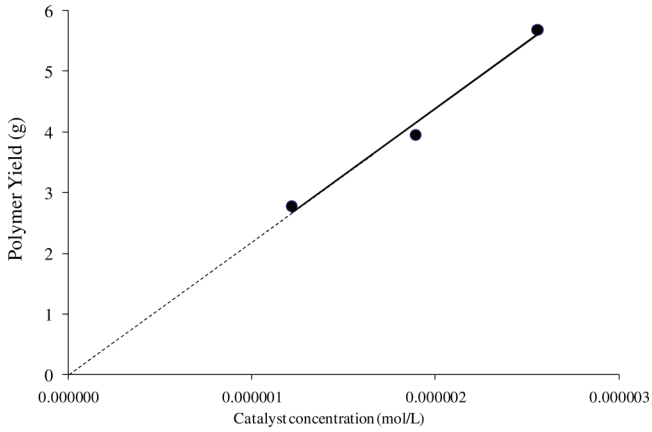

Figure 7. Polymer yield versus catalyst concentration for runs C-1, C-2, and C-3.

that the line passes through the origin, as expected. Ethylene flow rate curves for these three polymerizations are shown in Figure 8a. As a further test, we plotted the corresponding

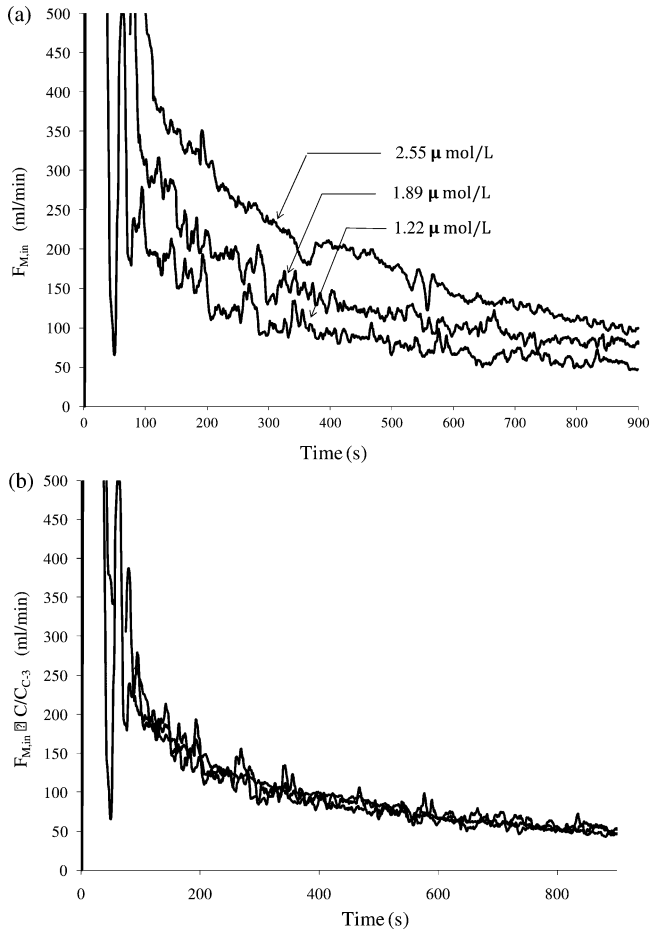

Figure 8. (a) Ethylene feed flow rate for runs C-1, C-2, and C-3. Legends indicate catalyst concentrations. (b) Products of ethylene flow rates times catalyst ratio $C/C_{C\text{-}3}$ for the same runs.

products of ethylene flow rates times catalyst ratio $C/C_{C\text{-}3}$, where $C_{C\text{-}3}$ is the catalyst concentration of run C-3, selected as the base, and C is the catalyst concentration of the other runs. All curves merge into a single one, proving that ethylene flow

dx.doi.org/10.1021/ma202577n | Macromolecules 2012, 45, 1777–1791

rate is proportional to catalyst concentration in the reactor (Figure 8b).

Comparing the polymerization yields for runs 160A and 160B with 160C and 160D shows that doubling catalyst concentration doubles polymer yield. The same conclusion is reached when the polymer yields for runs 180A, 180B, and 180C are compared. Therefore, there is enough evidence to show that the polymer yield is proportional to the catalyst concentration in the reactor, at least at high MAO/CGC ratios and when the change in catalyst concentration is within the range investigated in this study. These experimental findings are in disagreement with eq 15, which results from the direct application of a second order decay profile to polymerizations with CGC.

Effect of Catalyst Concentration on Polymer Molecular Weight. A good estimate of variance for M_n and M_w is necessary to check whether catalyst concentration affects molecular weight averages. Since variances for M_n and M_w are independent of ethylene concentration and they are nearly the same (Compare spread of molecular weights data in Table 1), combining variances using the pooled estimator of variances can provide these estimates. The pooled estimates of the common standard deviation[27] for M_w and M_n based on the data in Table 1 were found to be 5864 and 4200, respectively. This variability includes errors from molecular weight measurements and polymerization replicates. The difference between the mean M_w of polyethylene samples made at two levels of catalyst concentration at 160 psig (runs 160A to 160D) is 6931, which is less than two times of pooled estimate of the common standard deviation (2 × 5864). The difference between the mean M_n of the same samples is 1,150 which is again less than two times of pooled estimate of the common standard deviation for M_n (2 × 4200). This means that the difference between the means of average molecular weights at the two levels of catalyst concentrations results from random error variable. A similar calculation was performed for the two levels of catalyst concentration at 180 psig, reaching the same conclusion. Therefore, there is no evidence that changing catalyst concentration affects average molecular weights under the investigated polymerization conditions.

Modified Deactivation Mechanism. As demonstrated above, a simple second order catalyst decay mechanism cannot predict a linear relationship between polyethylene yield and catalyst concentration. However, the experimental results described in the previous section show that such a linear relationship is indeed observed for the range of conditions investigated in this study. Therefore, it is necessary to propose a mechanism that can describe the nonfirst order catalyst decay rate and, at the same time, account for the linear relation between polymer yield and catalyst concentration in the reactor.

In order to model the catalyst decay behavior with CGC−Ti, three elementary steps were assumed: thermal deactivation, MAO-promoted deactivation and reactivation. The thermal deactivation step is given by the reaction below,

$$C_t \xrightarrow{k_{dth}} C_{dp} \tag{16}$$

where k_{dth} denotes the thermal deactivation rate constant, and C_{dp} are the permanently deactivated sites. MAO-promoted (or, possibly TMA-prompted, since TMA is always often present in equilibrium with MAO) deactivation and reactivation reactions are represented as,

$$C_t + \text{MAO} \xrightarrow{k_d} C_d \tag{17}$$

$$C_d + \text{MAO} \xrightarrow{k_a} C_t \tag{18}$$

where C_d is a reversibly deactivated (or dormant) catalyst site that can be reactivated by reaction with MAO. This type of reversible deactivation mechanism has been used before to model the catalyst decay behavior of Cp_2ZrCl_2 for the polymerization of ethylene and propylene.[28,29]

The corresponding molar balances for C_t and C_d are given by

$$\frac{dC_t}{dt} = -k_{dth}C_t - k_d[\text{MAO}]C_t + k_a[\text{MAO}]C_d \tag{19}$$

$$\frac{dC_d}{dt} = -k_a[\text{MAO}]C_d + k_d[\text{MAO}]C_t \tag{20}$$

Since MAO is present at a much higher concentration than CGC, $k_a[\text{MAO}]$ and $k_d[\text{MAO}]$ may be assumed to be invariant during polymerization and will be represented by the lumped constants k'_a and k'_d, respectively.

Equations 19 and 20 can be solved with Laplace transforms under the initial conditions $C_t = C_0$ and $C_d = 0$ at $t = 0$ to yield eq 21 (details of this derivation are given in Appendix B, Supporting Information:

$$C_t = \frac{C_0}{(s_1 - s_2)}[(s_1 + k'_a)e^{s_1 t} - (s_2 + k'_a)e^{s_2 t}] \tag{21}$$

where s_1 and s_2 are constants defined as,

$$s_1 = \frac{1}{2}[\sqrt{(k_{dth} + k'_d + k'_a)^2 - 4k_{dth}k'_a} - (k_{dth} + k'_d + k'_a)] \tag{22}$$

$$s_2 = -\frac{1}{2}[\sqrt{(k_{dth} + k'_d + k'_a)^2 - 4k_{dth}k'_a} + (k_{dth} + k'_d + k'_a)] \tag{23}$$

The molar balance for monomer concentration in a semibatch reactor is given by

$$\frac{d[M]}{dt} = \frac{F_{M,in}}{V_R} - R_p \tag{24}$$

Since monomer concentration is kept constant, we conclude that,

$$F_{M,in} = R_p V_R \tag{25}$$

Combining eqs 9, 21, and 25 leads to the final expression for the monomer feed flow rate to the reactor for a catalyst that follows the trigger mechanism and deactivates according to the steps proposed in eqs 16-18,

$$F_{M,in} = \frac{k_p K[M]^2 C_0 V_R}{(1 + K[M])(s_1 - s_2)}[(s_1 + k'_a)e^{s_1 t} - (s_2 + k'_a)e^{s_2 t}] \tag{26}$$

dx.doi.org/10.1021/ma202577n | *Macromolecules* 2012, 45, 1777−1791

Finally, the polymer yield, in moles, can be obtained by the integration of eq 26,

$$n = \frac{k_p K[M]^2 C_0 V_R}{(1 + K[M])(s_1 - s_2)}\left[\frac{(s_1 + k'_a)}{s_1}(e^{s_1 t} - 1) - \frac{(s_2 + k'_a)}{s_2}(e^{s_2 t} - 1)\right] \quad (27)$$

Different from eq 15, eq 27 predicts that the polymer yield depends linearly on catalyst concentration in the reactor, in agreement with the experimental findings shown in Figures 7 and 8.

Estimation of Kinetic Parameters. Equation 26 can be rearranged to the following form,

$$\frac{(1 + K[M])F_{M,in}}{K[M]^2} = \frac{k_p C_0 V_R}{s_1 - s_2}[(s_1 + k'_a)e^{s_1 t} - (s_2 + k'_a)e^{s_2 t}] \quad (28)$$

The right-hand side (RHS) of eq 28 is a function of polymerization time, catalyst concentration, reactor volume, and temperature-dependent rate constants, while the left-hand side (LHS) depends on monomer concentration, reactor feed flow rate, and the equilibrium constant K. Therefore, if we plot eq 28 LHS versus time for the runs performed at varying monomer concentrations but same catalyst concentration, reactor volume, and temperature, we expect all curves to merge into a single one, given that we have chosen a proper value for the equilibrium constant K.

The optimum value for K can be obtained by minimizing the following objective function,

$$\chi = \frac{\int\left[\left(\frac{(1 + K[M])F_{M,in}}{K[M]^2}\right)_{max} - \left(\frac{(1 + K[M])F_{M,in}}{K[M]^2}\right)_{min}\right] dt}{\int\left[\frac{(1 + K[M])F_{M,in}}{K[M]^2}\right]_{a_v} dt} \quad (29)$$

where the subscripts "max" and "min" are the maximum and minimum values of eq 28 LHS for all runs at time t, and a_v refers to its average value for all runs at time t. In fact, by minimizing this objective function, the area of the error band relative to total area under the average monomer consumption rate is also minimized. Half of the value of the objective function at the optimum point would be the maximum value of the error in predicting polymer yield with eq 27. The optimum K value estimated by minimizing the objective function defined in eq 29 was found to be equal to 1.1.

Figure 9 shows the plot of eq 28 LHS versus time for all the polymerization runs in Table 7 using K = 1.1. All curves merge relatively well into a single 'master" curve, especially taking into consideration that, due to normal random error during the polymerizations, perfect overlapping would be extremely unlikely. Since the reactor temperature and pressure fluctuate more at the beginning of the polymerization, more variability is observed at shorter polymerization times.

Equation 28 was used to estimate the model parameters k'_a, $k_pC_0V_R$, s_1, and s_2 by fitting the average value of the LHS of eq 28 for all runs using MATALB curve fit toolbox. The first 70 s of the data were not used in curve fitting due to initial lag in measuring ethylene flow rate. The parameter estimates, with their approximate 95% confidence intervals, are shown in Table 4.

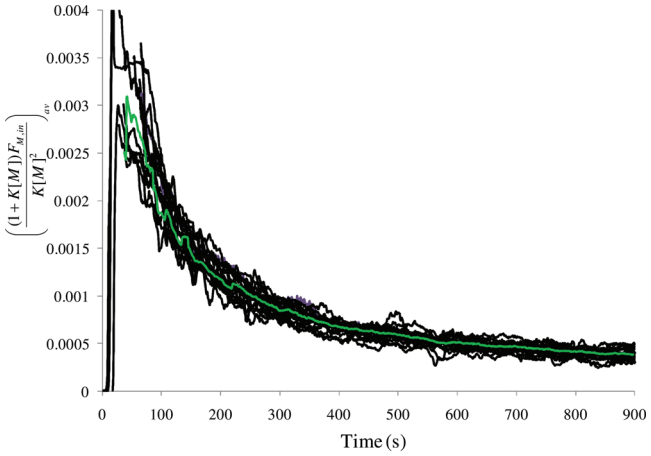

Figure 9. Plot of LHS of eq 28, $\{((1 + K[M])F_{M,in})/(K[M]^2)\}_{av}$, versus time for all the polymerization runs in Table 1.

Table 4. Model Parameters

parameter	estimated values with approximate 95% confidence interval
k'_a	$3.375 \times 10^{-3} \pm 1.5 \times 10^{-4}$ s^{-1}
$k_pC_0V_R$	$6.149 \times 10^{-3} \pm 1.34 \times 10^{-4}$ L.s^{-1}
s_1	$-1.169 \times 10^{-2} \pm 3.7 \times 10^{-4}$ s^{-1}
s_2	$-1.202 \times 10^{-3} \pm 4.5 \times 10^{-5}$ s^{-1}

None of the confidence intervals include zero, indicating that all the parameters are statistically significant.

Figure 10 shows the experimental LHS of eq 28 averaged for all runs superimposed with the RHS of eq 28 with the model parameters estimated in Table 4.

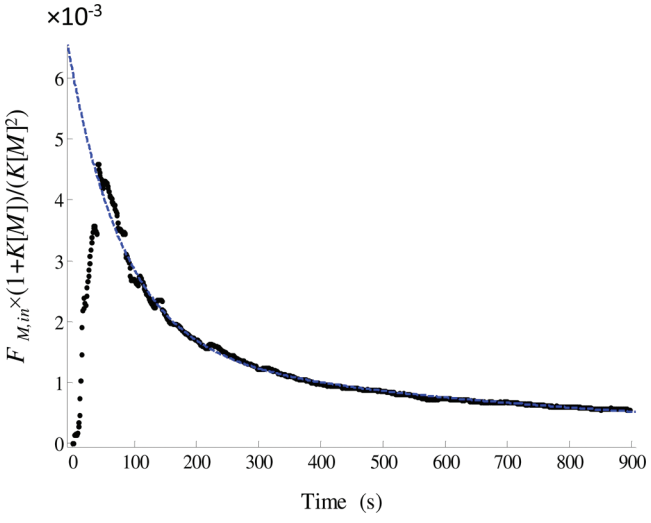

Figure 10. Plot of the experimental LHS term of eq 28, averaged for all runs, versus time. The dotted curve shows the fitted curve.

Values for k_{dth} and k'_d can be calculated using the expressions below, obtained by solving eqs 22 and 23 simultaneously,

$$k_{dth} = \frac{s_1 s_2}{k'_a} \quad (30)$$

$$k'_d = -(s_1 + s_2) - \frac{s_1 s_2}{k'_a} - k'_a \quad (31)$$

dx.doi.org/10.1021/ma202577n | Macromolecules 2012, 45, 1777–1791

Table 5 tabulates the point estimates of the all kinetic parameters required for the model represented by eq 26.

Table 5. Estimated Values of Kinetic Parameters for Eq 26

parameter	estimated values
k'_a	3.746×10^{-3} s^{-1}
k_p	5.046×10^{4} $L.mol^{-1}.s^{-1}$
k_{dth}	3.633×10^{-3} s^{-1}
k'_d	5.144×10^{-3} s^{-1}
K	1.1

Figure 11 shows how the experimental ethylene feed flow rates are well represented by eq 26 using the parameters

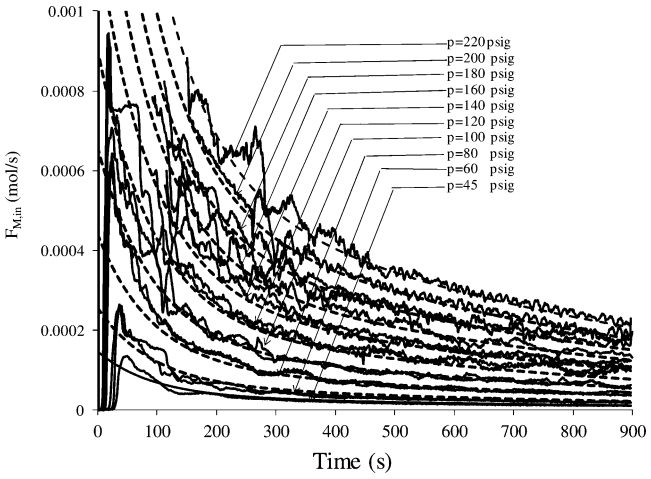

Figure 11. Comparison between experimental ethylene feed flow rates and model predictions with eq 26 using parameters listed in Table 5. Dashed curves are model predictions.

reported in Table 5. The excellent agreement between model fit and experimental results demonstrates that the proposed model describes remarkably well the relation between ethylene pressure and ethylene uptake rate as a function of time.

The polymer yield at the end of the polymerizations was predicted using the kinetic parameters reported in Table 5 and eq 27. Figure 12 compares experimental and predicted polymer yields for a wide range of ethylene concentrations. Once again,

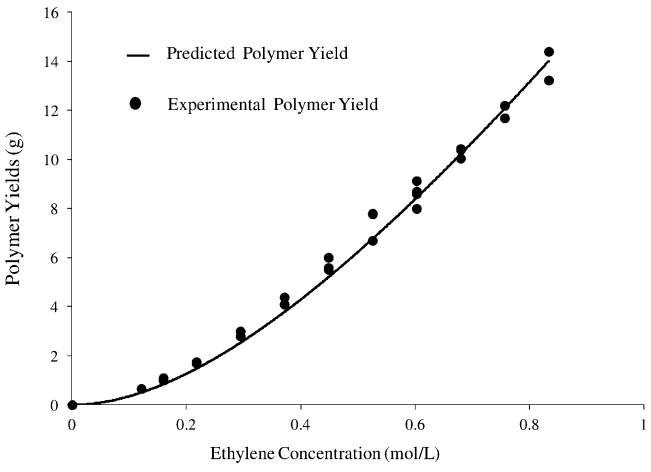

Figure 12. Comparison between experimental and predicted polymer yields.

excellent agreement was observed between experimental data and model predictions.

The findings on CGC deactivation behavior can be summarized as follows:

- Assuming a first order model alone (thermal decay or deactivation by impurities) cannot explain CGC deactivation. A second order model can explain CGC deactivation as a function of time, but it is unable to explain the effect of catalyst concentration.
- Assuming reversible activation and deactivation with MAO can explain the effect of catalyst concentration, but it cannot explain the effect of time because the consequence of this assumption would be the following equation for ethylene flow rate into the reactor, obtained by solving the relevant differential equations,

$$F_{M,in} = \frac{k_p K[M]^2 C_0 V_R}{(1 + K[M])(k'_a + k'_d)} [k'_a + k'_d e^{-(k'_a + k'_d)t}] \quad (32)$$

When time approaches infinity, the value for monomer flow rate reaches the limiting value

$$F_{M,in} = \frac{k_p K[M]^2 C_0 V_R k'_a}{(1 + K[M])(k'_a + k'_d)} \quad (33)$$

This limiting behavior contradicts the experimental findings of the present investigation because our observations indicate that ethylene uptake curves go to zero at very long polymerization times (total catalyst deactivation).

In conclusion, in addition to reversible activation and deactivation with MAO, thermal deactivation is also required to explain the effect of monomer concentration, catalyst concentration, and time on the polymerization rate of ethylene with CGC under the conditions investigated in this study.

Effect of Monomer Concentration on Molecular Weight. Figure 13 shows how M_n, M_w, and PDI of polyethylene made with CGC vary with total reactor pressure. The PDI remains

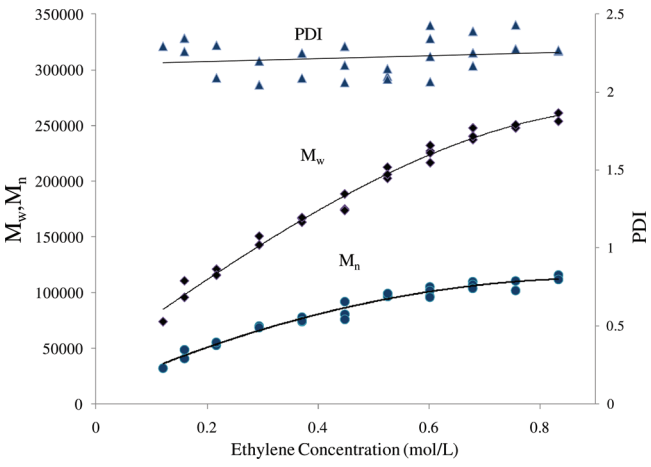

Figure 13. Variation of M_n, M_w, and PDI with ethylene concentration.

practically constant in all polymerizations, with values in a narrow range between 2 and 2.5, as theoretically expected for a single-site catalyst. Both M_n and M_w initially increase with polymerization pressure and then tend to constant values, which is consistent with a chain growth mechanism controlled by transfer to ethylene.

dx.doi.org/10.1021/ma202577n | Macromolecules 2012, 45, 1777–1791

Estimation of Chain Transfer Rate Constants. Transfer to monomer, to metal alkyl, to transfer agents such as H_2, and β-hydride elimination, are among the main chain transfer mechanisms for polymerization with coordination catalysts.[14,23]

In the absence of hydrogen, the number-average molecular weight, M_n, is related to the relative rate of propagation to chain transfer reactions through the following equation,

$$\frac{mw}{M_n} = \frac{R_M + R_{\beta H} + R_{Al}}{R_P} \tag{32}$$

where R_P is the rate of propagation, R_M, $R_{\beta H}$, and R_{Al} are the rate of transfer to monomer, β-hydride elimination, and transfer to MAO, respectively, and mw is monomer molar mass.

According to the mechanism we are proposing herein, when a monomer approaches a complexed catalyst site, two reactions may take place: monomer propagation, where the monomer molecule is inserted into the growing polymer chain, as represented in eq 2, or transfer to ethylene, forming a dead polymer chain with a terminal double bond (macromonomer) and a catalyst site attached to a single monomer unit, as described in eq 33,

$$P^*{\cdot}M + M \xrightarrow{k_M} \overline{\overline{P}} + P^*{\cdot}M \tag{33}$$

where $\overline{\overline{P}}$ denotes a polymer chain with a terminal double bond. Notice that the trigger mechanism formalism, assuming that one monomer molecule remains complexed to the active site, was kept in eq 33.

Macromonomers can also be formed via β-hydride elimination, in which the hydrogen atom attached to the β carbon in the chain is transferred to the metal center, as described in the following equation,

$$P^*{\cdot}M \xrightarrow{k_{\beta H}} \overline{\overline{P}} + P^*{\cdot}M \tag{34}$$

The rates of macromonomer formation by these two transfer mechanisms are given by the expressions,

$$R_M = k_M[P^*{\cdot}M][M] \tag{35}$$

$$R_{\beta H} = k_{\beta H}[P^*{\cdot}M] \tag{36}$$

Substituting the expression for $[P^*{\cdot}M]$ given in eq 6 into eqs 35 and 36,

$$R_M = \frac{k_M K[M]^2 C_t}{1 + K[M]} \tag{37}$$

$$R_{\beta H} = \frac{k_{\beta H} K[M] C_t}{1 + K[M]} \tag{38}$$

Similarly, for chain transfer to MAO

$$R_{Al} = \frac{k_{Al}[Al] K[M] C_t}{1 + K[M]} \tag{39}$$

Finally, substituting eqs 9, 37, 38, and 39 into eq 32 gives,

$$\frac{mw}{M_n} = \frac{k_M}{k_p} + \frac{k_{\beta H} + k_{Al}[Al]}{k_p} \times \frac{1}{[M]} \tag{40}$$

or,

$$\frac{M_n}{mw} = \frac{[M]}{\frac{k_M}{k_p}[M] + \frac{k_{\beta H} + k_{Al}[Al]}{k_p}} \tag{41}$$

Figure 14 shows the plot of mw/M_n versus the reciprocal of ethylene concentration in the reactor. The slope and intercept

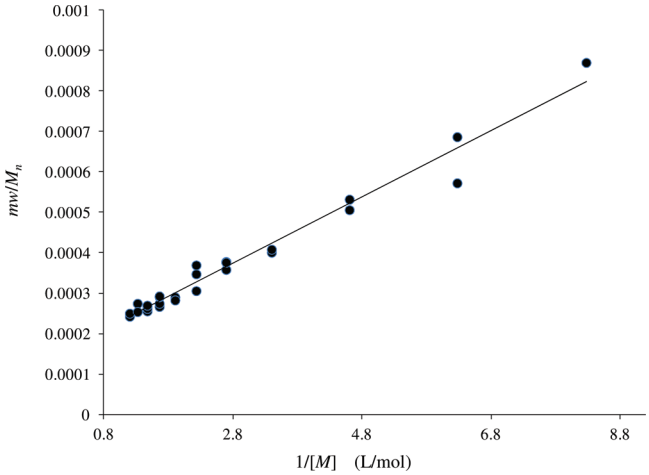

Figure 14. Plot of $1/M_n$ versus $1/[M]$; see eq 40.

of the line provide the point estimates for k_M / k_p and $(k_{\beta H} + k_{Al}[Al])/k_p$, respectively, which are reported in Table 6.

Table 6. Summary of Chain Transfer Parameter Estimation Using Linear and Nonlinear Regression

parameter	linear regression	estimated standard error	nonlinear regression	estimated standard error
k_M/k_p	$1.43 \times 10^{-4} \pm 1.8 \times 10^{-5}$	8.68×10^{-6}	$1.5 \times 10^{-4} \pm 1.6 \times 10^{-5}$	8×10^{-6}
$(k_{\beta H} + k_{Al}[Al])/k_p$	$8.2 \times 10^{-5} \pm 5.6 \times 10^{-6}$	2.71×10^{-6}	$7.86 \times 10^{-5} \pm 8.9 \times 10^{-6}$	4.33×10^{-6}

Figure 15 plots M_n/mw versus monomer concentration. Nonlinear regression of eq 41 was performed by minimizing

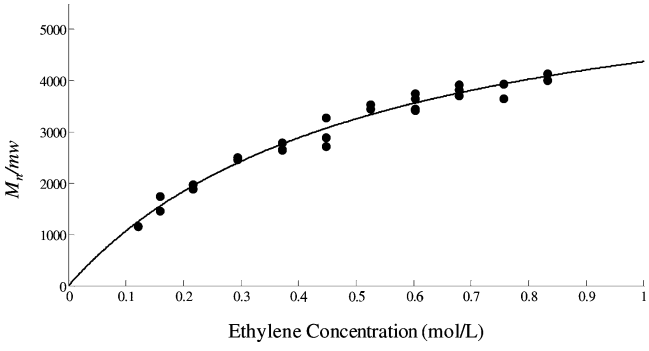

Figure 15. Curve fitting for M_n data using eq 41.

the sum of the squares of the residuals to obtain k_M / k_p and $(k_{\beta H} + k_{Al}[Al])/k_p$. Assuming that the variability in ethylene concentration is negligible, the approximate confidence interval for the parameters can also be calculated. Table 6 summarizes the results of 95% confidence interval calculations for the

dx.doi.org/10.1021/ma202577n | Macromolecules 2012, 45, 1777–1791

parameters using linear regression and the corresponding approximate ones using nonlinear regressions. The parameter estimates using both techniques are very similar and describe very well how M_n varies with ethylene pressure.

Effect of MAO Concentration on Polymer Microstructure. Thirteen polymerization runs were performed to study the effect of MAO concentration on the microstructural properties of the resulting polymer. Temperature and ethylene pressure were kept constant during all polymerizations. Catalyst concentration was the same for all polymerizations, except for run 453, where it was necessary to reduce the Al/Ti to its lowest value. Polymerization conditions are summarized in Table 7.

Table 7. Polymerization Conditions (MAO Effect)[a]

run	MAO (mol Al/L)	Al/Ti
441	0.0076	12 400
442	0.0122	19 900
443	0.0213	34 900
444	0.0030	4900
445	0.0167	27 400
446	0.0076	12 400
447	0.0122	19 900
448	0.0304	49 500
454	0.0030	4900
455	0.0122	19 900
456	0.0213	34 900
457	0.0076	12 400
453[b]	0.0030	1200

[a]Catalyst concentration = 0.62 μmol/L, polymerization temperature = 120 °C, and polymerization pressure = 120 psig. [b]Catalyst concentration =2.44 μmol/L.

Table 8 summarizes molecular weight-average measurements and polymer yield for all runs.

Table 8. Polymer Yields and Molecular Weight Averages

run	M_w	M_n	PDI	polymer yield (g)
441	177 200	68 100	2.6	2.4
442	184 900	80 500	2.3	3.5
443	164 200	82 000	2.2	5.92
444	153 700	39 900	3.85	0.97
445	175 500	76 900	2.28	5.02
446	180 800	69 000	2.62	2.84
447	183 500	78 400	2.34	3.84
448	191 200	88 100	2.17	7.77
454	168 000	48 200	3.49	1.24
455	177 800	76 700	2.32	4.12
456	188 700	83 600	2.26	6.94
457	152 600	62 700	2.43	2.62
453	147 700	37 800	3.91	3.01

The polymer yield increases with MAO concentration in the reactor, as shown in Figure 16. Interestingly, the polymer yield for sample 453, which was made at higher catalyst concentration than the other runs, does not lie on the curve showing the trend for the samples made at a lower catalyst concentrations. However, if the yield for sample 453 is normalized by multiplying it by the catalyst concentration of the other samples and then dividing it by its own catalyst concentration, this point also falls on the same trend line, as indicated in Figure 16. This confirms that polymer yield is linearly related to catalyst concentration, as observed before.

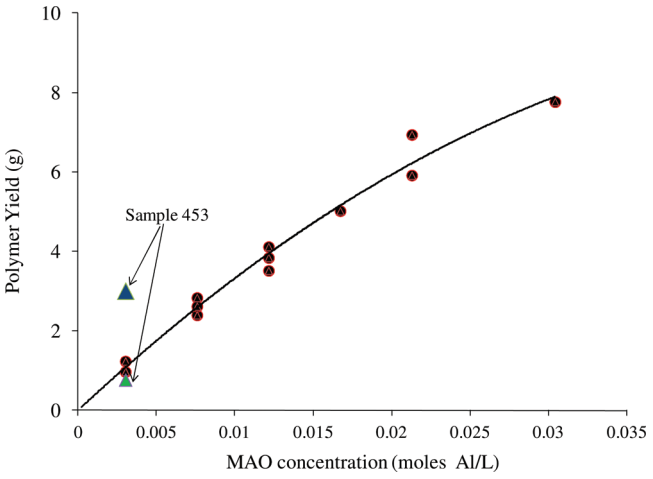

Figure 16. Polymer yield versus MAO concentration.

Figure 17 illustrates how PDI, M_n, and M_w vary with Al/Ti ratio. Decreasing Al/Ti ratio down to about 20 000 does not

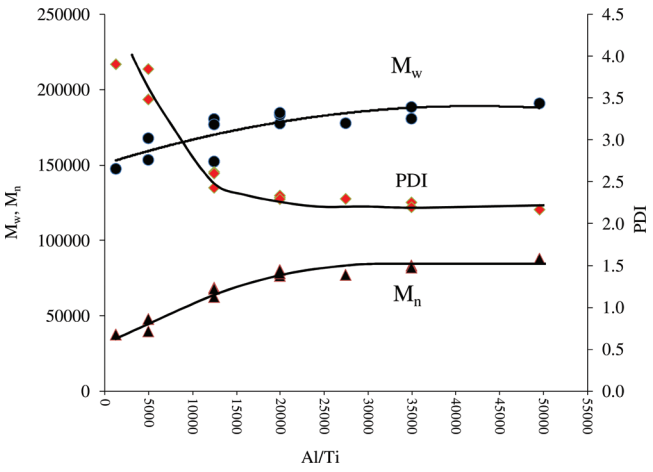

Figure 17. Molecular weight averages and PDI as a function Al/Ti.

affect molecular weight averages and PDI, but a further decrease will reduce M_n and M_w, and increase polydispersity.

The effect of Al/Ti on molecular weight averages will be discussed in the next section.

Long Chain Branch Formation. Figure 18 shows the 15° light scattering signal intensity versus GPC elution volume for all the polymerization runs listed in Table 7. For samples made under high MAO concentration or high Al/Ti ratio (Al/Ti > 20 000), no significant shoulder or bimodality is observed. At low Al/Ti ratios (Al/Ti < 12 000 and lower) a shoulder appears at low elution volumes, becoming more significant as the Al/Ti ratio decreases. To confirm that this high molecular weight shoulder comes from long chain branching, Sample 453, which was synthesized at the lowest Al/Ti ratio of all samples shown in Table 7, was analyzed by ^{13}C NMR.

Figure 19 compares the proton-decoupled ^{13}C NMR spectra of samples 453 and 448. Seven well resolved peaks were observed with the chemical shifts positioned at 14.2, 22.9, 32.2, 34.57, 27.28, 38.2, and 33.97 ppm for sample 453. To account for the peaks observed in this spectrum, the structure shown in

dx.doi.org/10.1021/ma202577n | Macromolecules 2012, 45, 1777–1791

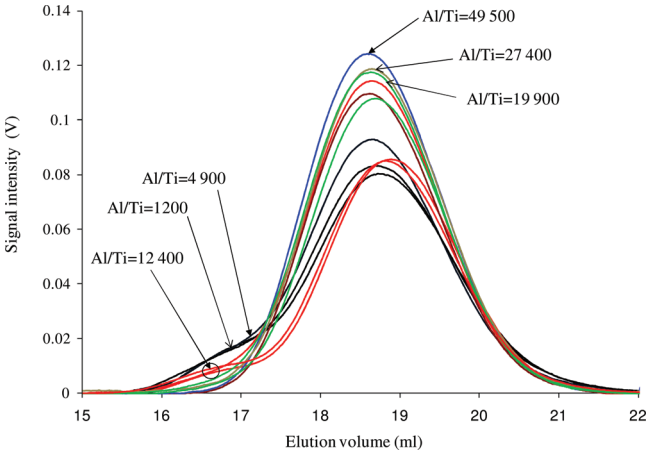

Figure 18. Light scattering 15° signal intensity versus GPC elution volume for samples made under different Al/Ti ratios.

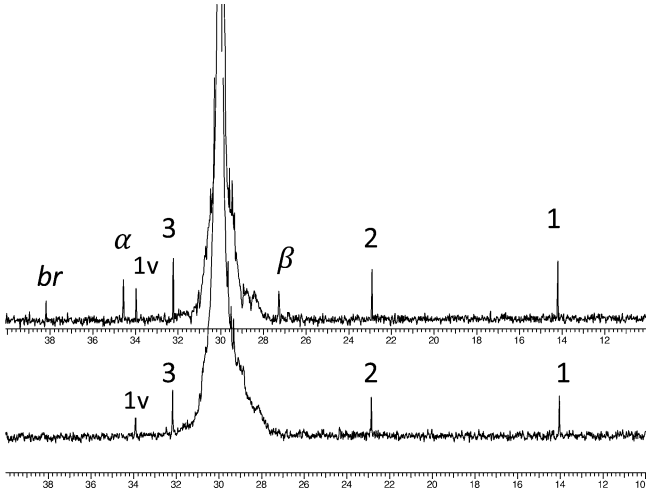

Figure 19. ^{13}C NMR spectrum of samples 453 (top) and 448 (bottom).

Figure 20 was assumed. On the basis of the Grant and Paul rules, the previous chemical shifts correspond to carbons 1, 2, 3,

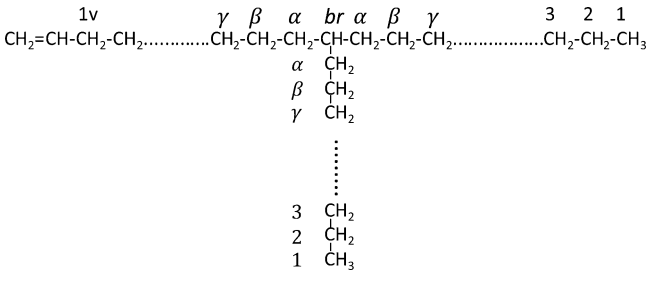

Figure 20. Chemical structure of polyethylene containing long chain branches made by CGC.

α, *β*, *br*, and 1v, respectively. Other carbon types have chemical shifts located at 30 or near 30 ppm so they would be obscured by the main peak at 30 ppm. Inspection of the spectrum in Figure 19 confirms the presence of LCBs in sample 453. The log [*η*] × log MW plot of sample 453 depicted in Figure 21 further confirms the presence of LCBs in this sample.

The increase in PDI observed when the Al/Ti ratio was reduced can be partially attributed to the formation of LCBs, as

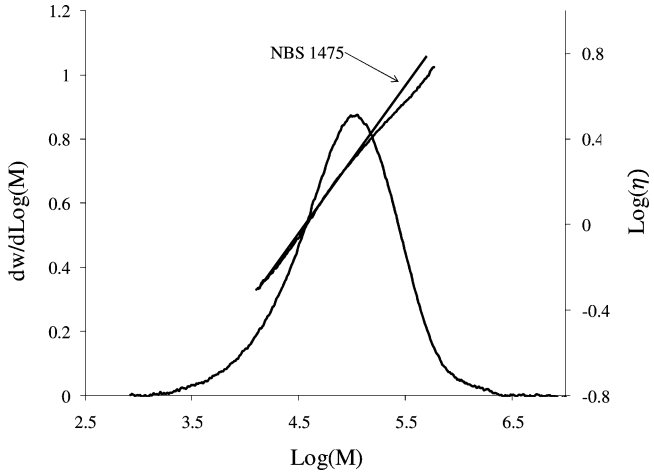

Figure 21. Molecular weight distribution and intrinsic viscosity plot of sample 453.The intrinsic viscosity plot for the linear polyethylene standard NBS 1475 is shown for comparison.

shown in ^{13}C NMR spectra for sample 453, but the observed increase is too high to be credited only to the presence of LCBs.

Sample 448, which was made at high Al/Ti ratio, was also analyzed using ^{13}C NMR spectroscopy. Four peaks, corresponding to 1, 2, 3, and 1v carbons were observed, but no LCB peak was detected (Figure 19). In addition, its log [*η*] × log MW plot was linear, indicating that LCB frequency in the sample is negligible. The summary of ^{13}C NMR analysis results for these two samples is given in Table 9.

Table 9. ^{13}C NMR analysis for Samples 453 and 448[a]

sample	λ_{vinyl}	λ_{CH3}	n_{LCB}
453	0.39	0.78	0.23
448	0.064	0.29	0

[a] λ_{vinyl} = Number of unsaturated chain ends per 1000 C, λ_{CH3} = Number of saturated chain ends per 1000 C, n_{LCB} = Average number of long chain branches per chain.

The unsaturated chain-end density (λ_{vinyl}, number of unsaturated chain ends per 1000 carbon atoms), saturated chain end density (λ_{CH_3}, number of saturated chain ends per 1000 carbon atoms) and long chain branch density (λ_{LCB}, number of long chain branches per 1000 carbon atoms) were calculated using the following equations,[13]

$$\lambda_{vinyl} = 1000\frac{IA_{1v}}{IA_{Tot}} \quad (42)$$

$$\lambda_{CH_3} = 1000\frac{IA_2 + IA_3}{2IA_{Tot}} \quad (43)$$

$$\lambda_{LCB} = 1000\frac{IA_\alpha}{3IA_{Tot}} \quad (44)$$

where IA_{1v}, IA_2, IA_3, IA_α, and IA_{Tot} are the integral areas of allylic, 2, 3, *α* and total carbons,

dx.doi.org/10.1021/ma202577n | Macromolecules 2012, 45, 1777–1791

The long chain branch frequency (n_{LCB}, average number of long chain branches per chain) was estimated using the following equation,[13]

$$n_{LCB} = \frac{2\lambda_{LCB}}{\lambda_{CH3} + \lambda_{vinyl} - \lambda_{LCB}} \quad (45)$$

To better understand why the molecular weight averages decreased when the Al/Ti ratio was reduced, the λ_{vinyl} of seven randomly selected polymer samples (456, 448, 445, 453, 454, 455, 446) made at different Al/Ti ratios were measured using FTIR spectroscopy. Figure 22 plots the λ_{vinyl} versus Al/Ti ratio

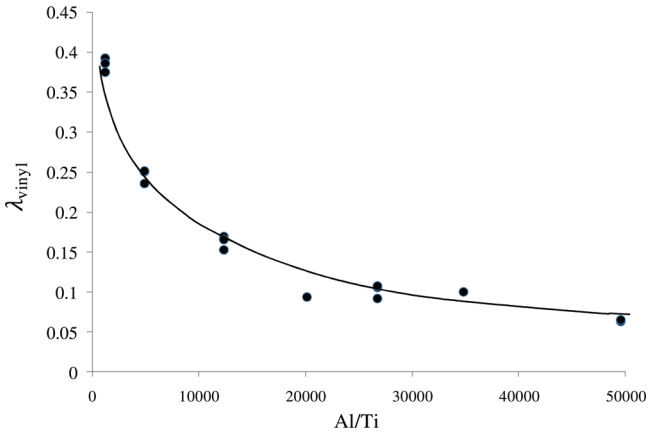

Figure 22. Unsaturated chain end density (λ_{vinyl}) as a function of Al/Ti ratio.

for these samples. (The multiple points at each Al/Ti level are FTIR analysis replicates, not polymerization replicates, so the variability at each Al/Ti level reflects variability in λ_{vinyl} measurements.) Since λ_{vinyl} for sample 448, made at the high Al/Ti ratio of 49 500, is low and the sample has no LCBs, it seems that high Al/Ti ratios slow down chain transfer reactions that lead to the formation of vinyl-terminated chains (macromonomers), while the rate of transfer to MAO increases. It also appears that the decrease in the rate of macromonomer formation reactions is more pronounced than the increase in the rate of chain transfer to MAO as the Al/Ti ratio is increased. The overall effect of these two rate changes is that molecular weight initially increases with increasing Al/Ti ratio until it finally levels off, while the concentration of macromonomer decreases. Therefore, when Al/Ti ratio decreases, the rate of macromonomer formation increases, the molecular weight decreases, and more LCBs are formed.

Figure 23 shows how the unsaturated chain end frequency (n_{vinyl}), or the average number of unsaturated chain ends per polymer chain, varies as a function of the Al/Ti ratio. The n_{vinyl} was calculated with the expression,

$$n_{vinyl} = \frac{\lambda_{vinyl} \times M_n}{14\,000} \quad (46)$$

It is interesting to notice that at low Al/Ti ratios n_{vinyl} is approximately equal to 1. This indicates that most chains have one vinyl terminal group and, consequently, that chain transfer to MAO is negligible when the Al/Ti ratio is relatively low. Since n_{vinyl} decreases with increasing Al/Ti and chain transfer to MAO does not produce vinyl terminated chains, transfer to MAO is likely to become more relevant at higher Al/Ti ratios.

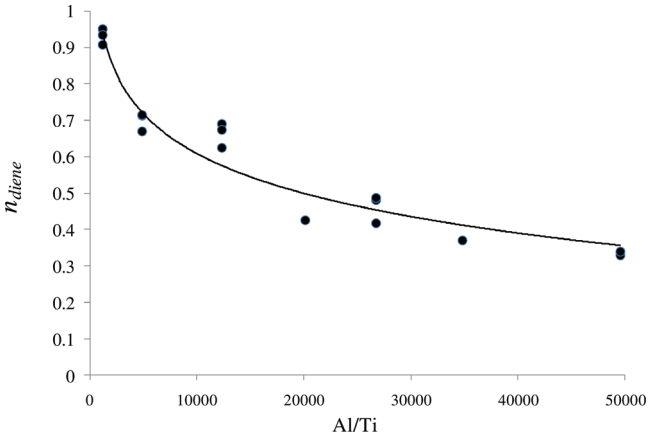

Figure 23. Unsaturated chain end frequency (n_{diene}) versus Al/Ti ratio.

Figure 24 compares the MWD of sample 448 made with Al/Ti = 49 500 with those of Samples 444 and 453, produced

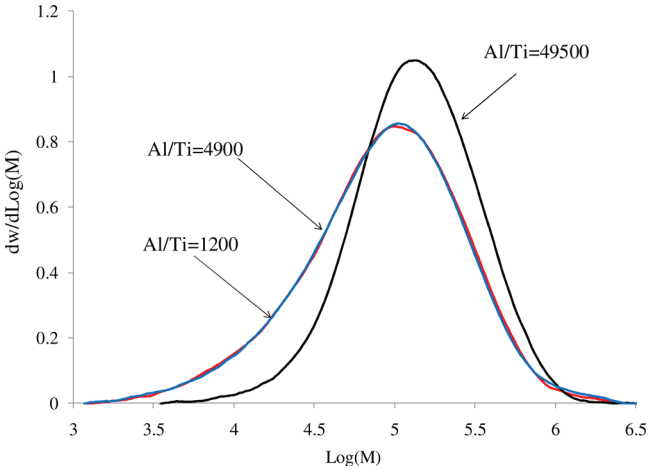

Figure 24. Molecular weight distributions for samples 444, 453, and 448 made under different Al/Ti ratios.

with Al/Ti ratios of 4900 and 1200, respectively. The fraction of low molecular weight chains increases when the MAO concentration decreases. It can be speculated that this lower molecular weight chains are more likely to be vinyl-terminated. It is also interesting to notice that, for these samples, MWD depends on MAO concentration, not on Al/Ti ratio, because samples 453 and 444 were made at the same MAO concentration but at different Al/Ti ratios of 1200 and 4200, respectively.

Effect of Monomer Concentration on Long Chain Branching at low Al/Ti Ratio (Al/Ti = 916). Long chain branches are formed with metallocene catalysts when macromonomers are copolymerized with a growing polymer chain; thus, decreasing ethylene concentration in the reactor is expected to increase LCB formation. The experimental results discussed in the previous section show that low MAO concentration favors the formation of macromonomers, which is a prerequisite for LCB formation. In this section we analyze the effect of changing ethylene concentration at low MAO concentration on LCB formation.

The effect of ethylene concentration was investigated by varying the total reactor pressure from 40 to 210 psig at a temperature of 120 °C. Nine polymer samples were made at five different pressures (Table 10). MAO and catalyst

dx.doi.org/10.1021/ma202577n | Macromolecules 2012, 45, 1777–1791

Table 10. Polymerization Conditions (Monomer Concentration Effect with Al/Ti = 916)[a]

run	733	734	735	736	737	738	741	742	745
total reactor pressure (psig)	120	160	80	80	120	205	120	40	40

[a]Catalyst concentration = 4.9 μmol/L. Temperature = 120 °C. Al/Ti = 916.

concentration, polymerization time and temperature were kept the same in all runs. Molecular weight averages, polymer yields, and LCB frequency estimates are presented in Table 11.

Table 11. Molecular Weight Averages and Polymer Yields (Monomer Concentration Effect with Al/Ti = 916)

run	pressure (psig)	M_w	M_n	PDI	polymer yield (g)	n_{LCB}[a]
733	120	142 200	40 200	3.5	4.57	0.2
734	160	176 700	46 400	3.8	6.64	0
735	80	113 400	31 400	3.6	2.04	0.27
736	80	113 600	32 400	3.5	2.50	0.25
737	120	137 600	38 600	3.6	4.79	0.21
741	120	158 900	46 300	3.4	4.69	0.18
742	40	94 000	23 400	4.0	0.65	0.32
738	205	195 300	55 100	3.5	10.22	0
745	40	105 200	24 900	4.2	0.77	0.3

[a]Estimated using the Zimm−Stockmeyer equation.

Figure 25 plots polymer yield versus monomer concentration. As observed for high Al/Ti (see Figure 2), a nonfirst

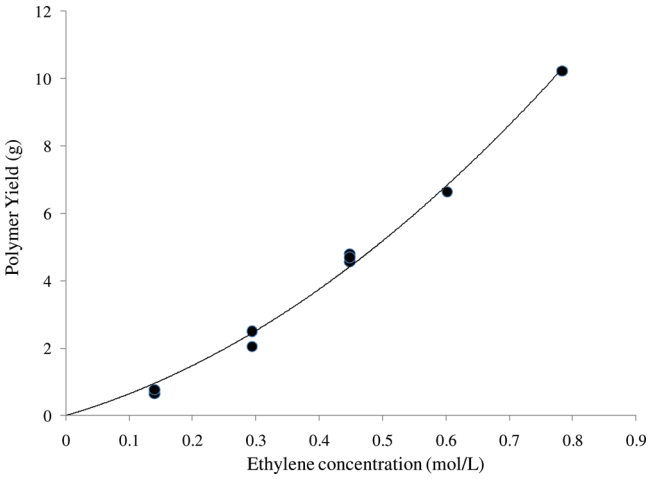

Figure 25. Polymer yield as a function of ethylene concentration (Al/Ti=916).

order dependence on monomer concentration is also noticed in this case.

Plots of the 15° GPC light scattering detector signal intensity versus elution volume for all polymer samples are shown in Figure 26. At an ethylene pressure of 120 psig, a shoulder is observed on the low elution volume region (high molecular weight), which corresponds to long chain branched polymer chains, as demonstrated in Figure 19. Decreasing ethylene pressure accentuates this bimodality. The area under the high molecular weight peak (low elution volume) increases as ethylene pressure decreases, implying that LCB formation is more significant at lower pressures.

Figure 27 compares the MWDs of all samples, and log $[\eta] \times$ log MW plots for the linear polyethylene standard NBS 1475

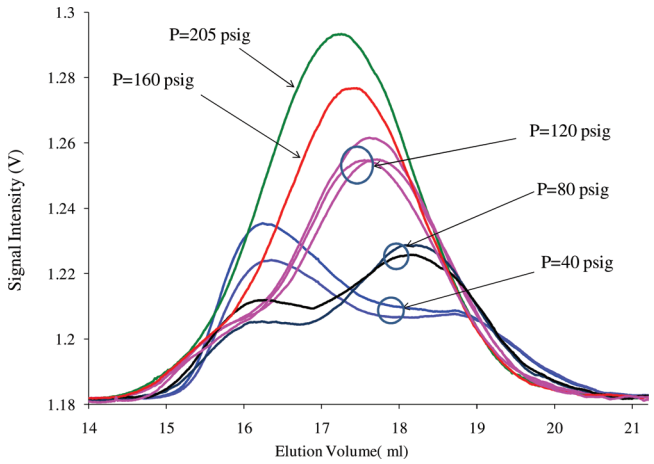

Figure 26. GPC light scattering 15° detector signal intensity versus elution volume for samples in Table 10.

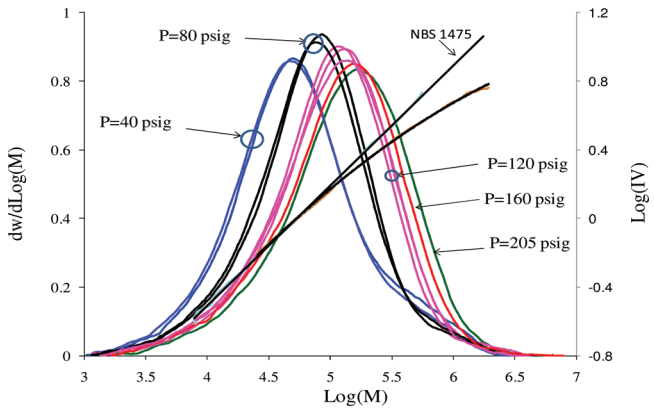

Figure 27. Molecular weight distribution of the polyethylene samples made at low Al/Ti ratio and log $[\eta] \times$ log MW plot for sample 745 (P = 40 psig) and linear polyethylene standard NBS 1475.

and Sample 745 (made at 40 psig). The nonlinear log $[\eta] \times$ log MW curve for Sample 745 is a clear indication of the presence of LCBs. The high molecular weight shoulders seen for the samples made at 120, 80, and 40 psig are also indicative of the presence of LCBs. Zimm-Stockmayer approach[30] was used to estimate the LCB frequency for these samples (Table 11), confirming that decreasing ethylene pressure in the reactor leads to more long chain branching in the polymer.

Figure 28 shows how M_n, M_w and PDI vary with ethylene concentration. PDI is almost constant at high ethylene concentrations, but starts to increase for values lower than 0.4 mol/L. This increase in PDI at lower ethylene concentrations can be attributed, in part, to an increase in the rate of LCB formation due to the decreasing ethylene concentration. Although at high ethylene concentrations (ethylene pressures of 160 psig and higher) no sign of LCB was detected by the GPC viscometer, PDI still remains higher that the theoretical value of two expected for polyethylene made with single-site catalysts at uniform conditions, which indicates that not all increase in PDI can be attributed to long

dx.doi.org/10.1021/ma202577n | Macromolecules 2012, 45, 1777−1791

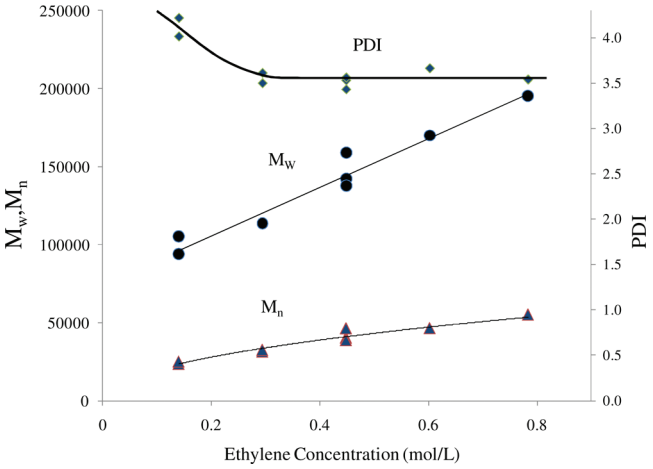

Figure 28. Effect of ethylene concentration on M_n, M_w, and PDI at low MAO concentration.

chain branching. In fact, true single site behavior is not observed for this catalyst when MAO concentration is low.

Finally, Figure 29 compares M_n and M_w for the two sets of samples made at low and high Al/Ti ratios. Weight and

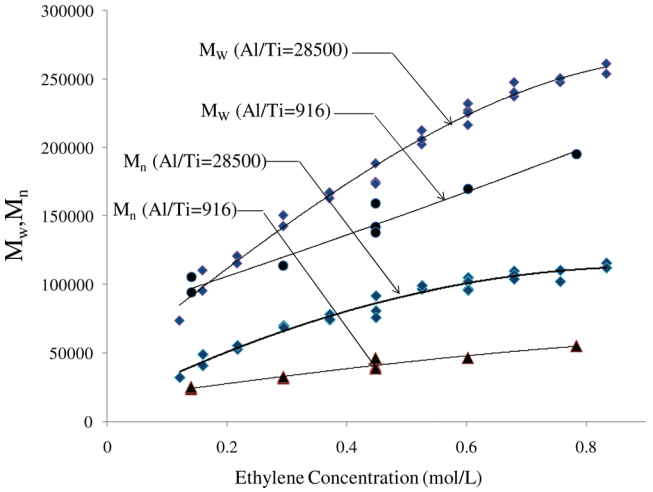

Figure 29. Effect of ethylene concentration and Al/Ti ratio on molecular weight averages.

number-average molecular weights are higher when the polymers are made at larger Al/Ti ratios, but this difference decreases for lower ethylene pressures, as expected.

CONCLUSIONS

The kinetics of ethylene solution polymerization using the CGC/MAO system was studied in a semibatch reactor at high temperature using a wide range of ethylene, CGC and MAO concentrations and the results were described with a novel mathematical model that captured the main features of the polymerization kinetics and molecular weight response. The propagation reaction order was found to be first order with respect to catalyst concentration, while the order with respect to ethylene concentration changed from 1 to 2 as a function of ethylene pressure. Reversible activation and deactivation with MAO along with thermal deactivation was proposed to explain the effect of time, monomer and catalyst concentration on the measured polymerization rates. Detailed parameter estimates for the leading polymerization and chain transfer constants were estimated for this model and it proved to be able to describe the experimental data remarkably well. It is important to emphasize that the mechanism-based model proposed herein describes all the collected experimental data very well, but it is just a mathematical model for polymerization kinetics; alternative models may be derived that reach a similar description, although none such alternative model was found by the authors in this investigation.

Decrease in MAO concentration leads to the production of polymer chains with terminal vinyl groups, which may be incorporated subsequently into growing polymer chains to produce long chain branched polymers. Polymer molecular weight decreases by lowering MAO concentration, while PDI increases. Part of the increase in PDI due to the lowering of MAO concentration can be attributed to LCB formation, whereas the rest results from non single-site behavior of the catalyst at low MAO concentration. Decrease in monomer concentration leads to the production of polymer chains with increased LCB frequencies while the MAO concentration is low.

ASSOCIATED CONTENT

Supporting Information

Two appendices with expanded mathematical calculations. This material is available free of charge via the Internet at http://pubs.acs.org.

AUTHOR INFORMATION

Notes

The authors declare no competing financial interest.

REFERENCES

(1) Braunschweig, H.; Breitling, F. M. *Coord. Chem. Rev.* **2006**, *21*–*22*, 2691–2720.
(2) Odian, G. *Principles of Polymerization*, 4th ed.; John Wiley & Sons: New York, 2004; p 675.
(3) Chen, Y.; Fu, P.; Stern, C.; Marks, T. *Organometallics* **1997**, *26*, 5958–5963.
(4) McKnight, A.; Waymouth, R. *Chem. Rev.* **1998**, *7*, 2587–2598.
(5) Yan, D.; Wang, W.; Zhu, S. *Polymer* **1999**, *7*, 1737–1744.
(6) Beigzadeh, D.; Soares, J.; Hamielec, A. *J. Appl. Polym. Sci.* **1999**, *11*, 1753–1770.
(7) Wang, W.; Kharchenko, S.; Migler, K.; Zhu, S. *Polymer* **2004**, *19*, 6495–6505.
(8) Wang, W.-J.; Zhu, S.; Park, S. J. *Macromolecules* **2000**, *16*, 5770–5776.
(9) Kolodka, E.; Wang, W.; Zhu, S.; Hamielec, A. *Macromolecules* **2002**, *27*, 10062–10070.
(10) Wen-Jun, W.; Zhibin, Y.; Hong, F.; Zhu, S.; Bo-Geng, L. *Polymer* **2004**, *16*, 5497–5504.
(11) Beigzadeh, D.; Soares, J. B. P.; Duever, T. A. *Polym. Chem.* **2004**, *12*, 3055–3061.
(12) Young, M.; Ma, C. *J. Polym. Eng.* **2002**, *2*, 75–93.
(13) Wang, W. J.; Yan, D.; Zhu, S.; Hamielec, A. *Macromolecules* **1998**, *25*, 8677–8683.
(14) Huang, J.; Rempel, G. *Prog. Polym. Sci.* **1995**, *3*, 459–526.
(15) ASTM D5576–00(2006) *Standard Practice for Determination of Structural Features in Polyolefins and Polyolefin Copolymers by Infrared Spectrophotometry*; ASTM: Philadelphia, PA, 2006; Vol. *08.03*
(16) Lee, L. S.; Hsu, H. L. *Fluid Phase Equilib.* **2005**, *2*, 221–230.
(17) Chakravarti, S.; Ray, W. *J. Appl. Polym. Sci.* **2001**, *12*, 2901–2917.
(18) Chakravarti, S.; Ray, W. *J. Appl. Polym. Sci.* **2001**, *8*, 1096–1119.

(19) Xu, Z.; Chakravarti, S.; Ray, W. *J. Appl. Polym. Sci.* **2001**, *1*, 81−114.
(20) Chien, J.; Yu, Z.; Marques, M.; Flores, J.; Rausch, M. *J. Polym. Sci., Polym. Chem.* **1998**, *2*, 319−328.
(21) Kissin, Y.; Mink, R.; Nowlin, T.; Brandolini, A. *Top. Catal.* **1999**, *1*−*4*, 69−88.
(22) Bergstra, M.; Weickert, G. *Macromol. Mater. Eng.* **2005**, *6*, 610−620.
(23) Hamielec, A.; Soares, J. *Prog. Polym. Sci.* **1996**, *4*, 651−706.
(24) Bohm, L. L. *J. Appl. Polym. Sci.* **1984**, *1*, 279−289.
(25) Shaffer, W.; Ray, W. *J. Appl. Polym. Sci.* **1997**, *6*, 1053−1080.
(26) Schnuss, A.; Reichert, K. *Makromol. Chem., Rapid Commun.* **1990**, *7*, 315−320.
(27) Montgomery, D. C.; Runger, G. *Applied statistics and propability for engineers*, 3rd ed.; John Wiley and Sons Inc.: New York, 2003.
(28) Fischer, D.; Mulhaupt, R. *J. Organomet. Chem.* **1991**, *1*−*2*, C7−C11.
(29) Jiang, S.; Wang, L.; Zhang, P.; Feng, L. *Macromol. Theory Simul.* **2002**, *1*, 77−83.
(30) Mehdiabadi, S., *Synthesis, Characterization and Polymerization Kinetic Study of Long Chain Branched Polyolefins Made with Two Single-Site Catalysts*, Ph.D. Thesis, University of Waterloo: Waterloo, Canada, 2011; p 95.

Macromolecules

Article

pubs.acs.org/Macromolecules

Acrylamide-Based Copolymers Bearing Photoreleasable Thiols for Subsequent Thiol−Ene Functionalization

Guillaume Delaittre,[†,‡,§] Thomas Pauloehrl,[†,§] Martin Bastmeyer,[‡,§] and Christopher Barner-Kowollik*[,†,§]

[†]Preparative Macromolecular Chemistry, Institut für Technische Chemie und Polymerchemie, Karlsruhe Institute of Technology (KIT), Engesserstr. 18, 76128 Karlsruhe, Germany

[‡]Zoologisches Institut, Zell- und Neurobiologie, Karlsruhe Institute of Technology, Haid-und-Neu-Str. 9, 76131 Karlsruhe, Germany

[§]Center for Functional Nanostructures (CFN), Karlsruhe Institute of Technology (KIT), Wolfgang-Gaede-Str. 1a, 76131 Karlsruhe, Germany

Supporting Information

ABSTRACT: A new set of monomers is presented in order to incorporate thiols into radical polymers using a protecting chemistry/photocleavage route. The (co)polymerization kinetics of an *o*-nitrobenzyl thioether-containing acrylamide derivative are reported. The presence of the *o*-nitrobenzyl moiety is found to strongly affect the polymerization. Nevertheless, water-soluble copolymers with *N*,*N*-dimethylacrylamide (DMAAm) as a comonomer are obtained either by free radical polymerization ($10\,000 \leq M_n \leq 17\,500$ g mol^{-1}; $1.5 \leq$ PDI ≤ 1.8) or by reversible addition−fragmentation transfer (RAFT)-mediated controlled/living radical polymerization ($2000 \leq M_n \leq 5700$ g mol^{-1}; $1.1 \leq$ PDI ≤ 1.2). Deprotection under UV light ($\lambda = 366$ nm) at ambient temperature is followed by UV/vis monitoring of the protecting group release, which proceeds to completion between 40 min and 2 h within the studied range of concentration as demonstrated by ^{1}H NMR spectroscopy. Thiol−maleimide addition is subsequently carried out and found to proceed with a nearly quantitative yield (ca. 90%) as measured by ^{1}H NMR. Different block copolymers ($9400 \leq M_n \leq 16\,500$ g mol^{-1}; $1.3 \leq$ PDI ≤ 1.4) with a PDMAAm water-soluble block, a polystyrene hydrophobic block, or a poly(*N*-isopropylacrylamide) thermosensitive block as the first segment and possessing the photoreleasable thiol moieties in the second block are subsequently synthesized by RAFT-mediated polymerization. We finally demonstrate the orthogonal sequential deprotection and reaction with benzyl maleimide of two different thiol species originating from the thiocarbonylthio functionality and the *o*-nitrobenzyl protected lateral groups, respectively.

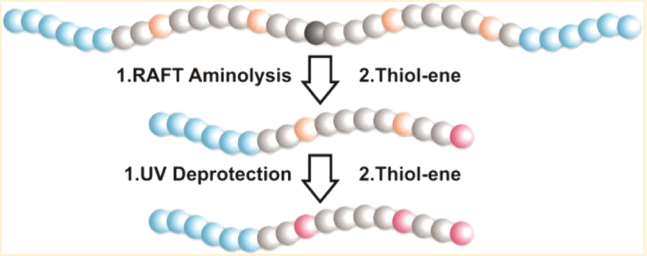

INTRODUCTION

The past 5 years have witnessed a significant growth of interest in the use of *click* methodologies in polymer and materials chemistry.[1] Since macromolecules are difficult to quantitatively modify and bear multiple functional groups, the efficiency and orthogonality of *click* reactions has indeed very often proven to be useful.[2] Although the most prominent technique was initially the azide−alkyne cycloaddition,[3] its generally required use of copper as a catalyst has led to a gradual shift of attention toward copper-free chemistries such as thiol−ene and thiol−yne additions,[4] (hetero) Diels−Alder [4 + 2] cycloaddition,[5] some very efficient nucleophilic substitutions,[6] oxime formation,[7] nitrile oxide−alkyne cycloaddition,[8] or ring-opening of epoxides.[9] Copper-free synthetic methods are particularly interesting when bio-related applications are envisioned. Thiol-based *click* conjugations have shown to be very powerful in various fields of application.[10] Thiols can react very efficiently with themselves to form disulfide bridges and with electron-withdrawing group-substituted enes such as (meth)acrylates or maleimides via a radical pathway or Michael addition.[4] Furthermore, they are also able to strongly bind to a wide range of metal surfaces, for instance, silver or gold.[11]

Radical polymerization is arguably the most versatile polymerization technique since it is tolerant to most functional groups. However, there are some exceptions and thiols are one of them due to their large transfer constants in the polymerization of vinyl monomers.[12] Indeed, they are regularly employed to reduce the molecular weight or introduce a specific functionality in radically prepared macromolecules.[13] Consequently, sulfhydryl groups need to be introduced after the polymerization or to be protected (or masked) when they are initially present. For example, the pyridyl disulfide group (PyDS) has been often incorporated—especially when bioapplications were targeted—by using functional monomers,[14] initiators,[15] or RAFT agents.[16] PyDS has also been attached by amidation to amino-containing polymers using *N*-succinimidyl 3-(2-pyridyldithio)propionate.[17] Matyjaszewski

Received: December 9, 2011
Revised: January 26, 2012
Published: February 8, 2012

   dx.doi.org/10.1021/ma202670d | Macromolecules 2012, 45, 1792−1802

Scheme 1. General Sequential Deprotection/Thiol−Ene Functionalization Strategy Applied to a RAFT Polymerization-Made Block Copolymer Possessing the Protected Thiol Groups as a Comonomer Unit in One Block

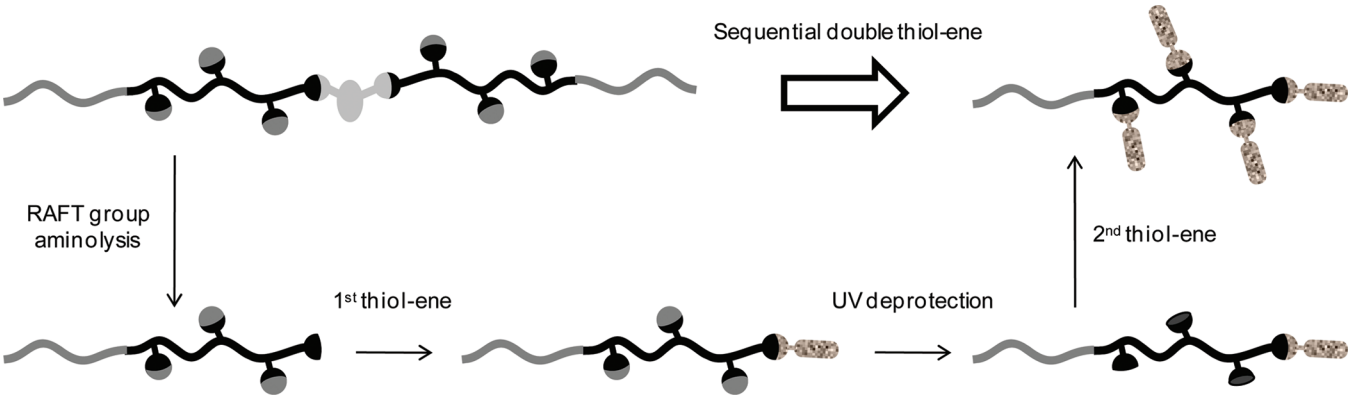

and colleagues employed a bifunctional ATRP initiator composed of a disulfide linker to obtain midchain-functionalized polystyrene (PS) which was eventually reduced by DTT to yield PS-SH.[18] Li et al. also introduced thiols using an alkyl disulfide yet as a lateral group.[19] Classical protecting-group chemistry has also been employed to prepare ATRP initiators[20−22] or nitroxides[23] bearing a thiol group which was subsequently activated after functioning to mediate the polymerization. In the case of RAFT-mediated controlled/living polymerization thiocarbonylthio compounds are used as controlling agent, but they can also be regarded as masked thiols since methods such as aminolysis, hydrolysis, and metal hydride reduction will lead to the mercapto-end-functionalized chains.[24]

In the context of pure postpolymerization (i.e., the incorporation of previously absent sulfur atoms), alkyl halides such as ATRP-made polymers have been substituted using thiourea to form isothiouronium salts which were subsequently hydrolyzed to give thiol-capped polymers.[25,26] Very recently, Boyer et al. reported a nucleophilic substitution of Br-capped polymers employing methanethiosulfonate followed by basic hydrolysis[27] while Paris and co-workers used potassium thioacetate to obtain end-thiolated polymers via hydrolysis of the intermediate thioester-capped chains.[28]

Protecting group chemistry is very often employed in pure organic chemistry, particularly when complex structures are targeted.[29] It consists in the reversible protection of one or several functional groups which can potentially react while performing a modification meant to occur on another part of the molecule. It also allows in some applications the activation of specific functions when desired. While chemically driven deprotections have been employed to a high extent in polymer chemistry, the use of light-induced deprotection has been the subject of much less attention. The phototriggered release of chemical groups is very attractive as it allows not only for temporal control of the reaction but also for its spatial control. For instance, the *o*-nitrobenzyl group and its methoxy-substituted derivatives have been often used, e.g., for polymer functionalization,[30] reversible bioconjugation,[31] or surface photopatterning.[32]

In the current study, we introduce two novel functional monomers which bear a light-cleavable protected-thiol substituent. The polymerizability of the acrylamide monomer via a free radical mechanism is studied. Subsequently, the ability of the so-formed copolymers to release thiols and undergo Michael addition is evidenced. The RAFT process is then used to generate well-defined block copolymers incorporating the masked thiols in one block. Finally, sequential Michael addition reactions are performed at the chain end after aminolysis of the thiocarbonylthio moiety and along the chain after photodeprotection (Scheme 1).

EXPERIMENTAL SECTION

Materials. Cysteamine hydrochloride (98%, ABCR), 2-nitrobenzyl bromide (98%, ABCR), lithium hydroxide (98%, Alfa Aesar), acryloyl chloride (96%, Alfa Aesar), methacryloyl chloride (97%, ABCR), triethylamine (TEA, 99+%, Merck), sodium hydrogen carbonate ($NaHCO_3$, 99%, Roth), 2-aminoethanol (99%, Fluka), tri-*n*-butylphosphine (TBP, ≥90%, Fluka), dimethylphenylphosphine (DMPP, 99%, Sigma-Aldrich), 1,4-dioxane (99+%, Acros), and acetonitrile (HPLC grade, Acros) were used as received. Ethanol, methanol, chloroform, ethyl acetate, toluene, and *n*-hexane were of all from VWR (Normapur grade) and also used as received. 2,2′-Azobisbutyronitrile (AIBN, 98%, Sigma-Aldrich) was recrystallized twice from methanol and stored at −19 °C. *N*,*N*-Dimethylacrylamide (DMAAm, 99%, Sigma-Aldrich) and styrene (99%, Acros) were passed through a column of basic alumina (VWR) to remove the inhibitor and stored at −19 °C. *N*-Isopropylacrylamide (NiPAAm) was recrystallized twice from toluene/*n*-hexane 1:1 v/v. Dichloromethane (VWR, Normapur) was dried on 4 Å molecular sieves. Dibenzyltrithiocarbonate (DBTTC)[33] and benzyl maleimide[34] were synthesized according to previously reported procedures.

*Monomer Synthesis. 2-((2-Nitrobenzyl)thio)ethanamine (**1**).* **1** was synthesized according to a previously reported procedure.[35] In a 150 mL beaker, lithium hydroxide (1.2506 g, 51.2 mmol) was dissolved in deionized water (25 mL) and ethanol (75 mL) was added. The resulting suspension was subsequently introduced into a 250 mL double-necked round-bottom flask containing cysteamine hydrochloride (2.9141 g, 25.1 mmol). A 150 mL dropping funnel was connected and filled with a solution of 2-nitrobenzyl bromide (5.5214 g, 25.0 mmol) in ethanol (100 mL). The solution was subsequently added dropwise to the cysteamine mixture over a period of 15 min at ambient temperature. The mixture was further stirred at 35 °C for 40 min. Ethanol was removed by rotary evaporation, and 100 mL of deionized water was added. The heterogeneous mixture was poured into a separating funnel and extracted with dichloromethane (3 × 150 mL). The organic fractions were combined, dried over sodium sulfate, filtered, and evaporated. The residue was subsequently purified by flash column chromatography using dichloromethane/methanol 4:1 to give the pure product as a yellow viscous oil (3.5365 g, 67%). The compound was rapidly used for further reactions since limited degradation was observed upon storage. ^{1}H NMR ($CDCl_3$, 250 MHz, δ): 7.96 (d, 1H), 7.26−7.59 (m, 3H), 4.07 (s, 2H), 2.85 (t, 2H), 2.57 (t, 2H), 1.67 (s, 2H) ppm.

dx.doi.org/10.1021/ma202670d | *Macromolecules* 2012, 45, 1792−1802

*N-(2-((2-Nitrobenzyl)thio)ethyl)acrylamide (**2**).* In a 250 mL double-necked round-bottom flask, **1** (3.5365 g, 16.7 mmol) and triethylamine (2.80 mL, 19.8 mmol) were dissolved in dry dichloromethane (150 mL). A dropping funnel was connected to the flask and filled with a solution of acryloyl chloride in dry dichloromethane (20.2 mmol in 30 mL). The flask was cooled to 0 °C, and the acryloyl chloride solution was added dropwise under vigorous stirring over a period of 30 min. The mixture was then allowed to warm to ambient temperature and left to stir for another 15 h. After washing with 2 × 40 mL of brine and 40 mL of a $NaHCO_3$-saturated solution, the organic phase was dried over magnesium sulfate, filtered, and evaporated. The residue was purified by flash column chromatography using chloroform/ethyl acetate 9:1 as an eluent to give an opaque yellow oil which gave a yellow solid upon standing (3.5143 g, 79%). ^{1}H NMR ($CDCl_3$, 250 MHz, δ): 7.91 (d, 1H), 7.32−7.54 (m, 3H), 6.17 (dd, 1H), 6.10−5.90 (broad, 1H), 6.03 (dd, 1H), 5.59 (dd, 1H), 4.02 (s, 2H), 3.42 (q, 2H), 2.58 (t, 2H) ppm.

*N-(2-((2-Nitrobenzyl)thio)ethyl)methacrylamide (**3**).* The same procedure as for **2** was employed, except that methacryloyl chloride was used instead of acryloyl chloride. Briefly, **1** (0.8278 g, 3.9 mmol) and triethylamine (0.53 mL, 4.0 mmol) were dissolved in dry dichloromethane (70 mL). Subsequently, a solution of methacryloyl chloride in dichloromethane (4.1 mmol in 15 mL) was slowly added. After purification by flash column chromatography using chloroform/ethyl acetate 9:1 as an eluent, **3** was obtained as a viscous yellow oil (0.5542 g, 51%). ^{1}H NMR ($CDCl_3$, 250 MHz, δ): 7.91 (d, 1H), 7.54−7.32 (m, 3H), 6.37−6.17 (broad, 1H), 5.64 (m, 1H), 5.27 (m, 1H), 4.02 (s, 2H), 3.40 (q, 2H), 2.59 (t, 2H), 1.90−1.88 (m, 3H) ppm.

*Polymerizations. (Co)polymerizations of **2** and DMAAm.* In a 10 mL round-bottom flask, monomer(s), AIBN, and—if necessary—DBTTC were dissolved in 1,4-dioxane. For a collation of all polymerization conditions, please refer to Table 1. The mixture was deoxygenated by purging with nitrogen over a period of 30 min. The polymerization was triggered by immersing the flask into an oil bath preheated to 70 °C. Samples were periodically withdrawn to follow the reaction kinetics. A portion was diluted in $CDCl_3$ to determine the conversion by ^{1}H NMR. Another portion was evaporated and dissolved in DMAC (+ 1 wt % LiBr) for size-exclusion chromatography analysis.

Table 1. Experimental Conditions of the (Co)polymerizations at 70 °C in 1,4-Dioxane of *N*-(2-((2-Nitrobenzyl)thio)ethyl) Acrylamide 2 and DMAAm Reported in the Present Study

entry	symbol[c]	[M]/[AIBN]	2:DMAAm (mol/mol)	[DBTTC]/[AIBN]
A[a]		20	100:0	
B[a]		20	15:85	
C[b]	●	100	15:85	
D[b]	×	50	15:85	
E[b]	■	50	0:100	
F[b]	♦	50	39:61	
G[b]	○	50	59:41	
H[b]	▲	50	15:85	2
I[b]	□	50	15:85	1

[a][M] = 2.6 M. [b][M] = 0.5 M. [c]The symbols noted in the Table refer to Figures 1 and 2.

*Synthesis of P(DMAAm-co-**2**) (**4**).* Test polymer **4** was produced to evaluate the possibility of thiol photodeprotection followed by thiol−maleimide addition. The mixture was prepared according to entry B (Table 1): In a 10 mL round-bottom flask, monomer **2** (0.2063 g, 0.77 mmol), DMAAm (0.4345 g, 4.34 mmol), and AIBN (0.0423 g, 0.26 mmol) were dissolved in 1,4-dioxane (2 mL). The mixture was deoxygenated by purging with nitrogen for 30 min and then immersed in an oil bath preheated to 70 °C. After 21 h, the flask was cooled to ambient temperature. The polymer was recovered as a slightly yellow powder by 2-fold precipitation in *n*-hexane at ambient temperature (^{1}H NMR, acetone-d_6) $([\mathbf{2}]/[M])_{polymer}$ = 14 mol % (30 wt %).

*Synthesis of the PDMAAm-TTC-PDMAAm MacroRAFT Agent (**7**).* In a 50 mL round-bottom flask, DMAAm (3.9607 g, 39.6 mmol), DBTTC (0.2320 mg, 0.80 mmol), and AIBN (0.0522 g, 0.32 mmol) were dissolved in 1,4-dioxane (15.9 mL). The mixture was deoxygenated by purging with nitrogen over a period of 1 h. The polymerization was triggered by immersing the flask into an oil bath preheated to 70 °C. After 40 min, the polymerization was stopped by cooling the flask to ambient temperature. ^{1}H NMR analysis of the raw mixture in $CDCl_3$ indicated a conversion of 35%. The reaction mixture was concentrated by rotary evaporation, and the polymer was obtained as a yellow powder by 2-fold precipipation in *n*-hexane followed by filtration on a glass filter. (SEC/DMAC) M_n = 3000 g mol^{-1}; PDI = 1.10 (^{1}H NMR, acetone-d_6) M_n = 2600 g mol^{-1}.

*Synthesis of PDMAAm-b-P(DMAAm-co-**2**)-TTC-P(DMAAm-co-**2**)-b-PDMAAm (**8**).* In a 10 mL round-bottom flask, macroRAFT agent **7** (0.1081 g, 0.04 mmol), DMAAm (0.2153 g, 2.15 mmol), monomer **2** (0.1018 g, 3.82 mmol), and AIBN (0.0083 g, 0.05 mmol) were dissolved in 5 mL of 1,4-dioxane. The mixture was deoxygenated by purging with nitrogen over a period of 30 min. The polymerization was triggered by immersing the flask into an oil bath preheated to 70 °C. After 16.5 h, the polymerization was stopped by cooling the flask down to ambient temperature. ^{1}H NMR analysis of the raw mixture in $CDCl_3$ indicated a conversion of 86%. The reaction mixture was slightly concentrated under vacuum, and the polymer was obtained as a light-yellow powder by 2-fold precipipation in *n*-hexane at ambient temperature followed by filtration on a glass filter. (SEC/DMAC) M_n = 8200 g mol^{-1}; PDI = 1.32. (^{1}H NMR, acetone-d_6) $([\mathbf{2}]/[M])_{polymer}$ = 11 mol % (25 wt %); M_n = 9400 g mol^{-1}.

*Synthesis of the PS-TTC-PS MacroRAFT Agent (**9**).* In a 10 mL round-bottom flask, AIBN (0.0420 g, 0.26 mmol) and DBTTC (0.1483 g, 0.51 mmol) were dissolved in styrene (4.0083 g, 38.1 mmol). The mixture was deoxygenated by purging with nitrogen over a period of 30 min. The polymerization was triggered by immersing the flask into an oil bath preheated to 60 °C. After 7 h, the polymerization was stopped by cooling the flask down to ambient temperature. ^{1}H NMR analysis of the raw mixture in acetone-d_6 indicated a conversion of 33%. The reaction mixture was diluted with a small volume of THF, and the polymer was obtained as a yellow powder by 2-fold precipipation in cold methanol followed by filtration on a glass filter. (SEC/DMAC) M_n = 3800 g mol^{-1}; PDI = 1.12.

*Synthesis of PS-b-P(DMAAm-co-**2**)-TTC-P(DMAAm-co-**2**)-b-PS (**10**).* In a 10 mL round-bottom flask, macroRAFT agent **9** (0.1567 g, 0.04 mmol), DMAAm (0.2153 g, 2.15 mmol), monomer **2** (0.1018 g, 3.82 mmol), and AIBN (0.0083 g, 0.05 mmol) were dissolved in 5 mL of 1,4-dioxane. The mixture was deoxygenated by purging with nitrogen over a period of 30 min. The polymerization was triggered by immersing the flask into an oil bath preheated to 70 °C. After 16.5 h, the polymerization was stopped by cooling the flask down to ambient temperature. ^{1}H NMR analysis of the raw mixture in $CDCl_3$ indicated a conversion of 77%. The reaction mixture was slightly concentrated under vacuum, and the polymer was obtained as a light-yellow powder by 2-fold precipipation in *n*-hexane at ambient temperature followed by filtration on a glass filter. (SEC/DMAC) M_n = 6500 g mol^{-1}; PDI = 1.27. (^{1}H NMR, acetone-d_6) M_n = 9950 g mol^{-1}.

*Synthesis of the P(DMAAm-co-**2**)-TTC-P(DMAAm-co-**2**) macroRAFT Agent (**11**).* In a 10 mL round-bottom flask, monomer **2** (0.2805 g, 1.05 mmol), DMAAm (0.6125 g, 6.12 mmol), DBTTC (0.0404 g, 0.14 mmol), and AIBN (0.0262 g, 0.16 mmol) were dissolved in 1,4-dioxane (13.7 mL). The mixture was deoxygenated by purging with nitrogen for 1 h and then immersed in an oil bath preheated to 70 °C. After 5.5 h, the flask was cooled down to ambient temperature. A monomer conversion of 50% was determined by ^{1}H NMR. The polymer was recovered as a light-yellow powder by 2-fold precipitation in *n*-hexane at ambient temperature. (SEC/DMAC) M_n = 3800 g mol^{-1}; PDI = 1.10. (^{1}H NMR, acetone-d_6) M_n = 3800 g mol^{-1}.

*Synthesis of the P(DMAAm-co-**2**)-b-PNiPAAm-TTC-PNiPAAm-b-P(DMAAm-co-**2**) (**12**).* In a 10 mL round-bottom flask, macroRAFT

agent **11** (0.0385 g, 0.01 mmol), NiPAAm (0.2187 g, 1.93 mmol), and AIBN (0.7 mg, 4 μmol) were dissolved in 1,4-dioxane (3 mL). The mixture was deoxygenated by purging with nitrogen over a period of 30 min. The polymerization was triggered by immersing the flask into an oil bath preheated to 70 °C. After 14 h, the polymerization was stopped by cooling the flask down to ambient temperature. ^{1}H NMR analysis of the raw mixture in $CDCl_3$ indicated a conversion of about 90%. The reaction mixture was concentrated by rotary evaporation, and the polymer was obtained as a yellow powder by 2-fold precipitation in *n*-hexane followed by filtration on a glass filter. (SEC/DMAC) M_n = 16 500 g mol^{-1}; PDI = 1.36.

Polymer-Analogue Modifications. Photodeprotection Kinetics. Copolymer **4** was dissolved in acetonitrile at different concentrations and transferred to a 1 cm square quartz cell. The cell was placed 5 mm in front of a hand-held TLC lamp (8 W) and irradiated at 366 nm at ambient temperature. At timed intervals the cuvette was placed in a UV spectrometer to monitor the absorbance of the solution at 345 nm, corresponding to the maximum of absorption of photoreleased *o*-nitrosobenzaldehyde.

*Synthesis of Fully Deprotected P(DMAAm-co-**2**) **4** (**5**).* Copolymer **4** (0.1044 g, 0.12 mmol protected thiol groups) was dissolved in acetonitrile (39 mL). The solution was transferred in three 15 mL headspace vials (Pyrex, diameter 20 mm), which were airtight crimped employing SBR seals with PTFE inner linear. The mixture was deoxygenated by purging with nitrogen for 30 min. The vials were placed 5 mm in front of a hand-held TLC lamp (8 W) and irradiated at 366 nm at ambient temperature for 2.5 h. Polymer **5** was recovered by precipitation in cold *n*-hexane (0.7740 g, 89%). ^{1}H NMR in acetone (see Figure 4) showed no trace of residual protecting groups.

*Michael Addition on Fully Deprotected P(DMAAm-co-**2**) **5** (**6**).* Copolymer **5** (60 mg, 81 μmol thiol groups), benzyl maleimide (0.2046 g, 1.29 mmol), and DMPP (0.1 mg, 0.7 μmol) were dissolved in acetonitrile (4 mL). The mixture was deoxygenated by purging with nitrogen for 30 min, after which deoxygenated TEA (100 μL, 0.72 mmol) was added using a nitrogen-purged syringe. After 15 h, polymer **6** was recovered by precipitation in cold *n*-hexane. ^{1}H NMR in acetone (see Figure 4) revealed a functionalization yield of 92%.

*Synthesis of PDMAAm-b-P(DMAAm-co-**2**)-SH (**13**).* In a 10 mL round-bottom flask, **8** (0.5996 g, ca. 64 μmol according to M_n determined by ^{1}H NMR) was dissolved in acetonitrile (9.7 mL) together with TBP (21 μL, 85 μmol). The resulting yellow mixture was deoxygenated by purging with nitrogen for 30 min. Using a nitrogen-purged syringe, deoxygenated 2-aminoethanol (49 μL, 0.81 mmol) was added. After stirring 18 h at ambient temperature, a pale yellow solution was obtained. Polymer **13** was recovered by precipitation in cold *n*-hexane. (SEC/DMAC) M_n = 7200 g mol^{-1}; PDI = 1.37.

*Synthesis of ω-((1-Benzyl-2,5-dioxopyrrolidin-3-yl)thio)-PDMAAm-b-P(DMAAm-co-**2**) (**14**).* In a 10 mL round-bottom flask, **13** (0.4200 g, ca. 89 μmol end-chain thiol groups according to M_n(**8**) determined by ^{1}H NMR) and benzyl maleimide (0.1029 g, 0.55 mmol) were dissolved in acetonitrile (11.1 mL). The resulting slightly yellow solution was deoxygenated by purging with nitrogen for 40 min. Using a nitrogen-purged syringe, deoxygenated TBP (12 μL, 49 μmol) was added, followed 20 min later by TEA (45 μL, 0.33 mmol). After 18 h polymer **14** was recovered by precipitation in cold *n*-hexane. ^{1}H NMR in acetone (see Figure 6) revealed a functionalization yield of 95%. (SEC/DMAC) M_n = 8000 g mol^{-1}; PDI = 1.24.

*Synthesis of Fully Deprotected ω-((1-Benzyl-2,5-dioxopyrrolidin-3-yl)thio)-PDMAAm-b-P(DMAAm-co-**2**) **14** (**15**).* Copolymer **14** (90.7 mg, 85 μmol protected thiol groups) was dissolved in acetonitrile (30 mL). The solution was transferred into three 15 mL headspace vials (Pyrex, diameter 20 mm), which were airtight crimped employing SBR seals with PTFE inner linear. The mixture was deoxygenated by purging with nitrogen for 30 min. The vials were placed 5 mm in front of a hand-held TLC lamp (8 W) and irradiated at 366 nm at ambient temperature for 2.5 h. Polymer **15** was recovered by precipitation in cold *n*-hexane. ^{1}H NMR in acetone (see Figure 6) showed no trace of residual protecting groups. (SEC/DMAC) M_n = 6200 g mol^{-1}; PDI = 1.17.

*Michael Addition on Fully Deprotected ω-((1-Benzyl-2,5-dioxopyrrolidin-3-yl)thio)-PDMAAm-b-P(DMAAm-co-**2**) **15** (**16**).* Copolymer **15** (32.7 mg, 35 μmol thiol groups), benzyl maleimide (0.0818 g, 0.44 mmol), and DMPP (0.04 mg, 0.3 μmol) were dissolved in acetonitrile (3 mL). The mixture was deoxygenated by purging with nitrogen for 30 min, after which deoxygenated TEA (40 μL, 0.29 mmol) was added using a nitrogen-purged syringe. After 15 h, copolymer **16** was recovered by precipitation in cold *n*-hexane. ^{1}H NMR in acetone (see Figure 6) revealed a functionalization yield of 89%. (SEC/DMAC) M_n = 8200 g mol^{-1}; PDI = 1.35.

Characterizations. ^{1}H NMR spectroscopy was carried out on either a Bruker AM 250 or a Bruker AM 400 spectrometers at 250 or 400 MHz, respectively. The δ-scale is referenced to tetramethylsilane (δ = 0.00 ppm) as internal standard. Size-exclusion measurements were performed on a Polymer Laboratories/Varian PLGPC 50 Plus system comprising a Polymer Laboratories 5.0 mm bead-size guard column (50 × 7.5 mm^2), followed by three PL columns and a differential refractive-index detector. The eluent was *N*,*N*′-dimethylacetamide (DMAc) at 50 °C with a flow rate of 1 mL min^{-1}. The SEC system was calibrated using linear poly(styrene) (PS) standards ranging from 160 to 6 × 10^6 g mol^{-1} and linear poly(methyl methacrylate) standards ranging from 700 to 2 × 10^6 g mol^{-1}. The resulting molecular weight distributions were determined by universal calibration using Mark–Houwink parameters for PS (K = 14.1 × 10^{-5} dL g^{-1}, α = 0.70).[36] Molecular weights relative to PS are reported in the current contribution. UV/vis spectra were recorded on a Varian Cary 300 Bio spectrophotometer.

RESULTS AND DISCUSSION

Monomer Synthesis. When a statistical copolymerization is conducted, one usually prefers to use comonomers of a rather similar electronic and steric structure. For the sake of versatility, we thus synthesized two monomers starting from the same substituent building block: one acrylamide for copolymerizations with other acrylamides or acrylates and one methacrylamide to use together with other methacrylamides or methacrylates (see Scheme 2). It could be verified that these

Scheme 2. Synthetic Routes to Photocleavable Protected Thiol-Containing Monomers[a]

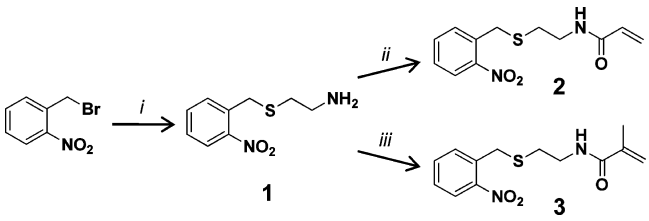

[a]Reagents and conditions: (i) LiOH, cysteamine hydrochloride, H_2O/EtOH, 35 °C; (ii) acryloyl chloride, triethylamine, DCM, 0 °C → ambient temperature; (iii) methacryloyl chloride, triethylamine, DCM, 0 °C → ambient temperature.

two monomers were photosensitive since a clear change in their UV–vis spectra was observed after irradiation at 366 nm (see Figure S3). In the current study, we will focus on the incorporation of these photoreactive monomers into various macromolecular architectures.

Polymerizability of the *o*-Nitrobenzyl-Protected 2-Mercaptoethyl (Meth)acrylamides. The following part is dedicated to a study on the polymerizability of acrylamide **2**. Indeed, incorporating nitrobenzyl moieties via a prepolymerization approach does not seem straightforward since these groups

dx.doi.org/10.1021/ma202670d | *Macromolecules* 2012, 45, 1792–1802

are known to act as retarders or even inhibitors in free-radical polymerization.[37] Nevertheless, some examples can be found in the literature. For instance, although they were unable to obtain homopolymers, Voit and co-workers succeeded in incorporating *N*-nitroveratryloxycarbonyl-protected amines into methyl methacrylate-based polymers.[32a] Gohy and co-workers reported the successful controlled synthesis of homopolymers of nitrobenzyl methacrylate by ATRP, however, only up to 30% conversion.[38] Recently, Grubbs and colleagues successfully employed alkoxyamines bearing nitrobenzyl groups on both the nitroxide and the initiating fragment sides to efficiently control the free-radical polymerization of methyl methacrylate.[39]

We initially proceeded to homopolymerize **2** employing conditions similar to those reported by Voit and colleagues (Table 1, entry A). Contrary to their findings, we observed a conversion of 34% after 24 h at 60 °C (M_n = 22 500 g mol^{-1}; PDI = 1.8). The experiment proves the polymerizability of **2**, yet higher conversions are usually desirable. It was thus decided that a copolymerization approach was feasible, since in most applications (e.g., bioconjugation or surface grafting) the incorporation of few reactive groups along the polymer chain is sufficient for the final purpose. An alternative acrylamide was selected for this purpose, namely *N*,*N*-dimethylacrylamide (DMAAm). Indeed its polymer has the advantage of being organo- and water-soluble and to some extent biocompatible.[40] We initially employed a molar ratio **2**/DMAAm of 15:85 since it represents a reasonable minimal amount of incorporated groups. The copolymerizations were conducted at 70 °C in 1,4-dioxane with two initial AIBN concentrations. With [M]/[AIBN] = 100, the polymerization proceeded relatively slowly and only reached 50% after 8 h (refer to Figure 1): a value at which a conversion plateau was observed. Using a higher concentration of radical initiator ([M]/[AIBN] = 50) permitted to convert 92% of the monomer mixture into polymer in ca. 20 h (Figure 1). Subsequently, the initiator concentration was kept constant and the monomer mixture composition was varied (see Table 1). When DMAAm was reacted alone, the polymerization proceeded relatively rapidly with more than 90% of the monomer being consumed in 4 h.

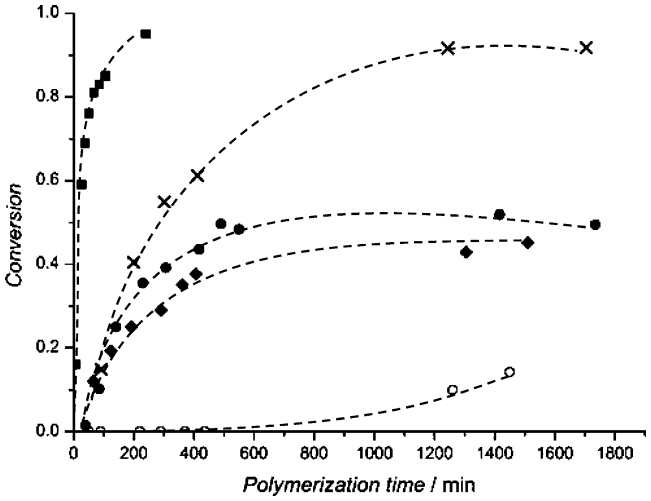

Figure 1. Evolution of the global monomer conversion vs time for the free-radical (co)polymerization of **2** with DMAAm at 70 °C in 1,4-dioxane with variable initiator concentrations and comonomer mixture compositions (see Table 1). The dashed lines are drawn to guide the eye.

Increasing the proportion of **2** and keeping the overall monomer concentration constant resulted in significantly decreased polymerization rates (refer to Figure 1). Examination of the macromolecular characteristics also revealed a strong impact of the nitrobenzene groups on the chain length. Indeed, while molecular weights ranging from ca. 65 and 40 kg mol^{-1} were obtained for the homopolymerization of DMAAm, 3−4 times lower molecular weights were found when 15 mol % of **2** was present in the copolymerization mixture. For a given conversion range, a continuous decrease of MW was observed for an increase in [**2**] (see Figure 2).

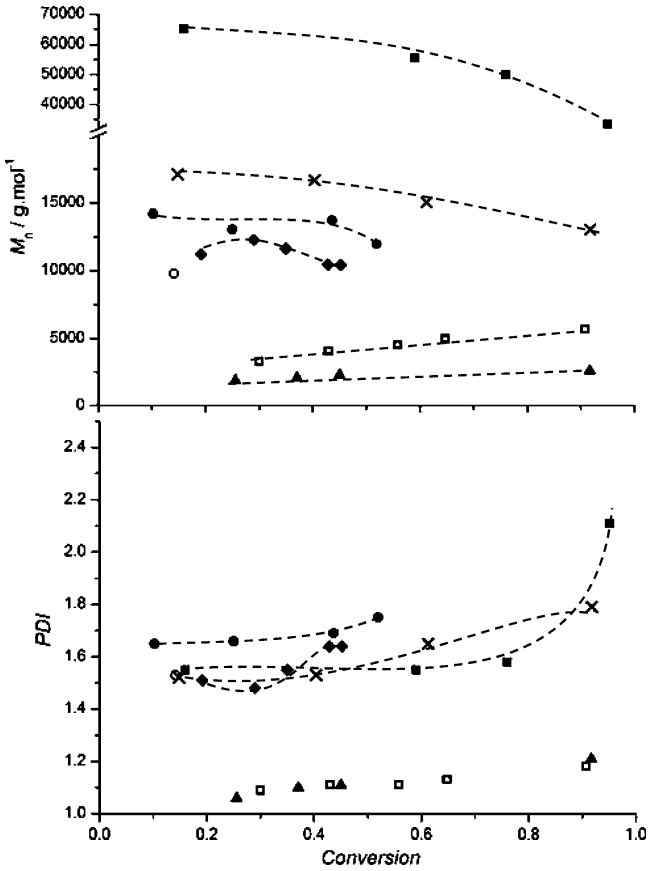

Figure 2. (top) Evolution of the number-average molar masses vs conversion for the free-radical and RAFT-mediated living/controlled radical (co)polymerizations of **2** with DMAAm at 70 °C in 1,4-dioxane with different initiator concentrations and comonomer mixture compositions (see Table 1). (bottom) Corresponding polydispersity indices. The dashed lines are drawn to guide the eye.

We additionally found that **3** was able to copolymerize with methyl methacrylate (see Figure S4). However, the remainder of our study will focus on the acrylamide derivative **2**. The use of **3** for obtaining polymethacrylamide-based polymers will be the subject of a future publication.

In addition to providing a means to calculate the overall monomer conversion, monitoring by ^{1}H NMR revealed that the incorporation of **2** was rather similar to that of DMAAm. Particularly, purified copolymer **4** (Scheme 3), obtained at the highest monomer conversion (92%, entry D), revealed that the *o*-nitrobenzyl thioether moieties remained intact throughout the polymerization and that the comonomer ratio in the copolymer was rather similar to the comonomer feed, 14:86 and 15:85, respectively (see Figure S5). Consequently, we

dx.doi.org/10.1021/ma202670d | *Macromolecules* 2012, 45, 1792−1802

Scheme 3. Photodeprotection of P(DMAAm-*co*-2) Copolymer at 366 nm Followed by Base-Catalyzed Michael Addition with Benzyl Maleimide

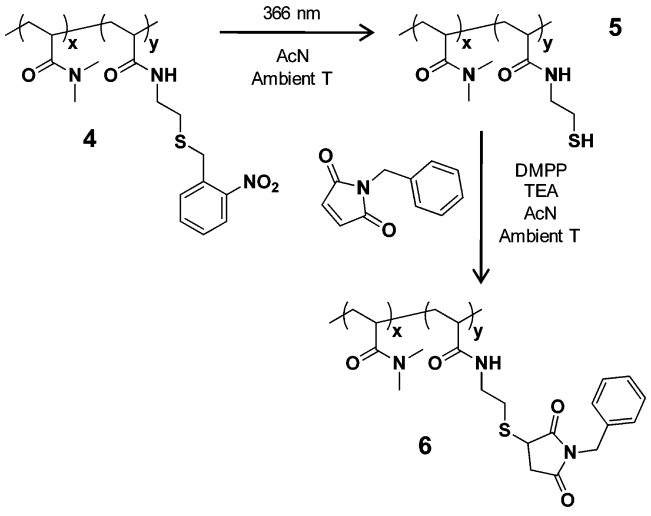

evaluated the possibility of releasing thiols along the polymer chains and of subsequently reacting them with Michael acceptors such as maleimide derivatives.

Deprotection and Subsequent Functionalization. The deprotection reaction was performed using a simple hand-held UV lamp (8 W) generally used in laboratories to read TLC plates. The irradiation was carried out at ambient temperature in acetonitrile at 366 nm (refer to Scheme 3), where the absorbance of the polymer due to the presence of the *o*-nitrobenzyl groups is substantial (see Figure S6). Although irradiation at lower wavelengths (UV-C) would probably favor a faster deproctection due to a relatively higher absorbance, we reasoned that the employment of UV-A radiation was more promising in view of potential bioapplications. The drawback is that the photoreleased *o*-nitrosobenzaldehyde possesses a maximum of absorbance at 345 nm.[41] It is thus necessary to work under diluted conditions: a polymer concentration of a few g L^{-1}, which is in fact a typical concentration range in biochemistry.

For a concentration of 3 g L^{-1} of copolymer **4** (3.4 mM) the absorbance at 345 nm does not show any further change after being irradiated for ~2 h. ^{1}H NMR analysis of the purified polymer indicates that at this stage quantitative deprotection is achieved. Indeed, the spectrum of copolymer **5** (Figure 4, middle spectrum) shows no more distinct aromatic peaks, and the signal at ca. 4 ppm accounting for the methylene protons bound to the carbon bridging the sulfur atom and the benzyl ring in copolymer **4** completely disappeared.

Figure 3 clearly evidences the influence of the concentration on the deprotection kinetics. While quantitative deprotection was achieved in about 2 h at 3 g L^{-1}, only 25 min was sufficient to reach 97% deprotection at 0.35 g L^{-1}.

After purification by precipitation, the fully deprotected copolymer **5** was subsequently subjected to reaction with benzyl maleimide in presence of a catalytic amount of dimethylphenylphosphine—acting as a reducing agent to suppress disulfide bridging—and triethylamine as basic catalyst. The reaction was performed at ambient temperature overnight. After removal of the excess maleimide and catalysts, copolymer **6** was recovered and analyzed by ^{1}H NMR (Figure 4, see bottom spectrum). Two new peaks could be observed, both

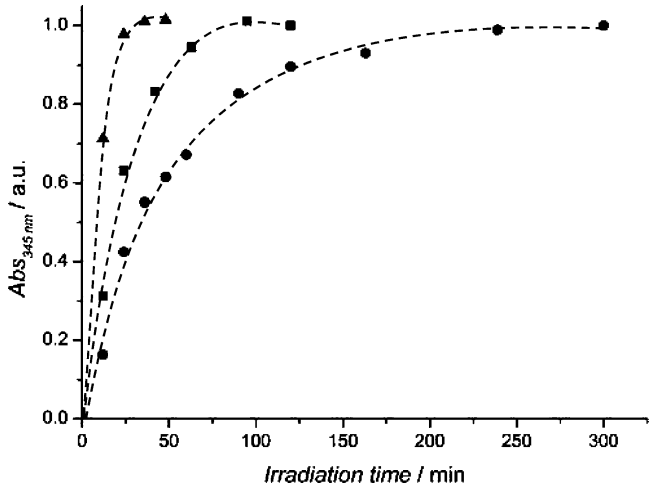

Figure 3. Normalized evolution of the absorbance at 345 nm of copolymer **4** (P(DMAAm$_{86}$-*co*-**2**$_{14}$)) solutions in acetonitrile vs time of irradiation at 366 nm at ambient temperature for different concentrations: 0.35 (▲), 1 (■), and 3 g L^{-1} (●). The dashed lines are drawn to guide the eye.

originating from the maleimide derivative: one at 4.65 ppm accounting for the methylene protons in the α-position of the benzyl ring and one between 7.15 and 7.45 ppm representing the aromatic protons. The absence of ethylenic protons at 6.65 ppm confirms that all excess maleimide was efficiently removed during purification and that the two aforementioned peaks are contributions solely due to grafted benzyl maleimide. Taking as a reference the side chain protons between 2.2 and 3.8 ppm and comparing the aromatic protons of **6** to those of the protected copolymer **4**, we calculate a global deprotection/functionalization sequence yield of 92%.

After having evidenced the efficiency of our system, we focused on obtaining better-defined architectures such as amphiphilic and thermosensitive block copolymers exhibiting the photocleavable group in the hydrophilic block, which could be of interest to construct surface-reactive nanoparticles,[42] nanovesicles,[43] or nanogels.[44]

Well-Defined Macromolecular Architectures. Although nitroxide-mediated polymerization could have been chosen since alkoxyamines are efficient controlling agents in radical polymerization of acrylamides,[45] we opted for reversible-addition−fragmentation transfer (RAFT) polymerization since we had in mind that the thiocarbonylthio moiety present at the end or in the middle of RAFT polymers could provide an additional and orthogonal source of thiols.[24] Furthermore, ATRP of acrylamide derivatives is not straightforward.[46] We employed dibenzyl trithiocarbonate (DBTTC) as RAFT agent since trithiocarbonates allow to efficiently mediate the radical polymerization of acrylamides.[47]

Two kinetic runs were performed using the best conditions found for the free-radical copolymerization of **2** and DMAAm, i.e., giving the highest conversion (entry D). Each experiment was performed with a different concentration of RAFT agent corresponding to [DBTTC]/[AIBN] = 2 or 1 respectively for entries H and I. As expected, in the case of an ideal chain transfer mechanism, the polymerization rate was not affected by the presence of the RAFT agent as conversion vs time plots for entries H and I were very similar to that of entry D (see Figure S8). However, the macromolecular characteristics were strongly altered (refer to Figure 2). Polymers with much lower

dx.doi.org/10.1021/ma202670d | *Macromolecules* 2012, 45, 1792−1802

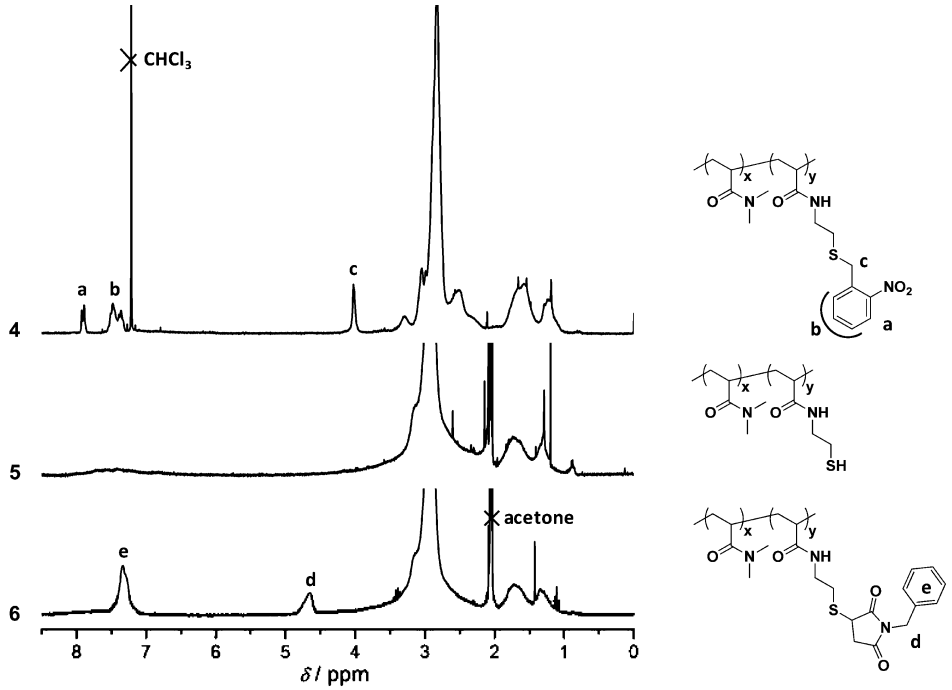

Figure 4. ^{1}H NMR spectra of purified copolymers after, from top to bottom, free-radical copolymerization of **2** with DMAAm (**4**), photodeprotection of a 3 g L^{-1} solution of **4** for 2 h (**5**), and reaction of **5** with benzyl maleimide (**6**).

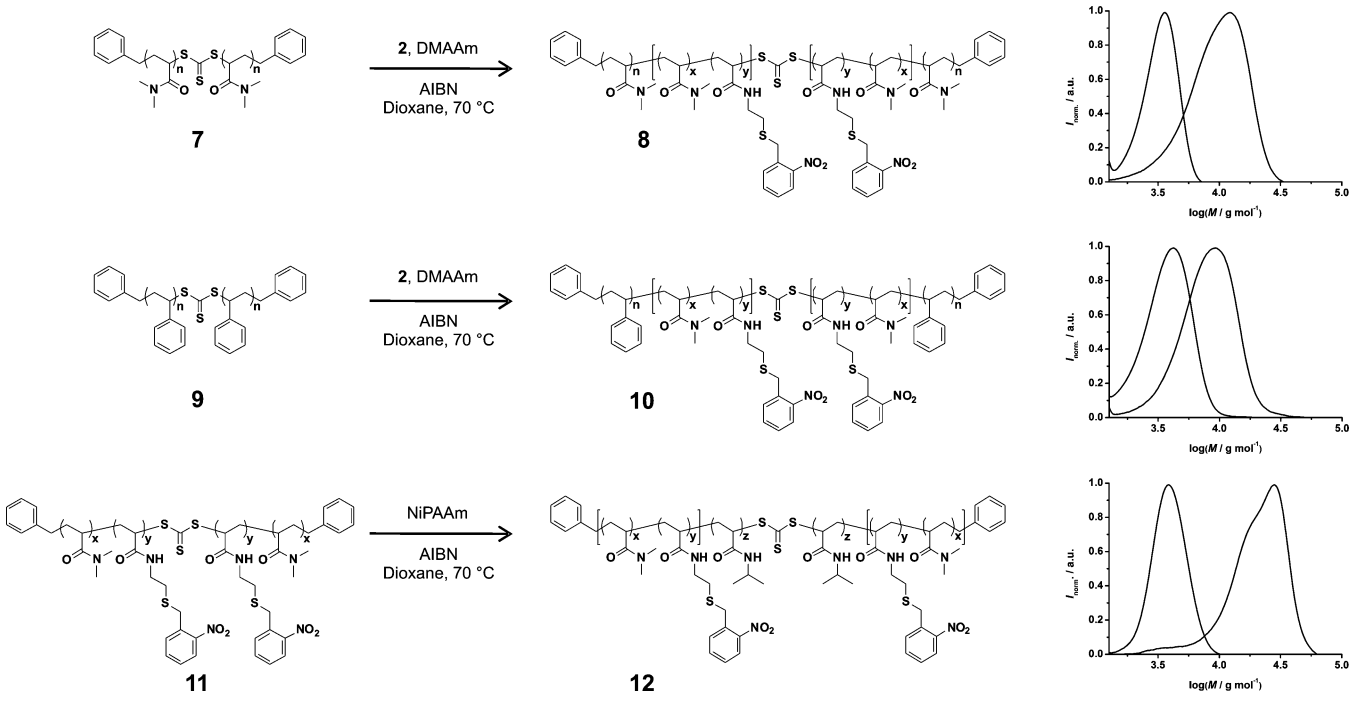

Figure 5. Synthesis of functional triblock copolymers by RAFT-mediated polymerization exhibiting the *o*-nitrobenzyl-protected thiols in either their inner (top and middle rows) or their outer (bottom row) block(s).

molecular weights ranging between 2000 and 5000 g mol^{-1} and polydispersity indices between 1.06 and 1.21 were identified by size-exclusion chromatography. Particularly, the progressive complete shift of the SEC traces with increasing monomer conversion demonstrated the controlled character of the polymerization (see Figure S9). Using PDMAAm or PS macromolecular RAFT agents **7** and **9**, respectively, allowed us to synthesize well-defined bishydrophilic and amphiphilic block copolymers, respectively (Figure 5). In each case, triblock copolymers comprising a middle block possessing the protected thiol units were obtained with rather low polydispersities, i.e., 1.32 and 1.27 for copolymers **8** and **10**, respectively. To further prove the living character of copolymers of **2** and DMAAm obtained in the presence of DBTTC, we synthesized P(DMAAm-*co*-**2**) macromolecular RAFT agent **11** using conditions similar to those of entry H (Table 1) and stopped the polymerization at a monomer conversion of 0.5 (Figure 5). We subsequently performed the RAFT polymerization of *N*-

dx.doi.org/10.1021/ma202670d | *Macromolecules* 2012, 45, 1792–1802

isopropylacrylamide (NiPAAm) in the presence of **11** and AIBN at 70 °C in 1,4-dioxane. The targeted degree of polymerization of the PNiPAAm block was purposely set at a high value (ca. 200) and the polymerization performed to a high monomer conversion (95%) to clearly evidence the consumption of **11**. The overlay of the SEC traces of **11** and of the corresponding product of the NiPAAm RAFT-mediated polymerization (Figure 5, bottom right) shows a distinct shift toward higher molecular weights together with a shoulder and a tail, both at lower molecular weights. The latter certainly originates from dead chains present in macroRAFT agent **11**, while the nonsymmetrical distribution may have arisen from irreversible termination by recombination, highly possible for polymerization of acrylamide derivatives at high conversion.

With the synthesis of copolymers by RAFT-mediated polymerization, we had not only in mind to produce well-defined (block) copolymers but also to introduce an additional masked thiol moiety. Indeed, aminolysis of the thiocarbonylthio compounds eliminates the RAFT end or middle group to yield ω-mercapto polymers (see Introduction). We envisaged that it should be possible to orthogonally deprotect/functionalize both types of thiols in a sequential manner. We thus reacted the block copolymer **8** with 2-aminoethanol in acetonitrile at ambient temperature in presence of tri-*n*-butylphosphine as a reducing agent (see Scheme 4). The effectiveness of the reaction can be assessed via both SEC and UV/vis spectroscopy. Although the number-average molecular weight of polymer **13** was not the half of that **8**—which can be explained by a nonsymmetrical structure or potential disulfide coupling as suggested by the increase in polydispersity—the successful removal of the trithiocarbonate moiety could be evidenced by disappearance of its characteristic UV absorbance maximum at ~310 nm (see Figure S10). ^{1}H NMR performed on the purified diblock copolymer **13** showed that the *o*-nitrobenzyl protecting group was insensitive to the aminolysis process (Figure 6, second row).

The released end-chain thiol functionality present in copolymer **13** was subsequently reacted with benzyl maleimide employing conditions previously described for the Michael addition on the deprotected thiol lateral groups of free-radical polymer **4** to produce benzyl maleimidothioether-capped copolymer **14**. A similar yield of 95% was calculated by ^{1}H NMR (refer to Figure 6). The purified copolymer **14** was then subjected to the same treatment as copolymer **4**, i.e., UV irradiation at 366 nm for 2 h to quantitatively produce copolymer **15** bearing multiple lateral thiol groups followed by triethylamine-catalyzed Michael addition with benzyl maleimide at ambient temperature to yield copolymer **16**. Again, a similar thiol−ene reaction yield of 89% was calculated from the relative integration of the aromatic protons signal to that of other lateral group protons between 2.2 and 3.8 ppm. Finally, it is important to note that the integrity of the well-defined polymeric backbones was maintained throughout all the consecutive modifications as demonstrated by similar molecular weight distributions ($1.17 \leq \text{PDI} \leq 1.25$) within a similar molecular weight range ($7200 \leq M_n \leq 8200$ g mol^{-1}) for copolymers **13**, **14**, **15**, and **16**. However, it remains difficult to draw any numerical interpretation due to the different nature of these copolymers and thus a different hydrodynamic behavior in size-exclusion chromatography.

Scheme 4. Synthetic Strategy for the Orthogonal Double Thiol-Maleimide Michael Addition via Sequential Aminolysis of the Thiocarbonylthio Moieties and *o*-Nitrobenzylthioether UV Deprotection

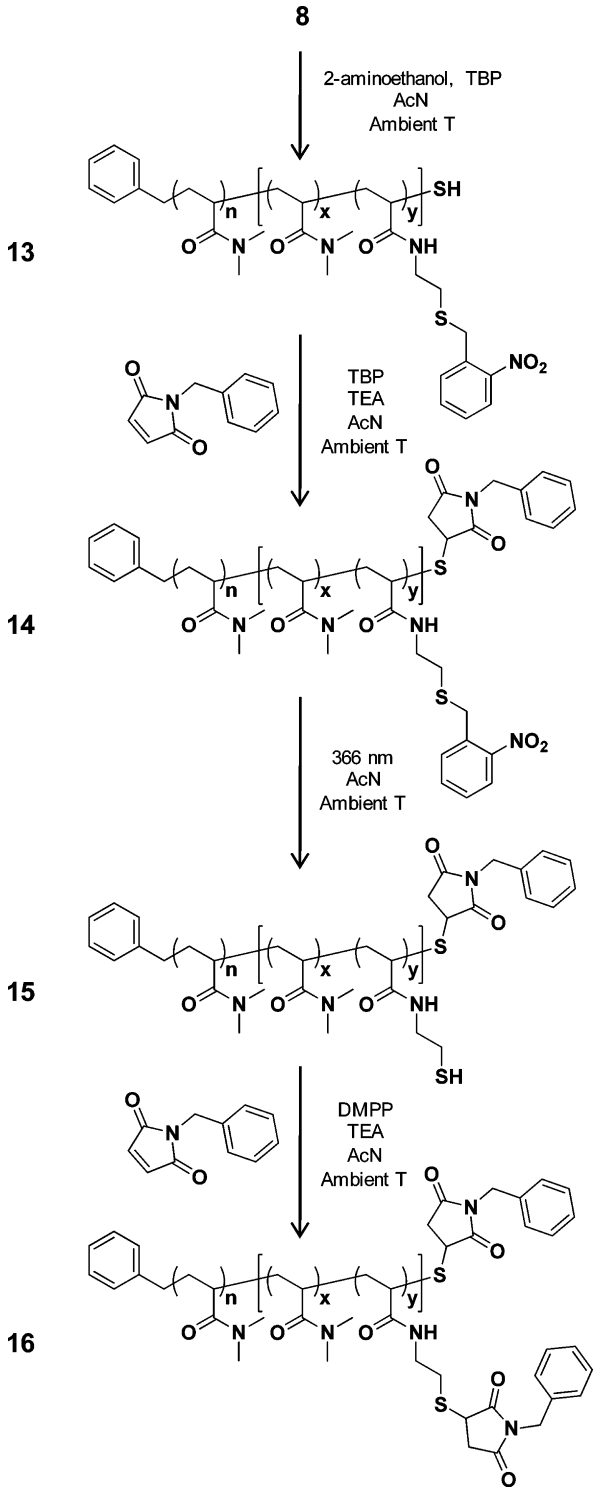

CONCLUSIONS

The synthesis of two new (meth)acrylamide derivatives bearing a UV-sensitive *o*-nitrobenzyl protected thiol group is reported. Despite the disturbing nature of the *o*-nitrobenzyl group in free-radical processes which retards the polymerization, it was possible to obtain statistical copolymers with *N,N*-dimethyla-

dx.doi.org/10.1021/ma202670d | *Macromolecules* 2012, 45, 1792−1802

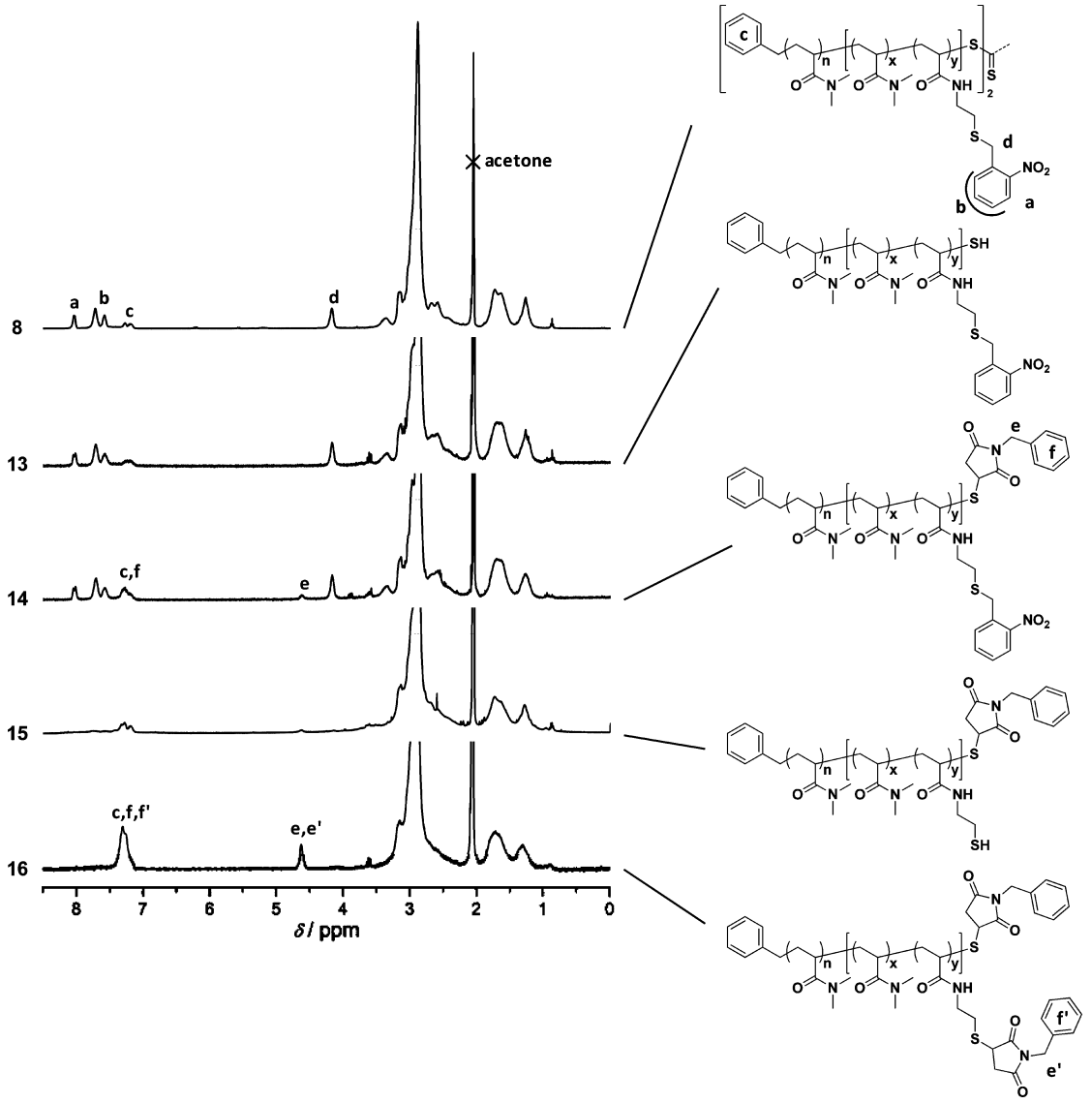

Figure 6. ^{1}H NMR spectra of purified copolymers after, from top to bottom, RAFT-mediated copolymerization of **2** with DMAAm (**8**), aminolysis of **8** (**13**), capping of end-chain released thiol by benzyl maleimide (**14**), photodeprotection of **14** for 2 h (**15**), and reaction of **15** with benzyl maleimide (**16**).

crylamide (DMAAm) in relatively high yields with an appropriate design of the reaction conditions. The protecting group remained intact throughout the polymerization process and could thus be used to trigger the release of multiple thiol groups along polymeric chains by UV irradiation. The deprotection rate was found to be concentration-dependent, probably due to the strongly absorbing nature of the photoreleased caging group in the irradiation wavelength domain. Nevertheless, full deprotection and close-to-quantitative subsequent thiol-maleimide functionalization (92%) could be achieved. In a further effort to create well-defined functional polymeric materials, RAFT-mediated polymerization was utilized to produce block copolymers possessing one statistical block consisting of DMAAm units and the protected thiol acrylamide derivative as a first segment and hydrophilic PDMAAm, hydrophobic polystyrene, or thermosensitive poly(*N*-isopropylacrylamide) as a second one. Importantly, a PDMAAm-based block copolymer was employed to demonstrate the effective orthogonal double deprotection/Michael addition of thiols originating from aminolyzed RAFT thiocarbonylthio midchain group and light-cleavable *o*-nitrobenzylthioether lateral groups, with high efficiency (95 and 89%, respectively).

■ ASSOCIATED CONTENT

Supporting Information

Additional NMR spectra, UV/vis absorption curves, and SEC traces. This material is available free of charge via the Internet at http://pubs.acs.org.

■ AUTHOR INFORMATION

Corresponding Author

*E-mail: christopher.barner-kowollik@kit.edu.

Notes

The authors declare no competing financial interest.

■ ACKNOWLEDGMENTS

C.B.-K. acknowledges financial support from the Karlsruhe Institute of Technology (KIT) in the context of the *Excellence*

Initiative for leading German universities as well as the German Research Council (DFG) and the Ministry of Science and Arts of the state of Baden-Württemberg. G.D. thanks the *Alexander von Humboldt Foundation* for financial support via a Humboldt Research Fellowship for Postdoctoral Researchers. T.P.'s Ph.D. studies are funded by the *Fonds der Chemischen Industrie*.

■ REFERENCES

(1) (a) Hawker, C. J.; Wooley, K. L. *Science* **2005**, *309*, 1200. (b) Binder, W. H.; Sachsenhofer, R. *Macromol. Rapid Commun.* **2007**, *28*, 15. (c) Barner-Kowollik, C.; Inglis, A. J. *Macromol. Chem. Phys.* **2009**, *210*, 987. (d) Iha, R. K.; Wooley, K. L.; Nystrom, A. N.; Burke, D. J.; Kade, M. J.; Hawker, C. J. *Chem. Rev.* **2009**, *109*, 5620. (e) Golas, P. L.; Matyjaszewski, K. *Chem. Soc. Rev.* **2010**, *39*, 1338. (f) Sumerlin, B. S.; Vogt, A. P. *Macromolecules* **2010**, *43*, 1. (g) Barner-Kowollik, C.; Du Prez, F. E.; Espeel, P.; Hawker, C. J.; Junkers, T.; Schlaad, H.; Van Camp, W. *Angew. Chem., Int. Ed.* **2011**, *50*, 60.

(2) Kolb, H. C.; Finn, M. G.; Sharpless, K. B. *Angew. Chem., Int. Ed.* **2001**, *40*, 2004.

(3) (a) Meldal, M.; Tornøe, C. W. *Chem. Rev.* **2008**, *108*, 2952. (b) Lutz, J.-F. *Angew. Chem., Int. Ed.* **2007**, *46*, 1018. (c) Dirks, A. J.; Cornelissen, J. J. L. M.; van Delft, F. L.; van Hest, J. C. M.; Nolte, R. J. M.; Rowan, A. E.; Rutjes, F. P. J. T. *QSAR Comb. Sci.* **2007**, *26*, 1200. (d) Meldal, M. *Macromol. Rapid Commun.* **2008**, *29*, 1016. (e) Lundberg, P.; Hawker, C. J.; Hult, A.; Malkoch, M. *Macromol. Rapid Commun.* **2008**, *29*, 998. (f) Aragão-Leoneti, V.; Campo, V. L.; Gomes, A. S.; Field, R. A.; Carvalho, I. *Tetrahedron* **2010**, *66*, 9475.

(4) (a) Hoyle, C. E.; Bowman, C. N. *Angew. Chem., Int. Ed.* **2010**, *49*, 1540. (b) Hoogenboom, R. *Angew. Chem., Int. Ed.* **2010**, *49*, 3415. (c) Hoyle, C. E.; Lowe, A. B.; Bowman, C. N. *Chem. Soc. Rev.* **2010**, *39*, 1355.

(5) (a) Sinnwell, S.; Inglis, A. J.; Davis, T. P.; Stenzel, M. H.; Barner-Kowollik, C. *Chem. Commun.* **2008**, 2052. (b) Inglis, A. J.; Sinnwell, S.; Stenzel, M. H.; Barner-Kowollik, C. *Angew. Chem., Int. Ed.* **2009**, *48*, 2411. (c) Nebhani, L.; Gerstel, P.; Atanasova, P.; Bruns, M.; Barner-Kowollik, C. *J. Polym. Sci., Polym. Chem.* **2009**, *47*, 7090. (d) Paulöhrl, T.; Inglis, A. J.; Barner-Kowollik, C. *Adv. Mater.* **2010**, *22*, 2788. (e) Inglis, A. J.; Nebhani, L.; Altintas, O.; Schmidt, F.-G.; Barner-Kowollik, C. *Macromolecules* **2010**, *43*, 5515. (f) Goldmann, A. S.; Tischer, T.; Barner, L.; Bruns, M.; Barner-Kowollik, C. *Biomacromolecules* **2011**, *12*, 1137.

(6) (a) Ott, C.; Hoogenboom, R.; Schubert, U. S. *Chem. Commun.* **2008**, 3516. (b) Becer, C. R.; Babiuch, K.; Pilz, D.; Hornig, S.; Heinze, T.; Gottschaldt, M.; Schubert, U. S. *Macromolecules* **2009**, *42*, 2387. (c) Babiuch, K.; Becer, C. R.; Gottschaldt, M.; Delaney, J. T.; Weisser, J.; Beer, B.; Wyrwa, R.; Schnabelrauch, M.; Schubert, U. S. *Macromol. Biosci.* **2011**, *11*, 535.

(7) (a) Li, R. C.; Broyer, R. M.; Maynard, H. D. *J. Polym. Sci., Part A: Polym. Chem.* **2006**, *44*, 5004. (b) Heredia, K. L.; Maynard, H. D. *Org. Biomol. Chem.* **2007**, *5*, 45. (c) Heredia, K. L.; Tolstyka, Z. P.; Maynard, H. D. *Macromolecules* **2007**, *40*, 4772. (d) Kopping, J. T.; Tolstyka, Z. P.; Maynard, H. D. *Macromolecules* **2007**, *40*, 8593. (e) Christman, K. L.; Broyer, R. M.; Schopf, E.; Kolodziej, C. M.; Chen, Y.; Maynard, H. D. *Langmuir* **2011**, *27*, 4715.

(8) (a) Singh, I.; Zarafshani, Z.; Lutz, J.-F.; Heaney, F. *Macromolecules* **2009**, *42*, 5411. (b) Singh, I.; Zarafshani, Z.; Heaney, F.; Lutz, J.-F. *Polym. Chem.* **2011**, *2*, 372.

(9) Tsarevsky, N. V.; Bencherif, S. A.; Matyjaszewski, K. *Macromolecules* **2007**, *40*, 4439.

(10) Kade, M. J.; Burke, D. J.; Hawker, C. J. *J. Polym. Sci., Part A: Polym. Chem.* **2010**, *48*, 743.

(11) Love, J. C.; Estroff, L. A.; Kriebel, J. K.; Nuzzo, R. G.; Whitesides, G. M. *Chem. Rev.* **2005**, *105*, 1103.

(12) Ueda, A.; Nagai, S. In *Polymer Handbook*, 4th ed.; Brandrup, J., Immergut, E. H., Grulke, E. A., Eds.; Wiley: New York, 1999; p II/97.

(13) Chiefari, J.; Rizzardo, E. In *Handbook of Radical Polymerization*, 2nd ed.; Matyjaszewski, K., Davis, T. P., Eds.; John Wiley and Sons: New York, 2002; p 629.

(14) (a) Nagel, B.; Gajovic-Eichelmann, N.; Scheller, F. W.; Katterle, M. *Langmuir* **2010**, *26*, 9088. (b) Crownover, E. F.; Convertine, A. J.; Stayton, P. S. *Polym. Chem.* **2011**, *2*, 1499.

(15) (a) Bontempo, D.; Heredia, K. L.; Fish, B. A.; Maynard, H. D. *J. Am. Chem. Soc.* **2004**, *126*, 15372. (b) Heredia, K. L.; Bontempo, D.; Ly, T.; Byers, J. T.; Halstenberg, S.; Maynard, H. D. *J. Am. Chem. Soc.* **2005**, *127*, 16955. (c) Iwasaki, Y.; Omichi, Y.; Iwata, R. *Langmuir* **2008**, *24*, 8427. (d) Vázquez-Dorbatt, V.; Tolstyka, Z. P.; Chang, C.-W.; Maynard, H. D. *Biomacromolecules* **2009**, *10*, 2207.

(16) (a) Liu, J.; Bulmus, V.; Barner-Kowollik, C.; Stenzel, M. H.; Davis, T. P. *Macromol. Rapid Commun.* **2007**, *28*, 303. (b) Boyer, C.; Liu, J.; Wong, L.; Tippett, M.; Bulmus, V.; Davis, T. P. *J. Polym. Sci., Part A: Polym. Chem.* **2008**, *46*, 7207. (c) Chang, C.-W.; Nguyen, T. H.; Maynard, H. D. *Macromol. Rapid Commun.* **2010**, *31*, 1691.

(17) van Dijk-Wolthuis, W. N. E.; van de Wetering, P.; Hinrichs, W. L. J.; Hofmeyer, L. J. F.; Liskamp, R. M. J.; Crommelin, D. J. A.; Hennink, W. E. *Bioconjug. Chem.* **1999**, *10*, 687.

(18) Tsarevsky, N. V.; Matyjaszewski, K. *Macromolecules* **2002**, *35*, 9009.

(19) Li, L.; Jiang, X.; Zhuo, R. *J. Polym. Sci., Part A: Polym. Chem.* **2009**, *47*, 5989.

(20) Carrot, G.; Hilborn, J.; Hedrick, J. L.; Trollsås, M. *Macromolecules* **1999**, *32*, 5171.

(21) Ye, M.; Zhang, D.; Han, L.; Tejada, J.; Ortiz, C. *Soft Matter* **2006**, *2*, 243.

(22) Javakhishvili, I.; Hvilsted, S. *Biomacromolecules* **2009**, *10*, 74.

(23) Hill, N. L.; Jarvis, J. L.; Pettersson, F.; Braslau, R. *React. Funct. Polym.* **2008**, *68*, 361.

(24) (a) Barner, L.; Perrier, S. In *Handbook of RAFT Polymerization*; Barner-Kowollik, C.; Wiley-VCH: Weinheim, 2008; p 455. (b) Willcock, H.; O'Reilly, R. K. *Polym. Chem.* **2010**, *1*, 149. (c) Moad, G.; Rizzardo, E.; Thang, S. H. *Polym. Int.* **2011**, *60*, 9.

(25) Garamszegi, L.; Donzel, C.; Carrot, G.; Nguyen, T. Q.; Hilborn, J. *React. Funct. Polym.* **2003**, *55*, 179.

(26) Uygun, M.; Tasdelen, M. A.; Yagci, Y. *Macromol. Chem. Phys.* **2010**, *211*, 103.

(27) Boyer, C.; Soeriyadi, A. H.; Roth, P. J.; Whittaker, M. R.; Davis, T. P. *Chem. Commun.* **2011**, *47*, 1318.

(28) Liras, M.; García, O.; Quijada-Garrido, I.; París, R. *Macromolecules* **2011**, *44*, 1335.

(29) *Greene's Protective Groups in Organic Synthesis*; Wuts, P. G. M., Greene, T. W., Eds.; John Wiley and Sons: New York, 2007.

(30) Pauloehrl, T.; Delaittre, G.; Bastmeyer, M.; Barner-Kowollik, C. *Polym . Chem.* **2012**, DOI: 10.1039/C1PY00372K.

(31) (a) Kostiainen, M. A.; Smith, D. K.; Ikkala, O. *Angew. Chem., Int. Ed.* **2007**, *46*, 7600−7604. (b) Kostiainen, M. A.; Kasyutich, O.; Cornelissen, J. J. L. M.; Nolte, R. J. M. *Nature Chem.* **2010**, *2*, 394−399.

(32) (a) Braun, F.; Eng, L.; Trogisch, S.; Voit, B. *Macromol. Chem. Phys.* **2003**, *204*, 1486. (b) Ryan, D.; Parviz, B. A.; Linder, V.; Semetey, V.; Sia, S. K.; Su, J.; Mrksich, M.; Whitesides, G. M. *Langmuir* **2004**, *20*, 9080. (c) Brown, A. A.; Azzaroni, O.; Huck, W. T. S. *Langmuir* **2009**, *25*, 1744.

(33) (a) Aoyagi, B.; Endo, T. *J. Polym. Sci., Part A: Polym. Chem.* **2009**, *47*, 3702. (b) Bivigou-Koumba, A. M.; Kristen, J.; Laschewsky, A.; Mueller-Buschbaum, P.; Papadakis, C. M. *Macromol. Chem. Phys.* **2009**, *210*, 565.

(34) Clevenger, R. C.; Turnbull, K. D. *Synth. Commun.* **2000**, *30*, 1379.

(35) Gosh, S.; Tochtrop, G. P. *Tetrahedron Lett.* **2009**, *50*, 1723.

(36) Strazielle, C.; Benoit, H.; Vogl, O. *Eur. Polym. J.* **1978**, *14*, 331.

(37) Bajpai, U. D. N.; Bajpai, A. K.; Bajpai, J. *J. Appl. Polym. Sci.* **1991**, *42*, 2005.

(38) Schumers, J.-M.; Fustin, C.-A.; Can, A.; Hoogenboom, R.; Schubert, U. S.; Gohy, J.-F. *J. Polym. Sci., Part A: Polym. Chem.* **2009**, *47*, 6504−6513.

(39) Greene, A. C.; Grubbs, R. B. *Macromolecules* **2010**, *43*, 10320.

(40) Nakayama, Y.; Matsuda, T. *Langmuir* **1999**, *15*, 5560.

(41) (a) Il'ichev, Y. V.; Schwörer, M. A.; Wirz, J. *J. Am. Chem. Soc.* **2004**, *126*, 4581. (b) Marriott, G.; Miyata, H.; Kinosita, K. *Biochem. Int.* **1992**, *26*, 943.
(42) (a) Nagasaki, Y.; Okada, T.; Scholz, C.; Iijima, M.; Kato, M.; Kataoka, K. *Macromolecules* **1998**, *31*, 1473. (b) Lu, J.; Shi, M.; Shoichet, M. S. *Bioconjugate Chem.* **2008**, *20*, 87. (c) Nicolas, N.; Bensaid, F.; Desmaële, D.; Grogna, M.; Detrembleur, C.; Andrieux, K.; Couvreur, P. *Macromolecules* **2008**, *41*, 8418. (d) Bae, J. W.; Lee, E.; Park, K. M.; Park, K. D. *Macromolecules* **2009**, *42*, 3437. (e) Delaittre, G.; Justribó-Hernández, G.; Nolte, R. J. M.; Cornelissen, J. J. L. M. *Macromol. Rapid Commun.* **2011**, *32*, 19.
(43) Opsteen, J. A.; Brinkhuis, R. P.; Teeuwen, R. L. M.; Löwik, D. W. P. M.; van Hest, J. C. M. *Chem. Commun.* **2007**, 3136.
(44) Meng, Z.; Hendrickson, G. R.; Lyon, L. A. *Macromolecules* **2009**, *42*, 7664.
(45) Delaittre, G.; Rieger, J.; Charleux, B. *Macromolecules* **2011**, *44*, 462 and references therein.
(46) (a) Teodorescu, M.; Matyjaszewski, K. *Macromolecules* **1999**, *32*, 4826. (b) Rademacher, J. T.; Baum, M.; Pallack, M. E.; Brittain, W. J.; Simonsick, W. J. *Macromolecules* **1999**, *33*, 284. (c) Xia, Y.; Yin, X.; Burke, N. A. D.; Stöver, H. D. H. *Macromolecules* **2005**, *38*, 5937.
(47) (a) Moad, G.; Rizzardo, E.; Thang, S. H. *Aust. J. Chem.* **2005**, *58*, 379. (b) Favier, A.; Charreyre, M.-T. *Macromol. Rapid Commun.* **2006**, *27*, 653.

Macromolecules

Article

pubs.acs.org/Macromolecules

Size-Tunable Nanoparticle Synthesis by RAFT Polymerization in CO_2-Induced Miniemulsions

Siqing Cheng, S. R. Simon Ting, Frank P. Lucien, and Per B. Zetterlund*

Centre for Advanced Macromolecular Design (CAMD), School of Chemical Engineering, The University of New South Wales, Sydney, NSW 2052, Australia

Supporting Information

ABSTRACT: A novel environmentally friendly low-energy emulsification method that relies on pressurization with CO_2 to low pressure has been applied to reversible addition−fragmentation chain transfer (RAFT) polymerization of styrene-in-water miniemulsions with the anionic surfactant Dowfax 8390. This method circumvents traditional high-energy homogenization, and over a certain CO_2 pressure range, a transparent miniemulsion is formed. RAFT polymerization of styrene using benzyldodecyl trithiocarbonate and the aqueous phase initiator VA-044 was carried out successfully in CO_2-induced miniemulsions at 50 °C with good control/livingness. Interestingly, the particle size could be conveniently tuned via the CO_2 pressure without altering the recipe, with 6.00, 6.50, and 7.50 MPa generating number-average particle diameters of 98, 89, and 48 nm, respectively, at ∼70% conversion. The smallest particle size corresponded to the pressure range within which the emulsion was transparent.

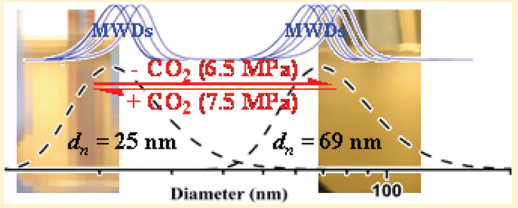

INTRODUCTION

Miniemulsions (also referred to as nanoemulsions) are kinetically stable but thermodynamically unstable submicrometer-sized (typically in the diameter range 50−500 nm) dispersions of oil (e.g., vinyl monomer) in water.[1] The miniemulsion concept was originally introduced by Ugelstad et al.,[2] who proposed the notion of polymerization within small monomer droplets (monomer droplet nucleation) during emulsion polymerization. Miniemulsion polymerization is distinct from the traditional emulsion polymerization process in that polymer particles are generated from monomer droplets, as opposed to nucleation in the continuous phase via micellar and/or homogeneous nucleation. This mechanistic aspect is the reason for the attractiveness of miniemulsion polymerization for nanoparticle synthesis. Since miniemulsion polymerization possesses the inherent advantage that ideally each monomer droplet is transformed into a polymer particle and diffusion across the aqueous phase is not required,[3] the process conveniently lends itself to synthesis of hybrid polymer particles,[4] hollow polymer particles,[4a] and implementation of controlled/living radical polymerization (CLRP).[5] Since miniemulsions are thermodynamically unstable, energy input is required for their formation, traditionally in the form of high-energy homogenization via ultrasonication or high-pressure homogenization. This requirement remains an impediment to industrial implementation of miniemulsion polymerization, and it is therefore of interest to develop alternative low-energy methods to generate miniemulsions for polymerization as well as to device convenient methods to tune the droplet/particle size.

Considerable efforts have been geared toward development of methods for low-energy generation of miniemulsions, mainly for nonpolymerization purposes.[1b] The approaches available mainly make use of accessible catastrophic phase transitions occurring during the emulsification process due to the change in the spontaneous curvature of the surfactant as a result of the variation in the physicochemical properties of the system, such as changing temperature (phase inversion temperature (PIT) method[6]), adjusting the composition of the system (emulsion inversion point (EIP) method[7]), or using additives to change the pH[8] or ionic strength.[9] In addition to the obvious benefit of low energy, such methods may also be advantageous with regards to reproducibility and generation of uniform droplet size distributions. High-energy homogenization methods normally generate fairly ill-defined droplet size distributions and are sensitive to process variables such as the power, the size and shape of the container, and the location of the sonifier tip.

Recently, miniemulsions based on low-energy emulsification have been attracting attention for synthesis of polymeric nanoparticles. Spernath et al.[10] reported miniemulsion polymerization of lauryl acrylate based on the sequential use of high-energy homogenization and the PIT method. Sadtler et al.[11] and Galindo-Alvarez et al.[12] synthesized poly(ethylene oxide)-covered nanoparticles using miniemulsion polymerization of styrene in connection with the EIP and PIT methods, respectively, for miniemulsion generation. In our recent work,[13] miniemulsion polymerization of styrene based on the EIP low-energy emulsification method was implemented successfully. An alternative means of effecting low-energy miniemulsion formation is based on *in situ* formation of

Received: December 20, 2011
Revised: February 2, 2012
Published: February 8, 2012

surfactant at the oil–water interface;[14] this method has been implemented successfully for both conventional radical polymerization and nitroxide-mediated radical polymerization (NMP). Some of the above approaches are of limited use for polymerizations; the required composition changes (EIP method) are not always easily achieved in practice, and a variation in temperature (PIT method) is not practical in connection with radical polymerization initiated by thermal initiators. The development of effective, controllable, environmentally benign, and low-energy emulsification methods for preparation of miniemulsions for polymerizations is challenging and of great importance.

As an attractive green solvent, supercritical or compressed CO_2 has been widely used in many chemical and industrial processes because it is readily available, inexpensive, and nontoxic and its physical properties can be tuned continuously by pressure and/or temperature.[15] The dissolution of compressed CO_2 in aqueous solution can change the properties of the aqueous solution considerably, and thus the properties of aqueous solutions can be tuned by controlling the CO_2 pressure. The ability to control the properties of an aqueous surfactant solution by CO_2 is interesting[16]—the properties of the surfactant aggregates in aqueous solution can be tuned by the CO_2 pressure because of the tunable nature of compressed CO_2. This principle has been widely applied successfully in reversibly controlling the properties of solutions containing surfactant by pressurization and depressurization, e.g., reverse micelles,[17] creating CO_2 continuous microemulsion or CO_2/water emulsions,[18] and triggering phase transitions between different surfactant aggregates.[19] Most interestingly, a recent investigation[20] demonstrated that CO_2 can induce the formation of miniemulsions (in the absence of high-energy mixing) in a wide range of water-to-oil volume ratios in the presence of a low concentration of surfactant. Miniemulsions obtained in this way have been applied to the synthesis of nanomaterials, enhanced oil recovery, and polymerizations in preliminary investigations.[20,21] This novel means of preparing miniemulsions is of great interest not only because it circumvents the traditional high-energy mixing approaches but also because the formation and breakage of the miniemulsion can be controlled reversibly by pressurization and depressurization without contaminants (e.g., salt to break the emulsion). Although the exact miniemulsion formation mechanism remains to be clarified,[20] this technique clearly has great potential for miniemulsion polymerization.

CLRP[22] makes it possible to prepare polymer of predetermined microstructure and various complex architectures by free radical means, and the past decade has seen significant progress in the area of CLRP in dispersed systems.[5e,f] Reversible addition–fragmentation chain transfer (RAFT) polymerization is one of the most frequently employed techniques.[23] RAFT miniemulsion polymerization can be challenging mainly due to issues related to colloidal stability (superswelling) but can be implemented with success under appropriate conditions.[5f,24] To date, the only examples of miniemulsion CLRP based on low-energy emulsification are our works on NMP[14c] and RAFT[25] polymerization in miniemulsion using *in situ* surfactant formation without use of high-energy homogenization.

In the current work, we investigated—for the first time—RAFT polymerization of styrene in aqueous miniemulsion induced by compressed CO_2, i.e., in the absence of traditional high-energy mixing techniques. It is demonstrated that polymeric nanoparticles of diameters <100 nm comprising well-defined polymer can be prepared, with the additional advantage of the particle size being tunable via the CO_2 pressure.

EXPERIMENTAL SECTION

Materials. Water was distilled and deionized before use. Styrene (St; 99%, Aldrich) was purified by passing through a column with basic aluminum oxide (Ajex) to remove inhibitor. The RAFT agent

Scheme 1. Benzyl Dodecyltrithiocarbonate (BDT)

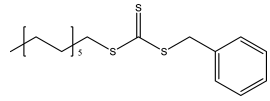

benzyldodecyl trithiocarbonate (BDT; Scheme 1) was prepared according to methods described elsewhere.[26] The water-soluble initiator 2,2′-azobis[2-(2-imidazolin-2-yl)propane] dihydrochloride (VA-044; Wako Pure Chemicals), liquid CO_2 (99.5%, Coregas), the surfactant disulfonated alkyl diphenyl oxide sodium salt (Dowfax 8390, 33 wt % in water from Dow Chemical), and hexadecane (HD; 99%, Aldrich) were used as received. All other chemical agents were purchased from Sigma-Aldrich, supplied at the highest purity available.

Phase Behavior Investigation. The apparatus used for observing the phase behavior of the emulsion system was similar to that used previously.[15g,27] It consisted of a custom-made sight gauge reactor with an internal volume of 40 mL, a magnetic stirrer, and a high-pressure syringe pump (Isco, 260D). The temperature in the reactor was controlled by a Julabo FP35 heater/cooler unit with a Pt 100 sensor via circulating oil through internal channels encased in the reactor block. The pressure gauge used was composed of a pressure transducer (Druck, PDCR 911) and an indicator. In a typical experiment, Dowfax 8390/styrene/water/HD was mixed by general magnetic stirring for ~40 min to obtain a milky-white emulsion before addition to the reactor. After thermal equilibrium was attained, CO_2 was charged into the reactor to the desired pressure, and the phase behavior was observed via the viewing window.

Miniemulsion Polymerization Procedures. The apparatus described above for the phase behavior investigation was also used for the polymerizations. In a typical experiment, the reaction mixture of styrene/HD/BDT/Dowfax 8390/VA-044/water (11.6 wt % styrene rel water, 8 wt % HD rel styrene, and 33 wt % Dowfax 8390 rel

Table 1. Recipes for RAFT Miniemulsion Polymerizations[a]

recipe	St/g	Dowfax 8390/g	water/g	HD/g	BDT/g	VA-044/g
A	1.0	0.33	8.59	0.08	0.009	0.0026
B	1.0	0.10	8.80	0.08	0.009	0.0026

[a][St]/[BDT] = 400; [BDT]/[VA-044] = 3; HD rel St = 8 wt %.

styrene; recipe A in Table 1) was mixed by general magnetic stirring for ~40 min to obtain a milky-white emulsion, purged with nitrogen for 10 min before it was charged into the nitrogen-purged reactor and sealed off, and subsequently subjected to nitrogen bubbling for 20 min via an inlet located at the bottom of the reactor. The polymerizations were conducted at 50 °C at the CO_2 pressure that gave a transparent emulsion (7.50 MPa) as well as at two lower pressures of 6.50 and 6.00 MPa. After the desired time, the CO_2 was released, and the collected reaction mixture was cooled in an ice/water bath.

Two recipes (Table 1) were investigated for the miniemulsion polymerizations based on ultrasonication (instead of CO_2 approach). The composition in recipe A was the same as that in the CO_2-induced miniemulsion polymerizations above, while the only difference in recipe B was that the Dowfax 8390 concentration was reduced (10 vs 33 wt % rel styrene). In a typical experimental procedure for

dx.doi.org/10.1021/ma202744f | *Macromolecules* 2012, 45, 1803–1810

miniemulsion polymerization based on ultrasonication, the reaction mixture of styrene/HD/Dowfax 8390/VA-044/BDT/water was subjected to ultrasonication (Digital sonifier, model 450, Branson) in an ice−water bath at 70% amplitude for 10 min. Approximately 10 mL of the resultant miniemulsion was transferred to a glass bottle and then sealed with a rubber septum, Parafilm, and copper wire. After purging by nitrogen for 30 min, the rubber septum was sealed using vacuum grease. Polymerization was carried out in an oil bath at 50 °C under magnetic stirring. The polymerizations were stopped at prescribed times by cooling the glass bottles in ice water.

Measurements and Characterization. St conversions were determined by a Shimadzu GC-17A gas chromatograph with H_2 as carrier gas, equipped with a J&W Scientific 30 m AT-WAX column and an autosampler, employing tetrahydrofuran (THF) as solvent and *N*,*N*-dimethylformamide (DMF) as internal standard.

Polymer molecular weights and molecular weight distributions were determined by gel permeation chromatography (GPC) with a Shimadzu modular system with THF as eluent at 40 °C at a flow rate of 1.0 mL/min with injection volume of 40 μL. The GPC was equipped with a DGU-12A solvent degasser, a LC-10AT pump, A CTO-10A column oven and an ECR 7515-A refractive index detector, and a Polymer Laboratories 5.0 μm bead-size guard column (50 × 7.8 mm^2) followed by four 300 × 7.8 mm^2 linear Phenogel columns. The system was calibrated against polystyrene standards ranging from 500 to 10^6 g/mol.

The number (d_n)- and weight- (d_w)-average particle diameters and their distributions were measured using dynamic light scattering (DLS; Malvern Nano-ZS) operating a 4 mW He−Ne laser at 633 nm at the backscattering angle of 173° at 25 °C. All DLS measurements were carried out in the absence of CO_2 (the polymerizations were stopped at prescribed times by depressurization and subsequent cooling of the reactor to ambient temperature, followed by sampling for DLS). All miniemulsion samples were measured directly without dilution after polymerization. All results are based on an average of five runs, each run taking 20 s.

Particle sizes were further confirmed by transmission electron microscopy (TEM). The TEM micrographs were obtained using a JEOL 1400 transmission electron microscope at the voltage of 100 V. The magnification was calibrated against a diffraction grating replica (accuracy ±5%). The specimens were prepared by casting an aqueous solution of the polymerized miniemulsion (1 g/dm^3 of polymer) onto a Formvar-coated copper grid followed by natural drying. A negative staining technique using 2 wt % phosphotungstic acid (PTA) was applied to the samples.

RESULTS AND DISCUSSION

Phase Behavior. As previously observed for the water/sodium bis(2-ethylhexyl) sulfosuccinate (AOT)/isooctane system,[20] a turbid styrene/HD/Dowfax 8390/water emulsion (11.6 wt % styrene rel water, 8 wt % HD rel styrene, and 33 wt % Dowfax 8390 rel styrene; recipe A in Table 1 without RAFT agent and initiator) under stirring at 50 °C became increasingly translucent as CO_2 was charged to the system and eventually completely transparent when the CO_2 pressure reached ∼7.50 MPa. The pressure range of the transparent region was ∼0.50 MPa. Subsequently, with continuously increasing CO_2 pressure, the transparent emulsion gradually changed to turbid again (Figure 1). As previously confirmed by small-angle X-ray scattering (SAXS), electrical conductivity measurements, as well as some applications for synthesis of nanomaterials by Han and co-workers,[20,21] the reversible phase behavior change of the emulsion from milky white to transparent with CO_2 pressure is ascribed to the change in the size of the emulsion droplets, the smallest droplets corresponding to the transparent region.

The above observations were all made during magnetic stirring in the high-pressure reactor. If the stirring is stopped while the system is still pressurized, phase separation does occur. In the absence of CO_2, complete phase separation of the turbid styrene/HD/Dowfax 8390/water system after stopping the stirring occurred after ∼4 h. However, under the same conditions but under CO_2 pressurization, the time to complete phase separation was significantly prolonged. At the CO_2 transparent pressure of 7.50 MPa, it took ∼48 h for complete phase separation to occur. At higher CO_2 pressures up to ∼8.10 MPa, the emulsion was turbid but still very stable, taking at least 20 h for complete phase separation to occur after stopping the stirring. However, when the CO_2 pressure exceeded ∼8.10 MPa, another clear immiscible liquid layer appeared on the surface of the solution. The upper liquid phase was assumed to be a CO_2-rich phase, as suggested by an increase in the thickness of the layer with increasing pressure. This type of phase separation is commonly associated with the dissolution of compressed CO_2 in aqueous−organic mixed solvents.[28] Given the fact that the system does phase separate in the absence of stirring, it can be concluded that it is thermodynamically unstable; i.e., it is not a microemulsion even in the pressure region that gives a transparent emulsion. Importantly, these findings also suggest that the droplet size can be tuned via the CO_2 pressure. In addition, when the investigated system was depressurized, the phase behavior was found to be reversible, i.e., the transparent emulsion was recovered at ∼7.50 MPa. The mechanistic aspects of these phenomena remain to be clarified but may be related to the insertion of CO_2 molecules into the interfacial film, resulting in a change in the curvature.[18c,20,29]

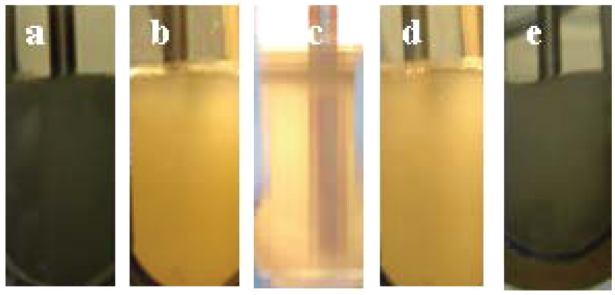

Figure 1. Photographs of the styrene/HD/Dowfax 8390/water system (33 wt % Dowfax 8390 rel St; 8 wt % HD rel St; 11.6 wt % St rel water as per recipe A in Table 1) at 50 °C and CO_2 pressures of (a) 3.00, (b) 7.13, (c) 7.50, (d) 7.86, and (e) 8.00 MPa.

The pressure P_T is defined as the pressure at which the emulsion becomes transparent. In order to optimize the experimental conditions for miniemulsion formation with regards to polymerization, P_T was measured as a function of various experimental parameters (based on recipe A of Table 1 without BDT and VA-044). Figure 2a shows P_T plotted vs the amount of surfactant Dowfax 8390 at different temperatures, revealing how P_T decreases with increasing surfactant content and increases with increasing temperature. Evidently, higher temperatures are unfavorable for miniemulsion formation induced by CO_2, presumably because the solubility of CO_2 decreases with increasing temperature. The dependence on surfactant concentration is quite natural, given that a greater number of surfactant molecules will provide increased colloidal stability. Both the temperature and the surfactant content need to be carefully considered for a miniemulsion polymerization initiated thermally; a certain temperature is required for thermal decomposition of the radical initiator, and the surfactant content should not exceed that at which the surfactant concentration in the aqueous phase exceeds the

dx.doi.org/10.1021/ma202744f | *Macromolecules* 2012, 45, 1803−1810

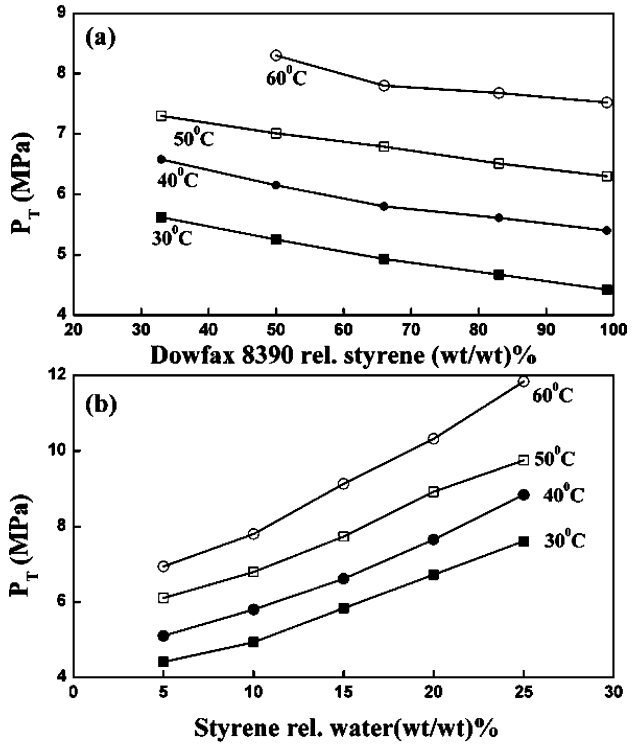

Figure 2. P_T (minimum CO_2 pressure at which emulsion becomes transparent) as a function of (a) weight fraction surfactant Dowfax 8390 rel styrene at different temperature (8 wt % HD rel St; 11.6 wt % St rel water) and (b) St weight content (wt % rel to water) at different temperature (33 wt % Dowfax 8390 and 8 wt % HD rel St).

critical micelle concentration (cmc) (as this would result in micellar nucleation—not desirable in a miniemulsion polymerization). Figure 2b shows that P_T increases with increasing styrene content at different temperatures. Considering the above dependencies of P_T on the recipe and the temperature, it was decided to conduct the miniemulsion polymerizations below 60 °C using a fairly high surfactant concentration and a relatively low styrene content, the main objective being to minimize the required CO_2 pressure. It would be possible to employ less surfactant, but a higher CO_2 pressure would then be required to obtain a similar droplet size. Here it is worth pointing out that the apparent cmc for sodium dodecyl sulfate (SDS) in a styrene miniemulsion can be as high as 5 times greater than that in water due to the high total surface area of the styrene droplets (which adsorbs surfactant);[30] i.e., the presence of micelles is not expected in the present system under CO_2 pressure.

RAFT Polymerization in CO_2-Induced Miniemulsion. RAFT polymerizations of styrene using BDT as RAFT agent (Scheme 1) were carried out in CO_2-induced miniemulsions at 50 °C employing the water-soluble initiator VA-044. The miniemulsion composition was 33 wt % Dowfax 8390 rel styrene, 11.6 wt % styrene rel water, 8 wt % HD rel to styrene, $[\text{styrene}]_0/[\text{BDT}]_0 = 400$, and $[\text{BDT}]_0/[\text{VA-044}]_0 = 5$ (recipe A, Table 1). The presence of small amounts of BDT and VA-044 had a negligible effect on the CO_2 transparent pressure P_T, which remained ~7.50 MPa at 50 °C. Preliminary experiments showed that miniemulsion formation occurred more readily at pressures slightly below than slightly above P_T, and therefore RAFT polymerizations were conducted at pressures of 6.00 and 6.50 MPa in addition to P_T (7.50 MPa).

At all three CO_2 pressures, the polymerizations proceeded with good colloidal stability with no visible coagulum or phase separation. DLS data of particle size as a function of conversion for all three CO_2 pressures are displayed in Figure 3. There is a

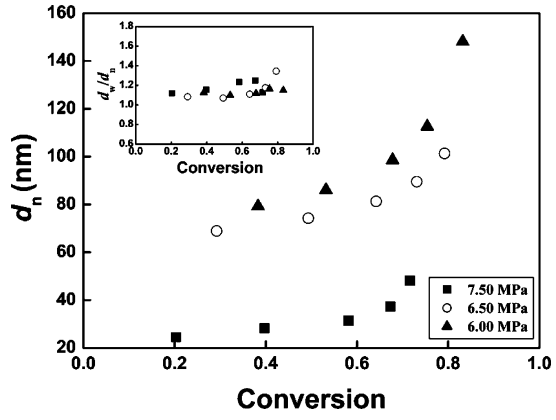

Figure 3. Number-average diameter (d_n) and polydispersities (d_w/d_n) vs conversion for CO_2-induced RAFT miniemulsion polymerization of styrene initiated by VA-044 at 50 °C using Dowfax 8390 as surfactant at pressures of 6.00, 6.50, and 7.50 MPa with [St]/[BDT] = 400 and [BDT]/[VA-044] = 3 (33 wt % Dowfax 8390 rel St; 8 wt % HD rel St; 11.6 wt % St rel water).

clear trend in decreasing particle size with increasing pressure, with the smallest particle size of $d_n \approx 30$ nm obtained at P_T (7.50 MPa), which is considerably smaller than for a "normal" miniemulsion generated via high-energy mixing and closer in size to a microemulsion. Figure 4 shows an overlay of particle

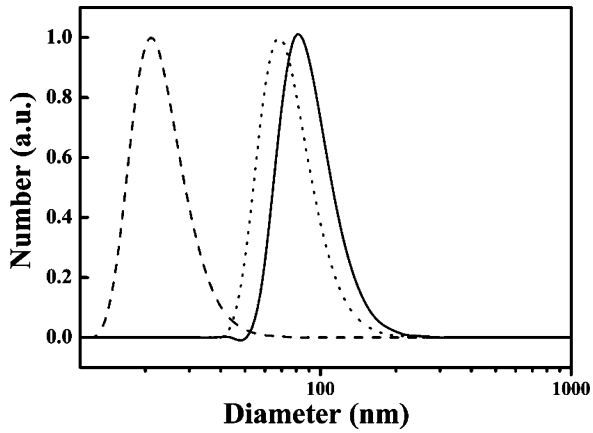

Figure 4. Particle size distributions based on number for CO_2-induced RAFT miniemulsion polymerization of styrene initiated by VA-044 at 50 °C using Dowfax 8390 as surfactant at CO_2 pressures of 7.50 (– – –), 6.50 (···), and 6.00 (—) MPa after polymerization for 8 h (conversion = 20.3, 29.2, and 38.3% for 7.50, 6.50, and 6.00 MPa, respectively) with [St]/[BDT] = 400 and [BDT]/[VA-044] = 3 (33 wt % Dowfax 8390 rel St; 8 wt % HD rel St; 11.6 wt % St rel water).

size distributions obtained by DLS at approximate conversions of 30% for all three pressures, clearly revealing how the particle size decreases with increasing CO_2 pressure in this pressure range. The same trend is also clearly evident in TEM micrographs of particles obtained at ~30% conversion for the three pressures (Figure 5). These data demonstrate that it is possible to tune the particle size via the CO_2 pressure without altering the miniemulsion recipe. It is quite challenging to tune

dx.doi.org/10.1021/ma202744f | Macromolecules 2012, 45, 1803–1810

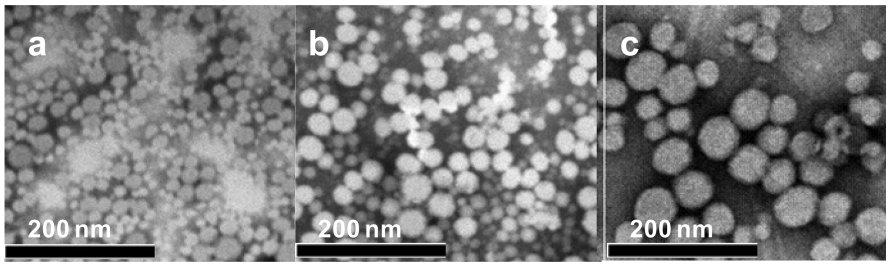

Figure 5. TEM micrographs of polystyrene particles obtained by CO_2-induced RAFT miniemulsion polymerization of styrene initiated by VA-044 at 50 °C using Dowfax 8390 as surfactant at CO_2 pressures of (a) 7.50, (b) 6.50 and (c) 6.00 MPa after polymerization for 8 h (conversion = 20.3, 29.2, and 38.3% for 7.50, 6.50, and 6.00 MPa, respectively) with [St]/[BDT] = 400 and [BDT]/[VA-044] = 3 (33 wt % Dowfax 8390 rel St; 8 wt % HD rel St; 11.6 wt % St rel water).

the particle size using high-energy miniemulsification—this would normally be done by varying the surfactant content and/or the mixing energy (e.g., ultrasonication power).[3b] The width of the particle size distributions (as judged by d_w/d_n; inset in Figure 3) were approximately the same for all pressures investigated. At all pressures, the particle size remained close to constant up to ~60% conversion, beyond which there was a gradual increase. Based on an ideal miniemulsion, each monomer droplet would be converted to a polymer particle with perfect preservation of droplet identity; i.e., the particle size would remain constant with conversion. In the present case, the increasing trend in particle size with conversion at high conversion is presumably a consequence of colloidal stability issues. One can speculate that this may occur because the stabilizing effect of CO_2 is reduced as monomer is gradually converted to polymer.

Figure 6 shows conversion−time data, revealing that there is a fairly modest but significant decrease in polymerization rate

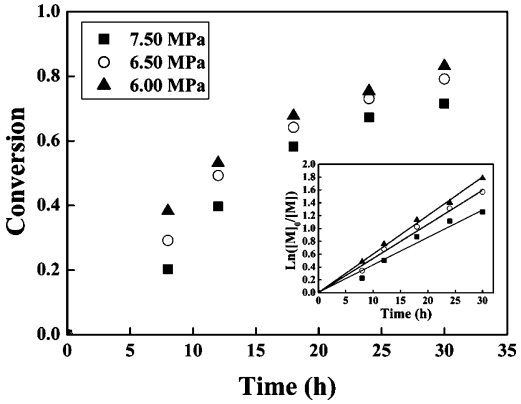

Figure 6. Conversion vs time and first-order plot (inset) for CO_2-induced RAFT miniemulsion polymerization of styrene initiated by VA-044 at 50 °C using Dowfax 8390 as surfactant at pressures of 6.00, 6.50, and 7.50 MPa with [St]/[BDT] = 400 and [BDT]/[VA-044] = 3 (33 wt % Dowfax 8390 rel St; 8 wt % HD rel St; 11.6 wt % St rel water).

(R_p) with increasing pressure. The inset shows that the first-order plots are close to linear. The change in R_p with pressure may be related to the change in particle size caused by the CO_2 pressure and/or some other property of the system that is a function of the CO_2 pressure. RAFT miniemulsion systems can exhibit retardation as a result of exit of the RAFT R-group (the radical expelled on fragmentation of the initial low molecular weight RAFT agent),[31] and the rate of exit would increase with decreasing particle size, in agreement with the trend seen in Figure 6. Moreover, if the system is zero−one[32] in nature, an intrinsic retardative effect can be caused by the RAFT agent relative to the corresponding bulk system.[33] The smaller the average particle size, the greater is the number fraction of particles of the particle size distribution that are zero−one, and thus the stronger is the retardation. This retardative effect has its origin in the fact that a certain fraction of radicals in the system are RAFT adduct (intermediate) radicals that are unable to propagate, thereby decreasing the number of propagating radicals per particle. The average numbers of propagating radicals per particle ($\bar{n}$) during the initial stage of the polymerizations were calculated from eq 1:

$$\bar{n} = \frac{N_A V_p}{k_p}\left\{\frac{d(\ln([St]_0/[St]))}{dt}\right\} \quad (1)$$

where N_A is Avogadro's number, V_p is the average particle volume (with $V_p = {}^1/_6\pi d_W{}^3$), k_p is the propagation rate coefficient (237 M^{-1} s^{-1} [34]), and $[St]_0$ and [St] are the initial and instantaneous styrene concentrations in the organic phase, respectively. Based on the initial slopes of the first-order plots, $\bar{n}$ = 1.6×10^{-2}, 1.0×10^{-2}, and 6.0×10^{-4} for 6.00, 6.50, and 7.50 MPa, respectively. The fact that $\bar{n} \leq 0.5$ is consistent with (but does not prove) that the systems are zero−one in nature.[32]

It has also been shown theoretically that variation in monomer concentration between particles may cause retardation in RAFT miniemulsion polymerization when the diameter is less than 100 nm.[33b,35] This effect would increase in magnitude with decreasing particle size. A decrease in particle size would lead to reduced termination rates due to compartmentalization (segregation of propagating radicals), thus causing an increase in R_p with decreasing particle size.[35,36] However, in the present system, such an effect is apparently outweighed by the retardative mechanisms outlined above. Finally, it can of course not be excluded that the CO_2 pressure may influence other properties of the system that in turn affect R_p.

It is well-known that pressurization of an organic solvent with CO_2 results in a CO_2-expanded solvent, i.e., an increase in volume. It thus needs to be considered whether the styrene droplets in the present work may swell with CO_2 because such an increase in volume would dilute the system and therefore influence the polymerization kinetics. The volumetric expansion of an organic solvent with CO_2 is primarily a function of the solubility of CO_2 in the solvent.[15e] In preliminary work, we observed that the volumetric expansion of pure styrene in CO_2 was around 50 vol % at the polymerization conditions employed. The associated solubility of CO_2 is ~50 mol %.[37] However, when styrene droplets are suspended in an aqueous

dx.doi.org/10.1021/ma202744f | Macromolecules 2012, 45, 1803−1810

solution, the CO_2 concentration attained in the droplets is governed by the solubility of CO_2 in the aqueous phase. Since it is well-known that CO_2 is poorly soluble in water, even at elevated pressure (<5 wt % at reaction conditions), the CO_2 concentration in the droplets is expected to be much lower than that observed in the simple styrene/CO_2 binary system. Thus, the volumetric expansion of the styrene droplets in the aqueous miniemulsion can safely be considered to be negligible. This was also confirmed visually, as no increase in the total level of liquid in the reactor was observed in the presence of CO_2 and over the course of the polymerization.

The molecular weight distributions (MWDs) were monomodal and shifted to higher molecular weights with increasing conversion in all cases (Figure 7). The values of M_n increased

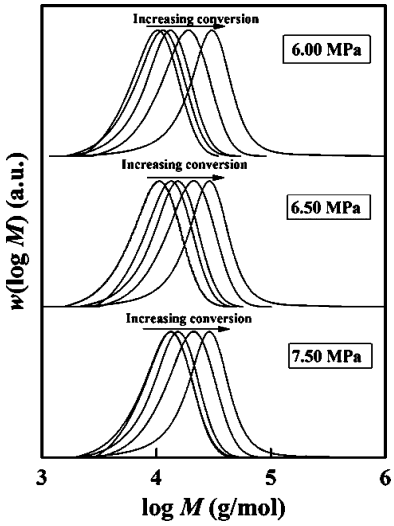

Figure 7. Molecular weight distributions (normalized to peak height) for CO_2-induced RAFT miniemulsion polymerization of styrene initiated by VA-044 at 50 °C using Dowfax 8390 as surfactant at pressures of 6.00, 6.50, and 7.50 MPa with [St]/[BDT] = 400 and [BDT]/[VA-044] = 3 (33 wt % Dowfax 8390 rel St; 8 wt % HD rel St; 11.6 wt % St rel water).

close to linearly with respect to conversion in excellent agreement with $M_{n,th}$ (theoretical M_n ($M_{n,th}$) = ([St]$_0$/[BDT]$_0$) × MW_{St} × α, where α is fractional St conversion) below 60% conversion with polydispersities (M_w/M_n) below 1.5 (Figure 8), indicating good control/livingness. Beyond 60% conversion, M_n deviates upward from $M_{n,th}$ and M_w/M_n gradually increases. Interestingly, there is no clear trend in the M_n and M_w/M_n data with CO_2 pressure—the CO_2 pressure has no discernible effect on M_n, and any effect on M_w/M_n is masked by scatter in the data. Additionally, it is noted that above 60% conversion the M_n vs conversion plots at all three pressures exhibited very similar upward deviations from $M_{n,th}$. These deviations in M_n are also accompanied by a gradual increase in M_w/M_n, and the onset of these phenomena corresponds to the conversion level at which the particle size started to increase with conversion (Figure 3) at all CO_2 pressures investigated. It can be speculated that the increase in particle size (presumably caused by coagulation or possibly Ostwald ripening) may have caused some loss in control, possibly as a result of alteration in the ratio [St]/[BDT] at the polymerization loci. It is also possible that the onset of diffusion control of the addition step of the chain transfer reaction (addition of propagating radical to RAFT end group) at

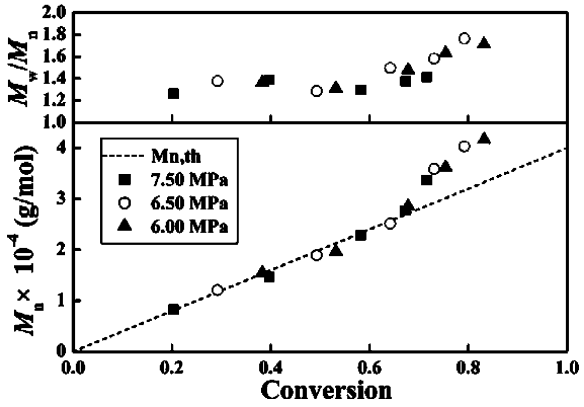

Figure 8. Number-average molecular weights (M_n) and polydispersities (M_w/M_n) vs conversion for CO_2-induced RAFT miniemulsion polymerization of styrene initiated by VA-044 at 50 °C using Dowfax 8390 as surfactant at pressures of 6.00, 6.50, and 7.50 MPa with [St]/[BDT] = 400 and [BDT]/[VA-044] = 3 (33 wt % Dowfax 8390 rel St; 8 wt % HD rel St; 11.6 wt % St rel water).

intermediate/high conversion may have resulted in an increase in M_w/M_n (although this would not affect M_n).[38]

RAFT Polymerization in Miniemulsion using Ultrasonication. In order to shed further light on the effect of CO_2 on RAFT polymerization in CO_2-induced miniemulsions, the polymerization was repeated using ultrasonication instead of CO_2 to induce the original miniemulsion (recipe A in Table 1). The miniemulsion was somewhat translucent before and after polymerization, and the particle size after polymerization (24 h; 96% conversion) was very small; d_n = 59 nm (d_w = 87 nm). However, the polymerization did not proceed with control/livingness, as evidenced by a very broad MWD (Figure 9; M_w/

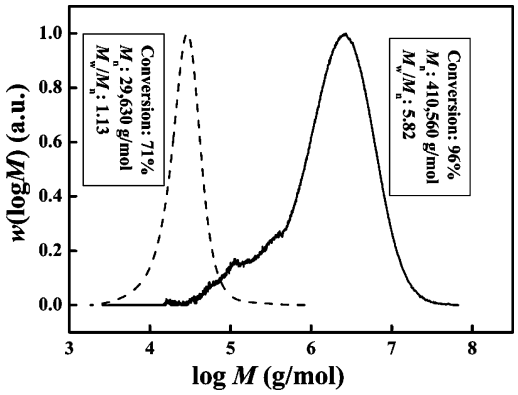

Figure 9. Molecular weight distributions from RAFT miniemulsion polymerization of styrene for 24 h at 50 °C using ultrasonication for two different Dowfax 8390 concentrations (w/w) rel to St phase: 33% (—), 10% (- - -).

M_n = 5.82) and M_n = 410 550 g/mol ($M_n \gg M_{n,th}$). The polymerization (with ultrasonication) was repeated with a lower surfactant content (10 wt % rel to St as opposed to 33 wt %; recipe B in Table 1), resulting in d_n = 132 nm (d_w = 143 nm) at 71% conversion (24 h), and this time the control/livingness was excellent as manifested by a very narrow MWD (Figure 9; M_w/M_n = 1.13) and $M_n \approx M_{n,th}$.

It is likely that the polymerization proceeded based on an emulsion polymerization mechanism at the higher surfactant concentration. The highly hydrophobic RAFT agent would be

dx.doi.org/10.1021/ma202744f | Macromolecules 2012, 45, 1803–1810

unable to diffuse sufficiently rapidly across the aqueous phase from droplets to particles, thus resulting in the RAFT mechanism breaking down. It is probable that at this high surfactant concentration the initial monomer droplets were not sufficiently small to adsorb enough surfactant, and micelles thus existed in the aqueous phase, causing micellar nucleation. The presence of CO_2 may have suppressed formation of micelles due to the gas antisolvent effect, thereby promoting surfactant adsorption on monomer droplets as discussed in relation to the CO_2-promoted solubility of oil in microemulsion.[39] At the lower surfactant concentration, micelles would not have been present, and therefore the polymerization proceeded as a miniemulsion polymerization and thus with good control/livingness.

CONCLUSIONS

A novel technique for generation of miniemulsions by use of low-pressure CO_2, thus circumventing traditional high-energy mixing methods, has been successfully applied to the synthesis of polymeric nanoparticles in aqueous miniemulsion by use of controlled/living radical polymerization. More specifically, RAFT polymerization of a styrene-in-water miniemulsion was conducted using the RAFT agent benzyldodecyl trithiocarbonate and the aqueous phase initiator VA-044 with the anionic surfactant Dowfax 8390 at 50 °C. Satisfactory control/livingness was obtained as evidenced by generally good agreement between M_n and $M_{n,th}$, and MWDs shifting to higher molecular weights with increasing conversion and remaining relatively narrow.

Over a certain CO_2 pressure range, near 7.5 MPa, a transparent miniemulsion is formed, indicating the formation of droplets smaller than for traditional miniemulsions. Importantly, an additional advantage of this system is that the particle size can be conveniently tuned via the CO_2 pressure without changing the recipe, with 6.00, 6.50, and 7.50 MPa, generating number-average particle diameters of 98, 89, and 48 nm, respectively (~70% conversion). The smallest particle size corresponded to the pressure range within which the emulsion was transparent. The present system has potential to significantly expand the general scope of miniemulsion polymerization, in particular with respect to size-tunable synthesis of polymeric nanoparticles, while still benefiting from the established advantages of miniemulsion polymerization associated with monomer droplet nucleation.

ASSOCIATED CONTENT

Supporting Information

Droplet/particle size distributions as functions of conversion as obtained by dynamic light scattering. This material is available free of charge via the Internet at http://pubs.acs.org.

AUTHOR INFORMATION

Corresponding Author

*Tel +61 2 9385 4331; Fax +61 2 9385 6250; e-mail p.zetterlund@unsw.edu.au.

Notes

The authors declare no competing financial interest.

ACKNOWLEDGMENTS

P.B.Z. is grateful for an ARC Future Fellowship, an ARC Discovery grant (DP1093343), and strategic funding from UNSW.

REFERENCES

(1) (a) Mason, T. G.; Wilking, J. N.; Meleson, K.; Chang, C. B.; Graves, S. M. *J. Phys.: Condens. Matter* **2006**, *18*, R635–R666. (b) Solans, C.; Izquierdo, P.; Nolla, J.; Azemar, N.; Garcia-Celma, M. J. *Curr. Opin. Colloid Interface Sci.* **2005**, *10*, 102–110. (c) Tadros, T.; Izquierdo, P.; Esquena, J.; Solans, C. *Adv. Colloid Interface Sci.* **2004**, *108–109*, 303–318.

(2) (a) Ugelstad, J.; El-Aasser, M. S.; Vanderhoff, J. W. *J. Polym. Sci., Polym. Lett. Ed.* **1973**, *11*, 503–513. (b) Schork, F. J.; Luo, Y.; Smulders, W.; Russum, J. P.; Butté, A.; Fontenot, K. Miniemulsion Polymerization. *Polymer Particles* **2005**, 129–255.

(3) (a) Asua, J. M. *Prog. Polym. Sci.* **2002**, *27*, 1283. (b) Landfester, K. *Macromol. Rapid Commun.* **2001**, *22*, 896.

(4) (a) Landfester, K. *Angew. Chem., Int. Ed.* **2009**, *48*, 4488–4507. (b) van Berkel, K. Y.; Hawker, C. J. *J. Polym. Sci., Part A: Polym. Chem.* **2010**, *48*, 1594–1606. (c) Faucheu, J.; Gauthier, C.; Chazeau, L.; Cavaillé, J.-Y.; Mellon, V.; Lami, E. B. *Polymer* **2010**, *51*, 6–17.

(5) (a) de Brouwer, H.; Tsavalas, J. G.; Schork, F. J.; Monteiro, M. J. *Macromolecules* **2000**, *33*, 9239–9246. (b) Saka, Y.; Zetterlund, P. B.; Okubo, M. *Polymer* **2007**, *48*, 1229–1236. (c) Zetterlund, P. B.; Nakamura, T.; Okubo, M. *Macromolecules* **2007**, *40*, 8663–8672. (d) Simms, R. W.; Cunningham, M. F. *Macromolecules* **2007**, *40*, 860–866. (e) Cunningham, M. F. *Prog. Polym. Sci.* **2008**, *33*, 365–398. (f) Zetterlund, P. B.; Kagawa, Y.; Okubo, M. *Chem. Rev.* **2008**, *108*, 3747–3794. (g) Zetterlund, P. B.; Saka, Y.; Okubo, M. *Macromol. Chem. Phys.* **2009**, *210*, 140–149. (h) Oh, J. K.; Perineau, F.; Charleux, B.; Matyjaszewski, K. *J. Polym. Sci., Part A: Polym. Chem.* **2009**, *47*, 1771–1781. (i) Guo, Y.; Liu, J. Q.; Zetterlund, P. B. *Macromolecules* **2010**, *43*, 5914–5916. (j) Li, W. W.; Yoon, J. A.; Matyjaszewski, K. *J. Am. Chem. Soc.* **2010**, *132*, 7823–7825. (k) Oliveira, M. A. M.; Boyer, C.; Nele, M.; Pinto, J. C.; Zetterlund, P. B.; Davis, T. P. *Macromolecules* **2011**, *44*, 7167–7175. (l) Averick, S. E.; Magenau, A. J. D.; Simakova, A.; Woodman, B. F.; Seong, A.; Mehl, R. A.; Matyjaszewski, K. *Polym. Chem.* **2011**, *2*, 1476–1478.

(6) (a) Shinoda, K.; Saito, H. *J. Colloid Interface Sci.* **1969**, *30*, 258–263. (b) Morales, D.; Gutierrez, J. M.; Garcia-Celma, M. J.; Solans, Y. C. *Langmuir* **2003**, *19*, 7196–7200. (c) Fernandez, P.; André, V.; Rieger, J.; Kühnle, A. *Colloids Surf., A* **2004**, *251*, 53–58.

(7) (a) Forgiarini, A.; Esquena, J.; Gutiérrez, C.; Solans, C. *Langmuir* **2001**, *17*, 2076–2083. (b) Sajjadi, S. *Langmuir* **2006**, *22*, 5597–5603. (c) Sole, I.; Maestro, A.; Gonzalez, C.; Solans, C.; Gutierrez, J. M. *Langmuir* **2006**, *22*, 8326–8332. (d) Wang, L.; Mutch, K. J.; Eastoe, J.; Heenan, R. K.; Dong, J. *Langmuir* **2008**, *24*, 6092–6099.

(8) Salager, J. L. In *Encyclopedia of Emulsion Technology*; Marcel Dekker: New York, 1988; Vol. 3.

(9) (a) Nishimi, T.; Miller, C. A. *Langmuir* **2000**, *16*, 9233–9241. (b) Lamaallam, S.; Bataller, H.; Dicharry, C.; Lachaise, J. *Colloids Surf., A* **2005**, *270–271*, 44–51.

(10) (a) Spernath, L.; Magdassi, S. *Polym. Adv. Technol.* **2007**, *18*, 705–711. (b) Spernath, L.; Regev, O.; Levi-Kalisman, Y.; Magdassi, S. *Colloids Surf., A* **2009**, *332*, 19–25.

(11) Sadtler, V.; Rondon-Gonzalez, M.; Acrement, A.; Choplin, L.; Marie, E. *Macromol. Rapid Commun.* **2010**, *31*, 998–1002.

(12) Galindo-Alvarez, J.; Boyd, D.; Marchal, P.; Tribet, C.; Perrin, P.; Marie-Begue, E.; Durand, A.; Sadtler, V. *Colloids Surf., A* **2011**, *374*, 134–141.

(13) Cheng, S.; Guo, Y.; Zetterlund, P. B. *Macromolecules* **2010**, *43*, 7905–7907.

(14) (a) Prokopov, N. I.; Gritskova, I. A. *Russ. Chem. Rev.* **2001**, *70*, 791–800. (b) Parker, D. K.; Feher, F. J.; Mahadevan, V. Controlled polymerization. US Patent 6992156 Jan 31, 2006. (c) Guo, Y.; Liu, J.; Zetterlund, P. B. *Macromolecules* **2010**, *43*, 5914–5916. (d) El-Jaby, U.; Cunningham, M.; McKenna, T. F. L. *Macromol. Rapid Commun.* **2010**, *31*, 558–562. (e) Guo, Y.; Zetterlund, P. B. *Polymer* **2011**, *52*, 4199–4207.

(15) (a) Eckert, C. A.; Knutson, B. L.; Debenedetti, P. G. *Nature* **1996**, *383*, 313–318. (b) Jacobson, G. B.; Lee, C. T.; Johnston, K. P.; Tumas, W. *J. Am. Chem. Soc.* **1999**, *121*, 11902–11903. (c) Kendall, J. L.; Canelas, D. A.; Young, J. L.; DeSimone, J. M. *Chem. Rev.* **1999**, *99*,

543−563. (d) McHale, R.; Aldabbagh, F.; Zetterlund, P. B.; Okubo, M. *Macromol. Rapid Commun.* **2006**, *27*, 1465−1471. (e) Jessop, P. G.; Subramaniam, B. *Chem. Rev.* **2007**, *107*, 2666−2694. (f) Zetterlund, P. B.; Aldabbagh, F.; Okubo, M. *J. Polym. Sci., Part A: Polym. Chem.* **2009**, *47*, 3711−3728. (g) Pu, D. W.; Lucien, F. P.; Zetterlund, P. B. *J. Polym. Sci., Part A: Polym. Chem.* **2011**, *49*, 4307−4311.

(16) Zhang, J.; Han, B. *J. Supercrit. Fluids* **2009**, *47*, 531−536.

(17) Feng, X.; Zhang, J.; Chen, J.; Han, B.; Shen, D. *Chem.—Eur. J.* **2006**, *12*, 2087−2093.

(18) (a) Hoefling, T. A.; Enick, R. M.; Beckman, E. J. *J. Phys. Chem.* **1991**, *95*, 7127−7129. (b) Beckman, E. J. *Science* **1996**, *271*, 613. (c) Eastoe, J.; Gold, S.; Rogers, S.; Wyatt, P.; Steytler, D. C.; Gurgel, A.; Heenan, R. K.; Fan, X.; Beckman, E. J.; Enick, R. M. *Angew. Chem., Int. Ed.* **2006**, *118*, 3757−3759. (d) Eastoe, J.; Gold, S.; Rogers, S.; Wyatt, P.; Steytler, D. C.; Gurgel, A.; Heenan, R. K.; Fan, X.; Beckman, E. J.; Enick, R. M. *Angew. Chem., Int. Ed.* **2006**, *45*, 3675−3677.

(19) (a) Zhang, J.; Han, B.; Li, W.; Zhao, Y.; Hou, M. *Angew. Chem., Int. Ed.* **2008**, *47*, 10119−10123. (b) Zhang, J.; Han, B.; Zhao, Y.; Li, W.; Liu, Y. *Phys. Chem. Chem. Phys.* **2011**, *13*, 6065−6070. (c) Zhao, Y.; Zhang, J.; Wang, Q.; Li, J.; Han, B. *Phys. Chem. Chem. Phys.* **2011**, *13*, 684−689.

(20) Zhang, J.; Han, B.; Zhang, C.; Li, W.; Feng, X. *Angew. Chem., Int. Ed.* **2008**, *47*, 3012−3015.

(21) Zhao, Y.; Zhang, J.; Li, W.; Zhang, C.; Han, B. *Chem. Commun.* **2009**, 2365−2367.

(22) Braunecker, W. A.; Matyjaszewski, K. *Prog. Polym. Sci.* **2007**, *32*, 93−146.

(23) (a) Chiefari, J.; Chong, Y. K.; Ercole, F.; Krstina, J.; Jeffery, J.; Le, T. P. T.; Mayadunne, R. T. A.; Meijs, G. F.; Moad, C. L.; Moad, G.; Rizzardo, E.; Thang, S. H. *Macromolecules* **1998**, *31*, 5559−5562. (b) Moad, G.; Rizzardo, E.; Thang, S. H. *Aust. J. Chem.* **2009**, *62*, 1402−1472.

(24) (a) Luo, Y.; Tsavalas, J.; Schork, F. J. *Macromolecules* **2001**, *34*, 5501−5507. (b) Yang, L.; Luo, Y. W.; Li, B. G. *J. Polym. Sci., Part A: Polym. Chem.* **2006**, *44*, 2293−2306. (c) Qi, G.; Schork, F. J. *Langmuir* **2006**, *22*, 9075−9078.

(25) Ting, S. R. S.; Min, E. H.; Zetterlund, P. B. *Aust. J. Chem.* **2011**, *64*, 1033−1040.

(26) Ting, S. R. S.; Gregory, A. M.; Stenzel, M. H. *Biomacromolecules* **2009**, *10*, 342−352.

(27) Pu, D. W.; Lucien, F. P.; Zetterlund, P. B. *J. Polym. Sci., Part A: Polym. Chem.* **2010**, *48*, 5636−5641.

(28) (a) Rajasingam, R.; Tran, T.; Lucien, F. P. *J. Supercrit. Fluids* **2005**, *33*, 69−76. (b) Hallett, J. P.; Ford, J. W.; Jones, R. S.; Pollet, P.; Thomas, C. A.; Liotta, C. L.; Eckert, C. A. *Ind. Eng. Chem. Res.* **2008**, *47*, 2585−2589.

(29) Mohamed, A.; Trickett, K.; Chin, S. Y.; Cummings, S.; Sagisaka, M.; Hudson, L.; Nave, S.; Dyer, R.; Rogers, S. E.; Heenan, R. K.; Eastoe, J. *Langmuir* **2010**, *26*, 13861−13866.

(30) Chang, H. C.; Lin, Y. Y.; Chern, C. S.; Lin, S. Y. *Langmuir* **1998**, *14*, 6632−6638.

(31) (a) Tsavalas, J. G.; Schork, F. J.; de Brouwer, H.; Monteiro, M. J. *Macromolecules* **2001**, *34*, 3938−3946. (b) Prescott, S. W.; Ballard, M. J.; Rizzardo, E.; Gilbert, R. G. *Macromol. Theory Simul.* **2006**, *15*, 70−86. (c) Lansalot, M.; Davis, T. P.; Heuts, J. P. A. *Macromolecules* **2002**, *35*, 7582−7591. (d) Butte, A.; Storti, G.; Morbidelli, M. *Macromolecules* **2001**, *34*, 5885−5896.

(32) Gilbert, R. G. *Emulsion Polymerization: A Mechanistic Approach*; Academic Press: London, 1995.

(33) (a) Tobita, H. *Macromol. Theory Simul.* **2009**, *18*, 120−126. (b) Tobita, H. *Macromol. Theory Simul.* **2011**, *20*, 709−720. (c) Luo, Y.; Wang, R.; Yang, L.; Yu, B.; Li, B.; Zhu, S. *Macromolecules* **2006**, *39*, 1328−1337.

(34) Buback, M.; Gilbert, R. G.; Hutchinson, R. A.; Klumperman, B.; Kuchta, F. D.; Manders, B. G.; ÒDriscoll, K. F.; Russell, G. T.; Schweer, J. *Macromol. Chem. Phys.* **1995**, *196*, 3267−3280.

(35) Tobita, H. *Macromol. Theory Simul.* **2009**, *18*, 108−119.

(36) Tobita, H.; Yanase, F. *Macromol. Theory Simul.* **2007**, *16*, 476−488.

(37) Akgun, M.; Emel, D.; Baran, N.; Akgun, N. A.; Deniz, S.; Dincer, S. *J. Supercrit. Fluids* **2004**, *31*, 27−32.

(38) Peklak, A. D.; Butte, A. *Macromol. Theory Simul.* **2006**, *15*, 546−562.

(39) (a) Zhang, R.; Liu, J.; He, J.; Han, B.; Wu, W.; Jiang, T.; Liu, Z.; Du, J. *Chem.—Eur. J.* **2003**, *9*, 2167−2172. (b) Li, D.; Han, B.; Liu, Z.; Liu, J.; Zhang, X.; Wang, S.; Zhang, X.; Wang, J.; Dong, B. *Macromolecules* **2001**, *34*, 2195−2201.

Macromolecules

Article

pubs.acs.org/Macromolecules

Combined Techniques for the Characterization of Polyfluorene Copolymers and Correlation with their Optical Properties.

Filippo Samperi,*[,†] Salvatore Battiato,[†] Concetto Puglisi,[†] Umberto Giovanella,[‡] Raniero Mendichi,[‡] and Silvia Destri[‡]

[†]Istituto di Chimica e Tecnologia dei Polimeri (ICTP) UOS Catania, CNR, Via Gaifami 18, 95126 Catania Italy

[‡]Istituto per lo Studio delle Macromolecole, CNR, Via Bassini 15, 20133 Milano, Italy

Supporting Information

ABSTRACT: New red- and green-emitting copolymers, hereafter *core*-copolymers, bearing a 4,7-bis(thiophen-2-yl)-benzothiadiazole and a benzothiadiazole residue respectively as bridging *core* between two identical polymeric arms were synthesized by Suzuki coupling reaction of the dibromine derivative of such chromophores and essentially borolane-ended alternating copolymers [namely **P(TPAF)**] of triphenylammine disubstituted fluorene and dialkylsubstituted fluorene. All polymer samples were characterized by ^{1}H NMR and in particular by MALDI−TOF MS. MALDI mass spectra allow the identification of many end groups of the initial blue-emitting macromers and therefore of the side reactions occurring during Suzuki polycondensation. The average molar masses were determined by two different SEC apparatus, one calibrated with conventional polystyrene narrow standards and the other with an absolute calibration curve built up by SEC/MALDI−TOF MS analysis of selected SEC fractions of polydisperse red and green *core*-copolymers. MALDI mass spectra of these fractions give reliable information on their composition, which combined with their integrated area calculated from the corresponding normalized SEC curves, enable the estimation, for the first time, of the percentage of macromolecules containing the dyes composing the neat *core*-copolymers. Optical characterization, performed by UV−visible absorption and photoluminescence measurements, of the same SEC fractions gives results in agreement with the different compositions determined by their MALDI mass spectra.

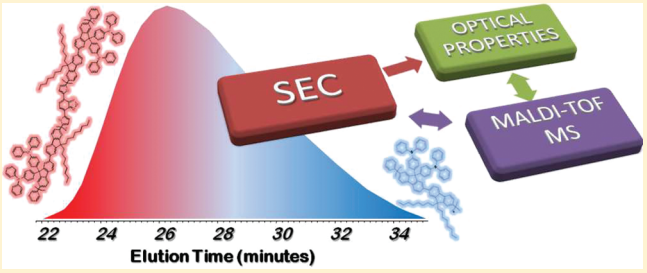

1. INTRODUCTION

Conjugated aromatic polymers have been largely used in the last two decades for preparing active layers in optoelectronic devices as organic light-emitting diodes (OLEDs),[1] bulk heterojunction photovoltaic cells[2] and electronic ones like organic field-effect transistors.[3] In particular, in the fabrication of the former group of devices, alternating copolymers are employed and organometallic polycondensations are considered a useful and reliable synthesis method. In the preparation of polymers containing fluorene, benzothiadiazole, and thiophene residues, the Suzuki coupling plays a very important role starting from diboronic acid or diboronic acid ester as 4,4,5,5-tetrametyl-1,3,2-dioxoborolane or 1,3-propane-1,3,2-dioxoborolane of a monomer and the dibromine or diiodide derivatives of the comonomer.[4−23] For introducing at the same time different emitting dyes in a polymeric skeleton or both electron donor and acceptor side groups more than one dihalide derivative has to be used in a one step synthesis. This strategy, experienced by Chuang et al.[4] for preparing active layers suitable for white-emitting OLEDs (WOLEDs), leads however to a not defined mixture of chemically different polymers due to the different reactivity of dihalide species and also to the intrinsic nature of the Suzuki coupling. Alternatively, we tried another approach to obtain WOLEDs[5] enabling us to determine more precisely the amount of blue, green, and red emitting polymeric species constituting the blend for the device active layer. Two molecular dyes, benzothiadiazole (**Btz**) as the green emitter and 4,7-bis(thiophen-2-yl)benzothiadiazole (**ThBtzTh**) as the red emitter, were individually inserted as bridging *core* between two identical polymeric blue emitting arms. The polymeric arms, as well as the pure blue emitting compound in the blend, consist of a fluorene-based alternating copolymer **P(TPAF)** made by a triphenylamine disubstituted fluorene unit (**TPA**) and a dialkyl substituted fluorene (**F**) one. We have already shown that such an insertion of TPA moieties resulted in reduced interchain interactions, an enhanced hole injection, and increased morphological stability with respect to conventional polyfluorenes (PFs).[6] Moreover, the presence of bulkier side groups contributed to tune resonant energy transfer (RET) process from donor toward the acceptor entities of the polymeric chains,[7] otherwise too efficient to observe the contemporary emission from all the chromophores necessary for the white emission. The blue-emitting copolymer was synthesized by Suzuki polycondensation, while the green

Received: October 13, 2011
Revised: January 19, 2012
Published: February 9, 2012

and red emitting *core*-copolymers were prepared via the two following steps. In the former, 9,9-bis(4-diphenylaminophenyl)-2,7-dibromofluorene and 9,9-dioctylfluorene-2,7-diboronic acid bis(1,3-propanediol) ester were copolymerized using $(Ph_3P)_4Pd$ as the catalyst capping the growing chains with phenylboronic acid pinacol ester. Two preformed macromers successively reacted with the dibromide derivatives of green and red dyes; 7-dibromo-benzothiadiazole (**Br_2Btz**) and 4,7-bis(5-bromothiophen-2-yl)benzothiadiazole (**Br_2(ThBtzTh)**) respectively. Base, catalyst and solvent of the former Suzuki reaction were not replaced. However, also following this approach the precise determination of the relative amounts of the blue, green, and red polymers in the active blend was hard to reach. Considering the mechanistic aspects of the Suzuki coupling described in literature for other polymers based on thiophene and phenylene residues[8,9] or on fluorene residue[10] and the related side reactions using $(Ph_3P)_4Pd$ catalyst,[11,12] we decided to investigate the composition of so-called green and red *core*-copolymers. In this paper we aim to detect the potential presence of blue-emitting **P(TPAF)**, determine its amount and correlate the optical properties of the *core*-copolymers to both the percentages of the dye actually inserted and to its position along the polymeric backbone. We have adopted different reaction protocols to carried out the final cross coupling reaction between each dye and the preformed macromers giving rise to materials with different properties. The product of each reaction has been first investigated by means of ^{1}H NMR and size exclusion chromatography (SEC) analyses, and then by matrix assisted laser desorption/ionization time of flight mass spectrometry (MALDI−TOF MS), to obtain reliable knowledge of the structure and the chemical composition of the final products, as a function of the reaction parameters [**P(TPAF)** characteristics and reagent molar ratio]. MALDI−TOF MS should allow the identification of each macromolecular component,[24−31] its various end groups, and therefore should afford a deeper insight in both the Suzuki polycondensation reaction mechanism and the limiting side reactions. This technique has already been successfully applied to the characterization of several conjugated aromatic polymers such as polyfluorenes (PF)s and polythiophenes (PT)s.[8−10,13−15,31,32] Moreover, advanced information on the chemical composition of the red and green *core*-copolymers have been obtained by means of the powerful *off-line* SEC/MALDI−TOF MS coupling method.[24,25,29] The characterization of several homopolymers[24−28] and also of copolymers such as copolyesters,[24,25] and alternating thiophene-phenylene copolymers,[8] has already taken advantage of this tool. In the present paper, it has been applied for the first time to the characterization of fluorene based copolymers having relative higher molar mass. The polydisperse polymers have been fractionated into several fractions of narrow molar mass dispersity (D < 1.05) which have been analyzed by MALDI−TOF MS. Thus, absolute average molar masses (MM, M_w and M_n) have been measured for each fraction and used to calibrate the SEC curves of the polydisperse polymer (self-calibration). Combining SEC and MALDI MS data of each SEC fraction, we propose an equation that permits, for the first time on the base to the best of our knowledge, the calculation of the weight percentage of the molecular species bearing a dye unit composing the crude *core*-copolymers. Optical characterization of the crude copolymers and SEC fractions has been carried out to correlate the optical properties with the chemical composition. In fact, from changes in the absorption and photoluminescence (PL) spectra, details about both the presence of the red and green emitting dyes and their position within the polymer chain (inner or outer) are obtained, and totally agree with mass spectrometry data. Therefore, the *off-line* SEC/MALDI−TOF MS coupling tool here presented can be extended to any conjugated copolymer obtained by organometal catalyzed polycondensation even with MM higher than 20.000 g/mol.

2. EXPERIMENTAL SECTION

2.1. Materials. All reagents, unless otherwise specified, were obtained from Aldrich or Acros and used as received. All solvents used for the chemical reactions were dried by standard procedures. All manipulations involving air-sensitive reagents were performed under an atmosphere of dry nitrogen. Tetrakis(triphenylphosphine)-palladium ($(Ph_3P)_4Pd$) was stored in inert atmosphere for few days only. **Br_2(ThBtzTh)** was prepared by bromination of **ThBtzTh** obtained by Stille coupling of **Br_2Btz** and tributyl(2-thienyl)stannane.

2.2. Syntheses. *2.2.1. Synthesis of P(TPAF)−Borolane Macromers.* **P(TPAF)** macromers were synthesized as reported elsewhere[16] starting from homemade 9,9-bis(4-diphenylaminophenyl)-2,7-dibromofluorene (**1**) and 9,9-dioctylfluorene-2,7-diboronic acid bis(1,3-propanediol) (**2**), as depicted in Scheme 1 (route a). In a typical procedure, 0.8 g (0.98 mmol) of **1** and 568 mg (0.98 mmol) of **2** were dissolved in 14 mL of anhydrous toluene. The catalyst $(Ph_3P)_4Pd$ (11.4 mg, 9.86 μmol, 1%$_{eq}$), 2.12 mL of a K_2CO_3 2 M aqueous solution, and Aliquat (0.987 mmol) were added to the solution. The reaction was stirred at 90 °C for 6 h; then the brominated end groups were capped by adding 201 mg (0.98 mmol) of phenylboronic acid pinacol ester (**3**) and stirred for 18 h at 90 °C. A black precipitate stuck to the vessel walls was formed. The reaction mixture was diluted with 20 mL of toluene and passed through a Celite pad, then the copolymer was precipitated from methanol (100 mL). The precipitate was collected and extracted with acetone using a Soxhlet apparatus to give 700 mg (59% yield) of tailored macromer **P(TPAF)−Borolane** terminated [referred as **P(TPAF)1** in Scheme 1]. In a different run the reaction duration time was increased up to 10 h and 604 mg (2,96 mmol) of quencher **3** (3:1 molar ratio with respect to each comonomer) were added to the mixture which was stirred for 15 h at 90 °C obtaining a polymer (referred thereafter as **P(TPAF)2**) with a 63% of yield.

2.2.2. Synthesis of Green and Red core-Copolymers. Green and red *core*-copolymers were synthesized by means of Suzuki coupling reaction of a macromer **P(TPAF)−Borolane** terminated with **Br_2Btz** and with **Br_2(ThBtzTh)**, respectively, as highlighted in Scheme 1 (routes b and c).

In a typical procedure, 150 mg of macromer **P(TPAF)2** were dissolved in toluene and (0.32 mg, 0.27 μmol) of $Pd(Ph_3P)_4$ from a previously prepared toluene solution together with 7.5 mL of [2M] K_2CO_3 aqueous solution and a drop of Aliquat were added. A toluene solution of **Br_2Btz** (3.67 mg, 12.5 μmol in 4.0 mL) or **Br_2(ThBtzTh)** (5.73 mg, 12.5 μmol in 4 mL) to get green and red *core*-copolymers respectively, was dropped in the reaction medium at 90 °C under stirring. The mixture was further stirred for 15 h, then phenylbromide (373 mg, 2.38 mmol) was added as a quencher of unreacted **P(TPAF)2** and the stirring and heating were prolonged for 24 h. The solution was filtered through a Celite column and the polymer was precipitated in methanol. Extraction with acetone was used to remove any residue of dyes obtaining 50 mg of green [**P(TPAF)2-Btz** sample] and 62 mg of red [**P(TPAF)2-ThBtzTh** sample] *core*-copolymers, respectively.

The macromer/dibromide ratio, and the dropping modality of dibromide solutions were changed in the different runs and will be reported in the Results and Discussion, and summarized in Table 1.

2.3. Measurements. *2.3.1. NMR Spectroscopy.* ^{1}H NMR spectra were recorded at 25 °C using a Bruker ARX400 and Bruker Advance 400 MHz spectrometers. Toluene-d_8 and

Scheme 1. Synthesis of Macromers and *core*-Copolymers

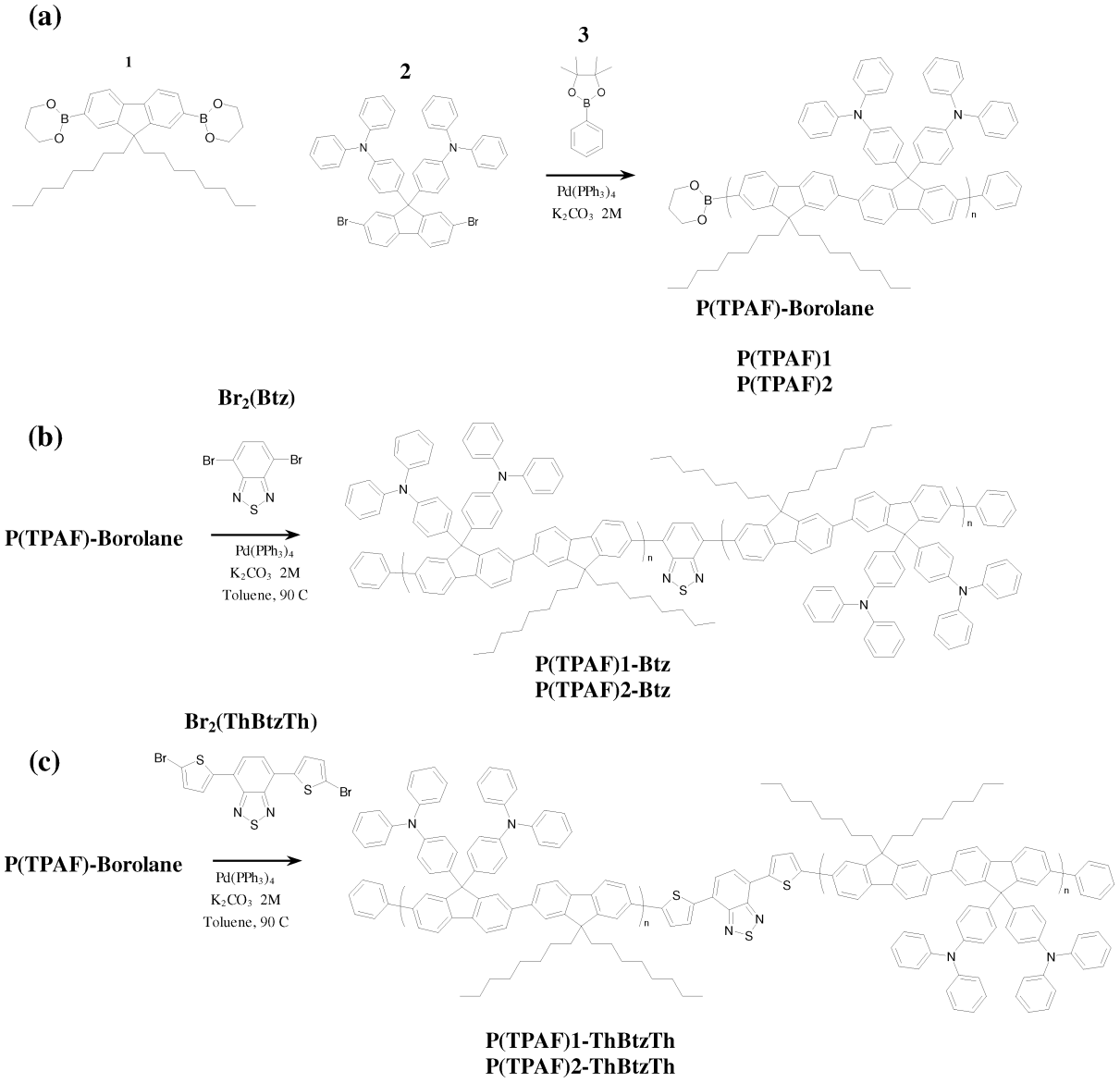

Table 1. Experimental Parameters, Average Molar Masses (M_n and M_w), and Polydispersity ($D = M_w/M_n$) of the P(TPAF)s Studied

				SEC[b]			SEC–MALDI[c]		
samples	P(TPAF)/dye–Br_2 (equiv/equiv)	dye–Br_2 catalyst (%)	dye insertion[a] (%)	M_n (g/mol)	M_w (g/mol)	D (g/mol)	M_n (g/mol)	M_w (g/mol)	D (g/mol)
P(TPAF)1	–			3400	5250	1.55	3640	5660	1.56
P(TPAF)1-Btz	1:1	8	32	4160	7350	1.77	4370	7740	1.77
P(TPAF)1-ThBtzTh	1:1	8	24	3900	6500	1.67	3730	6550	1.76
P(TPAF)2	–			6000	11 600	1.93	5230	11860	2.27
P(TPAF)2-Btz	5:1	4	34	6900	13 800	2.00	7050	13950	1.98
P(TPAF)2-ThBtzTh	5:1	4	45	8600	19 600	2.28	8420	20900	2.48

[a]Dye insertion means the percentage of P(TPAF) chains bearing the dye units, the values are calculated with a variance of ±0.2. [b]Calculated by SEC system calibrated toward polystyrene standards. [c]Calculated by *off-line* SEC–MALDI–TOF MS coupling method.

sym-tetrachloroethane-d_2 ($C_2D_2Cl_4$) were used as solvents. ^{1}H NMR spectra of the SEC fractions were recorded by a Bruker A-CF 200 spectrometer at 25 °C, using $C_2D_2Cl_4$ as locking agent in a microprobe NMR tube. The polymer fractions, obtained after evaporation of tetrahydrofun (THF) used as eluent in the SEC runs, were dissolved in toluene-d_8.

^{31}P NMR spectra were recorded in solution of $C_2D_2Cl_4$ at 25 °C by a Varian-Inova instrument operating at 200 MHz, using H_3PO_4 (85%) as external reference. All ^{31}P NMR spectra are decoupled from the proton, and the chemical shifts are reported in ppm with respect to the used reference. The data were enhanced with 1D Win-NMR software by applying the Lorentz–Gauss function, using appropriate

dx.doi.org/10.1021/ma202301j | *Macromolecules* 2012, 45, 1811–1824

line broadening and Gaussian broadening parameters in order to improve the peaks resolutions.

2.3.2. Size Exclusion Chromatography (SEC). In a first step, the whole molar mass dispersity (MMD), relative averages (M_n, M_w, M_z) and polydispersity index ($D = M_w/M_n$) of all polymers were determined by a conventional size exclusion chromatography (SEC)[33] system calibrated toward polystyrene (PS) standards, using THF as mobile phase, 0.8 mL/min of flow rate and 35 °C of temperature. In a conventional SEC system the molar mass of polymers is not absolute but relative to PS narrow MMD standards. The conventional chromatographic system consisted of an integrated Alliance 2695 chromatographic system (degasser, pump and injector) from Waters (Milford, MA) and a 2414 differential refractometer (DRI) used as concentration detector. The column set was composed of two PLgel Mixed C columns (5 μm of particle size) from Polymer Laboratories (Shropshire, U.K.).

In a second step, polymers were accurately fractionated and the obtained fractions were characterized off-line by means of the absolute MALDI−TOF MS method. The SEC fractionation of green and red *core*-copolymers was carried out by means of a Waters 515 apparatus, equipped with four Ultrastyragel HR columns (ID = 7.8 mm, L = 300 mm, 5 μm of particle size) in the order HR-4, HR-3, HR-2, and HR-1 connected in series, a Waters R401 DRI detector, THF as mobile phase, 1 mL/min of flow rate. The SEC traces were recorded and processed using a Clarity-GPC software provided by DataApex. In a typical fractionation, 100 μL of a polymer solution in THF (≈5 mg/mL of concentration) was injected and fractions were taken every 25 s (0.25 mL) using a Waters fraction collector positioned after the DRI detector. For each sample 40−50 fractions were collected. The solvent of SEC fractions was reduced at 30−50 μL under nitrogen flow, and the absolute molar masses of selected fractions were determined by MALDI−TOF MS. Furthermore, some fractions were afterward reinjected in the SEC apparatus as standards for absolute molar mass calibration of P(TPAF)-based polymers.

2.3.3. MALDI−TOF Mass Spectrometry. The MALDI−TOF mass spectra were recorded in reflector or linear delayed extraction mode, using a Voyager-DE STR instrument (Perseptive Biosystem) mass spectrometer, equipped with a nitrogen laser (λ = 337 nm, pulse width = 3 ns), working in a positive ion mode. The accelerating voltage was 20 KV, grid voltage and delay time (delayed extraction, time lag), were optimized for each sample to achieve the higher mass resolution ($M/\Delta M$). Laser irradiance was maintained slightly above threshold. *trans*-2-[3-(4-*tert*-Butylphenyl)-2-methyl-2-propenylidene]malononitrile (acronym: DCTB) 0.1 M in THF and 1,8-dihydroxy-9,10-dihydroanthracen-9-one (dithranol) 0.1 M in THF were used as matrices. Samples of P(TPAF) based polymers used for the MALDI analyses were prepared as follows: 10 μL of polymer solution (5 mg/mL in THF), were mixed with 10 or 30 μL of a matrix solution (0.1 M in THF). Then 1 μL of each analyte/matrix mixture was spotted on the MALDI sample holder and slowly dried to allow analyte/matrix cocrystallization. The best spectra were recorded using DCTB, obtaining a mass resolution of about 800−1000 in linear mode and 3000−5000 in reflector mode, in the mass range from m/z 1000 to m/z 4000. For the analysis of polymer SEC fractions 1 μL of each selected concentrated SEC solution was mixed with 1 or 3 μL of the matrix solution (DCTB). Then, the same procedure used for the MALDI analyses of the polydisperse P(TPAF) based polymers was followed. The MALDI spectra of the SEC fractions recorded in linear mode were processed by the PGRAM program provided by Perseptive Biosystem, which uses mass-spectral intensities to compute the quantities known as the most-probable molecular weight (M_p), number-average molar mass, weight-average molar mass, and polydispersity index. The M_w values were used to build an absolute molar mass calibration of SEC traces of all polymers.

2.3.4. Optical Measurements. UV−vis absorption spectra of toluene solutions were measured with a Lambda 900 Perkin-Elmer spectrometer. Continuous wave photoluminescence (PL) spectra were recorded using a SPEX 270 M monochromator equipped with a N_2-cooled CCD detector, by exciting with a monochromated xenon lamp.

3. RESULTS AND DISCUSSION

3.1. Synthesis. Polymerization via Suzuki coupling is commonly considered a step growth process when a AA monomer reacts with a BB one resulting in an alternating copolymer. Like in others step growth polymerizations the best care must be taken about stoichiometry balance to obtain high molecular weight. Consequently, the monomers purity has to be as high as possible and any oxygen contamination should be avoided. In literature there are examples reporting procedures for small molecules coupling where these constrains are not respected and Suzuki coupling is even carried out in aerobic condition using air stable catalyst.[22] However, if applied to polycondensation, the molar mass for the resulting polymer was not as high as that obtained under anaerobic conditions due to limiting oxidation of boronic derivatives.[10,23] In the present work the Suzuki coupling approach has been applied to synthesize two types of conjugated polymers (referred here as *core*-copolymer) bearing a BTz unit or a ThBTzTh unit, as green or red chromophore, respectively. In both *core*-copolymer synthesis the former step is a step growth process while the latter is just a coupling of two equivalents of a purified macromer **P(TPAF)−Borolane** [**P(TPAF)1** and **P(TPAF)2** samples in Table 1] with the dibromide derivative of the dyes as shown in Schemes 1b and 1c for **Br_2Btz** and **Br_2(ThBtzTh)**, respectively.

The reaction conditions of these steps were modified in the different runs (see Table 1) by changing: (i) the molar ratio between *core* dye and macromer **P(TPAF)**; (ii) the addition procedure of the dibromide derivative of each dye (either by slowly dropping during the first 8 h of reaction, for synthesis of **P(TPAF)1-Btz** and **P(TPAF)1-ThBtzTh**, or by slowly dropping in three different times during the reaction going on, in the synthesis of **P(TPAF)2-Btz** and **P(TPAF)2-ThBtzTh**).

As already reported,[5] the insertion of Btz and ThBtzTh dyes in the polymer chains was proved by both optical measurements and ^{1}HNMR spectroscopy. Solution UV−vis absorption spectra are dominated by P(TPAF) absorption peaked at 388 nm, while the photoluminescence spectra of diluted solutions [10^{-5} M] clearly showed a green emission with a maximum at 530 nm for the material containing Btz or a red emission at 638 nm for that one with ThBtzTh cromophore. At the end of the step growth polymerization different species have been formed as already shown for coupling of other monomers[8−10,13] using ^{1}H NMR spectroscopy coupled with MALDI-TOF MS characterization.[8−10,13−15,17,18,34] To guaranty the material emission property, ^{1}H NMR spectra were recorded in $C_2D_2Cl_4$ which makes the assignment of the ending groups protons following Slugovc results[10] more difficult although two distinct set of signals appear at 7.30−7.40 ppm and at 7.40−7.50 ppm (see Figure 1Sa, Supporting Information). The former can be attributed to three protons of hydrogen terminated **F** unit, while the latter should be better assigned to protons of an end phenyl ring coming from either the end-capping reagent (phenylboronic acid pinacol ester) or from aryl−aryl scrambling reaction between palladium and phosphine −bound aryls than to protons in ortho position of a bromo end group.[17] A third set of very low intensity signals appeared at 6.80−6.90 ppm and can be assigned to two protons of dioctyl **F** unit featuring a hydroxyl end group in agreement with Slugovc results.[10] In the aliphatic region the protons of boronic acid esters were not picked out. In the chemical structure of *core*-copolymers many aromatic residues are present whose protons give a lot of signals in the range 6.8−8.7 ppm preventing the

detection and precise determination of all the species containing the chromophore: end-polymers, brominate-end-polymers, *core*-copolymers. Hence, just an estimate of the amount of the inserted dye is accessible. However, the use of more solvents: toluene-d_8 and $C_2D_2Cl_4$, in different experiments (Figures 1Sb and 1Sc, Supporting Information) allows for the assignment in **P(TPAF)1-Btz** sample of protons of Btz unit linked to alkylfluorene residues near 7.6 ppm in toluene-d_8 (Figure 2S, Supporting Information) using bis(9,9-dioctylfluoren-2-yl-4,7-benzothiadiazole) (**F_2Btz**) as model compound, while we could not recognize the protons of Btz moiety linked to a **F** residue and bearing a bromo atom as in the model compound 4-(9,9-dioctylfluoren-2-yl)-7-bromobenzothiadiazole (**FBtzBr**) in both solvents. By comparison with the ^{1}H NMR spectra of model compounds: **Br_2(ThBtzTh)**, **ThBtzTh**, and 4-(5-bromothien-2-yl)-7-(thien-2-yl)-benzothiadiazole (**BrThBtzTh**) in $C_2D_2Cl_4$ (see the assignments summarized in Supporting Information, Section 1) we could assign the signals at 8.08−8.10 ppm to thiophene protons linked to **F** ring at one side and to Btz moiety at the other one, and to **F** protons, while the Btz protons can be found in the range 7.86−7.88 together with other fluorene protons. However, in this case the detection of signals attributable to proton of either terminal thiophene ring or terminal thiophene ring featuring a bromo atom was impossible even by considering the spectrum of a **P(TPAF)-ThBtzTh** end-capped tailored polymer obtained by Suzuki coupling of macromer **P(TPAF)2** with the cromophore **BrThBtzTh**. Likely, is even more complicate the identification of ThBtzTh units along the red *core*-copolymer chains composing the samples **P(TPAF)1-ThBtzTh** and **P(TPAF)2-ThBtzTh**. The SEC analyses of the green and red *core*-copolymers reveal, as shown in Figure 1 and in Figure 3S (Supporting Information), that their average molar masses increase with respect to those of the corresponding parent macromer (see Table 1). These results confirm that the Suzuki coupling reaction of the macromers with the green and red dye monomers **Br_2Btz** and **Br_2(ThBtzTh)** occurred.

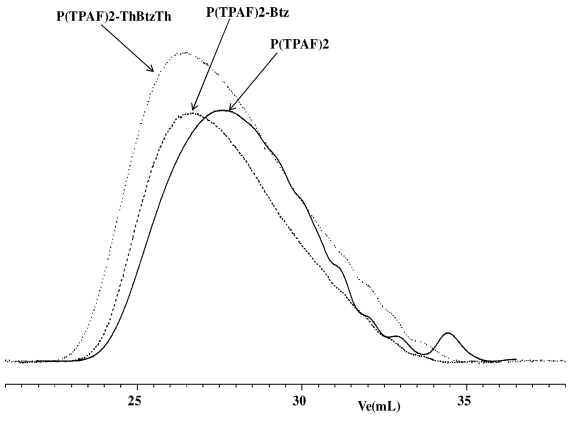

Figure 1. SEC traces of **P(TPAF)2**, **P(TPAF)2-Btz**, and **P(TPAF)2-ThBtzTh** samples.

3.2. MALDI Characterization. To corroborate finding from NMR spectra and, furthermore, to gain more information on product dispersity and the end groups of the polymer chain composing the samples studied, MALDI−TOF mass spectra were also acquired. Figure 2a displays MALDI mass spectrum of the tailored macromer **P(TPAF)2** which composition must be completely defined to understand the (b) and (c) reaction steps of Scheme 1. It shows, in the mass range m/z 1000−11000, 17 clusters of homologous peaks separated by about 1039.3−1039.6 Da, which corresponds to the mass of the P(TPAF) repeating unit (1039.4 Da), each cluster has been assigned to linear P(TPAF) chains bearing different end groups. Calibrated mass spectra permit a pertinent assignment of almost all families of peaks, and the corresponding structures are displayed in Chart 1. The assignments are also summarized in the Table 1S (Supporting Information) together with the corresponding masses. The MALDI mass spectrum in Figure 2a shows mass peaks in the higher mass molecular weights range corresponding to oligomers up to n = 10 (10-mers), and exemplifies the complexity of the reaction products. A similar mass spectrum was recorded for the corresponding tailored macromer **P(TPAF)1** (see Figure 4S, Supporting Information) synthesized using the same molar ratio of the reagents **1** and **2** and an equimolar amount of the quencher **3** as indicated in Scheme 1a. However, some differences emerge looking more carefully the spectra of both samples as can be seen in Figures 2b and 2c, which display a section ranging from m/z 1600 to m/z 2700 of the mass spectra of both macromers **P(TPAF)2** and **P(TPAF)1**, respectively, recorded in reflectron mode. In the mass spectra of **P(TPAF)2**, as well in Figure 2b, the most intense peak series appears at m/z 1243.5 + n1039.4 and is labeled with the symbol C_n. This mass series was assigned to the P(TPAF) chains terminated with phenyl (Ph) and pinacol boronic ester groups (referred herein as β'; see Chart 2).

On the other hand, in the mass spectrum of the macromer **P(TPAF)1** the most intense peaks, correspond to the potassiated ions of the macromolecules terminated with Ph and propapanediol boronic ester (namely thereafter as β) groups and are labeled with the symbol C'_n (see Figure 4S, Supporting Information), as well in Figure 2c. These findings suggest that the propapanediol−boronic −pinacol−boronic ester−ester exchange could be mostly promoted using a large excess of phenyl−pinacol boronate (**3**) as quencher, as well as in the synthesis of the macromer **P(TPAF)2**. The P(TPAF) macromolecules generally form radical cations ($M^{\bullet+}$) in the MALDI source, in accordance with published studies on similar polymer samples,[8−10,30,32,34,35] however the families of macromolecules terminated with 1,3-propanediol boronic esters (β) give potassiated ions ($M + K^+$), as was proved using also CF_3COONa salt as doping agent in matrices. In this case only the families of P(TPA)F chains terminated with propanediol boronic esters give both sodiated ($M + Na^+$) and potassiated ions, whereas the other P(TPA)F macromolecules give only radical cations. Chains terminated with hydroxyl groups (OH) (species E'_n, G'_n, and M in Chart 1 and in Table 1S, Supporting Information) appear as both potassiated and nonpotassiated ions. Contrary to P(TPAF) oligomers terminated with at least one propapanediol-boronic ester, those having a pinacol-boronic ester end groups (species C_n in Chart 1) do not give potassiated or sodiated ions in our MALDI conditions. This behavior can be due to the greater steric hindrance of the pinacol-boronic ester with respect to the propapanediol-boronic ester. The presence of the families of peaks belonging to P(TPAF) chains bearing boronic esters (β and β') as end groups (species C_n, C'_n, D_n, G_n, G'_n, H_n, I_n, L_n, Q_n, and R_n in Chart 1) in the spectra of both macromers (Figure 2 and Figure 4S, Supporting Information, respectively) confirms that the experimental conditions used in performing Suzuki polycondensation reaction lead to linear chains terminated essentially with these reactive end groups. Therefore, these borolane ended P(TPAF) chains may allow

dx.doi.org/10.1021/ma202301j | *Macromolecules* 2012, 45, 1811−1824

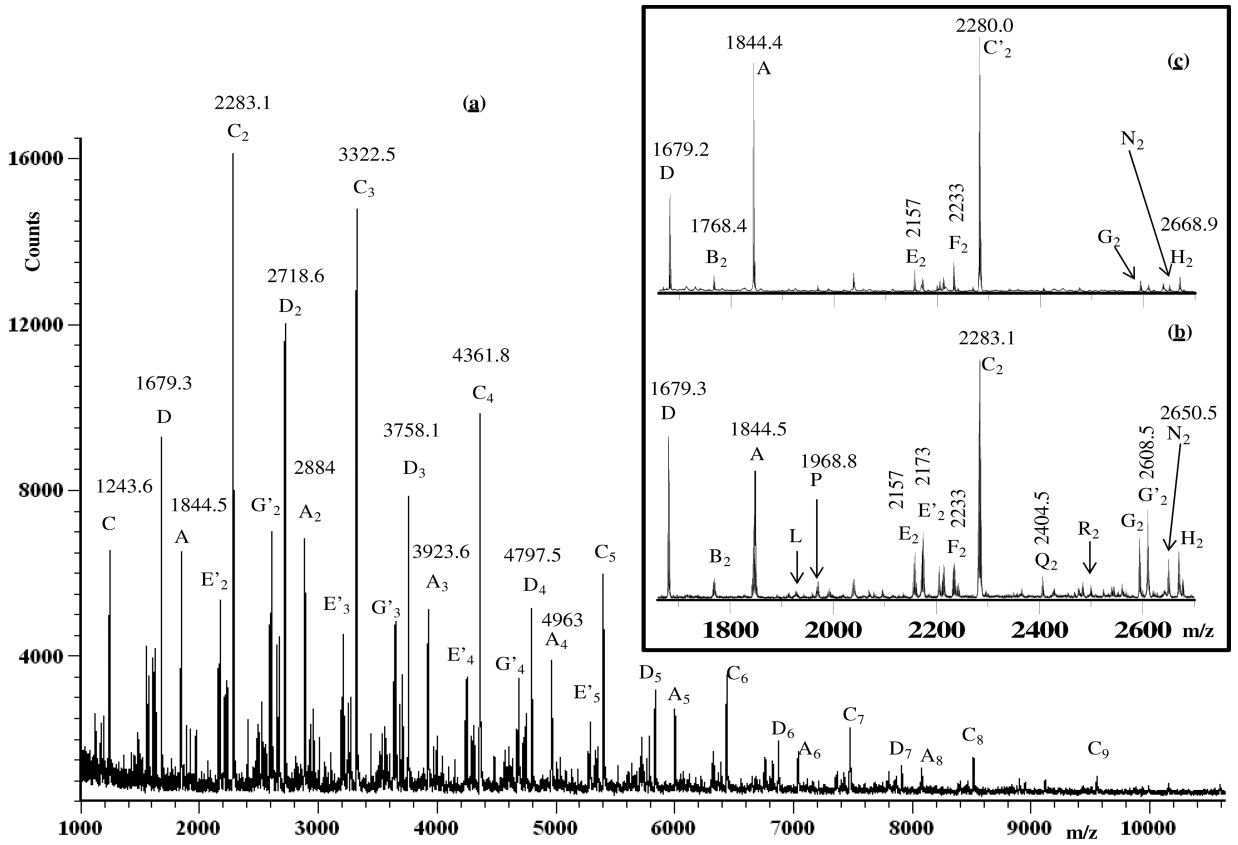

Figure 2. (a) MALDI−TOF mass spectrum (in linear mode) of pristine **P(TPAF)2** macromer; (b and c) enlarged section of MALDI mass spectra (in reflectron mode) of **P(TPAF)2** and **P(TPAF)1** macromers, respectively.

Chart 1. Structural Assignments of Peak Series Belonging to Blue-Emitting Species Present in the MALDI−TOF Mass Spectra of Macromers [P(TPAF)1 and P(TPAF)2] and *core*-Copolymers[a,b]

A_n= Ph-(TPAF)$_n$-TPA-Ph
B_n= Ph-(TPAF)$_n$-TPA-H
C_n= Ph-(TPAF)$_n$-β'
C'_n= Ph-(TPAF)$_n$-β
D_n= β'-F-(TPAF)$_n$-β
E_n= Ph-(TPAF)$_n$-H
E'_n= Ph-(TPAF)$_n$-OH
F_n= Ph-(TPAF)$_n$-Ph
G_n= β-F-(TPAF)$_n$-H
G'_n= β-F-(TPAF)$_n$-OH
H_n= β-F-(TPAF)$_n$-Ph
I_n= Ph-TPA-(TPAF)$_n$-β
L_n= Pd-TPA-(TPAF)$_n$-β
M_n= H-F-(TPAF)$_n$-OH
N_n= Pd-F-(TPAF)$_n$-Ph
P_n= Ph-(TPAF)$_n$-TPA-PO$_2$Ph$_2$
Q= Ph_2OP-(TPAF)$_n$-β
R= Ph_2PPd-(TPAF)$_n$-β'
T_n= H-(TPAF)$_n$-P-Ph
U_n= H-F-(TPAF)$_n$-H
U'_n= H-F-(TPAF)$_n$-OH
V_n= H-F-(TPAF)$_n$-Ph
V'_n= Ph-F-(TPAF)$_n$-Ph
V^*_n= HO-F-(TPAF)$_n$-Ph

[a]Species **T**, **U**, **U′**, **V**, **V′**, and **V*** were observed in particular in the mass spectra of red and green *core*-copolymers.. [b]The molecular structure and the mass of each unit and end group are portrayed in Chart 2.

for the synthesis of copolymers containing chromophore units in the backbone by reacting with **Br_2Btz** and **Br_2(ThBtzTh)** (Scheme 1, parts b and c). However, the mass spectra of both macromers show also other series of peaks belonging to P(TPAF) chains terminated with unreactive groups at both side, such as phenyl/phenyl (species A_n and F_n in Chart 1), hydrogen/phenyl (species B_n and E_n in Chart 1), hydroxy/phenyl (species E'_n in Chart 1), and hydrogen/hydroxy (species M_n in Chart 1). Therefore, the identification of P(TPAF) chains terminated with hydrogen, hydroxyl and phenyl groups

dx.doi.org/10.1021/ma202301j | *Macromolecules* 2012, 45, 1811−1824

Chart 2. Structure and Molar Mass of the Repeating Unit, of each Moiety, End Group, and Chromophore Present in the Polyfluorenes Species Revealed by MALDI−TOF MS Analysis

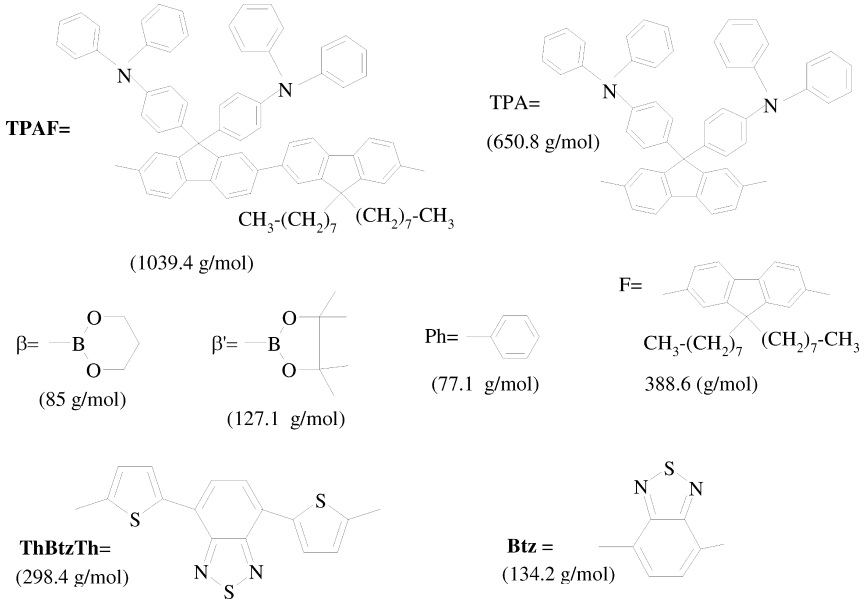

clearly reveals that, in accord to the literature,[8,10,18,20] concomitant side reactions (debromination, hydrolytic deboronation, hydroxy deboronation) occur during the Suzuki polycondensation reaction between dibromide and diboronate monomers (Scheme 2). Palladium-mediated dehalogenation is a well-understood process that occurs via β-hydride elimination from Ar−Pd(II)−alkoxy species followed by reductive elimination of Ar−H.[10,36,37]

As already presented during NMR discussion also phenyl/phenyl terminated chains can origin from the exchange between phosphorus-bound aryl moiety and palladium-bound aryl group as depicted in Scheme 3b, an unfortunate drawback of the Suzuki coupling occurring very frequent if not encumbered phosphine are used. MALDI mass spectra of both macromers show also the presence of weak intensity peaks due to the radical cations corresponding to families of oligomers having palladium and phosphorus derivatives (species L_n, N_n, P_n, Q_n, and R_n in parts b and c of Figure 2 and also in Figure 4S, Supporting Information; see assignments in Chart 1 and in Table 1S, Supporting Information). The formation of chains with incorporated phosphorus-moiety was confirmed by ^{31}P NMR spectra of both macromers, which showed after 38 000 scans two very weak signals at δ 38.2 and 35.2 ppm), corresponding to the phosphine oxide region of the spectrum. The weakness of these signal confirms, as well as the MALDI spectra, that only a very small percentage of the phosphorus containing units are incorporated into the polymer, and that this uptake is low relative to polymerization degree. Under these conditions, the phosphorus containing units should serve as cappers rather than as branch points, in agreements with the hypothesis suggested by Jannsen et al.[9] Side reactions which give rise to oligomers with phosphorus-moieties into the polymer backbone were already observed in the synthesis of poly(*p*-phenylene)s by Suzuki coupling polymerization.[12,38]

Taking into account that the mole ratio of each individual species is generally proportional to the MS detector response,[24,25,28] we have calculated the relative percentage of P(TPAF) chains terminated with reactive borolane ester groups composing the macromers **P(TPAF)1** and **P(TPAF)2**, from the corresponding mass spectra. This assumption is reasonable for MALDI spectra of polymers with a narrow molar mass dispersity. However, is also reasonable if the analysis is limited to a portion of the spectrum. Using the intensity of each peak series present in the mass range from m/z 1000 up to m/z 8000 and the eq 1, we have calculated that P(TPAF) chains terminated with reactive borolane ester groups are about 66 ± 2% in the macromer **P(TPAF)2**, and about 55 ± 2% in the macromer **P(TPAF)1**.

$$\%\ \mathrm{mol}_{\mathrm{PF-Borolane}} = \left(\sum I_{\mathrm{PF-Borolane}}\right)/\left(\sum I_{\mathrm{PF-Borolane}} + \sum I_{\mathrm{PF-unreactive}}\right)\cdot 100 \quad (1)$$

where $\sum I_{\mathrm{PF\text{-}Borolane}}$ and $\sum I_{\mathrm{PF\text{-}unreactive}}$ represent the sum of the intensity of each peak family corresponding to the P(TPAF) macromolecules terminated with borolane ester groups (i.e., species C_n, C'_n, D_n, G_n etc. in Chart 1) and with unreactive moieties at both ends (i.e., families A_n, B_n, E_n, F_n etc., in Chart 1), respectively.

Scheme 2

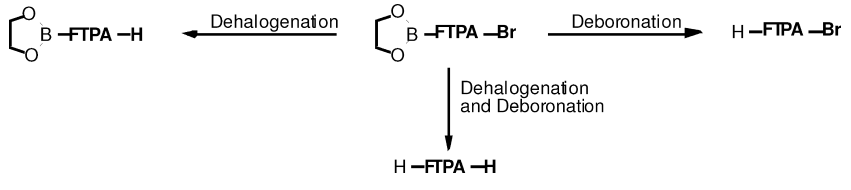

dx.doi.org/10.1021/ma202301j | *Macromolecules* 2012, 45, 1811−1824

Scheme 3

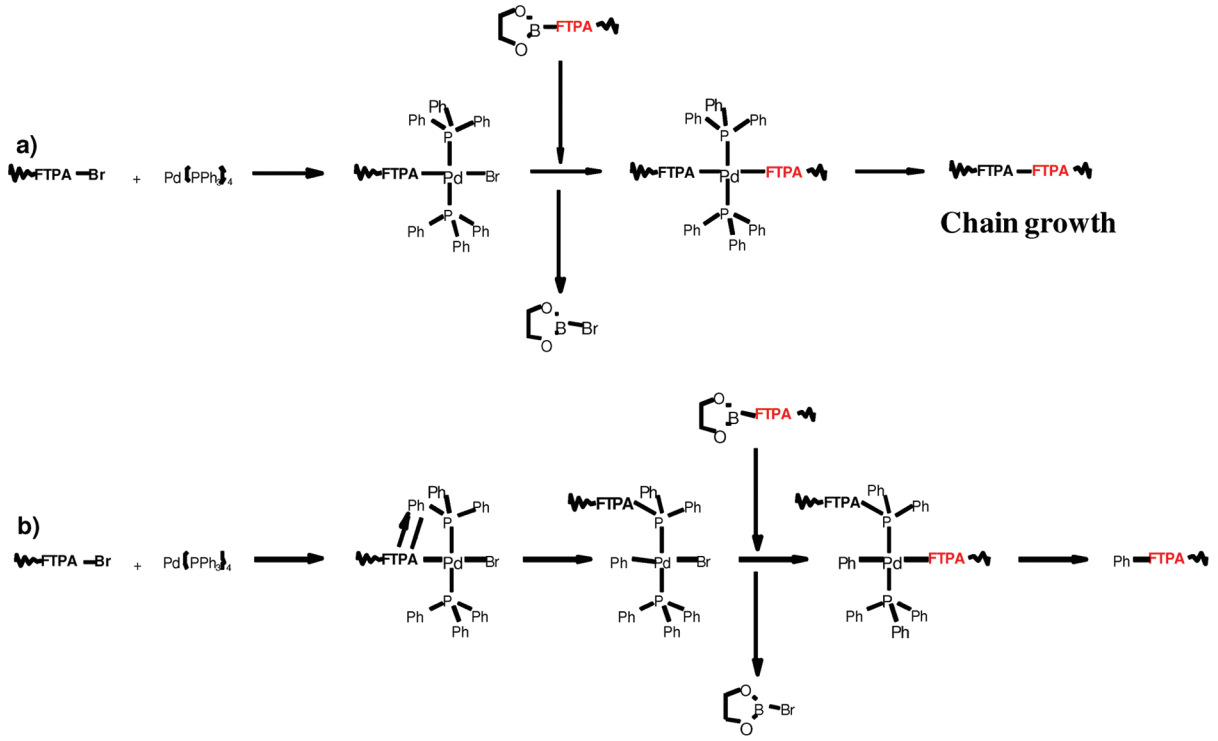

Like P(TPAF) macromers, all green and red *core*-copolymers were also analyzed by MALDI−TOF MS using DCTB as matrix, to obtain more reliable information on their chemical composition. In Figure 3 and in Figure 5S, Supporting Information, are displayed the mass spectra of pristine polydisperse *core*-copolymers **P(TPAF)2-ThBtzTh** and **P(TPAF)2-Btz**, respectively. These Figures, as expected on the base of the composition results found by MALDI−TOF analysis of the parent macromers discussed above, show intense peaks due to the P(TPAF) chains bearing unreactive end groups (i.e., families A_n, E_n, E'_n, F_n, etc. and U_n, V_n, T_n, etc. sketched in Chart 1 and described in Tables 1S and 2S, Supporting Information for parent macromers and

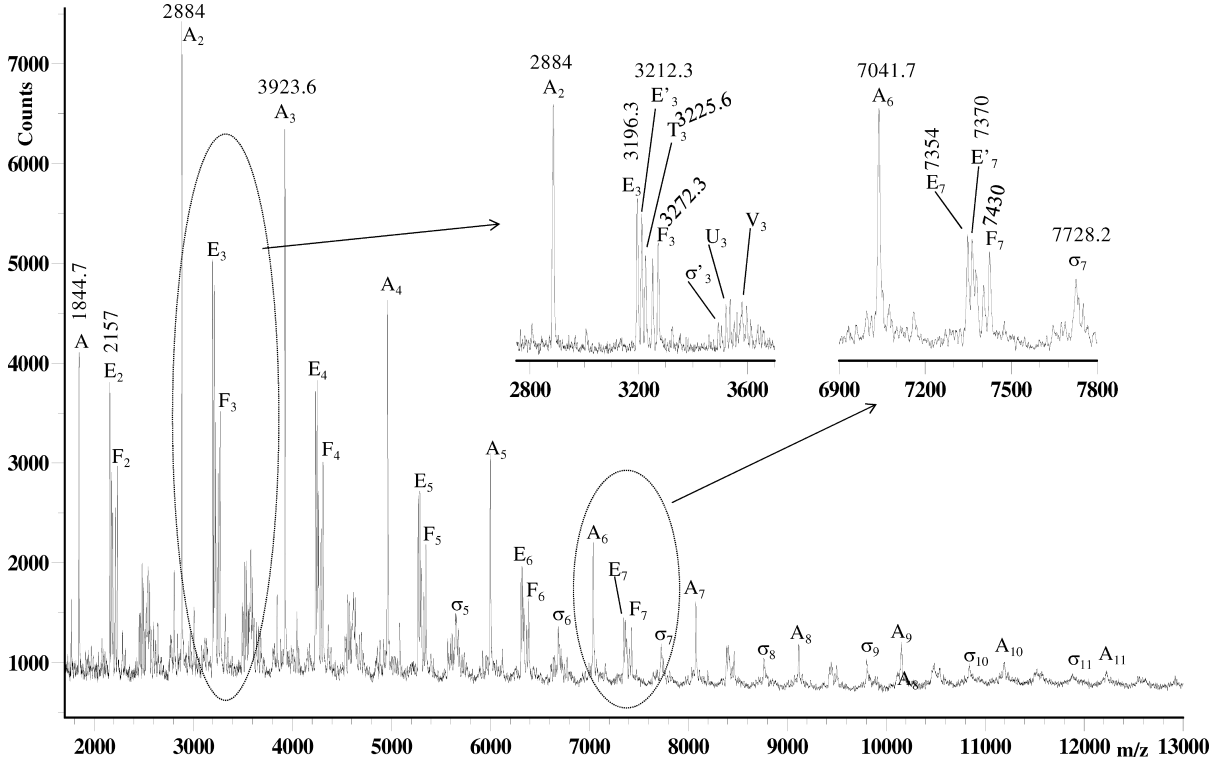

Figure 3. MALDI−TOF mass spectrum (in linear mode) of the pristine red *core*-copolymer **P(TPAF)2-ThBtzTh**.

dx.doi.org/10.1021/ma202301j | *Macromolecules* 2012, 45, 1811−1824

Chart 3. Structural Assignments of *core*-Copolymer Species Revealed by Means of MALDI−TOF MS Analysis of Red and Green *core*-Copolymers[a,b]

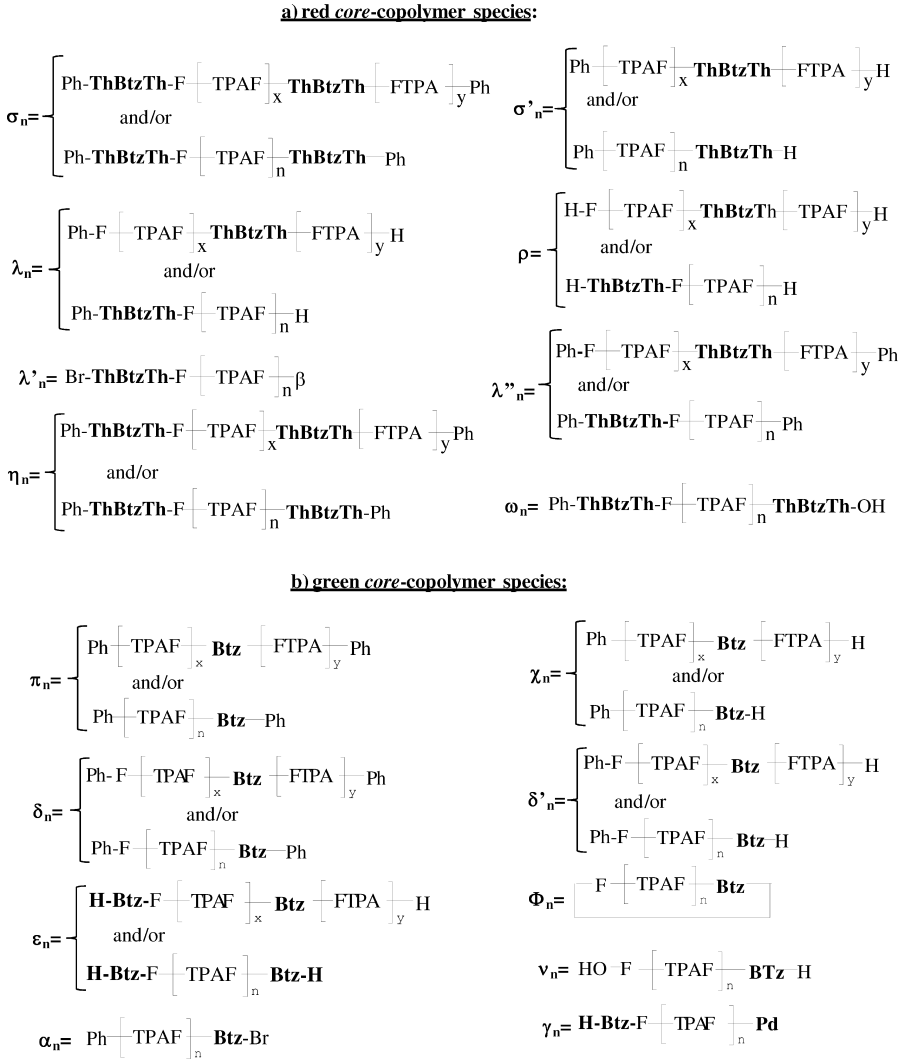

[a]The assignments of blue-emitting species are summarized in the Chart 1; [b]$n = x + y$.

core-polymers, respectively), as highlighted in the inset of both figures. The most intense peaks correspond to the P(TPAF) chains terminated with phenyl groups at both ends (species A_n in Chart 1). In the mass range higher than m/z 3000 were also observed some signals corresponding to the molecular ions ($M^{\bullet+}$) of the copolymer chains containing a dye group (ThBtzTh or Btz): species σ_n, σ'_n, λ_n, λ'_n λ''_n, etc., for **P(TPAF)2-ThBtzTh** sample; species π_n, δ_n, δ'_n etc., for green *core*-polymer **P(TPAF)2-Btz**. The pertinent assignment of the peak series belonging to *core*-copolymer chains are summarized in the Chart 3 and in Tables 2S (red) and 3S (green), Supporting Information). In the low mass range of the mass spectra of the **P(TPAF)2-Btz** sample were also observed weak signals corresponding to cyclic oligomers containing a Btz unit (species Φ_n in Chart 3). The formation of cycles has been already pinpointed in the synthesis of aromatic conjugated polymers by Suzuki polycondensation.[8] The mass spectrum in Figure 5S, Supporting Information, shows also low intense peaks corresponding to the P(TPAF) macromers terminated with pinacol boronic ester (species C_n in Chart 1), indicating the incomplete conversion of these reactive chain ends. Similar mass spectra were recorded for the *core*-copolymers **P(TPAF)1-ThBtzTh** and **P(TPAF)1-Btz** (see Figures 6S and 7S, Supporting Information) which were synthesized using a macromer P(TPAF)/dye-dibromide-derivative ratio five times lower and by adding the bromide solution along all the reaction. In these mass spectra, as well as in those of samples coming from **P(TPAF)2** macromer, mass peaks attributable to P(TPAF)s containing the dye unit (ThBtzTh or Btz) were observed with low intensity only in the mass range higher than 4000 Da. As can be observe in Figure 3 and in Figure 5S, Supporting Information, the relative intensity of peaks due to the dye-bearing species increases in mass range higher than m/z 5000, with respect to that of the unreactive PFTPA chains belonging to mass series A_n. SEC curves of all *core*-copolymers (Figure 1 and Figure 3S, Supporting Information) calibrated with PS narrow standards, provide a large dispersity of average molar masses ($D > 1.9$), as reported in Table 1. Moreover, they show that their macromolecular components have molecular masses ranging from 1000 up to 20 000 g/mol or higher. Therefore, we believe that PFTPA *core*-copolymers chains have mostly molar mass higher than 10 000 g/mol and then are not detected in the MALDI−TOF mass spectra of the neat polydisperse samples. In fact, it is known that in MALDI−TOF MS analysis of polydisperse

dx.doi.org/10.1021/ma202301j | *Macromolecules* 2012, 45, 1811−1824

polymer low molecular mass species are more easily desorbed than high molecular mass ones, determining discrimination effect and often macromolecules with molar mass higher than 10 000−15 000 g/mol were not revealed.[24−29] As affirmed in the literature,[24,25,29] MALDI−TOF MS gives absolute determinations of average molar masses (M_w and M_n), in particular only for polymers with a narrow dispersity ($D = M_w/M_n < 1.1$) it succeeds independently of their structure, while fails for polymeric materials with a higher polydispersity ($D > 1.1$), as well as for the *core*-copolymers here investigated. To obtain more reliable information on the chemical composition and on the absolute average molar masses of all *core*-copolymers, we have applied the powerful *off-line* SEC/MALDI−TOF MS coupling method.[24,25,29] The four *core*-copolymers reported in Table 1 were fractionated into narrow molar mass fractions by analytical SEC runs, obtaining about 40−50 fractions for each sample. The average molar masses (MM; M_w and M_n) of several selected narrow polydisperse fractions were then measured by MALDI-TO MS and the values calculated were used to "self-calibrate" starting SEC curves. For all samples the absolute calibration curves agree with the eq 2 that, therefore, was used to calculate the MM of all samples synthesized; calculated values are summarized in Table 1. The calibration curves calculated by SEC−MALDI TOF MS analysis of **P(TPAF)1-ThBtzTh** and **P(TPAF)2-ThBtzTh** sample are displayed in Figure 8S, Supporting Information.

$$\log M_w = 11.22 - 0.3911V_e + 4.66 \times 10^{-3}(V_e)^2 \qquad (2)$$

Table 1 shows that the MM calculated by SEC−MALDI−TOF MS agree with those calculated by an apparatus SEC calibrated with narrow PS standards, confirming the potentiality of the method. The MALDI TOF mass spectra of the narrowly distributed SEC fraction give considerable information on the real composition of the *core*-copolymers. In Figure 4 an illustrative example of the MALDI mass spectra of selected SEC fractions of the **P(TPAF)2-ThBtzTh** sample eluted at 22.625 (F1), 24.625 (F9), 27.125 (F19), 28.625 (F25), and 29.875 mL (F30), are reported. All MALDI−TOF mass spectra confirm a narrow dispersity ($D < 1.04$) for each sample obtained by SEC fractionation. MALDI mass spectra of other **P(TPAF)2-ThBtzTh** SEC fractions are portrayed in Figure 9S, Supporting Information. As can be seen in both the Figures, the mass spectra of fractions eluted at Ve higher than 29.875 mL (i.e., see spectrum of the fraction F25 in Figure 4), beside the peaks corresponding to the mono charged molecular ions (labeled as M^+), also show those due to the double charged ions (M^{2+}) and those due to the adduct dimer ions (M_2^+). Some spectra exhibit also the extensive multimer formation: i.e., trimeric ions (M_3^+), tetrameric ions (M_4^+), and pentameric ions (M_5^+). The intensity of these multimer ions and those of on the ions M^{2+} increases as increases the applied laser intensity; the spectra displayed in Figure 4 and in Figure 9S, Supporting Information are recorded using a minimum laser irradiance (threshold) useful to obtain a meaningful signal/noise ratio. The average molar masses of each fraction were calculated using only the intensity of mass peaks belonging to monocharged ions (M^+). Similar mass spectra were also obtained for the SEC fraction collected for **P(TPAF)1-ThBtzTh** copolymer, and some remarkable spectra are portrayed in Figure 10S, Supporting Information. As shown in Figures 4 and 9S, Supporting Information, MALDI−TOF mass spectra of the SEC fractions display well-resolved peaks from m/z 1000 to m/z 15 000−20 000, allowing for both the assignment of each peak to the corresponding macromolecule and the identification of the end groups. Consequently the most-probable structures can be identified, in particular those corresponding to the chains bearing the dye moiety (i.e., **ThBtzTh**). The assignments of the mass peak series displayed in Figures 4 and 9S, Supporting Information are highlighted in Chart 1 (blue-emitting species) in Chart 3 (dye-species), and also in Tables 1S and 2S, Supporting Information. In detail, as an example here we discuss these data in the following. They reveal that SEC fractions taken at elution volume (V_e) higher than 28.625 mL (fractions F25−F45) are mostly constituted of unreactive P(TPAF) oligomers (blue-emitting component: species A_n, B_n, E_n, E'_n, F_n P_n, T_n, V_n, V'_n and V^*_n, in Chart 1). Peaks belonging to the macromolecules bearing the dye-ThBtzTh units (i.e., species σ_n, σ'_n, λ_n, λ''_n, etc. in Chart 3) appear with an intensity that decreases as increases the V_e. Fractions **P(FTPA)2-ThBtzTh** eluted at $V_e > 32.875$ mL (see mass spectrum of fraction F45 in Figure 9S, Supporting Information) do not contain any dye-species. The intensity of mass peaks corresponding to the dyes containing chains (families σ_n, σ'_n, λ_n, λ'_n, λ''_n, etc in Chart 3) increases with respect to those of blue emitting P(FTPA) macromolecules in the mass spectra of the SEC fractions eluted in the range between 28.6 and 24.7 mL (see spectra of fractions F25, F19, F15, and F11 in Figure 4 and in Figure 9S, Supporting Information). Peaks corresponding to the P(FTPA) chains A_n and E_n are observed with a negligible intensity in the mass spectrum of SEC fraction F10 and disappear in that of the F9 one, which presents families of peaks belonging only to the dye bearing **P(FTPA)-ThBtzTh** species, as can be observed in Figure 4. SEC fractions eluted at V_e lower than 26.0 mL gave low or unresolved mass peaks, however in accord to the spectrum of the fraction F9 displayed in Figure 4; hence, we can affirm that they contain only dyes bearing *PFTPA-ThBtzTh* macromolecules (i.e., species σ_n, σ'_n, λ_n, λ'_n, λ''_n, ω_n, and η_n in Chart 3). Therefore, the MALDI mass spectra of the SEC fractions confirm that the *core*-copolymer **P(FTPA)2-ThBtzTh** is a mixture of blue-species P(FTPA) and of dye-containing **P(FTPA)-ThBtzTh** macromolecules which are the main species at higher molar mass. As can be observe in Figure 10S, Supporting Information, in the case of the copolymer **P(FTPA)1-ThBtzTh** only the SEC fractions F1−F4 eluted at lower V_e contain just red-dye bearing **P(FTPA)-ThBtzTh** macromolecules, while the SEC fractions from F5 up to F24 contain a mixture of **P(FTPA)-ThBtzTh** and P(FTPA) type chains in different ratios (see Table 5S, Supporting Information). SEC fractions of **P(FTPA)1-ThBtzTh** taken at Ve higher than 32.175 mL (F31) present only blue P(FTPA) species. This result can be ascribable to the low MM of the **P(FTPA)1-ThBtzTh** with respect to **P(FTPA)2-ThBtzTh** sample (see Table 1). The different composition of the SEC fractions taken from **P(FTPA)2-ThBtzTh** at different Ve was also qualitatively confirmed by ^{1}H NMR analysis, since the proton spectra present some signal with different relative intensity as can be observe in Figure 11S, Supporting Information. Unfortunately, as discussed above, the NMR analysis does not permit an unambiguous characterization of the composition of each polymer fraction. A similar behavior was also observed in the SEC−MALDI mass spectra of the **P(FTPA)1-Btz** and **P(FTPA)2-Btz** green copolymers, and will be discussed in a next work together to their optical properties. The SEC−MALDI spectra discussed above could further provide important and

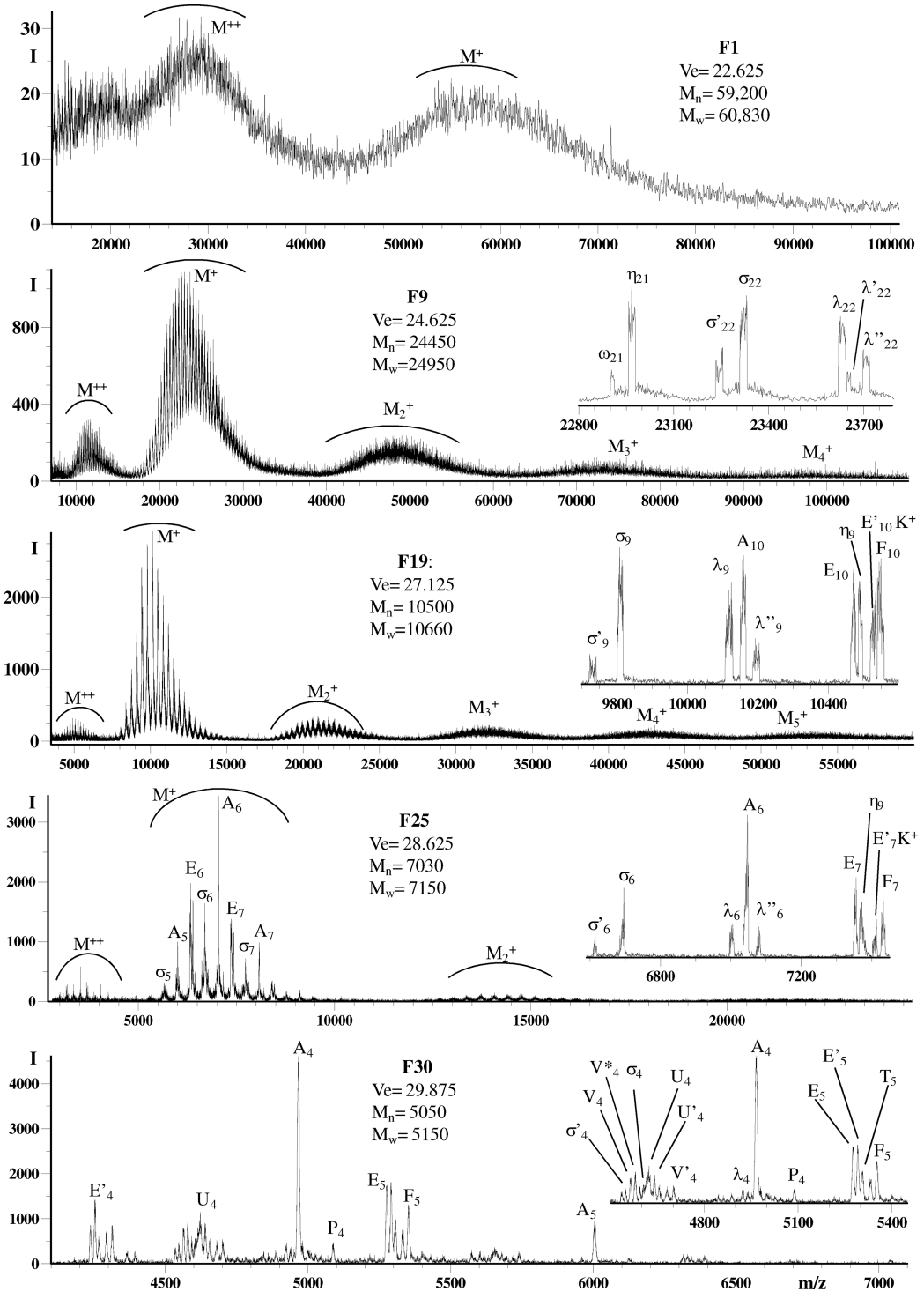

Figure 4. MALDI–TOF mass spectra of some SEC fractions of the **P(TPAF)2-ThBtzTh** sample.

useful information on the chemical composition of the red-*core*-copolymers **P(FTPA)1-ThBtzTh** and **P(FTPA)2-ThBtzTh**. Since each SEC fraction is constituted of macromolecules with a narrow molar mass dispersity and, as mentioned above the mole ratio of each individual species is proportional to the MS detector response in MALDI analysis, we have set ourselves to reach the ambitious goal to calculate the weight percentages of dye-containing (red or green) and blue (**P(TPFA)**) components of the *core*-copolymers here studied, using the integrated area of each SEC fraction and the molar fraction of the two components (dye-containing and blue) calculated from the corresponding MALDI spectra.

The weight percent of the macromolecules bearing the dye unit (% $W_{\text{PF-Dye}}$) composing the polydisperse *core*-copolymers, were calculated using the eq 3 (see also the theory in section 2, Supporting Information)

$$\%\, W_{\text{PF-Dye}} = \sum_{i=1}^{n} [W_{\text{fi}}(X_{\text{PF-Dye}})_{\text{fi}}] \times 100 \qquad (3)$$

dx.doi.org/10.1021/ma202301j | *Macromolecules* 2012, 45, 1811–1824

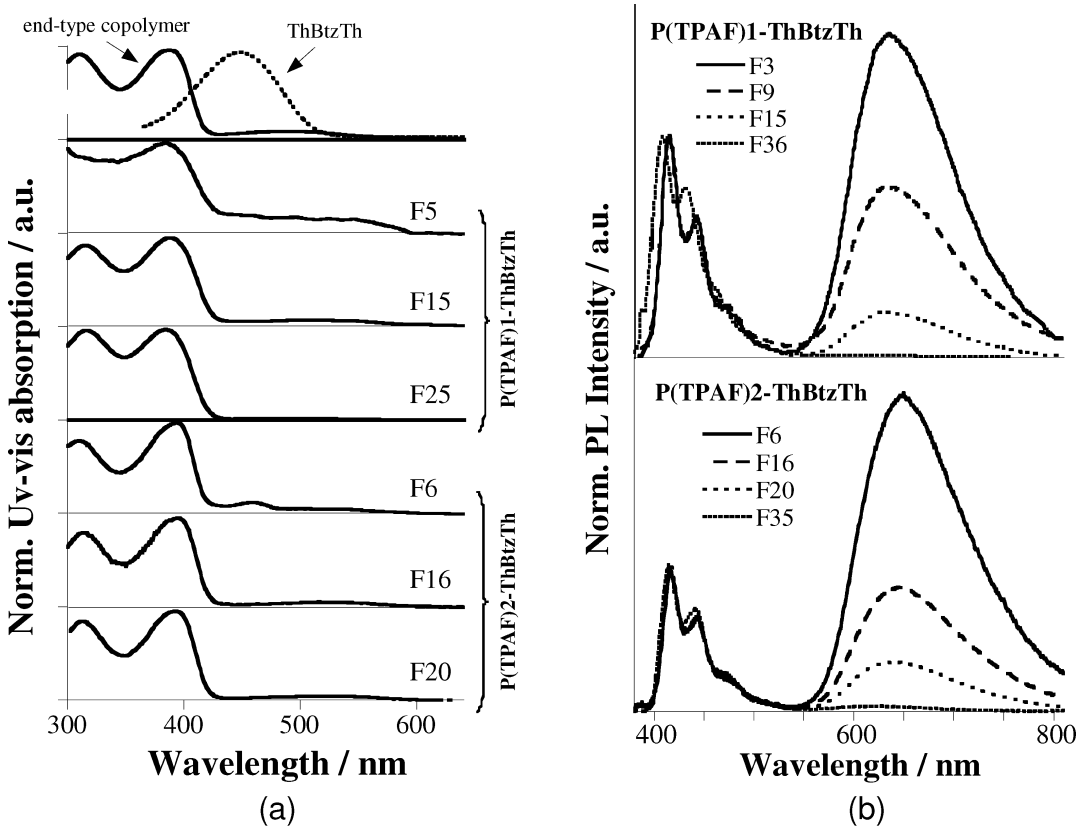

Figure 5. (a) Normalized UV−vis absorption (vertically shifted for clarity) and (b) PL spectra of **P(TPAF)1-ThBTzTh** (top) and **P(TPAF)2-ThBTzTh** (bottom) copolymer's selected fractions. The absorption spectra of ThBtzTh chromophore and end-capped **P(TPAF)-ThBTzTh** copolymer in toluene diluted solutions are reported for comparison. PL spectra are obtained by exciting the donor copolymer at 380 nm.

where W_{fi} is the area of the fraction *fi* calculated from the normalized area of the SEC curve; and $(X_{PF\text{-}Dye})_{fi}$ indicates the molar fraction of all species containing the dye unit present in the SEC fraction *fi*, calculated from the corresponding mass spectra. The calculated $\%W_{PF\text{-}Dye}$ values are noted in Table 1. In Tables 4S and 5S of Supporting Information are summarized for each SEC fraction both the molar fraction of the two components (red-dye-containing species and blue-emitting macromolecules) calculated from the corresponding MALDI−TOF mass spectra and their area derived from the SEC curves of the neat *core*-copolymers **P(TPAF)1-ThBtzTh** and **P(TPAF)2-ThBtzTh**, respectively. The knowledge of the actual composition of each copolymer and also of its fractions can allow for a better understanding of the optical properties, as will be discussed below. Moreover, we can say that is mandatory to correlate the different absorption and luminescence properties to the changes of synthesis procedure.

As can be observe looking the Chart 3 and also Tables 2S and 3S, Supporting Information, many of the structures of P(TPAF) chains containing the dye unit (ThBTzTh or Btz) cannot be assigned unequivocally to a macromolecule having this group in the main chain or as end-capper. However, we hypothesize that in the macromolecules with high molar mass the dye unit is mostly in the backbone, while it does as end group in those ones having lower molar mass (i.e., < 3000−4000 g/mol). This hypothesis is supported by the optical properties measured for the SEC fractions: see following discussion.

3.3. Optical Characterization. The differences between **P(TPAF)2-ThBtzTh** and **P(TPAF)1-ThBtzTh** red *core*-copolymers evidenced by MALDI analysis are confirmed by optical characterizations. In this section the comparison between the absorption and emission properties of the two red *core*-copolymers is presented. Figure 5 shows UV−vis absorption (a) and PL (b) spectra of various SEC fractions taken in the SEC run of **P(TPAF)1-ThBtzTh** and **P(TPAF)2-ThBtzTh** copolymers. In the absorption spectra of diluted toluene solution of the fractions F6, F8, and F10 of **P(TPAF)2-ThBtzTh**, corresponding to higher average molar mass and all dye-containing copolymers (see MALDI analysis and Table 5S, Supporting Information, for elution volumes), three distinct peaks are present thus indicating that the electronic configurations of the two components, P(TPAF) and ThBTzTh, are partially not mixed.[39] The 390 nm peak is attributed to the $\pi-\pi^*$ transition of P(TPAF) chains[6] and the push−pull property induced by the ThBTzTh electron acceptor unit within the chain is responsible for the long wavelength transition at 515 nm. The additional 460 nm peak, being similar to that of isolated and distorted **ThBTzTh** in solution (Figure 5a) and progressively weakened as the molar mass decreases (see Figure 12S, Supporting Information), arises from a chain distortion that is consistent with a *core*-copolymer configuration in which two long arms are twisted with respect to the inner dye. This peak is not present in the spectra of higher average molar mass **P(TPAF)1-ThBtzTh** fractions F1-to-F6 that are fully constituted by dye-bearing macromolecules as well (Table 4S, Supporting Information). In the middle range molecular weight fractions, F8-to-F25 for **P(TPAF)1-ThBtzTh** and F11-to-F28 for **P(TPAF)2-ThBtzTh**, the 390 nm/515 nm peak intensity ratio is increased because the percentage of P(TPAF) chains

dx.doi.org/10.1021/ma202301j | *Macromolecules* 2012, 45, 1811−1824

containing ThBTzTh is progressively reduced (see Tables 4S and 5S, respectively, Supporting Information). The disappearance of the 460 nm peak and the blue-shift of the 515 nm peak (see Figures 12S and 13S, Supporting Information) are due to the planarization of the ThBtzTh rings among themselves or with respect to a P(TPAF) arm and to a higher probability to find acceptor dye as end-capping unit of the chain instead as a inner one. In fact, these results totally agree with MALDI spectra data, and in particular the relative intensity of peak series σ_n and σ'_n, because the chromophore unit ThBtzTh should be mostly present as end-chain in the red *core*-macromolecules σ'_n and in the skeleton of those belonging to species σ_n. Finally, the comparison with the UV−vis absorption spectrum of the **ThBtzTh** end-capped copolymer model **P(TPAF)-ThBtzTh**, that shows only the 490 nm centered absorption band beside the main 390 nm peak (Figure 5a and Figure 13aS, Supporting Information), confirms this statement. The resonant energy transfer (RET) from directly excited P(TPAF), the excitation donor, toward the *core* dye, which behaves as the acceptor, guaranteed by the almost complete spectral overlap between the absorption of the ThBtzTh (and Btz in the green one) dye and the emission of P(TPAF) copolymer,[5,39,40] is a tool to investigate the products composition. The intramolecular REF efficiency, as measured in the diluted solutions, takes place only within the dye-containing chains and affects the donor/acceptor emission intensity depending on both donor/acceptor concentration ratio and acceptor position along the P(TPAF) main chain (Figure 13S, Supporting Information, and unpublished results). PL spectra of selected diluted toluene solution **P(TPAF)1-ThBtzTh** and **P(TPAF)2-ThBtzTh** fractions, reported in Figure 5b, show both features of P(TPAF) and ThBtzTh emission. The dominant 645 nm peak of ThBtzTh progressively decreases and blue-shifts as copolymer molecular weight decreases, in agreement with both the diminishing number of copolymer chains containing the red chromophore and the different positioning of the ThBtzTh moiety that comes closer to the chain termination. This shift is more evident in **P(TPAF)2-ThBtzTh** than in **P(TPAF)1-ThBtzTh** (see Figure 13bS, Supporting Information) accounting for a larger amount of end-capped macromolecules even at higher average molar mass in the latter red *core*-copolymer.

A similar discussion applies to **P(TPAF)-Btz** copolymers optical properties (see Figure 14S, Supporting Information).

4. CONCLUSIONS

Red- and green-emitting *core*-copolymers based on fluorene residues have been prepared by Suzuki coupling. MALDI−TOF mass spectra confirm that hydrolytic deboronation, dehalogenation, aryl−aryl scrambling, and boronic ester−ester exchange side reactions occur during the synthesis of conjugated aromatic polymers by Suzuki polycondensation. The compositions of the red and green *core*-copolymers have been characterized by means of MALDI−TOF MS analysis of their narrow distributed SEC fractions. An appropriate combination of SEC−MALDI TOF MS data has allowed to calculate, for the first time on the base of the literature about the SEC−MALDI of polymers that we have consulted, the percentage of polymer chains bearing the chromophore units. This finding is consistent with the changes in the optical properties of red or green *core*-copolymers having different average molar masses, which were synthesized following various Suzuki coupling protocols. On the base of the spectral shifts of the SEC fraction absorption and emission bands, we conclude that the chromophore units are mostly present as end group in the dye−polymer chains with relative low average molar masses (MM), whereas they are in the backbone of those having high average MM. This remarkable result explains also the variation in the optical properties of the two red type polymers **P(TPAF)1-ThBtzTh** and **P(TPAF)2-ThBtzTh** which have different average MM. By *off-line* SEC−MALDI method were also calculated the absolute average molar masses of the polyfluorene samples studied, and the values agree with those calculated using a SEC−viscosimetry apparatus calibrated with PS standards. In conclusion, the *off-line* SEC/MALDI−TOF MS coupling analysis here presented can be a valuable tool to determine the actual composition of any conjugated copolymer obtained by organometal catalyzed polycondensation even with MM higher than 20 000.

■ ASSOCIATED CONTENT

Supporting Information

(1) ^{1}H NMR data on some model compounds; (2) theoretical approach, calculation of the percentage of components of the polydisperse polymer samples, combining SEC and SEC/MALDI−TOF MS data; (3) ^{1}H NMR spectra of macromers and of *core*-copolymers recorded in different solvents; (4) SEC curves and MALDI−TOF mass spectra of macromer P(TPAF)-1 and of the corresponding *core*-copolymers; (5) MALDI−TOF mass spectra of *core*-copolymers; (6) MALDI mass spectra of some SEC fractions of red *core*-copolymers **P(TPAF)2-ThBtzTh** and **P(TPAF)1-ThBtzTh**; (7) figures that display the optical characterization of some SEC fractions and a model compound; (8) tables with structural assignments of the mass peaks present in the MALDI−TOF mass spectra of macromers and *core*-copolymers; (9) tables that report the SEC and SEC−MALDI−TOF MS data of red *core*-copolymers **P(TPAF)1-ThBtzTh** and **P(TPAF)2-ThBtzTh**. This material is available free of charge via the Internet at http://pubs.acs.org.

■ AUTHOR INFORMATION

Corresponding Author

*E-mail: fsamperi@unict.it.

Notes

The authors declare no competing financial interest.

■ ACKNOWLEDGMENTS

The financial support for this research work from the Italian Project PRIN 2009PRAM8L_004, Progetto Cariplo SOFT-PV 2009-2671 and the National Council Research (CNR), are gratefully acknowledged . The authors thank Dr. Mariacecilia Pasini for her contribution in *core*-copolymers preparation and Mr. Daniele Piovani for his contribution in *core*-copolymer SEC fractionation.

■ REFERENCES

(1) (a) Abbel, R.; Schenning, A. P. H. J.; Meijer, E. W. *J. Polym. Sci., Part A: Polym. Chem.* **2009**, *47*, 4215−4233. (b) Köhnen, A.; Irion, M.; Malte, C.; Gather, M. C.; Rehmann, N.; Zacharias, P.; Meerholz, K. *J. Mater. Chem.* **2010**, *20*, 3301−3306.

(2) (a) Inganäs, O.; Fengling Zhang, F.; Andersson, M. R. *Acc. Chem. Res.* **2009**, *42*, 1731−1739. (b) Helgesen, M.; Roar Søndergaard, R.; Krebs, F. C. *J. Mater. Chem.* **2010**, *20*, 36−60. (c) Topham, D.; Andrew, J.; Parnell, A. J.; Hiorns, R. C. *J. Polym. Sci..Part B: Polym. Phys.* **2011**, *49*, 1131−1156. (d) Dennler, G.; Scharber, C. M.; Brabec, C. J. *Adv. Mater.* **2009**, *21*, 1323−1328.

(3) Facchetti, A. *Chem. Mater.* **2011**, *23*, 733−758.
(4) Chuang, C.-Y.; Shih, P.-I.; Chien, C.-H.; Wu, F.-I.; Shu, C.-F. *Macromolecules* **2007**, *40*, 247−252.
(5) Giovanella, U.; Betti, P.; Bolognesi, A.; Destri, S.; Melucci, M.; Pasini, M.; Porzio, W.; Botta, C. *Org. Electron.* **2010**, *11*, 2012−2018.
(6) Giovanella, U.; Pasini, M.; Destri, S.; Porzio, W.; Botta, C. *Synth. Met.* **2008**, *158*, 113−119.
(7) Pasini, M.; Giovanella, U.; Betti, P.; Bolognesi, A.; Botta, C.; Destri, S.; Porzio, W.; Vercelli, B.; Zotti, G. *Chem. Phys. Chem.* **2009**, *10*, 2143−2149.
(8) Jayakannan, M.; Van Dongen, J. L. J.; Janssen, R. A. J. *Macromolecules* **2001**, *34*, 5386−5393.
(9) Jayakannan, M.; Lou, X.; Van Dongen, J. L. J.; Janssen, R. A. *J. Polym. Sci., Part A: Polym. Chem.* **2005**, *43*, 1454−1462.
(10) Kappaun, S.; Zelzer, M.; Bartl, K.; Saf, R.; Stelzer, F.; Slugovc, C. *J. Polym. Sci., Part A: Polym. Chem.* **2006**, *44*, 2130−2138.
(11) Goodson, F. E.; Wallow., T. I.; Novak, B .M. *J. Am. Chem. Soc.* **1997**, *119*, 12441−12453.
(12) Goodson, F. E.; Wallow., T. L.; Novak, B .M. *Macromolecules* **1998**, *31*, 2047−2056.
(13) Chen, H.; He, M.; Pei, J.; Liu, B. *Anal. Chem.* **2002**, *74*, 6252−6258.
(14) Yokoyama, A.; Suzuki, H.; Kubota, Y.; Ohuchi, K.; Higashimura, H.; Yokozawa, T. J. *Am. Chem. Soc.* **2007**, *129*, 7236−7237.
(15) Miyakoshi, R.; Yohoyama, A.; Yokozawa, T. *J. Polym. Sci., Part A: Polym. Chem.* **2008**, *46*, 753−765.
(16) Bolognesi, A.; Betti, P.; Destri, S.; Giovanella, U.; Moreau, J.; Pasini, M.; Porzio, W. *Macromolecules* **2009**, *42*, 1107−1113.
(17) Sakamoto, J.; Rehahn, M.; Wegner, G.; Schluter, D. *Macromol. Rapid Commun.* **2009**, *30*, 653−687.
(18) Weber, S. K.; Galbrecht, F.; Scherf, U. *Org. Lett.* **2006**, *8*, 4039−4041.
(19) Murage, J.; Eddy, J. W.; Zimbalist, J. R.; McIntyre, T. B.; Wagner, Z. R.; Goodson, F. E. *Macromolecules* **2008**, *41*, 7330−7338.
(20) Zhou, E.; Cong, J.; Yamakawa, S.; Wei, Q.; Nakamura, M.; Tajima, K.; Yang, C.; Hashimoto, K. *Macromolecules* **2010**, *43*, 2873−2879.
(21) Wang, J.; Zhang, C.-Q.; Zhong, C.-M.; Hu, S.-J.; Mo, Y.-Q.; Chen, X.; Wu, H.-B. *Macromolecules* **2011**, *44*, 17−19.
(22) Tao, B.; Boykin, D. W. *J. Org. Chem.* **2004**, *69*, 4330−4335.
(23) Kan, Y. K.; Deria, P.; Caroll, P. J.; Therien, M. J. *Org. Lett.* **2008**, *10*, 1341−1344.
(24) Montaudo, G.; Montaudo, M. S.; Samperi, F. In *Matrix-Assisted Laser Desorption Ionisation/Mass Spectrometry of Polymers*; Montaudo, G., Lattimer, R. P., Eds.; CRC Press: Boca Raton, FL, 2002; Vol *1*, p 419.
(25) Montaudo, G.; Samperi, F.; Montaudo, M. S. *Prog. Polym. Sci.* **2006**, *31*, 277−357.
(26) Räder, H. J.; Schrepp, W. *Acta Polym.* **1998**, *49*, 272−293.
(27) Pasch, H.; Schrepp, W. In *MALDI-TOF Mass spectrometry of polymers*; Springer: Berlin, 2003; p 298.
(28) Nielen, M. W. F. *Mass Spectrom. Rev.* **1999**, *18*, 309−344.
(29) Montaudo, G.; Garozzo, D.; Montaudo, M. S.; Puglisi, C.; Samperi, F. *Macromolecules* **1995**, *28*, 7983−7989.
(30) Langeveld-Voss, B. M. W.; Janssen, R. A. J.; Spiering, A. J. H.; van Dongen, J. L. J.; Vonk, E. C.; Claessens, H. A. *Chem.Commun.* **2000**, 81−82.
(31) Vonk, E. C.; Langeveld-Voss, B. M. W.; Van Dongen, J. L. J.; Janssen, R. A. J.; Claessens, H. A.; Cramers, C. A. *J. Chromatogr. A* **2001**, *911*, 13−26.
(32) Remmers, M.; Müller, B.; Martin, K.; Rüder, H.-J.; Kühler, W. *Macromolecules* **1999**, *32*, 1073−1079.
(33) Mendichi, R.; Giacometti Schieroni, A. In *Current Trends in Polymer Science*; Pandalai, S. G., Ed.; TWR Network: Trivandrum, India, 2001; Vol. *6*, p 17.
(34) Ma, Z.; Qiang, L.-L.; Wang, Fan; Y., -Y.; Pu, K.-Y.; Yin, R.; Huang, W. *J. Mass. Spectrom.* **2007**, *42*, 20−24.
(35) Wang, Q.; Tian, H.; Geng, Y.; Wang, F. *Macromolecules* **2011**, *44*, 1256−1260.
(36) Navarro, O.; Kaur, H.; Mahjoor, P.; Nolan, S. P. *J. Org. Chem.* **2004**, *69*, 3173−3180.
(37) Alonso, F.; Beletskaya, I. P.; Yus, M. *Chem. Rev.* **2002**, *102*, 4009−4084.
(38) Morita, D. K.; Stille, J. K.; Norton, J. R. *J. Am. Chem. Soc.* **1995**, *117*, 8576−8581.
(39) Hou, Q.; Xu, Y.; Yang, W.; Yuan, M.; Peng, J.; Cao, Y. *J. Mater. Chem.* **2002**, *12*, 2887−2892.
(40) Lakowicz, J. R. In *Principles of Fluorescence Spectroscopy*, 2nd ed., Kluwer Academic Plenum Publishers: New York, 1999; pp 367−394.

Macromolecules

Article

pubs.acs.org/Macromolecules

Liquid Crystalline Polythiophene Bearing Phenylnaphthalene Side-Chain

Mari Watanabe,[†,‡] Kazuhiko Tsuchiya,[§] Toshinobu Shinnai,[§] and Masashi Kijima*[,†,‡,∥]

[†]Institute of Materials Science, Graduate School of Pure and Applied Sciences, University of Tsukuba, 1-1-1 Tennodai, Tsukuba, Ibaraki 305-8573, Japan

[‡]Tsukuba Research Center for Interdisciplinary Materials Science, University of Tsukuba, 1-1-1 Tennodai, Tsukuba, Ibaraki 305-8573, Japan

[§]Central Research Laboratory, Technology & Development Division, Kanto Chemical Co., Inc., 1-7-1 Inari, Soka, Saitama 340-0003, Japan

[∥]Division of Materials Science, Faculty of Pure and Applied Sciences, University of Tsukuba, 1-1-1 Tennodai, Tsukuba, Ibaraki 305-8573, Japan

Supporting Information

ABSTRACT: Polythiophene bearing a 2-phenylnaphthalene side group at 3-position was synthesized from a 2,5-dibromothiophene monomer by two polymerization methods, i.e., Yamamoto dehalogenative polycondensation using $Ni(cod)_2$ and Ni-catalyzed chain-growth polymerization. Polymers prepared by the former method had good solubility for organic solvents, 6300−8400 g mol^{-1} of number-average molecular weights, absorption bands at around 300 and 385 nm due to $\pi-\pi^*$ transitions at the phenylnaphthalene moiety and polythiophene backbone, a main fluorescence emission band at around 540 nm from the polythiophene backbone in solution and film state, and presence of enantiotropic liquid crystalline phases which enabled to construct an arrayed state. On the other hand, the latter polymer showed considerably red-shifted absorption and emission bands at around 444 and 585 nm in solution and 509 and 720 nm in film state respectively, but had poor solubility and unresolved mesophases.

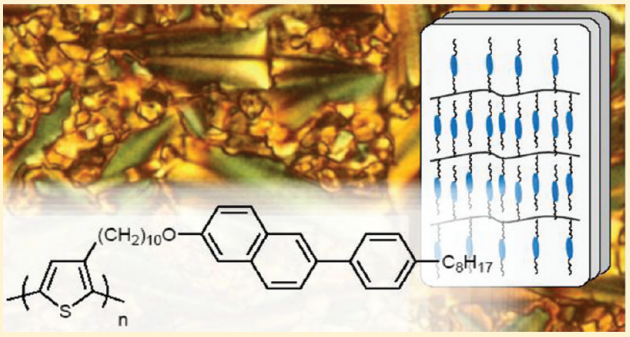

INTRODUCTION

Conjugated polymers bearing a liquid crystalline side-chain have been studied for the purpose of adding specific functionalities of birefringence, self-orientation, and induced anisotropy to semiconducting polymer backbones.[1−3] They are prospective candidate of elaborate functional materials as well or better than main-chain type liquid crystalline conjugated polymers,[4,5] because their electrical and optical properties are expected to be controlled by the molecular orientation of various liquid crystalline side chains and furthermore macroscopic alignment of them can be progressed by an external perturbation such as shear stress, electric or magnetic field.[6−8]

Polythiophene derivatives have been drawing much attention for their wide-spreading potential of applications, such as organic light emitting diodes,[9−11] polymer solar cells,[12−15] and organic field effect transistors.[16,17] Therefore, they have also been investigated as π-conjugated backbone of the side-chain type polymer liquid crystals. For development of liquid crystallinity of polythiophenes, selective 2,5-polymerization of thiophene having mesogenic group at 3-position was crucial[18] and several methods have successfully produced characteristic liquid crystalline polythiophenes, respectively.[3,7,19−23] However, the excellent liquid crystalline polythiophenes, in which a fair percentage of insulating parts occupied, have faced a dilemma of sacrificing inherent electrical and optical properties of polythiophene. Replacement of the insulating side chains by semiconducting ones might be a solution and development strategy. Therefore, several conjugated polymers bearing semiconducting side chains have been synthesized and their basic properties were surveyed.[24]

2-Phenylnapthalene derivatives have been received much attention as a calamitic liquid crystalline photoconductor with ambipolar and high carrier transport properties.[25,26] It is considered that calamitic thermotropic liquid crystals are suitable as the side chain of polythiophene that should take a lamellar structure. In this paper, 2,5-dibromothiophene monomer having 2-phenylnaphthalene side chain at 3-position was prepared by two methods. The former is conventional 2,5-polymerization of 3-substituted polythiophenes using $Ni(cod)_2$ known as Yamamoto method[27] under different conditions to

Received: November 8, 2011
Revised: January 27, 2012
Published: February 9, 2012

   dx.doi.org/10.1021/ma202469g | Macromolecules 2012, 45, 1825−1832

give two polythiophenes with different degree of polymerization (**PTPhN1a** and **PTPhN1b**) whose regioregularity of head-to-tail is uncontrolled, and the latter is Ni-catalyzed chain-growth method[28,29] to provide a 3-substituted polythiophene with high regioregularity of head-to-tail conformation, **PTPhN2**, as summarized in Scheme 1. Furthermore, basic properties of these polymers were investigated by comparing their conformations, molecular weights, absorption−emission characteristics, and thermotoropic liquid crystalline behaviors.

Scheme 1. Polymerization Methods

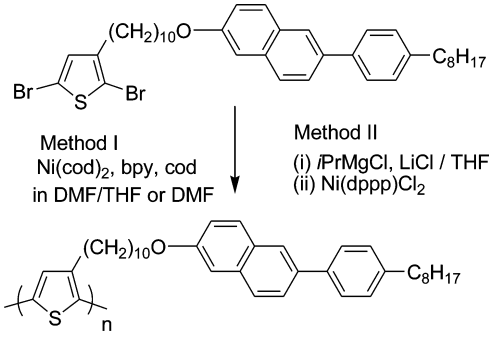

PTPhN1a : Method I (DMF/THF), regiorandom
1b : Method I (DMF), regiorandom
PTPhN2 : Method II, head-to-tail

EXPERIMENTAL SECTION

General Data. Average molecular weights of the polymers were determined by gel permeation chromatography (GPC) calibrated with polystyrene standards using THF as an eluent. ^{1}H and ^{13}C nuclear magnetic resonance (NMR) spectra were measured with a JEOL JNM-ECS 400 at a resonance frequency of 400 MHz for ^{1}H and 100 MHz for ^{13}C in $CDCl_3$ at room temperature. A Bruker AVANCE 600 was also used to measure NMR spectra at a resonance frequency of 600 MHz for ^{1}H and 150 MHz for ^{13}C in chlorobenzene-d_5 at room temperature for **PTPhN1b** and at 120 °C for **PTPhN2**. IR spectra were recorded on a JASCO FT/IR 550 spectrometer. UV−vis absorption and photoluminescence (PL) spectra were recorded on a Shimadzu UV-3100PC and a Hitachi F-4500. The thermal properties of compounds were analyzed by differential scanning calorimetry (DSC) using SII EXSTAR 6000 at a heating/cooling rate of 10 °C min^{-1}. The optical textures of mesophases were observed by a Nikon ECLIPSE E 600 POL and a Nikon ECLIPSE LV 100 polarizing optical microscope (POM) with a Linkam TH-600PM thermocontroller. X-ray diffraction (XRD) measurements were performed using a Rigaku RINT2100 and a PANalytical X'pert diffractometer with Cu−K_α radiation (λ= 1.5418 Å). Electrochemical measurements of drop-cast films of the polymers on an electrode were performed by cyclic voltammetry using a Hokuto Denko HB-305 function generator and a HAL3001 potentiostat equipped with a Pt disk electrode as the working electrode, a Pt plate as a counter electrode, and a saturated calomel electrode (SCE) as a reference electrode. The measurements were carried out at a scanning rate of 50 mV s^{-1} in acetonitrile (0.1 mol dm^{-3} Et_4NBF_4) under an Ar atmosphere. Ionization potentials (vs vacuum) of the polymers were estimated from the onset of their first oxidation peak (E_{onset}) in the cyclic voltammograms on the basis that ferrocene/ferrrocenium is 4.8 eV below the vacuum level.[30,31]

Materials. Following compounds shown in Scheme 2 were prepared according to methods described in a preceding report[24] with a little modification and the experimental details were described in Supporting Information; 2-(10-bromodecyloxy)tetrahydro-2H-pyran (**1**), 3-(10-tetrahydro-2*H*-pyran-2-yloxydecyl)thiophene (**2**), 3-thiophenedecanol (**3**), 2,5-dibromo-3-thiophenedecanol (**4**), 4-octylphenylboronic acid (**5**), 2-Methoxy-6-(4-octylphenyl)naphthalene (**6**). Other chemicals used in this study were purchased from Kanto Chemical Co., Inc., Tokyo Chemical Industry Co., Ltd., Nacalai Tesque Inc., Sigma-Aldrich Co., LLC., Merck & Co., Inc., or Acros Organics of Thermo Fisher Scientifics, and used without further purification unless stated. THF and DMF were purified by distillation according to common methods.

Synthesis. *2-(4-Octylphenyl)-6-hydroxynaphthalene (7).* Into **6** (2.66 g, 7.68 mmol) in dry CH_2Cl_2 (100 mL) boron tribromide (15.3 mL, 1.0 mol dm^{-3} in CH_2Cl_2) was added dropwise under N_2 atmosphere at 0 °C. After stirring at room temperature overnight, water was poured into the reaction solution at 0 °C. The product was extracted with CH_2Cl_2,

Scheme 2. Synthetic Routes of the Compounds

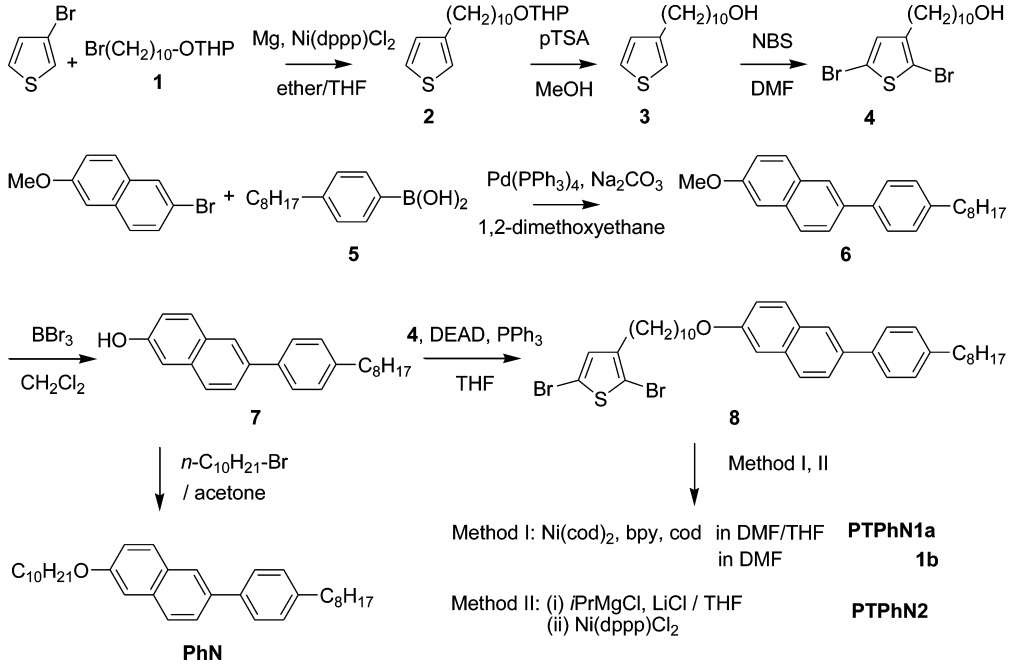

dx.doi.org/10.1021/ma202469g | *Macromolecules* 2012, 45, 1825−1832

washed with aqueous $NaHCO_3$ and water, and dried over anhydrous Na_2SO_4. Recrystallization from toluene gave **7** as a solid product (2.01 g, 78.8% yield). ^{1}H NMR (400 MHz, $CDCl_3$, δ ppm): 0.89 (t, 3H), 1.28 (br, 10H), 1.66 (m, 2H), 2.66 (t, 2H), 5.04 (s, 1H), 7.12 (dd, 1H), 7.17 (d, 1H), 7.28 (d, 2H), 7.61 (d, 2H), 7.68−7.75 (m, 2H), 7.80 (d, 1H), 7.96 (s, 1H). ^{13}C NMR (100 MHz, $CDCl_3$, δ ppm): 14.11, 22.67, 29.27, 29.38, 29.50, 31.53, 31.89, 35.63, 109.29, 118.09, 125.36, 126.25, 126.77, 127.02, 128.89, 129.18, 130.09, 133.61, 136.40, 138.42, 141.99, 153.39.

*2,5-Dibromo-3-{10-[6-(4-octylphenyl)naphthalene-2-yloxy]-decyl}thiophene (**8**).* To a solution of **4** (1.06 g, 2.66 mmol), **7** (0.86 g, 2.59 mmol), and triphenylphosphine (0.85 g, 3.24 mmol) in dry THF (20 mL), diethyl azodicarboxylate (DEAD) (1.5 mL, 40% in toluene) was added at 0 °C, which was stirred at room temperature for 3 days. The product was purified by column chromatography on silica gel (CH_2Cl_2/hexane, 1:1) and recrystallization from acetone, which gave a colorless solid (1.18 g, 62.1% yield). ^{1}H NMR (400 MHz, $CDCl_3$, δ ppm): 0.88 (t, 3H), 1.31 (br, 20H), 1.46−1.57 (m, 4H), 1.66 (m, 2H), 1.85 (m, 2H), 2.50 (t, 2H), 2.65 (t, 2H), 4.08 (t, 2H), 6.77 (s, 1H), 7.13−7.17 (m, 2H), 7.27 (d, 2H), 7.61 (d, 2H), 7.69 (dd, 1H), 7.75−7.78 (m, 2H), 7.94 (d, 1H). ^{13}C NMR (100 MHz, $CDCl_3$, δ ppm): 14.10, 22.67, 26.09, 29.06, 29.24, 29.27, 29.32, 29.37, 29.43, 29.45, 29.50, 29.52, 29.54, 31.53, 31.89, 35.63, 68.05, 106.39, 107.92, 110.29, 119.36, 125.25, 125.93, 127.00, 127.09, 128.87, 129.12, 129.55, 130.95, 133.65, 136.22, 138.51, 141.88, 142.97, 157.14. Anal. Calcd for $C_{38}H_{48}OSBr_2$: C 64.04, H 6.79, N 0.00. Found: C 63.89, H 6.52, N 0.06.

*2-(4-Octylphenyl)-6-decyloxynaphthalene (**PhN**).* 1-Bromodecane (95.0 μL, 0.46 mmol) and **7** (152 mg, 0.46 mmol) in acetone (4 mL) were refluxed for 3 days in the presence of K_2CO_3 (94 mg, 0.68 mmol). The mixture was washed with water/CH_2Cl_2 and the organic layer was dried over anhydrous Na_2SO_4. The product was purified by column chromatography on silica gel (CH_2Cl_2/hexane, 1:1) and recrystallization from hexane, yielding a colorless solid (92 mg, 42.6% yield). ^{1}H NMR (400 MHz, $CDCl_3$, δ ppm): 0.88 (t, 3H), 1.28 (br, 24H), 1.50 (m, 2H), 1.66 (m, 2H), 1.85 (m, 2H), 2.65 (t, 2H), 4.07 (t, 2H), 7.13−7.18 (m, 2H), 7.27 (d, 2H), 7.61 (d, 2H), 7.69 (dd, 1H), 7.76 (d, 2H), 7.94 (d, 1H). ^{13}C NMR (100 MHz, $CDCl_3$, δ ppm): 14.11, 22.67, 26.10, 29.25, 29.27, 29.33, 29.38, 29.42, 29.50, 29.57, 29.59, 31.54, 31.89, 35.62, 68.05, 106.33, 119.36, 125.25, 125.91, 126.99, 127.09, 128.86, 129.09, 129.54, 133.64, 136.18, 138.50, 141.86, 157.14.

*Poly(3-{10-[6-(4-octylphenyl)naphthalene-2-yloxy]decyl}-thiophene-2,5-diyl) (**PTPhN**).* Method I: Nickel bis(cycloocadiene) ($Ni(cod)_2$) (235 mg, 0.85 mmol), 2,2′-bipyridine (bpy) (135 mg, 0.86 mmol), and 1,5-cyclooctadiene (cod) (96 μL, 0.78 mmol) in dry DMF (2 mL) were stirred at room temperature under N_2 atmosphere for 30 min. Then the monomer **8** (297 mg, 0.42 mmol) in dry THF (2 mL) was added into the catalyst solution, which was stirred at 80 °C for 3 days. The reaction mixture was poured into the solution of MeOH containing aqueous HCl, and the resultant precipitate was successively purified by reprecipitation from MeOH and acetone, respectively. **PTPhN1a** was obtained as a yellow solid (220 mg, 95% yield). ^{1}H NMR (400 MHz, $CDCl_3$, δ ppm): 0.88 (br, 3H), 1.15−1.87 (m, 28H), 2.47−2.80 (m, 4H), 3.99 (br, 2H), 6.95−7.20 (m, 3H), 7.20−7.29 (br, 2H), 7.48−7.79 (m, 5H), 7.89 (br, 1H). ^{13}C NMR (100 MHz, $CDCl_3$, δ ppm): 14.11, 22.67, 26.12, 29.28, 29.40, 29.50, 29.59, 30.61, 31.53, 31.89, 35.61, 67.98, 106.26, 119.31, 125.18, 125.84, 126.94, 127.09, 128.82, 129.06, 129.51, 133.63, 136.10, 138.43, 141.80, 157.10.

Similarly, the monomer **8** (205 mg, 0.29 mmol) in dry DMF (3.5 mL) was added into the solution of $Ni(cod)_2$ (252 mg, 0.92 mmol), 2,2′-bipyridine (149 mg, 0.95 mmol), and 1,5-cyclooctadiene (80 μL, 0.58 mmol) in dry DMF (0.7 mL), and the reaction mixture was stirred at 80 °C for 3 days under N_2 atmosphere. The reaction mixture was precipitated from the MeOH containing aqueous HCl solution, and reprecipitated from MeOH and acetone, respectively, affording **PTPhN1b** as a yellow solid (151 mg, 95% yield). NMR spectra of **PTPhN1b** were identical with those of **PTPhN1a**.

Method II: Into the monomer **8** (252 mg, 0.35 mmol) and LiCl (18 mg, 0.4 mmol) in dry THF (1.5 mL), was added *i*PrMgCl (2.0 mol dm^{-3} in THF, 180 μL) at 0 °C, which was stirred at 0 °C for 1 h. After addition of dry THF (2.0 mL), the part of the reaction mixture (0.5 mL) was sampled for analysis of metalated intermediates.[32] Then [1.3-bis(diphenylphosphino)propane]dichloronickel(II) ($Ni(dppp)Cl_2$) (4 mg, 0.008 mmol) was added to the reaction mixture, which was stirred at room temperature overnight. After addition of an aqueous HCl solution, the reaction mixture was extracted with chloroform for several times to obtain a polymer-dispersed organic layer, which was washed with water and dried over $CaCl_2$. The product dissolved in hot *o*-dichlorobenzene was reprecipitated from MeOH, acetone, and chloroform/acetone, affording **PTPhN2** as a purple solid (104 mg, 62% yield). ^{1}H NMR (600 MHz, chlorobenzene-d_5, δ ppm): 0.87 (t, 3H), 1.33 (br, 20H), 1.47 (m, 4H), 1.66 (br, 2H), 1.77 (br, 2H), 2.54 (m), 2.61 (br, 2H), 2.88 (m), 3.99 (br, 2H), 6.96−7.25 (m, 5H), 7.55 (br, 2H), 7.57−7.68 (m, 3H), 7.87 (br, 1H). ^{13}C NMR (150 MHz, chlorobenzene-d_5, δ ppm): 13.94, 22.81, 26.57, 29.48, 29.68, 29.75, 29.87, 29.96, 30.65, 30.82, 31.44, 32.13, 35.93, 68.81, 108.07, 119.59, 125.57, 125.80, 126.12, 126.24, 127.35, 127.48, 128.00, 128.41, 128.50, 128.58, 128.69, 128.77, 128.83, 128.96, 129.10, 129.21, 129.27, 129.43, 129.54, 129.62, 129.83, 130.05, 134.42, 135.50, 134.85, 136.859, 139.19, 141.99, 157.96.

Estimation of Regioregularity and Degree of Polymerization by ^{1}H NMR. Regioregularity (rr) of the 3-substituted polythiophenes (content of head-to-tail linkages in the polymer chains) was estimated from integration values of α-methylene proton signals of a head-to-tail linkage at about 2.8 ppm (I_{ht}) and a head-to-head linkage at about 2.58 ppm (I_{hh}) using an equation, $rr = I_{ht}/(I_{ht} + I_{hh})$, by ^{1}H NMR analysis.[33] Practically, in the cases of **PTPHN1a** and **PTPHN1b** measured in $CDCl_3$ with the JEOL JNM-ECS 400, I_{hh} was roughly determined by subtracting overlapping integration of α-methylene protons (2H) at 2.61 ppm of the (4-octylphenyl)naphthalene moiety from total integration of signals in the region of 2.47−2.65 ppm. In the cases of ^{1}H NMR analysis of **PTPHN1b** and **PTPHN2** in chrorobenzene-d_5 measured with the Bruker AVANCE 600, rr was more properly calculated using eq 1 with I'_{ht} (2.95−2.77 ppm), I'_{hh} (2.77−2.65 ppm), and an integration value of α-methylene protons of polymer terminals (I'_{term}) (2.58−2.40 ppm).[34,35] Similarly, number-average degree of polymerizations (dp) of **PTPHN1b** and **PTPHN2** were estimated using eq 2 with these integration values.

$$rr = I'_{ht}/(I'_{ht} + I'_{hh} + I'_{term}) \quad (1)$$

$$dp = (I'_{ht} + I'_{hh} + I'_{term})/I'_{term} \quad (2)$$

RESULTS AND DISCUSSION

Synthesis. Synthetic routes for the monomer **8**, model liquid crystal (**PhN**), and polymers (**PTPhN**) are summarized in Scheme 2. 2,5-Dibromothiophene derivative **4** was synthesized from 3-bromothiophene and the THP protected 10-bromodecanol **1** by Kumada−Tamao−Corriu cross coupling,[36] followed by dibromination with NBS. On the other hand, phenylnaphthalene derivative **7** was prepared from 2-bromo-6-methoxynaphthalene and **5** by Suzuki−Miyaura cross coupling[37] and successive ether cleavage reaction. The monomer **8** was synthesized from the thiophene moiety **4** and phenylnaphthalene moiety **7** by Mitsunobu reaction.[38] The model liquid crystal, 2-phenylnaphthalene derivative **PhN**, was also synthesized by Williamson reaction of 1-bromodecane and **7** for the purpose of comparison with the polymers. **PTPhN1a** and **PTPhN1b** were obtained by polymerization of the monomer **8** by Yamamoto method[27] (method I) in DMF-THF and in DMF, respectively. **PTPhN2** was obtained from the same monomer **8** by Ni-catalyzed chain-growth polymerization method[28,29] (method II).

General Properties. The polymerization results and average molecular weights and rr of **PTPhN1** and **PTPhN2** are summarized in Table 1. **PTPhN1a** and **PTPhN1b** exhibited good solubility for organic solvents such as chloroform and THF at room temperature, while **PTPhN2** was insoluble in such solvents, but soluble in hot chlorobenzene or hot *o*-dichlorobenzene. The GPC analysis showed that the number-average molecular weight (M_n) and polydispersity (M_w/M_n) were 6300 g mol^{-1} and 1.24 for **PTPhN1a** and 8400 g mol^{-1} and 1.62 for **PTPhN1b**, respectively. GPC analysis of **PTPhN2** was not carried out because of the insolubility for the THF eluent. Head-to-tail content (rr) of **PTPhN1** could be roughly estimated to be about 30% from ^{1}H NMR spectra at 400 MHz in $CDCl_3$ in the region of 2.2−3.2 ppm for α-methylene protons of 3-substituted polythiophene. In order to compare rr between **PTPHN1** and **PTPHN2**, it was precisely examined by 600 MHz ^{1}H NMR in chlorobenzene-d_5 at room temperature for **PTPhN1b** and at 120 °C for **PTPhN2** (Figure 1). A sharp and strong peak at about 2.61 ppm is assigned to α-methylene protons of the 4-octylphenylnaphthalene moiety (B), and the other signals are due to α-methylene protons of the 3-substituent moiety of various thiophene units (A). Signals observed between 2.95 and 2.76 ppm (A_1), 2.76−2.65 ppm (A_2), and 2.58−2.40 ppm (A_3) are assigned to regioregular units, regioirregular ones and chain-end ones, respectively.[33−35] From these integration areas, rr of **PTPhN1b** and **PTPhN2** could be estimated from eq 1 (see Experimental Section) to be 29.9% and 76.3% . On the basis of this NMR analysis, number-average degree of polymerization (dp) and M_n of **PTPhN1b** and **PTPhN2** can be estimated using eq 2 with these integration values (see Experimantal Section). Interestingly, M_n values of two polymers estimated by NMR are in the range of 4000−5000 g mol^{-1} and are not so much different. Considerable difference between M_n for **PTPhN1b** obtained by respective two methods is due to overestimation of M_n usually observed in rigid poly(3-alkylthiophene)s by GPC.[39]

Consequently, the characteristic poor solubility of **PTPhN2** compared to **PTPhN1** was suggested to be caused by the higher rr, probably which caused strong intermolecular interaction between the main chains and side chains. Other than the NMR investigation, the good rr for **PTPhN2** is also supported by the fact that an intermediate, 3-substituted 2-bromo-5-chloromagnesiothiophene, produced 4 times larger than a 5-bromo-2-chloromagnesio derivative in the initial stage.[32] which was confirmed by ^{1}H NMR analysis of the sampling according to the procedure described in the Experimental Section. The poor solubility of **PTPhN2** brought about precipitation of polymeric products in an early stage of polymerization, which rather lowered dp than expected from the molar ratio of the monomer/Ni catalyst about 44 and at the same time lowered rr.

Table 1. Polymerization Results and Average Molecular Weights and Regioregularity of the Polymers

polymer	yield/%	M_n/g mol^{-1} (M_w/M_n)	dp[a]	rr/%[b]
PTPhN1a	95	6300 (1.24)[c]	11.4[c]	(30)
PTPhN1b	95	8400 (1.62),[c] 4650[d]	15.2,[c] 8.4[d]	29.9 (30)
PTPhN2	62	4090[d]	7.4[d]	76.3

[a]Number-average degree of polymerization. [b]Regioregularity determined by 600 MHz (and 400 MHz) ^{1}H NMR. [c]Determined by GPC. [d]Determined by ^{1}H NMR.

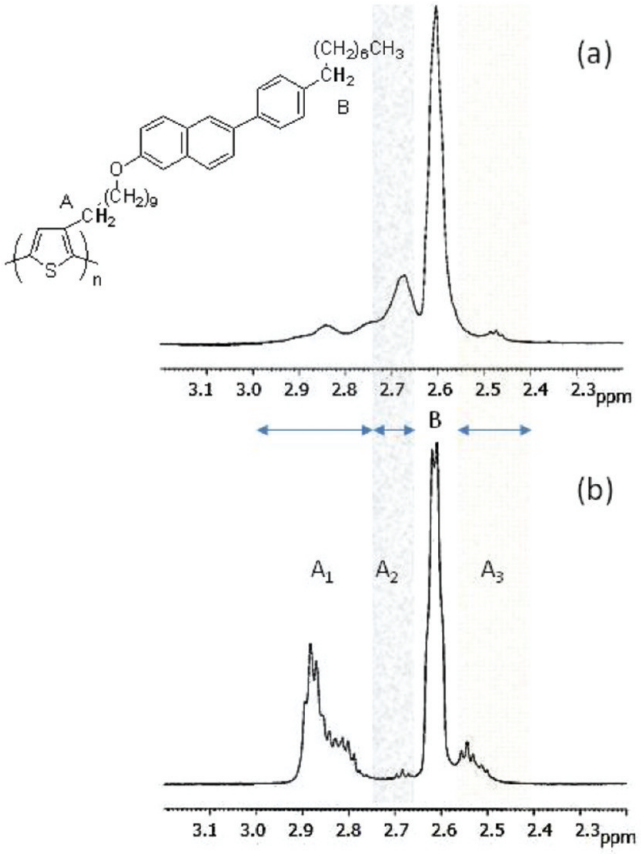

Figure 1. ^{1}H NMR (600 MHz) spectra of **PTPhN1b** (a) at room temperature and **PTPhN2** (b) at 120 °C in chlorobenzene-d_5 in the range 2.2−3.2 ppm.

Photoabsorption and Fluorescence Properties. UV−vis absorption spectra of the polymers in solution and in thin solid film state are shown in Figure 2 and Figure 3, and their optical data of absorption and PL are summarized in Table 2. Absorption spectra of **PTPhN1a** and **PTPhN1b** were basically same in solution and in film state, and showed two characteristic absorption bands due to $\pi-\pi^*$ transition of the phenylnaphthalene moiety in the ultraviolet region around 300 nm and polythiophene backbones in the visible light region around 385 nm. The assignment is considered reasonable in comparison with spectrum of **PhN** shown in Figure 2. The

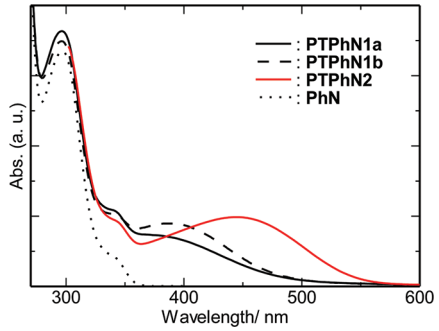

Figure 2. Normalized UV−vis spectra of chloroform solutions of **PTPhN1a** (black solid line), **PTPhN1b** (black dashed line), **PhN** (black dotted line), and an *o*-dichlorobenzene solution of **PTPhN2** (red solid line).

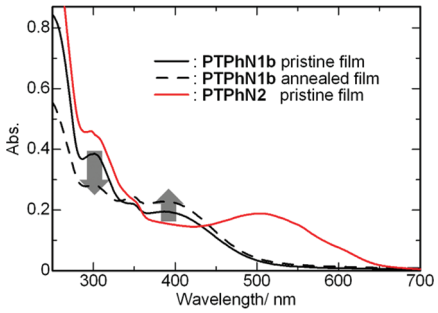

Figure 3. UV−vis spectra of a pristine film (black solid line) and an annealed film heat treated at 140 °C (black dashed line) of **PTPhN1b** and pristine film of **PTPhN2** (red solid line, *y* axis is Abs. (arbitrary unit)) on a quartz glass plate.

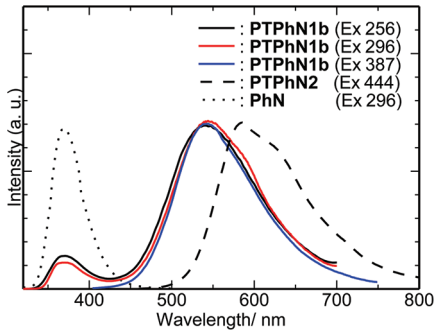

Figure 4. Normalized PL spectra of chloroform solutions of **PTPhN1b** excited at 256 nm (black solid line), 296 nm (red solid line), 387 nm (blue solid line), **PhN** excited at 296 nm (black dotted line), and *o*-dichlorobenzene solution of **PTPhN2** excited at 444 nm (black dashed line).

latter band observed in the region rather blue-shifted than usual 3-substituted polythiophenes and little difference between absorption λ_{max} in solution and film state suggest that π-conjugation of the polythiophene backbones is significantly restricted by the large side chains and their rr. A little bathochromic and hyperchromic shift of the latter band observed for **PTPhN1b** by comparison with **PTPhN1a** is due to longer π-conjugation of the higher molecular weight polymer. These results suggest that polymerization performed successfully. In contrast, the latter band of **PTPhN2** was considerably bathochromic shifted compared to **PTPhN1** especially in the film states. The absorption λ_{max} of **PTPhN2** in $CHCl_3$ (444 nm) suggests that the $\pi-\pi^*$ transition energy is lower than those of regioirregular poly(3-alkylthiophene)s (λ_{max} = 428 nm)[33] and a regioregular octamer of 3-octylthiophene (λ_{max} = 422 nm)[40] and higher than that of regioregular poly(3-hexylthiophene (λ_{max} = 456 nm),[33] Considering this, the optical characteristic of **PTPhN2** is basically corresponding to the estimated rr (76.3%) and dp (7.4). Optical bandgaps (E_g) between energy levels of highest occupied molecular orbital (E_{HOMO}) and the lowest unoccupied molecular orbital (E_{LUMO}) of **PTPhN1** and **PTPhN2** estimated from absorption edge in the film state were 2.25 and 1.86 eV, respectively. E_{HOMO} of **PTPhN1a** and **PTPhN1b** were estimated at about −5.50 eV from onset oxidation potential of their cyclic voltammograms, and consequently, E_{LUMO} were calculated being about −3.25 eV from the values of E_g and E_{HOMO}. In the same way, E_{HOMO} and E_{LUMO} of **PTPhN2** were estimated to be −5.34 and −3.46 eV. These results indicate that **PTPhN2** has not only the narrower E_g but also larger electron accepting ability and lower ionization ability than **PTPhN1**.

When **PTPhN1** are excited with light energies at 256, 296, and 387 nm, they showed a characteristic emission band around 540 nm in chloroform (Figure 4) and 550 nm in the film state. The PL band is due to emission from the polythiophene backbone and not from the phenylnaphthalene moiety, which can be confirmed by comparing with PL spectra of poly(3-hexylthiophene) polymerized under the same conditions (λ_{max} = 550 nm in chloroform) and **PhN** (λ_{max} = 369 nm in chloroform). This result suggests that Förster resonance energy transfer[41] efficiently occurs from the phenylnaphthalene side group to the polythiophene backbone in the solution and film states taking into consideration that the PL band of the phenylnaphthalene side group overlaps with the absorption band of the polythiophene main chain. On the other hand, **PTPhN2** showed an emission peak from polythiophene backbones at 585 nm in solution and 720 nm in film state, which are almost same with those of regioregular poly(3-hexylthiophene).[33]

Liquid Crystalline Behavior. Thermal behavior of **PTPhN** and **PhN** was investigated by temperature-controlled POM and DSC, and the DSC thermograms are shown in Figure 5 and phase transition temperatures and changes of enthalpy (ΔH) of the polymers and **PhN** are summarized in Table 3. The DSC analysis showed that the phase transitions for **PTPhN1a** and **PTPhN1b** were enantiotropic. The POM analysis revealed that all mesophases of **PTPhN1** showed fan-shaped textures typical of smectic phases (Sm), and sizes of domains were respectively large about several tens of μm regardless of their different average size of molecular weights (Figure 6a,b). **PTPhN1a** made a fan-shaped texture at around 115 °C under heating process, and it was changed into a broken one at about 122 °C. Further heating to 149 °C led to disappearance of the birefringence, which corresponds to transition into isotropic liquid phase (Iso). On the other hand, **PTPhN1b** showed one distinct smectic liquid crystalline phase, and the phase transition temperatures of glass phase (G)-Sm and Sm-Iso were higher than those of **PTPhN1a**. These results suggest that the higher molecular weight heightens phase transition temperatures of **PTPhN1**, while the higher polydispersity

Table 2. Optical Properties and Energy Levels of the Polymers

	UV−vis λ_{max}/nm		PL λ_{max}/nm				
polymer	solution	film[c]	solution	film[c]	E_g/eV[d]	E_{HOMO}/eV[e]	E_{LUMO}/eV[f]
PTPhN1a	385[a]	386	534[a]	550	2.25	−5.51	−3.26
PTPhN1b	387[a]	387	541[a]	559	2.25	−5.50	−3.26
PTPhN2	444[b]	509	585[b]	720	1.86	−5.34	−3.46

[a]In chloroform. [b]In *o*-dichlorobenzene. [c]Drop-cast films on a quartz plate. [d]Calculated from absorption edge of the films. [e]Estimated from onset of the oxidation peak from cyclic voltammerty. [f]Calculated from HOMO level and the optical bandgap.

dx.doi.org/10.1021/ma202469g | *Macromolecules* 2012, 45, 1825−1832

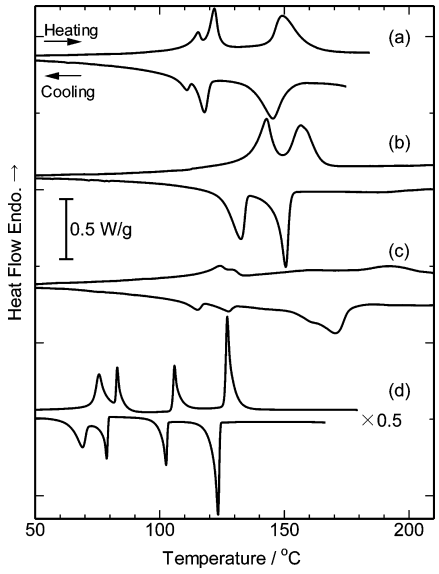

Figure 5. DSC thermograms of **PTPhN1a** (a), **PTPhN1b** (b), **PTPhN2** (c), and **PhN** (d) in the second sweeps with a scan rate of 10 °C min^{-1}.

Table 3. Phase Transition Temperatures and Changes of Enthalpy of Compounds[a,b]

	phase transition temperature/°C (ΔH /J g^{-1})[c]	
compound	heating process	cooling process
PTPhN1a	G 115 (6.7) SmE 122 (10.4) SmA 149 (19.9) Iso	Iso 146 (−19.4) SmA 118 (−8.2) SmE 111 (−5.9) G
PTPhN1b	G 143 (19.9) Sm 157 (16.7) Iso	Iso 151 (−17.4) Sm 132 (−16.3) G
PTPhN2	G 124[d] Sm 192[d] Iso	Iso 171[d] Sm 115[d] G
PhN	K 76 (16.1) SmE 83 (7.9) SmB 106 (9.8) SmA 127 (21.4) Iso	Iso 123 (−21.5) SmA 103 (−8.4) SmB 79 (−10.1) SmE 69 (−15.6) K

[a]Abbreviations: K, crystal; G, glass state; SmA, B, E, defined smectic phases as A, B, E; Sm, unresolved smectic phases; Iso, isotropic liquid. [b]Liquid crystalline phases were determined by DSC, POM, and XRD. [c]Determined from second DSC traces at a scan rate of 10 °C min^{-1}. [d]Approximate transition temperatures of undefined mesophases.

makes phase transitions indistinct. Meanwhile, **PTPhN2** did not show any distinct mesophases both in DSC and POM analyses, and the observed POM texture was a polygonal (Figure 6c). This is ascribed to the strengthened interactions between main chains as well as side mesogenic groups caused by the high rr.

The phase transition behaviors of **PTPhN1** thought to be dominantly affected by liquid crystalline properties of the phenylnaphthalene side chain. As listed in Table 3, **PhN** showed three enantiotropic smectic phases (SmE, SmB, SmA) between crystal phase (K) and Iso, whose behavior is similar to those of series of phenylnaphthalene liquid crystals reported previously.[42] The ΔH of phase transition from Sm to Iso was within 17−20 J g^{-1} for **PTPhN1** and 21 J g^{-1} for **PhN**, which approximately equated to 10 kJ mol^{-1}. Although **PTPhN1a** and **PTPhN1b** had different phase transition temperatures and different number of distinct mesophases, their total ΔH between G and Iso are almost equal to 37 J g^{-1} in the heating process and −34 J g^{-1} in the cooling one. These results suggest that similar change of molecular arrangement occurs at the side chain moieties in **PTPhN1** between the states of G and Iso.

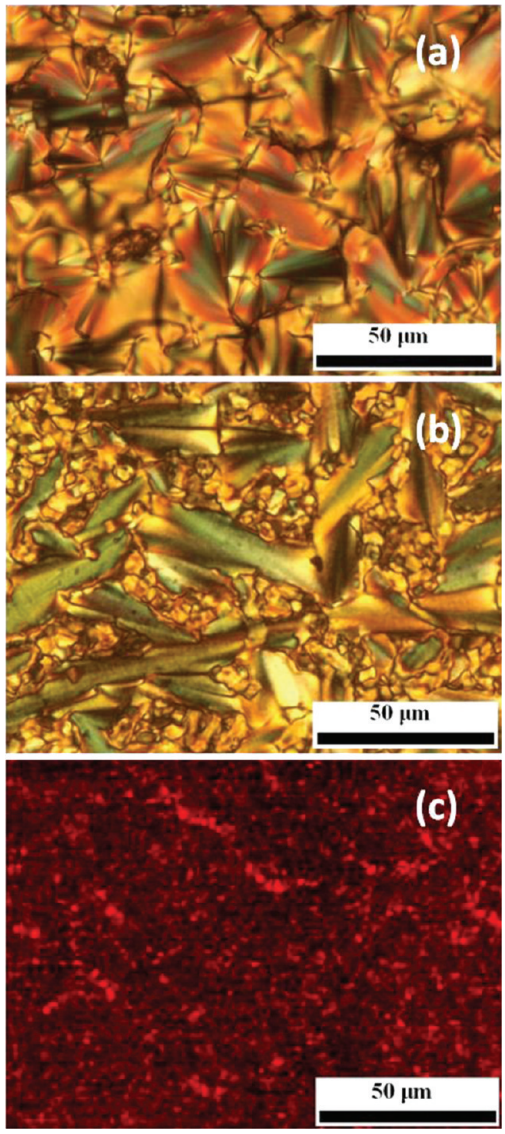

Figure 6. Polarized optical micrographs of **PTPhN1a** at 128 °C in the heating process (a), **PTPhN1b** at room temperature after isotropic phase transition, annealing at 140 °C, and successive rapid cooling (b), and **PTPhN2** at room temperature after isotropic phase transition, annealing at 150 °C, and rapid cooling (c).

A typical molecular arrangement of **PTPhN1** was predicted from X-ray diffraction (XRD) observations of a pristine drop-cast film and an annealed sample of **PTPhN1b** on a Si substrate. The annealed sample was prepared by heat-treating at 175 °C (Iso) of the pristine film, cooling down and annealing at 140 °C (Sm) for several minutes, and rapidly cooling down to room temperature in a G state. As shown in Figure 7, the polymer film samples showed two characteristic XRD signal patterns, and the annealing sharpened and intensified both signals with enhancement of molecular arrangements. The former is a series of sharp peaks at $2\theta = 2.5°$ ($c \approx 35$ Å), 4.8 and 7.4 due to a layered distance of the phenylnaphthalene side chains, which is assigned to Miller indices, (001)−(003). The layer spacing of ca. 35 Å is almost corresponding to a length of the side chain moiety in the most extended conformation. As a result, the layered distance should be equivalent to interchain distance of the polythiophene backbones. The latter is distinct peaks at $2\theta = 19.3°$ and 20.7° on broad multiple signals around

dx.doi.org/10.1021/ma202469g | *Macromolecules* 2012, 45, 1825−1832

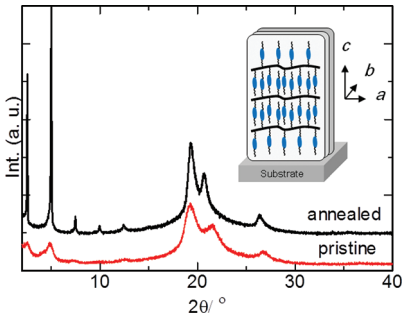

Figure 7. XRD spectra of pristine (red) and annealed (black) films of **PTPhN1b** and a suggested molecular arrangement.

15−30°, which is sum of the signals due to distances of phenylnaphthalene moieties taking SmE domains involving reflections such as (200), (020), (110), (220) with lattice constants of a = 9.2 Å and b = 8.6 Å. Therefore, a layered π-stacked distance between polythiophene sheets should come to be 4.3 Å. **PTPhN1a** and **PTPhN2** in G state basically showed same XRD signal pattern of the pristine film of **PTPhN1b**. In addition, heat treatment of **PTPhN1a** at 125 °C changed the pattern to typical of SmA showing a layer distance (36 Å) read from a sharp peak at 2θ = 4.8° and an intermolecular distance (4.6 Å) between the mesogenic side chains read from a broad signal at 2θ = 19.3°, while the pattern was almost invariant against thermal annealing for **PTPhN2**.

Furthermore, comparison of the UV−vis absorption spectra of the pristine and annealed films of **PTPhN1b** (Figure 3) showed that the annealed film had a stronger absorbance at around 400 nm due to the polythiophene backbone and weaker absorbances at around 250 and 300 nm due to the phenylnaphthalene moiety relative to those of the pristine film. These results also support the molecular orientation of **PTPhN1** illustrated in Figure 7, because the perpendicular oriented phenylnaphthalene moiety on a substrate hard to absorb perpendicular incident radiation and, in contrast, the parallel oriented polythiopehene backbones with torsion angles in some degree are favorable for the light absorption.

CONCLUSIONS

2-Phenylnaphthalene liquid crystals that are ambipolar carrier transporting semiconductor were introduced into 3-position of thiophene as the side chain functionality. The synthesized thiophene monomer was polymerized by Yamamoto method using $Ni(cod)_2$,[27] and also polymerized by chain-growth method using $Ni(dppp)Cl_2$.[28,29] **PTPhN1a** and **PTPhN1b** prepared by the former method under the different conditions were well soluble in organic solvents, and the observed general characteristics of M_n (6000−9000 g mol^{-1}), absorption λ_{max} (ca. 385 nm), and PL emission λ_{max} (530−560 nm) were ordinary for 3-substituted polythiophenes obtained by this method. PL spectral analysis of **PTPhN1** in solution and solid states suggested that energy transfer from the phenylnaphthalene side-chain to the polythiophene backbone effectively occurred by the Förster mechanism. **PTPhN1** showed smectic mesophases between G and Iso in the enantiotropic phase transitions. From the total ΔH of phase transitions, changes of molecular arrangements of **PTPhN1** along the phase transitions were revealed to be intrinsically same, while their transition temperatures were different. The molecular arrangement of **PTPhN1b** in the liquid crystalline phase was examined by XRD and UV−vis spectroscopies with a cooled sample in glassy state. The patterns of XRD signals and the anisotropy of UV−vis absorbance suggested that the phenylnaphthalene side chains vertically oriented against to the polythiophene backbones to construct a polymer array. The observed distance of smectic layer ($c \approx 35$ Å) of the side chains is thought to correspond to the distance between the polythiophene backbones. In addition, a lamellar structure made by sheets of the rigid polymer backbones and interdigitated flexible side chains are suggested to take a SmE arrangement. Consequently, the arrayed **PTPhN1** in the smectic states are expected to be reflected by the semiconducting characteristics of phenylnaphthalene liquid crystals,[25,26,42] because the mesophases observed for **PTPhN** are basically caused by aggregation of the phenylnaphthalene side chains. On the other hand, **PTPhN2** prepared by the latter method is expected to have good photoabsorption and semiconducting characteristics due to the fairly high regioregularity of polythiophene backbones. However, this attempt brought about production of the extremely low soluble polymer and its phase transition behaviors were obscure as observed in DSC and POM in spite of having M_n comparable to **PTPhN1**, which is a dilemma should be overcome by considering intermolecular interactions between polymer main chains as well as side groups.

ASSOCIATED CONTENT

Supporting Information

Synthetic procedures of compounds (**1**−**6**) and ^1H NMR spectra of the polymers. This material is available free of charge via the Internet at http://pubs.acs.org.

AUTHOR INFORMATION

Corresponding Author

*Fax: +81-29-853-4490. Telephone: +81-29-853-6905. E-mail: kijima@ims.tsukuba.ac.jp.

Notes

The authors declare no competing financial interest.

ACKNOWLEDGMENTS

The authors thank Dr. H. Goto, University of Tsukuba, for the use of GPC and polarizing microscopes, and Chemical Analysis Division, Research Facility Center for Science and Technology, University of Tsukuba, for facilities of the NMR, elemental analysis, DSC, UV−vis, and PL measurements.

REFERENCES

(1) Akagi, K. *J. Polym. Sci., Part A, Polym. Chem.* **2009**, *47*, 2463−2485.
(2) Abe, S.; Kijima, M.; Shirakawa, H. *J. Mater. Chem.* **2000**, *10*, 1509−1510.
(3) Chien, L.; Chien, Y.; Zhou, D.; Zha, F.; Li, D.; Yao, K. *Macromol. Chem. Phys.* **2011**, *212*, 24−41.
(4) Bao, Z.; Chen, Y.; Cai, R.; Yu, L. *Macromolecules* **1993**, *26*, 5281−5286.
(5) Neher, D. *Macromol. Rapid Commun.* **2001**, *22*, 1365−1385.
(6) Goto, H.; Akagi, K.; Shirakawa, H.; Oh, S.; Araya, K. *Synth. Met.* **1995**, *71*, 1899−1900.
(7) Osaka, I.; Goto, H.; Itoh, K.; Akagi, K. *Synth. Met.* **2001**, *119*, 541−542.
(8) Geng, J.; Zhou, E.; Li, G.; Lam, J. W. Y.; Tang, B. Z. *J. Polym. Sci., Part B, Polym. Phys.* **2004**, *42*, 1333−1341.
(9) Andersson, M. R.; Thomas, O.; Mammo, W.; Svensson, M.; Theander, M.; Inganäs, O. *J. Mater. Chem.* **1999**, *9*, 1933−1940.

(10) Ahn, S. -H.; Czae, M.; Kim, E. -R.; Lee, H. *Macromolecules* **2001**, *34*, 2522−2527.
(11) Evenson, S. J.; Mumm, M. J.; Pokhodnya, K. I.; Rasmussen, S. C. *Macromolecules* **2011**, *44*, 835−841.
(12) Park, S. H.; Roy, A.; Beaupré, S.; Cho, S.; Coates, N.; Moon, J. S.; Moses, D.; Leclerc, M.; Lee, K.; Heeger, A. J. *Nat. Photonics* **2009**, *3*, 297−303.
(13) Biniek, L.; Chochos, C. L.; Leclerc, N.; Hadziioannou, G.; Kallitsis, J. K.; Bechara, R.; Lévêque, P.; Heiser, T. *J. Mater. Chem.* **2009**, *19*, 4946−4951.
(14) Piliego, C.; Holcombe, T. W.; Douglas, J. D.; Woo, C. H.; Beaujuge, P. M.; Fréchet, J. M. J. *J. Am. Chem. Soc.* **2010**, *132*, 7595−7597.
(15) Liang, Y.; Yu, L. *Acc. Chem. Res.* **2010**, *43*, 1227−1236.
(16) Liu, J.; Zhang, R.; Sauvé, G.; Kowalewski, T.; McCullough, R. D. *J. Am. Chem. Soc.* **2008**, *130*, 13167−13176.
(17) Rieger, R.; Beckmann, D.; Pisula, W.; Steffen, W.; Kastled, M.; Müllen, K. *Adv. Mater.* **2010**, *22*, 83−86.
(18) Kijima, M.; Akagi, K.; Shirakawa, H. *Synth. Met.* **1997**, *84*, 237−238.
(19) Koide, N.; Iida, H. *Mol. Cryst. Liq. Cryst.* **1995**, *261*, 427−436.
(20) Osaka, I.; Shibata, S.; Toyoshima, R.; Akagi, K.; Shirakawa, H. *Synth. Met.* **1999**, *102*, 1437−1438.
(21) Kohono, H.; Saitoh, F.; Miyahara, T.; Koide, N. *Polym. J.* **2003**, *35*, 945−950.
(22) Goto, H.; Dai, X.; Narihiro, H.; Akagi, K. *Macromolecules* **2004**, *37*, 2353−2362.
(23) Tahar-Djebbar, I.; Nekelson, F.; Heinrich, B.; Donnio, B.; Guillon, D.; Kreher, D.; Mathevet, F.; Attias, A. *Chem. Mater.* **2011**, *23*, 4653−4656.
(24) Tsuchiya, K.; Oikawa, K.; Yamazaki, H.; Kijima, M.; Abe, S. *Jpn. Kokai Tokkyo Koho* JP 2005008860 A 20050113, 2005.
(25) Funahashi, M.; Hanna, J. *Appl. Phys. Lett.* **1997**, *71*, 602−604.
(26) Funahashi, M.; Hanna, J. *Appl. Phys. Lett.* **1998**, *73*, 3733−3735.
(27) Yamamoto, T.; Morita, A.; Miyazaki, Y.; Maruyama, T.; Wakayama, H.; Zhou, Z.; Nakamur, Y.; Kanbara, T. *Macromolecules* **1992**, *25*, 1214−1223.
(28) Iovu, M. C.; Sheina, E. E.; Gil, R. R.; McCullough, R. D. *Macromolecules* **2005**, *38*, 8649−8656.
(29) Miyakoshi, R.; Yokoyama, A.; Yokozawa, T. *J. Am. Chem. Soc.* **2005**, *127*, 17542−17547.
(30) Pommerehne, J.; Vestweber, H.; Guss, W.; Mahrt, R. F.; Bässler, H.; Porsch, M.; Daub, J. *Adv. Mater.* **1995**, *7*, 551−554.
(31) Agrawal, A. K.; Jenekhe, S. A. *Chem. Mater.* **1996**, *8*, 579−589.
(32) Loewe, R. S.; Ewbank, P. C.; Liu, J.; Zhai, L.; McCullough, R. D. *Macromolecules* **2001**, *34*, 4324−4333.
(33) Chen, T.; Wu, X.; Rieke, R. D. *J. Am. Chem. Soc.* **1995**, *117*, 233−244.
(34) Bras, J.; Pépin-Donat, B. *Magn. Reson. Chem.* **2001**, *39*, S7−67.
(35) Beryozkina, T.; Senkovskyy, V.; Kaul, E.; Kiriy, A. *Macromolecules* **2008**, *41*, 7817−7823.
(36) Tamao, K.; Kodama, S.; Nakajima, I.; Kumada, M. *Tetrahedron* **1982**, *38*, 3347−3354.
(37) Miyaura, N.; Suzuki, A. *Chem. Rev.* **1995**, *95*, 2457−2483.
(38) Mitsunobu, O.; Yamada, M. *Bull. Chem. Soc. Jpn.* **1967**, *40*, 2380−2382.
(39) Liu, J.; Loewe, R. S.; McCullough, R. D. *Macromolecules* **1999**, *32*, 5777−5785.
(40) Zak, Z.; Lapkowski, M.; Guillerez, S.; Bidan, G. *Synth. Met.* **2001**, *152*, 185−188.
(41) Förster, T. *Ann. Phys.* **1948**, *437*, 55−75.
(42) Maeda, H.; Funahashi, M.; Hanna, J. *Mol. Cryst. Liq. Cryst.* **2000**, *346*, 183−192.

Macromolecules

Article

pubs.acs.org/Macromolecules

High Open-Circuit Voltage Solar Cells Based on New Thieno[3,4-*c*]pyrrole-4,6-dione and 2,7-Carbazole Copolymers

Ahmed Najari,[†] Philippe Berrouard,[†] Chiara Ottone,[‡] Mathieu Boivin,[§] Yingping Zou,[†,⊥] David Gendron,[†] William-Olivier Caron,[†] Philippe Legros,[†] Claudine N. Allen,[§] Saïd Sadki,[‡] and Mario Leclerc*[,†]

[†]Canada Research Chair on Electroactive and Photoactive Polymers, Department of Chemistry, Université Laval, Quebec City, (Quebec), Canada G1V 0A6

[‡]INAC, UMR 5819-SPrAM (CEA, CNRS, Univ. J. Fourier-Grenoble I), LEMOH, F- 38054 Grenoble, France

[§]Centre d'optique, photonique et laser (COPL), Département de physique, de génie physique et d'optique, Université Laval, Québec (Québec), Canada, G1V 0A6

[⊥]College of Chemistry and Chemical Engineering, Central South University, Changsha 410083, China

Supporting Information

ABSTRACT: New alternating copolymers derived from thieno-[3,4-*c*]pyrrole-4,6-dione (TPD) and 2,7-carbazole moieties have been synthesized by Suzuki cross-coupling reaction and characterized. These polymers combine interesting properties such as good solubility and excellent thermal and air stability. The present studies indicate that the combination of TPD and 2,7-carbazole building blocks can be a very effective way to lower the HOMO energy level and ultimately to enhance the V_{oc} of polymer solar cells. The V_{oc} reported here (up to 1.07 V) is one of the highest observed for polymer:[60]PCBM bulk heterojunction devices, and preliminary results on the photovoltaic devices (power conversion efficiencies up to 1.8%) indicate that performance could probably be improved by increasing the molecular weights and by fine-tuning the electronic properties and the morphology.

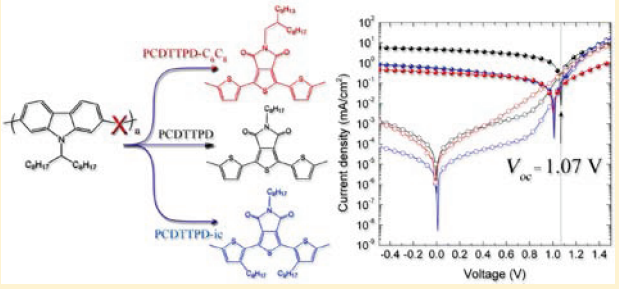

INTRODUCTION

Polymer bulk heterojunction (BHJ) solar cells offer a compelling option for tomorrow's photovoltaics due to many interesting features such as low cost, light weight, and flexibility.[1−3] BHJ solar cells based on the blends of regioregular poly(3-hexylthiophene)s (P3HT) and [6,6]-phenyl C61-butyric acid methyl ester ([60]PCBM) have been investigated extensively in the past decade, and power conversion efficiencies (PCE)s as high as 4−5% have been reported.[4−6] However, the PCE is critically limited by the relatively low open-circuit voltage (V_{oc} ≈ 0.5−0.6 V). Usually, the V_{oc} originates from the energy difference between the highest occupied molecular orbital (HOMO) of the polymer and the lowest unoccupied molecular orbital (LUMO) of the fullerene derivative.[7] Therefore, polymers with a deep HOMO level will potentially lead to an enhanced V_{oc} and a possibly higher PCE when blended with PCBM. Along these lines, some push−pull copolymers based on 2,7-carbazole derivatives have demonstrated promising potential as photovoltaic materials.[8−11] Among them, poly(*N*-9′-heptadecanyl-2,7-carbazole-*alt*-5,5-(4′,7′-dithienyl-2′,1′,3′-benzothiadiazole) (PCDTBT) has a low-lying HOMO energy level of −5.5 eV, showing a V_{oc} of 0.9 V when mixed with [70]PCBM. Tao et al. have achieved a PCE of 7.1% using PCDTBT:[70]PCBM on an area of 1.0 cm^2.[12] Also, Heeger et al. reported a PCE of 7.2% based on PCDTBT and using [70]PCBM as electron acceptor, TiO_X as an optical spacer, and a structured antireflection coating.[13]

Because the HOMO level of alternating push−pull copolymers is mainly determined by the donor moiety, the relatively low-lying HOMO energy level of PCDTBT seems to be related to the presence of the weak electron-donating carbazole unit. Indeed, when this moiety is copolymerized with different electron-withdrawing units as benzothiadiazole BT,[8,9,12,13] 1,4-diketopyrrolopyrrole (DPP),[10,14] or pyridine derivatives,[9] the HOMO energy levels of the resulting copolymers remain most of the time between −5.3 and −5.5 eV. For all these reasons, the 2,7-carbazole unit can be an excellent candidate to generate a high V_{oc} in bulk heterojunction polymer solar cells.

In parallel, thieno[3,4-*c*]pyrrole-4,6-dione (TPD)-based polymers were first introduced by Tour and Zhang,[15] and recently, Leclerc et al. have reported for the first time the use of these copolymers in solar cells.[16] For instance, the electron-withdrawing TPD moiety copolymerized with an electron-donating benzo[1,2-*b*;3,4-*b*]dithiophene (BDT) unit presented a HOMO energy level (−5.56 eV) which led to a V_{oc} of 0.85 V

Received: November 21, 2011
Revised: January 29, 2012
Published: February 9, 2012

Scheme 1. Synthesis of Polymers

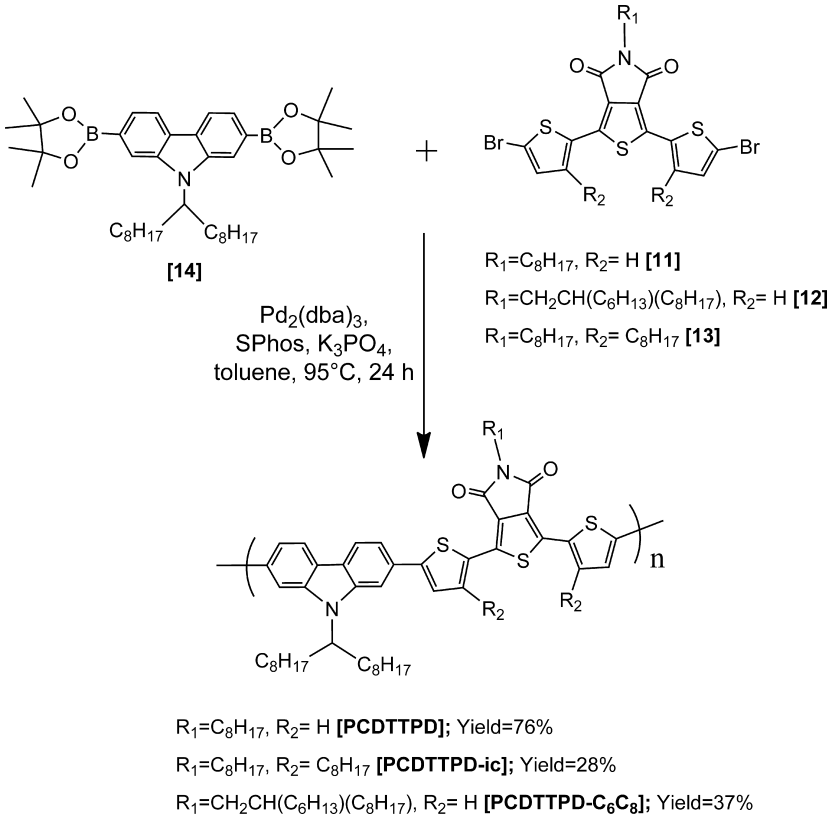

in the resulting photovoltaic devices.[17] By using the same polymer, Fréchet et al.[18] reported a power conversion efficiency up to 6.8% with the addition of 1,8-diiodooctane (DIO) during the processing of the film. Tao et al.[19] achieved a PCE of 7.3% (V_{oc} of 0.88 V) with a new copolymer made of dithienosilole and TPD units (PDTSTPD). By using a dithienogermole comonomer (DTG-TPD), Reynolds et al.[20] reported a comparable performance (PCE of 7.3% with a V_{oc} of 0.85 V). Finally, Wei et al.[21] have fabricated a BHJ solar cell device incorporating a bithiophene comonomer (PBTTPD) which also exhibited a PCE of 7.3% (V_{oc} of 0.92 V). In short, most bulk heterojunction solar cells based on thieno[3,4-*c*]pyrrole-4,6-dione derivatives exhibit also relatively high open-circuit voltage.[22] In other words, the electron-withdrawing TPD unit contributes to slightly decrease the HOMO energy level of the resulting push−pull copolymers while keeping the LUMO energy levels around −3.8 eV.

In this work, we therefore present new alternating copolymers based on thieno[3,4-*c*]pyrrole-4,6-dione (TPD) and 2,7-carbazole moieties, namely PCDTTPD, PCDTTPD-ic, and PCDTTPD-C_6C_8 (see Scheme 1). It is believed that by combining both comonomers promising conjugated copolymers for photovoltaic applications could emerge.

RESULTS AND DISCUSSION

First, a TPD unit (monomer **6**, see Supporting Information) was directly copolymerized with a 2,7-carbazole unit (monomer **14**, see Scheme 1) without any spacer (PCTPD, see Supporting Information), but a low number-average molecular weight, $\bar{M}_n$, of 3 kg/mol (polymerization degree (PD) ∼ 5) was obtained with a polydispersity index (PDI) of 1.5. As previously observed, Suzuki coupling does not seem to be a useful tool with TPD units.[23] However, TPD units are highly suitable moieties for direct arylation reactions,[24,25] and the same polymer was then prepared by direct arylation polycondensation reaction (see Supporting Information). This reaction gave a PCTPD with a $\bar{M}_n$ of 34 kg/mol and PDI of 1.3. The resulting copolymer has electrochemical (E_g^{el}) and optical (E_g^{opt}) bandgaps of 2.36 eV. The HOMO and LUMO energy levels are localized at −5.88 and −3.52 eV, respectively. However, this large band gap copolymer is clearly not promising for photovoltaic applications, and it was not further investigated in this study. In fact, the optimal band gap, considering the solar emission spectrum, should range between 1.3 and 1.9 eV.[17]

To decrease the band gap, unsubstituted and substituted thiophene spacers were added. As shown in Scheme 1, different comonomers were polymerized through Suzuki cross-coupling polymerization to afford PCDTTPD, PCDTTPD-ic, and PCDTTPD-C_6C_8. Further details about the synthesis of monomers ([**1**] to [**13**]) and related polymers are described in the Supporting Information. An end-capping reaction was performed by using bromobenzene and phenylboronic acid to increase the stability of the polymer.[26] PCDTTPD, PCDTTPD-ic, and PCDTTPD-C_6C_8 have a $\bar{M}_n$ of 13, 18, and 6 kg/mol, respectively (see Table 1). Thermogravimetric

Table 1. Polymerization and Thermal Data of Polymers

polymers	$\bar{M}_n$ (kg/mol)	$\bar{M}_w$ (kg/mol)	PDI	T_g (°C)	T_d (°C)
PCDTTPD	13	24	1.8		450
PCDTTPD-ic	18	24	1.3	80	425
PCDTTPD-C_6C_8	6	10	1.7		390

dx.doi.org/10.1021/ma202540j | *Macromolecules* 2012, 45, 1833−1838

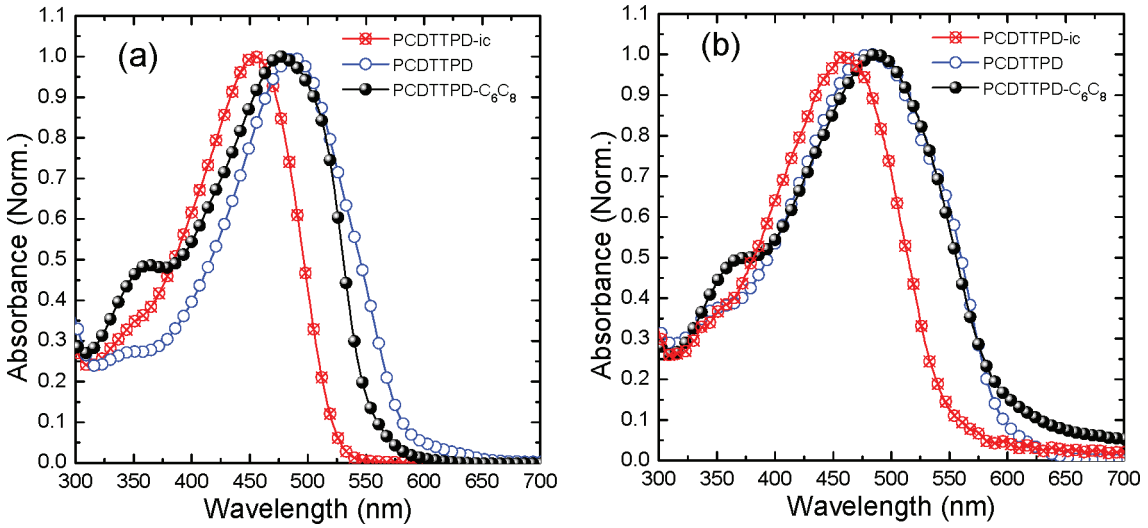

Figure 1. UV−vis absorption spectra of PCDTTPD, PCDTTPD-ic, and PCDTTPD-C_6C_8 in $CHCl_3$ solution (a) and in the solid state (b).

Table 2. Optical and Electrochemical Properties of the Polymers

	UV−vis absorption spectra				cyclic voltammetry (vs Ag/Ag^+)				
	solution	film			p-doping[a]		n-doping[a]		
polymers	λ_{max} (nm)	λ_{max} (nm)	λ_{onset} (nm)	E_g^{opt} (eV)	E_{on}^{ox} (V)	HOMO[b] (eV)	E_{on}^{red} (V)	LUMO[b] (eV)	E_g^{el} (eV)
PCDTTPD	487	484	604	2.05	1.01	−5.71	−0.96	−3.74	1.97
PCDTTPD-ic	454	458	560	2.21	0.77	−5.47	−1.31	−3.39	2.02
PCDTTPD-C_6C_8	480	487	602	2.06	0.80	−5.50	−1.20	−3.50	1.93

[a]p-doping and n-doping represent the electrochemical oxidation and reduction, respectively. The term electrochemical p-doping and n-doping is generally understood as a process that involves both oxidation and reduction of the conducting polymer backbone and the concomitant changes in the electronic structure. [b]HOMO = $-e(E_{on}^{ox} + 4.7)$ (eV) and LUMO = $-e(E_{on}^{red} + 4.7)$ (eV).

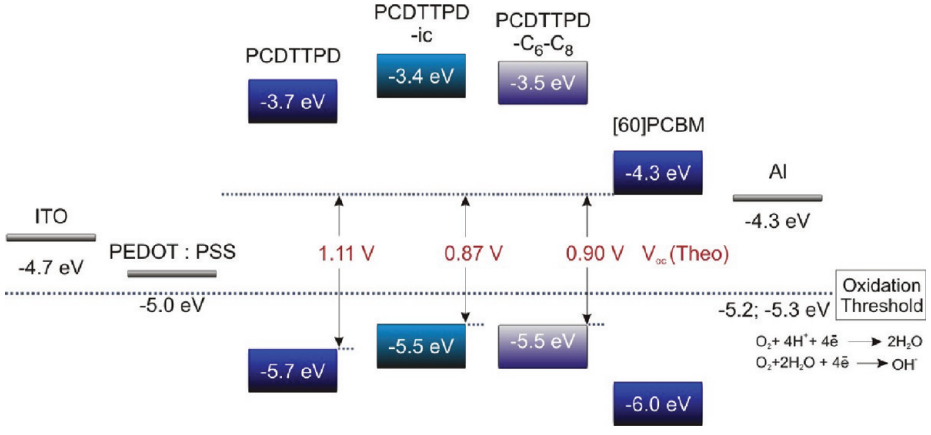

Figure 2. Energy levels diagram of the polymers and [60]PCBM.

analyses (TGA) (Figure 1S) show that these polymers possess a good stability up to 450 °C under nitrogen. DSC measurements did not indicate any glass transition temperature (T_g) for PCDTTPD and PCDTTPD-C_6C_8 but revealed a T_g around 80 °C for PCDTTPD-ic. All polymers are soluble in common solvents such as chloroform, THF, chlorobenzene (CB), 1,2-dichlorobenzene (ODCB), and 1,2,4-trichlorobenzene (TCB).

The optical properties were investigated by UV−vis−NIR absorption spectroscopy (see Figure 1 and Table 2). The UV−vis−NIR absorption spectra show broad absorption bands in solution and in the solid state around 480−487 nm for PCDTTPD and PCDTTPD-C_6C_8, while those of PCDTTPD-ic are observed around 458 nm. These results seem to indicate that the substituted thiophene spacers seem to affect the optical properties of those copolymers. Indeed, this blue shift could be explained by a slightly twisted conformation due to the presence of alkyl chains.[27] The optical bandgap determined from the polymers film absorption onset are around 2.0 eV for the polymers having unsubstituted thiophene spacers and 2.2 eV for PCDTTPD-ic.

The HOMO and LUMO energy levels of polymers were determined by cyclic voltammetry (CV). These data are summarized in Figure 2 and Table 2. Based on the recorded oxidation potentials for PCDTTPD, PCDTTPD-ic, and PCDTTPD-C_6C_8 (HOMO energy levels at −5.71, −5.47,

dx.doi.org/10.1021/ma202540j | Macromolecules 2012, 45, 1833−1838

Table 3. Photovoltaic Data for ITO/PEDOT:PSS/Polymer:[60]PCBM/Al Devices

polymers	thickness (nm)	J_{sc} (mA cm^{-2})	V_{oc} (V)	FF	PCE (%)	J_0 (A/m^2)
PCDTTPD	53	−4.72	1.07	0.36	1.82	3.5×10^{-17}
PCDTTPD-ic	82	−0.56	1.01	0.25	0.14	4.8×10^{-17}
PCDTTPD-C_6C_8	91	−0.35	1.00	0.39	0.13	4.4×10^{-17}

and −5.50 eV, respectively), the polymers should be stable in ambient air conditions.[28] The HOMO and LUMO energy levels of the polymers were estimated from the onset oxidation and reduction potentials, assuming a SCE level to be at −4.7 eV below the vacuum level.[29] It should be noted that the structural difference between the PCDTTPD and PCDTTPD-C_6C_8 is almost negligible, but a HOMO energy level difference of 0.2 eV is observed between both polymers. This observation could be explained by the presence of the chain in the TPD unit. Indeed, compared to a linear chain, a branched side chain increases the electron density in the polymer, so in this case the oxidation may be easier. However, it is important also to mention that the electrochemistry is a dynamic method and different parameters need to be taking into account as the thickness of the film, the porosity of the polymer, etc.

On the basis of these electrochemical data and taking into account a LUMO energy level at −4.3 eV for [60]PCBM and using the semiempirical estimation of the eq 1,[7] the theoretical open-circuit voltages (V_{oc}) calculated for PCDTTPD, PCDTTPD-ic, and PCDTTPD-C_6C_8 should be around 1.10, 0.87, and 0.90 V, respectively (Figure 2)

$$V_{oc} = \frac{1}{e}[|E^{donor}_{HOMO}| - |E^{PCBM}_{LUMO}|] - 0.3 \quad (1)$$

where e is the elementary charge and the value of 0.3 V is an empirical factor.[30] Indeed, Vanderwal et al. have observed that there is a correlation between the V_{oc} and the energetic difference between the HOMO of the donor (polymer) and the LUMO of the acceptor (PCBM).[31] As the authors highlighted, an increase of the LUMO level of the fullerene or the utilization of donor polymers with optimized energetic levels represent the most efficient pathways for increasing the V_{oc} of a polymer−PCBM solar cells. Also, the reduction of nonradiative pathways and the increase of the carrier lifetime should result to a decrease of the dark saturation current (J_0) and, therefore, to an increase of the V_{oc} value. By using the eq 2,[31] J_0 was estimated around to (3.0−4.0) × 10^{-17} A/m^2 for all polymers (see Table 3)

$$V_{oc} = \frac{k_B T}{e} \ln\left(\frac{J_{sc}}{J_0} + 1\right) \quad (2)$$

where k_B is the Boltzmann constant and T is the temperature.

Because of the interesting electronic and optical of the copolymers (preferred energy levels and proper absorption spectra), BHJ solar cells were fabricated with a configuration of glass/ITO/PEDOT:PSS/polymer:[60]PCBM/Al. After spin-coating a layer of 50 nm of poly(3,4-ethylene dioxythiophene):poly(styrenesulfonate) (PEDOT:PSS) onto a precleaned indium−tin oxide (ITO)-coated glass substrate, polymer/[60]PCBM blends (1:1 (PCDTTPD) or 1:2 (PCDTTPD-ic and PCDTTPD-C_6C_8), w/w) solution in ODCB were deposed by spin-coating and dried under vacuum at room temperature for 15 h. The devices were completed by evaporating Al metal as the electrode. The solar cells active area is 25 mm^2. The detailed conditions of the device fabrication and characterization are fully described in the Supporting Information. The photovoltaic performance presented in Figure 3 was realized under AM 1.5G illumination of 100 mW cm^{-2}.

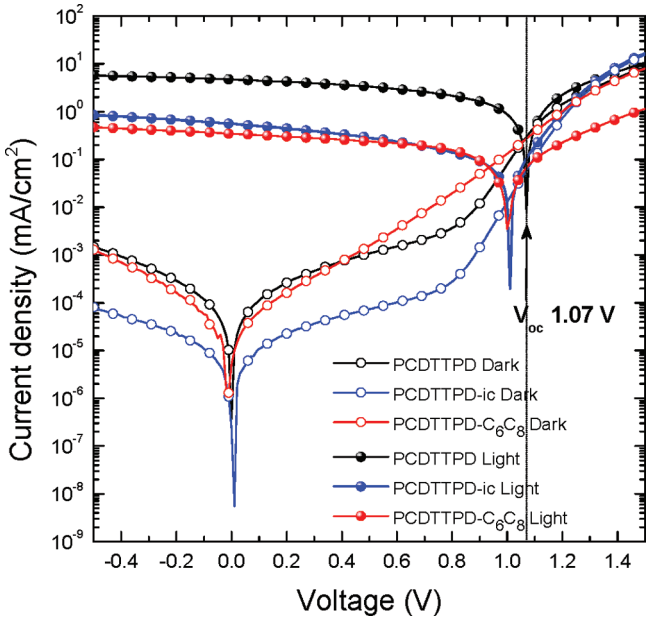

Figure 3. J−V curves of the polymer solar cells based on PCDTTPD in the dark and under the illumination of AM 1.5 G, 100 mW cm^{-2}.

The polymer PCDTTPD was able to reach a current density of 4.72 mA cm^{-2}, a moderate fill factor of 0.36, and a very high open-circuit voltage (V_{oc}) of 1.07 V. It is worth noting that this open-circuit voltage agrees with its anticipated value. As a result, a power conversion efficiency (PCE) of 1.82% has been achieved in these first measurements. In the case of PCDTTPD-ic and PCDTTPD-C_6C_8, very low PCEs were achieved. However, for fair comparisons, it could be important to vary the device configurations (such as annealing, solvents, additives, electrodes, acceptors, etc.) for each polymer. Such optimizations should be carried out in the near future.

Photovoltaic properties such as PCE, open-circuit voltage (V_{oc}), short-circuit current density (J_{sc}), fill factor (FF), and the dark saturation current (J_0) are listed in Table 3. These performances can be partially explained by the morphology observed using atomic force microscopy (AFM) (see Figure 4). In fact, AFM images of PCDTTPD:[60]PCBM show some percolation pathways compared to those obtained with PCDTTPD-ic:[60]PCBM and PCDTTPD-C_6C_8:[60]PCBM blends, where the presence of holes (more or less wide and deep, see Figure 3S) into the bulk heterojunction could easily disturb or limit the transport of the charges to the electrodes. The presence of different chains on the polymers probably implies a steric hindrance in solid state in the case of PCDTTPD-ic and PCDTTPD-C_6C_8 which involve a change of the conformation and the morphology. In this regard, the

dx.doi.org/10.1021/ma202540j | Macromolecules 2012, 45, 1833−1838

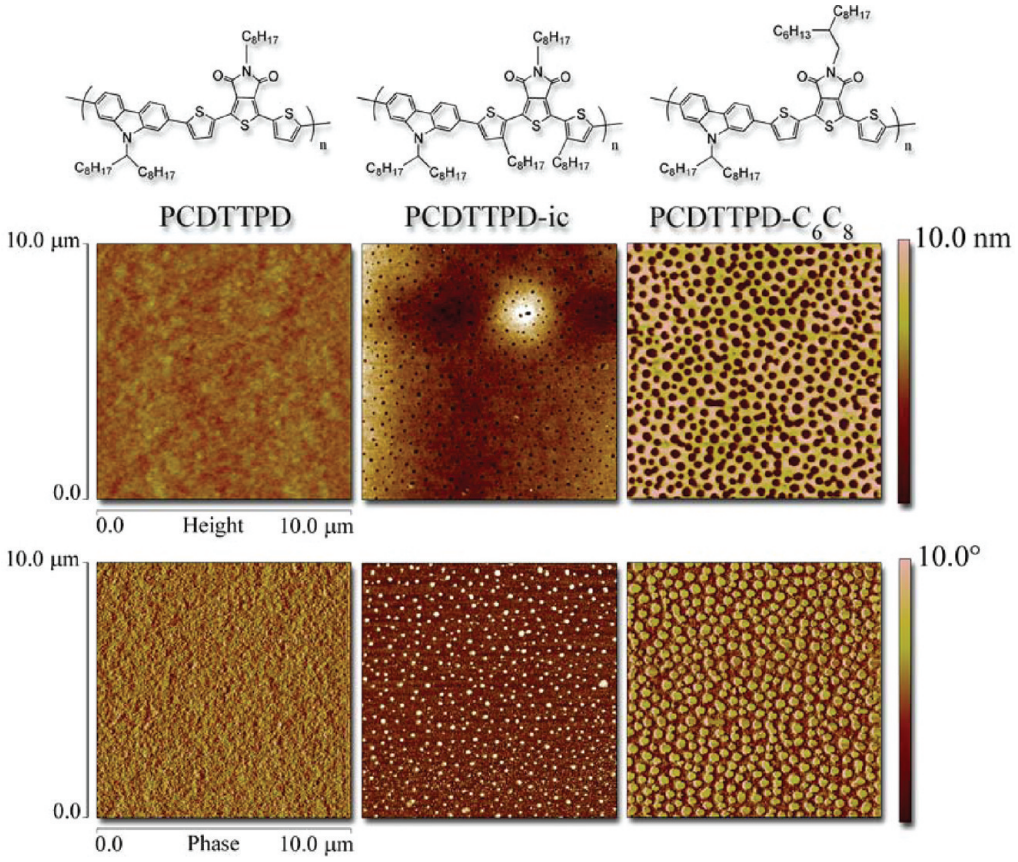

Figure 4. AFM images acquired by tapping mode (height and phase images are shown for polymers/[60]PCBM blends).

interaction with [60]PCBM is completely different for these polymers compared to PCDTTPD.

CONCLUSION

New poly(2,7-carbazole-*alt*-TPD) derivatives (PCDTTPD, PCDTTPD-ic, and PCDTTPD-C_6C_8) were designed and synthesized. These polymers combine interesting properties such as good solubility and excellent thermal and air stability. Preliminary results with photovoltaic devices based on PCDTTPD:[60]PCBM show a power conversion efficiency close to 2.0% with a high V_{oc} of 1.07 V. The present studies indicate that the combination of TPD and 2,7-carbazole building blocks can be a very effective way to lower the HOMO energy level and ultimately to enhance the V_{oc} of polymer solar cells. The V_{oc} reported here is one of the highest observed for a polymer:[60]PCBM bulk heterojunction devices.[32−36] We also firmly believe that by optimizing nanoscale morphology of these PCDTTPD-based devices through different polymer/[60 or 70]PCBM ratios, processing additives, or annealing, higher PCE values should be obtained. Higher molecular weights through direct arylation polycondensation reactions could also be an asset.

ASSOCIATED CONTENT

Supporting Information

Experimental details, synthesis of the monomers and polymers, instrumentation, fabrication details, and characterization procedures of the organic photovoltaic devices. This material is available free of charge via the Internet at http://pubs.acs.org.

AUTHOR INFORMATION

Corresponding Author

*E-mail: Mario.Leclerc@chm.ulaval.ca.

Notes

The authors declare no competing financial interest.

ACKNOWLEDGMENTS

The authors kindly thank Rodica Neagu-Plesu for SEC measurements. This work was supported by grants from NSERC.

REFERENCES

(1) Günes, S.; Neugebauer, H.; Sariciftci, N. S. *Chem. Rev.* **2007**, *107*, 1324−13338.
(2) Coakley, K. M.; McGehee, M. D. *Chem. Mater.* **2004**, *16*, 4533−4542.
(3) Brabec, C. J.; Dyakonov, V.; Scherf, U. In *Organic Photovoltaics: Materials, Device Physics, and Manufacturing Technologies*; John Wiley & Sons: New York, 2008.
(4) Li, G.; Shrotriya, V.; Huang, J.; Yao, Y.; Moriarty, T.; Emery, K.; Yang, Y. *Nature Mater.* **2005**, *4*, 864−868.
(5) Kim, J. Y.; Kim, S. H.; Lee, H. H.; Lee, K.; Ma, W.; Gong, X.; Heeger, A. J. *Adv. Mater.* **2006**, *18*, 572−576.
(6) Kim, K.; Liu, J.; Namboothiry, M. A. G.; Carroll, D. L. *Appl. Phys. Lett.* **2007**, *90*, 163511−163514.
(7) Scharber, M. C.; Mühlbacher, D.; Koppe, M.; Denk, P.; Waldauf, C.; Heeger, A. J.; Brabec, C. J. *Adv. Mater.* **2006**, *18*, 789−794.
(8) Blouin, N.; Michaud, A.; Leclerc, M. *Adv. Mater.* **2007**, *19*, 2295−2300.
(9) Blouin, N.; Michaud, A.; Gendron, D.; Wakim, S.; Blair, E.; Neagu-Plesu, R.; Belletête, M.; Durocher, G.; Tao, Y.; Leclerc, M. *J. Am. Chem. Soc.* **2008**, *130*, 732−742.

(10) Zou, Y.; Gendron, D.; Aïch, R. B.; Najari, A.; Tao, Y.; Leclerc, M. *Macromolecules* **2009**, *42*, 2891−2894.
(11) Zou, Y.; Gendron, D.; Neagu-Plesu, R.; Leclerc, M. *Macromolecules* **2009**, *42*, 6361−6365.
(12) Chu, T. Y.; Alem, S.; Tsang, S.-W.; Tse, S.-C.; Wakim, S.; Lu, J.; Dennler, G.; Waller., D.; Gaudiana, R.; Tao, Y. *Appl. Phys. Lett.* **2011**, *98*, 253301−253303.
(13) Sun, Y.; Takacs, C. J.; Cowan, S. R.; Seo, J. H.; Gong, X.; Roy, A.; Heeger, A. J. *Adv. Mater.* **2011**, *23*, 2226−2230.
(14) Jo, J.; Gendron., D.; Najari, A.; Moon, J. S.; Cho, S.; Leclerc, M.; Heeger, A. J. *Appl. Phys. Lett.* **2010**, *97*, 203303−203305.
(15) Zhang, Q. T.; Tour, J. M. *J. Am. Chem. Soc.* **1997**, *119*, 5065−5066.
(16) Zou, Y.; Najari, A.; Berrouard, P.; Beaupré, S.; Aïch, B.-R.; Tao, Y.; Leclerc, M. *J. Am. Chem. Soc.* **2010**, *132*, 5330−5331.
(17) Boudreault, P.-L. T.; Najari, A.; Leclerc, M. *Chem. Mater.* **2011**, *23*, 456−469.
(18) Piliego, C.; Holcombe, T. W.; Douglas, J. D.; Woo, C. H.; Beaujuge, P. M.; Fréchet, J. M. J. *J. Am. Chem. Soc.* **2010**, *132*, 7595−7597.
(19) Chu, T.-Y.; Lu, J.; Beaupré, S.; Zhang, Y.; Pouliot, J.-R.; Wakim, S.; Zhou, J.; Leclerc, M.; Li, Z.; Ding, J.; Tao, Y. *J. Am. Chem. Soc.* **2011**, *133*, 4250−4253.
(20) Amb, C. M.; Chen, S.; Graham, K. R.; Subbiah, J.; Small, C. E.; So, F.; Reynolds, J. R. *J. Am. Chem. Soc.* **2011**, *133*, 10062−10065.
(21) Su, M.-S.; Kuo, C.-Y.; Yuan, M.-C.; Jeng, U.-S.; Su, C.-J.; Wei, K.-H. *Adv. Mater.* **2011**, *23*, 3315−3319.
(22) Najari, A.; Beaupré, S.; Berrouard, P.; Zou, Y.; Pouliot, J.-R.; Lepage-Pérusse, C.; Leclerc, M. *Adv. Funct. Mater.* **2011**, *21*, 718−728.
(23) Berrouard, P.; Grenier, F.; Pouliot, J.-R.; Gagnon, E.; Tessier, C.; Leclerc, M. *Org. Lett.* **2011**, *13*, 38−41.
(24) Berrouard, P.; Najari, A.; Pron, A.; Gendron, D.; Morin, P.-O.; Pouliot, J.-R.; Veilleux, J.; Leclerc, M. *Angew. Chem., Int. Ed.* **2011**, DOI: 10.1002/anie.201106411.
(25) Fujinami, Y.; Kuwabara, J.; Lu, W.; Hayashi, H.; Kanbara, T. *ACS Macro Lett.* **2012**, *1*, 67−70.
(26) Park, J. K.; Jo, J.; Seo, J. H.; Park, Y. D.; Lee, K.; Heeger, A. J.; Bazan, G. C. *Adv. Mater.* **2011**, *23*, 2430−2435.
(27) Leclerc, M.; Martinez Diaz, F.; Wegner, G. *Makromol. Chem.* **1989**, *190*, 3105−3116.
(28) de Leeuw, D. M.; Simenon, M. M. J.; Brown, A. R.; Einerhand, R. E. F. *Synth. Met.* **1997**, *87*, 53−59.
(29) Thompson, B. C.; Kim, Y. G.; Reynolds, J. R. *Macromolecules* **2005**, *38*, 5359−5362.
(30) Cowan, S. R.; Roy, A.; Heeger, A. J. *Phys. Rev. B* **2010**, *82*, 245207−245216.
(31) Minnaert, B.; Burgelman, M. *Prog. Photovoltaics* **2007**, *15*, 741−748.
(32) Zhang, F.; Jespersen, K. G.; Björström, C.; Svensson, M.; Andersson, M. R.; Sundström, V.; Magnusson, K.; Moons, E.; Yartsev, A.; Inganäs, O. *Adv. Funct. Mater.* **2006**, *16*, 667−674.
(33) Chen, X.; Schulz, G. L.; Han, X.; Zhou, Z.; Holdcroft, S. *J. Phys. Chem. C* **2009**, *113*, 8505−8512.
(34) Schulz, G. L.; Chen, X.; Holdcroft, S. *Appl. Phys. Lett.* **2009**, *94*, 023302−023304.
(35) Zheng, Q.; Jung, B. J.; Sun, J.; Katz, H. E. *J. Am. Chem. Soc.* **2010**, *132*, 5394−5404.
(36) Vandewal, K.; Tvingstedt, K.; Gadisa, A.; Inganäs, O.; Manca, J. V. *Nature Mater.* **2009**, *8*, 904−909.

Macromolecules

Article

pubs.acs.org/Macromolecules

Online Monitoring of Styrene Polymerization in Miniemulsion by Hyperpolarized ^{129}Xenon NMR Spectroscopy

Mathis Duewel, Nicolas Vogel, Clemens K. Weiss, Katharina Landfester, Hans-Wolfgang Spiess, and Kerstin Münnemann*

Max Planck Institute for Polymer Research, Ackermannweg 10, 55128 Mainz, Germany

Supporting Information

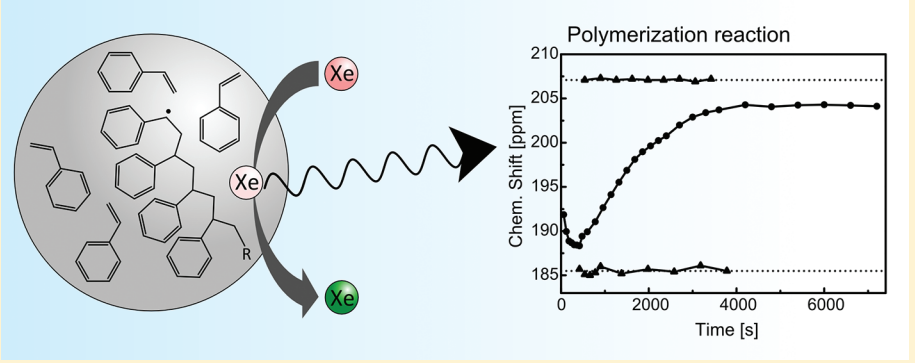

ABSTRACT: Online monitoring of a miniemulsion polymerization of styrene by hyperpolarized ^{129}Xe NMR spectroscopy is presented. The chemical shift of ^{129}Xe directly reports on the monomer/polymer ratio in the reaction mixture and therefore on the conversion of the reaction. The method allows for monitoring the progress of a polymerization with high time resolution and without sample extraction. The results obtained by ^{129}Xe NMR spectroscopy were successfully validated by comparison with results of calorimetry. Further characterization of the polymer dispersions with regard to the solids content and the particle diameters proved the comparability of both methods. Small deviations in the kinetic data and the properties of the polymer suspension from both methods are explained by the loss of monomer during the ^{129}Xe NMR experiments due to the used setup. In the future, ^{129}Xe NMR might also be applied for online monitoring of other chemicals reactions, e.g., allowing for determining the kinetics of thermoneutral reactions.

INTRODUCTION

Many chemical and physical properties of polymers depend on the numerous parameters of the polymerization process. Adjusting the polymer properties can thus be achieved by tailoring the polymerization process.[1] Online monitoring methods offer an efficient control of the reaction, which leads to products with constant quality at minimal costs.[2] The most valuable ones work without the need of sample extraction. Common techniques to monitor industrial polymerization reactions are reaction calorimetry, optical spectroscopy methods like IR or Raman spectroscopy, and process gas chromatography.[3,4] The widely used calorimetric measurements are suitable for immediate reaction control, but only for exo- or endothermic reactions.

NMR spectroscopy is another useful tool for online monitoring of polymerization reactions, providing valuable information about the composition of the reaction mixture.[5−7] It has been shown that online NMR spectroscopy for monitoring polymerizations can provide an acceptable time resolution using ^{1}H NMR and ^{13}C NMR.[2,8] However, the intrinsic low sensitivity of NMR measurements and the need of time-consuming signal averaging often lead to problems in achieving this, which is especially true for ^{13}C at natural abundance limiting the achievable time resolution to a few minutes. Isotopic enrichment of ^{13}C would help to overcome this problem but is much too costly. Moreover, ^{1}H NMR mostly requires the use of expensive deuterated solvents hampering its application for industrial processes.

Several so-called hyperpolarization methods can overcome the lack of sensitivity of NMR spectroscopy, allowing for an excellent time resolution in dynamic measurements. They create a large nonequilibrium population of the Zeeman energy levels of the used nucleus thus achieving signal enhancements of several orders of magnitude compared to the thermal case.[9−11] Different hyperpolarization methods like dynamic nuclear polarization (DNP),[12] para-hydrogen induced polarization (PHIP),[13,14] or the hyperpolarization of noble gases by spin-exchange optical pumping (SEOP)[15,16] have been developed until now. In this work, hyperpolarization of the noble gas ^{129}Xe via spin-exchange optical pumping was applied

Received: November 30, 2011
Revised: January 22, 2012
Published: February 8, 2012

using an apparatus described elsewhere.[17] During the process of SEOP, angular momentum is transferred from the photons of circular polarized laser light to the electron spins of valence electrons of rubidium and subsequently to the nuclear spins of xenon gas.[15,16] The hyperpolarization process takes place outside the NMR spectrometer, before the gas is brought into contact with the sample.

The signal enhancement in NMR spectroscopy due to the hyperpolarization of ^{129}Xe offers the possibility of fast measurements and the online monitoring of dynamic processes.[18−20] Furthermore, one can take advantage of two other properties of the ^{129}Xe nucleus: First, the large polarizability of the xenon electron cloud by its physical and chemical environment leads to a large chemical shift range of ^{129}Xe NMR. This sensitivity allows for reporting of sample properties by the chemical shift of the Xe atom without the need of covalent bonding between the Xe atom and the sample molecules. Many examples of gaseous ^{129}Xe NMR exploiting this effect can be found in the material science of porous media.[21−23] Another useful property of Xe is its solubility in liquid phases, both organic and aqueous, which allows for the use of ^{129}Xe in liquid reaction mixtures.

The polymerization techniques of emulsion and miniemulsion polymerization reactions are widely used in industry and science because of their good reaction heat dissipation, the constant, low viscosity of the reaction mixture, and high achievable conversion rates. The droplets of a miniemulsion serve as a kind of nanoreactor for the reaction which equals to a bulk polymerization inside the droplets. In addition to the preparation of "simple" polymeric nanoparticles by radical polymerization, miniemulsion polymerization allows using a broad range of monomers, conducting polyreactions as e.g. polycondensation, or polyaddition reactions,[24−26] which are not accessible with conventional emulsion polymerization. It further offers the possibility to encapsulate a variety of materials to generate functional nanoparticles.[27,28] The presence of the aqueous phase in emulsion and miniemulsion polymerization reactions can pose severe difficulties for ^{1}H NMR measurements due to the very prominent water signal which can superimpose other signals stemming from the reaction educts or products. By using ^{129}Xe NMR, the presence of a large proton background signal does not interfere with the measurements.

In this contribution, the real-time monitoring of a free radical polymerization of styrene in a miniemulsion is demonstrated, using a continuous flow of hyperpolarized ^{129}Xe through the reaction mixture. A short description of the monitoring of a batch polymerization of methyl methacrylate at 35 G was given by Gloeggler et al.[29] However, to our knowledge, the current paper gives the first full length report demonstrating that hyperpolarized ^{129}Xe can be used for online monitoring of a polymerization reaction. By combining all properties of hyperpolarized ^{129}Xe as described above, it is used here as an NMR probe in a polymerization reaction of an industrially important monomer in the complex environment of a miniemulsion. The absence of xenon from common chemical substances leads to the absence of any undesired background signal rendering the interpretation of the sparse Xe spectra very convenient. In this work, only two distinct peaks of xenon inside the reaction mixture are recorded. The resulting simple NMR spectra can be analyzed in a very straightforward manner by the determination of the chemical shift of the ^{129}Xe peaks giving access to the conversion of the polymerization. Therefore, the kinetics of two polymerization reactions were recorded by hyperpolarized ^{129}Xe NMR spectroscopy using two oil-soluble azo-initiators with different decomposition temperatures. In order to prove the validity of the method, the progress of the polymerization reaction observed by ^{129}Xe NMR was compared to results obtained by calorimetry. Calorimetric measurements on similar emulsion and miniemulsion systems can also be found in the literature.[30−33] To allow for better comparison and to exclude any time-dependent changes of the miniemulsion, small samples of the same batch of miniemulsion were measured simultaneously by ^{129}Xe NMR spectroscopy and calorimetry. Thereafter, the conversion of the different samples and reactions were determined by measuring the solids content. To check for differences between the polymer colloids obtained from the individual reactions monitored by NMR and calorimetry, the mean particle diameters were measured by photon cross-correlation spectroscopy (PCCS) and scanning electron micrographs.

MATERIALS AND METHODS

For the miniemulsions, styrene, sodium dodecyl sulfate (SDS), hexadecane (all purchased from Sigma-Aldrich, Germany), the initiators 2,2′-azobis(2-methylbutyronitrile) (V59, 10 h half-life decomposition temperature 340 K), and 2,2′-azobis(4-methoxy-2,4-dimethylvaleronitrile) (V70, 10 h half-life decomposition temperature 303 K, both initiators purchased from Wako, Japan) were used. The miniemulsions were prepared by mixing 24 g of ultrapure H_2O (Milli-Q-grade), 6 g of distilled styrene (57.6 mmol), 60 mg of SDS as surfactant (0.21 mmol), 250 mg of hexadecane as hydrophobic agent (1.1 mmol), and either 100 mg of V59 (0.52 mmol) or 100 mg of V70 (0.32 mmol) as initiator and the treatment with ultrasound (1/2 in. tip, 90% amplitude, Branson Sonifier 450D) for 2 min, applied in 10 s pulses with 10 s break. During and after the emulsification, the miniemulsions were ice-cooled to reduce any possible polymerization prior to the measurements.

For the hyperpolarization of ^{129}Xe, xenon (purity 4.7, natural abundance, Westfalen AG, Germany), nitrogen (purity 5.0, Westfalen AG, Germany), helium (purity 4.6, Westfalen AG, Germany), and rubidium (purity 99.8%, Alfa Aesar GmbH & Co KG) were used. The Xe was polarized in a polarizer built by the Research Center Jülich in a gas mixture consisting of 1% Xe, 8% N_2, and 91% He. The polarizer was used in a continuous mode during the whole reaction time with a gas flow of around 70 mL/min at a pressure of 7 bar. The gas mixture containing the polarized ^{129}Xe was directly used for the NMR measurements without pressure reduction or replenishment of the diluted Xe gas.

For dissolving the hyperpolarized ^{129}Xe in the reaction mixture, hollow-fiber membranes (hydrophobic surface, made from polypropylene, pore sizes ∼30 nm, Membrana GmbH, Germany) were used.[34−36] The experimental setup for the ^{129}Xe NMR measurements is sketched in Figure 1. The membranes allow for the molecular dissolution of Xe gas into the bulk of the sample without the loss of hyperpolarization. The use of the membrane avoids the formation of gas bubbles or foam and thus minimizes susceptibility artifacts. After an equilibration concentration of Xe in the sample is reached, Xe gas also diffuses back through the membrane, thus providing a continuous exchange of hyperpolarized and due to NMR pulses and T_1 relaxation depolarized ^{129}Xe atoms in the sample. The membranes were glued into homemade tube caps made from poly(ether ether ketone) (PEEK) providing in- and outlets for the gas mixture as well as a tight seal applicable for pressures of up to 8 bar and temperatures of up to at least 350 K. In order to minimize any diffusional losses of organic monomer across the hydrophobic membrane into the gas flow, remotely controlled nonmagnetic pneumatic valves were used near the sample tube inside the NMR magnet to create a bypass around the sample tube in between subsequent measurements.

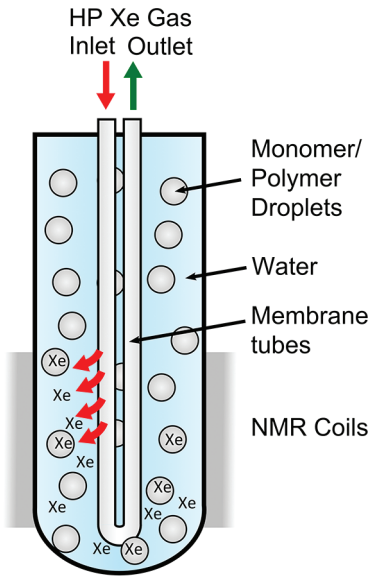

Figure 1. Sketch of the NMR sample tube containing the miniemulsion and the hollow fiber membranes inside the NMR coil. The hydrophobic membrane allows for the passage of hyperpolarized ^{129}Xe in and out the reaction mixture. The inlet and outlet of the membrane are connected to the gas flow of the polarizer.

All NMR experiments were carried out in a 7 T NMR magnet equipped with a Tecmag console. Pressure-resistant NMR tubes (o.d. 10 mm, i.d. 5 mm) were used for all experiments.

For the time-resolved polymerization monitoring, 1.5 mL of the miniemulsion was put into the sample tube together with the membranes (see Figure 1). After an initial pressurizing step, the gas flow containing hyperpolarized ^{129}Xe was fed through the membranes into the still cool sample tube for 2 min, allowing for the initial dissolution of Xe gas into the sample. Subsequently, the sample tube was inserted into the NMR magnet heated to 343 K. The insertion of the sample tube was considered as the time t = 0 for the polymerization reaction. Starting after 1 min of reaction, ^{129}Xe NMR spectra were recorded. For each spectrum of the time-resolved measurements, four scans with a repetition delay of 10 s were recorded to allow for a sufficient signal-to-noise ratio. For the first 10 min of reaction time, spectra were recorded every minute, for the next 30 min every 3 min, then until the first hour of reaction time every 5 min, and finally for the second hour of reaction time every 10 min.

All ^{129}Xe NMR spectra were analyzed by using Matlab for fitting the ^{129}Xe NMR spectra and determining the chemical shifts as the center of gravity of the adsorbed or dissolved Xe peaks. The peak of the free Xe gas was used as a reference and set to 0 ppm. In the case of two distinct peaks for the dissolved ^{129}Xe (beginning of the reaction), both peaks have been fitted and the mean center of gravity of both peaks was calculated and used for the further evaluation.

For the mole-fraction-dependent experiments, polystyrene (mole weight 100 000 g mol^{-1}, polymer standard, PSS, Germany) and styrene (Sigma-Aldrich, Germany) were used. Nine mixtures of styrene and polystyrene were made with styrene mole fractions ranging from 0.95 to 0.3. Thermal ^{129}Xe NMR spectra of pure styrene, pure polystyrene, and the nine different monomer–polymer mixtures were recorded by averaging the thermal Xe NMR signal for several hundred scans after evacuating the sample tube and pressurizing it with up to 3 bar of Xe gas.

The calorimetric measurements were carried out on a μRC-micro reaction heat calorimeter (Thermal Hazard Technology, UK) at 343 K. The sample volume was 1 mL. The solids content was determined by evaporation of the liquid phase from the dispersion at 323 K under a pressure of 50 mbar and weighing the solid residue. Particle sizes were measured by photon cross-correlation spectroscopy (PCCS) using a Nanophox PCCS (Sympatec GmbH, Germany). For the measurement, 35 μL of the dispersion was diluted with 1.5 mL of Milli-Q water. Scanning electron micrographs were recorded on a Gemini 1530 microscope (Carl Zeiss AG, Germany). From the electron micrographs, mean particle diameters were determined from 150 polymer particles for each polymerization. Size exclusion chromatography (SEC) was performed at 303 K with a Waters Alliance 2000 autosampler and a Waters 510 HPLC pump using PSS-SDV columns with pore sizes of 500, 1 × 10^4, and 1 × 10^5 Å, respectively. The signals were detected on an Erma UV detector (λ = 254 nm) and a SOMA RI detector. The eluent and the solvent for the samples was THF, the elugrams were calibrated against PS standards.

RESULTS AND DISCUSSION

Figure 2 shows representative NMR spectra of ^{129}Xe atoms dissolved in the miniemulsion after the cold sample was

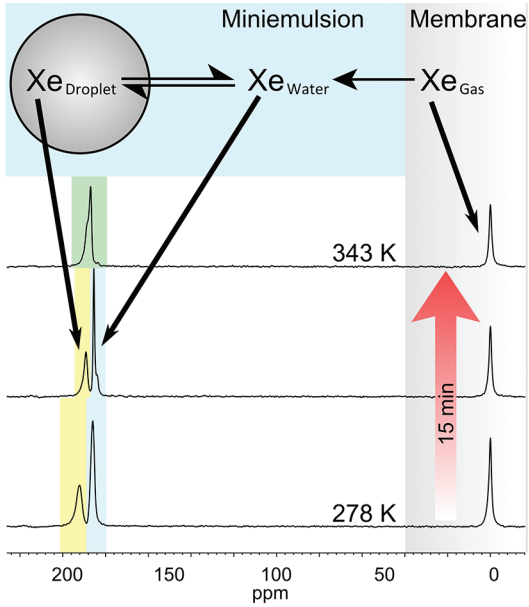

Figure 2. NMR spectra of hyperpolarized ^{129}Xe dissolved in the miniemulsion. According to the number of phases, up to three Xe peaks are observable. The right peak in the spectra corresponds to the free Xe gas located in the hollow fiber membranes, whereas the middle and the left peak correspond to Xe dissolved in the aqueous (blue background) and organic (yellow) environment, respectively. The cold sample (278 K) was heated during the first minutes in the NMR spectrometer to 343 K giving rise to a faster exchange of the Xe atoms between the organic and aqueous phase and the appearance of an exchange peak (green).

introduced in the spectrometer and heated to the temperature of the polymerization. Three distinct peaks can be observed corresponding to Xe in different physical and chemical environments. The peak of free Xe gas inside the hollow-fiber membranes has the lowest chemical shift and can be used as an internal reference (0 ppm). The Xe atoms dissolved in the different phases (aqueous and organic) of the miniemulsion give rise to the peaks at 186 and 192 ppm, respectively.

In the case of a relatively slow exchange of the xenon atoms between the continuous aqueous phase and the discontinuous organic phase, as it is the case for room temperature and below, two distinct peaks can be observed in the NMR spectra (lower spectra in Figure 2). Heating the sample to 343 K (temperature of the polymerization) results in higher exchange rates and the two distinct peaks start to merge until only one exchange peak

dx.doi.org/10.1021/ma202605n | Macromolecules 2012, 45, 1839–1846

is visible (upper spectra in Figure 2; this process is also visible in the spectra of the first 15 min in Figure 4, see below).

In order to easily monitor polymerization reactions by ^{129}Xe NMR spectroscopy, a (preferably linear) dependence of the chemical shift of the dissolved ^{129}Xe on the conversion of the polymerization should exist. In miniemulsion polymerizations, however, four contributions to the chemical shift of dissolved Xe must be considered:

First, there are the interactions between ^{129}Xe atoms and H_2O molecules of the continuous phase whose contribution to the total chemical shift can be considered constant during the reaction because the amount of water in the system does not change substantially. Second, interactions exist between the dissolved ^{129}Xe atoms themselves, but the contribution is very small due to the very low Xe density in these experiments (only 1% of Xe in the gas mixture) and can be neglected. Furthermore, there are two chemical shift contributions in the organic phase of the miniemulsion stemming from the interactions between the ^{129}Xe atoms and the monomer and polymer molecules. The first contribution is decreasing during the reaction as the amount of the monomer molecules is depleting; the latter contribution is growing during the reaction as the polymerization degree increases.

By taking into account all the described contributions, the behavior of the chemical shift can be calculated by the equation[37−39]

$$\begin{aligned}\delta_{\text{dissolved Xe}} = &-\sigma_0^{\text{Xe-mono}}(T)[\text{mono}](T)\\ &-\sigma_0^{\text{Xe-poly}}(T)[\text{poly}](T)\\ &-\sigma_0^{\text{Xe-H}_2\text{O}}(T)[\text{H}_2\text{O}](T)\\ &-\sigma_1^{\text{Xe-Xe}}(T)[\text{Xe}](T)\end{aligned} \quad (1)$$

$\delta_{\text{dissolved Xe}}$ is the resulting chemical shift of ^{129}Xe dissolved in the miniemulsion. The constants $\sigma_0^{\text{Xe-mono}}$, $\sigma_0^{\text{Xe-poly}}$, $\sigma_0^{\text{Xe-H}_2\text{O}}$, and $\sigma_1^{\text{Xe-Xe}}$ are the shielding contributions due to interactions of Xe with the monomer, the polymer, the water of the aqueous phase, and itself, respectively. The terms [mono], [poly], [H_2O], and [Xe] depict the amount of monomer, polymer, water, and xenon in the miniemulsion, and T is the temperature.

By omitting the Xe−Xe interactions as described above and assuming the Xe−H_2O interactions and the temperature constant, the equation simplifies to

$$\begin{aligned}\delta_{\text{dissolved Xe}} = &-\sigma_0^{\text{Xe-mono}}[\text{mono}] - \sigma_0^{\text{Xe-poly}}[\text{poly}]\\ &-\text{const}\end{aligned} \quad (2)$$

With [poly] = 1 − [mono], the equation can be further simplified, giving the following linear dependence on the mole fraction of the monomer [mono]:

$$\begin{aligned}\delta_{\text{dissolved Xe}} = &(\sigma_0^{\text{Xe-poly}} - \sigma_0^{\text{Xe-mono}})[\text{mono}]\\ &-\sigma_0^{\text{Xe-poly}} - \text{const}\end{aligned} \quad (3)$$

In order to check for the linear dependence of the chemical shift on the monomer concentration, the chemical shifts of ^{129}Xe in pure styrene and pure polystyrene (M_w = 100 000 g mol^{-1}) as well as in nine mixtures of styrene and polystyrene with increasing monomer to polymer ratios were determined. In Figure 3, the chemical shift of dissolved ^{129}Xe is plotted versus the mole fraction of the polymer and the mole fraction

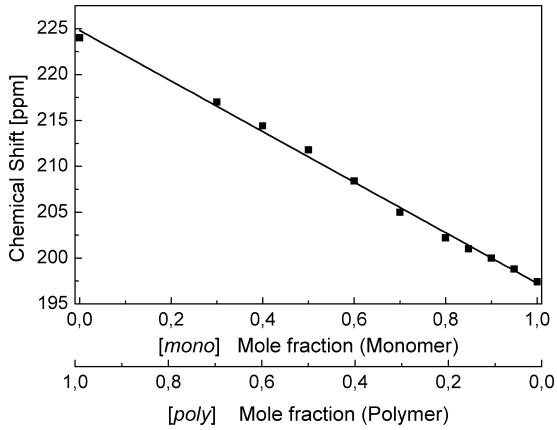

Figure 3. Plot of the chemical shift of ^{129}Xe versus the mole fraction of a monomer/polymer mixture. The points are the chemical shift values of pure polystyrene (M_w = 100 000 g mol^{-1}), nine mixtures of styrene and polystyrene with decreasing polymer ratio, and pure styrene. A linear fit of the data points is shown as a solid line.

of the monomer in the mixture. A linear dependence of the chemical shift on the sample composition is clearly observed. The values were fit linearly, yielding the following relationship between chemical shift and the mole fraction of the monomer [mono]:

$$\delta_{\text{Xe,mix}} = -27.6\ \text{ppm}\cdot[\text{mono}] + 224.8\ \text{ppm} \quad (4)$$

In this contribution, the studied polymerization reactions took place in a miniemulsion, a heterophase system, which is not only consisting of the mixture of styrene and polystyrene but also of water. Thus, the fit values based on eq 4 cannot be used to directly determine the conversion of the reaction mixture in the following dynamic experiments because of the contribution of the aqueous phase to the chemicals shift in miniemulsions. However, it will be demonstrated in the following that the underlying dependence of the chemical shift shown above is just as well applicable to the monitoring of complex systems like miniemulsion polymerization reactions.

A series of ^{129}Xe NMR spectra recorded during the miniemulsion polymerization of styrene are presented in Figure 4. The plot shows a zoomed region containing the peaks of the hyperpolarized ^{129}Xe dissolved in the reaction mixture in the range of 186−205 ppm. For the sake of visibility, not all recorded spectra from the start to the end of the reaction are depicted. During the course of the polymerization, a clear shift of the ^{129}Xe peaks to higher chemical shift values is observed. Thus, the progress of the reaction is directly observable from the evolution of the ^{129}Xe NMR signal. In the beginning, a temperature effect is visible as the xenon peaks move to smaller chemical shift values (compare first and second spectra in Figure 4). This shift is attributed to the heating of the sample from 278 to 343 K. In the first spectra the heating effect counters and partially compensates the effect of the starting polymerization reaction, which simultaneously causes an increase in chemical shift. The resulting "equilibration time" due to heating is in fact comparable with the time which is needed for the heating of the sample in the calorimeter used in these studies (see below).

Figure 4 shows also the already mentioned merging of the two ^{129}Xe peaks stemming from the aqueous and the organic phase of the miniemulsion to only one exchange peak due to changes in the exchange rate in the course of the experiment

dx.doi.org/10.1021/ma202605n | Macromolecules 2012, 45, 1839−1846

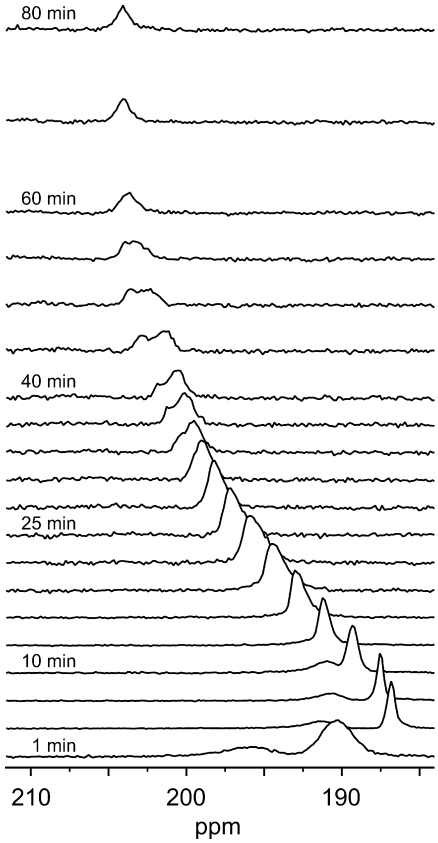

Figure 4. Time series of ^{129}Xe NMR spectra recorded during a miniemulsion polymerization reaction at 343 K (initiated with V70). The plot shows the chemical shift range of the dissolved Xe. The insertion of the sample tube into the heated magnet was used as the starting time t = 0 min. The spectra depict a strong dependence of the Xe chemical shift on the progress of the polymerization.

(compare spectra before and after 10 min in Figure 2). The exchange rate increases as the temperature inside the sample increases. However, substantial broadening and distortion of the dissolved ^{129}Xe peak occurs between 30 and 60 min reaction time. The line broadening can be attributed to an increase of viscosity inside the monomer/polymer droplets which leads to a decreased mobility of the Xe atoms and the polymer chains. The decreased mobility cause a rise of dipolar interactions between Xe atoms and protons resulting in a net dipolar broadening of the ^{129}Xe NMR lines.[40,41]

In this study, time-resolved spectra for two different polymerization reactions for a reaction time of 120 min were obtained by using two different azo-initiators, namely V59 and V70 (full names and 10 h half-life decomposition temperatures are denoted in the Materials and Methods section). At the reaction temperature of 343 K, polymerization reactions started by the two initiators follow the expected miniemulsion mechanism described by Bechthold et al.[30] (see Supporting Information). However, the two initiators used here decompose at very different rates at 343 K. The very fast decomposition of V70 compared to V59 leads to a shorter nucleation phase and a faster on/off mechanism for the polymerization reaction initiated by V70, resulting in a higher reaction rate at the beginning of the polymerization. The faster on/off mechanism leads to shorter polymer chains compared to the reaction initiated by V59 (for SEC results, see Supporting Information). The different molecular weights of the polymer suspensions allow us to the check for a dependence of the chemical shift of ^{129}Xe on the molecular weight of the polymers. A more detailed mechanistic insight into the two reactions from calorimetric data and the molecular weight distributions can be found in the Supporting Information.

For both polymerization reactions, the chemical shift of the dissolved ^{129}Xe was determined for each spectrum of the time series and plotted in Figure 5. The open and filled circles in

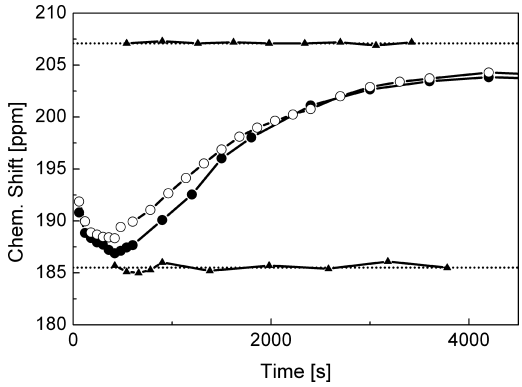

Figure 5. Plot of the chemical shift of ^{129}Xe versus reaction time with V70 as initiator (open circles), resulting in a faster increase in the chemical shift, and V59 as initiator (filled circles), resulting in a slower increase. The triangles correspond to the Xe chemical shift in a fully polymerized colloid of the same particle size (207.0 ppm) and a miniemulsion containing only monomer droplets (185.5 ppm) at 343 K. The lines are for guiding the eyes.

Figure 5 show the development of the chemical shift of the dissolved ^{129}Xe for the reaction initiated by V70 and V59, respectively. As expected due to the shorter nucleation phase, the chemical shift of the dissolved Xe in the reaction with the initiator V70 shows a faster increase than the one obtained in the reaction employing the initiator V59. For longer reaction times, the chemicals shift values of both reactions become the same due to the complete conversion of both polymerizations. Accordingly, the difference in the molecular weights of the products of the two polymerizations does not influence the chemical shift of ^{129}Xe in our experiments.

For comparison, Figure 5 also shows the two extremes for the chemical shift of the dissolved ^{129}Xe in theses polymerizations (triangles). The lower limit at 185.5 ppm represents ^{129}Xe dissolved in a miniemulsion at a temperature of 343 K containing only monomer, no polymer. It has been determined using a miniemulsion consisting of all reaction components except the initiator. Because of the lack of the initiator, no reaction could take place in the sample. The curve of the chemical shift of the reaction mixture nearly reaches the lower boundary (counteraction between thermal effect and shift due to the ongoing reaction).

The upper limit at 207.0 ppm is given by the chemical shift of dissolved Xe in a completely polymerized miniemulsion at a temperature of 343 K. It was measured by using a colloidal polymer suspension of the same particle size as in the miniemulsions. During the monitored polymerization reactions, the chemical shift values do not reach this boundary but stay ~3 ppm lower. This chemical shift difference can be attributed to the manufacturing of the colloid particles. The particles have been subjected to a dialysis process which removes any residual monomer, surfactant and charged, soluble oligomers from the

system. Thus, the colloid particles obtained in this manner differ from the in situ particles in the reaction mixture, giving rise to the observed difference in chemical shift.

To check the validity of the ^{129}Xe NMR monitoring method presented here, calorimetric measurements of the polymerization reactions were also carried out for polymerization reactions with the two initiators. In order to allow for a good comparison between the results obtained from calorimetry and ^{129}Xe NMR spectroscopy, two samples from the same miniemulsion batch were simultaneously measured by the two methods for each polymerization reaction. Thus, any change of the miniemulsion or any polymerization reaction prior to the start of the experiment can be ruled out for the interpretation of the differences between ^{129}Xe NMR and calorimetry.

The effect measured by a calorimeter is the heat flow in dependence of time which directly correlates with the reaction kinetics of the observed reaction. Thus, reaction heat calorimetry is a differential method. The chemical shift data measured by the NMR experiments depend on the polymerization degree or reaction conversion. Therefore, NMR reaction monitoring is an integral method. To compare the data from the two methods, the calorimetric data were numerically integrated.

Figure 6 shows the integrated calorimetric data (red line) and the corresponding ^{129}Xe NMR data (black circles) for both

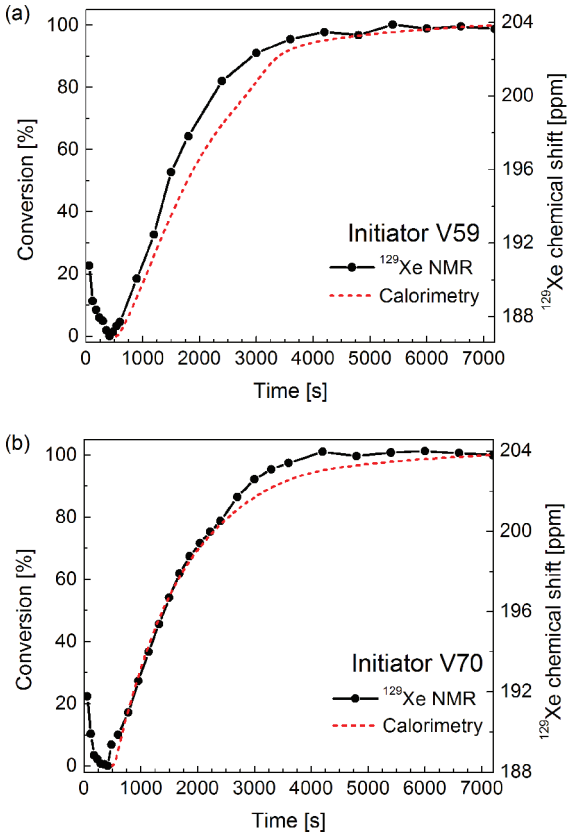

Figure 6. Comparison between the (integrated) calorimetry data (red dotted line) and the ^{129}Xe NMR data (solid line with filled circles showing the measured chemical shift) for the polymerization initiated by V59 (a) and V70 (b). The left *y*-axis shows the conversion, and the right *y*-axis shows the corresponding ^{129}Xe chemical shift values.

polymerization reactions. For the calorimetric data, the point of zero conversion was chosen as the time from which the reaction heat becomes exothermic (the first point of the positive slope, at t = 500 s). Comparably, the lowest chemical shift values derived from the ^{129}Xe NMR data for each of the two experimental series are assumed to be the points of zero conversion (at t = 420 s for both ^{129}Xe NMR experiments). After a reaction time of 7200 s, full conversion can be expected for both miniemulsion polymerization reactions (see calorimetric data in Supporting Information). Therefore, the calorimetric data have been scaled to conversion = 100% after 7200 s. Accordingly, the highest chemical shift values derived from the ^{129}Xe NMR data have been scaled to 100% conversion in order to reflect the anticipated full conversion. Both methods show a good qualitative agreement, demonstrating the validity of our approach. For the polymerization reaction initiated by V70 we even observe an excellent agreement for conversion rates up to 65%. However, small differences occur for high conversion rates for both polymerizations and the reactions seem to be slightly faster when observed by ^{129}Xe NMR. In order to reveal the differences of both observation methods, a thorough characterization of the polymerization products was performed.

To this end, the solids content of the four miniemulsions as well as the mean diameter of the particles were determined (see Table 1). For both ^{129}Xe NMR experiments, the solids content is lower and the particle diameters are smaller than for the corresponding calorimeter experiments. As there was no visible coagulum of the miniemulsion particles, this would suggest a lower conversion in the polymerizations measured by ^{129}Xe NMR, thereby contradicting the previously mentioned observation of a faster reaction observed by ^{129}Xe NMR. In order to reconcile the observed differences, we consider a mass loss of the monomer occurring during the ^{129}Xe NMR experiments. This mass loss is attributed to a diffusion of the hydrophobic monomer across the hydrophobic membrane into the dry gas flow and was tried to be minimized by a bypass of the gas flow between subsequent measurements. However, the loss of monomer could not be totally avoided due to the necessary Xe supply during the measurements. Such a loss of monomer during the polymerization reactions leads to both a higher polymer−monomer ratio after shorter reaction times (higher chemical shift in ^{129}Xe NMR) as well to smaller particle diameters.

Despite the mass loss, the accordance between the polymerizations observed by calorimetry and ^{129}Xe NMR is quite good. Because of the large concentration of monomer in the droplets at the start of the polymerization, the significance of the monomer loss is small for short reaction times. For longer reactions times, the significance of monomer loss increases which can lead to the larger difference in the observed conversions measured by calorimetry and ^{129}Xe NMR (see reaction initiated by V59 in Figure 6a). However, the mass loss of the hydrophobic monomer can be suppressed in future experiments by optimization of the experimental setup, for example, by the use of another type of hollow fiber membrane. Besides the described experimental imperfections in this work, the accuracy of the ^{129}Xe NMR method is limited only by the signal-to-noise ratio (SNR) which influences the accuracy of the determination of the chemical shift of ^{129}Xe and the achievable time resolution. A higher SNR—and thus a better accuracy of the presented method—could be achieved by using

dx.doi.org/10.1021/ma202605n | *Macromolecules* 2012, 45, 1839–1846

Table 1. Characterization of the Polymer Dispersions after Polymerization

	solids content [wt %]			particle diameter [nm] by PCCS		particle diameter [nm] from micrographs	
	calorimetry	^{129}Xe NMR	theory	calorimetry	^{129}Xe NMR	calorimetry	^{129}Xe NMR
V70	20.4	16.3	20.8	94.4 ± 12.0	87.7 ± 12.0	71.6 ± 13.4	66.6 ± 14.6
V59	19.6	16.5	20.8	105.6 ± 12.0	93.9 ± 12.0	88.8 ± 11.0	76.9 ± 11.0

a polarizer setup giving a higher ^{129}Xe polarization rate[10] or by using isotopically enriched Xe gas.

The solids content in the calorimeter experiments is only 0.4% and 1.2% lower than the theoretical value for a complete reaction which highlights the very high conversion achievable by miniemulsion polymerizations.[24,31] According to the calorimetric data (see Supporting Information), the conversion reached 100% for the calorimeter experiments after a reaction time of 7200 s, which corresponds well with the very small deviation from the theoretical solids content.

To obtain an insight into the particle size distributions for the two methods, SEM images of the particles from each polymerization reaction were acquired. Normally, the droplet size and the size distribution in a miniemulsion polymerization of a given amount of monomer are determined by the amount of surfactant in the reaction mixture and fixed in the emulsification step. Because of the hydrophobic nature of the membrane surfaces present during the ^{129}Xe NMR experiments, possible changes in particle size distribution were considered due adsorption and desorption processes of the droplets to and from the membrane surface. Figure 7 shows two SEM images

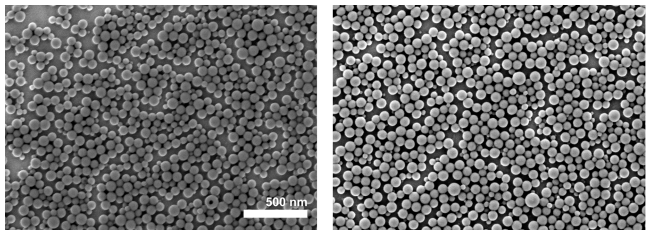

Figure 7. Scanning electron micrographs of the polymer suspensions after the polymerization. Left side: V70 ^{129}Xe NMR; right side: V70 calorimetry.

for the fast polymerization from the reaction inside the NMR spectrometer and in the calorimeter. No major differences in the particle size distribution can be found for all experiments. Besides the mentioned loss of monomer in the ^{129}Xe NMR experiments, the products and the course of the polymerization reactions in both methods seem to be very well comparable.

CONCLUSION

In this work, the chemical shift dependence of ^{129}Xe on the conversion of polymerization reactions has been demonstrated. Using this dependence and the large NMR signal of hyperpolarized ^{129}Xe, the online monitoring of a chemical reaction by ^{129}Xe NMR was successfully accomplished. Kinetic data for free-radical polymerization reactions of an industrially important monomer with two different reaction rates were obtained with good time resolution. In order to approve the validity of our method, the results of the ^{129}Xe NMR measurements were compared to calorimetric measurements. Both methods showed a good qualitative agreement except for minor differences at higher conversion rates that could be explained by a monomer loss during the ^{129}Xe NMR experiments which can most likely be circumvented by optimization of the experimental setup. The comparability of both methods was proven by a thorough characterization of the polymer products. Hyperpolarized ^{129}Xe NMR can thus provide an excellent method to investigate polymerizations exhibiting very complicated ^{1}H and ^{13}C NMR spectra due to the simplicity of the ^{129}Xe NMR spectra and the simple relationship of the ^{129}Xe chemical shift on the composition of the reaction mixture. Furthermore, the application of hyperpolarized ^{129}Xe NMR spectroscopy for the online monitoring of copolymerization reactions could allow to follow the conversion of each monomer independently which cannot be done by calorimetry. However, this would be only possible in favorable cases where the two monomers exhibit very different chemical shift values of the dissolved ^{129}Xe and extensive calibration measurements for the chemical shift of ^{129}Xe dissolved in mixtures of the used comonomers would be necessary. ^{129}Xe NMR might also be well applicable for the online monitoring of other chemical reactions apart from polymerizations. It might, for example, allow for time-resolved measurements of thermoneutral reactions which cannot be assessed by calorimetry. The presented method would very probably be applicable to larger reactors by implementing a pump-around loop which could bring a sample volume inside a (high-field) NMR magnet. In this case already existing "flow-through membrane modules" could be used for dissolution of the hyperpolarized ^{129}Xe prior to the NMR measurement.[36] Given the indepence of the signal amplitude of hyperpolarized samples from the magnetic field strength, the use of a low-field NMR spectrometer for routine reactor monitoring seems feasible under the condition of sufficiently large chemical shift dispersion.

ASSOCIATED CONTENT

Supporting Information

Data from calorimetry, the calculated average number of radicals, and the molecular weight distributions of the polymer suspensions obtained in the calorimeter experiments. This material is available free of charge via the Internet at http://pubs.acs.org.

AUTHOR INFORMATION

Corresponding Author

*E-mail: muenne@mpip-mainz.mpg.de.

Notes

The authors declare no competing financial interest.

ACKNOWLEDGMENTS

We thank S. Appelt and W. Häsing (FZ Jülich) for the development of the xenon polarizer. N. Vogel acknowledges funding from the Materials Science in Mainz (MAINZ) graduate school.

REFERENCES

(1) Matyjaszewski, K.; Gnanou, Y.; Leibler, L. *Macromolecular Engineering: Precise Synthesis, Materials Properties, Applications*; Wiley-VCH Verlag GmbH & Co. KGaA: New York, 2007.
(2) Guthausen, G.; Vargas, M. A.; Cudaj, M.; Hailu, K.; Sachsenheimer, K. *Macromolecules* **2010**, *43* (13), 5561−5568.
(3) Fonseca, G. E.; Dube, M. A.; Penlidis, A. *Macromol. React. Eng.* **2009**, *3* (7), 327−373.
(4) Frauendorfer, E.; Wolf, A.; Hergeth, W. D. *Chem. Eng. Technol.* **2010**, *33* (11), 1767−1778.
(5) Haddleton, D. M.; Perrier, S.; Bon, S. A. F. *Macromolecules* **2000**, *33* (22), 8246−8251.
(6) Gramm, S.; Komber, H.; Schmaljohann, D. *J. Polym. Sci., Part A: Polym. Chem.* **2005**, *43* (1), 142−148.
(7) Abdollahi, M.; Sharifpour, M. *Polymer* **2007**, *48* (1), 25−30.
(8) Landfester, K.; Spiegel, S.; Born, R.; Spiess, H. W. *Colloid Polym. Sci.* **1998**, *276* (4), 356−361.
(9) Ruth, U.; Hof, T.; Schmidt, J.; Fick, D.; Jansch, H. J. *Appl. Phys. B* **1999**, *68* (1), 93−97.
(10) Ruset, I. C.; Ketel, S.; Hersman, F. W. *Phys. Rev. Lett.* **2006**, *96* (5), xxxx.
(11) Ardenkjaer-Larsen, J. H.; Fridlund, B.; Gram, A.; Hansson, G.; Hansson, L.; Lerche, M. H.; Servin, R.; Thaning, M.; Golman, K. *Proc. Natl. Acad. Sci. U. S. A.* **2003**, *100* (18), 10158−10163.
(12) Carver, T. R.; Slichter, C. P. *Phys. Rev.* **1956**, *102* (4), 975−980.
(13) Bowers, C. R.; Weitekamp, D. P. *J. Am. Chem. Soc.* **1987**, *109* (18), 5541−5542.
(14) Münnemann, K.; Spiess, H. W. *Nature Phys.* **2011**, *7* (7), 522−523.
(15) Walker, T. G.; Happer, W. *Rev. Mod. Phys.* **1997**, *69* (2), 629−642.
(16) Appelt, S.; Baranga, A. B.; Erickson, C. J.; Romalis, M. V.; Young, A. R.; Happer, W. *Phys. Rev. A* **1998**, *58* (2), 1412−1439.
(17) Shah, N. J.; Unlu, T.; Wegener, H. P.; Halling, H.; Zilles, K.; Appelt, S. *NMR Biomed.* **2000**, *13* (4), 214−219.
(18) Kilian, W.; Seifert, F.; Rinneberg, H. *Magn. Reson. Med.* **2004**, *51* (4), 843−847.
(19) Han, S.; Kuhn, H.; Hasing, F. W.; Münnemann, K.; Blumich, B.; Appelt, S. *J. Magn. Reson.* **2004**, *167* (2), 298−305.
(20) Schröder, L.; Meldrum, T.; Smith, M.; Schilling, F.; Denger, P.; Zapf, S.; Wemmer, D.; Pines, A. *World Congr. Med. Phys. Biomed. Eng.* **2009**, *25* (13), 176−179.
(21) Sozzani, P.; Comotti, A.; Simonutti, R.; Meersmann, T.; Logan, J. W.; Pines, A. *Angew. Chem., Int. Ed.* **2000**, *39* (15), 2695−2698.
(22) Moudrakovski, I.; Soldatov, D. V.; Ripmeester, J. A.; Sears, D. N.; Jameson, C. J. *Proc. Natl. Acad. Sci. U. S. A.* **2004**, *101* (52), 17924−17929.
(23) Emmler, T.; Heinrich, K.; Fritsch, D.; Budd, P. M.; Chaukura, N.; Ehlers, D.; Ratzke, K.; Faupel, F. *Macromolecules* **2010**, *43* (14), 6075−6084.
(24) Schork, F. J.; Luo, Y. W.; Smulders, W.; Russum, J. P.; Butte, A.; Fontenot, K. *Polym. Part.* **2005**, *175*, 129−255.
(25) Landfester, K. *Annu. Rev. Mater. Res.* **2006**, *36*, 231−279.
(26) Landfester, K.; Crespy, D. *Beilstein J. Org. Chem.* **2010**, *6*, 1132−1148.
(27) Landfester, K.; Weiss, C. In *Modern Techniques for Nano- and Microreactors/-reactions*; Caruso, F., Ed.; Springer: Berlin, 2010; Vol. *229*, pp 1−49.
(28) Weiss, C.; Landfester, K. In *Hybrid Latex Particles*; van Herk, A. M., Landfester, K., Eds.; Springer: Berlin, 2011; Vol. *233*, pp 185−236.
(29) Glöggler, S.; Blümich, B.; Appelt, S. *Magn. Reson. Porous Media* **2011**, *1330*, 101−104.
(30) Bechthold, N.; Landfester, K. *Macromolecules* **2000**, *33* (13), 4682−4689.
(31) Li, D. H.; Sudol, E. D.; El-Aasser, M. S. *J. Appl. Polym. Sci.* **2006**, *101* (4), 2304−2312.
(32) Blythe, P. J.; Klein, A.; Phillips, J. A.; Sudol, E. D.; El-Aasser, M. S. *J. Polym. Sci., Part A: Polym. Chem.* **1999**, *37* (23), 4449−4457.
(33) Taratula, O.; Dmochowski, I. J. *Curr. Opin. Chem. Biol.* **2010**, *14* (1), 97−104.
(34) Baumer, D.; Brunner, E.; Blümler, P.; Zänker, P. P.; Spiess, H. W. *Angew. Chem., Int. Ed.* **2006**, *45* (43), 7282−7284.
(35) Cleveland, Z. I.; Möller, H. E.; Hedlund, L. W.; Driehuys, B. *J. Phys. Chem. B* **2009**, *113* (37), 12489−12499.
(36) Amor, N.; Zänker, P. P.; Blümler, P.; Meise, F. M.; Schreiber, L. M.; Scholz, A.; Schmiedeskamp, J.; Spiess, H. W.; Münnemann, K. *J. Magn. Reson.* **2009**, *201* (1), 93−99.
(37) Buckingham, A. D.; Pople, J. A. *Discuss. Faraday Soc.* **1956**, *22*, 17−21.
(38) Jameson, C. J.; Jameson, A. K.; Cohen, S. M. *J. Chem. Phys.* **1973**, *59* (8), 4540−4546.
(39) Jameson, C. J.; Dedios, A. C. *J. Chem. Phys.* **1992**, *97* (1), 417−434.
(40) Kentgens, A. P. M.; Vanboxtel, H. A.; Verweel, R. J.; Veeman, W. S. *Macromolecules* **1991**, *24* (12), 3712−3714.
(41) Saunders, M.; JimenezVazquez, H. A.; Khong, A. *J. Phys. Chem.* **1996**, *100* (39), 15968−15971.

Macromolecules

Article

pubs.acs.org/Macromolecules

Easily Attainable Phenothiazine-Based Polymers for Polymer Solar Cells: Advantage of Insertion of *S,S*-dioxides into its Polymer for Inverted Structure Solar Cells

Gyoungsik Kim,[†] Hye Rim Yeom,[†] Shinuk Cho,[‡] Jung Hwa Seo,[§] Jin Young Kim,[†] and Changduk Yang*[,†]

[†]Interdisciplinary School of Green Energy and KIER-UNIST Advanced Center for Energy, Low Dimensional Carbon Materials Center, Ulsan National Institute of Science and Technology (UNIST), Ulsan 689-798, South Korea

[‡]Department of Physics and EHSRC, University of Ulsan, Ulsan 680-749, South Korea

[§]Department of Materials Physics, Dong-A University, Busan 604-714, South Korea

Supporting Information

ABSTRACT: Two donor− (D−) acceptor (A) type polymers based on a soluble chromophore of phenothiazine (PT) unit that is a tricyclic nitrogen−sulfur heterocycle, have been synthesized by introducing an electron-deficient benzothiadiazole (BT) building block copolymerized with either PT or phenothiazine-*S,S*-dioxide (PT-*SS*) unit as an oxidized form of PT. The resulting polymers, **PPTDTBT** and **PPTDTBT-*SS*** are fully characterized by UV−vis absorption, electrochemical cyclic voltammetry, X-ray diffraction (XRD), and DFT theoretical calculations. We find that the maximum absorption of **PPTDTBT** is not only markedly red-shifted with respect to that of **PPTDTBT-*SS*** but also its band gap as well as molecular energy levels are readily tuned by the insertion of *S,S*-dioxides into the polymer. The main interest is focused on the electronic applications of the two polymers in organic field-effect transistors (OFETs) as well as conventional and inverted polymeric solar cells (PSCs). **PPTDTBT** is a typical p-type polymer semiconductor for OFETs and conventional PSCs based on this polymer and $PC_{71}BM$ show a power conversion efficiency (PCE) of 1.69%. In case of **PPTDTBT-*SS***, the devices characteristics result in: (i) 1 order of magnitude higher hole mobility ($\mu = 6.9 \times 10^{-4}$ cm^2 V^{-1} s^{-1}) than that obtained with **PPTDTBT** and (ii) improved performance of the inverted PSCs (1.22%), compared to its conventional devices. Such positive features can be accounted for in terms of closer packing molecular characteristics owing either to the effects of dipolar intermolecular interactions orientated from the sulfonyl groups or the relatively high coplanarity of **PPTDTBT-*SS*** backbone.

INTRODUCTION

The dramatic growing need for renewable energy supply is increasing the demand for new technologies for photovoltaic energy conversion. Polymeric solar cells (PSCs) have attracted much attention due to their potentials for low cost, lightweight, and good compatibility with the roll-to-roll process for making flexible large area devices.[1−5] So far, the most efficient polymer solar cell system is built on the concept of bulk-heterojunction (BHJ) structure, which uses a blend of an electron-donor polymer and an electron-acceptor fullerene.[3] Recently, power conversion efficiencies (PCEs) of 6−8% have been realized by using new conjugated polymer donors[6−10] or novel fullerene-derived acceptors.[11−13]

Aside from achieving higher PCEs, improving the stability of PSCs is equally important. In general, conventional PSCs are comprised of a BHJ active layer sandwiched between an acidic poly(3,4-ethylenedioxythiophene):poly(styrenesulfonate)- (PEDOT:PSS-) coated indium tin oxide (ITO) anode and a low work-function metal cathode (e.g., Al and Ca). In such a device structure, not only does the cathodes easily oxidize in air but also the acidic PEDOT:PSS-ITO can suffer interfacial degradation over the operating lifetime.[14] As alternative to the regular device configuration, PSCs with an inverted device structure have been developed, which enables the use of stable and printable high work-function metals (e.g., Ag and Au) as hole collecting top electrodes and n-type low work-function metal oxides (e.g., TiO_x and ZnO) as electron collecting bottom electrodes.[15,16] Thus, with advances made on the aforementioned efficiency front, the lifetime and reliability of PSCs are also envisaged by utilizing the inverted PSC configuration through the replacement of the low work-function metal cathode and the elimination of PEDOT:PSS layer.

Recently, several classes of narrow bandgap donor− (D−) acceptor (A) type polymers have been developed to better harvest the solar spectrum with deeper HOMO energies that can be helpful in realizing high open circuit voltage (V_{OC}) and PCEs, as the V_{OC} value of PSCs is directly proportional to the offset between the HOMO level of electron donor and the LUMO level of electron acceptor.[5,17−19] Among them, poly(2,7-carbazole-*alt*-dithienylbenzothiadiazole) (PCDTBT) showed particularly interesting achievement of a PCE in excess of 6% from a BHJ cell with V_{OC} value approaching 0.9 V as well as remarkable stability at higher temperature for extended periods of time.[17,20] More recently, efficient, air-stable inverted BHJ solar cells based on PCDTBT fabricated with a low-temperature annealed sol−gel-derived ZnO film as an electron transport layer have also been demonstrated.[15]

Received: December 8, 2011
Revised: January 15, 2012
Published: February 3, 2012

dx.doi.org/10.1021/ma202661b | *Macromolecules* 2012, 45, 1847−1857

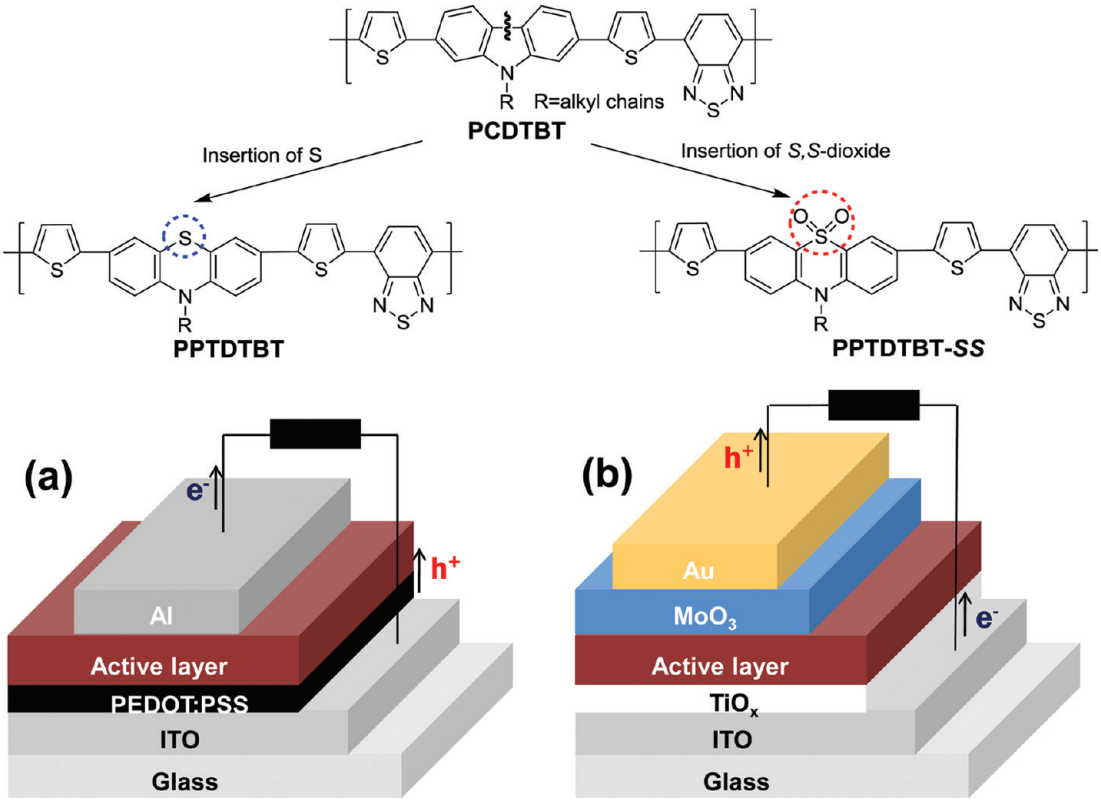

Figure 1. Molecular structures of PCDTBT and phenothiazine-based polymers. Schematic depiction of the conventional structure (a) and inverted structure (b) of the PSCs used by our research group.

However, to prepare the tricyclic 2,7-carbazole monomer, 4,4′-dibromobiphenyl must first undergo a nitration reaction followed by a Cadogan ring closure reaction.[21] The relatively long synthetic routes will limit their future commercial application in PSCs. To realize potentially low manufacturing costs, it is critical to obtain readily synthesized polymers from commercial products.

In this regard, we focused our attention to the well-known phenothiazine building block, considering the following: (i) Heterocyclic phenothiazine unit is structurally similar to the carbazole moiety but it contains an additional sulfur atom. As a more powerful electron-rich molecule, the phenothiazine is better suited for the development of enhanced intramolecular charge transfer (ICT) polymers. In addition, its "butterfly" nonplanar structure impedes π-stacking aggregation and intermolecular excimer formation, resulting in diverse opto-electronic applications.[22−26] (ii) Not only is phenothiazine cheap and commercially available but also it can be easily tailored by connecting solubilizing groups to the N atom to improve solubility. This is important since the barrier for preparation of materials in terms of a cost effectiveness must be overcome to realize the commercial potentials of PSCs. (iii) Following oxidation of phenothiazines to phenothiazine-*S*,*S*-dioxides, the electron-withdrawing sulfones would reduce the electron density in the polymer backbone, most likely rendering it more resistant toward the oxidation while simultaneously tuning the electronic properties. In particular, we hypothesized that the hydrophilicity of the SO_2 groups can promote the compatibility and low contact resistance through the potential interaction with oxides in the inverted BHJ solar cells integrated with metal oxide materials as an electron transport and an hole transport between the ITO/BHJ and BHJ/metal interfaces.

Herein, we report two new polymers incorporating either phenothiazine or its oxidized analogue phenothiazine-*S*,*S*-dioxide as the donor and benzothiadiazole as the acceptor, namely poly(*N*-(2-decyltetradecyl)-3,7-phenothiazine-*alt*-5,5-(4′,7′-di-2-thienyl-2′,1′,3′-benzothiadiazole)) (**PPTDTBT**) and poly(*N*-(2-decyltetradecyl)-3,7-phenothiazine-*S*,*S*-dioxide-*alt*-5,5-(4′,7′-di-2-thienyl-2′,1′,3′-benzothiadiazole)) (**PPTDTBT-*SS***), respectively (Figure 1). These polymers are tested in both conventional and inverted solar cell devices using the fullerene derivative (see Figure 1a and b). We find that PSCs based on **PPTDTBT** in a conventional architecture can reach PCE as high as 1.69%, whereas the utilization of its oxidized form **PPTDTBT-*SS*** into inverted solar cells shows improved performance (PCE = 1.22%), when compared to that of its conventional devices. The results obtained here are very helpful for molecular design strategies to obtain inverted solar cells with higher device performance.

■ RESULTS AND DISCUSSION

The synthetic routes to the intermediates and the polymers (**PPTDTBT** and **PPTDTBT-*SS***) are outlined in Scheme 1. Synthesis of 4,7-dibromo-2,1,3-benzothiadiazole (**1**), 4,7-di-2-thienyl-2,1,3-benzothiadiazole (**2**), and 4,7-bis(5-bromo-2-thienyl)-2,1,3-benzothiadiazole (**3**) were prepared by following the literature procedures.[27] In order to guarantee good solubility of phenothiazine-based polymers, the bulky branched side chain (2-decyltetradecyl) was introduced onto the nitrogen atom on the phenothiazine unit. Dibromination of **4** by *N*-bromosuccinimide (NBS) in DMF afforded 3,7-dibromo-*N*-(2-decyltetradecyl)phenothiazine (**5**) in 93% yield which was transformed into the corresponding diboronic ester **6** via lithiation and subsequent quenching with 2-isopropoxy-4,4,5,5-

dx.doi.org/10.1021/ma202661b | *Macromolecules* 2012, 45, 1847−1857

Scheme 1. Synthesis of PPTDTBT and PPTDTBT-*SS*[a]

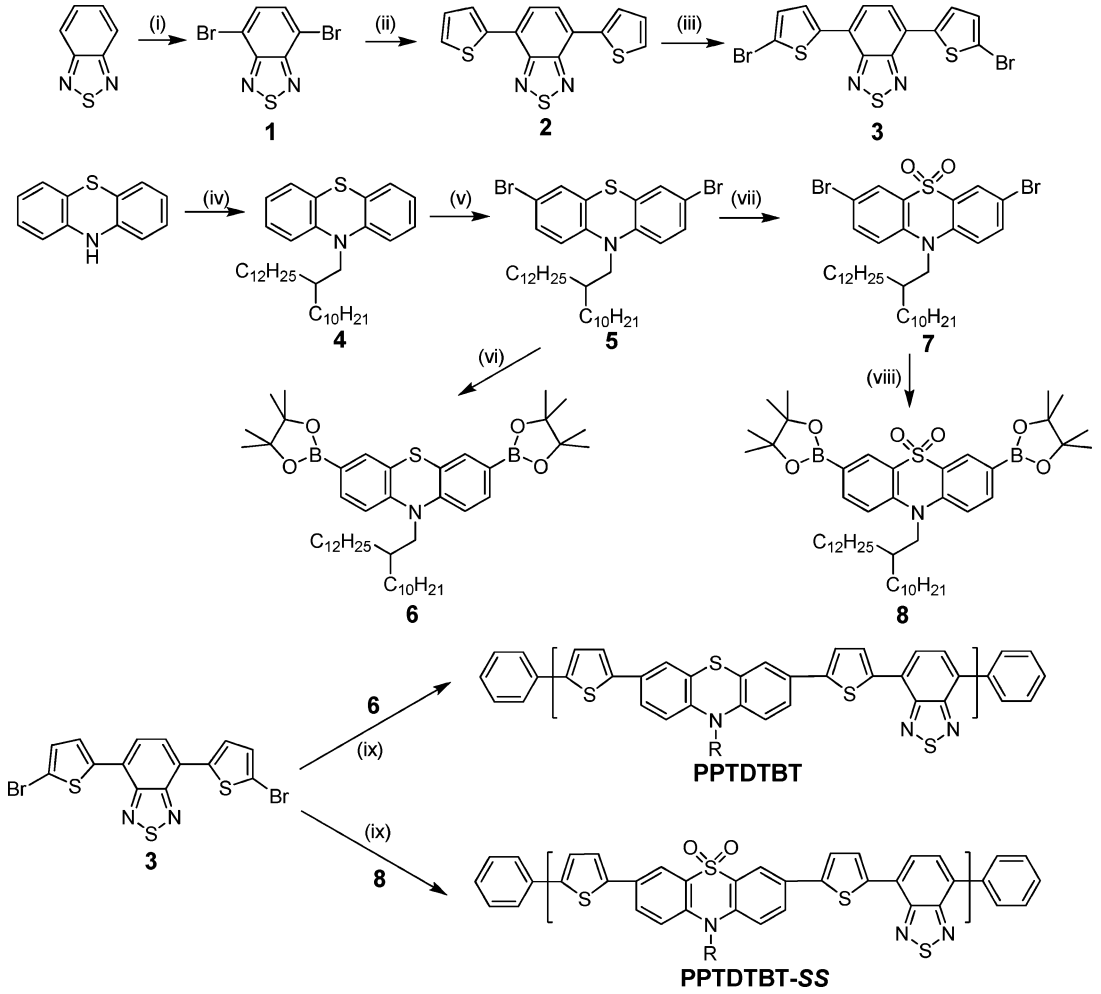

[a]Reagents and conditions: (i) Br_2, HBr, reflux; (ii) 2-(tributylstannyl)thiophene, THF, $Pd(pph_3)_4$, reflux; (iii) NBS, DMF, RT; (iv) 2-Decyltetradecyl bromide, NaN, DMF, RT; (v) NBS, DMF, RT; (vi) *n*-BuLi, THF, −78 °C, 2-isopropoxy-4,4,5,5-tetramethyl-1,3,2-dioxaborolane; (vii) H_2O_2, acetic acid, 90 °C; (viii) Bis(pinacolato)diboron, DMF, KOAc, $PdCl_2$(dppf), reflux; (ix) Suzuki polymerization, toluene, H_2O, K_3PO_4, P(*o*-tol)$_3$, $Pd_2(dba)_3$, 90 °C.

tetramethyl-1,3,2-dioxaborolane (58%) to generate the comonomer. Separately, compound **5** was oxidized with hydrogen peroxide under acetic acid (52%) according to a previously reported protocol[28] to obtain phenothiazine-*S*,*S*-dioxide **7**. Treatment of **7** with bis(pinacolato)diboron under $PdCl_2$(dppf)/KOAc/DMF led to the phenothiazine-*S*,*S*-dioxide diboronic ester **8** in 64% yield.

With all the monomers ready, Suzuki polycondensations (Scheme 1) were carried out at 90 °C for 72 h in degassed toluene/water using K_3PO_4 as an organic base, $Pd_2(dba)_3$ as a catalyst, and P(*o*-tol)$_3$ as the corresponding ligand, affording **PPTDTBT** and **PPTDTBT-*SS*** respectively. The target polymers were purified by reprecipitation and Soxhlet extraction with methanol, acetone, and chloroform. They show good solubility in common solvents such as chloroform, dichloromethane, toluene, THF, and chlorobenzene. Note that **PPTDTBT-*SS*** has somewhat lower solubility in the nonpolar solvents than that of **PPTDTBT** because of the increased polarity as well as the hydrophilicity that result from the introduction of the sulfone groups in the polymer backbone. Gel-permeation chromatography (GPC) analysis against polystyrene standard exhibits a number-averaged molecular mass (M_n) of 9.8×10^3 and 7.6×10^3 g/mol and polydispersity (PDI) of 1.27 and 1.21 for **PPTDTBT** and **PPTDTBT-*SS***, respectively.

Optical and Electrochemical Properties. The UV−vis spectra of two polymers (**PPTDTBT** and **PPTDTBT-*SS***) in chloroform solution and solid films on the quartz are shown in Figure 2. The spectroscopic data of the polymers are summarized in Table 1. **PPTDTBT** film are characterized with a strong, broad and structureless absorption band at 582 nm, corresponding to the intramolecular charge-transfer (ICT) transition, together with a strong absorption band at shorter wavelength (~395 nm) due to higher energy transitions such as $\pi-\pi^*$ transitions. Notably, such optical features are remarkable similarity to those of the analogous PCDTBT (λ_{max} = 398 and 576 nm), but **PPTDTBT** has a slightly lower optical band gap (E_g^{opt} = 1.79 eV) from the absorption edge of the thin film than PCDTBT (1.88 eV). Compared to **PPTDTBT** showing the absorption maxima, **PPTDTBT-*SS*** in the solid state exhibits a nearly identical high-energy peak at 387 nm but a hypsochromic shift of the ICT band at 535 nm, resulting in a larger optical band gap (1.95 eV). This indicates that, as expected, the donating strength of phenothiazine-*S*,*S*-dioxide

dx.doi.org/10.1021/ma202661b | *Macromolecules* 2012, 45, 1847−1857

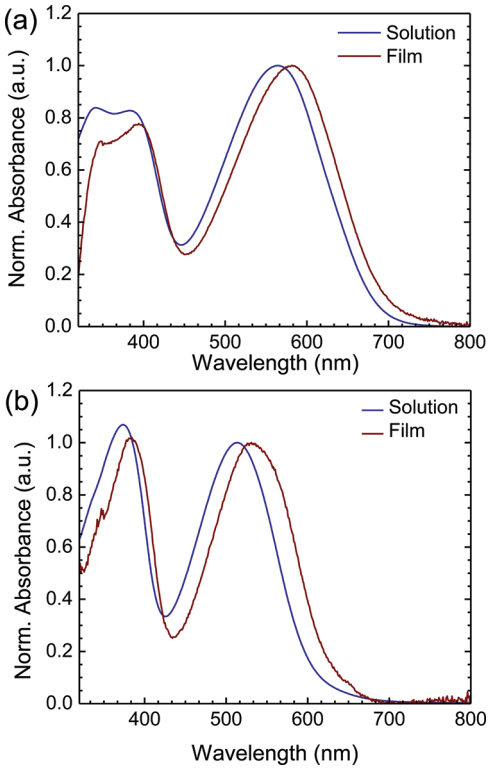

Figure 2. UV−vis absorption spectra of **PPTDTBT** (a) and **PPTDTBT-*SS*** (b).

that contains the electron-withdrawing sulfonyl group is weaker than that of the phenothiazine moiety, leading to relatively reduced ICT character in **PPTDTBT-*SS***.

Electrochemical cyclic voltammetry (CV) was performed to determine the highest occupied molecular orbital (HOMO) and lowest unoccupied molecular orbital (LUMO) energy levels of the polymers (Figure 3). The CV curves were recorded referenced to an Ag/Ag^+ (0.1 M n-Bu_4NPF_6) electrode, which was calibrated by a ferrocene-ferrocenium (Fc/Fc^+) redox couple (4.8 eV below the vacuum level). The electrochemical characteristics of the estimated energy levels (HOMO and LUMO) and electrochemical band gap (E_g^{elec}) are listed in Table 1. The HOMO and LUMO energy levels are calculated to be −5.41 and −3.63 eV for **PPTDTBT** and −5.60 and −3.60 eV for **PPTDTBT-*SS***, respectively. Considering the relatively low HOMO levels of the polymers, a high V_{OC} can be expected.[29] The LUMO levels of the polymers are positioned 0.3 eV above the $PC_{71}BM$ (−4.3 eV) to ensure a downhill driving force for charge separation to $PC_{71}BM$. The electrochemical HOMO−LUMO gaps of the both polymers are very similar to those of optical band gaps. Apparently, the LUMO value of **PPTDTBT** matches well with that of PCDTBT (−3.6 eV) whereas its higher HOMO level, in comparison with PCDTBT (−5.5 eV), indicates the increase of donor strength due to the insertion of the additional electron-rich sulfur atoms. For **PPTDTBT-*SS*** interchanged the phenothiazine with a phenothiazine-*S*,*S*-dioxide segment, the HOMO (−5.6 eV) is found to be lower than of that of **PPTDTBT** owing to the presence of the electron-deficient SO_2 groups in the polymer backbone, which can be beneficial to the better air-stability and higher V_{OC} of the PSCs based on the polymer as donor.[30]

X-ray Analyses. To evaluate the crystallinity of the polymer, X-ray diffraction (XRD) measurements were taken of thick films prepared from chlorobenzene on SiO_2/Si substrate. The thickness of the films was determined to be 1.5−55 μm by profilometry. Figure 4 shows the XRD data of the thin films of **PPTDTBT** and **PPTDTBT-*SS***, respectively. **PPTDTBT-*SS*** reveals a distinct primary diffraction feature at 2θ = 4.67°, corresponding to d-spacing of 18.9 Å and a secondary broad peak at 2θ = 21.2° (d = 4.2 Å) related to π−π stacking between the polymer main chains is also observed. Contrastingly, the XRD pattern of **PPTDTBT** exhibits only the secondary broad peak shifting to 17.51° (d = 5.10 Å). These results suggest a higher structural organization in the solid state for **PPTDTBT-*SS*** compared to **PPTDTBT**.

Organic Field Effect Transistors. To investigate the potential of the two new polymers in plastic electronics, organic field-effect transistors (OFETs) were fabricated in the top contact geometry as described in the Experimental Section (Figure 5). Figure 5b shows the transfer characteristics, $|I_{ds}|$ vs V_{gs} and $|I_{ds}|^{1/2}$ vs V_{gs} (both at V_{ds} = −60 V), of OFETs fabricated using **PPTDTBT** and **PPTDTBT-*SS***, respectively, as the active layer. These I_{ds} vs V_{gs} curves obtained from both **PPTDTBT** and **PPTDTBT-*SS*** exhibit clear signature of p-type behavior. The saturated charge carrier mobilities of the polymers are calculated using the saturation current equation: $I_{ds} = (\mu WC_i/2L)(V_{gs} - V_T)^2$.[31] An hole mobility ($\mu$) as high as 9.8×10^{-5} $cm^2\ V^{-1}\ s^{-1}$ (threshold voltage (V_T) = −11.5 V) with a current on/off ratio (I_{on}/I_{off}) of 2.5×10^2 is estimated for OFETs produced from **PPTDTBT**. Interestingly, despite the insertion of the electron-deficient SO_2 groups as well as the relatively lower molecular weight, the hole carrier mobility is increased by about 1 order of magnitude in **PPTDTBT-*SS*** OFETs ($\mu = 6.9 \times 10^{-4}$ $cm^2\ V^{-1}\ s^{-1}$, V_T = −21.0 V, $I_{on}/I_{off} = 7.7 \times 10^2$), compared to **PPTDTBT**. Although a concrete evidence of the high performance with **PPTDTBT-*SS*** OFETs is lacking at this stage, we think this is partially contributed either from (i) the reduced contact resistance between the semiconductor and the source/drain electrodes arising from the favorable interfacial dipoles between *S*,*S*-dioxide groups and Au electrodes or (ii) the well-interconnected thin film morphology due to the interaction between the polar *S*,*S*-dioxides. The enhanced intermolecular interactions would bring the polymer chain into a close proximity as evidenced by the XRD results, which can facilitate charge hopping in the polymer.

DFT Electronic Structure Calculations. To shed light on the difference in the electronic properties and energies of

Table 1. UV−Vis Absorption and Electrochemical Properties of the Polymers

polymer	λ_{max} [nm] solution	λ_{max} [nm] film	E_g^{opt} (eV)[a]	HOMO (eV)[b]	LUMO (eV)[b]	E_g^{elec} (eV)
PPTDTBT	390, 564	395, 582	1.79	−5.41	−3.63	1.78
PPTDTBT-*SS*	377, 515	387, 535	1.95	−5.60	−3.60	2.00

[a]Calculated from the absorption band edge of the copolymer film, $E_g^{opt} = 1240/\lambda_{edge}$. [b]Thin films in CH_3CN/n-Bu_4NPF_6, versus ferrocenium/ferrocene at 50 mVs^{-1}. HOMO and LUMO estimated from the onset oxidation and reduction potentials, respectively, assuming the absolute energy level of ferrocene/ferrocenium to be 4.8 eV below vacuum. E_g^{elec} (eV) = −(LUMO − HOMO).

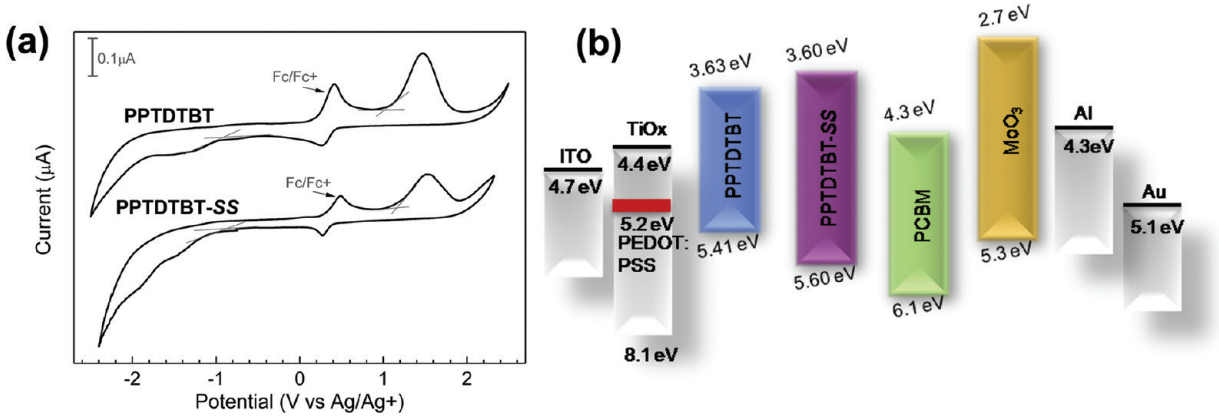

Figure 3. (a) Cyclic voltammograms of **PPTDTBT** (top) and **PPTDTBT-*SS*** (bottom) thin films on the Pt electrode in 0.1 M n-Bu_4NPF_6 acetonitrile solution at room temperature. (b) Energy level diagrams of individual layers used in conventional and inverted structure.

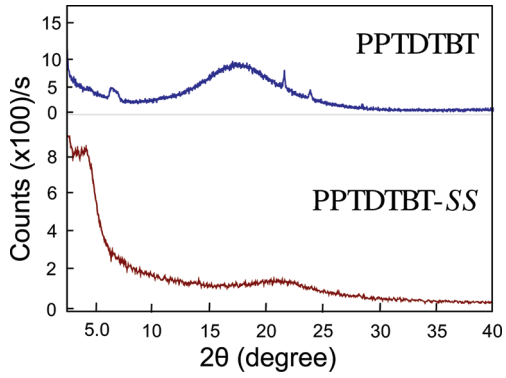

Figure 4. X-ray diffraction (XRD) patterns of drop-cast films of polymers on SiO_2/Si substrates.

frontier orbitals between the two polymers, computational studies using density functional theory (DFT) approaches were carried out. Oligomers $(\mathbf{PTDTBT})_n$ and $(\mathbf{PTDTBT\text{-}SS})_n$ with n = 1 and 2 were subjected to the calculations, with the alkyl chains replaced by methyl groups for simplicity. The optimized geometries and electron density distributions of the polymers were calculated with the B3LYP function and 6-31G* basis (Figure 6 and Figure S1 in the Supporting Information). As shown in Figure 6, the HOMO isosurfaces of the both $(\mathbf{PTDTBT})_n$ and $(\mathbf{PTDTBT\text{-}SS})_n$ are well spread over the whole conjugated backbones, whereas the LUMOs are mainly localized on BT units, respectively, which verifies the p-type behaviors obtained from the OFET study. In addition, the calculated bandgaps for $(\mathbf{PTDTBT})_2$ (1.80 eV) and $(\mathbf{PTDTBT\text{-}SS})_2$ (1.99 eV) are in considerable coincidence with the electrochemical analyses above. It is found that the phenothiazine and phenothiazine-*S*,*S*-dioxide rings are folded along the S···N vector, having the aspect angles of 21° and 15°, respectively, in qualitative agreement with their single crystal X-ray diffraction studies.[28] We note a relatively larger dihedral angle between PT and DTBT-*SS* units (θ = 160°) in the optimized geometry, when compared to that between PT and DTBT (θ = 153°). So it can be seen from the data that the coplanarity of **PPTDTBT-*SS*** is better than that in **PPTDTBT**. This implies that the backbone of **PPTDTBT-*SS*** brings about larger effective π–π interactions in the solid state, which matches qualitatively well with the XRD data. Furthermore, this can explain satisfactorily our interpretation of the better **PPTDTBT-*SS*** OFET results above.

Polymer Solar Cells. To demonstrate potential applications of the two polymers in PSCs, we used **PPTDTBT** and **PPTDTBT-*SS*** as an electron donor and $PC_{71}BM$ as an electron acceptor and fabricated conventional PSCs with a BHJ structure of ITO/PEDOT:PSS/polymers:$PC_{71}BM$/Al. The main focus of the current study is to elucidate the improved device performance of inverted PSCs by introducing SO_2 functionality in the polymer backbone through potential interaction with oxide materials. Thus, the PSCs with inverted configuration stacked from bottom to top (ITO/TiO_x/polymers:$PC_{71}BM$/MoO_3/Au) were also prepared, where MoO_3 as the hole transport layer and TiO_x as the electron transport layer were deposited. TiO_x was employed as the electron selective layer due to its high electron affinity (LUMO = ~4.4 eV).[32] Since the valence band edge of TiO_x is much lower than those of HOMOs of both the polymers and $PC_{71}BM$, the TiO_x layer serves also as a hole blocking layer. Similarly, the MoO_3 layer was used to block the electron flow because of its small electron affinity and to enhance hole transport to the anode.[33] The device structures of regular and inverted polymer solar cells are shown in Figure 1, parts a and b, and Figure 3b illustrates the energy level diagrams for each component, respectively. All data were obtained under white light AM1.5G illumination from a calibrated solar simulator with irradiation intensity of 100 mW/cm^2. The active layers through a very broad altering range from 1:1 to 1:4 (w/w) of polymer:$PC_{71}BM$ in either chlorobenzene (CB) or *o*-dichlorobenzene (ODCB) were evaluated. The optimized weight ratios of polymer to $PC_{71}BM$ for **PPTDTBT** and **PPTDTBT-*SS*** are 1:2 and 1:1.5, respectively. Device current density/voltage ($J - V$) characteristics are shown in Figure 7 and the parameters listed in Table 2.

PCEs up to 1.69% is observed for the conventional **PPTDTBT**:$PC_{71}BM$ solar cells with a V_{OC} of 0.77 V, a short circuit current density (J_{SC}) of 5.75 mA cm^{-2}, and a fill factor (FF) of 38%. Under the same white light illumination, the **PPTDTBT-*SS***:$PC_{71}BM$-based regular cell exhibits a J_{SC} of 4.03 mA cm^{-2}, a V_{OC} of 0.81 V, and a FF of 30%. It yields a substantially lower PCE of 0.97% because of its decreased photocurrent, when compared to that of **PPTDTBT**:$PC_{71}BM$. This can be mainly attributed to **PPTDTBT-*SS***'s intrinsic absorption limit in the visible region due to the relatively large energy bandgap. It is worthy to mention that as expected from the oxidation potential, the V_{OC} for the cell with **PPTDTBT-*SS*** is higher than that of **PPTDTBT**.

dx.doi.org/10.1021/ma202661b | *Macromolecules* 2012, 45, 1847–1857

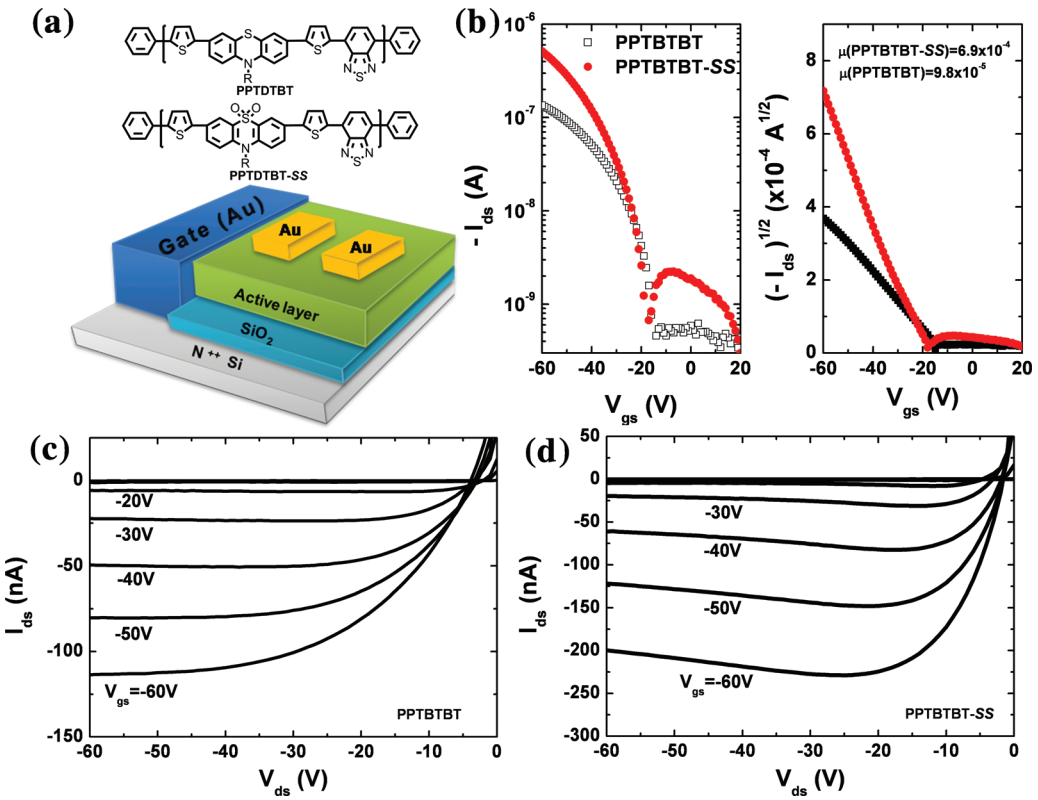

Figure 5. (a) Chemical structures of the polymers and schematic representation of OFETs structure (L = 50 μm, W = 1.5 mm). (b) Transfer curves in saturated regime with **PPTDTBT** (black line) and **PPTDTBT-*SS*** (red line). The output characteristics of **PPTDTBT** (c) and **PPTDTBT-*SS*** (d), respectively.

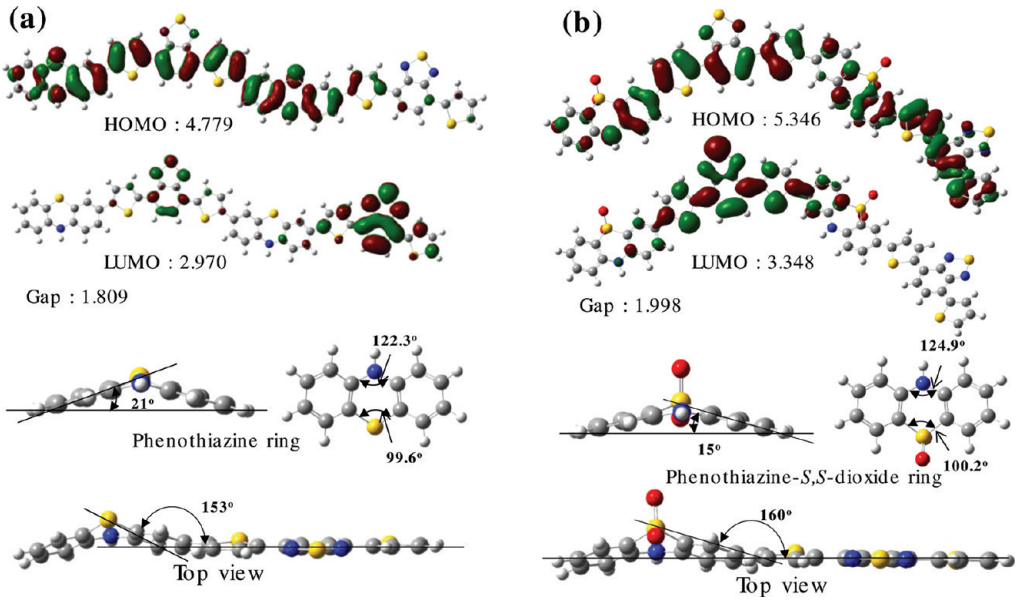

Figure 6. DFT-optimized geometries and charge-density isosurfaces for the HOMO and LUMO levels of (a) (**PTDTBT**)$_2$ and (b) (**PTDTBT-*SS***)$_2$ model systems (top) and optimized structures of phenothiazine and phenothiazine-*S*,*S*-dioxide rings and their top views, respectively (bottom).

Despite the aforementioned advantages of the inverted cells, the majority studies on the inverted cells were based on P3HT as active materials,[32,34] while only few new conjugated polymers had been tested in such configuration.[15,35,36] Therefore, comparison of the photovoltaic properties of new materials in both conventional and inverted cells is very important to fully evaluate the performance of new polymers. The J–V curves for the inverted polymer solar cells obtained under white light illumination (AM1.5 G, 100 mW/cm^2) are shown in Figure 7. The corresponding PCE is 1.47 and 1.22% for **PPTDTBT**:PC$_{71}$BM and **PPTDTBT-*SS***:PC$_{71}$BM, respectively (Table 2). In the both inverted devices, despite the fact that the absorption spectra of the active layer films in the two device types are identical, a decrease in the J_{SC} (4.80 mA cm^{-2} for **PPTDTBT**:PC$_{71}$BM and 4.11 mA cm^{-2} for **PPTDTBT-*SS***:PC$_{71}$BM, respectively) is clearly observed, resulting the

dx.doi.org/10.1021/ma202661b | *Macromolecules* 2012, 45, 1847–1857

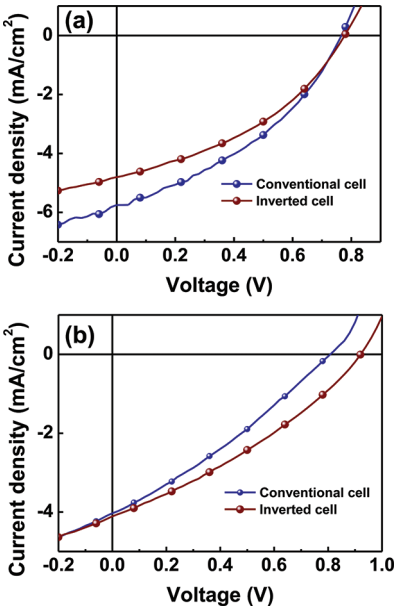

Figure 7. $J - V$ characteristics of the PSCs based on **PPTDTBT** (a) and **PPTDTBT-*SS*** (b) under illumination of AM1.5G, 100 mW/cm^2.

low overall performances. One possible explanation for this phenomenon is that, in the inverted cell, a small fraction of the incident light is observed by the evaporated Au top electrode. It is roughly estimated that 30% of the incident light with wavelength <650 nm is not absorbed by the active layer on the first pass, so clearly the reflectivity of the top electrode plays a non-negligible role in the total number of photons absorbed by the blend. Thus, it is plausible that the enhanced reflectivity of the Al electrodes used in the normal cell causes the photocurrent to be slightly higher.[37]

Surprisingly, in contrast, the inverted cell of **PPTDTBT-*SS***:$PC_{71}BM$ exhibits a slight improved J_{SC} and a much higher V_{OC} value (0.92 eV) than that of the conventional configuration with **PPTDTBT**:$PC_{71}BM$, which suggests that the recombination behavior and morphology are different for the two architectures. A likely rationale for this positive effect may be attributed to a combination of the following factors: The hydrophilicity of SO_2 groups would facilitate intimate contact on both the electrodes and thus facilitate efficient charge transfer between the active layer and the electrodes. In addition, we cannot rule out that the dipole moment induced by the polar SO_2 units in **PPTDTBT-*SS*** could be the origin of the improvement in the device performance since a higher V_{OC} can indicate a larger electrostatic field across the device structure,[32] although other explanations are still possible. Further investigation of these films using electrostatic force and surface potential microscopy in underway.

The accuracy of the photovoltaic measurements can be confirmed by the incident photon-to-electron conversion efficiency (IPCE) of the devices. Figure 8 shows the IPCE curves of both the conventional and inverted PSCs fabricated under the optimized conditions as those used for the $J-V$ measurements. All devices show a broad photoresponse spreading from 300 to 700 nm, with maximum around 570 nm. However, the IPCE of the device is within 40% for almost the whole absorption range. From this observation, we believe that the IPCE of the devices can be improved by increasing the thickness of the active layer without hampering charge separation and transport properties. However, because of their more or less limited solubility for the fabrication of practical PSCs, it is difficult to obtain high thickness for the active layer by using high concentration of the polymer blends. Currently, the preparation of dithienylbenzothiadiazole with two flexible alkoxyl chains in an effort to improve solubility is ongoing. Obviously, the IPCE value for the conventional **PPTDTBT**:$PC_{71}BM$ is the highest, which agrees with the highest J_{SC} value of the devices. To evaluate the accuracy of the photovoltaic results, the J_{SC} values were calculated by integrating the IPCE data with the AM 1.5G reference spectrum. The J_{SC} values obtained using integration and J-V measurements are rather close (within 7% error), which indicates that the photovoltaic results are reliable.

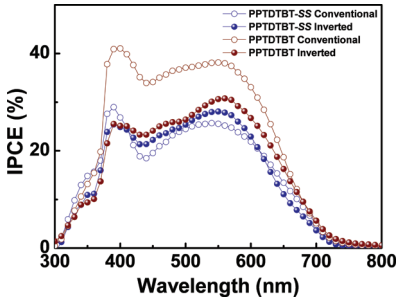

Figure 8. Incident photon-to-current efficiency (IPCE) spectra of the polymer:$PC_{71}BM$ solar cells.

Morphology. The nanoscale morphologies of both the conventional and inverted polymer/$PC_{71}BM$ films were studied using tapping-mode atomic force microscopy (AFM). Surface topography (left) and phase images (right) were taken for each film and are shown in Figure 9. Both the regular and inverted **PPTDTBT**:$PC_{71}BM$ blends are very similar and exhibit a rather uniform smooth film formation which suggests the absence of large features that might reduce the interface between polymer and fullerene potentially limiting device performance.[38,39] In contrast, **PPTDTBT-*SS***:$PC_{71}BM$ blends in both conventional and inverted structures (Figure 9, c and d) give very inhomogeneous features in which voids with a diameter of ~300 nm are present. This indicates poor miscibility between **PPTDTBT-*SS*** and $PC_{71}BM$. This implies that the presence of SO_2 groups makes **PPTDTBT-*SS*** strongly hydrophilic, which

Table 2. Photovoltaic Performance of Blends of the Polymers with Fullerenes

device structure	composite	d (nm)[a]	J_{SC} (mA cm^{-2})	V_{OC} (V)	FF	PCE (%)
conventional	**PPTDTBT**:$PC_{71}BM$ (1:2)	50	5.75	0.77	0.38	1.69
	PPTDTBT-SS:$PC_{71}BM$ (1:1.5)	50	4.03	0.81	0.30	0.97
inverted	**PPTDTBT**:$PC_{71}BM$ (1:2)	28	4.80	0.78	0.39	1.47
	PPTDTBT-*SS*:$PC_{71}BM$ (1:1.5)	32	4.11	0.92	0.32	1.22

[a]Thickness of the active layer.

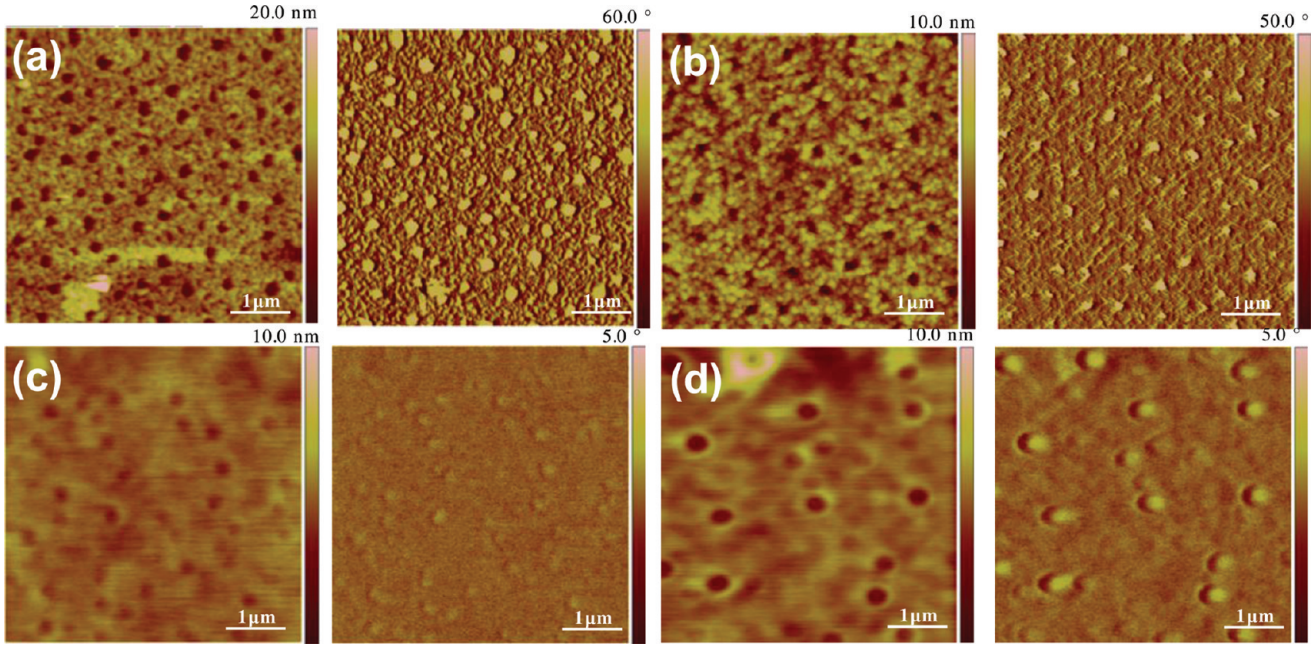

Figure 9. Tapping-mode AFM images (5 μm × 5 μm) of **PPTDTBT**:$PC_{71}BM$ (conventional (a); inverted (b)) and **PPTDTBT-*SS***:$PC_{71}BM$ (conventional (c); inverted (d)) films used in making the devices (under optimized device conditions). The topography of each film is shown in the left panels, and the corresponding phase images in the right panels.

is, in large part, responsible for the relatively low PCEs in the conventional cells, but this can positively affect the inverted PSCs adopting transporting metal oxides between the ITO/BHJ and BHJ/metal interfaces because of the potential interaction with oxides. This observation is in good agreement with the *J-V* characteristics tested in this study.

■ CONCLUSIONS

Considering low cost PSCs into account, an easily accessible donor, phenothiazine, which is stronger than commonly used 2,7-carbazole donors due to an additional sulfur atom, has been copolymerized with electron-deficient benzothiadiazole building block to yield new conjugated polymer **PPTDTBT**. By virtue of the enhanced strength of ICT, the "strong donor−acceptor" polymer (**PPTDTBT**) shows more bathocromically shifted absorption spectrum (λ_{max} = 582 nm) and lower band gap (E_g^{elec} = 1.78 eV) in comparison with its analogous polymer (PCDTBT) that in particular has been subject to increasing interest in the polymer research community. Through the sulfur oxidation in the phenothiazine unit, the corresponding oxidized form polymer **PPTDTBT-*SS*** is also prepared and characterized in parallel following our design motif. The strong polarity of SO_2 groups would enhance the compatibility and low contact resistance in the inverted BHJ solar cells integrated two metal oxides. Both the **PPTDTBT** and **PPTDTBT-*SS*** show moderate mobilities as p-type polymer semiconductors in OFETs. Interestingly, the carrier mobility of **PPTDTBT-*SS*** is about 1 order of magnitude higher than that of **PPTDTBT**, which is presumably ascribed to the closer packing driven either from the dipolar intermolecular interactions associated with the presence of the sulfonyl groups or the relatively enhanced coplanarity of **PPTDTBT-*SS***, supported by the DFT calculations as well as XRD results. The performance of the PSCs containing the polymer **PPTDTBT** reaches PCEs of 1.69% and 1.47% for conventional and inverted structure devices when using $PC_{71}BM$ as electron acceptor, respectively. On the other hand, despite the fact that relatively low-lying HOMO of **PPTDTBT-*SS*** enhances the V_{OC}, the current density in the **PPTDTBT-*SS***:$PC_{71}BM$-based regular cell is low and limits the PCE to 0.97%. This is likely a consequence of a reduced solar absorption of **PPTDTBT-*SS***'s caused by the relatively large energy bandgap. Delightfully, when it comes to incorporating **PPTDTBT-*SS*** into the inverted configuration cell with TiO_x and MoO_3 as electron-selective and hole-selective layers, respectively, the estimated PCE of 1.22% is achieved from the combination with the improved V_{OC} and J_{SC}. Current work on π-conjugated polymer structural modification has been aimed at understanding the influence of polymer polarity in inverted solar cells. Our results indicate that the introduction of *S,S*-dioxide units into the polymer backbone is a useful strategy for the design of high performance inverted solar cells.

■ EXPERIMENTAL SECTION

Materials and Instruments. All starting materials were purchased either from Aldrich or Acros and used without further purification. THF was distilled over sodium/benzophenone. ^{1}H NMR and ^{13}C NMR spectra were recorded on a Varian VNRS 600 MHz (Varian USA) spectrophotometer using $CDCl_3$ as solvent and tetramethylsilane (TMS) as the internal standard and MALDI MS spectra were obtained from Ultraflex III (Bruker, Germany). UV−vis-NIR spectra were taken on Cary 5000 (Varian USA) spectrometer. Number-average (M_n) and weight-average (M_w) molecular weights, and polydispersity index (PDI) of the polymer products were determined by gel permeation chromatography (GPC) with Agilent 1200 HPLC Chemstation using a series of mono disperse polystyrene as standards in THF (HPLC grade) at 308 K. Cyclic voltammetry (CV) measurements were performed on AMETEK VersaSTAT 3 with a three-electrode cell in a nitrogen bubbled 0.1 M tetra-*n*-butylammonium hexafluorophosphate (n-Bu_4NPF_6) solution in acetonitrile at a scan rate of 50 mV/s at room temperature. A used as the Ag/Ag^+ (0.1 M of $AgNO_3$ in acetonitrile) reference electrode, platinum counter electrode and polymer-coated platinum working electrode, respectively. The Ag/Ag^+ reference electrode was calibrated using a

dx.doi.org/10.1021/ma202661b | *Macromolecules* 2012, 45, 1847−1857

ferrocene/ferrocenium redox couple as an internal standard, whose oxidation potential is set at −4.8 eV with respect to zero vacuum level. The HOMO energy levels were obtained from the equation HOMO = $-(E_{ox}^{onset} - E_{(ferrocene)}^{onset} + 4.8)$ eV. The LUMO levels of polymers were obtained from the equation LUMO = $-(E_{red}^{onset} - E_{(ferrocene)}^{onset} + 4.8)$ eV.

OFET Device Preparation and Measurement. All p-type OFETs were fabricated on heavily doped n-type silicon (Si) wafers each covered with a thermally grown silicon dioxide (SiO_2) layer with thickness of 200 nm. The doped Si wafer acts as a gate electrode, and the SiO_2 layer functions as the gate insulator. The active layer was deposited by spin-coating at 2500 rpm. All solutions were prepared at 0.5 wt % concentration in chlorobenzene. The thickness of the deposited films was about 60 nm. Prior to vapor-deposition of source-drain electrodes, the films were dried on a hot plate stabilized at 80 °C for 30 min. All fabrication processes were carried out in a glovebox filled with N_2. Source and drain electrodes using Au were deposited by thermal evaporation using a shadow mask. The thickness of source and drain electrodes was 50 nm. Channel length (L) and channel width (W) was 50 μm and 1.5 mm, respectively. Electrical characterization was performed using a Keithley semiconductor parametric analyzer (Keithley 4200) under N_2 atmosphere. The electron mobility (μ) was determined using the following equation in the saturation regime

$$I_{ds} = (WC_i/2L) \times \mu \times (V_{gs} - V_T)^2$$

where C_i is the capacitance per unit area of the SiO_2 dielectric (C_i = 15 nF/cm^2) and V_T is the threshold voltage.

Fabrication of Conventional and Inverted Photovoltaic Cells. Two-type photovoltaic cells were fabricated on ITO-coated glass substrates. The ITO-coated glass substrates were first cleaned with detergent, ultrasonicated in water, acetone and isopropyl alcohol, and dried overnight in an oven. In conventional cells, PEDOT:PSS(Al 4083) was spin-cast on cleaned ITO substrates after a UV-ozone treatment for 15 min and heated at 140 °C for 10 min in air. Subsequently, the active layer was coated in a glovebox. The solution containing a mixture of **PPTDTBT**:$PC_{71}BM$ (1:2) in a solvent (chlorobenzene) with a concentration of 11 mg/mL and **PPTBTDT-*SS***:$PC_{71}BM$ (1:1.5) in a solvent (dichlorobenzene) with a concentration of 13 g/mL was spin-cast on top of PEDOT:PSS film. After then, the top electrode (Al) was deposited on the active layer in a vacuum (<10^{-6} Torr) thermal evaporator. Inverted solar cells were fabricated on ITO-coated glass substrates. A TiO_x precursor solution was prepared using the sol−gel method. The TiO_x precursor solution was spin-cast on cleaned ITO substrates after a UV-ozone treatment for 15 min and heated at 80 °C for 10 min in air for conversion to TiO_x by hydrolysis. Subsequently, the TiO_x-coated substrates were transferred into a glovebox. A solution containing a mixture of **PPTDTBT**:$PC_{71}BM$ (1:2) in a solvent (chlorobenzene) with a concentration of 11 mg/mL was spin-cast on top of TiO_x films at 1500 rpm 60 s and **PPTBTDT-*SS***:$PC_{71}BM$ (1:1.5) in a solvent (dichlorobenzene) with a concentration of 13 g/mL was spin-cast on top of TiO_x films at 600 rpm 60 s. Then, a thin layer of MoO_3 film (≈5 nm) was evaporated on top of the active layer. Finally, the anode (Au, ≈95 nm) was deposited on the active layer in a vacuum (<10^{-6} Torr) thermal evaporator. The cross-sectional area of each of the electrode defines the active area of the device as 13.5 mm^2. Photovoltaic cell measurements were carried out inside the glovebox using a high quality optical fiber to guide the light from the solar simulator equipped with a Keithley 2635A source measurement unit. The J−V curves for the devices were measured under AM 1.5G illumination at 100 mW cm^{-2}. The IPCE spectra for the PSCs were measured on an IPCE measuring system.

Synthesis of *N*-2-Decyltetradecylphenothiazine (4). To a mixture of phenothiazine (6.2 g, 31.1 mmol) and sodium hydride (60% in mineral oil, 1.0 g, 41.7 mmol) in anhydrous DMF (40 mL), 2-decyltetradecyl bromide (16.8 g, 40.2 mmol) was slowly added at room temperature under argon. The mixture was stirred at room temperature overnight, which was poured into water and extracted with diethyl ether. The separated organic layer was dried over $MgSO_4$ and removed under reduced pressure. The crude product was purified by column chromatography (silica gel, hexane) to afford 13.6 g (82%) of **4** as a colorless oil. ^{1}H NMR (600 MHz, $CDCl_3$): δ (ppm) 7.14 (m, 4H), 6.92−6.86 (m, 4H), 3.73 (d, 2H, J = 6.6 Hz), 2.00 (m, 1H), 1.41−1.26 (m, 40H), 0.91−0.88 (t, 6H, J = 7.2 Hz). ^{13}C NMR (150 MHz, $CDCl_3$): δ (ppm) 145.94, 127.66, 127.17, 126.03, 122.43, 116.05, 51.65, 36.25, 34.60, 32.10, 31.81, 30.11, 29.94, 29.86, 29.83, 29.81, 29.80, 29.77, 29.74, 29.73, 29.63, 29.62, 29.53, 29.51, 28.00, 26.40, 22.86, 14.29, 14.27. Anal. Calcd: C, 80.68; H, 10.72; N, 2.61; S, 5.98. Found: C: 80.91, H: 10.82, N: 2.74, S: 5.71. MALDI−TOF−MS m/z: $[M]^{+\bullet}$ = 535.34; calcd, 535.91.

Synthesis of 3,7-Dibromo-*N*-2-decyltetradecylphenothiazine (5). *N*-Bromosuccinimide (3.65 g, 20.53 mmol) was slowly added to a solution of **4** (5.0 g, 9.33 mmol) in anhydrous DMF (50 mL). The reaction mixture was stirred at room temperature overnight, which was quenched by water and extracted with diethyl ether. The separated organic layer was washed with water and brine, then dried over $MgSO_4$. The solvent was removed under reduced pressure. The crude product was purified by column chromatography(silica gel, hexane) to afford 6.0 g (93%) of **5** as a yellow oil. ^{1}H NMR (600 MHz, $CDCl_3$): δ (ppm) 7.25 (m, 4H), 6.69 (d, 2H, J = 1.8 Hz), 3.64 (d, 2H, J = 7.2 Hz), 1.89 (m, 1H), 1.36−1.22 (m, 40H), 0.89 (t, 6H, J = 7.2 Hz). ^{13}C NMR (150 MHz, $CDCl_3$): δ (ppm) 144.75, 130.20, 129.99, 127.49, 117.30, 114.91, 51.88, 34.60, 32.09, 32.08, 31.66, 30.06, 29.85, 29.82, 29.77, 29.75, 29.59, 29.52, 29.50, 26.33, 22.85, 14.28. Anal. Calcd: C, 62.33; H, 7.99; Br, 23.04; N, 2.02; S, 4.62. Found: C: 63.34, H: 8.11, N: 2.17, S: 4.53. MALDI−TOF−MS m/z: $[M]^{+\bullet}$ = 693.17; calcd, 693.7.

Synthesis of *N*-2-Decyltetradecyl-3,7-bis(4,4,5,5-tetramethyl-1,3,2-dioxaborolanyl)phenothiazine (6). A portion of 4.43 mL of *n*-butyllithium (1.6 M in hexane, 7.08 mmol) was added dropwise to a solution of **5** (2.0 g, 2.83 mmol) in anhydrous THF (40 mL) under argon atmosphere at −78 °C. After 30 min, 2-isopropoxy-4,4,5,5-tetramethyl-1,3,2-dioxaborolane (1.32 mL, 7.08 mmol) was injected to the reaction mixture. The resulting mixture was warmed up to room temperature and stirred overnight. Then, the reaction was quenched by water and extracted with a diethyl ether. The separated organic layer was washed with water and brine, then dried over $MgSO_4$ and removed under reduced pressure. The crude product was purified by column chromatography (silica gel, 10% ethyl acetate in hexane) to afford 1.3 g (58%) as a yellow-green sticky solid. ^{1}H NMR (600 MHz, $CDCl_3$): δ (ppm) 7.56 (d, 4H, J = 7.8 Hz), 6.83 (d, 2H, J = 7.8 Hz), 3.74 (d, 2H, J = 6.6 Hz), 1.94 (m, 1H), 1.37−1.2 (m, 64H), 0.89 (t, 6H, J = 6.6 Hz). ^{13}C NMR (150 MHz, $CDCl_3$): δ (ppm) 148.07, 134.07, 133.98, 125.27, 115.46, 83.80, 34.79, 32.09, 32.07, 31.78, 30.11, 29.81, 29.75, 29.62, 29.51, 29.48, 26.43, 24.99, 22.48. Anal. Calcd: C, 73.18; H, 10.11; B, 2.74; N, 1.78; O, 8.12; S, 4.07; Found: C: 73.44, H: 10.01, N: 1.94, S: 3.86, O: 7.82. MALDI−TOF−MS m/z: $[M]^{+\bullet}$ = 787.53; calcd, 787.83.

Synthesis of 3,7-Dibromo-*N*-2-decyltetradecylphenothiazine-*S*,*S*-dioxide (7). Hydroperoxide (35%, 10 mL) was added dropwise to a solution of **5** (2 g, 2.9 mmol) in acetic acid (30 mL) was stirred at 90 °C overnight. After cooled down, the water was added and extracted with ethyl acetate. The separated organic layer was and washed with water and brine, then dried over $MgSO_4$ and removed under reduced pressure. The crude product was purified by column chromatography (silica gel, 10% ethyl acetate in hexane) to afford 1.1 g (52%) of **7** as a colorless solid. ^{1}H NMR (600 MHz, $CDCl_3$): δ (ppm) 8.17 (d, 2H, J = 2.4 Hz), 7.67 (d, 2H, J = 7.2 Hz), 7.24 (s, 2H), 4.04 (d, 2H, J = 6.6 Hz), 1.94 (m, 1H), 1.29−1.20 (m, 40H), 0.89 (t, 6H, J = 7.2 Hz). ^{13}C NMR (150 MHz, $CDCl_3$): δ (ppm) 140.83, 135.92, 126.99, 126.41, 119.03, 114.72, 32.06, 30.90, 29.95, 29.84, 29.80, 29.74, 29.71, 29.62, 29.51, 29.49, 26.22, 22.84, 14.27. Elemental Analysis: C, 59.58; H, 7.64; Br, 22.02; N, 1.93; O, 4.41; S, 4.42; Found: C: 59.84, H: 7.70, N: 2.01, S: 4.21, O: 4.22. MALDI-TOF-MS m/z: $[M]^{+\bullet}$ = 727.23; calcd, 725.7.

Synthesis of N-2-decyltetradecyl-3,7-bis(4,4,5,5-tetramethyl-1,3,2-dioxaborolanyl)phenothiazine-S,S-dioxide (8). Compound 7 (0.7 g, 0.96 mmol), bis(pinacolato)diboron (0.97 g, 3.84 mmol), potassium acetate (0.66 g, 6.72 mmol), and Pd Cl_2(dppf) (42

mg, 57.6 μmol) in anhydrous DMF (20 mL) were stirred at 120 °C overnight. The reaction was quenched by water and extracted with ethyl acetate. The separated organic layer was washed with water and brine, then dried over $MgSO_4$ and removed under reduced pressure. The crude product was purified by column chromatography (silica gel, 30% ethyl acetate in hexane) to afford 0.5 g (64%) of **8** as light-yellow solid. ^{1}H NMR (600 MHz, $CDCl_3$): δ (ppm) 8.58 (s, 2H), 7.97 (d, 2H, J = 8.4 Hz), 7.33 (d, 2H, J = 8.4 Hz), 4.13 (d, 2H, J = 7.2 Hz), 1.98 (m, 1H), 1.35−1.19 (m, 64H), 0.88 (t, 6H, J = 7.2 Hz). ^{13}C NMR (150 MHz, $CDCl_3$): δ (ppm) 143.64, 138.72, 131.02, 125.88, 116.21, 84.28, 32.08, 31.05, 29.99, 29.80, 29.71, 29.67, 29.51, 29.47, 25.18, 25.02, 22.84, 14.28. Anal. Calcd: C: 70.32, H: 9.71, B: 2.64, N: 1.71, O: 11.71, S: 3.91. Found: C: 70.52, H: 9.68, N: 1.88, S: 3.61, O: 11.62. MALDI−TOF−MS m/z: $[M]^{+\bullet}$ = 819.53; calcd, 819.83.

Poly(*N*-(2-decyltetradecyl)-3,7-phenothiazine-*alt*-5,5-(4′,7′-di-2-thienyl-2′,1′,3′-benzothiadiazole)) (PPTDTBT). In a Schlenk flask, monomer **6** (0.21 g, 0.266 mmol) and 4,7-bis(5-bromothiophenyl)-2,1,3-benzothiadiazole (0.12 g, 0.266 mmol) was dissolved in toluene (7 mL), to this a solution of K_3PO_4 (286 mg, 1.34 mmol), tri*o*-tolylphosphine (10 mg, 0.03 mmol) and deionized water (1.5 mL) was added. The mixture was vigorously stirred at room temperature under argon. After 30 min, $Pd_2(dba)_3$ (10 mg, 0.011 mmol)was added to the reaction mixture and stirred at 90 °C for 3 days (end-capped with phenylboronic acid and bromobenzene). Finally, the solution was precipitated in a mixture of methanol and ammonia (4:1 v/v, 250 mL). This was filtered off through 0.45 μm nylon filter, washed on Soxhlet apparatus with methanol (1 d) and acetone (1 d). Then, 160 mg (72%) of the polymer was recovered as a violet-powder (M_n = 9.8 × 10^3 g/mol, PDI = 1.27). ^{1}H NMR (600 MHz, $CDCl_3$): δ (ppm) 8.11 (br, 2H), 7.88 (br, 2H), 7.50 (br, 2H), 7.32 (br, 4H) 6.91 (br, 2H), 3.79 (br, 2H), 2.04 (br, 1H), 1.8 (br, 6H), 1.42−1.24 (br, 40H), 0.87−0.84 (br, 6H).

Poly(*N*-(2-decyltetradecyl)-3,7-phenothiazine-S,S-dioxide-*alt*-5,5-(4′,7′-di-2-thienyl-2′,1′,3′-benzothiadiazole)) (PPTDTBT-SS). In a Schlenk flask, monomer **8** (0.214 g, 0.266 mmol) and 4,7-bis(5-bromothiophenyl)-2,1,3-benzothiadiazole (0.12 g, 0.266 mmol) was dissolved in toluene (7 mL), to this a solution of K_3PO_4 (286 mg, 1.34 mmol), tri*o*-tolylphosphine (10 mg, 0.03 mmol) and deionized water (1.5 mL) was added. The mixture was vigorously stirred at room temperature under argon. After 30 min, $Pd_2(dba)_3$ (10 mg, 0.011 mmol) was added to the reaction mixture and stirred at 90 °C for 3 days (end-capped with phenylboronic acid and bromobenzene). Finally, the solution was precipitated in a mixture of methanol and ammonia (4:1 v/v, 250 mL). This was filtered off through 0.45 μm nylon filter, washed on Soxhlet apparatus with methanol (1 d) and acetone (1 d). Then 0.14 g (61%) of the polymer was recovered as a deep-red powder (M_n = 7.6 × 10^3 g/mol, PDI = 1.21). ^{1}H NMR (600 MHz, $CDCl_3$): δ (ppm) 8.42 (br, 2H), 8.15 (br, 2H), 7.93 (br, 4H), 7.50−7.40 (br, 4H) 4.16 (br, 2H), 2.07 (br, 1H), 1.27−1.23 (br, 40H), 0.90−0.85 (br, 6H).

■ ASSOCIATED CONTENT

Supporting Information

DFT-optimized geometries and charge-density isosurfaces for the HOMO and LUMO levels of (a) $(\mathbf{PTDTBT})_1$ and (b) $(\mathbf{PTDTBT\text{-}SS})_1$ model, ^{1}H NMR spectra of polymers, polymers:PCBM blend transistors, solar cell performance of polymer:$PC_{61}BM$, and GPC data. This material is available free of charge via the Internet at http://pubs.acs.org.

■ AUTHOR INFORMATION

Corresponding Author

*E-mail: yang@unist.ac.kr. Telephone: +82-52-217-2920. Fax: +82-52-217-2909.

Notes

The authors declare no competing financial interest.

■ ACKNOWLEDGMENTS

This work was supported by Basic Science Research Program through the National Research Foundation of Korea (NRF) funded by the Ministry of Education, Science and Technology (2010-0002494) and the National Research Foundation of Korea Grant funded by the Korean Government (MEST) (2010-0019408), (2010-0026163), (2010-0026916), and (NRF-2009-C1AAA001-0093020).

■ REFERENCES

(1) Cheng, Y. J.; Yang, S. H.; Hsu, C. S. *Chem. Rev.* **2009**, *109*, 5868.
(2) Gunes, S.; Neugebauer, H.; Sariciftci, N. S. *Chem. Rev.* **2007**, *107*, 1324.
(3) Yu, G.; Gao, J.; Hummelen, J. C.; Wudl, F.; Heeger, A. J. *Science* **1995**, *270*, 1789.
(4) Kim, G.; Yun, M. H.; Anant, P.; Cho, S.; Jacob, J.; Kim, J. Y.; Yang, C. *Chem.—Eur. J.* **2011**, *17*, 14681.
(5) Cheedarala, R. K.; Kim, G. H.; Cho, S.; Lee, J.; Kim, J.; Song, H. K.; Kim, J. Y.; Yang, C. *J. Mater. Chem.* **2011**, *21*, 843.
(6) Wang, E. G.; Ma, Z. F.; Zhang, Z.; Vandewal, K.; Henriksson, P.; Inganas, O.; Zhang, F. L.; Andersson, M. R. *J. Am. Chem. Soc.* **2011**, *133*, 14244.
(7) Price, S. C.; Stuart, A. C.; Yang, L. Q.; Zhou, H. X.; You, W. *J. Am. Chem. Soc.* **2011**, *133*, 4625.
(8) Huo, L. J.; Zhang, S. Q.; Guo, X.; Xu, F.; Li, Y. F.; Hou, J. H. *Angew. Chem., Int. Ed.* **2011**, *50*, 9697.
(9) Piliego, C.; Holcombe, T. W.; Douglas, J. D.; Woo, C. H.; Beaujuge, P. M.; Fréchet, J. M. J. *J. Am. Chem. Soc.* **2010**, *132*, 7595.
(10) Chen, H. Y.; Hou, J. H.; Zhang, S. Q.; Liang, Y. Y.; Yang, G. W.; Yang, Y.; Yu, L. P.; Wu, Y.; Li, G. *Nat. Photonics* **2009**, *3*, 649.
(11) Zhao, G. J.; He, Y. J.; Li, Y. F. *Adv. Mater.* **2010**, *22*, 4355.
(12) Cheng, Y. J.; Hsieh, C. H.; He, Y. J.; Hsu, C. S.; Li, Y. F. *J. Am. Chem. Soc.* **2010**, *132*, 17381.
(13) He, Z.; Zhong, C.; Huang, X.; Wong, W.-Y.; Wu, H.; Chen, L.; Su, S.; Car, Y. *Adv. Mater.* **2011**, *23*, 4636.
(14) Jørgensen, M.; Norrman, K.; Krebs, F. C. *Sol. Energy Mater. Sol. Cells.* **2008**, *92*, 686.
(15) Sun, Y. M.; Seo, J. H.; Takacs, C. J.; Seifter, J.; Heeger, A. J. *Adv. Mater.* **2011**, *23*, 1679.
(16) Hau, S. K.; Yip, H.-L.; Leong, K.; Jen, A. K.-Y. *Org. Electron.* **2009**, *10*, 719.
(17) Park, S. H.; Roy, A.; Beaupre, S.; Cho, S.; Coates, N.; Moon, J. S.; Moses, D.; Leclerc, M.; Lee, K.; Heeger, A. J. *Nat. Photonics* **2009**, *3*, 297.
(18) Blouin, N.; Michaud, A.; Gendron, D.; Wakim, S.; Blair, E.; Neagu-Plesu, R.; Belletete, M.; Durocher, G.; Tao, Y.; Leclerc, M. *J. Am. Chem. Soc.* **2008**, *130*, 732.
(19) Svensson, M.; Zhang, F. L.; Veenstra, S. C.; Verhees, W. J. H.; Hummelen, J. C.; Kroon, J. M.; Inganäs, O.; Andersson, M. R. *Adv. Mater.* **2003**, *15*, 988.
(20) Cho, S.; Seo, J. H.; Park, S. H.; Beaupre, S.; Leclerc, M.; Heeger, A. J. *Adv. Mater.* **2010**, *22*, 1253.
(21) Cadogan, J. I. G.; Cameron-Wood, M.; Mackie, R. K.; Searle, R. J. G. *J. Chem. Soc.* **1965**, 4831.
(22) Padhy, H.; Huang, J. H.; Sahu, D.; Patra, D.; Kekuda, D.; Chu, C. W.; Lin, H. C. *J. Polym. Sci., Part A: Polym. Chem.* **2010**, *48*, 4823.
(23) Sang, G. Y.; Zou, Y. P.; Li, Y. F. *J. Phys. Chem. C* **2008**, *112*, 12058.
(24) Liu, Y.; Cao, H.; Li, J.; Chen, Z.; Cao, S.; Xiao, L.; Xu, S.; Gong, Q. *J. Polym. Sci., Part A: Polym. Chem.* **2007**, *45*, 4867.
(25) Cho, N. S.; Park, J. H.; Lee, S. K.; Lee, J.; Shim, H. K.; Park, M. J.; Hwang, D. H.; Jung, B. J. *Macromolecules* **2006**, *39*, 177.
(26) Kong, X. X.; Kulkarni, A. P.; Jenekhe, S. A. *Macromolecules* **2003**, *36*, 8992.
(27) Liu, B.; Najari, A.; Pan, C. Y.; Leclerc, M.; Xiao, D. Q.; Zou, Y. P. *Macromol. Rapid Commun.* **2010**, *31*, 391.

(28) Kamtekar, K. T.; Dahms, K.; Batsanov, A. S.; Jankus, V.; Vaughan, H. L.; Monkman, A. P.; Bryce, M. R. *J. Polym. Sci., Part A: Polym. Chem.* **2011**, *49*, 1129.
(29) Scharber, M. C.; Wühlbacher, D.; Koppe, M.; Denk, P.; Waldauf, C.; Heeger, A. J.; Brabec, C. L. *Adv. Mater.* **2006**, *18*, 789.
(30) Brabec, C. J.; Cravino, A.; Meissner, D.; Sariciftci, N. S.; Fromherz, T.; Rispens, M. T.; Sanchez, L.; Hummelen, J. C. *Adv. Funct. Mater.* **2001**, *11*, 374.
(31) Kang, S.-M.; Leblebici, Y. *CMOS Digital Integrated Circuits: Analysis and Design*; McGraw-Hill: New York, 1996.
(32) Chen, L. M.; Hong, Z. R.; Li, G.; Yang, Y. *Adv. Mater.* **2009**, *21*, 1434.
(33) Sun, Y. M.; Takacs, C. J.; Cowan, S. R.; Seo, J. H.; Gong, X.; Roy, A.; Heeger, A. J. *Adv. Mater.* **2011**, *23*, 2226.
(34) Ma, H.; Yip, H.-L.; Huang, F.; Jen, A. K.-Y. *Adv. Funct. Mater.* **2010**, *20*, 1371.
(35) Zhang, Y.; Hau, S. K.; Yip, H.-L.; Sun, Y.; Acton, O.; Jen, A. K.-Y. *Chem. Mater.* **2010**, *22*, 2696.
(36) Hsieh, C.-H.; Cheng, Y.-J.; Li, P.-J.; Chen, C.-H.; Dubosc, M.; Liang, R.-M.; Hsu, C.-S. *J. Am. Chem. Soc.* **2010**, *132*, 4887.
(37) Waldauf, C.; Morana, M.; Denk, P.; Schilinsky, P.; Coakley, K.; Choulis, S. A.; Brabec, C. J. *Appl. Phys. Lett.* **2006**, *89*, 233517.
(38) van Duren, J. K. J.; Yang, X. N.; Loos, J.; Bulle-Lieuwma, C. W. T.; Sieval, A. B.; Hummelen, J. C.; Janssen, R. A. J. *Adv. Funct. Mater.* **2004**, *14*, 425.
(39) Wienk, M. M.; Kroon, J. M.; Verhees, W. J. H.; Knol, J.; Hummelen, J. C.; van Hal, P. A.; Janssen, R. A. J. *Angew. Chem., Int. Ed.* **2003**, *42*, 3371.

■ NOTE ADDED AFTER ASAP PUBLICATION

This article posted ASAP on February 3, 2012. Scheme 1 has been revised. The correct version posted on February 7, 2012.

Macromolecules

Article

pubs.acs.org/Macromolecules

Physical and Structural Effects of Adding Ultrahigh-Molecular-Weight Poly[(*R*)-3-hydroxybutyrate] to Wild-Type Poly[(*R*)-3-hydroxybutyrate]

Taizo Kabe,[†] Takeharu Tsuge,[‡] Ken-ichi Kasuya,[§] Akio Takemura,[†] Takaaki Hikima,[∥] Masaki Takata,[⊥] and Tadahisa Iwata*[,†,⊥]

[†]Graduate School of Agricultural and Life Sciences, The University of Tokyo, 1-1-1 Yayoi, Bunkyo-ku, Tokyo 113-8657, Japan

[‡]Interdisciplinary Graduate School of Science and Engineering, Tokyo Institute of Technology, 4259 Nagatsuta, Midori-ku, Yokohama 226-8502, Japan

[§]Graduate School of Engineering, Gunma University, 1-5-1 Tenjin-cho, Kiryu, Gunma 376-8515, Japan

[∥]Research Infrastructure Group, RIKEN Harima Institute/SPring-8 Center, Kouto, Sayo-cho, Sayo-gun, Hyogo 679-5148, Japan

[⊥]Structural Materials Science Laboratory, RIKEN Harima Institute, SPring-8, 1-1-1 Kouto, Sayo-cho, Sayo-gun, Hyogo 679-5148, Japan

Supporting Information

ABSTRACT: Blend films containing wild-type poly[(*R*)-3-hydroxybutyrate]] (P(3HB)) and ultrahigh-molecular-weight P(3HB) (UHMW-P(3HB)) (compositions of 5/95 and 10/90 w/w) were prepared by solvent-casting and subsequent cold-drawing. The thermal properties, crystallization behavior, mechanical properties, and highly ordered structure of the blend films were analyzed by differential scanning calorimetry, polarized optical microscopy, a tensile test, and wide- and small-angle X-ray diffraction measurements with synchrotron radiation. The maximum radial growth rate of spherulites and corresponding temperature were identical for films of different composition. However, the half-time of crystallization of the blend films was shorter than that of P(3HB) because UHMW-P(3HB) behaves as a nucleating agent. The tensile strength, Young's modulus, and elongation at break of a 5/95 blend film after cold-drawing to 12 times of the original length were 242 MPa, 1.50 GPa, and 88%, respectively, which are higher than those of an UHMW-P(3HB) cold-drawn film and similar to those of common plastic films as poly(ethylene terephthalate). The wide-angle X-ray diffraction results indicated that the cold-drawn films with high tensile strength contained both 2_1 helix (α-form) and planar zigzag (β-form) conformations. Addition of a small amount of UHMW-P(3HB) to P(3HB) caused the β-form to appear in blend films at a high drawing ratio. A mechanism for forming β-form crystals in the blend films is proposed. Enzymatic degradation of the cold-drawn blend films is demonstrated using polyhydroxybutyrate depolymerase, suggesting that the rate of enzymatic degradation can be controlled by addition of UHMW-P(3HB).

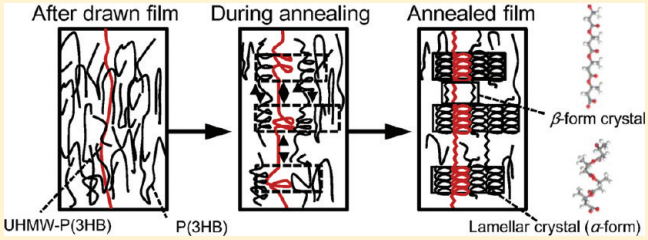

INTRODUCTION

Microbially produced polymers, which are synthesized from renewable carbon sources such as sugars and oils, are of interest for solving environment and resource problems. Poly[(*R*)-3-hydroxybutyrate] (P(3HB)), which can be biosynthesized by bacteria, is a type of polyhydroxyalkanoate (PHA) with thermoplastic properties[1,2] and is an alternative to petroleum-based plastics.[3] Furthermore, this microbial polyester is degraded in the natural environment by extracellular poly-hydroxybutyrate depolymerases secreted by some microorganisms.

However, the mechanical properties of P(3HB), which undergoes secondary crystallization at room temperature, are poor compared to those of common petrochemical polymers because its glass transition temperature (T_g) is lower than room temperature.[4,5] Several groups have attempted to improve the mechanical properties of P(3HB) and analyze its crystal structures.[6] The mechanical properties of P(3HB) have been improved by biosynthesis of P(3HB) copolymers,[7,8] preparation of a P(3HB) composite,[9] and blending P(3HB) with other polymers.[10−12]

Increasing the molecular weight and optimizing the drawing method are typical techniques used to improve the mechanical properties of films and fibers. Ultrahigh-molecular-weight P(3HB) (UHMW-P(3HB)) can be biosynthesized by the genetically modified bacterium *Escherichia coli*.[13] Iwata et al. successfully obtained UHMW-P(3HB) films with a high tensile strength of 287 MPa by hot-drawing near the melting

Received: October 12, 2011
Revised: January 26, 2012
Published: February 13, 2012

temperature and using a one-step drawing technique.[14] However, hot-drawing is only suitable for UHMW-P(3HB) with $M_w > 3.0 \times 10^5$. Accordingly, they developed a new cold-drawing method that improved the tensile strength of P(3HB) films.[15] This method is an attractive way to improve mechanical properties of wild-type (typical molecular weight) P(3HB) and its copolymers. The tensile strength of wild-type P(3HB) increased to 195 MPa using this cold-drawing method. Furthermore, in the case of drawn films, the tensile strength remained unchanged over time because the mobility of the oriented molecular chains is suppressed, which prevents secondary crystallization.[14]

It is difficult to produce UHMW-P(3HB) by high-density cultivation so it must be used effectively. Adding a small amount of UHMW-P(3HB) into wild-type P(3HB) might enhance its structure and mechanical properties. The first aim of this work is to investigate the effect of adding UHMW-P(3HB) to wild-type P(3HB) on crystallization using differential scanning calorimetry (DSC) and polarized optical microscopy (POM). UHMW-P(3HB)/wild-type P(3HB) blend films of high strength were produced using a cold-drawing technique. The physical properties and highly ordered structure of these films were investigated by tensile measurements and wide- and small-angle X-ray diffraction using synchrotron radiation.

A means of effectively using UHMW-polymer that has often been reported is to form blends of polyethylene (PE). These blend films, which consist of low-molecular-weight PE with a small amount of UHMW-PE, showed improved mechanical properties such as tensile strength and elongation at break compared with films lacking an UHMW component.[16] These findings show that inclusion of an UHMW component can improve the mechanical properties of a film. Other researchers have reported that the UHMW component behaves as the "shish" part of a "shish-kebab" structure.[17,18] Accordingly, it is expected that the same phenomena will be observed in cold-drawn UHMW-P(3HB)/P(3HB) blend films.

P(3HB) molecular chains with two types of molecular conformations—a 2_1 helix conformation[19,20] (α-form) which is the basic conformation in lamellar crystals and a planar zigzag conformation[21] (β-form) which appears in drawn P(3HB) films and fibers with high tensile strength—have been reported.[22,23] The β-form is considered to be generated from amorphous regions between lamellar crystals with the α-form formed in the two-step drawing process. In this paper, we propose a new mechanism for the formation of the β-form in cold-drawn UHMW-P(3HB)/P(3HB) blend films. P(3HB) is a known biodegradable plastic, so the effect of a small amount of UHMW-P(3HB) in blend films on the rate of enzymatic degradation by extracellular PHB depolymerase isolated from the environment was also investigated.

EXPERIMENTAL SECTION

Materials. P(3HB) was supplied by ICI Co. [weight-average-molecular-weight (M_w) = 5.2×10^5 and polydispersity (PDI) = 1.6]. UHMW P(3HB) [$M_w = 2.7 \times 10^6$ and PDI = 1.9] was biosynthesized from glucose by recombinant *E. coli* JM109 according to the method of Kahar et al.[24] Both P(3HB) samples were purified by reprecipitation from chloroform solution using *n*-hexane and then dried under vacuum at 30 °C for 3 days.

Preparation of Blend Films and Cold-Drawn Blend Films. Blend films with two compositions (UHMW-P(3HB)/P(3HB) = 5/95 and 10/90 (w/w)) were prepared by dissolving appropriate amounts of the different P(3HB) samples in chloroform, followed by solution casting. The M_w and PDI of 5/95 and 10/90 blend samples were $M_w = 0.73 \times 10^6$, PDI = 2.23 and $M_w = 0.77 \times 10^5$, PDI = 2.27, respectively. Blend films were obtained after solvent evaporation at room temperature and subsequent vacuum drying. The four films prepared with blend ratios of UHMW-P(3HB)/P(3HB) of 0/100, 5/95, 10/90, and 100/0 are named P(3HB), 5/95, 10/90, and UHMW-P(3HB), respectively.

All of the solvent-cast films were converted to amorphous films by placement in a hot press at 200 °C for 30 s and subsequent quenching in iced water below T_g. The films were cold-drawn in ice water using a hand-drawing machine. Cold-drawn films, which were fixed to the hand-drawing machine, were annealed at 100 °C for 2 h in an oven. All samples were investigated after aging for at least 3 days at room temperature.

Thermal Properties of Blend Films. The melting temperature (T_m) and T_g of the blend films were measured by DSC (Perkin-Elmer, DSC8500). The temperature was calibrated using indium. The first heating cycle was carried out at a rate of 20 °C/min from −50 to 200 °C, maintained at 200 °C for 1 min, and the cooled to −50 °C at a rate of −200 °C/min. T_g and T_m were determined from DSC curves obtained for the second heating cycle at a rate of 20 °C/min.

Radial Growth Rate of Spherulites. The growing morphology of spherulites was observed by a POM (Nikon, ECLIPSE E600 POL) equipped with crossed polarizers, a temperature jump stage (Japan High Tech., LK300A) and a CCD camera (Shimadzu, Moticam2000). P(3HB), UHMW-P(3HB), and blend films were first heated on a hot stage from room temperature to 200 °C and maintained there for 1 min. The sample was moved to a neighboring hot stage and then isothermally crystallized at 60, 70, 80, 90, or 100 °C. The growth of spherulites was plotted as a function of time. The growth of the radius of each spherulite was calculated from the slope of the curve.

Half-Time of Crystallization. The half-time of crystallization was measured by DSC. The first heating scan was carried out at a rate of 50 °C/min from 40 to 200 °C and then held for 1 min at 200 °C. The sample was cooled to a desired temperature at a rate of 200 °C/min to allow isothermal crystallization. The observed endothermic peak during the isothermal step was the integral of the endothermic peak as a function of time. The half-time of crystallization ($t_{1/2}$) is defined as half of the time needed to crystallize the sample.

Mechanical Properties of Cold-Drawn Blend Films. The tensile strength, Young's modulus, and elongation at break of the films were determined using a tensile testing machine (EZ-test, Shimadzu Co., Japan) at a cross-head speed of 20 mm/min. The gauge length and sample width were 10 mm and ∼3 mm, respectively.

The stability of cold-drawn blend film were investigated after a period of time. The cold-drawn 10/90 blend film with drawing ratio of 12 was chosen for aging because can be prepared easily. The stress−strain curves of the blend films before and after aging for 600 days were compared.

Synchrotron Wide-Angle X-ray Diffraction and Small-Angle X-ray Scattering Measurements. Synchrotron wide-angle X-ray diffraction (WAXD) and small-angle X-ray scattering (SAXS) measurements were carried out at the BL45XU beamline (wavelength, λ = 0.09 nm) in SPring-8, Harima, Japan. The camera lengths in the WAXD and SAXS measurements, which were calibrated using cerium oxide and silver behenate, were 106 and 2433 mm, respectively. The diffraction patterns were recorded with a CCD camera (C7300-12-NR, Hamamatsu Photonics, Japan). The crystallinity was calculated from the integrals of the crystalline phase in relation to the overall integral.[25] The long period (L_p) was determined using the Bragg equation ($L_p = \lambda/(2 \sin \theta)$) from the maximum peak of the meridional scattering of the SAXS patterns.

Enzymatic Degradation. Enzymatic degradation of P(3HB), UHMW-P(3HB), and blend films with a total area of about 2 cm^2 were carried out using extracellular PHB depolymerase from *Ralstonia pickettii* T1. Each film was placed in a solution of potassium phosphate buffer (pH 7.4, 1 mL) and enzymatic solution (200 μg/mL in potassium phosphate buffer, 5 μL) and incubated at 37 °C. Degradation was measured as the weight loss over time. The film specimens were weighed every 12 h over a period of 36 h. The weight

dx.doi.org/10.1021/ma202285c | Macromolecules 2012, 45, 1858−1865

loss was plotted as a function of degradation time. Enzymatic degradation rates were calculated from the slope of this curve.

RESULTS AND DISCUSSION

DSC Measurements. The DSC curves of P(3HB), UHMW-P(3HB), and blend films are shown in Figure 1, and

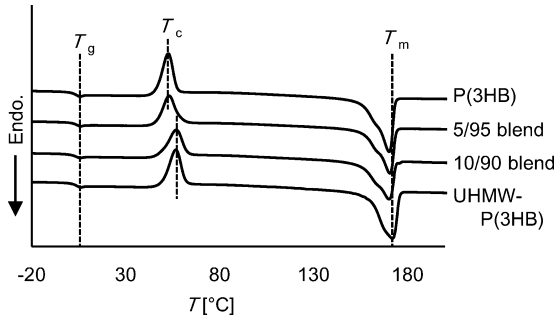

Figure 1. DSC heating curves for P(3HB), 5/95 blend, 10/90 blend, and UHMW-P(3HB) films.

Table 1. Thermal Properties of P(3HB), UHMW-P(3HB), and Blend Films

sample	T_g (°C)	T_c (°C)	T_m (°C)	ΔH (J/g)	crystallinity (%)
P(3HB)	1.8	53	170	110	75
5/95	2.2	53	170	94	65
10/90	2.1	57	170	94	65
UHMW-P(3HB)	2.4	57	172	110	75

T_g, T_c, T_m, and ΔH are listed in Table 1. T_g of all films were around 2 °C, and exothermic peaks (T_c) derived from cold crystallization of P(3HB), 5/95, 10/95 blend, and UHMW-P(3HB) appeared at 53, 53, 57, and 57 °C, respectively. This slight increase of T_c in the 10/90 blend seems to be caused by the addition of UHMW-P(3HB) decreasing the mobility of the P(3HB) chains. P(3HB) and UHMW-P(3HB) films had T_m of 170 and 172 °C, respectively. The 5/95 and 10/90 blend films showed T_m similar to P(3HB) at about 170 °C. The slightly higher T_m of the UHMW-P(3HB) film compared with the other films is caused by the larger lamellar thickness of UHMW-P(3HB) than those of the other samples, as listed in Table 2.

Radial Growth Rate of Spherulites and Half-Time of Crystallization. During isothermal crystallization, the crystallinity is controlled by the volume of lamellar crystals and nucleation frequency. During isothermal crystallization, the total volume of spherulites per unit volume (X) at time t is designated by[26]

$$X = 1 - \exp(-X_0) \tag{1}$$

$$X_0 = \int_0^t N v \, d\tau \tag{2}$$

$$X = 1 - \exp\left(-\int_0^t I\tau\left(\frac{4\pi}{3}\right)\{G(t-\tau)\}^3 d\tau\right) \tag{3}$$

N and v are the number of spherulites and the volume of one spherulite grown from one nucleus. I, G, t, and τ are nucleation rate, radial growth rate of spherulites, observation time, and the induced time of nucleus formation, respectively. t is $t_{1/2}$ when X is 0.5. Therefore, the equation relating I, G, and $t_{1/2}$ is

$$t_{1/2}{}^5 = \frac{15 \ln 2}{4\pi I G^3} \tag{4}$$

$t_{1/2}$ and G were measured to determine the overall rate of crystallization and growth rate of crystalline volume, allowing the effect of UHMW-P(3HB) on crystallization behavior to be investigated.

Figure 2 shows G of the spherulites as a function of isothermal crystallization temperature. For all of the samples,

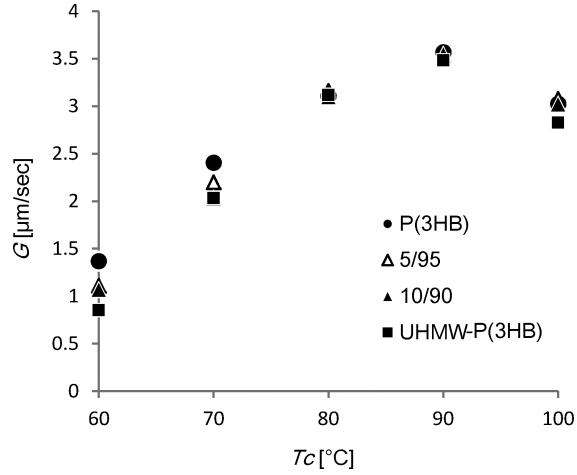

Figure 2. Radial growth rate (G) of spherulites as a function of crystallization temperature (T_c).

maximum values of G were obtained at around 90 °C. However, G at each crystallization temperature were larger with the order P(3HB) > blends > UHMW-P(3HB). Addition of

Table 2. Mechanical Properties, Crystallinity, Long Period, Lamellar Thickness, and (020) Orientation of Blend Films at Various Drawing Ratios and UHMW-P(3HB) Contents

samples	drawing ratio (λ)	tensile strength (MPa)	elongation at break (%)	Young's modulus (GPa)	crystallinity (%)	long period (L_p) (nm)	lamella thickness (Ip) (nm)	(020) orientation
P(3HB)	1	9	6	0.18	70	8.83	6.18	
	12	161	45	2.83	78	8.51	6.64	95.6
5/95	1	11	8	0.11	67	7.96	5.33	
	12	242	88	1.5	75	7.74	5.81	95.6
10/90	1	10	10	0.21	67	8.25	5.53	
	12	211	74	2.51	72	7.93	5.71	95
UHMW	1	40	10	0.8	68	9.68	6.58	
	10	191	56	1.62	73	11.22	8.19	95.6

dx.doi.org/10.1021/ma202285c | Macromolecules 2012, 45, 1858–1865

UHMW-P(3HB) with lower mobility appears to prevent crystallization of P(3HB) chains, reducing G. This phenomenon of decreasing G upon addition of high-M_w species has also been reported for other polymers such as isotactic polystyrene[27] and poly(tetramethyl-*p*-silphenylene)siloxane.[28]

Figure 3 shows $t_{1/2}$ as a function of isothermal crystallization temperature of the P(3HB), UHMW-P(3HB), and blend films.

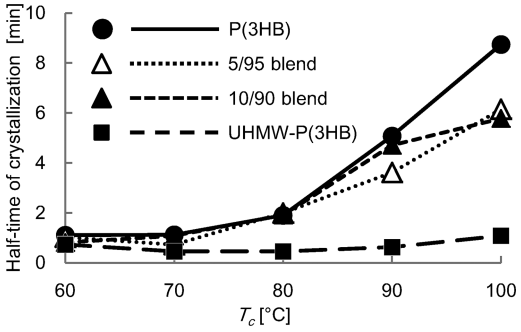

Figure 3. Crystallization half-time ($t_{1/2}$) as a function of crystallization temperature (T_c).

The $t_{1/2}$ value of UHMW-P(3HB) is the smallest of the four samples and was almost the same regardless of isothermal crystallization temperature. However, $t_{1/2}$ of P(3HB) and the blend samples increased with the isothermal crystallization temperature. The shortest $t_{1/2}$ of each sample is at around 60 °C. Considering that G of all of the samples was the largest at around 90 °C, I is another important factor contributing to this phenomenon. I for UHMW-P(3HB) is quite high compared with that of wild type P(3HB). The measured $t_{1/2}$ of UHMW-P(3HB) is expected to be a result of considerable entanglement of chains. The $t_{1/2}$ of the blends have an intermediate value between those of UHMW-P(3HB) and P(3HB). Addition of 5 or 10% UHMW-P(3HB) to P(3HB) resulted in an increase in crystallization rate at high temperatures of 90 to 100 °C, indicating that the addition of UHMW-P(3HB) accelerates the formation of nuclei because G did not change between samples. Based on the experimental results obtained for G (Figure 2) and $t_{1/2}$ (Figure 3), the addition of UHMW-P(3HB) to P(3HB) induces nucleation during the isothermal crystallization process. Polarization optical microscope graphics of each samples annealed at 100 °C for morphological observation are shown in Figure 4. As can be seen Figure 4, an increase in the number of crystals was observed by addition of UHMW-P(3HB).

Mechanical Properties of the Films. Figure 5 shows the mechanical properties of cold-drawn and annealed films of P(3HB), UHMW-P(3HB), and 5/95 and 10/90 blend films as a function of the cold-drawing ratio. The tensile strength, elongation at break, and Young's modulus of four kinds of cold-drawn films together with solvent-cast films (drawing ratio = 1) are summarized in Table 2. P(3HB), 5/95, and 10/90 blend films can be stretched up to 12 times their original length while the UHMW-P(3HB) film can only be stretched 10 times. The low drawing ratio of UHMW-P(3HB) seems to be related to its high degree of entanglement. The tensile strength curves of P(3HB) and UHMW-P(3HB) increase linearly with increasing drawing ratio. On the other hand, the tensile strength curves of the 5/95 and 10/90 blend films increase gradually up to a drawing ratio of 8, above which it increases abruptly. The cold-drawn 5/95 and 10/90 blend films demonstrated better mechanical properties than the P(3HB) and UHMW-P(3HB) cold-drawn films. The tensile strength, Young's modulus, and elongation at break of the 12 times drawn 5/95 blend film were 242 MPa, 1.50 GPa, and 88%, respectively. In general, the tensile strength of drawn films was increased by the orientation of molecular chains. However, the increase of the tensile strength of blend films drawn more than 8 times might be explained by changes in the highly ordered structure at a drawing ratio between 8 and 10 as well the aligned orientation of molecular chains.

The elongation at break of each sample, as shown in Figure 4B, increased with increasing drawing ratio up to around 6 and then decreased. When the drawing ratio is low, the molecular chains in the films gradually orient in the direction of drawing as the drawing ratio increases. Accordingly, the elongation at break increases. However, the elongation at break of drawn films with a drawing ratio of more than 6 decreased because the molecular chains have already become as aligned as possible.

The stress−strain curves of cold-drawn 10/90 blend film and the film aged for 600 days are displayed in Figure 6. The tensile strength and elongation at break of cold-drawn films were did not change after aging for 600 days. It is known that the tensile strength of undrawn P(3HB) film decreases due to secondary crystallization at room temperature. In this case, the high stability of cold-drawn film was demonstrated due to the high crystallinity and highly orientated molecular chain formed by cold-drawing. It has become clear that the stability of cold-drawn P(3HB) film was maintained even after aging for 600 days.

Wide-Angle X-ray Diffraction Analysis. The tensile strength of blend films drawn to more than 10 times their original length increased significantly compared with less drawn films. WAXD and SAXS measurements were performed to investigate the relationship between the structure of the films and their physical properties.

Figure 7A shows a typical WAXD pattern of an undrawn and annealed 5/95 blend film. The WAXD patterns of all samples are shown in Figure S1 of the Supporting Information. The ring patterns for the undrawn film indicate the random orientation

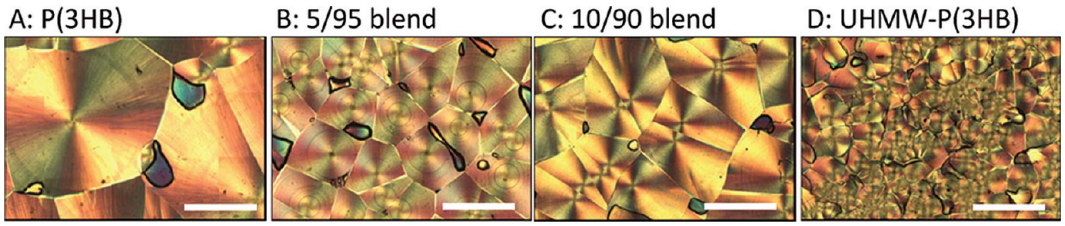

Figure 4. Polarization optical microscope graphics of each samples annealed at 100 °C: (A) P(3HB), (B) 5/95 blend, (C) 10/90 blend, and (D) UHMW-P(3HB). White bar indicates a scale at 500 μm.

dx.doi.org/10.1021/ma202285c | *Macromolecules* 2012, 45, 1858−1865

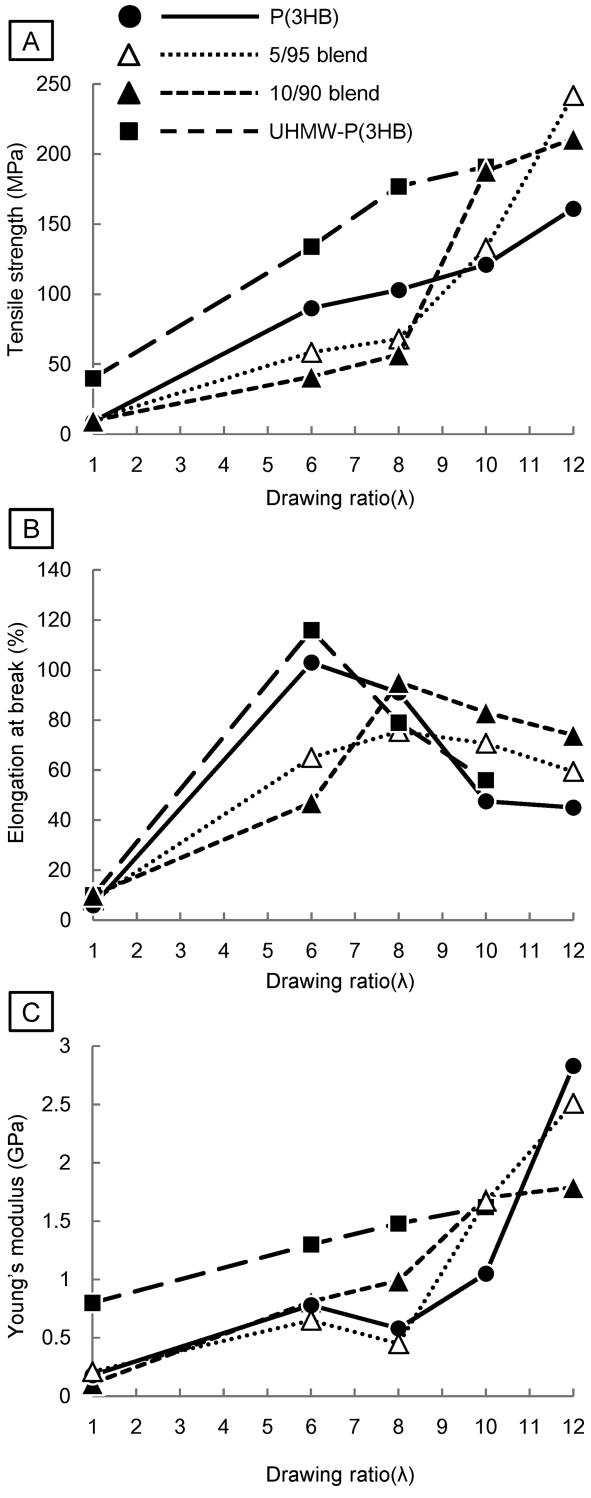

Figure 5. Mechanical properties of cold-drawn films annealed at 100 °C for 2 h. (A) Tensile strength, (B) elongation at break, and (C) Young's modulus as functions of drawing ratio. A drawing ratio of 1 is the undrawn film.

of lamellar crystals. On the other hand, the WAXD pattern of a 5/95 blend film with a cold-drawn ratio of 12 indicated the orientation of lamellar crystals with an α-form crystal structure (Figure 7B). Yokouchi et al. and Okamura and Marchessault reported that the α-form crystal structure of P(3HB) indexed with orthorhombic unit cell parameters of a = 0.576 nm, b = 1.320 nm, and c (fiber axis) = 0.596 nm and a space group of

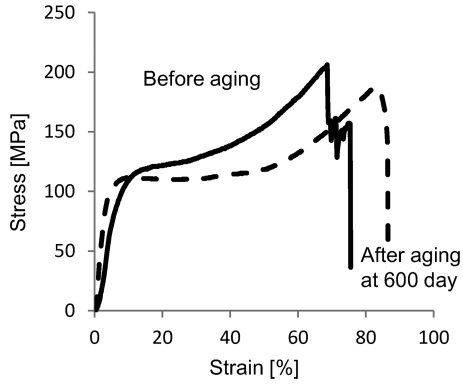

Figure 6. Stress–strain curves of cold-drawn 10/90 blend films at drawing ratio of 12. Solid line and dashed line indicate immediately after prepared film and aged film after 600 days, respectively.

$P2_12_12_1$. In addition, a reflection arising from oriented β-form crystals can be observed in the equatorial line. Orts et al.[21] observed the β-form, which is a planar zigzag conformation, in a cold-drawn poly[(*R*)-3-hydroxybutyrate-*co*-(*R*)-3-hydroxyvalerate] film. Furthermore, they reported that drawn films of P(3HB) and P(3HB) copolymers with high mechanical strength are of the β-form. It seems that the β-form of P(3HB) has improved physical properties compared with the α-form. However, the three-dimensional crystal structure for the β-form has not yet been reported. The *c*-axis was calculated to be 0.474 and 0.469 nm by Ort et al.[21] and Tanaka et al.,[29] respectively.

Figure 8A shows cropped WAXD patterns of drawn films of P(3HB), 5/95 blend, 10/90 blend, and UHMW-P(3HB) at their maximum drawing ratio. The cropped area is that indicated by a rectangle in Figure 7B. The black borders in Figure 8 are the domain showing β reflections. A reflection from the β-form did not appear in the WAXD pattern of UHMW-P(3HB). However, one can see reflections from the β-form in the WAXD patterns of drawn 5/95 and 10/90 blend films. The intensity of the β reflection for the drawn 5/95 blend film was higher than that for the 10/90 blend. In the case of P(3HB), the reflection of the β-form was slight. The intensity of the β reflection in Figure 8A was integrated as a function of azimuth to give intensity profiles to quantitatively assess the presence of the β-form, as shown in Figure 8B. The intensity profiles of all samples are shown in Figure S2 of the Supporting Information. It is difficult to calculate the crystallinity of the β-form because the diffraction from the β-form was not observed sharply except for the β-reflection at the equatorial line. It is expected that molecular chains with a β-form structure pack roughly along the fiber axis (*c*-axis), allowing reflections of the β-form to be detected on the equatorial line. This result indicates that molecular chains with β-form were aligned at the lattice plane (*hk*0). However, clear reflections are not observed at the layer line in WAXD, indicating that the chains pack roughly along the fiber axis.

The intensity ratio of β reflections ($R_{(\beta/\alpha)}$) to α(020) reflections can be defined as

$$R_{(\beta/\alpha)} = \int I_{\beta}\, dI / \int I_{\alpha(020)}\, dI \quad (5)$$

$\int I_{\alpha(020)}\, dI$ was calculated by integrating the α(020) reflection. Figure 9 shows $R_{(\beta/\alpha)}$ for each sample as a function of drawing ratio. Until a drawing ratio of 8, $R_{(\beta/\alpha)}$ was 0 because the β-form was not present in any of the drawn films. On the other hand, $R_{(\beta/\alpha)}$ increased at drawing ratios over 10 for the drawn films

dx.doi.org/10.1021/ma202285c | *Macromolecules* 2012, 45, 1858–1865

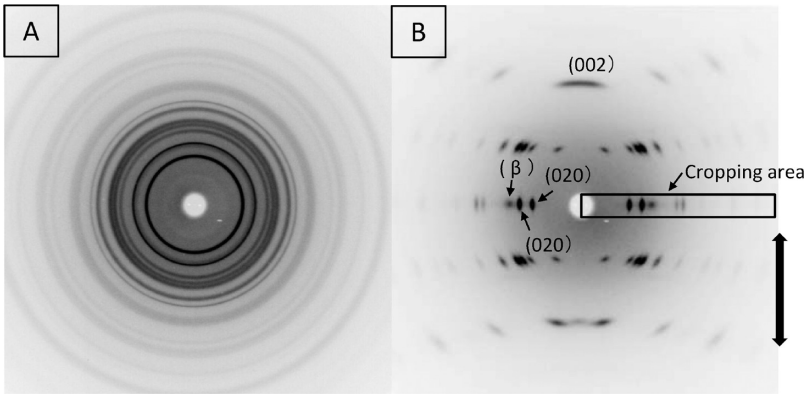

Figure 7. WAXD patterns of (A) undrawn 5/95 blend film and (B) 5/95 blend film at a drawing ratio of 12. The arrow indicates the drawing direction.

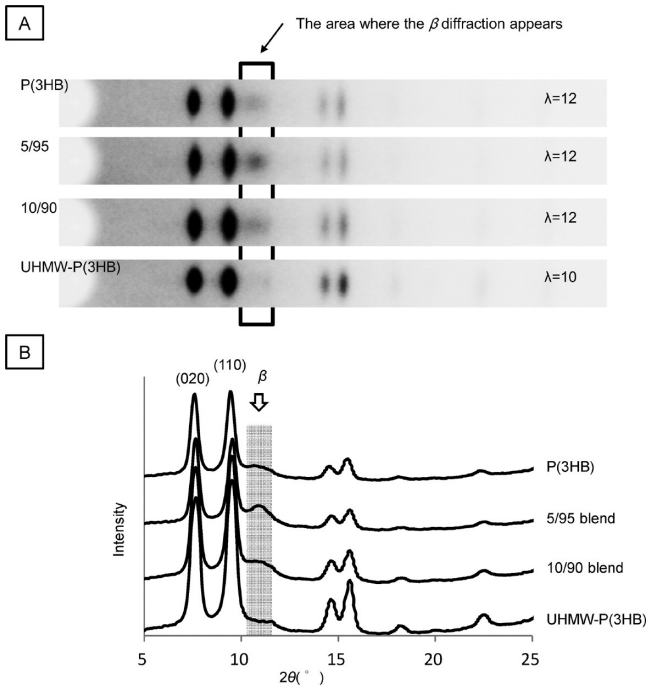

Figure 8. (A) Equatorial line of WAXD pattern of drawn films. λ indicates the maximum drawing ratio. (B) Line profile of drawn films.

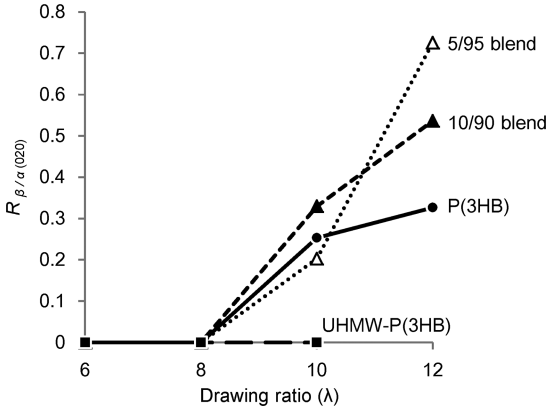

Figure 9. Intensity ratio of the β-form reflection to the (020) reflection of the α-form.

expect the UHMW-P(3HB) film. $R_{(\beta/\alpha)}$ of the blend films increased significantly compared with that of P(3HB). In particular, $R_{(\beta/\alpha)}$ values drastically increased for the 5/95 blend film at higher drawing ratios, which correlates with the tensile strength (Figure 5), indicating that the β-form (planar zigzag conformation) strongly increases the tensile strength of drawn films. Furthermore, the addition of a small amount of UHMW-P(3HB) chains seemed to induce generation of the β-form. The mechanism of generation of the β-form in blend films will be discussed later.

Small-Angle X-ray Scattering Analysis. Figure 10 shows typical SAXS profiles of 5/95 blend films that are (A) undrawn and with a drawing ratio of (B) 6 and (C) 12. The SAXS patterns of all samples are shown in Figure S3 of the Supporting Information. The ring pattern in (A) indicates an isotropic periodic structure such as spherulites. The SAXS pattern of the 6 times drawn 5/95 blend film (B) showed two strong signals at the meridian. This scattering means that a periodic structure of oriented lamellar crystals exists parallel to the drawing direction.

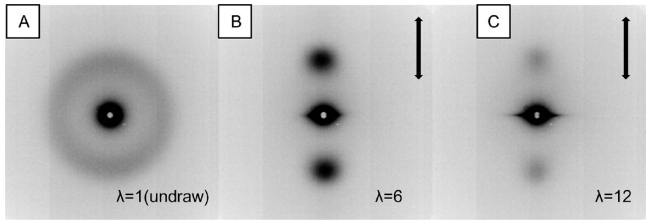

Figure 10. SAXS patterns of a 5/95 blend film that is (A) undrawn and with a drawing ratio of (B) 6 and (C) 12. The arrow indicates the drawing direction.

In the SAXS pattern of the 5/95 blend film with a drawing ratio of 12, the intensity of two signals at the meridian was lower than that of the blend film that had a drawing ratio of 6. This phenomenon seems to indicate that the difference of electron density decreased due to β-form crystals forming between lamellar crystals because the change in density between α-form and β-form crystals is smaller than that between α-form crystals and amorphous regions. A streak pattern was observed on the equator line, as shown in Figure 8C. This streak pattern indicates the appearance of a highly ordered structure, such as that resembling a shish-kebab, parallel to the drawing direction.

dx.doi.org/10.1021/ma202285c | *Macromolecules* 2012, 45, 1858–1865

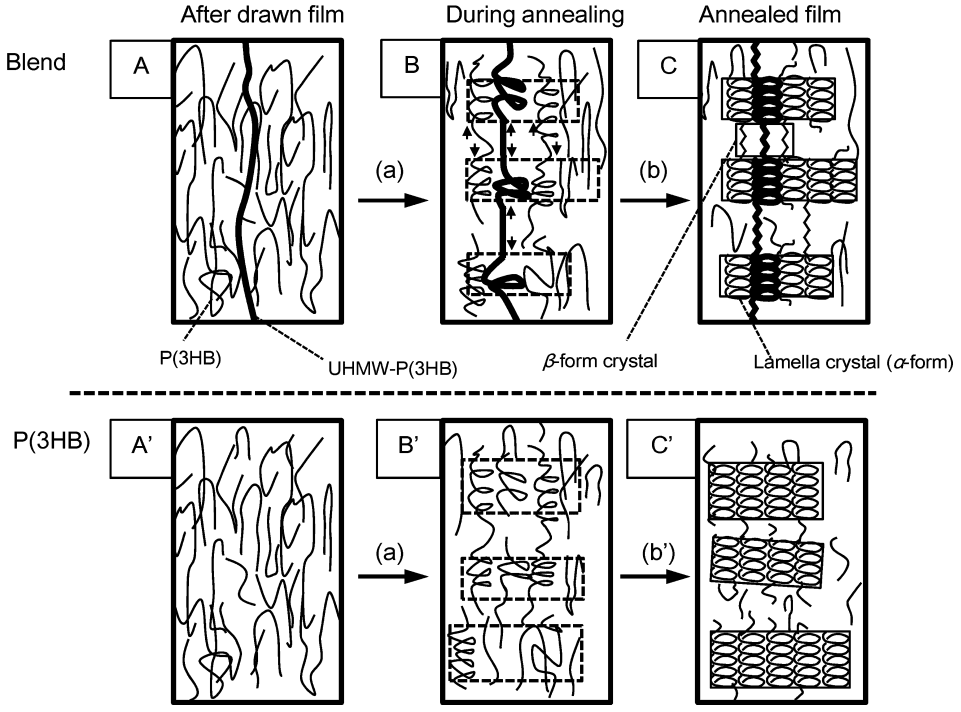

Figure 11. Schematic illustrations showing the proposed mechanism for generating β-form structures in blend and P(3HB) films. (A) Initial crystallization of lamellar crystals (α-form). (B) Generating the β-form in an amorphous region during further crystallization. (B′) Movement of lamellar crystals during further crystallization. The β-form was formed from tie-chains fixed between lamellar crystals during annealing.

The thickness of lamellar crystals (l_p) and their L_p are summarized in Table 2 together with physical properties. The l_p, which is ca. 8 nm, in the drawn UHMW-P(3HB) film is greater than that in the drawn P(3HB) film (~6 nm). The l_p values of 5/95 and 10/90 blends are slightly smaller than that of P(3HB), suggesting that the UHMW-P(3HB) chains in the blend films exist in the β-form between α-form lamellar crystals. If the UHMW-P(3HB) chains in the blend films form lamellar crystals with only themselves, the lamellar crystals in blend films will be thicker than those in the P(3HB) film. However, l_p of 5/95 and 10/90 blend films were smaller than that in the P(3HB) film, which supports the UHMW-P(3HB) chains adopting the β-form.

Proposed Formation Mechanism of the β-Form in Cold-Drawn Blend Films. Until now, it was considered that the β-form was generated from amorphous regions between lamellar crystals by two-step drawing.[30] However, in this experiment, two-step drawing was not used. Accordingly, we propose a new generation mechanism of the β-form in cold-drawn blend films. Based on our experimental results, a model for the formation of the β-form in cold-drawn and annealed blend films is presented, as depicted in Figure 11. When cold-drawing was applied to the blend films, the molecular chains become aligned along the drawing direction (Figure 11A). Lamellar crystals were generated by the annealing process. The UHMW-P(3HB) chains seem to cocrystallize with P(3HB) chains in lamellar crystals (Figure 11B). The UHMW-P(3HB) in blend film was expected to give the many forming tie chain as against P(3HB). The lamellar crystals including UHMW-P(3HB) chains are fixed by the presence of these chains, and as a result, these lamellar crystals seem to be unable to move freely. The UHMW-P(3HB) chains between lamellar crystals were pulled in the direction of lamellar crystals as the growth of the lamellar crystals progresses. This causes the UHMW-P(3HB) chains between lamellar crystals to adopt the β-form (planar zigzag) (Figure 11C). It is probable that the β-form structure is also formed from P(3HB) chains between lamellar crystals fixed by UHMW-P(3HB) chains. In the case of only P(3HB) (Figure 11A′–C′), it seems that forming the β-form structure is difficult because the pulling force toward the direction of the lamellar crystals is absorbed by movement of unfixed lamellar crystals (Figure 11C′). In addition, the tie-chain in P(3HB) is expected less than that in blend.

Enzymatic Degradation. Figure 12 shows the enzymatic degradation rates for the blend films together with P(3HB) and

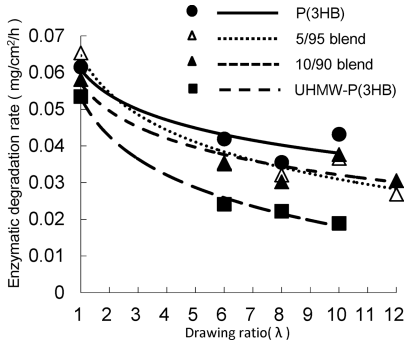

Figure 12. Enzymatic degradation rate of P(3HB), blend, and UHMW-P(3HB) films in an aqueous solution of polyhydroxybutyrate depolymerase at 37 °C.

UHMW-P(3HB) films at different drawing ratios. The degradation rates of UHMW-P(3HB) films were lower than those of P(3HB) and blend films. The degradation rates of each sample decreased with increasing drawing ratio. This is caused by the increase in crystallinity and lamellar thickness with drawing ratio. Comparing the P(3HB), blend, and UHMW-

dx.doi.org/10.1021/ma202285c | Macromolecules 2012, 45, 1858–1865

P(3HB) films, the slow degradation rate of UHMW-P(3HB) seems to be caused by thick lamellar crystals. The order of the enzymatic degradation rate was P(3HB) > blend > UHMW-P(3HB). This result indicates the addition of UHMW-P(3HB) to P(3HB) can control the degradation rate as well as the drawing procedure.

CONCLUSION

Blend films consisting of wild-type P(3HB), which is a typical microbial plastic, and a small amount of UHMW-P(3HB) were prepared. G reached a maximum value at around 90 °C for all of the samples, and at each crystallization temperature the order of G was P(3HB) > blend > UHMW-P(3HB). However, addition of UHMW-P(3HB) reduced $t_{1/2}$. Thus, addition of UHMW-P(3HB) chains appeared to increase the frequency of crystal nucleation. A cold-drawing technique was applied to the films. It has become clear that the stability of cold-drawn P(3HB) film was maintained even after aging for 600 days. WAXD measurements of the drawn films revealed the presence of β-form crystals, which are observed in high strength films. Measurement of the quantity of the β-form crystals showed that there is a correlation between the strength of a film and the amount of β-form structure. The addition of UIHMW-P(3HB) into wild-type P(3HB) improved the mechanical properties and increased the amount of β-form crystals in the resulting films. A new generation mechanism of β-form structures in blend films was proposed. The rate of enzymatic degradation of the films was P(3HB) > blend > UHMW-P(3HB).

ASSOCIATED CONTENT

Supporting Information

Wide- and small-angle X-ray diffraction patterns; intensity profiles from equatorial area on WAXD pattern. This material is available free of charge via the Internet at http://pubs.acs.org.

AUTHOR INFORMATION

Corresponding Author

*E-mail atiwata@mail.ecc.u-tokyo.ac.jp; Ph +81-3-5841-7888; Fax +81-3-5841-1304.

Notes

The authors declare no competing financial interest.

ACKNOWLEDGMENTS

This work was supported by a Grant-in-Aid for Scientific Research of Japan (A) No.22245026 (2010) and the New Energy and Industrial Technology Development Organization (NEDO) of Japan.

REFERENCES

(1) Doi, Y. *Microbial Polyesters*; VCH: New York, 1990.
(2) Steinbuschel, A.; Valentin, H. E. *FEMS Microbiol. Lett.* **1995**, *128*, 219−228.
(3) Lenz, R. W.; Marchessault, R. H. *Biomacromolecules* **2005**, *6*, 1−8.
(4) Scandola, M.; Ceccorulli, G.; Pizzoli, M. *Makromol. Chem., Rapid Commun.* **1989**, *10*, 47−50.
(5) De Koning, G. J. M.; Lemstra, P. J. *Polymer* **1993**, *19*, 4089−4094.
(6) Barham, P. J.; Keller, A.; Otun, E. L. *J. Mater. Sci.* **1984**, *19*, 2781−2794.
(7) Sudesh, K.; Abe, H.; Doi, Y. *Prog. Polym. Sci.* **2000**, *25*, 1503.
(8) Tsuge, T. *J. Biosci. Bioeng.* **2002**, *94*, 579−584.
(9) Park, J. W.; Doi, Y.; Iwata, T. *Macromolecules* **2005**, *38*, 2345−2354.
(10) Abe, H.; Matsubara, I.; Doi, Y. *Macromolecules* **1995**, *28*, 844−853.
(11) Ha, C.; Cho, W. *Prog. Polym. Sci.* **2002**, *27*, 759−809.
(12) Park, J. W.; Doi, Y.; Iwata, T. *Biomacromolecules* **2004**, *5*, 1557−1566.
(13) Kusaka, S.; Abe, H.; Lee, S. Y.; Doi, Y. *Appl. Microbiol. Biotechnol.* **1997**, *47*, 140−143.
(14) Aoyagi, Y.; Doi, Y.; Iwata, T. *Polym. Degrad. Stab.* **2003**, *79*, 209−216.
(15) Iwata, T.; Tsunoda, K.; Aoyagi, Y.; Kusaka, S.; Yonezawa, N.; Doi, Y. *Polym. Degrad. Stab.* **2003**, *79*, 217−224.
(16) Tincer, T.; Coskun, M. *Polym. Eng. Sci.* **1993**, *33*, 1243−1250.
(17) Yang, L.; Somani, R. H.; Sics, I.; Hsiao, B. S.; Kolb, R.; Fruitwala, H.; Ong, C. *Macromolecules* **2004**, *37*, 4845−4859.
(18) Ogino, Y.; Fukushima, H.; Matsuba, G.; Takahashi, N.; Nishida, K.; Kanaya, T. *Polymer* **2006**, *47*, 5669−5677.
(19) Okamura, K.; Marchessault, R. H. In *Conformation of Biopolymers*; Romachandra, G. N., Ed.; Academic Press: New York, 1967; Vol. 2, pp 709−720.
(20) Yokouchi, M.; Chatani, Y.; Tadokoro, H.; Teranishi, K.; Tani, K. *Polymer* **1973**, *14*, 267−272.
(21) Orts, W. J.; Marchessault, R. H.; Bluhm, T. L.; Hamer, G. K. *Macromolecules* **1990**, *23*, 5368−5370.
(22) Iwata, T.; Aoyagi, Y.; Fujita, M.; Yamane, H.; Doi, Y.; Suzuki, Y.; Takeuchi, A.; Uesugi, K. *Macromol. Rapid Commun.* **2004**, *25*, 1100−1104.
(23) Iwata, T. *Macromol. Biosci.* **2005**, *5*, 689−701.
(24) Kahar, P.; Agus, J.; Kikkawa.; Taguchi, K.; Doi, Y.; Tsuge, T. *Polym. Degrad. Stab.* **2005**, *87*, 161−169.
(25) Vonk, C. G. *J. Appl. Crystallogr.* **1973**, *6*, 148−152.
(26) Avrami, M. *J. Chem. Phys.* **1939**, *7*, 1103−1112.
(27) Lemstra, P. J.; Postma, J.; Challa, G. *Polymer* **1974**, *15*, 757−759.
(28) Magill, J. H. *J. Appl. Phys.* **1964**, *35*, 3249−3258.
(29) Tanaka, F.; Doi, Y.; Iwata, T. *Polym. Degrad. Stab.* **2004**, *85*, 893−901.
(30) Iwata, T.; Fujita, M.; Aoyagi, Y.; Doi, Y.; Fujisawa, T. *Biomacromolecules* **2005**, *6*, 1803−1809.

Macromolecules

Article

pubs.acs.org/Macromolecules

On the Polymerization Behavior of Telomers: Metathesis versus Thiol–Ene Chemistry

Hatice Mutlu,[†] Andrei N. Parvulescu,[‡] Pieter C. A. Bruijnincx,[‡] Bert M. Weckhuysen,[‡] and Michael A. R. Meier[†,*]

[†]Institute of Organic Chemistry, Karlsruhe Institute of Technology, Fritz-Haber-Weg-6, Building 30.42, 76131 Karlsruhe, Germany

[‡]Debye Institute of Nanomaterials Science, Inorganic Chemistry & Catalysis, Utrecht University, Universiteitsweg 99, 3584 CG Utrecht, The Netherlands

ABSTRACT: The potential of butadiene ditelomers for the synthesis of polymers has been investigated for the first time following two different approaches: acyclic diene metathesis (ADMET) polymerization and thiol–ene polyaddition. The feasibility of both step-growth polymerization methods has been investigated by focusing on the particular polymerization behavior of these unusual monomers. It has been shown that ring-closing metathesis of the studied ditelomers predominates in the first steps of ADMET, followed by oligomerization and double bond isomerization. On the other hand, during thiol–ene polyaddition, additional isomerization reactions, converting allyl ether moieties to vinyl ether moieties, were observed. Generally, the thiol–ene polymerization approach led to higher molecular weight polymers with better characteristics and interesting material properties.

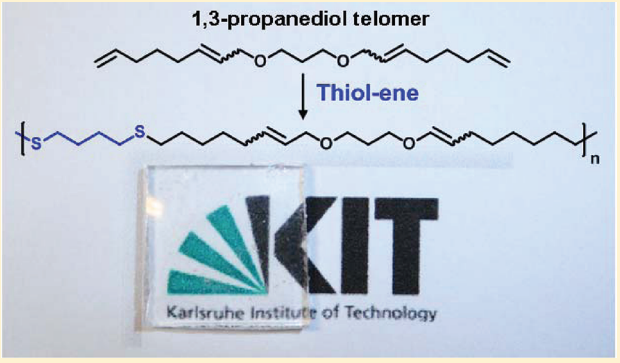

INTRODUCTION

Along with the idea of substituting petroleum-based feedstocks with renewable ones, the development of more sustainable and environmentally benign technologies for the production of versatile building blocks and polymers has become one of the most important items on the agenda of industry as well as academia.[1] In light of this general desire for more efficient and at the same time environmentally friendlier processes, the addition of nucleophiles to olefins and alkynes, typical examples of 100% atom-efficient reactions, can be considered as particularly attractive green processes. Among these reactions, the telomerization reaction,[2] a synthetic methodology originally discovered by Smutny in 1967,[3] is reported to provide linear dimerization products of 1,3-dienes (such as 1,3-butadiene and isoprene) via 1,6- or 3,6-addition of an appropriate nucleophile (e.g., alcohols,[4] water,[5] amines and ammonia,[6] sugar[7] and polyols,[8] starch,[9] and carbon dioxide[10]) in good yields for countless applications. This valuable process enables, for instance, the synthesis of intermediates for natural products or fine chemicals synthesis[11] and the preparation of amphiphilic compounds that find use as surfactants or emulsifiers if the proper diene/nucleophile combination is selected.[12] In addition, if the applicability of telomers, in particular α,ω-diene ones, could be extended to polymerization reactions, this would open up new opportunities for building high molecular weight and value-added materials. Notably, our literature survey has shown only a limited number of studies reporting the use of telomers as monomers for polymer synthesis. One example is the copolymerization of ethylene with 2,7-octadienyl methyl ether, a monotelomer available from the telomerization of 1,3-butadiene with methanol and palladium catalysts.[13] However, ditelomers have not yet been investigated for step-growth polymerizations. Since telomers contain double bonds, it should be possible to polymerize them using acyclic diene metathesis (ADMET) polymerization. This polymerization technique is advantageous since the catalysts employed are tolerant toward many functional groups, the reaction conditions are mild, and a wide range of molecular architectures are accessible.[14] Another well-established concept, the radical-initiated thiol–ene reaction,[15] has also been widely applied in the field of polymer science.[16] The so-called thiol–ene click reaction, discovered in 1905 by Posner,[17] is a well-known example of this type of reaction. Extensive investigations in the context of the reaction mechanism, polymerization kinetics, and monomer reactivity[18] have revealed that, in addition to being highly efficient under benign reaction conditions (compatible with water and oxygen), the thiol–ene coupling reaction is regioselective, metal-free, orthogonal to many functional groups, and provides quantitative or near-quantitative yields with simple or no chromatographic separation required.[14,19] Furthermore, some studies have already focused on the direct synthesis of linear oligomers and polymers through step-growth and addition/chain polymerizations of diolefins with dithiols.[20]

Received: December 7, 2011
Revised: January 24, 2012
Published: February 6, 2012

dx.doi.org/10.1021/ma2026572 | *Macromolecules* 2012, 45, 1866–1878

Thus, in order to broaden the application possibilities of butadiene telomers, we report here a comparative study on the polymerization of α,ω-diene telomers using two straightforward and simple chemical pathways: the acyclic diene metathesis and thiol−ene polymerizations as versatile tools to convert such valuable monomers into potentially useful macromolecular materials.

EXPERIMENTAL SECTION

Materials and Instrumentation. Thin layer chromatography (TLC) was performed on silica gel TLC cards (layer thickness 0.20 mm, Fluka). Permanganate reagent was used as developing solution.

All ^{1}H and ^{13}C nuclear magnetic resonance (NMR) spectra were acquired in $CDCl_3$ (99.8 atom % D, Armar Chemicals) as solvent using Bruker AVANCE DPX spectrometers operating at 300 and 400 MHz for ^{1}H NMR and 75.5 and 100 MHz for ^{13}C NMR. Chemical shifts (δ) are given in ppm relative to the internal standard tetramethylsilane (TMS, δ = 0.00 ppm) for ^{1}H NMR. The ^{1}H NMR spectra were referenced to the residual proton impurities in the $CDCl_3$ at δH 7.26 ppm. The ^{13}C NMR spectra were referenced to $^{13}CDCl_3$ at δC 77.00 ppm. For the analysis of the polymers the relaxation time was set to 5 s.

Molecular weight and PDI (M_w/M_n) values of the polymers were obtained by SEC (GPC) using a LC-20A system from Shimadzu equipped with an SIL-20A autosampler and an RID-10A refractive index detector in THF (flow rate 1 mL min^{-1}) at 50 °C. The analysis was performed on three different column systems; (A): PLgel 5 μm MIXED-D column (Varian, 300 mm × 7.5 mm, 10000 Å) with SDV gel 5 μm precolumn (PSS, 50 mm × 8.0 mm), (B): two PSS SDV column system (5 μm 300 mm × 7.5 mm, 1000 Å, 10000 Å) and (C): three PSS SDV column system (5 μm 300 mm × 7.5 mm, 100 Å, 1000 Å, 10000 Å). All determinations of molar mass were performed relative to linear poly(methyl methacrylate) standards (Polymer Standard Service, M_P 1100−981000 Da).

Differential scanning calorimetry (DSC) experiments were carried out under a nitrogen atmosphere at a heating rate of 10 °C min^{-1} with a DSC821e (Mettler Toledo) calorimeter up to a temperature of 250 °C using a sample mass in the range of 8−15 mg. Data from second heating scans are reported unless special heating treatments were applied. The glass transition temperature, T_g, is reported as the midpoint of the heat capacity change.

Thermogravimetric analysis (TGA) was performed on a TGA/SDTA851e instrument (Mettler Toledo) at a heating rate of 10 °C × min^{-1} under nitrogen. The weights of the samples were of about 8 mg.

All chemicals were used as received: $Pd(dba)_2$ (dba, bis(dibenzylideneacetone) (Aldrich), TOMPP (tris(*o*-methoxyphenyl)phosphine), 1,3-propanediol (>99%, Fluka), 1,3-butadiene (Linde Gas), 1,4-benzoquinone (**BQ**, >99%, Aldrich), 1-octanethiol (>98.5%, Aldrich), 1,4-butanedithiol (**DT1**, >97%, Aldrich), 2-mercaptoethyl ether (**DT2**, >95%, Aldrich), 3,6-dioxa-1,8-octanedithiol (**DT3**, >95%, Aldrich), benzylidenebis(tricyclohexylphosphine) dichlororuthenium (**C1**, Grubbs catalyst first generation, Aldrich), benzylidene [1,3-bis(2,4,6-trimethylphenyl)-2-imidazolidinylidene] dichloro-(tricyclohexylphosphine) ruthenium (**C2**, Grubbs catalyst second generation, Aldrich), (1,3-bis(2,4,6-trimethylphenyl)-2-imidazolidinylidene)dichloro(*o*-isopropoxyphenylmethylene) ruthenium (**C3**, Hoveyda−Grubbs catalyst second generation, Aldrich), [1,3-bis(2,4,6-trimethylphenyl)-2-imidazolidinylidene]dichloro [2-(1-methylacetoxy)-phenyl]methylene ruthenium(II) (**C4**, Umicore $M5_1$), ethyl vinyl ether (99%, Aldrich), 2,2′-azobis(2-methylpropionitrile) (**AIBN**, 98%, Aldrich) was used after recrystallization from methanol. All solvents (technical grade) were used without purification.

General Procedure for Ditelomers (1, 2, and 3) Synthesis. A standard telomerization procedure[4a] was adapted in order to maximize ditelomer formation for 1,3-propanediol. The reactions were performed inside a 100 mL stainless steel Parr autoclave. In a typical run, the autoclave was first loaded with the alcohol (0.12 mol), $Pd(dba)_2$ (4.85×10^{-5} mol) and the ligand TOMPP (tris(*o*-methoxyphenyl)-phosphine) (3.8×10^{-4} mol) at room temperature after which the autoclave was cooled to −40 °C. 1,3-Butadiene was directly condensed in the reactor and the autoclave was heated to the reaction temperature of 80 °C and kept at that temperature until the pressure had dropped to less than 3 bar after around 12 h (indicating that the reaction was finished). An excess of butadiene (1,3-butadiene:alcohol molar ratio of 6:1) was employed in all experiments in order to ensure complete telomerization of the alcohol. Three different phosphine to metal ratios were used in the telomerization of 1,3-butadiene with 1,3-propanediol: 4:1 (telomer **1**), 8:1 (telomer **2**), and 16:1 (telomer **3**). After purification of the products, the amount of the ditelomer of 1,3-propanediol was calculated to be more than 91%. The telomer products were isolated by column chromatography, for which a silica gel column (internal diameter: 50 mm, height: 250 mm, dead volume: 70 mL) was loaded with the telomer products. Two column volumes of hexane were eluted and discarded, after which the telomers were separated using a hexane:diethyl ether (9:1 v/v) mixture as the eluent. Pooled fractions were dried in vacuum and purity checked by ^{1}H NMR. The linear-to-branched (l/b) ratio was determined from the GC and NMR analysis of the isolated products.

Thiol−Ene Model Reaction. The thiol−ene model reactions were performed in a carousel reaction station RR98072 (Radleys Discovery Technologies, U.K.). Into a reaction tube, 0.5 g (1.71 mmol) of the ditelomer and 1.0 g of 1-octanethiol (6.84 mmol) were introduced and degassed via 3 times 200 mbar vacuum and subsequent Ar purge. The reaction were conducted either radically (model reaction A) or thermally induced (model reaction B) under solvent-free conditions at the desired reaction temperature (75 and 70 °C for the respective model reactions A and B). In the case of radical-initiated reactions, 2.5 mol % (0.04 mmol) of **AIBN** was added to the reaction mixture. The reactions were followed with TLC with hexane−ethyl acetate (15:1, v:v) as eluent. Moreover, the monomer conversion was calculated from integration of corresponding ^{1}H NMR signals. A relaxation time (d_1) of 5 s was used in the ^{1}H NMR analyses in order to obtain reliable integral values. The reaction products were purified by column chromatography with hexane−ethyl acetate (15:1, v:v) as eluent.

Model Reaction Products. ^{1}H NMR (300 MHz, $CDCl_3$, δ in ppm): 6.20 (d, −CH=C*H*−O−CH_2−, J = 12.6 Hz, $1H_{trans}$), 5.91 (dd, −CH=C*H*−O−CH_2−, J = 6.2, 1.3 Hz, $1H_{cis}$), 5.72−5.62 (m, −C*H*=CH−CH_2O−$_{trans\ isomer}$, −C*H*=CH_2 $_{branched\ telomer}$), 5.58−5.48 (m, −CH=C*H*−CH_2−O−$_{trans\ isomer}$, −C*H*=C*H*−CH_2−O−$_{cis\ isomer}$), 5.17−5.11 (m, −CH=CH_2 $_{branched\ telomer}$), 4.81−4.68 (m, −C*H*=CH−O−CH_2−, $1H_{trans}$), 4.37−4.25 (m, −C*H*=CH−O−CH_2−, $1H_{cis}$), 3.99 (d, J = 4.8 Hz, −CH=CH−CH_2−O−$_{cis\ isomer}$), 3.89 (d, J = 5.9 Hz, −CH=CH−CH_2−O−$_{trans\ isomer}$), 3.79−3.64 (m, −CH=CH−O−CH_2−CH_2−CH_2−O−), 3.48 (t, J = 6.4 Hz, −O−CH_2−CH_2−CH_2−O−), 2.57−2.46 (m, −CH_2−S−CH_2−), 2.10−1.98 (m, −CH_2−CH=CH−), 1.90−1.79 (m, −O−CH_2−CH_2−CH_2−O−, −CH=CH−O−CH_2−CH_2−CH_2−O−), 1.67−1.52 (m, −S−CH_2−CH_2−CH_2−), 1.42−1.31 (m, −CH_2−), 0−92−0.84 (t, −CH_3).

^{13}C NMR (75 MHz, $CDCl_3$, δ in ppm): 146.18 (−CH=*C*H−O−CH_2− $_{cis\ isomer}$), 144.99 (−CH=*C*H−O−CH_2−$_{trans\ isomer}$), 134.31 (−CH=CH−CH_2−O−$_{trans\ isomer}$), 134.17 (−CH=CH−CH_2−O−$_{cis\ isomer}$), 126.95 (−CH=*C*H−CH_2O−$_{cis\ isomer}$), 126.80 (−CH=*C*H−CH_2O−$_{trans\ isomer}$), 106.78 (−*C*H=CH−O−CH_2−$_{cis\ isomer}$), 104.09 (−CH=CH−O−CH_2−$_{trans\ isomer}$), 74.88 (−CH=CH−O−CH_2−CH_2−CH_2−O−), 71.80 (−CH=CH−CH_2−O−$_{trans\ isomer}$), 67.38 (−O−CH_2−CH_2−CH_2−O−), 66.65 (−CH=CH−CH_2−O−$_{cis\ isomer}$), 32.35 (−CH_2−S−CH_2−), 32.29 (−CH_2−S−CH_2−), 32.15 (−CH_2−CH=CH−O−), 31.93 (−CH_2−CH=CH−CH_2−O−), 30.37 (−O−CH_2−CH_2−CH_2−O−), 30.13 (−CH=CH−O−CH_2−CH_2−CH_2−O−), 29.79 (−S−CH_2−CH_2−CH_2−CH_2−), 29.72 (−S−CH_2−CH_2−CH_2−), 28.90 (−S−CH_2−CH_2−CH_2−), 28.67 (−CH_2−CH_2−CH_2=CH−), 28.4 (−CH_2−CH_2−CH_2−CH_3), 22.27 (−CH_2−CH_3), 14.14 (CH_3).

Polymerization Reactions. *General Procedure for ADMET Polymerizations.* The ADMET reactions were performed in a carousel reaction station RR98072 (Radleys Discovery Technologies, UK). Ditelomer **1**, **2**, or **3** (0.5 g, 1.71 mmol) was added into the carousel tube. Different amounts of catalysts (**C1**, **C2**, **C3**, or **C4**; see Figure 1) were added separately. The influence of the reaction conditions on the obtained molecular weight was studied (Tables 1, 2, and 3). Ethylene gas (byproduct) was removed by applying gas or

dx.doi.org/10.1021/ma2026572 | *Macromolecules* 2012, 45, 1866−1878

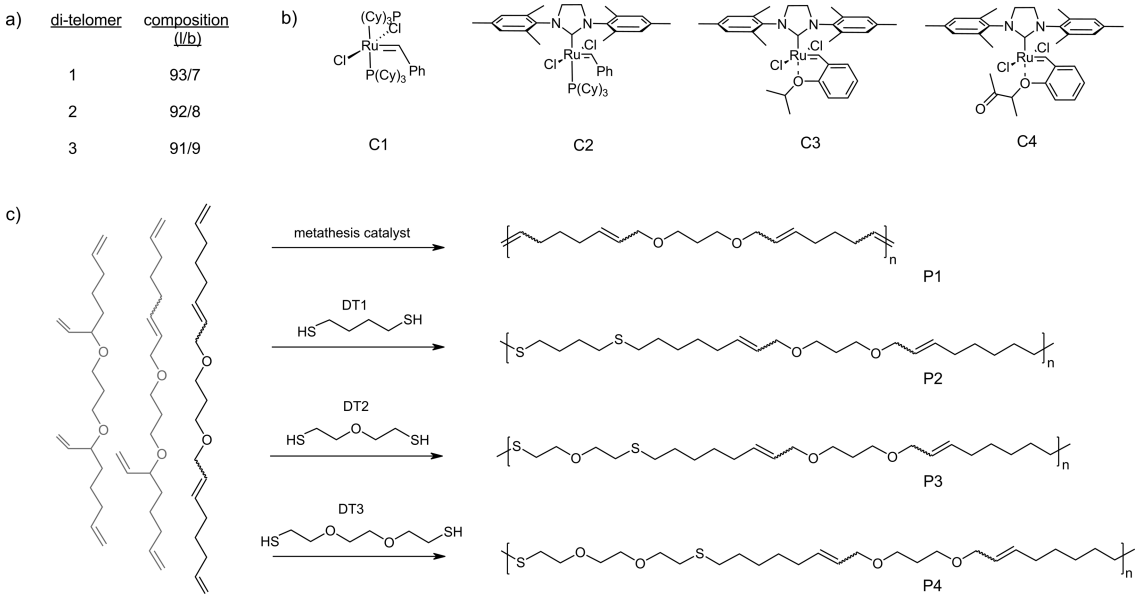

Figure 1. (a) Ditelomer composition as obtained via GC–MS and NMR analysis; (b) metathesis catalysts applied during ADMET studies of the ditelomers; (c) schematic representation of the applied polymerization techniques and idealized products.

Table 1. Selected Results of ADMET Studies of Telomer 1 in the Presence of C1 at Different Reaction Temperatures after 4 h Reaction Time

entry[a]	catal (mol %)	T (°C)	M_w[b] (Da)	PDI[b] (M_w/M_n)
1	**C1** [0.2]	40	600	1.35
2	**C1** [0.4]	40	650	1.27
3	**C1** [0.8]	40	650	1.32
4	**C1** [1.0]	40	700	1.26
5	**C1** [1.6]	40	750	1.48
6	**C1** [2.0]	40	820	1.50
7	**C1** [0.4]	50	830	1.50
8	**C1** [0.4]	60	750	1.48
9	**C1** [0.4]	70	690	1.42

[a]Additional conditions applied during polymerization: argon was applied for 4 h, unless otherwise specified. [b]GPC was performed on crude reaction samples, quenched with ethyl vinyl ether, in THF, containing BHT, with PMMA calibration; M_w is the weight-average molecular weight detected via GPC.

vacuum continuously. The reactions were cooled down to room temperature and quenched in THF by adding ethyl vinyl ether (500-fold excess to the catalyst) with stirring for 30 min at room temperature. Samples were taken periodically to determine the monomer conversion and the molar mass (distribution) of the resulting polymers using ^{1}H, ^{13}C NMR spectroscopy, as well as GPC analysis. The final reaction mixtures were precipitated in ice cold methanol. The yields varied in the range of 50–85%.

General Procedure for Thiol–Ene Polymerizations. The thiol–ene polymerization reactions were performed in a carousel reaction station RR98072 (Radleys Discovery Technologies, U.K.). Into a reaction vessel 0.5 g (1.71 mmol) of the ditelomer (**1**, **2**, or **3**) and the corresponding dithiol compound (see Table 4) were introduced and degassed via 3 times 200 mbar vacuum and subsequent Ar purge. Afterward, the reaction was let to stir magnetically (500 rpm) at the desired reaction temperature (35–70 °C) until the reaction became very viscous and could not be stirred anymore (Table 4). In some cases, desired amounts of **AIBN** (1.0–2.5 mol %) were added to the reaction mixture and reacted at 75 °C (Table 4). The final reaction mixtures were precipitated in ice cold methanol. The yields varied in the range of 70–92%.

Table 2. Selected Results of ADMET Studies of Telomer 1 in the Presence of C2, C3, and C4 at Different Reaction Temperatures after 4 h Reaction Time

entry	catal (mol %)	conditions[a]	T (°C)	M_w[b] (Da)	PDI[b] (M_w/M_n)
1	**C2** [0.4]	–	40	2200	1.82
2	**C2** [0.4]	**BQ** [0.8]	40	750	1.39
3	**C2** [0.4]	–	60	1500	1.64
4	**C2** [0.4]	–	80	890	1.54
5	**C3** [0.4]	–	40	1100	1.69
6	**C3** [2.0]	–	40	1900	1.74
7	**C3** [2.0]	**BQ** [4.0]	40	4650	1.98
8	**C3** [1.0]	–	80	1900	1.75
9	**C3** [1.0]	**BQ** [2.0]	80	4000	2.01
10	**C3** [1.0]	**BQ** [8.0]	80	4900	2.65
11[c]	**C3** [1.0]	**BQ** [8.0]	80	5600	2.17
12	**C4** [1.0]	–	80	1750	1.78
13	**C4** [1.0]	**BQ** [8.0]	80	1950	1.84
14[c]	**C4** [1.0]	**BQ** [8.0]	80	5450	2.33
15[d]	**C3** [1.0]	**BQ** [8.0]	80	9400 (6350)[e]	5.73 (2.48)[e]
16[d]	**C4** [1.0]	**BQ** [8.0]	80	3800 (2750)[e]	2.71 (2.50)[e]

[a]Additional conditions applied during polymerization: argon was applied for 4 h, unless otherwise specified; BQ: amount of benzoquinone in % with respect to monomer. [b]GPC was performed on crude reaction samples, quenched with ethyl vinyl ether, in THF, containing BHT, with PMMA calibration; M_w is the weight-average molecular weight detected via GPC. [c]Vacuum was applied for 4 h instead of gas flow. [d]Reactions were performed for 48 h with continuous argon flow for the first 4 h. [e]GPC data for crude reaction samples after 24 h, quenched with ethyl vinyl ether, in THF, containing BHT, with PMMA calibration.

Spectroscopic Data of Representative Thiol–Ene Polymers. **P2.** ^{1}H NMR (300 MHz, $CDCl_3$, δ in ppm): 5.85–5.72 (m, $-CH{=}CH_2$), 5.72–5.62 (m, $-CH{=}CH-CH_2-O-_{trans\ isomer}$, $-CH{=}CH_{2\ branched\ telomer}$), 5.58–5.48 (m, $-CH{=}CH-CH_2-O-_{trans\ isomer}$, $-CH{=}CH-CH_2-O-_{cis\ isomer}$), 5.17–5.11 (m, $-CH{=}CH_{2\ branched\ telomer}$), 5.01–4.92 (m, $-CH{=}CH_2$), 3.99 (d, J = 4.8 Hz, $-CH{=}CH-CH_2-O-_{cis\ isomer}$), 3.89 (d, J = 5.9 Hz, $-CH{=}CH-$

dx.doi.org/10.1021/ma2026572 | *Macromolecules* 2012, 45, 1866–1878

Table 3. ADMET Screening of Monomers 2 and 3 at 80°C with 1.0 mol % C3 (or C4) and 8.0 mol % BQ[b]

entry	monomer	catal (mol %)	T (°C)	M_w[a] (Da)	PDI[a] (M_w/M_n)
1	**2**	**C3** [1.0]	80	5350	4.35
2	**2**	**C4** [1.0]	80	4950	3.85
3	**3**	**C3** [1.0]	80	3500	5.84
4	**3**	**C4** [1.0]	80	4220	3.61

[a]GPC was performed to crude reaction samples, quenched with ethyl vinyl ether, in THF, containing BHT, with PMMA calibration; M_w is the weight-average molecular weight detected via GPC. [b]Additional conditions were applied during polymerization: vacuum was applied for 4 h, unless otherwise specified.

Table 4. Reaction Conditions and Analytical Data of Selected Thiol−Ene Polymerizations[d]

entry	monomer:thiol (ratio)	T (°C)	rxn time (h)	M_w[a] (Da)	PDI[a] (M_w/M_n)
1[b]	**1**:**DT1** = 1:1	35	24 (72)	2180	1.85
2	**1**:**DT1** = 1:1	50	48	19 820	5.60
3[c]	**1**:**DT1** = 1:1	70	24	124 200	27.00
4	**1**:**DT2** = 1:1	35	72	49 900	9.88
5	**1**:**DT2** = 1:1	50	96	48 100	6.40
6	**1**:**DT2** = 1:1	70	56	40 200	9.46
7	**1**:**DT3** = 1:1	50	48	53 800	8.61
8	**1**:**DT1** = 1:0.95	50	72	6380	2.91
9	**1**:DT1 = 0.95:1	50	56	20 300	5.08
10	**1**:**DT2** = 1:0.95	50	96	20 600	3.61
11	**1**:**DT2** = 0.95:1	50	96	480 000	53.0
12	**1**:**DT1** = 1:1 (2.5 mol % AIBN)	75	1	12 100	3.22
13	**1**:**DT2** = 1:1 (2.5 mol % AIBN)	75	1	13 150	5.01
14	**1**:**DT3** = 1:1 (2.5 mol % AIBN)	75	1	32 600	5.74
15	**1**:**DT3** = 1:1 (1.0 mol % AIBN)	75	4	8350	2.49

[a]GPC was performed to crude reaction samples in THF, containing BHT, with PMMA calibration; M_w is the weight-average molecular weight detected via GPC. [b]Reaction was performed for 72 h, however there was no difference between the GPC data of 24 and 72 h. [c]GPC data is for the corresponding soluble part of the crude reaction mixture. [d]Additional conditions applied during polymerization: reaction mixtures were degassed via 3 times 200 mbar vacuum and subsequent Ar purge, unless otherwise specified.

CH_2−O−$_{trans\ isomer}$), 3.48 (t, J = 6.4 Hz, −O−CH_2−CH_2−CH_2−O−), 2.57−2.46 (m, −CH_2−S−CH_2−, −CH_2−SH $_{end\ group}$), 2.10−1.98 (m, 1H, −CH_2−CH=CH−), 1.90−1.79 (m, 1H, −O−CH_2−CH_2−CH_2−O−, −CH_2−CH_2−SH $_{end\ group}$), 1.74−1.63 (m, −S−CH_2−CH_2−CH_2−CH_2−S−), 1.63−1.52 (m, 1H, −S−CH_2−CH_2−CH_2−), 1.52−1.42 (m, −CH_2−CH_2−CH=CH_2 $_{end\ group}$), 1.42−1.31 (m, −CH_2−).

^{13}C NMR (75 MHz, $CDCl_3$, δ in ppm): 138.80 (−CH=CH_2), 134.31 (−CH=CH−CH_2−O−$_{trans\ isomer}$), 134.17 (−CH=CH−CH_2−O−$_{cis\ isomer}$), 126.95 (−CH=CH−CH_2−O−$_{cis\ isomer}$), 126.80 (−CH=CH−CH_2−O−$_{trans\ isomer}$), 114.73 (−CH=CH_2), 71.80 (−CH=CH−CH_2−O−$_{trans\ isomer}$), 67.38 (−O−CH_2−CH_2−CH_2−O−), 66.65 (−CH=CH−CH_2−O−$_{cis\ isomer}$), 33.40 (−CH_2−CH=CH_2), 33.22 (−CH_2−CH_2−SH), 32.35 (−CH_2−S−CH_2−), 32.29 (−CH_2−S−CH_2−), 31.93 (−CH_2−CH=CH−), 30.37 (−O−CH_2−CH_2−CH_2−O−), 29.72 (−S−CH_2−CH_2−CH_2−), 28.95 (−S−CH_2−CH_2−CH_2−CH_2−S−), 28.90 (−S−CH_2−CH_2−CH_2−), 28.67 (−CH_2−CH_2−CH=CH−), 28.47 (−CH_2−CH_2−CH=CH_2), 24.41 (HS−CH_2−CH_2−).

P3. ^{1}H NMR (300 MHz, $CDCl_3$, δ in ppm): 5.85−5.71 (m, −CH=CH_2), 5.71−5.61 (m, −CH=CH−CH_2−O−$_{trans\ isomer}$, −CH=CH_2 $_{branched\ telomer}$), 5.58−5.48 (m, −CH=CH−CH_2−O−$_{trans\ isomer}$, −CH=CH−CH_2−O−$_{cis\ isomer}$), 5.17−5.11 (m, −CH=CH_2 $_{branched\ telomer}$), 5.01−4.92 (m, −CH=CH_2), 3.99 (d, J = 4.9 Hz, −CH=CH−CH_2−O−$_{cis\ isomer}$), 3.89 (d, J = 6.1 Hz, −CH=CH−CH_2−O−$_{trans\ isomer}$), 3.70 (t, J = 6.6 Hz, −O−CH_2−CH_2−SH $_{end\ group}$), 3.60 (t, J = 6.6 Hz, −S−CH_2−CH_2−O−CH_2−), 3.47 (t, J = 6.4 Hz, −O−CH_2−CH_2−CH_2−O−), 2.87 (t, J = 6.6 Hz, −O−CH_2−CH_2−SH $_{end\ group}$) 2.68 (t, J = 6.9 Hz, −S−CH_2−CH_2−O−), 2.53 (t, J = 7.4 Hz, −S−CH_2−CH_2−CH_2−), 2.10−1.98 (m, 1H, −CH_2−CH=CH−), 1.88−1.79 (m, 1H, −O−CH_2−CH_2−CH_2−O−), 1.64−1.52 (m, 1H, −S−CH_2−CH_2−CH_2−), 1.52−1.42 (m, −CH_2−CH_2−CH=CH_2 $_{end\ group}$), 1.42−1.33 (m, −CH_2−).

^{13}C NMR (75 MHz, $CDCl_3$, δ in ppm): 138.81 (−CH=CH_2), 134.30 (−CH=CH−CH_2−O−$_{trans\ isomer}$), 134.21 (−CH=CH−CH_2−O−$_{cis\ isomer}$), 126.91 (−CH=CH−CH_2−O−$_{cis\ isomer}$), 126.78 (−CH=CH−CH_2−O−$_{trans\ isomer}$), 114.74 (−CH=CH_2), 71.80 (−CH=CH−CH_2−O−$_{trans\ isomer}$), 70.87 (−S−CH_2−CH_2−O−CH_2−CH_2−S−), 69.40 (−O−CH_2−CH_2−SH), 67.37 (−O−CH_2−CH_2−CH_2−O−), 67.30 (−O−CH_2−CH_2−CH_2−O−), 66.63 (−CH=CH−CH_2−O−$_{cis\ isomer}$), 33.40 (−CH_2−CH=CH_2), 32.74 (−S−CH_2−CH_2−O−CH_2−CH_2−S−), 32.33 (−CH_2−S−CH_2−), 31.70 (−CH_2−CH=CH−), 30.35 (−O−CH_2−CH_2−CH_2−O−), 29.79 (−S−CH_2−CH_2−CH_2−), 28.87 (−S−CH_2−CH_2−CH_2−), 28.59 (−CH_2−CH_2−CH=CH−), 28.53 (−O−CH_2−CH_2−SH), 28.44 (−CH_2−CH_2−CH=CH_2).

P4. ^{1}H NMR (300 MHz, $CDCl_3$, δ in ppm): 5.87−5.72 (m, −CH=CH_2), 5.72−5.63 (m, −CH=CH−CH_2−O−$_{trans\ isomer}$, −CH=CH_2 $_{branched\ telomer}$), 5.59−5.50 (m, −CH=CH−CH_2−O−$_{trans\ isomer}$, −CH=CH−CH_2−O−$_{cis\ isomer}$), 5.18−5.12 (m, −CH=CH_2 $_{branched\ telomer}$), 5.03−4.93 (m, −CH=CH_2), 4.00 (d, J = 4.8 Hz, −CH=CH−CH_2−O−$_{cis\ isomer}$), 3.90 (d, J = 5.9 Hz, −CH=CH−CH_2−O−$_{trans\ isomer}$), 3.74 (t, J = 6.7 Hz, −O−CH_2−CH_2−SH $_{end\ group}$), 3.66−3.60 (m, −CH_2−O−CH_2−CH_2−O−CH_2−), 3.49 (t, J = 6.4 Hz, −O−CH_2−CH_2−CH_2−O−), 2.89 (t, J = 6.7 Hz, −O−CH_2−CH_2−SH $_{end\ group}$) 2.70 (t, J = 7.0 Hz, −S−CH_2−CH_2−O−), 2.53 (t, J = 7.3 Hz, −S−CH_2−CH_2−CH_2−), 2.09−1.99 (m, −CH_2−CH=CH−), 1.90−1.80 (m, −O−CH_2−CH_2−CH_2−O−), 1.64−1.53 (m, −S−CH_2−CH_2−CH_2−), 1.53−1.43 (m, −CH_2−CH_2−CH=CH_2 $_{end\ group}$), 1.43−1.33 (m, −CH_2−).

^{13}C NMR (75 MHz, $CDCl_3$, δ in ppm): 134.45 (−CH=CH−CH_2−O−$_{cis\ isomer}$), 134.24 (−CH=CH−CH_2−O−$_{trans\ isomer}$), 126.77 (−CH=CH−CH_2−O−$_{trans\ isomer}$), 126.44 (−CH=CH−CH_2−O−$_{cis\ isomer}$), 71.76 (−CH=CH−CH_2−O−$_{trans\ isomer}$), 71.19 (−S−CH_2−CH_2−O−CH_2−CH_2−O−CH_2−CH_2−S−), 70.43 (−S−CH_2−CH_2−O−CH_2−CH_2−O−CH_2−CH_2−S−), 67.34 (−O−CH_2−CH_2−CH_2−O−), 32.68 (−S−CH_2−CH_2−O−CH_2−CH_2−O−CH_2−CH_2−S−), 32.28(−S−CH_2−CH_2−CH_2−), 31.28 (−CH_2−CH=CH−), 30.32 (−O−CH_2−CH_2−CH_2−O−), 29.79 (−S−CH_2−CH_2−CH_2−), 28.84 (−S−CH_2−CH_2−CH_2−), 28.56 (−CH_2−CH_2−CH=CH−).

RESULTS AND DISCUSSION

Recently, research in industry and academia is particularly focused on applying benign reaction conditions and using precursors based on renewable feedstocks. In this sense, the 100% atom-efficient Pd-catalyzed telomerization of readily available and cheap 1,3-butadiene with renewable 1,3-propanediol is an elegant way to synthesize the herein studied monomers with minimum environmental impact.[21] It must be pointed out that 1,3-propanediol can be obtained directly either from corn or any plant oil as a renewable raw material,[22] and thus the telomerization process can, in principle, be integrated in a 100% biomass-based synthesis platform as long as butadiene is obtained from renewable sources, for instance from bioethanol.[23] With the application as surfactant precursor in mind, previous studies were aimed at optimizing conditions for formation of the monotelomer of 1,3-propanediol.[20] However, as the ditelomer product was required for our polymerization studies, telomerization conditions were adapted by using a larger excess of butadiene (1,3-butadiene:1,3-propanediol molar ratio of 6:1) and a longer reaction time at 80 °C under solvent-free conditions.

dx.doi.org/10.1021/ma2026572 | Macromolecules 2012, 45, 1866−1878

Using the Pd/TOMPP complex as telomerization catalyst, the ditelomers were obtained with full conversion of the diol substrate and a yield of 92%. The structures of the 1,3-propanediol-based ditelomers were confirmed by the means of ^{1}H NMR and ^{13}C NMR with a 95% (*E*)-configuration of the double bond in the hydrophobic chains. Telomerization products are almost inevitably obtained as a mixture of the linear (1-addition product) and branched (3-addition) octadienes. Controlling the linear to branched ratio (l/b; the linear product is often preferred) remains a challenge. It is known that higher phosphine to palladium ratios result in increased stability of the catalyst, but also in lower l/b ratios. As full conversion to the ditelomer, but also a l/b ratio that is as high as possible is required for the present application, a balance needs to be struck in the P/Pd ratio.[2] Thus, in order to achieve a selective synthesis of the linear (versus branched, designated as l/b ratio) ditelomer, the ratio of phosphine to metal was varied from 4:1, 8:1 to 16:1. The final diethers consisted of different linear/branched ratios as shown in Figure 1. As expected, a slight decrease (from 93% to 91%) was observed when the relative amount of phosphine was increased to 16 equiv.

ADMET Polymerizations. The efficacy of the telomers (**1**, **2**, and **3**) as monomers was evaluated using two polymerization methods. The first route focuses on the reactivity of the ditelomers in the presence of metathesis catalysts. As mentioned in the Introduction, it is well-known that, in addition to the construction of many complex and important low molecular weight molecules, the metathesis reaction has enabled the synthesis of diverse polymers.[24] So far, concerning the transformation of the hydrophobic chain of different monotelomers [such as (*E*)-1-phenoxy-2,7-octadiene or the (peracetylated)-octadienyl ether of xylose], the activity of several Ru-based Grubbs first and second generation catalysts, as well as Re- and W-based complexes, has been investigated.[25] In those cases where Ru-based catalysts were used, compounds corresponding to a metathesis involving internal double bonds were observed. However, up to date olefin metathesis has not been applied to ditelomers. As the ditelomers can be considered α,ω-dienes, they would be suitable monomers for acyclic diene metathesis (ADMET) polymerization. Nevertheless, ditelomers also possess internal double bonds and thus cannot be considered traditional α,ω-dienes, but participation of the internal olefins in ADMET would nonetheless still lead to polymer formation. Therefore, the ADMET reactions of monomers **1**, **2**, and **3** were investigated (Figure 1). The readily available Ru-based metathesis catalysts should be more suitable for these ditelomers, given their functional group tolerance.[13] In order to study the scope and limitations of the ADMET polymerization, extensive optimization studies involving changes of catalyst, temperature and substrate (the effect of l/b ratio) were carried out. Since ADMET polymerization is ideally performed in bulk monomer to maximize monomer concentration and favor formation of polymer,[26] the reactions were performed under solvent-free conditions. Moreover, ADMET chemistry relies on ethylene removal, which drives the reaction in this step-growth polymerization.[13] Therefore, unless otherwise specified, a continuous gas flow (argon or nitrogen) was applied throughout the reactions, which were run for 4 h. Furthermore, all results presented stem from at least two individual reactions. Monitoring of these reactions by GPC and NMR provided the necessary insights to fully understand the polymerization behavior of these new monomers. The primary screening of the ADMET reaction of telomers **1**, **2**, and **3** was focused on the effects of catalyst loading and temperature on the conversion to the desired polymer. The crucial point in this study was to retain the internal double bonds of the monomers unreacted. Ru–benzylidene metathesis catalysts are known to have better activities at mild temperatures.[27] Furthermore, low reaction temperatures reduce the extent of the possible isomerization during ADMET. Thus, the efficiency of some classical metathesis catalysts such as Grubbs first (**C1**) and second (**C2**) generations were initially compared at 40 °C with monomer **1**, which possesses the highest l/b ratio (Table 1 and Table 2). When 0.2 mol % **C1**, one of the most widely studied metathesis catalysts, in relation to the ditelomer was used (Table 1, entry **1**), **1** was recovered along with 30% dimeric product. Since further gradual increasing of the catalyst loading up to 2.0 mol % (entries 2–6) did not significantly change this result, a catalyst loading of 0.4 mol % **C1** was chosen for exploring the effect of the temperature on **C1**. Although it has been reported that **C1** does hardly show any side reactions up to a polymerization temperature of 90 °C,[28] temperatures higher than 70 °C were not applied here, because of catalyst decomposition in the current system.[29] Therefore, in attempts to favor higher conversions, the reaction temperature was varied from 50 until 70 °C. However, the higher reaction temperature was found not to have a considerable effect on the polymerization reaction, as evidenced by GPC (Table 1, compare entries 7–9). Moreover, also longer reaction times did not result in higher molecular weights, leading us to conclude that **C1**, at least under the applied bulk conditions, is unsuitable for the polymerization of these telomers.

The catalyst screening showed that **C2** (0.4 mol %) was more effective at low temperature, with better consumption of **1** (entries 1, 3 and 4, Table 2). However, also this catalyst did not afford high molecular weight polymers. Efforts to increase the molecular weight by increasing the catalyst amount from 0.4 to 2.0 mol % at 40 °C showed similar trends as in the case of **C1**.

Hoveyda–Grubbs second generation catalyst (**C3**) possesses metathesis efficiency similar to Grubbs second generation catalyst (**C2**), but with different substrate specificity. It was already reported that **C3** was employed successfully in many ADMET reactions.[13] Under the initial conditions (i.e., at 40 °C and 0.4 mol % of catalyst) only 50% of oligomer formation with 35% monomer recovery was observed together with 15% undefined low molecular weight product formation (GPC data). Thus, high catalyst loadings were used to improve the yield of high molecular weight products. Reactions of **1** with loadings of 0.4, 0.8, 1.0, and 2.0 mol % of **C3** gave low-molecular-weight oligomers with conversions increasing with the catalyst loading (up to 80% at 2.0 mol % of **C3**). Encouraged by this result, the ADMET reaction of **1** in the presence of 1.0 mol % of **C3** was performed at 80 °C, a typical polymerization temperature for ADMET reactions. The results of this experiment indicated high activity of **C3** after 4 h at 80 °C. However, even at 90% conversion, appreciably high molecular weights were not achieved. On the other hand, unidentified low molecular weight products were observed at higher retention times by GPC. The use of 2.0 mol % **C3** resulted in lower conversion of **1** with high amount of undefined small product formation (detected by GPC). A switch to another metathesis catalyst with chelating alkylidene ligand, **C4** (Figure 1b), gave similar results at 80 °C with loadings of 1.0 mol % as with **C3** (cf. entries 8 and 12 in Table 2).

After these studies, it became apparent that the reason for the inability to achieve a higher degree of polymerization could be the *in situ* isomerization of the double bonds during metathesis.[30] Previous studies showed that, depending on the nature of the reacting olefinic partners, the reaction conditions, as well as the nature of the catalyst, double bond isomerization reactions may occur.[31] Double bond isomerization occurs as result of ruthenium hydride formation, which can be suppressed by the addition of hydride scavengers, e.g., 1,4-benzoquinone (**BQ**).[30] Thus, catalysts **C2**, **C3**, and **C4** were examined with the same set of experiments in the presence of **BQ.** Rather unexpectedly, the inclusion of **BQ** did not show efficient isomerization inhibition at 40 °C for **C2**; in contrast, a drop of the molecular weight was detected, as observed by GPC (Table 2, entries 1 and 2). On the other hand, at 80 °C with a loading of 1.0 mol % **C3** and 8.0 mol % **BQ**, an increase of the molecular weight up to 4900 Da was observed (entry 10, Table 2). To investigate whether the **BQ** addition would favor an increase in molecular weight through longer reaction times, reactions 10 and 13 in Table 2 were reproduced and run for 48 h with initial argon flow for 4 h (entries 15 and 16, respectively). The GPC data of the reactions showed the catalysts to be still active even after 24 h in the presence of **BQ** with the molecular weight values clearly increasing.

Since the kinetics during ADMET are dictated by the removal of ethylene, a possible reason why ADMET mainly produced low molecular weight polymers, even in the presence of the isomerization inhibitor, could be inefficient ethylene removal. Therefore, an efficient ethylene removal by applying vacuum, instead of inert gas flow, was investigated. Indeed, when ADMET was performed under vacuum for 4 h in case for **C3** (entry 11, Table 2), the efficiency was substantially improved. For catalyst **C4**, the effect of applied vacuum was more pronounced (compare entries 13 and 14, Table 2), showing higher monomer conversions (monitored via NMR and GPC). Moreover, running the reactions detailed in entries 11 and 13 of Table 2 overnight (after applying vacuum for 4 h) resulted in highly viscous, sticky materials that were soluble in chloroform.

Monomer **1** is a mixture of linear and branched telomers with an l/b ratio of 93/7. Since the branched monomers possess 3 or 4 terminal double bonds, they act as branching points leading to the formation of hyperbranched structures. In order to get a more accurate picture of both the mechanism and the scope and limits of the reaction, the other two monomers **2** and **3**, which possess lower l/b ratios, were reacted under the optimized conditions: 1.0 mol % **C3** (or **C4**) at 80 °C under vacuum for 4 h. The results presented in Table 3 show a clear tendency for both catalysts (**C3** and **C4**): the molecular weights increase with the branching ratio of the monomers, which supports the polymerizations to highly branched systems and is due to the presence of a higher amount of more reactive terminal double bonds. Furthermore, the same set of experiments was performed for 24 h, with continuous vacuum for the first 4 h. The results of this set are also in line with the formation of hyperbranched structures. Furthermore, in the case of monomers **2** and **3**, the higher content of branched telomers led to gelation caused by cross-linking. Once cross-linked, the characterization of these materials (entries 3 and 4 in Table 3) was troublesome as they were no longer soluble in any common solvents such as THF, $CHCl_3$, DMSO, and DMF.

Presumably, in the reactions performed with constant flow of argon, the failure in directing the reaction of monomer **1** toward high molecular weight was due to other interfering intra- and intermolecular metathesis reactions. The intramolecular metathesis of a α,ω-diene could yield ethylene and an unsaturated carbocycle (or heterocycle) via ring-closing metathesis (RCM), whereas the intermolecular reaction would result in the release of ethylene with oligomer or polymer formation via ADMET. The GPC traces for almost all products in Table 1 and Table 2 were multimodal, with several distinct peaks in the low molecular weight range, suggesting that low molecular weight cyclic products were formed along with linear chains. Thus, to gain more evidence whether the RCM was occurring, control experiments under dilute solvent conditions (dichloromethane as solvent) with two different catalyst amounts (0.4 and 5.0 mol % **C2** or **C3** per **1**) were performed. Surprisingly, even under the dilute solvent conditions, oligomer formation as well as RCM took place in the first 30 min of the reactions (under continuous gas flow). To better understand the polymerization mechanism of monomer **1** ^{1}H NMR analysis was performed at different reaction times with additional 2D-NMR, ^{1}H,^{1}H−COSY, and heteronuclear multiple-quantum correlation (HMQC) experiments to confirm the structures drawn in Figure 2. The NMR analysis of both control experiments and ADMET polymerizations at different reaction times clearly showed that RCM of the terminal and internal double bonds did take place (with release of cyclopentene, see Figure 2), yielding a mixture of products (RCM products and new monomer structure suitable for further ADMET). Cyclopentene and 1,6-heptadiene were collected from the ADMET reaction as distillate. Along with these compounds, a ring-opening metathesis compound (dimer) was observed in the distillate as determined by ^{1}H NMR and GC−MS. The isolated mixture of cyclopentene and 1,6-heptadiene amounted to 1/5th of the total reaction mixture. The rate and the yield of RCM reaction depended on the reaction conditions, e.g., whether argon flow or vacuum was applied; under vacuum, the RCM was observed only in the first 5 min of the reaction. However, with a continuous gas flow, the RCM occurred for approximately 45 min. The formation of the ring-closing product between the terminal and internal double bond was evidenced by ^{1}H NMR, which showed a decrease of the terminal double bond proton resonances at 5.81 (5, in Figure 2a) and 4.97 ppm (4) and the appearance of new terminal double bond protons at 5.91 (1) and 5.20 ppm (2) belonging to the allylic ether. Furthermore, it was observed that the products from step a in Figure 2 subsequently reacted via ADMET, either with themselves or with unreacted monomers, thus giving a mixture of products as shown in Figure 2b. These metathesis reactions led to polymer formation (as observed by GPC); however, ^{1}H NMR analysis of the products also revealed that further double bond isomerization took place (Figure 3). The vinyl ether signals observed (hydrogens 1, 2, 3, and 4 in Figure 3), which have similar intensities as the signals belonging to the internal olefins formed by direct ADMET, illustrate this. The isomerization of the allylic (ether) double bonds to the vinyl position gave a 1:1 mixture of *trans* (1 and 2 in Figure 3) and *cis* (3 and 4) isomers. While this can be considered a nondisturbing side reaction in most polymerizations, the isomerization of allyl ethers to vinyl ethers has to be considered as it can lead to slow catalyst deactivation (ethyl vinyl ether[32] is the typical reagent used to quench metathesis reactions catalyzed with ruthenium alkylidenes). Moreover, a small amount of terminal double bond isomerization was also observed (Figure 3). Along with the aforementioned points, in ADMET polymerization the

dx.doi.org/10.1021/ma2026572 | *Macromolecules* 2012, 45, 1866−1878

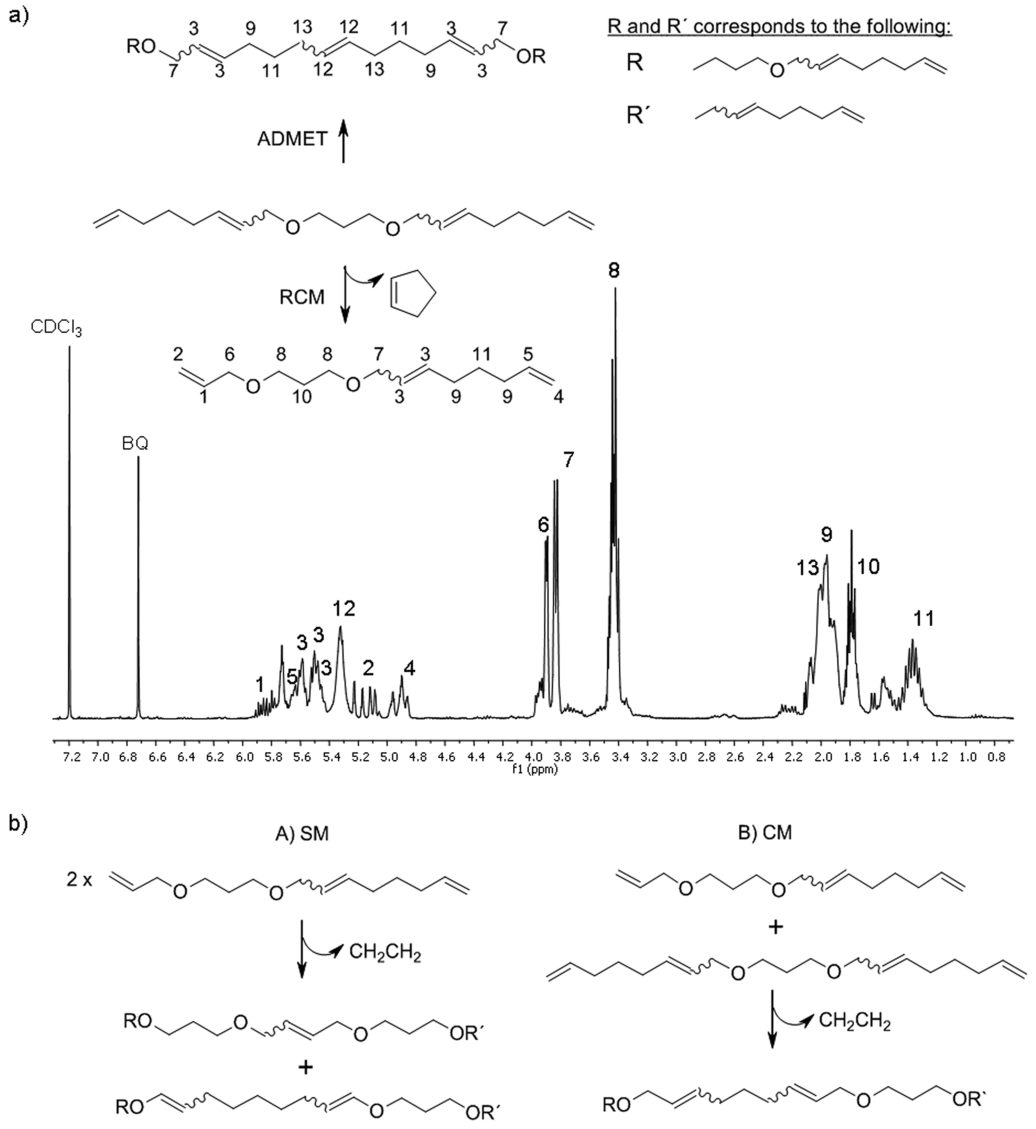

Figure 2. Study of the polymerization mechanism by means of NMR analysis: (a) initial reactions observed (first 30 min of ADMET reaction) (entry 11, Table 1); (b) subsequent reactions of RCM product.

polymerizability of a monomer can be limited by the number of methylene spacers between the olefin and the ether oxygen.[33] Thus, it could be that, to some extent, also the so-called "negative neighbouring group effect" is a reason for the somewhat poor polymerization results. Moreover, in some cases, self- and cross-metathesis reactivity was observed for monomers with only one methylene spacer present.[34] Finally, oligomerization of diallylic ethers has been reported before.[35] All this contributes to the observed rather poor polymerizability of the ditelomers via ADMET.

In summary, although it is possible to react the monomers with low catalyst loadings and relatively low temperatures via metathesis, the presence of branched telomers in the monomer mixture caused cross-linking at high monomer conversions. Moreover, ADMET was not sufficiently regioselective, allowing RCM events to take place. In addition, olefin isomerization events led to vinyl ether moieties within the polymer backbones.

Thiol–Ene Polymerizations. Thiols have a strong tendency to react with terminal double bonds in radical-initiated reactions. Therefore, in order to establish an alternative polymerization pathway for monomers **1**, **2** and **3**, the transformation of the ditelomers was also investigated in the presence of thiols as comonomers.

Initially, the model compound 1-octanethiol was reacted with telomer **1** under radical-initiated (model reaction A) or thermally induced (model reaction B) conditions using a molar ratio of 4:1 (thiol:**1**). Although low temperatures are generally favorable for thiol–ene additions, elevated reaction temperatures are required to avoid high viscosity or crystallization during polymerization. Furthermore, it was shown that in dithiol/diene mixtures, which are free of oxygen, radicals can also form spontaneously under initiator-free conditions.[19] Therefore, the model reaction was carried out at 70 °C without initiator. Although Hawker and colleagues showed that thiol–ene coupling reactions do not strictly require deoxygenation[36] when performed under solvent-free conditions, both model reactions were nonetheless kept under vacuum (200 mbar) for 5 min prior to exposing to heat and/or addition of initiator in order to remove oxygen, which is an efficient radical scavenger in these types of reactions.[35] The dithioether generated from the reaction performed in the presence of the radical initiator (**AIBN**) was the expected anti-Markovnikov diaddition product

dx.doi.org/10.1021/ma2026572 | *Macromolecules* 2012, 45, 1866–1878

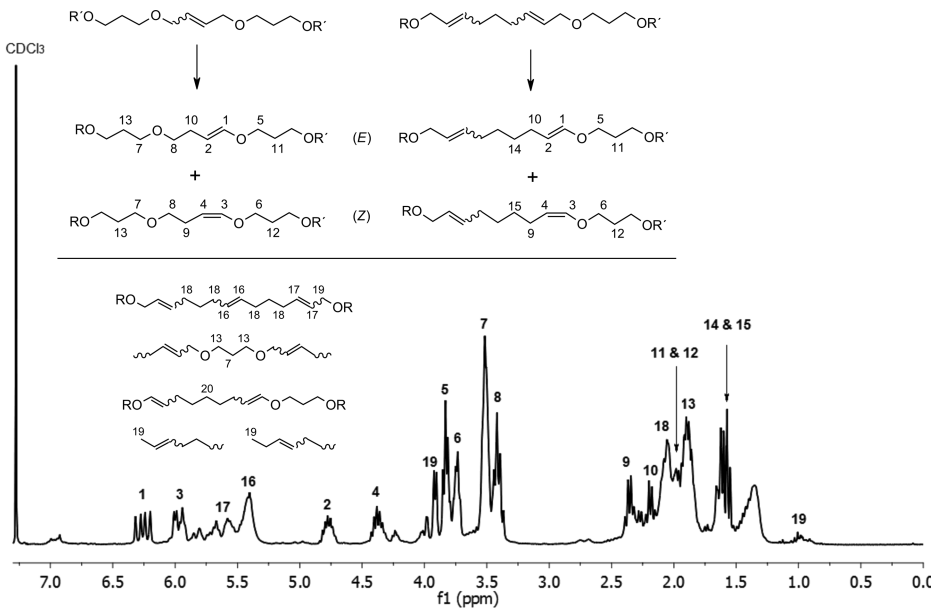

Figure 3. NMR spectra of a sample of the crude reaction mixture of entry 11, Table 1, taken after 2 h, showing the isomerization occurring during the ADMET reaction.

(Figure 4). As illustrated by the disappearance of the protons associated with the terminal double bonds (5.78 and 4.96 ppm) and homoallylic (1.46 ppm) signals, and the appearance of proton signals corresponding to the thioether product (methylenes in α- (2.52 ppm) and β-position (1.60 ppm) to the sulfur atom, the conversion was found to be essentially quantitative after 1 h at 75 °C (for complete description of the NMR data see the Experimental Section). Interestingly, the ^{1}H NMR spectra displayed also new significant signals at δ_H 6.20 (d, J = 12.6 Hz, 1H$_{trans}$), 5.91 (dd, J = 6.2, 1.3 Hz, 1H$_{cis}$), 4.81–4.68 (m, 1H$_{trans}$) and 4.37–4.25 (m, 1H$_{cis}$) due to a migration of the internal allyl ether double bonds to the vinylic position (*cis* and *trans* isomers were observed), along with a corresponding decrease of the integral value of the internal double bond signal (Figure 4). The thermally induced reaction without added initiator, on the other hand, resulted in a lower yield (90%) (model reaction B) after a significantly longer reaction time (20 h) at 70 °C. However, in this case, the aforementioned internal double bond migration occurred to a much lesser extent; just 3% internal allyl ether double bond migration was detected in contrast to 27% migration in case of model reaction A (compare results in Figure 4). While the extent of olefin migration may not be substantial under standard thiol–ene addition conditions, its occurrence is of considerable fundamental importance, since it involves hydrogen atom transfer between thiyl and allylic species.[37]

Thiols are efficient hydrogen donors, and since C–H bonds are stronger than S–H bonds [bond dissociation energy (BDE) = 91 kcal/mol],[38] thiyl radicals are usually regarded as unreactive with respect to hydrogen abstraction. Hydrogen atom transfer reactions are usually very sensitive to enthalpic polar effects, however. It was indeed reported that thiyl radicals can abstract hydrogen atoms from thermodynamically favorable allylic systems[36] in water/alcohol mixtures as well as from other C–H activated compounds.[39] Since an allylic C–H bond is unusually weak (BDE = 82 kcal/mol),[37] the free radical abstraction of such hydrogens is easier than for nonallylic hydrogens. The migration of the double bond could thus be explained by the mechanism proposed in Figure 5. This involves a favorable allylic hydrogen abstraction, followed by trapping of either the intermediate allylic radical or the more stable additional resonance form (step b in Figure 5) by a thiol to regenerate the initial structure or to form the internal vinyl ether (in the latter case). It should be noted that the hydrogen atom transfer between the electron-rich C–H bond in the ditelomer and the electrophilic thiyl radical is favored, if there is an appropriate polarity match between radical and the alkene (step a in Figure 5).[40] The same assumption could be applied for step c (Figure 5), where the hydrogen atom is transferred from the electrophilic thiol, acting here as a hydrogen atom donor, to the nucleophilic carbon-centered radical.

The model study thus shows that the use of radical initiator shortens the reaction time and results in double bond migration. This migration, leads to a vinyl ether function displaying a different reactivity that might be further exploited in another context.

Encouraged by the successful model study, and in order to demonstrate the feasibility of ditelomers in thiol–ene polymerizations, three different dithiols were investigated: 1,4-butanedithiol (**DT1**), 2-mercaptoethyl ether (**DT2**), and 3,6-dioxa-1,8-octanedithiol (**DT3**), under comparable conditions, in the absence or presence of radical initiator. Compared to the model reactions, the synthesis of polymers could present a number of additional challenges regarding efficiency. Although the internal double bonds of the ditelomers showed quite low reactivity at 70 °C during the model studies, the polymerizations were conducted at three different temperatures in order to obtain more detailed information about the effect of the temperature on the reactivity of the internal double bonds. Monomer **1**, possessing the highest l/b ratio (Figure 1a), was used in the initial optimization studies. The polymerizations were followed by GPC and NMR. The reactions were run until a viscosity increase was qualitatively observed, and then quenched by cooling to room temperature and diluted with an excess of THF to avoid cross-linking. All of the major impurities, including excess reactant and the initiator residue, were easily removed by repeated precipitation, and no chromatography was required.

dx.doi.org/10.1021/ma2026572 | *Macromolecules* 2012, 45, 1866–1878

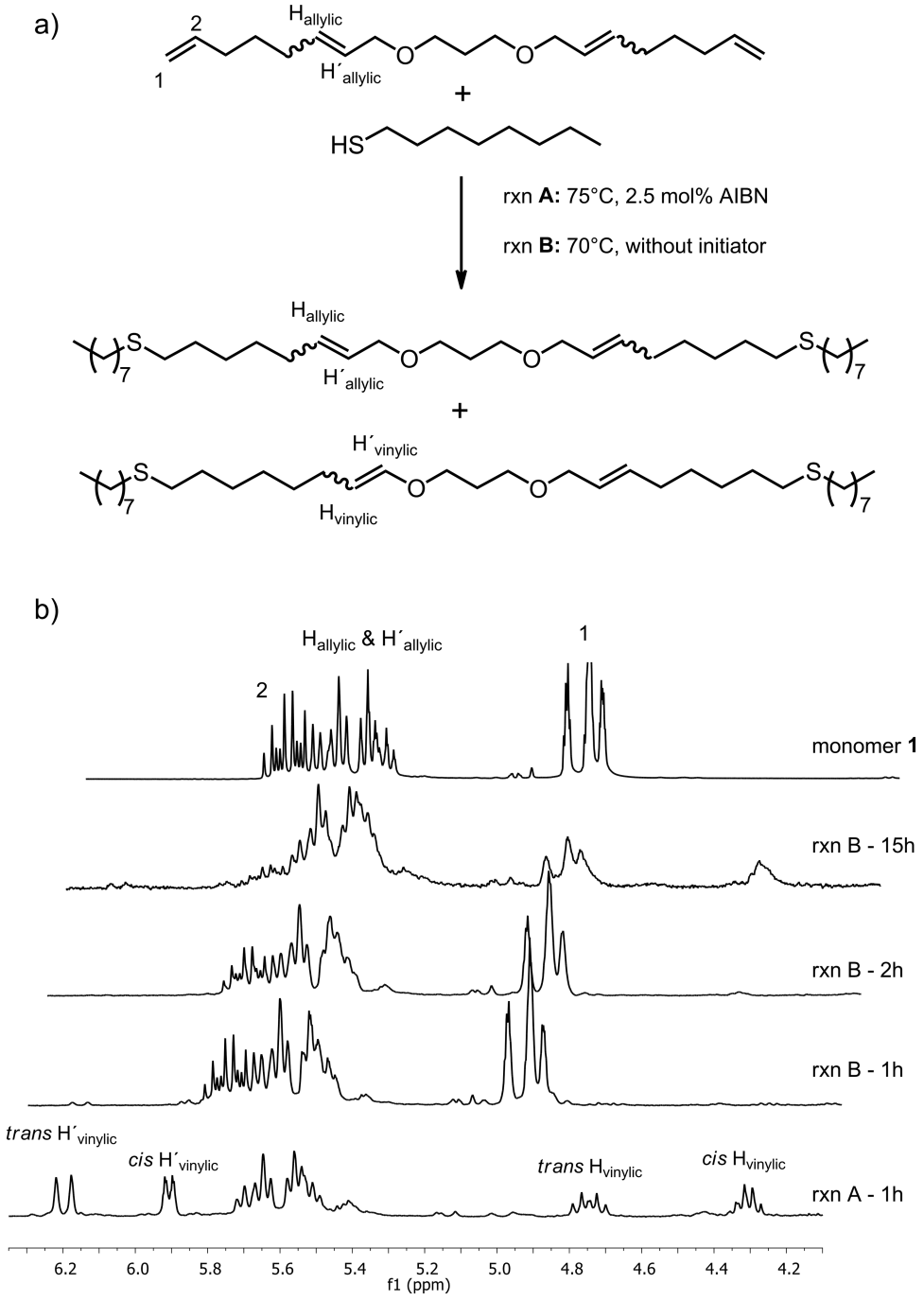

Figure 4. (a) Schematic representation of the model reactions mimicking the products from thiol−ene polymerization. (b) ^{1}H NMR spectra ($CDCl_3$; 300 MHz) comparison of the model thiol−ene reactions A and B with the corresponding monomer: ditelomer **A** (black line, crude reaction mixture of model reaction A, 1 h, with AIBN; blue line, crude reaction mixture of model reaction B, 1 h, without AIBN; light gray line, model reaction B, 2 h; dark gray line, model reaction B, 15 h; red line, monomer: ditelomer **A**).

Monomer **1** was polymerized at 35, 50, and 70 °C with **DT1**, first without the initiator AIBN. The GPC analysis showed that, even after 72 h at 35 °C, the thiol−ene reaction did not occur as efficiently as expected, and only low-molecular-weight oligomers (molecular weight <3000 Da) were formed (Table 4, entry 1). Generally, the results confirmed the internal double bonds to be less reactive than the terminal ones, which is known from literature and is a result of the reversibility of the C−S bond formation.[41] The NMR data of the reaction run at 50 °C (entry 2, Table 4) revealed characteristic peaks attributed to the formation of thioether bonds as well as the repeat units of thiol monomer and signals from the telomer backbone, which indicated that the reaction occurred. Moreover, the data shows that the internal double bonds remain almost unreacted. When the reaction was performed at 70 °C (Table 4, entry 3), a successful polyaddition was observed; however, prolonging the reaction times (more than 24 h) resulted in gelation. As with the model reactions described above, in the experiments performed at 50 and 70 °C, the internal double bond migration from the allylic to vinylic position was again observed.

To explore the influence of the dithiol structure on the reactivity of **1**, **DT2** was selected as it contains an ether group

dx.doi.org/10.1021/ma2026572 | *Macromolecules* 2012, 45, 1866−1878

and thus resembles more the structure of the 1,3-propanediol ditelomers. The reactions were conducted in analogy to those with **DT1**. Online GPC monitoring of the reactions revealed that the conversion of the ditelomer and of the dithiol were better in comparison to **DT1** (Figure 6a).

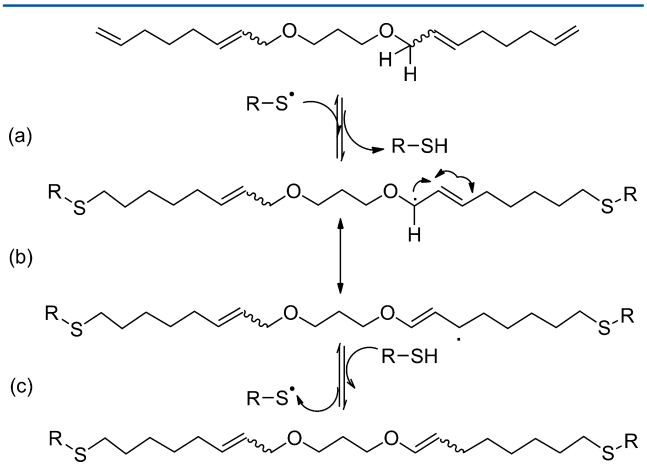

Figure 5. Thiyl radical-mediated olefin migration.

The ^{1}H NMR spectra of entries 4, 5, and 6 (Table 4) showed little variation (Figure 6b). As a common feature, the internal double bonds did not react, as calculated by comparison of the integrals of the characteristic multiplet centered at ~5.53 ppm (^{1}H of the internal double bond), and the triplet at ~3.50 ppm (4H from the 1,3-propanediol core of monomer **A**, which should not vary throughout the reaction). On the other hand, the integral value of the terminal double bond peak at ~4.95 ppm decreased, confirming the successful thiol–ene coupling. The conversion of the terminal double bonds could be calculated from the characteristic multiplet centered at 4.95 ppm and the triplet at 3.50 ppm. The product obtained at 50 °C showed 75% conversion of terminal double bonds, while the products obtained at 35 and 70 °C showed 84 and 82% conversion, respectively. The polymerization at 35 °C gave the highest conversion of terminal double bonds, but it also resulted in an unsymmetrical molecular weight distribution with high PDI (compare Figure 6). On the other hand, the polymerization at 70 °C gave a higher terminal double bond conversion than at 50 °C, but since the increase both in terminal double bond conversion and in molecular weight (GPC) was small, 50 °C was taken as temperature for further optimization of the reaction conditions. In the initial experiments, the dithiol

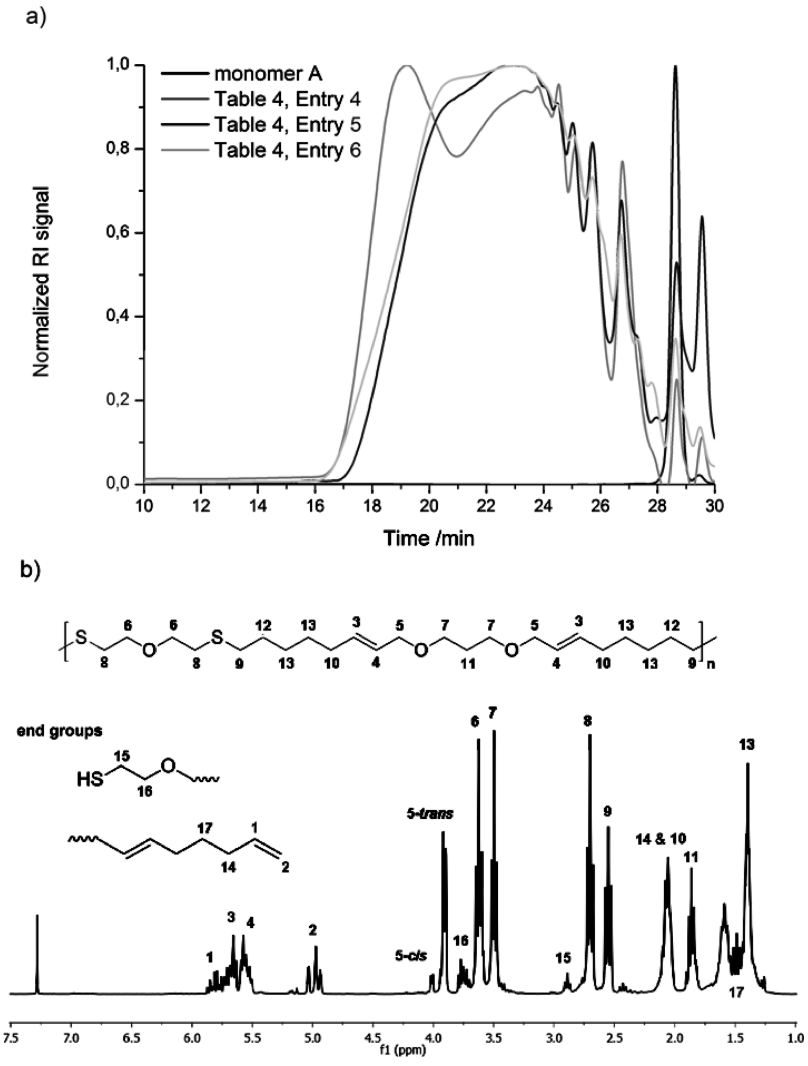

Figure 6. (a) Crude GPC chromatograms and (b) representative NMR data of the thiol–ene reaction product of **DT2** at three different temperatures (35, 50, and 70 °C). (The GPC data was obtained from SEC system with method A.)

dx.doi.org/10.1021/ma2026572 | *Macromolecules* 2012, 45, 1866–1878

amount used was calculated considering the ditelomer samples as pure linear ditelomers. To account for the small percentage of branched ditelomers present (Figure 1a), the effect of varying the ditelomer/dithiol ratio, from 1:1 to 0.95:1 and to 1:0.95, on the polymerizations at 50 °C was studied. Since the branched telomers contain extra terminal double bonds that can more easily react with the dithiols, an increase in the thiol ratio should favor branching reactions and thus should lead to higher molecular weights and higher PDIs (entry 11, Table 4). This was confirmed by the GPC traces of **DT1** (Table 4, entries 2, 8 and 9) and **DT2** (Table 4, entries 5, 10 and 11). The GPC analysis of the samples from the reaction of **1** with slight excess of thiol **DT2** (0.95:1) indeed showed an increase of molecular weight compared to the 1:1 reaction (75% conversion), which was in accordance with the observed 82% conversion of terminal double bonds (determined by ^{1}H NMR); however, ^{1}H NMR analysis also revealed 8% conversion of the internal olefins. Excess of ditelomer (1:0.95) resulted in a drop in conversion of the terminal double bonds to 70%, again in accordance with the lower M_w observed by GPC. These results demonstrate that variation in the temperature did not have a pronounced effect on the reactivity of the internal olefins, but a small excess of dithiol did have a considerable effect on the molecular weights.

Next, **DT3**, was tested in the thiol−ene polymerization of the ditelomers. The third dithiol **DT3** tested, was expected to have a positive effect on the polymerization results in terms of improved compatibility (miscibility) between both monomers (1:1 ratio at 50 °C, Table 4, entry 7). The GPC data of the 24 h crude reaction mixture revealed 92% monomer conversion to the polymer. The higher double bond conversion (80% by ^{1}H NMR) obtained at short reaction time further confirmed the improved polymerization compared to **DT1** and **DT2**.

Since the thermally induced thiol−ene polymerization reactions needed long polymerization times (at least 48 h), AIBN was applied as radical initiator (2.5 mol % to ditelomer molecule) to reduce the reaction time. The AIBN-initiated polymerizations were completed in 1 h (reaction mixture was not stirring anymore) with conversions of 95% for entry 14, Table 4 (by GPC). As with the previously obtained products, the polymers were completely soluble, although dissolution took time (around 6 h for the polymer with the highest molecular weight). The difference in solubility was attributable to the molecular weight difference. Since the high concentrations of radicals present in the reaction mixture increases the probability of side reactions, also lower AIBN loadings were tested for monomer **1**. From NMR and GPC analysis, it became clear that an initiator loading of 1.0 mol % already results in 95% conversion (by GPC, no carbons corresponding to the end groups detected in ^{13}C NMR). Almost no double bond migration is observed by ^{1}H NMR, thus more well-defined polymers were synthesized (Table 4, entry 15). In the same fashion, additional experiments were performed with monomer **2** and **3** in order to study the effect of the l/b ratio on the polymerizations performed in the presence of AIBN. Indeed, the higher the branching ratio, the higher the molecular weight and also the less well-defined structures with broad PDI values were obtained.

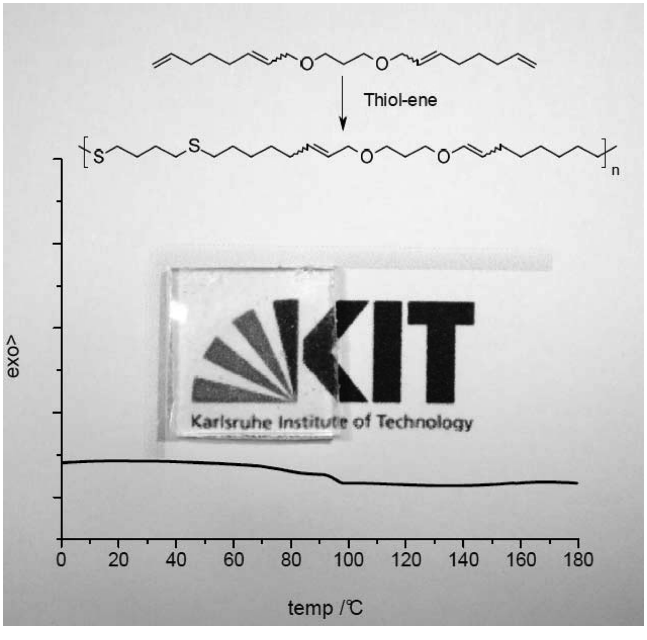

Figure 7. DSC chromatogram for the polysulfide of entry 2 from Table 4.

Both the thermally and radical-induced thiol−ene reactions were initially affected by difficulties in reaching the quantitative conversions targeted for polymer synthesis. However, variation of the ditelomer to dithiol ratio and the type of dithiol, led to optimized reaction conditions allowing for the formation of high molecular weight products. Very interestingly, the three dithiols yielded thermoplastic polysulfides of different structures, which could be shaped as transparent and colorless films by casting THF solutions (graphical abstract and Figure 7). To ascertain the thermal properties of the obtained thiol−ene polymers, DSC analysis was performed. The majority of the samples, even when subjected to different heating rates during DSC analysis, did not show any thermal transition in the studied temperature range (from −75 to +250 °C). However, a small T_g at 99 °C (at 20 °C/min) was observed for the polysulfide from entry 2, Table 4, suggesting that the rest of polysulfides possibly have T_gs in the same range, but are not detectable by DSC (Figure 7). It should be noted that the ditelomers monomers have no detectable glass or melting transitions in the studied temperature range and that the investigated polymer (entry 2, Table 4) can be reshaped by redissolution and solvent casting for several times, suggesting that it is not cross-linked. From the TGA analysis performed on the same polymer, it could be seen that the polymers display acceptable thermal stability under nitrogen. Under the given experimental conditions 5% mass loss of the polymer was detected at 306 °C.

CONCLUSION

The potential of ditelomers obtained from 1,3-propanediol as monomers for the synthesis of polymers via ADMET and thiol−ene polymerizations has been assessed. Regarding the ADMET pathway, it was shown that the products obtained were different depending on the method used to remove the released ethylene. When a flow of argon was used, mostly ring-closing metathesis products were obtained together with oligomers. On the other hand, when vacuum was applied, low molecular weight polymers were obtained in a ring-closing metathesis−ADMET−olefin isomerization sequence. The thiol−ene polyaddition with different dithiols led to higher molecular weights than the ADMET polymerization. The polymerizations in the presence of a radical initiator (AIBN) were considerably faster than the thermally initiated ones. In both cases, isomerization of the allyl ether to vinyl ether was observed, in a more prominent fashion in the presence of AIBN. The high molecular weight polymers obtained via the thiol−ene route behaved as shapeable and completely transparent thermoplastics.

dx.doi.org/10.1021/ma2026572 | *Macromolecules* 2012, 45, 1866−1878

AUTHOR INFORMATION

Corresponding Author

*E-mail: m.a.r.meier@kit.edu.

Notes

The authors declare no competing financial interest.

ACKNOWLEDGMENTS

H.M. would like to thank to Dr. Lucas Montero de Espinosa for the fruitful NMR discussions. P.C.A.B., A.N.P. and B.M.W. would like to thank ASPECT-ACTS for financial support. Peter J. C. Hausoul is thanked for his assistance with the synthesis of the telomer monomers.

REFERENCES

(1) (a) Meier, M. A. R.; Metzger, J. O.; Schubert, U. S. *Chem. Soc. Rev.* **2007**, *36*, 1788−1802. (b) Biermann, U.; Bornscheuer, U.; Meier, M. A. R.; Metzger, J. O.; Schäfer, H. J. *Angew. Chem., Int. Ed.* **2011**, *50*, 3854−3871. (c) Gandini, A. *Macromolecules* **2008**, *41*, 9491−9504. (d) Montero de Espinosa, L.; Meier, M. A. R. *Eur. Polym. J.* **2011**, *47*, 837−852. (e) Ronda, J. C.; Lligadas, G.; Galià, M.; Cádiz, V. *Eur. J. Lipid Sci. Tech.* **2011**, *113*, 46−58.

(2) Behr, A.; Becker, M.; Beckmann, T.; Johnen, L.; Leschinski, J.; Reyer, S. *Angew. Chem., Int. Ed.* **2009**, *48*, 3598−3614 and references cited therein.

(3) Smutny, E. J. *J. Am. Chem. Soc.* **1967**, *89*, 6793−6794.

(4) (a) Jackstell, R.; Harkal, S.; Jiao, H.; Spannenberg, B.; Rottger, D.; Nierlich, F.; Elliot, M.; Niven, S.; Cavell, K.; Navarro, O.; Viciu, M.; Nolan, S.; Beller, M. *Chem.—Eur. J.* **2004**, *10*, 3891−3900. (b) Tschan, M. J.-L.; Garcia−Suarez, E. J.; Freixa, Z.; Launay, H.; Hagen, H.; Benet-Buchholz, J.; van Leeuwen, P. W. N. M. *J. Am. Chem. Soc.* **2010**, *132*, 6463−6473.

(5) Lee, B. I.; Lee, K. H.; Lee, S. *J. Mol Catal. A: Chem.* **2000**, *156*, 283−287.

(6) (a) Behr, A.; Johnen, L.; Vorholt, A. J. *ChemCatChem* **2010**, *2*, 1271−1277. (b) Grotevendt, A.; Bartolome, M.; Spannenberg, A.; Nielsen, D. J.; Jackstell, R.; Cavell, K. J.; Oro, L. A.; Beller, M. *Tetrahedron Lett.* **2007**, *48*, 9203−9207. (c) Prinz, T.; Driessen-Hölscher, B. *Chem.—Eur. J.* **1999**, *5*, 2069−2076.

(7) (a) Desvergnes-Breuil, V.; Pinel, C.; Gallezot, P. *Green Chem.* **2001**, *3*, 175−177. (b) Estrine, B.; Bouquillon, S.; Henin, F.; Muzart, J. *Appl. Organomet. Chem.* **2007**, *21*, 945−946.

(8) (a) Behr, A.; Urschey, M. *Adv. Synth. Catal.* **2003**, *345*, 1242−1246. (b) Palkovits, R.; Nieddu, I.; Klein Gebbink, R. J. M.; Weckhuysen, B. M. *ChemSusChem* **2008**, *1*, 193−196. (c) Grotevendt, A.; Jackstell, R.; Michalik, D.; Gomez, M.; Beller, M. *ChemSusChem* **2009**, *2*, 63−70.

(9) Mesnager, J.; Quettier, C.; Lambin, A.; Rataboul, F.; Perrard, A.; Pinel, C. *Green Chem.* **2010**, *12*, 475−482.

(10) Behr, A.; Bahke, P.; Klinger, B.; Becker, M. *J. Mol Catal. A: Chem* **2007**, *267*, 149−156.

(11) (a) Rodriguez, A.; Normen, M.; Spur, B. W.; Godfroid, J.-J.; Lee, T. H. *Eur. J. Org. Chem.* **2000**, 2991−3000. (b) Tsuji, J.; Kobayashi, Y.; Takahasi, T. *Tetrahedron Lett.* **1980**, *21*, 483−486. (c) Tsuji, J.; Shimizu, I.; Suzuki, H.; Naito, Y. *J. Am. Chem. Soc.* **1979**, *101*, 5070−5072. (d) Tsuji, J.; Yasuda, H.; Mandai, T. *J. Org. Chem.* **1978**, *43*, 3606−3607. (e) Tsuji, J.; Mandai, T. *Tetrahedron Lett.* **1978**, *19*, 1817−1820. (f) Tsuji, J.; Mizutani, K.; Shimizu, I.; Yamamoto, K. *Chem. Lett.* **1976**, 773−774.

(12) (a) von Rybinski, W.; Hill, K. *Angew. Chem.* **1998**, *110*, 1394−1412; *Angew. Chem., Int. Ed.* **1998**, *37*, 1328−1345;(b) Gruber, B.; Weese, K. J.; Hoagland, S. M.; Mueller, H. P.; Hill, K.; Behr, A. (Henkel) DE 4242467, 1992. (c) Gruber, B.; Weese, K. J.; Hoagland, S. M.; Mueller, H. P.; Hill, K.; Behr, A. (Henkel) WO 1990, 13531, 1990; *Chem. Abstr.* **1991**, *115*, 137003.

(13) Fernandes, M.; Kaminsky, W. *Macromol. Chem. Phys.* **2009**, *210*, 585−593.

(14) (a) Mutlu, H.; Montero de Espinosa, L.; Meier, M. A. R. *Chem. Soc. Rev.* **2011**, *40*, 1404−1445 and references cited therein. (b) Opper, K. L.; Wagener, K. B. *J. Polym. Sci., Part A: Polym. Chem.* **2011**, *49*, 821−831 and references cited therein.

(15) Hoyle, C. E.; Bowman, C. N. *Angew. Chem., Int. Ed.* **2010**, *49*, 1540−1573.

(16) (a) Jonkheijm, P.; Weinrich, D.; Koehn, M.; Engelkamp, H.; Christianen, P. C. M.; Kuhlmann, J.; Maan, J. C.; Nuesse, D.; Schroeder, H.; Wacker, R.; Breinbauer, R.; Niemeyer, C. M.; Waldmann, H. *Angew. Chem., Int. Ed.* **2008**, *47*, 4421−4424. (b) Chen, G. J.; Amajjahe, S.; Stenzel, M. H. *Chem. Commun.* **2009**, 1198−1200. (c) ten Brummelhuis, N.; Diehl, C.; Schlaad, H. *Macromolecules* **2008**, *41*, 9946−9947. (d) Campos, L. M.; Meinel, I.; Guino, R. G.; Schierhorn, M.; Gupta, N.; Stucky, G. D.; Hawker, C. J. *Adv. Mater.* **2008**, *20*, 3728. (e) Goldmann, A. S.; Walther, A.; Nebhani, L.; Joso, R.; Ernst, D.; Loos, K.; Barner-Kowollik, C.; Barner, L.; Muller, A. H. E. *Macromolecules* **2009**, *42*, 3707−3714. (f) Sagar., K.; Gopalakrishnan, N.; Christiansen, M. B.; Kristensen, A.; Ndoni, S. *J. Micromech. Microeng.* **2011**, *21*, DOI: 10.1088/0960-1317/21/9/095001.

(17) Posner, T. *Chem. Ber.* **1905**, *38*, 646−657.

(18) (a) Kharasch, M. S.; Mayo, F. R. *Chem. Ind.* **1938**, *57*, 752. (b) Marvel, C. S.; Chambers, R. R. *J. Am. Chem. Soc.* **1948**, *70*, 993−998. (c) Marvel, C. S.; Caesar, P. D. *J. Am. Chem. Soc.* **1951**, *73*, 1097−1099. (d) The Chemistry of the Thiol Group; Patai, S., Ed.; Wiley: New York, 1974. (e) Jacobine, A. F. In *Radiation Curing in Polymer Science and Technology III*; Fouassier, J. P., Rabek, J. F., Eds.; Elsevier: London, 1993; Chapter 7, pp 219−268.

(19) Dondoni, A. *Angew. Chem., Int. Ed.* **2008**, *47*, 8995−8997. (b) Hoyle, C. E.; Lee, T. Y.; Roper, T. *J.Polym. Sci. Pol. Chem.* **2004**, *42*, 5301−5338.

(20) (a) Klemm, E.; Sensfuss, S. *J. Macromol. Sci.—Chem.* **1991**, *28*, 875−883. (b) Koyama, E.; Sanda, F.; Endo, T. *Macromolecules* **1998**, *31*, 1495−1500. (c) Shin, J.; Matsushima, H.; Chan, J. W.; Hoyle, C. E. *Macromolecules* **2009**, *42*, 3294−3301. (d) Acosta, R.; Garcia, A. E.; Martinez, M. G.; Berlanga, M. L. *Carbohydr. Polym.* **2009**, *78*, 282−286. (e) Lluch, C.; Ronda, J. C.; Galià, M.; Lligadas, G.; Cádiz, V. *Biomacromolecules* **2010**, *11*, 1646−1653. (f) Türünç, O.; Montero de Espinosa, L.; Meier, M. A. R. *Macromol. Rapid Commun.* **2011**, *32*, 1357−1361.

(21) (a) Palkovits, R.; Parvulescu, A. N.; Hausoul, P. J. C.; Kruithof, C. A.; Klein Gebbink, R. J. M.; Weckhuysen, B. M. *Green Chem.* **2009**, *11*, 1155−1160. (b) Hausoul, P. J. C.; Bruijnincx, P. C. A.; Klein Gebbink, R. J. M.; Weckhuysen, B. M. *ChemSusChem* **2009**, *2*, 855−858. (c) Palkovits, R.; Nieddu, I.; Kruithof, C. A.; Klein Gebbink, R. J. M.; Weckhuysen, B. M. *Chem.—Eur. J.* **2008**, *14*, 8995−9005. (d) Hausoul, P. J. C.; Parvulescu, A. N.; Lutz, M.; Spek, A. L.; Bruijnincx, P. C. A.; Klein Gebbink, R. J. M.; Weckhuysen, B. M. *Angew. Chem., Int. Ed.* **2010**, *49*, 7972−7975.

(22) Kraus, G. A. *CLEAN—Soil, Air, Water* **2008**, *36*, 648−651 and references therein.

(23) Korstanje, T. J.; Jastrzebski, J. T. B. H.; Klein Gebbink, R. J. M. *ChemSusChem* **2010**, *3*, 695−697.

(24) (a) Chauvin, Y. *Angew. Chem., Int. Ed.* **2006**, *45*, 3741−3747. (b) Schrock, R. R. *Angew. Chem., Int. Ed.* **2006**, *45*, 3748−3759. (c) Grubbs, R. H. *Angew. Chem., Int. Ed.* **2006**, *45*, 3760−3765. (d) Hoveyda, A. H.; Zhugralin, A. R. *Nature* **2007**, *450*, 243−251. (e) Casey, C. P. *J. Chem. Educ.* **2006**, *83*, 192−195.

(25) (a) Damez, C.; Bouquillon, S.; Hénin, F.; Muzart, J. *Eur. J. Org. Chem.* **2006**, *20*, 4565−4567. (b) Bouquillon, S. *C. R. Chim.* **2011**, *14*, 716−725.

(26) Watson, M. D.; Wagener, K. B. *Macromolecules* **2000**, *33*, 8963−8970.

(27) Vougioukalakis, G. C.; Grubbs, R. H. *Chem. Rev.* **2010**, *110*, 1746−1787.

(28) (a) Fokou, P. A.; Meier, M. A. R. *J. Am. Chem. Soc.* **2009**, *131*, 1664−1665. (b) Fokou, P. A.; Meier, M. A. R. *Macromol. Rapid Commun.* **2010**, *31*, 368−373.

(29) Ulman, M.; Grubbs, R. H. *J. Org. Chem.* **1999**, *64*, 7202−7207.

(30) (a) Michaut, A.; Rodriguez, J. *Angew. Chem., Int. Ed.* **2006**, *45*, 5740−5750. (b) Tori, M.; Mizutani, R. *Molecules* **2010**, *15*, 4242−4260. (c) Maynard, H. D.; Grubbs, R. H. *Tetrahedron Lett.* **1999**, *40*, 4137−4140. (d) Lehman, S. E.; Schwendeman, J. E.; O'Donnell, P. M.; Wagener, K. B. *Inorg. Chim. Acta* **2003**, *345*, 190−198. (e) Schmidt, B. *Eur. J. Org. Chem.* **2004**, 1865−1880.
(31) Hong, S. H.; Sanders, D. P.; Lee, C. W.; Grubbs, R. H. *J. Am. Chem. Soc.* **2005**, *127*, 17160−17161.
(32) Sanford, M. S.; Ulman, M.; Grubbs, R. H. *J. Am. Chem. Soc.* **2001**, *123*, 749−750.
(33) (a) Patton, J. T.; Boncella, J. M.; Wagener, K. B. *Macromolecules* **1992**, *25*, 3862−3867. (b) Wagener, K. B.; Brzezinska, K.; Anderson, J. D.; Younkin, T. R.; Steppe, K.; DeBoer, W. *Macromolecules* **1997**, *30*, 7363−7369.
(34) Lin, Y. A.; Chalker, J. M.; Davis, B. G. *J. Am. Chem. Soc.* **2010**, *132*, 16805−16811.
(35) Brzezinska, K.; Wolfe, P. S.; Watson, M. D.; Wagener., K. B. *Macromol. Chem. Phys.* **1996**, *197*, 2065−2074.
(36) (a) Killops, K. L.; Campos, L. M.; Hawker, C. J. *J. Am. Chem. Soc.* **2008**, *130*, 5062. (b) Heidecke, C. D.; Lindhorst, T. K. *Chem.−Eur. J.* **2007**, *13*, 9056−9067.
(37) (a) Lunazzi, L.; Placucci, G.; Grossi, L. *J. Chem. Soc., Chem. Commun.* **1979**, *12*, 533−534. (b) Schoeneich, C.; Asmus, K.-D.; Dillinger, U.; Bruchhausen, F. *Biochem. Biophys. Res. Commun.* **1989**, *161*, 113−120.
(38) McMillen, D. F.; Golden, D. M. *Annu. Rev. Phys. Chem.* **1982**, *33*, 493−532 and references cited therein.
(39) (a) Zhao, R.; Lind, J.; Merenyi, G.; Eriksen, T. E. *J. Am. Chem. Soc.* **1994**, *116*, 12010−12015. (b) Robins, M. J.; Ewing, G. J. *J. Am. Chem. Soc.* **1999**, *121*, 5823−5824. (c) Nauser, T.; Schoneich, C. *J. Am. Chem. Soc.* **2003**, *125*, 2042−2043.
(40) Roberts, B. P. *Chem. Soc. Rev.* **1999**, *28*, 25.
(41) Roper, T. M.; Guymon, C. A.; Jönsson, E. S.; Hoyle, C. E. *J. Polym. Sci., Part A: Polym. Chem.* **2004**, *42*, 6283−6298.

Macromolecules

Article

pubs.acs.org/Macromolecules

Fluorescent, Thermoresponsive Oligo(ethylene glycol) Methacrylate/9-(4-Vinylbenzyl)-9*H*-carbazole Copolymers Designed with Multiple LCSTs via Nitroxide Mediated Controlled Radical Polymerization

Benoît H. Lessard, Edwin Jee Yang Ling, and Milan Marić*

Department of Chemical Engineering, McGill Institute of Adv. Mater. (MIAM), Centre for Self-Assembled Chemical Structures (CSACS), McGill University, 3610 University Street, Montréal, Québec, Canada H3A 2B2

Supporting Information

ABSTRACT: 9-(4-Vinylbenzyl)-9*H*-carbazole (VBK) was used as the "controlling" comonomer for nitroxide mediated polymerization with 10 mol % SG1 free nitroxide relative to BlocBuilder initiator at 80 °C of oligo(ethylene glycol) methyl ether methacrylate (8−9 ethylene glycol (EG) units) ($OEGMA_{8-9}$), 2-(2-methoxyethoxy)ethyl methacrylate (MEO_2MA) and for an $OEGMA_{8-9}$/MEO_2MA-mixed feed. The synthesis of MEO_2MA/VBK and $OEGMA_{8-9}$/VBK copolymers and MEO_2MA/$OEGMA_{8-9}$/VBK terpolymers exhibited linear increases in number-average molecular weight ($\bar{M}_n$) versus conversion X, up until X = 0.6, with final copolymers characterized by relatively narrow, monomodal molecular weight distributions ($\bar{M}_w/\bar{M}_n$ < 1.4, in most cases). A series of MEO_2MA/$OEGMA_{8-9}$/VBK terpolymers were synthesized and by varying the $OEGMA_{8-9}$:MEO_2MA feed ratios, the terpolymers exhibited tunable lower critical solution temperatures in water (28 °C < LCSTs < 81 °C). MEO_2MA/$OEGMA_{8-9}$/VBK terpolymers were deemed sufficiently pseudo-"living" to reinitiate a second batch of MEO_2MA/$OEGMA_{8-9}$/VBK, with few apparent dead chains, as indicated by the monomodal shift in the GPC chromatograms. The resulting MEO_2MA/$OEGMA_{8-9}$/VBK block copolymers were designed so that each block exhibited a distinct LCST, which was confirmed by UV−vis and dynamic light scattering. In addition to controlling the terpolymerization, the VBK units imparted thermo-responsive fluorescence into the final copolymers.

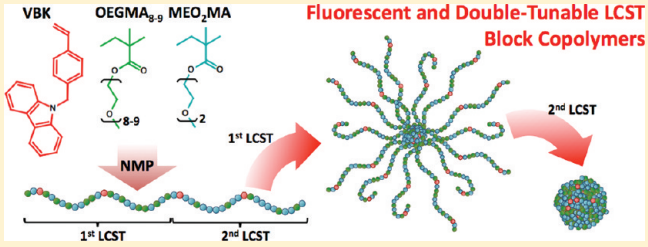

INTRODUCTION

Thermo-responsive polymers undergo a sharp physical change as a response to a small change in temperature. Thermo-responsive polymers have found application in polymer drug delivery vehicles,[1,2] biochemical sensors,[3−7] environmentally friendly photoresists,[8] intracellular uptake micelles,[9] and controlled-bacterial aggregation materials.[10] Thermo-responsive polymers can exhibit a lower critical solution temperature (LCST) in aqueous solution, meaning they are free-flowing water-soluble chains at lower temperatures but agglomerate or precipitate out of solution above a certain temperature (i.e., the LCST). For example, poly(*N*-isopropylacrylamide) (poly(NIPAAm))[11−14] and poly(2-(dimethylamino)ethyl methacrylate) (poly(DMAEMA))[15−17] exhibit LCSTs of 32 and 46 °C, respectively. The tuning of the polymer's LCST is highly attractive to impart more versatility and functionality into the polymer. For example, hydrophobic[18] or hydrophilic[15,19] comonomers are often incorporated into the final copolymer by statistical copolymerization to modify the LCST. Other methods of modifying LCST behavior involve using more complex microstructures such as block copolymers or star polymers. For example, Li et al. synthesized a poly(styrene)-poly(DMAEMA)−poly(NIPAAm) star block copolymer which micellized in water and exhibited two discernible thermo-induced micellar collapses.[20] Kotsuchibashi et al. synthesized poly(NIPAAm)-*block*-poly(NIPAAm-*co*-*N*-(isobutoxymethyl)-acrylamide) block copolymers, which underwent an initial transition from water-soluble polymers to micelles and a second transition from micelles to large aggregates when heated in an aqueous solution.[21] In these cases, the materials exhibited multiple, distinct LCSTs corresponding to the respective segments.[20,21] Several other examples of thermo-responsive block copolymers with two distinct phase transitions have been reported in the literature.[22−28]

Recently, Lutz and co-workers synthesized a series of thermo-responsive copolymers based on oligo(ethylene glycol) methyl ether methacrylates with 8−9 ethylene glycol (EG) units ($OEGMA_{8-9}$) and 2-(2-methoxyethoxy)ethyl methacrylate with 2 EG units (MEO_2MA, Scheme 1).[29,30] The authors showed that by changing the ratio of $OEGMA_{8-9}$:MEO_2MA, a sharp and tunable LCST in water between 26 and 90 °C was attainable.[29,31,32] However, to obtain such well-defined LCSTs, the control of the molecular weight and copolymer composition was imperative. Lutz and co-workers used atom transfer radical polymerization (ATRP), a controlled radical polymerization (CRP) method, to synthesize $OEGMA_{8-9}$/

Received: December 6, 2011
Revised: January 28, 2012
Published: February 10, 2012

dx.doi.org/10.1021/ma202648k | *Macromolecules* 2012, 45, 1879−1891

Scheme 1. Terpolymerization of 2-(2-Methoxyethoxy)ethyl Methacrylate (MEO_2MA), Oligo(ethylene glycol) Methyl Ether Methacrylate ($OEGMA_{8\text{-}9}$) and 9-(4-Vinylbenzyl)-9*H*-carbazole (VBK) by Nitroxide-Mediated polymerization Using BlocBuilder, Followed by a Subsequent Chain Extension of the Final Thermo-Responsive Terpolymer with a Fresh Batch of VBK, MEO_2MA, and $OEGMA_{8\text{-}9}$ (with a Different MEO_2MA:$OEGMA_{8\text{-}9}$ Compared to the First Block), Resulting in a Block Copolymer That Exhibits Dual Lower Critical Solution Temperatures (LCST) in Water

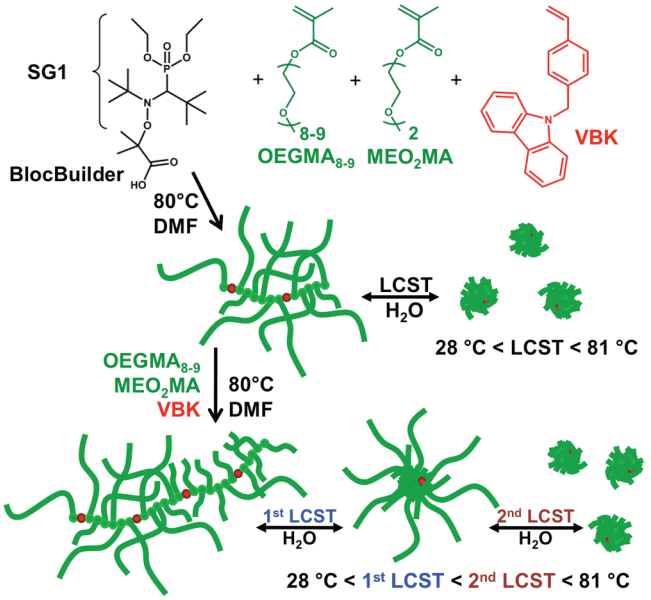

MEO_2MA copolymers to impart this composition control.[29,30] Other CRP techniques, such as reversible addition−fragmentation chain transfer (RAFT) polymerization, have also effectively controlled the molecular weight distribution and the composition of OEGMA-based copolymers.[33−36] However, the use of ATRP and RAFT can be problematic in some cases due to the presence of metallic species or thiol groups in the product, which could be detrimental in the desired application. An alternative CRP method termed nitroxide mediated controlled radical polymerization (NMP)[37,38] is a robust controlled polymerization technique that often only requires a single initiating species. Like ATRP, NMP features a reversible termination between dormant and active chains to control the radical species concentration, which in turn permits control of the molecular weight distribution and microstructure. In contrast to ATRP or RAFT, no additional purification of the final polymer is necessary prior to being used for sensitive electronic or biological applications.[37−39]

Traditionally, the major drawback of NMP was that it could only polymerize styrenics in a controlled manner. However, the development of second-generation initiating systems based on 2,2,5-trimethyl-4-phenyl-3-azahexane-3-nitroxide (TIPNO)[40] and [*tert*-butyl[1-(diethoxyphosphoryl)-2,2-dimethylpropyl]-amino]oxidanyl (SG1, Scheme 1)[41] have permitted the homopolymerization of various monomers such as acrylates[42−45] and acrylamides[18,37] which were previously unattainable by first-generation initiating systems such as 2,2,6,6-tetramethylpiperidinyloxyl (TEMPO). However, the homopolymerization of methacrylates by NMP was still elusive. Methacrylates have a high equilibrium constant between dormant and active chains, which result in the generation of a large number of free radicals in the initial stages of the polymerization. These radicals undergo irreversible termination characterized by a plateau of the number-average molecular weight ($\bar{M}_n$) versus conversion (X).[46] The use of additional nitroxide, to quench the excess of free radicals, results in a significant increase in β-hydrogen transfer from the propagating poly(methacrylate) chain to the SG1 nitroxide, also resulting in irreversible termination.[47] However, Charleux and co-workers discovered that the use of a small amount of a "controlling" comonomer, characterized by a lower K, can be used to decrease the average equilibrium constant ($\langle K \rangle$) and control the copolymerization of the methacrylate.[46,48,49] Originally the comonomer of choice was styrene, requiring 4.4−8.8 mol % relative to methyl methacrylate (MMA) to control the copolymerization.[46] The use of styrene has been successfully used to control many methacrylates such as ethyl methacrylate,[50] glycidyl methacrylate,[51] *tert*-butyl methacrylate,[52] benzyl methacrylate,[53] methacrylic acid,[54] and oligo(ethylene glycol) methyl ether methacrylates (4−5 EG units).[55,56] While the low incorporation of styrene into the copolymer may not significantly affect the mechanical properties of the methacrylate-rich copolymer,[50] its incorporation can hinder other properties such as cell cytotoxicity[39] or water-solubility.[57] Therefore, the use of other "controlling" comonomers such as acrylonitrile (AN)[39,58,59] and 4-styrenesulfonate[57] have been introduced to eliminate such problems that arise with the use of styrene and broaden the scope of comonomer applicability. Recently, our group has introduced the use of 9-(4-vinylbenzyl)-9*H*-carbazole (VBK) as a "controlling" comonomer for MMA.[60] Not only did the copolymerization require as little as 1 mol % of VBK to control the copolymerization effectively, the pendant carbazole group on the VBK introduced hole-transport properties into the final copolymer.[60] VBK has also been used to control the copolymerization of DMAEMA resulting in a thermo/pH responsive, fluorescent copolymer.[18]

Nicolas and co-workers have recently shown that the controlled copolymerization of oligo(ethylene glycol) methyl ether methacrylates (4−5 EG units) and acrylonitrile is possible by using an SG1-based alkoxyamine, 2-([*tert*-butyl[1-(diethoxyphosphoryl)-2,2-dimethylpropyl]amino]oxy)-2-methylpropionic acid unimolecular initiator (BlocBuilder) in an ethanol/water solution at 71−85 °C, resulting in polymers with low polydispersity that were water-soluble and biocompatible.[39] Schubert and co-workers synthesized $OEGMA_{8-9}$-based copolymers using pentafluorostyrene (PFS) as a "controlling" comonomer, resulting in final statistical copolymers with various PFS:$OEGMA_{8-9}$ ratios and relatively narrow molecular weight distributions ($\bar{M}_w/\bar{M}_n$ =1.22−1.73).[61] While considerable research in the field of thermo-responsive pendant EG based acrylates has been accomplished using NMP,[28,62] very little literature can be found concerning the polymerization of MEO_2MA, $OEGMA_{8-9}$ or a mixture of MEO_2MA with $OEGMA_{8-9}$ by NMP.[61]

In this study, VBK was used to copolymerize $OEGMA_{8-9}$ and MEO_2MA with varying amounts of VBK in the feed ($f_{VBK,0}$ = 0.01−0.20). The effect of feed composition on kinetics, polymerization control and final composition will be discussed. Second, a series of MEO_2MA/$OEGMA_{8-9}$/VBK terpolymers, with various MEO_2MA/$OEGMA_{8-9}$ ratios (while keeping the VBK content constant) were synthesized and their LCSTs in water were determined (Scheme 1). The effect of temperature on the terpolymer fluorescence was also investigated. Finally, characteristic terpolymers were used as macroinitiators to reinitiate a fresh batch of MEO_2MA/$OEGMA_{8-9}$/VBK ternary mixtures, resulting in a

dx.doi.org/10.1021/ma202648k | *Macromolecules* 2012, 45, 1879−1891

Table 1. Experimental Formulations for 2-(2-Methoxyethoxy)ethyl Methacryate (MEO_2MA)/9-(4-Vinylbenzyl)-9*H*-carbazole (VBK) and Oligo(ethylene glycol) Methyl Ether Methacrylates ($OEGMA_{8-9}$)/VBK Random Binary Copolymerizations Performed at 80°C in a 50 wt % *N*,*N*-Dimethylformamide (DMF) Solution

expt ID[a]	$[BB]_0$[b] (mol L^{-1})	$[SG1]_0$ (mol L^{-1})	$[VBK]_0$ (mol L^{-1})	$[MEO_2MA]_0$ (mol L^{-1})	$[OEGMA_{8-9}]_0$ (mol L^{-1})	$[DMF]_0$ (mol L^{-1})	$f_{VBK,0}$[c]
MEO_2MA/VBK-1	0.0115	0.0011	0.02	1.51	0	9.36	0.01
MEO_2MA/VBK-5	0.0121	0.0012	0.08	1.49	0	9.76	0.05
MEO_2MA/VBK-10	0.0121	0.0012	0.15	1.38	0	9.68	0.10
MEO_2MA/VBK-20	0.0074	0.0007	0.18	0.72	0	5.95	0.20
$OEGMA_{8-9}$/VBK-1	0.0124	0.0013	0.01	0	0.68	9.90	0.01
$OEGMA_{8-9}$/VBK-5	0.0122	0.0012	0.03	0	0.66	9.99	0.05
$OEGMA_{8-9}$/VBK-10	0.0123	0.0012	0.07	0	0.64	9.84	0.10
$OEGMA_{8-9}$/VBK-20	0.0123	0.0013	0.15	0	0.59	9.92	0.20

[a]Experimental identification (expt ID) for OEGMA with VBK and MEO_2MA with VBK copolymerizations are given by VBK/OEGMA -Y and VBK/MEO_2MA -Y, respectively, with VBK representing 9-(4-vinylbenzyl)-9*H*-carbazole, OEGMA representing oligo(ethylene glycol) methyl ether methacrylate, MEO_2MA representing 2-(2-methoxyethoxy)ethyl methacrylate, and *Y* representing the initial mol % of VBK in the feed. All copolymerizations were done in 50 wt % DMF solution with target average molecular weight of approximately 25 kg·mol $^{-1}$ while using an initial molar ratio of SG1 relative to BlocBuilder = $r = [SG1]_0/[BB]_0 = 0.1$. [b]$[BB]_0$ is initial concentration of BlocBuilder initiator. [c]$f_{VBK,0}$ is the initial molar fraction of VBK in the feed.

double thermo-responsive block copolymer (Scheme 1). These findings illustrate the versatility of NMP and its ability to synthesize potentially biocompatible, fluorescent block copolymers with tunable multi-LCSTs, which could find application in next-generation sensors or drug delivery vehicles.

EXPERIMENTAL SECTION

Materials. *N*,*N*-Dimethylformamide (DMF, >95%, certified ACS), ethyl ether (anhydrous, >95%, BHT stabilized/certified ACS) and tetrahydrofuran (THF, >99.5%, HPLC grade) were obtained from Fisher Scientific and used as received. Deuterated chloroform ($CDCl_3$, >99%), used for ^{1}H NMR spectroscopy, was obtained from Cambridge Isotopes Laboratory and also used as received. 2-(2-Methoxyethoxy)ethyl methacrylate, also known as di(ethylene glycol) methyl ether methacrylate (MEO_2MA, 188 g·mol^{-1}, 95%, 100 ppm hydroquinone monomethyl ether as inhibitor) and oligo(ethylene glycol) methyl ether methacrylate ($OEGMA_{8-9}$, average molecular weight $\bar{M}_n$ = 475 g·mol^{-1}, contained 100 ppm MEHQ as inhibitor and 300 ppm BHT as inhibitor) were obtained from Sigma-Aldrich and used as received. 9-(4-Vinylbenzyl)-9H-carbazole (VBK, >95%) was synthesized according to the literature.[63] 2-([*tert*-Butyl[1-(diethoxyphosphoryl)-2,2-dimethylpropyl]amino]oxy)-2-methylpropanoic acid (BlocBuilder-MA, 99%) and [*tert*-butyl[1-(diethoxyphosphoryl)-2,2-dimethylpropyl]amino]oxidanyl (SG1, >85%) were obtained from Arkema and used without further purification.

Random Copolymerization of 2-(2-Methoxyethoxy)ethyl Methacrylate with 9-(4-Vinylbenzyl)-9*H*-carbazole (MEO_2MA/VBK) and Oligo(ethylene glycol) Methyl Ether Methacrylate with 9-(4-Vinylbenzyl)-9*H*-carbazole ($OEGMA_{8-9}$/VBK). All MEO_2MA/VBK and $OEGMA_{8-9}$/VBK copolymerizations were performed in a 50 mL three-neck round-bottom glass reactor equipped with a condenser (cooled with a 50 vol % ethylene glycol to water mixture being circulated using a Neslab 740 chiller). The reactor temperature was modulated using a heating mantle connected to a temperature controller, which measured the temperature inside the reactor with a thermocouple located in the thermal well, also connected to the reactor. Once assembled, the reactor was filled with the reagents and a stir bar, prior to being placed on a magnetic stir plate. All copolymerizations were done in 50 wt % DMF solution with target number-average molecular weight of 25 kg·mol^{-1} at complete conversion and with varying amounts of VBK relative to MEO_2MA or $OEGMA_{8-9}$ (initial molar feed composition of VBK of $f_{VBK,0}$ = 0.01−0.20). All experimental formulations can be found in Table 1. As an example, the synthesis of MEO_2MA/VBK-5 is shown as an example. To the reactor was added VBK (0.46 g, 1.7 mmol), MEO_2MA (6.10 g, 32.4 mmol), BlocBuilder (0.10 g, 0.26 mmol), SG1 (0.008 g, 0.03 mmol) and DMF (15.5 g). The condenser and the third opening of the reactor were sealed using a rubber septum prior to inserting a needle and bubbling the mixture for 30 min with ultra pure nitrogen. The reactor was then heated with a heating rate of 10 °C·min^{-1}, while maintaining a light nitrogen purge, until the temperature reached 80 °C. The "start" of the copolymerization, t = 0 min, was arbitrarily assigned as the time when the reactor temperature reached 80 °C. Samples were periodically drawn from the reactor by syringe and characterized by GPC and ^{1}H NMR spectroscopy without further purification. After cooling, the crude product was separated from the monomer by dialysis (membrane MWCO = 3500 g·mol^{-1}, Spectrum Laboratories) against water for a week. The recovered polymer was then dried in a vacuum oven at 60 °C to remove the residual solvent. For the specific example cited, the final copolymer was characterized by a yield of 2.49 g (conversion X = 0.49, determined by ^{1}H NMR spectroscopy) with number-average molecular weight, $\bar{M}_n$ = 12.1 kg·mol^{-1}, a polydispersity index of $\bar{M}_w/\bar{M}_n$= 1.34 (determined by gel permeation chromatography (GPC) using THF as an eluent at 40 °C and poly(styrene) standards) and a final molar VBK copolymer composition of F_{VBK} = 0.08 (determined by ^{1}H NMR spectroscopy).

Terpolymerization of 2-(2-Methoxyethoxy)ethyl Methacrylate (MEO_2MA), Oligo(ethylene glycol) Methyl Ether Methacrylate ($OEGMA_{8-9}$), and 9-(4-Vinylbenzyl)-9*H*-carbazole (VBK). All MEO_2MA/$OEGMA_{8-9}$/VBK terpolymerizations were performed in an identical setup as the MEO_2MA/VBK and $OEGMA_{8-9}$/VBK copolymerizations and by following the identical procedure as the copolymerizations. The terpolymerizations were done in 50 wt % DMF solution with target number-average molecular weights of 25−425 kg·mol^{-1} and all the corresponding formulations can be found in Table 2. For the terpolymerizations, the amount of VBK was kept constant ($f_{VBK,0}$ = 0.02), while the amounts of MEO_2MA relative to $OEGMA_{8-9}$ were varied for all terpolymerizations. As an example, the synthesis of OM40/60 was performed by adding VBK (0.10 g, 0.37 mmol), MEO_2MA (2.07 g, 11.0 mmol), $OEGMA_{8-9}$ (3.27 g, 7.27 mmol), BlocBuilder (0.034 g, 0.89 mmol), SG1 (0.003 g, 0.01 mmol), and DMF (8.50 g) to the reactor followed by nitrogen bubbling of 30 min. The mixture was then heated to 80 °C and samples were drawn periodically by syringe. The final product was separated from the unreacted monomer by osmosis (membrane MWCO = 3500 g·mol^{-1}, Spectrum Laboratories) against water for a week and dried in the vacuum oven at 60 °C to remove the residual solvent. For the specific example cited, the final copolymer was characterized by a yield, after transfer losses from the dialysis and recovery, of 1.48 g (X = 0.49) with $\bar{M}_n$ = 28.7 kg·mol^{-1}, $\bar{M}_w/\bar{M}_n$= 1.34 (determined by GPC using THF as an eluent and poly(styrene) standards), F_{VBK} < 0.01 and F_{MEO2MA} = 0.68 (final composition determined by ^{1}H NMR spectroscopy).

Chain Extension of 2-(2-Methoxyethoxy)ethyl Methacrylate, Oligo(ethylene glycol) Methyl Ether Methacrylate and 9-(4-Vinylbenzyl)-9*H*-carbazole (MEO_2MA/$OEGMA_{8-9}$/VBK) Terpolymers with a Fresh Batch of MEO_2MA/$OEGMA_{8-9}$/VBK. All

dx.doi.org/10.1021/ma202648k | *Macromolecules* 2012, 45, 1879−1891

Table 2. Experimental Formulation for Various Oligo(ethylene glycol) Methyl Ether Methacrylates/2-(2-Methoxyethoxy)ethyl Methacryate/9-(4-Vinylbenzyl)-9*H*-carbazole (OEGMA$_{8-9}$/MEO$_2$MA/VBK) Random Terpolymerizations and Chain Extensions Performed at 80°C in a 50 wt % *N,N*-Dimethylformamide (DMF) Solution

expt ID[a]	$[BB]_0$[b] (mmol L^{-1})	$[SG1]_0$ (mmol L^{-1})	$[VBK]_0$ (mol L^{-1})	$[MEO_2MA]_0$ (mol L^{-1})	$[OEGMA_{8-9}]_0$ (mol L^{-1})	$f_{VBK,0}/f_{MEO2MA,0}$[c]	$\bar{M}_{nTarget}$
OM5/95	15.62	1.69	0.037	1.85	0.10	0.02/0.94	25.7
OM10/90	12.92	1.30	0.037	1.66	0.17	0.02/0.89	30.7
OM20/80	9.50	0.93	0.031	1.23	0.30	0.02/0.79	39.2
OM30/70	7.94	0.83	0.029	1.02	0.42	0.02/0.69	49.0
OM40/60	6.28	0.63	0.026	0.79	0.52	0.02/0.59	61.9
OM50/50	4.66	0.57	0.024	0.59	0.59	0.02/0.49	82.0
OM60/40	3.45	0.38	0.022	0.44	0.65	0.02/0.40	110.6
OM70/30	2.58	0.29	0.002	0.32	0.74	0.02/0.30	153.0
OM80/20	1.66	0.21	0.020	0.19	0.80	0.02/0.19	242.0
OM90/10	0.85	0.10	0.019	0.09	0.84	0.02/0.10	472.5
expt ID[a]	$[Macro.]_0$ (mmol L^{-1})	$[VBK]_0$ (mol L^{-1})	$[MEO_2MA]_0$ (mol L^{-1})	$[OEGMA_{8-9}]_0$ (mol L^{-1})	$f_{VBK,0}/f_{MEO2MA,0}$[c]	$\bar{M}_{nTarget}$	
OM5/95-OM50/50	2.29	0.031	0.66	0.63	0.02/0.50	181.6	
OM10/90-OM50/50	0.79	0.026	0.66	0.63	0.02/0.50	522.5	
OM80/20-OM20/80	0.65	0.037	0.96	0.22	0.02/0.79	211.4	

[a]Experimental identification (expt ID) for OEGMA$_{8-9}$, MEO$_2$MA and VBK terpolymerizations are given by OM*X*/*Y*, with "O" representing oligo(ethylene glycol) methyl ether methacrylate, "D" representing 2-(2-methoxyethoxy)ethyl methacrylate and *X*/*Y* representing the respective, initial mol % of OEGMA$_{8-9}$:MEO$_2$MA in the feed. For the chain extensions, the expt ID is given by OMX/*Y*−OMZ/*W* where OM*X*/*Y* represents the expt ID of the macroinitiator used for the chain extension and for OMZ/*W*, the "O" represents oligo(ethylene glycol) methyl ether methacrylate, "M" representing 2-(2-methoxyethoxy)ethyl methacrylateand *Z*/*W* representing the approximate initial mol % of OEGMA$_{8-9}$:MEO$_2$MA in the feed, respectively. All polymerizations were done in 50 wt % DMF solution, in the case of the terpolymerizations the $[DMF]_0$ = 8.2 mol L^{-1} and in the case of the chain extensions $[DMF]_0$ = 13.0 mol L^{-1}. [b]$[BB]_0$ represents the initial concentration of BlocBuilder initiator. [c]$f_{VBK,0}$ and $f_{MEO2MA,0}$ are the respective initial molar fractions of VBK and MEO$_2$MA in the feed.

Table 3. Molecular Characterization for 2-(2-Methoxyethoxy)ethyl Methacryate (MEO$_2$MA)/9-(4-Vinylbenzyl)-9*H*-carbazole (VBK) and Oligo(ethylene glycol) Methyl Ether Methacrylates (OEGMA$_{8-9}$)/VBK Random Binary Copolymers Synthesized at 80°C in a 50 wt % *N,N*-Dimethylformamide (DMF) Solution

expt ID[a]	*X*[b]	t_{polym} (min)	$\bar{M}_n$[c] (kg/mol)	$\bar{M}_w/\bar{M}_n$[c]	F_{VBK}[d]	F_{MEO2MA}[d]	$F_{OEGMA8-9}$[d]	water-soluble[e]
MEO$_2$MA/VBK-1	0.48	216	14.7	1.64	<0.01	>0.99	0	no
MEO$_2$MA/VBK-5	0.49	313	12.1	1.34	0.08	0.92	0	no
MEO$_2$MA/VBK-10	0.42	355	9.6	1.24	0.16	0.84	0	no
MEO$_2$MA/VBK-20	0.21	424	7.1	1.19	0.36	0.64	0	no
OEGMA$_{8-9}$/VBK-1	0.50	189	12.6	1.28	<0.01	0	>0.99	yes
OEGMA$_{8-9}$/VBK-5	0.50	286	11.2	1.28	0.09	0	0.91	yes
OEGMA$_{8-9}$/VBK-10	0.27	386	8.3	1.19	0.27	0	0.73	no
OEGMA$_{8-9}$/VBK-20	0.23	368	5.0	1.11	0.27	0	0.73	no

[a]Experimental identification (Exp. ID) for OEGMA with VBK and MEO$_2$MA with VBK copolymerizations are given by VBK/OEGMA-*Y* and VBK/MEO$_2$MA-*Y*, respectively, with VBK representing 9-(4-vinylbenzyl)-9*H*-carbazole, OEGMA representing oligo(ethylene glycol) methyl ether methacrylate, MEO$_2$MA representing 2-(2-methoxyethoxy)ethyl methacrylate and *Y* representing the initial mol % of VBK in the feed. All copolymerizations were done in 50 wt % DMF solution with target average molecular weight of 25 kg·mol^{-1}. [b]Monomer conversion, as determined by ^{1}H NMR spectroscopy. [c]Number-average molecular weight ($\bar{M}_n$) and polydispersity index ($\bar{M}_w/\bar{M}_n$) were determined using gel permeation chromatography (GPC) run in THF at 35 °C and calibrated against poly(styrene) standards. [d]F_{VBK}, F_{MEO2MA}, and $F_{OEGMA8-9}$ are the final molar composition of VBK, MEO$_2$MA, and OEGMA$_{8-9}$ in the copolymer, as determined by ^{1}H NMR spectroscopy. [e]Water-solubility of the final polymer was checked in neutral pH solution at room temperature.

MEO$_2$MA/OEGMA$_{8-9}$/VBK chain extensions were performed in an identical setup and by following the identical procedure to the copolymerizations and terpolymerizations. Similar to the terpolymerizations, the amounts of MEO$_2$MA relative to OEGMA$_{8-9}$ were varied all while keeping the amount of VBK constant ($f_{VBK,0}$ = 0.02) for all chain extension polymers. However, the ratios of MEO$_2$MA:OEGMA$_{8-9}$ for each block were manipulated so as to attain a different LCST for each block. All the corresponding formulations can be found in Table 2. As an example, the synthesis of OM10/90-OM50/50 was performed by adding VBK (0.05 g, 0.16 mmol), MEO$_2$MA (0.85 g, 4.52 mmol), OEGMA$_{8-9}$ (2.05 g, 7.27 mmol), DMF (4.3 g) and the macroinitiator (OM10/90, 0.11 g, 0.006 mmol, $\bar{M}_n$ = 18.5 kg·mol^{-1} and $\bar{M}_w/\bar{M}_n$= 1.55, see Table 2 and Table 4 for full characterization data of the macroinitiator) to the reactor. The mixture was bubbled with nitrogen for 30 min prior to being heated to 80 °C. Thereafter, samples were drawn periodically by syringe and used for monitoring the chain growth. After cooling, the final samples were separated from the MEO$_2$MA/OEGMA$_{8-9}$ monomers by osmosis (membrane MWCO = 3500 g·mol^{-1}, Spectrum Laboratories) against water for 4 days followed by vacuum filtration to remove the unreacted VBK. OM10/90-OM50/50: yield of 0.1 g with $\bar{M}_n$ = 35.2 kg·mol^{-1}, $\bar{M}_w/\bar{M}_n$= 1.69 (determined by GPC using THF as an eluent and poly(styrene) standards), F_{VBK} = 0.04, F_{MEO2MA} = 0.91 and $F_{OEGMA8-9}$ = 0.05 (final composition determined by ^{1}H NMR spectroscopy). The low yield is a result of the transfer losses from the reactor to dialysis membrane and from the dialysis membrane to the final storage vial.

Characterization. The molecular weight distribution was measured using gel permeation chromatography (GPC, Water Breeze) with THF as the mobile phase, which was run at a flow rate of 0.3 mL min^{-1}. The GPC was equipped with a guard column and with 3 Waters Styragel HR columns (HR1 with molecular weight measurement range of 0.1 to 5 kg·mol^{-1}, HR2 with molecular weight measurement range of 0.5 to 20 kg·mol^{-1} and HR4 with molecular

Table 4. Experimentally Derived Kinetic Parameters for 2-(2-Methoxyethoxy)ethyl Methacryate (MEO_2MA)/9-(4-Vinylbenzyl)-9*H*-carbazole (VBK) and Oligo(ethylene glycol) Methyl Ether Methacrylates ($OEGMA_{8-9}$)/VBK Copolymerizations Done at 80°C in 50 wt % *N*,*N*-Dimethylformamide (DMF) Solutions

expt ID[a]	r[b]	$f_{VBK,0}$[c]	$\langle k_P \rangle [P^\bullet]$[c] ($s^{-1}$)	$\langle k_P \rangle \langle K \rangle$[c] ($s^{-1}$)
MEO_2MA/VBK-1	0.10	0.01	$(2.9 \pm 0.2) \times 10^{-5}$	$(2.8 \pm 0.2) \times 10^{-6}$
MEO_2MA/VBK-5	0.10	0.05	$(3.0 \pm 0.2) \times 10^{-5}$	$(3.1 \pm 0.2) \times 10^{-6}$
MEO_2MA/VBK-10	0.10	0.10	$(1.5 \pm 0.3) \times 10^{-5}$	$(1.6 \pm 0.3) \times 10^{-6}$
MEO_2MA/VBK-20	0.10	0.20	$(9.1 \pm 1.5) \times 10^{-6}$	$(9.1 \pm 1.5) \times 10^{-7}$
$OEGMA_{8-9}$/VBK-1	0.10	0.01	$(2.8 \pm 0.6) \times 10^{-5}$	$(2.9 \pm 0.7) \times 10^{-6}$
$OEGMA_{8-9}$/VBK-5	0.10	0.05	$(2.9 \pm 0.5) \times 10^{-5}$	$(2.8 \pm 0.5) \times 10^{-6}$
$OEGMA_{8-9}$/VBK-10	0.10	0.10	$(1.0 \pm 0.1) \times 10^{-5}$	$(1.0 \pm 0.1) \times 10^{-6}$
$OEGMA_{8-9}$/VBK-20	0.11	0.20	$(8.5 \pm 0.8) \times 10^{-6}$	$(9.1 \pm 0.8) \times 10^{-7}$

[a]Experimental identification (expt ID) for OEGMA with VBK and MEO_2MA with VBK copolymerizations are given by VBK/OEGMA-*Y* and VBK/MEO_2MA-*Y*, respectively, with VBK representing 9-(4-vinylbenzyl)-9*H*-carbazole, OEGMA representing oligo(ethylene glycol) methyl ether methacrylate, MEO_2MA representing 2-(2-methoxyethoxy)ethyl methacrylate and *Y* representing the initial mol % of VBK in the feed. All copolymerizations were done in 50 wt % DMF solution with target average molecular weight of 25 kg·mol $^{-1}$. [b]Initial molar ratio of SG1 free nitroxide to BlocBuilder alkoxyamine used in the copolymerization: $r = [SG1]_0/[BlocBuilder]_0$ [c]Product of the average propagation rate constant, $\langle k_P \rangle$, and the average equilibrium constant, $\langle K \rangle$. Error derived from standard error in slope of scaled conversion ($\ln(1 - X)^{-1}$) versus time plots.

weight measurement range 5 to 600 kg·mol^{-1}), which were heated to 40 °C during the analysis. The GPC was equipped with both ultraviolet (UV 2487) and differential refractive index (RI 2410) detectors. The molecular weights were determined by calibration against linear, nearly monodisperse poly(styrene) standards. Final copolymer composition was estimated by ^{1}H NMR spectroscopy. The ^{1}H NMR spectra were obtained using a 200 MHz Varian Gemini 2000 spectrometer using $CDCl_3$ solvent in 5 mm Up NMR tubes and by performing a minimum of 32 scans per sample. The copolymer composition was determined by the ratio of the methylene protons corresponding to VBK units (δ = 5.2−5.4 ppm, Ar−CH_2−N−) and the resonances corresponding to the proton adjacent to the ester next to the backbone of the methacrylate (δ = 4.0−4.1 ppm, O−CH_2−CH_2) for MEO_2MA and for $OEGMA_{8-9}$). For the terpolymers, the composition of MEO_2MA, $OEGMA_{8-9}$ and VBK was determined by comparing the signal due to protons adjacent to the ester next to the backbone of the methacrylate (δ = 4.0−4.1 ppm, O−CH_2−CH_2, 2H for MEO_2MA and 2H for $OEGMA_{8-9}$), the protons adjacent to the ester within the repeat unit of EG of the methacrylate (δ = 3.5−3.75 ppm, −CH_2−O−[−CH_2−CH_2−O−]$_n$−, 6H for MEO_2MA and 34H for $OEGMA_{8-9}$) and the methylene protons corresponding to the VBK units (δ = 5.2−5.4 ppm, Ar−CH_2−N−). The individual monomer conversion was determined by comparing the vinyl peaks (δ = 6.6, 5.6, and 5.1 ppm for VBK and δ = 5.45 and 6.05 ppm for $OEGMA_{8-9}$ and MEO_2MA) of the respective monomers, to the methoxy group (δ = 4.0 and 4.1 ppm, for $OEGMA_{8-9}$ and MEO_2MA) and the methylene group (δ = 5.2−5.4 ppm, corresponding to the VBK) corresponding to the respective monomers and copolymers. The overall monomer conversion (X) for the MEO_2MA/VBK and $OEGMA_{8-9}$/VBK copolymerizations was then determined by eq 1:

$$X = f_{VBK,0} X_{VBK} + f_{OEGMA8-9,0} X_{OEGMA8-9} \quad \text{and}$$
$$X = f_{VBK,0} X_{VBK} + f_{MEO2MA,0} X_{MEO2MA} \qquad (1)$$

where X_{VBK}, $X_{OEGMA8-9}$, X_{MEO2MA} are the individual monomer conversions for VBK, $OEGMA_{8-9}$, and MEO_2MA, respectively and $f_{VBK,0}$, $f_{MEO2MA,0}$, and $f_{OEGMA8-9,0}$ are initial mol fractions in the feed for VBK, $OEGMA_{8-9}$, and MEO_2MA, respectively. Cloud point temperatures (CPTs) were determined by dynamic light scattering (DLS) and UV−vis spectroscopy from 3 g·L^{-1} solutions of terpolymer in neutral water (purified by reverse osmosis). DLS measurements were performed with a Malvern Zetasizer Nano equipped with a 532 nm 50 mW green laser. For the terpolymers, the samples were heated in 1 °C increments, allowed to equilibrate for 1 min followed by 12 measurements, which were then averaged together to give one value at the temperature of interest (average heat cycle ≈6−8 h). For the poly(MEO_2MA-*ran*-$OEGMA_{8-9}$-*ran*-VBK)-*block*-poly(MEO_2MA-*ran*-$OEGMA_{8-9}$-*ran*-VBK) block copolymers, the samples were heated in increments of 0.2 °C, allowed to equilibrate for 1 min followed by 10 measurements, which were averaged together to give one value at the corresponding temperature (average heat cycle ≈14−16 h). The CPTs for the terpolymers were taken once the scaled Z-average diameter reached 0.5 and was reported as the average of three experiments. The dual CPTs for the poly(MEO_2MA-*ran*-$OEGMA_{8-9}$-*ran*-VBK)-*block*-poly(MEO_2MA-*ran*-$OEGMA_{8-9}$-*ran*-VBK) block copolymers were estimated as the temperature of the midpoint between the measurement plateau. UV−Vis measurements were performed with a Cary 5000 UV−Vis−NIR spectrometer (Agilent Technologies) equipped with a Peltier thermostated (6 × 6) multicell holder equipped with temperature controller and magnetic stirring. Using a heating rate of 0.5 °C min^{-1}, the CPT was taken once the scaled absorbance, at 500 nm, reached 0.5. Fluorescence measurements were performed with a Cary Eclipse fluorescence spectrophotometer equipped with a xenon flash lamp and Peltier thermostated (4) multicell holder with temperature controller. Quartz cuvettes filled with 3 mg L^{-1} solutions were excited at a wavelength of 330 nm at various temperatures.

RESULTS AND DISCUSSION

Prior to synthesizing a MEO_2MA/$OEGMA_{8-9}$/VBK terpolymer, a better understanding of the effect of VBK on its respective copolymerization with MEO_2MA and of $OEGMA_{8-9}$ by NMP was required. Therefore, a series of MEO_2MA/VBK and $OEGMA_{8-9}$/VBK copolymers with various $f_{VBK,0}$ were synthesized at 80 °C (Table 1). The molecular weight characteristics, the final copolymer composition and the water-solubility of the poly(VBK-*ran*-MEO_2MA) and poly(VBK-*ran*-$OEGMA_{8-9}$) copolymers are summarized in Table 3.

Kinetics of the Random Copolymerizations of 2-(2-Methoxyethoxy)ethyl Methacrylate with 9-(4-Vinylbenzyl)-9*H*-carbazole (MEO_2MA/VBK) and Oligo(ethylene glycol) Methyl Ether Methacrylate with 9-(4-Vinylbenzyl)-9*H*-carbazole ($OEGMA_{8-9}$/VBK). The average equilibrium constant, $\langle K \rangle$, is defined in terms of the concentration of propagating macroradicals [P$^\bullet$], free nitroxide [N$^\bullet$] and the dormant alkoxyamine terminated species [P−N] (eq 2).

$$\langle K \rangle = \frac{[P^\bullet][N^\bullet]}{[P{-}N]} \qquad (2)$$

An average equilibrium constant is used since the polymerization is a statistical copolymerization consisting of two monomers, which may have very different individual equilibrium constants. The semilogarithmic kinetic plots of $\ln[(1 - X)^{-1}]$

dx.doi.org/10.1021/ma202648k | *Macromolecules* 2012, 45, 1879−1891

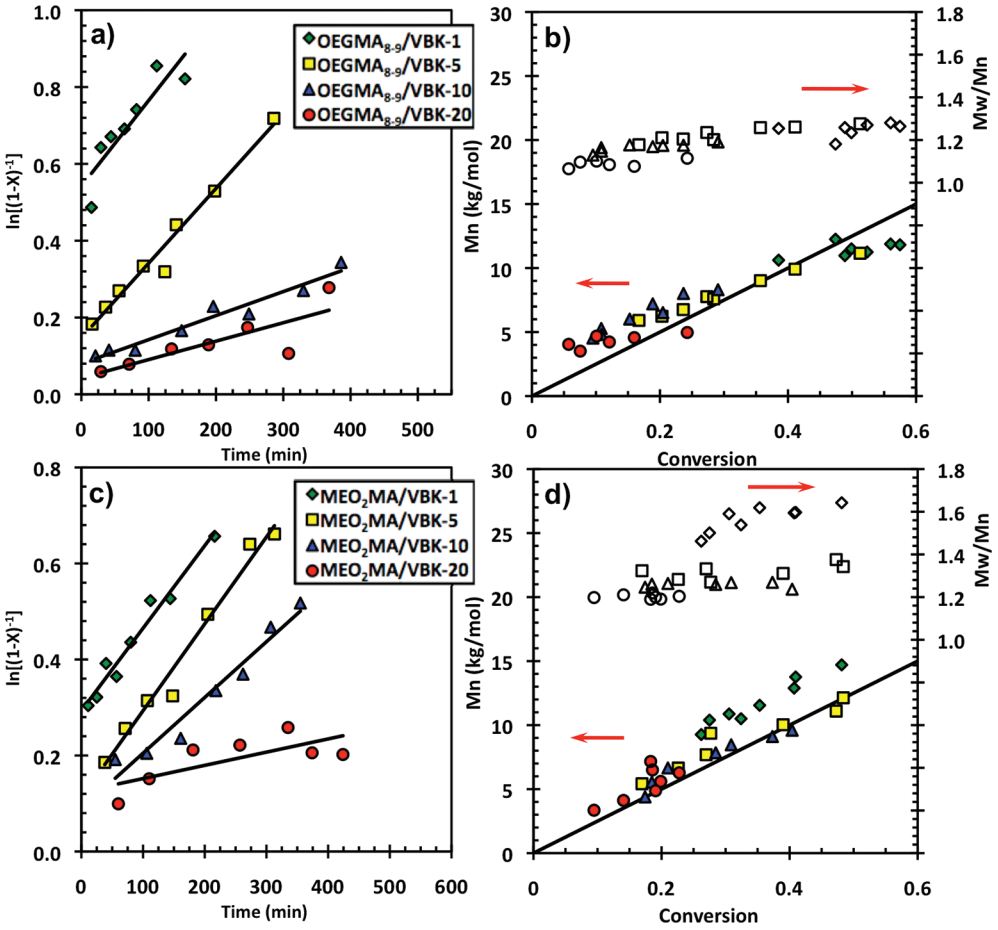

Figure 1. (a and c) Semilogarithmic plot of conversion ($\ln((1-X)^{-1})$ (X = conversion) versus time for 2-(2-methoxyethoxy)ethyl methacrylate-9-(4-vinylbenzyl)-9*H*-carbazole (MEO_2MA/VBK) and oligo(ethylene glycol) methyl ether methacrylate/VBK ($OEGMA_{8-9}$/VBK) copolymerizations, respectively, as functions of different initial feed compositions. (b and d), Number-average molecular weight $\bar{M}_n$ versus X for MEO_2MA/VBK and $OEGMA_{8-9}$/VBK copolymerizations, respectively. The legend in part a corresponds to the experiments displayed in both part a and part b, while, the legend in part c corresponds to the experiments in parts c and d. The empty symbols in parts b and d correspond to the $\bar{M}_w/\bar{M}_n$ versus X for the respective copolymerization corresponding to the respective filled symbol.

versus time for MEO_2MA/VBK and $OEGMA_{8-9}$/VBK are illustrated in Figure 1a and Figure 1b, respectively. The apparent rate constant, $\langle k_P\rangle[P^\bullet]$, which is the product of $\langle k_P\rangle$, the average propagation rate constant, and $[P^\bullet]$, the concentration of propagating macro-radicals, was determined from the slopes found in Figure 1, calculated typically from about 4−5 sample points taken in the linear region of the $\ln[(1-X)^{-1}]$ versus time plots. Generally, in the early stages of the polymerization, it can be assumed that the initial concentration of nitroxide $[N^\bullet]_0$ is sufficiently high so that $[N^\bullet] = [N^\bullet]_0$ and that [P−N] is approximately equal to the initial concentration of initiator ($[P-N] = [\text{BlocBuilder}]_0$). By taking these assumptions into account, the apparent rate constant can be related to the $\langle K\rangle$ as the product $\langle k_P\rangle\langle K\rangle$. Equation 2 thus is converted to the following form where r is the initial molar ratio of free nitroxide relative to BlocBuilder initiator ($r = [SG1]_0/[\text{BlocBuilder}]_0$) after multiplying eq 2 by $\langle k_P\rangle$.

$$\langle k_P\rangle\langle K\rangle \cong \langle k_P\rangle\frac{[P^\bullet][SG1]_0}{[\text{BlocBuilder}]_0} = \langle k_P\rangle[P^\bullet]r \qquad ([3])$$

For the systems studied here, the $\langle k_P\rangle[P^\bullet]$ reported were taken during the early stages of polymerization where linear growth of $\bar{M}_n$ versus conversion was observed (typically during the first 60 min of the polymerization where the previously mentioned assumptions held reasonably well). The experimental $\langle k_P\rangle\langle K\rangle$ values obtained for the MEO_2MA/VBK and $OEGMA_{8-9}$/VBK copolymerizations were compared and are summarized in Table 4. The experimental $\langle k_P\rangle\langle K\rangle$ tended to decrease slightly with increasing initial feed composition of VBK. For example, with $f_{VBK,0} = 0.01$, $\langle k_P\rangle\langle K\rangle_{MEO2MA/VBK} = (2.2 \pm 0.2) \times 10^{-6}$ s^{-1} and $\langle k_P\rangle\langle K\rangle_{OEGMA8-9/VBK} = (3.0 \pm 0.4) \times 10^{-6}$ s^{-1}. At a higher $f_{VBK,0} = 0.10$, $\langle k_P\rangle\langle K\rangle_{MEO2MA/VBK} = (1.6 \pm 0.2) \times 10^{-6}$ s^{-1} and $\langle k_P\rangle\langle K\rangle_{OEGMA8-9/VBK} = (9.6 \pm 0.9) \times 10^{-7}$ s^{-1} (see Table 4 for all $\langle k_P\rangle\langle K\rangle$). This observation was previously reported for MMA/VBK copolymerizations and is due to the low k_pK associated with VBK homopolymerizations at 80 °C.[60] The general increase in $\langle k_P\rangle\langle K\rangle$ as a function of decreasing VBK content suggested the polymerizations were becoming less controlled, and this was reflected in higher polymerization rates (Table 4) and generally broader molecular weight distributions (Table 3). It appears that regardless of the VBK content in the feed, there is no significant difference between $\langle k_P\rangle\langle K\rangle_{OEGMA8-9/VBK}$ and $\langle k_P\rangle\langle K\rangle_{MEO2MA/VBK}$. As a comparison, MMA/VBK copolymerization done in a dilute DMF solution at 80 °C with $f_{VBK,0} = 0.05$ resulted in $\langle k_P\rangle\langle K\rangle_{MMA/VBK} = (5.4 \pm 0.1) \times 10^{-6}$ s^{-1}.[60] Similarly, DMAEMA/VBK copolymerization in DMF at 80 °C with $f_{VBK,0} = 0.05$ also resulted in $\langle k_P\rangle\langle K\rangle_{DMAEMA/VBK} = (5.4 \pm 0.3) \times 10^{-6}$ s^{-1}.[18] Therefore,

dx.doi.org/10.1021/ma202648k | *Macromolecules* 2012, 45, 1879−1891

the $\langle k_P \rangle \langle K \rangle$ of MMA/VBK and DMAEMA/VBK is roughly 2 times greater than $\langle k_P \rangle \langle K \rangle_{MEO2MA/VBK}$ and $\langle k_P \rangle \langle K \rangle_{OEGMA8-9/VBK}$, when the copolymerization is performed in DMF at 80 °C with $f_{VBK,0}$ = 0.05. As mentioned earlier, $\langle k_P \rangle$ is an average of k_Ps corresponding to the respective monomers being copolymerized. Literature values for k_P of some oligo(ethylene glycol) methacrylates have been previously determined using pulsed laser polymerization (PLP) and can be used to make comparisons with respect to $\langle k_P \rangle \langle K \rangle$. The k_P corresponding to MEO_2MA done in bulk at 80 °C is $k_{P,\ MEO2MA,80\ °C}$ = 1460 $L \cdot mol^{-1} \cdot s^{-1}$,[64] and is very similar to that of MMA done in bulk at 80 °C, $k_{P,\ MMA,80\ °C}$ = 1297 $L \cdot mol^{-1} \cdot s^{-1}$.[65] These values suggest that K_{MEO2MA} must therefore be not very different compared to K_{MMA}, when polymerized in DMF at 80 °C. It has been reported that as the size of the EG chain increases, the corresponding k_P's also increase.[64] For example, the k_P corresponding to $OEGMA_3$ (oligo(ethylene glycol) methyl ether methacrylate with 3 EG units) done in bulk at 80 °C has $k_{P,OEGMA3,80\ °C}$ = 2270 $L \cdot mol^{-1} \cdot s^{-1}$.[64] However, no k_P for $OEGMA_{8-9}$ has been reported and therefore any comparison drawn between K_{MEO2MA} and $K_{OEGMA8-9}$ would be speculative.

The use of VBK as a "controlling" comonomer for MEO_2MA and $OEGMA_{8-9}$ resulted in a linear increase in $\bar{M}_n$ versus X up until X = 0.6, regardless of the $f_{VBK,0}$ used (Figure 1b and d). The growth in chains can be easily monitored by the shift in GPC chromatograms (see Supporting Information, Figure S1). The decrease in $OEGMA_{8-9}$ monomer concentration also appears in the GPC chromatograms due to its relatively high molecular weight (Figure S1, observe the peaks at an elution time of ≈32 min). In the case of MEO_2MA/VBK using $f_{VBK,0}$ = 0.01, the experimentally obtained $\bar{M}_n$ was slightly higher than the theoretical $\bar{M}_n$ and the copolymerizations experienced a slight broadening of the molecular weight distribution ($\bar{M}_w/\bar{M}_n \approx 1.6$), indicating a decrease in apparent initiator efficiency. Also, there is an offset at early polymerization time, suggesting chains were rapidly being formed, and there was not enough comonomer to provide sufficient control. Similar decreases in initiator efficiencies have been previously reported for the copolymerization of MMA/S[46] and MMA/VBK,[60] as the concentration of "controlling" comonomer was decreased. In the case of $OEGMA_{8-9}$/VBK using $f_{VBK,0}$ = 0.01, the experimentally obtained $\bar{M}_n$ does not appear to follow the theoretical $\bar{M}_n$. However, the molecular weight distribution remained relatively narrow ($\bar{M}_w/\bar{M}_n \leq 1.3$). For MMA/VBK copolymerizations, the use of 1 mol % VBK relative to MMA seemed to be the lowest VBK feed concentration that could be feasibly used to obtain a controlled polymerization.[60] For the copolymerizations of MEO_2MA/VBK and $OEGMA_{8-9}$/VBK, it appears that 1 mol % VBK in the feed is not sufficient to keep the polymerization controlled completely. Both the MEO_2MA/VBK and $OEGMA_{8-9}$/VBK copolymerizations were characterized by linear growth of $\bar{M}_n$ versus X and by final copolymers characterized by narrow molecular weight distributions with $\bar{M}_w/\bar{M}_n < 1.4$ as long as $f_{VBK,0} > 0.01$.

2-(2-Methoxyethoxy)ethyl Methacrylate with 9-(4-Vinylbenzyl)-9*H*-carbazole (MEO_2MA/VBK) and Oligo(ethylene glycol) Methyl Ether Methacrylate with 9-(4-Vinylbenzyl)-9*H*-carbazole ($OEGMA_{8-9}$/VBK) Statistical Copolymerizations: Copolymer Composition. Since the nitroxide-mediated copolymerization of MEO_2MA/VBK and $OEGMA_{8-9}$/VBK has not been studied using the BlocBuilder/SG1 initiating system, it was necessary to uncover the effect of feed composition on the copolymer composition. The results would then be useful for subsequent tailoring of copolymer composition, which is expected to have a strong effect on the water-solubility of the final copolymer. Several MEO_2MA/VBK and $OEGMA_{8-9}$/VBK copolymerizations were carried out while varying $f_{VBK,0}$ between 0.01 to 0.2 (Table 1). As previously mentioned, the copolymer composition was determined by ^1H NMR spectroscopy. Table 3 indicates the compositions of the various MEO_2MA/VBK and $OEGMA_{8-9}$/VBK random copolymers synthesized with various initial feed formulations. Generally, the composition of VBK is richer in the copolymer than in the initial copolymerization feed (Table 3). The preferential addition of VBK relative to MEO_2MA or $OEGMA_{8-9}$ is consistent with the observations for VBK/MMA[60] and VBK/DMAEMA[18] copolymerizations. The composition of copolymer samples taken early in the MEO_2MA/VBK and $OEGMA_{8-9}$/VBK copolymerizations (X < 0.2) were plotted as a function of feed composition (Figure 2). As a comparison, the copolymer composition of MMA/VBK was fit to a terminal model (e.g.: Mayo–Lewis equation[66]) using reactivity ratios, r_{MMA} = 0.24 ± 0.14 and r_{VBK} = 2.7 ± 1.5, which were previously determined for MMA/VBK copolymers by NMP using the identifical initiator system, solvent and polymerization temperature.[60] The terminal model for MMA/VBK is represented in Figure 2 as the dashed line. It is evident that, for the composition range studied ($f_{VBK,0}$ = 0.01–0.20), MEO_2MA/VBK and $OEGMA_{8-9}$/VBK copolymerizations were behaving in a similar fashion to the MMA/VBK copolymerization, illustrated by a preferential addition of VBK to itself, with regards to the respective methacrylate. For the purpose of this study, oligo-EG methacrylate-rich copolymers and terpolymers were synthesized with low $f_{VBK,0}$ to maintain water-solubility. As previously mentioned, very little VBK in the feed was necessary to be effective as a methacrylate-"controlling" comonomer and to impart fluorescence ($f_{VBK,0}$ = 0.01–0.05).[18,60] However, too much VBK in the feed resulted in a water-insoluble product ($F_{VBK,0}$ > 0.07 yielded water-insoluble copolymers).[18]

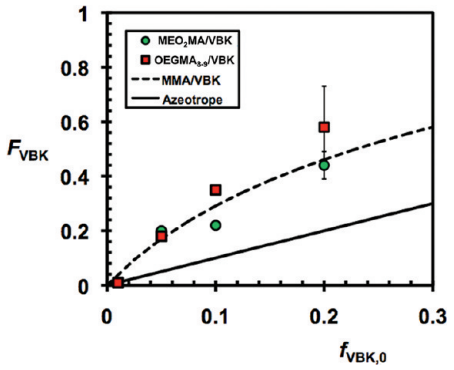

Figure 2. 9-(4-Vinylbenzyl)-9*H*-carbazole (VBK) copolymer composition F_{VBK} with respect to initial VBK feed composition $f_{VBK,0}$ for various methacrylate/VBK copolymerizations at 80 °C in dimethylformamide (DMF). Experimentally obtained compositions for 2-(2-methoxyethoxy)ethyl methacrylate/VBK (MEO_2MA/VBK) copolymers and oligo(ethylene glycol) methyl ether methacrylate/VBK ($OEGMA_{8-9}$/VBK) copolymers are represented by the circles and squares, respectively. The dashed line represents the theoretical fit to a terminal model (Mayo–Lewis equation) using r_{MMA} = 0.24 ± 0.14 and r_{VBK} = 2.7 ± 1.5, which were previously determined for methyl methacrylate/VBK copolymerizations (MMA/VBK).[60] The solid line represents the azeotropic composition ($r_{MMA} = r_{VBK} = 1$).

dx.doi.org/10.1021/ma202648k | *Macromolecules* 2012, 45, 1879–1891

Table 5. Molecular Characterization for Various Oligo(ethylene glycol) Methyl Ether Methacrylates/2-(2-Methoxyethoxy)ethyl Methacryate/9-(4-Vinylbenzyl)-9*H*-carbazole (OEGMA$_{8-9}$/MEO$_2$MA/VBK) Random Terpolymers and Block Copolymers

expt ID[a]	$\bar{M}_n$ (kg/mol)[b]	$\bar{M}_w/\bar{M}_n$[b]	F_{VBK}[c]	F_{MEO2MA}[c]	$F_{OEGMA8-9}$[c]	CPT[d] (°C) DLS (UV)
OM5/95	12.0	1.58	<0.01	0.93	0.07	27.9 (30.1)
OM10/90	18.5	1.55	0.02	0.88	0.09	32.2 (34.6)
OM20/80	23.1	1.28	<0.01	0.90	0.10	45.5 (49.5)
OM30/70	23.4	1.28	0.02	0.70	0.28	54.1 (54.4)
OM40/60	28.7	1.34	<0.01	0.68	0.32	65.4 (66.4)
OM50/50	35.9	1.28	0.03	0.53	0.44	67.4 (69.6)
OM60/40	22.9	1.38	0.03	0.41	0.55	73.3 (71.7)
OM70/30	43.2	1.22	0.05	0.25	0.70	73.1 (78.3)
OM80/20	39.2	1.20	<0.01	0.24	0.76	76.5 (80.9)
OM90/10	47.7	1.27	<0.01	0.02	0.98	>90[e](>90)[e]
expt ID[a]	$\bar{M}_n$ (kg/mol)[b]	$\bar{M}_w/\bar{M}_n$[b]	F_{VBK}[c]	F_{MEO2MA}[c]	$F_{OEGMA8-9}$[c]	1st CPT/2nd CPT[d] (°C) DLS$_1$ (UV) $_1$/DLS$_2$ (UV) $_2$
OM5/95-OM50/50	39.6	1.30	<0.01	0.51	0.49	31.2(39.3)/62.4(65.1)
OM10/90-OM50/50	35.2	1.69	0.04	0.91	0.05	39.2(41.2)/53.8(67.8)
OM80/20-OM20/80	91.9	1.95	0.02	0.38	0.60	40.8(44.5)/72.4(72.8)

[a]Experimental identification (expt ID) for OEGMA$_{8-9}$, MEO$_2$MA and VBK terpolymerizations are given by OMX/*Y*, with "O" representing oligo(ethylene glycol) methyl ether methacrylate, "M" representing 2-(2-methoxyethoxy)ethyl methacrylate, and *X*/*Y* representing the approximate initial mol % of OEGMA$_{8-9}$/MEO$_2$MA in the feed, respectively. For the chain extensions, the expt ID is given by OMX/*Y*-OMZ/*W* where OMX/*Y* represents the expt ID of the macroinitiator used for the chain extension and for OMZ/*W*, the "O" represents oligo(ethylene glycol) methyl ether methacrylate, "M" represents 2-(2-methoxyethoxy)ethyl methacrylate and *Z*/*W* represents the approximate initial mol % of OEGMA$_{8-9}$/MEO$_2$MA in the feed, respectively. [b]Number-average molecular weight ($\bar{M}_n$) and polydispersity index ($\bar{M}_w/\bar{M}_n$) were determined using gel permeation chromatography (GPC) run in THF at 35 °C and calibrated against poly(styrene) standards. [c]F_{VBK}, F_{MEO2MA}, and $F_{OEGMA8-9}$ are the final molar composition of VBK, MEO$_2$MA, and OEGMA$_{8-9}$ in the copolymer, as determined by ^{1}H NMR spectroscopy. [d]Cloud point temperature (CPT) was determined by dynamic light scattering (DLS) and UV−vis spectroscopy (UV/vis) for a 3 g·L^{-1} polymer and water solution. [e]No CPT was observed between 20 and 90 °C.

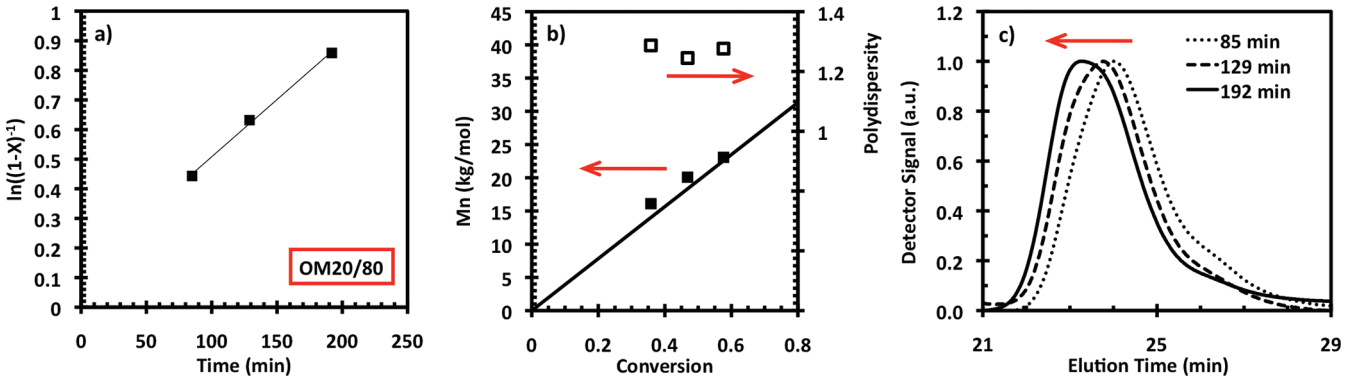

Figure 3. Characteristic (a) semilogarithmic plot of conversion ($\ln((1-X)^{-1})$ (X = conversion) versus time, (b) number-average molecular weight $\bar{M}_n$ versus X, and (c) gel permeation chromatograms for the terpolymerization of 2-(2-methoxyethoxy)ethyl methacrylate/oligo(ethylene glycol) methyl ether methacrylate/9-(4-vinylbenzyl)-9*H*-carbazole (MEO$_2$MA/OEGMA$_{8-9}$/VBK). The synthesis represented here is OM20/80 and its formulation can be found in Table 2 while the terpolymer characterization is summarized in Table 5.

Controlled Terpolymerization of 2-(2-Methoxyethoxy)ethyl Methacrylate, Oligo(ethylene glycol) Methyl Ether Methacrylate and 9-(4-Vinylbenzyl)-9*H*-carbazole (MEO$_2$MA/OEGMA$_{8-9}$/VBK). As mentioned in the previous section, the MEO$_2$MA/VBK and OEGMA$_{8-9}$/VBK binary copolymerizations resulted in a controlled copolymerization as long as $f_{VBK,0}$ > 0.01. Therefore, a series of MEO$_2$MA/OEGMA$_{8-9}$/VBK terpolymers were synthesized at 80 °C (Table 2), with variable feed ratios of MEO$_2$MA:OEGMA$_{8-9}$ while keeping the VBK composition constant but sufficiently high to ensure good control ($f_{VBK,0}$ = 0.02). The terpolymers were targeted since varying the MEO$_2$MA:OEGMA$_{8-9}$ ratio permitted tuning of the LCST. The molecular weight characteristics and the final composition for the poly(VBK-*ran*-MEO$_2$MA-*ran*-OEGMA$_{8-9}$) random terpolymers are found in Table 5. The final terpolymers were characterized by relatively narrow molecular weight distributions with $\bar{M}_w/\bar{M}_n$= 1.20−1.58 and $\bar{M}_n$ = 12.0−47.7 kg·mol^{-1} (Table 5). A characteristic scaled conversion ($\ln(1-X)^{-1}$) versus polymerization time and $\bar{M}_n$ versus X plot for a terpolymerization (OM20/80) are depicted in Figure 3a and Figure 3b, respectively. While only three samples were taken during the course of the terpolymerization, it appears that $\bar{M}_n$ increased linearly with X (up to $X \approx 0.6$) and that the $\bar{M}_w/\bar{M}_n$ remained relatively low with $\bar{M}_w/\bar{M}_n$< 1.30. The corresponding GPC chromatograms depict the $\bar{M}_n$ growth with time (Figure 3c). It would appear that the MEO$_2$MA/OEGMA$_{8-9}$/VBK terpolymerization was behaving in a similar fashion to the MEO$_2$MA/VBK and OEGMA$_{8-9}$/VBK binary copolymerizations. The use of as little as $f_{VBK,0}$ = 0.02 resulted in a controlled terpolymerization of MEO$_2$MA/OEGMA$_{8-9}$/VBK by NMP using the BlocBuilder/SG1 initiating system. Similar to the MEO$_2$MA/VBK and OEGMA$_{8-9}$/VBK copolymerizations, VBK can be used as a "controlling" comonomer for the terpolymerization of DEGM/OEGMA$_{8-9}$/VBK and was

dx.doi.org/10.1021/ma202648k | *Macromolecules* 2012, 45, 1879−1891

characterized by narrow molecular weight distributions for a wide range of $OEGMA_{8-9}$:MEO_2MA ratios (Table 5).

Chain Extension of 2-(2-Methoxyethoxy)ethyl Methacrylate, Oligo(ethylene glycol) Methyl Ether Methacrylate and 9-(4-Vinylbenzyl)-9*H*-carbazole (MEO_2MA/$OEGMA_{8-9}$/VBK) Terpolymers. A series of characteristic MEO_2MA/$OEGMA_{8-9}$/VBK terpolymers were used to reinitiate a fresh batch of MEO_2MA/$OEGMA_{8-9}$/VBK in DMF at 80 °C (see Table 2 for formulations). The molecular weight characteristics of the poly(MEO_2MA-*ran*-$OEGMA_{8-9}$-*ran*-VBK)-*block*-poly(MEO_2MA-*ran*-$OEGMA_{8-9}$-*ran*-VBK) block copolymers are found in Table 5. The terpolymer macroinitiators underwent an increase in $\bar{M}_n$ from 12.0 to 39.2 kg·mol^{-1} to 35.2−91.9 kg·mol^{-1} after chain extension and their molecular weight distributions broadened with from $\bar{M}_w/\bar{M}_n$ = 1.20−1.69 to 1.30−1.95 (Table 5). The $\bar{M}_n$ increased linearly versus conversion while the $\bar{M}_w/\bar{M}_n$ remained relatively low ($\bar{M}_w/\bar{M}_n \approx$ 1.3), illustrating the controlled behavior of the polymerization of OM5/95-OM50/50, a characteristic chain extension of MEO_2MA/$OEGMA_{8-9}$/VBK terpolymer (Figure 4).

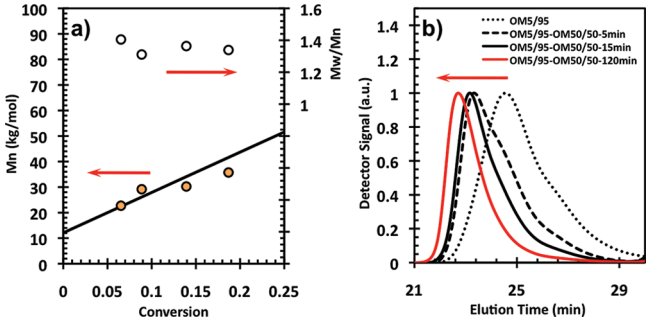

Figure 4. Characteristic a) $\bar{M}_n$, $\bar{M}_w/\bar{M}_n$ versus conversion and b) gel permeation chromatograms for chain extension from an OM5/95 macroinitiator using a second batch of 2-(2-methoxyethoxy)ethyl methacrylate/oligo(ethylene glycol) methyl ether methacrylate/9-(4-vinylbenzyl)-9*H*-carbazole (MEO_2MA/$OEGMA_{8-9}$/VBK). The feed compositions for the second batches of monomer are listed in Table 2. The molecular characteristics of the final block copolymers are summarized in Table 5.

The GPC chromatograms exhibited a slight tail, which could be a result of some irreversibly terminated macroinitiators. Similar tails have been previously reported for methacrylate-rich copolymers by NMP.[50] However, the majority of the chains appeared to be growing steadily, resulting in a block copolymer with two distinct segments. The addition of the second block was also characterized by the change in composition from the macroinitiator to the final block copolymer (Table 5). For example, the macroinitiator OM80/20 had a composition F_{VBK} < 0.01, F_{MEO2MA} = 0.24 and $F_{OEGMA8-9}$ = 0.76. After being used to reinitiate a MEO_2MA-rich ternary mixture, the final OM80/20-OM20/80 block copolymer had an overall composition of F_{MEO2MA} = 0.38 and $F_{OEGMA8-9}$ = 0.60. These results indicate that poly(VBK-*ran*-MEO_2MA-*ran*-$OEGMA_{8-9}$) terpolymers synthesized by NMP were pseudo-"living" enough to reinitiate a second ternary batch of monomers to make block copolymers where each of the blocks had distinct MEO_2MA:OEGMA compositions.

Terpolymer Solution Properties. The final $OEGMA_{8-9}$/VBK and MEO_2MA/VBK copolymers were mixed with neutral water (purified by reverse osmosis) to determine water-solubility. At room temperature, $OEGMA_{8-9}$/VBK copolymers with $F_{VBK} \leq$ 0.09 were determined to be water-soluble, while all MEO_2MA/VBK copolymers were determined to be water-insoluble at room temperature, even with VBK compositions as low as 1 mol % (Table 3). These results are expected; the incorporation of a hydrophobic comonomer such as VBK will obviously reduce the water-solubility of the final copolymer. A similar water-solubility range ($F_{VBK} \leq$ 0.07) was observed for poly(DMAEMA-*ran*-VBK) copolymers.[18] Because of the relatively short pendant EG chains (2 repeat units), poly(MEO_2MA) exhibits relatively low LCSTs ≈ 28 °C.[31] However, by the inclusion of a hydrophobic comonomer (such as VBK), the LCST drops below room temperature and therefore the resulting poly(MEO_2MA-*ran*-VBK) copolymers were not soluble in neutral water at room temperature (≈ 25 °C). However, poly($OEGMA_{8-9}$)s have longer EG side chains (8−9 repeat units) and are known to exhibit LCSTs ≈ 90 °C[31] and therefore the poly($OEGMA_{8-9}$-*ran*-VBK) copolymers remained completely water-soluble at room temperature up to relatively high VBK contents.

As previously mentioned, copolymers consisting of $OEGMA_{8-9}$ and MEO_2MA can result in water-soluble copolymers, which will exhibit CPTs between 25 and 90 °C, depending on the ratio of $OEGMA_{8-9}$ to MEO_2MA. A series of MEO_2MA/$OEGMA_{8-9}$/VBK terpolymers were synthesized with varying $OEGMA_{8-9}$:MEO_2MA ratios, while maintaining $f_{VBK,0}$ = 0.02 (see Table 2 for formulations and Table 5 for characterization). The CPTs of the terpolymers were determined by DLS and UV−vis spectroscopy. The final terpolymer composition, molecular weight characterization and corresponding CPT for each terpolymer can be found in Table 5. The obtained CPTs for the respective terpolymers increased from 28 to 81 °C as the ratio of $OEGMA_{8-9}$:MEO_2MA increased (Table 5). Characteristic DLS and UV−vis spectra are shown in Figure 5a and Figure 5b. The resulting CPTs determined by DLS and UV−vis for each terpolymer exhibited LCST differences of about 0−4 °C, depending on the technique used. Similar slight discrepancies have been observed in our previous work using DMAEMA/VBK copolymers and block copolymers, and is a result of the differences in detection methods.[18] The UV−vis spectra (Figure 5b) indicate a completely thermo-reversible transition with a slight hysteresis of 1−3 °C between the heating and cooling cycle of each copolymer. Similar "tunability" of copolymer LCSTs in aqueous solutions with identical concentration (3 g•L^{-1}), have previously been obtained using poly($OEGMA_{8-9}$-*ran*-MEO_2MA) copolymers synthesized by ATRP.[31] Just like the copolymers made by ATRP, NMP can be used to synthesize a library of well-defined $OEGMA_{8-9}$/MEO_2MA copolymers in a controlled manner, which have a tunable LCST, except that additional functionality was imparted by using a small amount of VBK as the "controlling" comonomer in the BlocBuilder-mediated NMP.

Block Co(terpolymer) Solution Properties. The final poly(MEO_2MA-*ran*-$OEGMA_{8-9}$-*ran*-VBK)-*block*-poly(MEO_2MA-*ran*-$OEGMA_{8-9}$-*ran*-VBK) block copolymers synthesized by chain extension from MEO_2MA/$OEGMA_{8-9}$/VBK terpolymers were also investigated, to determine their potential for thermo-responsive behavior with multiple LCSTs. The characteristic DLS and UV−vis spectra are shown in Figure 6. Because of the distinct segments of the block copolymer which possess different $OEGMA_{8-9}$:MEO_2MA ratios (see Table 5 for characterization data), the final block copolymer exhibited two distinct CPTs (Figure 6 and Figure 7). For example OM10/90-OM50/50 exhibited a CPT characterized by a sudden increase in particle size (Z_{AVG} ≈ 400 nm) at T = 39.2 °C corresponding

dx.doi.org/10.1021/ma202648k | *Macromolecules* 2012, 45, 1879−1891

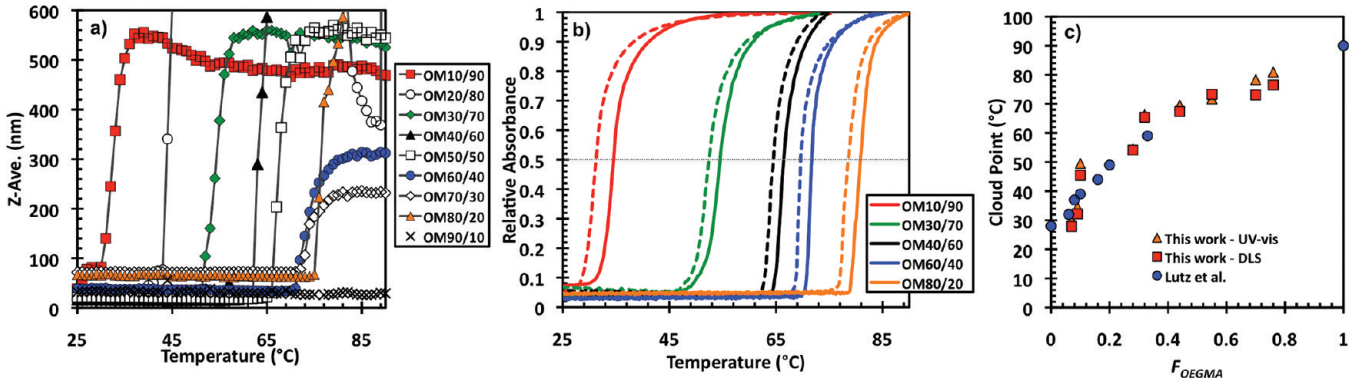

Figure 5. Cloud point temperature (CPT) determined by (a) dynamic light scattering (DLS) and by (b) UV−vis spectroscopy of characteristic poly(OEGMA$_{8-9}$-*ran*-MEO$_2$MA-*ran*-VBK) terpolymers (see Table 5 for complete characterization and identification of samples) in neutral water (pH = 7). CPTs were determined using 3 g·L^{-1} solutions. The dotted lines in part b represent the relative absorbance during the cooling process. As a comparison, the resulting CPTs obtained using DLS and UV−vis in parts a and b are plotted as a function of F_{OEGMA} in part c along with the corresponding literature values for poly(OEGMA$_{8-9}$-*ran*-MEO$_2$MA) binary copolymers obtained from Lutz et al.[31].

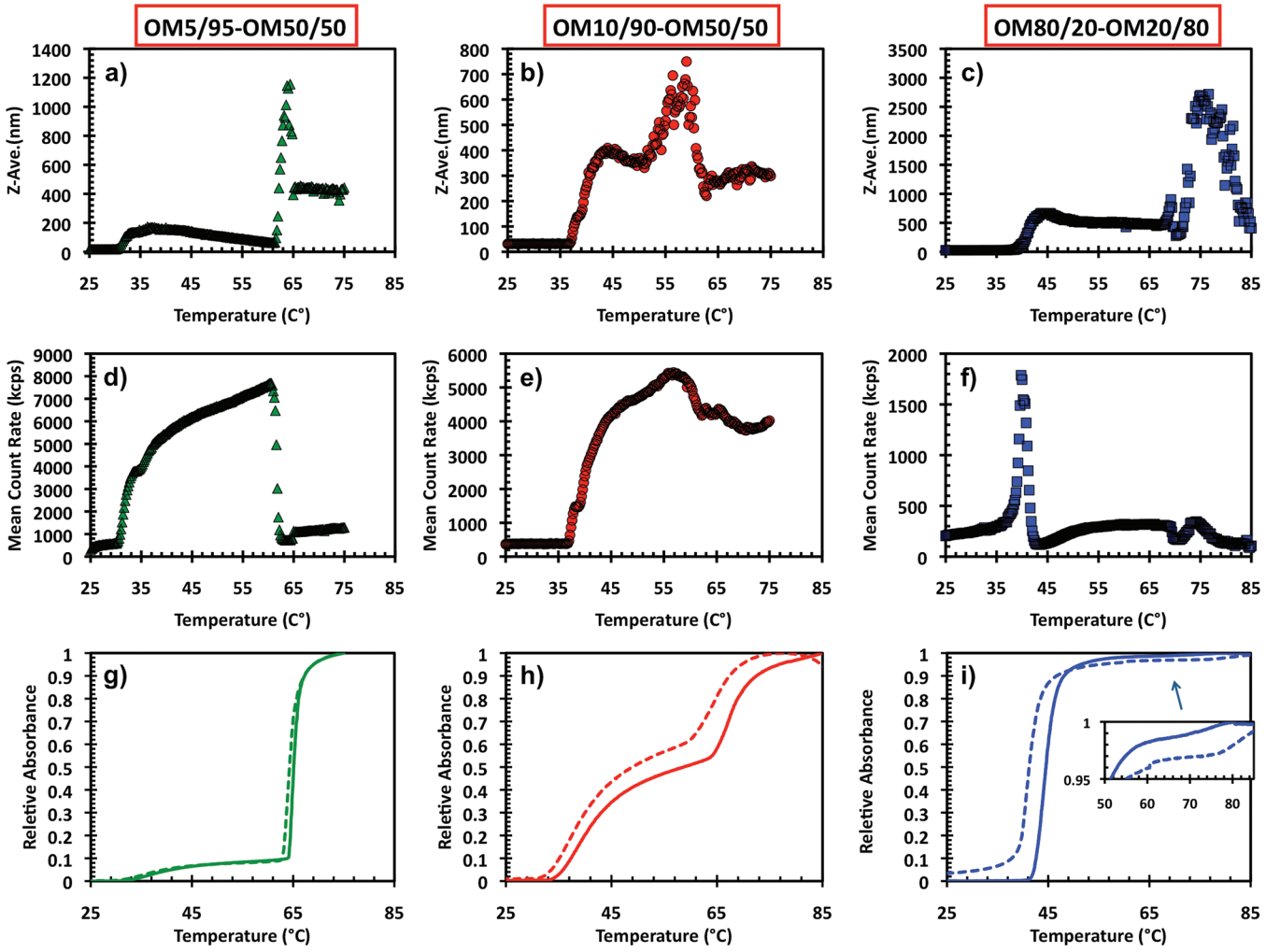

Figure 6. Dual cloud point temperature (CPT) determination by dynamic light scattering (DLS), where parts a−c represent the *Z*-average diameter with respect to temperature and parts d−f represent the mean count rate for OM5/95-OM50/50, OM10/90-OM50/50 and OM80/20-OM20/80 block copolymers, respectively. The corresponding temperature modulated UV−vis spectra for (g) OM5/95-OM50/50, (h) OM10/90-OM50/50, and (i) OM80/20-OM20/80 block copolymers are also represented. The inset in part i represents a close-up of the upper region of the spectrum. The molecular characteristics of the final block copolymers along with the respective CPTs can be found in Table 5. CPTs were determined using 3 g·L^{-1} solutions in all cases.

to the OM10/90 segment and a second CPT corresponding to a second increase in particle size (Z_{AVG} > 800 nm) at T = 53.8 °C corresponding to the OM50/50 segment (Figure 6b). The mean count of the particles was also plotted (Figure 6e) and shows good agreement with the transitions observed by tracking the change in Z_{AVG}. The first CPT (corresponding to OM10/90)

dx.doi.org/10.1021/ma202648k | *Macromolecules* 2012, 45, 1879−1891

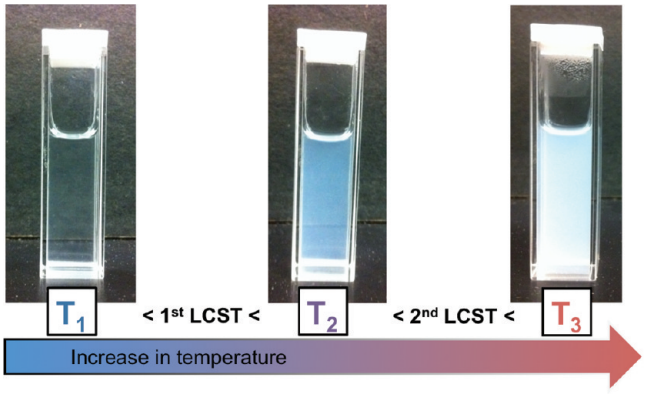

Figure 7. Visual observation of dual cloud point temperature (CPT) is shown for a sample heated to three temperatures bracketing the CPTs of the corresponding block copolymers where each block has different $MEO_2MA/OEGMA_{8-9}$ ratios. In this example, a 3 g·L^{-1} solution of OM10/90-OM50/50 is depicted at various temperatures. The solution is water-soluble at T_1 (room temperature) but becomes translucent as it is heated to T_2 while above the second CPT at T_3, the solution turned milky. The molecular characteristics of the final block copolymers along with the respective CPTs can be found in Table 5.

in the block copolymer is slightly higher (CPT = 39.2 °C by DLS) than the CPT previously determined for the OM10/90 macroinitiator (CPT = 32.2 °C by DLS − Table 5). This increase in CPT is due to the addition of a second more water-soluble block (below the second CPT as the second block was more water-soluble). The hydrophilic block improves the hydration of the responsive block and, due to the entropy-driven nature of the phase separation, leads to a higher CPT. Kotsuchibashi et al. reported micelle formation for poly(NIPAAm)-*block*-poly(NIPAAm-*co*-N-(isobutoxymethyl)-acrylamide) block copolymers when heating between the two corresponding LCSTs.[21] Similar observations have also been reported between poly(DMAEMA-*ran*-VBK) and poly(DMAEMA-*ran*-VBK)-*block*-poly(*N*,*N*-dimethylacrylamide) as the addition of the water-soluble poly(*N*,*N*-dimethylacrylamide) segment resulted in an increase in LCST and the formation of micelles above the LCST.[18] The second CPT observed for OM10/90-OM50/50 at T = 53.8 °C was a result of the chain extension that was formulated to mimic the OM50/50 terpolymer (segment OM50/50), which was previously determined to have an CPT = 67.4 °C. Using a similar reasoning as above, the second block of thermo-responsive terpolymer was now coupled to a water-insoluble segment (when the temperature is above the first CPT but below the second CPT) and now less energy was required to render the entire block copolymer insoluble, hence resulting in a decrease in the second CPT for the OM50/50 block of the block copolymer. Similarly, OM80/20-OM20/80 exhibited a CPT characterized by a sudden increase in particle size ($Z_{AVG} \approx$ 500 nm) at T = 40.8 °C corresponding to the OM20/80 segment (assuming the composition used in the formulation results in a segment with similar final composition as the OM20/80 terpolymer previously synthesized) and a second CPT corresponding to a second increase in particle size (Z_{AVG} > 2000 nm) at T = 72.4 °C corresponding to the OM80/20 segment, which was the macroinitiator used for the chain extension (see Table 2 for the formulation and Table 5 for characterization data and Figure 6 for the transitions). Similar to OM10/90-OM50/50, the first CPT for OM80/20-OM20/80 is slightly higher than the obtained CPT value for the corresponding OM80/20 terpolymer and the second CPT is slightly lower than the CPT previously determined for the OM20/80 macroinitiator (Table 5 and Figure 6). The corresponding UV−vis spectra can also be found in Figure 6g) for OM5/95-OM50/50, Figure 6h) for OM10/90-OM50/50 and Figure 6i) for OM80/20-OM20/80 and provide evidence of dual responsiveness of the block copolymers, in good agreement with the data obtained using DLS (see Table 5 for CPTs and Figure 6). As an example, Figure 7 displays visually the double thermo-responsive behavior of OM10/90-OM50/50. The UV−vis spectra in Figure 6g−i) also indicate that the thermo-responsive behavior is again completely reversible, even for the block copolymers, resulting in only a slight hysteresis of 1−4 °C between the heating and cooling cycles.

The properties described in Figure 5 and Figure 6 illustrates the power of compositional and microstructural control imparted by NMP into essentially pure $MEO_2MA/OEGMA_{8-9}$ copolymers (with a minimal amount of VBK). These dual thermo-responsive materials could potentially be used in the fabrication of multilevel sensors or more complex drug delivery vehicles, without using multiple functional monomers, but rather just by modifying the composition of $OEGMA_{8-9}$ relative to MEO_2MA in the respective blocks.

Terpolymer Fluorescence. In addition to "controlling" the polymerization of MEO_2MA and $OEGMA_{8-9}$, the VBK unit introduces hole transport and fluorescence properties into the final copolymer due to the carbazole moiety. The fluorescence spectra of the terpolymers OM50/50 and OM10/90, when excited at λ = 330 nm, exhibit two major emission peaks at 350 and 366 nm, corresponding to the carbazole group in the VBK unit (Figure 8).[18,63] As the temperature increases, the corresponding fluorescence intensity decreases (Figure 8). Similar

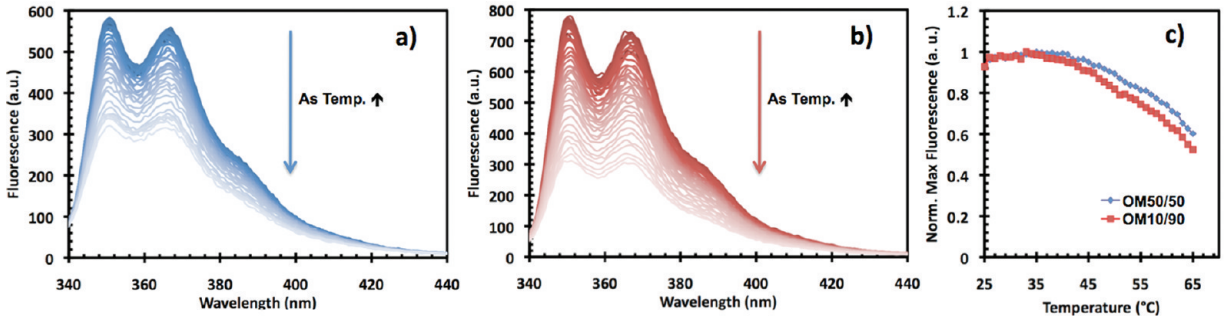

Figure 8. Temperature modulated fluorescence spectra for (a) OM50/50 and (b) OM10/90. (c) Normalized maximum fluorescence with respect to temperature for both OM50/50 and OM10/90. Fluorescence measurements were determined from 3 mg·L^{-1} solutions using an excitation wavelength of 330 nm at various temperatures.

dx.doi.org/10.1021/ma202648k | *Macromolecules* 2012, 45, 1879−1891

increases in fluorescence quenching was previously reported for poly(DMAEMA-*ran*-VBK) copolymers.[18] The decrease in intensity appears to be constant over the temperature range of 25 to 65 °C with no apparent "step" or change in rate of fluorescence quenching with respect to the corresponding LCSTs (LCST for OM10/90 ≈ 32−35 °C and LCST for OM50/50 ≈ 67−70 °C). Regardless, the incorporation of as little as 1−2 mol % of VBK into the final terpolymer resulted in a significant fluorescence response throughout a large temperature range, even with solutions as dilute as 3 mg·L^{-1}.

CONCLUSION

A series of MEO_2MA/VBK and $OEGMA_{8-9}$/VBK copolymers were synthesized in a controlled manner by NMP using BlocBuilder/SG1 at 80 °C. The binary copolymerizations exhibited linear increases in $\bar{M}_n$ versus X, up to $X \approx 0.60$ while maintaining relatively narrow molecular weight distributions with $\bar{M}_w/\bar{M}_n < 1.4$ when using $f_{VBK,0} > 0.01$ (and $\bar{M}_w/\bar{M}_n < 1.6$ when using $f_{VBK,0} = 0.01$). The experimentally obtained $\langle k_P \rangle \langle K \rangle$ values for the MEO_2MA/VBK and $OEGMA_{8-9}$/VBK copolymerizations were similar to each other and were approximately 2 times less than reported $\langle k_P \rangle \langle K \rangle$ values for MMA/VBK and DMAEMA/VBK copolymerizations performed at similar conditions. The binary copolymer composition, in the studied compositional range, was also similar to that of MMA/VBK copolymerizations, indicating a preferential addition of VBK to itself relative to the respective methacrylate. MEO_2MA/$OEGMA_{8-9}$/VBK terpolymerizations with fixed VBK controller content and various MEO_2MA:$OEGMA_{8-9}$ ratios, resulted in controlled polymerizations and narrow molecular weight distributions (in most cases: $\bar{M}_w/\bar{M}_n < 1.3$). Depending on the final relative MEO_2MA:$OEGMA_{8-9}$ composition, the terpolymers exhibited various CPTs between ∼28−81 °C. Therefore, by tuning the composition, it is possible to tune the LCST of the resulting terpolymer. Finally, characteristic terpolymers were used to initiate a second terpolymerization of MEO_2MA/$OEGMA_{8-9}$/VBK, giving rise to block copolymers consisting of two distinct blocks characterized by different compositions of MEO_2MA to $OEGMA_{8-9}$. The block copolymers exhibited dual CPTs corresponding to each terpolymer segment. In summary, NMP permitted the synthesis of block copolymers where each block had a distinct MEO_2MA:$OEGMA_{8-9}$ composition, that yielded specific, tunable CPTs for each block between ∼28−81 °C. The inclusion of VBK as the "controlling" BlocBuilder-mediated monomer not only allowed the synthesis of such materials in a controlled fashion but also introduced thermo-responsive fluorescence into the final block copolymers.

ASSOCIATED CONTENT

Supporting Information

Gel permeation chromatograms. This material is available free of charge via the Internet at http://pubs.acs.org.

AUTHOR INFORMATION

Corresponding Author

*Telephone: (514) 398-4272. Fax: (515) 398-6678. E-mail: milan.maric@mcgill.ca.

Notes

The authors declare no competing financial interest.

ACKNOWLEDGMENTS

The authors thank the NSERC Discovery Grant for financial support. They also thank NSERC for the Alexander Graham Bell CGS fellowship given to B.L. The authors also thank Bruce Lennox for the use of his temperature-modulated UV−vis spectrometer and fluorescence spectrophotometer, along with Dr. Paul Gaudet for his aid in training on the use of these devices. We also thank Scott Schmidt and Noah Macy of Arkema, Inc., for their help in obtaining BlocBuilder and SG1.

REFERENCES

(1) Wei, H.; Zhang, X.; Cheng, C.; Cheng, S.-X.; Zhuo, R.-X. *Biomaterials* **2007**, *28*, 99.
(2) Kedar, U.; Phutane, P.; Shidhaye, S.; Kadam, V. *Nanomed. Nanotechnol. Biol. Med.* **2010**, *6*, 714.
(3) Ryu, S.; Yoo, I.; Song, S.; Yoon, B.; Kim, J.-M. *J. Am. Chem. Soc.* **2009**, *131*, 3800.
(4) Shimada, T.; Ookubo, K.; Komuro, N.; Shimizu, T.; Uehara, N. *Langmuir* **2007**, *23*, 11225.
(5) Pietsch, C.; Schubert, U. S.; Hoogenboom, R. *Chem. Commun.* **2011**, *47*, 8750.
(6) McDonagh, C.; Burke, C. S.; MacCraith, B. D. *Chem. Rev.* **2008**, *108*, 400.
(7) Wolfbeis, O. S. *Adv. Mater.* **2008**, *20*, 3759.
(8) Ionov, L.; Diez, S. *J. Am. Chem. Soc.* **2009**, *131*, 13315.
(9) Akimoto, J.; Nakayama, M.; Sakai, K.; Okano, T. *Biomacromolecules* **2009**, *10*, 1331.
(10) Pasparakis, G.; Cockayne, A.; Alexander, C. *J. Am. Chem. Soc.* **2007**, *129*, 11014.
(11) Wang, S.; Cheng, Z.; Zhu, J.; Zhang, Z.; Zhu, X. *J. Polym. Sci., Part A: Polym. Chem.* **2007**, *45*, 5318.
(12) Topp, M.; Dijkstra, P.; Talsma, H.; Feijen, J. *Macromolecules* **1997**, *30*, 8518.
(13) Suchao-in, N.; Chirachanchai, S.; Perrier, S. B. *Polymer* **2009**, *50*, 4151.
(14) Chang, C.; Wei, H.; Feng, J.; Wang, Z.-C.; Wu, X.-J.; Wu, D.-Q.; Cheng, S.-X.; Zhang, X.-Z.; Zhuo, R.-X. *Macromolecules* **2009**, *42*, 4838.
(15) Fournier, D.; Hoogenboom, R.; Thijs, H. M. L.; Paulus, R. M.; Schubert, U. S. *Macromolecules* **2007**, *40*, 915.
(16) Chiu, Y.-C.; Kuo, C.-C.; Hsu, J.-C.; Chen, W.-C. *ACS Appl. Mater. Interfaces* **2010**, *2*, 3340.
(17) Burillo, G.; Bucio, E.; Arenas, E.; Lopez, G. P. *Macromol. Mater. Eng.* **2007**, *292*, 214.
(18) Lessard, B.; Marić, M. *J. Polym. Sci., Part A: Polym. Chem.* **2011**, *49*, 5270.
(19) París, R.; Quijada-Garrido, I. *Eur. Polym. J.* **2010**, *46*, 2156.
(20) Li, J.; He, W.-D.; Han, S.-c.; Sun, X.-l.; Li, L.-y.; Zhang, B.-y. *J. Polym. Sci., Part A: Polym. Chem.* **2009**, *47*, 786.
(21) Kotsuchibashi, Y.; Ebara, M.; Yamamoto, K.; Aoyagi, T. *J. Polym. Sci., Part A: Polym. Chem.* **2010**, *48*, 4393.
(22) Kotsuchibashi, Y.; Yamamoto, K.; Aoyagi, T. *J. Colloid Interface Sci.* **2009**, *336*, 67.
(23) Xie, D.; Ye, X.; Ding, Y.; Zhang, G.; Zhao, N.; Wu, K.; Cao, Y.; Zhu, X. X. *Macromolecules* **2009**, *42*, 2715.
(24) Skrabania, K.; Kristen, J.; Laschewsky, A.; Akdemir, Ö.; Hoth, A.; Lutz, J.-F. *Langmuir* **2006**, *23*, 84.
(25) Arotçaréna, M.; Heise, B.; Ishaya, S.; Laschewsky, A. *J. Am. Chem. Soc.* **2002**, *124*, 3787.
(26) Dimitrov, I.; Trzebicka, B.; Müller, A. H. E.; Dworak, A.; Tsvetanov, C. B. *Prog. Polym. Sci.* **2007**, *32*, 1275.
(27) Weiss, J.; Bottcher, C.; Laschewsky, A. *Soft Matter* **2011**, *7*, 483.
(28) Hua, F.; Jiang, X.; Zhao, B. *Macromolecules* **2006**, *39*, 3476.
(29) Lutz, J.-F. *J. Polym. Sci., Part A: Polym. Chem.* **2008**, *46*, 3459.
(30) Lutz, J.; Akdemir, Ö.; Hoth, A. *J. Am. Chem. Soc.* **2006**, *128*, 13046.
(31) Lutz, J.-F.; Hoth, A. *Macromolecules* **2006**, *39*, 893.

(32) Lutz, J.-F. *Adv. Mater.* **2011**, *23*, 2237.
(33) Becer, C.; Hahn, S.; Fijten, M. W. M.; Thijs, H. M. L.; Hoogenboom, R.; Schubert, U. S. *J. Polym. Sci., Part A: Polym. Chem.* **2008**, 7138.
(34) Pietsch, C.; Fijten, M. W. M.; Lambermont-Thijs, H. M. L.; Hoogenboom, R.; Schubert, U. S. *J. Polym. Sci., Part A: Polym. Chem.* **2009**, *47*, 2811.
(35) Jochum, F. D.; zur Borg, L.; Roth, P. J.; Theato, P. *Macromolecules* **2009**, *42*, 7854.
(36) Jochum, F. D.; Roth, P. J.; Kessler, D.; Theato, P. *Biomacromolecules* **2010**, *11*, 2432.
(37) Hawker, C. J.; Bosman, A. W.; Harth, E. *Chem. Rev.* **2001**, *101*, 3661.
(38) Grubbs, R. *Polym. Rev.* **2011**, *51*, 104.
(39) Chenal, M.; Mura, S.; Marchal, C.; Gigmes, D.; Charleux, B.; Fattal, E.; Couvreur, P.; Nicolas, J. *Macromolecules* **2010**, *43*, 9291.
(40) Benoit, D.; Chaplinski, V.; Braslau, R.; Hawker, C. J. *J. Am. Chem. Soc.* **1999**, *121*, 3904.
(41) Benoit, D.; Grimaldi, S.; Robin, S.; Finet, J.-P.; Tordo, P.; Gnanou, Y. *J. Am. Chem. Soc.* **2000**, *122*, 5929.
(42) Lacroix-Desmazes, P.; Lutz, J.-F.; Chauvin, F.; Severac, R.; Boutevin, B. *Macromolecules* **2001**, *34*, 8866.
(43) Lessard, B.; Graffe, A.; Maric, M. *Macromolecules* **2007**, *40*, 9284.
(44) Lessard, B.; Maric, M. *Macromolecules* **2008**, *41*, 7870.
(45) Lessard, B.; Schmidt, S. C.; Maric, M. *Macromolecules* **2008**, *41*, 3446.
(46) Charleux, B.; Nicolas, J.; Guerret, O. *Macromolecules* **2005**, *38*, 5485.
(47) Dire, C.; Belleney, J.; Nicolas, J.; Bertin, D.; Magnet, S.; Charleux, B. *J. Polym. Sci., Part A: Polym. Chem.* **2008**, *46*, 6333.
(48) Nicolas, J.; Dire, C.; Mueller, L.; Belleney, J.; Charleux, B.; Marque, S. R. A.; Bertin, D.; Magnet, S.; Couvreur, L. *Macromolecules* **2006**, *39*, 8274.
(49) Nicolas, J.; Mueller, L.; Dire, C.; Matyjaszewski, K.; Charleux, B. *Macromolecules* **2009**, *42*, 4470.
(50) Lessard, B.; Maric, M. *J. Polym. Sci., Part A: Polym. Chem.* **2009**, *47*, 2574.
(51) Moayeri, A.; Lessard, B.; Maric, M. *Polym. Chem.* **2011**, *2*, 2084.
(52) Lessard, B.; Tervo, C.; De Wahl, S.; Clerveaux, F. J.; Tang, K. K.; Yasmine, S.; Andjelic, S.; D'Alessandro, A.; Maric, M. *Macromolecules* **2010**, *43*, 868.
(53) Zhang, C.; Lessard, B.; Maric, M. *Macromol. React. Eng.* **2010**, *4*, 415.
(54) Dire, C.; Charleux, B.; Magnet, S.; Couvreur, L. *Macromolecules* **2007**, *40*, 1897.
(55) Nicolas, J.; Couvreur, P.; Charleux, B. *Macromolecules* **2008**, *41*, 3758.
(56) Dire, C.; Nicolas, J.; Brusseau, S.; Charleux, B.; Magnet, S.; Couvreur, L. In *Controlled/Living Radical Polymerization: Progress in RAFT, DT, NMP & OMRP*; American Chemical Society: Washington, DC, 2009; Vol. *1024*, p 303.
(57) Belleney, J.; Magnet, S.; Couvreur, L.; Charleux, B. *Polym. Chem.* **2010**, *1*, 720.
(58) Chenal, M.; Boursier, C.; Guillaneuf, Y.; Taverna, M.; Couvreur, P.; Nicolas, J. *Polym. Chem.* **2011**, *2*, 1523.
(59) Nicolas, J.; Brusseau, S.; Charleux, B. *J. Polym. Sci., Part A: Polym. Chem.* **2010**, *48*, 34.
(60) Lessard, B.; Ling, E. J. Y.; Morin, M. S. T.; Maric, M. *J. Polym. Sci., Part A: Polym. Chem.* **2011**, *49*, 1033.
(61) Becer, C. R.; Kokado, K.; Weber, C.; Can, A.; Chujo, Y.; Schubert, U. S. *J. Polym. Sci., Part A: Polym. Chem.* **2010**, *48*, 1278.
(62) Hua, F.; Jiang, X.; Li, D.; Zhao, B. *J. Polym. Sci., Part A: Polym. Chem.* **2006**, *44*, 2454.
(63) Zhang, W.; Yan, Y.; Zhou, N.; Cheng, Z.; Zhu, J.; Xia, C.; Zhu, X. *Eur. Polym. J.* **2008**, *44*, 3300.
(64) Siegmann, R.; Jeličić, A.; Beuermann, S. *Macromol. Chem. Phys.* **2010**, *211*, 546.
(65) García, N.; Tiemblo, P.; Guzmán, J. *Macromolecules* **2007**, *40*, 4802.
(66) Mayo, F. R.; Lewis, F. M. *J. Am. Chem. Soc.* **1944**, *66*, 1594.

Macromolecules

Article

pubs.acs.org/Macromolecules

Crystallization Behavior and Crystal Orientation of Poly(ε-caprolactone) Homopolymers Confined in Nanocylinders: Effects of Nanocylinder Dimension

Shintaro Nakagawa,[†] Ken-ichi Kadena,[†] Takashi Ishizone,[†] Shuichi Nojima,*[,†] Takafumi Shimizu,[‡] Kazuo Yamaguchi,[‡,§] and Seiichi Nakahama[§]

[†]Department of Organic and Polymeric Materials, Graduate School of Science and Engineering, Tokyo Institute of Technology, H-125, 2-12-1 Ookayama Meguro-Ku, Tokyo 152-8552, Japan

[‡]Department of Chemistry, Faculty of Science, Kanagawa University, Hiratsuka, Kanagawa 259-1293, Japan

[§]Research Institute for Photofunctionalized Materials, Kanagawa University, Hiratsuka, Kanagawa 259-1293, Japan

Supporting Information

ABSTRACT: The crystallization behavior and crystal orientation of poly(ε-caprolactone) (PCL) homopolymers and PCL blocks spatially confined in identical nanocylinders have been investigated using differential scanning calorimetry (DSC) and two-dimensional wide-angle X-ray diffraction (WAXD) as a function of cylinder diameter D. The PCL homopolymers confined in nanocylinders were prepared using microphase separation of PCL-*block*-polystyrene (PCL-*b*-PS) copolymers with a photocleavable *o*-nitrobenzyl group (ONB) between PCL and PS blocks and the subsequent cleavage of ONB by irradiating UV light. The time evolution of PCL crystallinity χ_{PCL} showed a first-order kinetics for both PCL blocks and PCL homopolymers confined in all the nanocylinders investigated. However, the D dependence of crystallization rates for PCL blocks was more drastic than that for PCL homopolymers, and consequently various D-dependent interrelations were observed between crystallization rates of PCL blocks and PCL homopolymers. The crystal orientation was also dependent on D; the *b*-axis of PCL crystals oriented parallel to the cylinder axis both for PCL blocks and PCL homopolymers confined in the nanocylinder with D = 13.0 nm, whereas the (110) plane of PCL crystals was normal to the cylinder axis in the nanocylinders with $D \geq 14.9$ nm. The difference in the degree of crystal orientation was not detected between PCL blocks and PCL homopolymers confined in nanocylinders with $D \geq 14.9$ nm.

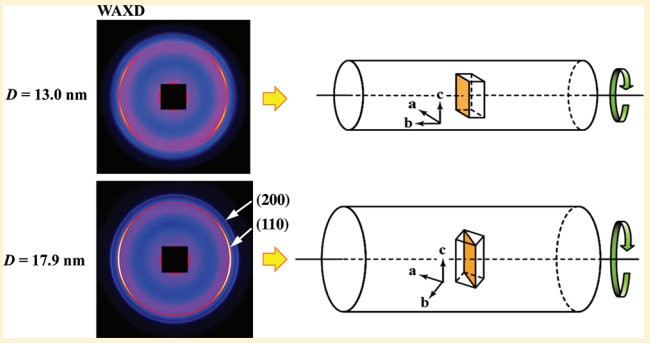

1. INTRODUCTION

When flexible polymers are spatially confined in isolated nanodomains (e.g., nanocylinders or nanospheres), they sometimes show peculiar dynamic behaviors as compared with those without spatial confinement. Crystallization is one of the dynamic behaviors or self-organization processes widely observed in polymer systems, and it is known, for example from the studies on confined crystallization of block copolymers,[1−3] that the crystallization behavior depends significantly on the geometry and dimension of isolated nanodomains.

The crystallization behavior and crystal orientation of homopolymers confined in isolated nanocylinders were first investigated using anode aluminum oxide (AAO) with largely varying cylinder diameters.[4−10] These results indicate a variety of crystallization behaviors and crystal orientations depending on the diameter, crystallization temperature, and molecular weight of constituent homopolymers. For example, Shin et al.[7] investigated the characteristics of lamellar crystals (i.e., thickness, crystallinity, and orientation) for confined polyethylene (PE) homopolymers and concluded that the cylinder diameter affected the lamella thickness and crystallinity of PE crystals, though they always showed preferential orientation in nanocylinders. The crystallization behavior of homopolymers confined in nanocylinders was also pursued using computer simulation,[11−15] where a characteristic crystallization process, i.e., a transient increase in the degree of crystal orientation, was predicted at the early stage of crystallization.[15]

Isolated nanodomains can be also prepared using microphase separation of block copolymers, where the crystalline block is spatially confined in nanodomains with the dimension comparable to the molecular size. Several kinds of crystalline−amorphous diblock copolymers have been used so far[16−28] to investigate the characteristic crystallization of confined blocks, and the crystallization behavior and resulting crystal orientation are explained in terms of the geometry and dimension of confined nanodomains. For example, Chung et al. investigated[28] the crystal

Received: November 24, 2011
Revised: January 4, 2012
Published: February 10, 2012

Table 1. Molecular Charateristics of PCL-*b*-PS Copolymers Used in This Study

sample code	M_n of PCL blocks[a] (g/mol)	M_n of PS blocks[a] (g/mol)	total M_n[a] (g/mol)	M_w/M_n[b]	PCL:PS (vol %)	morphology[c]	D[d] (nm)	p[e] (%)
PCL−PS1	7 900	24 100	32 000	1.05	25:75	cylinder	13.0	0
PCL/PS1	7 900	24 100	32 000	1.05	25:75	cylinder	13.0	80
PCL−PS2	9 400	27 900	37 300	1.03	25:75	cylinder	14.9	0
PCL/PS2	9 400	27 900	37 300	1.03	25:75	cylinder	14.9	86
PCL−PS3	12 400	48 900	61 300	1.03	20:80	cylinder	17.9	0
PCL/PS3	12 400	48 900	61 300	1.03	20:80	cylinder	17.9	86
PCL−PS4	22 600	70 000	92 600	1.08	24:76	cylinder	27.0	0
PCL/PS4	22 600	70 000	92 600	1.08	24:76	cylinder	27.0	82

[a]Determined by ^{1}H NMR. [b]Determined by GPC. [c]Observed using 1D-SAXS and/or TEM. [d]Cylinder diameter calculated from the primary peak position in 1D-SAXS curves and the vol % of PCL blocks. [e]Maximum photocleavage yield obtained by GPC.

orientation of poly(ε-caprolactone) (PCL) blocks in PCL-*block*-poly(4-vinylprydine) (PCL-*b*-P4VP) copolymers as a function of nanocylinder diameter and concluded that the *b*-axis of PCL crystals (i.e., fastest growth axis) oriented parallel to the cylinder axis in larger cylinders, whereas randomly oriented PCL crystals were formed in smaller cylinders.

It is easily supposed that the crystallization of block chains confined in isolated nanodomains is restricted by two factors: (1) *space confinement*, i.e., the crystalline blocks are spatially confined within curved nanodomains, and (2) *chain confinement*, i.e., the crystalline blocks are inherently tethered with the nanodomain interface at the chain end. For understanding the effects of two confinements separately on crystallization, we prepared poly(δ-valerolactone) (PVL) or poly(ε-caprolactone) (PCL) homopolymers confined in isolated nanodomains surrounded with amorphous polystyrene (PS) matrices[29,30] because the chain confinement does not work during crystallization of confined homopolymers. A photocleavable *o*-nitrobenzyl group (ONB) was introduced between different blocks in PVL-*b*-PS or PCL-*b*-PS to prepare such systems and then cleaved by irradiating UV light after microphase separation. The crystallization behavior and crystal orientation of confined homopolymers were compared with those of block chains just before photocleavage. We found from these studies that the crystallization of both PVL blocks and PVL homopolymers confined in an identical nanodomain was controlled by the first-order kinetics, and the initial crystallization rate of PVL blocks was slightly faster than that of PVL homopolymers though the final crystallinity of PVL homopolymers was significantly higher than that of PVL blocks. Furthermore, we studied the crystal orientation of PCL blocks and PCL homopolymers both confined in an identical nanocylinder and concluded that the PCL lamellar crystals oriented preferentially in nanocylinders irrespective of crystallization temperature T_c for two cases. However, the degree of crystal orientation increased remarkably for PCL homopolymers with increasing T_c while it improved slightly for PCL blocks, yielding a large difference in the PCL crystal orientation between two chains at higher T_c (≥−45 °C).

In this study, we investigate the crystallization behavior and crystal orientation of PCL blocks and PCL homopolymers both confined in identical nanocylinders as a function of cylinder diameter D. This is because many studies on the crystallization of block chains confined in nanocylinders have revealed that the lateral dimension of nanocylinders considerably affects the crystallization behavior and crystal orientation. From the experimental results, we elucidate the effects of space confinement and chain confinement on the crystallization of long chains confined in nanocylinders with various dimensions.

2. EXPERIMENTAL SECTION

2.1. Samples and Sample Preparation. The samples used in this study are poly(ε-caprolactone)-*block*-polystyrene (PCL-*b*-PS) diblock copolymers with a photocleavable *o*-nitrobenzyl group (ONB) between PCL and PS blocks. The photocleavage reaction of ONB in PCL-*b*-PS is shown in our previous publication.[30] It should be noted that several kinds of photocleavable block copolymers are recently synthesized and used for various studies on nanostructured polymer materials.[31−37] We synthesized four PCL-*b*-PS copolymers with different cylinder diameters. The results of molecular characterization are summarized in Table 1, where "PCL−PS" in the sample code represents the normal block copolymer before photocleavage, and "PCL/PS" represents the sample after photocleavage, i.e., the binary system with PCL homopolymers spatially confined in PS matrices. The vol % of PCL blocks in all the samples, calculated from the ^{1}H NMR results and the specific volumes of PS[38] and PCL[39] homopolymers, is 20−25%, from which we expect the cylindrical microdomain structure with the PCL block inside. PCL−PS1 was used in our previous study,[30] and PCL−PS2, PCL−PS3, and PCL−PS4 were newly synthesized for the present study to investigate the D dependence of the crystallization behavior and crystal orientation for PCL blocks and PCL homopolymers. Unfortunately, the amount of PCL−PS4 was not enough, and we could obtain the melting temperature and crystallinity of PCL chains in PCL−PS4 and PCL/PS4 but not investigate the crystallization behavior and crystal orientation of PCL chains.

The glass transition temperature of PS matrices T_g is ca. 100 °C and the melting temperature of PCL blocks confined in nanocylinders is ca. 40−55 °C (Figure 2), so that vitrification of PS matrices will prevent macrophase separation between PCL and PS homopolymers after photocleavage, and eventually we can prepare PCL homopolymers confined in nanocylinders embedded in the PS matrix. It is, therefore, possible to repeatedly crystallize and melt the PCL homopolymers by always keeping the sample temperatures below T_g.

We prepared two kinds of samples by the solution-casting method using toluene; thin films with the thickness of ca. 50 μm to observe the crystallization behavior using differential scanning calorimetry (DSC) and thick films with the thickness of ca. 0.7 mm to investigate the crystal orientation using two-dimensional small-angle X-ray scattering (2D-SAXS) and 2D wide-angle X-ray diffraction (2D-WAXD). This is because the 2D-SAXS and 2D-WAXD methods need thicker samples to get enough scattering intensity, but a pile of thin films may lead to the misorientation of nanocylinders existing in the sample. The detailed method to orient nanocylinders is described in our previous publication.[30]

2.2. Photocleavage. The block junction (i.e., *o*-nitrobenzyl group) was cleaved by irradiating UV light with wavelength longer than 300 nm (USHIO Optical Modulex, USH-500SC) to get PCL homopolymers confined in nanocylinders surrounded with glassy PS homopolymers, which were originally formed by microphase separation of PCL-*b*-PS copolymers. This photocleavage process is completely irreversible; that is, once the block junction is broken it never recombines into the copolymer.[31]

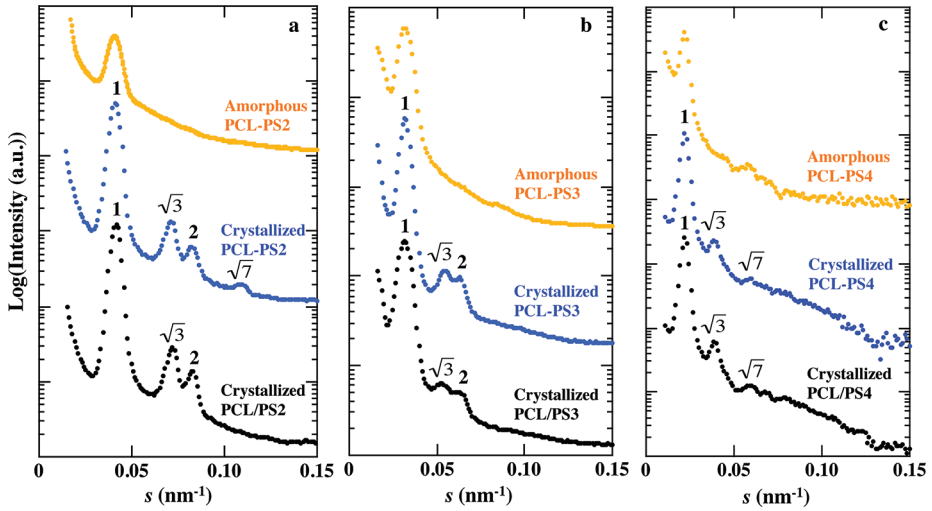

Figure 1. 1D-SAXS curves of PCL−PS2 and PCL/PS2 (a), PCL−PS3 and PCL/PS3 (b), and PCL−PS4 and PCL/PS4 (c) at amorphous and crystallized states indicated. The SAXS curves of uncleaved samples (yellow and blue curves) are shifted upward for legibility.

We used two irradiation conditions depending on the film thickness: 1 W/cm^2 and 1 h for the thin film and 10 W/cm^2 and 40 h for the thick film. The samples before and after UV irradiation were examined using gel permeation chromatography (GPC) to get the photocleavage yield of block copolymers, which was evaluated from the ratio of GPC peak areas for PCL-*b*-PS copolymers and PS homopolymers (see Figure S1 in Supporting Information). The yield shown in Table 1 is less than 100% for every case, which does not imply that the system has two nanocylinders, one consisting of PCL homopolymers and the other PCL blocks, but the uncleaved PCL blocks will be uniformly distributed in every nanocylinder, as described in our previous publications.[29,30]

2.3. Differential Scanning Calorimetry (DSC) Measurements. A Perkin-Elmer DSC Diamond was used with a heating rate of 10 °C/min to obtain the melting temperature of PCL chains and the glass transition temperature of PS chains and also evaluate the crystallinity of PCL chains χ_{PCL} as a function of crystallization time at several crystallization temperatures. The value of χ_{PCL} was calculated from the melting endothermic peak area assuming that the heat of fusion for perfect PCL crystals was 135 J/g.[39]

2.4. One-Dimensional Small-Angle X-ray Scattering (1D-SAXS) Measurements. First of all, the microdomain structure formed in the amorphous and crystallized PCL-*b*-PS copolymers was investigated using 1D-SAXS with synchrotron radiation, which was performed at Photon Factory in High Energy Accelerator Research Organization, Tsukuba Japan, with a small-angle X-ray equipment for solution installed at beamline BL-10C. Details of the equipment and the instrumentation are already described.[40−42] The scattered intensity was recorded with a one-dimensional position-sensitive proportional counter (PSPC), by which isotropic scattering from the sample was obtained as a function of s (= $(2/\lambda)[\sin\theta]$; λ, X-ray wavelength (= 0.1488 nm); 2θ, scattering angle). The cylinder diameter D was calculated from the angular position of the primary peak in SAXS curves and the vol % of PCL blocks existing in the system.

2.5. Two-Dimensional SAXS (2D-SAXS) and Wide-Angle X-ray Diffraction (2D-WAXD) Measurements. The orientation of nanocylinders was verified with 2D-SAXS and the PCL crystal orientation in oriented nanocylinders was measured by 2D-WAXD, both using Rigaku Nanoviewer with a rotating anode X-ray generator operating at 45 kV and 60 mA. The wavelength used was 0.1542 nm of Cu Kα radiation. The detector of both measurements was an image plate (FUJI Film BAS-SR 127) with the size of 10 × 10 cm^2, and the accumulation time was 6−12 h depending on the sample. The azimuthal plots of the (110) and (200) reflections arising from PCL crystals (Figure 8) were derived after subtracting the amorphous halo from PS and uncrystallized PCL chains, and the degree of PCL crystal orientation[43] was evaluated as a function of D for PCL blocks and PCL homopolymers crystallized at different crystallization temperatures.

3. RESULTS AND DISCUSSION

3.1. Characterization of Nanocylinders. Figure 1 shows the 1D-SAXS curves measured at room temperature for PCL−PS2 (and PCL/PS2) (a), PCL−PS3 (PCL/PS3) (b), and PCL−PS4 (PCL/PS4) (c) in amorphous and crystallized states, where the crystallized samples were obtained by annealing at −50 °C for 4 h in advance because the crystallization of PCL blocks does not take place at room temperature. The 1D-SAXS curves from amorphous and crystallized PCL−PS1 are already presented,[30] which are similar to those from PCL−PS2 except that the primary peak position shifts moderately to larger s due to the lower molecular weight of PCL−PS1. The SAXS intensity from amorphous samples (yellow curves) is weak, and the higher-order peaks cannot be observed, which is ascribed to the small difference in electron density between amorphous PS (332 e/nm^3 below 100 °C[38]) and amorphous PCL (354 e/nm^3 at 25 °C[39]). When the PCL blocks are crystallized (blue curves), the PCL nanocylinders have heterogeneous electron density distribution with PCL crystals (393 e/nm^3[39]) and amorphous PCL, so that we have the strong SAXS intensity with clear higher-order scattering peaks. These peak positions correspond exactly to a ratio of $1:\sqrt{3}:2:(\sqrt{7})$, indicating that the cylindrical microdomain structure is formed. Judging from the vol % of PCL blocks in the system (20−25 vol % in Table 1), the nanocylinder consists of PCL blocks surrounded with the PS matrix. In addition, we can find that the SAXS curves from photocleaved samples (black curves) are substantially identical with those from crystallized block copolymers (blue curves), meaning the nanocylinder is completely preserved after photocleavage, and therefore the PCL homopolymers are spatially confined within identical nanocylinders in which the PCL blocks have been confined before photocleavage. The formation of nanocylinders in PCL−PS1 was also verified using transmission electron microscopy (TEM) in our previous study.[30]

The diameter of nanocylinders D for each sample was evaluated from the primary peak position in SAXS curves and the vol % of PCL blocks in the system and found to be 13.0 nm for PCL−PS1 (and also PCL/PS1), 14.9 nm for PCL−PS2 (PCL/PS2), 17.9 nm for PCL−PS3 (PCL/PS3), and 27.0 nm for

PCL−PS4 (PCL/PS4), as summarized in Table 1. It should be noted that D changes linearly with $M_n^{2/3}$ (M_n: total molecular weight of copolymers) after the minor correction of composition,[44] though the molecular weight range is not sufficiently wide.

3.2. Melting Temperature and Crystallinity of PCL Blocks and PCL Homopolymers. We reported in our previous study on a poly(δ-varelolactone)-*block*-polystyrene (PVL-*b*-PS) copolymer[29] that the melting temperature and crystallinity of PVL chains were almost constant irrespective of crystallization temperature T_c in the limited T_c range and concluded that the space confinement did not permit additional crystallization at the late stage (e.g., lamella thickening) as usually observed in the crystallization of bulk homopolymers. This fact is also true for the present systems in the limited T_c range ($-60\ ^\circ C \le T_c \le -48\ ^\circ C$ for PCL−PS1, $-50\ ^\circ C \le T_c \le -40\ ^\circ C$ for PCL−PS2 and PCL−PS3, and $-40\ ^\circ C \le T_c \le -20\ ^\circ C$ for PCL−PS4), and therefore it is possible to directly compare the melting temperature and crystallinity of PCL chains in each sample crystallized at different T_c. It should be noted that the crystallizable temperature is extremely low as compared with bulk PCL homopolymers (i.e., $T_c \sim 40\ ^\circ C$[45]) and not so different among PCL−PS1, PCL−PS2, and PCL−PS3, from which we can expect that all the PCL blocks (as well as PCL homopolymers) crystallize by the same crystallization mechanism which is substantially different from the mechanism in bulk PCL homopolymers, as described in sections 3.3 and 3.4.

Figure 2 shows the melting temperature $T_{m,PCL}$ (a) and crystallinity χ_{PCL} (b) of PCL blocks and PCL homopolymers

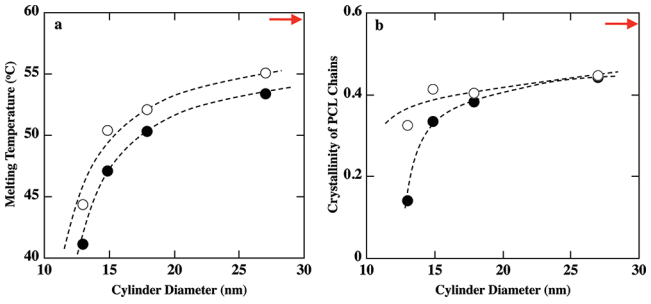

Figure 2. Melting temperature (a) and crystallinity (b) of PCL blocks (closed circle) and PCL homopolymers (open circle) plotted against cylinder diameter. The red arrows indicate the results of bulk PCL homopolymers (M_n = 11 000) crystallized at 40 °C for 300 min.[45] The dashed curves are a guide for the eye only.

plotted against D. The red arrows in Figure 2 indicate the results of bulk PCL homopolymers (M_n = 11 000) without space confinement,[45] from which we find that the space confinement seriously affects the melting temperature and crystallinity of PCL chains. We find from Figure 2a that $T_{m,PCL}$ decreases steeply with decreasing D for both chains. Because the melting temperature of bulk homopolymers is, in general, related intimately to the thickness of lamellar crystals, the large decrease in $T_{m,PCL}$ suggests that the lateral dimension of confined cylinders critically controls the PCL lamella thickness, in particular, at smaller D ($\le$14.9 nm). This fact is consistent with the previous reports on cylindrically confined block chains, where the smaller (and therefore thinner) crystals are formed at smaller D.[7,23,28] In addition, Figure 2a shows that $T_{m,PCL}$ of PCL homopolymers is always higher than that of PCL blocks in every sample, suggesting more restriction is imposed on the crystallization of PCL blocks as compared with that of PCL homopolymers.

We find from Figure 2b that the difference in χ_{PCL} is very large between PCL blocks and PCL homopolymers at D = 13.0 nm, which is mainly ascribed to the extremely small χ_{PCL} for PCL−PS1. However, this difference is considerably reduced with increasing D to be negligibly small at $D \ge 17.9$ nm, suggesting that the tethering effect of PCL blocks on χ_{PCL} is prominent only at extremely small D. It is known from the studies on the crystallization of block chains confined in nanocylinders[28] and of homopolymers confined in AAO[8] that the final crystallinity of constituent chains is intimately related to the crystal orientation, and this orientation is mainly driven by the crystallization mechanism in confined space. Therefore, it is necessary to observe the crystallization behavior and crystal orientation of PCL blocks and PCL homopolymers and try to find the relationship between them.

3.3. Crystallization Behavior of PCL Blocks and PCL Homopolymers. The process of isothermal crystallization was pursued using DSC for PCL blocks and PCL homopolymers confined in various nanocylinders. Figure 3 shows the typical

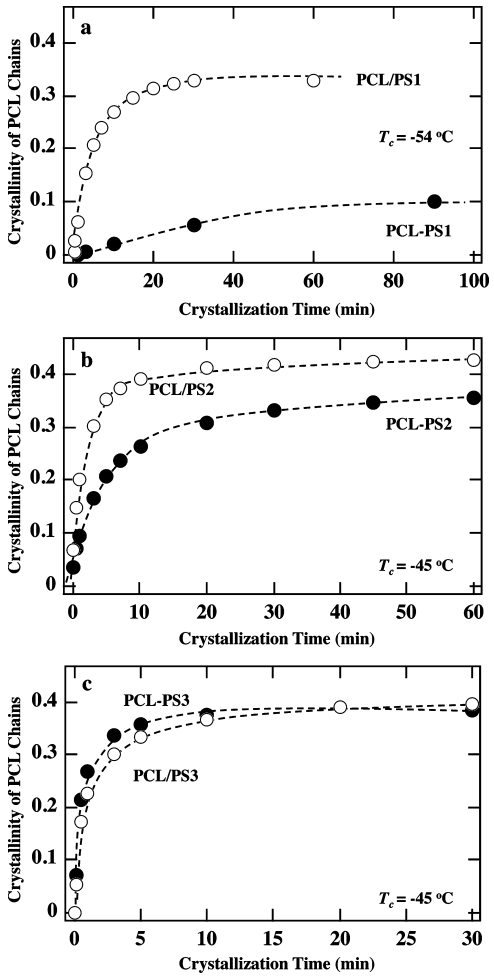

Figure 3. Crystallinity of PCL blocks (closed circles) and PCL homopolymers (open circles) plotted against crystallization time for PCL−PS1 and PCL/PS1 (a), PCL−PS2 and PCL/PS2 (b), and PCL−PS3 and PCL/PS3 (c). The crystallization temperature T_c is indicated in each panel. The dashed curves are a guide for the eye only.

time evolution of χ_{PCL} for three samples, where T_c is chosen in such a way that the crystallization rates of PCL homopolymers are comparable. The time evolution of χ_{PCL} is extremely

dx.doi.org/10.1021/ma202566f | Macromolecules 2012, 45, 1892−1900

different between PCL blocks in PCL−PS1 and PCL homopolymers in PCL/PS1 (Figure 3a); χ_{PCL} increases very slowly for PCL blocks and reaches the small crystallinity (~0.15) even after a long time (>300 min), whereas χ_{PCL} for PCL homopolymers increases steeply at the early stage followed by an asymptotic increase, yielding a large difference in the final χ_{PCL} between two chains (Figure 2b). However, the crystallization rate is improved remarkably for PCL blocks in PCL−PS2, and the time evolution of χ_{PCL} is similar to that for PCL homopolymers in PCL/PS2 to result in a moderate difference in the crystallization rate between two chains (Figure 3b). On the contrary, χ_{PCL} of PCL blocks in PCL−PS3 is slightly larger than that of PCL homopolymers in PCL/PS3 at the early stage (Figure 3c). This result is qualitatively similar to that previously reported on the crystallization of PVL blocks and PVL homopolymers confined in an identical nanocylinder (D = 15.7 nm),[29] where we speculated that the chain confinement (i.e., tethering effect of block chains) accelerated nucleation to yield the increasing crystallization rate of PVL blocks as compared with that of PVL homopolymers.

It is surprising that the interrelation of crystallization rates between PCL blocks and PCL homopolymers confined in identical nanocylinders depends drastically on D, as shown in Figure 3, and this is one of the new findings in the present study. This D dependence can be explained successfully by considering two factors simultaneously working on the formation of critical nuclei (or nucleation) during crystallization: (1) decelerated chain mobility of PCL blocks and PCL homopolymers due to the space confinement and (2) accelerated nucleation of PCL blocks due to the chain confinement.

The space confinement is very effective at smaller D to considerably slow down the mobility of PCL blocks and PCL homopolymers, and the chain confinement moreover decelerates the mobility of PCL blocks to yield a significant difference in the mobility between two chains. That is, the chain mobility of PCL blocks in PCL−PS1 is unusually reduced due to the combination of two confinements to result in extremely slow nucleation, whereas the PCL homopolymers in PCL/PS1 have the moderate mobility and the time necessary for nucleation is fairly shorter than that of PCL blocks. Consequently, we have a large difference in the time evolution of χ_{PCL} between two chains at D = 13.0 nm (Figure 3a). The effect of space confinement grows weak with increasing D to gradually recover the chain mobility, and accordingly the nucleation rate increases steadily for both PCL blocks and PCL homopolymers. As a result, χ_{PCL} of PCL blocks in PCL−PS2 increases steeply at the early stage, though the chain confinement still works effectively to moderately reduce the chain mobility of PCL blocks, yielding the slower crystallization rate as compared with that of PCL homopolymers in PCL/PS2 (Figure 3b). The effect of space confinement is further reduced at D = 17.9 nm to have sufficient chain mobility to form the critical nucleus. In this case, the chain confinement is advantageous to nucleation because the tethered chain end is slower-moving, which is favorable to form the crystal embryo. Consequently the crystallization rate of PCL blocks is larger than that of PCL homopolymers at D = 17.9 nm (Figure 3c), though the final χ_{PCL} of PCL homopolymers is slightly higher than that of PCL blocks (Figure 2b), probably because of a variety of crystal growth modes for PCL homopolymers.[12]

3.4. Analysis of Crystallization Behavior. The time evolution of χ_{PCL} shown in Figure 3 for PCL blocks and PCL homopolymers is completely different from the sigmoidal evolution usually observed in homopolymer crystallization without space confinement.[45] That is, we detect no induction time just before crystallization in Figure 3 even if the whole crystallization process is extremely slow. This crystallization process is generally approximated with the first-order kinetics,[29] where it is assumed that nucleation controls the crystallization process because of the instantaneous crystal growth within isolated nanodomains. This fact is verified using several crystalline blocks confined in spherical or cylindrical nanodomains,[46−48] where the crystallization rate at crystallization time t_c is proportional to the uncrystallized fraction remaining at t_c. That is

$$\frac{d\chi'_{PCL}(t_c)}{dt_c} \propto 1 - \chi'_{PCL}(t_c)$$

where $\chi'_{PCL}(t_c)$ represents the normalized crystallinity of PCL chains at t_c, i.e., $\chi'_{PCL}(t_c) = \chi_{PCL}(t_c)/\chi_{PCL}(\infty)$. Therefore, the plot of $\ln\{1 - \chi'_{PCL}(t_c)\}$ against t_c should be linear, and the slope is proportional to the crystallization rate of this process, that is, the crystallization rate is larger as the slope is steeper.

Figure 4 shows the plot of $\ln\{1 - \chi'_{PCL}(t_c)\}$ against t_c for the data presented in Figure 3. We find a linear relationship for

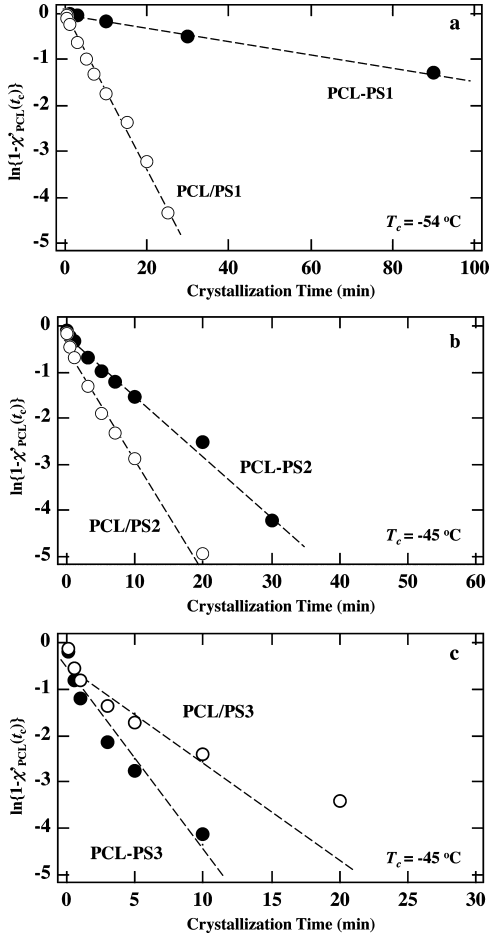

Figure 4. $\ln\{1 - \chi'_{PCL}(t_c)\}$ of PCL blocks (closed circles) and PCL homopolymers (open circles) plotted against crystallization time for PCL−PS1 and PCL/PS1 (a), PCL−PS2 and PCL/PS2 (b), and PCL−PS3 and PCL/PS3 (c). The dashed lines are best linear least-squares fit.

every case, indicating that nucleation controls the crystallization process in all samples. It should be noted that we have the

dx.doi.org/10.1021/ma202566f | Macromolecules 2012, 45, 1892−1900

moderate deviation from the linearity at the late stage crystallization of PCL blocks and PCL homopolymers at D = 17.9 nm (Figure 4c), for which the estimation of $\chi_{PCL}(\infty)$ may be responsible. Figure 5 shows the half-time of crystallization plotted

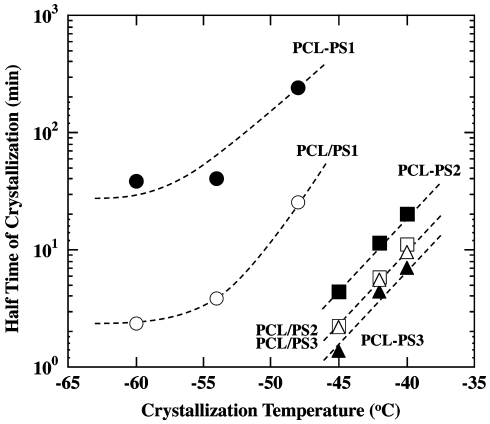

Figure 5. Half-time of crystallization plotted against crystallization temperature for PCL blocks in PCL−PS1, PCL−PS2, and PCL−PS3 (closed symbols) and PCL homopolymers in PCL/PS1, PCL/PS2, and PCL/PS3 (open symbols). The dashed curves are a guide for the eye only.

against T_c for all the samples investigated, where $\tau_{1/2}$ was evaluated from the slope k in Figure 4 through $\tau_{1/2} = -\ln 2/k$. The value of $\tau_{1/2}$ is a measure for the crystallization rate; it is larger as $\tau_{1/2}$ is smaller. It is clear from Figure 5 that the crystallization rate of PCL blocks and PCL homopolymers with D = 13.0 nm is extremely slow as compared with that of PCL chains with $D \geq$ 14.9 nm, suggesting that the space confinement works effectively on the crystallization at extremely small D. The effect of space confinement is gradually reduced, and eventually PCL homopolymers have sufficient mobility for nucleation when D reaches 14.9 nm, which is suggested by the fact that $\tau_{1/2}$ of PCL homopolymers in PCL/PS2 is almost equal to that in PCL/PS3. In addition to the space confinement, the chain confinement works on PCL blocks. It decelerates the overall chain mobility of PCL blocks in PCL−PS2 (D = 14.9 nm) to yield the slightly decreasing crystallization rate, whereas it accelerates nucleation at the tethering point (D = 17.9 nm) to increase the total crystallization rate, as discussed in section 3.3. It is also found from Figure 5 that the crystallization rate decreases significantly with increasing T_c for all PCL chains. This fact is reminiscent of the crystallization behavior observed in homopolymers without space confinement, for which the thermodynamic factor to make the critical embryo (e.g., the degree of supercooling) will be responsible.

3.5. Orientation of Nanocylinders. In order to investigate the crystal orientation of PCL chains confined in various nanocylinders using 2D-WAXD, it is necessary to uniaxially orient the nanocylinders existing in the system. This process was performed by applying the rotational shear to the block copolymers at 120 °C to obtain the disk samples with the diameter of ca. 20 mm and thickness of 0.7 mm, and the specimen for 2D-SAXS and 2D-WAXD experiments was cut out from the disk. The 2D-SAXS measurements were carried out at room temperature to verify the uniaxial orientation of nanocylinders after crystallization of PCL chains at −50 °C to enhance the X-ray contrast between the nanocylinder and matrix.

Figure 6 shows the 2D-SAXS patterns of crystallized PCL−PS3 (upper panels) and PCL/PS3 (lower panels) when viewed

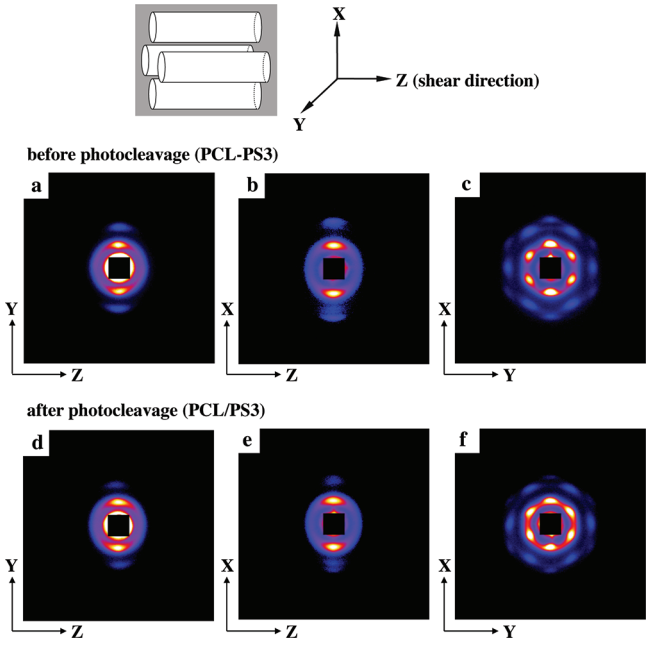

Figure 6. 2D-SAXS patterns viewed from X direction (a, d), Y direction (b, e), and Z direction (c, f) for PCL−PS3 (upper panels) and PCL/PS3 (lower panels). The definition of each direction against the shear direction is shown in the illustration (top), where Z is the shear direction and X and Y are perpendicular to the shear direction.

from X (a, d), Y (b, e), and Z (c, f) directions, where Z represents the shear direction and X and Y are perpendicular to the shear direction (see the illustration of Figure 6, top). We had similar 2D-SAXS patterns for PCL−PS1 (already shown in our previous study[30]) and also for PCL−PS2 (not shown here). We find two or three diffraction spots on the meridian arising from the parallel stacks of nanocylinders when viewed from X and Y directions (a, b, d, e), whereas the hexagonally symmetrical pattern is observed when viewed from the Z direction (c, f). These 2D-SAXS patterns clearly indicate that the nanocylinders are uniaxially oriented parallel to the shear direction (Z direction). Furthermore, we find that the 2D-SAXS patterns of PCL/PS3 viewed from each direction (d, e, f) are identical with those of PCL−PS3 (a, b, c), meaning that the oriented nanocylinders are completely preserved after photocleavage.

3.6. Crystal Orientation of PCL Blocks and PCL Homopolymers. The crystal orientation of PCL blocks and PCL homopolymers was investigated using 2D-WAXD. The results of PCL−PS1 and PCL/PS1 were already reported as a function of crystallization temperature (−60 °C ≤ T_c ≤ −40 °C).[30] Figure 7 shows the typical 2D-WAXD patterns of PCL−PS3 (a) and PCL/PS3 (b) crystallized at −40 °C when viewed from X direction (perpendicular to the shear direction), and the 2D-WAXD patterns viewed from Y direction are omitted because they should be the same in principle to those from X direction. The 2D-WAXD patterns of PCL−PS2 and PCL/PS2 are identical with Figure 7. We find two major diffractions in Figure 7 in addition to the diffuse scattering arising from the amorphous components existing in the system (i.e., amorphous PS and uncrystallized PCL). The diffractions can be successfully assigned using the crystallographic data available for the unit cell of PCL crystals[49] to be the

dx.doi.org/10.1021/ma202566f | Macromolecules 2012, 45, 1892−1900

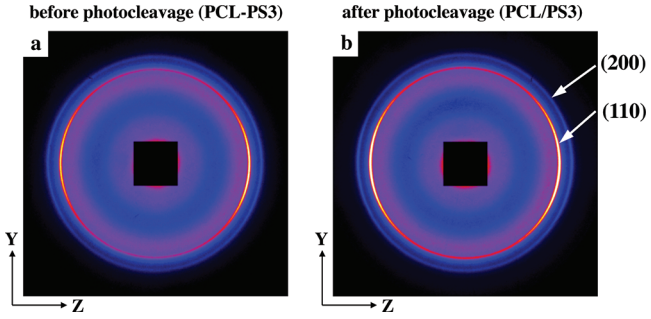

Figure 7. 2D-WAXD patterns viewed from *X* direction for PCL−PS3 (a) and PCL/PS3 (b) both crystallized at −40 °C. The *X* direction is perpendicular to the shear direction.

(110) reflection for the stronger diffraction at $2\theta = 21.41°$and the (200) reflection for the weaker diffraction at $2\theta = 23.76°$, as shown in Figure 7b. It is also known[49] that other diffraction intensities are considerably weak as compared with above two diffractions, so that it is reasonable that we have only two diffractions when the total crystallinity of PCL chains is extremely small (~0.1) as is the case of our samples.

We find from Figure 7 that the (110) reflection of PCL−PS3 and PCL/PS3 shows two strong arcs centered at the equator, which are entirely different from that of PCL−PS1 and PCL/PS1; four reflection peaks are clearly observed at off-axis regions instead of two reflections (see Figure S2 in Supporting Information). In order to quantitatively compare the 2D-WAXD patterns for each sample, we evaluated the (110) and (200) reflection intensities as a function of azimuthal angle ϕ using the analytical method described previously,[30] and the results are shown in Figure 8, where ϕ = 0° and 180°

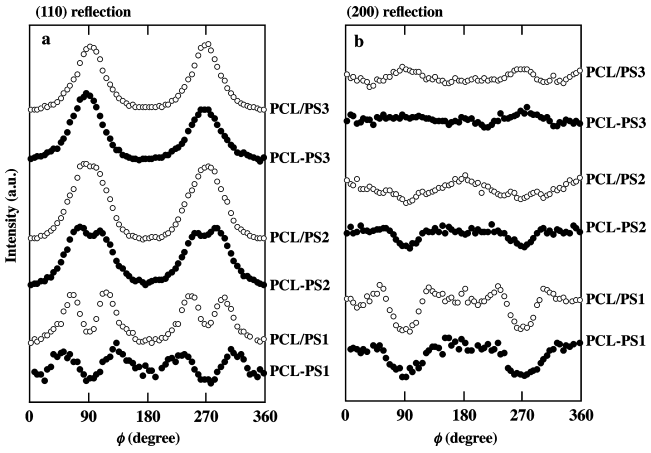

Figure 8. Intensities of the (110) reflection (a) and (200) reflection (b) plotted against azimuthal angle ϕ for each sample indicated. The crystallization temperature is −44 °C for PCL−PS1 and −40 °C for other samples.

corresponds to the meridian. We find from Figure 8a that the ϕ dependence of the (110) reflection changes significantly depending on the samples investigated; the symmetrical two peaks against ϕ = 90° or 270° observed for PCL−PS1 move toward the equator (ϕ = 90° or 270°) for PCL/PS1 and PCL−PS2, and eventually they merge into one for PCL/PS3 and PCL−PS3 (D = 17.9 nm). The ϕ dependence of the (200) reflection intensity is also moderately dependent on the samples; we find the arcs centered at the meridian (ϕ = 0° and 180°) for PCL/PS1 and PCL−PS1, but the ϕ dependence of the (200) reflection intensity for PCL/PS3 and PCL−PS3 does not show any definite peaks within the experimental error. We can conclude from Figure 8 that the crystal orientation both for PCL blocks and PCL homopolymers depends significantly on D. However, we do not detect any difference in the crystal orientation between PCL−PS3 and PCL/PS3 at different T_c ($-50\ °C \le T_c \le -40\ °C$).

3.7. Analysis of Crystal Orientation. The (110) and (200) reflections observed for PCL−PS1 and PCL/PS1 were successfully explained in our previous study[30] by assuming that the *b*-axis of PCL crystals (i.e., fastest growth axis[50]) was parallel to the cylinder axis; that is, the PCL crystals predominantly grew one-dimensionally in the nanocylinder with D = 13.0 nm. In this orientation, the (110) reflections should appear at ϕ = 58°, 122°, 238°, and 302° and the (200) reflections at ϕ = 0° and 180°, which agree satisfactorily with the peak positions observed in the 2D-WAXD patterns of PCL/PS1 and PCL−PS1 shown in Figure 8a. This crystal orientation is also reported for the cylindrically confined PCL blocks in PCL-*b*-P4VP[28] and *syn*-polystyrene homopolymers confined in AAO,[8] where it is concluded that the strong spatial restriction along *X* and *Y* directions is responsible for the one-dimensional crystal growth to yield the extremely reduced crystallinity of confined chains.

The (110) reflections centered at ϕ = 90° and 270° in the 2D-WAXD patterns of PCL−PS3 and PCL/PS3 (Figure 8a) can be explained if we assume that the (110) plane of PCL crystals (i.e., the fastest growth direction of bulk PCL homopolymers[50]) is normal to the cylinder axis. That is, the PCL crystals grow preferentially along the direction normal to the (110) plane in the nanocylinders with D = 17.9 nm. This crystal orientation will produce undetectably weak (200) reflection peaks at off-axis regions, which also agrees with the experimental results shown in Figure 8b. The change in the growth direction of PCL crystals (i.e., the change in crystal orientation) will arise from the increasing dimension along *X* and *Y* directions of confined nanocylinders, by which PCL crystals can grow along the *a*-axis (not fastest growth axis) as well as the *b*-axis (fastest growth axis) in order to increase the total crystallinity. That is, the growth mode of PCL crystals is two-dimensional (along the (100) plane) in larger nanocylinders, whereas it is one-dimensional (along the *b*-axis) in smaller nanocylinders, and eventually this difference in the mode of crystal growth yields significant differences in the crystallization rate and crystallinity between PCL−PS1 (or PCL/PS1) and PCL−PS3 (PCL/PS3). The difference in the crystal growth mode is schematically shown in Figure 9 between PCL homopolymers confined in smaller (D = 13.0 nm) and larger (D = 17.9 nm) nanocylinders. It should be noted that to our knowledge this is the first example to observe the two-dimensional crystal growth of block chains confined in nanocylinders.

The significant shift of the (110) reflection position observed in the 2D-WAXD patterns of PCL/PS1 and PCL−PS2 (Figure 8a) is somewhat puzzling. We have two possibilities for the reason for such shift. One possibility is that the diffraction pattern of PCL−PS2 (or PCL/PS1) is the superposition of those of PCL−PS1 and PCL−PS3. That is, the nanocylinder mainly consists of two PCL crystals with different orientations; one with the *b*-axis parallel to the cylinder axis and the other with the (110) plane normal to the cylinder axis. We can qualitatively explain the small variation in the (200) reflection pattern of PCL−PS2 (or PCL/PS1) (Figure 8b) using this model. The other possibility is that the lateral dimension increases with increasing D, and accordingly the crystal growth along the *a*-axis is gradually recovered to be detectable in larger

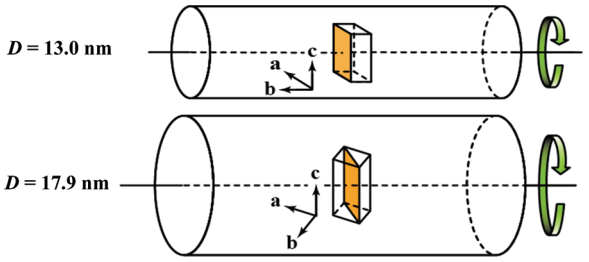

Figure 9. Schematic illustration showing the relationship between the cylinder axis and the growth direction of PCL crystals. The rectangle in the cylinder represents the enlarged unit cell of PCL crystals, and the growth plane is indicated by yellow. The PCL crystals grow predominantly along the *b*-axis in the smaller nanocylinder (upper), whereas they grow along the direction normal to the (110) plane in the larger nanocylinder (lower).

nanocylinders. As a result, the *b*-axis of growing PCL crystals deviates continuously from the initial orientation (parallel to the cylinder axis) with increasing *D*. However, more information is necessary to determine the detailed crystallization mechanism of PCL chains confined in the nanocylinders with intermediate *D*.

We already reported[30] that the degree of crystal orientation was significantly different at higher T_c (≥ -45 °C) between PCL blocks in PCL–PS1 and PCL homopolymers in PCL/PS1. However, the difference was not detected among PCL/PS2, PCL–PS2, PCL/PS3, and PCL–PS3 at every T_c investigated (-50 °C $\leq T_c \leq -40$ °C). That is, the degree of PCL crystal orientation confined in larger nanocylinders ($D \geq 14.9$ nm) is almost the same for PCL blocks and PCL homopolymers irrespective of T_c, which was verified by evaluating the degree of PCL crystal orientation f[43] from the ϕ dependence of (110) reflection intensities (Figure 8a). The result is shown in Supporting Information (Figure S3). In summary, the degree of PCL crystal orientation is clearly different at higher T_c (≥ -45 °C) between PCL blocks and PCL homopolymers in the smaller nanocylinder ($D = 13.0$ nm), whereas it is insignificant in the larger nanocylinders ($D \geq 14.9$ nm) irrespective of T_c investigated (-50 °C $\leq T_c \leq -40$ °C).

4. CONCLUSIONS

We investigated the crystallization behavior and crystal orientation of poly(ε-caprolactone) (PCL) homopolymers and PCL blocks confined in identical nanocylinders embedded in the polystyrene (PS) matrix as a function of cylinder diameter *D*. The PCL homopolymers confined in nanocylinders were prepared using microphase separation of PCL-*b*-PS copolymers followed by photocleavage at the block junction between PCL and PS blocks. The following conclusions were obtained from this study.

(1) The time evolution of PCL crystallinity χ_{PCL} showed a first-order kinetics both for PCL blocks and PCL homopolymers confined in all the nanocylinders investigated ($D = 13.0–17.9$ nm), meaning that the crystallization is controlled by nucleation. The *D* dependence of the crystallization rate for PCL blocks is more drastic than that for PCL homopolymers. As a result, various interrelations of crystallization rates were observed depending on *D* between PCL homopolymers and PCL blocks.

(2) The PCL crystals oriented predominantly such that the *b*-axis of PCL crystals was parallel to the cylinder axis for PCL blocks and PCL homopolymers confined in the smaller nanocylinder ($D = 13.0$ nm), whereas the (110) plane of PCL crystals was normal to the cylinder axis (i.e., the *b*-axis was not parallel to the cylinder axis) for both PCL chains in larger nanocylinders ($D \geq 14.9$ nm). That is, the growth mode of PCL crystals is definitely different to yield a moderate difference in χ_{PCL} between smaller ($D = 13.0$ nm) and larger ($D \geq 14.9$ nm) nanocylinders. The difference in the degree of crystal orientation could not be detected between PCL blocks and PCL homopolymers confined in larger nanocylinders ($D \geq 14.9$ nm).

■ ASSOCIATED CONTENT

Ⓢ Supporting Information

Figures S1–S3. This material is available free of charge via the Internet at http://pubs.acs.org.

■ AUTHOR INFORMATION

Corresponding Author

*Phone+81-3-5734-2132; Fax +81-3-5734-2888; e-mail snojima@polymer.titech.ac.jp.

■ ACKNOWLEDGMENTS

The 1D-SAXS measurements have been performed under the approval of Photon Factory Advisory Committee (No. 2010G014).

■ REFERENCES

(1) Muller, A. J.; Balsamo, V.; Arnal, M. L. *Adv. Polym. Sci.* **2005**, *190*, 1.
(2) Nandan, B.; Hsu, J. Y.; Chen, H. L. *J. Macromol. Sci., Part C* **2006**, *46*, 143.
(3) Castillo, R. V.; Muller, A. J. *Prog. Polym. Sci.* **2009**, *34*, 516.
(4) Steinhart, M.; Senz, S.; Wehrspohn, R. B.; Gosele, U.; Wendorff, J. H. *Macromolecules* **2003**, *36*, 3646.
(5) Steinhart, M.; Goring, P.; Dernaika, H.; Prabhukaran, M.; Gosele, U.; Hempel, E.; Thurn-Albrecht, T. *Phys. Rev. Lett.* **2006**, *97*, 027801.
(6) Wu, H.; Wang, W.; Yang, H.; Su, Z. *Macromolecules* **2007**, *40*, 4244.
(7) Shin, K.; Woo, E.; Jeong, Y. G.; Kim, C.; Huh, J.; Kim, K. W. *Macromolecules* **2007**, *40*, 6617.
(8) Wu, H.; Wang, W.; Huang, Y.; Su, Z. *Macromol. Rapid Commun.* **2009**, *30*, 194.
(9) Martin, J.; Mijangos, C.; Sanz, A.; Ezquerra, T. A.; Nogales, A. *Macromolecules* **2009**, *42*, 5395.
(10) Lutkenhaus, J. L.; McEnnis, K.; Serghei, A.; Russell, T. P. *Macromolecules* **2010**, *43*, 3844.
(11) Yamamoto, T. *Polymer* **2009**, *50*, 1975.
(12) Wang, M.; Hu, W.; Ma, Y.; Ma, Y. Q. *J. Chem. Phys.* **2006**, *124*, 244901.
(13) Miura, T.; Mikami, M. *Phys. Rev. E* **2007**, *75*, 031804.
(14) Qian, Y.; Cai, T.; Hu, W. *Macromolecules* **2008**, *41*, 7625.
(15) Cai, T.; Qian, Y.; Ma, Y.; Ren, Y.; Hu, W. *Macromolecules* **2009**, *42*, 3381.
(16) Quiram, D. J.; Register, R. A.; Marchand, G. R.; Adamson, D. H. *Macromolecules* **1998**, *31*, 4891.
(17) Weimann, P. A.; Hajduk, D. A.; Chu, C.; Chaffin, K. A.; Brodil, J. C.; Bates, F. S. *J. Polym. Sci., Part B* **1999**, *37*, 2053.
(18) Zhu, L.; Mimnaugh, B. R.; Ge, Q.; Quirk, R. P.; Cheng, S. Z. D.; Thomas, E. L.; Lotz, B.; Hsiao, B. S.; Yeh, F.; Liu, L. *Polymer* **2001**, *42*, 9121.
(19) Huang, P.; Zhu, L.; Cheng, S. Z. D.; Ge, Q.; Quirk, R. P.; Thomas, E. L.; Lotz, B.; Hsiao, B. S.; Liu, L.; Yeh, F. *Macromolecules* **2001**, *34*, 6649.
(20) Lee, W.; Chen, H. L.; Lin, T. L. *J. Polym. Sci., Part B* **2002**, *40*, 519.
(21) Sun, L.; Zhu, L.; Ge, Q.; Quirk, R. P.; Xue, C.; Cheng, S. Z. D.; Hsiao, B. S.; Avila-Orta, C. A.; Sics, I.; Cantino, M. E. *Polymer* **2004**, *45*, 2931.
(22) Ho, R. M.; Tseng, W. H.; Fan, H. W.; Chiang, Y. W.; Lin, C. C.; Ko, B. T.; Huang, B. H. *Polymer* **2005**, *46*, 9362.

(23) Huang, P.; Guo, Y.; Quirk, R. P.; Ruan, J.; Lotz, B.; Thomas, E. L.; Hsiao, B. S.; Avila-Orta, C. A.; Sics, I.; Cheng, S. Z. D. *Polymer* **2006**, *47*, 5457.
(24) Vasilev, C.; Reiter, G.; Pispas, S.; Hadjichristidis, N. *Polymer* **2006**, *47*, 330.
(25) Castillo, R. V.; Arnal, M. L.; Muller, A. J.; Hamley, I. W.; Castelletto, V.; Schmalz, H.; Abetz, V. *Macromolecules* **2008**, *41*, 879.
(26) Myers, S. B.; Register, R. A. *Macromolecules* **2010**, *43*, 393.
(27) Gitsas, A.; Floudas, G.; Butt, H. J.; Pakula, T.; Matyjaszewski, K. *Macromolecules* **2010**, *43*, 2453.
(28) Chung, T. M.; Wang, T. C.; Ho., R. M.; Sun, Y. S.; Ko, B. T. *Macromolecules* **2010**, *43*, 6237.
(29) Nojima, S.; Ohguma, Y.; Namiki, S.; Ishizone, T.; Yamaguchi, K. *Macromolecules* **2008**, *41*, 1915.
(30) Nojima, S.; Ohguma, Y.; Kadena, K.; Ishizone, T.; Iwasaki, Y.; Yamaguchi, K. *Macromolecules* **2010**, *43*, 3916.
(31) Yamaguchi, K.; Kitabatake, T.; Izawa, M.; Fujiwara, T.; Nishimura, H.; Futami, T. *Chem. Lett.* **2000**, *29*, 228.
(32) Kang, M.; Moon, B. *Macromolecules* **2009**, *42*, 455.
(33) Schumers, J. M.; Fustin, C. A.; Gohy, J. F. *Macromol. Rapid Commun.* **2010**, *31*, 1588.
(34) Schumers, J. M.; Gohy, J. F.; Fustin, C. A. *Polym. Chem.* **2010**, *1*, 161.
(35) Cao, M.; Wang, J. Q.; Chen, P. C.; Xu, J. T.; Fan, Z. Q. *J. Polym. Sci., Part A* **2010**, *48*, 3834.
(36) Cabane, E.; Malinova, V.; Meier, W. *Macromol. Chem. Phys.* **2010**, *211*, 1847.
(37) Yang, H.; Jia, L.; Wang, Z.; Di-Cicco, A.; Levy, D.; Keller, P. *Macromolecules* **2011**, *44*, 159.
(38) Richardson, M. J.; Savill, N. G. *Polymer* **1977**, *18*, 3.
(39) Crescenzi, V.; Manzini, G.; Calzolari, G.; Borri, C. *Eur. Polym. J.* **1972**, *8*, 449.
(40) Nojima, S.; Tsutsui, H.; Urushihara, M.; Kosaka, W.; Kato, N.; Ashida, T. *Polym. J.* **1986**, *18*, 451.
(41) Nojima, S.; Hashizume, K.; Rohadi, A.; Sasaki, S. *Polymer* **1997**, *38*, 2711.
(42) Nojima, S.; Kikuchi, N.; Rohadi, A.; Tanimoto, S.; Sasaki, S. *Macromolecules* **1999**, *32*, 3727.
(43) Miyazaki, T.; Hoshiko, A.; Akasaka, M.; Sakai, M.; Takeda, Y.; Sakurai, S. *Macromolecules* **2007**, *40*, 8277.
(44) Ohta, T.; Kawasaki, K. *Macromolecules* **1986**, *19*, 2621.
(45) Nojima, S.; Inokawa, D.; Kawamura, T.; Nitta, K. *Polym. J.* **2008**, *40*, 986.
(46) Loo, Y. L.; Register, R. A.; Ryan, A. J. *Phys. Rev. Lett.* **2000**, *84*, 4120.
(47) Chen, H. L.; Wu, J. C.; Lin, T. L.; Lin, J. S. *Macromolecules* **2001**, *34*, 6936.
(48) Nojima, S.; Toei, M.; Hara, S.; Tanimoto, S.; Sasaki, S. *Polymer* **2002**, *43*, 4087.
(49) Chatani, Y.; Okita, Y.; Tadokoro, H.; Yamashita, Y. *Polym. J.* **1970**, *1*, 555.
(50) Beekmans, L. G. M.; Vancso, G. J. *Polymer* **2000**, *41*, 8975.

Macromolecules

Article

pubs.acs.org/Macromolecules

FTIR-ATR Study of Water Distribution in a Short-Side-Chain PFSI Membrane

Maria-Chiara Ferrari,[†] Jacopo Catalano,[‡] Marco Giacinti Baschetti,* Maria Grazia De Angelis, and Giulio Cesare Sarti

Dipartimento di Ingegneria Chimica, Mineraria e delle Tecnologie Ambientali (DICMA), Alma Mater Studiorum-Università di Bologna, via Terracini 28, 40131 Bologna, Italy

ABSTRACT: Fourier transform infrared–attenuated total reflectance (FTIR-ATR) spectroscopy was used to study in detail water vapor sorption in a short-side-chain perfluorosulfonic acid ionomer membrane suitable for use as electrolyte in proton exchange membranes fuel cells. The analysis of the membrane IR spectra, at different values of relative humidity (0.00–0.50) and at 35 °C, allows to identify four types of water molecules, characterized by decreasing strength of interaction with the polymer sulfonate groups. The actual concentration of the different water species inside the membrane was determined by calibrating the IR absorbance data with independent measurements of total water vapor uptake. The sorption of the different populations of water can be represented by Langmuir isotherms: the first population is directly attached to sulfonate sites, while the others form subsequent layers, adsorbed one onto the other in a shell-like structure. To describe the overall sorption behavior of the different populations, four adjustable parameters are required, which are consistent with literature data, thus supporting the validity of the physical model considered.

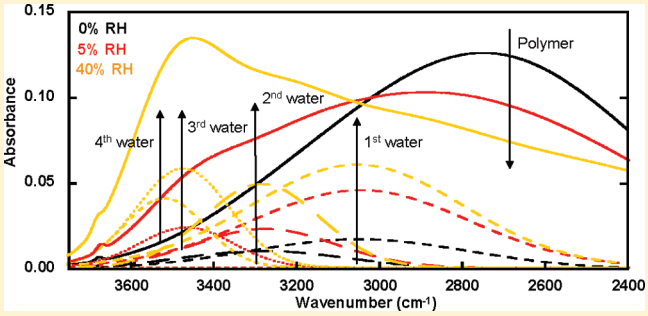

INTRODUCTION

Perfluorosulfonic acid ionomeric (PFSI) membranes are used in proton exchange membranes fuel cells (PEM-FCs) due to their good proton conductivity in humid conditions. These materials are characterized by a poly(tetrafluoroethylene) backbone with fluorinated side chains terminated by sulfonate ionic groups; their mass transport behavior is due to the complex structure formed by the hydrophilic groups attached to a hydrophobic skeleton. Upon hydration, two phases separate inside the PFSI membranes: a hydrophobic one, mainly constituted by the perfluorinated chains, and a hydrophilic one, formed by the sulfonic acid groups and the water molecules, which is responsible for the high proton conductivity shown by these materials in hydrated conditions.[1,2] The benchmark for PFSI materials is Nafion,[2−5] which was first used in the chloralkali processes due to its ion conductivity properties and later applied to fuel cell systems. In the past 20 years, however, because of the great advances in fuel cell technology, many alternative PFSI membranes have been synthesized and proposed with the aim to obtain better thermal and mechanical properties.[2,3,6,7] In the present work, the attention is focused on the properties of Aquivion (formerly known as Hyflon Ion),[8−10] a short-side-chain PFSI polymer produced by Solvay Solexis S.p.A, which is attracting increasing interest thanks to the similarities with Nafion and to its potentially higher thermal and chemical resistance.[11−13] Some of the water and methanol transport parameters for Aquivion were already measured and reported in previous works showing the same qualitative behavior encountered in the other PFSI films and confirming its great similarity with Nafion membranes.[14−19]

Because of the high dependence of PFSI proton conductivity on hydration, a complete understanding of the water sorption process in these membranes is essential to optimize their use in fuel cell operations, and various works can be found in the literature in which the total water vapor uptake of several PFSI films was measured in different conditions.[3−7,14−17] The water sorption in these materials, however, is known to occur through a complex mechanism due to the biphasic nature of the hosting matrix and to the nonhomogeneous strength of interaction between water molecules and sulfonate groups. This complex phenomenon is usually described by considering that different water families are present inside the polymer, as proved with different experimental techniques.[20−25] In particular, Baias et al. used NMR to distinguish between free and bound water[20] while Kim et al. analyzed the state of water with DSC and NMR,[21] identifying three different water populations (strongly bound to the polymer, loosely bound, and free water), although they reported that, most likely, there is a continuous distribution of water states, as stated also by Ye et al.[24]

In previous works,[14,15] we measured the total water vapor uptake at each activity in the short-side-chain PFSI membrane

Received: September 15, 2011
Revised: January 13, 2012
Published: February 13, 2012

used in this study and modeled the results by considering the amount of water vapor absorbed in the membrane as the sum of two contributions: a linear one, related to the physical absorption of free water molecules evenly distributed in the matrix, and a nonlinear one, related to the localized adsorption of water molecules onto sulfonate sites. The latter mode of sorption involves a strong interaction between water and hydrophilic groups, consistent with the fact that these water molecules remain permanently attached to the membrane even after complete evacuation at zero activity, unless relatively high temperatures are applied.[15]

The above description may represent not only qualitatively but, in many regards, also quantitatively the overall process of water sorption into the membrane considered; however, it oversimplifies the actual mechanism by classifying sorbed water molecules into two types only, one interacting and the other not interacting with the polar groups of the polymer. More reasonably, according also to Ye et al.,[20] one should consider a continuous sequence of water molecules, characterized by decreasing strength of interaction with sulfonic sites, and correspondingly located at increasing distances from them. Such a continuous structure is difficult to quantify and analyze in practice and possibly is not even necessary for fuel cell engineering purposes. In more practical terms, one can consider a discrete number of water populations, each one characterized by decreasing strength of interaction with sulfonate sites and interacting more directly with the nearby water molecules.[26]

To investigate such interactions, a detailed IR analysis of dry and hydrated Aquivion has been performed in this work, and the spectral features were investigated, taking advantage of the structural similarity with Nafion, for which several IR data are available.[27−41] It has to be said, however, that most of those studies regarded dry PFSI membranes, leading to a detailed description of the dry polymer spectrum in both H^+ and Na^+ forms, but a complete and satisfactory explanation of the hydrated IR spectra has not yet been provided,[29,31,34,40] and a thorough quantitative analysis of the spectra after equilibration at different activities is still missing.[41]

With the above aim in mind, in the present work we investigate the IR spectrum of Aquivion using the time-resolved FTIR-ATR spectroscopy. Such a technique enables us to label molecules on the basis of their interactions, such as hydrogen bonding, with other penetrant molecules or with the polymeric matrix, and to follow their evolution with time and penetrant activity.[42−45] FTIR-ATR spectroscopy, indeed, has already been applied to study water sorption and diffusion in Nafion, demonstrating great potential to elucidate the complex mechanisms which control such processes.[46−48]

The water sorption behavior of Aquivion was investigated at 35 °C and at water activities up to 50%; the different IR spectra of the hydrated membrane were carefully analyzed through a spectral deconvolution process. The different peaks related to different species of water molecules in the hydrated IR spectrum of the ionomer often appear merged into a single, broad, cumulative absorption band, which needs to be properly deconvoluted to identify and quantify the contribution of the individual peaks. The hydrated PFSI spectra were thus suitably deconvoluted to obtain the different absorption peaks which are related to the different water families present in the polymers and are characterized by different degree of interaction with the acid sulfonic groups. The area of each peak was then converted into the actual concentration through calibration with sorption and dilation data obtained with independent measurements. Such a quantitative analysis allowed to determine the actual sorption isotherm of each water family considered and to obtain a physically consistent description of the sorption process. The trends obtained for the concentration of each water family in the polymer can be described on the basis of a simple model expressly developed to account for the different mechanisms of sorption of the various water populations.

EXPERIMENTAL SECTION

Materials. Aquivion is a short-side-chain PFSI material that consists of a hydrophobic poly(tetrafluoroethylene) backbone with perfluorovinyl ether short side chains terminated by sulfonic acid

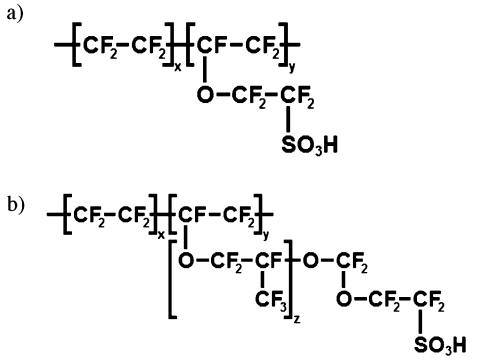

Figure 1. Molecular structure of (a) Aquivion and (b) Nafion 117.

($-SO_3H$) groups. As can be seen in Figure 1, Aquivion has a side chain shorter than other PFSI materials such as Nafion, a feature that may confer to this material good stability at high temperature and good mechanical properties. The short-side-chain ionomers also have a lower equivalent weight than longer-side-chain ionomers at equal molar concentration of sulfonic groups.

The sulfonyl fluoride (SO_2F) form of the polymer is obtained from the free radical copolymerization of tetrafluoroethylene (TFE) and perfluorosulfonylfluorodivinyl ether (SFVE);[8] after synthesis, the $-SO_2F$ groups are converted to $-SO_3H$ by immersion in alkaline aqueous solutions at medium temperature (80 °C) and subsequent treatment with a strong acid solution.

The ionomer was kindly provided by Solvay Solexis SpA as a 160 μm thick extruded membrane with an equivalent weight of 800 g_{pol}/mol_{-SO_3H} and was stored in distilled water for at least 24 h before testing.

FTIR-ATR Measurements. A Nicolet Avatar FTIR spectrometer has been used, equipped with a mercury−cadmium−telluride detector, to improve measurement accuracy. A schematic of a FTIR-ATR cell is presented in Figure 2;[49] a high refractive index crystal, placed in the spectrometer, traps the incident IR beam which is totally reflected on the crystal surface. At each reflection an evanescent wave rises from the surface, which is absorbed by the material placed onto the crystal, allowing the acquisition of its IR spectrum. The FTIR-ATR technique has been widely used to study the sorption process in polymeric materials; in this application, the polymer of interest adheres on the ATR crystal, and the diffusion of penetrants is studied by monitoring the time evolution of the penetrant characteristic absorption bands in the polymer spectrum. A detailed description of the technique and of the related theory can be found in the literature.[50,51]

In the present work experiments were conducted using a multiple reflection zinc selenide crystal (refractive index 2.42), with 45° beveled faces, placed in a horizontal flow-through ATR cell produced by Specac Inc., also shown in Figure 2. The cell is provided with a heating system that allows temperature control through the circulation of water from a heating bath. The data were collected by adding and averaging 32 scans per each spectrum with a resolution of 4 cm^{-1}; this

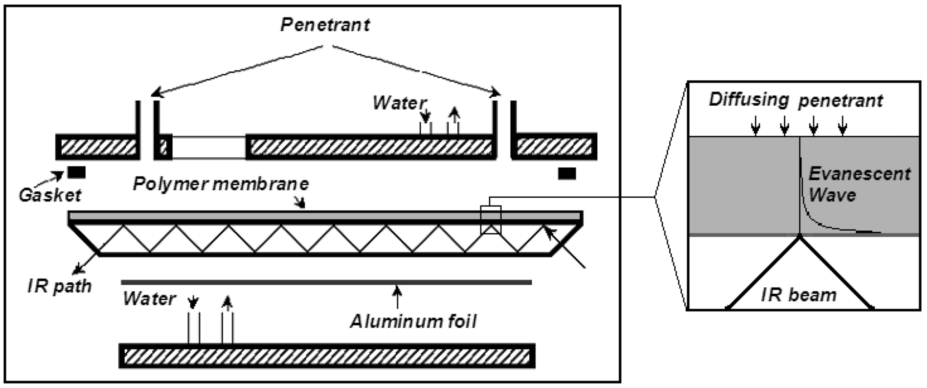

Figure 2. Schematic of the ATR cell: the polymer is attached onto the ATR crystal, and the penetrant enters from the ducts in the upper part of the cell and diffuses in the film. The IR beam is entrapped in the crystal so that only the diffused penetrant can be detected by the instrument; in the magnification window a schematic of the ATR principle is reported.

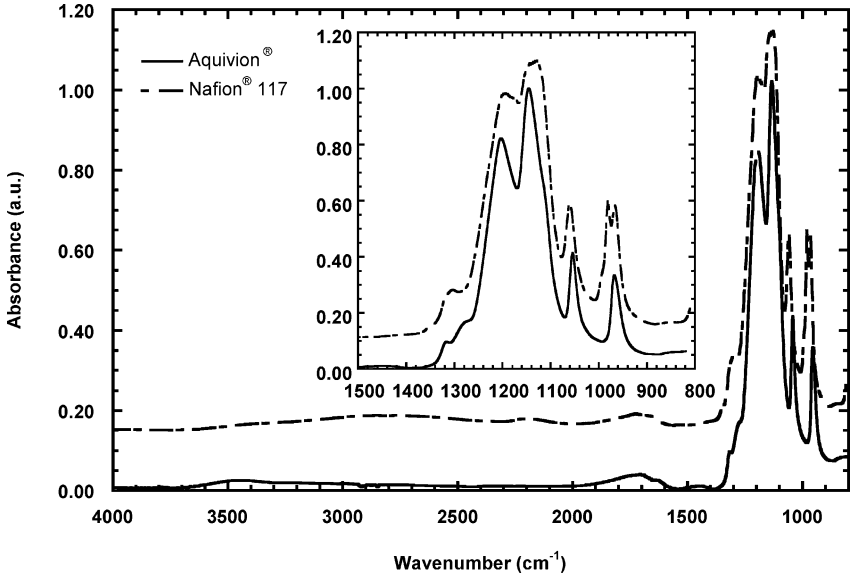

Figure 3. FTIR-ATR spectrum of Aquivion at room temperature in atmospheric humidity compared to that of Nafion 117 (shifted for the sake of clarity). Inset: magnification of the region containing the characteristic bands of the polymer.

setup was chosen to recover spectra with sufficient velocity (about 40 s per spectrum) while maintaining a good signal-to-noise ratio.

Particular care has been devoted to ensure the adhesion of the extruded ionomer onto the crystal in order to obtain reliable results.[46] Before every sorption experiment, a background spectrum of the ATR crystal was collected. A wet sample of membrane, precut in the hydrated condition, was placed onto the crystal, and the cell was tightened. The sample was dried overnight by flowing dry air through the cell and then evacuated for 4 h at the test temperature, 35 °C. It is well-known[15,16] that water is completely removed from the PFSI membranes only if the sample is evacuated at high temperature (about 120 °C in the case of Aquivion): therefore, at the beginning of each FTIR-ATR experiment the film was "dry" with respect to the experimental temperature; i.e., no further water could be removed at that temperature, although it was not completely water-free.

Differential sorption experiments were conducted by contacting the polymer with pure water vapor at a given partial pressure and subsequently increasing water pressure stepwise, once equilibrium was attained at the prior conditions (i.e., no more change in the spectrum could be detected over time). The sorption process was studied at 35 °C and up to an activity of about 0.5; the activity upper limit is cautiously imposed by the occurrence of condensation phenomena in some cold spots of the system. It is worthwhile to mention that, with this technique, both transient mass uptake and equilibrium sorption data can be obtained: in this work we focus our attention only on the equilibrium sorption behavior, when no flux and no concentration gradients are present in the membranes, and leave the analysis and modeling of transient sorption as well as the determination of the diffusion coefficients to a future work.

Sorption and Dilation Measurements. With the aim of obtaining a calibration of the spectrometer measurements, independent sorption and dilation measurements were performed in the same operative range used for the ATR-FTIR experiments.

It is indeed well-known that, for a given species i, IR measurements are obtained in terms of absorbance, A, which is directly related to concentration, c (in moles of water per polymer volume), according to the so-called Beer–Lambert's law that can be written as

$$c_i = \frac{1}{\delta \varepsilon_i} A_i \qquad (1)$$

where δ represents the path length traveled by the IR beam in the polymer and ε is the molar extinction coefficient which represents the proportionality constant between concentration and IR absorbance.

Water vapor sorption measurements were performed in a pressure decay system already described in previous paper[15] on Aquivion samples previously treated under vacuum and at 120 °C for about 4 h to ensure removal of all the water from the specimen. Although some water vapor sorption data were available for this ionomer, they were obtained on membranes not completely dry, and they do not allow to

dx.doi.org/10.1021/ma202099p | Macromolecules 2012, 45, 1901–1912

quantify accurately the total water content in the membrane but just the differential weight gain from the initial, partially hydrated state of the membrane. Indeed, while in FTIR-ATR experiments all the water is visible in the spectra, in manometric or gravimetric sorption experiments the water initially present in the membrane cannot be detected, and uncertainty on the initial amount of water in the membrane can lead to inconsistent water uptake results.

It must be also noticed that sorption measurements provide the water concentration in the ionomer on a weight base, while the use of eq 1 requires volumetric concentrations; because of high membrane swelling, therefore, an estimate of the polymer density at each different relative humidity (RH) is needed for proper comparison. For this purpose, ionomer dilation was measured by using an optical dilatometer able to detect displacements in the order of 1 μm; these data have been already presented in a separate work where all the details concerning the experimental techniques are described and the results are thoroughly discussed.[19]

RESULTS AND DISCUSSION

IR Spectra Analysis. The spectrum of Aquivion equilibrated with atmospheric humidity is reported in Figure 3 together with the one obtained for a Nafion sample in the same conditions. As expected, the two materials show the same characteristic peaks, their chemical structure being very similar; therefore, we will assume that Aquivion behaves like Nafion as far as the spectral features are concerned.

The main absorption bands that characterize the polymer are located in the interval of wavenumbers between 900 and 1500 cm^{-1}, which is enlarged in the inset of Figure 3 for clarity sake. The two fairly intense peaks at 1155 and 1220 cm^{-1} can be related to the symmetric and asymmetric stretching vibrations of −CF bonds of the backbone, respectively,[28,32,33,37] while the peak at 1060 cm^{-1} and the shoulder at 1300 cm^{-1} are attributed to the symmetric and asymmetric stretching of $-SO_3^-$ arising from water-induced dissociation of $-SO_3H$ groups.[28,32,33] Finally, the stretching of the C−O−C bonds is related to the band at 971 cm^{-1}.[28,32,33] The only difference between the two materials is a peak at 982 cm^{-1} clearly visible in the spectrum of Nafion and absent in that of Aquivion: such a peak is attributed[33,37] to the stretching of −CF in the $(-CF_2-CF(R)-CF_3-)$ groups of the side chains that, indeed, are not present in Aquivion (see Figure 1). Finally, the bands related to the undissociated $-SO_3H$ groups are expected to appear at 1410 and 910 cm^{-1},[28,32,33] but they are not visible in the spectra shown, suggesting that the humidity present in ambient air dissociates the great majority of the sulfonic groups in both materials; this fact was already noticed by different authors in PFSI membrane not adequately dried[25,29] and is in agreement with the work of Leuchs and Zundel, who found about 90% dissociation of trifluofomethanesulfonic acid, CF_3SOH_3, with just one mole of water per sulfonic group.[52]

For the hydrated polymer membrane, the portion of the spectra between the wavenumbers 1500 and 3800 cm^{-1} is usually related to the vibration of −OH bonds in water[28,32,33] and, therefore, is expected to undergo the major changes during water sorption. In particular, the region between 1500 and 2000 cm^{-1} is associated with the bending vibrations of water molecules, while the stretching vibrations of −OH can be found between 2400 and 3800 cm^{-1}.[28,32,33]

The latter region of the polymer spectra is plotted in Figure 4 at each differential hydration step, with water activity varying from 0.0 to 0.50. It can be seen that, with increasing water content in the membrane, the spectrum undergoes some modifications: in particular, the bands related to the −OH groups become detectable while a large band centered around 2720 cm^{-1} decreases. The latter band is not unequivocally identified in the literature: some authors relate such a peak to undissociated $-SO_3H$[31,37] while others relate it to the presence of an Evans window;[28] that is a local minimum due to overtones of bending modes and Fermi resonance and is responsible for the appearance of two apparent maxima at 2720 and 2200 cm^{-1}. The present data do not allow to identify the correct explanation, although the absence of the peaks at 910 and 1410 cm^{-1} corresponding to undissociated $-SO_3H$ seems to stand against the first interpretation. In any event, the intensity of the band at 2720 cm^{-1} is unanimously believed to decrease upon sorption, in agreement with the experimental findings, due to progressive dissociation of SO_3H group in presence of water and/or to the swelling of the membrane upon hydration. In general, the behavior of the peak at 2720 cm^{-1} is very likely affected also by the change of the peaks at lower wavenumber such as those related to water bending (1500−2000 cm^{-1}) as well as those related to polymer, such as the one present at 2375 cm^{-1} that is due to an overtone of polymer skeletal modes[28] and decreases with increasing water content due to polymer swelling.

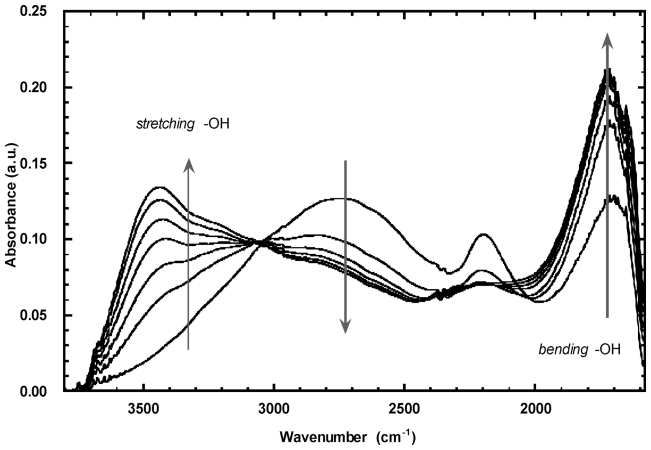

Figure 4. Evolution of the regions of bending (1500−2000 cm^{-1}) and stretching (3000−3800 cm^{-1}) vibrations of −OH in the Aquivion spectrum upon hydration at 35 °C.

Water sorption can be monitored by considering the water bending region or that related to the stretching of −OH bonds (2400−3800 cm^{-1}). In this work we focused on the latter region, where the absorption band is wider and a large amount of information can be collected by decomposing the spectrum in all its contributions.

The broad absorption band of the −OH stretching vibrations (2400−3800 cm^{-1}) has several components that can be identified based on the degree of interaction between water molecules and sulfonic groups. The analysis of spectra at different RH, reported in Figure 4, shows that the band area does not increase uniformly and that its shape changes with increasing water content. This behavior is due to the fact that different kinds of water molecules, with different degree of hydrogen bonding, are absorbed at different values of relative humidity.[28,33]

Identification of Different Water Populations: Spectra Deconvolution. The mass fraction of each family can be obtained through a decomposition of the band, which allows to follow separately the peaks related to each type of water molecules. To that aim, a fitting procedure was implemented

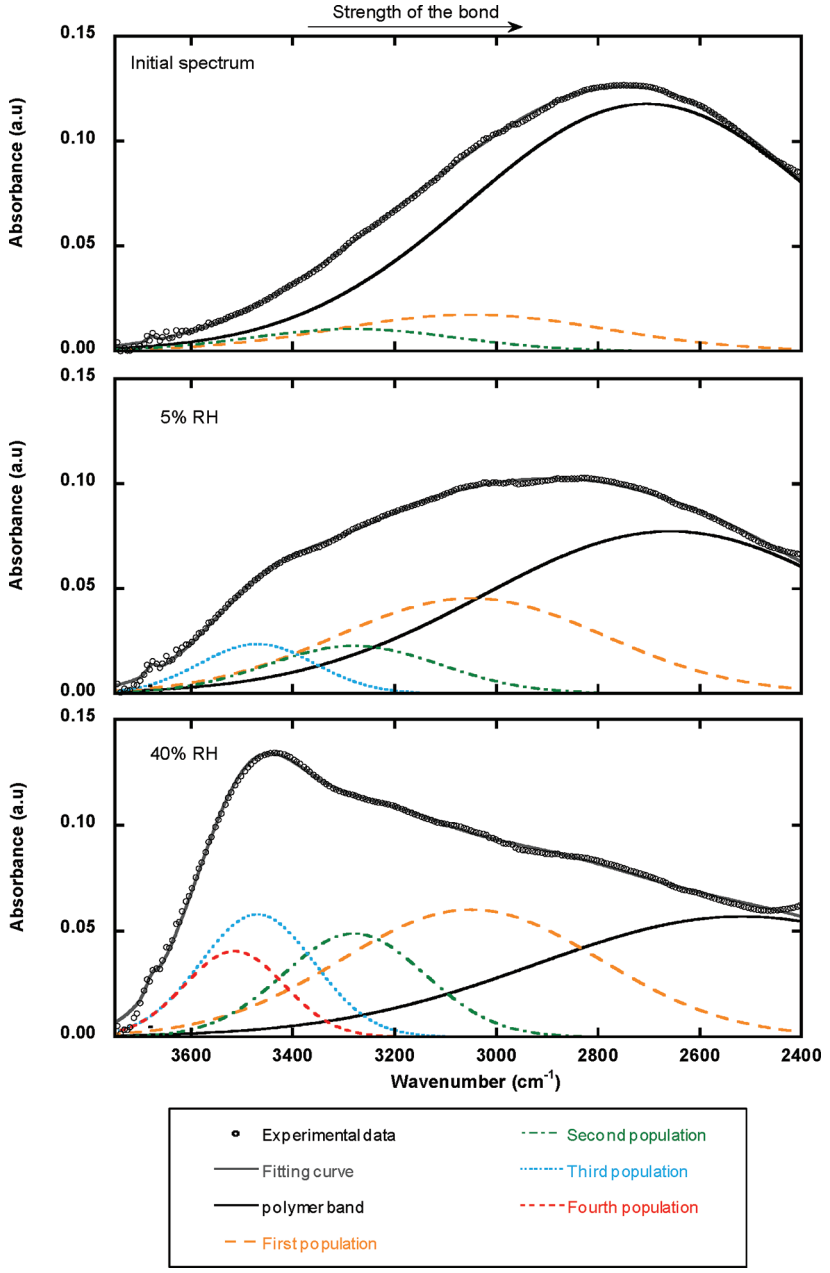

Figure 5. Region of stretching of the −OH groups of the Aquivion spectrum at different humidities: (a) at 0% RH, (b) at 5% RH, and (c) at 40% RH.

using the software Fityk,[53] distributed under the terms of the GNU General Public License. For each water activity, a baseline correction between 1580 cm^{-1} (starting point of the −OH bending band) and 3720 cm^{-1} (termination of the water stretching peak) was used. The minimum number of bands needed to reach a satisfactory description of the experimental data was determined through multiple fitting runs in which the peaks shape was fixed to the Gaussian function, while all the other parameters were allowed to vary. This method lead to the detection of the center position of each peak, which was used as a reference for the following hydration steps.

In particular, proceeding toward higher hydration, the position of the water-related peaks determined in previous steps was kept fixed, while their height and width was allowed to vary. On the other hand, the band centered at about 2700 cm^{-1} and extending well below the region of interest was allowed to move in order to account for the influence of spectral features present at lower wavenumber, such as the skeletal modes overtone peak at 2375 cm^{-1}, as well as the overtones of OH bending of sulfonic groups hydrogen bonded to water,[38] which were not considered in the deconvolution. This approach was chosen after a careful analysis of the whole spectral region between 1500 and 3800 cm^{-1}; spectral decomposition of this region, for which up to 11 different peaks were used, indicated that, while the behavior of OH stretching bands was substantially independent from the initial guess on band position and always showed a physically consistent evolution with the increasing water content, the peaks at lower wavenumber were strongly dependent on the initial guesses and frequently showed non monotonous behavior with increasing hydration, which was hardly explainable through a physical approach.

dx.doi.org/10.1021/ma202099p | *Macromolecules* 2012, 45, 1901−1912

In this concern, the use of a band with adjustable position at about 2700 cm^{-1} resulted to be an optimal solution to obtain consistent and objective data processing, since it allowed to separate the two spectral regions while having a negligible effect on the behavior of the peaks found in the deconvolution of water stretching region.

Focusing the attention on this region, it can be seen that the number of bands needed to describe the observed data increases with the water content in the polymer, as it is clearly shown from the three significant spectra presented in Figure 5 at 0%, 5%, and 40% RH. Three different bands can be identified in the ionomer dried under vacuum for 4 h at the experimental temperature (Figure 5a): one located at a wavelength of 2720 cm^{-1}, which as said before was related to the polymer, and two located at 3005 and 3280 cm^{-1}, related to water molecules interacting with sulfonic groups with decreasing strength (i.e., the interaction strength decreases as the wavenumber increases).[28,33,39]

At 5% RH, a third water-related peak appears in the region of less strongly bonded water molecules, precisely at 3470 cm^{-1}; the absorbance of the other water peaks, previously determined, changes slightly while the polymer-related band is much smaller than in the previous step and shifts toward lower wavenumbers (Figure 5b). If the water content in the membrane is further increased, a fourth water-related band at 3515 cm^{-1} appears. In Figure 5c, the spectrum at 40% RH shows clearly the four water populations respectively associated with the peaks at 3005, 3280, 3470, and 3515 cm^{-1}, as reported in Table 1, and characterized by decreasing degree of interaction with polar polymer sites.

Table 1. Characteristics Features of Different Water Families in the System: IR Peak Position and Band Width (fwhm), Fitted Extinction Coefficients ($\varepsilon_{eff,i}$), and Model Constants (K_i)

water population	IR peak center position (cm^{-1})	fwhm[a] (cm^{-1})	$\varepsilon_{eff,i}$ (cm^3/mol)	K_i
1st	3005	592 (2%)	1.56×10^4	100
2nd	3280	389 (6%)	1.19×10^4	20
3rd	3470	264 (3%)	1.19×10^4	3.5
4th	3515	241 (2%)	6.29×10^3	2.5

[a]The value in parentheses in fwhm column represent the maximum percent variation of this quantity at the different RH values inspected.

Concerning this result, a few considerations are in order: first of all, it should be stressed that number of deconvoluted peaks equal to 4 is the minimum required to obtain a satisfactory description of the experimental data. A different number of bands could be used to describe the OH stretching region; however, using two or three peaks did not allow to obtain a good fit unless more complex, and with more parameters, peak shapes (such as the so-called split-Gaussian) were used, while a higher number of peaks lead to minor improvements in the final fitting and in some cases generated unphysical behavior in the fitting results.

In addition, despite the complexity of the procedure followed, deconvolution results obtained were very stable and highly consistent, both internally and with respect to previous works; the width of different water peaks, also reported in Table 1, showed indeed very small variations at different RH, indicating that the obtained bands are related to precise molecular features that did not vary substantially during absorption, while the positions of the different water peaks are in good agreement with what proposed by other authors investigating water content in PFSI polymers.[30,38,39] In particular, the peaks found between 3300 and 3000 cm^{-1} have been related by many authors to water hydrogen bonded to sulfonic groups[38,39] or hydronium ions[28,30] while the bands related to H_3O^+ as well as those of internal sulfonic groups hydrogen bonding are expected to appear[30,38] in the range of 2900−3000 cm^{-1}, so that they are more difficult to be precisely assigned. However, by following the integrated absorbance of the peaks with time, shown in Figure 6, it can be noticed that the amount of all populations increases with time during polymer hydration, according to a kinetics qualitatively consistent with a mass diffusion process. Thus, also for the first population, the contribution of water OH stretching seems to be predominant, while the internal mode of undissociated SO_3H group, if present, seems to be placed at lower wavenumber and thus comprised in the wide peak at 2700 cm^{-1}. It is also clear from the same Figure 6 that the kinetic behavior of the first family differs from that of the others; the analysis of diffusion kinetics however is out of our present aim and will be presented and discussed in a future paper.

In the present work, instead, the attention is focused on the equilibrium values of water uptake. From the four water-related peaks identified with the above procedure, one can estimate the relative amount of the corresponding water families, by calculating the integral absorbance of the different bands as a function of water activity. The results, reported in Figure 7, clearly show that as the water content in the membrane increases, the first family of water rapidly reaches a plateau, while the area associated with weakly bonded molecules continues to increase. That is in agreement with the idea that the first water molecules entering the system react with sulfonic groups to produce hydronium ions, while the following ones substantially solvate with successive water layers and, consequently, have lower interaction energy with sulfonic groups.

Sorption Data and Absorbance−Concentration Relationship. The data provided by FTIR spectrometry and reported in Figure 7 are expressed in terms of absorbance; in order to obtain the penetrant concentration in the sample, an independent measurement of the water uptake is required.[51] As stated above, the relationship between the equilibrium values of concentration and absorbance A is given by the Beer−Lambert's law, reported in eq 1, which can be also be rewritten as follows:

$$\lambda = c\frac{m_{eq}}{\rho_{pol}} = \frac{1}{\delta\varepsilon}A\frac{m_{eq}}{\rho_{pol}} = \frac{1}{\varepsilon_{eff}}\frac{m_{eq}A}{\rho_{pol}} \quad (2)$$

where λ is the concentration of the species under study, expressed in moles of water per mole of $-SO_3H$, c is water concentration in moles per unit polymer volume, ρ_{pol} is the polymer density in hydrated conditions, and m_{eq} is the equivalent weight of the polymer expressed in g/mol_{SO_3H}. While in transmission IR spectroscopy ε and δ are generally considered as constants, in the ATR experiments the latter quantity is related to the penetration depth of evanescent wave[50,51] and changes with the absorption bands wavelength; thus, an effective extinction coefficient, ε_{eff}, is commonly used, as defined in eq 2.

In principle, however, variations of the effective molar extinction coefficient ε_{eff} with the wavenumber can be related

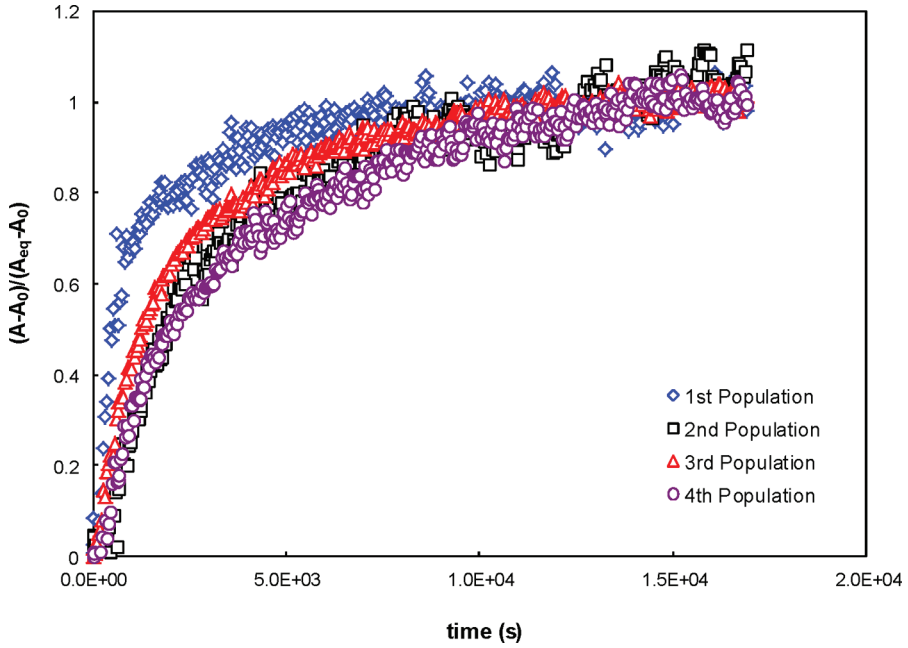

Figure 6. Time evolution of the integrated absorbance of the peaks related to the different water populations. The data refer to a sorption step in which the activity was increased from 0.1 to 0.2.

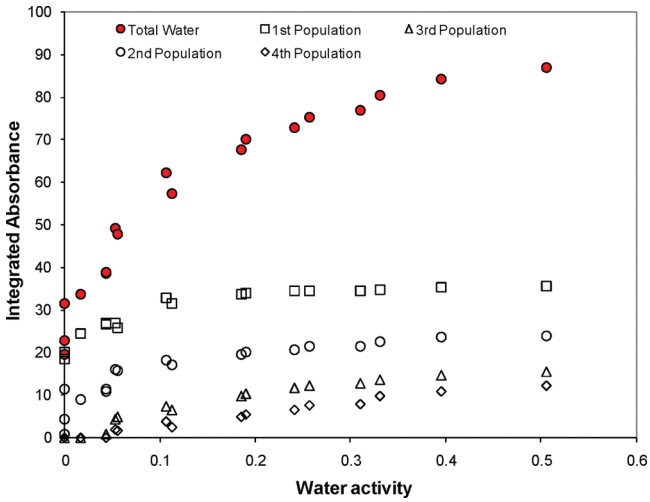

Figure 7. Evolution of integrated absorbance, as a function of water vapor activity for the different peaks identified in the Aquivion IR spectrum during the deconvolution process.

not only to changes of optical path length such as in FTIR-ATR but also to changes in the material absorbance due to variation of its refractive index or to the fact that a single peak, in complex spectra, can have contributions from different functional groups. These aspects have somehow prevented the quantitative study of water absorption in polymers using FTIR spectroscopy,[54,55] since deviation of the system from Beer–Lambert's law can lead to significant errors in the solubility calculation.[44,45] However, a quantitative description can be obtained also for the complex system by using multiple ε_{eff} values, whose evaluation requires reliable sorption data from separate independent source and a multiparameter calibration procedure.

In the present case, water solubility and polymer swelling were carefully measured in independent tests carried out on ionomer samples obtained from the same sheet as those examined in FTIR-ATR experiments.

The resulting data are presented in Figure 8; in particular, solubility is reported in terms of λ versus activity and shows the

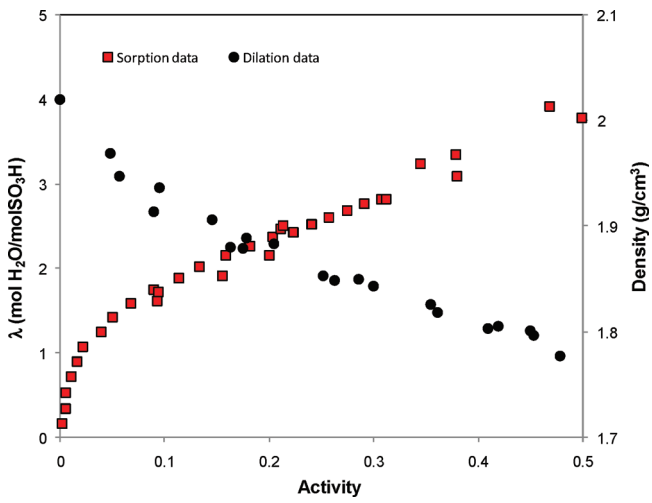

Figure 8. Water sorption in Aquivion and related change in polymer density as a function of water activity at 35 °C.

usual shape observed in sulfonated polymers, characterized by an initial steep increase of the mass uptake at low activities, followed by a linear part with lower slope at intermediate relative humidities. The final upturn of the sorption isotherm usually apparent at relative humidity higher than 70%[4,15] is not visible in the present data, since the activity range investigated was limited to about 0.5.

In the same Figure 8, also the density changes for the hydrated sample are presented, as calculated from the data and the procedure reported in ref 19. As expected, polymer density has an opposite trend with respect to water uptake, since it decreases due to polymer swelling upon sorption; parallel to

dx.doi.org/10.1021/ma202099p | Macromolecules 2012, 45, 1901–1912

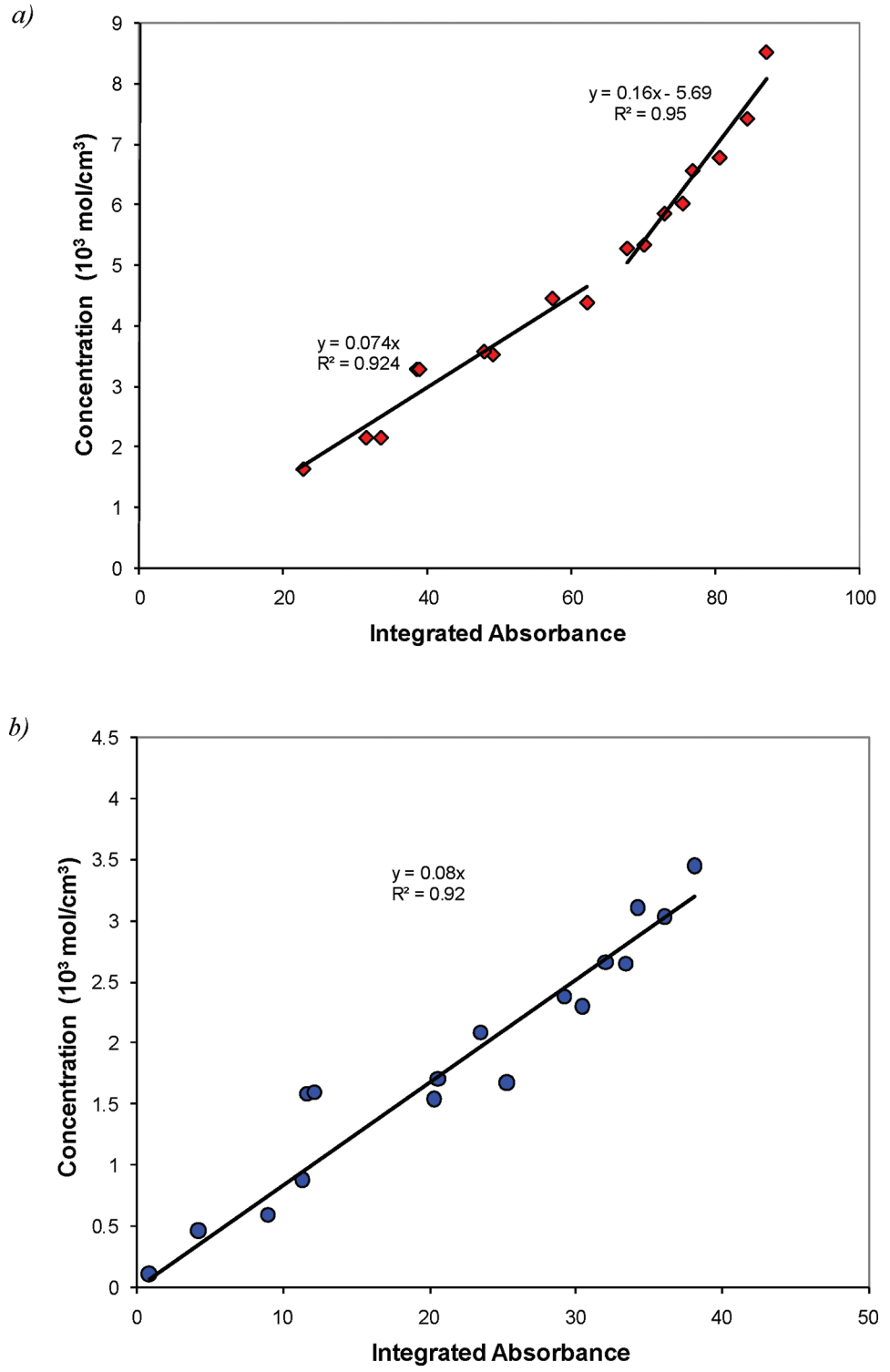

Figure 9. Calibration curve obtained from water concentration measured in a pressure decay apparatus (mol/cm^3) and integrated IR absorbance data at 35 °C, evaluated by considering (a) the contribution of all the water populations and (b) the contribution of the second and third populations only.

the sorption isotherm, the density change is particularly steep at low activity while it becomes substantially linear, with a lower slope, at the higher activities inspected.

From these data a direct relationship can be built between λ and A once the correct value of ε_{eff} for each water family is found. To that aim, the plot of the total water concentration in the membrane versus the total area of the water peaks in the −OH stretching region is presented in Figure 9a. Its behavior is not represented by a single straight line and shows an increase in slope at high absorbance, suggesting that the molar extinction coefficients decrease with increasing wavenumber and decreasing strength of interaction between water molecules and sulfonate sites. A multiple parameter regression is therefore required to obtain the values of the four extinction coefficients

dx.doi.org/10.1021/ma202099p | *Macromolecules* 2012, 45, 1901−1912

corresponding to the different water families, however, a simpler procedure is sufficient, in the present case, since the data are well described by a bilinear trend with two different regions characterized by two different slopes. The calibration for ε_{eff} can therefore be performed in a straightforward manner on the basis of the following assumptions:

(i) The first family, related to water directly interacting with the sulfonic groups, reaches a saturation value at $\lambda = 1$, which means that every water molecule in that family interacts with a single sulfonic group. The extinction coefficient $\varepsilon_{eff,1}$ is thus immediately evaluated from Figure 7, considering that absorbance value at saturation for the first population ($A \sim 35$ au) corresponds to $\lambda = 1$; the calculated value is then $\varepsilon_{eff,1} = 1.56 \times 10^4$ cm^3/mol.

(ii) From Figure 7 it is also seen that, for activities higher than 30%, the first and the second water populations have essentially reached their plateau, while the concentration of the fourth population increases 2 times more than that of the third one. This range of activities corresponds to integrated absorbance values higher than 70 a.u. and concentrations higher than $5 \times 10^3 \times$ mol/cm^3 (Figure 9a), where a change in slope of the calibration curve is apparent. The value of the slope in this range, therefore, can be mainly related to the molar extinction coefficient of the fourth population of water molecules, leading to a $\varepsilon_{eff,4}$ value of about 6.29×10^3 cm^3/mol.

The values of $\varepsilon_{eff,2}$ and $\varepsilon_{eff,3}$, can now be obtained by best fitting the water absorbance data once the contributions to c of the first and fourth families have been subtracted, as is shown in Figure 9b. Despite some scatter of the data, the plot clearly shows a linear behavior of the absorbance of the second and third family versus the corresponding water content, with a negligible difference between the extinction coefficient for these two families. In particular, a value of $\varepsilon_{eff,2} = \varepsilon_{eff,3}$ of about 1.19×10^4 cm^3/mol is obtained from the linear regression of the experimental data; the results of the regression are also shown in Figure 9b and are characterized by a correlation coefficient $R^2 = 0.92$, confirming the internal consistency of the procedure followed.

Using the above values for the effective molar extinction coefficients, summarized in Table 1 for clarity sake, the total water sorption isotherm is obtained as reported in Figure 10, from which the very good agreement with experimental solubility data is clearly appreciated. In the same figure, the sorption isotherms of the different populations are also reported as a function of water activity, illustrating their contribution to the total water uptake. In particular, by analyzing the different families, it can be noticed that the first one reaches the final plateau when the total value of λ is between 1.5 and 2, in very good agreement with the value of 1.6 mol of water per mole of acid found by Leuchs and Zundel[52] in the case of concentrated solution of CF_3SO_3H. The second and third populations are characterized by sorption isotherms with downward curvature, similar to those of adsorbing materials; the sorption of these molecules is thus somehow limited by the finite ability of sulfonic groups to coordinate water molecules, and therefore these two families are still related, to some extent, to the hydrophilic nuclei. On the contrary, the sorption isotherm of the fourth family has an almost linear behavior, typical of molecules physically absorbed in liquid and liquid-like structures such as rubbers, suggesting that the fourth population is formed by water not directly interacting with the sulfonic groups, but surrounded by other water molecules with which it interacts through water−water hydrogen bonding.

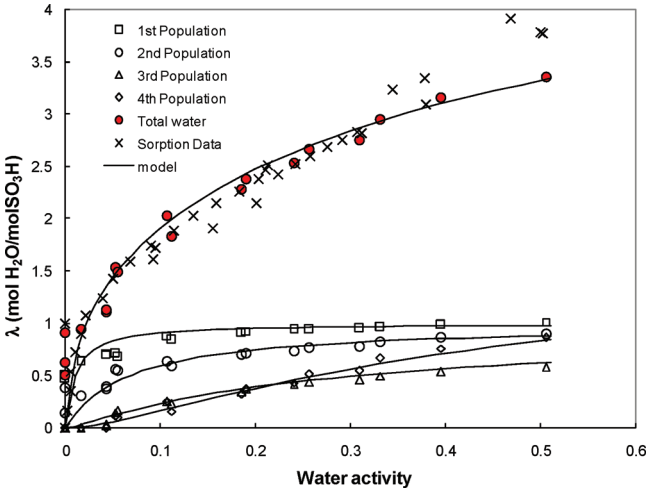

Figure 10. Water sorption isotherm in Aquivion at 35 °C collected with the FTIR-ATR spectrometer and with a pressure decay apparatus. The isotherms of the different species of water identified from the FTIR-ATR experiments are also reported. The lines represent the fit obtained with the model presented in this work.

The behavior of the different water families inside the polymer thus clearly suggests that water sorption in PFSI membranes is a complex process that, from a physical point of view, can be described as a sort of multilayer adsorption of water molecules on acid sulfonic groups followed by a physical absorption in the hydrophilic phase which has been formed. It is worthwhile to notice that, while the quantitative, relative amount of the different water families is strongly related to the calibration procedure considered, being thus affected by some degree of uncertainty, the physical process described is essentially related to the qualitative behavior of the different absorption bands present in the polymer spectra at different degrees of hydration and is thus independent of the calibration procedure followed.

MODELING EQUILIBRIUM SORPTION

The qualitative physical description considered in analyzing the polymer spectra and the procedure followed for the calibration between absorbance and water concentration can be further supported by a quantitative agreement between experimental results and a mathematical model describing the various steps considered in the process. To that aim, we adapted to our findings on the different water populations the models already proposed for similar systems, which describe the total water uptake in an ionomeric matrix considering a series of solvating reactions between water and sulfonic groups.[6,26,57] In particular, we considered that each sulfonic group is surrounded by a three-layer structure of water molecules. Following the results by Paddinson and co-workers, who studied the short-side-chain PFSI hydrated structure through a series of first principles electronic structure calculations,[58,59] we can describe the system as in Figure 11 in which a possible representation of the different layers is presented. Paddisons and co-workers indeed showed that structures with hydronium or Zundel ions in the vicinity of sulfonic groups are preferred in short-side-chain PFSI, when $\lambda \leq 3$, while other water molecules can directly interact with both the SO_3^- or H_3O^+ system;[58] such a result was also confirmed by molecular dynamics simulation conducted on a similar polymer structure for $\lambda = 3$.[59] Therefore, it is supposed that the first water family is formed

dx.doi.org/10.1021/ma202099p | Macromolecules 2012, 45, 1901−1912

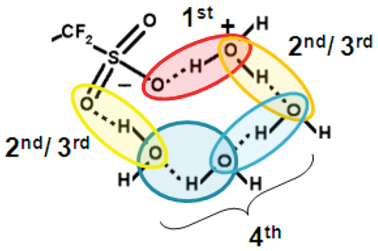

Figure 11. Possible structure of water around sulfonic groups at low hydration levels and relationship with different water families observed in the IR spectrum. Tentative assignments of hydrogen-bonding interaction observed in the IR spectra are also highlighted in the figure.

by the water molecules directly interacting with the $-SO_3H$ groups, leading to their dissociation, while the second and third populations, that begin to appear at higher hydration levels are bound to the inner family in a shell-like structure; in particular, the hypothesis is made that they can interact directly with the dissociated sulfonic groups or with the hydronium ions. The fourth population finally represents the water present in the outer shell, which is only marginally influenced by the sulfonic groups and interacts only with water molecules of the previous hydration shell (second and third population) or with the rest of free water which can be substantially considered as physically absorbed in the hydrophilic part of the polymer.

This model structure obviously offers a simplified view of a more complex reality, but it appears plausible at least in the inspected range of water concentrations, where the number of water molecules in the system is still relatively low. In particular, such geometry was selected among the other possible ones to stress the fact that, in the outer shell, the free water can be involved in more than one hydrogen bond per molecule, thus increasing its molar absorbance and lowering ε_4; this fact justifies the quite high difference observed between the absorption coefficient of the fourth family and that of the other ones.

From a mathematical point of view, the equilibrium sorption of the different populations can be represented through the use of multiple Langmuir isotherms, describing the adsorption of subsequent layers onto the inner ones: the first water family directly interacts with the sulfonated groups (indicated by the subscript "sites"), while the second and third are adsorbed on the $SO_3H{\cdot}(H_2O)$ clusters, and the fourth one on the sites available in the inner shell formed by the second and third type of water molecules as indicated in Figure 11. This mathematical approach was chosen for its simplicity among the many others possible; indeed, the use of more rigorous models, such as those based on a series of adsorption reaction in mutual equilibrium,[26,60,61] imply for the present structure a rather complex mathematical development, without increasing the accuracy of the results. In the present case, therefore, the least onerous mathematical description was adopted, and the following set of equations was used to describe the system behavior:

$$c_1 = K_1 \frac{a_w}{1 + K_1 a_w} c_{sites} \quad (3)$$

$$c_2 = K_2 \frac{a_w}{1 + K_2 a_w} c_1 \quad (4)$$

$$c_3 = K_3 \frac{a_w}{1 + K_3 a_w} c_1 \quad (5)$$

$$c_4 = K_4 \frac{a_w}{1 + K_4 a_w} (c_2 + c_3) \quad (6)$$

The equilibrium constants of the Langmuir isotherms, K_1, K_2, K_3, and K_4 are obtained by best fitting each curve to the data collected with FTIR-ATR experiments and reported in Figure 10. Interestingly, the value of the first constant, K_1, is large (on the order of 100) and comparable with data available for the first dissociation constant of polystyrenesulfonates,[57] while the other constants have progressively decreasing values of about 20, 3.5, and 2.5, respectively, in agreement with the weaker interaction with the acid groups. The parameters obtained are also reported in Table 1, while the results of the modeling are presented in Figure 10.

Of course, the present analysis together with the associated model structure is appropriate for the water concentration range inspected; at higher activities, more complex water structures are expected to occur, with the formation of Zundel ions as well as extensive clustering of free water that substantially change the IR response of the different populations and make more difficult to discriminate among the contributions of the different families.[30,34]

At the relative humidities experimentally considered, on the other hand, the agreement between the model and the experiments for the total water uptake is rather good, as visible in Figure 10, where the model calculations are represented by solid lines. The model actually represents very well the experimental findings for each population and describes correctly the details of the sorption behavior in the range of activity in which the strongly interacting water populations reach their maxima as well as beyond this point where the contribution of the fourth population, initially negligible, becomes important.

Such an agreement is reached with the use of one single fitting parameter for each curve, and the maximum errors are found in the lower activity range, where the lack of data and the uncertainty related to the initial amount of water absorbed in the polymer affect the sensitivity and the reliability of the experimental measurements.

The approach proposed is thus physically consistent and allows to describe correctly the experimental behavior observed; the results support the validity of the assumptions considered in the model and in processing the data.

■ CONCLUSIONS

Water sorption in Aquivion was studied through the FTIR-ATR technique. The analysis of IR spectra at different relative humidities allowed to distinguish among different populations of water on the basis of their interaction with the terminal sulfonic group of the side chain of the ionomer. The decomposition of −OH stretching band between 2400 and 3800 cm^{-1}, in particular, leads to consider the presence of four water populations appearing at different degrees of hydration and characterized by a decreasing strength of interaction with the sulfonic groups. Based on the comparison of total water absorbance with independent solubility measurement, a proper calibration curve was obtained, and the IR results were described in terms of concentration. The sorption isotherm of each water family was thus determined: the first three water populations are characterized by isotherms with downward curvature, typical of adsorbing materials that reach a saturation, while the fourth one shows an almost linear dependence on water activity, which suggests that the corresponding water

group was not directly interacting with the polymer acidic sites. The corresponding model description was presented, considering the different water populations as directly interacting, in a sequence of shells, with the sulfonic groups, through Langmuir-type adsorption mechanisms. The agreement with the observed experimental data is rather satisfactory, indicating both the consistency of the qualitative physical representation of the process and the robustness of the model proposed.

The FTIR-ATR technique allows to study the water sorption mechanism in detail and to understand the multiple mechanisms through which water is absorbed into the PFSI membrane.

AUTHOR INFORMATION

Corresponding Author

*E-mail: marco.giacinti@unibo.it.

Present Addresses

[†]Institute for Materials and Processes, The University of Edinburgh, King's Buildings, Mayfield Road, Edinburgh EH9 3JL, UK.

[‡]Center for Inorganic Membrane Studies, Department of Chemical Engineering, Worcester Polytechnic Institute, 100 Institute Rd., 01609 Worcester, MA.

Notes

The authors declare no competing financial interest.

REFERENCES

(1) *Fuel Cell Handbook*, 7th ed.; EG&G Technical Services, Inc., 2004; Contract DE-AM26-99FT40575.

(2) Heitner-Wirguin, C. *J. Membr. Sci.* **1996**, *120*, 1−33.

(3) Pushpa, K. K.; Nandan, D.; Iyer, R. M. *J. Chem. Soc., Faraday Trans. 1* **1988**, *84*, 2047−2056.

(4) Zawodzinski, T. A.; Derouin, C.; Radzinski, S.; Sherman, R. J.; Smith, V. T.; Springer, T. E.; Gottesfeld, S. *J. Electrochem. Soc.* **1993**, *140*, 1041−1047.

(5) Zawodzinski, T. A.; Neeman, M.; Sillerud, L. O.; Gottesfeld, S. *J. Phys. Chem.* **1991**, *95*, 6040−6044.

(6) Takata, H.; Mizuno, N.; Nishikawa, M.; Fukada, S.; Yoshitake, M. *Int. J. Hydrogen Energy* **2007**, *32*, 371−379.

(7) Van Nguyen, T.; Vanderborgh, N. *J. Membr. Sci.* **1998**, *143*, 235−248.

(8) Arcella, V.; Ghielmi, A.; Merlo, L.; Gebert, M. *Desalination* **2006**, *199*, 6−8.

(9) Arcella, V.; Troglia, C.; Ghielmi, A. *Ind. Eng. Chem. Res.* **2005**, *44*, 7646−7651.

(10) Arcella, V.; Ghielmi, A.; Tommasi, G. *Ann. N. Y. Acad. Sci.* **2003**, *984*, 226−244.

(11) Danilczuk, M.; Perkowski, A. J.; Schlick, S. *Macromolecules* **2010**, *43*, 3352−3358.

(12) Mohamed, H. F. M.; Kobayashi, Y.; Kuroda, C. S.; Ohira, A. *Macromol. Chem. Phys.* **2011**, *212*, 708−714.

(13) Stassi, A.; Gatto, I.; Passalacqua, E.; Antonucci, V.; Aricò, A. S.; Merlo, L.; Oldani, C.; Pagano, E. *J. Power Sources* **2011**, DOI: 10.1016/j.jpowsour.2010.12.084.

(14) Catalano, J.; Giacinti Baschetti, M.; De Angelis, M. G.; Sarti, G. C.; Sanguineti, A.; Fossati, P. *Desalination* **2009**, *240*, 341−346.

(15) De Angelis, M. G.; Lodge, S.; Giacinti Baschetti, M.; Sarti, G. C.; Doghieri, F.; A. Sanguineti, A.; Fossati, P. *Desalination* **2006**, *193*, 398−404.

(16) Morris, D. R.; Sun, X. *J. Appl. Polym. Sci.* **1993**, *50*, 1445−1452.

(17) Yamamoto, Y.; Ferrari, M. C.; Giacinti Baschetti, M.; De Angelis, M. G.; Sarti, G. C. *Desalination* **2006**, *200*, 636−638.

(18) Gorri, D.; De Angelis, M. G.; Giacinti Baschetti, M.; Sarti, G. C. *J. Membr. Sci.* **2008**, *322*, 383−391.

(19) Catalano, J.; Myezwa, T.; De Angelis, M. G.; Giacinti Baschetti, M.; Sarti, G. C. *Int. J. Hydrogen Energy* **2011**, DOI: 10.1016/j.ijhydene.2011.07.047.

(20) Baias, M.; Demco, D. E.; Blümich, B.; Möller, M. *Chem. Phys. Lett.* **2009**, *473*, 142−145.

(21) Kim, Y. S.; Dong, L.; Hickner, M. A.; Glass, T. E.; Webb, V.; McGrath, J. E.; et al. *Macromolecules* **2003**, *36*, 6281.

(22) Lee, D. K.; Saito, T.; Benesi, A. J.; Hickner, M. A.; Allcock, H. R. *J. Phys. Chem. B* **2011**, *115*, 776−783.

(23) Lu, Z.; Polizos, G.; Macdonald, D. D.; Manias, E. *J. Electrochem. Soc.* **2008**, *155*, B163.

(24) Ye, G.; Janzen, N.; Goward, G. R. *Macromolecules* **2006**, *39*, 3283−3290.

(25) Zhao, Q.; Majsztrik, P.; Benziger, J. *J. Phys. Chem. B* **2011**, *115*, 2717−2727.

(26) Choi, P.; Datta, R. *J. Electrochem. Soc.* **2003**, *150*, E601−E607.

(27) Basnayake, R.; Peterson, G. R.; Casadonte, D. J.; Korzeniewsky, C. *J. Phys. Chem. B* **2006**, *110*, 23938−23943.

(28) Buzzoni, R.; Bordiga, S.; Ricchiardi, G.; Spoto, G.; Zecchina, A. *J. Phys. Chem.* **1995**, *99*, 11937−11951.

(29) Falk, M. *Can. J. Chem.* **1980**, *58*, 1495−1501.

(30) Gruger, A.; Rèegis, A.; Schmatko, T.; Colomban, P. *Vibr. Spectr.* **2001**, *26*, 215−225.

(31) Iwamoto, R.; Oguro, K.; Sato, M.; Iseki, Y. *J. Phys. Chem. B* **2002**, *106*, 6973−6978.

(32) Korzeniewsky, C.; Snow, D. E.; Basnayake, R. *Appl. Spectrosc.* **2006**, *60*, 599−604.

(33) Laporta, M.; Pegoraro, M.; Zanderighi, L. *Phys. Chem. Chem. Phys.* **1999**, *1*, 4619−4628.

(34) Ludvigsson, M.; Lindgren, J.; Tegenfeldt, J. *Electrochim. Acta* **2000**, *45*, 2267−2271.

(35) Quezado, S.; Kwak, J. C. T.; Falk, M. *Can. J. Chem.* **1984**, *62*, 958−966.

(36) Wang, Y.; Kawano, Y.; Aubuchon, S. R.; Palmer, R. A. *Macromolecules* **2003**, *36*, 1138−1146.

(37) Ostrowska, J.; Narebska, A. *Colloid Polym. Sci.* **1983**, *261*, 93−98.

(38) Ostrowska, J.; Narebska, A. *Colloid Polym. Sci.* **1984**, *262*, 305−310.

(39) Warren, D. S.; Mc. Quillan, A. J. *J. Phys. Chem. B* **2008**, *112*, 10535−10543.

(40) Maréchal, Y. *J. Mol. Struct.* **2003**, *648*, 27−47.

(41) Hofmann, D. W. M.; Kuleshova, D.; D'Aguanno, B.; Di Noto, V.; Negro, E.; Conti, F.; Vittadello, M. *J. Phys. Chem. B* **2009**, *113*, 632−639.

(42) Elabd, Y. A.; Giacinti Baschetti, M.; Barbari, T. A. *J. Polym. Sci., Part B: Polym. Phys.* **2003**, *41*, 2794−2807.

(43) Elabd, Y. A.; Barbari, T. A. *AIChE J.* **2001**, *47*, 1255−1262.

(44) Sammon, C.; Deng, C.; Mura, C.; Yarwood, J. *J. Mol. Liq.* **2002**, *101*, 35−54.

(45) Sammon, C.; Deng, C.; Yarwood, J. *Polymer* **2003**, *44*, 2669−2677.

(46) Hallinan, D. T.; Elabd, Y. A. *J. Phys. Chem. B* **2007**, *111*, 13221−13230.

(47) Hallinan, D. T.; Elabd, Y. A. *J. Phys. Chem. B* **2009**, *113*, 4257−4266.

(48) Hallinan, D. T.; De Angelis, M. G.; Giacinti Baschetti, M.; Sarti, G. C.; Elabd, Y. A. *Macromolecules* **2010**, *43*, 4667−4678.

(49) Giacinti Baschetti, M.; Piccini, E.; Barbari, T. A.; Sarti, G. C. *Macromolecules* **2003**, *36*, 9574−9584.

(50) Harrick, N. J. *Internal Reflection Spectroscopy*; Interscience Publications: New York, 1967.

(51) Hong, S. U.; Barbari, T. A.; Sloan, J. M. *J. Polym. Sci., Part B: Polym. Phys.* **1997**, *35*, 1261−1267.

(52) Leuchs, M.; Zundel, G. *J. Chem. Soc., Faraday Trans. 2* **1978**, *74*, 2256−2267.

(53) http://www.unipress.waw.pl/fityk/.

(54) Cotugno, S.; Larobina, D.; Mensitieri, G.; Musto, P.; Ragosta, G. *Polymer* **2001**, *42*, 6431−6438.

(55) Musto, P.; Ragosta, G.; Mensitieri, G.; Lavorgna, M. *Macromolecules* **2007**, *40*, 9614−9627.
(56) Kusoglu, A.; Santare, M. H.; Karlsson, A. M. *Polymer* **2009**, *50*, 2481−2491.
(57) Glueckauf, E.; Kitt, G. P. *Proc. R. Soc. London, Ser. A* **1955**, *228*, 322−341.
(58) Paddison, S. J. *Annu. Rev. Mater. Res.* **2003**, *33*, 289−319.
(59) Hristov, I. H.; Paddison, S. J.; Paul, R. *J. Phys. Chem. B* **2008**, *112*, 2937.
(60) Choi, P.; Jalani, N. H.; Datta, R. *J. Electrochem. Soc.*. **2005**, *152*, E84−E89.
(61) Wu, X.; Wang, X.; He, G.; Benziger, J. *J. Polym. Sci., Part B: Polym. Phys.* **2011**, *49*, 1437−1445.

Macromolecules

Article

pubs.acs.org/Macromolecules

Study of the Formation of Poly(vinyl alcohol) Films

Sushanta Ghoshal, Paul Denner, Siegfried Stapf, and Carlos Mattea*

Department of Technical Physics II/Polymer Physics, Institute of Physics, Faculty of Mathematics and Natural Science, Ilmenau University of Technology, PO Box 10 05 65, D-98684 Ilmenau, Germany

Supporting Information

ABSTRACT: The film formation of poly(vinyl alcohol) of different molecular weights from concentrated solution has been observed in real time by means of low-field nuclear magnetic resonance (NMR) methods. The drying of films was followed with a depth resolution of 50 μm up to the formation of the final film of typically 300 μm thickness, and the molecular mobility was determined with spatial resolution by analyzing the NMR relaxation times (T_2, T_1) behavior. A gradient in the molecular dynamics was observed from T_1 data during evaporation process up to an intermediate time when the film shrinkage rate decreases significantly; T_2 indicates dynamical heterogeneity as well, persisting up to complete removal of water. The relaxation times suggest an increase of local molecular order which is more pronounced toward the air/film interface. Wide-angle X-ray diffraction confirms the formation of an ordered region at this interface with a crystallinity higher—depending on molecular weight—than at the bottom side of the film.

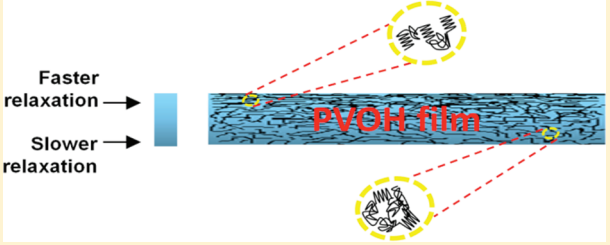

1. INTRODUCTION

Synthetic polymers are established and abundantly used mainly due to their low price, availability, and physical and chemical properties.[1] However, they are responsible for producing an enormous amount of waste in daily life, a problem of ever-growing importance to mankind.[2] There is a small number of synthetic polymers which are known for their environment friendly behavior. Poly(vinyl alcohol) (PVOH), synthesized by Herrmann and Haehnel in 1924, is one of those synthetic polymers that is biodegradable and biocompatible and possesses good mechanical properties.[3]

Commercially available PVOH has a broad range of hydrolysis and degree of polymerizations which open the field of versatile applications in fibers, cosmetics industry, adhesives, textile and paper sizing, asbestos alternatives, and pharmaceutical and biomedical materials.[4−6] PVOH is a good film-forming polymer which has applications in different industrial sectors, for instance, as a high oxygen barrier film, membranes, packaging materials, and polarizing film as PVOH−iodine complex.[7−10] Water is used as a common solvent for the production of semicrystalline PVOH film. Above the glass transition temperature ($T_g \approx 85$ °C) fully hydrolyzed PVOH is completely soluble in water.[11] The drying process during the formation of the PVOH film from the aqueous solution is vital as the final structure and the characteristic properties of the film depend on this process.[12] A number of references[12−16] have been devoted to study the drying of the PVOH solution. There, a "skin" formation process has been reported which consists of a glassy layer formation on top of the evaporating solution. This process is related to the shifting of the glass transition temperature (T_g) due to the change in the solvent concentration. As the PVOH film is semicrystalline in nature, the removal of solvent during the film formation process will drive both the crystallization and the amorphous phase (glass) formation process. In particular, the glass transition temperature of the PVOH−water mixture will increase. As a consequence, a glassy layer may develop at the air−sample interface as the solvent removal rate is faster in this part of the sample, compared with the bulk solution system. On the other hand, the development of a crystalline skin is reported in ref 17 on the basis of the change in evaporation rate during the film formation. In this reference, magnetic resonance imaging (MRI) studies of PVOH cast from aqueous solution as a function of time show nonuniform water distribution at certain drying conditions, coupled with a crystalline layer at the top surface of the solution. However, detailed microscopic experimental studies explaining these observations as well as the structural characterization of the final film addressing these phenomena are scarce.

In recent years single-sided low-field nuclear magnetic resonance (NMR) scanners[18,19] are established as a suitable tool to study noninvasively the film formation with a microscopic resolution as it has been demonstrated in refs 20 and 21 in the case of biopolymer gelatin and PVOH film, respectively. Using this technique, the new feature reported in the present work is the experimental demonstration of the presence of gradual heterogeneities in PVOH in an aqueous solution during film formation. In addition, the X-ray diffraction (XRD) technique is used to study the film which is capable of providing information on structure of the final state of a film at a molecular level. The film formation of PVOH of three different molecular weights (see below) is investigated in order to observe the molecular weight dependency. Water is used as a

Received: October 19, 2011
Revised: January 26, 2012
Published: February 15, 2012

solvent and compared with previous results obtained using deuterated water as a solvent.[21] The NMR studies presented here reveals a progressive process leading to a hardening of the top regions of the film assessed by the relaxation times T_2 and T_1 gradually growing at the bottom part of the sample. The heterogeneity identified by the NMR study is confirmed by the XRD study of the film.

In order to find universal features during the film formation process of polymers, the comparison with other film formation process is worthwhile. Note that during the film formation of a biopolymer like gelatin in solution with different concentrations,[20,22] a different type of heterogeneity was observed. That system is homogeneous at the beginning of the film formation when the sample is cast. At a later stage of drying, heterogeneities appear and the bottom part of the sample shows lower values of T_2 than the upper part. This is an opposite behavior as observed in the PVOH solution system. Biopolymers are structurally complex and so are the processes involved in the formation of films out of them. The study of the film formation of polymers having simpler structures, like PVOH will certainly bring useful insights into the field of film formation processes.

2. EXPERIMENTAL SECTION

2.1. Sample Preparation. PVOH (MOWIOL grade) was obtained from Sigma-Aldrich, Germany, and used without further purification. Three different molecular weights of PVOH—27 000, 61 000, and 125 000—were used in this study with a degree of hydrolysis >98% for all the samples. While most experiments were carried out with the sample of MW = 61 000 (indicated as 61K), comparative measurements were repeated under similar experimental conditions for MW = 27 000 (27K) and MW = 125 000 (125 K). Two solvents were used: monodistilled water and deuterium oxide (D_2O). D_2O (100 atom % D) was purchased from Carl Roth GmbH + Co., Germany. The PVOH was dried at 110 °C to remove the moisture. Each sample was then kept in a desiccator in a moisture-free atmosphere at ambient temperature for storage. The same protocol was used for the preparation of all the samples to be diluted either with H_2O or D_2O. Table 1 shows the composition of the samples used in this work.

Table 1. Preparation of the 25% PVOH Solution (w/v) for Different Studies Using Either H_2O or D_2O as Solvent

sample label	mol wt of PVOH solute	solvent	study	final film thickness (μm)
a	27K	H_2O	T_1 and T_2 at 11.7 MHz, XRD	380 ± 25
b	61K	H_2O	T_1 and T_2 at 11.7 MHz, XRD	340 ± 12
c	125K	H_2O	T_1 and T_2 at 11.7 MHz, XRD	268 ± 15
d	61K	H_2O	T_1 and T_2 at 40 MHz	
e	61K	D_2O	T_1 and T_2 at 40 MHz	
f	61K	H_2O	diffusion	
g	61K	D_2O	diffusion	

Prior to carrying out the experiments, either distilled water or deuterium oxide was used to prepare the 25% (w/v) PVOH–H_2O or 25% (w/v) PVOH–D_2O solutions, respectively. In order to obtain a homogeneous mixture and to avoid local gelation, each of the above samples was heated and stirred at 90 °C for 1 h, with the beaker being covered completely (but not sealed) during this period. Following this step, the covered beaker containing the homogeneous mixture was placed in an oven and was kept at the same temperature for further 5 h to eliminate air bubbles. After cooling down, the viscous solution was cast on a polystyrene Petri dish of 55 mm diameter for the film formation experiment (see section 2.2). Note that when PVOH is used as hydrogel, the gel is induced only after several cycles of a freezing–thawing process.[23,24] However, no gel formation was observed after several hours of preparation in the present work.

2.2. NMR Experiments with Single-Sided NMR Scanner. Each of the viscous solutions was placed on a single-sided NMR scanner (NMR MOUSE, ACT GmbH, Germany) with the sensor having a sensitive area of about 10 mm by 10 mm, placed underneath the center of the Petri dish. The detailed experimental setup is illustrated elsewhere.[22] The device, having an accessible vertical range of 2.1 mm, is operated at 11.7 MHz for ^{1}H Larmor frequency, and possesses a static gradient of the magnetic field of 11.5 T/m. The digital resolution is determined by the combination of the spectral width, acquisition time, and the gradient strength.[25] The minimum 180° pulse separation is determined by the acquisition time of the echo preceded and followed by the dead-time of the system of 23 μs. It was set to 87.5, 66.5, 56.5, and 53.5 μs for the resolution of 50, 100, 200, and 300 μm, respectively. The Carr–Purcell–Meiboom–Gill (CPMG) pulse sequence[26] was applied to obtain the vertical profiles and to accumulate T_2-weighted echo trains by moving the scanner relative to the sample as well as to measure the effective time of echo decays. The 90° rf pulse length was set to 3.5 μs.

For the samples a, b, and c (see Table 1), the position of the sensor was moved in steps of 100 μm with a slice thickness of 50 μm from the beginning. The polystyrene substrate is defined as "zero" height in the following discussion. Each point in the profile corresponds to the sum of the area of the second to fifth echo. A total of 2048 echoes were acquired for computing the effective transverse relaxation times T_2 layer by layer. The signal decays for each point in the profile followed either single- or double-exponential behavior and were fitted accordingly (see Discussion section). The waiting time between pulse trains, as well as the number of repetitions, was adjusted according to the longest T_1 at a particular time in the experiment, in order to keep the signal unaffected by longitudinal relaxation weighting, but maximizing signal-to-noise ratio for a given experimental run. Following each T_2 profile, a second experiment was carried out where a saturation recovery pulse sequence [90°–τ–90°][27] was used with 18 τ values (logarithmically spaced) for determining T_1. T_2 values of the fully dried films obtained from sample c were also measured as a function of height using CPMG pulse sequence in three separate experiments for different echo times and keeping the remaining parameters constant (32 echoes, 250 ms repetition time, and 2048 scans).

For the diffusion measurements, sample f (25% (w/v) PVOH–H_2O) and sample g (25% (w/v) PVOH–D_2O) were prepared and the stimulated echo sequence[28] in combination with the static magnetic field gradient of the sensor was used. The measurements were performed right after the casting, sealing the container to avoid evaporation. For this measurement an encoding time τ = 0.0055–1.9 ms, diffusion time Δ = 2 ms, and repetition time of 3 and 5 s (for the sample f and g, respectively) were used. All experiments were performed at room temperature. During the whole NMR measurement, the temperature of the magnet was stable within ±0.5 °C. At the position of the sample, a minor increase in the temperature was detected due to the heating of the rf coil. This heating was well below 0.5 °C.

2.3. NMR Experiments at 40 MHz. The PVOH solutions were measured right after preparation using sealed 8 mm NMR tubes avoiding both evaporation and proton exchange with the atmospheric humidity. The proton relaxation measurements were performed using a Minispec unit (Bruker Optics, Germany) operating at 40 MHz ^{1}H Larmor frequency, and with a temperature controller. All measurements were carried out at 21.5 ± 0.5 °C. An inversion recovery pulse sequence [180°–τ–90°][29,30] was used with 30 τ values (logarithmically spaced) to measure the spin–lattice relaxation time (T_1). The spin–spin relaxation time (T_2) was obtained applying the CPMG pulse sequence with a 90°–180° pulse separation of 40 μs at a 180° pulse width of 3.5 μs.

dx.doi.org/10.1021/ma2023292 | Macromolecules 2012, 45, 1913–1923

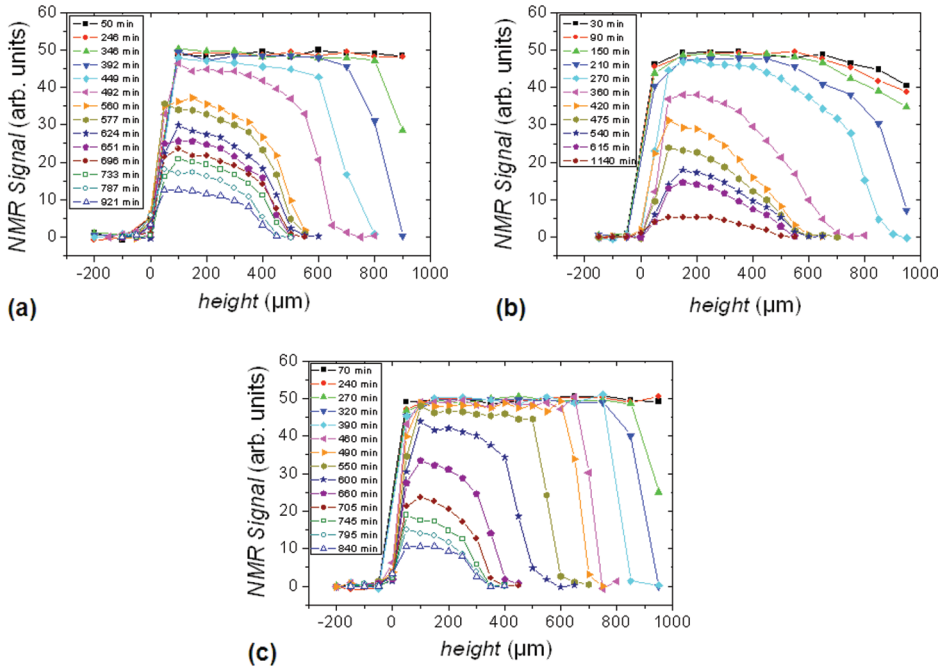

Figure 1. NMR profiles of the PVOH solutions of (a) 27K, (b) 61K, and (c) 125K at different drying times as indicated.

2.4. X-ray Diffraction (XRD) Measurements. Structural details of the PVOH film were examined by comparing the XRD pattern of both sides of the same film. The XRD patterns were acquired with a Philips X'Pert PRO diffractometer, equipped with a wide-range PW 3050/6X goniometer which is capable to measure 0.001°/step. The calibration was carried out prior to each of the measurements and a minimum offset for Ω (incident angle) and 2θ (diffraction angle) with 50% of the beam parallel to the surface of the sample were achieved. The experiment was carried out at room temperature using Cu Kα radiation (λ = 0.154 nm) generated at a voltage of 35 kV and 30 mA current. The fixed angle incident beam method[21] was used where Ω = 0.5° was fixed throughout the experiment. The sample was scanned between 2θ = 1.5° and 68° with a step size of 0.050°, scanning speed of 2°/min, and a count time of 100 s per point. Prior to the measurements, the sample was stored in the same environmental conditions as employed for the NMR experiments. The amorphous part of the spectra was subtracted using conventional method to show the impact of the difference in crystalline parts of the both sides of the film.

3. RESULTS

3.1. Profiling of the Sample. As stated in the Experimental Section, the sample was placed on top of the scanning device and vertical profiles were obtained by moving the scanner from top to bottom at a step size of 100 μm at the beginning and 50 μm at a later stage with a resolution of 50 μm in both cases. The NMR profiles of samples a, b, and c are shown in Figures 1a, 1b, and 1c, respectively, as a function of height at different time intervals while the system is evolving under the solvent evaporation. The time scale shown in this figure is the time after sample casting. Between two successive profiles, T_1 was measured (see section 3.4).

The right edge of the profiles corresponds to the air−sample interface, whereas 0 μm at the left-hand side shows the substrate−sample interface. All the samples possess an initial height of more than 1000 μm, and the air−sample interface is becoming observable due to progressive shrinkage after 346, 210, and 270 min of evaporation time for samples a, b, and c, respectively. Note that the apparent shift of the substrate−sample interface by ∼50 μm is an averaging effect and a consequence of the change of step size of the scanner which is reduced from 100 to 50 μm.

It is seen that the maximum profile intensity shown by all three samples are the same (within experimental error) which means that the molecular weight of the PVOH samples does not, at first sight, have an influence on the signal intensity. The signal of the profiles is a consequence of the number density of protons in PVOH and water. Because of the settings of the NMR experiment, there is no T_1 weighting, but a T_2 influence cannot be completely excluded. Its influence is negligible in the profiles (see following section); the profile is therefore only an indicator for the film thickness but not for the distribution of polymer within the film.

3.2. Rate of Evaporation. In Figure 2, the decrease in the sample height as a function of evolving time is shown. The sample height has been calculated as the width of the profiles, defined by the values of 5% of the maximum intensity where the signal can still be distinguished reliably from the noise level. On the basis of this assumption, the rate of evaporation $\dot{E}$, defined as the slope of the fitted lines, was calculated for each sample. Two evaporation regimes are observed in all the samples.

The first stage of evaporation has similar rates for samples a and b. For sample c this value is slightly smaller, which means that a very high molecular weight of PVOH may affect the evaporation process. The second regime of evaporation appears after around 560, 420, and 700 min of drying time for samples a, b, and c, respectively. Note that the rates decrease by almost 1 order of magnitude for all the samples. The relative humidity and temperature of the laboratory were not controlled but tend to be 40 ± 5% and 21 °C ± 2 °C, respectively, which may influence the average drying time.

3.3. T_2 Study in Single-Sided NMR. Each point in the profile of Figure 1 is obtained from an individual CPMG echo train. It is found that at the earlier evaporation times

dx.doi.org/10.1021/ma2023292 | Macromolecules 2012, 45, 1913−1923

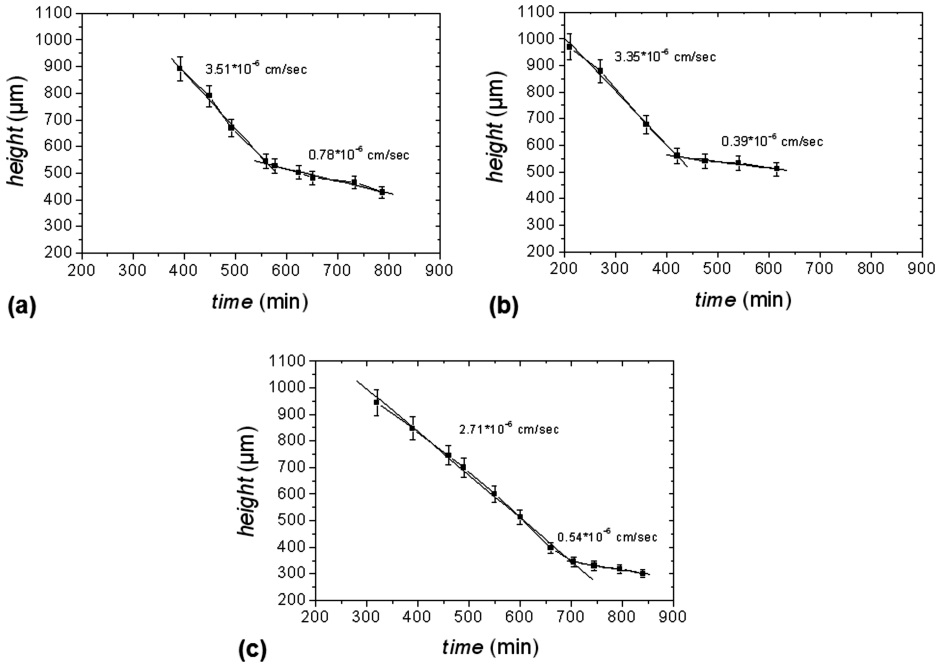

Figure 2. Film thickness estimated from the profile widths in Figure 1 (see text) as a function of drying time. Linear fits to the experimental data are shown. (a), (b), and (c) correspond to samples of 27K, 61K, and 125K PVOH, respectively. Numbers indicate fitted evaporation rates (i.e., film thickness change per time).

the echo decay curves can be fitted with a biexponential function

$$S(t) = A_{\text{short}} \exp(-t/T_{2\text{short}}) + A_{\text{long}} \exp(-t/T_{2\text{long}}) \quad (1)$$

where $S(t)$ is the area under the echo signal.

The short T_2 decay is expected to correspond to the relaxation of the protons of the PVOH molecule that are not able to exchange (nonlabile protons). The long decay corresponds to the water protons as well as to the OH protons of PVOH that exchange with the solvent. The relative weight of the two contributions, A_{short} and A_{long}, can be estimated based on the initial polymer concentration and the state of evaporation as is obtained from the remaining film thickness, assuming approximately constant density throughout the experiment (see Discussion section).

The long and short T_2 components as a function of sample height are shown in Figures 3 and 4, respectively, from the beginning to a later stage of film formation process which is indicated by the evaporation time. Note that due to presence of the strong B_0 gradient, the T_2 obtained in the single-sided NMR device is the combination of transverse relaxation and potential contributions of the longitudinal relaxation as well as magnetic field inhomogeneity and should therefore, strictly speaking, be considered as *effective* T_2 times (see Discussion section). It is found that a $T_{2,\text{long}}$ of around 90 ms at different heights can be seen in the first hour of the drying process for all samples. $T_{2,\text{long}}$ values decrease with time until the end of the measurement period due to both the process of film formation and solvent evaporation.

From the relaxation behavior of the bottom part of the sample, it is also evident that the $T_{2,\text{long}}$ values decrease around 2 orders of magnitude (~90 to ~2 ms) during the drying period. Figure 4 shows that $T_{2,\text{short}}$ is around 10 ms after 1 h of casting for each sample, which is decreased to around 0.1 ms until the short components are not anymore detectable. The relative amounts of the fast decaying components, calculated as $A_{\text{short}}/(A_{\text{short}} + A_{\text{long}})$, are shown in Figure 5.

The fundamental observation in these figures is that the T_2 relaxation times change at different layers for each measurement. From about 400 to 500 min onward, the echo of the sample/air interface layer in all the samples could only be fitted with a monoexponential function to obtain the corresponding T_2 value (see Figure 3). For further evaporation times this feature extends to inner layers and at the end covers the complete sample. This state is reached after 1000 ± 100 min.

Note that the pulse separation used in these experiments is 87.5 μs, which means the first echo is generated after this time. The solidlike component, which decays within 100 μs,[31] will thus be difficult to observe. This is the reason why only one component is observed at the later stage of drying which indicates the formation of a solidlike structure at the top surface of the sample. At the later stages of the evaporation process, both T_2 components are found to gradually decrease toward the film/air interface. There is no such height dependence of T_2 at the beginning of the experiment, indicating that at this stage of the film formation process the dynamics in the solution is uniform. In the PVOH solution prepared using D_2O,[21] the same type of T_2 dependency as a function of sample height was observed. Moreover, the T_2 values of this sample are similar to the shorter T_2 of samples a, b, and c. The difference in gradual change of T_2 all along the layers in different experiments due to the drying effects are bigger than any change in T_2 that could happen in the time taken for a single profile. The relative difference between the maximum and minimum T_2 within the film as a function of drying time, as a measure of dynamic sample heterogeneity, was found to gradually increase from the beginning to about 60 ± 10%, for both the fast and slow components, and then stabilize inside the experimental error.

3.4. T_1 Study in Single-Sided NMR. As stated in section 3.1, T_1 and T_2 measurements of the same sample are performed

dx.doi.org/10.1021/ma2023292 | *Macromolecules* 2012, 45, 1913–1923

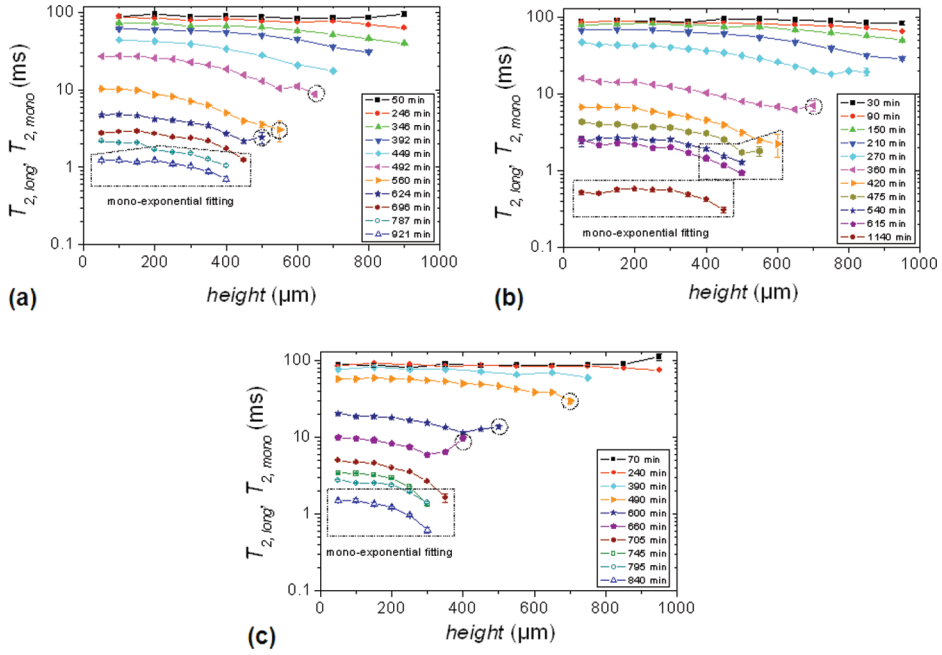

Figure 3. Effective T_2 relaxation times of the slower decaying components at different heights. (a), (b), and (c) correspond to samples of 27K, 61K, and 125K PVOH, respectively. The layer positions correspond to coordinates introduced in Figure 1. At the later stage of drying, the echo decays were fitted monoexponentially which is indicated by the circles and boxes.

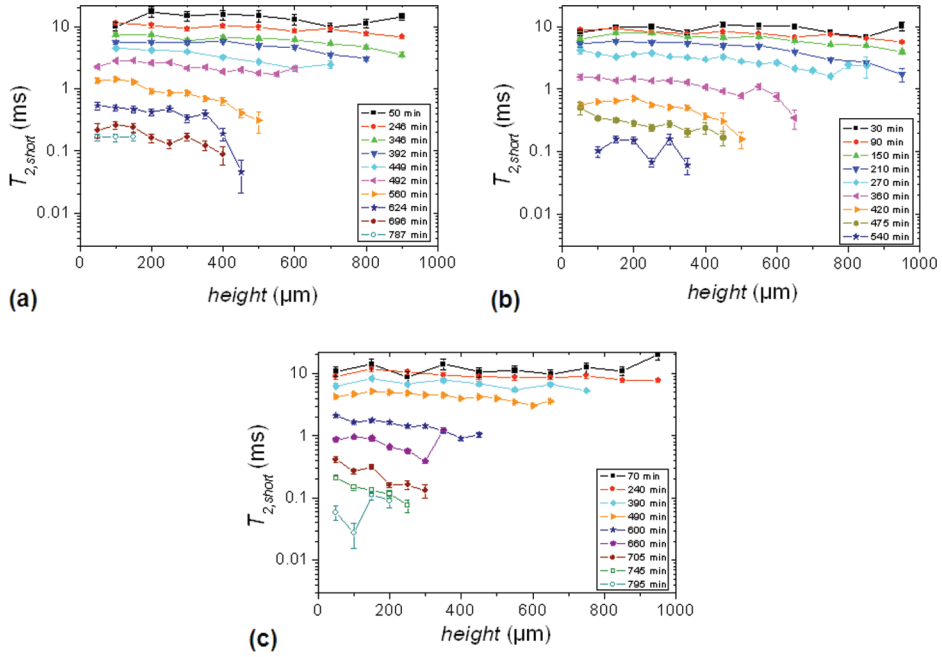

Figure 4. As in Figure 3, but for the faster decaying components.

as a function of height. A monoexponential function was fitted to all the magnetization recovery curves in these experiments to obtain the corresponding spin−lattice relaxation time (T_1) values. The results of the T_1 measurements of the samples a, b, and c are shown in Figure 6 as a function of sample height at different drying times.

3.5. T_1 and T_2 Study at 40 MHz. T_1 and T_2 of freshly prepared PVOH solutions using H_2O and D_2O (labeled as sample d and e, respectively) are studied in a more homogeneous magnetic field at 40 MHz ^{1}H Larmor frequency. The values of T_1 and T_2 for both short and long components, respectively, are shown in Table 2. It is observed that both samples prepared using H_2O and D_2O have two components while with the single-sided NMR scanner at 11.7 MHz, only one component is found as described in section 3.4. T_1 of the single component of the PVOH solution prepared using H_2O at 11.7 MHz has to be compared with the long T_1 component at 40 MHz. The sample prepared using D_2O as a solvent has a higher long component of T_1, while the short component remains almost the same. HDO molecules formed due to the exchange of labile protons from the −OH group of the PVOH chain with the deuterium atom of the solvent are responsible for the longer T_1

dx.doi.org/10.1021/ma2023292 | Macromolecules 2012, 45, 1913−1923

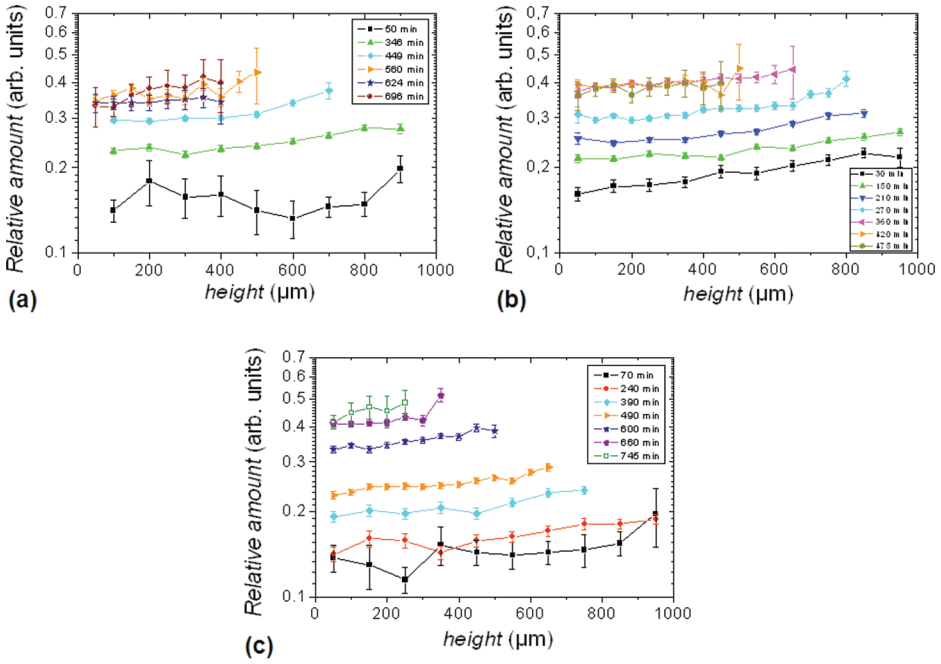

Figure 5. Relative amount of the fast decaying component of transverse relaxation for the measurements shown in Figures 3 and 4.

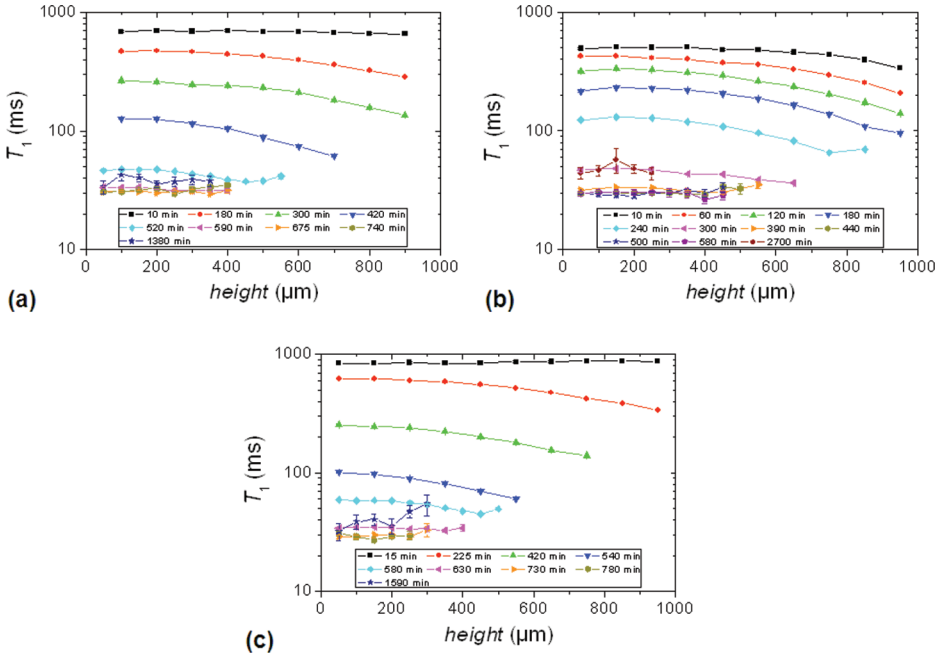

Figure 6. Evolution of T_1 with drying time. (a), (b), and (c) correspond to samples of 27K, 61K, and 125K PVOH, respectively. The layer positions correspond to coordinates introduced in Figure 1.

Table 2. T_1 and T_2 Relaxation Times and % Relative Amount of the Short and Long Components of Sample d (61K PVOH in H_2O) and Sample e (61K PVOH in D_2O) Measured Right after Preparation at 40 MHz Proton Larmor Frequency

	T_1 study				T_2 study			
	short (±1%)		long (±1%)		short (±1%)		long (±1%)	
sample	T_1 (ms)	rel amount (%)	T_1 (ms)	rel amount (%)	T_2 (ms)	rel amount (%)	T_2 (ms)	rel amount (%)
d	41	12.7	668	87.3	17	15.6	390	84.4
e	50	74.6	1115	25.4	18	75.8	688	24.2

value. A similar tendency is seen in the T_2 values (see Table 2). T_2 values of the short components match with the results obtained in the single-sided NMR. Generally speaking, all the values of T_2 of the short components of the fresh samples obtained in both instruments are between 10 and 20 ms. Note that the T_2 values of the long component of the H_2O-prepared sample in this study is

dx.doi.org/10.1021/ma2023292 | Macromolecules 2012, 45, 1913−1923

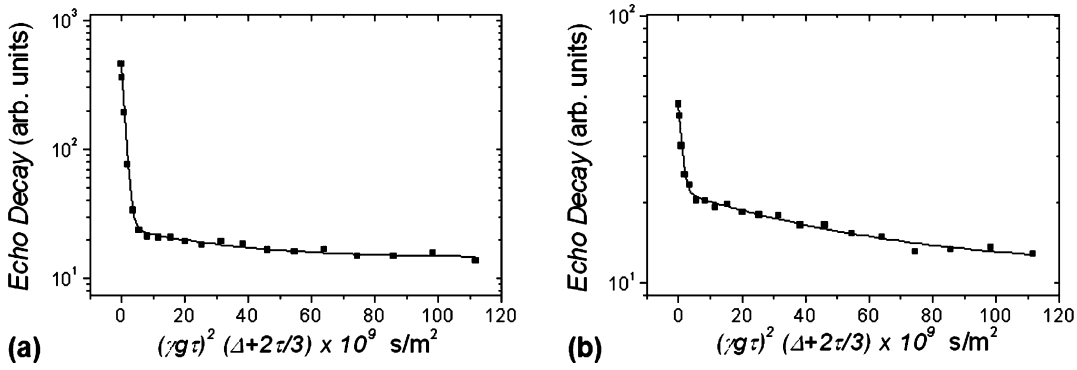

Figure 7. Stimulated echo decay curves of (a) sample f (61K PVOH in H_2O) and (b) sample g (61K PVOH in D_2O) measured in the single-sided NMR scanner right after the sample preparation. The solid lines are biexponential fittings to the experimental data.

390 ms, whereas it is around 90 ms for all the samples studied in single-sided NMR (see section 3.3). A possible magnetic field dependence of T_2 is expected to be much weaker and does not explain the difference. The relative amount of the short and long components calculated from the T_1 and T_2 experiments are given in Table 2 (see Discussion section).

3.6. Diffusion Study in Single-Sided NMR. The strong gradient of the single-sided NMR scanner is used to perform the diffusion experiments using a stimulated echo pulse sequence. Figure 7 shows the echo decays of sample f (H_2O as a solvent) and sample g (D_2O as a solvent) right after preparation. The signal of the residual ^1H in the solvent from the sample g is strongly suppressed by a repetition time much shorter than the corresponding T_1. In this figure, two components can clearly be distinguished. The diffusion attenuation for the two components in the slow-limit exchange can be written as[25]

$$A_{\mathrm{diff}}(\tau) = A_{\mathrm{short}} \exp\left\{-KD_{\mathrm{short}} - \left(\frac{2\tau}{T_{2\mathrm{short}}} + \frac{\Delta}{T_{1\mathrm{short}}}\right)\right\} + A_{\mathrm{long}} \exp\left\{-KD_{\mathrm{long}} - \left(\frac{2\tau}{T_{2\mathrm{long}}} + \frac{\Delta}{T_{1\mathrm{long}}}\right)\right\} \quad (2)$$

where $K = (\gamma G\tau)^2(\Delta + 2\tau/3)$. γ, G, τ, and Δ represent gyromagnetic ratio of protons, gradient strength, encoding time, and diffusion time, respectively. Note that for samples f and g both conditions, $\tau \ll T_2$ and $\Delta \ll T_1$, are satisfied. As a result, these two relaxation times will not affect the diffusion measurement.

3.7. Study of the Dried Film Using XRD. The X-ray diffractograms of the films obtained from the samples a, b, and c are shown in the Figure 8 where the 2θ angles were scanned between 1.5° and 68°. All XRD patterns are showing the crystalline structure only. The amorphous contribution has been subtracted.[32] XRD patterns of both the upper and lower parts of all the studied samples show a characteristic crystalline peak at a scattering angle of $2\theta \approx 19.5°$. The XRD patterns of the upper part of each film show a second peak at $2\theta \approx 41°$, which is not distinguishable due to low signal-to-noise ratio in the XRD pattern of the lower part of the films. The parameter % crystallinity is defined below which is a simplified indication of the true crystallinity:[33]

$$\%\ \text{crystallinity} = \{(\text{total area} - \text{amorphous area}) \text{ of the XRD pattern}\} / (\text{total area of the XRD pattern}) \times 100 \quad (3)$$

Note that the raw XRD pattern is composed of the superposition of the signal intensity (fraction) from the scattering centers corresponding to the crystalline and amorphous part. The amorphous area is determined from the correction of the baseline for the amorphous region obtained in the lower part of the XRD pattern. To determine the crystallite size present in the upper and lower parts of the final film, Scherrer's equation[34] is applied:

$$d = \frac{k\lambda}{B\cos\theta} \quad (4)$$

where λ is the X-ray wavelength (0.154 nm), B is the full width at half-maximum (FWHM) of the characteristic crystalline peak (at $2\theta = \sim 19.5°$), θ is the Bragg angle, and k is the Scherrer constant having a value of 0.9 used for PVOH as can be seen in ref 35.

Table 3 shows the intensities of the peaks at the scattering angle of $2\theta \approx 19.5°$, full width at half-maximum (FWHM) of these peaks, and the % crystallinity (estimated from eq 3) obtained from the raw XRD patterns. The intensities at both sides of the film are influenced by several factors like roughness and curvature of the sample. The % crystallinity on the other hand is independent of these factors and is the relevant parameter in the context of the present study (see below).

4. DISCUSSION

Two stages of evaporation are found in all systems as it can be seen in Figure 2. This behavior can be interpreted as a dynamical change produced after the average water concentration decreases below a certain value where there is almost no free water anymore, but still the polymer retain high mobility. A similar observation is described in ref 17 where the two regimes are attributed to the formation of a "skin layer" at the air–sample interface. It is stated that this skin, having insufficient mobile ^1H to be visualized during profiling, consists of a relatively high crystalline fraction which makes it particularly impermeable. Consequently, evaporation rate becomes slower as it is reflected from the two evaporation rates. The thickness

dx.doi.org/10.1021/ma2023292 | Macromolecules 2012, 45, 1913–1923

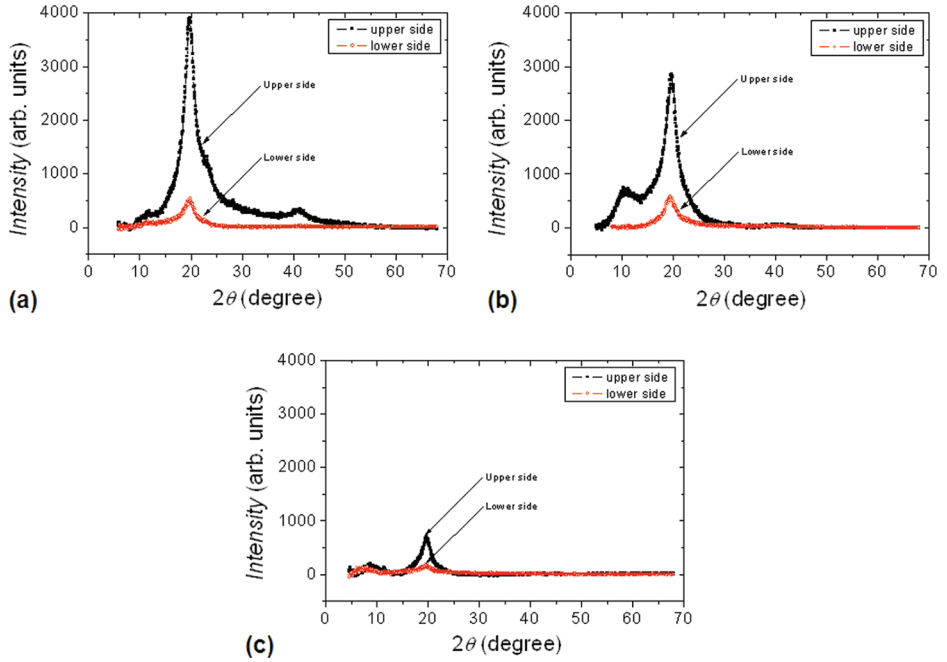

Figure 8. X-ray patterns of the completely dried film. (a), (b), and (c) correspond to samples prepared from 27K, 61K, and 125K PVOH in H_2O, respectively.

Table 3. Maximum Intensity of the Peaks and Full Width at Half-Maximum (FWHM) at $2\theta \approx 19.5°$ and % Crystallinity of the Upper Layers Comparing to the Lower Layers in Sample a (27K PVOH in H_2O), Sample b (61K PVOH in H_2O), and Sample c (125K PVOH in H_2O) Calculated from the Fitting of the XRD Patterns Shown in Figure 8

	intensity of the peak (±4%) at $2\theta \approx 19.5°$ (arb units)		fwhm of the peak (±4%) at $2\theta \approx 19.5°$ ($\Delta(2\theta)$)		crystallinity (±4%) (%)	
sample	upper side	lower side	upper side	lower side	upper side	lower side
a	3403	434	2.2	2.2	64.8	38.1
b	2468	523	2.4	2.6	55.4	34.2
c	648	144	2.3	3.8	31.0	22.0

of any eventual "skin layer" is in any case much smaller than the minimum resolution of the scanner (30 μm). The different evaporation regimes correlate with the change in the shape of the profiles in their solution–air interface. The sharper decay is associated with the faster evaporation rate.

In the general case, the NMR relaxation rate of polymers in solution is proportional to the so-called segmental correlation time[36,37]

$$\frac{1}{T_1} \propto \tau_s \approx \frac{b^2 a_H \eta}{k_B T} \tag{5}$$

where b is the Kuhn segment length, a_H is the hydrodynamic radius of the segments, and η is the viscosity of the medium surrounding the segment. T is the absolute temperature, and k_B is the Boltzmann constant. As the evaporation takes place, the mobility of the polymer chains decreases due to the increase in the viscosity of the solution, and as a consequence, the NMR relaxation process is affected. In the case of pure water, T_1 and T_2 have an inverse dependence with the viscosity as well,[38] but this dependence not necessarily holds for the case of water in a polymer–water solution. As mentioned above, the detection of a "skin layer" using this single-sided scanner is difficult. However, the remarkable fact in this work by NMR is the evidence of a gradual slowing down of the molecular dynamics in the direction of the evaporating surface. This is indicated by the two experimental parameters T_1 and T_2. T_1 values of all the samples show common features. For instance, T_1 values decrease as a function of time as a result of the solvent evaporation. Before the minimum T_1 is reached, the bottom parts of all the samples show longer T_1 than the corresponding upper part following similar spatial patterns than T_2 along the height of the film. The different values of T_1 along the sample height provide additional evidence that the drying of the PVOH film is inhomogeneous.

The two components of T_2 allow certain discrimination of the dynamics of the polymer itself and its solution. The component with a shorter relaxation constant may be assigned to the nonlabile protons of the polymer backbone. This fast decaying component increases with time of film formation all along the system (see Figure 5). As the evaporation of the solvent continues, the concentration of the solute increases as well as the contribution of the polymer main chains in the NMR signal which explain this trend. From the figure it is clear that the relative amount in each of the samples grows slightly toward the top part.

The values of the slow diffusion component corresponding to the polymer are $(3.2 \pm 0.1) \times 10^{-11}$ and $(1.8 \pm 0.4) \times 10^{-11}$ m^2/s for the samples f and g, respectively (Figure 7). On the other hand, the fast diffusion coefficient reflects the exchange of protons between the backbone and the solvent. Sample f has a fast diffusion coefficient of $(1.1 \pm 0.1) \times 10^{-9}$ m^2/s while for sample g the value is $(0.94 \pm 0.06) \times 10^{-9}$ m^2/s. Both diffusion coefficients are about half the value of bulk water, a consequence of the high viscosity of the solution.

The diffusion process is playing an important role in the understanding of the heterogeneities in the dynamics observed during film formation. In order to have a quantitative insight, an analysis similar to that stated in ref 17 can be made computing

dx.doi.org/10.1021/ma2023292 | Macromolecules 2012, 45, 1913–1923

the relation between the rate of the vertical convection and the diffusion of the polymer molecules:

$$\varsigma = \frac{\xi \dot{E}}{D} \tag{6}$$

Here ξ is the layer thickness, $\dot{E}$ is the value of the thickness change as shown in Figure 2 in m/s, and D is the diffusion coefficient of the polymer molecules. When $\varsigma \ll 1$, diffusion dominates in the solution and the film remain homogeneous throughout. For the cases when $\varsigma \geq 1$, the difference in concentration cannot be compensated by diffusion, giving rise to a higher polymer concentration in the upper part of the solution. Taking the values of $\dot{E}_1$ from Figure 2b, one obtains $\varsigma \approx 1.05$ for samples f. This means that drying is taking place in a so-called heterogeneous regime.

With these values in mind, one needs to verify the validity of the observed *effective* T_2 times in comparison to the actual T_2 times. In a strong magnetic field gradient, the signal decays not only due to relaxation but also due to diffusion. In a CPMG sequence of pulse separation τ, the diffusional decay at the jth echo is theoretically proportional to $\exp[-1/12(\gamma^2 G^2 \tau^2) D j\tau]$ while the relaxation contribution is proportional to $\exp[-j\tau/T_2]$. Assuming a self-diffusion coefficient of 10^{-9} m^2/s, the constant magnetic field gradient of G = 11.5 T/m leads to a decay of about $\exp[-6\ \mathrm{s}^{-1}\ j\tau\ ]$ if the longest pulse separation of τ = 87.5 μs is used. In other words, this additional decay can falsely be interpreted as relaxation, and in the limit of T_2, an *effective* T_2 of about 160 ms would be obtained, putting a limit for the longest measurable relaxation time. This explains, in part, the discrepancy between the T_2 values of the fresh sample measured at the two different spectrometers (see section 3.3 and 3.5). On the other hand, as T_2 becomes shorter during the drying process, it quickly approaches the true value since relaxation now dominates the diffusion contribution (supported also by the decrease in D as the sample's viscosities increase). For all practical purposes, the measured decay constants during the drying process represent a very good approximation to the true transverse relaxation rates.

A second influence is brought about by the imperfection of the π pulse excitations in this inhomogeneous magnetic field; this will lead to a superposition of coherence pathways that has the effect of "contaminating" the real T_2 with a contribution of the—longer—T_1. Depending on the exact shape of the B_0 and B_1 fields, this contribution can be computed.[39] In our study, the possible influence of T_1 on the CPMG measurements was estimated by comparing samples with known relaxation properties and was found to be negligible for the fitting procedure used, which involved integrating the complete echoes. This finding is further supported by the fact that, while the decrease of both relaxation times with height coordinate appears to be similar, T_1 approaches a constant value well before T_2 does.

Using water as a solvent, one has to pay attention to the contribution of the ^{1}H of the different subsystems in order to achieve a correct interpretation of the experimental NMR results. For this reason, T_1 and T_2 relaxation times are measured in a slightly higher and more homogeneous magnetic field of a proton Larmor frequency of 40 MHz. Generally, in a 25% PVOH−H_2O solution, 21.4% protons from the PVOH molecule containing 4 protons in the repeating unit and 78.6% protons from the H_2O molecule containing 2 protons in each molecule contribute to the NMR signal. Taking into account that 1 proton is exchangeable (labile protons) among 4 protons in the PVOH molecule, further calculation shows that around 16% of the total NMR signal comes from the nonlabile protons of the PVOH polymer backbone whereas the remaining 84% of the signal is contributed by the H_2O molecule and the labile protons of PVOH molecule. Table 2 shows a very similar distribution of relative weight of the short (as well as long) components as obtained from the experimental values of T_1 and T_2 measurements of sample d in 40 MHz. In case of PVOH−D_2O solution, 75% nonlabile protons from the PVOH backbone chain and 25% labile protons in the solution or in exchange will give rise to the signal. The relative weight obtained from the T_1 and T_2 measurements of sample e show around 75% slow decaying and 25% fast decaying components as can be seen in Table 2. Furthermore, from Figure 5, it is clear that at the first experimental hour the relative amount of the fast decaying components is 15−20% which matches with the estimated value as described above. NMR proves clearly, as long as the system has still a sufficiently high mobility, that inhomogeneities appear in the solution during practically all the film formation process. During solidification, at advanced evolution times, rigid domains are extended in the entire sample limiting the application of the NMR technique employed in the current work as can be seen in Figure S1 (see Supporting Information for discussion). The heterogeneities observed during evolution will have a signature after solidification, and this is nicely proven in Figure 8.

A source of the difference in the XRD peak intensities, besides roughness or curvature at both sides of the sample, is the presence of more crystalline domains in the upper part of the sample.[40] The total crystallinity decreases for the film sample prepared from the PVOH of higher molecular weight. The relative amount of crystallinity (see eq 3) further supports this observation. From the FWHM values (see Table 3) it is found, using eq 4, that the crystalline domains have a characteristic size in the order of 5 nm in all the samples independent of the side that is measured and its relative amount of crystallinity. Quantitatively, the upper and lower sides of the films prepared from samples a, b, and c have a difference in the relative amount of crystallinity in the range of 10−25% (see Table 3).

The mechanism that account for the observed heterogeneities takes place necessarily during film formation. For each of the samples, the T_1 and T_2 values of both components (Figures 3, 4, and 6) decrease and the relative amount of the fast decaying components (Figure 5) increases gradually with the increment in the sample height and evolution time. At later stage of drying, the $T_{2\mathrm{short}}$ relaxation times are not anymore detectable. This indicates a solidlike structure formation in the vicinity of the top surface of the samples. As expressed above, these results point toward the fact that the sample is not homogeneous during drying, giving rise to the nonhomogeneous structure of the film. The appearance of the single components at the upper part of the samples as shown in the T_2 study (Figure 3) is a strong evidence that the solid phase is in the process of formation at the corresponding evolution times. The gradual formation of the semicrystalline polymer domains occurs henceforth from top to bottom of the film. The system undergoes a glass transition and becomes semicrystalline as the evaporation on the top surface increases locally the concentration of polymer to a critical concentration at a certain time. The distribution of the solute (PVOH) concentration in the system[41] arises due to the water evaporation. Right after casting, the water−PVOH solution is a uniform fluid with high viscosity. The drying process regulates water transport in the whole system. At the beginning this transport involves diffusion

dx.doi.org/10.1021/ma2023292 | Macromolecules 2012, 45, 1913−1923

of water molecules through the continuous solution, but at later stages, percolation of water through interstitial spaces between solidified semicrystalline PVOH takes place. The gradient of the solvent and solute concentrations[42] induced by evaporation[12,41] generates a net flux of water in the direction of the evaporation front causing a difference in concentration. Diffusion processes will tend to reestablish a uniform concentration, but the slow diffusivity of the polymers prevents any equilibration in the time scale of the total film formation process. When a concentration gradient is induced, provided that there is enough mobility in the system, it will remain at advanced times where the fluid system becomes highly viscous. The solidification phase transition then will reflect the concentration inhomogeneity.

5. CONCLUSIONS

The film formation of PVOH of different molecular weights in water solution and the final films obtained in the course of time were studied by NMR relaxation and X-ray diffractometry, respectively. The shrinking rate was followed by NMR imaging with a single-sided NMR profiler. The current study reports NMR measurements mainly on the ^{1}H nuclei of the samples. Despite the fact that a considerable amount of NMR signal is generated from the protons in the solution (water), the results are in complete agreement with the case where D_2O is used as a solution instead, as it is confirmed in a previous study.[21]

By the determination of the relaxation parameters T_1 and T_2, it could be traced out that the effect of the evaporation of the solvent molecules in the dynamics of the solution induces a dynamic heterogeneity of the polymer molecules across the film thickness for all the molecular weights. The local evaporation process taking place at the solution−air interface further influences the migration of polymer chains, inducing differences in concentration along the whole system. The direct consequence is the reduction in the mobility of the polymer chains toward the surface where evaporation takes place. These spatial heterogeneities influence the local dynamical behavior of the system and the profile of relaxation times becomes progressively asymmetric during the evolution time. The shorter relaxation times on the top surface at later stages of film formation indicate the presence of more immobile polymer chains. Once the system has completely solidified below a certain water content, the measured T_2 relaxation times reflect the dynamics of the amorphous part (as expressed above, the single-sided scanner is not sensitive to solid NMR signals). This reveals that the amorphous domain has different dynamics along the film. Taking into account that more crystallization domains are found on top of the film from the XRD study, together with the fact that the polymer system is well below the glass transition temperature, the dynamics of the amorphous part is restricted by the presence of the crystalline domains in the sense of confinement; i.e., there is a geometrical confinement. The effect of the molecular weight on the structure of the films is the formation of a more crystalline phase at the top surface for the PVOH which has the lowest molecular weight. This can be seen in Table 3, where the ratio of crystallinity between the upper and the lower parts decreases with the increase in molecular weight.

In conclusion, an evidence of heterogeneous dynamical restriction of the amorphous part of the final film by the presence of more crystalline domains is found in the final film along the vertical direction, induced during its formation process and influenced by the molecular weight of the polymer.

■ ASSOCIATED CONTENT

Ⓢ Supporting Information

T_2 constants at different layers of the completely dried film from sample c (containing 25% PVOH (125K) in H_2O). This material is available free of charge via the Internet at http://pubs.acs.org.

■ AUTHOR INFORMATION

Corresponding Author

*E-mail: carlos.mattea@tu-ilmenau.de

Notes

The authors declare no competing financial interest.

■ ACKNOWLEDGMENTS

S.G. gratefully acknowledges Deutscher Akademischer Austauschdienst (DAAD) for the scholarship (PKZ: A/07/80278) to pursue his PhD research.

■ REFERENCES

(1) Feldman, D.; Barbalata, A. *Synthetic Polymers: Technology, Properties, Applications*; Chapman & Hall: London, UK, 1996.
(2) *Chemistry and Technology of Biodegradable Polymers*; Griffin, G., Ed.; Springer: Berlin, 1993.
(3) Steinbüchel, A.; Matsumura, S. *Biopolymers: Miscellaneous Biopolymers and Biodegradation of Synthetic Polymers*; Wiley-VCH: New York, 2003.
(4) Stephans, L. E.; Foster, N. *Macromolecules* **1998**, *31*, 1644−1651.
(5) Finch, C. A., Ed. *Poly(vinyl Alcohol)- Developments*, 2nd ed.; Wiley: New York, 1997.
(6) Shibayama, M.; Kurokawa, H.; Nomura, S.; Roy, S.; Stein, R. S.; Wu, W. L. *Macromolecules* **1990**, *23*, 1438−1443.
(7) Valentín, J. L.; López, D.; Hernández, R.; Mijangos, C.; Saalwächter, K. *Macromolecules* **2009**, *42*, 263−272.
(8) Tripathi, S.; Mehrotra, G. K.; Dutta, P. K. *Int. J. Biol. Macromol.* **2009**, *45* (4), 372−376.
(9) Chang, J. B.; Hwang, J. H.; Park, J. S.; Kim, J. P. *Dyes Pigm.* **2011**, *88* (3), 366−371.
(10) Yang, C.-C.; Lee, Y.-J. *Thin Solid Films* **2009**, *517* (17), 4735−4740.
(11) Hodge, R. M.; Bastow, T. J.; Edward, G. H.; Simon, G. P.; Hill, A. J. *Macromolecules* **1996**, *29*, 8137−8143.
(12) Wong, S.; Altinkaya, S. A.; Mallapragada, S. K. *J. Polym. Sci., Part B: Polym. Phys.* **2005**, *43*, 3191−3204.
(13) Ngui, M. O.; Mallapragada, S. K. *J. Polym. Sci., Part B: Polym. Phys.* **1998**, *36*, 2771−2780.
(14) Ngui, M. O.; Mallapragada, S. K. *J. Appl. Polym. Sci.* **1999**, *72*, 1913−1920.
(15) Ngui, M. O.; Mallapragada, S. K. *Polymer* **1999**, *40*, 5393−5400.
(16) Wong, S.; Altinkaya, S. A.; Mallapragada, S. K. *Polymer* **2004**, *45*, 5151−5161.
(17) Ciampi, E.; McDonald, P. J. *Macromolecules* **2003**, *36*, 8398−8405.
(18) Blümich, B.; Perlo, J.; Casanova, F. *Prog. Nucl. Magn. Reson. Spectrosc.* **2008**, *52*, 197−269.
(19) Mitchell, J.; Blümler, P.; McDonald, P. J. *Prog. Nucl. Magn. Reson. Spectrosc.* **2006**, *48*, 161−236.
(20) Ghoshal, S.; Mattea, C.; Denner, P.; Stapf, S. *J. Phys. Chem. B* **2010**, *114*, 16356−16363.
(21) Ghoshal, S.; Denner, P.; Stapf, S.; Mattea, C. *Chem. Phys. Lett.* **2011**, *515*, 231−234.
(22) Ghoshal, S.; Mattea, C.; Stapf, S. *Chem. Phys. Lett.* **2010**, *485*, 343−347.
(23) Peppas, N. A. *Makromol. Chem.* **1975**, *176*, 3433−3440.
(24) Yang, H.; Cheng, R.; Xie, H.; Wang, Z. *Polymer* **2005**, *46*, 7557−7562.

(25) Kimmich, R. *NMR Tomography, Diffusometry, Relaxometry*; Springer-Verlag: Berlin, 1997.
(26) Meiboom, S.; Gill, D. *Rev. Sci. Instrum.* **1958**, *29*, 688−691.
(27) Bloembergen, N. *Nuclear Magnetic Resonance*; W.A. Benjamin: New York, 1961.
(28) Hahn, E. L. *Phys. Rev.* **1950**, *80*, 580−594.
(29) Carr, H. Y.; Purcell, E. M. *Phys. Rev.* **1954**, *94*, 630−638.
(30) Vold, R.; Waugh, J.; Klein, M.; Phelps, D. *J. Chem. Phys.* **1968**, *48*, 3831−3832.
(31) Hills, B. P. *Mol. Phys.* **1992**, *76* (3), 509−523.
(32) Park, S.; Baker, J. O.; Himmel, M. E.; Parilla, P. A.; Johnson, D. K. *Biotechnol. Biofuels* **2010**, *3*, 1−10.
(33) He, B. B. *Two-Dimensional X-ray Diffraction*; John Wiley & Sons, Inc.: Hoboken, NJ, 2009.
(34) Scherrer, P. *Nachr. Ges. Wiss. Göttingen* **1918**, *26*, 98−100.
(35) Miyazaki, T.; Hoshiko, A.; Akasaka, M.; Saki, M.; Takeda, Y.; Sakurai, S. *Macromolecules* **2007**, *40*, 8277−8284.
(36) Kimmich, R.; Fatkullin, N. *Advan. Polym. Sci.* **2004**, *170*, 1−113.
(37) Doi, M.; Edwards, S. F. *The Theory of Polymer Dynamics*; Clarendon: Oxford, 1986.
(38) Abragam, A. *The Principles of Nuclear Magnetism*; Oxford University Press: London, 1961.
(39) Hürlimann, M. D.; Griffin, D. D. *J. Magn. Reson.* **2000**, *143*, 120−135.
(40) Ricciardi, R.; Auriemma, F.; Rosa, C.; de; Lauprêtre, F. *Macromolecules* **2004**, *37*, 1921−1927.
(41) Kabalnov, A.; Wennerström, H. *Soft Matter* **2009**, *5*, 4712−4718.
(42) Krantz, W.; Ray, R.; Sani, R.; Gleason, K. *J. Membr. Sci.* **1986**, *29*, 11−36.

Macromolecules

Article

pubs.acs.org/Macromolecules

Multishape Memory Effect of Norbornene-Based Copolymers with Cholic Acid Pendant Groups

Yu Shao, Christine Lavigueur, and X. X. Zhu*

Department of Chemistry, Université de Montréal, C.P. 6128, Succursale Centre-ville, Montreal, QC H3C 3J7, Canada

Supporting Information

ABSTRACT: Multishape memory copolymers were prepared through copolymerization of two norbornene derivatives: one based on cholic acid and the other on triethylene glycol monomethyl ether. The glass transition temperature (T_g) of the copolymers can be tuned over a temperature range from −58 to 176 °C. Most of these copolymers displayed a very broad T_g over a 20 °C range which can allow a multishape memory effect. The shape memory properties of the copolymer incorporating an equal molar amount of both monomers have been studied in detail. The multishape memory effect was investigated by dynamic mechanical analysis using a thermomechanical programming process, in which multiple steps created two, three, and four temporary shapes. The polymer displayed good shape fixing and recovery in different thermal processing stages over the broad glass transition range. This series of copolymers with broad and tunable T_g's may be useful as functional materials with multishape memory effect.

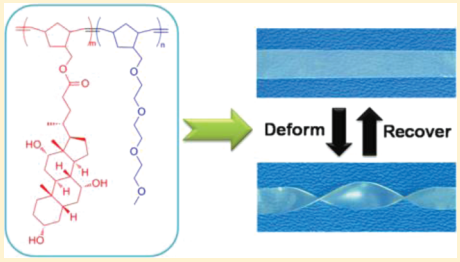

INTRODUCTION

Shape memory polymers (SMP) are stimuli-responsive materials with the ability to change their shape upon exposure to external stimuli[1−3] such as light,[4−7] heat,[8−10] or magnetic field.[11] In a typical thermally induced shape memory polymer,[12] the permanent shape is determined by chemical[13] or physical[14] cross-links, and the temporary shapes are fixed through crystallization or vitrification. When heated to a temperature higher than a certain switching temperature, these materials have the ability to revert to their permanent shape. Shape memory polymers are of great significance for biomedical applications,[15,16] such as smart suture materials,[17] responsive stents for cardiovascular engineering,[18] self-expandable implants for minimally invasive surgery,[19] controlled drug release,[20] and fasteners.[17]

The potential application of a shape memory polymer is determined by the number of temporary shapes which can be memorized in each shape memory cycle. Furthermore, it is difficult to tailor polymer structure to tune the shape memory transition temperatures for the targeted applications.[14,21] To address these issues, much effort has been devoted to the development of multishape memory polymers.[22−26] However, polymer systems displaying multiple shape memory effects are mostly limited to chemically cross-linked and semicrystalline polymers or block copolymers.[22,27,28] Kasi et al.[29] reported side-chain liquid crystalline polymers with dual transition temperatures. Chemical cross-links and crystalline moieties were incorporated into the polymer chain to obtain a triple-shape memory effect. The complicated structure of the resulting polymers makes it difficult to tune their processing and mechanical properties. Other factors can also limit potential application, such as maximum strain, modulus, elastic energy storage density, recovery temperature, response time, and cycle life.[3] Tunable polymer systems are much needed, particularly for biomedical applications.

Bile acids are natural compounds present in large quantities in humans and most animals and all possess a steroidal backbone, which gives them a rigidity similar to that of aromatic derivatives.[30] Cholic acid is the most important naturally-ocurring bile acid and is an ideal building block for new biomaterials.[31−35] The incorporation of cholic acid moieties within a polymer should provide rigidity and biocompatibility to the polymer.[33,36,37]

Ring-opening metathesis polymerization (ROMP) is a useful synthetic method because it provides good control of the polymerization process and has a high level of tolerance toward polar groups.[38−40] Norbornene derivatives, which are ideal monomers for ROMP, may be coupled to bile acids via the hydroxyl group at position 3 or the carboxyl group at position 24 on the steroid skeleton.[41] Polymerization of other monomers based on bile acids with or without additional comonomers affords polymers with bile acid pendant groups.[29,42] Such materials displayed tunable hydrophilicity, solubility, glass transition temperature, and mechanical properties.

In this study, two norbornene derivatives were prepared in good yields—one incorporating cholic acid (NCA) and the other triethylene glycol monomethyl ether (NTEG)—and a series of copolymers were obtained from their copolymerization by ROMP. The multishape memory properties of a representative copolymer were investigated in detail by dynamic mechanical analysis (DMA).

Received: November 14, 2011
Revised: January 29, 2012
Published: February 10, 2012

   dx.doi.org/10.1021/ma202506b | *Macromolecules* 2012, 45, 1924−1930

EXPERIMENTAL SECTION

Materials. Cholic acid, 5-norbornene-2-methanol (mixture of endo and exo, 98%), triethylene glycol monomethyl ether, 4-(dimethylamino)pyridine (DMAP), ethyl vinyl ether, sodium hydride (NaH), 1-ethyl-3-(3-(dimethylamino)propyl)carbodiimide hydrochloride (EDC·HCl), and (1,3-bis(2,4,6-trimethylphenyl)-2-imidazolidinylidene)dichloro(phenylmethylene)(tricyclohexylphosphine)-ruthenium (Grubbs' catalyst second generation) were purchased from Aldrich (purest grade available from this supplier) and solvents from VWR. Tetrahydrofuran (THF), dichloromethane (DCM), and *N*,*N*-dimethylformamide (DMF) were dried using a solvent purification system from Glass Contour. Hexane, methanol, and ethyl acetate were used without further purification. Toluene-4-sulfonic acid-2-[2-(2-methoxyethoxy)ethoxy]ethyl ester ($TosO(CH_2CH_2O)_3Me$) was synthesized following a literature procedure.[43]

Characterization. IR spectra were recorded on an Excalibur HE series FTS 3100 instrument from Digilab. ^1H and ^{13}C NMR spectra were recorded on a Bruker AV400 spectrometer operating at 400 MHz for protons and 100 MHz for ^{13}C. $CDCl_3$ and DMSO-d_6 were used as solvents.

Size exclusion chromatography (SEC) was performed on a Breeze system from Waters equipped with a 717 plus autosampler, a 1525 binary HPLC pump, and a 2410 refractive index detector using three consecutive Waters columns (Phenomenex, 5 μm, 300 mm × 7.8 mm; styragel HR4, 5 μm, 300 mm × 7.8 mm; styragel HR6, 5 μm, 300 mm × 3.8 mm). DMF for SEC was filtered using 0.2 μm nylon Millipore filters. The flow rate of the eluent (DMF) was 1 mL/min. Poly(methyl methacrylate) standards (2500−608 000 g/mol) were used for calibration.

Thermogravimetric analyses (TGA) were performed on a Hi-Res TGA 2950 (TA Instruments) under a flow of nitrogen. T_{dec} was defined as the onset of the decomposition temperature. Differential scanning calorimetry (DSC) measurements were carried out on a DSC Q1000 (TA Instruments) at a heating/cooling rate of 10 °C/min. T_g was defined as the midpoint of change in slope on the second heating run, and the T_g range was determined by the onset and offset of the changes in heat capacity of the samples.

Polymer films for mechanical tests were prepared by evaporating a concentrated THF solution (300 g/L) of the desired polymer in a Teflon mold at room temperature and atmospheric pressure for 24 h and then at 100 °C under reduced pressure for another 24 h. Smaller rectangular samples (6.0 mm × 2.0 mm) were cut from these films and used for mechanical tests (the dimensions of the films were measured with a digital calliper with a precision of 0.01 mm). Dynamic mechanical analysis (DMA) was carried out on a DMA2980 from TA Instruments. For multifrequency experiments, a preload force of 0.005 N, an amplitude of 10 μm, a temperature sweeping rate of 1 °C/min, and a frequency of 1 Hz were used. The T_g ranges measured by DMA were determined by the onset and offset of the changes in the storage modulus of the polymers. For controlled force (stress−strain) experiments, a preload force of 0.005 N and a force ramp of 0.1 N/min were used. For shape memory experiments, the controlled force mode was used. At least three consecutive cycles were performed for each sample. In shape memory experiments, the polymer is deformed at an elevated temperature (deformation temperature, T_d) and the deformed temporary shape is fixed upon cooling (fixing temperature, T_f). It is then heated to a recovery temperature (T_r) to recover the permanent shape. In a typical triple-shape memory experiment, the sample was kept at 85 °C for 5 min and then stretched at 0.2 N/min. The DMA chamber was then cooled to 60 °C while maintaining the applied stress for 10 min. The sample was unloaded and kept at 60 °C for 30 min to fix the first temporary shape. Stress was reapplied, and the DMA chamber was cooled to 30 °C and kept isothermal for 5 min. After unloading the sample and remaining isothermal for 5 min to fix the second temporary shape, the sample was heated to 60 °C and kept isothermal for 60 min to recover the first temporary shape. Finally, the sample was heated to 85 °C and kept isothermal for 30 min to recover the permanent shape.

Preparation of the Materials. *Cholic Acid-Based Norbornene Monomer (NCA).* 5-Norbornene-2-methanol (2.0 g, 16.1 mmol), cholic acid (6.6 g, 16.1 mmol), and DMAP (0.2 g, 1.6 mmol) were dissolved in 40 mL of anhydrous DCM under argon. The reaction mixture was cooled to 0 °C, and then EDC·HCl (3.7 g, 19.3 mmol) was added. After 1 h, the reaction mixture was warmed to room temperature and stirred for 16 h. The organic phase was washed with 0.1 M HCl (50 mL), 10% $NaHCO_3$ (50 mL), and brine (50 mL × 3). After drying the organic layer over Na_2SO_4 and removing the solvent under vacuum, the residue was purified by column chromatography on silica gel (ethyl acetate:hexane = 10:1) to give a white solid (5.4 g, 65%); mp: 67.4 °C by DSC (10 °C/min). FT-IR (ATR mode): ν (cm^{-1}) = 3385 (OH), 2934, 2865 (CH_2), 1732, 1712 (C═O), 1076 (C−O). ^1H NMR (400 MHz, $CDCl_3$): δ (ppm) = 6.19−5.94 (m, 2H), 4.19−4.13, 4.01−3.95, 3.89−3.85, 3.70−3.65 (m, 2H), 4.01 (s, 1H), 3.88 (s, 1H), 3.48 (br s, 1H), 2.86−2.72 (m, 2H), 2.44−0.55 (m, 38H). ^{13}C NMR (100 MHz, $CDCl_3$): δ (ppm) = 174.7, 138.0, 137.3, 136.6, 132.6, 73.4, 72.4, 68.8, 68.2, 60.8, 49.8, 47.6, 46.9, 45.4, 44.3, 44.1, 42.6, 42.2, 41.9, 40.1, 40.0, 38.4, 38.2, 35.7, 35.2, 35.1, 31.8, 31.4, 30.9, 30.0, 29.4, 28.7, 27.9, 26.9, 23.6, 22.9, 21.5,17.7, 14.6, 12.9. HRMS (ESI Pos): found for $C_{32}H_{50}NaO_5$ $[M + Na]^+$: 537.3561 *m*/*z*; calculated 537.3551 *m*/*z*.

Triethylene Glycol-Based Norbornene Monomer (NTEG). 5-Norbornene-2-methanol (1.0 g, 8.1 mmol) was added dropwise to a suspension of NaH (0.3 g, 12.5 mmol) in 40 mL of dry DMF under an argon atmosphere. The mixture was stirred at room temperature for 10 min and at 60 °C for 1 h. $TosO(CH_2CH_2O)_3Me$ (3.9 g, 12.3 mmol) dissolved in 5 mL of DMF was added at room temperature. The mixture was stirred at room temperature for 10 min and then at 60 °C for 12 h, after which 50 mL of water was added and the layers were separated. The aqueous layer was extracted with ethyl acetate (30 mL × 3), and the combined organic layers were washed with 10% $NaHCO_3$ (50 mL) and brine (50 mL × 3), dried over $MgSO_4$, and concentrated *in vacuo*. The residue was purified by column chromatography on silica gel (ethyl acetate:hexane = 1:3) to afford a colorless oil (1.4 g, 62%). FT-IR (ATR mode): ν (cm^{-1}) = 2915, 2864 (CH_2), 1687 (C═C), 1103 (C−O). ^1H NMR ($CDCl_3$, 400 MHz): δ (ppm) = 6.10−5.90 (m, 2H), 3.65−3.52, 3.19−3.03 (m, 14H), 3.36 (s, 3H), 2.88−2.73 (m, 2H), 2.33, 1.68 (br s, 1H), 2.35−2.32, 1.10−1.05 (m, 1H), 1.28−1.20 (m, 2H), 0.49−0.44 (m, 1H). ^{13}C NMR (100 MHz, $CDCl_3$): δ (ppm) = 137.5, 132.9, 76.5, 75.5, 72.4, 71.1, 71.0, 70.9, 70.6, 59.5, 49.8, 45.4, 44.3, 44.0, 42.6, 41.9, 39.2, 39.1, 30.1, 29.5. HRMS (ESI Pos): found for $C_{15}H_{26}NaO_4$ $[M + Na]^+$: 293.1725 *m*/*z*; calculated 293.1723 *m*/*z*.

Polymerization. All polymerizations were performed under an argon atmosphere. Solvents were degassed by a freeze−pump−thaw procedure. A typical ROMP was carried out as the following. NCA and NTEG in various ratios (total: 2.0 mmol) were dissolved in THF (3.9 mL). Grubbs' catalyst second generation (1.7 mg, 2.0×10^{-3} mmol) was added to the monomer solution at 50 or 25 °C with stirring. After 3 h, ethyl vinyl ether (50 μL, 0.5 mmol) was added, and the solution was stirred for 1 h. The reaction mixture was poured into methanol or hexane. The precipitate was collected and dried *in vacuo* to yield the polymer as a solid. As an example of a typical yield, 731 mg of poly(NCA−NTEG)$_{1:1}$ was obtained (93% yield). The ^1H NMR peak assignments for the homopolymers and a copolymer, poly(NCA−NTEG)$_{1:1}$, are shown in Figure S2 (Supporting Information).

RESULTS AND DISCUSSION

Synthesis and Characterization of Monomers and Copolymers. The commercially available 5-norbornene-2-methanol was chosen as the starting material because it has a large ring strain and can be readily polymerized by ROMP by the use of Grubbs' catalyst.[38,44] The targeted monomers can be made in a single step (Scheme S1, Supporting Information). In recent literature, the hydroxyl groups of bile acid derivatives were protected and deprotected for the reaction with

dx.doi.org/10.1021/ma202506b | *Macromolecules* 2012, 45, 1924−1930

Scheme 1. Synthesis of the Copolymers by ROMP Using Grubbs' Catalyst Second Generation

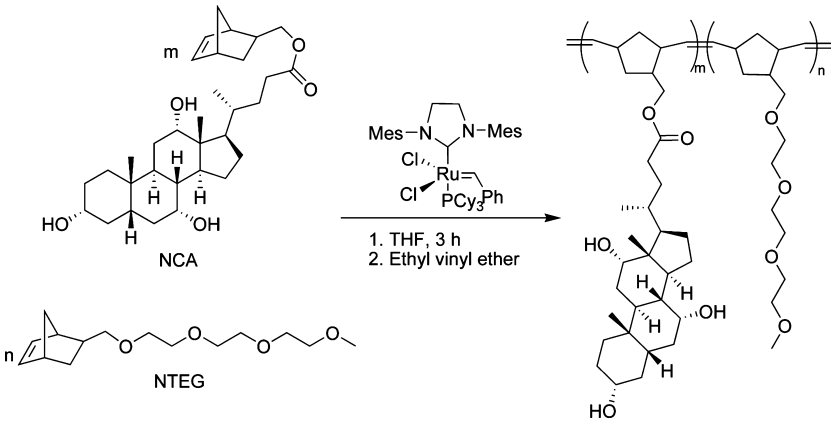

Table 1. Polymerization Conditions and Properties of Copolymers with Various Ratios of NCA to NTEG

polymer[a]	NCA:NTEG[b]	T[c] (°C)	yield (%)	M_n[d] (g/mol)	PDI[d]	T_g[e] (°C)	T_g range[f] (°C)	T_g range[g] (°C)
poly(NCA)	1:0	50	97.2	340 000	1.8	176	173−177	
poly(NCA−NTEG)$_{4:1}$	1:0.25	50	96.0	297 000	1.5	136	132−139	
poly(NCA−NTEG)$_{2:1}$	1:0.55	25	99.1	453 000	2.1	105	99−110	82−108
poly(NCA−NTEG)$_{1:1}$	1:0.95	25	93.3	473 000	2.5	64	54−72	53−77
poly(NCA-NTEG)$_{1:2}$	1:2.27	25	94.6	614 000	2.6	27	17−42	17−51
poly(NCA−NTEG)$_{1:3}$	1:3.43	25	91.0	505 000	2.3	10	−1−24	
poly(NTEG)	0:1	25	88.4	96 000	1.2	−58	−67 to −51	

[a]Polymerization conditions: [monomer]:[Grubbs catalyst] = 1000:1, [monomer] = 0.5 M in THF, 3 h. The numbers in the subscript are those of the monomers molar ratios in the feed. [b]NCA:NTEG: molar ratio in the copolymers calculated from the ratio of proton NMR peak integrations. [c]Polymerization temperature. [d]Measured by SEC. [e]Measured by DSC. T_g defined as the midpoint in the change of heat capacity. [f]Determined by the onset and offset of the changes in the heat capacity. [g]Determined by the onset and offset of the changes in the storage modulus of the sample.

norbornene methanol.[41] We found that this is unnecessary. NCA was obtained (65% yield) without any protection of the hydroxyl groups of cholic acid. NTEG was used as comonomer to tune the physical and mechanical properties of the polymers. NTEG was synthesized by coupling $TosO(CH_2CH_2O)_3Me$ and 5-norbornene-2-methanol (62% yield) in a manner similar to a literature procedure.[43] The ^{1}H NMR spectra of NCA and NTEG with key peak assignments are shown in Figure S2 (Supporting Information).

ROMP was carried out in THF with NCA and NTEG, using Grubbs' catalyst second generation (Scheme 1). The polymers made are listed with the experimental conditions in Table 1. Poly(NCA) and poly(NCA-NTEG)$_{3:1}$ were synthesized at a higher temperature (50 °C) because the solubility of the resulting polymers was too low at room temperature in THF. The yields obtained after precipitation was between 88 and 99% for all polymerizations. Table 1 shows that most copolymers have relatively high PDIs due to a higher rate of propagation than initiation with the Grubbs' catalyst. When the content of NTEG is above 30 mol % in the copolymers, they are easy to dissolve in common organic solvents such as THF and $CHCl_3$ and can form films easily by solvent casting. The copolymers with T_g below room temperature behave as elastomers at ambient temperatures.

The ^{1}H NMR spectrum of the polymer (an example is shown in Figure S2D, Supporting Information) shows the appearance of peaks in the range of δ = 5.43−5.14 ppm (−C*H*=C*H*− groups of the copolymer main chain) and the disappearance of the peak of the double bond of the two monomers at 6.04 ppm, suggesting that the monomers were completely consumed. The ratio of the integration of the O−CH_3 signal at 3.40 ppm to that of the −CH_3 signal on the cholic acid residue at 0.57 ppm in the copolymer corresponds to the monomer feed ratio, indicating that the monomers were nearly completely converted. In most cases, the content of NTEG unit in the copolymers was somewhat higher than that in the feed, which may be due to a greater reactivity of NTEG than NCA which may have a high steric hindrance in the copolymerization process.

Thermogravimetric analysis showed that all the polymers have a good thermal stability below 350 °C, except poly(NTEG) which begins to degrade slowly at 200 °C (Figure S3, Supporting Information). Figure 1A shows that all of the polymers display a glass transition temperature (T_g) without any evidence of melting, suggesting that they are probably amorphous. Figure 1B shows that the T_g varies linearly as a function of the comonomer content in the copolymers. When the amount of NTEG units in the copolymers is increased from 0 to 100%, the T_g decreases from 176 to −58 °C. Copolymerization of a rigid cholic acid-based monomer with a flexible comonomer such as NTEG allows the fine-tuning of the T_g of the resulting copolymers. It therefore provides a simple method for tailoring the glass transition temperature to meet the specific requirements of certain applications. One of the characteristics of these copolymers is their very broad T_g. From the onset to the end of the glass transition in the DSC curves (Figure 1A and Table 1), this interval ranges from 4 °C for poly(NCA) to over 25 °C for poly(NCA−NTEG)$_{1:3}$. The same phenomena were also investigated by DMA experiments for poly(NCA−NTEG)$_{2:1}$, poly(NCA−NTEG)$_{1:1}$, and poly(NCA−-NTEG)$_{1:2}$ (Figure S5, Supporting Information). Xie anticipated that amorphous polymers with a broad glass

dx.doi.org/10.1021/ma202506b | *Macromolecules* 2012, 45, 1924−1930

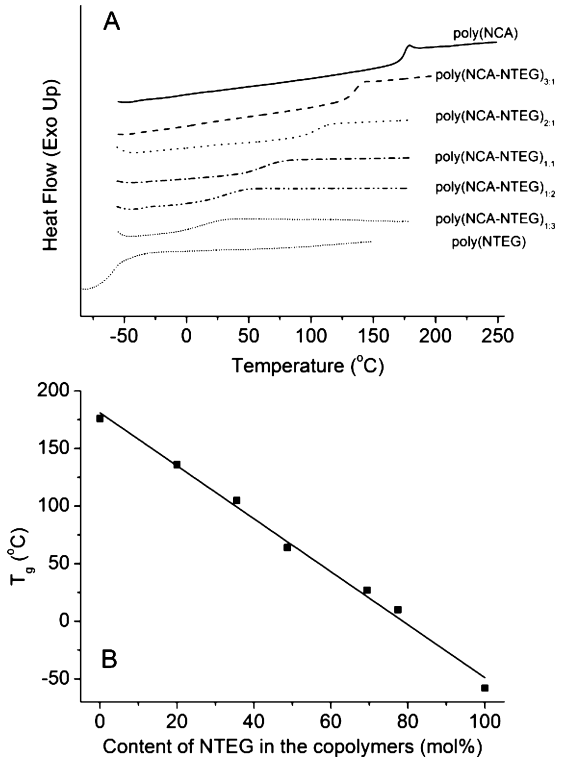

Figure 1. Thermal properties of the polymers: (A) DSC curves of the copolymers with various ratios of NCA to NTEG showing their glass transition temperatures; (B) variation of the T_g of the copolymers as a function of molar content of NTEG in the copolymers.

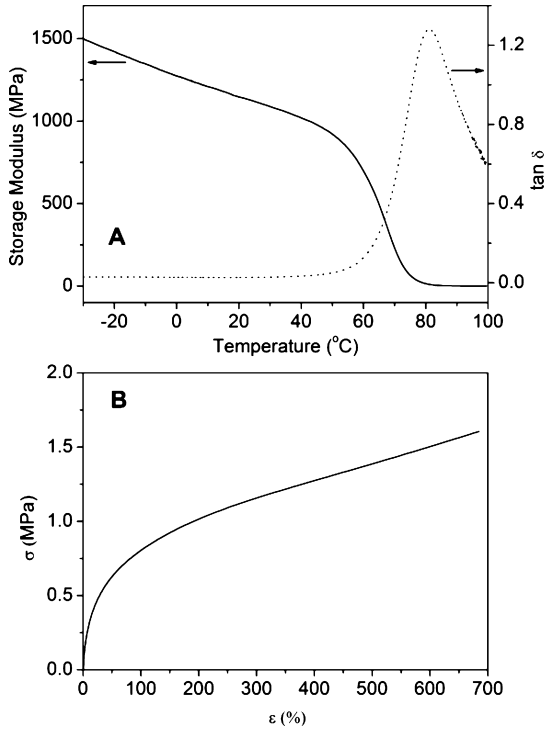

Figure 2. (A) DMA curve of poly(NCA–NTEG)$_{1:1}$ (frequency: 1 Hz), where tan δ is the ratio of the loss modulus (E'') to the storage modulus (E'). (B) Stress–strain plot of poly(NCA–NTEG)$_{1:1}$ at 85 °C (stress: σ; strain: ε; the maximum elongation corresponds to the travel limit of the equipment geometry rather than the elongation at break).

transition may have multishape memory effect.[14] Inspired by this idea, our polymers with broad glass transition temperature are explored for multishape memory effects.

Shape Memory Properties. The shape memory properties of poly(NCA–NTEG)$_{1:1}$, made with a 1:1 ratio of NCA to NTEG, have been investigated in details as a representative example of the copolymers in this series.

The DMA shows that poly(NCA–NTEG)$_{1:1}$ has a broad glass transition from 53 to 77 °C (multifrequency mode, 1 Hz), as shown in Figure 2A. Below these temperatures, the material is hard (storage modulus E' = 1.16 GPa at 40 °C), whereas above these temperatures, it displays typical rubberlike elasticity (E' = 5.79 MPa at 85 °C), with maximum elongations higher than 600% (geometrical limit of the DMA equipment), as shown in Figure 2B. At strains up to 600%, the polymer is still able to recover its original shape when reheated at 85 °C without any applied force, demonstrating its excellent recovery ability.

Two parameters are used to quantify the shape memory effect: the shape fixity (R_f), which is the ability to fix a mechanical deformation (temporary shape), and the shape recovery (R_r), which is the ability to recover the permanent shape. They are calculated by the use of the following expressions:[14]

$$R_f = \frac{\varepsilon(N)}{\varepsilon_{load}(N)} \times 100\% \quad (1)$$

$$R_r = \frac{\varepsilon(N) - \varepsilon_{rec}(N)}{\varepsilon(N) - \varepsilon_{rec}(N-1)} \times 100\% \quad (2)$$

where ε_{load} is the maximum strain imposed on the sample, ε is the strain after unloading the applied force, ε_{rec} is the strain after the completion of the recovery step, and N is the cycle number.

Before measuring the shape memory performance of the polymer, the polymer films were annealed at 85 °C to remove any residual stress/strain from the polymer processing step. In a typical thermal dual-shape memory experiment (Figure 3), the

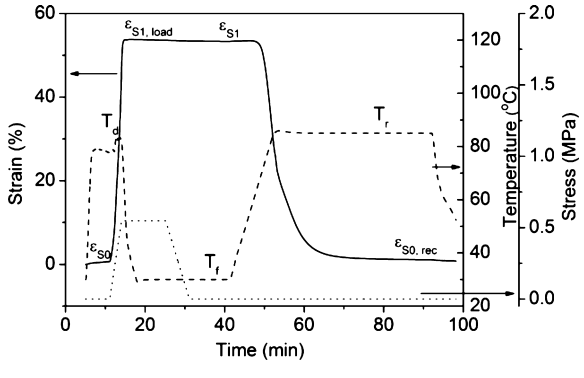

Figure 3. Dual-shape memory properties of poly(NCA–NTEG)$_{1:1}$ at a deformation (T_d) and recovery temperatures (T_r) of 85 °C and at a fixing temperature (T_f) of 30 °C (R_f = 99.2%, R_r = 98.6%).

sample was stretched to 53% strain at 85 °C (deformation temperature, T_d, above T_g) and then cooled to 30 °C (fixing temperature, T_f, below T_g). The temporary shape was completely fixed (R_f = 99.2%). When reheated to 85 °C

dx.doi.org/10.1021/ma202506b | Macromolecules 2012, 45, 1924–1930

(recovery temperature, T_r, above T_g), the permanent shape was recovered (R_r = 98.6%).

Poly(NCA−NTEG)$_{1:1}$ displays high performance dual-shape memory effect when deformed and recovered above the upper end of its T_g, as indicated by the R_f and R_r values approaching 100% (Table 2). This high performance is maintained over several cycles (Table 2 and Figure S4, Supporting Information). The high shape fixity (R_f > 99%) in all cycles indicates that vitrification in the glassy state (30 °C) is efficient in freezing chain mobility and storing elastic energy. Heating the polymer to 85 °C for a period (generally 40 min) leads to a high shape recovery (R_f > 98%). No irreversible creep appeared, even under a strain of 187% in the fifth cycle, showing that the polymer chains remained entangled despite the absence of chemical cross-links. It appears that the polymer chains and side groups provide sufficiently strong interactions to make the polymer recover its original shape.

Table 2. Strain, Shape Fixity (R_f), and Shape Recovery (R_r) of Poly(NCA−NTEG)$_{1:1}$ over Several Cycles[a]

cycle no.	strain (%)	R_f (%)	R_r (%)
1	164.7	99.5	98.7
2	171.7	99.5	99.0
3	177.7	99.5	99.2
4	180.9	99.5	99.4
5	187.4	99.5	99.4

[a]Deformation: 85 °C, 5 min; applied force: 0.6 N; shape fixing: 30 °C, 30 min; shape recovery: 85 °C, 40 min.

Multishape memory effect of the polymers generally can be investigated by two heating programming processes:[27] non-continuous[24,29] and continuous.[23] Continuous heating is more suitable in the study of shape memory polymers that have two or more distinct switching domains, providing obviously independent transition temperatures (T_{trans}). The polymers in this work represent a new class of materials, which has one broad T_g. Within the broad T_g range, multiple temporary shapes can be fixed and recovered by changing the temperature in rather small increments. Since these temperature intervals are narrow, noncontinuous heating was selectively used in the study of these polymers.[26]

A triple-shape memory experiment was performed on poly-(NCA-NTEG)$_{1:1}$, as shown in Figure 4. The permanent shape S0 was deformed at 85 °C (T_{d1}) and fixed at 60 °C (T_{f1}) to yield the first temporary shape (S1). The sample was further deformed at 60 °C (T_{d2}) and fixed at 30 °C (T_{f2}) to yield the second temporary shape (S2). Upon reheating to 60 °C (T_{r1}), the first temporary shape was recovered ($S1_{rec}$). Further heating to 85 °C (T_{r2}) allowed the recovery of the permanent shape ($S0_{rec}$). Equations 1 and 2 are expanded to eqs 3 and 4 to calculate the R_f and R_r for the triple-shape memory effect.

$$R_f(S1 \rightarrow S2) = \frac{\varepsilon_{S2} - \varepsilon_{S1}}{\varepsilon_{S2,load} - \varepsilon_{S1}} \times 100\% \quad (3)$$

$$R_r(S2 \rightarrow S1) = \frac{\varepsilon_{S2} - \varepsilon_{S1,rec}}{\varepsilon_{S2} - \varepsilon_{S1}} \times 100\% \quad (4)$$

In the multiple-stage shape memory experiment, the polymer displayed the ability to memorize a complex thermomechanical history. Within the broad T_g range, deformation at a lower temperature was more difficult than at a higher temperature, requiring a higher stress to obtain a comparable deformation. Shape fixing was much more efficient at lower temperatures, with a lower shape fixity for the deformation fixed at 60 °C (R_f(S0→S1) = 70.2%) than for the one fixed at 30 °C (R_f(S1→S2) = 97.2%). Shape recovery was excellent at both temperatures, with both R_r(S2→S1) and R_r(S1→S0) higher than 96%.

The quadruple-shape memory effect of poly(NCA−NTEG)$_{1:1}$ was also demonstrated, as shown in Figure 5. Although shape fixing was not optimal when performed at high temperatures, good shape recovery was obtained for all steps, indicating that the T_g of this polymer is sufficiently broad for it to memorize at least four distinct shapes. Theoretically, a broad glass transition temperature can be considered as an infinite number of transitions, leading to the possibility of an infinite number of memorized shapes in a multishape memory sequence.[14]

The broadness of the T_g determines the temperature span related to the shape memory behavior of these polymers. The fixing temperatures T_f can be within or below the T_g, while recovery temperatures T_r must be within or above the T_g, higher than the T_f. The shape fixity decreased near the offset of the T_g, but the shape memory effects observed at these temperatures were reproducible and reliable. The recovery forces induced by the thermoplastic character of the polymers

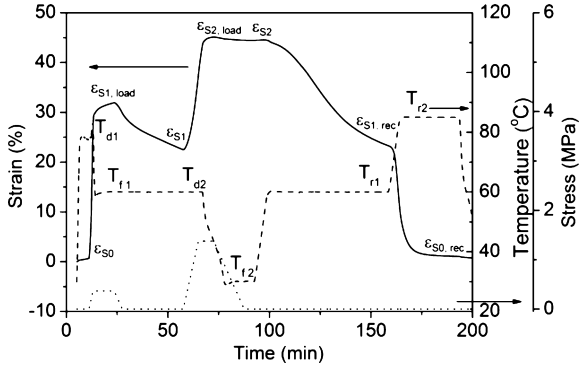

Figure 4. Triple-shape memory properties of poly(NCA−NTEG)$_{1:1}$ (T_{d1} = T_{r2} = 85 °C, T_{f1} = T_{d2} = T_{r1} = 60 °C, and T_{f2} = 30 °C). R_f(S0→S1) = 70.2%, R_f(S1→S2) = 97.2%, R_r(S2→S1) = 96.7%, and R_r(S1→S0) = 96.4%.

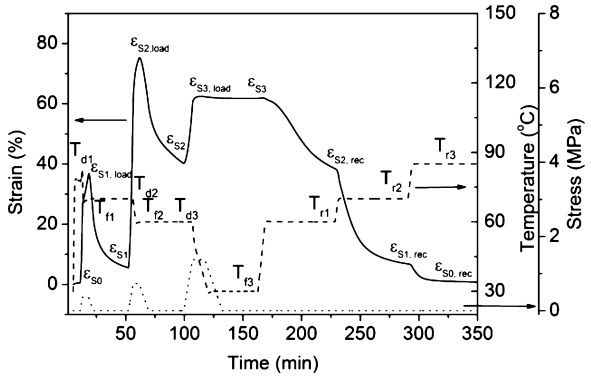

Figure 5. Quadruple-shape memory effect of poly(NCA−NTEG)$_{1:1}$ (T_{d1} = T_{r3} = 85 °C, T_{f1} = T_{d2} = T_{r2} = 70 °C, T_{f2} = T_{d3} = T_{r1} = 60 °C, T_{f3} = 30 °C). R_f(S0→S1) = 6.7%, R_f(S1→S2) = 49.6%, R_f(S2→S3) = 97.1%, R_r (S3→S2) = 109.0%, R_r(S2→S1) = 96.4%, and R_r (S1→S0) = 94.0%.

dx.doi.org/10.1021/ma202506b | Macromolecules 2012, 45, 1924−1930

are apparently different at different temperature within the T_g range. Throughout this range, the temporary shapes deformed at high temperature can be kept at lower temperature.

Nagata reported that high-molecular-weight nonchemically cross-linked polynorbornene showed shape memory effect, which was attributed to physical entanglement of the chains acting as fixed structures.[45] It is likely that physical entanglement of the high-molecular-weight copolymer chains is responsible for the permanent shape in our polymer system. The ability to memorize multiple temporary shapes is due to the broad glass transition temperature.[14] Hydrogen-bonding interactions[46] between polymer side chains may also play a role in fixing and recovering the multiple temporary shapes.

CONCLUSION

A series of copolymers with a polynorbornene main chain, and cholic acid and triethylene glycol side groups were successfully synthesized through ROMP. The T_g of the copolymers are broad and tunable and vary linearly with the monomer ratio over a wide temperature range (−58 to 176 °C). The broad T_g's enable the polymers to have multishape memory effects. The copolymer tested displayed very high performance dual-shape memory effects over several cycles and also showed triple- and quadruple-shape memory effects. Only one copolymer was selected for detailed studies, but the other copolymers in this series also show shape memory properties. For typical shape memory polymers, the T_g is regarded as one temperature point not a range, above or below which a temporary shape is recovered or fixed. To the best of our knowledge, Xie's work[14,26] and ours are the first studies to explore the broad T_g of polymers for multishape memory behaviors. The polymers in Xie's work are based on perfluorosulfonic acid ionomer and thus are not easy for bulk processing. The polymers in this work may prove to be more versatile in their applications due to their more varied properties, such as stiffness, modulus, T_g, etc. Other polymers with broad T_g's[48] may be also studied for such properties.

The multishape memory properties of these copolymers are inherently different from traditional shape memory polymers. Although shape memory effect has been observed for norbornene-based polymers,[45,47] to the best of our knowledge, these copolymers based on norbornene monomer with cholic acid side group are the first example of multishape memory polymers in the absence of any chemical cross-links. The mechanism of multishape memory effects is still a subject to be further studied. The present results may contribute to the design and understanding of multishape memory polymers with a broad glass transition. These polymers may find applications as biomedical implants and coatings due to the generally good biocompatibility of cholic acid and PEG.

ASSOCIATED CONTENT

Supporting Information

Synthetic routes of NCA and NTEG, DSC curves of poly(NCA), poly(NCA−NTEG)$_{1:1}$, and poly((NCA−NTEG)$_{1:2}$, ^{1}H NMR spectra of NCA and NTEG in $CDCl_3$, and poly(NTEG), poly(NCA−NTEG)$_{1:1}$, and poly(NCA) in DMSO-d_6, TGA curves of all the polymers, consecutive dual-shape memory cycles of poly(NCA−NTEG)$_{1:1}$, DMA curves of poly(NCA−NTEG)$_{2:1}$, poly(NBCA−NBTEG)$_{1:1}$, poly(NCA−NTEG)$_{1:2}$. This material is available free of charge via the Internet at http://pubs.acs.org.

AUTHOR INFORMATION

Notes

The authors declare no competing financial interest.

ACKNOWLEDGMENTS

Financial support from NSERC of Canada, FQRNT of Quebec, and the Canada Research Chair program is gratefully acknowledged. Authors thank Dr. Kun Zhang for helpful discussions and Mr. Sylvain Essiembre and Mr. Pierre Ménard-Tremblay for their technical support. The authors are members of CSACS funded by FQRNT and GRSTB funded by FRSQ.

REFERENCES

(1) Behl, M.; Lendlein, A. *Mater. Today* **2007**, *10*, 20−28.
(2) Lee, H.-F.; Yu, H. H. *Soft Matter* **2011**, *7*, 3801−3807.
(3) Leng, J.; Lan, X.; Liu, Y.; Du, S. *Prog. Mater. Sci* **2011**, *56*, 1077−1135.
(4) Lendlein, A.; Jiang, H.; Junger, O.; Langer, R. *Nature* **2005**, *434*, 879−882.
(5) Lee, K. M.; Koerner, H.; Vaia, R. A.; Bunning, T. J.; White, T. J. *Soft Matter* **2011**, *7*, 4318−4324.
(6) Wu, L.; Jin, C.; Sun, X. *Biomacromolecules* **2011**, *12*, 235−241.
(7) Kumpfer, J. R.; Rowan, S. J. *J. Am. Chem. Soc.* **2011**, *133*, 12866−12874.
(8) Weiss, R. A.; Izzo, E.; Mandelbaum, S. *Macromolecules* **2008**, *41*, 2978−2980.
(9) Zhou, J.; Schmidt, A. M.; Ritter, H. *Macromolecules* **2010**, *43*, 939−942.
(10) Lendlein, A.; Kelch, S. *Angew. Chem., Int. Ed.* **2002**, *41*, 2034−2057.
(11) Mohr, R. *Proc. Natl. Acad. Sci. U. S. A.* **2006**, *103*, 3540−3545.
(12) Yakacki, C. M.; Shandas, R.; Safranski, D.; Ortega, A. M.; Sassaman, K.; Gall, K. *Adv. Funct. Mater.* **2008**, *18*, 2428−2435.
(13) Liu, C. D.; Chun, S. B.; Mather, P. T. *Macromolecules* **2002**, *35*, 9868−9874.
(14) Xie, T. *Nature* **2010**, *464*, 267−270.
(15) Sokolowski, W.; Metcalfe, A.; Hayashi, S.; Yahia, L. H.; Raymond, J. *Biomed. Mater. (Bristol, U. K.)* **2007**, *2*, S23−S27.
(16) Yakacki, C. M.; Gall, K. *Adv. Polym. Sci.* **2010**, *226*, 147−175.
(17) Lendlein, A. *Science* **2002**, *296*, 1673−1676.
(18) Metcalfe, A.; Desfaits, A.-C.; Salazkin, I.; Yahia, L. H.; Sokolowski, W. M.; Raymond, J. *Biomaterials* **2003**, *24*, 491−497.
(19) Yakacki, C. M.; Shandas, R.; Lanning, C.; Rech, B.; Eckstein, A.; Gall, K. *Biomaterials* **2007**, *28*, 2255−2263.
(20) Wache, H. M.; Tartakowska, D. J.; Hentrich, A.; Wangner, M. H. *J. Mater. Sci.* **2003**, *14*, 109−112.
(21) Xie, T.; Xiao, X.; Cheng, Y.-T. *Macromol. Rapid Commun.* **2009**, *30*, 1823−1827.
(22) Bellin, I.; Kelch, S.; Lendlein, A. *J. Mater. Chem.* **2007**, *17*, 2885−2891.
(23) Luo, X.; Mather, P. T. *Adv. Funct. Mater.* **2010**, *20*, 2649−2656.
(24) Pretsch, T. *Smart Mater. Struct.* **2010**, *19*, 015006.
(25) Zotzmann, J.; Behl, M.; Hofmann, D.; Lendlein, A. *Adv. Mater.* **2010**, *22*, 3424−3429.
(26) Li, J.; Xie, T. *Macromolecules* **2011**, *44*, 175−180.
(27) Behl, M.; Lendlein, A. *J. Mater. Chem.* **2010**, *20*, 3335−3345.
(28) Behl, M.; Razzaq, M. Y.; Lendlein, A. *Adv. Mater.* **2010**, *22*, 3388−3410.
(29) Ahn, S.-k.; Deshmukh, P.; Kasi, R. M. *Macromolecules* **2010**, *43*, 7330−7340.
(30) Gautrot, J. E.; Zhu, X. X. *J. Mater. Chem.* **2009**, *19*, 5705−5716.
(31) Denike, J. K.; Zhu, X. X. *Macromol. Rapid Commun.* **1994**, *15*, 459−465.
(32) Zhu, X. X.; Nichifor, M. *Acc. Chem. Res.* **2002**, *35*, 539−546.
(33) Gautrot, J. E.; Zhu, X. X. *Macromolecules* **2009**, *42*, 7324−7331.
(34) Zhang, J.; Zhu, X. *Sci. China, Ser. B: Chem.* **2009**, *52*, 849−861.

(35) Zhang, Y. H.; Akram, M.; Liu, H. Y.; Zhu, X. X. *Macromol. Chem. Phys.* **1998**, *199*, 1399−1404.
(36) Gautrot, J. E.; Zhu, X. X. *Angew. Chem., Int. Ed.* **2006**, *45*, 6872−6874.
(37) Gautrot, J. E.; Zhu, X. X. *Chem. Commun.* **2008**, *14*, 1674−1676.
(38) Conrad, R. M.; Grubbs, R. H. *Angew. Chem., Int. Ed.* **2009**, *48*, 8328−8330.
(39) Leitgeb, A.; Wappel, J.; Slugovc, C. *Polymer* **2010**, *51*, 2927−2946.
(40) Bielawski, C. W.; Grubbs, R. H. *Prog. Polym. Sci.* **2007**, *32*, 1−29.
(41) Ogawa, S.; Takano, S.; Fujimori, H.; Itoh, T.; Kaita, S.; Iida, T.; Wakatsuki, Y. *React. Funct. Polym.* **2010**, *70*, 563−571.
(42) Benrebouh, A.; Zhang, Y. H.; Zhu, X. X. *Macromol. Rapid Commun.* **2000**, *21*, 685−690.
(43) Gajanan, M. P.; Bhasker, B.; Jochen, W.; Siegfried, B.; Klaus, W.; Michael, R. B. *Dalton Trans.* **2009**, *41*, 9043−9051.
(44) Maynard, H. D.; Okada, S. Y.; Grubbs, R. H. *J. Am. Chem. Soc.* **2001**, *123*, 1275−1279.
(45) Nagata, N. *Kagaku* **1990**, *45*, 554−557.
(46) Li, J. H.; Lewis, C. L.; Chen, D. L.; Anthamatten, M. *Macromolecules* **2011**, *44*, 5336−5343.
(47) Liu, C.; Mather, P. T. *J. Appl. Med. Polym.* **2002**, *6*, 47−52.
(48) Kim, J.; Mok, M. M.; Sandoval, R. W.; Woo, D. J.; Torkelson, J. M. *Macromolecules* **2006**, *39*, 6152−6160.

Macromolecules

Article

pubs.acs.org/Macromolecules

Experimental Determination of Hansen Solubility Parameters for Select POSS and Polymer Compounds as a Guide to POSS–Polymer Interaction Potentials

Henry W. Milliman,[†] David Boris,[‡] and David A. Schiraldi*[,†]

[†]Department of Macromolecular Science and Engineering, Case Western Reserve University, Cleveland, Ohio 44106, United States

[‡]Kodak Research Laboratories, Rochester, New York 14650, United States

ABSTRACT: Polyhedral oligomeric silsesquioxanes (POSS) have been incorporated into a wide range of polymers over the past two decades in an attempt to enhance their thermal and mechanical properties. Properties of POSS/polymer blends/composites are highly dependent on the uniformity of POSS dispersion and thus are particularly sensitive to the magnitude of interaction between POSS and added fillers/polymers. Methods to characterize these interactions in terms of solubility parameters have been recently examined in the literature using group contribution calculations. The present work presents a method for measuring three-dimensional Hansen solubility parameters for polymers and POSS which allows for the direct calculation of interaction potentials. These measured solubility parameters predict POSS/polymer interactions more accurately than group contribution calculations and accurately predict the uniformity of POSS dispersion and the resultant property enhancements.

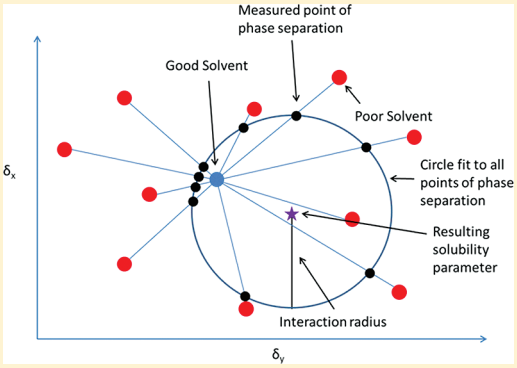

INTRODUCTION

Polyhedral oligomeric silsesquioxanes (POSS) are a class of hybrid molecules which consist of an inorganic siloxane core which is functionalized with any of a number of organic substituents. POSS has been incorporated into polymers though copolymerization,[1,2] grafting,[3] and blending[4−7] over the past two decades in hopes of providing property enhancements similar to that seen in the traditional composite field in which rigid inorganic particles are incorporated into polymers to provide thermal and mechanical reinforcement.[8,9] Early research in the field of nanocomposites indicated that inorganic particles require compatibilization to produce strong interactions with a polymer, resulting in reinforcement and a strong interface.[10,11] This compatibilization is generally accomplished by modifying the surface of the particles with an organic moiety to closely match the chemical structure of the polymer. POSS molecules have attracted attention as molecular-scale equivalents to organically modified particles because they are hybrid materials containing rigid inorganic cores modified by a huge variety of pendant group functionalities. Over 100 different POSS molecules are commercially available with different organic functionalities for matching and blending with desired matrix polymer. The challenge is to predict which POSS functionality will enhance properties when incorporated into a given polymer. In the case of copolymerization or grafting of a POSS material to a polymer, the choice of modifier will be based on the specific chemistry needed for a given reaction scheme. In the case of melt-blending though, a different set of criteria must be met. In a melt blend POSS behaves as a large molecule, and can exist in a number of states once incorporated into a polymer. In many cases the POSS will simply phase separate due to a lack of compatibility with the polymer. If a high degree of attractive interaction is present, the POSS can be dispersed on the nanometer scale or even in a completely dissolved state.[12,13] In the case of molecular dispersion it can act as a plasticizer.[14] If there are specific interactions (hydrogen bonding), the system can behave similarly to that of a copolymer or grafted system.[15]

If the desired system is one in which a high degree of POSS/polymer interaction is present, how does one go about selecting an optimal POSS additive for a specific polymeric matrix? A simple examination of the chemical structure is not sufficient as it is difficult to ascertain what the effects the silicate core and molecular geometry will have on the interaction potential of POSS. For this reason several researchers have turned to evaluating POSS/polymer combinations in terms of solubility parameters.[16−18] By assigning solubility parameter values to different POSS and polymer species, predictions about dispersion and compatibility can be made. If the difference in solubility parameters between the POSS and polymer is very low, it is expected that there will be a high degree of POSS polymer interaction, yielding favorable results similar to a graft or copolymer system, while if the difference is very high it is assumed that the system would phase separate yielding a decrease in the desired physical properties.

Received: December 11, 2011
Revised: January 31, 2012
Published: February 7, 2012

Work from Morgan et al. describes interaction potentials as calculated using the Hoy method of group contribution calculation.[16] These calculations result in a single parameter value for the square root of cohesive energy density. Chin et al. also relate the level of dispersion of POSS to solubility parameters in terms of the three-dimensional Hansen solubility parameter which contains separate terms for the contribution of dispersion, polar, and hydrogen bonding forces.[16−18] The contribution of hydrogen bonding is ignored in that work though, as is the contribution of the core silicate to the calculated solubility parameter.

To obtain accurate solubility parameters, it was our goal to independently and directly measure the Hansen solubility parameters of a variety of polymers and POSS grades. These experimental results can then be used to test the assumptions used for group contribution or other calculation methods.

Solubility of a given solvent−solute pair is governed by the free energy of mixing

$$\Delta G_M = \Delta H_M - T\Delta S_M \tag{1}$$

where ΔG_M is the Gibbs free energy of mixing, ΔH_M is the enthalpy of mixing, T is the absolute temperature, and ΔS_M is the entropy of mixing.[19] In order for spontaneous mixing to occur, $\Delta G_M \leq 0$. In the case of high molecular weight species, dissolution is accompanied by a relatively small positive change in entropy, and thus the enthalpy of mixing is the dominant term. Hildebrand and Scott[20] proposed that enthalpy of mixing could be described as

$$\Delta H_M = V_{mix}[(\Delta E_1^V/V_1)^{1/2} - (\Delta E_2^V/V_2)^{1/2}]^2\Phi_1\Phi_2 \tag{2}$$

where V_{mix} is the volume of the mixture, ΔE_i^V is the energy of vaporization of species i, V_i is the molar volume, and Φ_i is the molar volume. The cohesive energy, E, of a material is the energy required to break all intermolecular forces. When divided per unit volume the value for cohesive energy density is obtained:

$$\text{CED} = \frac{E}{V} = (\Delta H_{vap} - RT)/V \tag{3}$$

The Hildebrand solubility parameter then is defined as the square root of cohesive energy density:

$$\delta = \left(\frac{E}{V}\right)^{1/2} \tag{4}$$

Equation 2 can be rewritten in terms of the Hildebrand solubility parameter (eq 4) to give the heat of mixing per unit volume of a two part mixture:

$$\frac{\Delta H_M}{V} = (\delta_1 - \delta_2)^2\Phi_1\Phi_2 \tag{5}$$

In order for $\Delta G_M \leq 0$, the heat of mixing must be smaller than the entropic term in eq 1; therefore, the difference in solubility parameters $(\delta_1 - \delta_2)$ must remain small. The major shortcoming of the Hildebrand method, though, is that it does not take into account specific interactions between molecules, like hydrogen bonding. To expand on this idea, Hansen proposed breaking the cohesive energy into three parts, corresponding to three types of interactions:[21]

$$E = E_D + E_P + E_H \tag{6}$$

where the total cohesive energy (E) is composed of individual terms for contributions from dispersion (D), polar−polar (P), and hydrogen bonding (H) forces. Dividing this equation by the molar volume gives the square of the total (Hildebrand) solubility parameter as the sum of the squares of the Hansen D, P, and H components.

$$\frac{E}{V} = \frac{E_D}{V} + \frac{E_P}{V} + \frac{E_H}{V} \tag{7}$$

$$\delta^2 = \delta_D{}^2 + \delta_P{}^2 + \delta_H{}^2 \tag{8}$$

These three parameters can be measured experimentally (as will be described later) such that solubility "distance" (Ra) can be calculated for any polymer−solvent (and POSS/polymer) combination. In order to maximize POSS/polymer interactions, one must simply choose a filler/matrix combination which minimizes this distance.

$$(Ra)^2 = 4(\delta_{D2} - \delta_{D1})^2 + (\delta_{P2} - \delta_{P1})^2 + (\delta_{H2} - \delta_{H1})^2 \tag{9}$$

In this equation, the factor of "4" is predicted by the Prigogine corresponding states theory of polymer solutions when the geometric mean is used to estimate the interaction in mixtures of dissimilar molecules and has been found to be convenient when plotting solubility data as a sphere.[22]

Conceptually, the method for determining Hansen solubility parameters (HSP) is to define a sphere in three-dimensional Hansen space (with dispersion, polar, and hydrogen bonding forces as the three axes) in which all of the good solvents (including solvent mixtures) for the solute exist inside the sphere while all of the poor solvents are excluded from the sphere. The three component values for HSP are well-known for a large number of common solvents, and thus each solvent is represented by a point in a Hansen three-dimensional space. By replacing some of the good solvent with a poor solvent (creating a mixture), we move along the line connecting the good solvent solubility parameter to the poor solvent solubility parameter. At some point the polymer or solute will phase separate, which defines a boundary on that line. By repeating this process with a number of poor solvents, a sphere can be fit in which all of the soluble mixture (points) are within the sphere while all of the nonsoluble mixtures are outside of it. The center of this sphere is then the three-dimensional solubility parameter of the solute with the radius of the sphere defined as the radius of interaction. Figure 1 represents this concept in two dimensions.

Once solubility parameters have been determined for different POSS and polymer combinations the distance between these two compounds in Hansen space can be calculated by eq 9. The distance defines how far separated two components are in solubility space. Dividing the solubility distance by the minimum interaction radius (smaller of the two) one arrives with a value of "relative energy distance" (RED), which in effect measures the mutual compatibility of the two materials. If the RED is 0, then the solubility parameters are exactly matched and the materials are soluble with no energy difference. If the RED is less than 1, then the two compounds are strongly compatible and predicted to be mutually soluble. A value at or close to 1 is a boundary condition, and progressively higher values indicate lower affinities. If the distance is greater than the larger of the interaction radii, then the blend should phase separate. These values will be used

dx.doi.org/10.1021/ma202685j | Macromolecules 2012, 45, 1931−1936

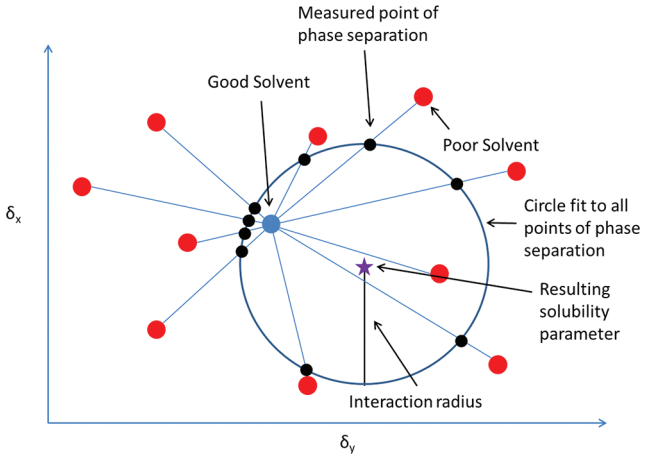

Figure 1. Graph showing conceptual method for solubility parameter determination. For ease of viewing only two dimensions are shown.

to predict when certain POSS−polymer combinations will show a high degree of interaction, with lower values predicting high interactions and higher values predicting little to no interaction and phase separation.

The present work will serve to show how well POSS dispersion, interaction potential, and phase separation can be predicted with this method as well as show the deficiencies of other methods which make use of calculations with problematic assumptions. Specifically, a previous study by the Schiraldi group[15] will be analyzed in terms of solubility parameter. In this work it was found that a high degree of POSS/polymer interactions (and associated property enhancements) were found for a blend of phenoxy resin and trisilanolphenyl POSS while the same POSS blended with polycarbonate (PC) showed phase separation and decreased properties. For the comparison to other methods, the work of Morgan[16] and Chin[17,18] will also be examined to show how the direct measurement of three-dimensional solubility parameters can lead to a better understanding of the phase behavior of these blends without the need for assumptions.

EXPERIMENTAL SECTION

Materials. The following solvents were used, either as good or poor solvents, and were all obtained from Fisher with 99% or higher purity, free of inhibitors and dried over molecular sieves before use: dichloromethane, tetrahydrofuran, hexane, toluene, methyl ethyle ketone, 1-propanol, cyclohexane, acetonitrile, methanol, *N,N*-dimethylformamide, ethanol, dimethyl sulfoxide, heptane, propylene glycol, hexafluoroisopropanol, and triethylene glycol. Hansen solubility parameters for these solvents were obtained from ref 21.

Aminopropylisobutyl POSS (AM0265), phenylisobutyl POSS (MS0813), phenylisooctyl POSS (MS0814), and trisilanolphenyl POSS (SO1458) were purchased from Hybrid Plastics Inc. and used as received. Polysulfone was obtained from Solvay Advanced Polymers (Udel P-1700 NT 11) with a reported melt flow index of 6.5 g/10 min at 343 °C and 2.16 kg. PKFE phenoxy resin was obtained from InChem Resins Inc. (Rock Hill, SC), with reported number-average and weight-average molecular weights of 16 000 and 60 000 g/mol, respectively. Calibre 200-14 an unstabilized polycarbonate resin was supplied by Styron LLC.

Solution Preparation. Initially, good and poor solvents for each of the seven analytes were determined qualitatively by making ca. 1% weight solutions in a variety of solvents. The data needed to construct a sphere in three-dimensional Hansen space consists of a series of volume fraction values of good/poor mixtures where the last clear solution and first visibly phase separated solution is noted. Here is the procedure: Once a good solvent had been determined a standard solution of the polymer/POSS of interest was prepared such that 1 mL of this solution would contain 50 mg of the compound of interest (2.5 g in 50 mL). Using an autopipet, 1 mL of solution was added to each of 50 glass vials. The solvent was then removed by vacuum leaving 50 mg of polymer/POSS in the vial. The initial series consisted of volume ratios of (good solvent:poor solvent) 90:10, 80:20, 70:30, 60:40, 50:50, 40:60, 30:70, 20:80, and 10:90, with a total volume of 5 mL. The appropriate volume of good solvent was added to each of the vials and left overnight to allow complete dissolution. Next, the appropriate volume of each of 6−10 bad solvents was added to each series of solutions. The vials were shaken to ensure complete mixing and left for 1 week to equilibrate, reducing any kinetic effects of dissolution. Once equilibrated a record was made for each series of which solutions remained clear and which showed signs of phase separation. These values were then used to build models for each of the compounds.

The models were constructed using a Microsoft Excel solving routine in which the boundary conditions were defined such that the last condition of solubility would be contained within a sphere while the first condition of insolubility would be contained outside of said sphere. The model contained as many parameters as solvent series were prepared for a particular compound. Since there are four parameters (dispersion, polar, hydrogen bonding, and interaction radius), the minimum number of inputs is four, though in many cases 6−7 data series were used. The model was optimized by minimizing the average distance between the radius as defined by the boundary condition recorded and the radius predicted by the model. In this way the three-dimensional Hansen solubility parameters (with interaction radius) were measured and modeled for a variety of POSS molecules and polymers.

RESULTS AND DISCUSSION

In total, three polymers and four POSS grades were measured and modeled. The structures and short names of these compounds are listed in Figure 2. The initial results for solubility parameters are listed in Table 1. Values are given for each of the three parameters (in units of $MPa^{1/2}$), interaction radius (unitless), and total solubility parameter (in units of $MPa^{1/2}$ and $(cal/cm^3)^{1/2}$), as calculated from eq 8. It should be noted that two different approaches were taken to calculate these values. The first approach solved for the model points in a way to minimize the deviation from the measured boundary points (best fit). The second solved for the model points in such a way as to minimize the total interaction radius. In most cases the values given by either approach were quite similar, and so values shown in Table 1 are produced using the best fit model

To gauge how well these values predict POSS−polymer interactions, the work of Schiraldi and Iyer[15] was analyzed in terms of solubility parameters. In that work it was found that a blend of trisilanolphenyl POSS (SO1458) and polycarbonate showed a lack of POSS−polymer interactions and therefore phase separated, yielding decreased physical properties. By blending the same POSS with PKFE phenoxy resin, though, a different trend was found. In that system an increase in modulus and glass transition temperature was noted and explained by the presence of hydrogen bonding and $\pi-\pi$ stacking which resulted in a pseudografted POSS structure. Now knowing the experimental solubility parameter values for each of these compounds calculations can be carried out (using eq 9) which will provide the relative energy difference between each of the polymers and the POSS grade which was used. The results from these calculations are listed in Table 2. From these calculations it is clear that trisilanolphenyl POSS has a significantly smaller relative energy difference to PKFE (1.11) than to PC (1.87) and therefore a higher interaction potential.

dx.doi.org/10.1021/ma202685j | *Macromolecules* 2012, 45, 1931−1936

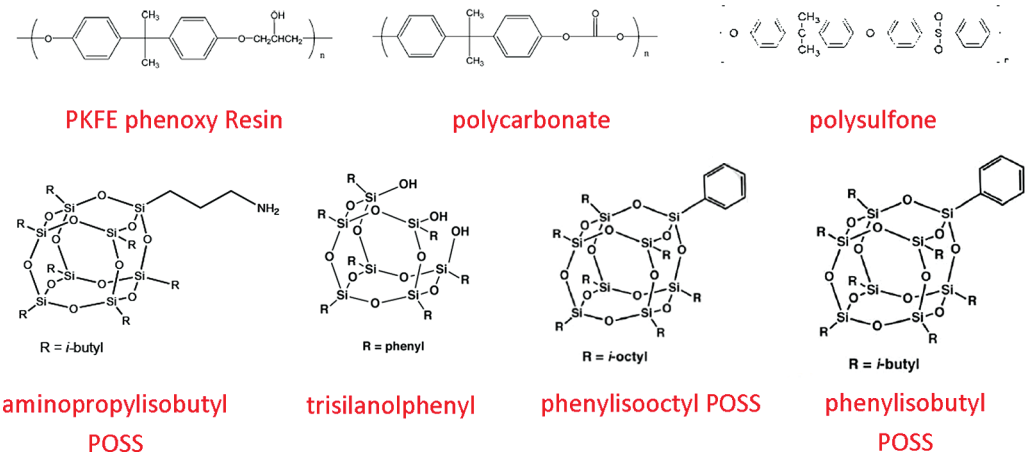

Figure 2. Structures and short names for polymers and POSS grades tested.

Table 1. Solubility Parameters for Select Compounds

compd	δ_D	δ_P	δ_H	r	δ_T, $MPa^{1/2}$	δ_T, $(cal/cm^3)^{1/2}$
PC	19.35	6.43	5.80	6.23	21.20	10.36
PKFE	22.05	9.06	9.58	12.62	25.69	12.56
PSF	19.02	5.90	6.13	4.29	20.84	10.18
SO1458	16.60	16.72	5.23	15.07	24.14	11.80
AM0265	16.85	0.00	11.83	10.83	20.58	10.06
MS0813	16.93	5.69	7.23	4.30	19.30	9.43
MS0814	16.31	8.32	8.75	7.00	20.29	9.92

Table 2. Calculation of Relative Energy Difference (RED) for POSS−Polymer Combinations

	δ_D	δ_P	δ_H	r	RED (SO1458)
PC	19.35	6.43	5.80	6.23	1.87
PKFE	22.05	9.06	9.58	12.62	1.11
PSF	19.02	5.90	6.13	4.29	2.77
SO1458	16.60	16.72	5.23	15.07	0.00

The value of 1.11 for the SO1458−PKFE combination predicts that the two are almost soluble. In this case the results are clearly predicted by use of solubility parameters. While this model does not take into account the processing and thermal history of the blends, the results are consistent with the predicted values. These Hansen solubility parameters were developed using a solution technique and are most accurate when comparing to solution blended systems. The predicted results for dispersion and reinforcement in this study, however, are confirmed through this method.

It was this previous work which led to additional research by Schiraldi et al. which incorrectly predicted that similarities in chemical structure between polysulfone (PSF) and trisilanolphenyl POSS would lead to a high degree of interaction between blend components resulting in polymer properties enhancements.[23] It was assumed that polysulfone would behave more similarly to phenoxy resin than polycarbonate due to its polarity and the potential for hydrogen bonding to sulfone groups. The calculation of "RED" for SO1458 and PSF though yields a result of 2.77; this large difference means that PSF has a significantly lower interaction potential than PC which is why a highly phase-separated morphology and decreased mechanical properties were observed in these blends. This example illustrates the futility in predicting POSS/polymer interactions based on chemical structures alone. While polysulfone could be assumed to behave in a similar manner as phenoxy resin in POSS blends, it exhibited lower compatibility than was previously observed with the poorly matched polycarbonate polymer. By measuring values for solubility parameters of POSS−polymer combinations, the nature and the magnitude of the interactions can be understood and predictions can be made about whether a phase separated or dispersed blend will result without the need to perform experiments.

The values determined herein were then used to revisit other examples from the literature. As was mentioned previously, a number of workers in the field have begun to try to correlate solubility parameters to POSS−polymer interactions, though they are using different techniques to find the solubility parameters which may lead to inaccurate determinations. Morgan et al.[16] tried to use the Hoy solubility parameters of nylon-6, with calculated values for octaisobutyl POSS and trisilanolphenyl POSS. The Hoy method of group contribution calculations were used to determine single value solubility parameters, generating the listed in Table 3. Since values were

Table 3. Solubility Parameters As Calculated Using the Hoy Method[16]

	$\sum G_i$ $(kcal\ cm^3/mol)^{1/2}$	δ $(cal/cm^3)^{1/2}$
PA6	1.10	11.0
octaisobutyl-POSS	7.43	7.8
trisilanolphenyl-POSS	7.93	9.8

not determined for octaisobutyl POSS in the present work, only the values for nylon-6 (provided by ref 21) and trisilanolphenyl POSS (SO1458) will be considered.

From these values the authors hypothesize that the nylon-6 will have a higher degree of interaction with trisilanolphenyl POSS because the values for solubility parameter are closer than that of octaisobutyl POSS. While this may be true there is no discussion of how close those values need to be to produce a strong interaction. With a single value solubility parameter there is no way of taking into account interaction radius or understanding how the different component contributions of solubility parameter affect the real difference in interaction potential. If those same materials are considered using the Hansen method to calculate a "RED", a much different result is

dx.doi.org/10.1021/ma202685j | Macromolecules 2012, 45, 1931−1936

Table 4. Hansen Solubility Values and RED Calculation for PA6−SO1458 Combination

	δ_D	δ_P	δ_H	r	RED (SO1458)
PA6	17.00	10.6	3.4	5.10	2.82
SO1458	16.60	16.72	5.23	15.07	0.00

noted (Table 4). Using this approach, a RED value of 2.82 is determined which would suggest that there is actually a very large difference in solubility parameters and that the nylon-6-SO1458 blend should show a phase-separated morphology, which indeed is the result which was reported.

This example shows that solubility parameters can be effectively used to predict POSS/polymer interactions, but it is necessary to use a more sophisticated model which takes into account each of the interaction forces independently and which does not rely on the calculation of single values based on group contribution methods.

Other recent work has also highlighted how solubility parameter could be useful for understanding POSS−polymer interactions. Work by Chin et al. also uses group contribution calculations to make estimations of interaction potentials.[17,18] The importance of using three parameter Hansen solubility parameters is stressed by Chin; however, assumptions were then made which could lead to errors in accurately predicting interaction potentials. In order to perform the calculations using the Hoftyzer and van Krevelen method, two assumptions were made: (1) hydrogen bonding was assumed to have no impact based on the symmetry of the molecule, and (2) the core POSS cage's contribution to the overall solubility parameter was neglected. The results of these calculations are listed in Table 5. In that work aminopropylisobutyl POSS is the

Table 5. Calculated Solubility Parameters for Select Compounds[17]

	δ_d ($J^{1/2}$ $cm^{-3/2}$)	δ_p	δ_h	δ
PA6	15.9	34.6	13.4	18.0
aminopropylisbutyl-POSS	17.5	0	0	17.5
aminopropylisooctyl-POSS	18.6	0	0	18.6
aminopropylphenyl-POSS	19.2	1.5	0	19.3

only POSS used which has been measured and modeled so it will be discussed here.

As stated earlier, the authors have made the assumption that there is no hydrogen bonding contribution and that the POSS cage has no contribution. This however is refuted by the results shown previously (Table 1) which show that indeed hydrogen bonding has a large contribution to the total solubility parameter. In the case of aminopropylisobutyl POSS (AM0265/AB POSS) hydrogen bonding plays a significant role in the solubility behavior of the compound (δ_H = 11.83). The authors have presented the total solubility parameters for nylon-6 and a series of POSS types without explaining the connection between the difference in solubility parameter and the resultant interaction potential. The authors state that since the value for nylon-6 is closest to aminopropylisobutyl POSS, it has the highest degree of interaction and therefore the best dispersion; however, the difference between nylon-6 and aminopropylisobutyl POSS is 0.5, while the difference between nylon-6 and aminopropylisooctyl POSS is negligibly different at 0.6. Using the Hansen value for nylon-6 and the measured value for AM0265, a relative energy difference calculation can be carried out (Table 6), which shows a

Table 6. Hansen Solubility Values and RED Calculation for PA6−AM0265 Combination

	δ_D	δ_P	δ_H	r	RED (AM0265)
PA6	17.00	10.6	3.4	5.10	0.71
AM0265	16.85	0.00	11.83	10.83	0.00

distance of 0.71. This RED predicts that the POSS would be soluble in the nylon matrix which is indeed the result that is reported. In this case our conclusions are consistent with what the author reports, but our method of prediction is more advanced and we contend considerably more accurate.

It is not our goal to treat the previous work as incorrect or insubstantial. On the contrary, their work correctly anticipates the need for an accurate method for predicting and interpreting POSS/polymer interactions, and the proposed group contribution calculations are one method to move in that direction. Unfortunately, though, in order to perform those calculations, unnecessary assumptions are made which can lead to misleading results. By using the experimental determination of Hansen solubility parameter as described here, direct measurements can be made which separate the contributions from the many forces which determine interaction potentials between molecules. Using this information, relative energy difference calculations can be made which can quantitatively determine the degree of interaction between polymer and POSS.

CONCLUSIONS

In this work an experimental method for the determination of Hansen solubility parameters was presented and used to determine solubility parameter values for a number of polymers and POSS grades. Using these solubility parameters, it was then possible to carry out relative energy distance calculations for various POSS−polymer combinations. The results from these calculations accurately predict the solubility, the POSS−polymer interactions and resultant POSS−dispersion uniformity compared to reported experimental results in the literature. Specifically, the behavior of POSS/phenoxy resin and POSS/polycarbonate blends was examined, and it was shown that the solubility parameter values for the POSS/polymer combinations used in that work accurately predict the very different observed behaviors in these blends. It was also shown that more recent work on POSS/polysulfone blends that showed a phase-separated morphology can be explained due to a high relative energy difference which was not predicted by simple evaluation of the chemical structures of the POSS and polymer used.

Examples of solubility parameter estimations using group contribution calculations were also examined and compared to the values which had been determined using the Hansen method. It was determined that these calculation methods are inaccurate and specifically make unjustifiable assumptions. By experimentally determining the Hansen solubility parameters for a given POSS−polymer combination without any a priori assumptions, we get accurate prediction of POSS−polymer interactions and therefore POSS dispersion uniformity. These works did, however, highlight the need for these types of experimental evaluations to understand and predict POSS dispersion. Future work in this area will determine to what degree processing and thermal history affect the accurate prediction of these values. The current model has no way to account for the degree of mixing achieved by blending or differences in cooling rates from the melted state. These factors

dx.doi.org/10.1021/ma202685j | Macromolecules 2012, 45, 1931−1936

may affect the ability of the POSS and polymer to associate in an ideal manner. In some cases these factors may have an effect which may be greater than the interaction potentials which would be present in a solution blended system.

AUTHOR INFORMATION

Corresponding Author

*Tel 216-368-4243; e-mail das44@case.edu.

Notes

The authors declare no competing financial interest.

ACKNOWLEDGMENTS

Funding for this work by NSF CMMI grant #0727231 is gratefully acknowledged.

REFERENCES

(1) Li, S.; Simon, G. P.; Matisons, J. G. *J. Appl. Polym. Sci.* **2010**, *115*, 1153.

(2) Wu, J.; Haddad, T. S.; Kim, G.; Mather, P. T. *Macromolecules* **2007**, *40*, 544.

(3) Zheng, L.; Farris, R. J.; Coughlin, E. B. *Macromolecules* **2001**, *34*, 8034.

(4) Fang, Y. F.; Chen, S. *J. Polym. Sci., Part A: Polym. Chem.* **2009**, *47*, 1136.

(5) Sanchez-Soto, M.; Illescas, S.; Milliman, H.; Schiraldi, D. A.; Arostegui, A. *Macromol. Mater. Eng.* **2010**, *295*, 846.

(6) Zeng, J.; Kumar, S.; Iyer, S.; Gonzalez, R. I.; Schiraldi, D. A. *High Perform. Polym.* **2005**, *17*, 403.

(7) Bauman, T. F.; Jones, T. V.; Wilson, T.; Saab, A. P.; Maxwell, R. S. *J. Polym. Sci., Part A: Polym. Chem.* **2009**, *47*, 2589.

(8) Giannelis, E. P. *Adv. Mater.* **1996**, *8*, 29.

(9) Ahmadi, S. J.; Huang, Y. D.; Li, W. *J. Mater. Sci.* **2004**, *39*, 1919.

(10) Lagaly, G. *Appl. Clay Sci.* **1999**, *15*, 1.

(11) Jancar, J.; Douglas, J. F.; Starr, F. W.; Kumar, S. K.; Cassagnau, P.; Lesser, A. J.; Sternstein, S. S. *Polymer* **2010**, *51*, 3321.

(12) Kopesky, E. T.; Haddad, T. S.; Cohen, R. E.; McKinley, G. H. *Macromolecules* **2004**, *37*, 8992.

(13) Li, G. Z.; Wang, L.; Toghiani, H.; Daulton, L.; Koyama, K.; Pittman, U. *Macromolecules* **2001**, *34*, 8686.

(14) Soong, S.; Cohen, R. E.; Boyce, M. C. *Polymer* **2007**, *48*, 1410.

(15) Iyer, S.; Schiraldi, D. A. *Macromolecules* **2007**, *40*, 4942.

(16) Misra, R.; Fu, B. X.; Plagge, A.; Morgan, S. E. *J. Polym. Sci., Part B: Polym. Phys.* **2009**, *47*, 1088.

(17) Lim, S.; Hong, E.; Song, Y.; Choi, H. J.; Chin, I. *J. Mater. Sci.* **2011**.

(18) Lim, S.; Hong, E.; Song, Y.; Choi, H. J.; Chin, I. *J. Mater. Sci.* **2010**, *45*, 5984.

(19) Miller-Chou, B. A.; Koenig, J. L. *Prog. Polym. Sci.* **2003**, *28*, 1223.

(20) Hildebrand, J. H.; Scott, R. L. *The Solubility of Nonelectrolytes*, 3rd ed.; Dover Publications: New York, 1964.

(21) Hansen, C. M. *Hansen Solubility Parameters, A Users Handbook*; CRC Press: Boca Raton, FL, 2000.

(22) Prigogine, I. (in collaboration with Bellemans, A., and Marthot, A.) *The Molecular Theory of Solutions*; North-Holland: Amsterdam, 1957.

(23) Milliman, H. W.; Sánchez-Soto, M.; Arostegui, A.; Schiraldi, D. A. *J. Appl. Polym. Sci.*, accepted for publication.

Macromolecules

Article

pubs.acs.org/Macromolecules

Quantitative Water Uptake Study in Thin Nylon-6 Films with NMR Imaging

N. J. W. Reuvers,[†] H. P. Huinink,*[,†] H. R. Fischer,[‡] and O. C. G. Adan[†,‡]

[†]Department of Applied Physics, Eindhoven University of Technology, P.O. Box 513, NL-5600MB

[‡]TNO, De Rondom 1, Eindhoven, P.O. Box 6235, NL-5600HE

ABSTRACT: Nylon-6 is widely used as an engineering plastic. Compared to other synthetic polymers, nylon-6 absorps significant amounts of water. Although the typical sorbed amounts and diffusivity of water are well-known, less is known about the relation between the diffusivity and the water content. Attempts have been made in the past to obtain such relationship from moisture content profiles as measured with NMR imaging. However, these studies were mainly performed at high temperatures and without a proper calibration of the signal. In particular, at room temperature, far below the T_g of dry nylon, plasticizing effects of water will result in a strong contribution of the polymer signal. Therefore, we have studied water uptake in 200 μm nylon-6 films in this temperature range near room temperature with NMR imaging. By calibrating the NMR signal with vapor sorption data, we were able to obtain moisture content profiles. A strongly nonlinear relation between the NMR signal and the moisture was observed at room temperature, which proves that contribution of the polymer to the NMR signal can neither be neglected nor assumed to be constant in time. Furthermore, glass transition temperature measurements combined with the water distribution provide plasticization profiles during water uptake. On the basis of the moisture content profiles, the moisture content dependency of the diffusion coefficient for water uptake is deduced through a Matano−Boltzmann analysis. This relation appeared to be highly nonlinear at room temperature. The self-diffusion coefficient was calculated through combination of the sorption-isotherm and the diffusion coefficient. Exposure of a nylon film to heavy water showed that water affects only a small fraction of the amorphous nylon phase. Water transport most likely occurs in this fraction of the amorphous phase. It is concluded that the heterogeneity of the amorphous phase is an important issue for a profound understanding of water transport in nylon-6 films.

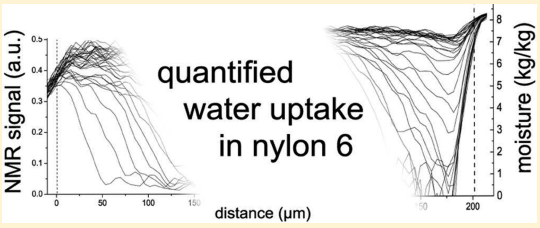

INTRODUCTION

Polyamides, also known as nylons, are widely used as engineering plastic and textile fiber mainly due to their excellent properties. In particular, the mechanical properties are attractive for many applications and remain unaffected in a wide range of temperatures. Nylon is also easy to process, for example by extrusion molding, which is reflected in the large variety of geometries encountered in every day life.

The chemical structure of nylons consists of amide groups separated by a number of methylene units. Therefore, a variety of polyamides exist, consisting of either one single α,ω aminoacid monomer like nylon-6 (PA6) and nylon-12 or two monomers, a dicarboxylic acid and a diamine like nylon 4.6 or 6.6. The number of successive carbon atoms in the polymer backbone between the amide groups is given by the index and influences material properties such a stiffness, melting point or water absorption.[1] The latter feature is especially caused by the hydrophilic character of the amide functionality.

Nylons absorb amounts of water far larger than other synthetic polymers. This paper focuses on the transport properties and characteristics of nylon-6, where the amide groups are only separated by 6 carbon atoms. This material can accommodate water mass fractions up to 9%, as reported in the literature.[2−8]

Nylon, a semicrystalline material, consists of a crystalline part where polymer chains are nicely stacked and a disordered or amorphous part. It is generally accepted that water penetrates polymers in general and nylon-6/6.6 in particular through the amorphous phase.[9−11] Water weakens hydrogen bonds between neighboring amide groups and lifts the steric hindrance of the polymer chains by mobilizing them. Consequently, the amorphous phase is plasticized, the glass transition temperature T_g [K] is lowered and the mechanical properties are altered. Reimschuessel[12] and Yokouchi and co-workers[13] describe the correlation between mechanical properties, such as the modulus of elasticity E [Pa], and the glass transition temperature T_g.

A first systematic study of the interaction between the amorphous phase and water resulted in an hypothesis regarding the exact sorption mechanism.[14] According to Puffr et al. sorption occurs in three "steps": the first involves tightly bound water, the second loosely bound water, which both interact with amide groups in the form of a single or double hydrogen bond. The third step is the clustering of water. It is generally accepted

Received: December 16, 2011
Revised: January 17, 2012
Published: February 7, 2012

that water sorption occurs in a few number of steps as described above.[3,5,11,15−19] Only a few authors, like Le Huy and Rault[20] and L. S. Loo,[21] suggest that all water is bound to the amide group in the same way.

The key parameter for characterizing and understanding the water uptake in nylon-6 is the diffusion coefficient. Absolute values have been obtained in various studies, but are difficult to compare as they are dependent on morphological parameters such as crystallinity,[16] the experimental technique used to determine the diffusion coefficient,[8,22−24] and the temperature.[9] The reported diffusion coefficients range from 1×10^{-14} m^2 s^{-1} to 5×10^{-13} m^2 s^{-1}.[3,7,9,24] In general, it is observed that the diffusion coefficient increases with concentration.[7,24] A single study[3] reports a maximum in the diffusion coefficient at a relative humidity of 50%. All aforementioned numbers are obtained gravimetrically, which is a bulk method, and no spatial information about the diffusion process is obtained.

To obtain spatial information in a non destructive way NMR imaging can be used. By far the most extensive 1D imaging study was conducted by Blackband and his co-workers.[25] In this study, blocks of nylon-6.6 were immersed in water and detailed experimental results are generated for a temperature of 100 °C. This includes the uptake profiles as measured by NMR and the resulting diffusion coefficient. Gravimetric experiments revealed a mass uptake proportional to $t^{1/2}$, especially at temperatures higher than 50 °C. Finally, from the resulting NMR signal profiles a concentration dependent diffusion coefficient was obtained using the Boltzmann transformation.[25] Fyfe et al.[26] performed another set of experiments investigating the water absorption into nylon-6.6 at a temperature of 100 °C. In their study the fast low angle shot (FLASH) NMR technique was employed. The results obtained by gravimetric analysis and NMR imaging pointed to a Case-I process, i.e., Fickian diffusion.

In all these NMR imaging studies no attention was paid to the exact amount of water during the uptake process. The signal intensities are directly interpreted as water quantities.[25,27] Only D. Y. Artemov[28] pointed out the complexity of the NMR signal of water in nylon. The signal contribution of plasticized polymer, which appears simultaneously with ingressing water, should not be underestimated. In particular, below the glass transition of the dry nylon, the signal of the nylon itself will strongly increase with the water content due to plasticization.

In our study, the combined process of water uptake and plasticization of nylon-6 films is studied at room temperature with quantitative NMR imaging. By converting signal profiles into moisture content distributions on the basis of a gravimetric calibration procedure, a quantitative relationship between the diffusivity and the water content is obtained and the importance of plasticization is shown. To understand the signal component that is due to polymer plasticization, experiments using D_2O are conducted. The morphology of the nylon films is characterized and the relation between the water content and the glass transition temperature is established. For a better understanding of the diffusion process the concentration dependency of the diffusion coefficient is calculated from the moisture content profiles.

MATERIAL

Preparation. Films of polyamide 6 are prepared from commercially available polyamide 6 (Akulon K123, M_w = 25.000, DSM, The Netherlands). Films are made by compression molding of dried pellets at a temperature of 280 °C for 10 min between two steel plates, separated by a spacer of 200 μm. The obtained films, having a thickness of 200 μm, were stored prior to experiments in a container containing silica gel as drying agent.

For the water uptake measurements in the NMR, films are cut into circular disks with a diameter of approximately 11 mm. These disks were attached to a 140 μm thick microscope cover glass using silicone glue (type: Dow Corning 3140). Subsequently, a glass cylinder is glued on top of the cover glass surrounding the nylon film. Before an experiment the films are stored in an oven at 100 °C for 5 h in order to remove residual traces of moisture. Weight loss was not measured anymore after 5 h.

Material Properties. *Sorption Isotherm.* The sorption isotherm describes the relation between moisture content and relative humidity or water activity. In the present study the sorption isotherm was determined by gravimetry, Figure 1. The mass of the dry films is measured m_d [g] before storage at a certain relative humidity RH[%] in a climate chamber. The relative humidity in the climate chamber is created using saturated salt solutions. Saturated salt solutions of LiCl, CH_3COOK, $MgCl_2{\cdot}6H_2O$, K_2CO_3, $Mg(NO_3)_2$, $NaNO_3$, NaCl, KCl, KNO_3, and K_2SO_4 give a stable equilibrium relative humidity of 12, 22, 33, 43, 53, 65, 75, 85, 93, and 97% respectively.[29] After several days of storage in the climate chambers, the wet weight is obtained m_w [g]. The moisture content θ is calculated as:

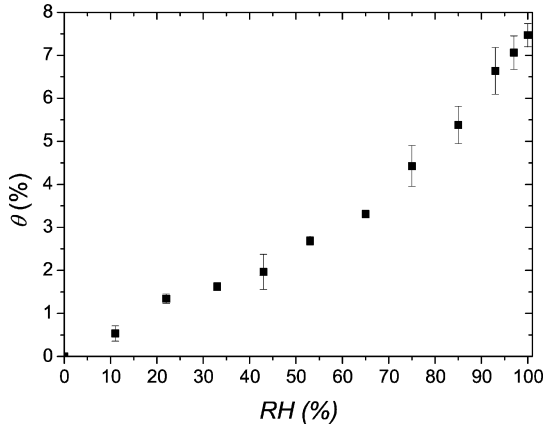

Figure 1. The sorption isotherm of a nylon-6 film. The figure shows the weight increase (θ,% by mass) with respect to the dry state as a function of the relative humidity (RH, %). The disproportional increase of the moisture content above 65% RH is due to the formation of water clusters.

$$\theta = \frac{m_w - m_d}{m_d} \times 100\% \quad (1)$$

Note that the moisture content is defined as a mass-to-mass percentage.

In our case, the moisture content θ of a fully saturated film is 7.4%. In the literature moisture content values are reported in the range from 4%[17] up to 10%.[3,7,16] The moisture content increases disproportional above relative humidities of 65% with respect to the lower humidities. Despite the differences in raw material (e.g., molecular weight) and processing conditions (influences of crystallinity[30]), the shape of the obtained sorption isotherm is similar to the ones in literature.

Crystallinity. The crystalline part forms a barrier to water transport and must be characterized to understand the water uptake behavior. Wide angle X-ray scattering (WAXS) experiments using a Philips pw1830 diffractometer (Cu Kα) was employed to determine the structure of the crystalline phase. In all cases, two intense peaks were detected at angles 2θ equal to 20.2 and 23.9 deg. These reflections are

attributed to the 200 and 002−202 planes in the α-phase,[6,9,31] thus being the main component in the crystalline phase.

To measure the degree of crystallinity of the samples, differential scanning calorimetry measurements (DSC) using a Mettler 822e were conducted under a nitrogen atmosphere. The heating rate was 10 K/min in a range between 253 to 533 K. An analysis of the melting peak, using a value of 240 J/g[10,31] for the melting enthalpy of a 100% crystalline sample, resulted in a crystallinity of 23% for the film samples.

Glass Transition Temperature. As the glass temperature drops due to ingressing water, more hydrogen nuclei on the polymer backbone are mobilized and appear in the NMR signal. For understanding the NMR signal quantitatively the T_g gives vital information.

The glass transition temperature was determined using DMTA (Dynamic Mechanical Thermal Analysis) on a Thermal Analysis DMA2980. The sample was placed in the tensile testing clamps and heated between 223 and 373 K with a heating rate of 5 K/min. The measurements are performed using an amplitude of 20 μm at a frequency of 1 Hz. The glass transition temperature was assigned to the maximum of the tan Δ. An alternate definition for the glass transition temperature like the maximum of the loss modulus only lowers the T_g with 10 K.

The samples were conditioned in the same way as for the gravimetry measurements. Since the employed DMTA was not equipped with a RH control, an error will occur in the DMTA measurements at relative humidities that differ from the surrounding RH in the room. Moisture loss of these samples by evaporation during fixation and the first moments of cooling down of the DMTA could lead to an overestimation of the T_g. The maximal effect of evaporation will only be present at two samples of the highest RH (93% and 97%), and was estimated by examining samples immersed in liquid water. These samples were fully wetted and thereafter exposed to environmental relative humidity. The mass of these samples is measured before and after this evaporation period. Assuming a time of 5 min for fixation and cooling, such an exposure to air at room temperature will lower the moisture content only by 0.7%.

NMR SETUP AND IMAGING

Originating from the field of medicine, NMR imaging has become more and more available throughout the last decades. This has led to the application of NMR imaging to the field of material research.[32] NMR imaging is based on the principle that nuclei in a magnetic field resonate at a frequency proportional to the magnetic field strength.[33] The frequency $\omega = \gamma\,(2\pi)^{-1}|\vec{B}|$ is called the Larmor frequency, where $\gamma\,(2\pi)^{-1}$ is the gyromagnetic ratio which equals 42.58 MHz/T for ^{1}H nuclei.

Application of a spatial dependent magnetic field $|\vec{B}| = |\vec{B}_0| + G_z z$ results in a unique frequency for each position, which allows to obtain spatial information from a sample. The strength of the gradient in the field determines the resolution. To obtain a resolution of several micrometers, needed for measuring thin films the so- called GARField approach is used.[34,35] By special shaped magnetic pole tips, a gradient in the magnitude of the magnetic field, $G_z = \partial\,|\vec{B}|/\partial z$ [T/m], is created (see Figure 2). In the present study a setup having a field gradient G_z = 42 T/m and a B_0 of 1.4 T is used. A reference sample of 0.02 M $CuSO_4$ is measured before each experiment to correct for inhomogeneity of the excitation profile.

Pulsed NMR will give a signal decay that can be described by the longitudinal relaxation time $T_1[s]$ and the transverse relaxation time $T_2[s]$. The signal can be described with

$$S = \frac{\rho}{\rho_w}\left[1 - \exp\left(\frac{-t_r}{T_1}\right)\right]\exp\left(\frac{-t_{\exp}}{T_2}\right) \tag{2}$$

where ρ [mol m^{-3}] and ρ_w are the hydrogen densities in the sample and liquid water, respectively. In this equation, t_{exp} is the experimental time and t_r [s] is the time between two subsequent experiments. For a multipulse experiment the experimental time t_{exp} [s] is subdivided in a number of pulses n with a certain time spacing 2τ [s]. For imaging purposes, the NMR signal intensity or signal profiles are used and these are the signal intensities at a t_{exp} of 2τ.

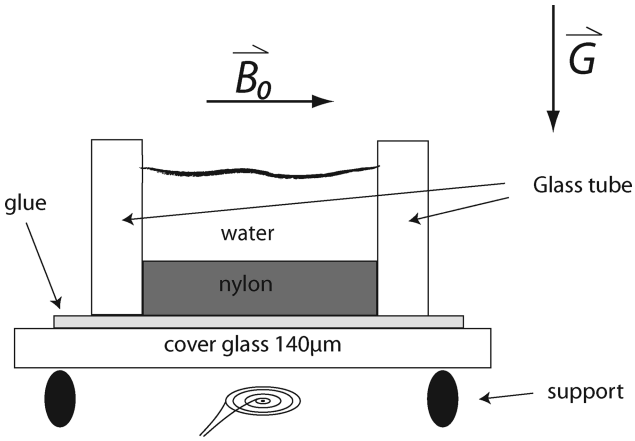

Figure 2. A schematic picture of the sample for a water uptake experiment. The nylon film is precisely placed in a glass tube (cylinder) and glued on a glass plate. This glass tube surrounds the sample and is used to contain the water for the experiments. The static field B_0 is oriented parallel with the nylon film. The high gradient G in this static field enables the high resolution.

Materials contain different types of hydrogen nuclei. Both the environment and the mobility of the nucleus lead to a difference in transverse relaxation. Crystallites or entanglements will severely limit motions of nuclei and give a fast decay (short T_2) while parts in the amorphous phase or dangling chains have a higher mobility and will contribute to a higher value of T_2. In the simpliest case a monoexponential decay can be used to fit the measured decay. The transversal decay is often analyzed using a multiexponential decay curve.[2,36−41] Neglecting the longitudinal relaxation and the noise in the experiments, such a multiexponential decay is described by eq 3. Each component is governed by an amplitude A_i and a relaxation time $T_{2,i}$.

$$S(n) = \sum_{i=1}^{N} A_i \exp\left(\frac{-2\tau n}{T_{2,i}}\right) \tag{3}$$

The transversal signal decay is very sensitive to the polymer structure and mobility and is therefore a measure for the effect of water on the nylon matrix. Often several exponential components are used to interpret the signal decay. Without interpreting the components of the multiexponential decay, a more practical approach to characterize the signal decay is based on an average relaxation time $\langle T_2\rangle$:[41]

$$\langle T_2\rangle = \sum_{i=1}^{N} \frac{S(2\tau i)}{S(2\tau)} \times t_e \tag{4}$$

To obtain the hydrogen density profiles and relaxation times, the Ostroff-Waugh (OW) pulse sequence is used (α_x^o−τ−[α_y^o−τ−echo−τ−]$_n$).[42] In this sequence α is a nominal 90^o pulse. To cover the relaxation curve a train of 256 pulses is given. The effective pulse duration is 1 μs which excites a slice of 450 μm. The inter echo time 2τ is set to 100 μs with an acquisition time (t_{aq}) of 90 μs.

An inter echo time of 100 μs together with an acquisition time of 90 μs theoretically gives a resolution of 6 μm, $\Delta z = (\gamma G t_{aq})^{-1}$. However due to misalignment with the B_0 field the actual resolution can be less.

NMR measurements of the water uptake process are conducted with 1024 averages and a repetition time of t_r = 0.5 s. As a consequence, measuring a single profile takes 17 min. Experiments with equilibrated films are conducted using a higher number of averages (8192).

In order to control the RH the NMR insert is equipped with a climate chamber. The temperature inside the chamber is set by

dx.doi.org/10.1021/ma202719x | *Macromolecules* 2012, 45, 1937−1945

pumping temperature controlled water through the walls of this chamber. The chamber RH is created by means of a flow controller that mixes dry air and water in the desired ratio and injects it into the chamber.

RESULTS

This section describes the experimental results concerning water uptake on a nylon-6 film. The NMR signal was calibrated, meaning that signal intensities are related to the amount of water in the film. The rate of the diffusion process was examined by calculation of the diffusion coefficient. By means of a relaxation study, heavy water and DMTA measurements the interaction between water and the polymer matrix is examined

Water Uptake and Signal Calibration. Measuring the uptake process results in NMR signal profiles as shown in Figure 3. Such signal profiles should be considered as a superposition of a plasticizing front and a water front. The signal on the vertical axis shows the number of mobile ^{1}H nuclei probed ($T_2 \geq 100$ μs) with respect to water. The horizontal axis is the distance with respect to the water/polymer interface.

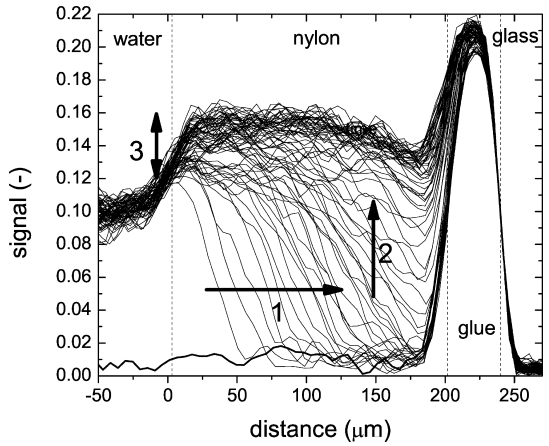

Figure 3. NMR signal profiles measured during the uptake of water by a 200 μm nylon film. The water on top of the nylon layer is visible at the left side of the figure, whereas the glue underneath the layer is visible at the right side of the figure. The time between subsequent profiles is 17 min. It takes water 6 h (1) to reach the bottom of the film and then another 4 h (2) to fill the film completely. Polymer plasticization is most clearly shown near the water/nylon interface (3).

The right-hand side of Figure 3 corresponds to the glass plate on the bottom of the sample as shown in Figure 2. Whereas glass is not detected in the NMR the layer of silicon glue, the nylon film and the water above the nylon film can clearly be distinguished. Their signal intensities are explained by the relation between the T_1 and T_2 of the material and the experimental parameters t_e and t_r. The relatively long T_1 of the water ($t_r/T_1 < 1$) surpresses the signal from the water.

The bold line in Figure 3 displays the situation before water is introduced and the nylon is still dry. Three different processes can be distinguished. Two of them occur chronologically: (1) a front develops and reaches the bottom ($t < 6$ h) and (2), water distributes homogeneously throughout the film ($6 < t < 10$ h). From the beginning of the experiment a slower process (3) occurs which is most clearly observed as a signal rise near the glass polymer interface.

To quantify the diffusion of water the actual moisture content θ should be considered instead of the NMR signal. To convert the NMR signal into moisture content both the mass and the NMR signal of samples equilibrated at a certain RH have been measured. Figure 1 shows the sorption isotherm as obtained by gravimetry. The signal intensity of equilibrated samples is obtained by measuring a serie of samples conditioned at different relative humidities using the climate chamber in the NMR equipment. Figure 4 shows the moisture content as a function of the measured NMR signal intensity. The data is fitted with a double exponential growth function. This fit is shown as a dashed line in Figure 4.

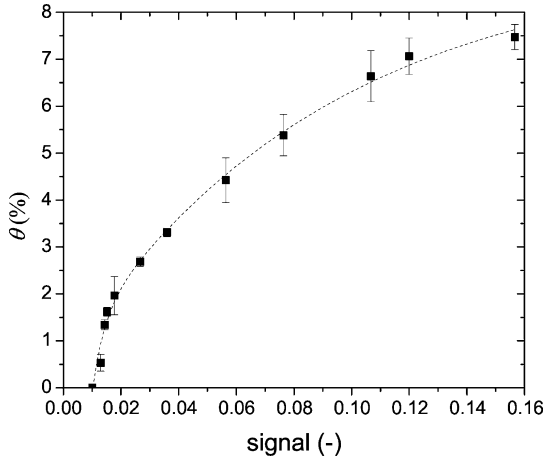

Figure 4. Signal calibration curve. This curve describes the relation between the NMR signal and the moisture content θ of nylon films equilibrated with water vapor at various RH values. The figure shows that the relation between signal and θ is nonlinear. The fit (dashed line) through the data (■) is used to convert signal profiles into moisture profiles.

Obviously the relation between θ and the NMR signal is nonlinear. The curve shows that at low water content the signal intensity is very insensitive to water content changes. With increasing water content the signal becomes more sensitive to the water content. At high water content, a small amount of water leads to a large signal variation which is probably due to plasticization of the polymer matrix.

Now the relationship between the NMR signal and the water content is known, the NMR profiles can be converted into moisture content profiles. Figure 5 shows the original NMR profiles (a) and the moisture content profiles (b) after application of the signal calibration. As long as the moisture content is below 2% the signal coming from the moist nylon is too low to be detected, since the signal-to-noise ratio of the chosen number of averages (1024) is not high enough.

The most distinct effect of the calibration is visible at the water/nylon boundary and in the late stage of the uptake process (as indicated by 3 in Figure 3). In the late stage, when the film is almost saturated, an homogeneous NMR signal rise in the profiles is detected. This slow signal increase is hardly visible in the water content profiles, meaning that only little (additional) water is ingressing into the film at this stage. The late stage rise in the NMR signal is a result of further plasticization of the polymer matrix. Polymer chains become more mobile and their hydrogen atoms start to contribute to the signal.

dx.doi.org/10.1021/ma202719x | Macromolecules 2012, 45, 1937–1945

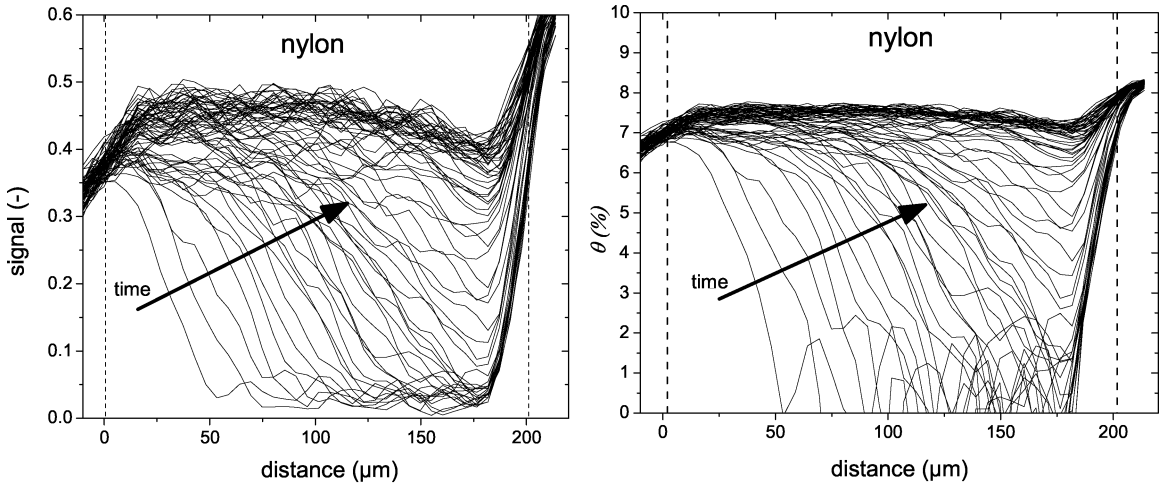

Figure 5. Transfering NMR signal profiles (a) into moisture content profiles (b). The figure shows the two main effects of the signal calibration on the shape of the profiles. The slow, homogeneous signal increase is hardly visible in the moisture content profiles. Very little water enters the film at this stage, mainly plasticization occurs. The curvature of the moisture content profiles is also changed. At low signal intensities, the curves are lifted upward, meaning that the water content at low signal intensities is underestimated when the NMR signal profiles would be used for quantification.

Furthermore, the calibration introduces extra curvature in the profiles. In particular, at signal intensities lower than 0.08 the profiles are tilted upward. Figure 4 already shows that a supposed linear relation between signal and moisture content results in underestimation of the moisture content at low signal intensities. At low moisture content the water strongly interacts with a rather immobile amorphous phase, which results in fast relaxation of the signal[40] and thereby underestimation of the signal.

Although the calibration has been used to quantify the signal its applicability to dynamic water uptake processes still has to be proven. The calibration curve is obtained by measuring the signal from samples that have been equilibrated with a defined RH. The uptake proces however is a nonequilibrium situation. Our calibration will be only applicable if local equilibrium occurs throughout the nylon film during water ingress. This means that the state of the polymeric matrix is only determined by the local water content. To check the validity of the calibration, the average relaxation time and intensity of the first echo has been investigated for both the calibration samples and the uptake process. The average relaxation time $\langle T_2 \rangle$ is very sensitive for the local polymer mobility and is therefore a measure for the effect of water on the nylon.

Figure 6 shows the average decay time as a function of the signal intensity for both the calibration and the uptake process. The solid squares are the values obtained in the signal calibration experiment and the open circles refer to the signal at 125 μm, with respect to the water/nylon interface, during a water uptake experiment as shown in Figure 3. There is a good match between the data points from the uptake experiment and the signal calibration measurement, showing a unique coupling between the signal intensity of the first echo and $\langle T_2 \rangle$. This justifies the use of the calibration curve for nonequilibrium processes like water uptake in nylon-6.

Finally it can be concluded that NMR signal intensity profiles (as shown in Figure 3) and obtained by others[27,43] do not give a correct representation of the water content in the film. When the amorphous phase becomes plasticized, the hydrogen nuclei on the polymer backbone start to contribute to the signal.

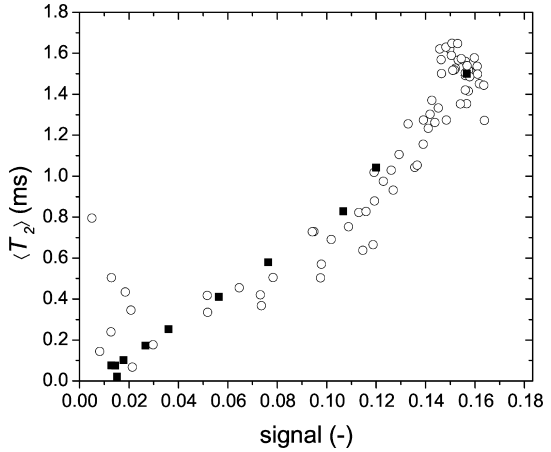

Figure 6. Average relaxation time $\langle T_2 \rangle$ as a function of the signal intensity for calibration (■) and uptake experiment (○). The average relaxation time is taken at a distance of 125 μm from the nylon/water interface. The similarity of both calibration experiment and a water uptake experiment proves that the static calibration can be used for obtaining water content profiles during uptake.

Furthermore, water exhibits a fast signal decay due to interaction with the polymer and cannot be detected by the NMR equipment. For these reasons the relation between signal and water content is not linear. This will especially be the case when experiments are performed below T_g of the dry nylon.

Uptake Kinetics. The water uptake can be analyzed by the non linear diffusion equation, eq 5. In this equation is θ the mass fraction of moisture (i.e., moisture content), t[s] the time and D[m^2/s] the effective diffusion coefficient.

$$\frac{\partial \theta}{\partial t} = \frac{\partial}{\partial x}\left(D(\theta)\frac{\partial \theta}{\partial x}\right) \tag{5}$$

To quantify the diffusion coefficient the Matano−Boltzmann method is used.[44] The essence of this method is that the spatial coordinate is transformed into a new coordinate $\lambda = x/\sqrt{t}$. For a detailed analysis we refer to Crank.[45]

dx.doi.org/10.1021/ma202719x | Macromolecules 2012, 45, 1937−1945

Since this Boltzmann transformation assumes an infinite geometry and constant boundary conditions, a limited number of profiles ($1 < t < 6$ h) is selected for the transformation. The outcome of the Boltzmann transformation is shown in Figure 7.

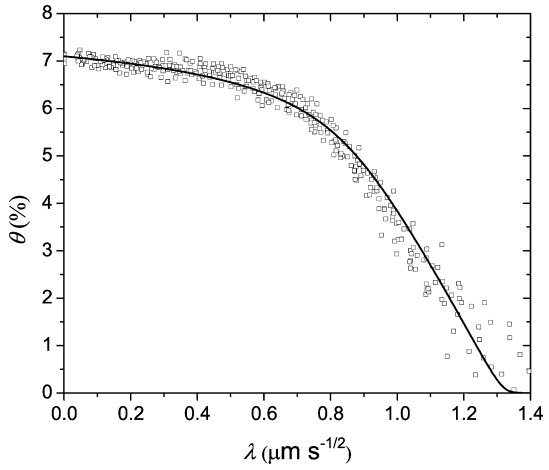

Figure 7. Moisture content (θ) profiles as a function of $\lambda = x/(t)^{1/2}$, wherein λ is the Boltzmann transformation, x is the distance with respect to water/nylon interface and t is the time. The data points (□) are obtained from the Boltzmann transformation of the moisture content profiles and the solid line represents the simulated profiles.

The open squares in this figure are the data points and the black line is the Boltzmann transformation of a simulation, which will be discussed later on. All data points coincide on a single master curve, proving that the diffusion coefficient depends on the moisture content only and that the nonlinear diffusion equation (eq 5) can be used to describe water ingress in this system.

The moisture content dependent diffusion coefficient can be calculated according to

$$D(\theta) = -\frac{1}{2}\left(\frac{d\theta}{d\lambda}\right)_{\theta}^{-1} \int_0^{\theta} \lambda \, d\theta' \tag{6}$$

A spline is used to calculate the diffusion coefficient according to eq 6. For water contents lower than 2% this spline is extrapolated linearly. The concentration dependence of the diffusion coefficient is shown in Figure 8. The diffusion coefficient increases with concentration, which is in agreement with previous studies.[7,16,19,24] Only one particular study reported a maximum for the diffusion coefficient at an RH of 50% at 23 °C.[3] Moreover, the magnitude of the obtained diffusion coefficient is in agreement with values reported in the literature (1×10^{-14} to 1×10^{-13} m^2 s^{-1} at 25 °C[8]).

In contrast with previous studies on nylon-6.6, a highly nonlinear relation between the moisture content and the diffusion coefficient is observed.[25,27] At a moisture content above 5%, the diffusion coefficient rises exponentially, whereas previous studies report a linear relation between the concentration and the diffusion coefficient in the entire moisture content range.

Knowing the concentration dependency of the diffusion coefficient, the nonlinear diffusion equation (eq 5) is solved numerically. The black line in Figure 7 shows the Boltzmann transformation of the calculated moisture profile. Measurement and simulation are in good agreement, indicating that the correct relation for the diffusion coefficient has been obtained.

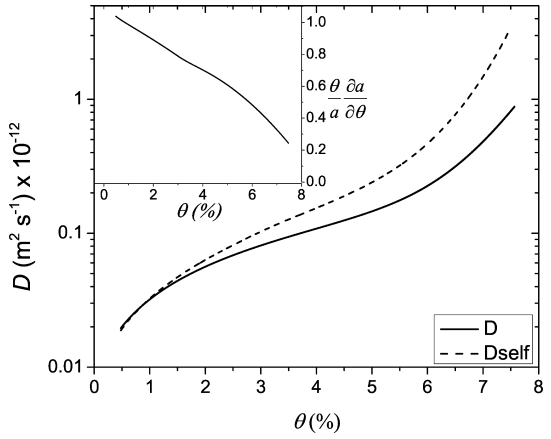

Figure 8. Effective diffusion coefficient D and self-diffusion coefficient D_{self} as a function of moisture content θ. Both coefficients exhibit a highly nonlinear dependency on the moisture content. The inset shows the storage term $(\theta\partial a)/(a\partial\theta)$ as a function of moisture content. Water storage capacity increases faster above θ = 5% and limits the effective diffusion coefficient.

Furthermore, this shows that the effective diffusion coefficient is only a function of the moisture content $D(\theta)$, so implicit time dependency. For the transport process this implies the absence of memory effects and thus a local equilibrium in the system.

The diffusion coefficient as discussed above expresses the effective rate of transport in a transient situation, while the self-diffusion coefficient gives information about the motion of water in absence of a concentration gradient and nett transport. Assuming that all volume changes are small the concentration is proportional to the moisture content as measured by the NMR.

$$\theta \approx \frac{cM_{w,H_2O}}{\rho_d} \times 100\% \tag{7}$$

Where M_{w,H_2O} [g mol^{-1}] is the molecular weight of water and ρ_d [kg m^{-3}] is the density of dry nylon. The relation between the effective diffusion coefficient and the self-diffusion coefficient can be found in textbooks.[45]

$$D(\theta) \equiv D_{self}\frac{\theta}{a}\left(\frac{\partial a}{\partial \theta}\right)_T \tag{8}$$

In principle, the self-diffusion coefficient can be interpreted in terms of free-volume models,[46,47] which is beyond the scope of this paper.

Using eq 8 and the sorption isotherm, the self-diffusion coefficient can be calculated. This is shown in Figure 8, pointing out that for θ > 5% the value of the self-diffusion coefficient starts to deviate significantly from the effective diffusion coefficient.

This self-diffusion coefficient will be larger than the diffusion coefficient because of storage effects represented by the term $(\theta\partial a)/(a\partial\theta)$ in eq 8. The effective diffusion coefficient that determines the speed of the water front in the nylon layer is limited by the presence of the storage term. In case that θ rises steeply around a certain value of a, the tangent $(\partial\theta/\partial a)$ is steeper than the line θ/a, which makes the complete term $(\theta\partial a)/(a\partial\theta)$ smaller than one.

The inset in Figure 8 shows the storage term as a function of moisture content. The storage term almost decreases linearly up until a moisture content of 5%. At higher moisture content, the difference between the effective and the self-diffusion

dx.doi.org/10.1021/ma202719x | Macromolecules 2012, 45, 1937−1945

coefficient is the largest because the water storage capacity increases with moisture content. It is concluded that the effective diffusion coefficient for water uptake at room temperature shows a highly nonlinear concentration dependency.

Plasticization. The amorphous phase is the place for storage and transport of water. More insight into the effect of water on the amorphous phase (plasticization) is obtained by exposing the nylon film to D_2O. The measurements are conducted using an excess of D_2O because the hydrogen on the amide group (N−H) is likely to exchange.[48] The resulting signal will solely consist of hydrogen nuclei on the polymer backbone (−CH_2−) in the amorphous phase of the film. Figure 9 shows the profile of a film equilibrated with D_2O. Thereafter

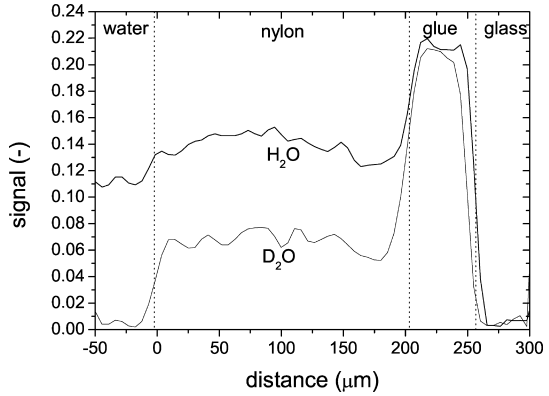

Figure 9. Signal intensities as a function of depth in a nylon layer exposed to D_2O and H_2O. Signal intensities were measured after equilibration. The D_2O results depict that half of the signal with respect to H_2O originates from the plasticized polymer.

the heavy water is removed and normal water is put on top of the film. A profile of the equilibrium situation for H_2O is also shown in Figure 9.

This experiment shows that roughly half of the signal in a saturated film comes from water, whereas the other half originates from mobilized polymer. Quantitatively, it can be argued that for every observable monomer of nylon about 5.5 molecules H_2O appear in the signal of a water uptake experiment. According to the theory of Puffr et al.,[14] who stated that water in nylon is bound to specific sites (the amine groups) or exist as clusters. For bound water they found that three water molecules are bound to two neighboring amide groups.[4,14,15] Following the ideas of Puffr et al. and assuming that all detectable water is associated with all detectable nylon monomers, this would mean that 1.5 molecules of water are bound by the amide group of a mobile monomer and 4 molecules of water are organized in a cluster in the neighborhood of this monomer.

The signal intensities of the water and the deuterium signal can be understood by calculating the expected signal based on the proton densities of nylon ρ_N [m^{-3}] and water ρ_w [m^{-3}]. The signal fraction due to water equals:

$$S = \frac{\rho_w}{\rho_w + \rho_N} \tag{9}$$

The ratio of ρ_w and ρ_N can be related to the moisture content θ:

$$\theta = \frac{\rho_w}{\rho_N}\frac{11}{2}\frac{M_{w,H_2O}}{M_{w,nylon6}} \times 100\% \tag{10}$$

Using the molecular weight of a nylon monomer $M_{w,nylon6}$ [g/mol] of 113 and a signal ratio ρ_w/ρ_N of 0.08 (see Figure 9), θ is estimated to be 7%. As this value is in close agreement with the value obtained by gravimetry (i.e., 7.5%), it is concluded that all water is observed in a saturated system.

Similarly, the fraction of the amorphous phase visible in our NMR measurements is calculated. The expected signal from the total amorphous phase is equal to

$$S = \frac{\rho_a}{\rho_w + \rho_N} \tag{11}$$

wherein ρ_a is the proton density of the amorphous phase. The density of the crystalline and amorphous phase are respectively 1.23 kgl^{-1} and 1.08 kgl^{-1}. Compensating for the degree of crystallinity it can be shown that ρ_a equals $0.72\rho_N$.[31] Combining the eqs 10 and 11 and setting θ to 7.5%, the signal of the total amorphous phase should be 0.75. The signal intensity of the D_2O saturated nylon-6 in Figure 9 is much lower: 0.07. This indicates that water only influences a small part of the amorphous phase: 10%.

The reason for this small fraction is the heterogeneous structure of the amorphous phase, as described by Litvinov and co-workers.[40] The amorphous phase is composed of a soft amorphous region and a rigid noncrystalline interfacial region. They stated that the rigid fraction is not affected by water and has a signal decay much shorter than 100 μs. This rigid fraction is not detected in our measurements. Murthy et al.[48,49] also distinguished two types of amorphous domains in highly crystalline nylon: a small fraction (1/3) inside the lamellae stacks and a larger fraction outside. Absorbed D_2O was mainly found in the amorphous region outside the lamellae. For understanding the kinetics of water transport the existence of this heterogeneity is a crucial issue. Apparently the amorphous phase has preferential zones where water is absorbed or can be transported.

As plasticization in the equilibrated state has been examined and quantified the glass transition temperature during a dynamic uptake process is discussed now. Figure 10 shows

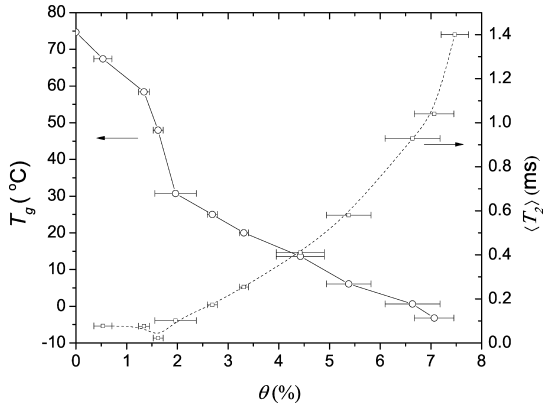

Figure 10. Glass transition temperature T_g and the average relaxation time $\langle T_2 \rangle$ as a function of the moisture content θ. An increase in moisture content decreases the T_g and increases the average relaxation time.

dx.doi.org/10.1021/ma202719x | Macromolecules 2012, 45, 1937−1945

the glass transition temperature and average relaxation time as a function of moisture content. The process of plasticization during water uptake can be visualized by looking at the glass transition temperature. For understanding the NMR signal, the T_g as a function of moisture content is important. The T_g is measured as a function of moisture content with DMTA at the same relative humidity values as the sorption isotherm enabling a direct conversion from *RH* to moisture content. The T_g of the dry nylon is 75 °C and drops to −3 °C for an almost saturated film (θ = 7%). At low moisture content the T_g decreases with increasing moisture content. Above a moisture content of about 2% it drops at a lower rate. A similar behavior was also measured by others who measured a fast decrease of T_g up to a moisture content of 4% followed by a slower decrease going to 10% of moisture.[50]

When the glass transition temperature drops below room temperature due to the uptake of moisture, the amorphous phase will be mobilized. The glass temperature drops to room temperature at θ > 3% as can be seen in Figure 10. The connection between the glass transition temperature and the NMR signal can be made by analyzing $\langle T_2 \rangle$, which is also plotted in Figure 10. The $\langle T_2 \rangle$ as a function of the water content is extracted from the calibration data set. The relaxation time starts to increase at moisture content of 2.5%. The first fraction of water ($\theta \leq$ 2.5%) will be strongly bound to the polymer matrix[40] and therefore exhibits a fast signal decay. As NMR is more sensitive to local mobility changes the NMR relaxation time increases before the glass transition temperature reaches room temperature. The increase in relaxation time brings the signal decay in the detectable range $\langle T_2 \rangle$ > 100 μs.

With the help of the DMTA data (Figure 10) NMR signal profiles are converted into T_g profiles. The results are depicted in Figure 11, providing a unique view on material properties

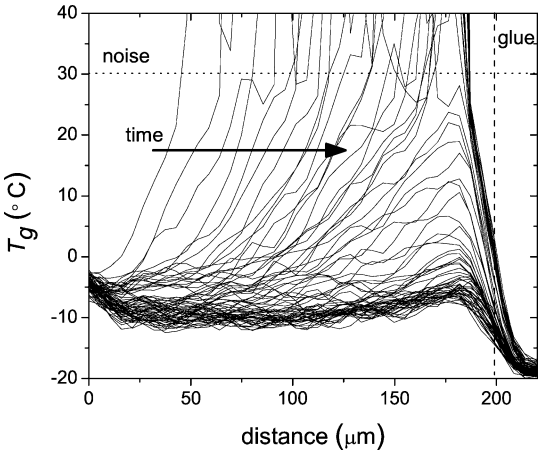

Figure 11. Time dependent evolution of the glass transition temperature in the nylon film during moisture uptake. The profiles show that the local T_g decreases when moisture penetrates the film. The time interval between subsequent profiles is 17 min. The horizontal dotted line at 30 °C is the experimental noise level, above which the T_g values cannot be trusted.

(e.g., stiffness) of the nylon as moisture penetrates the film. Such data can be used as input for numerical studies. The noise level of the NMR excludes the first 2% of moisture from detection during an uptake measurement as concluded earlier. This implies that data from T_g above 30 °C cannot be trusted, as indicated by the horizontal dashed line in Figure 11. At 30° the T_g approaches the experimental temperature and the polymer will be mobilized significantly, bringing the $\langle T_2 \rangle$ within the detection limits. Combined with the NMR data, the DMTA measurements provide a unique spatial distribution of the T_g during water uptake.

CONCLUSION

The water uptake of 200 μm thick nylon-6 films at room temperature was explored using NMR. The uptake process was measured at room temperature both spatially and time-resolved, providing a unique view at the processes. The relation between the NMR signal and the moisture content was established by simultaneously measuring the mass and the NMR signal of films at various relative humidities. On the base of such calibration, the NMR signal profiles were converted into moisture content profiles. The calibration was validated by coupling signal intensities to average transverse relaxation times. A highly nonlinear relation between signal and moisture content was observed, which underlines the need for calibration. This will especially be the case when water ingress is studied at temperatures below the glass transition temperature of the dry nylon. The most important effect of the calibration is the distinction between water ingress and plasticization. The calibration showed that the signal increase in the late state of the process when the film is nearly saturated, is mainly due to polymer plasticization.

By applying a Matano−Boltzmann analysis a highly nonlinear relation between the water content and the diffusion coefficient was found. The diffusion coefficient exponentially increases as a function of the moisture content. This does not agree with previous studies that report a linear relation, which underlines the necessity of a proper calibration. Analysis shows that this diffusion coefficient is a combination of two parts; the self-diffusion coefficient and a storage term, which is governed by the sorption isotherm. The self-diffusion coefficient increases more rapidly with the moisture content than the diffusion coefficient due to the local storage of water.

Heavy water experiments provide a profound insight in the plasticization of the amorphous phase. During uptake, the plasticized polymer gave rise to about half of the NMR signal intensity, whereas the other half originated from ingressing water. Water seems to affect only a small fraction (10%) of the amorphous phase due to the heterogeneity of the amorphous phase. As a consequence the water will diffuse along preferential pathways through the amorphous phase.

By combining the NMR signal and DMTA measurements, the spatial and temporal variations in the glass transition temperature during water uptake could be monitored. Such profiles give information about material properties like stiffness or swelling during water uptake.

NMR imaging gives spatially resolved information and enables nondestructive measurements. Our study stresses that a calibration of the NMR signal is a prerequisite for obtaining proper relationships for the diffusion coefficient and self-diffusion coefficient. Further, T_g profiles can be calculated, which enables a quantitative visualization of the plasticization process during water uptake.

AUTHOR INFORMATION

Corresponding Author

*E-mail: h.p.huinink@tue.nl.

Notes

The authors declare no competing financial interest.

■ ACKNOWLEDGMENTS

This research was funded by STW, NXP, and TNO. The authors would like to thank Hans Dalderop and Jef Noijen (TU/e)for their daily support. For help with sample preparation and DMTA measurements we would like to thank Koos van Lieshout and Irene Hovens (TNO).

■ REFERENCES

(1) A. K. van der Vegt; Govaert, L.E., *Polymeren van keten tot kunstof*; Delft University Press: Delft, The Netherlands, 1991.
(2) Adriaensens, P.; Pollaris, A.; Carleer, R.; Vanderzande, D.; Gelan, J.; Litvinov, V.; Tijssen, J. *Polymer* **2001**, *42*, 7943−7952.
(3) Hernandez, R.; Gavara, R. *J. Polym. Sci., Part B: Polym. Phys.* **1994**, *32*, 2367−2374.
(4) Lim, L.; Britt, I.; Tung, M. *J. Appl. Polym. Sci.* **1999**, *71*, 197−206.
(5) Frank, B.; Frubing, P.; Pissis, P. *J. Polym. Sci., Part B: Polym. Phys.* **1996**, *34*, 1853−1860.
(6) Murase, S.; Inoue, A.; Miyashita, Y.; Kimura, N.; Nishio, Y. *J. Polym. Sci., Part B: Polym. Phys.* **2002**, *40*, 479−487.
(7) Inoue, K.; Hoshino, S. *J. Polym. Sci., Part B: Polym. Phys.* **1976**, *14*, 1513−1526.
(8) Monson, L.; Braunwarth, M.; Extrand, C. *J. Appl. Polym. Sci.* **2008**, *107*, 355−363.
(9) Dr. Richard, Vieweg; Dr. Alfred, Müller, *Polyamide; Herstellung, Eigenschaften, Verarbeitung und Andwendung*; Carl Hansen Verlag: München, 1966.
(10) Avramova, N. *J. Appl. Polym. Sci.* **2007**, *106*, 122−129.
(11) Murthy, N. *J. Polym. Sci., Part B: Polym. Phys.* **2006**, *44*, 1763−1782.
(12) Reimschuessel, H. *J. Polym. Sci.* **1978**, *16*, 1229−1239.
(13) Yokouchi, M. *J. Polym. Sci.* **1984**, *22*, 1635−1643.
(14) Puffr, R.; Sebenda, J. *J. Polym. Sci., Part. C-Polym. Sym.* **1967**, 79−93.
(15) Xu, Y.; Wu, P. *J. Mol. Struct.* **2007**, *833*, 145−149.
(16) Kawasaki, K.; Sekita, Y. *J. Polym. Sci., Part A: Gen. Pap.* **1964**, *2*, 2437−2443.
(17) Rele, V.; Papir, Y. *J. Am. Phys. Soc.* **1975**, *20*, 284.
(18) Dlubek, G.; Redmann, F.; Krause-Rehberg, R. *J. Appl. Polym. Sci.* **2001**, *84*, 244−255.
(19) Sfirakis, A.; Rogers, C. *Polym. Eng. Sci.* **1980**, *20*, 294−299.
(20) Le Huy, H.; Rault, J. *Polymer* **1994**, *35*, 136−139.
(21) Loo, L.; Cohen, K., L. S.; Gleason. *Macromolecules* **1998**, *31*, 8907−8911.
(22) Ogawa, T.; Nagata, T.; Hamada, Y. *J. Appl. Polym. Sci.* **1993**, *50*, 981−987.
(23) Camacho, W.; Hedenqvist, M.; Karlsson, S. *Polym. Int.* **2002**.
(24) Asada, T.; Onogi, S. *J. Colloid Sci.* **1963**, *18*, 784−792.
(25) Mansfield, P.; Bowtell, R.; Blackband, S. *J. Magn. Reson.* **1992**, *99*, 507−524.
(26) Fyfe, C.; Randall, L.; Burlinson, N. *J. Polym. Sci., Part A: Polym. Chem.* **1993**, *31*, 159−168.
(27) Snaar, J.; Robyr, P.; Bowtell, R. *Magn. Res. Imag.* **1998**, *16*, 587−591.
(28) Artemov, D.; Samoilenko, A.; Iordanskii, A. *Vysokomolekulyarnye Soedineniya Ser. A* **1989**, *31*, 2473−2476.
(29) Greenspan, L. *J. Res. Natl. Bur. Stand., Sect. A-Phys. Chem.* **1977**, *81*, 89−96.
(30) Galeski, A.; Argon, A.; Cohen, R. *Makromol. Chem.* **1987**, *188*, 1195−1204.
(31) Penel-Pierron, L.; Depecker, C.; Seguela, R.; Lefebvre, J. *J. Polym. Sci., Part B: Polym. Phys.* **2001**, *39*, 484−495.
(32) Blümich, B.; Kuhn, W., *Magnetic Resonance Microscopy*.; VCH Verlagsgesellschaft: Weinheim, Germany, 1992.
(33) Vlaardingenbroek, M. T.; den Boer, J. A. *Magnetic Resonance Imaging*; Springer-Verlag: Berlin, Heidelberg, Germany, and New York, 1995.
(34) Glover, P. M.; Aptaker, P. S.; Bowler, J. R.; Ciampi, E.; McDonald, P. J. *J. Magn. Reson.* **1999**, *139*, 90−97.
(35) Erich, S. J. F.; Laven, J.; Pel, L.; Huinink, H. P.; Kopinga, H. P. *Appl. Phys. Lett.* **2005**, *52*, 210−216.
(36) Chelsea, R.; Fechete, R.; Culea, E.; Demco, D.; Blümich, B. *J. Magn. Reson.* **2009**, *196*, 178−190.
(37) Smith, E. *Polymer* **1976**, *17*, 761−767.
(38) McCall, D.; Anderson, E. *Polymer* **1963**, *4*, 93−103.
(39) Adriaensens, P.; Pollaris, A.; Rulkens, R.; Litvinov, V.; Gelan, J. *Polymer* **2004**, *45*, 2465−2473.
(40) Litvinov, V.; Penning, J. *Macromol. Chem. Phys.* **2004**, *205*, 1721−1734.
(41) Steinbrecher, G.; Scorei, R.; Cimpoiasu, V. M.; Petrisor, I. *J. Magn. Reson.* **2000**, 361−334.
(42) Ostroff, E. D.; Waugh, J. S. *Phys. Rev. Lett.* **1966**, *16*, 1097−1098.
(43) Mansfield, P.; Blackband, S. *J. Phys. C: Solid State Phys.* **1986**, L49−L52.
(44) Matano, C. *Jpn. J. Phys.* **1933**.
(45) Crank, J. *The Mathematics of diffusion*; Clarendon Press: Oxford, U.K., 1975.
(46) Vrentas, C.; Vrentas, J. S. *J. Polym. Sci., Part B: Polym. Phys.* **2002**, *41*, 501−507.
(47) Fujita, H. *Chem. Eng. Sci.* **1993**, *48*, 3037−3042.
(48) Murthy, N.; Stamm, M.; Sibilia, J.; Krimm, S. *Macromolecules* **1989**, *22*, 1261−1267.
(49) Murthy, N.; Akkapeddi, M. *Macromolecules* **1998**, *31*, 142−152.
(50) Kettle, G. *Polymer* **1977**, *18*, 742−743.

Macromolecules

Article

pubs.acs.org/Macromolecules

Orientation and Structure of Single Electrospun Nanofibers of Poly(ethylene terephthalate) by Confocal Raman Spectroscopy

Marie Richard-Lacroix and Christian Pellerin*

Département de chimie and Centre for Self-Assembled Chemical Structures, Université de Montréal, Montréal, QC, H3C 3J7, Canada

ABSTRACT: The ability to characterize individual electrospun fibers is essential in order to understand and control this complex process. In this paper, we demonstrate that confocal Raman microscopy is a powerful method to quantify molecular orientation and structure at the individual fiber level using poly(ethylene terephthalate) as a model system. Highly reproducible polarized spectra with an excellent signal-to-noise ratio were measured in 1 min or less for fibers with a diameter as little as 500 nm. The orientation of smaller fibers can also be probed using a calibration procedure. Our results reveal a very broad distribution of molecular orientation and structure within the samples: some individual fibers are completely isotropic and amorphous while others present a $\langle P_2 \rangle$ orientation parameter as large as 0.75. The development of this large orientation is accompanied by a *gauche*-to-*trans* structural conversion into the mesomorphous phase. Even the most highly oriented fibers only present a very small degree of crystallinity.

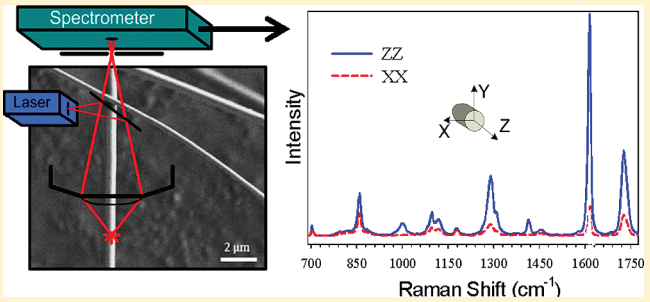

INTRODUCTION

Electrospinning is a technique that produces continuous fibers of various natural and synthetic polymer systems with typical diameters ranging from a few hundreds of nanometers to a few micrometers. In the past 2 decades, it has gained much attention for its versatility, simplicity, and efficiency for producing nanoscale materials for applications in catalysis, tissue engineering, filtration, biosensors, drug delivery, and electronic devices.[1,2] However, the widespread application of electrospun fibers is still limited by a poor understanding and control of their physical properties.[2]

Molecular orientation and crystallinity are parameters that strongly influence properties of nanofibers. Recent studies have demonstrated that the strong elongational forces experienced by the jet during the electrospinning process result in the formation of nanofibers with a high degree of molecular orientation and/or distinct crystal morphology for several highly crystalline polymers.[3−5] These fibers are usually characterized by techniques such as X-ray diffraction (XRD) and infrared spectroscopy that require performing measurements on large bundles in order to obtain acceptable signal-to-noise ratios. As a consequence, one must assume a uniform distribution of structural characteristics in the sample and, for molecular orientation, a perfect alignment of fibers within the bundle. In practice, electrospun nanofibers usually present a large distribution of diameters and morphology, are often only partially aligned, and sometimes contain defects such as beads due to jet instabilities during the electrospinning process.[6] The development of characterization techniques adapted to the size of individual nanofibers therefore appears as a critical need.

Selected-area electron diffraction (SAED) has been successfully used to characterize the orientation and crystalline structure within single nanofibers of highly crystalline polymers such as polyethylene,[7] nylon-6,[8] polylactide,[8] and poly(ε-caprolactone).[9] A high degree of orientation along the fiber axis was observed in all cases. However, SAED can require exhaustive sample preparation, depending on the thickness of the fiber, and precise quantification is affected by the sensitivity of most organic polymers to electron beam damage.[10] Another major limitation of diffraction techniques is that they are normally restricted to the analysis of the crystalline phase and are thus of limited use for fibers of amorphous or low-crystallinity polymers. As a matter of fact, increasing attention has been paid in the past years to the orientation of the amorphous phase in nanofibers. Several atomic force microscopy (AFM) studies of single fibers revealed a sharp increase of Young's modulus with a decreasing fiber diameter.[11,12] This observation was attributed to an anisotropy of the amorphous phase which would be induced by confinement when the fibers reach down a critical diameter.[12,13] This phenomenon still needs to be correlated with direct and quantitative orientation measurements at the single fiber level.

Confocal Raman spectroscopy offers many advantages for the study of individual fibers since it provides molecular level information about conformation, interactions, and crystallinity. Moreover, it enables distinguishing between the molecular orientation of the crystalline and amorphous phases. Bellan and Craighead first proposed using this technique to characterize the orientation of single nylon-6 electrospun nanofibers.[14] Unfortunately, the low signal-to-noise ratio of the four polarized spectra required to quantify orientation lead to values outside the theoretical range, casting a doubt on the applicability of Raman

Received: December 20, 2011
Revised: February 2, 2012
Published: February 15, 2012

spectroscopy for nanofibers. In fact, to our knowledge, no other successful results were published.

In this paper, we demonstrate that the molecular orientation of single electrospun fibers with diameters down to 500 nm can be quantified using confocal Raman spectroscopy. Nanofibers of poly(ethylene terephthalate) (PET) were used as a model system since its Raman spectrum is well understood. Spectra with an excellent signal-to-noise ratio can be recorded in less than a minute. We finally show that Raman spectroscopy can readily be used to quantify the distribution of conformations and crystallinity within a collection of single nanofibers.

THEORETICAL SECTION

The orientation distribution function (ODF) for uniaxially oriented samples such as fibers, $N(\theta)$, can be expressed as an expansion of even Legendre polynomials $P_l(\cos\theta)$:[15,16]

$$N(\theta) = \sum_{even}^{l} \left(l + \frac{1}{2}\right)\langle P_l\rangle P_l(\cos\theta) \tag{1}$$

The $\langle P_l\rangle$ coefficients, called order parameters, are determined experimentally. The brackets indicate that they represent the average value of the lth Legendre polynomial over the complete distribution of orientation. Polarized Raman spectroscopy gives access to the second and fourth coefficients of the series, $\langle P_2\rangle$ and $\langle P_4\rangle$, defined as[15−17]

$$\langle P_2\rangle = \frac{1}{2}(3\langle\cos^2\theta\rangle - 1) \tag{2}$$

$$\langle P_4\rangle = \frac{1}{8}(35\langle\cos^4\theta\rangle - 30\langle\cos^2\theta\rangle + 3) \tag{3}$$

$\langle P_2\rangle$ is 1 for a perfect orientation along the fiber axis (Z), 0 for an isotropic distribution, and −0.5 for a perfect orientation perpendicular to the fiber axis (X). According to the Schwarz inequalities, the $\langle P_4\rangle$ values are restricted to a certain range for any given $\langle P_2\rangle$ value:[15−17]

$$\frac{1}{18}(35\langle P_2\rangle^2 - 10\langle P_2\rangle - 7) \le \langle P_4\rangle \le \frac{1}{12}(5\langle P_2\rangle + 7) \tag{4}$$

The maximum and minimum $\langle P_4\rangle$ values are associated with unimodal and bimodal orientation distributions, respectively.[15−17] With knowledge of the $\langle P_2\rangle$ and $\langle P_4\rangle$ coefficients, the most probable ODF can be estimated using the entropy theory.[18]

In Raman spectroscopy, the scattered intensity for a given vibrational mode depends on the shape and orientation of its polarizability ellipsoid, which can be described by a second rank tensor, α, in terms of its principal components α_1, α_2, and α_3.[15,19]

$$\alpha = \begin{pmatrix} \alpha_1 & & \\ & \alpha_2 & \\ & & \alpha_3 \end{pmatrix} = \alpha_3 \begin{pmatrix} a_1 & & \\ & a_2 & \\ & & 1 \end{pmatrix} \tag{5}$$

where $a_1 = \alpha_1/\alpha_3$ and $a_2 = \alpha_2/\alpha_3$. Bower[20] developed the theory of orientation quantification by Raman spectroscopy by establishing a linear relationship between the measured polarized spectral intensities (I_s), the principal components of the Raman tensor, and the order parameters ($\langle P_2\rangle$ and $\langle P_4\rangle$) according to

$$I_s = I_0 \sum_{i,j} (l'_i l_j \alpha_{ij})^2 \tag{6}$$

where I_0 depends on instrumental factors such as the laser power, l'_i and l_j are the direction cosines of the polarization vector of the incident and scattered beam, respectively, and α_{ij} are the components of the Raman tensor expressed in the laboratory frame. The brackets represent the mean value over the distribution of orientation. Assuming uniaxial symmetry, there are only five independent and nonzero equations that describe this dependency. The so-called "complete method" involves recording 12 different Raman spectra in three different geometries.[21]

In confocal Raman spectroscopy, only the backscattering geometry is accessible so that a limited set of two parallel-polarized (ZZ and XX) and two cross-polarized (ZX and XZ) spectra can be measured. In this notation, the first letter corresponds to the polarization of the incident beam and the second to that of the selected component of the scattered beam. This limitation requires additional approximations to quantify $\langle P_2\rangle$ and $\langle P_4\rangle$, as described in detail by Rousseau et al.[19] Common constants can be eliminated by calculating the ratios of the experimental cross- and parallel-polarized spectra.[15,19,22] These two ratios, R_1 and R_2, are related to the α_{ij} elements of the tensor as described by

$$R_1 = \frac{I_{ZX}}{I_{ZZ}} = \frac{A\langle(\alpha_{ZX})^2\rangle + B\langle(\alpha_{ZY})^2\rangle}{A\langle(\alpha_{ZZ})^2\rangle + B\langle(\alpha_{ZY})^2\rangle} \tag{7a}$$

$$R_2 = \frac{I_{XZ}}{I_{XX}} = \frac{A\langle(\alpha_{XZ})^2\rangle + B\langle(\alpha_{XY})^2\rangle}{A\langle(\alpha_{XX})^2\rangle + B\langle(\alpha_{XY})^2\rangle} \tag{7b}$$

A and B are constants that take into account the depolarization of the incident and scattered beam in the focal plane associated with the use of a high numerical aperture (NA) objective.[23] B is not negligible when using a high NA objective and requires considering out-of-plane contributions of the Raman tensor to the measured spectral intensity. The $\langle(\alpha_{ij})^2\rangle$ terms in eq 7 contain four unknown parameters, namely a_1, a_2, $\langle P_2\rangle$, and $\langle P_4\rangle$. With the approximation that the Raman tensor has a cylindrical symmetry, that is $a_1 = a_2 = a$, the $\langle(\alpha_{ij})^2\rangle$ terms can be expressed as:[19]

$$\langle(\alpha_{XX})^2\rangle = {\alpha_3}^2\left(\frac{1}{15}(3 + 4a + 8a^2) - \frac{2}{21}(3 + a - 4a^2)\langle P_2\rangle + \frac{3}{35}(1 - a)^2\langle P_4\rangle\right) \tag{8a}$$

$$\langle(\alpha_{ZZ})\rangle^2 = {\alpha_3}^2\left(\frac{1}{15}(3 + 4a + 8a^2) + \frac{4}{21}(3 + a - 4a^2)\langle P_2\rangle + \frac{8}{35}(1 - a)^2\langle P_4\rangle\right) \tag{8b}$$

$$\langle(\alpha_{XZ})^2\rangle = \langle(\alpha_{ZX})^2\rangle = \langle(\alpha_{ZY})^2\rangle = {\alpha_3}^2(1 - a)^2\left(\frac{1}{15} + \frac{1}{21}\langle P_2\rangle - \frac{4}{35}\langle P_4\rangle\right) \tag{8c}$$

$$\langle(\alpha_{XY})^2\rangle = {\alpha_3}^2(1 - a)^2\left(\frac{1}{15} - \frac{2}{21}\langle P_2\rangle + \frac{1}{35}\langle P_4\rangle\right) \tag{8d}$$

The "a" parameter can be determined by measuring the polarized intensities of the band of interest for an isotropic sample. For such sample, R_1 and R_2 are equivalent to the depolarization ratio, ρ, since $\langle P_2\rangle$ and $\langle P_4\rangle$ are equal to zero, and can be expressed as:[19]

$$\rho = R_1 = R_2 = \frac{(A + B)(1 - a)^2}{A(8a^2 + 4a + 3) + B(1 - a)^2} \tag{9}$$

dx.doi.org/10.1021/ma202749d | Macromolecules 2012, 45, 1946−1953

It should be noted that the use of eq 9 to obtain "*a*" implies the approximation of a constant depolarization ratio over the whole range of orientation investigated. With knowledge of "*a*", one can finally solve eqs 7 and 8 to determine $\langle P_2 \rangle$ and $\langle P_4 \rangle$.

EXPERIMENTAL SECTION

Sample Preparation. Poly(ethylene terephthalate) (PET) flakes (Scientific Polymer Products) with an inherent viscosity of 0.58, trifluoroacetic acid and dichloromethane (Fisher Scientific) were used without further purification. Fibers were prepared from a 15% w/w solution of PET in a 50:50 w/w mixture of trifluoroacetic acid and dichloromethane. Solutions were introduced in a glass syringe equipped with a 0.41 mm diameter flat-end needle. A 27 kV positive voltage was applied to the needle tip using a CZE 1000R high-voltage power supply (Spellman High Voltage Electronics) while a 2 kV negative potential (Power Designs) was imposed on two parallel metallic rods to collect the electrospun fibers. The distance between the needle tip and the collector was 15 cm. Small quantities of fibers were then collected on a BaF_2 window and dried under vacuum for at least 4 h prior to analysis by Raman spectroscopy.

Raman Characterization. Spectra were recorded in the backscattering geometry with a LabRam HR800 spectrometer (Horiba Jobin Yvon) coupled with an Olympus BX41 microscope. The confocal hole and the slit width were fixed at 100 and 150 μm, respectively. A 632.8 nm He−Ne laser was focused on the fiber with a 100X long working distance objective (0.8 NA). The power at the sample was ~10.5 mW. A half wave plate was used to select the polarization of the incident laser beam and a polarizer was used to select the *X* or *Z* component of the scattered beam. A scrambler was placed before the 600 groove/mm holographic grating in order to minimize its polarization-dependent response.

Individual nanofibers isolated by several micrometers from their nearest neighbors were aligned with their long axis along the *Z* direction and polarized spectra were recorded in the order: *ZZ*, *ZX*, *XX*, *XZ*, *ZZ*(2). The fifth spectrum was recorded to detect any drift of the system during acquisition. Any series showing more than a 5% difference in the absolute intensity of the 1616 cm^{-1} band in the *ZZ* and *ZZ*(2) spectra was rejected. The depolarization ratio was determined with polarized measurements on isotropic amorphous PET films. Correction factors were applied to all spectra to compensate for the residual polarization dependence of the spectrometer. They were determined by recording polarized spectra of isotropic amorphous films of PET and polystyrene for a series of bands with known depolarization ratio.

RESULTS AND DISCUSSION

Orientation Quantification at the Single Nanofiber Level. The bottom of Figure 1 presents an example of a full set of parallel- and cross-polarized Raman spectra for a ~500 nm electrospun PET fiber in the 1575−1775 cm^{-1} spectral region. No smoothing or baseline corrections were applied. An excellent signal-to-noise ratio can be observed, on the order of 200:1 for the 1616 cm^{-1} band in the *ZZ* spectrum and of 100:1 in the cross-polarized spectra (*XZ* and *ZX*). This high spectral quality was achieved with a short acquisition time of only 30 s per spectrum. In fact, acceptable polarized spectra could be acquired with an integration time as short as 5 to 10 s, depending on samples, but six acquisitions were averaged in order to improve the signal-to-noise ratio.

The molecular orientation of this nanofiber was quantified using the intensity of the 1616 cm^{-1} band, which is assigned to the symmetric C═C stretching of the benzene ring.[24] The principal axis of its tensor is aligned along the C_1-C_4 axis with a tilt angle of 20° with respect to the main chain.[25] This band is of particular interest since it is reported to be representative of the overall orientation of the system thanks to its constant

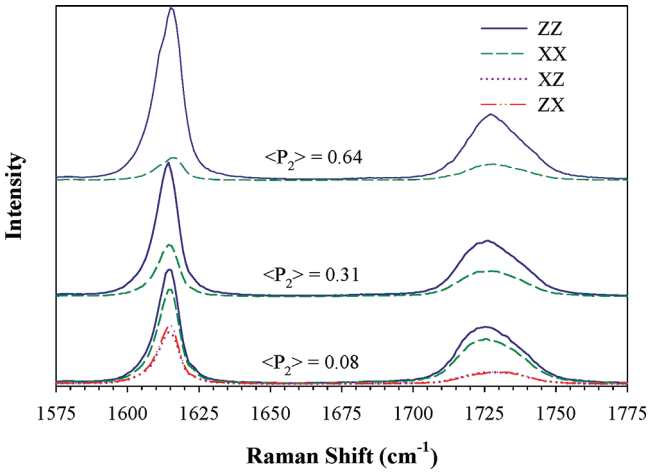

Figure 1. Polarized Raman spectra for three representative individual electrospun PET fibers in the 1575−1775 cm^{-1} spectral region. For clarity, the cross-polarized spectra (*XZ* and *ZX*) are only shown for one fiber.

bandwidth and position upon orientation and/or crystallization.[26,27] In contrast, the 1725 cm^{-1} band, which is due to symmetric stretching of the carbonyl groups, shifts and narrows with increasing crystallinity.[24,28,29] The orientation of this nanofiber is small with a $\langle P_2 \rangle$ value of 0.08 after adjustment for the 20° tilt angle of the 1616 cm^{-1} band. This result appears consistent with previous XRD studies on electrospun PET nonwovens that reported a small degree of orientation.[30]

Figure 1 also presents examples of polarized Raman spectra obtained for two other nanofibers with a ~500 nm diameter. For clarity, only the parallel-polarized Raman spectra (*ZZ* and *XX*) are shown. The spectra clearly demonstrate the nonuniformity of the orientation from fiber to fiber within the sample. Indeed, some nanofibers show a surprisingly high degree of orientation with $\langle P_2 \rangle$ values as high as 0.75. Such high values have never been reported for PET nanofibers and are unexpected for nanofibers composed of a low-crystallinity polymer. To our knowledge, $\langle P_2 \rangle$ values of this order of magnitude have only been observed for fibers composed of highly crystalline polymers such as poly(ε-caprolactone),[5] poly(ethylene oxide) (PEO)[3] and PEO complexes with urea.[31] The nonuniformity of orientation within the sample is consistent with the recent SAED study of Yoshioka et al.[7] on individual electrospun polyethylene nanofibers. In their case, a direct correlation was established between the molecular orientation and the diameter of the fibers. Such a clear dependence was not observed in this study for PET nanofibers, possibly because the diameter of most fibers was close to the spatial resolution of the optical microscope and could not be determined with high accuracy. This limited spatial resolution is the main weakness of Raman microscopy as compared to TEM-based electron diffraction.

As mentioned in the Theoretical Section, the calculation of these $\langle P_2 \rangle$ values assumes that the tensor of the 1616 cm^{-1} band is cylindrical and is not affected by changes in orientation and/or crystallinity, as first proposed by Purvis and Bower.[25] These assumptions have been questioned by Lesko et al.[26] and later by Yang and Michelson[32] who reported that the shape of this Raman tensor is not perfectly cylindrical and evolves with structural changes, leading to a larger error in the magnitude of $\langle P_2 \rangle$ and $\langle P_4 \rangle$ with increasing orientation. However, the

dx.doi.org/10.1021/ma202749d | *Macromolecules* 2012, 45, 1946−1953

consequence is a slight underestimation of $\langle P_2 \rangle$ so that the large values reported here for highly oriented PET nanofibers are not overestimated and comparisons from fiber to fiber are still reliable.

Figure 2 shows the polarized Raman spectra of the same three fibers in the 675−1175 cm^{-1} spectral region. The bands

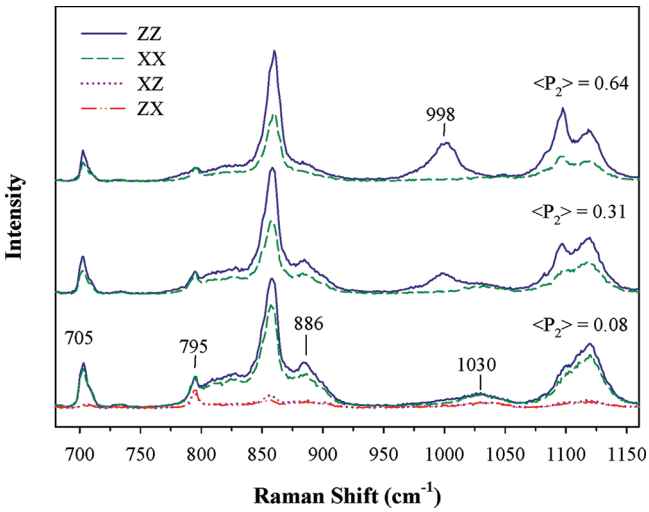

Figure 2. Polarized Raman spectra of single electrospun PET fibers in the 675−1175 cm^{-1} spectral region. For clarity, the cross-polarized spectra (*XZ* and *ZX*) are only shown for one fiber.

are considerably weaker, especially in the cross-polarized spectra since most of them have a small depolarization ratio,[25] but their signal-to-noise ratio is still sufficient to allow quantitative analysis. These spectra strongly support the quantitative nature of our orientation results. In particular, the 795 cm^{-1} band, which is due to a combination of C═O and ring ester C−C out-of-plane bending and ring torsion[33] is well-known for its insensitivity to orientation.[29] Its equivalence in both parallel-polarized spectra (ZZ and XX) for all samples demonstrates that the distribution of $\langle P_2 \rangle$ values observed from fiber to fiber is real and not an artifact due to incorrect focusing.

The 998 cm^{-1} band, which is associated with O−CH_2 and C−C stretching of the ethylene glycol unit in the *trans* conformation,[29] appears only in the ZZ spectra of oriented nanofibers and its intensity increases with orientation. A similar but more complicated behavior is observed for the 1096 cm^{-1} band which is also associated with the *trans* conformation.[24] This is in agreement with the *gauche*-to-*trans* rotational isomerization of the ethylene glycol units upon orientation.[34] These results indicate that the population of *trans* conformer increases with the overall orientation of the polymer chains and that their degree of orientation is extremely high in all cases. In contrast, the bands associated with *gauche* conformers[24] show the opposite behavior. In particular, the 1030 cm^{-1} band does not show any polarization dependence and only appears in the spectra of weakly oriented fibers while the 886 cm^{-1} band shows a drastic decrease in intensity in both parallel−polarized spectra upon orientation. These results suggest that the *gauche* conformers are essentially isotropic and that their fraction decreases with the overall orientation of the system. Similar behaviors were observed by Adar and Noether[29] and by Yang and Michelson[32,35] in their studies of spin-oriented PET fibers.

Over 15 PET nanofibers showing the intensity equivalence for the 795 cm^{-1} band and a high reproducibility between the ZZ and ZZ(2) spectra were analyzed. The $\langle P_2 \rangle$ and $\langle P_4 \rangle$ values were always found to be in the acceptable range defined by the limiting values of eq 4. These two order parameters were used to calculate the most probable orientation distribution of the polymer chains within nanofibers using the entropy theory.[18] Figure 3

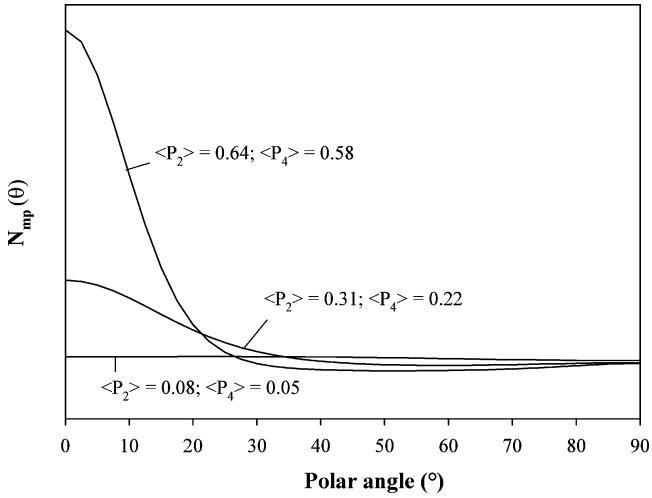

Figure 3. Most probable orientation distribution function determined for three single electrospun PET nanofibers.

shows the ODF determined for the three fibers shown as examples in Figures 1 and 2. For weakly oriented samples, the distribution is almost constant for all polar angles. For more oriented samples, both $\langle P_2 \rangle$ and $\langle P_4 \rangle$ follow a similar increasing trend. This leads in all cases to a unimodal ODF with its maximum along the fiber axis (polar angle of 0°). For the most highly oriented samples, the ODF is significantly narrowed as compared to the one associated with smaller $\langle P_2 \rangle$ values.

The results obtained here show a significant improvement in spectral quality as compared to those previously reported,[14] leading to a much better confidence in the validity of the quantitative analysis. We believe this is mainly due to the differences in sample handling and in the objective used. Indeed, even imperceptible fiber movements during the experiment are detrimental to the reproducibility between the ZZ and ZZ(2) spectra. The relationship between the absolute band intensities of the four polarized spectra, which is required to perform orientation quantification, therefore becomes compromised. To overcome this problem, small quantities of fibers were electrospun between two parallel rod collectors and carefully transferred on a BaF_2 window, a planar and Raman-inactive substrate in the spectral regions of interest. The samples were further dried under vacuum for a few hours in order to eliminate the residual solvent before measurement. It was found that if the fibers are allowed to completely dry before their transfer on the substrate, the focus equivalence is impossible to achieve. We believe that traces of solvent that are always trapped in nanofibers immediately after electrospinning, even when using volatile solvents, helped to initially adsorb the fibers on the substrate. This prevented any motion after the subsequent drying and enabled reproducible measurements, even a month after the fiber deposition. Attempts to use transmission electron microscopy grids were unsuccessful because the points of contact between the nanofibers and the substrate were not sufficient to prevent movements. The size of the laser spot on the sample is also a key factor in obtaining high signal-to-noise

dx.doi.org/10.1021/ma202749d | *Macromolecules* 2012, 45, 1946−1953

ratios. The diameter of the laser spot was approximately 700 nm with our 100× objective as compared with a 4 μm spot reported by Bellan and Craighead with a 50× objective.[14] As a consequence, the signal-to-noise ratio was drastically improved even if the total acquisition time was reduced from 600 s to less than 60 s for each polarized spectrum.

The very broad distribution of orientation level observed from fiber to fiber within the same electrospun sample reveals the need of characterizing a large number of fibers to properly describe these heterogeneous systems. In order to reduce the time necessary to perform such analysis, we established a calibration curve relating the orientation parameters to the intensity ratio of bands in a single polarized spectrum. The *ZZ* spectra appeared as the best option because of their larger signal-to-noise ratio. Figure 4 presents the linear relationship

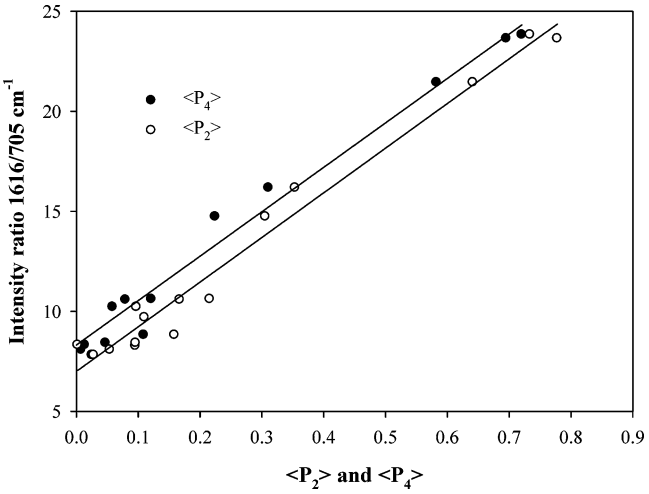

Figure 4. Calibration curves relating the 1616/705 cm^{-1} intensity ratio in the ZZ spectra to the $\langle P_2 \rangle$ and $\langle P_4 \rangle$ orientation parameters. A total of 15 PET nanofibers with diameters between 500 nm and 1 μm were used to establish these calibration curves.

established between the 1616/705 cm^{-1} band ratio and the $\langle P_2 \rangle$ and $\langle P_4 \rangle$ parameters. Both calibration curves show an excellent linearity with a correlation coefficient of 0.98. Interestingly, $\langle P_2 \rangle$ and $\langle P_4 \rangle$ evolve collinearly and $\langle P_4 \rangle$ is systematically slightly smaller than $\langle P_2 \rangle$. These order parameters result in unimodal ODFs that become narrower with increasing $\langle P_2 \rangle$ as shown in Figure 3 for selected examples. These calibration curves eliminate the need of recording the full set of polarized spectra and, importantly, to achieve spectral quality equivalence between the spectra before the measurement, which is the most time-consuming step of the experiment. Semiquantitative orientation information can therefore be obtained in less than 1 min based on the acquisition of a single *ZZ* spectrum. To our knowledge, such short measurement time for individual electrospun nanofibers has not been achieved by any other technique.

The orientation of 35 additional individual nanofibers from five independent samples (from different sample depositions) was quantified using this strategy in order to evaluate the distribution of orientation of the PET sample from a statistical point of view. The fibers appeared to separate into three non-overlapping clusters: approximately 70% of the fibers were only slightly oriented with an average $\langle P_2 \rangle$ value of 0.09 and a standard deviation of 0.04, 20% were very highly oriented with $\langle P_2 \rangle = 0.70 \pm 0.04$, and only 10% of the fibers had an intermediate level of orientation between these two extremes ($\langle P_2 \rangle = 0.32 \pm 0.08$). It should also be pointed out that large variations of orientation were also observed when analyzing points separated by tens of micrometers along some single fibers. It is clear that orientation quantification on bundles would have missed this fundamental information about the heterogeneity of the system.

In addition to enabling statistically meaningful studies, this calibration procedure enables evaluating the orientation of fibers with diameters smaller than 500 nm. Even if a very good signal-to-noise ratio can be obtained by increasing the acquisition time, we were not able to perform strict molecular orientation quantification for fibers with a size comparable to or smaller than the diffraction limit of the laser: the intensity equivalence for the 795 cm^{-1} band in the *ZZ* and *XX* spectra was no longer achievable. The calibration curves of Figure 4 enable to overcome this diameter limitation and to study orientation in thinner fibers. These calibration curves should remain valid even if the behavior of ultrathin fibers departs from that of the larger ones since the two bands are well-known for their insensitivity to morphological changes.

Structural Analysis at the Single Nanofiber Level. In addition to orientation, rich structural information can be obtained at the single nanofiber level using confocal Raman spectroscopy. It is well-known that PET chains can be organized into three distinct phases: the amorphous, the crystalline, and the mesomorphous phases. The amorphous phase is largely dominated by the *gauche* conformers of the ethylene glycol units while the *trans* conformation is adopted in the crystalline and mesomorphous phase.[36] These two phases are mainly differentiated by the organization of the terephthalate groups, which are randomly oriented in the mesomorphous phase and coplanar in the crystalline phase.[37] Cold-drawn PET films[38] and spin-oriented fibers[29] were shown to be dominated by the mesomorphous phase. On the other hand, samples stretched above T_g or annealed after the drawing process additionally give rise to crystallization.[39] This microstructure has a large impact on the physical properties of the samples. It is therefore interesting to evaluate the nature and the relative importance of the phases formed during the electrospinning process, as well as their homogeneity from fiber to fiber.

As mentioned when discussing Figure 2, the evolution of the 998 and 886 cm^{-1} bands clearly shows an increase in *trans* conformers when going from slightly to highly oriented fibers. Rodriguez-Cabello et al.[40] proposed quantifying the *gauche* and *trans* fractions (F_T and F_G) using these two bands and the 795 cm^{-1} band as an internal reference, which was later replaced by the 705 cm^{-1} band:[41]

$$F_T = p_1\left(\frac{I_{998}}{I_{705}}\right)_{iso} \qquad F_G = p_2\left(\frac{I_{886}}{I_{705}}\right)_{iso} \tag{10}$$

where p_1 and p_2 are coefficients that express the relative weight of the 998 and 886 cm^{-1} bands, respectively. To perform this calculation on oriented samples, one needs to eliminate the effect of orientation from the measured spectral intensity. Frisk et al.[42] developed a strict method to evaluate an "orientation insensitive" spectrum and Lefèvre et al.[43] later adapted it to Raman microspectroscopy. This method is hardly applicable here because using the cross-polarized spectra for three of the weakest bands of the spectrum leads to large errors. As a first approximation, the analogue of the infrared structural

absorbance was calculated using only the parallel-polarized spectra:[41]

$$\left(\frac{I_{band}}{I_{705}}\right)_{iso} = \left(\frac{I_{band}}{I_{705}}\right)_{ZZ} + 2\left(\frac{I_{band}}{I_{705}}\right)_{XX} \quad (11)$$

Since the band intensities are normalized in eq 11, it is not necessary to obtain the focus equivalence between the *XX* and *ZZ* spectra so that *trans* and *gauche* fractions can be calculated even for fibers smaller than 500 nm. The coefficients p_1 and p_2 were determined experimentally by rearranging eq 10 and were found to be 0.30 and 0.32, respectively, in excellent agreement with the reported ones.[40,41,44] It should be noted that the 705 cm^{-1} band, used for normalization, shows a small polarization dependence and that band fitting was not used to quantify the intensity of the 886 cm^{-1} band. These two factors did not have a significant influence on the determined coefficients.

Figure 5 shows the evolution of the *trans* and *gauche* fractions determined independently using eq 10 as a function of $\langle P_2 \rangle$ for

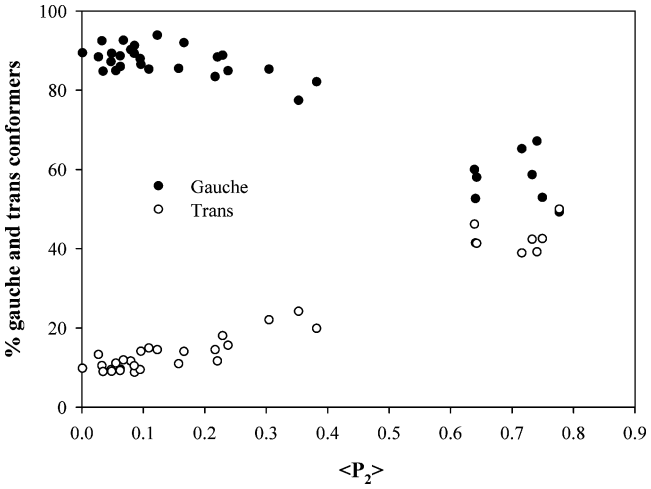

Figure 5. Evolution of the *gauche* and *trans* fractions as a function of $\langle P_2 \rangle$ in electrospun PET fibers.

a series of nanofibers covering the complete range of orientation obtained. Results show that unoriented or slightly oriented nanofibers contain 10−15% of *trans* conformers, which is consistent with the conformation distribution of totally amorphous and isotropic PET samples.[37,40] The population of *trans* conformers gradually increases with orientation and reaches 40−50% for the nanofibers with the highest $\langle P_2 \rangle$ values. The population of *gauche* conformers follows the opposite trend. This increase in *trans* fraction with orientation is in agreement with studies of fibers formed at high wind-up speed[34] and of films stretched to high draw ratios.[38,44] While this method is only semiquantitative because of the approximations associated with eq 11, it demonstrates very well the capability of Raman spectroscopy to follow small structural changes in individual nanofibers. It should also be pointed out that Figure 5 includes $\langle P_2 \rangle$ values that were calculated strictly or using the calibration curve shown in Figure 4. No distinction can observed between these two series, reinforcing the validity of the calibration method.

This increase in *trans* content with orientation can be either due to crystallization or to the formation of the mesomorphous phase. Crystallinity degrees must therefore be determined at the single fiber level to discriminate between these two possibilities. The simplest and most commonly used method is to follow the full width at half-maximum (fwhm) of the C═O stretching band at 1725 cm^{-1}. The carbonyl groups are randomly oriented in the amorphous and mesomorphous phases but are coplanar with the phenyl ring and *trans* to one another in the crystalline phase, resulting in a reduction of the bandwidth. Melveger[28] reported a linear relationship between the fwhm of this band and the density (d) of the polymer, which can then be related to the crystallinity through

$$d = \frac{-\text{fwhm}_{1725} + 305}{209} \quad (12a)$$

$$X_c = (d - d_a)/(d_c - d_a) \quad (12b)$$

where d_a = 1.335 g/cm^3 and d_c = 1.445 g/cm^3 are the density of the amorphous and crystalline phases, respectively.[32]

Figure 6 shows the evolution of the degree of crystallinity (labeled as model 1) as a function of $\langle P_2 \rangle$ for the series of

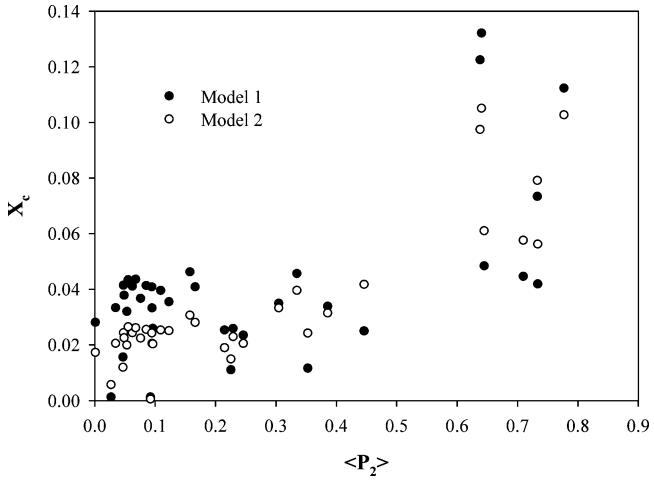

Figure 6. Evolution of the degree of crystallinity of PET nanofibers as a function of their $\langle P_2 \rangle$. The results of models 1 and 2 were calculated with eqs 12 and 13, respectively.

electrospun fibers presented in Figure 5. All crystallinity values are very small but two behaviors can be distinguished: nanofibers with a $\langle P_2 \rangle$ value smaller than 0.5 are almost totally amorphous (X_c < 0.05), while only the most highly oriented nanofibers show a non-negligible degree of crystallinity. X_c remains small, below 14%, for nanofibers with a *trans* content as high as 50%, suggesting that the overall orientation is mainly due to the formation of a highly oriented mesomorphous phase. By comparison, XRD patterns recorded on PET bundles (not shown) did not show any crystalline peaks. Kim et al.[30] also concluded to totally amorphous PET nanofibers using XRD when studying PET nonwovens formed under similar electrospinning conditions. This apparent discrepancy is due to the fact that the highly oriented fibers only account for ~20% of the sample. Crystallinity can hardly be detected for bundles because the ensemble measurement averages out the nanofibers characteristics.

For this simple quantification, only the *ZZ* spectra were used since the fwhm of the 1725 cm^{-1} was reported to be unaffected by orientation.[28] This approximation has been questioned for highly oriented samples.[45,46] To confirm these conclusions, crystallinity degrees were also determined using a more elaborate method proposed by Natarajan et al.[46] These authors showed that an improved correlation between the *ZZ* spectra

dx.doi.org/10.1021/ma202749d | *Macromolecules* 2012, 45, 1946−1953

and density can be obtained by combining the bandwidth of the 1725 cm^{-1} band with the intensity of the 998 cm^{-1} band (normalized to the 705 cm^{-1} band):

$$d = 1.398 - 0.0023\text{fwhm}_{ZZ1725} + 0.00305\left(\frac{I_{ZZ998}}{I_{ZZ705}}\right) + 0.00072\left(\frac{I_{ZZ998}}{I_{ZZ705}}\right)^2 \quad (13)$$

The results are shown in Figure 6 as model 2 and correlate very well with those of the simpler model 1. Differences can be attributed to a polarization dependence of the bandwidth of the 1725 cm^{-1} band and to small changes in the numerical coefficients of eq 13 since they depend on the NA of the objective.[46] It should be noted that both models rely on the assumption that the mesomorphous phase (largely dominated by *trans* conformers) has the same density as the amorphous phase (largely dominated by *gauche* conformers). This approximation leads to an overestimation of the crystallinity degree[47] so the conclusion that the significant increase in *trans* fraction with orientation (Figure 5) is mostly due to the formation of the mesomorphous phase is unaffected. Both models are experimentally simple since they only require one polarized spectrum and are therefore applicable to fibers with a diameter smaller than 500 nm.

It is possible to draw a general picture of the structure in the electrospun PET fibers. Results indicate that the largest fraction (~70%) of the fibers possess a weak orientation ($\langle P_2 \rangle$ below 0.2) and are essentially amorphous, as shown in Figure 6. Some fibers develop a much higher orientation that is almost completely due to *trans* conformers. Indeed, even if the 1616 cm^{-1} band provides the overall orientation of the system, the spectra of Figure 2 indicate that the orientation of the *trans* conformers is very high while the *gauche* conformers are essentially isotropic. Accordingly, Figure 5 shows that the increase in overall orientation and in the fraction of the *trans* conformers are closely related. These *trans* conformers are mostly found in the mesomorphous phase. The strong elongational forces experienced by the polymer chains during the electrospinning process enable the formation of this oriented phase, but the fast solvent evaporation limits the chains mobility and prevents the formation of the better organized crystalline phase. Figure 6 suggests that some nuclei can form by a stress induced crystallization process along the fiber axis for the most highly oriented nanofibers, but that they did not have the opportunity to grow. This behavior is similar to that observed for fibers and films drawn at room temperature[29,38] but is highly heterogeneous from fiber to fiber. It is plausible that this heterogeneity originates from a broad distribution of effective elongational forces experienced by fibers (or fiber sections) during the whipping process.

CONCLUSION

In this work, we demonstrated the great efficiency of Raman spectroscopy for characterizing molecular orientation and structural characteristics of individual electrospun nanofibers. Highly reproducible polarized Raman spectra of single PET nanofibers were obtained in less than a minute with an excellent signal-to-noise ratio. With the establishment of a calibration curve, a single polarized spectrum was shown to be sufficient to perform orientation quantification on a large number of nanofibers, including those with a diameter smaller than 500 nm. Quantitative orientation parameters ($\langle P_2 \rangle$ and $\langle P_4 \rangle$), *gauche* and *trans* isomer fractions, and crystallinity degrees were obtained on several individual PET nanofibers. A broad distribution of all these parameters was observed from fiber to fiber. It was shown that the mesomorphous phase rather than the crystalline phase was mainly dominant.

We believe that confocal Raman spectroscopy will become a major tool for the characterization of single nanofibers. This technique should improve our understanding of the parameters that control the molecular orientation and structural organization of polymer chains in electrospun nanofibers.

AUTHOR INFORMATION

Corresponding Author

*Telephone: (514) 340-5762. Fax: (514) 340-5290. E-mail: c.pellerin@umontreal.ca.

Notes

The authors declare no competing financial interest.

ACKNOWLEDGMENTS

This work was supported by a grant and a graduate scholarship (MRL) from the Natural Sciences and Engineering Research Council of Canada (NSERC). We are grateful to T. Lefèvre for useful discussions.

REFERENCES

(1) Sill, T. J.; von Recum, H. A. *Biomaterials* **2008**, *29*, 1989. Agarwal, S.; Wendorff, J. H.; Greiner, A. *Polymer* **2008**, *49*, 5603. Bhardwaj, N.; Kundu, S. C. *Biotechnol. Adv.* **2010**, *28*, 325. Greiner, A.; Wendorff, J. H. *Angew. Chem., Int. Ed.* **2007**, *46*, 5670. Wang, Z.-G.; Wan, L.-S.; Liu, Z.-M.; Huang, X.-J.; Xu, Z.-K. *J. Mol. Catal. B: Enzym.* **2009**, *56*, 189. Kumbar, S. G.; James, R.; Nukavarapu, S. P.; Laurencin, C. T. *Biomed. Mater.* **2008**, *3*, 034002.

(2) Baji, A.; Mai, Y.-W.; Wong, S.-C.; Abtahi, M.; Chen, P. *Comput. Sci. Technol.* **2010**, *70*, 703.

(3) Kakade, M. V.; Givens, S.; Gardner, K.; Lee, K. H.; Chase, D. B.; Rabolt, J. F. *J. Am. Chem. Soc.* **2007**, *129*, 2777.

(4) Fennessey, S. F.; Farris, R. J. *Polymer* **2004**, *45*, 4217. Kongkhlang, T.; Tashiro, K.; Kotaki, M.; Chirachanchai, S. J. *Am. Chem. Soc.* **2008**, *130*, 15460.

(5) Edwards, M. D.; Mitchell, G. R.; Mohan, S. D.; Olley, R. H. *Eur. Polym. J.* **2010**, *46*, 1175.

(6) Zuo, W.; Zhu, M.; Yang, W.; Yu, H.; Chen, Y.; Zhang, Y. *Polym. Eng. Sci.* **2005**, *45*, 704. Deitzel, J. M.; Kleinmeyer, J.; Harris, D.; Beck Tan, N. C. *Polymer* **2001**, *42*, 261. Lim, C. T.; Tan, E. P. S.; Ng, S. Y. *Appl. Phys. Lett.* **2008**, *92*, 141908. Tripatanasuwan, S.; Zhong, Z.; Reneker, D. H. *Polymer* **2007**, *48*, 5742.

(7) Yoshioka, T.; Dersch, R.; Tsuji, M.; Schaper, A. K. *Polymer* **2010**, *51*, 2383.

(8) Dersch, R.; Liu, T.; Schaper, A. K.; Greiner, A.; Wendorff, J. H. *J. Polym. Sci., Part A: Polym. Chem.* **2003**, *41*, 545.

(9) Chen, X.; Dong, B.; Wang, B.; Shah, R.; Li, C. Y. *Macromolecules* **2010**, *43*, 9918.

(10) Williams, D. B.; Carter, C. B. *Transmission Electron Microscopy.*, 2nd ed.; Springer: New York, 2009; Vol. *1*.

(11) Ji, Y.; Li, B.; Ge, S.; Sokolov, J. C.; Rafailovich, M. H. *Langmuir* **2005**, *22*, 1321. Liu, Y.; Chen, S.; Zussman, E.; Korach, C. S.; Zhao, W.; Rafailovich, M. *Macromolecules* **2011**, *44*, 4439.

(12) Burman, M.; Arinstein, A.; Zussman, E. *EPL-Europhys. Lett.* **2011**, *96*, 16006.

(13) Arinstein, A.; Burman, M.; Gendelman, O.; Zussman, E. *Nat. Nanotechnol.* **2007**, *2*, 59.

(14) Bellan, L. M.; Craighead, H. G. *Polymer* **2008**, *49*, 3125.

(15) Lefèvre, T.; Pellerin, C.; Pézolet, M. Characterization of molecular orientation. In *Molecular Characterization and Analysis of Polymers*; Chalmers, J. M., Meier, R. J., Eds.; Elsevier: Amsterdam, 2008; Vol. *53*, p 295.

(16) Tanaka, M.; Young, R. *J. Mater. Sci.* **2006**, *41*, 963.
(17) Bower, D. I. *J. Polym. Sci., Polym. Phys. Ed.* **1981**, *19*, 93.
(18) Nomura, S.; Kawai, H.; Kimura, I.; Kagiyama, M. *J. Polym. Sci., Part A-2: Polym. Phys.* **1970**, *8*, 383.
(19) Rousseau, M.-E.; Lefèvre, T.; Beaulieu, L.; Asakura, T.; Pézolet, M. *Biomacromolecules* **2004**, *5*, 2247.
(20) Bower, D. I. *J. Polym. Sci., Polym. Phys. Ed.* **1972**, *10*, 2135.
(21) Pigeon, M.; Prud'homme, R. E.; Pézolet, M. *Macromolecules* **1991**, *24*, 5687.
(22) Lagugné-Labarthet, F.; Buffeteau, T.; Sourisseau, C. *J. Phys. Chem. B* **1998**, *102*, 5754.
(23) Turrell, G. *J. Raman Spectrosc.* **1984**, *15*, 103.
(24) Štokr, J.; Schneider, B.; Doskočilová, D.; Lövy, J.; Sedláček, P. *Polymer* **1982**, *23*, 714.
(25) Purvis, J.; Bower, D. I. *J. Polym. Sci., Polym. Phys. Ed.* **1976**, *14*, 1461.
(26) Lesko, C. C. C.; Rabolt, J. F.; Ikeda, R. M.; Chase, B.; Kennedy, A. *J. Mol. Struct.* **2000**, *521*, 127.
(27) Jarvis, D. A.; Hutchinson, I. J.; Bower, D. I.; Ward, I. M. *Polymer* **1980**, *21*, 41.
(28) Melveger, A. J. *J. Polym. Sci., Part A-2: Polym. Phys.* **1972**, *10*, 317.
(29) Adar, F.; Noether, H. *Polymer* **1985**, *26*, 1935.
(30) Kim, K.; Lee, K.; Khil, M.; Ho, Y.; Kim, H. *Fibers Polym.* **2004**, *5*, 122.
(31) Liu, Y.; Antaya, H.; Pellerin, C. *J. Polym. Sci., B: Polym. Phys.* **2008**, *46*, 1903.
(32) Yang, S.; Michielsen, S. *Macromolecules* **2003**, *36*, 6484.
(33) Boerio, F. J.; Bailey, R. A. *J. Polym. Sci.: Polym. Lett. Ed.* **1974**, *12*, 433.
(34) Garton, A.; Carlsson, D. J.; Holmes, L. L.; Wiles, D. M. *J. Appl. Polym. Sci.* **1980**, *25*, 1505.
(35) Yang, S.; Michielsen, S. *Macromolecules* **2002**, *35*, 10108. Yang, S.; Michielsen, S. *J. Polym. Sci., B: Polym. Phys.* **2004**, *42*, 47.
(36) Manley, T. R.; Williams, D. A. *Polymer* **1969**, *10*, 339.
(37) Cole, K. C.; Ajji, A.; Pellerin, É. *Macromolecules* **2002**, *35*, 770.
(38) Pellerin, C.; Pézolet, M.; Griffiths, P. R. *Macromolecules* **2006**, *39*, 6546.
(39) Ajji, A.; Guèvremont, J.; Cole, K. C.; Dumoulin, M. M. *Polymer* **1996**, *37*, 3707. Cole, K. C.; Ajji, A.; Pellerin, É. *Macromol. Symp.* **2002**, *184*, 1.
(40) Rodríguez-Cabello, J. C.; Quintanilla, L.; Pastor, J. M. *J. Raman Spectrosc.* **1994**, *25*, 335.
(41) Kawakami, D.; Hsiao, B. S.; Burger, C.; Ran, S.; Avila-Orta, C.; Sics, I.; Kikutani, T.; Jacob, K. I.; Chu, B. *Macromolecules* **2004**, *38*, 91.
(42) Frisk, S.; Ikeda, R. M.; Chase, D. B.; Rabolt, J. F. *Appl. Spectrosc.* **2003**, *57*, 1053.
(43) Lefèvre, T.; Rousseau, M.-E.; Pézolet, M. *Appl. Spectrosc.* **2006**, *60*, 841.
(44) Rodríguez-Cabello, J. C.; Merino, J. C.; Quintanilla, L.; Pastor, J. M. *J. Appl. Polym. Sci.* **1996**, *62*, 1953.
(45) Everall, N.; Tayler, P.; Chalmers, J. M.; MacKerron, D.; Ferwerda, R.; van der Maas, J. H. *Polymer* **1994**, *35*, 3184.
(46) Natarajan, S.; Michielsen, S. *J. Appl. Polym. Sci.* **1999**, *73*, 943.
(47) Lin, S.-B.; Koenig, J. L. *J. Polym. Sci., Polym. Phys. Ed.* **1982**, *20*, 2277.

Macromolecules

Article

pubs.acs.org/Macromolecules

Reduction of Dielectric Hysteresis in Multilayered Films via Nanoconfinement

Matthew Mackey,[†] Donald E. Schuele,[†] Lei Zhu,[†,*] Lionel Flandin,[‡] Mason A. Wolak,[§] James S. Shirk,[§] Anne Hiltner,[†,∥] and Eric Baer[†,*]

[†]Department of Macromolecular Science and Engineering, Case Western Reserve University, Cleveland, Ohio 44106, United States

[‡]LEPMI, UMR 5279, CNRS, Université de Savoie, F-73376 Le Bourget Du Lac Cedex, France

[§]US Naval Research Laboratory, Washington, D.C. 20375, United States

ABSTRACT: Micro/nanolayer coextrusion was used to fabricate polycarbonate (PC)/poly(vinylidene fluoride) (PVDF) layered films with significantly reduced dielectric losses while maintaining high energy density. The high-field polarization hysteresis was characterized for layered films as a function of PVDF layer thickness (6000 to 10 nm) and composition (10 to 70 vol % PVDF), and was found to decrease with decreasing layer thickness and PVDF content. To gain a mechanistic understanding of the layer thickness (or nanoconfinement) effect, wide-angle X-ray diffraction, polarized Fourier transform infrared spectroscopy, and broadband dielectric spectroscopy were employed. The results revealed that charge migration, instead of dipole flipping, was responsible for the hysteresis in multilayered films. The absence of PVDF dipole-flipping was attributed to the nonuniform electric field distribution in the layered structure, where the field in PVDF layers were calculated to be significantly lower than that in PC layers due to large contrast in dielectric constant (~3 for PC versus ~12 for PVDF). The charges were likely to be impurity ions in the form of catalyst residue or surfactants from suspension polymerization. The characteristics of the dielectric spectroscopy relaxation indicated that ions mostly existed in the PVDF layers, and PC/PVDF interfaces prevented them from entering adjacent layers. Therefore, as the layer thickness decreases to nanometer scales, the amount of ion movement, dielectric loss, and hysteresis were decreased. This study provides clear evidence of the nanoconfinement effect in multilayered films, which advantageously decreases the hysteresis loss.

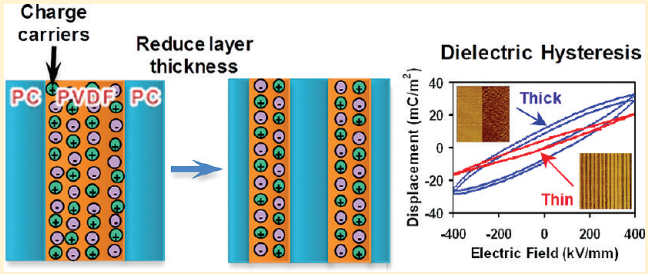

INTRODUCTION

Capacitors are vital in nearly all microelectronics and electronic devices, ranging from cell phones and computers to automotive vehicles and power systems.[1−3] The common uses include signal coupling/decoupling and filtering, high current sourcing, power conditioning, and pulsed power (or energy storage). Currently, there are several important motivations for developing dielectric capacitors with increased energy density and low loss. First, it is necessary for capacitors to keep pace with the global trend of electronics miniaturization. Second, with the drive to decrease fossil fuel dependence, compact/lightweight and reliable capacitors are required for applications such as hybrid electric vehicles[4] and grid converters for renewable energy sources.[5] The maximum energy density that can be stored in an insulating material is proportional to the dielectric constant times the square of the breakdown strength.[6] Therefore, highly insulating materials with both a high dielectric constant and high breakdown strength are desired. To maintain high performance and reliability, it is also necessary to maintain low losses (i.e., low-field dissipation factor and high-field hysteresis loss) since losses reduce the discharged energy density, cause dielectric heating, and limit the frequency response of the capacitor.[1]

Polymer dielectrics have recently attracted substantial research interest because of their excellent manufacturing/processing advantages and electrical insulating properties. From a manufacturing point of view, polymers are easy to produce and process on a large scale, which makes them inexpensive. They are also lightweight with good mechanical properties. Regarding their electrical properties, polymers generally have a high breakdown strength and low losses.[7] Two widely used state-of-the-art polymer dielectrics are biaxially oriented polypropylene (BOPP) and poly(ethylene terephthalate) (PET), which have the following measured properties: material level energy density of 5−6 J/cm^3 at breakdown, dielectric constant of 2−3, breakdown strength of 600−700 MV/m, and tan δ of 0.0003−0.002.[2]

In spite of extensive and far-reaching research efforts, realization of high performance dielectric materials with increased energy density and low loss is still an important goal. One method of improving the energy density and performance is to combine two or more different materials by blending or *in situ* polymerization. Several common fillers for

Received: October 12, 2011
Revised: January 9, 2012
Published: February 3, 2012

Table 1. Details of the 50PC/50PVDF Multilayered Films and the Corresponding Thermal Properties

composition (vol %) (PC/PVDF)	no. of layers	film thickness (μm)	PVDF layer thickness (nm)	PVDF crystallinity (%)	T_m (°C)	T_c (°C)
PVDF control	-	12	-	51	171	131
PC control	-	12	-	-	T_g: 150	-
50/50	2	12	6000	48	171	132
50/50	2	6	3000	50	171	131
50/50	8	12	1500	46	171	131
50/50	8	6	750	45	171	132
50/50	32	12	380	45	171	130
50/50	32	6	187	43	172	132
50/50	256	12	50	42	171	128
50/50	256	6	25	42	171	129

high energy density polymer nanodielectrics include barium titanate,[8−12] lead zirconate titanate,[13] and titanium dioxide.[14,15] Other techniques aim to modify BOPP (or PET)[16] or synthesize specialized copolymers and terpolymers, e.g., poly(vinylidene fluoride-*co*-chlorotrifluoroethylene) [P(VDF-CTFE)] and P(VDF-*co*-trifluoroethylene-*co*-chlorotrifluoroethylene) [P(VDF-TrFE-CTFE)].[6,17,18] Often, the approaches produce an enhancement in one of the properties (e.g., energy density) but a reduction in another (e.g., dielectric and hysteresis losses). Other common issues include commercial viability, scale-up, cost, and mechanical/thermal stability, which are difficult for newly synthesized materials.[19,20]

To improve electrical properties while maintaining mechanical integrity and commercial viability requirements, we have used the novel polymer processing technique of micro/nanolayer coextrusion to produce layered structures. This processing technique includes the combination of 2 or 3 polymers in an ABABABAB, ABCABCABC, or ABCBABCB configuration, creating films with 2 to 4096 layers and layer thicknesses ranging from tens of micrometers down to less than 10 nm.[21] Prior research has shown that useful changes occur in the mechanical, optical,[22−24] and transport properties,[25] as the layer thickness is reduced to nanometer scales. From a dielectric standpoint, analogous changes are expected and electrical properties can be optimized by independently varying the layer thickness and film composition. The layered film containing one high dielectric constant material [P(VDF-*co*-hexafluoropropylene), P(VDF-HFP)] and one high breakdown strength material [polycarbonate (PC)] has been previously studied and shown to provide significant enhancements in breakdown strength.[26,27]

In this report, the nanoconfinement effect from multilayering of PC and PVDF on reducing low-field dielectric and high-field hysteresis losses is explored. It is found that ion migration in PVDF layers, rather than PVDF dipole switching, is responsible for both dielectric and hysteresis losses. Note that the PVDF is synthesized by suspension polymerization. Therefore, the ionic impurity should originate from surfactant residue. On the basis of a simulation study using the diffusion model by Sawada,[28,29] the diffusion coefficient and concentration of the impurity ions were estimated to be 2×10^{-13} m^2/s and <1 ppm (by weight), respectively. By decreasing the PVDF layer thickness down to a few tens of nanometers, both low and high field losses can be significantly reduced. On the basis of this finding, the synergistic effect of thin layers and additives on the physical properties may open a door to new engineering practice in many other applications.

EXPERIMENTAL SECTION

Materials. Two polymers were used in this study, one for its high breakdown strength and the other for its high dielectric constant. PC, Calibre 200−6 with a molecular weight of 24 500 g/mol from Dow Chemical Company, was chosen as the high breakdown strength material. PVDF homopolymer, Solef 6010 with a molecular weight of 64 000 g/mol from Solvay Solexis, was chosen as the high dielectric constant material. A set of PC/PVDF multilayered films was produced using microlayer coextrusion (Table 1). The films were coextruded with sacrificial polyethylene (PE) skin layers on both sides of the layered film in order to improve the film surface smoothness, handleability, and immunity to damage. This skin was peeled off before any measurements were carried out. In addition to the 50/50 PC/PVDF films in Table 1, compositions of 90/10, 70/30, 30/70, and 10/90 were also produced. A coextrusion temperature of 250 °C was chosen based on the rheological compatibility of the two polymers. The polymer rheology was characterized using a melt flow indexer (MFI), on Kayeness Galaxy 1, at a shear rate that is similar to extrusion conditions (10 s^{-1}). Prior to processing the PC resin, it was dried in a vacuum oven at 80 °C for 48 h.

Atomic Force Microscopy (AFM). The layered film cross sections were imaged using AFM. The samples were prepared by embedding the films in epoxy and microtoming at −40 °C with an ultramicrotome (Leica EM FC6). Phase and height images of the cross sections were recorded simultaneously at ambient temperature in air using the tapping mode of a Nanoscope IIIa MultiMode scanning probe (Digital Instruments, Santa Barbara, CA).

Dielectric Hysteresis Measurements. Electric displacement−electric field (D−E) hysteresis measurements were carried out on a Premiere II ferroelectric tester from Radiant Technologies, Inc. The applied voltage was a bipolar triangular waveform at 1 Hz. An electrostatic sandwich technique was used to apply electrodes, which were 5.8 μm metalized BOPP films, on both sides of the film.[30] An 80 μm thick Kapton mask with a 1 cm diameter hole was used to control the area under high fields. In each sample, electric fields from 100 to 500 MV/m were applied to the sample in 50 MV/m increments. This electrostatic sandwich setup performed better without any insulating oils because the oil could prevent two metalized BOPP films from coming together and establishing a tight contact with the test film. To ensure safety, all high field measurements were remotely controlled with a computer.

X-ray Diffraction. Wide-angle X-ray diffraction (WAXD) patterns were obtained by aligning the incident X-ray beam parallel to the extrusion direction (ED) of the film. The measurements were performed on a Rigaku MicroMax-002$^+$ diffractometer at 45 kV and 0.88 mA. A Confocal Max-Flux optics was used with a sealed tube microfocus X-ray source, giving a highly focused beam of monochromatic Cu Kα radiation (λ = 0.154 nm). The sample-to-detector distance was 140 mm, and the diffraction angle was calibrated using a CaF_2 standard. The patterns were collected using an image plate with a 50 μm pixel size.

Electric Field Dependent Polarized Fourier Transform Infrared (FTIR). Polarized FTIR under electric field was carried out on a Nexus 870 FTIR ESP from Nicolet with the polarizer fixed at the

perpendicular configuration, i.e., the angle between the film stretching direction and the polarizing light was 90°. Films were stretched about four times at 120 °C using a homemade uniaxial stretching machine in a Blue-M gravity oven. Carbon electrodes were evaporated onto both sides of the film using a Denton Bench Top Turbo III high vacuum evaporator. The thickness of carbon electrodes was optimized so that the resulting resistance was several kΩ with a baseline transmittance of 80−90%.[31−33] High electric fields were supplied with a Matsusada AMT-20B10−B high voltage amplifier.

Dielectric Spectroscopy. Broadband dielectric spectroscopy measurements were performed on a Novocontrol unit (0.001 Hz to 100 kHz, 25 to 200 °C) under a vacuum of 40 mTorr. Sample was prepared by evaporating 30 nm thick aluminum electrodes with 1 cm diameter to both sides of the test film.

RESULTS AND DISCUSSION

Effect of Layering on High-Field Polarization Hysteresis. The layer integrity and uniformity were examined using phase contrast atomic force microscopy (AFM), as shown in Figure 1. There were no structural defects in the multilayered films such as layer breakup or interlayer connection, which is the advantage of forced assembly using microlayer coextrusion.[21,25] The layer thickness and standard deviation were determined from the AFM images in Figure 1 to be 6200 ± 780 nm, 1600 ± 160 nm, 400 ± 90 nm, and 50 ± 10 nm for 50PC/50PVDF 2-, 8-, 32-, and 256-layer films, respectively. These measured thicknesses are in good agreement with the nominal layer thicknesses given in Table 1 in the Experimental Section. Here, an individual film is named as *xx*PC/*yy*PVDF (*LL* μm/*ZZ* nm), where *xx* and *yy* are volume percentages of PC and PVDF, *LL* is the total film thickness, and *ZZ* is the PVDF layer thickness. This nomenclature will be used throughout the paper.

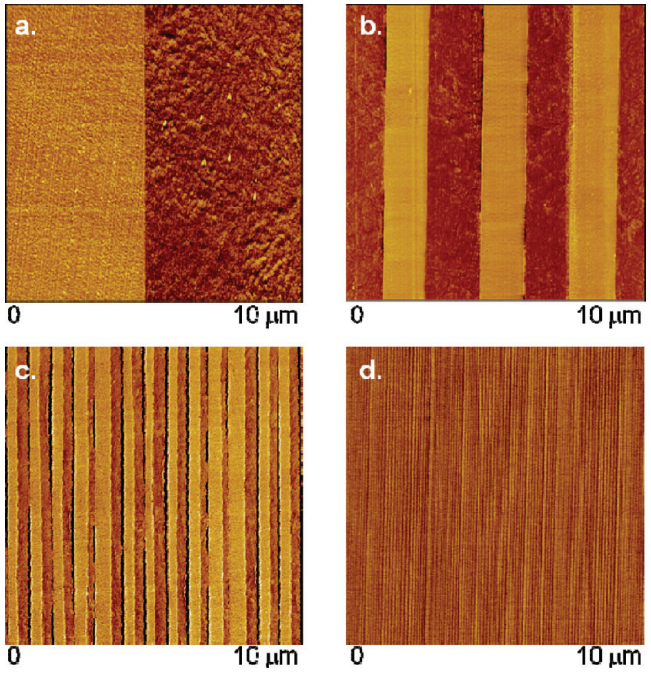

Figure 1. AFM phase images of 50PC/50PVDF layered film cross sections. Key: (a) 2 layers (12 μm/6000 nm); (b) 8 layers (12 μm/1500 nm); (c) 32 layers (12 μm/375 nm); (d) 256 layers (12 μm/50 nm). The light and dark colored layers are PC and PVDF, respectively.

To determine the effect of layer confinement on *D*−*E* hysteresis, measurements were carried out on PC/PVDF layered films and controls. For clarity, a single field sweep at 400 MV/m is shown for the two controls. For the layered films, field sweeps at 100, 200, 300, and 400 MV/m are shown. The PC control exhibited low hysteresis, which was expected for linear dielectric materials, and the PVDF control had a large hysteresis loop with dipole saturation at high fields, which was typical of ferroelectric materials (Figure 2a).[34] The hysteresis behavior of layered films showed intermediate levels of electric displacement relative to the controls, i.e., larger loops than PC but no dipole saturation at high fields (400−500 MV/m) as seen for the PVDF control (Figure 2).

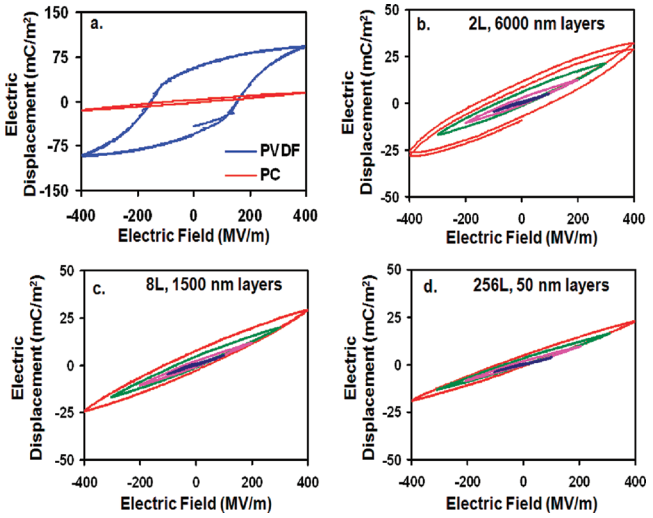

Figure 2. *D*−*E* hysteresis loops of monolithic controls and 50PC/50PVDF layered films with different layer thicknesses. Key: (a) monolithic PC and PVDF controls, 12 μm thick; (b) 2 layers (12 μm/6000 nm); (c) 8 layers (12 μm/1500 nm); (d) 256 layers (12 μm/50 nm). Each loop at a given electric field has two poling cycles. For parts b−d, blue, magenta, green, and red loops correspond to the poling field being 100, 200, 300, and 400 MV/m, respectively.

The effects of layer thickness, electric field, and film composition on dielectric hysteresis were studied for the PC/PVDF layered films. In parts b−d of Figure 2, reducing layer thickness caused a substantial decrease in the hysteresis. These results were quantified and generalized by calculating the hysteresis loop area as a function of layer thickness for several different compositions and electric fields (Figure 3). It was found that thinner layers had a beneficial effect on the hysteresis at different electric fields (300−500 MV/m) and compositions (10−70 vol % PVDF) (see Figure 3). When independently studying the effects of composition and electric field on hysteresis, the hysteresis loop area increased with increasing the PVDF content and electric field. When the PVDF volume fraction was 90 vol %, the high-field hysteresis loop substantially opened up and became similar to that of PVDF in Figure 2A (data not shown), suggesting that when the PC layer thickness was too thin as compared to the thickness of PVDF, the PC layers had almost no effect on reducing the hysteresis loss. Therefore, no comparison was made for PC/PVDF 10/90 multilayered films in Figure 3.

The above results provided us the following information. First, the composition effect indicated that PVDF layers were responsible for the hysteresis, which was consistent with the large hysteresis of the PVDF control. Regarding the effect of electric field, a higher field caused a greater electric displace-

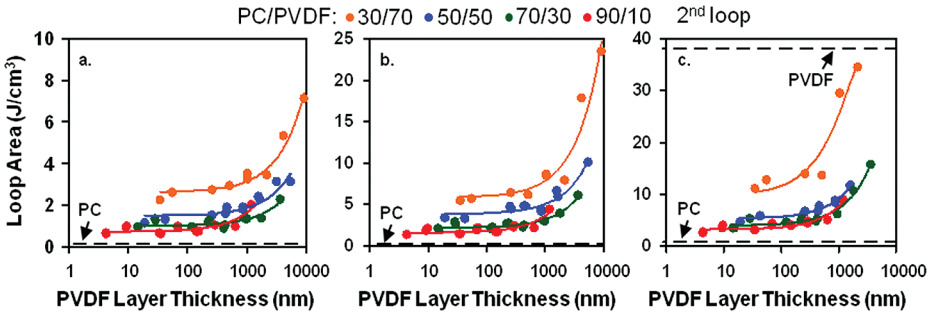

Figure 3. Hysteresis loop area of layered films as a function of PVDF layer thickness for different layer compositions at (a) 300 MV/m, (b) 400 MV/m, and (c) 500 MV/m, respectively.

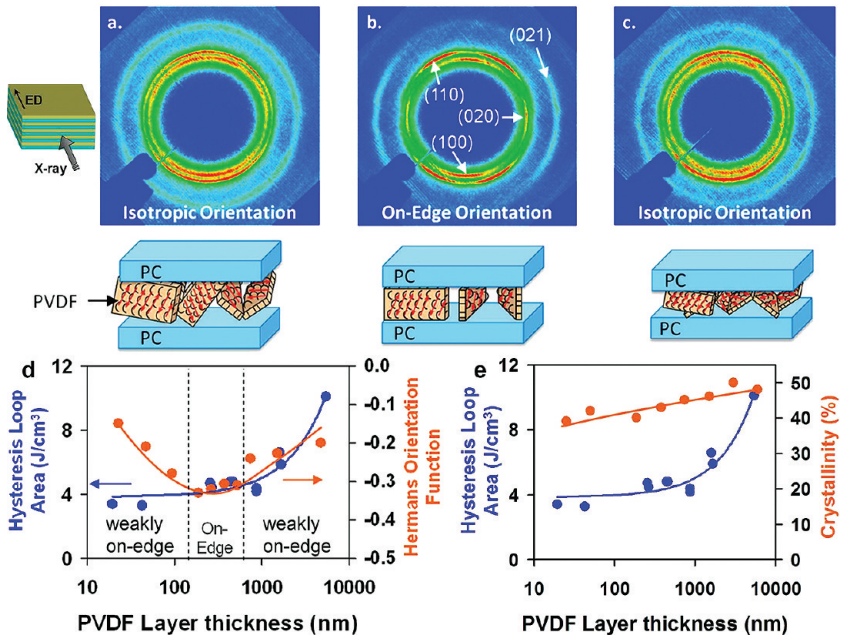

Figure 4. WAXD patterns of 50PC/50PVDF layered films: (a) 8 layers (12 μm/1500 nm); (b) 32 layers (12 μm/380 nm); (c) 256 layers (12 μm/50 nm). The X-ray beam is parallel to the extrusion direction (ED, see the inset scheme). (d) Hysteresis loop area and Hermans orientation function as a function of layer thickness for 50PC/50PVDF layered films. (e) Hysteresis loop area and PVDF crystallinity as a function of layer thickness for 50PC/50PVDF layered films.

ment, part of which originated from the irreversible polarizations (e.g., dipoles in ferroelectric crystals and ions in the amorphous phase).[7] The mechanism behind the layer thickness effect was, however, not immediately apparent. To determine why nanolayers had reduced hysteresis, polarized FTIR and broadband dielectric spectroscopy experiments were carried out to differentiate the effect of dipole switching from that of ion migration.

Ferroelectric Dipole Switching in Multilayered Films. The large dielectric hysteresis in PVDF-based polymers is most commonly attributed to dipolar switching where the dipoles in ferroelectric crystals rotate in response to an applied field.[34] In contrast to ferroelectric PVDF, paraelectric materials like PC, PET, and BOPP exhibit almost no hysteresis because orientational polarization does not exist in the sample.[7] Knowing that the hysteresis in layered films can originate from orientational polarization in PVDF layers, we propose that the possible hysteresis mechanism in layered films might originate from dipole switching, which can be experimentally determined using field-dependent polarized FTIR on uniaxially oriented films.

Because dipole switching is typically associated with ferroelectric crystals, we first examined the crystal orientation in the PVDF layers as a function of layer thickness, using WAXD. With decreasing the layer thickness, the crystal orientation went from weakly on-edge (Figure 4a) to on-edge (Figure 4b) and back to weakly on-edge (Figure 4c) with a maximum on-edge orientation occurring in films with 200 nm PVDF layers (Figure 4d). Here, weakly on-edge indicated that the crystallographic *a*-axes had some tendency of being perpendicular to the layers. This unexpected trend was reproducible and some explanation of the behavior was given in ref 35. The on-edge orientation is expected to contribute to increased rather than decreased hysteresis,[36] because the CH_2CF_2 dipoles are nearly perpendicular to the chain axes and in a plane parallel to applied field. Therefore, the WAXD results in Figure 4d implied that dipole switching should not correlate with the reduced hysteresis as PVDF layer thickness decreased. The crystallite size can be estimated using the Scherrer equation from the peak width of WAXD reflections in Figure 4. The peak width and thus crystallite size of WAXD reflections was not much affected by the layer thickness. Therefore, the reduced hysteresis could not be attributed to

dx.doi.org/10.1021/ma202267r | *Macromolecules* 2012, 45, 1954–1962

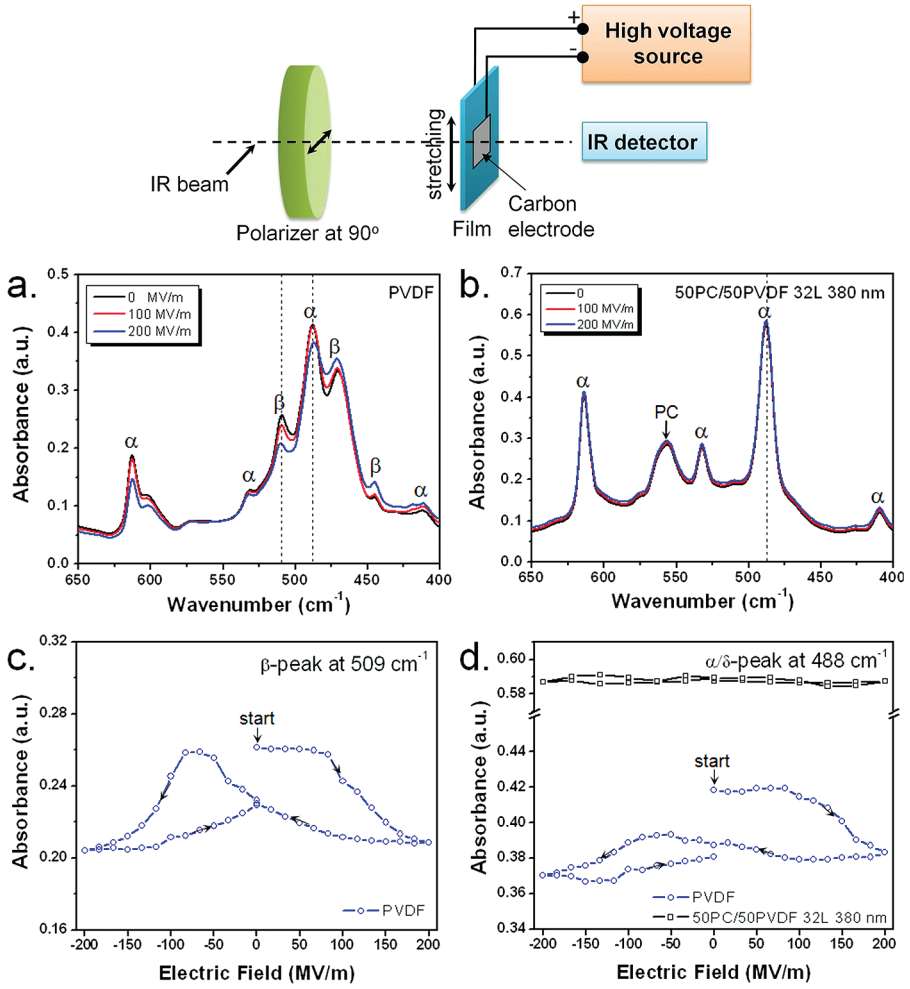

Figure 5. Polarized FTIR spectra of uniaxially oriented (a) PVDF and (b) 50PC/50PVDF (12 μm/380 nm) films under different electric fields. The stretching ratios were 400% and 370% for PVDF and 50PC/50PVDF (12 μm/380 nm) films, respectively. The polarized light is perpendicular to the film stretching direction (see the top panel for the polarized FTIR experimental setup). For clarity, each spectrum in part b is offset by 0.005 (absorbance) to avoid complete overlap. (c) The β-peak absorbance at 509 cm^{-1} and (d) the α/δ-peak absorbance at 488 cm^{-1} as a function of electrical field for uniaxially oriented PVDF and 50PC/50PVDF (12 μm/380 nm) films. The start and change of electric field are shown by arrows in (c) and (d).

changes in the crystallite size.[37] Because the dipole switching-derived hysteresis can only occur in the crystals, the crystallinity of PVDF as a function of layer thickness was also investigated (Figure 4e). The crystallinity decreased from 51% to 42% as the PVDF layer thickness decreased from 6000 to 25 nm. A 9% decrease in crystallinity, however, could not simply account for such a substantial decrease in hysteresis (Figure 4e).

Field-dependent polarized FTIR spectra for uniaxially oriented PVDF and 50PC/50PVDF (12 μm/380 nm) films are shown in Figure 5, parts a and b, respectively. Uniaxial stretching was used to maximize the 509 and 488 cm^{-1} absorbance intensities by orienting the CF_2 dipoles parallel to the polarized light. Our experimental result showed that uniaxial stretching did not change the shape and magnitude of hysteresis loops as compared to the unstretched film. The polarized light was perpendicular to the film stretching direction (see the top panel of Figure 5). Because the PVDF control film was stretched at 120 °C, both α and β characteristic peaks were seen in Figure 5a.[34,38] Upon varying the applied field, the absorbance for both β and α/δ peaks changed (note that PVDF α-phase will transform into δ-phase upon electric poling above 100 MV/m[39]). Typical results for the β-peak at 509 cm^{-1} and α/δ-peak at 488 cm^{-1} are shown in Figure 5, parts c and d, respectively. As expected, butterfly shaped hysteresis loops were observed in both figures, indicating that dipoles switched in response to the applied field.[34] For the 50PC/50PVDF (12 μm/380 nm) film, only α-phase was observed despite that it was stretched at 120 °C to 3.7 times its original length (see Figure 5b). Note that there was no significant interference of the PC absorbance in the range between 400 and 650 cm^{-1}. In addition, the absorbance of the α/δ-peak at 488 cm^{-1} does not vary with the applied electric field. From this result, we conclude that there is no dipole switching in PC/PVDF layered films. This can be understood from the following analysis. Assuming that relative dielectric constants for PC and PVDF are $\varepsilon_{r,PC} = 3$[26] and $\varepsilon_{r,PVDF} = 12$,[27,36] respectively, the nominal electric fields (E) in PC and PVDF layers in a serial capacitor model are as follows:[27,40]

$$E_{PC} = E_0\left[\phi_{PC}\left(1 - \frac{\varepsilon_{r,PC}}{\varepsilon_{r,PVDF}}\right) + \frac{\varepsilon_{r,PC}}{\varepsilon_{r,PVDF}}\right]^{-1} \quad (1)$$

dx.doi.org/10.1021/ma202267r | Macromolecules 2012, 45, 1954–1962

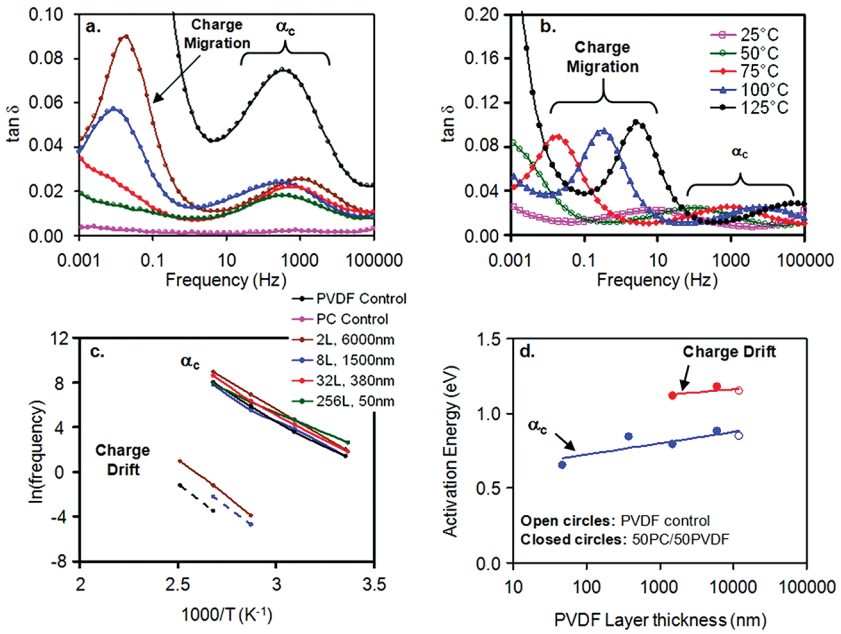

Figure 6. Dielectric spectroscopy of (a) 50PC/50PVDF layered films at 75 °C for different layer thicknesses and (b) the 50PC/50PVDF (6 μm/3000 nm) film as a function of frequency at different temperatures. Activation energy plots of 50PC/50PVDF (12 μm) layered films: (c) ln(peak frequency) as a function of reciprocal temperature and (d) activation energy as a function of layer thickness for both charge migration and α_c relaxation processes. The legends in part c are also for part a.

$$E_{PVDF} = E_0\left[\phi_{PC}\left(\frac{\varepsilon_{r,PVDF}}{\varepsilon_{r,PC}} - 1\right) + 1\right]^{-1} \quad (2)$$

Here E_0 is the external electric field and ϕ_{PC} is the volume fraction of PC. When the external electric field is 200 MV/m for a 50PC/50PVDF film, the nominal fields in PC and PVDF layers are calculated to be 320 and 80 MV/m, respectively. In addition, the coercive field could increase as the PVDF thickness decreased to the nanometer range, making dipole switching more difficult in layered films.[41,42] Therefore, we consider that it is the low nominal electric field in thin PVDF layers (80 MV/m) that prevent the dipole switching in the layered films. Further increase the poling electric field may be able to induce dipole flipping in PVDF. Nevertheless, this may exceed the electric breakdown field of the film and cannot be experimentally achieved.

Given no dipole-flipping in PVDF, we would like to ask: What is the possible reason for the reduced hysteresis as the PVDF layer thickness decreases? As we know, there are five types of polarization in polymers, namely, electronic, atomic, (dipolar) orientational, ionic, and interfacial polarizations.[7] Electronic and atomic polarizations take place in the optical and infrared frequencies. Therefore, there should be no loss at all from electronic and atomic polarizations at the 10 Hz poling frequency. Because PVDF dipoles do not flip, the observed hysteresis can only originate from ionic and/or interfacial (or Maxwell–Wagner–Sillars[7]) polarizations. If the observed hysteresis originates from interfacial polarization, the more layers in the multilayer film will have more interfaces and in turn will result in greater hysteresis loss. This is contradictory to the above experimental observation. Therefore, the observed hysteresis can only originate from ionic polarization. The question then is: Why the hysteresis decreases as the PVDF layer thickness decreases in PC/PVDF multilayer films?

Charge Migration. If charge migration exists, broadband dielectric spectroscopy can be used to detect the ion motion.[43,44] Measurements were carried out on the controls and 50PC/50PVDF layered films as a function of layer thickness and temperature (Figure 6). Two dielectric relaxations were observed over the frequency (0.001–100 kHz) and temperature (25–125 °C) ranges tested: one at a high frequency (1 kHz at 75 °C) which is not affected by layer thickness and another at a low frequency (0.02 Hz at 75 °C) which is layer thickness dependent. The high frequency relaxation peak occurred in both the PVDF control and layered films and is known in the literature as the α_c relaxation of α-form PVDF associated with the dipole wagging along the helical axes.[36,45] The α_c relaxation was not significantly affected by layer thickness because the molecular origins are much smaller than the thinnest layers. In contrast, the low frequency relaxation was affected by layer thickness, which indicates that the underlying mechanism had a length scale on the order of micrometers to nanometers; these characteristics are typical of ion migration.[43,44,46] On the basis of the tan δ of the controls (Figure 6a), the impurity ions are predominantly in the PVDF layers rather than the PC layers because the tan δ of the PVDF control increased sharply at low frequencies due to ionic conduction while the PC control was relatively flat over the entire frequency range (Figure 6a). The dielectric spectra for the 50PC/50PVDF (6 μm/3000 nm) film were also collected at temperatures ranging from 25 to 125 °C (Figure 6b). As expected from time–temperature superposition, the relaxations shifted to higher frequency with increasing temperature. This was used to calculate the activation energies of both charge migration and α_c processes for the layered films and PVDF control as a function of the layer thickness (Figure 6, parts c and d). Linear relationships between ln(peak frequency) and reciprocal temperature were obtained for both processes (Figure 6c), indicating that Arrhenius equation could be used to obtain the activation energies. Values of 0.85 and 1.15 eV (1

dx.doi.org/10.1021/ma202267r | Macromolecules 2012, 45, 1954–1962

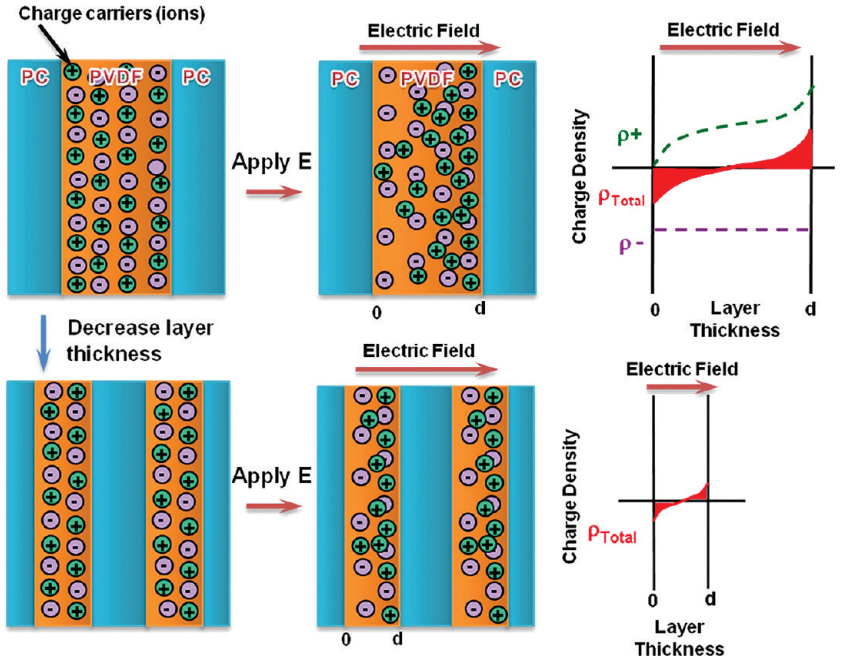

Figure 7. Schematic of charge migration in layered films: (top panel) thick layers and (bottom panel) thin layers. Both positive and negative ions are needed to maintain a zero net charge. For simplicity, it is assumed that only one of the charge carriers moves. After an electric field is applied, there is a gradient in charge concentration. Compared with thick PVDF layers, thin PVDF layers have less charge motion and total charge buildup.

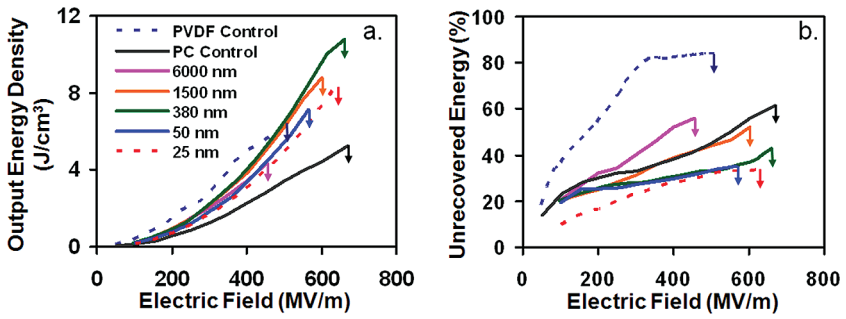

Figure 8. (a) Output energy density and (b) percent unrecovered energy of 50PC/50PVDF films as a function of electric field. To confirm reliability, each measurement was repeated twice.

eV = 96.3 kJ/mol) were obtained for the activation energies in the α_c and charge migration relaxations, respectively (Figure 6d). The activation energies of the α_c and charge migration processes were comparable with those reported in the literature.[44,47,48] Regarding the effect of layer thickness, the α_c activation energy decreased as the layers became thinner. This might be caused by the greater fraction of interphase material in films with thinner layers. The interphase usually exhibits a set of properties different from the bulk material.[49,50]

The details of charge migration[51] adapted to a layered film structure are explained as follows. Ions, in the form of surfactant residue (Solef 6010 is synthesized from suspension polymerization according to the manufacturer datasheet),[7] are initially homogeneously dispersed in the PVDF layer. To maintain charge neutrality, the same number of positive and negative charges exists. The charges are also assumed to be confined to their respective layers because the interfaces act as barriers to ion motion as a result of the potential barrier.[7] Alternatively, due to the high resistivity of PC (i.e., value of 10^{17} Ω-cm from manufacturer datasheet) compared to PVDF (i.e., 10^{14} Ω-cm from manufacturer datasheet), it is possible that the PC layers and interfaces act as blocking electrodes causing the ions to be confined in the PVDF. When an electric field is applied, one or both of the positive and negative charges migrate to the layer interface producing a drift current and an ion concentration gradient. The migration may occur through the free volume in a manner analogous to gas diffusion in polymers.[52] The charges build up at the layer interface(s) until the drift current is balanced by the diffusion current (due to thermal motion and the repulsion of like charges) (top panel in Figure 7). In films with thinner PVDF layers, the amount of ion motion and charge buildup at the interface is lower (bottom panel in Figure 7), which decreases the hysteresis at high fields and the amplitude of the charge migration dielectric loss peak at low fields. In addition, the small charge separation in thin layers allows them to relax to equilibrium faster than in thick layers, which allows for improved output energy density. Because the concentration of ionic impurity is estimated to be less than 1 ppm (by weight),[28] it is difficult to identify the chemical structure of these impurity ions.

Effect of Layering on Output Energy Density and Hysteresis Loss. Dielectric hysteresis directly affected the output (or discharged) energy density and percent unrecovered energy, which were determined by integrating the D-E

dx.doi.org/10.1021/ma202267r | *Macromolecules* 2012, 45, 1954–1962

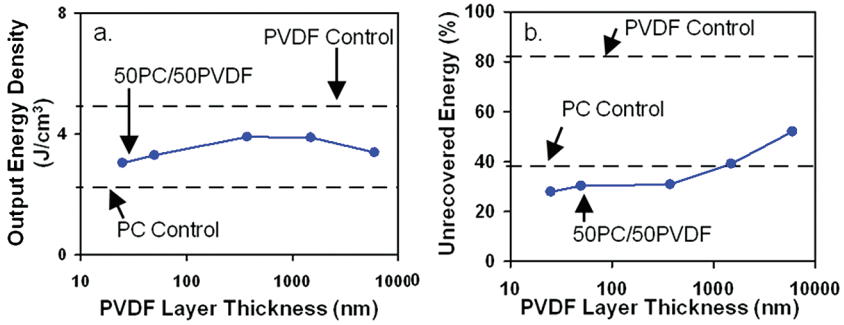

Figure 9. (a) Output energy density and (b) percent unrecovered energy of 50PC/50PVDF films as a function of layer thickness at 400 MV/m.

hysteresis loop of 50PC/50PVDF layered films and controls (Figure 8). Details of this calculation can be found in ref 19. The PVDF control had the highest output energy density at a given electric field below 450 MV/m, whereas the PC control had the lowest. The 50PC/50PVDF layered films were between these two controls; however, the enhanced breakdown strengths of the layered films resulted in higher output energy densities (e.g., the output energy density for the 50PC/50PVDF (12 μm, 380 nm) was as high as 11 J/cm^3). Regarding the percent unrecovered energy, both layered films and PC control had significantly lower unrecovered energy than the PVDF control. The percent unrecovered energy also decreased as the layers became thinner. For example, for the 50PC/50PVDF (12 μm, 380 nm) film the percent unrecovered energy density was lower than that of the PC control while still having an increased output energy density at breakdown. This indicated that the confined PVDF/PC layers were more efficient at discharging electric energy compared to the PC bulk control because the ion migration was hindered by the layered structure and interfaces. The result also showed that the 2-layer film had a low breakdown strength, indicating that more than two layers were required for high breakdown strength. A cross-plot of Figure 8 was produced at 400 MV/m to illustrate the layer thickness effect (Figure 9). Obviously, the layered structure with the PVDF layer thinner than 380 nm was effective at reducing hysteresis while also enhancing the output energy density.

■ CONCLUSIONS

Multilayered films with alternating PC and PVDF were fabricated with layer thicknesses ranging from 6000 nm to less than 10 nm and compositions from 10 to 70 vol % PVDF. The layered structure provided a beneficial effect, i.e., the hysteresis decreased with decreasing layer thickness. Using polarized FTIR and broadband dielectric spectroscopy techniques to investigate dipole switching and charge migration, respectively, the underlying mechanism responsible for the high-field hysteresis was determined to be charge migration in the PVDF layers. More specifically, the dielectric spectra of the layered films exhibited a low frequency relaxation process (E_a = 1.15 eV), which was attributed to charge migration and could be attenuated by decreasing layer thickness. This indicated that the layered structure and interfaces (or PC blocking layers) prevented the charge species from passing from one layer to the next. In films with thinner PVDF layers, the amount of ion motion and charge buildup at the interface was minimized. This in turn decreased the amplitude of the charge migration-induced dielectric loss peak and hysteresis. Therefore, layered structures can be utilized to eliminate the low and high field losses in impure materials, which is very beneficial since chemical purification processes are time-consuming and costly. The effect of improved hysteresis in the layered films was significant because they could achieve increased energy density and reduced loss at the same time. For example, the 50PC/50PVDF (12 μm/380 nm) film had an output energy density of 11 J/cm^3 but a percent unrecovered energy significantly lower even than that of the PC control. These findings also have important practical implications in other electronic applications that employ polymeric materials (i.e. semiconductor materials, liquid crystal displays, and electrical insulation). For insulating materials, it is desirable to remove and prevent the generation of charge carriers that may cause ionic or dc conduction. Other applications, however, may benefit from added ions to exploit ionic conduction. The multilayering technique demonstrated here has the potential for producing structures with enhanced properties for many of these other applications.

■ AUTHOR INFORMATION

Corresponding Author

*E-mail: lxz121@case.edu (L.Z.); exb6@case.edu (E.B.).

Notes

[‖]Professor Anne Hiltner passed away in September 2010.

■ ACKNOWLEDGMENTS

This research was generously supported by the National Science Foundation through the Center for Layered Polymeric Systems (CLiPS) Science and Technology Center (DMR-0423914) and the Office of Naval Research (N00014-10-1-0349). Jung-Kai Tseng is acknowledged for carrying out the polarized FTIR experiments.

■ REFERENCES

(1) Sarjeant, W. J.; Zirnheld, J.; MacDougall, F. W. *IEEE Trans. Plasm. Sci.* **1998**, *26*, 1368−1392.

(2) Sarjeant, W. J.; Clelland, I. W.; Price, R. A. *P. IEEE.* **2001**, *89*, 846−855.

(3) Tan, Q.; Irwin, P.; Cao, Y. *IEEJ Trans. Fund. Mater.* **2006**, *126*, 1152−1159.

(4) Husain, I., *Electric and Hybrid Vehicles: Design Fundamentals*; CRC Press: Boca Raton, FL, 2010.

(5) Teodorescu, R.; Liserre, M.; Rodríguez, P., *Grid Converters for Photovoltaic and Wind Power Systems*; Wiley: Chichester, U.K., 2011.

(6) Chu, B.; Zhou, X.; Ren, K.; Neese, B.; Lin, M. R.; Wang, Q.; Bauer, F.; Zhang, Q. M. *Science* **2006**, *313*, 334−336.

(7) Kao, K.-C., *Dielectric Phenomena in Solids: with Emphasis on Physical Concepts of Electronic Processes*. Elsevier Academic Press: Boston, MA, 2004.

(8) Kim, P.; Jones, S. C.; Hotchkiss, P. J.; Haddock, J. N.; Kippelen, B.; Marder, S. R.; Perry, J. W. *Adv. Mater.* **2007**, *19*, 1001−1005.
(9) Kim, P.; Doss, N. M.; Tillotson, J. P.; Hotchkiss, P. J.; Pan, M. J.; Marder, S. R.; Li, J.; Calame, J. P.; Perry, J. W. *ACS Nano* **2009**, *3*, 2581−2592.
(10) Li, J.; Claude, J.; Norena-Franco, L. E.; Seok, S. I.; Wang, Q. *Chem. Mater.* **2008**, *20*, 6304−6306.
(11) Guo, N.; DiBenedetto, S. A.; Kwon, D. K.; Wang, L.; Russell, M. T.; Lanagan, M. T.; Facchetti, A.; Marks, T. J. *J. Am. Chem. Soc.* **2007**, *129*, 766−767.
(12) Guo, N.; DiBenedetto, S. A.; Tewari, P.; Lanagan, M. T.; Ratner, M. A.; Marks, T. J. *Chem. Mater.* **2010**, *22*, 1567−1578.
(13) Tang, H.; Lin, Y.; Andrews, C.; Sodano, H. A. *Nanotechnology* **2011**, *22*, 015702.
(14) Maliakal, A.; Katz, H.; Cotts, P. M.; Subramoney, S.; Mirau, P. *J. Am. Chem. Soc.* **2005**, *127*, 14655−14662.
(15) Li, J.; Seok, S. I.; Chu, B.; Dogan, F.; Zhang, Q.; Wang, Q. *Adv. Mater.* **2009**, *21*, 217−221.
(16) Kita, H.; Okamoto, K.; Sakamoto, I. *Radiat. Phys. Chem.* **1986**, *28*, 393−397.
(17) Zhou, X.; Chu, B.; Neese, B.; Lin, M.; Zhang, Q. M. *IEEE Trans. Dielectr. Electr. Insul.* **2007**, *14*, 1133−1138.
(18) Lu, Y.; Claude, J.; Neese, B.; Zhang, Q.; Wang, Q. *J. Am. Chem. Soc.* **2006**, *128*, 8120−8121.
(19) Guan, F.; Wang, J.; Yang, L.; Tseng, J. K.; Han, K.; Wang, Q.; Zhu, L. *Macromolecules* **2011**, *44*, 2190−2199.
(20) Guan, F.; Wang, J.; Yang, L.; Guan, B.; Han, K.; Wang, Q.; Zhu, L. *Adv. Funct. Mater.* **2011**, *21*, 3176−3188.
(21) Ma, M.; Vijayan, K.; Hiltner, A.; Baer, E.; Im, J. *J. Mater. Sci.* **1990**, *25*, 2039−2046.
(22) Kazmierczak, T.; Song, H. M.; Hiltner, A.; Baer, E. *Macromol. Rapid Commun.* **2007**, *28*, 2210−2216.
(23) Jin, Y.; Tai, H.; Hiltner, A.; Baer, E.; Shirk, J. S. *J. Appl. Polym. Sci.* **2007**, *103*, 1834−1841.
(24) Weber, M. F.; Stover, C. A.; Gilbert, L. R.; Nevitt, T. J.; Ouderkirk, A. J. *Science* **2000**, *287*, 2451−2456.
(25) Wang, H.; Keum, J. K.; Hiltner, A.; Baer, E.; Freeman, B.; Rozanski, A.; Galeski, A. *Science* **2009**, *323*, 757−760.
(26) Wolak, M. A.; Pan, M. J.; Wan, A.; Shirk, J. S.; Mackey, M.; Hiltner, A.; Baer, E.; Flandin, L. *Appl. Phys. Lett.* **2008**, *92*, 113301.
(27) Mackey, M.; Hiltner, A.; Baer, E.; Flandin, L.; Wolak, M. A.; Shirk, J. S. *J. Phys. D: Appl. Phys.* **2009**, *42*, 175304.
(28) Sawada, A.; Tarumi, K.; Naemura, S. *Jpn. J. Appl. Phys.* **1999**, *38*, 1418−1422.
(29) Mackey, M.; Schuele, D. E.; Zhu, L.; Baer, E. 2012, to be submitted.
(30) Ho, J.; Ramprasad, R.; Boggs, S. *IEEE Trans. Dielectr. Electr. Insul.* **2007**, *14*, 1295−1301.
(31) Buchtemann, A.; Schulz, E. *Thin Solid Films* **1987**, *152*, L135−L138.
(32) Buchtemann, A.; Geiss, D. *Polymer* **1991**, *32*, 215−220.
(33) Buchtemann, A.; Schmolke, R. *J. Polym. Sci., Part B: Polym. Phys.* **1991**, *29*, 1299−1302.
(34) Nalwa, H. S., *Ferroelectric Polymers: Chemistry, Physics, and Applications*; Marcel Dekker, Inc.: New York, 1995.
(35) Mackey, M.; Flandin, L.; Hiltner, A.; Baer, E. *J. Polym. Sci., Part B: Polym. Phys.* **2011**, *49*, 1750−1761.
(36) Guan, F.; Pan, J.; Wang, J.; Wang, Q.; Zhu, L. *Macromolecules* **2010**, *43*, 384−392.
(37) Guan, F.; Wang, J.; Pan, J.; Wang, Q.; Zhu, L. *Macromolecules* **2010**, *43*, 6739−6748.
(38) Vijayakumar, R. P.; Khakhar, D. V.; Misra, A. *J. Appl. Polym. Sci.* **2010**, *117*, 3491−3497.
(39) Lovinger, A. J. *Science* **1983**, *220*, 1115−1121.
(40) Kuffel, E.; Zaengl, W. S.; Kuffel, J., *High Voltage Engineering: Fundamentals*, 2nd ed.; Butterworth-Heinemann: Oxford, U.K., and Boston, MA, 2000.
(41) Dawber, M.; Chandra, P.; Littlewood, P. B.; Scott, J. F. *J. Phys: Condens. Matter* **2003**, *15*, L393−L398.
(42) Blinov, L. M.; Fridkin, V. M.; Palto, S. P.; Bune, A. V.; Dowben, P. A.; Ducharme, S. *Usp. Fiz. Nauk* **2000**, *170*, 247−262.
(43) Rashmi; Narula, G. K.; Pillai, P. K. C. *J. Mater. Sci.* **1987**, *22*, 2006−2010.
(44) Fanggao, C.; Saunders, G. A.; Lambson, E. F.; Hampton, R. N.; Carini, G.; DiMarco, G.; Lanza, M. *J. Polym. Sci., Part B: Polym. Phys* **1996**, *34*, 425−433.
(45) Furukawa, T.; Wang, T. Measurements and Properties of Ferroelectric Polymers. In *The Applications of Ferroelectric Polymers*; Wang, T., Herbert, J. M., Glass, A. M., Eds.; Chapman and Hall: New York, 1988; Vol. *5*, pp 66−117.
(46) Haase, W.; Wróbel, S. *Relaxation Phenomena: Liquid Crystals, Magnetic Systems, Polymers, High-Tc Superconductors, Metallic Glasses*; Springer: New York, 2003.
(47) Tuncer, E.; Wegener, M.; Gerhard-Multhaupt, R. *J. Non-Cryst. Solids* **2005**, *351*, 2917−2921.
(48) Yano, S.; Okubo, N.; Takahashi, K. *Macromol. Symp.* **1996**, *108*, 279−289.
(49) Liu, R. Y. F.; Bernal-Lara, T. E.; Hiltner, A.; Baer, E. *Macromolecules* **2005**, *38*, 4819−4827.
(50) Liu, R. Y. F.; Jin, Y.; Hiltner, A.; Baer, E. *Macromol. Rapid Commun.* **2003**, *24*, 943−948.
(51) Pierret, R. F., *Semiconductor Device Fundamentals*. Addison-Wesley: Reading, MA, 1996.
(52) Miyamoto, T.; Shibayam., K. *J. Appl. Phys.* **1973**, *44*, 5372−5376.

Macromolecules

Article

pubs.acs.org/Macromolecules

Monolayers of Diblock Copolymer Micelles by Spin-Coating from *o*-Xylene on SiO_x/Si Studied in Real and Reciprocal Space

Jiun-You Liou and Ya-Sen Sun*

Department of Chemical and Materials Engineering, National Central University, Taoyuan 32001, Taiwan

Supporting Information

ABSTRACT: Polystyrene-*block*-poly(2-vinylpyridine), P(S-*b*-2VP), micelles of nanometer size and core−shell spherical shape were deposited as monolayers on silicon substrates (SiO_x/Si) with varied surface coverage using spin coating from polymer solutions in *o*-xylene of varied polymer concentration. Simply on varying the polymer solution, the micellar surface coverage on SiO_x/Si, spatial order, and organization of micelles were tailored in the monolayer regime. The surface morphology of P(S-*b*-2VP) micelles was explored with grazing-incidence small-angle X-ray scattering (GISAXS) and an atomic force microscope (AFM). Quantitative analysis and simulations of the X-ray scattering pattern were performed to derive the dependence of the structural and ordering parameters of micelles on the P(S-*b*-2VP) concentration. Four spatial arrangements were investigated. Upon progressively increased surface coverage with increasing concentration, disordered spherical micelles, loosely packed spherical micelles with hexagonal order, ordered spherical micelles with random loosely packed densities, and closely packed spherical micelles with short-range order were obtained sequentially. This system thus serves as a model for analysis of the impact of surface coverage as a function of polymer concentration on the shape, size, size distribution, and assembly of truncated micelles within two-dimensional monolayers on SiO_x/Si.

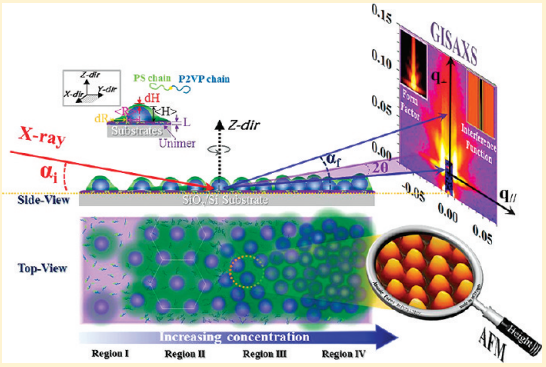

INTRODUCTION

Amphiphilic block copolymers (a-BCP) refer conventionally to long-chain amphiphiles, each of which contains a hydrophobic block and a hydrophilic block, linked by a covalent bond.[1,2] When a-BCP are dissolved in a selective solvent, the insoluble blocks tend to aggregate, whereas the soluble blocks maintain contact with the solvent, generating various micellar aggregates in solution.[1,2] In contrast, the behavior of an assembly of micelles of monolayer thickness on interfaces is diverse and versatile.[3−12] For micellar films of monolayer thickness on a solid, spherical micelles with the lateral order of a two-dimensional superlattice spontaneously develop on the solid surface that has a strong affinity with one block.[3−14] Simply on varying either the concentration of the polymer in a solvent or the spin rates, the monolayer a-BCP films were found to have ordered arrays of spherical micelles with tunable periodicity.[15] On grafting a layer of short PS chains to hinder efficiently the interfacial interactions at the substrate interface or on exposing the grafted layer to ozone and ultraviolet light for a varied duration, the morphological diversity of micelles or the hierarchical self-assembly of various micelles in monolayered films was finely tailored.[16,17] Beyond the morphological diversity of micelles on a solid interface, diverse morphologies were found for micelles on liquid surfaces. Varying the temperature effected fine-tuning of varied micellar morphologies on an ionic liquid surface,[18,19] or varying the surface pressure produced a two-dimensional self-assembly of micelles at a water/air interface.[20]

The surface morphology and lateral ordering of micellar assemblies on a substrate are generally addressed with direct imaging techniques involving a scanning electron microscope (SEM) and an atomic force microscope (AFM), but these techniques provide a localized view of the structural information with limited statistics and lack the ability to probe buried and inner structures within a film. In contrast to use of an AFM or SEM, grazing-incidence small-angle X-ray scattering (GISAXS) is a powerful tool to probe a surface or interface and the nanostructures buried in thin films.[21−32] The detectable length with X-ray scattering in a grazing-incidence geometry covers a range from less than 1 nm to hundreds of nanometers. Measurement of relief islands on a substrate or objects buried within a film near the critical angle of the substrate decreases the bulk scattering from the substrate. Through GISAXS modeling analysis with IsGISAXS software, experimental scattering data provide quantitative nanostructure information in and out of the plane of objects deposited on a substrate.[31,32]

By combining an AFM, GISAXS, and modeling of the scattering data, we quantitatively examined the size, size distribution, and lateral ordering of polystyrene-*block*- poly(2-vinylpridine), P(S-*b*-2VP), micelles on bare silicon substrates at varied surface coverage. The GISAXS data combined with

Received: November 29, 2011
Revised: February 3, 2012
Published: February 13, 2012

modeling analyses provide useful insights to characterize P(S-*b*-2VP) micelles in thin films over large areas. Our approach to prepare P(S-*b*-2VP) monolayers with varied coverage is based on spin coating from a selective solvent, *o*-xylene, containing micelles at varied mass fraction. P(S-*b*-2VP) existing as dispersed spherical micelles exhibited a narrow distribution of size in all solutions, whereas the spin-coated P(S-*b*-2VP) monolayers appeared as truncated spheres on substrates. We investigated systematically the dependence of truncated height, lateral radius, intermicellar spacing, and ordering of micelles on the P(S-*b*-2VP) concentration.

EXPERIMENTS

Sample Preparation. An asymmetric diblock copolymer P(S-*b*-2VP) having molar mass M_n = 118 500 g/mol (molar masses of the two blocks: M_n^{PS} = 48 500 g/mol and M_n^{P2VP} = 70 000 g/mol; molar mass distribution M_w/M_n = 1.13) (Polymer Source, Inc.) was used as received. Bare silicon wafers were cleaned in a piranha solution (3:7 v/v 30% H_2O_2:H_2SO_4) for 40 min, rinsed with deionized water, and dried under flowing N_2. Varied amounts of P(S-*b*-2VP) powders were dissolved in *o*-xylene. P(S-*b*-2VP) micellar films of varied surface coverage were prepared via spin coating (5000 rpm, 60 s) from *o*-xylene solutions of varied P(S-*b*-2VP) concentration in the range 0.1−1 mass %. For drying, the thin films were placed in a chamber at a maintained temperature 26 °C with humidity less than 20%.

Material Characterization. We investigated the surface of the thin films with an atomic force microscope (AFM, SPA400 Seiko) in the tapping mode. AFM images were recorded with scan ranges between 1 μm × 1 μm or 2 μm × 2 μm. We used aluminum-coated silicon cantilevers (length 150 μm, width 26 μm, thickness 300 μm); the force coefficient was ∼7.4 N/m, and the resonant frequency was 160 kHz. Measurements of small-angle X-ray scattering (SAXS) and grazing-incidence small-angle X-ray scattering (GISAXS) were performed with a Nano-Viewer (Rigaku) using Cu Kα X-rays (30 kV and 40 mA) with wavelength λ = 1.54 Å and exposure durations 20 min for GISAXS and 1 h for SAXS. The experimental GISAXS geometry is shown in Figure 1. GISAXS patterns were collected with

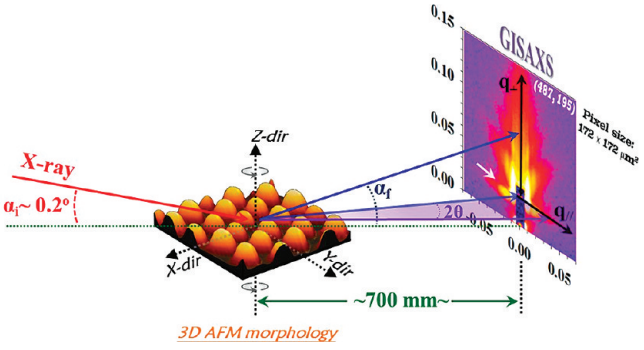

Figure 1. Schematic view of the experimental GISAXS setup. The sample is placed horizontally. The angle of incidence is α_i and the exit angle is α_f. A two-dimensional detector collects the scattered intensity, and a rod-shaped beamstop is placed before the detector to attenuate the intense direct and reflected beams. Shown is a 3D AFM topographic image revealing the surface morphology of a monolayer of truncated P(S-*b*-2VP) micelles on SiO_x/Si.

PLATUS 100 K of 83.8 × 33.5 mm^2 at incidence angle 0.2°, which is an optimal angle between the critical angles of samples and substrates. The scattering vector, q ($q = 4\pi/\lambda \sin\theta$, with scattering angle θ), in these patterns was calibrated with silver behenate. As an example, Figure 1 shows the anisotropic scattering pattern of a P(S-*b*-2VP) micellar film on a SiO_x/Si substrate prepared on spin coating at 5000 rpm from a P(S-*b*-2VP) solution (0.5%).

Analysis of SAXS Data. The scattered intensity is proportional to the product of the form and structure factors, $P(q)$ and $S(q)$.[33] The form factor is related to the shape of the scattering object and is given by the Fourier transform of its distribution of electron density. The structure factor is related to the spatial correlation about the object assembly and is expressed with a Fourier transform of the object−object pair correlation, considering a system of polydispersive homogeneous spheres with a small particle concentration, $S(q) \sim 1$. The SAXS data were analyzed with a model of polydisperse core−shell spheres, given by[34]

$$P(q) = \frac{\text{scale}}{V_t}\left[\frac{3V_c(\rho_c - \rho_s)j_1(qr_c)}{Qr_c} + \frac{3V_t(\rho_s - \rho_{solvent})j_1(qr_t)}{Qr_t}\right] + \text{bkg} \quad (1)$$

in which $j_1 = (\sin r - r\cos r)/r^2$ is a first-order Bessel function, radius is $r_t = r_c + t_s$, volume is $V_i = (4\pi/3)r_i^3$, subscripts "c" and "s" represent the P2VP core and PS shell, respectively, and t_s is the thickness of the shell. The Schultz distribution was introduced into the fitting to yield a polydispersity (PDI) in the core radius. As a result, the morphological parameters of the micelles, including the radius of the P2VP cores, the thickness of PS shells, and PDI, were extracted from the fits of SAXS data. The density of the poly(2-vinylpyridine) core is ρ_c = 1.05 mg μL^{-1}.[30] Knowing the initial mass (w^{P2VP}) of the P2VP block dissolved in *o*-xylene, we obtained the aggregation number (n_a) within each micelle and the number (n_m) of micelles in *o*-xylene according to expressions $n_a = \rho_c V_c/M_n^{P2VP}$ and $n_m = w^{P2VP}/\rho_c V_c$.[30]

Modeling of GISAXS Patterns and Profiles. In contrast to modeling of SAXS data that are mainly expressed in terms of a Born approximation (BA), the GISAXS data reveal complicated scattering patterns or profiles as a result of multiple scattering events in terms of a combination of reflection and refraction effects.[31,32] In this case, expressions of the scattering cross section of GISAXS patterns are best described with a distorted-wave Born approximation (DWBA). The software IsGISAXS was used to model the experimental GISAXS data.[31] To model the form factor, we tried varied micelle geometries, such as truncated spheres with or without a core−shell structure. The best agreements were obtained with use of a core−shell sphere with truncation along the substrate normal and the interference function of a hexagonal paracrystal of parameter D with Gaussian isotropic disorder σ_D/D. In addition to the scattered intensity from truncated micelles, a modulation of the intensity along direction $q_\perp$ is discerned (as indicated by a white arrow in Figure 1), which is associated with a homogeneous layer developed at the substrate interface.[23,35] To account for the observed intensity modulation along direction $q_\perp$, we introduced a parameter to describe the homogeneous layer of varied thickness L between a substrate and micellar objects in the simulations.

RESULTS AND DISCUSSION

P(S-*b*-2VP) Micelles in *o*-Xylene Solutions. *o*-Xylene is an effective solvent for the PS block but poor for the P2VP block. P(S-*b*-2VP) in a dilute, selective solvent is expected to form dispersed core−shell spherical micelles, each of which comprises a swollen layer of PS shell and a compact P2VP core.[15,30] To know quantitatively the average sizes and size distributions of the P(S-*b*-2VP) core−shell micelles in this work, we first employed SAXS measurements on the polymer solutions containing P(S-*b*-2VP) in *o*-xylene at mass fraction varied from 0.1 to 1 mass %. As Figure 2a shows, the SAXS profiles reveal only series of scattering maxima associated with the form factor. A feature of Bragg diffraction maxima corresponding to the structure factor is absent from Figure 2a, indicating that the dispersed micelles in *o*-xylene were disordered. We tested several models of various object shapes to fit the SAXS data with IGOR Pro software;[34] only fits with a model of polydispersed core−shell spheres agree satisfactorily

dx.doi.org/10.1021/ma2025946 | *Macromolecules* 2012, 45, 1963−1971

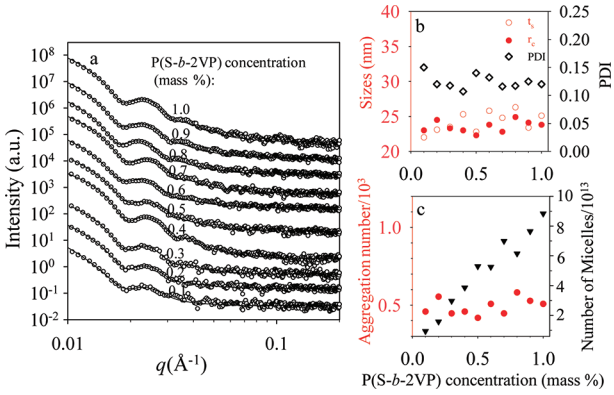

Figure 2. (a) Experimental SAXS data (symbols) and fitted curves (lines) for P(S-*b*-2VP) core−shell micelles at varied mass fractions in *o*-xylene. The curves are shifted for clarity along the *y*-axis. (b) Mean radius of P2VP cores (r_s, red filled circles), thickness of PS shells (t_s, red open circles), and polydispersity of the P2VP cores (PDI, black open diamonds) and (c) aggregation number (red filled diamonds) and number of micelles (black filled triangles) as deduced from the fits are plotted as a function of P(S-*b*-2VP) concentration.

with the experimental data, indicating that varying the P(S-*b*-2VP) concentration in the range 0.1−1 mass % leads to the formation of core−shell full spheres of only one type.

With simulation according to a model of polydispersed core−shell spheres, the mean radius r_c of the core, thickness t_s of the shell, and the polydispersity PDI of core−shell spheres were obtained, shown as a function of P(S-*b*-2VP) concentration in Figure 2b. Figure 2c shows plots of the aggregation number constituting a micelle and the micelle number vs concentration. This structural information indicates that increased concentration in the range 0.1−1 mass % P(S-*b*-2VP) in *o*-xylene led to an increased micelle number density. In addition, no structural transition to form cylindrical or lamellar micelles was induced on varying the concentration. The micelles hence retained the same core−shell spherical shape. The micelles in *o*-xylene exhibited a P2VP core radius 22.3−24.9 nm with a PS shell of thickness 22.0−26.3 nm and a polydispersity 0.12−0.15. The aggregation number n_a in *o*-xylene obtained from SAXS was 459 to 508.

Micellar Morphology of P(S-*b*-2VP) with Various Surface Coverages on SiO_x/Si. Monolayer films of P(S-*b*-2VP) micelles with varied surface coverage were prepared on silicon substrates on spin coating (5000 rpm, 60 s) from o-xylene solutions containing (S-*b*-2VP) at mass fractions in a range 0.1−1 mass %. AFM measurements were performed for surface morphological observations. The measured AFM topographic images for the micellar films are shown in Figure 3. Spin coating from these o-xylene solutions evidently led to only a single monolayer of P(S-*b*-2VP) micelles covering SiO_x at a varied surface density. Particularly at an incomplete surface coverage, the micelles appeared as discrete single nanodomains; no irregular agglomerates were found. The absence of irregular agglomerates is taken to indicate that long-range repulsions existed between the micelles on SiO_x/Si.[36]

With increased surface coverage, the micelles spun from *o*-xylene distributed on top of SiO_x/Si with four distinct spatial arrangements: (i) disordered spherical micelles of large diameter (0.1 mass %, Figure 3a), (ii) loosely packed spherical micelles with hexagonal order (0.2−0.5 mass %, Figure 3b−e), (iii) randomly ordered spherical micelles with loosely packed density (0.6−0.8 mass %, Figure 3f−h), and (iv) closely

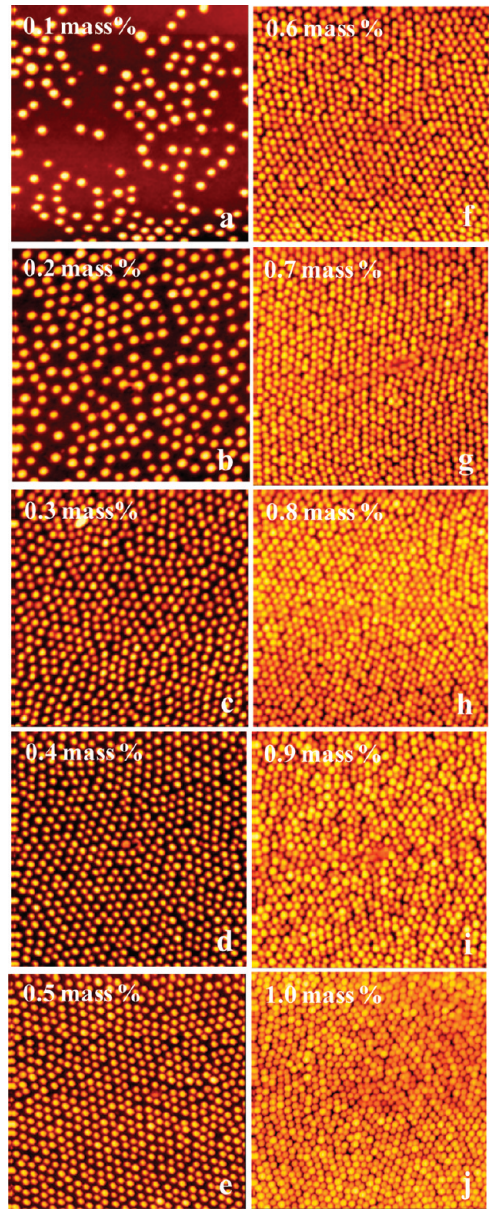

Figure 3. 2 μm × 2 μm AFM topographies for micelles on SiO_x/Si spun from *o*-xylene solutions containing P(S-*b*-2VP) micelles at mass fractions (a) 0.1, (b) 0.2, (c) 0.3, (d) 0.4, (e) 0.5, (f) 0.6, (g) 0.7, (h) 0.8, (i) 0.9, and (j) 1.0 mass %.

packed spherical micelles with short-range order (0.9−1.0 mass %, Figure 3i,j). No coalescence of P(S-*b*-2VP) spherical micelles to form ribbon-like nanostructures through intermicelle fusion occurred.[3−5,12] In addition, the lateral diameter of isolated micelles in case i was larger than that of micelles in cases ii, iii, and iv. For case i, because of a small coverage, each micelle was separate from its nearest neighbors by a large distance, and the micelles on SiO_x/Si were disordered. Measuring the dimensions (diameter and height) of the micelles at loosely packed densities is feasible through the AFM height profiles (Figure S1, Supporting Information). As for the sample having the highest coverage density, we scratched the film to visualize the cross-section profile of micelles by AFM (Figure S2, Supporting Information). The cross section of the AFM topography demonstrates that the thickness of the micellar film is approximately 22−28 nm, which length is indicative of the thickness of a P(S-*b*-2VP) monolayer.

dx.doi.org/10.1021/ma2025946 | *Macromolecules* 2012, 45, 1963−1971

These height profiles reveal that the micelle height is less than the lateral diameter, indicating that the micelles were truncated along the substrate normal, displaying as truncated spheres. The height of the truncated spheres depends intrinsically on the extent of wetting of micelles with a substrate.[36]

When the samples had moderate densities of micelles covering the surface with a narrow distribution of size (as spun from solutions of 0.2−0.5 mass %), monolayers of P(S-*b*-2VP) micelles with regular arrays were obtained (Figure 3b−e). Each micelle was separate from its nearest neighbors at a preferential mean distance in the range 106−87.2 nm. This spatial arrangement is described as loosely packed micelles with hexagonal order (case ii). In the range 0.2−0.5 mass % of coverage, increasing surface coverage made the intermicelle distance decrease and improved the spatial order. Because packing defects were present, the spatial arrangements of the ordered micelles on top of SiO_x/Si reveal, however, paracrystalline domains rather than perfect single-crystal monograins with an area greater than $2 \times 2\ \mu m^2$. It is worth noting that when the coverage of micelles is not high, we can discern that the bottom of the micelles was truncated to form a quasi-two-dimensional, circular mat, whereas the upper half retained a hemispherical cap shape (Figure S3, Supporting Information); this circular mat surrounding a hemispherical-shaped structure is speculated to comprise mainly collapsed micellar shells of PS due to solvent evaporation. When spun from 0.6−0.8 mass %, the micelles initiated contact with their neighbors and ordered themselves into strings and ordered domains. Within the strings each micelle had about two contact points with its neighbors, whereas within the ordered domains each micelle was in contact with more neighbors. This case is described as randomly ordered micelles with a loosely packed density on SiO_x/Si (case iii).[36]

When we increased the surface coverage (as spun from concentrations in the range 0.9−1 mass %), closely packed micelles with short-range order formed on top of SiO_x/Si (Figure 3i,j). At case iv, the spatial order of the P(S-*b*-2VP) micelles in the films was significantly lost, and some micelles in close contact were deformed, because when the micelles touched and adhered tightly together, they distorted into truncated spheres along the lateral direction. As a result, when a closely packed and dense layer of truncated micelles covered completely the substrate, the dense monolayer of truncated micelles resembled a bumplike structure placed on a continuous layer over a substrate.[15,30]

To characterize quantitatively the micellar nanostructure of the P(S-*b*-2VP) films on SiO_x/Si, we measured GISAXS at angle 0.2°. Figure 4 shows a comparison of the experimental GISAXS 2D patterns of these films together with the corresponding simulations. As Figure 4 a−j shows, the experimental GISAXS patterns of the micellar films do not display ring-banded scattering characteristic of monodispersed full spheres on a solid.[32] Accordingly, we exclude the possibility of the existence of monodispersed full spheres. Furthermore, the micellar films on SiO_x/Si show no feature of Kiessig fringes. Müller-Buschbaum et al. found that those fringes are associated with resonant diffuse scattering as a result of correlated interfaces.[37−42] The absence of fringes is thus taken to indicate the absence of an interfacial correlation at both interfaces of the P(S-*b*-2VP) micellar films. This absence of correlated interfaces is explained by the fact that the roughness at the free surface of micellar films is dominated by only a hemispherical-cap contour of truncated spheres and is not influenced by the underlying SiO_x/Si substrate.

The scattering pattern of the disordered micelles at the least coverage density in the first image (Figure 4a) shows two spots of attenuated intensity within the rod-shaped shadow of a copper beam stop; the top spot is from the specular beam, and the bottom spot is from the direct beam. The GISAXS pattern also shows scattering lobes along the $q_{\|}$ direction that are separated by strong calabash-shaped scattering near the rod-shaped shadow (indicated with an inclined arrow). Diffuse scattering rods inclined at an angle with respect to the surface normal are clearly observed in the GISAXS pattern; upon rotation of the sample, these rods do not reveal an azimuthal angular dependence of scattering. No Bragg diffraction streak characteristic of ordered structures is observed in the pattern. As the isolated micelles randomly distributed on top of SiO_x/Si at the least surface coverage (from 0.1 mass %), the scattering features shown in Figure 4a arise only from the intramicelle form factor describing the shape, dimension, and size distributions of an island.

Figure 4b−e shows the GISXS patterns of micelles spun from solutions of P(S-*b*-2VP) 0.2−0.5 mass % in *o*-xylene. In addition to the scattering features described above, the GISAXS patterns reveal symmetric sets of narrow Bragg diffraction streaks parallel to the $q_{\perp}$ direction. The positions of these Bragg diffraction streaks continuously shifted to large $q_{\|}$ with increased coverage. This shift indicates a change in the relative micellar position, i.e., a decreased intermicelle spacing. In comparison with Figure 4a, these samples reveal apparent inclined diffuse scattering rods. The intensity enhancement of the inclined diffuse scattering rods is due to an increased number of micelles on SiO_x/Si. The diffuse scattering rods interfere coherently with the narrow Bragg diffraction streaks, producing elongated bands with enhanced intensity. No diffraction spot resulting from 3D crystallites with a strong uniaxial preferred orientation about the substrate normal was present.[24] These features indicate the existence of the monolayer of micelles with a lateral order in the films. In contrast, the GISAXS patterns for randomly ordered micelles in a loosely packed surface coverage on SiO_x/Si show that the intensity of the inclined diffuse scattering rods gradually weakens with increasing coverage (Figure 4f−h); this weakening might be ascribed to shape and size variations of micelles, caused by the deformation of micelles along the lateral direction. Here we noted also a modulation of the intensity along the $q_{\|}$ direction (indicated by parallel arrows). Such modulation has been found when a homogeneous layer is formed between the substrate and particulate objects.[23,35] When a closely packed and dense layer of truncated micelles completely covers the substrate, only an apparent interference pattern is discernible because of the complete vanishing of inclined diffuse scattering rods (Figure 4i,j).

Figure 4a′−j′ illustrates the 2D GISAXS patterns simulated with IsGISAXS. In the first simulated GISAXS pattern (Figure 4a′), we used only the shape function of isolated core−shell spheres with truncation along the substrate normal and the DWBA approach; the interference function was excluded from this modeling pattern based on the observation of disordered micelles at the least surface coverage (Figure 3a). To account for the shape variations of truncated core−shell micelles, we used only the distribution width (σ_R) of the core radius for modeling. The simulation with IsGISAXS shown in Figure 4a′ agrees satisfactorily with the experimental GISAXS pattern. The form factor of truncated spheres reveals prominent features of scattering rods and lobes of which the scattering positions in

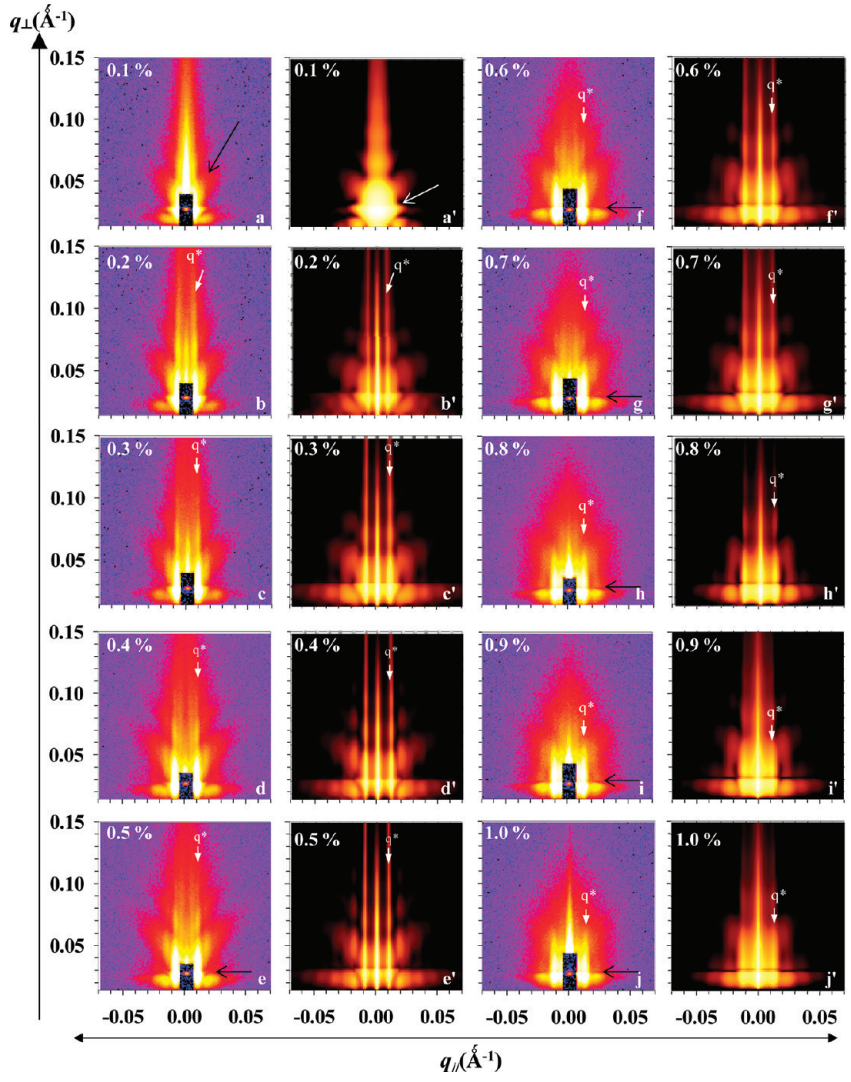

Figure 4. Measured (a–j) and simulated (a′–j′) 2D GISAXS patterns of micelles on SiO_x/Si spun from *o*-xylene solutions containing P(S-*b*-2VP) at mass fractions: (a, a′) 0.1, (b, b′) 0.2, (c, c′) 0.3, (d, d′) 0.4, (e, e′) 0.5, (f, f′) 0.6, (g, g′) 0.7, (h, h′) 0.8, (i, i′) 0.9, and (j, j′) 1.0 mass %. The intensity scale is logarithmic. Yellow color indicates bright intensity. Thick white arrows label the position of the principal diffraction Bragg rod.

the ($q_{||}$, $q_\perp$) space depend on the sizes (height and radius) of truncated micelles. A second prominent feature is the modulation present at the bottom of the strong calabash-shaped scattering (indicated with an inclined arrow). Such modulation is present only for truncated spheres having a core–shell structure, in which the core is P2VP and the shell is PS. The related simulation without the PS shell layer shows no modulation, whereas with a PS shell layer such modulation is present (see Figure S4).

For Figure 4b′–j′, the repeating Bragg reflections along $q_{||}$ are well reproduced with the interference function of a hexagonal paracrystalline. The position of the principal diffraction Bragg rod moves toward larger $q_{||}$, which accounts for a decreased interdomain spacing. Furthermore, the simulations taking account of a homogeneous layer reveal a pronounced modulation of the intensity; this modulation appears as a streak along the $q_{||}$ direction.

To improve our understanding of the in-plane and out-of-plane structural information about micelles, we implemented also perpendicular and parallel scan cuts on the 2D experimental GISAXS patterns to show the 1D scattering profiles. Figure 5 shows not only the measured data (symbols) but also the corresponding simulation cuts (solid lines) produced with the IsGISAXS software. Figure 5a shows the 1D off-detector-scan scattering profiles, which were extracted from the vertical cuts along $q_\perp$ at $q_{||}$ = 0.01 Å^{-1}. In Figure 5a, each off-detector-scan GISAXS profile shows an enhanced feature, known as the Yoneda peak, that is due to multiple scattering effects.[21−23,31,32] At a small surface coverage (from 0.1 mass % solution), the Yoneda feature is sharp, which appears at an exist angle at $q_\perp$ = 0.029 Å^{-1}. According to its position, we attribute the Yoneda feature to arise from only the SiO_x/Si substrate for the X-ray wavelength that we used. As spin-coated from solutions with polymer concentrations 0.2–1.0 mass %, the films reveal an additional Yoneda feature emerging at $q_\perp$ = 0.027 Å^{-1}, being slightly smaller than that of SiO_x/Si. This Yoneda feature is associated with critical angle $\alpha_c^{P(S\text{-}b\text{-}2VP)}$ of P(S-*b*-2VP). A superposition between the peaks yielded a round Yoneda feature with width covering from the critical angle $\alpha_c^{SiOx/Si}$ of SiO_x/Si to a value near $\alpha_c^{P(S\text{-}b\text{-}2VP)}$. The rounding occurred because an increased micelle coverage produced an enhanced absorption and refraction of both the incident and the scattered beams inside the micelle layer itself.[31,32] A second prominent feature is the intensity variation

dx.doi.org/10.1021/ma2025946 | *Macromolecules* 2012, 45, 1963–1971

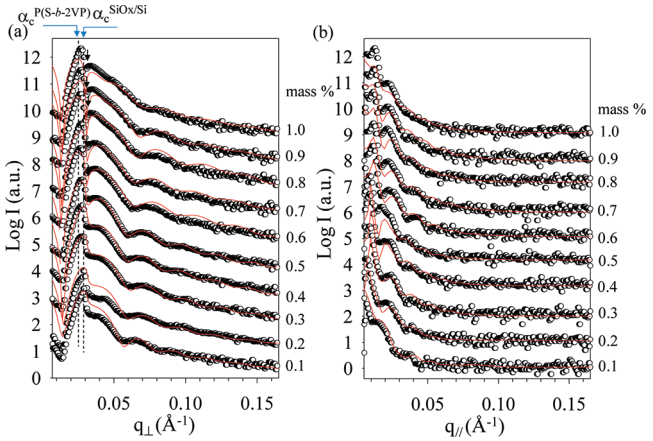

Figure 5. Intensity cross sections of GISAXS patterns shown in Figures 4a–j (experimental data) and 4a′–j′ (simulated patterns). The cuts were made (a) along the $q_\perp$ direction at $q_\parallel$ = 0.01 Å^{-1} and (b) along the $q_\parallel$ direction at the maximum intensity of the lobes. The intensities are shifted for clarity along the ordinate axis.

the first local minimum (indicated by arrowheads) observable for micelles with varied surface coverage. The first local minimum became deeper as the surface coverage of micelles increased, particularly when the micelles were deposited on SiO_x/Si by spin-coating from 0.6 to 1.0 mass % solutions. This deeper minimum is due to the presence of a homogeneous layer between a substrate and the micellar objects.[23,35]

As shown in Figure 5a, the 1D GISAXS profiles for the P(S-*b*-2VP) micelles reveal scattering fringes along the vertical direction. As those fringes are associated with the form factor of the micelles, the frequency of the fringes along $q_\perp$ observed for P(S-*b*-2VP) micelles on SiO_x/Si depends intrinsically on the micellar height. The scattering fringes smear when the micelles have close packing at large coverage (spun from 0.9 to 1.0 mass %). The smearing implies a broad distribution of size for the micelles.

Figure 5b shows the 1D in-plane scattering profiles, which were extracted from the cuts along $q_\parallel$ at the maximum intensity of the lobes. As Figure 5b shows, except the case of a small coverage of disordered micelles, other samples with concentrated micelles reveal scattered intensities in terms of the product of the form factor and the structure factor. The structure factor produces Bragg diffraction features appearing along the $q_\parallel$ direction, whereas the form factor yields fringes observable at medium and large $q_\parallel$. Figure 5b reveals a variation of the principal Bragg diffraction for loosely packed micelles with spatial order, continuously shifting toward large $q_\parallel$ values with varied surface coverage. The position of the principal Bragg diffraction feature is associated with the micellar spacing. The shifting therefore represents a modified micelle distance, i.e., a decreased distance from micelle to micelle. When the micelles are in close contact with each other, the principal Bragg diffraction feature reveals a slight variation in position.

Through the modeling simulations, the structural parameters of the core–shell micelles for the thin films prepared with spin-coating of polymer solutions of varied concentration were calculated. The structural parameters extracted from the fits are shown in Figure 6; symbols $\langle R\rangle$, $\langle H\rangle$, d*R*, d*H*, *L*, and *D* are described in Figure 7a. Figure 6a shows plots of the nearest-neighbor distance *D* and disorder parameter σ_D/D versus polymer concentration. Whereas the intermicelle distance *D* deceased with increased concentration, the disorder parameter

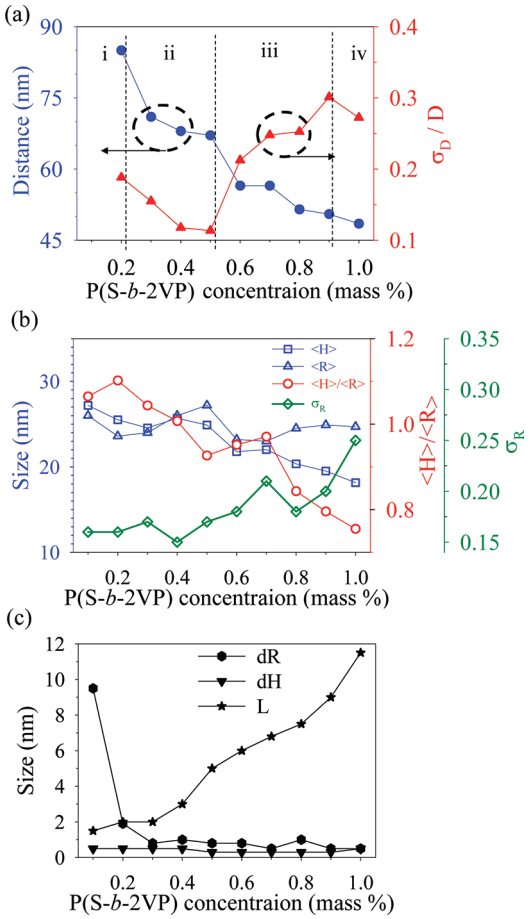

Figure 6. (a) Dependence of the nearest-neighbor distance (*D*: filled circles) and disorder parameter (σ_D/D: filled triangles) on concentration of P(S-*b*-2VP). (b) Plots show the variation of the core size (radius $\langle R\rangle$: open triangles; height $\langle H\rangle$: open squares), size distribution (σ_R: open diamonds), and ratio of height to radius ($\langle H\rangle$/$\langle R\rangle$: open circles) with concentration of P(S-*b*-2VP). (c) Dependence on concentration of thickness (d*R*: filled hexagons; d*H*: filled triangles down) of PS shells and thickness (*L*: filled stars) of the homogeneous layer at the substrate interface.

σ_D/D behaved differently. In regime i, micelles at a small density are deposited from a small concentration (0.1 mass %) onto SiO_x/Si; the micelles are disordered and lack a well-defined spacing between nearest neighbors. In regime ii (in the range 0.2–0.5 mass %), both *D* and σ_D/D decrease with increasing concentration, indicative of improved ordering and decreased intermicellar distance of micelles with increasing coverage. Further decreased *D* would lead to decreased micellar ordering, evident from increased σ_D/D with decreased *D* in regimes iii and iv. We selectively annealed micelles films in toluene and THF vapors. The hydroxyl surface of the substrate preferentially caused adsorption of P(S-*b*-2VP) chains at the interface of SiO_x/Si to form a wetting layer through growing at the expense of the disintegration of spherical micelles when the initially disordered spherical micelles were exposed to vapors (Figure S5). This result indicates that in the presence of a strong affinity between the pyridine groups of P2VP chains and the hydroxyl surface of the bare silicon wafer the ordering improvement of micelles is therefore unachievable by solvent annealing unless a layer of homopolymer brushes is grafted to hinder effectively the interactions at the substrate interfaces to prevent the P(S-*b*-2VP) adsorption onto SiO_x/Si.[16,17]

dx.doi.org/10.1021/ma2025946 | *Macromolecules* 2012, 45, 1963–1971

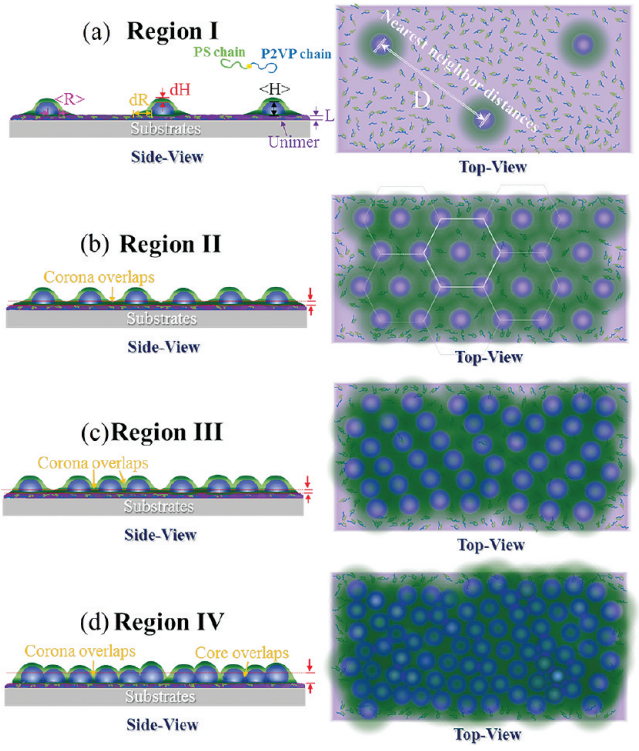

Figure 7. Schematic illustrations showing the real space of disordered micelles having a truncated core−shell structure on top of a homogeneous layer of P(S-*b*-2VP) chains anchored with SiO_x/Si (a, regime i), loosely packed spherical micelles with a hexagonal order (b, regime ii), randomly ordered micelles with a loosely packed density (c, regime iii), and closely packed spherical micelles with spatial order (d, regime iv). Labels $\langle R \rangle$, $\langle H \rangle$, d*R*, d*H*, *L*, and *D* denote respectively the central radius and height of P2VP cores, the thicknesses of PS shells, the thickness of a homogeneous layer underneath the micelles, and the nearest-neighbor distance.

The central core height $\langle H \rangle$ and radius $\langle R \rangle$ and the size distributions σ_R are shown in Figure 6b. Whereas the mean core radius of P2VP was constant, the core height of P2VP decreased with concentration. The ratio of $\langle H \rangle$ and $\langle R \rangle$ thus decreased from ca. 1.1 to 0.75 with increased surface coverage. For the σ_R polydispersity of the core radius of P2VP, two scenarios were recognized: σ_R first remained constant (∼0.15) for micelles spun from 0.1 to 0.5 mass % solutions and then increased for micelles spun from concentrations in the range 0.6−1.0 mass %. This increased σ_R is due to the deformation of micelles along the lateral direction when they are in close contact with their nearest neighbors at a large coverage.

Figure 6c shows plots of the shell thickness and the layer thickness versus polymer concentration. The micellar shells on SiO_x/Si reveal several prominent features; the first is that the PS shells in a dry state have anisotropic thickness, so that shell thickness d*H* normal to the substrate is different from shell thickness d*R* along the substrate. Particularly with spin-coating from a 0.1 mass % solution, d*R* (9.5 nm) is much greater than d*H* (0.5 nm). Furthermore, both d*H* and d*R* for micelles on SiO_x/Si are less than the isotropic thickness of the PS shell in solution. Through preferential swelling of the PS shell by *o*-xylene, the increased thickness of PS is comparable with the core radius of P2VP, even though the constituted volume fraction of PS is less than that of P2VP. During spin-coating, solvent evaporating from the PS block led, however, to a collapse of the micellar shells, but micelles with a swollen shell were soft: on coming in contact with a rigid surface, they became truncated along the substrate normal under the influence of the rigid surface. Both factors account for the anisotropic thickness of the micellar shells. Whereas the d*H* thickness remained nearly stable, the d*R* thickness decreased with concentration in the range 0.1−0.3 mass % and then remained stable. At that stage, the d*R* thickness was slightly larger than d*H*. According to Figure 6, we can express the coverage density in terms of $(\langle 2R \rangle + 2dR)/D$ where the numerator $(\langle 2R \rangle + 2dR)$ denotes the diameter of the core−shell micelle, whereas *D* is the nearest-neighbor distance. The surface coverage density increases from 0.147 to 1.040 as the polymer solution increases from 0.1 to 1 mass %. At the mass fractions of 0.9 and 1.0 mass %, the surface coverage is slightly larger than unity, indicative of a very dense monolayer.

In addition to the presence of micelles on top of SiO_x/Si, a homogeneous layer that resulted from adsorption of free P(S-*b*-2VP) chains was also present after spin-coating. Such a homogeneous layer at the substrate interface was revealed by Krausch, Krystyna, and co-workers with other techniques.[4−6,43] Our analysis of GISAXS data also confirm the existence of the homogeneous layer of free P(S-*b*-2VP) chains on the solid surface of SiO_x/Si. When micelles were spun from a solution with polymer concentration less than 0.3 mass %, the layer underneath the micelles was thin, less than 2 nm. The layer at the substrate interface varied, however, continuously with respect to concentration in the range 0.3−1 mass %. These changes reflect an increased *L* with increased coverage.

On the basis of our quantitative analysis and simulations of the X-ray scattering pattern, we propose a series of scenarios to describe the shape, size, size distribution, and assembly of truncated micelles within two-dimensional monolayers depending on the polymer concentration in solution. As spun from a small concentration, free P(S-*b*-2VP) chains exhibit a great tendency first to adsorb onto SiO_x/Si to form a thin homogeneous layer before micelle adsorption, as the surface of SiO_x/Si had a strong affinity for the P4VP block (see Figure 7a); as a result, the micelles settled on top of the homogeneous P(S-*b*-2VP) layer anchored with SiO_x/Si during spin-coating. At a small coverage, the micelles were disordered and lack a well-defined distance to nearest neighbors. In a dry state, solvent evaporation led to collapsed micellar shells of thin thickness. Furthermore, micelles deformed through truncation along the substrate normal when they adhered to a rigid flat surface. These micelles appeared as truncated micelles with anisotropic shell thickness on SiO_x/Si; the bottom of the truncated micelle was assumed to form a quasi-two-dimensional, circular mat whereas the upper half retained a hemispherical cap shape; around each hemisphere was looped a circular mat (top view, Figure 7a). This circular mat is speculated to comprise mainly PS chains, which we describe as a ring-banded region. As the surface micelle was still composed of the P2VP core and the PS shell, the size of such a surface micelle is still described by the sum of the core radius $\langle R \rangle$ and the shell thicknesses (d*R* and d*H*).

Upon spin-coating of polymer solutions in the range 0.2−0.5 mass %, the micelles were packed with a long-range hexagonal order on SiO_x/Si, in which the distance between nearest neighbors decreased with increased concentration. Before micellar contact, two-dimensional ring-banded maps made contact with their nearest counterparts, producing an increased thickness of the homogeneous layer (Figure 7b). In addition, the contact between ring-banded maps resulted also in improved in-plane ordering of micelles, even though the hemispherical caps were not in close contact. In this case, the presence of ring-banded

dx.doi.org/10.1021/ma2025946 | *Macromolecules* 2012, 45, 1963−1971

maps can be treated as additionally extended areas between the micelles. Because of these additional areas, the effective radius of the micelles was greater than their physical core−shell radius, thus yielding ordered micelles with a loosely packed density (regime ii, Figure 7b). Further increased surface coverage density produced much superposition of the ring-banded maps, consequently increasing the layer thickness at the substrate interface and decreasing the distance between the micelles (regime iii, Figure 7c). In regime iii, the hemispherical caps of micelles were in contact with their neighbors and ordered themselves into strings and ordered domains. The coexistence of strings and ordered domains accounts for the increased disorder parameter. When the micelles covered SiO_x/Si at large surface densities, a biaxial truncation occurred along both the lateral and normal directions because of the close contact and tight adherence of micelles. The bottom of the micelles was deformed to develop into a continuous layer, and the top retained a caplike structure upon further increased surface coverage. The lateral size and height distributions of spherical caps had a small degree of polydispersity. As a result, the morphology of a dense monolayer of micelles resembled a monolayer of bumps placed on a thick continuous layer (Figure 7d). Such a phenomenon is similar to that found for a highly ordered monolayer of PMMA beads by Frömsdorf.[25] In our case, however, the thick layer is comprised of not only the adhered bottom of micelles but also a thin layer of P(S-*b*-2VP) chains anchored with SiO_x/Si (Figure 7d).

CONCLUSION

Both real and reciprocal-space characterization has been used complementarily to investigate the monolayers of P(S-*b*-2VP) micelles with four spatial arrangements on SiO_x/Si. Although AFM maps directly probe the surface topography, the structural information obtained is limited to the size and spatial ordering of micelles in local areas. GISAXS enabled the detection of the inner film structures, including P2VP cores and PS shells, and the homogeneous layer underneath the core−shell micelles. Through modeling of GISAXS data, we obtained quantitative information about the dependence of P2VP cores, the PS shells within truncated micelles, and the homogeneous layer underneath the micelles on the polymer concentration during the spin-coating. According to the structural parameters, four scenarios are distinguished to describe satisfactorily the variations of size, size distribution, and spatial ordering of truncated micelles with varied density of coverage on top of SiO_x/Si.

ASSOCIATED CONTENT

Supporting Information

Height profiles of micelles on SiO_x/Si spun from *o*-xylene solutions containing P(S-*b*-2VP) micelles at various mass fractions (Figure S1), cross-section AFM image, 3D topography, and high profile of the surface morphology of a scratched film (initially spin-coated from 1 mass % polymer solution) (Figure S2), 3-dimensional AFM tomography of micelles as-spun from a solution of P(S-*b*-2VP) 0.2 mass % in *o*-xylene (Figure S3), simulated GISAXS pattern of a truncated sphere without PS shell (Figure S4), and AFM topographies of solvent-annealed thin films in toluene and THF vapors (Figure S5). This material is available free of charge via the Internet at http://pubs.acs.org.

AUTHOR INFORMATION

Corresponding Author

*E-mail: yssun@cc.ncu.edu.tw.

Notes

The authors declare no competing financial interest.

ACKNOWLEDGMENTS

The National Science Council provided support (NSC-100-2628-E-008-007-MY3 and NSC-100-2120-M-008-001-).

REFERENCES

(1) Riess, G. *Prog. Polym. Sci.* **2003**, *28*, 1107−1170.
(2) Förster, S.; Antonietti, M. *Adv. Mater.* **1998**, *10*, 195−217.
(3) Li, Z.; Zhao, Y.; Liu, M.; Rafailovich, M. H.; Sokolov, J.; Khougaz, K.; Eisenberg, A.; Lennox, R. B.; Krausch, G. *J. Am. Chem. Soc.* **1996**, *118*, 10892−10893.
(4) Meiners, J. C.; Ritzi, A.; Rafailovich, M. H.; Sokolov, J.; Mlynek, J.; Krausch, G. *Appl. Phys.* **1995**, *A61*, 519−524.
(5) Meiners, J. C.; Elbs, H.; Ritzi, A.; Mlynek, J.; Krausch, G. *J. Appl. Phys.* **1996**, *80*, 2224−2227.
(6) Meiners, J. C.; Quintel-Ritzi, A.; Mlynek, J.; Elbs, H.; Krausch, G. *Macromolecules* **1997**, *30*, 4945−4951.
(7) Spatz, J. P.; Eibeck, P.; Mössmer, S.; Möller, M.; Kramarenko, E. Y.; Khalatur, P. G.; Potemkin, I. I.; Khokhlov, A. R.; Winkler, R. G.; Reineker, P. *Macromolecules* **2000**, *33*, 150−157.
(8) Spatz, J. P.; Möller, M.; Noeske, M.; Behm, R. J.; Pietralla, M. *Macromolecules* **1997**, *30*, 3874−3880.
(9) Spatz, J. P.; Sheiko, S.; Möller, M. *Adv. Mater.* **1996**, *8*, 513−517.
(10) Kramarenko, E. Y.; Potemkin, I. I.; Khokhlov, A. R.; Winkler, R. G.; Reineker, P. *Macromolecules* **1999**, *32*, 3495−3501.
(11) Potemkin, I. I.; Kramarenko, E. Y.; Khokhlov, A. R.; Winkler, R. G.; Reineker, P.; Eibeck, P.; Spatz, J. P.; Möller, M. *Langmuir* **1999**, *15*, 7290−7298.
(12) Kim, T. H.; Huh, J.; Huang, J.; Kim, H.-C.; Kim, S. H.; Sohn, B.-H.; Park, C. *Macromolecules* **2009**, *42*, 6688−6697.
(13) Park, S.; Wang, J.-Y.; Kim, B.; Chen, W.; Russell, T. P. *Macromolecules* **2007**, *40*, 9059−9063.
(14) Hu, Y.; Chen, D.; Park, S.; Emrick, T.; Russell, T. P. *Adv. Mater.* **2010**, *22*, 2583−2587.
(15) Krishnamoorthy, S.; Pugin, R.; Brugger, J.; Heinzelmann, H.; Hinderling, C. *Adv. Funct. Mater.* **2006**, *16*, 1469−1475.
(16) Chang, C. Y.; Wu, P. J.; Sun, Y. S. *Soft Matter.* **2011**, *7*, 9140−9147.
(17) Chang, C. Y.; Lee, Y. C.; Wu, P. J.; Liou, J. Y.; Sun, Y. S.; Ko, B. T. *Langmuir* **2011**, *27*, 14545−14553.
(18) Lu, H.; Lee, D. H.; Russell, T. P. *Langmuir* **2010**, *26*, 17126−17132.
(19) Lu, H.; Akgun, B.; Wei, X.; Li, L.; Satija, S. K.; Russell, T. P. *Langmuir* **2011**, *27*, 12443−12450.
(20) Zhu, J.; Eisenberg, A.; Lennox, R. B. *J. Am. Chem. Soc.* **1991**, *113*, 5583−5588.
(21) Müller-Buschbaum, P. *Anal. Bioanal. Chem.* **2003**, *376*, 3−10.
(22) Müller-Muschbaum, P. In *Polymer Surfaces and Interfaces: Characterization and Applications*; Stamm, M., Ed.; Springer: Berlin, 2008; pp 17−46.
(23) Müller-Muschbaum, P. In *Applications of Synchrotron Light to Noncrystalline Diffraction in Materials and Life Sciences*; Ezquerra, T. A., Garcia-Gutierrez, M., Nogales, A.; Gomez, M., Eds.; Springer: Berlin, 2009; Vol. *776*, pp 61−89.
(24) Lee, B.; Park, I.; Yoon, J.; Park, S.; Kim, J.; Kim, K. W.; Chang, T.; Ree, M. *Macromolecules* **2005**, *38*, 4311−4323.
(25) Frömsdorf, A.; Čapek, R.; Roth, S. V. *J. Phys. Chem. B* **2006**, *110*, 15166−15171.
(26) Heitsch, A. T.; Patel, R. N.; Goodfellow, B. W.; Smilgies, D.-M.; Korgel, B. A. *J. Phys. Chem. C* **2010**, *114*, 14427−14432.
(27) Sun, Y. S.; Chien, S. W.; Wu, P. J. *Macromolecules* **2010**, *43*, 5016−23.
(28) Sun, Y. S.; Chien, S. W.; Liou, J. Y. *Macromolecules* **2010**, *43*, 7250−7260.
(29) Sun, Y. S.; Chien, S. W.; Liou, J. Y.; Su, C. H.; Liao, K. F. *Polymer* **2011**, *52*, 1180−1190.

(30) Frömsdorf, A.; Kornowski, A.; Pütter, S.; Stillrich, H.; Lee, L.-T. *Small* **2007**, *3*, 880−889.
(31) Lazzari, R. *J. Appl. Crystallogr.* **2002**, *35*, 406−421.
(32) Renaud, G.; Lazzari, R.; Leroy, F. *Surf. Sci. Rep.* **2009**, *64*, 255−380.
(33) Roe, R. J. *Methods of X-ray and Neutron Scattering in Polymer Science*; Oxford University Press: New York, 2000; Vol. *5*, p 155.
(34) Kline, S. R. *J. Appl. Crystallogr.* **2006**, *39*, 895−900.
(35) Meier, R.; Ruderer, M. A.; Diethert, A.; Kaune, G.; Körstgens, V.; Roth, S. V.; Müller-Muschbaum, P. *J. Phys. Chem. B* **2011**, *115*, 2899−2909.
(36) Israelachvili, J. N. *Intermolecular & Surface Forces*, 3rd ed.; Academic Press: New York, 2011; Chapter 109, pp 503−534.
(37) Müller-Buschbaum, P. *J. Phys.: Condens. Matter* **2003**, *15*, R1549−R1582.
(38) Müller-Buschbaum, P.; Gutmann, J. S.; Lorenz, C.; Schmitt, T.; Stamm, M. *Macromolecules* **1998**, *31*, 9265−9272.
(39) Müller-Buschbaum, P.; Stamm, M. *Macromolecules* **1998**, *31*, 3686−3692.
(40) Müller-Buschbaum, P.; Gutmann, J. S.; Lorenz-Haas, C.; Wunnicke, O.; Stamm, M.; Petry, W. *Macromolecules* **2002**, *35*, 2017−2023.
(41) Müller-Buschbaum, P.; Gutmann, J. S.; Wolkenhauer, M.; Kraus, J.; Stamm, M.; Smilgies, D.; Petry, W. *Macromolecules* **2001**, *34*, 1369−1375.
(42) Müller-Buschbaum, P.; Gutmann, J. S.; Kraus, J.; Walter, H.; Stamm, M. *Macromolecules* **2000**, *33*, 569−576.
(43) Krystyna, A.; Mourran, A.; Moeller, M. Surface micelles and surface-induced nanopatterns fromed by block copolymers. In *Ordered Polymeric Nanostructures at Surfaces*; Springer-Verlag: Berlin, 2006; Vol. *200*, pp 57−70.

Macromolecules

Article

pubs.acs.org/Macromolecules

Instabilities of PS/PMMA Bilayer Patterns with a Corrugated Surface and Interface

Zheng Zhang, Dae Up Ahn, and Yifu Ding*

Department of Mechanical Engineering, University of Colorado, Boulder, Colorado 80309-0427, United States

Supporting Information

ABSTRACT: We study the patterns spontaneously formed by bilayer polymer films upon annealing. Specifically, polystyrene (PS) films were spin-cast on topographically patterned poly(methyl methacrylate) (PMMA) substrates and subsequently annealed at temperatures above the glass transition temperature of both polymers. The influence of the molecular weight and the volume of PS on the morphological evolution of the corrugated liquid−liquid interface was examined. When the PS formed isolated stripes both on the mesas and within the trenches of the PMMA pattern, capillary instability was observed for these nonaxisymmetric PS threads. The kinetics of the capillary breakup depended on the thread-to-matrix viscosity ratio, and was dictated by the more viscous component. In contrast, the characteristic wavelength of the breakup only slightly depended on some viscosity ratio, and reached a minimum at the viscosity ratio around 1. When the PS was thick enough to form a continuous layer, the instability of the film further depended on the molecular weight of the PS. For a molecular weight of 13 kg/mol, the PS dewetted from PMMA via a random nucleation and growth mechanism. However, for a molecular weight of 2000 kg/mol, localized nucleation on top of the PMMA mesas led to a mesh-like PS morphology, which eventually broke up due to capillary instability. Therefore, by controlling the molecular weight and the spin-cast volume of the top layer, the kinetics of morphological evolution and the resulting patterns can be controlled.

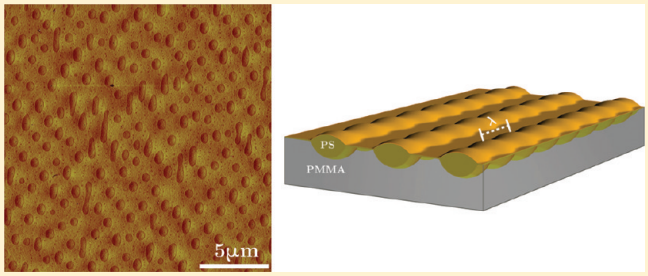

1. INTRODUCTION

Polymers, in thin films or nanostructured patterns, are subject to a range of surface and interfacial interactions. Understanding the characteristics of these interactions and the resulting instabilities is vital for achieving robust polymeric patterns and structures, especially during fabrication processes. The extent of these instabilities can be modulated by viscous and elastic effects. Understanding of these effects promises to create unique complex structures which are hard to approach with top-down lithographic methods.

Capillary fluctuations are ubiquitous at viscous polymer surfaces and interfaces. These fluctuations can lead to spontaneous rupture or dewetting of an ultrathin (<100 nm) polymer film on a nonwettable substrate, through a mechanism termed spinodal dewetting.[1] Thicker films are more resistant to these fluctuations. The fluctuations can be dramatically amplified under thermal[2] or electric[3,4] fields, which can rupture a normally stable film. In the absence of external fields, a thick polymer film can dewet from nonwettable substrates alternatively via a nucleation and growth mechanism.[5−7] Studies have shown that both types of dewetting can be guided or directed using topographically[8,9] or chemically[10,11] patterned substrates.

For polymer structures with large length-to-cross-section ratios, such as fibers, the capillary fluctuations along the axial direction can lead to rupture of the continuous structures. For a cylindrical liquid thread embedded within a viscous matrix, the characteristics of the capillary breakup, including both the wavelength and kinetics, are well captured by Tomotika's classical theory.[12] Intriguingly, recent experiments by Knops et al.[13] showed that the capillary breakup for multiple neighboring threads can occur simultaneously. Depending on the diameter of the threads, the distance between neighboring threads, and the thread-to-matrix viscosity ratio, these threads can break up via an "in-phase" or "out-of-phase" fashion.

Recently, we discovered that polystyrene (PS) threads (or stripes) cast on top of topographic poly(methyl methacrylate) (PMMA) patterns also showed simultaneous capillary breakup, creating a unique hierarchical composite film.[14,15] Here we present a systematic investigation of the influences of molecular weight and the as-cast volume of the PS on the morphological evolution of the PS/PMMA patterns upon thermal annealing. With proper control of these two factors, three regimes of phase evolution were observed: (1) a two-stage capillary breakup for low molecular weight and relatively small volume fraction of PS; (2) dewetting of PS on PMMA via random nucleation and growth for relatively thicker PS films with low molecular weight; (3) controlled nucleation of PS on PMMA mesas followed by capillary instability. Each type of phase

Received: December 14, 2011
Revised: January 26, 2012
Published: February 15, 2012

evolution resulted in a distinctive morphology featuring unique micro- and nanostructures.

2. EXPERIMENTAL SECTION

2.1. Materials. Monodisperse (PDI < 1.1) PMMA and PS were purchased from Polymer Source, Inc. and Scientific Polymer Products, Inc. All polymers were used as received, and their molecular weight and glass-transition temperature T_g are listed in Table 1. The T_gs of PS were estimated from literature.[16] As a confirmation of the reproducibility of the literature values, we sampled the T_gs of PS13k and PMMA12k for determination using the second Differential Scanning Calorimetry (NETZSCH DSC 204F1) scan at a heating rate of 20 °C/min.

Table 1. Molecular Weight and T_g of the Polymers Used in This Study

polymer	M_w (g/mol)	T_g (°C)	acronym
PMMA	12 000	107	PMMA12k
PS	4000	74[a]	PS4k
	13 000	87	PS13k
	31 600	97[a]	PS31.6k
	214 000	100[a]	PS214k
	2 000 000	100[a]	PS2000k

[a]Values obtained from ref 16.

2.2. Pattern Fabrication. PMMA thin films were first prepared by spin-coating toluene solutions containing 2.5 wt % of PMMA onto 0.38 mm thick silicon substrates that had previously been cleaned with piranha solution. The resulting PMMA films were subsequently annealed in a vacuum oven at 150 °C for 3 hours to remove the residual solvent. The initial thicknesses of the planar as-spincast PMMA films were determined to be ~150 nm. Surface grating patterns were fabricated onto the PMMA films via thermal embossing nanoimprint lithography (TE-NIL). The NIL process was performed on a nanoimprinter Eitrie 3 (Obducat Inc.) at 130 °C under a pressure of 4 MPa for 3 min. The same silicon mold was applied to all PMMA films in order to fabricate identical grating patterns with a pitch of 834 nm, a line-to-space ratio of 1, and a pattern height of 200 nm. AFM measurements of the as-imprinted PMMA patterns confirmed faithful replication of the mold pattern on all samples. Prior to the NIL, a self-assembled monolayer of tridecafluoro-1,1,2,2-tetrahydrooctyltrichlorosilane (Sigma-Aldrich, Inc.) was deposited on the surface of the mold through a vapor deposition process.[17] This effectively reduced adhesion between the mold and imprinted PMMA films, thus facilitating mold release at 70 °C (i.e., after PMMA was vitrified).

The PMMA used in this study had a molecular weight sufficiently below its critical molecular weight for entanglement ($M_c \approx 28$ kg/mol for bulk PMMA).[18,19] The patterned PMMA films were allowed adequate time for the residual stresses imposed by the NIL process to relax.[20,21] Subsequently, PS films were spin-cast onto the patterned PMMA films from 1-chloropentane (a selective solvent for PS[22]) solutions, with different weight fractions as specified in the discussion below, in order to obtain different thicknesses of the upper PS layer. The resulting PS/PMMA patterns were annealed at 60 °C (below the T_gs of both PS and PMMA) for 3 hours in vacuum to remove the residual solvents.

2.3. Characterization of Morphological Evolution upon Annealing. The PS/PMMA patterns were annealed under ambient conditions for different amounts of time, on a custom-made hot stage that had been calibrated with 7 melting-point standards (Sigma-Aldrich, Inc.) prior to use. The evolution of the surface morphology due to annealing was investigated with a Nikon LV150 optical microscope and a Dimension 3100 atomic force microscope (AFM). Furthermore, after selective removal of the top PS layer with cyclohexane, a selective solvent for PS,[23,24] we characterized the exposed PS/PMMA interface with AFM. All the AFM measurements were conducted using tapping mode with silicon cantilever probes that

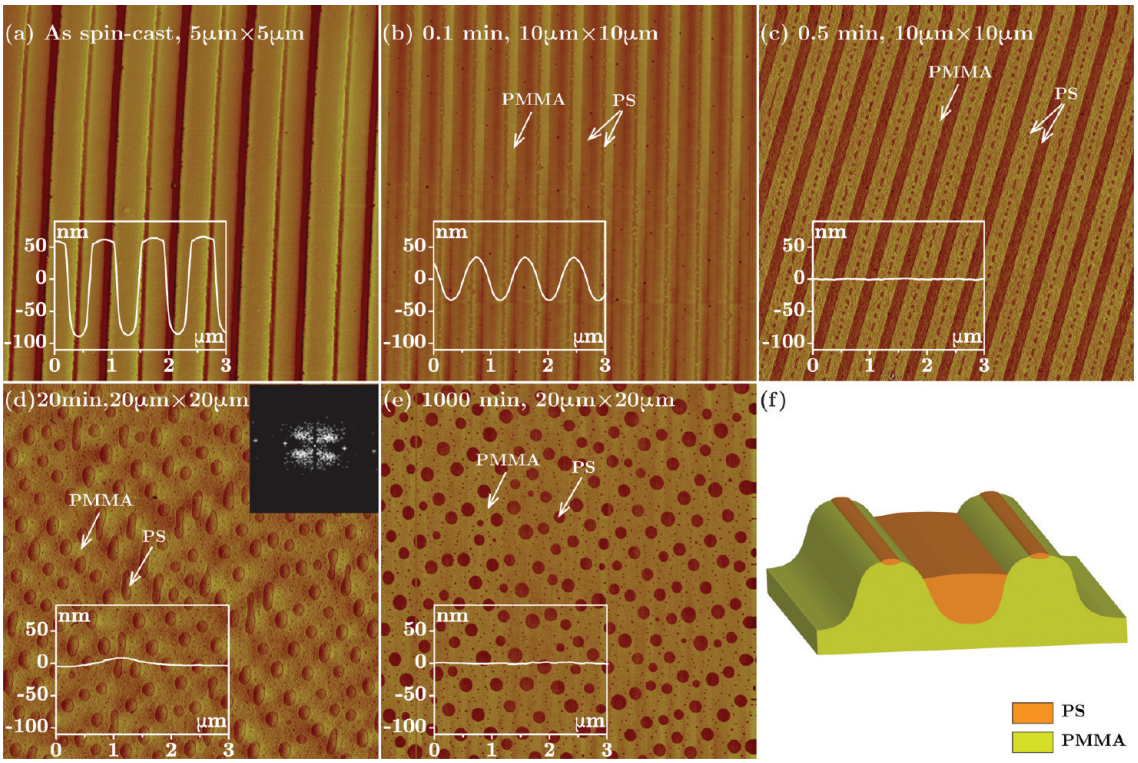

Figure 1. (a–e) AFM phase images of the PS214k/PMMA12k sample after annealing at 140 °C for different amounts of time, as labeled on each image. The insets are the representative cross-sectional profiles of each sample surface. (f) A schematic of the cross-section in part b.

dx.doi.org/10.1021/ma2026836 | Macromolecules 2012, 45, 1972–1981

have an estimated resonant frequency of 300 kHz and spring constants ranged from 25 to 75 N/m.

3. RESULTS AND DISCUSSION

3.1. Capillary Instabilities of PS Threads on PMMA Patterns.

3.1.1. Morphological Evolution. Recently, we reported the simultaneous breakup of PS13k threads that had been partially confined on PMMA12k patterns, when annealed at temperatures above the T_g of both polymers.[14] Here we first examine the generality of this capillary instability by varying the molecular weight of PS, ranged from 4 kg/mol to 2000 kg/mol, on identical PMMA12k substrates. For PS with molecular weight of 4 kg/mol up to 214 kg/mol, a type of two-step capillary instability was observed when the initial volume of PS cast on top of the PMMA pattern did not form a thick continuous layer, similar to what had been observed in the PS13k/PMMA12k.[14]

Figure 1 represents the distinctive stages during the morphological evolution in PS214k/PMMA12k. As detailed in the Experimental Section, the nanoimprinted PMMA pattern had a pattern height of 200 nm (see supplementary Figure S5, Supporting Information). After PS214k was cast onto the PMMA pattern, the average apparent pattern height became 143 nm, with PS distributed both on top of the mesas and within the trenches of the PMMA pattern. According to the mass conservation method described in our previous study,[14] we estimated the average thickness of PS214k on the mesas and trenches to be 12 and 63 nm, respectively. Just after 0.1 min of annealing at 140 °C, a temperature above the T_g of both polymers, the overall pattern height decreased to 67 nm (inset of Figure 1b), driven by the reduction of the overall polymer-surface energy. During this period, the PS on the PMMA mesas quickly retreated to the mesa centers, forming isolated narrow threads, while the PS in the trenches formed larger threads therein, as marked in Figure 1b, and schematically shown in Figure 1f.

After annealing for 0.5 min, the surface of the PS214k/PMMA system was completely smoothed out to minimize the polymer-surface area, resulting in a root mean square (RMS) surface roughness of $R_q \approx 0.49$ nm (see the inset of Figure 1c). During this period, the narrow PS threads on top of the PMMA mesas broke up into lines of droplets, driven by capillary instability seeking to minimize the total system energy (Figure 1c). Meanwhile, the width of the PS threads confined in the PMMA trenches shrank noticeably from 417 nm in the as-cast sample to ~300 nm. The mass transport associated with these subtle morphological changes was induced by the balance between the surface tension of the PS and the interfacial tension between the PS and PMMA, as discussed in the following section.

This intriguing surface pattern was preserved up to 10 min. Upon further annealing, the remaining larger PS threads also broke up into lines of droplets due to capillary instability. The characteristic wavelength of this capillary instability was determined to be 2.33 μm, from power spectrum density (PSD) analyses of the AFM phase images along the grating lines, after the threads completely broke up. As revealed in the FFT image (inset of Figure 1d), neighboring PS threads broke up simultaneously via an out-of-phase fashion, consistent with our previous report.[14] The sequential breakup of the two sets of PS threads led to a unique type of composite thin film: highly correlated PS214k droplets with a bimodal distribution in diameter (~600 nm for the larger droplets, ~65 nm for the smaller ones), all of which were partially embedded in the PMMA matrix. Upon further annealing, the morphological evolution was dominated by the coalescence among these PS droplets, reducing the PS/PMMA interfacial energy. Note that the overall surface of the film remained flat after the capillary breakup (cross-sectional profiles are shown in the insets of Figure 1d and e) and no dewetting of the PMMA matrix film was observed, since the SiO_x surface was wettable for the PMMA.

The aforementioned morphological evolution was observed for PS with molecular weights from 4 kg/mol to 214 kg/mol, as long as the as-cast PS on top of the PMMA pattern did not form a continuous thick layer (which will be discussed in section 3.2). Regardless, for these nonaxisymmetric PS threads that are partially embedded in the viscous PMMA matrix, there exists no theoretical model to describe the characteristic wavelength of the capillary instability and the corresponding breakup kinetics. In the following section, a static analysis of this system is presented first, and then experimental findings of the dependence of both the characteristic wavelength and breakup time on the viscosity ratio of the PS/PMMA are presented in section 3.1.3.

3.1.2. Static Analysis on the Capillary Instability of Nonaxisymmetric PS Threads. An axisymmetric liquid cylinder, with a radius r, completely embedded in an infinite immiscible viscous matrix breaks up into droplets due to Plateau–Rayleigh instability.[25,26] This is known to be caused by thermally induced surface fluctuations comprised of a rich spectrum of sinusoidal waves. As a sinusoidal fluctuation with a wavelength λ and amplitude α develops on the surface, conservation of the cylinder volume leads to a decrease in the average radius

$$r'^2 = r^2 - \alpha^2/2. \tag{1}$$

The total interfacial energy, E, of such a cylinder with a sinusoidal profile along the surface is[27]

$$E = 2\pi r'\lambda\gamma\left[1 + \left(\frac{\alpha\pi}{\lambda}\right)^2\right] \tag{2}$$

where γ is the interfacial tension between the thread and the matrix. From eq 1 and eq 2, it is clear that at the small perturbation limit, $\alpha\pi \ll \lambda$, E decreases with increasing fluctuating amplitude only for modes with wavelengths $\lambda > 2\pi r$.[28] Fluctuating waves with $\lambda < 2\pi r$ gradually damp out as they are energetically unfavorable.

In the following, we use a geometric analysis to determine the cutoff wavelength for the capillary instability of nonaxisymmetric liquid threads that are partially embedded in another viscous medium. Such threads were found at two different stages during annealing for our PS/PMMA system, for example, in the PS214k/PMMA12k system shown in Figure 1: ~80 nm wide PS threads on PMMA mesas as marked in Figure 1b, and ~300 nm wide PS threads originated from the PS cast into the PMMA trenches, as marked in Figure 1c. These PS threads were bounded by two interfaces, one air and the other PMMA. Since the cross-sectional length scale was well below the capillary length ($\kappa^{-1} = (\gamma/\rho g)^{1/2} \approx 1.8$ mm) of the PS at 140 °C, gravity was negligible compared to the surface/interfacial tension. The equilibrated cross sections of the two sets of PS threads, on mesas and within trenches, were similar in shape but different in size. In the following, we focus the

dx.doi.org/10.1021/ma2026836 | Macromolecules 2012, 45, 1972–1981

discussion on the larger PS threads confined within the PMMA trenches, because of the smaller experimental uncertainty.

As schematically shown in Figure 2, the cross-sectional shapes of the threads are determined by the balance of the

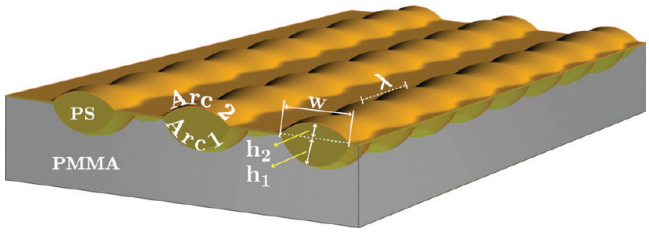

Figure 2. Schematic illustration of the sinusoidal fluctuations along the nonaxisymmetric PS threads that are partially embedded in the PMMA matrix. The geometry of the thread cross-section is marked (not actual size).

Laplace pressure at the PS−air surface with that at the PS/PMMA interface

$$\Delta P_{\text{Laplace}} = \frac{2\gamma_{S-M}}{r_1} = \frac{2\gamma_{PS}}{r_2} \tag{3}$$

where γ_{PS} and γ_{S-M} are the surface tension of the PS and the interfacial tension of the PS/PMMA, respectively. At a given annealing temperature, $\gamma_{PS} \gg \gamma_{S-M}$. For example, at 140 °C, γ_{PS} = 32.1 mN·m^{-1} (invariant in the range of PS molecular weights studied here) and γ_{S-M} = 1.6 mN·m^{-1}.[29] Therefore, the curvature of the PS/PMMA interface, Arc 1 (labeled in Figure 2), is significantly larger than that of the PS surface, Arc 2. Specifically, the radii of curvature of both arcs can be determined by

$$r_1 = \frac{w^2}{8h_1} + \frac{h_1}{2} \tag{4}$$

$$r_2 = \frac{w^2}{8h_2} + \frac{h_2}{2} \tag{5}$$

where the geometric parameters, w and h_1 can be determined by AFM measurements after selective removal of the PS. The corresponding central angles of both arcs are

$$\theta_1 = 2\arcsin\left(\frac{w}{2r_1}\right) \tag{6}$$

$$\theta_2 = 2\arcsin\left(\frac{w}{2r_2}\right) \tag{7}$$

When a thermally excited sinusoidal fluctuation with amplitude α and wavelength λ grows at the PS/PMMA interface, we assume that the corresponding fluctuation on the PS surface has the same wavelength but a much smaller amplitude $\alpha\gamma_{S-M}/\gamma_{PS}$, which is consistent with the observations from the AFM image (Figure 1c). At the small fluctuation limit, we derive the total surface/interfacial energy per unit length as

$$E(\alpha, \lambda) = \lambda\left\{\theta_1 r'_1\gamma_{S-M}\left[1 + \left(\frac{\alpha\pi}{\lambda}\right)^2\right] + \theta_2 r'_2\gamma_{PS}\left[1 + \frac{\left(\frac{\gamma_{S-M}}{\gamma_{PS}}\alpha\right)^2\pi^2}{\lambda^2}\right]\right\} \tag{8}$$

where the radii decreased according to eq 1. Unstable waves lead to reduction in E, which requires the first and second partial derivative of E, with respect to α at 0, should be zero and less than zero, respectively.[27] Taking the derivatives, we arrive at

$$\left.\frac{\partial E}{\partial \alpha}\right|_{\alpha=0} = 0 \tag{9}$$

$$\left.\frac{\partial^2 E}{\partial \alpha^2}\right|_{\alpha=0} = \frac{\gamma_{S-M}}{2\lambda}\left[\left(4\pi^2 r_1\theta_1 - \lambda^2\frac{\theta_1}{r_1}\right) + \left(4\pi^2\frac{\gamma_{S-M}}{\gamma_{PS}}r_2\theta_2 - \lambda^2\frac{\gamma_{S-M}\theta_2}{\gamma_{PS}r_2}\right)\right] < 0 \tag{10}$$

Equation 9 and 10 are necessary conditions for unstable waves to grow and lead to reduction in E. Equation 9 is ubiquitously satisfied and eq 10 yields only one legitimate inequality.

$$\lambda > 2\pi\sqrt{\frac{r_1\theta_1 + \frac{\gamma_{S-M}}{\gamma_{PS}}r_2\theta_2}{\frac{\theta_1}{r_1} + \frac{\gamma_{S-M}\theta_2}{\gamma_{PS}r_2}}} = 2\pi\sqrt{\frac{r_1(\theta_1 + \theta_2)}{\frac{\theta_1}{r_1} + \left(\frac{\gamma_{S-M}}{\gamma_{PS}}\right)^2\frac{\theta_2}{r_1}}} \tag{11}$$

Since $\theta_2 \ll \theta_1$ and $\gamma_{S-M} \ll \gamma_{PS}$, the inequality above can be simplified as

$$\lambda > 2\pi r_1 \tag{12}$$

i.e., only the initial radius of curvature at the PS/PMMA interface (Arc 1) is important for determining the cutoff wavelength, λ_c, above which the sinusoidal fluctuations on the strongly nonaxisymmetric liquid threads lead to a decrease of total system energy. In contrast, the PS−air surface plays only a minor role. Thus, the expression of λ_c for our nonaxisymmetric threads is the same as Plateau−Rayleigh's static analysis for an infinite perfect cylinder with identical radius r_1. By eq 11, we can estimate λ_c, for instance, in our PS31.6k/PMMA12k system, w = 400 nm, and h_1 = 140 nm. Solving eqs 3−7 gives the geometric parameters, r_1 = 212.0 nm, r_2 = 4150 nm, θ_1 = 2.47 rad, θ_2 = 0.096 rad. Plugging them in eq 11 gives λ_c for the nonaxisymmetric PS threads half-embedded in PMMA, $\lambda_c \approx$ 1.36 μm. From the experimental results shown below, the

dx.doi.org/10.1021/ma2026836 | Macromolecules 2012, 45, 1972−1981

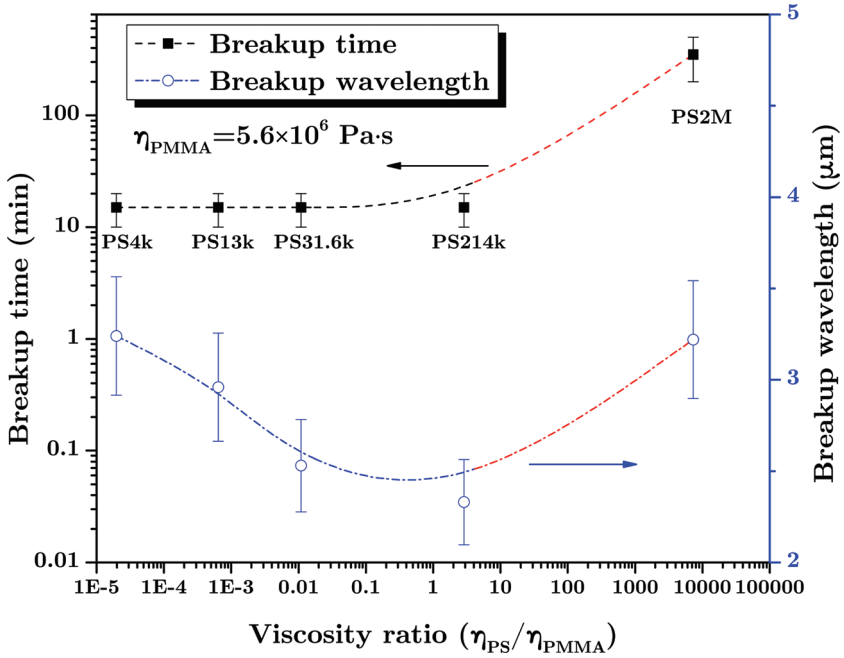

Figure 3. Influence of thread-to-matrix viscosity ratio on both the breakup time and characteristic wavelength of the capillary instability for the PS threads confined in the PMMA trenches after annealing at 140 °C. The dashed lines are a guide to the eye only.

minimum wavelength for the unstable capillary fluctuations for the partially embedded PS threads is indeed determined by the radius of curvature of the liquid−liquid interface r_1.

For our nonaxisymmetric threads, the following has to be taken into consideration additionally: (a) the different curvatures on the PS−air and the PS−PMMA side; (b) the difference between PS−air surface tension and PS−PMMA interfacial tension, and (c) the different viscosities of PMMA and air. An exact analytic or numeric treatment is still lacking in literature.

3.1.3. Characteristic Wavelength and Breakup Time of These Nonaxisymmetric PS Threads. As discussed above, all sinusoidal fluctuations with wavelengths above λ_c would lead to a reduction in the surface/interfacial energy of the system. However, oftentimes the morphology of the capillary breakup observed does not reflect such a broad distribution in wavelengths (Figure 1e). Rather, it reveals a characteristic/dominant wavelength. For an axisymmetric thread embedded in an immiscible viscous fluid matrix, Tomotika's pioneering theoretical work shows that the unstable sinusoidal fluctuations grow at significantly different rates.[12] The fastest growing mode quickly eclipses others and dominates the final morphology. Both the wavelength and the growth rate of the dominant mode is a known function of the initial cylinder radius and thread-to-matrix viscosity ratio.[12]

Here we provide first-hand experimental findings of both the characteristic wavelength and the breakup time of these nonaxisymmetric PS threads with varying molecular weights. As detailed in the Experimental Section, PS with molecular weight ranged from 4 kg/mol to 2000 kg/mol was examined while PMMA was kept identical, which allows for the thread-to-matrix viscosity ratio to span 10 orders of magnitude. Each sample was annealed at 140 °C, similar to the sample shown in Figure 1, and the evolving morphologies were determined with AFM. Similar to the PS214k/PMMA system discussed above, the characteristic wavelength for the capillary instability in each sample was determined from the PSD analysis of the AFM images. Furthermore, the breakup time, defined as the time at which the isolated droplets were formed, was obtained from the AFM measurements for each sample.

Figure 3 plots both the characteristic wavelength and the breakup time as a function of the thread-to-matrix viscosity ratio for all the samples studied. Here, the steady-state viscosity for both the monodisperse PS and PMMA were estimated from Majeste et al.[30] and Ahn et al.,[15] correspondingly. As shown in Figure 3, viscosities of the PS threads are significantly lower than that of the PMMA matrix for PS molecular weights smaller than 214 kg/mol, and become comparable to the matrix viscosity at 214 kg/mol. In this regime, the breakup time remains rather constant (~20 min) even though the thread-to-matrix viscosity ratio has increased 10 000 times, indicating that the breakup time is dictated by the invariant viscosity of the PMMA matrix. In contrast, as the PS molecular weight increases from 214 kg/mol to 2000 kg/mol, the thread viscosity becomes significantly larger than that of the PMMA matrix, and the breakup time increases dramatically from ~20 min to ~500 min. This suggests that the viscosity of the PS threads dictates the breakup kinetics.

From Figure 3, it is apparent that the more viscous component, either the threads or the matrix, is the rate-limiting factor for the breakup of the threads. Although a rigorous theoretical account of the kinetics of the capillary breakup of a nonaxisymmetric thread is still lacking, the qualitative trend is consistent with the two limiting cases in Tomotika's theory. Specifically, the growth rate, *in*, for an axisymmetric PS thread

dx.doi.org/10.1021/ma2026836 | *Macromolecules* 2012, 45, 1972−1981

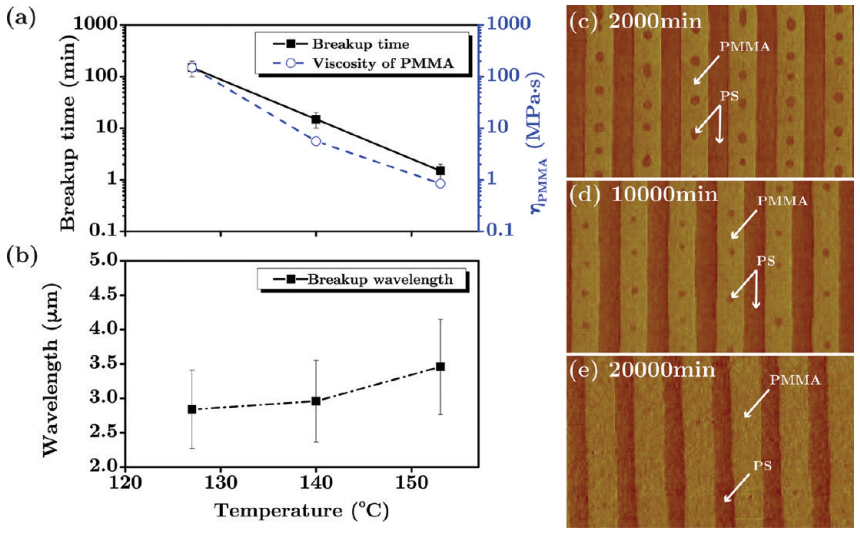

Figure 4. Influence of annealing temperature on (a) the time scale and viscosity of PMMA for the PS13k/PMMA12k system and (b) the characteristic wavelength of the capillary breakup. (c–e) AFM phase images (5 μm × 3 μm) of the sample surface after annealing at 114 °C for different amounts of time as labeled. The bright and dark regions correspond to the PMMA and PS domains, respectively.

completely embedded in a PMMA matrix, at the two extremes of viscosity ratios are

$$in = \begin{cases} \dfrac{1}{\eta_{PMMA}} \dfrac{\gamma_{S-M}\Omega_1(kr)}{2r}, & \eta_{PS}/\eta_{PMMA} \to 0 \\ \dfrac{1}{\eta_{PS}} \dfrac{\gamma_{S-M}\Omega_2(kr)}{2r}, & \eta_{PS}/\eta_{PMMA} \to \infty \end{cases} \tag{13}$$

where k is the wavenumber and r is the initial radius of the thread. $\Omega_1(kr)$ and $\Omega_2(kr)$ are nondimensional single-variable functions of kr, characterizing the growth rate of a perturbation with wavenumber k. Therefore, the more viscous component, thread or matrix, will dominate the growth rate or the breakup time of the threads, indicated by the viscosity terms in the denominators.

Since the viscosity of air is negligible compared to the polymers, the breakup kinetics is dictated by the PS/PMMA interface. This is also manifested by the morphology or the characteristic wavelength of the fastest growing mode. As shown in Figure 3, the characteristic wavelengths for all samples were around 3 μm, all of which were above the cutoff wavelength of each respective sample (~1.36 μm). The cutoff wavelength did vary slightly with the amount of PS cast. The error bars in the breakup time represent the upper and lower bound limited by experimental resolution, while for the breakup wavelength, they represent 10% off-peak values in our PSD fitting analysis. Interestingly, it appears that the breakup wavelength reaches a minimum when the thread-to-matrix viscosity ratio approaches 1. A calculation based on Tomotika's classical theory by Knops et al.[13] shows that, for a completely embedded axisymmetric viscous thread, the breakup wavenumber (inverse of breakup wavelength) reaches maximum at a thread-to-matrix viscosity ratio near 1 (see Figure 1 from ref 13). Although the exact physical system and geometries in our experiments were different from ref 13, the similarity indicates again the PS/PMMA interface plays a dominating role in choosing the fastest mode. On the other hand, if the PS/air surface was dominant, the fastest growing wavelength of a PS thread in air would tend to infinity,[12] disagreeing with the experimental results. As noted above, a rigorous theoretical work is still needed to describe both the wavelength and the growth rate associated with the fastest growing mode for a partially embedded nonaxisymmetric thread.

3.1.4. Influence of Annealing Temperature on the Capillary Instability of PS13k/PMMA12k. As discussed above, in the low thread-to-matrix viscosity ratio regime, the breakup time is controlled by the PMMA matrix viscosity. To further verify this, we annealed the samples at different temperatures. PS13k/PMMA12k system was annealed at 114, 127, 140, and 153 °C. At the three higher temperatures, the morphological evolutions, according to the AFM measurements, were similar to that shown in Figure 1.

The breakup time and characteristic wavelength of the capillary instability (for the larger PS threads confined in the PMMA trenches) are shown in Figure 4, parts a and b. Clearly, with the increase of annealing temperature, the breakup time was reduced dramatically while the breakup wavelength remained ~3 μm. It is known that PS and PMMA are "fragile" glass-forming liquids, whose viscosities have a similar dependence on temperatures.[31] Therefore, the viscosity ratio is not expected to vary significantly with the increase of annealing temperature, while the absolute values of the viscosities of both polymers decrease dramatically. Since reducing the PS viscosity over 5 orders of magnitude while keeping the matrix viscosity constant did not affect the breakup time, the significant reduction in breakup time with the increase of annealing temperature was most likely caused by the dramatic reduction in the matrix viscosity. In particular, Figure 4 shows 2 orders of magnitude of reduction in the viscosity of PMMA matrix, similar to the change observed in the breakup time.

The morphological evolution became extremely slow at 114 °C, a temperature slightly above the bulk T_g of PMMA (107 °C). Figure 4c–e show that the isolated larger PS threads remained unbroken even after 20000 min of annealing, once again suggesting that the PMMA viscosity dominated the breakup time of the PS threads. In comparison, the smaller PS threads (or stripes) on top of the PMMA mesas had completely broken up into droplets after 2000 min annealing. A similar

dx.doi.org/10.1021/ma2026836 | Macromolecules 2012, 45, 1972–1981

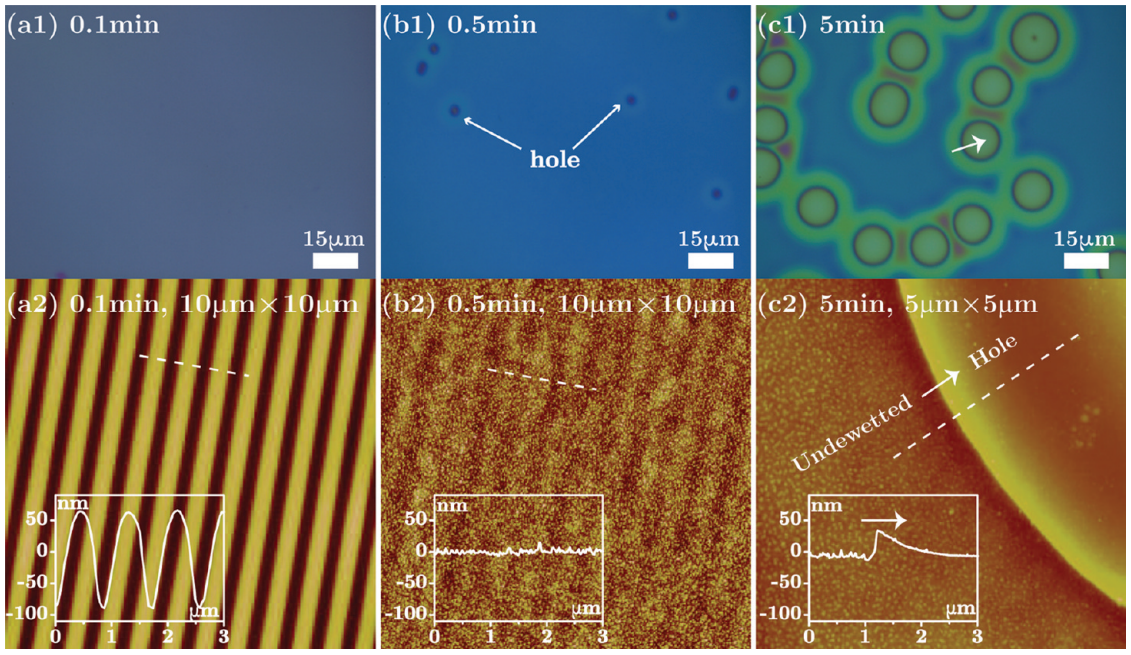

Figure 5. Morphologies of a thick PS layer, cast from 1.8 wt % solution, on the PMMA pattern, upon annealing at 153 °C for different amounts of time as labeled on the images. (a1−c1) Optical images of the sample surface. (a2−c2) Corresponding topographic AFM images of the PS/PMMA interface after selective removal of PS with cyclohexane. Insets in parts a2−c2 are the cross-sectional profiles.

trend was also observed for the partially embedded PS threads (Figure 1). In addition to the geometric reasons, it might also be that the effective viscosity of the PS within the ultrathin threads on the mesas (less than 20 nm, determined after selectively dissolve the PS) is much smaller than that of the larger ones. This could possibly be resultant from confinement-induced T_g reduction.[32] Interestingly, during extended annealing, the isolated PS droplets (radius ≈ (90−100) nm, depth ≈ (60−70) nm), gradually "sank" into the underlying PMMA, presumably to reduce the total surface/interfacial energy.

In contrast to the significant dependence of kinetics on the temperature, few variations in the breakup wavelength were found at the three annealing temperatures (Figure 4a). As discussed above, since the thread-to-viscosity ratio remained rather constant at different annealing temperatures and the geometry and boundary conditions were identical, the breakup wavelength was expected to be similar, as observed in Figure 4a.

3.2. Influence of the PS Film Thickness on the Instability of the PS/PMMA Patterns. The two-stage capillary instability discussed above was observed for all the systems, in which PS top layer did not form a thick continuous layer after short annealing. In order to draw a complete picture regarding the role of the PS film thickness, both PS13k and PS2000k films were cast onto the PMMA12k pattern from toluene solutions with varying concentrations. Their corresponding morphological evolutions upon thermal annealing are discussed below.

3.2.1. PS13k/PMMA12k. The deposition of PS onto topographically patterned surfaces via spin-coating is influenced by the interplay between flow and evaporation.[33,34] The spin-coating process of polymer solutions consists of two stages, flow-dominant stage and evaporation-dominant stage. Studies show that a critical film thickness divides the two stages. In the second stage, the fluid becomes so viscous that it ceases to flow.[33] After reaching this critical thickness, evaporation of the solvent dictates the partitioning of the PS. Qualitatively, when using higher concentrations of PS solutions, the critical thickness should be reached quicker,[35] leaving more PS deposited on the PMMA patterns. When the PS13k solution concentration was 0.5 and 1.0 wt %, the as-cast PS did not form a continuous layer. As a result, a similar two-stage capillary breakup was observed (similar to that in Figure 1) with slight differences in the breakup time and wavelength that were caused by the differences in the width (or the amount) of the PS threads. As expected, the PS droplets formed from the use of the 1.0 wt % solution were larger than those formed when using the 0.5 wt % solution (see Figure S1, Supporting Information).

In contrast, for PS cast from 1.8 and 2.5 wt % solutions, no capillary instability was observed. For example, for PS cast from 1.8 wt % solution, both the PS surface and PS/PMMA interface (Figure 5a1 and a2) smoothed out quickly upon annealing and reached a planar bilayer configuration (Figure 5b1 and b2). AFM images of the PS/PMMA interface pattern heights became as small as few nanometers (Figure 5b2), and circular holes were nucleated within the PS film (Figure 5b1). The growth of these holes eventually led to the complete dewetting of the PS, forming PS droplets on top of the PMMA (not shown). This nucleation and growth mechanism is similar to that of a 65 nm thick PS13k film on top of a viscous PMMA substrate.[14] Furthermore, the AFM measurements revealed a characteristic undercut profile (inset of Figure 5c2) after selectively removing the top PS layer. This type of interfacial profile at the dewetting rim in Figure 5c1 is consistent with that observed in the dewetting of PS planar film on top of a viscous PMMA film (regime I in ref 24).

3.2.2. PS2000k/PMMA12k Patterns. Both the capillary instability and dewetting described above are characteristic viscous instabilities driven by the minimization of surface/interfacial energy of the system via viscous dissipation. With an increase in molecular weight, the viscoelasticity of the polymers

dx.doi.org/10.1021/ma2026836 | *Macromolecules* 2012, 45, 1972−1981

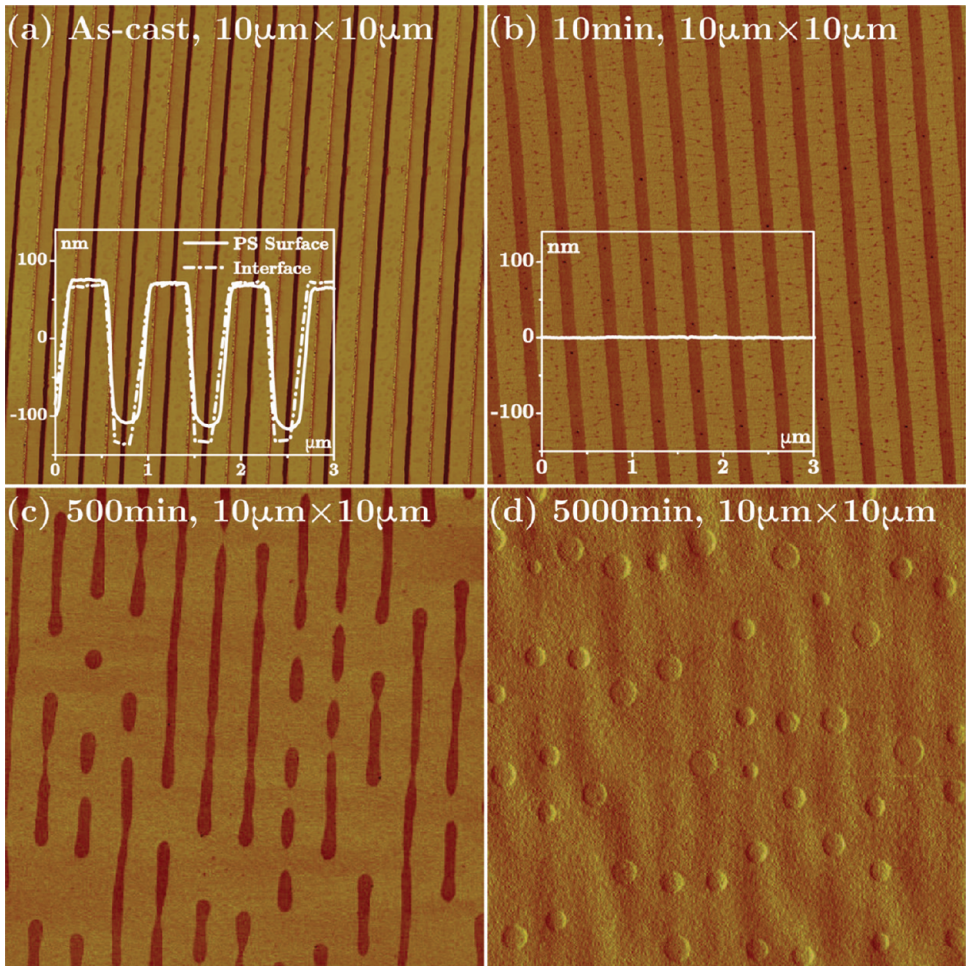

Figure 6. AFM phase images of PS2000k (cast from 0.6 wt % solution)/PMMA12k patterns after annealing at 140 °C for different amounts of time as labeled on the images. The inset in part a shows the representative cross-sectional profiles of both the PS surface and PS−PMMA interface. The inset in part b shows the cross-sectional profile of the surface.

becomes increasingly evident. Here, PS2000k films with varying thickness were cast onto the PMMA12k patterns, from toluene solutions with concentrations of 0.6, 0.8, and 1.0 wt %, to examine the influence of the viscoelasticity on the overall film instabilities.

Figure 6 shows that the morphological evolution in PS2000k0.6%/PMMA was similar to the one shown in Figure 1: a quick surface leveling led to isolated PS stripes/threads, which broke up via capillary instability. Because of the low concentration of PS solution used, the PS stripes left on top of the PMMA mesas were only around 3 nm thick (inset of Figure 6a), which did not show a clear capillary breakup. The capillary breakup of the larger threads confined in PMMA trenches (~23 nm thick after casting) shows that the breakup time (~500 min) was significantly longer than that of the lower molecular weight PS (~20 min) at the same annealing temperature, as shown in Figure 3.

In comparison, PS2000k cast from 0.8 and 1.0 wt % solution onto the PMMA pattern showed distinctive morphological evolutions, the latter of which is shown in Figure 7 (the images for PS2000k cast from 0.8% solution are provided in Figure S3, Supporting Information). The as-cast pattern has a cross-sectional profile showing round and smooth tops as opposed to the flat edged tops in PS2000k0.6%/PMMA system (Figure S2, Supporting Information). This curvature strongly suggests a continuous coverage of the PS2000k capping layer over the PMMA patterns. After 20 min, the surface of the PS decayed to ~6 nm tall (Figure 7a). The apexes of the PS lines were at the center of the PMMA trenches, while valleys corresponded to the PS on the PMMA mesas (Figure 7a).

After 50 min, holes were found to be nucleated in the PS upper layer on top of the PMMA mesas, where the PS film was the thinnest (Figure 7b). This time scale was significantly shorter than the capillary-breakup time for the isolated PS2000k threads in Figure 6. The growth/merging of these holes caused the PS threads to bend and form bridges between neighboring ones. The result was a mesh-like PS structures on top of the PMMA film after 100 min of annealing. The mesh-like structure in the PS2000k0.6%/PMMA system appears evidently different, in terms of diameter and connectivity, from PS2000k0.8%/PMMA system (Figure S3 in Supporting Information), which suggests concentration of spin-coating solution as a controlling parameter. This mesh-like network then evolved via local merging of PS threads, which eventually ruptured into isolated droplets via capillary instability after 1000 min (Figure 7, parts d and e). This rupture time was longer than that observed in Figure 6, because the average diameter/cross-section of the threads in the mesh-like structure was larger. Further annealing led to the shape changes of the isolated PS droplets driven by the interfacial tension (Figure

dx.doi.org/10.1021/ma2026836 | *Macromolecules* 2012, 45, 1972−1981

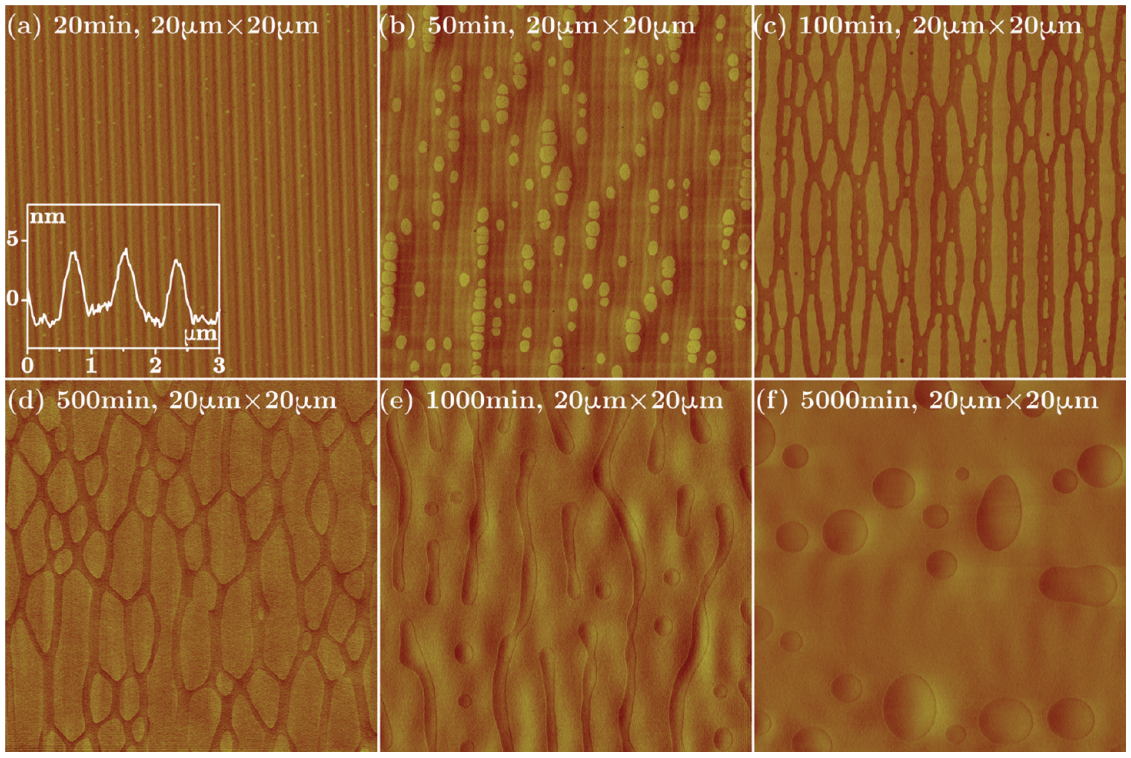

Figure 7. AFM phase images of PS2000k (cast from 1.0 wt % solution)/PMMA12k patterns after annealing at 140 °C for different amounts of time as labeled on the images. The inset in part a shows the cross-sectional profile of the sample surface for the corresponding sample.

7f). Clearly, the distribution of the diameter of the PS droplets is much broader than the one shown in Figure 6, due to the formation of the intermediate mesh-like morphology. Clearly, the elasticity of the highly entangled polymers, manifested in the bending of the lines, can signficantly influence the final morphology resulted from viscous instabilty.

4. CONCLUSIONS

In this study, we systematically examined the instability of the bilayer polymer patterns formed by casting of PS onto topographic PMMA patterns and subsequent thermal annealing at temperatures above the T_g of both polymers. A range of instabilities were observed depending on the molecular weight and amount of PS cast on the PMMA.

When the PS cast on the PMMA pattern did not form a continuous layer, a two-stage capillary instability was observed. Upon annealing, the PS quickly formed confined threads both on top of the PMMA mesas and within the PMMA trenches. These nonaxisymmetric PS threads, partially embedded in the PMMA matrix, broke up into isolated droplets via capillary instability. Systematic measurements showed that the breakup time depended on the thread-to-matrix viscosity and was dictated by the more viscous phase. In contrast, the characteristic wavelength of the capillary breakup only slightly depended on the viscosity ratio, and reached a minimum as the viscosity ratio approached 1. Although these experimental results can be qualitatively understood from the limiting cases of Tomotika's theory, an exact theoretical description of the capillary instability in such nonaxisymmetric threads is still lacking.

When the top PS layer was thick enough to form a continuous layer shortly after annealing, the instability of the film varied with the molecular weight of the PS. When the molecular weight of the PS was low, a planar PS/PMMA bilayer was formed after annealing. Subsequently, the PS upper layer dewetted from the PMMA via a random nucleation and growth mechanism. For high molecular weight PS, the PS/PMMA interface remained corrugated with a continuous PS layer on top. Localized nucleation in the PS layer occurred on top of the PMMA mesas, which resulted in a mesh-like PS morphology. Eventually, this PS fibrillar network broke into droplets due to capillary instability. Therefore, by controlling the molecular weight and spin-cast volume, a rich spectrum of micro- and nanoscale structures can be obtained that are potentially useful for a range of applications.

■ ASSOCIATED CONTENT

Supporting Information

AFM phase images, AFM height images, and a cross-sectional profile. This material is available free of charge via the Internet at http://pubs.acs.org/.

■ AUTHOR INFORMATION

Corresponding Author

*E-mail: Yifu.Ding@Colorado.edu.

Notes

The authors declare no competing financial interest.

■ ACKNOWLEDGMENTS

The authors acknowledge the funding support from the National Science Foundation under Grant No. CMMI-1031785. Acknowledgment is made to the donors of the Petroleum Research Fund, administered by the American Chemical Society, for partial support of this research (Grant Number: ACS-PRF 50581-DNI7).

REFERENCES

(1) Xie, R.; Karim, A.; Douglas, J. F.; Han, C. C.; Weiss, R. A. *Phys. Rev. Lett.* **1998**, *81*, 1251−1254.
(2) Schäffer, E.; Harkema, S.; Roerdink, M.; Blossey, R.; Steiner, U. *Macromolecules* **2003**, *36*, 1645−1655.
(3) Schäffer, E.; Thurn-Albrecht, T.; Russell, T. P.; Steiner, U. *Nature* **2000**, *403*, 874−877.
(4) Morariu, M. D.; Voicu, N. E.; Schäffer, E.; Lin, Z.; Russell, T. P.; Steiner, U. *Nat. Mater.* **2002**, *2*, 48−52.
(5) Reiter, G. *Phys. Rev. Lett.* **1992**, *68*, 75−78.
(6) Reiter, G. *Langmuir* **1993**, *9*, 1344−1351.
(7) Stange, T. G.; Evans, D. F.; Hendrickson, W. A. *Langmuir* **1997**, *13*, 4459−4465.
(8) Higgins, A. M.; Jones, R. A. L. *Nature* **2000**, *404*, 476−478.
(9) Herminghaus, S.; Brinkmann, M.; Seemann, R. *Annu. Rev. Mater. Res.* **2008**, *38*, 101−121.
(10) Rockford, L.; Liu, Y.; Mansky, P.; Russell, T. P.; Yoon, M.; Mochrie, S. G. J. *Phys. Rev. Lett.* **1999**, *82*, 2602−2605.
(11) Sehgal, A.; Ferreiro, V.; Douglas, J. F.; Amis, E. J.; Karim, A. *Langmuir* **2002**, *18*, 7041−7048.
(12) Tomotika, S. *Proc. R. Soc. London, Ser. A: Math. Phys. Sci.* **1935**, *150*, 322−337.
(13) Knops, Y. M. M.; Slot, J. J. M.; Elemans, P. H. M.; Bulters, M. J. H. *AIChE J.* **2001**, *47*, 1740−1745.
(14) Ahn, D. U.; Wang, Z.; Yang, R.; Ding, Y. *Soft Matter* **2010**, *6*, 4900−4907.
(15) Ahn, D. U.; Ding, Y. *Soft Matter* **2011**, *7*, 3794−3800.
(16) Ding, Y.; Kisliuk, A.; Sokolov, A. P. *Macromolecules* **2004**, *37*, 161−166.
(17) Jung, G.; Li, Z.; Wu, W.; Chen, Y.; Olynick, D. L.; Wang, S.; Tong, W. M.; Williams, R. S. *Langmuir* **2005**, *21*, 1158−1161.
(18) Ferry, J. *Viscoelastic properties of polymers*, 3rd ed.; Wiley: New York, 1980.
(19) Kumaraswamy, G.; Ranganathaiah, C. *Polym. Eng. Sci.* **2006**, *46*, 1231−1241.
(20) Ding, Y.; Ro, H.; Douglas, J.; Jones, R.; Hine, D.; Karim, A.; Soles, C. *Adv. Mater.* **2007**, *19*, 1377−1382.
(21) Ding, Y.; Ro, H. W.; Germer, T. A.; Douglas, J. F.; Okerberg, B. C.; Karim, A.; Soles, C. L. *ACS Nano* **2007**, *1*, 84−92.
(22) Ennis, D.; Betz, H.; Ade, H. *J. Polym. Sci., Part B: Polym. Phys.* **2006**, *44*, 3234−3244.
(23) Wang, C.; Krausch, G.; Geoghegan, M. *Langmuir* **2001**, *17*, 6269−6274.
(24) Lambooy, P.; Phelan, K. C.; Haugg, O.; Krausch, G. *Phys. Rev. Lett.* **1996**, *76*, 1110−1113.
(25) Rayleigh, L. *Philos. Mag.* **1892**, *34*, 145.
(26) Rayleigh, L. *Philos. Mag.* **1892**, *34*, 177.
(27) Son, Y.; Martys, N. S.; Hagedorn, J. G.; Migler, K. B. *Macromolecules* **2003**, *36*, 5825−5833.
(28) de Gennes, P.; Brochard-Wyart, F.; Quere, D. *Capillarity and wetting phenomena: drops, bubbles, pearls, waves*, 1st ed.; Springer: Berlin, 2003.
(29) Mark, J. E. *Physical Properties of Polymers Handbook*, 2nd ed.; Springer: New York, 2007.
(30) Majeste, J.; Montfort, J. P.; Allal, A.; Marin, G. *Rheol. Acta* **1998**, *37*, 486−499.
(31) Böhmer, R.; Ngai, K. L.; Angell, C. A.; Plazek, D. J. *J. Chem. Phys.* **1993**, *99*, 4201.
(32) Alcoutlabi, M.; McKenna, G. B. *J. Phys.: Condens. Matter* **2005**, *17*, R461−R524.
(33) Meyerhofer, D. *J. Appl. Phys.* **1978**, *49*, 3993.
(34) Yu, Z.; Hwu, J.; Liu, Y.; Gauzner, G.; Lee, K.; Kuo, D. *J. Appl. Phys.* **2011**, *110*, 014303.
(35) Hall, D. B.; Underhill, P.; Torkelson, J. M. *Polym. Eng. Sci.* **1998**, *38*, 2039−2045.

Macromolecules

Article

pubs.acs.org/Macromolecules

Thermoreversible Gel−Sol Behavior of Rod−Coil−Rod Peptide-Based Triblock Copolymers

Venkata Krishna Kotharangannagari,[†,‡,∥] Antoni Sánchez-Ferrer,[‡,∥] Janne Ruokolainen,[§] and Raffaele Mezzenga*[,‡]

[†]Department of Physics and Frimat Center for Nanomaterials, University of Fribourg, Chemin du Museé 3, 1700 Fribourg, Switzerland

[‡]Food & Soft Materials Science, Institute of Food, Nutrition & Health, ETH Zurich, Schmelzbergstrasse 9, 8092 Zurich, Switzerland

[§]Department of Applied Physics, AALTO University, P.O. Box 15100, 00076 Helsinki, Finland

Supporting Information

ABSTRACT: A series of peptide-based triblock copolymers consisting of poly(γ-benzyl-L-glutamate)-*b*-poly(dimethylsiloxane)-*b*-poly(γ-benzyl-L-glutamate) [PBLG-*b*-PDMS-*b*-PBLG] were synthesized using ring-opening polymerization (ROP). The chemical structure and degree of polymerizations were evaluated by ^{1}H NMR. These triblock copolymers form thermoreversible gels in toluene with critical gel concentration as low as 1.5 wt % and following trends which correlate directly with the secondary structure of the peptidic block. Fourier transform infrared spectroscopy (FTIR) studies indicate that the α-helical content is increased while β-sheets and random coil contents are systematically decreased with increasing volume fraction of the PBLG blocks. The gel−solution transition behavior of the triblock copolymers was examined using modulated dynamic light scattering (MDLS). It was observed that all the gels undergo gel−solution transition around 50 °C and revert back to its original state when cooling down to room temperature. Dye diffusion and diffusing wave spectroscopy (DWS) experiments showed a reduced mobility of both the dye molecules and tracer particles in the gels compared to that in solution state. The rheological studies on the organogels indicate that increasing molecular weight of the PBLG blocks or concentration of the triblock copolymers increase the gel strength considerably. Using transmission electron microscopy (TEM), the morphology of the organogels was shown to be prevalently formed by nanofibrils, with an average thickness in the range of 6−12 nm.

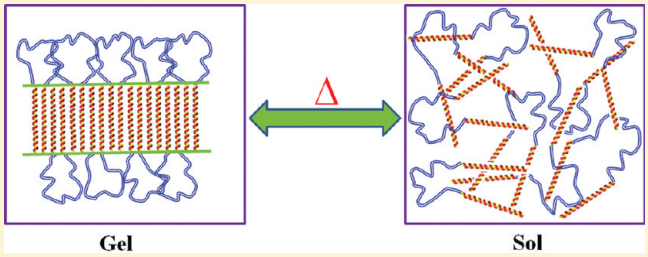

INTRODUCTION

The self-assembly behavior of rod−coil block copolymers is different from the common coil−coil block copolymers due to the presence of the rigid segment in their architectures and has attracted great attention in recent years.[1−7] When dissolved in solution, in some rod−coil block copolymer systems, the polymers can form nanostructured gels in solution instead of micelles.[8] Generally, the network formation in polymers can occur through chemical cross-linking between polymer chains or physical interactions through the entanglements or self-assembled supramolecular structures. These physical gels can exhibit reversible sol−gel transitions by changing temperature, pH, ionic strength, or concentration of the solution.[9]

Gels are a class of soft materials composed of a confined phase in a continuous three-dimensional network. On the basis of the solvent media, gels are classified in two kinds of systems: hydrogels (in aqueous medium) and organogels (in organic medium). Gels are predominantly composed of liquids; nevertheless, in terms of their mechanical response, they behave like a solid material. Moreover, in peptide-based block copolymers, gels can be further tuned by ionic interactions, coil−coil interactions, or hydrophobic association.[10−12]

In the case of peptide-based hydrogel systems, the gel formation is based on hydrophobic interactions due to the hydrophobicity of some amino acid residues (i.e., valine or leucine), which maintains the α-helix as a supramolecular self-assembled structure. Small peptide-based gels have been shown to undergo into molecular fibril networks and showed thermoreversibility and pH responsiveness.[13,14] Peptide-based rod−coil diblock copolymers can form hydrogels with various potential applications in biotechnology.[15−17]

Organogels have unique applications, which are not possible for hydrogels, and these organic-based gels are currently an area of active research.[18−20] The peptide-based block copolymer organogel formation is similar to that of hydrogels, typically through noncovalent interactions such as hydrogen bonding,

Received: December 5, 2011
Revised: February 1, 2012
Published: February 15, 2012

$\pi-\pi$ stacking, van der Waals interactions, and solvophobic interactions.[21−25]

Poly(γ-benzyl-L-glutamate) (PBLG) is a synthetic peptide, which forms α-helices at high degree of polymerization[26] by intramolecular hydrogen bonding.[27,28] This rigid-rod-like structure of PBLG[29−31] shows thermotropic liquid-crystalline order in bulk[32,33] and thermoreversible gelation behavior in solution.[34,35] Indeed, the synthesis and self-assembly of PBLG-based rod−coil block copolymers have been studied extensively due to its biocompatibility for several decades, and the resulting functional materials have several applications in the biomedical and tissue engineering field.[36−39]

The pure PBLG homopolymer form thermoreversible gels in solvents such as toluene or benzyl alcohol passing through a lyotropic liquid-crystalline phase before gelation,[40,41] and fibril-like network structures were found in pure PBLG homopolymer gels.[34] Recently, PBLG-based rod−coil diblock copolymers have been prepared, and their solutions showed thermoreversible gel formation in toluene.[42] The mechanism for the self-assembly behavior of the PBLG-based rod−coil block copolymers suggests that a wide variety of this kind of systems with novel architectures could generate supramolecular structures in solution. Very recently, the synthesis and gel formation in toluene of PBLG−POSS (polyhedral oligomeric silsesquioxane) diblock copolymers have been reported, where the POSS block protrusion from the ribbons prevented the aggregation of the nanoribbons and allowed the formation of clear gels.[43] Block copolymers of poly(Z-lysine) with different coil blocks showed an increase in the gel strength with increasing the molecular weight of the peptide block.[44]

Peptide-based rod−coil−rod triblock copolymers have been synthesized and studied in bulk state,[45−48] but the thermoreversible gel−sol behavior of such systems has never been explored before. For this purpose, we synthesized and characterized a series of six rod−coil−rod triblock copolymers consisting of PBLG-*b*-PDMS-*b*-PBLG, where the degree of polymerization of the peptide-based sequences was systematically modified. The choice for these polymers (PBLG and PDMS) was based on their biocompatibility, the rigidity and self-assembly features of the PBLG block, and the low T_g and high solubility in toluene of the PDMS segment. By controlling the degree of polymerization and the α-helical content of the peptide blocks, we were able to control the self-assembly behavior of PBLG rods and the gel formation of the triblock copolymers into fibril-like networks.

EXPERIMENTAL PART

Materials. L-Glutamic acid γ-benzyl ester (Fluka, ≥99.0%), triphosgene (Aldrich, 98%), *N*,*N*-dimethylformamide, DMF (Sigma-Aldrich, ≥99.8%, over molecular sieve), dichloromethane, DCM (Acros, 99.99%), methanol (Fluka, 99.8%), and toluene (Fluka, ≥99.7%) were used as received. Ethyl acetate (Sigma-Aldrich, ≥99.9%) and cyclohexane (Sigma-Aldrich, ≥99.9%) were dried and distilled over CaH_2 (Fluka, >97.0%) at normal pressure. Poly(dimethylsiloxane) (PDMS), diaminopropyl-terminated, was purchased from ABCR Chemicals, Germany. The (*E*)-4,4′-bis(hex-5-en-1-yloxy)azobenzene dye was synthesized accordingly to the literature.[49] Dried silica microspheres (540 nm diameter, SS03N, Bangs Laboratories) were dispersed in toluene at 10 wt % concentration.

Synthesis of (BLG-NCA) Monomer. The BLG-NCA monomer (γ-benzyl L-glutamate *N*-carboxyanhydride) was synthesized as published in our previous work.[26] Briefly, 15 g (63.2 mmol, 1 equiv) of γ-benzyl L-glutamate and 8.13 g (27.4 mmol, 0.43 equiv) of triphosgene were placed in a 500 mL two-necked round-bottomed flask equipped with a magnetic stirrer, condenser, and nitrogen inlet. The system was purged with nitrogen for 10 min, 250 mL of freshly distilled ethyl acetate over CaH_2 was added, and the reaction mixture was brought to 145 °C. After several hours (5−6 h), the reactants were completely soluble, and the reaction was cooled down to room temperature. The monomer was obtained by recrystallization from ethyl acetate/cyclohexane. Yield: 15.3 g (91%). ^{1}H NMR (360 MHz, $CDCl_3$): δ = 7.10−7.42 (5H, m, Ar), 6.62 (1H, s, NH), 5.04 (2H, s, Ar−CH_2), 4.29 (1H, t, α-CH, J = 6.0 Hz), 2.50 (2H, t, γ-CH_2, J = 6.6 Hz), 2.16 (1H, m, β-CH), 2.03 (1H, m, β-CH) ppm.

Synthesis of PBLG-*b*-PDMS-*b*-PBLG Triblock Copolymers. All triblock copolymers were obtained by using the procedure described in what follows. As a representative example, the synthesis of the triblock copolymer P25 ($PBLG_{24}$-$PDMS_{314}$-$PBLG_{24}$) is described. In a 25 mL round-bottomed flask, the BLG-NCA monomer was dissolved in dry DMF under a nitrogen atmosphere. In another 10 mL round-bottomed flask, the diamino-terminated poly(dimethylsiloxane) (H_2N-PDMS-NH_2) macroinitiator was dissolved in dry DMF under a nitrogen atmosphere. The monomer solution was transferred to the polymer solution by syringe. The resulting mixture was stirred at room temperature for 5 days under a nitrogen atmosphere. Afterward, the solvent was removed under vacuum, and the residue was dissolved in DCM. The resulting triblock copolymer was obtained as a white solid after reprecipitation with cold methanol followed by centrifugation (3000 rpm, 0 °C). The supernatant was then removed, and this process was repeated three times. Yield: 85−90%. ^{1}H NMR (360 MHz, $CDCl_3$): δ = 9.00−7.70 (43H, NH), 7.60−6.90 (241H, Ar), 5.50−4.60 (91, Ar−CH_2), 4.50−3.60 (47H, α-CH), 2.85−1.40 (212H, β-CH_2 and γ-CH_2), 1.00−0.70 (26H, Si−β-CH_2), 0.65−0.40 (10H, Si−α-CH_2), 0.35−0.00 (1874H, Si−CH_3) ppm.

Preparation of the Organogels. The gels of PBLG-*b*-PDMS-*b*-PBLG triblock copolymers were prepared in toluene according to the published procedure.[42] The required amounts of polymer and toluene were placed together in a sample vial. Afterward, the sealed vial was heated until the mixture became homogeneous. The polymer solution was brought to room temperature and maintained at this temperature for 48 h. Gelation was monitored—at first—by the test tube invert method. The lowest gelation concentration was identified as the critical concentration for the gelation (c_{gel}). The gel−sol transition temperature (T_{gel}) was measured by the procedure reported by Hirst et al.[50] All c_{gel} and T_{gel} values were measured in triplicates.

Techniques and Apparatus. ^{1}H NMR measurements were carried out at room temperature on a Bruker DPX-360 spectrometer operating at 360 MHz and using $CDCl_3$ as solvent.

Fourier transform infrared (FTIR) spectra of solid samples were measured at room temperature using a Bruker Tensor 27 FTIR spectrometer in attenuated total reflection (ATR) mode. For the gel samples, the FTIR measurements were performed on a Varian 640 instrument, placing the sample between two CaF_2 windows in transmission mode.

Modulated dynamic light scattering (MDLS) measurements were performed using a LS Instruments apparatus with a He−Ne laser beam (632.8 nm). The instrument is equipped with advanced modulated 3D cross-correlation technology, which suppresses the multiple scattering. Samples were prepared in glass cuvettes of 10 mm thickness. The scattered intensity fluctuations were collected at a fixed angle of 90° and averaged from three runs of 600 s each. The measurements were performed on selected samples at different temperature conditions ranging from 25 to 60 °C with 5 °C steps. Temperatures were controlled by a thermostat within an error of 0.1 °C.

Diffusing wave spectroscopy (DWS) measurements were carried out in a transmission mode using a commercial DWS apparatus (LS Instruments) with a He−Ne laser beam (λ = 632.8 nm). Samples were prepared and placed in quartz cuvettes with a 2 mm optical path length. The silica tracer nanoparticles (~20 μL) were added to the polymer solution, and the cuvette temperature was controlled with a Peltier temperature controller (±0.2 °C), keeping the samples 10 min at the required temperature before the measurement started. The observed autocorrelation function was determined with a digital

Scheme 1. Synthetic Route for the Obtaining the PBLG-*b*-PDMS-*b*-PBLG Triblock Copolymers

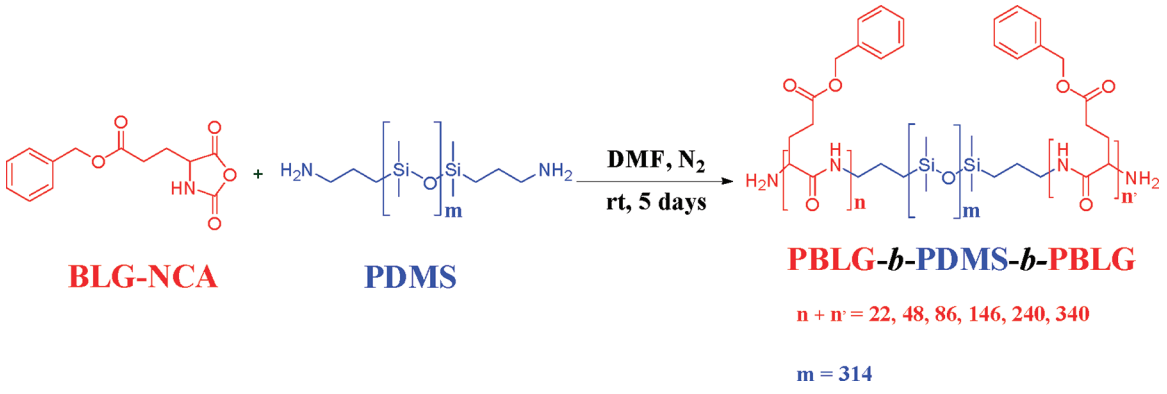

Table 1. Number-Average Molar Mass (M_n), Average Degree of Polymerization (DP_{PBLG}) of One PBLG Segment, Volume Fraction (ϕ_{PBLG}) of the Two PBLG Segments, Critical Gelation Concentration (c_{gel}), Gel−Sol Transition Temperature (T_{gel}), and the Theoretical Length of the Peptide Segment (L_α) in a α-Helix Conformation for the PBLG-*b*-PDMS-*b*-PBLG Triblock Copolymers

sample	block composition	M_n[a] (g mol^{-1})	$M_{n,PBLG}$[a] (g mol^{-1})	DP_{PBLG}[a]	ϕ_{PBLG}[b]	c_{gel} (wt %)	T_{gel} (°C)	L_α[c] (nm)
P13	$PBLG_{11}$-$PDMS_{314}$-$PBLG_{11}$	27 800	4 600	11	0.13	3.5	42	1.7
P25	$PBLG_{24}$-$PDMS_{314}$-$PBLG_{24}$	33 500	10 300	24	0.25	1.5	42	3.6
P38	$PBLG_{43}$-$PDMS_{314}$-$PBLG_{43}$	42 000	18 800	43	0.38	1.5	44	6.5
P51	$PBLG_{73}$-$PDMS_{314}$-$PBLG_{73}$	55 300	32 100	73	0.51	1.5	45	11
P63	$PBLG_{120}$-$PDMS_{314}$-$PBLG_{120}$	75 700	52 500	120	0.63	1.5	46	18
P71	$PBLG_{170}$-$PDMS_{314}$-$PBLG_{170}$	97 800	74 600	170	0.71	1.5	46	26

[a]Calculated by ^{1}H NMR . [b]Calculated from the following equation: $\phi_{PBLG} = M_{n,PBLG}\,\rho_{PBLG}^{-1}/(M_{n,PBLG}\,\rho_{PBLG}^{-1} + M_{n,PDMS}\,\rho_{PDMS}^{-1})$, where ρ_{PBLG} = 1.278 g cm^{-3} and ρ_{PDMS} = 0.97 g cm^{-3}. [c]Calculated from the following equation: $L_\alpha = 0.15 DP_{PBLG}$.

correlator, and the electric field autocorrelation function $g_2(t) - 1$ was acquired over 120 s.

The mechanical properties of the organogels were studied using an AR 2000 stress-controlled rheometer (TA Instruments) with steel cone−plate configuration (20 mm diameter cone with an angle of 2°). First, a stress sweep was performed from 0.1 to 100 Pa at a frequency of 1 Hz. After a rigorous preshear (6 rad s^{-1} in steady state, 2 min), the recovery of the gel was measured as a function of time under a stress of 0.1 Pa. Finally, a frequency sweep from 0.1 to 10 Hz was performed on the recovered gel under a stress of 0.1 Pa. The temperature of the plate was maintained at 25 °C. The gel strength was quantified by the evaluation of the shear storage modulus G'.

Transmission electron microscopy (TEM) images were acquired on a JEOL JEM-3200FSC electron microscope operating at 100 kV and bright field mode. TEM specimens were prepared by gently placing a few milligram fraction of organogel onto a carbon-coated copper grid; chemical staining to enhance phase contrast was carried out using vapors of an aqueous solution of RuO_4.

RESULTS AND DISCUSSION

In order to study the effect of the peptide volume fraction on the self-assembled gels, PBLG-*b*-PDMS-*b*-PBLG triblock copolymers were synthesized by systematically varying the PBLG content in the peptide sequence. The six different triblock copolymers with different degree of polymerization of the PBLG block were synthesized via ring-opening polymerization (ROP) of the γ-benzyl L-glutamate *N*-carboxyanhydride monomer (BLG-NCA)[51] using the corresponding PDMS diamino-terminated polymer (M_n = 23 200 g mol^{-1}) as macroinitiator according to the method described in the literature[28,52] and shown in Scheme 1. The required amounts of monomer and macroinitiator were dissolved in DMF and under a nitrogen atmosphere. After purification, the resulting triblock copolymers were fully characterized by ^{1}H NMR (Supporting Information, Figure SI-1). The degree of polymerization (DP), the average-number molecular weight (M_n), and the corresponding volume fraction of the peptide block (ϕ_{PBLG}) were evaluated by integrating the peak from the benzyl protons in the PBLG block—δ_{PBLG} (Ar−CH_2) = 5.50−4.60 ppm—and keeping the area of the peak from PDMS as constant—δ_{PDMS}(Si−CH_3) = 0.35−0.00 ppm. All the calculated values agreed with the stoichiometry used for the synthesis of the triblock copolymers and are summarized in Table 1.

For the preparation of the gels, the exact amounts of polymers and toluene were weighed in glass vials and heated to 75−80 °C for several minutes until homogeneous solutions were obtained. Afterward, the samples were brought to room temperature, and after 48 h the fully transparent gels were formed; by preparing different concentrations for each triblock copolymer, the critical gelation concentration (c_{gel}) could be determined (Table 1) and the phase diagram for the triblock copolymers constructed as shown in Figure 1. From the phase diagram, it can be observed that triblock copolymers with higher degree of polymerization can form gels at very low PBLG concentration. This trend seems to be consistent for all samples (dividing line in Figure 1) with critical gelation concentration of the triblock copolymer of 1.5 wt %. The only exception is that of the sample P13, which has very low degree of polymerization (DP = 11). As it will be shown below, this trend is the result of the very low α-helical content for this sample,[26] which does not promote the formation of gels. Moreover, the gel−sol transition temperature progressively increased when increasing the volume fraction of the PBLG blocks in the different samples (Supporting Information, Figure SI-2).

dx.doi.org/10.1021/ma2026379 | Macromolecules 2012, 45, 1982−1990

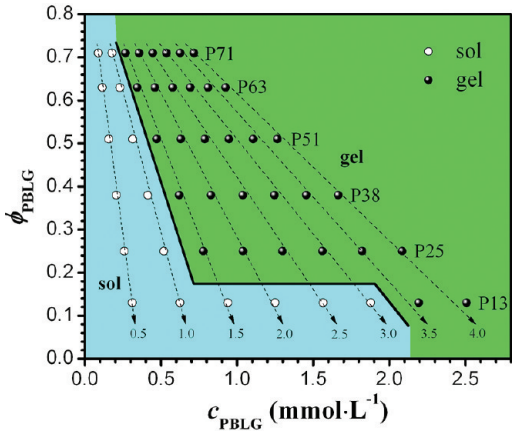

Figure 1. Phase diagram for PBLG-*b*-PDMS-*b*-PBLG triblock copolymer systems in toluene at 25 °C. (Note: the c_{PBLG} expresses the molar concentration of PBLG blocks, acting as physical linkers in the gelation process, and the numbers from the arrows are the weight percentage concentrations.)

In order to understand the influence of the secondary structure of these triblock copolymers on the gel properties, FTIR measurements were performed on all samples, both in solid state and in the gels. The FTIR spectra of all triblock copolymers in solid state clearly show characteristic absorption peaks of the peptide secondary structures (Figure 2a). The absorption peaks at 1650−1660 cm^{-1} (amide I) and at 1540−1550 cm^{-1} (amide II) are characteristic of the α-helix secondary structure.[53] The β-sheet population has absorption peaks at 1620−1640 and 1670−1680 cm^{-1},[54] and the random coil or turn populations at 1640−1650, 1660−1670, and 1680−1690 cm^{-1}, all in the amide I region.[55] The absorbance peak at 1731 cm^{-1} corresponds to the C=O stretching of the benzyl ester protecting group from the PBLG block. From the analysis of the amide I region and following the second derivative technique for the qualitative determination of the peaks maxima,[56] and the deconvolution technique[57] in a series of Lorentzian distributions, the populations of all secondary structures could be easily quantified[58] (Supporting Information, Figure SI-3a−d).

As shown in Figure 2a, the increase in the volume fraction of the PBLG block stabilized the α-helix content, while the β-sheet and random coil conformations decreased. The sample P13 showed mixture of α-helix and β-sheet populations, which is normal for PBLG blocks containing less than 18 residues, whereas the remaining polymers showed mainly α-helical content[26] with a gradual change in the secondary structure content as shown in Figure 2b. By increasing the volume fraction of the PBLG sequence, the α-helical content was increased from 56% to 89%, and the β-sheet and random coil

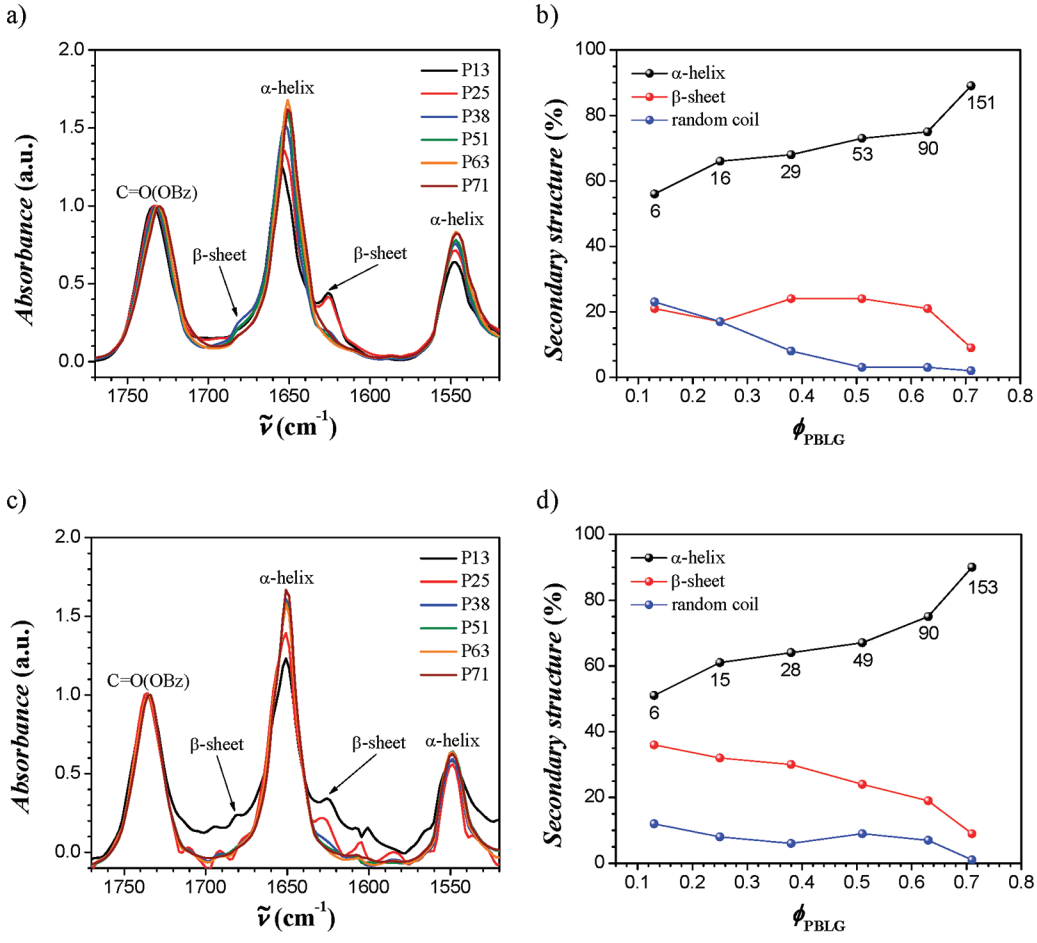

Figure 2. (a) FTIR spectra and (b) secondary structure populations for all triblock copolymers in solid state. (c) FTIR spectra and (d) secondary structure populations for all triblock copolymers in the gel state. Note: the numbers underneath black symbols are the average-number repeating units in the peptide block which contribute to the α-helical structure.

dx.doi.org/10.1021/ma2026379 | *Macromolecules* 2012, 45, 1982−1990

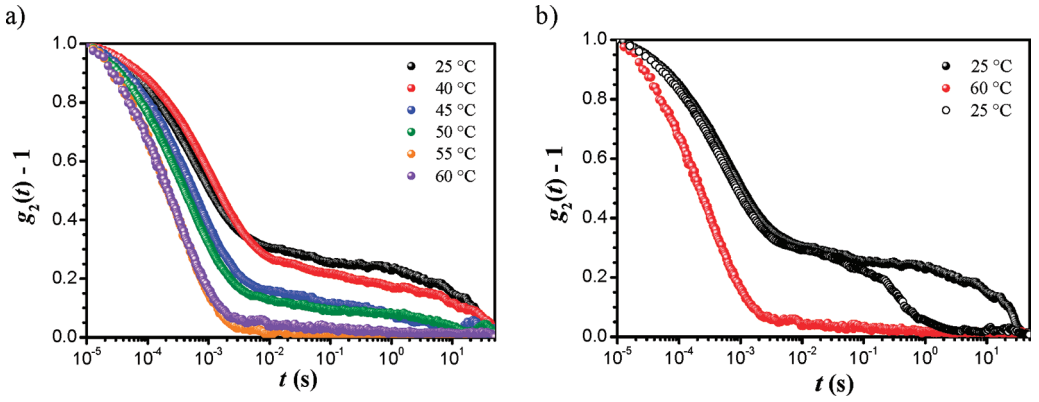

Figure 3. (a) Normalized electric field cross-correlation functions at different temperatures for the sample P63 at 2 wt % in toluene. (b) Normalized electric field cross-correlation functions at 25 °C, 60 °C, and back to 25 °C showing the thermoreversible behavior of the sample P63 at 2 wt % in toluene.

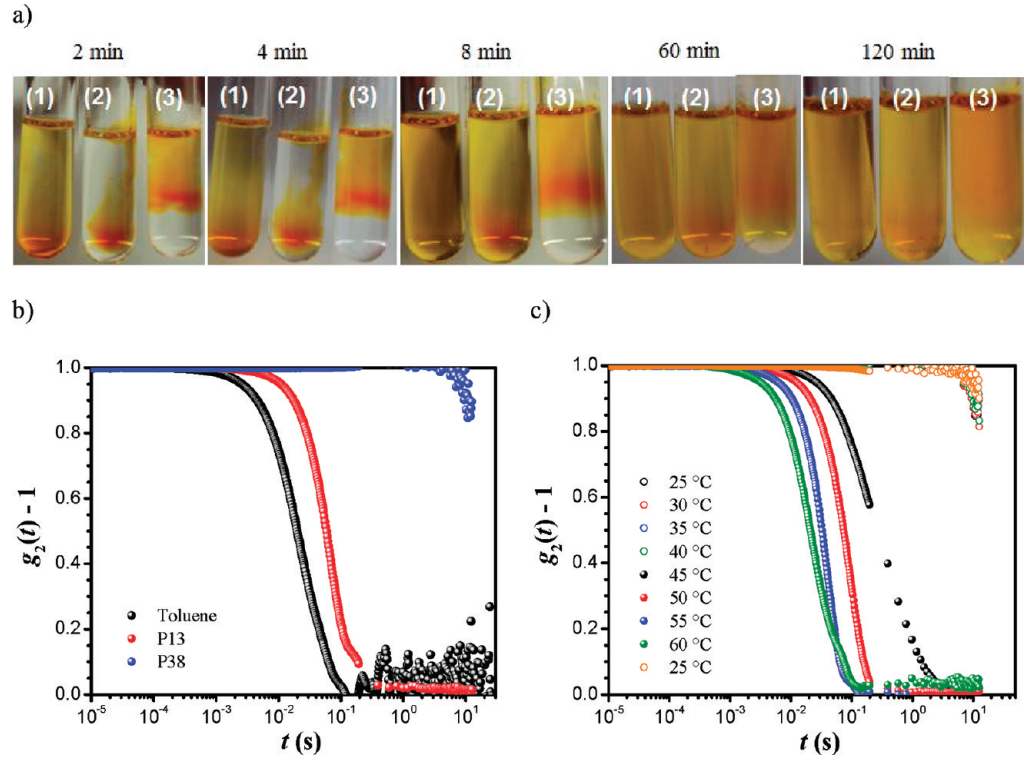

Figure 4. (a) Diffusion behavior of the azobenzene dye as a function of time in (1) toluene, (2) sample P13 at 2 wt % in toluene, and (3) sample P38 at 2 wt % in toluene at 25 °C. (b) Electric field autocorrelation function at 25 °C for the diffusion of silica tracer nanoparticles in pure toluene, in P13 and P38 at 2 wt % in toluene. (c) Electric field autocorrelation function at different temperatures for the sample P38 at 2 wt % in toluene.

populations decreased from 21% to 9% and from 23% to 2%, respectively.

Figure 2c shows the FTIR spectra of all block copolymers organogels at 25 °C and 2 wt %, with the exception of the sample P13, acquired at 4 wt %. The collected spectra agree nearly perfectly with those obtained in solid state. Thus, no significant differences were observed when the triblock copolymers formed the gel structure. In Figure 2d, the changes in α-helix population (from 51% to 90%), β-sheets (from 36% to 9%), and random coils (from 12% to 1%) as a function of the PBLG volume fraction are shown. Just small variations in the β-sheet and random coil populations can be observed, while the α-helix content remains nearly unaffected between solid and gel samples. We also run FTIR measurements at 50 °C to find out whether the gel−sol transition is originating from the loss of secondary structure rather than changes in solubility. However, identical FTIR spectra collected at 25 °C (gel state) and at 50 °C (sol state) (Supporting Information, Figure SI-3e) allow ruling out loss of secondary structure and confirm that the gel−sol behavior arises solely from changes in solubility of the PBLG block with temperature.

In order to follow the changes during the gel−sol transition and to observe the reversibility of the systems, modulated dynamic light scattering (MDLS) experiments on the gel samples in toluene were performed. At high concentrations, multiple scattering is expected in the measurements. Thus, in order to extract the single scattering information, we make use of a MDLS setup, equipped with two detectors which cross-correlate the scattered signal from the same volume and at the same scattering vector.[59] It is well-known that the intensity and

dx.doi.org/10.1021/ma2026379 | *Macromolecules* 2012, 45, 1982−1990

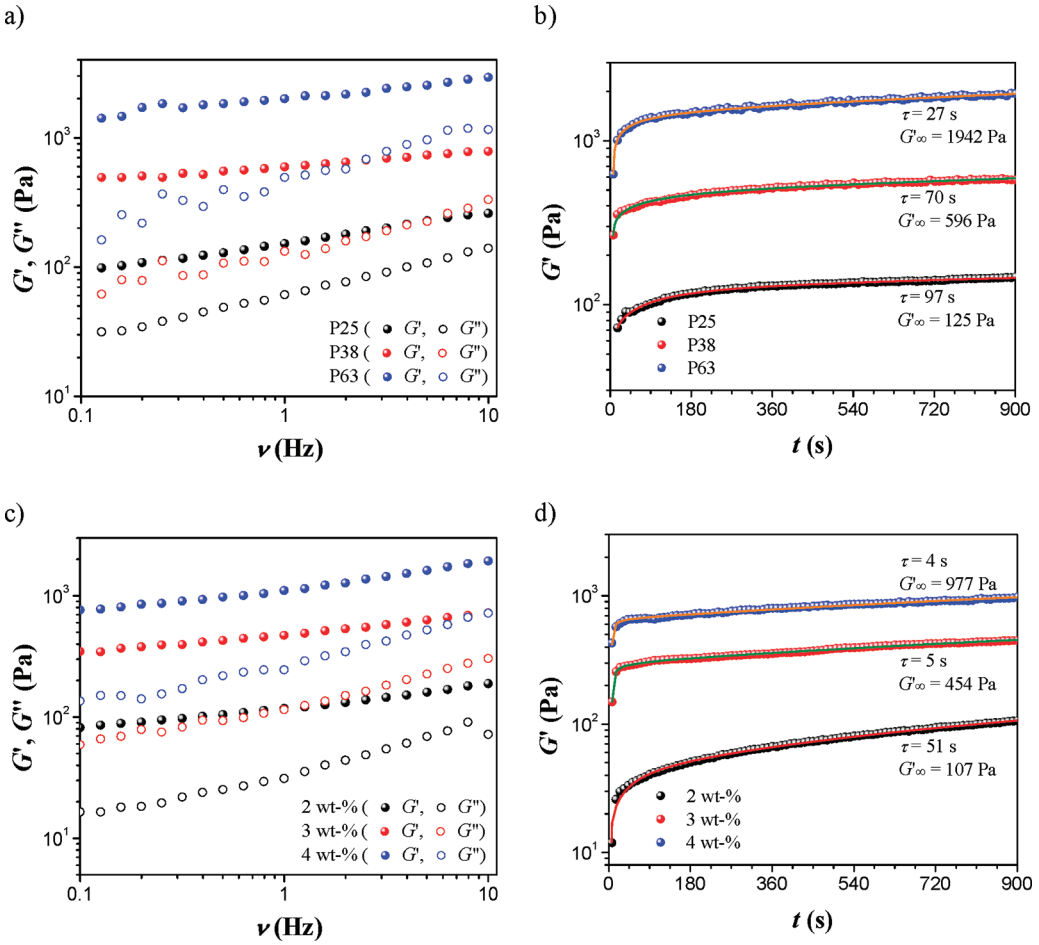

Figure 5. (a) Frequency sweeps experiments for the triblock copolymer P25, P38, and P63 at 2 wt % in toluene. (b) Recovery of the three organogels after a preshear at 6 rad s^{-1} for to 2 min. (c) Frequency sweeps experiments for the triblock copolymer P38 at different concentrations in toluene. (d) Recovery after a preshear at 6 rad s^{-1} for to 2 min.

electric fields correlation functions in gels decay at longer times compared to their corresponding solutions. Thus, a faster decay time should be observed when heating the gel samples above the gel−sol transition temperature. MDLS measurements were carried out on the samples P25 ($PBLG_{24}$-$PDMS_{314}$-$PBLG_{24}$), P38 ($PBLG_{43}$-$PDMS_{314}$-$PBLG_{43}$), and P63 ($PBLG_{120}$-$PDMS_{314}$-$PBLG_{120}$) at 2 wt % in the gel state from 25 to 60 °C with steps of 5 °C.

Figure 3a shows the normalized modulated electric field cross-correlation function[60] for the sample P63 at different temperatures. At 25 °C, a long relaxation decay time was observed (τ = 21 s), which is common of gel-like systems, together with a second exponential decay at shorter relaxation times (τ = 0.6 ms) indicative of fast molecular relaxations in the system. As soon as the temperature was gradually increased, the gel-like relaxation decay time vanished showing only one fast decay time (τ = 0.3 ms). These results confirmed the presence of a gel−sol transition which was confirmed by the fluidity of the sample when the triblock copolymer was no longer self-assembled into a network.

In Figure 3b, the thermoreversible behavior of the sample P63 in the gel state when heating the sample from 25 to 60 °C and cooling back to 25 °C is shown. Again, the sample at 25 °C showed the bimodal decay time with a slow and a fast relaxation times at τ = 21 s and τ = 0.6 ms, respectively. After heating the sample up to 60 °C, the relaxation decay time shortened to τ = 0.3 ms due to the disassembly of the network structure and the fast diffusion of the resulting macromolecules at higher temperature. When the sample was cooled down to 25 °C, the correlation function shifted back showing a bimodal decay time with higher decay times at τ = 0.4 s and 0.5 ms, which indicate the thermoreversible ability of the sample to form gels. Similar behavior was also observed for the other samples P25 and P38 (Supporting Information, Figure SI-4a−d).

In order to elucidate the nature of the gels, diffusion experiments were performed at 25 °C using two different triblock copolymers (P13 and P38) at 2 wt % concentration in toluene and an azobenzene dye [(*E*)-4,4′-bis(hex-5-en-1-yloxy)azobenzene]. At this concentration, the two selected triblock copolymers P13 and P38 were in the solution state and in the gel state, respectively. The azobenzene dye was dropped from the top and let diffuse showing different diffusion behavior depending on the nature of the media (Figure 4a). The counter experiment with toluene alone took over 4 min to show complete diffusion of the dye, while for samples P13 and P38 diffusion was completed within 8 and 120 min, respectively. This delay in the diffusion time can be explained by the reduced mobility of the dye molecules in the presence of the triblock copolymers and strongly affected when the sample is in the gel state. These results were consistent with those from DWS experiments shown in Figure 4b. At 25 °C, the auto-correlation function for the gel-like sample P38 decayed at

dx.doi.org/10.1021/ma2026379 | *Macromolecules* 2012, 45, 1982−1990

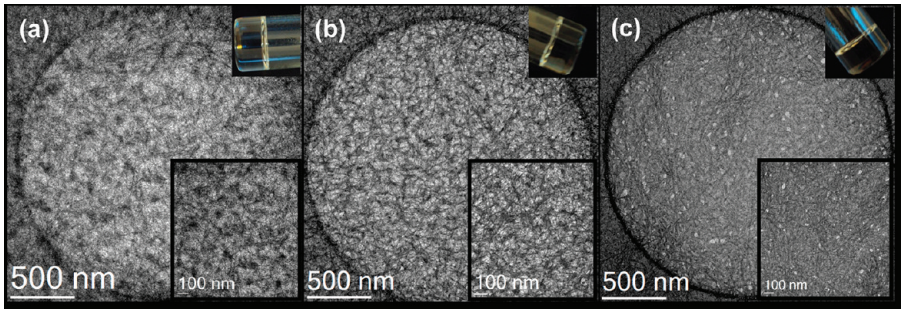

Figure 6. TEM images of the 2 wt % organogels: (a) P25, (b) P38, and (c) P63.

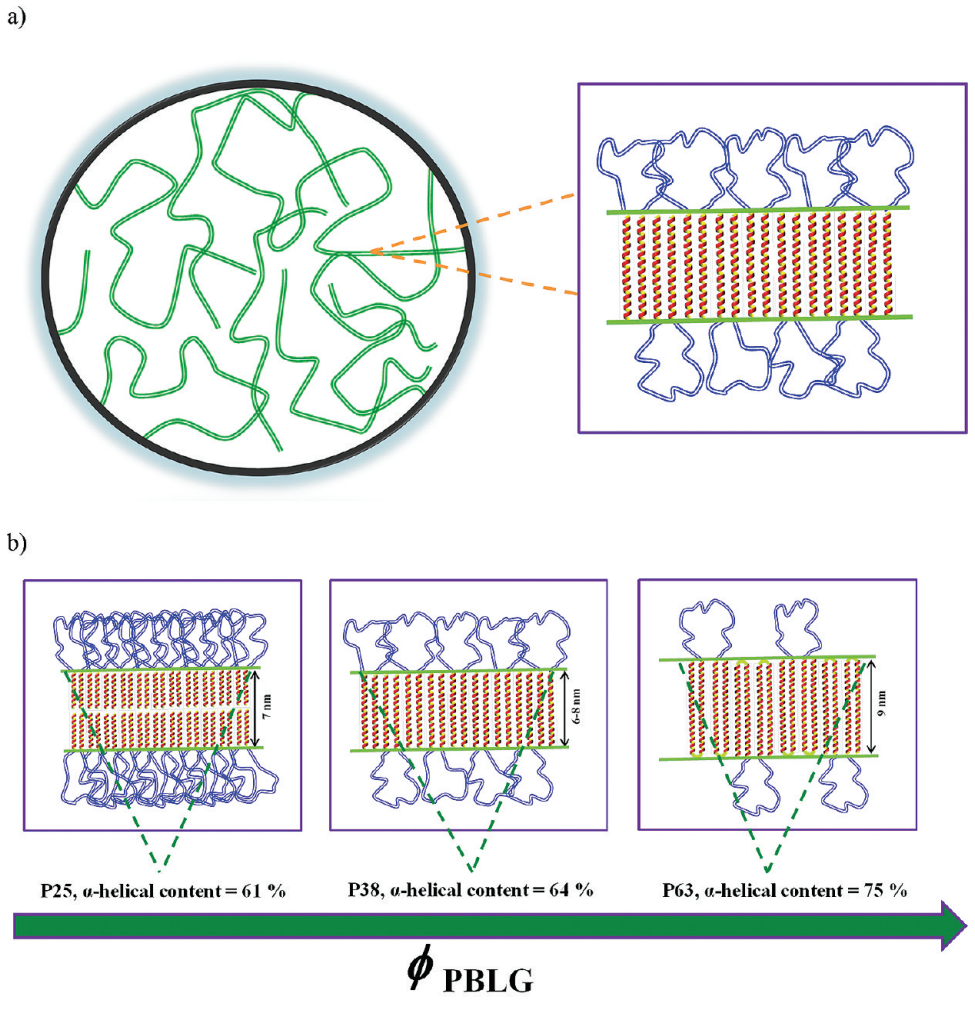

Figure 7. (a) Self-assembly of the peptide-base PBLG rods during the nanofibril formation for the PBLG-*b*-PDMS-*b*-PBLG triblock copolymers. (b) Schematic diagram for the changes in thickness due to the increase in volume fraction of the PBLG block: P25, a head-to-head morphology of the α-helical rods; P38, a monolayer morphology; and P63, a head-to-head packing of folded α-helical rods.

longer time (τ = 21 s), while the sol-like sample P13 and the nanoparticles in pure toluene decayed at shorter times (τ = 78 ms and τ = 29 ms, respectively).

In Figure 4c, a progressive change in the correlation function as a function of temperature is shown for the sample P38. The relaxation decay time was systematically decreasing with increasing temperature from 25 °C (τ = 21 s) to 60 °C (τ = 30 ms) and completely restored back to 25 °C (τ = 21 s). These results confirmed the presence of a reversible gel−sol transition.

Furthermore, rheology experiments were performed on the three selected samples P25, P38, and P63 in order to study the effect of the peptide's degree of polymerization of the triblock copolymers in the gel state at 2 wt %. Initially from the test tube invert method, the time required to form a gel was observed to decrease with increasing the molecular weight of the PBLG segment and concentration. Figure 5a shows the frequency sweeps with a systematic change in the shear modulus of the organogels for the three different molecular weights. At 2 wt % concentration, the storage (G') and loss (G'') moduli are directly proportional to the molecular weight of the peptide

dx.doi.org/10.1021/ma2026379 | *Macromolecules* 2012, 45, 1982−1990

rods. Before a preshear is applied to the samples, the storage moduli of the three gels at 1 Hz are 226, 1267, and 3042 Pa (Supporting Information, Figure SI-5a) for the samples P25, P38, and P63, respectively. When the volume fraction of the PBLG changes from ϕ_{PBLG} = 0.25 (P25) to ϕ_{PBLG} = 0.63 (P63), the gel strength increases more than 10 times, showing an enhancement on the mechanical properties of the material due to improved interaction between the large α-helixes at ϕ_{PBLG} = 0.63. After a preshearing at 6 rad s^{-1} for 2 min, the time for the recovery of all organogels was also determined. Figure 5b shows the time evolution of the three gels in toluene after their complete breakdown. After 15 min, the storage moduli at 1 Hz are 125, 596, and 1942 Pa for the samples P25, P38, and P63, respectively, and their recovery times were 97, 70, and 27 s, respectively. Thus, faster restructuring of the network are observed for the high molecular weight triblock copolymers due to the ease to reform the three-dimensional structures upon increase of the peptide blocks.

Figure 5c shows the change in storage modulus for the sample P38 at three different concentrations. Initially, the storage moduli of the three gel concentrations were 423 Pa (2 wt %), 357 Pa (3 wt %), and 832 Pa (4 wt %) (Supporting Information, Figure SI-5b). This increase of the storage modulus upon increasing concentration can be explained due to increasing density of physical interactions in the network with block copolymer content, leading to stronger gels. After applying a preshear at 6 rad s^{-1} for 2 min, the storage moduli were 107, 454, and 977 Pa for the 2, 3, and 4 wt % gel concentrations, respectively, and with recovery times of 51, 5, and 4 s. Thus, a recovery of the gel rigidity at different concentrations is observed, and at high concentration, the restructuring of the network becomes faster with block copolymer concentration (Figure 5d).

Moreover, transmission electron microscopy (TEM) experiments were performed in order to know the morphology of the self-assembled triblock copolymer organogels. The images revealed nanofibril-like morphology as shown Figure 6. After averaging the thicknesses of different nanofibrils, the widths of the corresponding self-assembled structures were found to range from 6 to 10 nm (P25), from 7 to 11 nm (P38), and from 8 to 12 nm (P63) depending on the degree of polymerization of the peptide block. These results compare reasonably well to those obtained from the calculations of the end-to-end distance of the PBLG blocks shown in Table 1.

The proposed mechanism for the establishment of these nanofibril structures is based on the microscopic phase separation of the triblock copolymers in toluene. It is well-known that the PBLG homopolymer phase separates when a homogeneous solution of this polymer is cooled down to room temperature.[42] In the case of block copolymers where a toluene-soluble middle PDMS block is present, this microphase separation increases the local concentration of PBLG blocks and force them to self-assemble into nanofibrils. On the basis of the range of diameters of the fibrils measured, and comparing it to the length of PBLG block, one may expect the PBLG rods to align perpendicular to the long axis (in a homeotropic-like alignment) of the phase separated nanofibril domains, in the case of P25 and P38; in the case of P63, the relatively thin fibrils compared to PBLG contour length suggests possible alternative packing mechanisms (such as α-helixes folding), but in all cases, the PBLG rich-nanofibrils intertwine into a 3-D network structure forming a gel.

Taking together the results of the FTIR, MDLS, rheology, and TEM analysis, the proposed mechanism for the self-assembly of the triblock copolymers in the gel state is presented in Figure 7a. All the triblock copolymers form thermoreversible organogels in toluene by the self-assembly of the rods at a concentration above their critical gelation threshold, which strongly depends on the α-helical content and the degree of polymerization of the PBLG block. The PBLG rods are confined within the core of the nanofibrils, whereas the PDMS coils remain exposed to—and swollen by—the toluene solvent molecules. Furthermore, considering the width of the fibrils, we are able to propose the packing mechanisms sketched in Figure 7b for the various triblock organogels. For the sample P25, a head-to-head morphology of the α-helix rods with 7 nm thickness is expected (homeotropic packing); for the sample P38, a monolayer morphology with 6−8 nm thickness is expected, while for the sample P63, a head-to-head packing of folded α-helix rods with 9 nm thickness is expected, in agreement with previous reports on folding of long α-helix rods.[27,61]

■ CONCLUSIONS

In summary, a series of six peptide-based triblock copolymers (PBLG-*b*-PDMS-*b*-PBLG) have been synthesized using ring-opening polymerization starting from a diamino-terminated PDMS macroinitiator. These triblock copolymers form thermoreversible organogels in toluene at the critical gelation concentration of 1.5 wt %. The degree of polymerization of the PBLG block and the concentration of triblock copolymer play a key role in the gel formation and the corresponding gel strengths. The secondary structure of the resulting gels shows an increase in the α-helical content as a function of the average-number molecular weight of the rod segment. The increased volume fraction of the PBLG block results in an improved and stronger tridimensional structure of the gel. These organogels undergo gel−solution transition around 50 °C and revert back to their original state when cooling down to room temperature. The presence of gel-like and sol-like structure was studied by diffusion experiments, where the reduced mobility of an azobenzene dye molecule and silica tracer nanoparticles was observed in the gel state when compared to the solution state. The gel strength of these triblock copolymers is enhanced with increasing the molecular weight of the PBLG or the triblock copolymer concentration, leading to a denser and stronger 3D network gel. These organogels have a nanofibril-like morphology with an average thickness in the range of 6−12 nm. These results show convincingly that the structure and strength of peptide-based thermoreversible organogels can be engineered via carefully design of the molecular architecture of the block copolymer precursors.

■ ASSOCIATED CONTENT

Ⓢ Supporting Information

^{1}H NMR spectra, the phase diagram showing the gel−sol transition as a function of concentration and temperature, the secondary structure evaluation from the FTIR experiments, MDLS plots, and rheological plots of the triblock copolymers. This material is available free of charge via the Internet at http://pubs.acs.org.

AUTHOR INFORMATION

Corresponding Author

*E-mail: raffaele.mezzenga@hest.ethz.ch.

Author Contributions

‖The first two authors contributed equally to this study.

Notes

The authors declare no competing financial interest.

ACKNOWLEDGMENTS

The authors thank Dr. Sreenath Bolisetty, Prof. Nader Taheri, and Dr. Jani Seitsonen for the support in DLS, rheology, and TEM experiments and kind discussions. This work was carried out with the financial support of the FRIMAT center for Nanomaterials and the Swiss Science National Foundation.

REFERENCES

(1) Lee, M.; Cho, B.; Zin, W. *Chem. Rev.* **2001**, *101*, 3869−3892.
(2) Reenders, M.; ten Brinke, G. *Macromolecules* **2002**, *35*, 3266−3280.
(3) Sary, N.; Mezzenga, R.; Brochon, C.; Hadziioannou, G.; Ruokolainen, J. *Macromolecules* **2007**, *40*, 3277−3286.
(4) Sary, N.; Rubatat, L.; Brochon, C.; Hadziioannou, G.; Ruokolainen, J.; Mezzenga, R. *Macromolecules* **2007**, *40*, 6990−6997.
(5) Sary, N.; Brochon, C.; Hadziioannou, G.; Mezzenga, R. *Eur. Phys. J. E* **2008**, *24*, 379−384.
(6) Pryamitsyn, V.; Ganesan, V. *J. Chem. Phys.* **2004**, *120*, 5824−5838.
(7) Jenekhe, S. A.; Chen, X. L. *Science* **1998**, *279*, 1903−1907.
(8) Li, K.; Guo, L.; Liang, Z.; Thiyagarajan, P.; Wang, Q. *J. Polym. Sci., Part A: Polym. Chem.* **2005**, *43*, 6007−6019.
(9) Olsen, B. D.; Segalman, R. A. *Mater. Sci. Eng., R* **2008**, *62*, 37−66.
(10) Horkay, F.; Tasaki, I.; Basser, P. J. *Biomacromolecules* **2001**, *2*, 195−199.
(11) Nam, K.; Watanabe, J.; Ishihara, K. *Int. J. Pharm.* **2004**, *275*, 259−269.
(12) Qu, X.; Wirsen, A.; Albertsson, A.-C. *J. Appl. Polym. Sci.* **1999**, *74*, 3186−3192.
(13) Pochan, D. J.; Schneider, J. P.; Kretsinger, J.; Ozbas, B.; Rajagopal, K.; Haines, L. *J. Am. Chem. Soc.* **2003**, *125*, 11802−11803.
(14) Schneider, J. P.; Pochan, D. J.; Ozbas, B.; Rajagopal, K.; Pakstis, L.; Kretsinger, J. *J. Am. Chem. Soc.* **2002**, *124*, 15030−15037.
(15) Breedveld, V.; Nowak, A. P.; Sato, J.; Deming, T. J.; Pine, D. J. *Macromolecules* **2004**, *37*, 3943−3953.
(16) Nowak, A. P.; Breedveld, V.; Pakstis, L.; Ozbas, B.; Pine, D. J.; Pochan, D.; Deming, T. J. *Nature* **2002**, *417*, 424−428.
(17) Park, M. H.; Joo, M. K.; Choi, B. G.; Jeong, B. *Acc. Chem. Res.* **2011**.
(18) Tew, G. N.; Pralle, M. U.; Stupp, S. I. *J. Am. Chem. Soc.* **1999**, *121*, 9852−9866.
(19) Gao, P.; Zhan, C.; Liu, L.; Zhou, Y.; Liu, M. *Chem. Commun.* **2004**, *10*, 1174−1175.
(20) Zhan, C.; Gao, P.; Liu, M. *Chem. Commun.* **2005**, *4*, 462−464.
(21) Markland, P.; Zhang, Y.; Amidon, G. L.; Yang, V. C. *J. Biomed. Mater. Res.* **1999**, *47*, 595−602.
(22) Suzuki, M.; Nakajima, Y.; Yumoto, M.; Kimura, M.; Shirai, H.; Hanabusa, K. *Org. Biomol. Chem.* **2004**, *2*, 1155−1159.
(23) Suzuki, M.; Sato, T.; Kurose, A.; Shirai, H.; Hanabusa, K. *Tetrahedron Lett.* **2005**, *46*, 2741−2745.
(24) Terech, P.; Weiss, R. G. *Chem. Rev. (Washington, DC, U. S.)* **1997**, *97*, 3133−3159.
(25) Van Esch, J. H.; Feringa, B. L. *Angew. Chem., Int. Ed.* **2000**, *39*, 2263−2266.
(26) Sánchez-Ferrer, A.; Mezzenga, R. *Macromolecules* **2010**, *43*, 1093−1100.
(27) Papadopoulos, P.; Floudas, G.; Klok, H.; Schnell, I.; Pakula, T. *Biomacromolecules* **2004**, *5*, 81−91.
(28) Floudas, G.; Papadopoulos, P.; Klok, H.; Vandermeulen, G. W. M.; Rodriguez-Hernandez, J. *Macromolecules* **2003**, *36*, 3673−3683.
(29) Flory, P. J. *Proc. R. Soc. London, Ser. A* **1956**, *234*, 73−89.
(30) Uematsu, I.; Uematsu, Y. *Adv. Polym. Sci.* **1984**, *59*, 37−73.
(31) Block, H. *In Poly(γ-benzyl-L-glutamate) and Other Glutamic Acid Containing Polymers*; Gordon and Breach Science Publishers: New York, 1983.
(32) Robinson, C.; Ward, J. C. *Nature* **1957**, *180*, 1183−1184.
(33) Yu, S. M.; Conticello, V. P.; Zhang, G.; Kayser, C.; Fournier, M. J.; Mason, T. L.; Tirrell, D. A. *Nature* **1997**, *389*, 167−170.
(34) Tohyama, K.; Miller, W. G. *Nature* **1981**, *289*, 813−814.
(35) Kuo, S. W.; Lee, H. F.; Huang, C. F.; Huang, C. J.; Chang, F. C. *J. Polym. Sci., Part A: Polym. Chem.* **2008**, *46*, 3108−3119.
(36) Lecommandoux, S.; Achard, M.; Langenwalter, J. F.; Klok, H. *Macromolecules* **2001**, *34*, 9100−9111.
(37) Carlsen, A.; Lecommandoux, S. *Curr. Opin. Colloid Interface Sci.* **2009**, *14*, 329−339.
(38) Holowka, E. P.; Pochan, D. J.; Deming, T. J. *J. Am. Chem. Soc.* **2005**, *127*, 12423−12428.
(39) Chécot, F.; Brûlet, A.; Oberdisse, J.; Gnanou, Y.; Mondain-Monval, O.; Lecommandoux, S. *Langmuir* **2005**, *21*, 4308−4315.
(40) Doty, P.; Bradbury, J. H.; Holtzer, A. M. *J. Am. Chem. Soc.* **1956**, *78*, 947−954.
(41) Tadmor, R.; Khalfin, R. L.; Cohen, Y. *Langmuir* **2002**, *18*, 7146−7150.
(42) Kim, K. T.; Park, C.; Vandermeulen, G. W. M.; Rider, D. A.; Kim, C.; Winnik, M. A.; Manners, I. *Angew. Chem., Int. Ed* **2005**, *44*, 7964−7968.
(43) Kuo, S.; Lee, H.; Huang, W.; Jeong, K.; Chang, F. *Macromolecules* **2009**, *42*, 1619−1626.
(44) Naik, S. S.; Savin, D. A. *Macromolecules* **2009**, *42*, 7114−7121.
(45) Papadopoulos, P.; Floudas, G.; Schnell, I.; Lieberwirth, I.; Nguyen, T. Q.; Klok, H. *Biomacromolecules* **2006**, *7*, 618−626.
(46) Ibarboure, E.; Rodríguez-Hernández, J.; Papon, E. *J. Polym. Sci., Part A: Polym. Chem.* **2006**, *44*, 4668−4679.
(47) Ibarboure, E.; Papon, E.; Rodríguez-Hernández, J. *Polymer* **2007**, *48*, 3717−3725.
(48) Ibarboure, E.; Rodríguez-Hernández, J. *Eur. Polym. J.* **2010**, *46*, 891−899.
(49) Sánchez-Ferrer, A.; Merekalov, A.; Finkelmann, H. *Macromol. Rapid Commun.* **2011**, *32*, 672−678.
(50) Hirst, A. R.; Smith, D. K.; Feiters, M. C.; Geurts, H. P. M.; Wright, A. C. *J. Am. Chem. Soc.* **2003**, *125*, 9010−9011.
(51) Kotharangannagari, V. K.; Sánchez-Ferrer, A.; Ruokolainen, J.; Mezzenga, R. *Macromolecules* **2011**, *44*, 4569−4573.
(52) Hammond, M. R.; Klok, H.; Mezzenga, R. *Macromol. Rapid Commun.* **2008**, *29*, 299−303.
(53) Holloway, P. W.; Mantsch, H. H. *Biochemistry* **1989**, *28*, 931−935.
(54) Dong, A.; Huang, P.; Caughey, W. S. *Biochemistry* **1990**, *29*, 3303−3308.
(55) Surewicz, W. K.; Mantsch, H. H. *Biochim. Biophys. Acta* **1988**, *952*, 115−130.
(56) Kauppinen, J. K.; Moffatt, D. J.; Mantsch, H. H.; Cameron, D. G. *Anal. Chem.* **1981**, *53*, 1454−1457.
(57) Kauppinen, J. K.; Moffatt, D. J.; Mantsch, H. H.; Cameron, D. G. *Appl. Sprectrosc.* **1981**, *35*, 271−276.
(58) Yang, W. J.; Griffiths, P. R.; Byler, D. M.; Susi, H. *Appl. Spectrosc.* **1985**, *39*, 282−287.
(59) Block, I. D.; Scheffold, F. *Rev. Sci. Instrum.* **2010**, *81*, 123107.
(60) Park, M. J.; Char, K. *Langmuir* **2004**, *20*, 2456−2465.
(61) Babin, J.; Taton, D.; Brinkmann, M.; Lecommandoux, S. *Macromolecules* **2008**, *41*, 1384−1392.

Macromolecules

Article

pubs.acs.org/Macromolecules

Dynamics and Large Strain Behavior of Self-Healing Hydrogels with and without Surfactants

Deniz C. Tuncaboylu,[†] Melahat Sahin,[†] Aslihan Argun,[†] Wilhelm Oppermann,*[,‡] and Oguz Okay*[,†]

[†]Department of Chemistry, Istanbul Technical University, 34469 Maslak, Istanbul, Turkey

[‡]Institute of Physical Chemistry, Clausthal University of Technology, 38678 Clausthal-Zellerfeld, Germany

Supporting Information

ABSTRACT: Polyacrylamide hydrogels formed via hydrophobic interactions between stearyl groups in aqueous micellar solution of sodium dodecyl sulfate (SDS) present two faces depending on which state they are. The gels containing SDS micelles exhibit, in addition to the fast mode, a slow relaxation mode in dynamic light scattering (DLS) and time-dependent elastic moduli, indicating the temporary nature of the hydrophobic associations having lifetimes of the order of seconds to milliseconds. The gels where SDS had been removed after their preparation behave similar to chemically cross-linked ones with time-independent elastic moduli, a high degree of spatial inhomogeneity, and a single relaxation mode in DLS. Because of this drastic structural change, the physical gels are insoluble in water with a gel fraction close to unity. In surfactant containing gels, a large proportion of physical cross-links dissociate under force, but they do so reversibly, if the force is removed they reform again. The reversible disengagements of the hydrophobic units building the physical cross-links leads to a self-healing efficiency of nearly 100%, while no such healing behavior was observed after extraction of SDS due to the loss of the reversible nature of the cross-linkages.

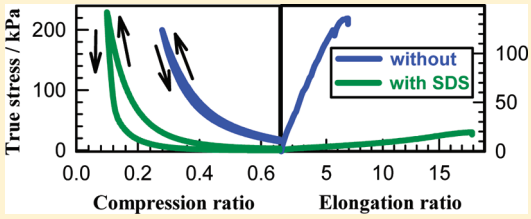

INTRODUCTION

Aqueous solutions of hydrophobically modified hydrophilic polymers constitute a class of soft materials with remarkable rheological properties.[1,2] Above a certain polymer concentration, the hydrophobic groups in such associative polymers are involved in intermolecular associations that act as reversible breakable cross-links creating a transient 3D polymer network. A simple method to obtain associative polymers is the free radical micellar polymerization technique, as first described by Candau and co-workers.[1−8] In this technique, a water-insoluble hydrophobic monomer solubilized within the micelles is copolymerized with a hydrophilic monomer such as acrylamide (AAm) in aqueous solutions by free-radical addition polymerization. Because of high local concentration of the hydrophobe within the micelles, the hydrophobic monomers are distributed as random blocks along the hydrophilic polymer backbone. One limitation of this technique is that large hydrophobes such as stearyl methacrylate (C18) or dococyl acrylate (C22) cannot be solubilized within the micelles due to the very low water solubility of these monomers.[9−12] Incorporation of blocks of large hydrophobes into a hydrophilic polymer backbone would produce strong and long-lived hydrophobic associations.

We have recently shown that large hydrophobes can be solubilized in a micellar solution of sodium dodecyl sulfate (SDS) provided that an electrolyte, such as NaCl, has been added in sufficient amount.[9] Salt leads to micellar growth[13,14] and, hence, solubilization of the hydrophobes within the grown SDS micelles. As illustrated in Figure 1, after solubilization of the large hydrophobes C18 or C22 within the wormlike SDS micelles of salt solutions, they could be copolymerized with AAm to obtain physical hydrogels. The surfactant-containing gels formed using C18 blocks as physical cross-links exhibit unique characteristics such as insolubility in water but solubility in SDS solutions, nonergodicity, self-healing, and a high degree of toughness.[9]

However, when SDS micelles are removed from the physical gels, they become fragile and do not exhibit the initial mechanical performances. Understanding what gives these surfactant-containing gels toughness and self-healing ability could be essential for the design of future self-healing soft materials and this was the aim of this study. Moreover, although the physical gels we reported before were in a state close to the critical gel state with a power-law frequency dependence in their viscoelastic moduli, they were insoluble in water with a gel fraction close to unity.[9] It was also of fundamental interest to explain the apparent contradiction that a critical gel could remain stable in water.

Here, we prepared physical gels by micellar copolymerization of AAm with 2 mol % C18 in aqueous SDS−NaCl solutions. The initial monomer concentration was varied over a wide range. By increasing the polymer concentration at the gel preparation, we were able to obtain strong gels enabling determination of their large strain behavior. We present and characterize in this paper two series of physical gels: one series still containing SDS micelles and another one where the SDS micelles had been removed after preparation. Dynamic

Received: December 9, 2011
Revised: January 24, 2012
Published: February 6, 2012

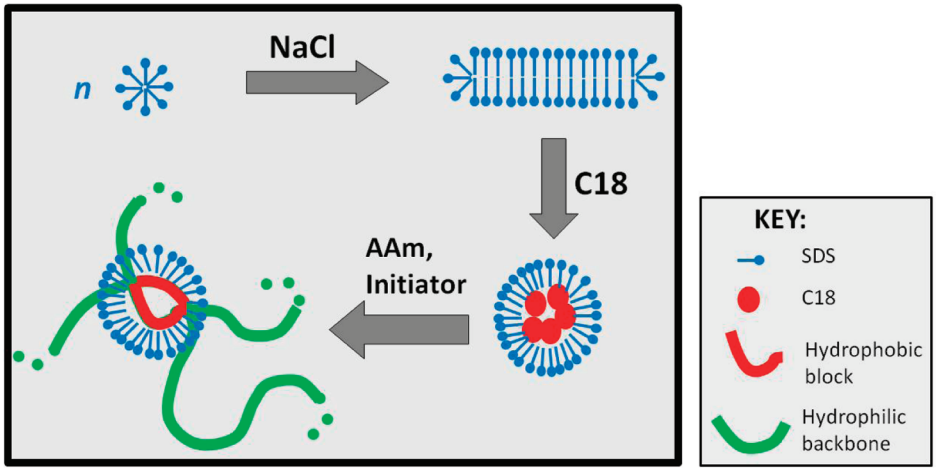

Figure 1. Cartoon showing the formation of surfactant containing physical gels in aqueous SDS−NaCl solutions via hydrophobic C18 blocks.

properties of the gels were investigated by dynamic light scattering (DLS) and rheometry, while their large-strain mechanical and self-healing performances were determined by uniaxial elongation or compression tests. We will show that the physical gels without SDS micelles behave similar to chemically cross-linked gels: they exhibit time-independent dynamic moduli and a single relaxation mode in DLS. When micelles are present, the hydrophobic interactions are weakened, thereby increasing the viscoelastic dissipation in the gel sample. This is the key factor for self-healing. After fracture, strong hydrophobic interactions localized across the damage surfaces together with the internal dynamics of surfactant containing gels leads to the renewal of hydrophobic associations and self-healing at room temperature.

EXPERIMENTAL PART

Materials. Acrylamide (AAm, Merck), sodium dodecyl sulfate (SDS, Sigma), ammonium persulfate (APS, Merck), *N,N,N′,N′*-tetramethylethylenediamine (TEMED, Merck), and NaCl (Merck) were used as received. Commercially available stearyl methacrylate (C18, Fluka) consists of 65% *n*-octadecyl methacrylate and 35% *n*-hexadecyl methacrylate. Micellar copolymerization of AAm with C18 was conducted at 25 °C for 24 h in the presence of an APS (3.5 mM)−TEMED (0.25% v/v) redox initiator system. SDS and NaCl concentrations were set to 7% w/v (0.24 M) and 0.5 M, respectively. C18 content of the monomer mixture was also fixed at 2 mol % while the total monomer concentration was varied between 5% and 15% w/v. The gel preparation procedure was the same as in our previous study.[9] For the swelling and mechanical measurements, the copolymerization reactions were carried out in plastic syringes of 4 mm internal diameters. For the dynamic light scattering measurements, the reactions were conducted in light scattering vials after filtration of the gelation solutions through Nylon membrane filters with a pore size of 0.2 μm.

Quantification of the Solubilization of C18 in SDS−NaCl Solutions. The amount of C18 solubilized in the micelles was estimated by measuring the transmittance of SDS−NaCl solutions containing various amounts of C18 on a T80 UV−vis spectrophotometer. The transmittance at 500 nm was plotted as a function of the added amount of C18 in the SDS−NaCl solution, and the solubilization extent of C18 was determined by the curve break (Figure S1).

Rheological Experiments. Gelation reactions were carried out at 25 °C within the rheometer (Gemini 150 rheometer system, Bohlin Instruments) equipped with a cone-and-plate geometry with a cone angle of 4° and diameter of 40 mm. The instrument was equipped with a Peltier device for temperature control. The reactions were monitored at an angular frequency ω of 6.3 rad/s and a deformation amplitude γ_0 = 0.01. After a reaction time of 3 h, the dynamic moduli of the reaction solutions approached limiting values (Figure S2). Then, frequency-sweep tests and stress-relaxation experiments were carried out at 25 °C, as described before.[9]

Dynamic Light Scattering (DLS) Measurements. DLS measurements were performed at 25 °C using ALV/CGS-3 compact goniometer (ALV, Langen, Germany) equipped with a cuvette rotation/translation unit (CRTU) and a He−Ne laser (22 mW, λ = 632.8 nm). The scattering angle θ was varied between 50° and 130°. Details about the instrument were described before.[9] The time-average intensity correlation functions $g_T^{(2)}(q\ \tau)$ of gels were acquired at 100 different sample positions selected by randomly moving the CRTU before each run. The acquisition time for each run was 30 s. The short-time limit of $g_T^{(2)}(q,\tau)$ can be related to an apparent diffusion coefficient, D_A, via[15,16]

$$D_A = -\frac{1}{2q^2}\lim_{\tau\to 0}\frac{d(\ln(g_T^{(2)}(q,\tau)-1))}{d\tau} \quad (1)$$

where q is the scattering vector, $q = (4\pi n/\lambda)\sin(\theta/2)$, n is the refractive index of the solvent, τ is the decay time, and subscript T denotes time average. For nonergodic media like polymer gels, D_A and, likewise, the time-averaged scattering intensity $\langle I(q)\rangle_T$ vary randomly with sample position. $\langle I(q)\rangle_T$ has two contributions: one from static inhomogeneities (frozen structure) and the other from dynamic fluctuations according to the following equation:[15−17]

$$\langle I(q)\rangle_T = I_C(q) + \langle I_F(q)\rangle_T \quad (2)$$

where $I_C(q)$ and $\langle I_F(q)\rangle_T$ are the scattered intensities due to the frozen structure and liquidlike concentration fluctuations, respectively. To separate $\langle I(q)\rangle_T$ into its two parts, we follow the method proposed by Joosten et al.[15] Treating the system by the partial heterodyne approach, one obtains

$$\frac{\langle I(q)\rangle_T}{D_A} = \frac{2\langle I(q)\rangle_T}{D} - \frac{\langle I_F(q)\rangle_T}{D} \quad (3)$$

The cooperative diffusion coefficient D and the fluctuating component of the scattering intensity $\langle I_F(q)\rangle_T$ of the present hydrogels were obtained by plotting $\langle I(q)\rangle_T/D_A$ vs $\langle I(q)\rangle_T$ data recorded at 100 different sample positions (Figure S3). The dynamic correlation length ξ was evaluated by $\xi = kT/(6\pi\eta D)$, where η is the viscosity of the medium (0.89 mPa·s) and kT is the Boltzmann energy.

For ergodic media like surfactant solutions, the scattered intensity contains only a fluctuating component and independent of sample position. $g_T^{(2)}(q,\tau)$ is then equivalent to an ensemble-averaged intensity correlation function and can be written as the Laplace

dx.doi.org/10.1021/ma202672y | Macromolecules 2012, 45, 1991−2000

transform of the distribution of relaxation rates, $G(\Gamma)$ (we disregard a coherence factor):

$$g_T^{(2)}(q, \tau) - 1 = [\int_0^\infty G(\Gamma) \exp(-\Gamma\tau)\, d\Gamma]^2 \quad (4)$$

where Γ is the characteristic relaxation rate. $G(\Gamma)$ values at five angles (50°, 70°, 90°, 110°, and 130°) were evaluated with an inverse Laplace transform of $g_T^{(2)}(q,\tau) - 1$ with the integrated ALV software (Figure S4). Relaxation rates of the fast (Γ_{fast}) and slow modes (Γ_{slow}) were obtained from the peak values of Γ in $G(\Gamma)$s. For a diffusion process, the relaxation rate of a particular mode is q^2 dependent and is related to the diffusion coefficient as $\Gamma = Dq^2$.

Gel Fractions and Swelling Measurements. Cylindrical hydrogel samples (diameter 4 mm, length about 6 cm) were immersed in a large excess of water at 24 °C for at least 15 days by replacing water every day to extract any soluble species. The masses m of the gel samples were monitored as a function of swelling time by weighing the samples. Relative weight swelling ratio m_{rel} of gels was calculated as $m_{rel} = m/m_0$, where m_0 is the initial mass of the gel sample. Then, the equilibrium swollen gel samples with relative masses $m_{rel,eq}$ were taken out of water and immersed in liquid nitrogen for 5 min before they were freeze-dried. The amount of SDS released from the gels during their swelling was estimated using the methylene blue (MB) method.[18] For this purpose, swelling tests were carried out as described above, except that the volume of external solution was fixed at 100 mL. Solution samples were taken at various time intervals, just before replacing water, and subjected to MB method. The amount of SDS released was calculated as $10^2 m_{SDS,t}/(m_0 C_{SDS})$, where $m_{SDS,t}$ is the mass of SDS in the external solution at time t and C_{SDS} is the initial SDS concentration of gel samples (0.07 g/mL). The cumulative release of SDS was obtained by summing up SDS released % data over all times. To check for completeness of SDS extraction from gels, dry samples were inspected by energy dispersive X-ray spectroscopy (EDS) performed on a scanning electron microscope (Jeol 6335F) using Oxford-INCA/ISIS software. EDS spectra were acquired and used for X-ray mapping of sulfur (detection limit: 0.1%) and other elements present in the samples.

The gel fraction W_g, that is, the conversion of monomers to the water-insoluble polymer (mass of cross-linked polymer/initial mass of the monomer), was calculated from the masses of dry, extracted polymer network and from the comonomer feed. The volume fractions of physically cross-linked PAAm after the gel preparation and in the equilibrium swollen gel, ν_2^0 and ν_2, respectively, were calculated as

$$\nu_2^0 = 10^{-2}\rho^{-1}C_0 W_g \quad (5a)$$

$$\nu_2 = \left[1 + \left(\frac{m_{rel,eq}}{\nu_2^0} - \rho\right)\right]^{-1} \quad (5b)$$

where ρ is the density of PAAm (1.35 g/mL).[19] The linear swelling ratio α of the gels with respect to the state of preparation was calculated from the polymer volume fractions as $\alpha = (\nu_2^0/\nu_2)^{1/3}$.

Uniaxial Compression Measurements. The measurements were performed in a thermostated room at 24 ± 0.5 °C on gel samples both in the state of preparation and after equilibrium swelling in water. Cyclic compression experiments were performed on a Zwick Roell test machine using a 10 N load cell. The cylindrical hydrogel sample of about 4 mm diameter and 6 mm length was placed between the plates of the instrument. Before the test, an initial compressive contact to 0.004 ± 0.003 N was applied to ensure a complete contact between the gel and the plates. Cyclic tests were conducted with a compression step performed at a constant crosshead speed of 5 mm/min to a maximum load (varied between 0.5 and 4 N), followed by immediate retraction to zero displacement and a waiting time of 2 min, until the next cycle of compression. Load and displacement data were collected during the experiment. Compressive stress was presented by its nominal σ_{nom} or true values σ_{true} (= $\lambda\sigma_{nom}$), which are the forces per cross-sectional area of the undeformed and deformed gel specimen, respectively, while the strain is given by λ, the deformation ratio (deformed length/initial length). The stress–strain isotherms at low compression ratios were measured by using an apparatus previously described by our group.[20] Briefly, cylindrical gel sample (diameter 4 mm, length 7 mm) was placed on a digital balance (Sartorius BP221S). A load was transmitted vertically to the gel through a rod fitted with a PTFE end-plate. The force acting on the gel was calculated from the reading of the balance while the resulting deformation was measured using a digital comparator (IDC type Digimatic Indicator 543-262, Mitutoyo Co.), which was sensitive to displacements of 10^{-3} mm. The force and the resulting deformation were recorded after 10 s of relaxation. The measurements were conducted up to about 20% compression with increments of ca. 1%. The modulus G_t of gels after a relaxation time t = 10 s was determined from the slope of the linear dependence

$$\sigma_{nom} = -G_t(\lambda - \lambda^{-2}) \quad (6)$$

Typical stress–strain data plotted according to eq 6 are shown in Figure S5 for the hydrogels before and after swelling in water.

Uniaxial Elongation Measurements. The measurements were performed on cylindrical hydrogel samples of about 4 mm in diameter on a Zwick Roell test machine using a 500 N load cell under the following conditions: crosshead speed = 50 mm/min, sample length between jaws = 13 ± 3 mm. The tensile strength and percentage elongation at break were recorded. For reproducibility, at least six samples were measured for each gel, and the results were averaged.

RESULTS AND DISCUSSION

Preparation of Physical Gels with and without Surfactant. Physical gels were prepared by the micellar copolymerization of AAm with C18 in aqueous SDS–NaCl solutions. C18 content of the monomer mixture (C18 + AAm) was fixed at 2 mol % while the initial monomer concentration C_0 was varied between 5% and 15%. The presence of NaCl in the reaction solution induced the micellar growth (see the next section) and, hence, solubilization of the hydrophobe C18 within the SDS micelles. The maximum solubility of C18 in the reaction solution was determined as 1.2% w/v, corresponding to C_0 = 15% (Figure S1). Indeed, transparent gels were obtained in the range of C_0 between 5% and 15% while at larger concentrations translucent gels were obtained. We therefore limited our investigation to gels formed at or below C_0 = 15%.

To obtain physical gels free of SDS micelles, the gel samples were extracted in water at 24 °C. Figure 2 shows the data

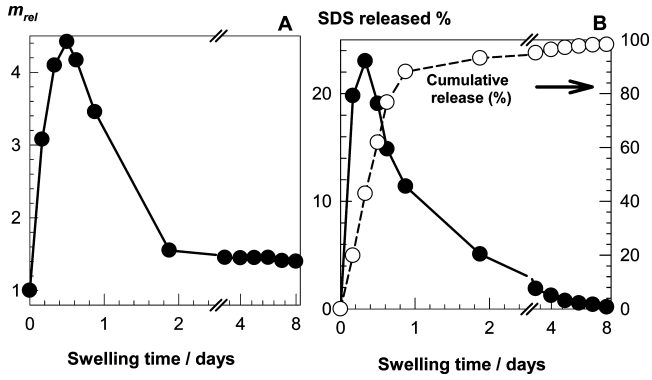

Figure 2. Relative weight swelling ratio m_{rel} of the physical gel (A) and the amount of SDS released from the gel (B) plotted against the swelling time in water. C_0 = 10%.

obtained during the extraction of a gel sample formed at C_0 = 10%, where the relative gel mass m_{rel} and the released amount of SDS from the gel (in %) are plotted as a function of the

dx.doi.org/10.1021/ma202672y | Macromolecules 2012, 45, 1991–2000

swelling time. At short swelling times, the gel exhibits a large swelling ratio due to the osmotic pressure of SDS counterions inside the gel network. As SDS is progressively extracted from the network, the osmotic effect disappears and the gel gradually converts into a nonionic gel having a markedly reduced swelling ratio ($m_{rel,eq}$ = 1.3 ± 0.2 for C_0 = 5−15%). Cumulative SDS release data in Figure 2B reveal that, after a swelling time of about 8 days, all SDS was extracted from the gels. Indeed, sulfur analyses of freeze-dried gel samples formed between C_0 = 5% and 15% gave no sulfur (<0.1%), indicating complete SDS extraction.

The characteristics of the physical gels before and after swelling in water are collected in Table 1. The average gel fraction W_g is 0.86 ± 0.02, demonstrating strong hydrophobic associations between the PAAm chains which could not be destroyed during the expansion of the gels in water. The polymer concentration ν_2 of the gels swollen to equilibrium is a little lower than the value ν_2^0 at the state of gel preparation. The linear swelling ratio α increases slightly with rising C_0 from 1.04 to 1.16, suggesting that the network chains are in the Gaussian regime.[20,21] Also, the fact that the equilibrium swelling ratio is considerably lower than the maximum swelling (cf. Figure 2A) is a strong indication that the network chains are in the Gaussian regime. In contrast, we observed that the gels which are soft at the state of preparation become stiff upon swelling in water. To quantify this behavior, we measured the elastic modulus G_t of cylindrical gel samples (diameter 4 mm, length 7 mm) after a relaxation time t of 10 s. Table 1 also contains the moduli data of gels before and after swelling in water. The equilibrium swollen gels exhibit 3−8-fold larger elastic moduli than those in the preparation state. As the degrees of dilution of the network chains before and after swelling are close together (Table 1), this increase reveals the occurrence of structural transformations during the removal of the surfactant micelles from the gel network.

Table 1. Properties of the Physical Gels with and without SDS

		after preparation state		after equilibrium swelling in water		
C_0 (% w/v)	W_g	G_t (kPa)	ν_2^0	G_t (kPa)	ν_2	α
5	0.83	*a*	0.031	*a*	0.027	1.04
6	0.87	0.14	0.039	*a*	0.032	1.06
7	0.86	0.34	0.045	2.0	0.037	1.06
8	0.88	0.64	0.052	4.8	0.042	1.07
9	0.86	1.0	0.057	6.8	0.045	1.08
10	0.87	1.5	0.064	8.1	0.049	1.09
15	0.83	4.9	0.092	13.0	0.058	1.16

[a]Gels were too weak to withstand the elasticity measurements.

Dynamics of Gelation Solutions and Physical Gels. DLS measurements were conducted at various preparation steps of the gelation solutions, i.e., before and after additions of NaCl, C18, or AAm into the SDS solution as well as after polymerization and after removal of SDS micelles. The time-average intensity correlation functions (ICFs) of the solutions and gels were recorded at five angles (θ) between 50° and 130°. Figures 3A and 3B show typical ICFs obtained at θ = 90° from solutions and gels, respectively. ICF of the SDS−water solution exhibits both fast and slow relaxation modes. This is similar to

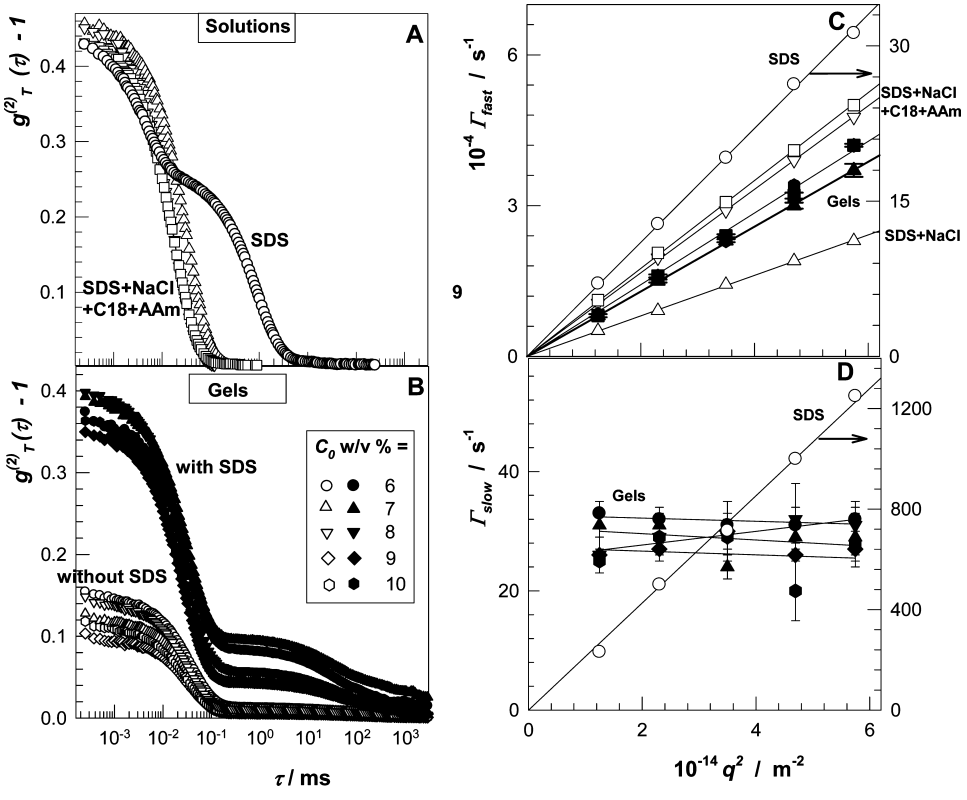

Figure 3. (A, B) ICFs of SDS solutions (A) and physical gels (B). θ = 90°. SDS solutions without (○) and with NaCl (△), NaCl + C18 (▽), and NaCl + C18 + AAm (□). The amounts of C18 and AAm correspond to the preparation recipe of 10% gel. However, amounts corresponding to 5−10% gels do not affect the results. Filled and open symbols in (B) represent data for gels with and without SDS, respectively. (C, D) Relaxation rates of the fast (Γ_{fast}) and slow modes (Γ_{slow}) plotted against q^2 for gels and solutions. The symbols are the same as in (A) and (B).

dx.doi.org/10.1021/ma202672y | Macromolecules 2012, 45, 1991−2000

polyelectrolyte solutions where a fast and a slow mode occur in salt-free conditions. These relaxations merge into one upon addition of salt.[22] Likewise, the addition of NaCl (0.5 M) and of monomers into the SDS solution results in the disappearance of the slow mode. After formation of the physical gels, a slow mode appears again on an even longer time scale (Figure 3B). However, when the SDS micelles are removed from the gels, the slow mode disappears.

Additional information can be obtained from the scattering vector dependencies of the relaxation rates. The relaxation rates of the fast (Γ_{fast}) and slow modes (Γ_{slow}) were obtained from the peak positions in the relaxation rate distribution functions $G(\Gamma)$, some examples of which are given in Figure S4. In Figures 3C and 3D, Γ_{fast} and Γ_{slow} are plotted against q^2, respectively. For SDS−water solution, Γ_{fast} and Γ_{slow} are both proportional to q^2, demonstrating diffusive processes. The hydrodynamic correlation length ξ on the basis of the fast mode was calculated as 0.5 nm for SDS micelles in water, while after addition of NaCl, it increases to 6.1 nm due to the formation of wormlike micelles.[9,23−25] Addition of C18 and AAm into the SDS−NaCl solution decreases again the correlation length to 3 nm due to the oil-induced structural change of wormlike micelles.[9,26−30] In contrast to the slow relaxation mode of the SDS solution, the slow mode of gels containing SDS (~30 ms) is independent of the scattering vector q (filled symbols in Figure 3D), demonstrating that it does not represent a diffusive process but is related to the structural relaxation of the physical network. Thus, the ICFs indicate a structural relaxation in physical gels on the time scales of milliseconds. This process only occurs in the presence of SDS micelles, it seems to disappear when the SDS is removed.

Rheological measurements are another means of studying the dynamic properties of the gels. Figures 4A and 4B show the frequency dependencies of the elastic modulus G' (filled symbols), viscous modulus G'' (open symbols), and tan δ (= G''/G', lines) for the gels (C_0 = 10%) with (A) or without SDS (B). In Figures 4C and 4D, the relaxation moduli $G(t)$ of the same gels, obtained from stress relaxation measurements, are plotted against time t at different strains γ_0. The gel containing SDS exhibits time-dependent dynamic moduli with a plateau modulus at high frequencies (10^2 rad/s) and a loss factor above 0.1 indicating the temporary nature of the hydrophobic associations having lifetimes of the order of seconds to milliseconds. After extraction of SDS, the dynamic moduli become nearly time independent and the loss factor decreases below 0.1 corresponding solidlike behavior. Similar results were also obtained for other gel samples formed at various concentrations (Figure S6).

On the basis of these measurements, we conclude that, when SDS micelles are present, the cross-links are reversible due to the local solubilization of the hydrophobic associations so that the gels are weak. After extraction of SDS, direct exposure of the hydrophobic associations to the aqueous environment increases their lifetimes so that the gels behave mostly like being covalently cross-linked ones with time-independent dynamic moduli and a single mode relaxation in DLS. The results also demonstrate that the presence of surfactant micelles is responsible for the slow mode of the physical gels. Previous studies show a slow relaxation in the micellar kinetics on the time scale of milliseconds to seconds, corresponding to the dissolution of a micelle into individual surfactant molecules.[31] Since the breakup of a micelle around the hydrophobic blocks

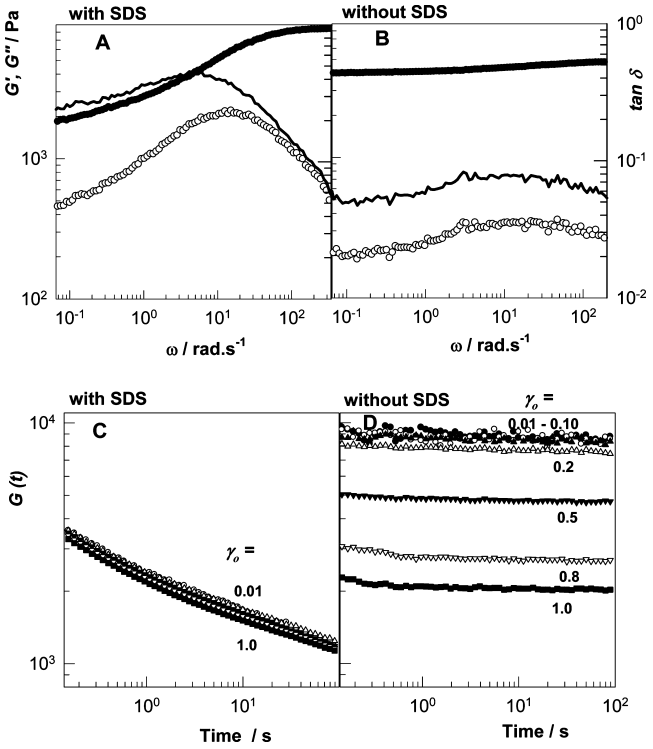

Figure 4. (A, B) G' (filled symbols), G'' (open symbols), and tan δ (lines) of gels with (A) and without SDS (B) shown as a function of angular frequency ω. C_0 = 10%; γ_0 = 0.01. (C, D) Relaxation modulus $G(t)$ as a function of time t for various strains γ_0 for gels with (C) and without SDS (D). C_0 = 10%; γ_0 = 0.01 (●), 0.05 (○), 0.10 (▲), 0.20 (△), 0.50 (▼), 0.80 (▽), and 1.0 s (■).

will enhance the hydrophobic interactions at this location, while its re-formation will decrease these interactions again, it is likely that the micellar kinetics and resulting temporary strong associations are responsible for the slow network relaxations in SDS containing physical gels.

Additionally, we point out that the water insolubility of the present physical gels, even those in a critical gel state,[9] is in accord with the above findings. During the swelling process, the removal of SDS from the gels increases the lifetime of the associations so that the gels become increasingly stable as SDS is progressively extracted. Conversely, if swelling is performed without extraction of SDS (this requires an excess of SDS in the swelling medium), the gels should dissolve due to the weak hydrophobic associations. This was indeed observed. In Figure 5, the relative mass m_{rel} of gel samples formed at C_0 = 10% is shown as a function of the swelling time in SDS−water solutions. At or above 5% SDS concentrations, the gels completely dissolve within 1−3 weeks while they remain stable at lower SDS concentrations. Because of the weakening of the hydrophobic associations with increasing surfactant concentration, the higher the SDS concentration in the external solution, the shorter the time period required for the gel-to-sol transition and the lower is the gel mass at this transition.

Structural Inhomogeneity of Gels with and without SDS. Figure 3B shows that the initial amplitude of the ICF significantly decreases after extraction of SDS micelles, indicating increasing extent of frozen concentration fluctuations. To account for the nonergodicity of gels, the time-averaged scattering intensity $\langle I \rangle_T$ at θ = 90° was recorded at a hundred different sample positions. Figure 6A shows the

dx.doi.org/10.1021/ma202672y | Macromolecules 2012, 45, 1991−2000

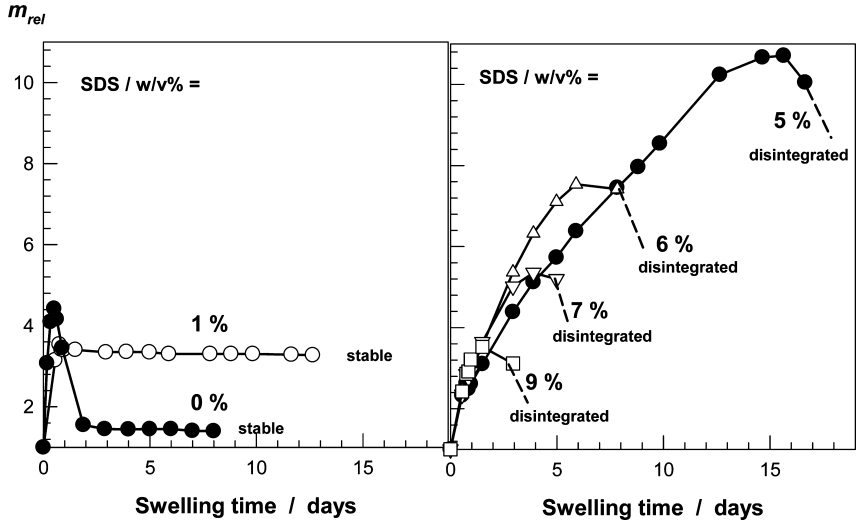

Figure 5. Relative weight swelling ratio m_{rel} of the gels formed at C_0 = 10% in aqueous SDS solutions shown as a function of the swelling time. SDS concentrations in the external solutions are indicated.

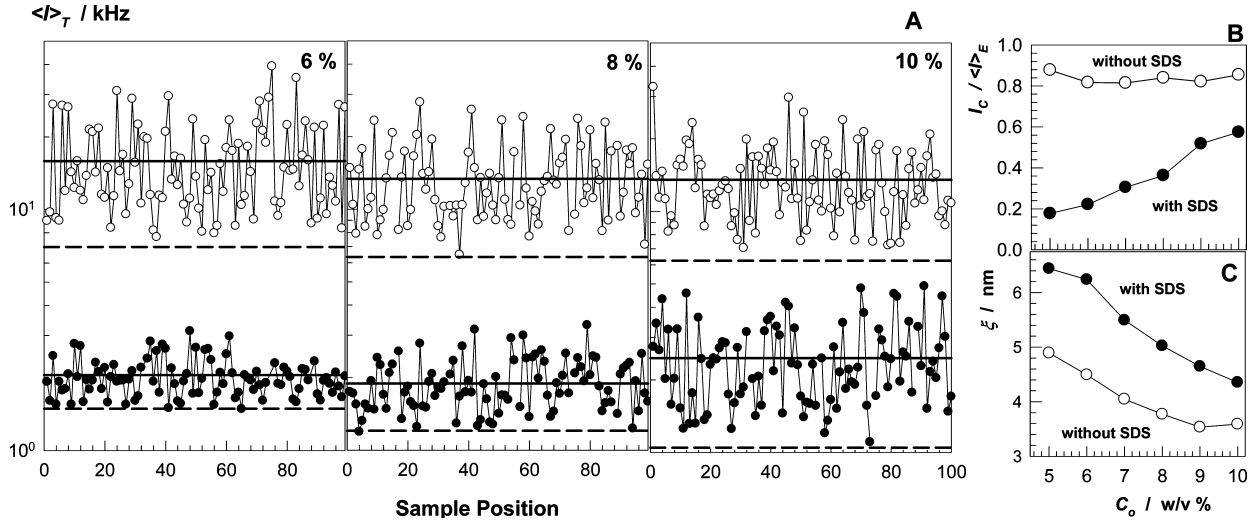

Figure 6. (A) Variation of $\langle I\rangle_T$ with the sample position of the physical gels with (●) and without SDS (○). The initial monomer concentrations C_0 are indicated. (B, C) Contribution of the static component $I_C/\langle I\rangle_E$ of the scattered intensity (B) and the dynamic correlation length ξ (C) plotted against C_0.

variations of $\langle I\rangle_T$ with randomly chosen sample position for gels with (filled symbols) and without SDS (open symbols). Note that $\langle I\rangle_T$ is averaged over a measurement time of 30 s. The solid lines represent the ensemble-averaged scattering intensity, $\langle I\rangle_E$, obtained by averaging $\langle I\rangle_T$ over all sample positions. The dashed lines represent that part of the scattering intensities $\langle I_F\rangle_T$ which is due to liquidlike concentration fluctuations. Almost 1 order of magnitude increase of the spatial fluctuations in $\langle I\rangle_T$ is observed after extraction of SDS micelles from the hydrogels. Since the relative swelling ratio $m_{rel,eq}$ of the physical gels without SDS is around 1.3, this increase cannot be attributed to the dilution of the network chains. However, the presence of SDS can markedly affect the scattering contrast. It is thus advisible to use a relative measure to capture the inhomogeneity. In Figure 6B, the relative contribution of the static component (frozen structure) of the scattered intensity, $I_C/\langle I\rangle_E$ is plotted against C_0. An appreciable portion of the thermal scattering from gels containing SDS is due to the presence of large SDS micelles; $I_C/\langle I\rangle_E$ monotonically increases from 20% to 60% with rising C_0 due to the suppression of the fluctuations by the polymer chains. In the absence of SDS, $I_C/\langle I\rangle_E$ of gels is independent of C_0 and equals to 83 ± 3%. Thus, the degree of the spatial gel inhomogeneity considerably increases after extraction of surfactant molecules. This increase is possibly related to the loss of reversibility of the cross-linkages and the resulting increase in the apparent cross-link density of gels at long experimental time scales (Table 1). We calculated the correlation length ξ of gels on the basis of their fast modes. In Figure 6C, ξ is plotted against C_0. ξ of surfactant containing gels is slightly decreasing from 6 to 4 nm, indicating decreasing mesh size with rising C_0, and it further decreases after extraction of SDS micelles.

Mechanical Properties of Gels. Inspection of the stress relaxation data in Figures 4C and 4D reveals that, at a given time scale, the modulus of gels containing SDS remains unchanged as the strain γ_0 is increased from 1% to 100%, while in the absence of SDS, it rapidly decreases with γ_0. In Figure 7A, the data are replotted as the variation of the relaxation modulus $G(t)$ of gels with increasing strain at fixed times. In the case of gels with SDS, the extent of the linear viscoelastic regime is

dx.doi.org/10.1021/ma202672y | *Macromolecules* 2012, 45, 1991−2000

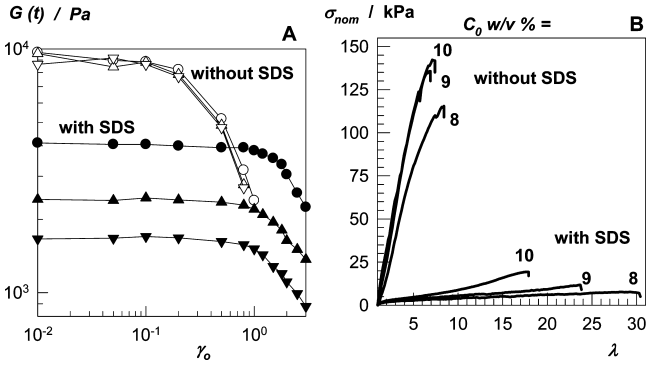

Figure 7. (A) Relaxation modulus $G(t)$ as a function of strain γ_0 for various times t for gels with (filled symbols) and without SDS (open symbols). t = 0.1 (circles), 1.0 (triangles up), and 10 s (triangles down). (B) Stress–strain curves of the physical gels with and without SDS formed at various C_0 indicated.

rather large, up to strains around 100%, whereas it is small and limited to strains up to ~10% for gels without SDS. This indicates a remarkable decrease of the toughness of gels after extraction of SDS micelles, as also observed by the uniaxial elongation tests conducted on cylindrical gel samples. Figure 7B represents tensile stress–strain data of the physical gels formed at three different concentrations C_0. In the presence of SDS, the elongation at break exceeds 1700%, and it further increases as C_0 is decreased. Without SDS, the gels break at about 700% strain and exhibit an order of magnitude larger ultimate strength as compared to the SDS containing gels.

The large strain properties of the physical gels with and without SDS were also compared by cyclic compression tests. The tests were conducted by compression of cylindrical gel samples at a constant crosshead speed to a predetermined maximum load, followed by immediate retraction to zero displacement. After a fixed waiting time of 2 min, the cycles were repeated several times. In all cases, the loading curve of the compressive cycle was different from the unloading curve, indicating damage in the gels and dissipation of energy during the cycle. In Figure 8A, three successive loading–unloading cycles of a gel sample formed at C_0 = 10% are shown as the dependence of the true stress σ_{true} on the deformation ratio λ. The behavior of virgin gel sample can be recovered when the sample is left to rest for 2 min without stress. The reversibility of loading/unloading cycles was observed in all gels with or without SDS. The perfect superposition of the successive loading curves demonstrates that the damage done to the gel samples during the loading cycle is recoverable in nature. This behavior is similar to that of the hydrogels formed by dynamic cross-links[32−34] but different from double-network gels showing irreversible fracture of the covalent bonds in the primary network.[35−37]

Figures 8B and 8C show the results of the loading/unloading experiments of the gels with increasing maximum load from 0.5 to 4 N. When SDS is present (B), a significant hysteresis is observed, while in the absence of SDS (C), the extent of hysteresis is low. In Figure 9A, the energy U_{hys} dissipated during the compression cycle calculated from the area between the loading and unloading curves is plotted against the maximum load. For gels without SDS, U_{hys} is below 3 kJ/m^3, while with SDS, it is much larger. The hysteresis increases with increasing maximum load, i.e., with increasing maximum strain during the loading step, or with decreasing monomer concentration C_0. The hysteresis energy U_{hys} of the present gels can be interpreted as the average dissociation energy U_{xl} of a hydrophobic association times the number of associations broken down during the compression cycle,[37,38] i.e.

$$U_{hys} = U_{xl}\nu_e f_\nu \tag{7}$$

where ν_e is the concentration of elastically effective hydrophobic associations, i.e., the cross-link density of physical gels, and f_ν is the fraction of associations broken during the loading/unloading cycle. We assume that the energy U_{xl} required for the detachment of the hydrophobe C18 from associations is of the order of 10^2 kJ/mol.[39,40] To estimate the cross-link density ν_e, the plateau moduli G_0 of gels are obtained from the constant value of G' at a high frequency (Figures 4A,B and Figure S6). Since G_0 corresponds to the shear modulus G, ν_e was calculated using the equation[41,42]

$$G = (1 - 2/\phi)\nu_e RT(\nu_2^0/\nu_2)^{2/3} \tag{8}$$

where ϕ is the functionality of the cross-links, R is gas constant, and T is the absolute temperature (K). The calculation using eq 8 assumes a phantom network behavior, which is generally appropriate for the transient networks. However, for the present gels formed by hydrophobic associations, since the average aggregation number is large,[43] the cross-link function-

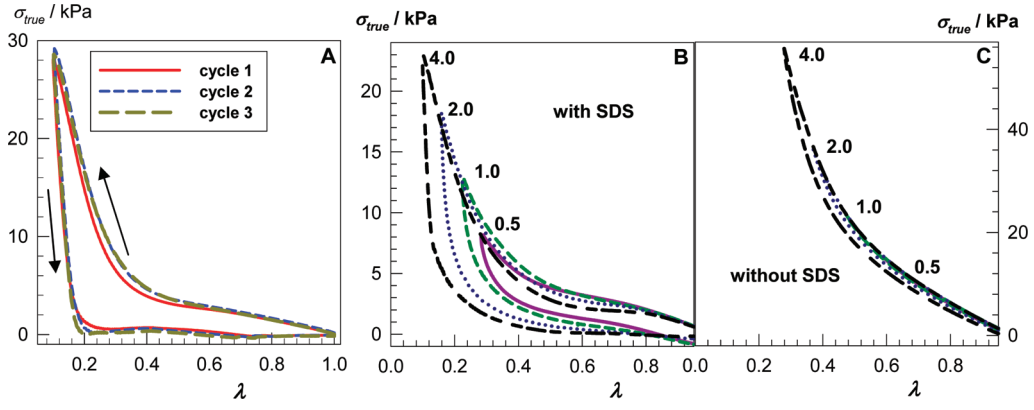

Figure 8. True stress σ_{true} vs deformation ratio λ curves from cyclic compression tests for the gel samples formed at C_0 = 10%. (A) Three successive loading/unloading cycles for a gel sample containing SDS. Maximum load = 5 N. (B, C) Loading/unloading cycles for gels with (B) and without SDS (C). The tests were conducted with increasing maximum load from 0.5 to 4 N, as indicated.

dx.doi.org/10.1021/ma202672y | Macromolecules 2012, 45, 1991–2000

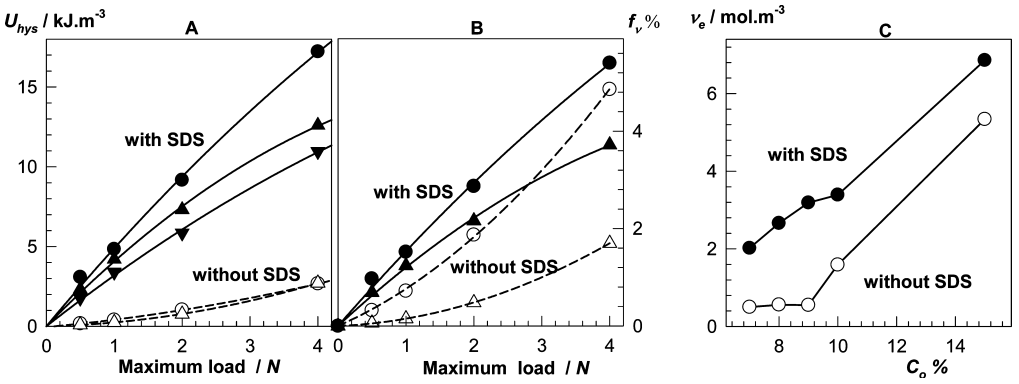

Figure 9. (A, B) Hysteresis energy U_{hys} (A) and the fraction f_ν of dissociated cross-links during the loading/unloading experiments (B) shown as a function of the maximum load. Data were from gels with (filled symbols) and without SDS (open symbols). C_0 = 9% (circles), 10% (triangles up), and 15% (triangles down). (C) Cross-link density ν_e of gels with (●) and without SDS (○) shown as a function of C_0.

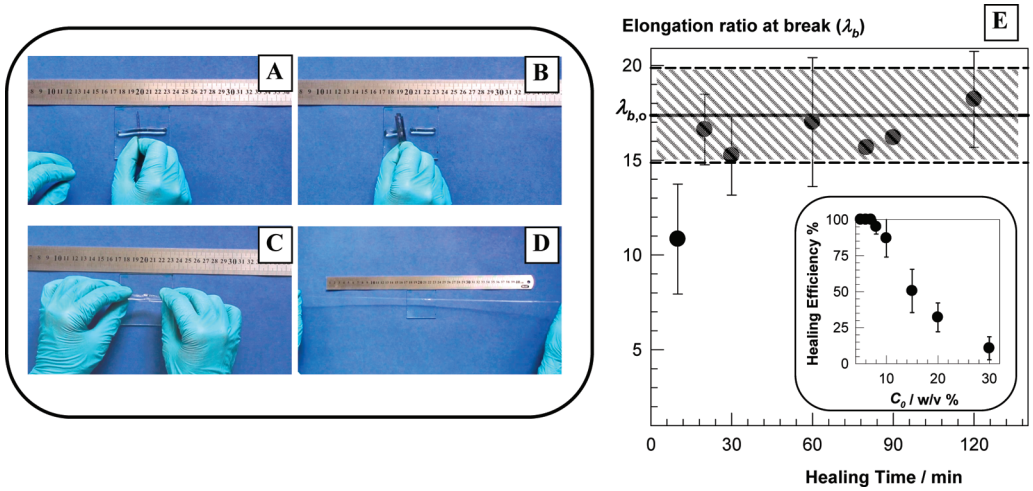

Figure 10. (A–D) Photographs of a gel sample formed at C_0 = 10%. After cutting into two pieces and pressing the fractured surfaces together for 10 min, they merge into a single piece. (E) Elongation ratio at break of healed gel samples (λ_b) formed at C_0 = 10% shown as a function of the healing time. The horizontal line and the dashed area represent the mean value and the standard deviation for the virgin gel sample. Inset to (E) shows the healing efficiency vs C_0 plot for a healing time of 30 min.

ality is also large, which will suppress the fluctuations of the cross-links about their mean positions,[44] so that the gels are expected to deform affinely, i.e., $(1 - 2/\phi) = 1$. Using the experimentally determined values of ν_2^0 and ν_2 (Table 1), together with the high-frequency elastic moduli G' (Figure S6), we calculated ν_e of gels with and without SDS and they are plotted in Figure 9C against C_0. Surfactant containing gels exhibit higher cross-link densities than the corresponding gels without SDS. This difference is possibly related to the effect of surfactant on the aggregation behavior of associating polymers in aqueous solutions. Since the presence of surfactant above its cmc weakens hydrophobic interactions, thereby reducing the aggregation number of hydrophobic blocks, the gels with SDS contain larger number of hydrophobic associations than without SDS, so that they exhibit higher cross-link densities. We have to mention that, at experimental time scales of the order of seconds, the apparent cross-link density of SDS containing gels is much lower than those without SDS due to the shorter lifetimes of the associations (cf. Figure 4).

Using the values of ν_e and U_{hys}, one may solve eq 7 for the fraction f_ν of physical cross-links reversibly broken during the compression cycles. The results are given in Figure 9B for the gels formed at C_0 = 9% and 10% plotted against the maximum load. When SDS is present (filled symbols), 1–6% of the physical cross-links dissociate under force, but reversibly, if the force is removed they re-form again. As C_0 is increased, f_ν decreases and becomes 0.3–2% at C_0 = 15%. In the absence of SDS (open symbols), this fraction is small at low maximum loads, indicating the stability of the associations, but it increases with increasing load and approaches to its value in SDS containing gels. The results thus reveal that there are a larger number of hydrophobic associations in physical gels with SDS, and these associations are easily broken; both of these properties contribute their significant hysteresis behavior in cyclic compression tests.

Reversible disengagements of the hydrophobic units from the associations under an external force point out the self-healing properties of surfactant containing physical gels. The Supporting Information movie shows the healing process of a gel sample formed at C_0 = 10%. The images in Figures 10A–D illustrate that when the fracture surfaces of a ruptured gel sample are pressed together at 24 °C, the two pieces merge into a single piece. The joint re-formed withstands very large extension ratios as the original gel sample before its fracture. No such self-healing behavior was observed after SDS had been extracted from the gel networks.

To quantify the healing efficiency, tensile testing experiments were performed using cylindrical gel samples of 5 mm diameter

and 6 cm length. The samples were cut in the middle, and then the two halves were merged together within a plastic syringe (of the same diameter as the gel sample) at 24 °C by slightly pressing the piston plunger. The healing time was varied from 10 to 130 min, and each experiment was carried out starting from a virgin sample. In Figure 10E, the elongation ratio at break of the healed gel sample (λ_b) formed at C_0 = 10% is plotted against the healing time. The horizontal solid line represents the average elongation ratio at break of the virgin sample ($\lambda_{b,0}$) with a standard deviation indicated by the dashed area (17.4 ± 2.5%). Healing efficiency, $\lambda_b/\lambda_{b,0}$, rapidly increases with the healing time, and after 20 min, a healing efficiency of nearly 100% was observed. We note that, although the stress−strain curves of the healed gels superimposed for all healing times, gel samples healed longer than 1 h broke at a different location than the healed zone. Experiments were also conducted using the gels formed at various C_0. In this set of experiments, the healing efficiency was determined for a fixed healing time of 30 min. As illustrated in the inset to Figure 10E, the healing efficiency remarkable decreases with C_0, i.e., with decreasing fraction of dissociable cross-links (Figure 9B); as a consequence, the damage created in the gel samples remained permanent at high polymer concentrations.

All the above dynamic and mechanical features of the physical gels suggest that the key factor leading to the self-healing behavior is the weakening of strong hydrophobic interactions due to the presence of surfactant molecules. Before fracture, this weakening creates an energy dissipation mechanism along the gel samples so that the degree of toughness significantly increases. After fracture, hydrophobes can easily find their partners in the other cut surface due to the hydrophobic interactions across the damage surfaces together with the help of the internal dynamics so that self-healing of the damaged gel samples occurs within a short period of time.

CONCLUSIONS

As a main finding of our experiments, several dynamic characteristics of self-healing hydrogels formed via micellar polymerization technique vanish after extraction of surfactant micelles. Physical gels containing SDS exhibit, in addition to the fast mode, a slow relaxation mode in DLS, indicating structural relaxations on the time scales of milliseconds. Time-dependent dynamic moduli of these gels also indicate the temporary nature of the hydrophobic associations having lifetimes of the order of seconds to milliseconds. After extraction of SDS, however, the gels behave similar to chemically cross-linked gels with time-independent dynamic moduli and a single relaxation mode in DLS. The results thus show that, when SDS micelles are present, the cross-links are reversible due to the local solubilization of the hydrophobic associations, while after extraction of SDS, direct exposure of the hydrophobic associations to the aqueous environment considerably increases their lifetimes. This structural change in the physical gels due to the removal of SDS is responsible for their insolubility in water and solubility in SDS solutions. A significant increase in the degree of spatial gel inhomogeneity was observed after extraction of surfactant molecules, which is also related to the breakdown of the reversible nature of the cross-linkages and resulting increase in the apparent cross-link density of gels at long time scales. In the presence of SDS, the gels are very tough and the elongation at break exceeds 1700% while without SDS, the gels break at about 700% strain and exhibit an order of magnitude larger ultimate strength. Results of the cyclic compression tests show that a large number of physical cross-links in SDS containing gels dissociate under force, but reversibly, if the force is removed, they re-form again. The reversible disengagements of the hydrophobic units building the physical cross-links leads to a healing efficiency of nearly 100%, while no such self-healing behavior was observed after extraction of SDS from the gel networks. The loss of self-healing ability of the present gels after their swelling limits their application areas to systems in which the gel samples have to be isolated from the environment.

ASSOCIATED CONTENT

Supporting Information

Figure S1, solubility of C18 in aqueous SDS−NaCl solutions; Figure S2, G' vs reaction time profiles of the micellar copolymerization of AAm and C18 and the limiting values of G' and tan δ as a function of C_0; Figure S3, the decomposition plots according to eq 3; Figure S4, the relaxation rate distribution functions $G(\Gamma)$ of surfactant solutions and gels; Figure S5, the stress−strain curves of the hydrogels; and Figure S6, the results of the frequency sweep tests conducted on the hydrogels with and without SDS. This material is available free of charge via the Internet at http://pubs.acs.org.

AUTHOR INFORMATION

Notes

The authors declare no competing financial interest.

ACKNOWLEDGMENTS

Work was supported by the Scientific and Technical Research Council of Turkey (TUBITAK) and International Bureau of the Federal Ministry of Education and Research of Germany (BMBF), TBAG-109T646. O.O. thanks the Turkish Academy of Sciences (TUBA) for the partial support.

REFERENCES

(1) Candau, F.; Selb, J. *Adv. Colloid Interface Sci.* **1999**, *79*, 149.
(2) Volpert, E.; Selb, J.; Candau, F. *Polymer* **1998**, *39*, 1025.
(3) Hill, A.; Candau, F.; Selb, J. *Macromolecules* **1993**, *26*, 4521.
(4) Regalado, E. J.; Selb, J.; Candau, F. *Macromolecules* **1999**, *32*, 8580.
(5) Candau, F.; Regalado, E. J.; Selb, J. *Macromolecules* **1998**, *31*, 5550.
(6) Kujawa, P.; Audibert-Hayet, A.; Selb, J.; Candau, F. *J. Polym. Sci., Part B: Polym. Phys.* **2004**, *42*, 1640.
(7) Kujawa, P.; Audibert-Hayet, A.; Selb, J.; Candau, F. *Macromolecules* **2006**, *39*, 384.
(8) Gao, B.; Guo, H.; Wang, J.; Zhang, Y. *Macromolecules* **2008**, *41*, 2890.
(9) Tuncaboylu, D. C.; Sari, M.; Oppermann, W.; Okay, O. *Macromolecules* **2011**, *44*, 4997.
(10) Chern, C. S.; Chen, T. J. *Colloids Surf., A* **1998**, *138*, 65.
(11) Leyrer, R. J.; Machtle, W. *Macromol. Chem. Phys.* **2000**, *201*, 1235.
(12) Lau, W. *Macromol. Symp.* **2002**, *182*, 283.
(13) Rehage, H.; Hoffman, H. *Mol. Phys.* **1991**, *74*, 933.
(14) (a) Missel, P. J.; Mazer, N. A.; Benedek, G. B.; Young, C. Y. *J. Phys. Chem.* **1980**, *84*, 1044. (b) Magid, L. J. *J. Phys. Chem. B* **1998**, *102*, 4064. (c) Hassan, P. A.; Raghauan, S. R.; Kaler, E. W. *Langmuir* **2002**, *18*, 2543. (d) Sutherland, E.; Mercer, S. M.; Everist, M.; Leaist, D. *J. Chem. Eng. Data* **2009**, *54*, 272.
(15) Joosten, J. G. H.; Mccarthy, J. L.; Pusey, P. N. *Macromolecules* **1991**, *24*, 6690.
(16) Pusey, P. N.; van Megen, W. *Physica A* **1989**, *157*, 705.
(17) Ikkai, F.; Shibayama, M. *Phys. Rev. Lett.* **1999**, *82*, 4946.

(18) ISO 7875-1, 1996. Water quality. Determination of surfactants. Part 1: Determination of anionic surfactants by measurement of the methylene blue index (MBAS). USO/TC 147.
(19) Kizilay, M. Y.; Okay, O. *Polymer* **2003**, *44*, 5239.
(20) Gundogan, N.; Melekaslan, D.; Okay, O. *Macromolecules* **2002**, *35*, 5616.
(21) The network chains are in the Gaussian regime up to a linear swelling ratio α around 1.5 (cf. ref 20). In this regime, the elastic modulus decreases with increasing degree of swelling.
(22) Förster, S.; Schmidt, M.; Antonietti, M. *Polymer* **1990**, *31*, 781.
(23) Young, C. Y.; Missel, P. J.; Mazer, N. A.; Benedek, G. B.; Carey, M. C. *J. Phys. Chem.* **1978**, *82*, 1375.
(24) Hayashi, S.; Ikeda, S. *J. Phys. Chem.* **1980**, *84*, 744.
(25) Magid, L. J.; Li, Z.; Butler, P. D. *Langmuir* **2000**, *16*, 10028.
(26) Molchanov, V. S.; Philippova, O. E.; Khokhlov, A. R.; Kovalev, Y. A.; Kuklin, A. I. *Langmuir* **2007**, *23*, 105.
(27) Kumar, S.; Bansal, D.; Din, K. *Langmuir* **1999**, *15*, 4960.
(28) Kunieda, H.; Ozawa, K.; Huang, K.-L. *J. Phys. Chem. B* **1998**, *102*, 831.
(29) Siriwatwechakul, W.; LaFleur, T.; Prud'homme, R. K.; Sullivan, P. *Langmuir* **2004**, *20*, 8970.
(30) Sato, T.; Acharya, D. P.; Kaneko, M.; Aramaki, K.; Singh, Y.; Ishitobi, M.; Kunieda, H. J. *J. Dispersion Sci. Technol.* **2006**, *27*, 611.
(31) Patist, A.; Oh, S. G.; Leung, R.; Shah, D. O. *Colloids Surf., A* **2001**, *176*, 3.
(32) Miquelard-Garnier, G.; Creton, C.; Hourdet, D. *Soft Matter* **2008**, *4*, 1011.
(33) Miquelard-Garnier, G.; Hourdet, D.; Creton, C. *Polymer* **2009**, *50*, 481.
(34) Lin, W. C.; Fan, W.; Marcellan, A.; Hourdet, D.; Creton, C. *Macromolecules* **2010**, *43*, 2554.
(35) Tanaka, Y.; Fukao, K.; Miyamoto, Y. *Eur. Phys. J. E* **2000**, *3*, 395.
(36) Tanaka, Y.; Kuwabara, R.; Na, Y. H.; Kurokawa, T.; Gong, J. P.; Osada, Y. *J. Phys. Chem. B* **2005**, *109*, 11559.
(37) Webber, R. E.; Creton, C.; Brown, H. R.; Gong, J. P. *Macromolecules* **2007**, *40*, 2919.
(38) Lake, G. J.; Thomas, A. G. *Proc. R. Soc. London, A* **1967**, *300*, 108.
(39) Annable, T.; Buscall, R.; Ettelaie, R.; Whittlestone, D. *J. Rheol.* **1993**, *37*, 695.
(40) Ng, W. K.; Tam, K. C.; Jenkins, R. D. *J. Rheol.* **2000**, *44*, 137.
(41) Flory, P. J. *Principles of Polymer Chemistry*; Cornell University Press: Ithaca, NY, 1953.
(42) Treloar, L. R. G. *The Physics of Rubber Elasticity*; Oxford University Press: Oxford, UK, 1975.
(43) Shashkina, Yu. A.; Zaroslov, Yu. D.; Smirnov, V. A.; Philippova, O. E.; Khokhlov, A. R.; Pryakhina, T. A.; Churochkina, N. A. *Polymer* **2003**, *44*, 2289.
(44) Mark, J. E.; Erman, B. *Rubberlike Elasticity. A Molecular Primer*; Cambridge University Press: Cambridge, UK, 2007.

Macromolecules

Article

pubs.acs.org/Macromolecules

Block Random Copolymers of *N*-Alkyl-Substituted Acrylamides with Double Thermosensitivity

Mohammad T. Savoji, Satu Strandman, and X. X. Zhu*

Department of Chemistry, Université de Montréal, CP 6128, Succursale Centre-ville, Montreal, QC H3C 3J7, Canada

Supporting Information

ABSTRACT: Block copolymers consisting of two segments of random copolymers of *N*-alkylacrylamides have been synthesized by a sequential reversible addition−fragmentation chain transfer (RAFT) polymerization. The copolymers in the form of A_nB_m-*b*-A_pB_q have been made of two blocks of *N*-*n*-propylacrylamide (nPA) and *N*-ethylacrylamide (EA) of different compositions to obtain polymers with stepwise thermosensitivity. The control of the RAFT polymerization was confirmed by studying the kinetics of the copolymerization process. The block random copolymer, poly(nPA$_x$-*co*-EA$_{1-x}$)-*block*-poly(nPA$_y$-*co*-EA$_{1-y}$), is well-defined and has a low polydispersity. The cloud points of the random copolymers can be tuned by varying the chemical composition of the copolymers. The diblock copolymer exhibited a two-step phase transition upon heating to 41.5 and 53.0 °C, corresponding to the cloud points of the individual blocks. Dynamic light scattering experiments also showed the stepwise aggregation properties of the copolymer in aqueous solutions.

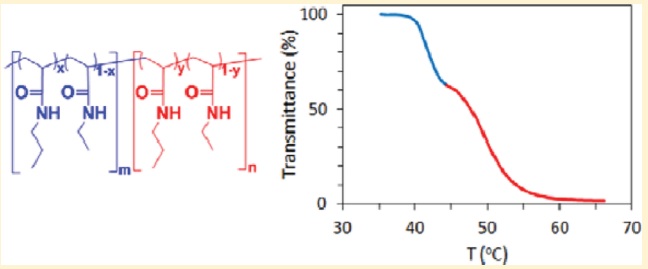

INTRODUCTION

Thermoresponsive polymers have been widely investigated for their potential in biomedical applications.[1−4] Many polymers based on N-alkyl-substituted acrylamides, the most well-known of which being poly(*N*-isopropylacrylamide), exhibit a lower critical solution temperature (LCST) in water.[5] The thermoresponsiveness of these polymers depends on the relative hydrophobicity or hydrophilicity of the *N*-alkylacrylamide monomers,[5,6] in addition to the effects of molar mass, concentrations, and additives. Increased hydrophobicity of the substitution groups leads to a lower phase transition temperature of the polymers obtained.[7−10] The cloud points (CPs) of the polymers can be tuned by the varying the chemical composition of the random copolymers based on N-alkyl-substituted (meth)acrylamides.[11−13] Diblock copolymers with dual thermoresponsive behavior have been synthesized by the incorporation of blocks with different cloud points.[4,14−19] We have made various di- and triblock copolymers of *N*-alkylacrylamides and showed that they exhibited multiple CPs in aqueous solutions,[20,21] corresponding to different stages of their aggregation.[22,23] The phase transitions are usually accompanied by changes in the micellar size or shape and solution properties. However, the choice of the substitution groups on such monomers limits the range of the phase transition temperatures. To tailor the properties of the materials, it would be ideal to have blocks available with a thermosensitivity at any desired temperature. This may be achieved by varying the chemical composition of a random copolymer.[12] Therefore, our approach is to make a block copolymer of two random copolymer sequeneces with different thermosensitivities. We choose to use the reversible addition−fragmentation chain transfer (RAFT) polymerization method[24,25] to grow two block of random copolymers of *N*-*n*-propylacrylamide (nPA) and *N*-ethylacrylamide (EA) with compositions adjusted for the desired transition temperatures. We report here the design, synthesis, and characterization of a diblock thermoresponsive copolymer with two distinct transition temperatures corresponding to the two random copolymers synthesized by sequential RAFT copolymerization.

EXPERIMENTAL SECTION

Materials. 2,2′-Azobis(isobutyronitrile) (AIBN) from Eastman Kodak was recrystallized from methanol and stored in dark bottles in a refrigerator. Acryloyl chloride, ethylamine, and *n*-propylamine were purchased from Aldrich and were used without further purification. *N*-*n*-Propylacrylamide (nPA) and *N*-ethylacrylamide (EA) were prepared by reacting acryloyl chloride with the corresponding alkylamines following a reported procedure.[26] 2-Dodecylsulfanylthiocarbonylsulfanyl-2-methylpropionic acid (DMP) was used as a highly efficient chain transfer reagent (CTA) and prepared according to the procedure reported by Lai et al.[27] Water was purified using a Millipore Milli-Q system. Anhydrous and oxygen-free dioxane was obtained by passage through columns packed with activated alumina and supported copper catalyst (Glass Contour, Irvine, CA).

Polymer Synthesis. The monomers nPA and EA were added at a predetermined ratio along with trithiocarbonate DMP as the CTA and AIBN as the initiator in a 100 mL Schlenk tube equipped with a magnetic stirrer bar. A fixed volume of anhydrous dioxane was then transferred to the Schlenk tube. The ratio of [monomers]:[DMP]:

Received: December 16, 2011
Revised: January 24, 2012
Published: February 8, 2012

[AIBN] was fixed at 200:1:0.1, and the total monomer concentration was 0.3 g/mL. The mixture was degassed by three freeze–pump–thaw cycles prior to immersing it in a preheated oil bath. The reaction temperature was set to 70 °C, and the reaction was conducted for 90 min before terminating it by exposing the reaction mixture to air and immersing it in an ice bath. The product was then precipitated in diethyl ether, filtered, and dried in vacuum oven at 60 °C to yield poly(nPA$_x$-*co*-EA$_{1-x}$)-CTA as a yellowish powder. The resulting random copolymer was then used as the DMP-ended macro-CTA in the second step to make a diblock copolymer using the reactant ratio [monomer]:[macro-CTA]:[AIBN] of 400:1:0.1. The procedure for diblock copolymerization was the same as for random copolymerization, except that DMP has been replaced by macro-CTA (Scheme 1). In the kinetic studies, aliquots of the reaction mixture were withdrawn during the course of the copolymerization and analyzed by size exclusion chromatography (SEC) and nuclear magnetic resonance (NMR) spectroscopy.

Scheme 1. RAFT Copolymerization of nPA and EA for the Preparation of Poly(nPA$_x$-*co*-EA$_{1-x}$) and Further Chain Extension Leading to a Diblock Random Copolymer Poly(nPA$_x$-*co*-EA$_{1-x}$)-*block*-poly(nPA$_y$-*co*-EA$_{1-y}$)

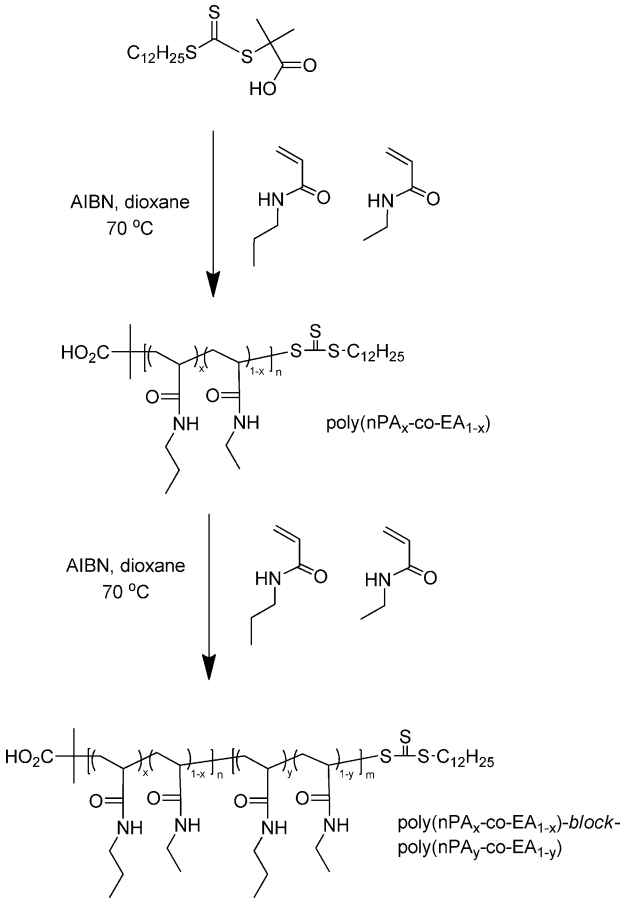

Polymer Characterization. Molar masses and polydispersity indices (PDI) of the polymers were obtained by SEC on a Waters 1525 system equipped with three Waters Styragel columns and a refractive index detector (Waters 2410) at 35 °C. *N,N*-Dimethylformamide (DMF) was employed as the mobile phase at a flow rate of 1 mL/min, and the system was calibrated by poly(methyl methacrylate) standards. In kinetic studies, the volatile species were removed in a vacuum oven at 60 °C from the samples taken at different time intervals during the course of the reaction.

The NMR spectra of the monomers and polymers in deuterated chloroform ($CDCl_3$) were determined on a Bruker AV-400 spectrometer operating at 400 MHz for protons. The chemical shifts are given in reference to the solvent peak at 7.26 ppm. The theoretical molar masses were calculated from the conversions given by ^{1}H NMR according to

$$\bar{M}_{n,th} = M_{CTA} + \frac{[monomer]}{[CTA]} \times M_{monomer} \times conversion \quad (1)$$

where M_{CTA} is the molar mass of the chain transfer agent and [monomer] and [CTA] are the initial monomer and CTA concentrations, respectively. $M_{monomer}$ is the weighted molar mass of the comonomers and calculated from the molar ratios of comonomers in the product obtained by ^{1}H NMR. The molar masses of the polymers were not determined by ^{1}H NMR because of the overlap of the methyl group signals from EA and from DMP end group at 0.99 ppm. For a block copolymer, [CTA] in eq 1 is replaced by the concentration of macro-CTA.

The CPs of the polymers were determined from the optical transmittance measured on a Cary 300 Bio UV–vis spectrophotometer equipped with a temperature-controlled sample holder. Samples were prepared by the dissolution of copolymers in distilled water in an ice–water bath, after which the solutions were homogenized by ultrasonication. The absorbance was measured at different wavelengths for the aqueous solution of polymers 1.0 mg/mL by continuous heating at rate of 0.1 °C/min over various temperature ranges or stepwise heating at 1 °C intervals with 20 min equilibration at each temperature, which was also the heating procedure used in the light scattering experiments where continuous heating was not possible. Here, the CP is defined as a temperature at which the differential of transmittance change with respect to the temperature at a certain wavelength is maximal.[28] Another definition is the temperature corresponding to a 10% or 50% reduction in the initial transmittance.[20,25,29] For individual blocks, the temperature at which 50% transmittance was lost upon heating was considered as the CP. For block copolymers, the CP is determined from the middle point between the onset and the offset of the transmittance curve as a function of temperature.

Dynamic light scattering (DLS) studies on the temperature-dependent aggregation behavior were carried out on a CGS-3 compact goniometer (ALV GmbH) equipped with an ALV-5000 multi tau digital real time correlator at chosen temperatures using a Science/Electronics temperature controller. The laser wavelength was 632 nm, and the scattering angle was fixed at 90°. All solutions were made with the concentration of 2.0 mg/mL and filtered through 0.22 μm Millipore filters to remove dust. The samples were heated at 1 °C intervals within 20 min equilibration time. The results were analyzed by CONTIN inverse Laplace transform algorithm. The decay rate distributions were transformed to an apparent diffusion coefficient and the apparent intensity-weighted hydrodynamic diameters of the polymers was obtained from the Stokes–Einstein equation.

RESULTS AND DISCUSSION

Kinetics of the RAFT Copolymerization of *N*-Alkyl-Substituted Acrylamides. *N*-*n*-Propylacrylamide and *N*-ethylacrylamide were copolymerized in dioxane at 70 °C using a monomer ratio of 70:30 (nPA:EA) and a reactant ratio of [monomers]:[CTA]:[initiator] of 200:1:0.1. The conversion was monitored by ^{1}H NMR spectroscopy of the samples withdrawn from the reaction mixture at regular time intervals and determined by comparing the integrated areas of the characteristic proton signals from the vinyl group of monomers in the region of 5.5–6.3 ppm with the integrated areas of the methyl signals of the polymer at 0.8–1.2 ppm (Figure S1, Supporting Information). Of course, the contribution of residual methyl group signals is subtracted from the total

dx.doi.org/10.1021/ma2027269 | *Macromolecules* 2012, 45, 2001–2006

integration in the region of 0.8−1.2 ppm (as explained in Figure S2).

The composition of the copolymer remained constant throughout the duration of the polymerization process as verified by ^{1}H NMR (Figure S2), which indicates the random nature of the copolymerization. The evolution of the molar mass with conversion is presented in Figure 1. The increase in

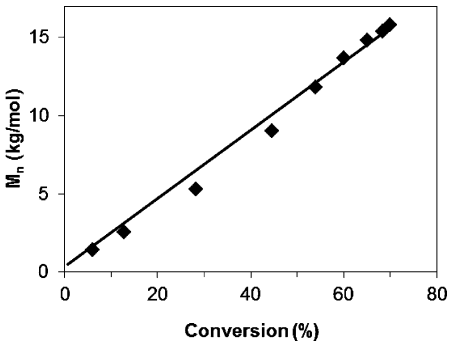

Figure 1. Number-average molar mass M_n as a function of conversion of the monomers for the RAFT copolymerization of nPA and EA at monomer ratio of 70:30 (nPA:EA). Solid line represents the theroretical molar masses calculated from eq 1.

molar mass follows the theoretical line up to 70% conversion, which shows the controlled character of the copolymerization. An increase in polydispersity is observed at higher conversions (Figure 2A) and a negative deviation from linearity in the

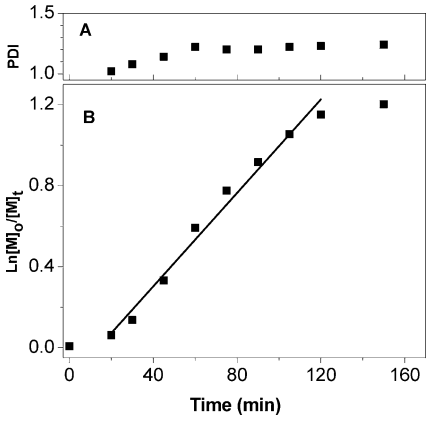

Figure 2. (A) Polydispersity index (PDI) and (B) semilogarithmic kinetic plot of the monomer conversion $\ln([M]_0/[M]_t)$ as a function of reaction time for the RAFT copolymerization of nPA and EA in dioxane at 70 °C with a monomer ratio [nPA]:[EA] of 70:30 and [monomers]:[CTA]:[initiator] ratio of 200:1:0.1. Solid line is a linear fit to part of the data to serve as a visual guide.

pseudo-first-order plot (Figure 2B) occurred after 120 min reaction time, both frequently reported for the RAFT polymerization of *N*-substituted acrylamides.[20,25,30−32] An inhibition period of ∼15 min at the beginning of polymerization is attributed to the slow fragmentation of CTA.[33−36] The kinetic data indicate that the concentration of the radical species is constant during the reaction, and thus, the polymerization is controlled in this range of conversions. The SEC chromatograms of the samples withdrawn at different reaction times (Figure S3) show that the higher polydispersities at high conversions arise from low-molar-mass tailing similar to our earlier observations[20] as well as those by other groups.[30,35,37]

In our earlier discussion, we showed that the negative deviation of the kinetic plot may not arise from the initiator-derived radicals but is rather related to the number of other radicals, which can be corrected to some degree by lowering the polymerization temperature.[20] This was our motivation for the choice of current reaction temperature (70 °C). The reactivities of *N*-alkylacrylamides are also known to depend on their structure, the polymerizations of *N,N*-dialkyl-substituted acrylamides being faster and more controlled than those of their monosubstituted counterparts with less negative deviation in the kinetic behavior.[20] In comparison with our earlier kinetic data on the homopolymerization of nPA with the same [CTA]:[initiator] ratio at the same temperature,[20] the copolymerization of nPA and EA shows better linearity up to higher conversions. Other monomers (*N-tert*-butylacrylamide, tBA, and *N,N*-dimethylacrylamide, DMA) with different mole fractions were also copolymerized under the same conditions, and they showed the same kinetic behavior as P(nPA$_{0.7}$EA$_{0.3}$) (data not shown). On the basis of the kinetic data, the reaction conditions are chosen to provide an active macro-CTA that can be employed in the subsequent block copolymerization.

CPs of the Random Copolymers. Various *N*-alkyl-substituted acrylamide homopolymers and corresponding random copolymers were synthesized and studied in our group.[12] Among them, *N-n*-propylacrylamide (nPA) and *N*-ethylacrylamide (EA) were selected for the current study. These monomers have different hydrophilicities and thus the corresponding copolymers have different CPs. A series of copolymers with different nPA:EA ratios were synthesized, and their thermoresponsiveness was tested in aqueous solutions. Table 1 shows the characteristics of the copolymers. The

Table 1. Chemical Compositions and CP of Poly(nPA$_x$-*co*-EA$_{1-x}$) Copolymers with Different Ratios of the Comonomers

polymer	M_n[a] (g/mol)	PDI[a]	nPA:EA ratio in final polymer[b]	CP (°C)[c]
PEA	19 800	1.08	100:0	>85
P(nPA$_{0.2}$EA$_{0.8}$)	15 200	1.24	19.1:80.9	75
P(nPA$_{0.4}$EA$_{0.6}$)	19 800	1.13	40.5:59.5	52
P(nPA$_{0.5}$EA$_{0.5}$)	12 000	1.18	49.8:50.2	45
P(nPA$_{0.6}$EA$_{0.4}$)	20 100	1.23	58.2:41.8	40
P(nPA$_{0.7}$EA$_{0.3}$)	13 200	1.11	69.9:30.1	37
P(nPA$_{0.8}$EA$_{0.2}$)	16 500	1.21	78.1:21.9	33
PnPA	12 800	1.10	0:100	20

[a]Determined by SEC. [b]Determined by ^{1}H NMR. [c]Determined by UV−vis spectroscopy at λ = 350 nm.

copolymer compositions are nearly identical to the feed ratios, supporting our earlier observations on the similar reactivity of *N*-alkylacrylamides[12] and suggesting that the copolymers are statistically random.

Figure 3 shows the CPs of poly(nPA$_x$-*co*-EA$_{1-x}$) random copolymers as a function of the mole fraction of EA in the random copolymer. The CP increases with an increase in the mole fraction of the more hydrophilic monomer EA and follows eq 2 as a function of the comonomer composition:[12]

$$T = \frac{\mu_1 T_1 + k\mu_2 T_2}{\mu_1 + k\mu_2} \quad (2)$$

dx.doi.org/10.1021/ma2027269 | *Macromolecules* 2012, 45, 2001−2006

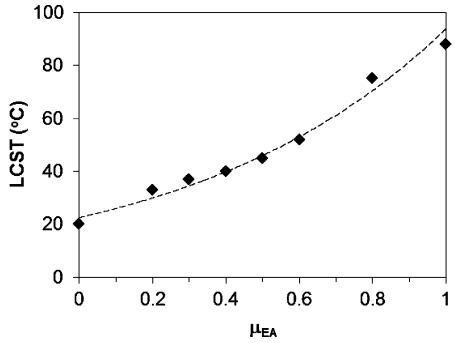

Figure 3. CPs of poly(nPA$_x$-*co*-EA$_{1-x}$) aqueous solution as a function of the mole fraction of EA, μ_{EA}. The dashed line shows the curve fitting to eq 2, yielding a k value of 0.69.

where T, T_1, and T_2 are the CPs of the random copolymer, PEA, and PnPA, respectively. μ_1 and μ_2 are the mole fractions of EA and nPA (note that $\mu_1 = 1 - \mu_2$), respectively, and k is a weighting parameter which can be deduced from curve fitting to the experimental data. A k value of 1 would be obtained in the case of a linear relationship of T vs μ_1. In the current case, the plot has a concave shape, yielding a k value of 0.69. In comparison, a k value of 0.51 was observed for the copolymers of EA and a more hydrophobic monomer, *N*-*tert*-butylacrylamide (tBA).[12] Figure 3 shows a 15 °C difference between the CPs of P(nPA$_{0.4}$EA$_{0.6}$) and P(nPA$_{0.7}$EA$_{0.3}$), enough to distinguish the phase transitions in a block copolymer. Therefore, these monomer ratios were chosen to build the two blocks of the copolymer.

Preparation of a Diblock Random Copolymer by RAFT Polymerization. A random copolymer of nPA and EA with a comonomer ratio of 70:30, P(nPA$_{0.7}$EA$_{0.3}$), was synthesized to serve as a macro-CTA (macro-chain transfer agent) for the chain extension. The polymerization was stopped at 60% conversion to avoid the formation of dead chain ends. The polymer was purified by a precipitation in diethyl ether prior to the addition of the second block so that it was free of monomers as shown by ^{1}H NMR spectroscopy (Figure S1, Supporting Information). The details of the macro-CTA copolymer are presented in Table 2.

Table 2. Conversions and the Compositions of Mono- and Diblock Random Copolymers

polymer	nPA:EA ratio in the blocks[a]	conv[a] (%)	M_n theor[b]	M_n SEC[c]	PDI[c]
P(nPA$_{0.7}$EA$_{0.3}$)	69.9:30.1	60	13 500	13 200	1.11
P(nPA$_{0.7}$EA$_{0.3}$)-*b*-P(nPA$_{0.4}$EA$_{0.6}$)	41.2:58.8	66	41 000	45 000	1.26

[a]Detemined by ^{1}H NMR. [b]Calculated from eq 1. [c]Determined by SEC.

As mentioned above, the comonomer ratio for building the second block was chosen to yield two separable phase transitions in aqueous solution. The conditions of the block copolymerization of nPA and EA at a feed ratio of 60:40 were the same as in the first copolymerization, but the ratio of reactants [monomer]:[macro-CTA]:[AIBN] was set at 400:1:0.1 to provide a longer second block that would allow a better solubilization of the final block copolymer above the CP of the first block. It is known that some monomers tend to produce more deactivated macro-CTAs in a RAFT copolymerization than the others. Although this phenomenon is not fully understood, we have earlier shown that macro-CTAs of *N*-monosubstituted acrylamides such as nPA and iPA mostly remain active, more than those of the disubstituted acrylamides.[20,21]

The results of the block copolymerization are summarized in Table 2, and the SEC chromatograms of the macro-CTA and the resulting block copolymer are shown in Figure 4, indicating

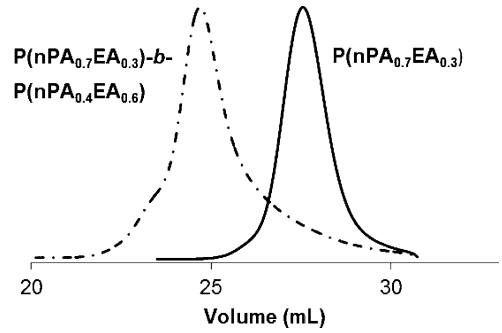

Figure 4. SEC chromatograms of P(nPA$_{0.7}$EA$_{0.3}$) (macro-CTA) and P(nPA$_{0.7}$EA$_{0.3}$)-*b*-P(nPA$_{0.4}$EA$_{0.6}$) (diblock copolymer).

the livingness of block copolymerization. The conversion of the second block was 66%, and the molar mass of the block random copolymer was well in accordance with the theoretical value calculated by eq 1. The polydispersity increased upon block copolymerization, indicating some loss of control over the RAFT polymerization process, commonly observed for macro-CTAs and associated with a small quantity of inactive species in the reaction.[38] The monomer composition of the P(nPA$_{0.4}$EA$_{0.6}$) block in Table 2 was calculated from the ^{1}H NMR spectra of macro-CTA and diblock copolymer (Figure S4). On the basis of the molar masses given by SEC and the monomer compositions, the block ratio of the P(nPA$_{0.7}$EA$_{0.3}$)-*b*-P(nPA$_{0.4}$EA$_{0.6}$) diblock copolymer is 1:2.4.

Solution Properties of Copolymers and Block Random Copolymer. To demonstrate the phase transitions of the individual blocks of P(nPA$_{0.7}$EA$_{0.3}$)-*b*-P(nPA$_{0.4}$EA$_{0.6}$) diblock random copolymer, the transmittance curves of aqueous solutions of P(nPA$_{0.7}$EA$_{0.3}$) and P(nPA$_{0.4}$EA$_{0.6}$) at a concentration of 1.0 mg/mL upon heating are shown in Figure 5A, indicating CPs of 37 and 52 °C, respectively. The molar masses of the random copolymers were 13 200 and 19 800 g/mol, respectively (Table 1).

Figure 5B shows two clear shifts in the transmittance of P(nPA$_{0.7}$EA$_{0.3}$)-*b*-P(nPA$_{0.4}$EA$_{0.6}$) solution with increasing temperature. When observed at 350 nm, the transmittance starts to decrease abruptly at 40 °C as the more hydrophobic P(nPA$_{0.7}$EA$_{0.3}$) block becomes insoluble upon heating, the middle point of the first transition being at 41.5 °C. When the temperature continues to rise, the second increase in the turbidity starts at 46 °C with a middle point of the transition at 53 °C, corresponding to the CP of P(nPA$_{0.4}$EA$_{0.6}$). The broadening of the phase transition temperatures may be influenced by the mutual and opposite effect of the two individual blocks: The more hydrophilic block drags the CP of the neighboring block to a higher temperature while the more hydrophobic one drags the other block to a lower CP. Fast continuous heating without equilibration led to lower apparent transition temperatures (Figure S5), as it may not allow enough

dx.doi.org/10.1021/ma2027269 | *Macromolecules* 2012, 45, 2001−2006

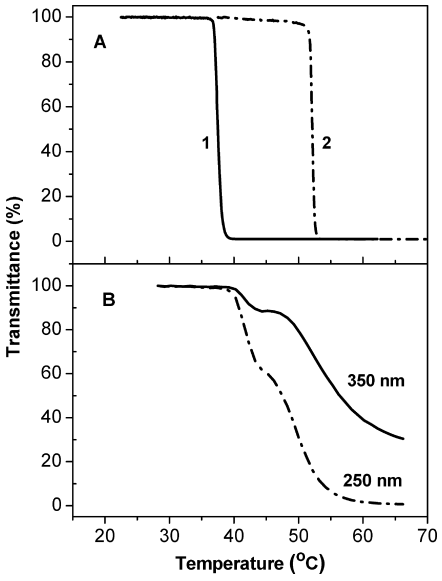

Figure 5. Temperature-dependent transmittance of 1.0 mg/mL aqueous solutions of (A) $P(nPA_{0.7}EA_{0.3})$ and $P(nPA_{0.4}EA_{0.6})$, observed at a wavelength of 350 nm and (B) $P(nPA_{0.7}EA_{0.3})$-*b*-$P(nPA_{0.4}EA_{0.6})$ at two wavelengths, 350 and 250 nm. The samples were heated by 1 °C intervals followed by an equilibration for 20 min.

time for the reorganization of individual blocks during the aggregation. The temperature-dependent transmittance of the diblock random copolymer depends on the detection wavelength (Figure S5). It is known that the scattering depends strongly on the wavelength of the light ($\sim\lambda^{-4}$).[39] This explains the higher transmittance at 350 nm than at 250 nm since the light of a shorter wavelength is more scattered than that of a longer wavelength. In addition, only the particles larger than the wavelength of light are visible at a certain observation wavelength. Therefore, at longer observation wavelengths, fewer particles are visible, leading to a lower apparent turbidity.[22]

The temperature dependence of apparent mean hydrodynamic diameter (D_h) of $P(nPA_{0.7}EA_{0.3})$-*b*-$P(nPA_{0.4}EA_{0.6})$ in a 2.0 mg/mL solution is demonstrated in Figure 6, and the

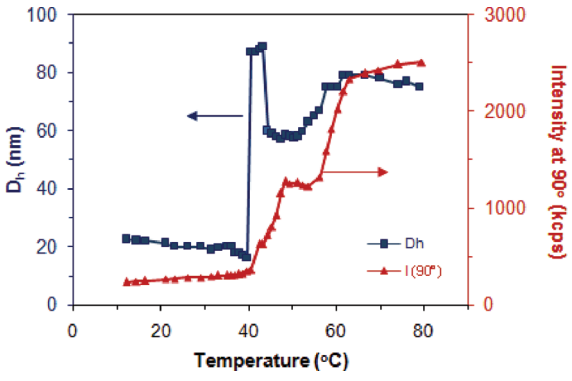

Figure 6. Temperature dependence of mean hydrodynamic diameter (D_h) and scattering intensity obtained by dynamic light scattering at 90° angle for a 2.0 mg/mL aqueous solution of $P(nPA_{0.7}EA_{0.3})$-*b*-$P(nPA_{0.4}EA_{0.6})$.

proposed mechanism for the aggregation process is shown in Scheme 2. At low temperatures, the solution consists of small micelles ($D_h \leq 22$ nm) possibly together with molecularly

Scheme 2. Schematic Illustration of the Aggregation Behavior of $P(nPA_{0.7}EA_{0.3})$-*b*-$P(nPA_{0.4}EA_{0.6})$ in Water upon Heating: (a) Molecularly Soluble Polymers and Small Micelles below 40 °C; (b) Dehydration of the $P(nPA_{0.7}EA_{0.3})$ Core at 40 °C; (c) Collapsed Aggregates at 44−53 °C; (d) Clusters above 53 °C

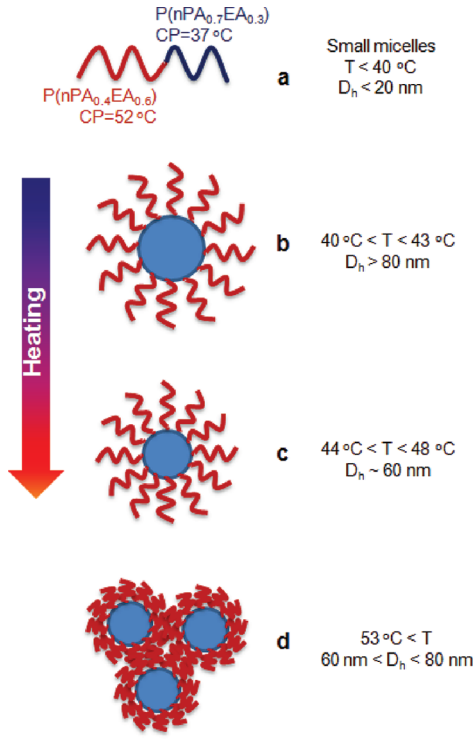

dissolved polymers, which compress upon heating prior to reaching the onset of the first CP. Such shrinking has been commonly observed for thermoresponsive polymers due to a coil-to-globule transition.[40−42] The micellization itself may stem from the hydrophobic $C_{12}H_{25}$ CTA end group of the block copolymer. The micelles start to aggregate when the temperature reaches the onset of the CP transition of the more hydrophobic $P(nPA_{0.7}EA_{0.3})$ block at 40 °C, and the mean diameter suddenly increases as the size distribution becomes bimodal due to the emergence of larger aggregates ($D_h \sim 88$ nm), similar to the observations by Laschewsky and co-workers on triblock copolymers.[43] Further heating results in a collapse of the core at 44−48 °C upon the dehydration of the hydrophobic block, after which the aggregated species remain stable. We have earlier described similar aggregation behavior with an initial increase in D_h followed by a collapse for a poly(*N*-*n*-propylacrylamide) homopolymer as well as for its diblock and triblock copolymers.[22] At 53 °C, the more hydrophilic $P(nPA_{0.4}EA_{0.6})$ block reaches its CP and becomes more hydrophobic, leading to its contraction in water and further clustering of the micelles. Scattering intensity increases gradually during the aggregation/collapse and clustering processes, with a plateau in between. At 63 °C, the size distribution is monomodal and the mean hydrodynamic diameter of clusters is 79 nm, followed by a small contraction due to further dehydration of the outer block upon heating.

■ CONCLUSIONS

RAFT polymerization has been successfully used to make random copolymers of *N*-alkyl-substituted acrylamides with

dx.doi.org/10.1021/ma2027269 | *Macromolecules* 2012, 45, 2001−2006

narrow molecular weight distributions. The kinetic study shows the controlled character of the RAFT copolymerization of the two monomers in the family of *N*-alkylacrylamides at conversions below 70%. The CP of the copolymers can be varied over a temperature range of 20−85 °C by adjusting the comonomer ratio, allowing the design of block copolymers of two random copolymers with different phase transition temperatures. The stepwise aggregation of the block copolymer at different temperatures has been clearly shown. While rising the temperature above the CP of the first block leads to clustering and subsequent collapse of the core of the aggregates, heating above the CP of the second block induces further clustering and contraction of the shell through the dehydration of outer block. Further studies by dynamic and static light scattering together with microscopic methods may help to better understand the aggregation process. These block random copolymers expand the scope of thermoresponsive polymers and give promise to novel materials with tailored stimuli-responsive properties.

■ ASSOCIATED CONTENT

Ⓢ Supporting Information

^{1}H NMR spectra of a reaction mixture and of a purified random copolymer, SEC traces of copolymers at different polymerization times, ^{1}H NMR spectra for the mono- and diblock copolymers, and UV−vis transmittance of the aqueous solution of the polymers at different wavelengths. This material is available free of charge via the Internet at http://pubs.acs.org.

■ AUTHOR INFORMATION

Notes

The authors declare no competing financial interest.

■ ACKNOWLEDGMENTS

Financial support from NSERC of Canada, the FQRNT of Quebec, and the Canada Research Chair program is gratefully acknowledged. The authors are members of CSACS funded by FQRNT and GRSTB funded by FRSQ. M.T.S. thanks the Department of Chemistry of Université de Montréal for the Camille Sandorfy Scholarship. The authors thank Prof. F. Winnik and Dr. X. Qiu for their help with the temperature-dependent DLS measurements.

■ REFERENCES

(1) Li, C.; Madsen, J.; Armes, S. P.; Lewis, A. L. *Angew. Chem., Int. Ed.* **2006**, *45*, 3510−3513.
(2) Pasparakis, G.; Alexander, C. *Angew. Chem., Int. Ed.* **2008**, *47*, 4847−4850.
(3) Stuart, M. A. C.; Huck, W. T. S.; Genzer, J.; Muller, M.; Ober, C.; Stamm, M.; Sukhorukov, G. B.; Szleifer, I.; Tsukruk, V. V.; Urban, M.; Winnik, F.; Zauscher, S.; Luzinov, I.; Minko, S. *Nature Mater.* **2010**, *9*, 101−113.
(4) Jochum, F. D.; Roth, P. J.; Kessler, D.; Theato, P. *Biomacromolecules* **2010**, *11*, 2432−2439.
(5) Aseyev, V.; Tenhu, H.; Winnik, F. In *Self Organized Nanostructures of Amphiphilic Block Copolymers II*; Müller, A. H. E., Borisov, O., Eds.; Springer: Berlin, 2011; Vol. *242*, pp 29−89.
(6) Liu, R.; Fraylich, M.; Saunders, B. *Colloid Polym. Sci.* **2009**, *287*, 627.
(7) Bütün, V.; Liu, S.; Weaver, J. V. M.; Bories-Azeau, X.; Cai, Y.; Armes, S. P. *React. Funct. Polym.* **2006**, *66*, 157−165.
(8) Principi, T.; Goh, C. C. E.; Liu, R. C. W.; Winnik, F. M. *Macromolecules* **2000**, *33*, 2958−2966.
(9) Soga, O.; van Nostrum, C. F.; Hennink, W. E. *Biomacromolecules* **2004**, *5*, 818−821.
(10) Sugihara, S.; Kanaoka, S.; Aoshima, S. *Macromolecules* **2004**, *37*, 1711−1719.
(11) Zhu, X. X.; Avoce, D.; Liu, H. Y.; Benrebouh, A. *Macromol. Symp.* **2004**, *207*, 187−191.
(12) Liu, H. Y.; Zhu, X. X. *Polymer* **1999**, *40*, 6985−6990.
(13) Avoce, D.; Liu, H. Y.; Zhu, X. X. *Polymer* **2003**, *44*, 1081−1087.
(14) Weiss, J.; Böttcher, C.; Laschewsky, A. *Soft Matter* **2011**, *7*, 483.
(15) Lee, H.-N.; Bai, Z.; Newell, N.; Lodge, T. P. *Macromolecules* **2010**, *43*, 9522−9528.
(16) Romão, R. I. S.; Beija, M.; Charreyre, M.-T. r. s.; Farinha, J. P. S.; Gonçalves da Silva, A. l. M. P. S.; Martinho, J. M. G. *Langmuir* **2009**, *26*, 1807−1815.
(17) Maki, Y.; Mori, H.; Endo, T. *Macromol. Chem. Phys.* **2010**, *211*, 45−56.
(18) Mertoglu, M.; Garnier, S.; Laschewsky, A.; Skrabania, K.; Storsberg, J. *Polymer* **2005**, *46*, 7726−7740.
(19) Dimitrov, I.; Trzebicka, B.; Müller, A. H. E.; Dworak, A.; Tsvetanov, C. B. *Prog. Polym. Sci.* **2007**, *32*, 1275−1343.
(20) Cao, Y.; Zhu, X. X.; Luo, J.; Liu, H. *Macromolecules* **2007**, *40*, 6481−6488.
(21) Cao, Y.; Zhu, X. X. *Can. J. Chem.* **2007**, *85*, 407−411.
(22) Cao, Y.; Zhao, N.; Wu, K.; Zhu, X. X. *Langmuir* **2009**, *25*, 1699−704.
(23) Xie, D.; Ye, X.; Ding, Y.; Zhang, G.; Zhao, N.; Wu, K.; Cao, Y.; Zhu, X. X. *Macromolecules* **2009**, *42*, 2715−2720.
(24) Braunecker, W. A.; Matyjaszewski, K. *Prog. Polym. Sci.* **2007**, *32*, 93−146.
(25) Smith, A. E.; Xu, X.; McCormick, C. L. *Prog. Polym. Sci.* **2010**, *35*, 45−93.
(26) Shea, K. J.; Stoddard, G. J.; Shavelle, D. M.; Wakui, F.; Choate, R. M. *Macromolecules* **1990**, *23*, 4497−4507.
(27) Lai, J. T.; Filla, D.; Shea, R. *Macromolecules* **2002**, *35*, 6754−6756.
(28) Idziak, I.; Avoce, D.; Lessard, D.; Gravel, D.; Zhu, X. X. *Macromolecules* **1999**, *32*, 1260−1263.
(29) Boutris, C.; Chatzi, E. G.; Kiparissides, C. *Polymer* **1997**, *38*, 2567−2570.
(30) de Lambert, B.; Charreyre, M.-T.; Chaix, C.; Pichot, C. *Polymer* **2005**, *46*, 623−637.
(31) Schilli, C. M.; Zhang, M.; Rizzardo, E.; Thang, S. H.; Chong, Y. K.; Edwards, K.; Karlsson, G.; Müller, A. H. E. *Macromolecules* **2004**, *37*, 7861−7866.
(32) Convertine, A. J.; Lokitz, B. S.; Lowe, A. B.; Scales, C. W.; Myrick, L. J.; McCormick, C. L. *Macromol. Rapid Commun.* **2005**, *26*, 791−795.
(33) Favier, A.; Charreyre, M.-T.; Chaumont, P.; Pichot, C. *Macromolecules* **2002**, *35*, 8271−8280.
(34) Lowe, A. B.; McCormick, C. L. *Prog. Polym. Sci.* **2007**, *32*, 283−351.
(35) Sumerlin, B. S.; Donovan, M. S.; Mitsukami, Y.; Lowe, A. B.; McCormick, C. L. *Macromolecules* **2001**, *34*, 6561−6564.
(36) Perrier, S.; Barner-Kowollik, C.; Quinn, J. F.; Vana, P.; Davis, T. P. *Macromolecules* **2002**, *35*, 8300−8306.
(37) Yusa, S.-i.; Shimada, Y.; Mitsukami, Y.; Yamamoto, T.; Morishima, Y. *Macromolecules* **2004**, *37*, 7507−7513.
(38) Stenzel, M. H. In *Handbook of RAFT Polymerization*; Barner-Kowollik, C., Ed.; Wiley-VCH Verlag GmbH: Weinheim, 2008; pp 315−372.
(39) Kerker, M. In *The Scattering of Light, and Other Electromagnetic Radiation*; Academic Press: New York, 1969; p 339.
(40) Lessard, D. G.; Ousalem, M.; Zhu, X. X.; Eisenberg, A.; Carreau, P. J. *J. Polym. Sci., Part B: Polym. Phys.* **2003**, *41*, 1627−1637.
(41) Wu, C.; Wang, X. *Phys. Rev. Lett.* **1998**, *80*, 4092−4094.
(42) Wang, X.; Qiu, X.; Wu, C. *Macromolecules* **1998**, *31*, 2972−2976.
(43) Weiss, J.; Laschewsky, A. *Langmuir* **2011**, *27*, 4465−4473.

Macromolecules

Article

pubs.acs.org/Macromolecules

PEG-L-PAF and PEG-D-PAF: Comparative Study on Thermogellation and Biodegradation

Eun Young Kang, Bora Yeon, Hyo Jung Moon, and Byeongmoon Jeong*

Department of Bioinspired Science (WCU), Department of Chemistry and Nano Science, Ewha Womans University, 52, Ewhayeodae-gil, Seodaemun-gu, Seoul, 120-750, Korea

Supporting Information

ABSTRACT: L-Polypeptides and D-polypeptides can be prepared from natural L-amino acids and non-natural D-amino acids, respectively. In this study, poly(ethylene glycol)−poly(L-alanine-*co*-L-phenyl alanine) (PEG-L-PAF) and poly(ethylene glycol)−poly(D-alanine-*co*-D-phenyl alanine) (PEG-D-PAF) with similar molecular weight and composition, but different stereochemistry were investigated, focusing on thermogelling behavior and biodegradation. The sol-to-gel transition temperature of both PEG-L-PAF and PEG-D-PAF aqueous solutions decreased from 26 to 7 °C as the concentration increased from 4.0 wt % to 9.0 wt %. Dynamic light scattering, transmission electron microscopy, circular dichroism spectra, and ^{13}C NMR spectra suggested that the sol-to-gel transition involved changes in molecular assemblies resulting from dehydration of PEG for both PEG-L-PAF and PEG-D-PAF. In particular, the significant differences between PEG-L-PAF and PEG-D-PAF were observed for histocompatibility as well as in vitro/in vivo degradation. Only PEG-L-PAF was significantly degraded by cathepsin B and elastase, as well as under in vivo conditions. The histocompatibility assayed by the H&E staining method showed that formation of the collagen capsule around the PEG-D-PAF gel was thicker than the PEG-L-PAF gel, indicating that acute inflammation was milder with PEG-L-PAF gel than with PEG-D-PAF gel. Current study emphasizes the significance of stereochemistry in biomaterial development.

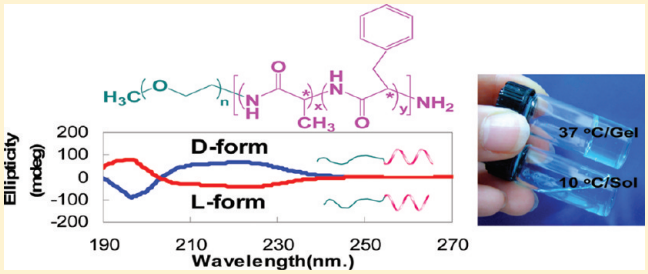

INTRODUCTION

Polypeptides have recently been drawing attention for uses as specific building blocks, drug delivery carriers, and tissue engineering scaffolds, due to the fact that they can be used to produce specific secondary structures or nanostructures by modulating their amino acid composition and sequences.[1−5] Amino acids, except for glycine, have a chiral center, which can be a natural L-form or a non-natural D-form. The application of polypeptides as biopharmaceutical intermediates or vaccines is based on the chemical or enzymatic conversions among this stereospecific species.[6−8] From a biomaterial point of view, a polypeptide can be degraded by proteolytic enzymes and the degradation of the polypeptide can be controlled by varying the stereospecificity of the constituent amino acids.[9−11]

Aqueous solutions of thermogelling polymer undergo sol-to-gel transition as the temperature increases. They are low-viscous aqueous solutions at low temperatures and become a semisolid gel at high temperatures, typically at the body temperature of warm-blooded mammal (37 °C). The phase transition polymeric systems have been extensively investigated as minimally invasive drug delivery depots, injectable tissue engineering scaffolds, and biomaterials that prevent postsurgical adhesion, due to the simple procedures required for encapsulating pharmaceutical agents or cells, followed by facile implantation of the depot at a target site.[12−17] In this case, the duration of the in situ formed gel is a very important parameter for practical applications. Ideally, the duration should be matched to the biomedical function of the system. Therefore, a gel should be eliminated after releasing all the encapsulated drug from the drug delivery system, and the tissue growth rate should be matched to the gel elimination rate for a tissue engineering scaffold.[18]

In this study, we synthesized thermogelling poly(ethylene glycol)−poly(alanine-*co*-phenyl alanine) (PEG−PAF) block copolymers of PEG-L-PAF and PEG-D-PAF with a similar molecular weight, but different chiralities. Alanine−phenyl alanine and alanine−alanine sequences are degraded by proteolytic enzymes in the subcutaneous layer of mammals such as cathepsin B, cathepsin C, elastase, and metalloproteinase-2 (MMP-2).[10,19,20] Therefore, the PAF was chosen as a degradable polypeptide block. As the sequence and other chemical factors affect thermogelling behavior, biodegradability, and biocompatibility,[21−23] we herein examine the effect of chirality of a thermogel consisting of PEG and PAF.

The PEG-L-PAF and PEG-D-PAF consist of naturally occurring L-amino acids and non-natural D-amino acids, respectively. The physicochemical properties, in vitro/in vivo

Received: December 29, 2011
Revised: February 10, 2012
Published: February 16, 2012

degradation profiles, and tissue compatibility of the PEG-L-PAF and PEG-D-PAF were compared.

EXPERIMENTAL SECTION

Materials. α-Amino-ω-methoxy-poly(ethylene glycol) (PEG) (M.W ~ 2000 Da) (ID Bio, Korea), N-carboxy anhydrides of L-alanine, *N*-carboxy anhydrides of D-alanine, *N*-carboxy anhydrides of L-phenyl alanine, and *N*-carboxy anhydrides of D-phenyl alanine (KPX Life Science, Korea) were stored at 4 °C in a desiccator filled with drying agents under high vacuum and used as needed. Toluene (Aldrich, USA) was dried over sodium before use. Chloroform (Aldrich, USA) and *N,N*-dimethylformamide (anhydrous) (Aldrich, USA) were treated with anhydrous magnesium sulfate before use.

Synthesis of PEG−PAF. PEG-L-PAF was prepared by ring-opening polymerization of the *N*-carboxy anhydrides of L-alanine and N-carboxy anhydrides of L-phenyl alanine in the presence of α-amino-ω-methoxy-poly(ethylene glycol).[10,24,25] PEG-D-PAF was similarly prepared by using *N*-carboxy anhydrides of D-alanine and *N*-carboxy anhydrides of D-phenyl alanine in the presence of α-amino-ω-methoxy-poly(ethylene glycol).

^{1}H and ^{13}C NMR Spectroscopy. ^{1}H NMR spectra of the PEG−PAF (in CF_3COOD) (500 MHz NMR spectrometer; Varian, USA) were used to determine the composition of the polymer. ^{13}C NMR spectral changes of the PEG−PAF (5.0 wt % in D_2O) were investigated as a function of temperature. The solution temperature was equilibrated for 20 min at each temperature.

Phase Diagram. The sol−gel transition of the polymer aqueous solution was investigated by the test tube inverting method. The aqueous polymer solution (1.0 mL) was added into a vial with an inner diameter of 11 mm. The transition temperature was determined by the flow (sol)−nonflow (gel) criterion with a temperature increment of 1 °C per step. Each data point is an average of 3 measurements.

Dynamic Mechanical Analysis. Changes in modulus of the polymer aqueous solutions were investigated by dynamic rheometry (Thermo Haake, Rheometer RS 1). The aqueous polymer solution was placed between parallel plates of 25 mm diameter with a gap of 0.5 mm. To minimize water evaporation during the experiment, the plates were enclosed in a water saturated chamber. The data were collected under conditions of controlled stress (4.0 dyn/cm^2) and a frequency of 1.0 rad/s. The heating rate was 0.5 °C/min.

Transmission Electron Microscopy (TEM). The PEG−PAF aqueous solution (10 μL; 0.01 wt %) at 10 °C was placed on the carbon grid and the excess solution was blotted with filter paper. The grids were dried at room temperature for 24 h. The microscopy image was obtained by JEM-2100F (JEOL) with an accelerating voltage of 200 kV.

Dynamic Light Scattering. The apparent size of PEG−PAF aggregates in water (1.0 wt %) was studied by a dynamic light scattering instrument (ALV 5000−60 × 0) as a function of temperature. The aqueous solution was equilibrated for 20 min at each temperature. A YAG DPSS-200 laser (Langen, Germany) operating at 532 nm was used as a light source. The results of dynamic light scattering were analyzed by the regularized CONTIN method. The decay rate distributions were transformed to an apparent diffusion coefficient. From the diffusion coefficient, the apparent hydrodynamic size of a polymer aggregate could be obtained by the Stokes−Einstein equation.

Circular Dichroism (CD) Spectroscopy. A CD spectrophotometer (J-810, JASCO) was used to study the ellipticity of the PEG−PAF aqueous solution as a function of polymer concentration at a fixed temperature of 20 °C in a polymer concentration range of 0.01−1.0 wt %. In addition, ellipticity of the PEG−PAF aqueous solution was obtained as a function of temperature at a fixed concentration of 0.01 wt % in a range of 10−50 °C at increments of 10 °C per step. The aqueous solution was equilibrated for 20 min at each temperature.

In Vitro Degradation. The in vitro degradation of PEG−PAF was studied over a 3 day period in phosphate buffered saline (150 mM) at pH = 7.4 for the control and chymotrypsin; in phosphate buffered saline (150 mM) with 1.0 mM $CaCl_2$ at pH = 7.4 for collagenase and elastase; in phosphate buffered saline (150 mM) with 0.02 wt % Triton X-100, 0.1 mM ethylene diamine tetraacetic acid, and 5 mM glutathione at pH = 5.5 for cathepsin B; and in Tris buffered solution (0.05 M) with 10 mM $CaCl_2$ at pH = 7.4 for MMP-2. The polymer concentration was fixed at 1.0 wt %. Five units of each enzyme were used for the in vitro study except for MMP-2, where a concentration of 2.5 μg/mL was used because information concerning the number of enzyme (MMP-2) units was not available. The recovered samples were extracted with *N,N*-dimethylformamide for molecular weight analysis by gel permeation chromatography.

In Vivo Degradation. Aqueous polymer solutions (0.5 mL; 5.0 wt % of PEG−PAF) contained in prefilled syringes were injected into the subcutaneous layer of rats using a 25 gauge syringe needle. Rats were sacrificed 1 day, 5 days, and 15 days after injection for the gel duration study. The remaining gel was removed from the rats and stored at −20 °C.

Histology. The histology around the implant site was investigated for 5 days after implantation. Neutral buffered formalin (NBF) solution was prepared by mixing formaldehyde solution (37−40%; 100 mL), sodium phosphate monobasic (4.0 g), sodium phosphate dibasic (6.5 g), and deionized water (900 mL). The tissue surrounding the gel was stored in NBF solution at −20 °C. After 24 h, the tissue was embedded in a frozen section compound (Leica, USA) and stored at −80 °C. Microcryotomed sections of tissue with a thickness of ~8 μm were stained with hematoxylin and eosin (H&E), and examined by microscopy (Olympus lX71-F22PM, Japan).

Animal Procedures. All experimental procedures using animals were conducted in accordance with the NIH Guide for the Care and Use of Laboratory Animals and were approved by the Committee of Ewha Womans University.

RESULTS AND DISCUSSION

The *N*-carboxy anhydrides of alanine and the *N*-carboxy anhydrides of phenyl alanine were copolymerized on the amine-terminated PEG to prepare the PEG−PAF.[10,19,20] The molecular weight of PEG−PAF was calculated by ^{1}H NMR spectra (CF_3COOD) (Figure 1). The end group of alanine

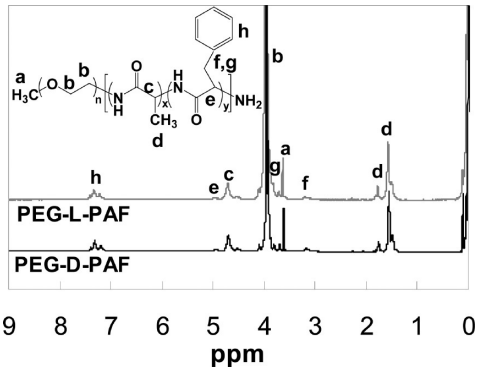

Figure 1. ^{1}H NMR spectra (CF_3COOD) of PEG-L-PAF and PEG-D-PAF.

(methyl) (1.7−1.9 ppm) was distinguished from internal alanine (methyl) (1.2−1.7 ppm) of the PEG−PAF in the ^{1}H NMR spectra. The integration of the peaks in ^{1}H NMR spectra at 1.2−1.9 ppm ($-CH_3$ of alanine), 3.8−4.1 ppm ($-CH_2CH_2O-$ of PEG), and 7.0−7.5 ppm (phenyl group of phenylalanine) was used to calculate the composition and the molecular weight of the PEG−PAF by the following equations.

$$CH_3O(CH_2CH_2O)_nCH_2CH_2\{[NHCOCH(CH_3)]_x [NHCOCH(CH_2C_5H_5)]_y\} - NH_2D^+$$

dx.doi.org/10.1021/ma202809c | *Macromolecules* 2012, 45, 2007−2013

n = 44 for PEG with a molecular weight of 2000 Da.

$$A_{1.2-1.9}/A_{3.8-4.1} = 3x/180$$

$$A_{7.0-7.5}/A_{3.8-4.1} = 5y/180$$

$A_{1.2-1.9}$, $A_{3.8-4.1}$, and $A_{7.0-7.5}$ are the areas of the peaks at 1.2−1.9 ppm, 3.8−4.1 ppm, and 7.0−7.5 ppm in the ^{1}H NMR of PEG−PAF. The number 180 is the number of protons related to PEG appearing at $A_{3.8-4.1}$. On the basis of the assignments, the structures of PEG-L-PAF and PEG-D-PAF were calculated to be EG_{44}-L-$A_{12}F_4$ and EG_{44}-D-$A_{13}F_4$, respectively. The molecular weight distribution determined by GPC was 1.1−1.2. The unimodal distribution of the polymer molecular weight in GPC shows that the PEG−PAF was well prepared (Supporting Information, Figure S1).

PEG−PAF aqueous solutions underwent sol-to-gel transition as the temperature increased. The phase diagram of the PEG−PAF aqueous solution was determined by the test tube inverting method (Figure 2a). A sol-to-gel transition of the polymer aqueous solutions was observed in a concentration range of 4.0−9.0 wt %. As the polymer concentration increased, the sol-to-gel transition temperature decreased from 26 to 7 °C. The small differences in the transition temperatures might result from the small differences in the polymer composition, sequence, or molecular weight distribution. Aqueous solutions of both PEG-L-PAF and PEG-D-PAF were not sufficiently rigid to stop the mass flow at concentrations <4.0 wt %; also the polymer aqueous solutions existed as a gel phase and sol−gel transition was not observed above 9.0 wt % in a temperature range of 0−60 °C. The sol-to-gel transition of the PEG−PAF aqueous solutions (5.0 wt %) accompanied large increases in the storage modulus (G') and the loss modulus (G''). At the same time, the crossing of G' over G'' was observed during the sol-to-gel transition (Figure 2b).[26,27] G' and G'' are the measures of an elastic component and a viscous component of a complex modulus (G^*). Therefore, the elastic component dominates the viscous component above the sol-to-gel transition temperature. The aqueous solution (5.0 wt %) of PEG with a molecular weight of 2000 Da that did not show a significant change in G′ or G″ were also compared. The G′ was smaller than G″ over the temperature range studied, suggesting that the PEG aqueous solution maintained its sol state (Figure 2b).

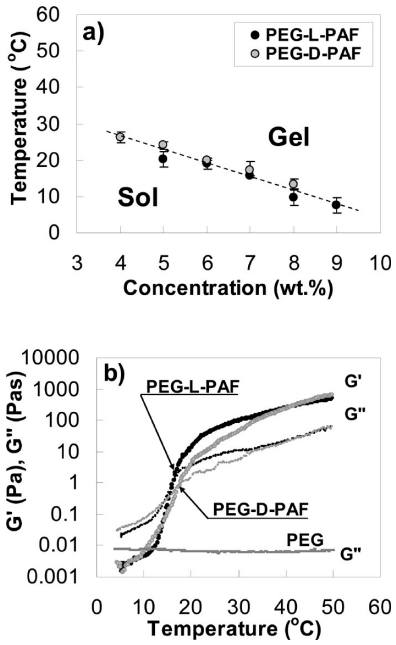

Figure 2. (a) Phase diagram of PEG−PAF aqueous solutions determined by the test tube inverting method (n = 3). (b) Modulus of the PEG−PAF aqueous solutions (5.0 wt %) as a function of temperature. G'' of α-amino-ω-methoxy−poly(ethylene glycol) (PEG) aqueous solution (5.0 wt %) is compared as a control. G' of the PEG aqueous solution was <0.001 Pa (data not shown).

PEG−PAF consists of the hydrophilic PEG block and the hydrophobic PAF block, therefore, the polymers self-assembled into micelles in water. The apparent sizes of the self-assemblies of PEG−PAF were measured by dynamic light scattering at a 1.0 wt % concentration. Particles with a size of 10−60 nm were observed at 10 °C, and random molecular aggregation led to formation of large particles (100−800 nm) with a broad size distribution as the temperature increased to 30 °C (Figure 3a and 3b). The molecular aggregation suggests that the intermolecular attraction between particles increases as the temperature increases, similar to the previous thermogelling polyesters, polycarbonates, polyphosphazenes, and polypeptides.[12−17,28−30] Supporting the dynamic light scattering results, spherical micelles with 20−100 nm in diameter were also observed by TEM, where the polymer aqueous solution at 10 °C was coated on the grid and dried at room temperature (Figure 3c).

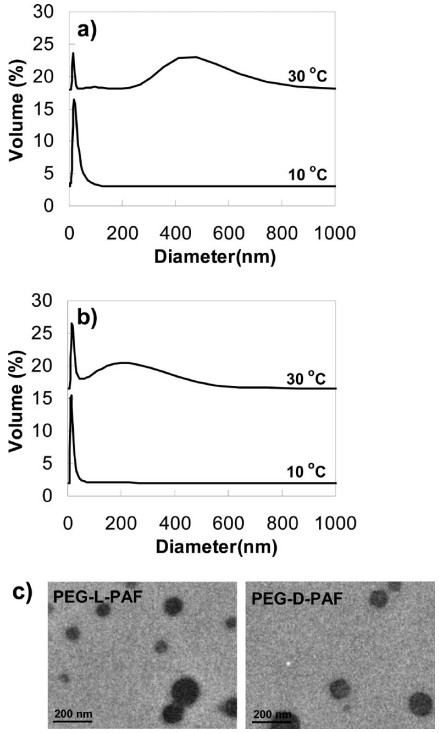

Figure 3. Apparent size of PEG-L-PAF (a) and PEG-D-PAF (b) as a function of temperature studied by dynamic light scattering of their aqueous solutions (1.0 wt %). (c) TEM images of PEG-L-PAF and PEG-D-PAF developed from their aqueous solutions (0.01 wt %).

As a chiroptical method, circular dichroism spectroscopy clearly distinguished the PEG-L-PAF and PEG-D-PAF. PEG-L-PAF showed a positive band centered at 196 nm and a negative band centered at 210 and 220 nm, suggesting a typical α-helix-structure for the polypeptide (Figure 4). On the other hand,

dx.doi.org/10.1021/ma202809c | Macromolecules 2012, 45, 2007−2013

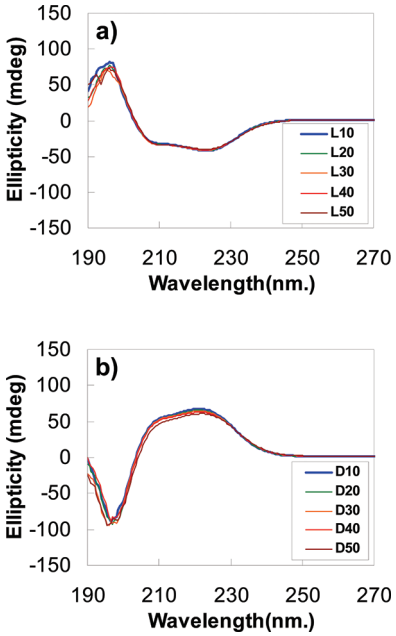

Figure 4. CD spectra of PEG-L-PAF and PEG-D-PAF aqueous solution (0.01 wt %) as a function of temperature. The legends of L*N* and D*N* indicate PEG-L-PAF at *N* °C and PEG-D-PAF at *N* °C, respectively.

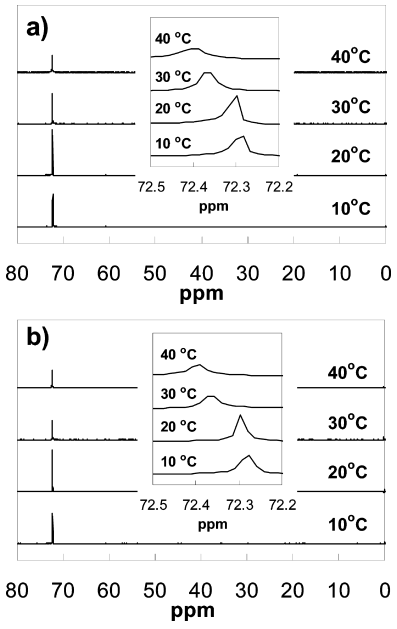

Figure 5. ^{13}C NMR spectra of PEG-L-PAF (a) and PEG-D-PAF (b) aqueous solution (5.0 wt % in D_2O) as a function of temperature.

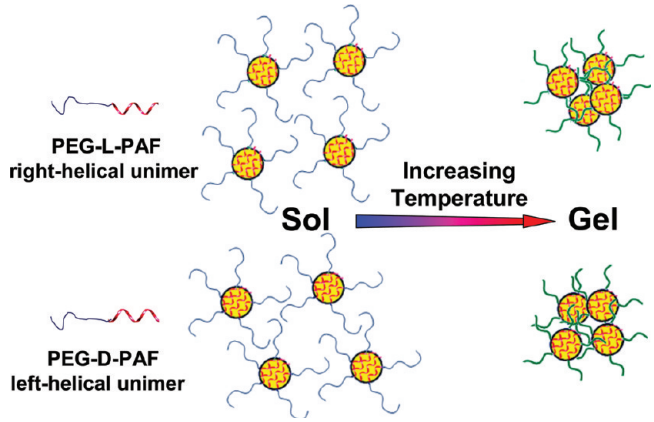

Figure 6. Schematic presentation of the sol-to-gel transition of the PEG-L-PAF (top) and PEG-D-PAF (bottom) aqueous solutions. Note the right and the left handed helixes for PEG-L-PAF and PEG-D-PAF, respectively.

the CD spectra of PEG-D-PAF showed a mirror image of PEG-L-PAF. The amphiphilic PEG−PAF molecules (PEG-L-PAF and PEG-D-PAF) assembled in water and lost their secondary structure information in the CD spectra at higher concentrations and gave a single negative band at 228 nm (Supporting Information, Figure S2).[24,31,32] Therefore, the CD spectra of PEG-L-PAF and PEG-D-PAF aqueous solutions were compared at 0.01 wt % in a temperature range of 10−50 °C in order to investigate the change in secondary structure as a function of temperature (Figure 4). Typical α-helical CD spectra with one minimum at 196 nm and 2 minima at 210 and 220 nm were maintained in a temperature range of 10−50 °C for PEG-L-PAF. CD spectra of PEG-D-PAF with an opposite sign of PEG-L-PAF also maintained their overall shapes in the same temperature range. The stability of the secondary structure of PEG−PAF is in contrast with the thermogelling of polyalanine-poloxamer-polyalanine, which showed a large increase in β-sheet conformation as the temperature increased.[33]

^{13}C NMR spectra of aqueous solutions (5.0 wt %) of both PEG-L-PAF and PEG-D-PAF showed a broadened and downfield shifted PEG peak from 72.3 to 72.4 ppm as the temperature increased from 10 to 40 °C (Figure 5). The sol-to-gel transition of the PEG−PAF aqueous solution significantly decreased the molecular motion of PEG, resulting in the broadening and collapsing of the PEG peaks in the ^{13}C NMR spectra.[12−17,28−30] The PAF did not appear in the ^{13}C NMR spectra in D_2O due to the core−shell structures of PEG−PAF in water, where the hydrophilic flexible PEG blocks form a shell and the hydrophobic PAF blocks is shielded as a core.

On the basis of the DLS study, TEM images, CD spectra and ^{13}C NMR spectra of PEG-L-PAF and PEG-D-PAF aqueous solutions, the sol-to-gel transition mechanism of the polymer aqueous solutions was suggested in Figure 6. Polypeptides of PEG-L-PAF and PEG-D-PAF form a right helix and left helix in water, respectively. The hydrophilic PEG dehydrated as the temperature increases as presented in thin blue lines at low temperature and thick green lines at high temperature in the figure. The hydrophobic PAF is presented as pink helices in the figure. Because of the amphiphilic nature of hydrophilic PEG and hydrophobic PAF, the polymer self-assembled into micelles in water with a size of tens nanometers at low temperatures, which aggregates into hundreds nanometers as the temperature increases. The sol-to-gel transition involves such a changes in molecular assemblies resulting from the dehydration of PEG conjugated to rigid hydrophobic PAF while preserving the secondary structure of PAF.

Differences between L-polypeptide and D-polypeptide regarding susceptibility to enzymatic degradation are well-known.[34] Even the incorporation of a few D-amino acids in a L-polypeptide increases its stability against proteolytic enzymes.[35,36] This point is very important for practical application of the polymer for drug delivery and tissue engineering because the degradation profile affects the rate of drug release or cell growth.

dx.doi.org/10.1021/ma202809c | *Macromolecules* 2012, 45, 2007−2013

The GPC profiles of the polymers were investigated after incubation of each polymer for 72 h in an aqueous solution (1.0 wt %) containing each enzyme (5 units) (Figure 7). The PEG-L-PAF was degraded by cathepsin B, and elastase, whereas PEG-D-PAF was quite stable against all the proteases studied in this research including cathepsin B, elastase, collagenase, chymotrypsin, and MMP-2.[9−11,37,38] Both PEG-L-PAF and PEG-D-PAF were stable in PBS. The previous thermogelling poly(L-alanine-*co*-L-leucine) was rather stable against cathepsin B, but was degraded by MMP.[39]

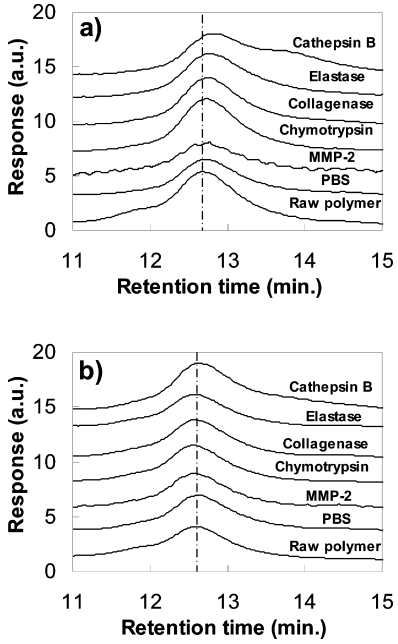

Figure 7. GPC profile of PEG-L-PAF (a) and PEG-D-PAF (b) after in vitro enzymatic degradation.

A transparent hydrogel was formed upon the subcutaneous injection of the PEG−PAF aqueous polymer solution (5.0 wt %; 0.5 mL/rat) by the temperature-sensitive sol-to-gel transition. Photos of remaining gels at the injection site were taken 1 day, 5 days, and 15 days after the injection (Figure 8). The PEG-L-PAF gel was decreased in size in 5 days and almost cleared in 15 days. The fibrous capsule around a gel, surface erosion, and biodegradation of a gel can induce a decrease in the apparent size of the implanted gel in the subcutaneous layer of rats. The tight gel of remaining PEG-D-PAF in 15 days was distinguished from the small loose gel of PEG-L-PAF in 15 days, suggesting the preferential biodegradation of the PEG-L-PAF. Degradation rate of a chitosan/β-glycerol phosphate thermogel increased as the ratio of chitosan to β-glycerol phosphate decreased.[40] The duration of polyester thermogels were controlled by composition and topology of the polymer.[16,22] Current paper emphasized the significance of stereochemistry in controlling the gel duration.

The GPC profile of the remaining gel after 15 days of implantation in the subcutaneous layer of rats also showed that the retention time increased from 12.7 min (raw PEG-L-PAF) to 14 min (in vivo implanted PEG-L-PAF), indicating the biodegradation of PEG-L-PAF in vivo (Figure S3, Supporting Information).

Histocompatibility around the in situ formed gels of PEG-L-PAF and PEG-D-PAF was also compared by the H&E staining method 5 days after injection of the polymer aqueous solutions into the subcutaneous layer. Collagen capsules (dense circles) were observed around the gel for both systems, however, the collagen capsule was thicker for PEG-D-PAF than PEG-L-PAF, indicating milder tissue irritation for PEG-L-PAF than PEG-D-PAF (Figure 9). Typical foreign body reactions around an implanted thermogel begin with acute inflammatory responses by macrophages, lymphocytes, and neutrophils, followed by fibrous tissue formation and infiltration of vascular microstructure.[22,41−43] It takes one to several weeks for the remodelling process by the regular tissue, depending on the polymer structure or duration of the gel. The relative short duration of PEG-L-PAF is contrast with the PEG-D-PAF, polyesters, and poly(ester urethane)s thermogels with >1 month of gel duration.[44−46]

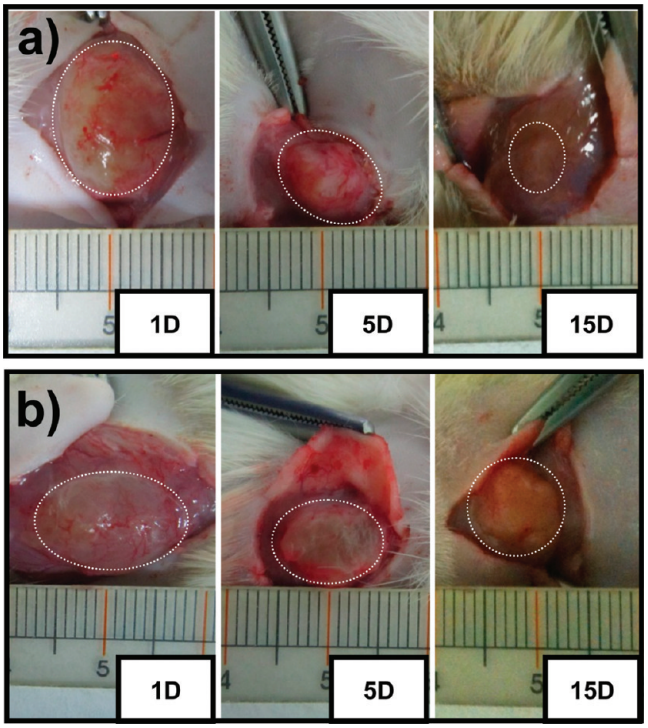

Figure 8. Gel duration of PEG-L-PAF (a) and PEG-D-PAF (b) after subcutaneous injection of the PEG−PAF aqueous solution (5.0 wt %; 0.5 mL/rat) into rats. The photos were taken 1 day, 5 days, and 15 days after the subcutaneous injection. Dotted-lines indicate the boundaries of the gel.

CONCLUSIONS

PEG-L-PAF and PEG-D-PAF block copolymers with similar molecular weights, but, different stereochemistry were compared for their solution behavior and biodegradation. Both polymers were similar in their phase diagrams of sol-to-gel transition and temperature-sensitive changes in their self-assemblies. However, their chirooptical properties as shown by circular dichroism spectra were opposite in sign. In particular, PEG-L-PAF and PEG-D-PAF showed significant differences in degradation in enzyme solution (in vitro) and duration of a gel in the subcutaneous layer of rats (in vivo). And, the formation of the collagen capsule around the PEG-D-PAF gel was thicker than the PEG-L-PAF gel, indicating that acute inflammation was milder for the PEG-L-PAF gel than the PEG-D-PAF gel.

dx.doi.org/10.1021/ma202809c | *Macromolecules* 2012, 45, 2007−2013

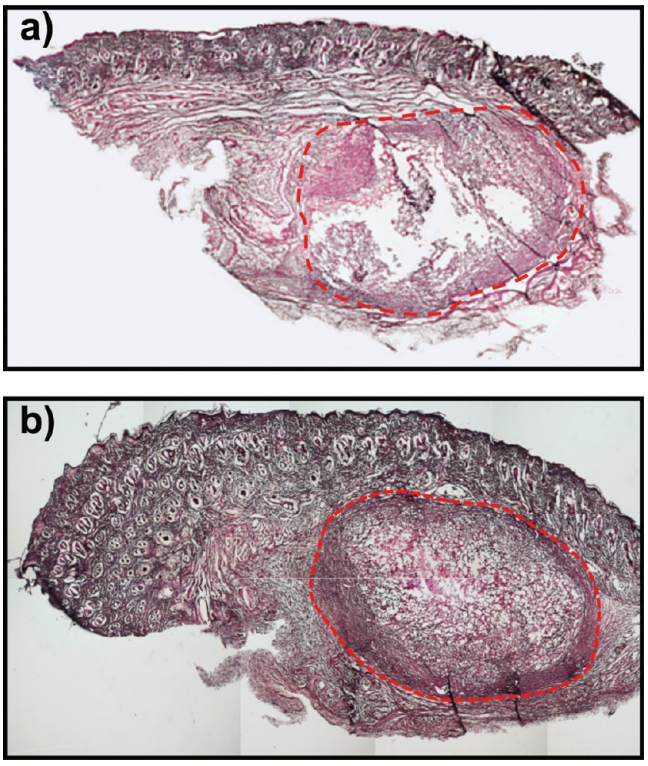

Figure 9. H&E staining images of PEG-L-PAF (a) and PEG-D-PAF (b) 5 days after subcutaneous injection of the PEG−PAF aqueous solution (5.0 wt %; 0.5 mL/rat) into rats. The gel is marked as dot-lines.

The current study suggests that stereochemistry of a thermogelling polypeptide plays a critical role in biocompatibility as well as biodegradability.

■ ASSOCIATED CONTENT

Ⓢ Supporting Information

GPC chromatograms of PEG-L-PAF and PEG-D-PAF, CD spectra of PEG-L-PAF and PEG-D-PAF aqueous solution as a function of concentration, and GPC profile of PEG−PAF 15 days after implantation in the subcutaneous layer of rats. This material is available free of charge via the Internet at http://pubs.acs.org.

■ AUTHOR INFORMATION

Corresponding Author

*Email: bjeong@ewha.ac.kr.

Notes

The authors declare no competing financial interest.

■ ACKNOWLEDGMENTS

This work was supported by National Research Foundation of Korea (NRF) grants funded by the Korea government (MEST) (Grant Nos. 2011-0000376, 2011-0001340, and R31-2008-000-10010-0)

■ REFERENCES

(1) Wright, E. R.; Conticello, V. P. *Adv. Drug Delivery Rev.* **2002**, *54*, 1057−1073.
(2) Kopecek, J. *Eur. J. Pharm. Sci.* **2003**, *20*, 1−16.
(3) Morihara, Y.; Ogata, S. I.; Kamitakahara, M.; Ohtsuki, C.; Tanihara, M. *J. Polym. Sci., Polym. Chem.* **2005**, *43*, 6048−6056.
(4) Lutolf, M. P.; Lauer-Fields, J. L.; Schmoekel, H. G.; Metters, A. T.; Weber, F. E.; Fields, G. B.; Hubbell, J. A. *Proc. Natl. Acad. Sci. U.S.A.* **2003**, *100*, 5413−5418.
(5) Lee, K. Y.; Mooney, D. *Chem. Rev.* **2001**, *101*, 1869−1879.
(6) Park, H.; Kim, K. M.; Lee, A.; Ham, S.; Nam, W.; Chin, J. *J. Am. Chem. Soc.* **2007**, *129*, 1518−1519.
(7) Wang, W.; Gan, H.; Sun, T.; Su, B.; Fuchs, H.; Vestweber, D.; Butz, S. *Soft Matter* **2010**, *6*, 3851−3855.
(8) Durani, S. *Acc. Chem. Res.* **2008**, *41*, 1301−1308.
(9) Garripelli, V. K.; Kim, J. K.; Son, S.; Kim, W. J.; Jo, S. *Acta Biomater.* **2011**, *7*, 1984−1992.
(10) Jeong, Y.; Joo, M. K.; Bahk, K. H.; Choi, Y. Y.; Kim, H. T.; Kim, W. K.; Sohn, Y. S.; Jeong, B. *J. Controlled Release* **2009**, *137*, 25−30.
(11) Kopecek, J.; Kopeckova, P. *Adv. Drug Delivery Rev.* **2010**, *62*, 122−149.
(12) Yu, L.; Ding, J. *Chem. Soc. Rev.* **2008**, *37*, 1473−1481.
(13) Loh, X. J.; Li, J. *Expert Opin. Ther. Patents* **2007**, *17*, 965−977.
(14) Huynh, D. P.; Im, G. J.; Chae, S. Y.; Lee, K. C.; Lee, D. S. *J. Controlled Release* **2009**, *137*, 20−24.
(15) Joo, M. K.; Park, M. H.; Choi, B. G.; Jeong, B. *J. Mater. Chem.* **2009**, *19*, 5891−5905.
(16) Park, M. H.; Joo, M. K.; Choi, B. G.; Jeong, B. *Acc. Chem. Res.* **2011**, *10*, DOI: 1021/ar200162j.
(17) Zhang, Z.; Ni, J.; Chen, L.; Yu, L.; Xu, J.; Ding, J. *Biomaterials* **2011**, *32*, 4725−4736.
(18) Cha, C.; Kohman, R. E.; Kong, H. *Adv. Funct. Mater.* **2009**, *19*, 3056−3062.
(19) Soyez, H.; Schacht, E.; Vanderkerken, S. *Adv. Drug Delivery Rev.* **1996**, *21*, 81−106.
(20) Braga, P. C.; Sasso, M. D.; Culici, M.; Bianchi, T.; Bordoni, L.; Marabini, L. *Pharmacology* **2006**, *77*, 130−136.
(21) Yu, L.; Zhang, Z.; Ding, J. *Biomacromolecules* **2011**, *12*, 1290−1297.
(22) Yu, L.; Zhang, Z.; Zhang, H.; Ding, J. *Biomacromolecules* **2010**, *11*, 2169−2178.
(23) Park, S. H.; Choi, B. G.; Moon, H. J.; Cho, S. H.; Jeong, B. *Soft Matter* **2011**, *7*, 6515−6521.
(24) Choi, Y. Y.; Joo, M. K.; Sohn, Y. S.; Jeong, B. *Soft Matter* **2008**, *4*, 2383−2387.
(25) Cai, X. J.; Dong, H. Q.; Xia, W. J.; Wen, H. Y.; Li, W. Q.; Yu, J. H.; Li, Y. Y.; Shi, D. L. *J. Mater. Chem.* **2011**, *21*, 14639−14645.
(26) Hu, J.; Ge, Z.; Zhou, Y.; Zhang, Y.; Liu, S. *Macromolecules* **2010**, *43*, 5184−5187.
(27) Borisova, O.; Billon, L.; Zaremski, M.; Grassl, B.; Bakaeva, Z.; Lapp, A.; Stepanek, P.; Borisov, O. *Soft Matter* **2011**, *7*, 10824−10833.
(28) Hwang, M. J.; Suh, J. M.; Bae, Y. H.; Kim, S. W.; Jeong, B. *Biomacromolecules* **2005**, *6*, 885−890.
(29) Lee, B. H.; Lee, Y. M.; Sohn, Y. S.; Song, S. C. *Macromolecules* **2002**, *35*, 3876−3879.
(30) Kim, S. Y.; Kim, H. J.; Lee, K. E.; Han., S. S.; Sohn, Y. S.; Jeong, B. *Macromolecules* **2007**, *40*, 5519−5525.
(31) Wang, J.; Gibson, M. I.; Barbey, R.; Xiao, S. J.; Klok, H. A. *Macromol. Rapid Commun.* **2009**, *30*, 845−850.
(32) Lim, Y.; Moon, K. S.; Lee, M. *Angew. Chem., Int. Ed.* **2009**, *121*, 1629−1633.
(33) Oh, H. J.; Joo, M. K.; Sohn, Y. S.; Jeong, B. *Macromolecules* **2008**, *41*, 8204−8209.
(34) Wade, D.; Moman, A.; Wahlin, B.; Drain, C. M.; Andreu, D.; Boman, H. G.; Merrifield, R. B. *Proc. Natl. Acad. Sci. USA.* **1990**, *87*, 4761−4765.
(35) Tugyi, R.; Uray, K.; Ivan, D.; Fellinger, E.; Perkins, A.; Hudecz, F. *Proc. Natl. Acad. Sci. U.S.A.* **2005**, *102*, 413−418.
(36) Sela, M.; Zisman, E. *FASEB J.* **1997**, *11*, 449−456.
(37) Brubaker, C. E..; Messersmith, P. B. *Biomacromolecules* **2011**, No. in press, DOI: dx.doi.org/10.1021/bm201261d.
(38) Kim, S.; Healy, K. E. *Biomacromolecules* **2003**, *4*, 1214−1223.
(39) Moon, H. J.; Choi, B. G.; Park, M. H.; Joo, M. K.; Jeong, B. *Biomacromolecules* **2011**, *12*, 1234−1242.

(40) Dang, Q. F.; Yan, J. Q.; Li, J. J.; Cheng, X. J.; Liu, C. S.; Chen, X. G. *Carbohyd. Polym.* **2011**, *83*, 171−178.
(41) Sun, B.; Ma, W.; Su, F.; Wang, Y.; Liu, J.; Wang, D.; Liu, H. *J. Mater. Sci.: Mater. Med.* **2011**, *22*, 2111−2118.
(42) Fredriksson, C.; Hedhammar, M.; Feinstein, R.; Nordling, K.; Kratz, G.; Johansson, J.; Huss, F.; Rising, A. *Materials* **2008**, *2*, 1908−1922.
(43) Zhou, H.; Zhang, Y. P.; Zhang, W. F.; Chen, X. G. *Carbohydr. Polym.* **2011**, *83*, 1643−1651.
(44) Park, D.; Wu, W.; Wang, Y. *Biomaterials* **2011**, *32*, 777−786.
(45) Huynh, C. T.; Kang, S. W.; Li, Y.; Kim, B. S.; Lee, D. S. *Soft Matter* **2011**, *7*, 8984−8990.
(46) Kang, Y. M.; Lee, S. H.; Lee, J. Y.; Son, J. S.; Kim, B. S.; Lee, B.; Chun, H. J.; Min, B. H.; Kim, J. H.; Kim, M. S. *Biomaterials* **2010**, *31*, 2453−2460.

Macromolecules

Article

pubs.acs.org/Macromolecules

Bithiophenesilane-Based Dendronized Polymers: Facile Synthesis and Properties of Novel Highly Branched Organosilicon Macromolecular Structures

S. A. Ponomarenko,[†,*] N. N. Rasulova,[†] Y. N. Luponosov,[†] N. M. Surin,[†] M. I. Buzin,[‡] I. Leshchiner,[§] S. M. Peregudova,[‡] and A. M. Muzafarov[†]

[†]Enikolopov Institute of Synthetic Polymeric Materials, Russian Academy of Sciences, 70 Profsoyuznaya St., Moscow, 117393, Russia

[‡]Nesmeyanov Institute of Organoelement Compounds, Russian Academy of Sciences, 28 Vavilova St., Moscow, 119991, Russia

[§]Department of Chemistry, Moscow State University, Leninskie gory, Moscow, 119992 Russia

Supporting Information

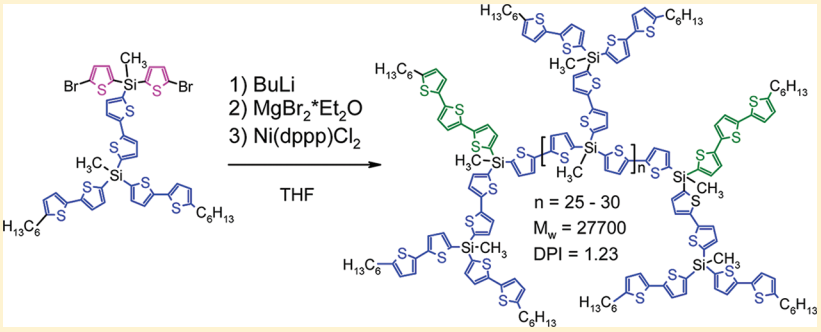

ABSTRACT: The synthesis of two novel bithiophenesilane-based dendronized polymers by a chain growth Kumada polymerization, their molecular properties in dilute solutions and thermal properties in the bulk are described and compared with those of bithiophenesilane dendrimers. GPC equipped with a dual light scattering detector has shown that the polymers exhibit narrow polydispersity indices (PDI = 1.22−1.23) and have a weight-average polymerization degree of 44 for **P1** and 30 for **P2**, which correspond to 88 and 120 bithiophenesilane fragments, respectively. Spectral-luminescent investigations showed that both polymers among with the bithiophenesilanes contain from 1 to 4 terthiophenesilane fragments in every macromolecule, which leads to the so-called "dendritic molecular antenna" effect. The intramolecular energy transfer efficiency was measured to be 50 and 70% for polymers **P1** and **P2** respectively, which, alongside with the results of viscometric studies, points out to the compact conformation of these macromolecules in solution, which is close to those of bithiophenesilane dendrimers.

INTRODUCTION

Macromolecules consisting of oligothiophenesilane repeating units are of significant interest to researchers from the point of view of their applications as functional materials in organic electronics and photonics.[1,2] Exhibiting good luminescent[3,4] and semiconducting properties,[5,6] they can be used as precursors in the preparation of conducting polymers,[7] as functional materials for emitting layer in polymer light emitting diodes[8] or as perspective donor materials for organic photovoltaic cells (solar cells).[9−11] Among them, bithiophenesilane systems exhibit a good fluorescence quantum yield Q_F, which is significantly higher than that of the bithiophene luminophore itself[12] and depends on the degree of branching of the molecule.[13] It was also shown that similar star-like molecules show Q_F significantly higher than that of the corresponding linear polymer, poly[(tetraethyldisilanylene)-bithiophene].[14] Recently, a family of bithiophenesilane dendrimers (**Gn(2−2)** in Scheme 1) with efficient photoluminescence in the violet-blue spectrum range was reported.[15−17] In the case of organosilicon dendritic molecules, consisting of bi- and terthiophenesilane fragments (**D1(3−2)** and **B1(3−2)** in Scheme 1), the "molecular antenna" effect was observed.[18] It was shown that this effect results from the existence of the efficient inductive-resonant transfer of the energy of electronic excitation from bithiophenesilane (donor) to terthiophenesilane (acceptor) fragments of the macromolecule.[19] A similar effect was observed also in some other bithiophenesilane-containing dendrimers.[20,21] Such properties of oligothiophenesilane systems are related, on the one hand, to the presence of $\sigma-\pi$ conjugation between an oligothiophene fragment and a silicon atom directly linked to it, and to the absence of conjugation between the neighboring oligothiophene fragments, separated by the silicon atom, on the other hand. It makes them different from fully conjugated hyper-

Received: October 29, 2011
Revised: January 30, 2012
Published: February 10, 2012

   dx.doi.org/10.1021/ma2024045 | *Macromolecules* 2012, 45, 2014−2024

Scheme 1. Structural Formulas of Bithiophenesilane-Containing Dendrimers.[17,18]

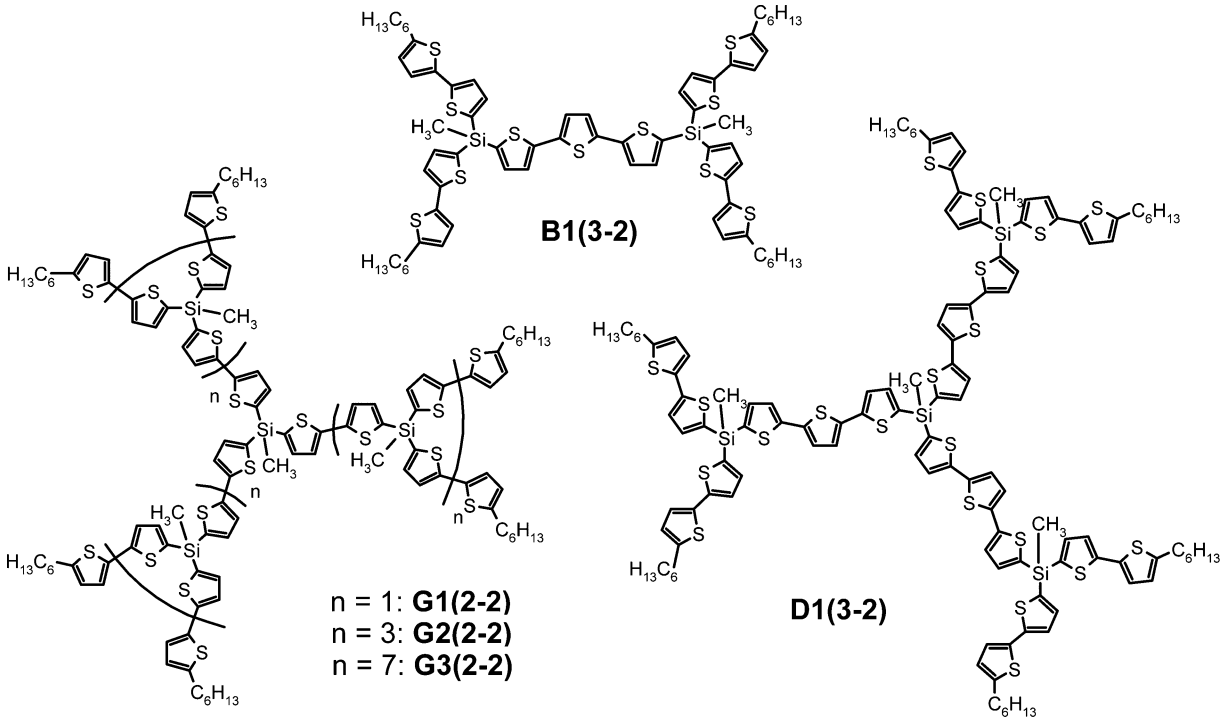

Scheme 2. General Structural Formulas of Bithiophenesilane-Containing Dendronized Polymers P1 and P2

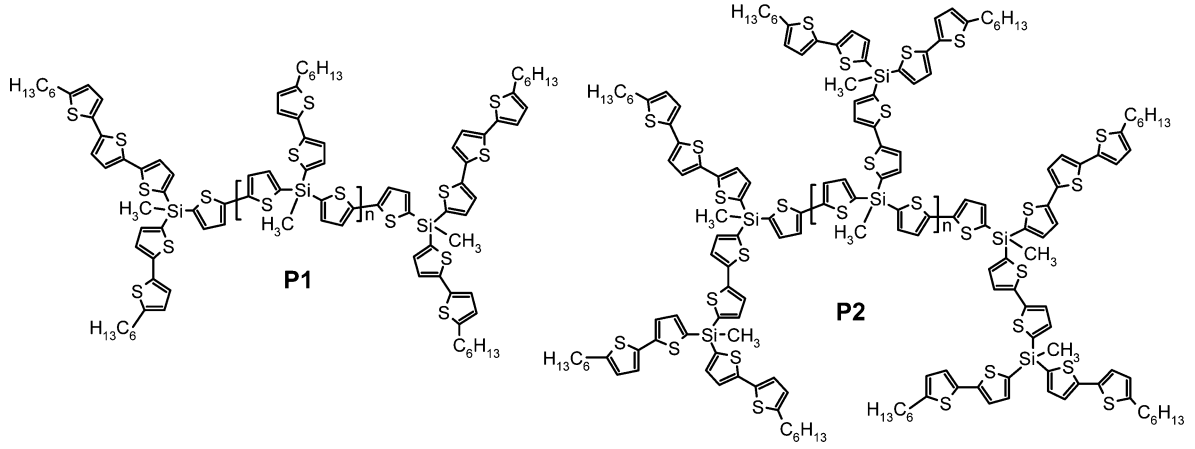

branched 2,3,5-polythiophenes[22] and polythiophene dendrimers[23,24] consisting of 2-, 3-, and 5-linked thiophene rings. The latter have a wide absorption spectrum in the vis spectrum range, which allows to use them as donor materials in organic solar cell.[25]

Dendronized polymers feature hybrid structures of both classical polymeric systems and dendrimers.[26,27] They are promising for applications in various areas, such as biological[28] and medical[29] sciences, catalysis in polymer chemistry[30] and others. An increased interest to such 3D macromolecules based on conjugated structures is governed by the perspectives of their utilization in optoelectronics, where they could serve as efficient light emitting materials.[31] However, most of the dendronized polymers reported before have a conjugated backbone and isolating dendritic wedges.[32−35] In this sense, the synthesis of dendronized polymers containing oligothiophene fragments linked to each other via silicon atoms both in the backbone and in the wedges (Scheme 2) looks intriguing. That is why the purpose of the present work was the elaboration of an efficient scheme of the synthesis of such systems and studying the influence of their specific molecular structure on the physical properties in comparison to bithiophenesilane-containing dendrimers obtained before.[17,18]

EXPERIMENTAL PART

Materials. *n*-Butyl lithium (1.6 M solution in hexane), 1,2-dibromoethane, magnesium, 1,3-bis(diphenylphosphino)-propanenickel(II) chloride Ni(dppp)Cl_2 (Acros Organics), were used as received without additional purification. THF, diethyl ether, toluene, and hexane were dried and purified according to the known techniques and then used as solvents. 5-hexyl-2,2′-bithiophene was prepared according to the technique described earlier.[36] The first generation of bithiophenesilane monodendron 2,2′-bithiophen-5-yl-[bis(5′-hexyl-2,2-bithiophen-5-yl)]methylsilane (**6**) was synthesized according the method described before.[17] The solvents were evaporated in vacuum under a pressure of up to 1 Torr at 40 °C.

dx.doi.org/10.1021/ma2024045 | *Macromolecules* 2012, 45, 2014−2024

GPC analysis was performed by means of a Shimadzu LC10A^{VP} series chromatograph (Japan) equipped with an RID-10A^{VP} refractometer and SPD-M10A^{VP} diode matrix as detectors and a Phenomenex column (USA) with a size of 7.8 × 300 mm^2 filled with the Phenogel sorbent with a pour size of 500 Å; THF was used as the eluent.

Light scattering experiments were performed on Shimadzu HPLC System, equipped with DGU14U degasser unit, LC-10AD pump, CTO-10A column oven with a Phenomenex column (USA) with a size of 7.8 × 300 mm^2 filled with the Phenogel sorbent with a pour size of 10^3 Å, RID-10A refractometer, Viscotek 270 Dual detector (RALS and LALS) and Omnisec 4.5 Software. The sample loop was 100 μL, angle RALS 90°, angle LALS 7°. The system was calibrated using polystyrene standard with M_w = 10050, dn/dc = 0.185 (Polymer Laboratories). The molar weight of the standard was chosen in the range of M_w of the samples under investigation for better accuracy of the measurements. Using the exact concentrations of the samples, close to 5.00 mg/mL, the values of dn/dc were determined from RI data, which were found to be 0.24 for both polymer samples investigated. Then this value was used by Omnisec 4.5 software to calculate the real M_w from the light scattering (RALS and LALS) data.

For thin layer chromatography, "Sorbfil" (Russia) plates were used. In the case of column chromatography, silica gel 60 ("Meck") was taken.

^{1}H NMR spectra were recorded at a "Bruker WP-250 SY" spectrometer, working at a frequency of 250.13 MHz and utilising the DMSO-d_6 signal (2.45 ppm) as the internal standard. ^{13}C and ^{29}Si NMR spectra were recorded using a "Bruker Avance II 300" spectrometer at 75 and 60 MHz, respectively. In the case of ^{1}H NMR spectroscopy, the compounds to be analyzed were taken in the form of 1% solutions in CCl_4-DMSO-d_6 mixture. In the case of ^{13}C and ^{29}Si NMR spectroscopy, the compounds to be analyzed were taken in the form of 5% solutions in $CDCl_3$. The spectra were then processed on the computer using the ACD Laboratories software.

Mass-spectrometry measurements were performed on the Micromass M@ldi MALDI−TOF MS instrument operating in the reflection mode. To prepare the samples separate solutions of the starting material and matrix in THF with concentrations of 1 mg/mL and a solution of salt (silver triflate) in deionized water at a concentration of 1 mg/mL were mixed and applied to a steel target (at ∼2 uL) to dry, volume ratio of 1:1:1. 2,5-dihydrobenzoic acid, 2-(4-hydroxyphenylazo)benzoic acid, and 3-indolacrilic acid where used as the matrix substance. The standard laser operating frequency was 10 Hz. Standard spectra were regularly obtained by combining approximately 100 single laser shot spectra.

Elemental analysis of C, H elements was carried out using CHN automatic analyzer CE1106 (Italy). Experimental error is 0.30−0.50%. Analysis of Br element was carried by visual titration technique using $Hg(NO_3)_2$ and diphenylcarbazone as indicator. The burning was done in the Sheninger flask using alkaline solution of hydrogen peroxide as an absorbent. Experimental error is 0.30−0.50%. Spectrophotometry technique was used for the Si analysis as described in ref 37.

The absorption and luminescence spectra were recorded over a range of 250−600 nm in dilute solutions in THF (UV-grade) with a concentration of 10^{-5}−10^{-6} M in order to avoid self-absorption. The luminescence measurements were performed on an ALS01 M multifunctional absorption-luminescence spectrometer, the detailed description of which can be found elsewhere.[13] The absorption spectra were recorded on a Shimadzu UV-2501PC spectrophotometer (Japan). Unless stated otherwise, all reactions were carried out under argon atmosphere using water-free solvents. The intrinsic viscosity of solutions was measured in THF at 25.0 ± 0.1 °C on an Ubbelohde viscometer with a capillary diameter of 0.3 mm using Schott AVS 370 System having a laser automatic level detection.

For the DSC measurements, the glass transition temperatures were obtained at a heating rate of 10 °C in argon atmosphere in a Mettler DSC-822e differential scanning calorimeter. TGA was performed on the "Derivatograth-C" (MOM, Hungary) in air and argon at a heating rate of 5 °C/min on samples of about 10 mg by weight.

Synthesis. *(5-Bromothiene-2-yl)lithium (**2**).* A solution of 3.09 g (12.8 mmol) 2,5-dibromothiophene (**1**) in 20 mL THF was cooled down to −78 °C, after which 8.0 mL (12.8 mol) of a solution of 1.6 M *n*-butyllithium in hexane was added slowly dropwise to it followed by stirring during 1 h at that temperature. The obtained solution of compound **2** was used immediately in the following stage of synthesis without isolation or purification of the product.

*(5-Bromothien-2-yl)magnesium Bromide (**3**).* 4.7 mL (8 mmol) of a solution of 1.6 M *n*-butyllithium in hexane was added slowly dropwise to a solution of 1.81 g (8 mmol) of 2,5-dibromothiophene in 50 mL of THF previously cooled down to −78 °C. The reaction mixture was then stirred for 1 h at that temperature. After that 0.01 mol of an ether complex of magnesium bromide (prepared *in situ* by the Grignard reaction from 1,2-dibromoethane and magnesium in ether) was added and the reaction mixture was stirred for additional 2 h. The obtained solution of compound **3** was used in the following stage of synthesis without isolation or purification of the product.

*Dichloro(5′-hexyl-2,2′-bithiophene-5-yl)methylsilane (**5**).* A solution of 1.6 g (6.4 mmol) of 5-hexyl-2,2′-bithiophene (**4**) in 45 mL of THF was cooled down to −78 °C followed by the slow dropwise addition to it of 4.0 mL (6.4 mmol) of a solution of 1.6 M *n*-butyllithium in hexane. The reaction mixture was stirred for 1 h at −78 °C. In a separate flask a solution of 11.2 mL (96 mmol) of methyltrichlorosilane in 15 mL of THF was cooled down to −78 °C, after which the previously obtained lithium derivative of compound **4** was added to it slowly dropwise. When the whole amount of it was added, the cooling bath was removed and the temperature of the reaction mixture was allowed to rise to 20 °C. An excess of methyltrichlorosilane was then distilled with toluene, and the solution of freshly synthesized compound **5** in toluene was used in the following stage of synthesis without isolation or purification of the product.

*Bis(5-bromo-2-thienyl)(5′-hexyl-2,2′-bithiophen-5-yl)-methylsilane (**M1**).* A solution of freshly prepared compound **5** in toluene was added dropwise to a freshly prepared solution of compound **2** (from 3.09 g (12.8 mmol) of 2,5-dibromothiophene and 8.0 mL (12.8 mmol) of solution of 1.6 M *n*-butyllithium and 20 mL of THF) in a THF−hexane mixture at −78 °C. After the completion of the reaction the reacting mixture was poured into 100 mL of water and 300 mL of diethyl ether. The organic layer was then separated, rinsed with water to pH = 7, dried over anhydrous Na_2SO_4, which was followed by evaporation of the solvent in a vacuum rotary evaporator. The reaction yield of the raw product was found to be 77% (according to GPC). It was purified by column chromatography on silica gel using a mixture of hexane−toluene (v/v 5:1) as the eluent, to yield 2.06 g (52%) of the pure compound **M1** as a light-yellow viscous liquid. ^{1}H NMR (DMSO-d_6/CCl_4): 0.88 (t, 3H, CH_3−CH_2−, J = 6.7 Hz), 0.89 (s, 3H, CH_3−Si), 1.25−1.40 (overlapping peaks, 6H, −CH_2−CH_2−CH_2− and CH_3−CH_2−CH_2−), 1.63 (m, 2H, −CH_2−CH_2−T, J = 7.3 Hz), 2.77 (t, 2H, −CH_2−T, J = 7.3 Hz), 6.70 (d, 1H, J = 3.7 Hz), 7.04 (d, 1H, J = 3.7 Hz), 7.20 (d, 2H, J = 3.7 Hz), 7.22−7.26 (overlapping peaks, 3H), 7.28 (d, 1H, J = 3.7 Hz). ^{13}C NMR (75 MHz, $CDCl_3$, δ, ppm): −0.47, 14.07, 22.55, 28.71, 30.15, 31.51, 31.54, 119.38, 124.15, 124.38, 124.88, 131.56, 134.02, 137.28, 137.54, 138.07, 145.61, 146.23. ^{29}Si NMR (60 MHz, $CDCl_3$, δ, ppm): −25.78. MALDI MS m/z 724.26 (M + Ag)$^+$, calculated 724.79. Anal. Calcd for $C_{23}H_{24}Br_2S_4Si$: C 44.80; H, 3.92; Br, 25.92; S, 20.80; Si, 4.55. Found: C, 44.97; H, 3.95; Br, 25.83; S, 20.75; Si, 4.50.

*{5′-[bis-(5′-hexyl-2,2′-bithiophene-5-yl)(methyl)silyl]-2,2′-bithiophene-5-yl}(dichloro)methylsilane (**7**).* First, 2.3 g (3.3 mmol) of 2,2′-bithiophen-5-yl-[bis(5′-hexyl-2,2-bithiophen-5-yl)]methylsilane (**6**) in 65 mL of THF was cooled down to −78 °C followed by the slow addition to it of 2.0 mL (3.3 mmol) of a solution of *n*-butyllithium in hexane, after which the reaction mixture was stirred during 1 h at −78 °C. In a separate flask, a solution of 6.5 mL (82 mmol) of methyltrichlorosilane in 20 mL of THF was cooled down to −78 °C, after which the previously obtained lithium-derivative of compound **6** was added to it slowly dropwise. When the full amount was added, the cooling bath was removed and the temperature slowly rose to 20 °C,

dx.doi.org/10.1021/ma2024045 | *Macromolecules* 2012, 45, 2014−2024

Scheme 3. Synthesis of Monomers M1 and M2 and Their Polymerization

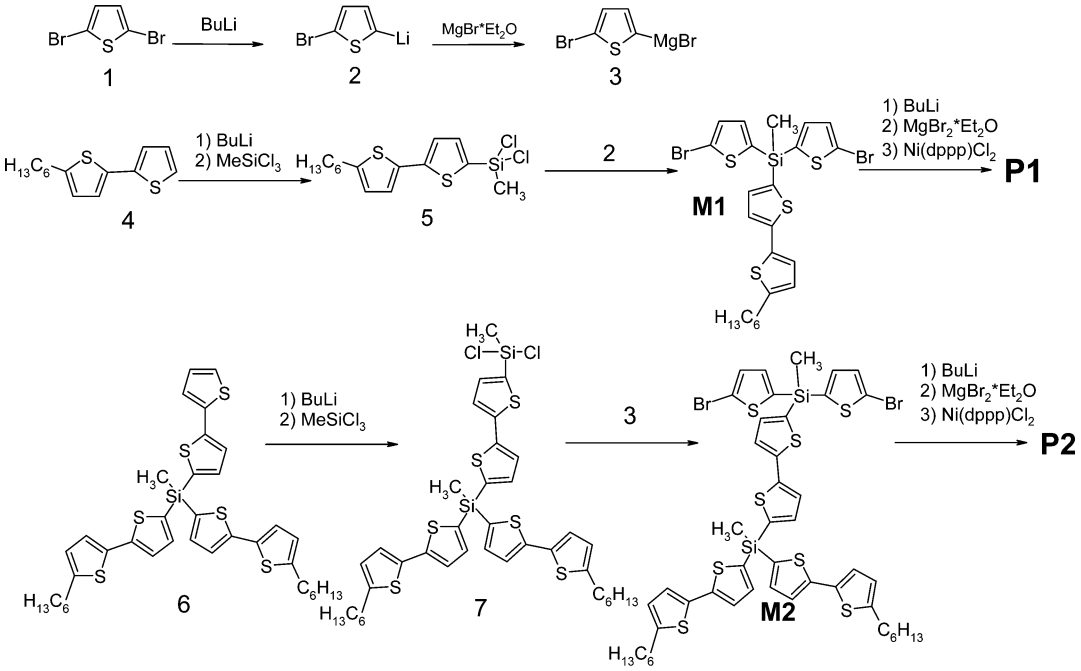

after which an excess of methyltrichlorosilane was distilled with toluene. The obtained solution of compound **7** in toluene was used in the following stage of synthesis without isolation or purification of the product.

*{5′-[Bis(5-bromo-2-thienyl)(methyl)silyl]-2,2′-bithiophen-5-yl}-[bis(5′-hexyl-2,2′-bithiophen-5-yl)]methylsilane (**M2**).* **A.** (via organolithium derivative **2**): A solution of compound **2** in a THF-hexane mixture (freshly obtained from 1.78 g (7.4 mmol) of 2,5-dibromothiophene, 45 mL of THF, and 4.6 mL (7.4 mmol) of a solution of 1.6 M *n*-butyllithium in hexane) was added to a solution of freshly prepared solution of compound **7** in toluene. After standard extraction described in the procedure of the synthesis of **M1**, the reaction yield of the product was 44% (according to GPC). It was purified by column chromatography on silica gel using a mixture of hexane–toluene (v/v 5:1) as the eluent, to yield 0.59 g (15%) of the pure product as a yellowish highly viscous liquid. ^{1}H NMR (DMSO-d_6/CCl_4, δ, ppm): 0.88 (t, 6H, CH_3–CH_2–, J = 6.7 Hz), 0.89 (s, 3H, CH_3–Si(T–Br)$_2$), 0.93(s, 3H, CH_3–Si), 1.24–1.38 (overlapping peaks, 12H, –CH_2–CH_2–CH_2– and CH_3–CH_2–CH_2–), 1.63 (m, 4H, –CH_2–CH_2–T, J = 7.3 Hz), 2.76 (t, 4H, –CH_2–T, J = 7.3 Hz), 6.69 (d, 2H, J = 3.7 Hz), 7.04 (d, 2H, J = 3.7 Hz), 7.20 (d, 3H, J = 3.7 Hz), 7.22–7.25 (overlapping peaks, 3H), 7.27–7.31 (overlapping peaks, 2H), 7.33 (d, 2H, J = 4.3) 7.39 (d, 2H, J = 3.7 Hz). ^{13}C NMR ($CDCl_3$, δ, ppm): −0.51, −0.22, 14.08, 22.56, 28.71, 30.15, 31.52, 31.54, 119.45, 123.99, 124.35, 124.84, 125.67, 125.80, 131.58, 132.78, 133.07, 134.26, 135.08, 137.05, 137.60, 137.83, 137.85, 138.11, 143.64, 144.50, 145.22, 145.99. ^{29}Si NMR ($CDCl_3$, δ, ppm): −25.70, −25.39. Anal. Calcd for $C_{46}H_{48}Br_2S_8Si_2$: C, 51.47; H, 4.51; Br, 14.89; S, 23.90; Si, 5.23. Found: C, 51.22; H, 4.61; Br, 14.92; S, 24.11; Si, 5.11. MALDI MS: m/z, 1180.98 $(M + Ag)^+$; calculated, 1180.85.

B (via organomagnesium derivative **3**). A solution of freshly prepared compound **7** in toluene was added quickly dropwise to a solution of compound **3** (freshly prepared from 1.85 g (7.6 mmol) of 2,5-dibromothiophene, 50 mL of THF, 4.7 mL (7.6 mmol) of 1.6. M *n*-butyllithium, and 10 mmol of an ether complex of magnesium bromide). After standard extraction described in the procedure of the synthesis of **M1**, the reaction yield of the product was 64% (according to GPC). It was purified by column chromatography on silica gel using a mixture of hexane–toluene (v/v 5:1) as the eluent, to yield 1.25 g (35%) of the pure product, which was fully identical to compound **M2**, obtained via organolithium derivative **2**.

*Poly[(5′-hexyl-2,2′-bithiophen-5-yl)(methyl)(2,2′-bithiophene-5,5′-diyl)silane] (**P1**).* A solution of 0.45 g (0.7 mmol) of compound **M1** in 15 mL of THF was cooled down to −78 °C, then a solution of 0.45 mL (0.7 mmol) of 1.6 M *n*-butyllithium in hexane was added dropwise to it. After that the reaction mixture was stirred for 1 h at a temperature of −78 °C. Then 1.2 mmol of an ether complex of magnesium bromide was added to the reaction mixture, after which the cooling bath was removed and the temperature slowly rose to 20 °C. In the next step, 3.9 mg (0.007 mmol) of [bis-(diphenylphosphino)propane]nickel(II) chloride Ni(dppp)Cl_2 was added to the reaction mixture followed by 2 h of stirring. Then the reaction mixture was poured into 150 mL of water and 300 mL of diethyl ether. The organic layer was separated, rinsed with water to pH = 7, dried over anhydrous Na_2SO_4 and evaporated in the vacuum rotary evaporator. The reaction yield was 74% (according to GPC). It was then purified from the residual amounts of the catalyst by means of column chromatography on silica gel using toluene as the eluent. Further purification was made by fractional precipitation, utilizing toluene as the solvent and hexane as the precipitating agent. As a result, 0.20 g (60%) of the pure polymer was isolated. ^{1}H NMR (DMSO-d_6/CCl_4, δ, ppm): 0.79–0.93 (overlapping peaks, 6H, CH_3–CH_2–, CH_3–Si), 1.20–1.37 (overlapping peaks, 6H, –CH_2–CH_2–CH_2– and CH_3–CH_2–CH_2–), 1.52–1.67 (broad peak, 2H, –CH_2–CH_2–T), 2.65–2.77 (broad peak, 2H, –CH_2–T), 6.60 (broad peak, 1H), 6.95 (broad peak, 1H), 7.13 (broad peak, 1H), 7.19–7.34 (overlapping peaks, 5H). ^{13}C NMR ($CDCl_3$, δ, ppm): −0.21, 14.06, 22.55, 28.71, 30.14, 31.50, 31.53, 124.02, 124.37, 124.83, 125.70, 132.67, 134.26, 134.45, 137.89, 144.03, 145.25, 145.96. ^{29}Si NMR ($CDCl_3$, δ, ppm): −25.29. Anal. Calcd for $C_{23}H_{26}S_4Si$: C, 60.21; H, 5.71. Found: C, 58.69; H, 5.53.

*Poly[{5′-[bis(5′-hexyl-2,2′-bithiophen-5-yl)(methyl)silyl]-2,2′-bithiophen-5,5′-yl}(methyl)(2,2′-bithiophen-5,5′-diyl)silane] (**P2**).* This procedure was carried out according to a technique similar to that of polymer **P1** described before from 0.51 g (0.48 mmol) of compound **M2**, 15 mL of THF, 0.3 mL (0.48 mmol) of 1.6 M *n*-butyllithium in hexane, 1.9 mmol of an ether complex of magnesium bromide, and 2.6 mg (0.005 mmol) of Ni(dppp)Cl_2. After standard extraction, the reaction yield of the product was 69% (according to GPC). After purification similar to that used in the case of polymer **P1**, 0.19 g (44%) of pure polymer **P2** was isolated. ^{1}H NMR (DMSO-d_6/CCl_4, δ, ppm): 0.79–0.91 (overlapping peaks, 12H, CH_3–CH_2–, CH_3-Si), 1.19–1.33 (overlapping peaks, 12H, –CH_2–CH_2–CH_2– and CH_3–

dx.doi.org/10.1021/ma2024045 | *Macromolecules* 2012, 45, 2014–2024

CH_2–CH_2–), 1.52–1.66 (broad peak, 4H, CH_2–CH_2–T), 2.64–2.75 (broad peak, 4H, –CH_2–T), 6.57 (broad peak, 2H), 6.92 (broad peak, 2H), 7.09 (broad peak, 2H), 7.16–7.31 (overlapping peaks, 10H). ^{13}C NMR ($CDCl_3$, δ, ppm): −0.19, 14.07, 22.55, 28.70, 30.13, 31.49, 31.53, 123.97, 124.35, 124.82, 125.68, 125.70, 125.75, 132.86, 134.17, 134.23, 134.28, 134.73, 137.83, 137.96, 143.90, 144.05, 144.15, 145.18, 145.91. ^{29}Si NMR ($CDCl_3$, δ, ppm): −25.40, −25.18. Anal. Calcd for $C_{46}H_{50}S_8Si_2$: C, 60.34; H, 5.50. Found: C, 59.79; H, 5.57.

RESULTS AND DISCUSSIONS

Among three general approaches to the synthesis of dendronized polymers ("grafting to", grafting from" and "macromonomer strategy")[26] the last one was selected for preparation of the bithiophenesilane dendronized polymers, since the creation of dendronized polymers having high molecular weights and containing no defects using the other approaches of synthesis is quite complicated. Its implementation requires, first, the preparation of precursors, which are dendritic monomers having difunctional reactive groups in the focal point, and, second, their subsequent polymerization. Among various reactions involving organometallic synthesis used in the synthesis of conjugated polymers, the Kumada reaction,[38] whose essence is the formation of biaryl C–C bond from arylhalogenides and their magnesium or zinc derivatives in the presence of palladium- or nickel-catalysts, is widely used. Earlier, such a reaction was applied for the synthesis of bithiophenesilane dendrimers.[15,16] The only, but significant, disadvantage of this reaction is the formation of symmetric byproduct caused by exchange of halogen and magnesiumhalogen reacting groups, which the Kumada reaction is known for. However, in the case of symmetric monomers this circumstance poses no obstacle, since the substitution of a bromine group on the thiophene ring with a magnesium bromide residue followed by the coupling reaction of the exchange products leads to the formation of the products of interest anyway. It is also known that during the synthesis of polythiophenes from their organometallic (magnesium or zinc) derivatives with the use of nickel catalysts, polymerization goes by the chain growth mechanism having "living" nature that leads to the formation of polymers with low polydispersity indices (PDIs).[39] That is why the reaction of the polymerization of difunctional bithiophenesilane-dendronized monomers under the Kumada conditions on the nickel catalyst was selected for the synthesis of dendronized polymers in the present work (Scheme 3).

The synthesis of dendronized polymers **P1** and **P2** was made in two main stages: (1) the preparation of branched monomers **M1** and **M2** and (2) their polymerization under the Kumada conditions. The synthesis of monomer **M1** and its polymerization were carried out as the model reactions in order to understand whether the progress of the reaction in the case of bithiophenesilane systems would be possible according to the chain growth mechanism at all. 5-Hexyl-2,2′-bithiophene (compound **4**) was chosen as the model compound, since it exhibits quite interesting optical characteristics[13] and it is a structural unit of the monodendron **M2** used further. Besides, as a result of the synthesis, it forms a bithiophenesilane comb-like polymer **P1** being a structural homologue of the dendronized polymer of interest **P2**, which will provide a chance to compare the properties of these polymers both between themselves and with those of the bithiophenesilane dendrimers of different generations obtained previously.[17]

Synthesis of Monomers. The synthesis of bis(5-bromo-2-thienyl)(5′-hexyl-2,2′-bithiophen-5-yl)-methylsilane (monomer **M1**) was carried out by reacting dichloro-(5′-hexyl-2,2′-bithiophen-5-yl)methylsilane (**5**) with a 2-fold molar excess of (5-bromo-2-thienyl)lithium (**2**) with a yield of 77%. Compound **2** was prepared *in situ* by the lithiation of 2,5-dibromothiophene (**1**) with *n*-butyllithium. The synthesis of compound **5** was performed by reacting a lithium-derivative of 5-hexyl-2,2′-bithiophene (**4**) with a 10-fold molar excess of methyltrichlorosilane for the purpose of the increasing of the yield of the target product of monosubstitution. The excess of methyltrichlorosilane was then distilled with toluene, and the solution of freshly synthesized compound **5** in toluene was used in the following reaction stage without its isolation or purification.

The synthesis of the second monomer—{5′-[bis(5-bromo-2-thienyl)(methyl)silyl]-2,2′-bithiophen-5-yl}[bis(5′-hexyl-2,2′-bithiophen-5-yl)]methyl silane (**M2**)—is similar to that previously described for **M1**. In this case the first generation of bithiophenesilane monodendron, 2,2′-bithiophen-5-yl-[bis-(5′-hexyl-2,2′-bithiophen-5-yl)]methylsilane (**6**), was utilized as the initial compound, whose synthesis was performed according to the technique described earlier. However, using the modification of the focal point of {5′-[bis(5-bromo-2-thienyl)-(methyl)silyl]-2,2′-bithiophen-5-yl}[bis(5′-hexyl-2,2′-bithiophen-5-yl)]methylsilane (**7**) by organolithium compound **2**, led to the reaction yield of compound **M2** of 44% only, whereas the use of organomagnesium derivative **3** allowed to increase the yield of **M2** to 64%. It may be explained by a decreased probability of the metal-bromide exchange reaction for organomagnesium derivatives as compared to their organolithium analogues that leads to formation of smaller amount of byproduct related to this process.

The purification of monomers **M1** and **M2** obtained was performed by classical column chromatography on silica gel. The purity and molecular structure of both monomers was proven by a combination of GPC analysis (Figure 1), MALDI–TOF MS, elemental analysis and ^{1}H, ^{13}C, ^{29}Si NMR spectroscopy (see Experimental Part and Figures S1–S6, S13, and S14 in the Supporting Information).

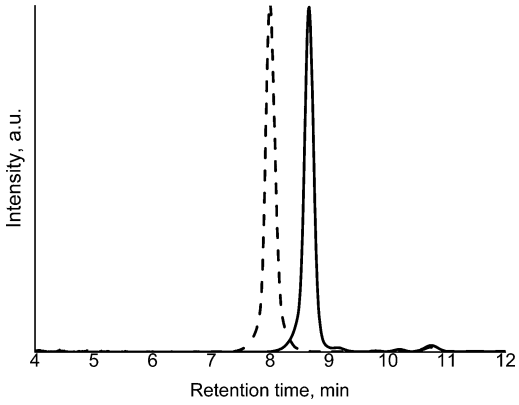

Figure 1. GPC curves for monomers **M1** (solid line) and **M2** (dashed line).

Synthesis of Polymers. Poly[(5′-hexyl-2,2′-bithiophen-5-yl)(methyl)(2,2′-bithiophen-5,5′-diyl)silane] (**P1**) was prepared by the Kumada reaction (Scheme 3) from monomer **M1**, which was first lithiated with an equimolar amount of *n*-butyllithium and then subjected to the lithium–magnesium exchange by the reaction with an ether complex of magnesium bromide. The synthesized organomagnesium derivative of monomer **M1** was

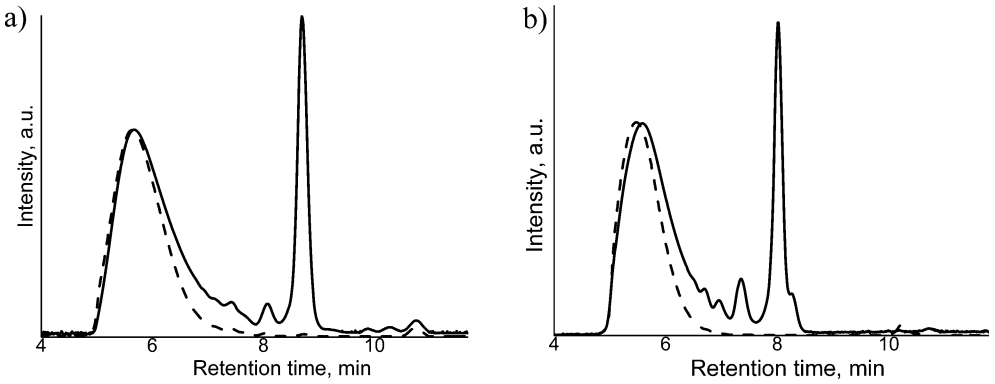

Figure 2. GPC curves of polymers **P1** (a) and **P2** (b). The solid and dashed lines correspond to the reaction mixture and the purified polymer, respectively.

Table 1. Molecular Characteristics of the Bithiophenesilane Dendrimers and Dendronized Polymers[a]

	PS		LS					
compound	M_w	PDI	M_w	PDI	M_w(LS)/M_w(PS) ratio	n	m	$[\eta]$, dL/g
G1(2−2)	2480	1.01	2250[b]	1.01	0.91	4	9	0.048
G2(2−2)	4990	1.01	5150[b]	1.01	1.03	10	21	0.055
G3(2−2)	9260	1.02	11 800[b]	1.02	1.27	22	45	0.070
P1	16 100	1.23	20 300	1.22	1.26	37−44	74−88	0.062
P2	18 700	1.19	27 700	1.23	1.48	25−30	100−120	0.101

[a]Notes: PS = molecular weight characteristics obtained using calibration according to the polystyrene standards, LS = molecular weight characteristics obtained using the dual light scattering detectors, n = average number of repeating units in the macromolecule, m = average number of bithiophene fragments in the macromolecule, and $[\eta]$ = values of intrinsic viscosity measured in THF at 25 °C. [b]Data for dendrimers are taken from ref 17.

subjected to polymerization at room temperature in the presence of the nickel catalyst Ni(dppp)Cl_2 resulting in the formation of polymer **P1**. The reaction was complete in 2 h with a reaction yield of 74% according to GPC analysis (Figure 2a).

The synthesis of poly[{5′-[bis(5′-hexyl-2,2′-bithiophen-5-yl)(methyl)silyl]-2,2′-bithiophen-5,5′-yl}(methyl)(2,2′-bithiophen-5,5′-diyl)silane] (**P2**) was performed according to the technique similar to that described above for **P1**, where **M2** was used as the macromonomer. As in the previous case, the polymerization reaction was complete within 2 h at room temperature (23 °C) with the reaction yield of 69% according to the GPC analysis (Figure 2b).

In both cases the purification of the polymers was made by hexane-induced fractional precipitation from their solutions in toluene. The molecular structure and purity of the polymers obtained were confirmed by GPC-analysis (Figure 2) and ^{1}H, ^{13}C, ^{29}Si NMR spectroscopy (see Experimental Part and Figures S7−S12 in the Supporting Information). The dendronized polymers obtained were highly soluble in low-polar organic solvents such as THF, toluene, chloroform, etc.

Molecular Characteristics. For the synthesized polymers, the values of the average molecular weights (M_w) and the polydispersity indices (PDIs) have been estimated by the following GPC-based methods: (1) using the calibration curves based on the narrow PDI polystyrene (PS) standards and (2) using a dual light scattering (LS) detector combined with a refractometer (Table 1). The data obtained indicate that despite the rigid-chain nature of the polymers under investigation, the values of their molecular weights estimated with respect to the polystyrene standards are significantly underrated in comparison to those obtained by the light scattering method known to provide true M_w values. This experimental observation can be rationalized by a more compact conformation of the molecules of the dendronized polymers as compared to the flexible-chain molecules of PS with the same molecular weight, which is probably related to their hyperbranched structure. Moreover, the ratio of the real values of M_w to those calculated according to the PS standards when going from **P1** to **P2** increases from 1.26 to 1.48. This increase in deviation from the M_w measured by PS-based standards may be connected with an increase of the branching of the monomer repeating unit from **M1** to **M2**, resulting in a more compact conformation of the macromolecule of the dendronized polymer **P2** as compared to the PS of the same molar weight. Similar tendency of increasing the deviation between the M_w measured by GPC on the base of the PS standards and by the light scattering detector was observed in the series of dendrimers **G1−G3** as well (Table 1). It is interesting to note that the phenomenon whereas the molecular masses measured by GPC based on polystyrene standards were different from the actual molar masses has been investigated for different dendrimers and long conjugated oligomers: for the dendrimers it was found that the GPC results underestimated their molar masses,[40] while in the case of rigid conjugated oligomers an effect of overestimation of the molar masses was observed.[41]

The GPC measurements have shown that the polymers synthesized exhibit quite narrow polydispersity indices (PDI = 1.22−1.23). These data indicate that the chain growth mechanism of the Kumada polymerization[38] is also valid for the synthesis of the polymers from rather bulky monomer **M1** and macromonomer **M2**. Estimations based on these GPC data gives a weight-average polymerization degree n = 44 for **P1** and n = 30 for **P2**, which correspond to the number of

dx.doi.org/10.1021/ma2024045 | Macromolecules 2012, 45, 2014−2024

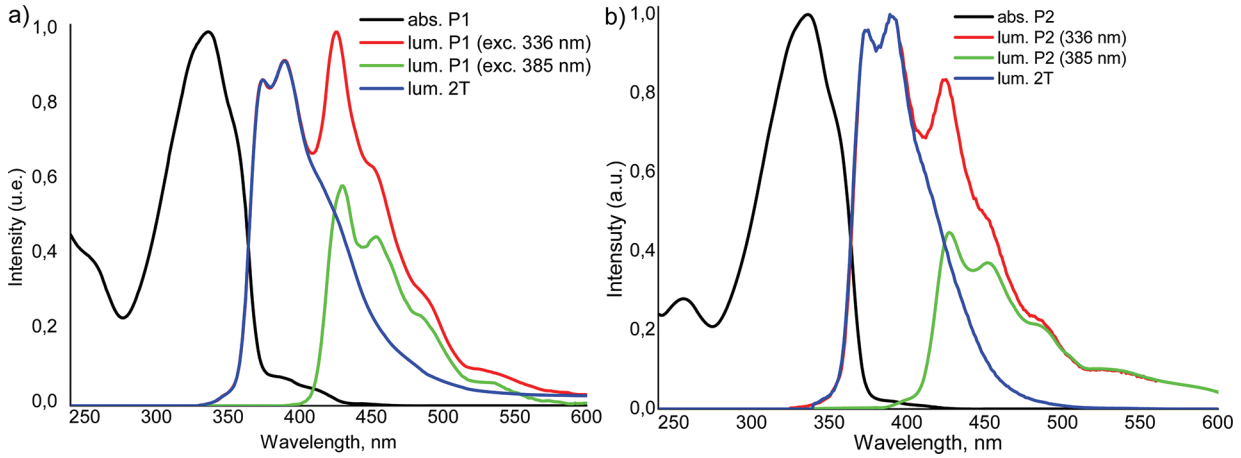

Figure 3. Absorption and luminescence spectra of dilute solutions of polymers **P1** (a) and **P2** (b) in THF. Luminescence spectra of bithiophene component (blue line) for both polymers was calculated by deduction of the luminescence of the polymer excited at 385 nm from the luminescence of the polymer excited at 336 nm.

Table 2. Optical Properties of Various Oligothiophenesilane Macromolecules and Their Low Molecular Weight Analogues[a]

compound	λ_{abs}, nm	ε, $M^{-1}\cdot cm^{-1}$	λ_{lum}, nm	Q_F, %	Q_{ETE}, %	ref
2T	303	-	362	1[b]	-	12
3T	354	-	407	7[b]	-	12
Hex-2T	308	13 000	374	1.8[b]	-	16
Hex-2T-TMS	320	19 000	380	5.8[b]	-	16
TMS-2T-TMS	322	20 000	381	6.0[b]	-	16
p-T_2SiMe_2[d]	326	-	371/387	24[c]	-	12
P1	336, 385	41 000	374/389/430/453	13	50 ± 15	this work
P2	336, 385	77 000	374/389/427/452	14	70 ± 15	this work
G1(2−2)	333	174 000	374/388	30	-	17
G2(2−2)	334	420 000	375/390	31	-	17
G3(2−2)	336	870 000	376/390	30	-	17
D1(3−2)	338, 388	147000, 114000	427/450	10	97 ± 3	18
B1(3−2)	337, 382	84000, 39 000	427/450	10	91 ± 3	18

[a]Measured in THF unless otherwise stated. Notes: λ_{abs} = absorption maximum, ε = molar extinction coefficient, λ_{lum} = luminescence maximum, Q_F = luminescence quantum yield, and Q_{ETE} = efficiency of intramolecular energy transfer. [b]In hexane. [c]In CH_2Cl_2. [d]Linear polymer: poly[5,5′-(dimethylsilylene)-2,2′-bithiophene].

bithiophenesilane fragments to be contained in average in one macromolecule m = 88 and 120, respectively (Table 1). The corresponding number-averaged values of n and m are also shown in Table 1 as a lower limit of the respective interval. It should be noted that dendronized polymers **P1** and **P2**, both by the number of 2T fragments and by the weight-average molar weight, correspond to the forth or even higher generation of the bithiophenesilane dendrimer, which was not possible to prepare in a regular manner.

The data obtained from the measurements of the intrinsic viscosity $[\eta]$ of the solutions of the dendronized polymers synthesized and their analogues—the bithiophenesilane dendrimers—are presented in Table 1 as well. The values of $[\eta]$ of all the macromolecules under investigation lies in a range of 0.048−0.101 dL/g, that is 2−4 times higher than the $[\eta]$ of more flexible polyallylcarbosilane dendrimers of various generations.[42] Besides, $[\eta]$ slightly increases with the increase of the molecular weight of the dendronized polymer, which is also observed in the studied family of bithiophenesilane dendrimers. At the same time, the dependency of the reduced viscosity on the concentration of the solution is more pronounced for the dendronized polymers than for the dendrimers, for which the reduced viscosity is practically independent of the dilution of their solutions (see Figure S15 in the Supporting Information). All in all, there are similarities in the hydrodynamic behavior of the bithiophenesilane dendrimers and dendronized polymers investigated, which confirm the conclusion about the compact conformation of the dendronized polymers.

Optical Properties. The absorption and luminescence spectra of the dilute solutions of dendronized polymers **P1** and **P2** in THF are presented in Figure 3. The absorption spectrum of polymer **P1** is almost identical to that of the star-like bithiophenesilane molecules.[13] The value of the molar extinction coefficient ε, being 41000 L $mol^{-1}cm^{-1}$ at a wavelength of 336 nm, calculated for one monomer unit, corresponds to the sum of ε for two bithiophenesilane fragments (Table 2). Thus, the formation of the absorption spectrum of the dendronized polymer occurs in the same way as in the case of the bithiophenesilane dendrimer.[19] At the same time, a weak long-wave band in the 370−400 nm range, which is impossible to explain by the absorption of the bithiophenesilane fragments, was observed in the absorption and excitation spectra of polymer **P1**. The luminescence spectrum of polymer **P1** excited at 336 nm lies in the range from 360 to 540 nm and has a complex structure and differs from the luminescence of

dx.doi.org/10.1021/ma2024045 | *Macromolecules* 2012, 45, 2014−2024

this polymer excited at 385 nm (Figure 3a). The letter spectra coincides with luminescence of dendrimer **D1(3−2)**, which shows limunescence from its 3T fragments.[18] The mathematical deconvolution of the luminescence spectral contour of polymer **P1** excited at 336 nm led the fact that it consists of the luminescence spectra of two components—bithiophenesilane (2T) with the main maxima at 374 and 389 nm and terthiophenesilane (3T) with the main maxima at 430 and 453 nm. It means that beside the 2T repeating units, polymer **P1** contains a certain amount of 3T fragments. Calculations carried out on the basis of the measured absorption spectra of polymer **P1** revealed that the molar ratio of 2T to 3T fragments in this polymer is close to 25: 1. Therefore, upon the average, one macromolecule of **P1** contains 3−4 terthiophene units, two of which located, most probably, at the ends of the polymer main chain, as shown in Scheme 2.

It should be noted that the presence of the 3T units in **P1** was detected by spectral-luminescence methods only because of their very low content (3−4%) and similarity of their chemical composition to 2T units. Therefore, they can be considered as defects of the polymer chain, formation of which can be related to a small (1−2%) decomposition of the monomer **M1** during its lithiation with *n*-butyllithium (see Scheme S1 in the Supporting Information). The lithium derivatives of the mono- and bithiophene fragments thus formed undergo the lithium−magnesium exchange reaction and participate in the following polymerization under the Kumada conditions. In the polymerization reaction they can serve either as monofunctional blocking agents, which form 2T or 3T end groups, thus limiting the macromolecule length, or as bifunctional comonomer units (presumably, magnesium derivatives of 2,5-disubstituted thiophene), forming a few (1−2 per one macromolecule) defects of 3T units in the main chain of polymer **P1**.

In spite of a small amount of 3T units in **P1**, they significantly change its luminescence spectra as compared to those of the bithiophenesilane dendrimers **Gn(2−2)** (Scheme 1).[17] It was found that under the excitation of **P1** into the spectral range of the maximal absorption of bithiophenesilane and weak absorption of terthiophenesilane (336 nm), the integral intensity of the fluorescence of bithiophenesilane and terthiophenesilane amounts to 69% and 31% respectively, which points out to the phenomenon of the nonradiative energy transfer of the electronic excitation from bi- to terthiophenesilane fragments. In the case of excitation at 336 nm (2T), the fluorescence quantum yield Q_F amounts to 13%, whereas under excitation at 385 nm (3T) its value drops to 8%. Thus, the Q_F of 2T fragments in polymer **P1** is significantly lower than that in the bithiophenesilane dendrimers (20−30%), but not approaching zero as it takes place in the case of efficient (90−97%) intramolecular energy transfer in the "dendritic molecular antenna" from bi- and terthiophene fragments of **B1(3−2)** and **D1(3−2)** (Scheme 1).[18] Therefore, the efficiency of nonradiative energy transfer in polymer **P1** is lower than that in the dendritic "molecular antenna" consisting of bi- and terthiophene fragments. The calculations of the energy transfer efficiency Q_{ETE} from 2T to 3T fragments carried out on the basis of the measured absorption and luminescence spectra of polymer **P1** by the method described before[18] yielded a value of Q_{ETE} close to 50%. The critical distance of energy transfer by inductive resonance mechanism for the system bithiophene-silicon-terthiophene amounts to 20−25 Å meaning that the average distance between a terthiophene fragment (acceptor) and a group of bithiophene fragments (donors) must not exceed 25 Å. In the case of the linearly arranged main chain of polymer **P1**, it amounts to approximately 100−110 Å (see Figure S16a in the Supporting Information), which should correspond to the efficiency of energy transfer of lower than 4%. Hence it is possible to conclude that a macromolecule of the polymer forms a coil with quite dense packing, in the case of which a bigger number of bithiophene fragments is located closer than 20−25 Å apart from the terthiophene fragment. It is in good agreement with the data obtained by the GPC and viscometry methods, also pointing out to the compact conformation of such macromolecules (see Figure S16c in the Supporting Information).

The formation of the absorption spectrum of dendronized polymer **P2** (Figure 3b) is similar to that of polymer **P1**. The value of the molar extinction coefficient ε, being 77000 L mol^{-1} cm^{-1} at a wavelength of 336 nm, calculated for one monomer unit, corresponds to the sum of ε for four bithiophenesilane fragments. During excitation spectra measurements preformed at 490 nm (in the luminescence range of 3T), a long wavelength band corresponding to the excitation spectrum of 3T was present in the excitation spectrum. Thus, the macromolecule of polymer **P2** also contains terthiophenesilane fragments. Calculations carried out on the basis of the measured absorption spectra of polymer **P2** revealed that the molar ratio of 2T to 3T fragments in this polymer is close to 68: 1. Therefore, one macromolecule of polymer **P2** contains approximately 2 terthiophene repeating units in average, which, most probably, located at the ends of the polymer chains as shown in Scheme 2. During excitation into the spectral range of the maximal absorption of 2T and weak absorption of 3T (336 nm), the integral intensity of the luminescence of 2T and 3T amounts to 69% and 31% respectively. At the same time, excitation at 336 nm (2T) and 385 nm (3T) results in Q_F of 14% and 8%, respectively. The calculations of the energy transfer efficiency from 2T to 3T fragments carried out on the basis of the measured absorption and luminescence spectra of polymer **P2** yielded a value of Q_{ETE} close to 70%. In the case of the most elongated configuration of the macromolecule of polymer **P2**, its 17 repeating units (68 bithiophene fragments falling on one terthiophene fragment) have a length of approximately 150−160 Å (see Figure S16d in the Supporting Information). In this case, the average distance of 2T structural units from 3T structural units amounts to 80−85 Å, which results in an efficiency of energy transfer of below 1%. In order to the energy transfer efficiency will be equal to 70%, as it was observed, the distance between the most part of the 2T fragments and the 3T fragment must not exceed a value of 18−22 Å that is possible in compact conformations of the macromolecules only (see Figure S16f in the Supporting Information).

Comparison of the optical characteristics (molar extinction coefficients, energy transfer efficiency, luminescence quantum yield) of the synthesized bithiophenesilane-containing dendronized polymers, dendrimers, and low molecular weight analogues of their structural fragments may be found in Table 2. The data presented there suggest that the basic optical properties exhibited by the obtained dendronized polymers are better than those of their low-molecular analogues (i.e., their molar extinction coefficients and luminescence quantum yield are higher) and somewhat poorer than those of the dendrimers with similar compositions (i.e., the energy transfer efficiency is lower as compared to dendrimer **D1(3−2)**).

dx.doi.org/10.1021/ma2024045 | *Macromolecules* 2012, 45, 2014−2024

Thermal Properties. The phase behavior and thermal stability of the dendronized polymers obtained were studied by means of the DSC and TGA methods (Table 3). The data recorded are shown in Figure 4. According to the results of DSC analysis (Figure 4a), both polymers turn out to be amorphous, whereas their glass transition temperatures T_g are practically the same being 19 and 17 °C for **P1** and **P2** respectively. This is significantly higher than T_g of the corresponding bithiophenesilane dendrimers of different generations **G1(2−2)**, **G2(2−2)**, and **G3(2−2)**, and even T_g of those containing terthiophene units **D1(3−2)** and **B1(3−2)** − all these dendrimers has T_g in the range from −25 to −1 °C. No crystallization of polymers **P1** and **P2** was observed as opposite to dendrimer **B1(3−2)**. These results might be explained by higher M_w of the dendronized polymers as compared to the molar weight of the dendrimers (see Table 1) and low content of the terthiophenesilane units in these polymers.

Table 3. Thermal Properties of the Bithiophenesilane-Containing Dendrimers and Dendronized Polymers[a]

compound	T_g, °C	T_m, °C	ΔH_m, J/g	T_{dec} (A), °C	T_{dec} (B), °C
G1(2−2)	−14	-	-	405	305
G2(2−2)	−2	-	-	430	310
G3(2−2)	−1	-	-	430	400
P1	19	-	-	415	340
P2	17	-	-	400	300
D1(3−2)	−2	-	-	405	290
B1(3−2)	−25	72	33.14	400	290

[a]Notes: T_g = glass transition temperature, T_m = melting temperature, ΔH_m = melting enthalpy, T_{dec}(A) = temperature at 1% weight loss measured by TGA in argon, and T_{dec}(B) = temperature at 1% weight loss measured by TGA in air.

TGA analysis (Figure 4b) demonstrated the stability of the dendronized polymers **P1** and **P2** to thermal-oxidative destruction up to 340 and 300 °C (1 wt % weight loss), and up to 415 and 400 °C (1 wt % weight loss) in the case of thermal decomposition. These results are comparable with those obtained for bithiophenesilane-containing dendrimers (Table 3).

Cyclic Voltammetry. Electrochemical properties of polymers **P1** and **P2** and dendrimers **G1(2−2)**, **G2(2−2)**, and **D1(3−2)** were studied by cyclic voltammetry (CVA). The measurements were carried out in the 1,2-dichlorobenzene: acetonitrile (4: 1) mixture of solvents using 0.1 M Bu_4NPF_6 as supporting electrolyte. The results are summarized in Table 4. All compounds showed an irreversible oxidation with two waves for **P1**, **P2** (Figure 5), **G1(2−2)**, and **D1(2−3)** and with three waves for **G2(2−2)** (see Figure S17B in the Supporting Information). The fact of irreversible oxidation can be explained by electrochemical instability trithienylsubstitited silanes. It is known from the literature that mono- and disubstituted thienylsilanes are electrochemically unstable,[43] whereas tetrasubstituted thienylsilanes can be oxidized reversibly.[10] The onsets of the first oxidation peaks for **P1**, **P2**, **G1(2−2)**, **G2(2−2)**, and **D1(3−2)** have the values of $E^{1/2}$ equal to 1.30, 1.24, 1.23, 1.23, and 1.38 V vs a saturated calomel electrode (SCE), respectively. The HOMO level was calculated using these data as described before.[44] Peaks of the reduction process were not observed for all the polymers and dendrimers under investigation up to a value of −2.2 V for the discharge

Table 4. Electrochemical Properties of the Bithiophenesilane-Containing Dendrimers and Dendronized Polymers[a]

compound	E_{ox}, V	$E^{1/2}{}_{ox}$, V	E_{el}(HOMO), eV
G1(2−2)	1.29, 1.50	1.23, 1.44	−5.63
G2(2−2)	1.29, 1.48, 1.64	1.23, 1.42, 1.58	−5.63
P1	1.36, 1.60	1.30, 1.54	−5.70
P2	1.30, 1.58	1.24, 1.52	−5.64
D1(3−2)	1.34, 1.55	1.28, 1.49	−5.68

[a]Notes: E_{ox} = oxidation potential *vs* SCE; $E^{1/2}{}_{ox}$ = standard oxidation potential calculated as $E^{1/2} = E_{ox} - 0.06$ V; E(HOMO) calculated as E(HOMO) = $-E^{1/2}{}_{ox}$ −4.40 eV (see ref 43 for detail).

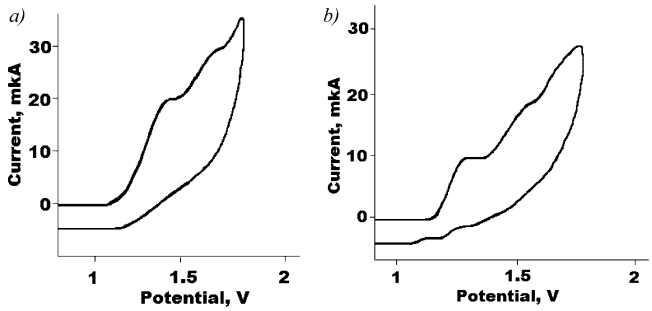

Figure 5. Electrochemical oxidation curves of **P1** (a) and **P2** (b).

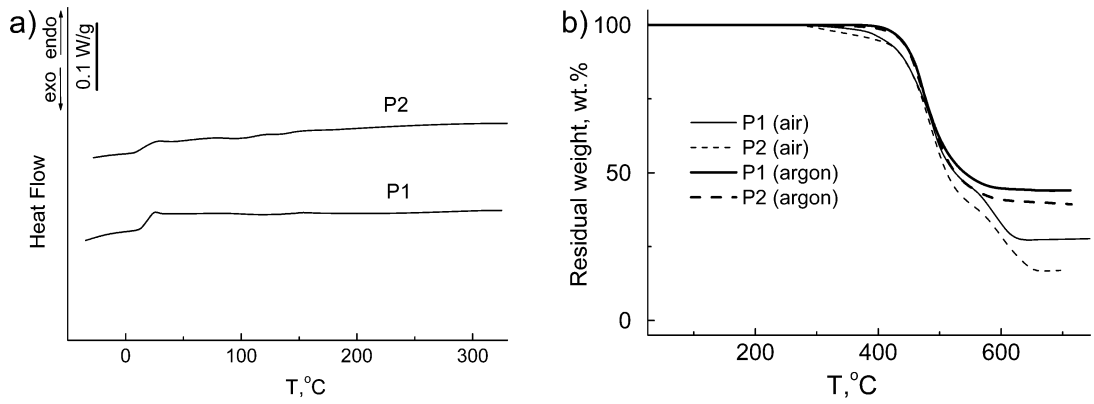

Figure 4. DSC (a) and TGA (b) curves of dendronized polymers **P1** and **P2**.

dx.doi.org/10.1021/ma2024045 | *Macromolecules* 2012, 45, 2014−2024

backgraound. As can be seen from the results obtained, the HOMO energy levels of bithiophenesilane dendrimers **G1(2−2)** and **G2(2−2)** (−5.63 eV) almost coincide with the HOMO energy level of polymer P2 (−5.64 eV), while the HOMO energy level of polymer P1 is much closer to the HOMO energy level of dendrimer **D1(3−2)**, containing both 2T and 3T fragments. Bearing in mind that the oxidation processes in such systems are governed by the most conjugated oligothiophene fragments, these results can be explained by the fact that concentration of 3T fragments in polymer **P2** is too small to be detected by CVA method and only 2T fragments are responsible for its oxidation. In contrast, the oxidation behavior of polymer **P1** is governed namely by 3T fragments. These results are in good agreement with optical measurements, which have shown that the ratio of 2T to 3T fragments in polymers **P1** and **P2** are 25: 1 and 68: 1, respectively.

CONCLUSIONS AND OUTLOOK

Thus, as a result of the present work, for the first time an efficient approach to the synthesis of bithiophenesilane dendronized polymers was developed and polymers **P1** and **P2** have been obtained. Both of them have low DPI (1.22−1.23), indicating that the polymerization under Kumada conditions used for their synthesis has a chain growth mechanism, like it was found before for much smaller monomer units of 3-hexylthiophene.[38] The polymers synthesized exhibited good solubility in a broad range of organic solvents, high thermal and thermal-oxidative stability up to 320 and 415 °C respectively, and interesting molecular and photo-optical properties. The measurements of the viscosity of the dilute solutions of the synthesized dendronized polymers and their analogues − the bithiophenesilane dendrimers − have shown that all of them have rather low values of the intrinsic viscosity $[\eta]$ (0.048−0.101 dL/g) that slightly increases with increasing the molar weight of the macromolecule. Similarities found in the hydrodynamic behavior of the bithiophenesilane dendrimers and dendronized polymers investigated, indicate that the dendronized polymers synthesized adopt the compact conformation in solutions.

Studies of the spectral-luminescent characteristics of the dilute solutions of dendronized polymers **P1** and **P2** pointed out to the presence of both bi- and terthiophene structural units in the polymers, whereas the ratio of the number of bithiophenesilane fragments to that of terthiophenesilane fragments is 25:1 in the case of polymer **P1** and 68:1 in the case of polymer **P2**. As a result, the nonradiative transfer of the electronic excitation energy from bi- to terthiophene fragment by the inductive resonance mechanism takes place for both polymers with an efficiency of 50 and 70% respectively. The obtained information affords ground to state that the configuration of the molecules of dendronized bithiophenesilane polymers possesses a shape of a coil with compact packing. Further works on bithiophenesilane-containing dendronized polymers with improved luminescence efficiency and their application in organic optoelectronics devices is in progress.

ASSOCIATED CONTENT

Supporting Information

NMR ^{1}H, ^{13}C, and ^{29}Si spectra, MALDI−TOF MS spectra, data of viscosity measurements, molecular models of **P1**, **P2**, cyclic voltammetry oxidation curves for **G1(2−2)**, **G2(2−2)**, and **D1(3−2)**, and schematic demonstration of formation of terthiophene units in polymer chains of **P1**. This material is available free of charge via the Internet at http://pubs.acs.org/.

AUTHOR INFORMATION

Corresponding Author

*E-mail: ponomarenko@ispm.ru.

Notes

The authors declare no competing financial interest.

ACKNOWLEDGMENTS

This work was supported by the Presidium of Russian Academy of Sciences (Program No. 22), Russian Foundation for Basic Research (grant No. 10-03-01009a), and Ministry of Education and Science of the Russian Federation (contract no. 16.740.11.0337). I.L. is grateful to Prof. Jayant Kumar (University of Massachusetts Lowell) for financial support during MALDI−TOF MS measurements.

REFERENCES

(1) Sauvajol, J. L.; Lère-Porte, J. P.; Moreau, J. J. E. In *Handbook of organic conductive molecules and polymers, volume 2, conductive polymers: synthesis and electrical properties*; Nalwa, N. S., Ed.; Wiley: Weinheim, Germany, 1997.

(2) Ponomarenko, S. A.; Kirchmeyer, S. *Adv. Polym. Sci.* **2011**, *235*, 33−110.

(3) Tang, H.; Zhu, L.; Harima, Y.; Yamashita, K.; Lee, K. K.; Naka, A.; Ishikawa, M. J. *Chem. Soc. Perkin. Trans.* **2000**, *2*, 1976−1979.

(4) Ishikawa, M.; Teramura, H.; Lee, K. K.; Schneider, W.; Naka, A.; Kobayashi, H.; Yamaguchi, Y.; Kikugawa, M.; Ohshita, J.; Kunai, A.; Tang, H.; Harima, Y.; Yamabe, T.; Takeuchi, T. *Organometallics* **2001**, *20*, 5331−5341.

(5) Ohshita, J.; Kim, D.-H.; Kunugi, Y.; Kunai, A. *Organometallics* **2005**, *24*, 4494−4496.

(6) Ohshita, J.; Izumi, Y.; Kim, D. H.; Kunai, A.; Kosuge, T.; Kunugi, Y.; Naka, A.; Ishikawa, M. *Organometallics* **2007**, *26*, 6150−6154.

(7) Bokria, J. G.; Kumar, A.; Seshadri, V.; Tran, A.; Sotzing, G. A. *Adv. Mater.* **2008**, *20*, 1175−1178.

(8) Jiang, X.; Zheng, Z.; Harima, Y.; Ohshita, J.; Sun, P. *J. Mater. Chem.* **2011**, *21*, 1902−1906.

(9) Roquet, S.; de Bettignies, R.; Leriche, P.; Cravino, A.; Roncali, J. *J. Mater. Chem.* **2006**, *16*, 3040−3045.

(10) Kleymyuk, E. A.; Troshin, P. A.; Luponosov, Y. N.; Khakina, E. A.; Moskvin, Yu.L.; Peregudova, S. M.; Babenko, S. D.; Meyer-Friedrichsen, T.; Ponomarenko, S. A. *Energy Environ. Sci.* **2010**, *3*, 1941−1948.

(11) Troshin, P. A.; Ponomarenko, S. A.; Luponosov, Y. N.; Khakina, E. A.; Egginger, M.; Meyer-Friedrichsen, T.; Elschner, A.; Peregudova, S. M.; Buzin, M. I.; Razumov, V. F.; Sariciftci, N. S.; Muzafarov, A. M. *Sol. Energy Mater. Sol. Cells* **2010**, *94*, 2064−2072.

(12) Herrema, J. K.; Gill, E. R.; Wildeman, J.; Gill, R. E.; Wieringa, R. H.; van Hutten, P. F.; Hadziioannou, G. *Macromolecules* **1995**, *28*, 8102−8116.

(13) Shumilkina, E. A.; Borshchev, O. V.; Ponomarenko, S. A.; Surin, N. M.; Pleshkova, A. P.; Muzafarov, A. M. *Mendeleev Commun.* **2007**, *17*, 34−36.

(14) Naka, A.; Matsumoto, Y.; Itano, T.; Hasegawa, K.; Shimamura, T.; Ohshita, J.; Kunai, A.; Takeuchi, T.; Ishikawa, M. *J. Organomet. Chem.* **2009**, *694*, 346−352.

(15) Ponomarenko, S. A.; Muzafarov, A. M.; Borshchev, O. V.; Vodopyanov, E. A.; Demchenko, N. V.; Myakushev, V. D. *Russ. Chem. Bull.* **2005**, *54*, 684−690.

(16) Borshchev, O. V.; Ponomarenko, S. A.; Surin, N. M.; Kaptyug, M. M.; Buzin, M. I.; Pleshkova, A. P.; Demchenko, N. V.; Myakushev, V. D.; Muzafarov, A. M. *Organometallics* **2007**, *26*, 5165−5173.

(17) Luponosov, Y. N.; Ponomarenko, S. A.; Surin, N. M.; Muzafarov, A. M. *Org. Lett.* **2008**, *10*, 2753−2756.

(18) Luponosov, Y. N.; Ponomarenko, S. A.; Surin, N. M.; Borshchev, O. V.; Shumilkina, E. A.; Muzafarov, A. M. *Chem. Mater.* **2009**, *21*, 447−455.
(19) Surin, N. M.; Borshchev, O. V.; Luponosov, Y. N.; Ponomarenko, S. A.; Muzafarov, A. M. *Russ. J. Phys. Chem. A* **2010**, *84*, 1979−1985.
(20) Borshchev, O. V.; Ponomarenko, S. A.; Kleymyuk, E. A.; Luponosov, Y. N.; Surin, N. M.; Muzafarov, A. M. *Russ. Chem. Bull.* **2010**, *59*, 797−805.
(21) Polinskaya, M. S.; Borshchev, O. V.; Luponosov, Y. N.; Surin, N. M.; Muzafarov, A. M.; Ponomarenko, S. A. *Mendeleev Commun.* **2011**, *21*, 89−91.
(22) Xu, M. H.; Pu, L. *Tetrahedron Lett.* **2002**, *43*, 6347−6350.
(23) Xia, C.; Fan, X.; Locklin, J.; Advincula, R. C. *Org. Lett.* **2002**, *4*, 2067−2070.
(24) Ma, C. Q.; Mena-Osteritz, E.; Debaerdemaeker, T.; Wienk, M. M.; Janssen, R. A. J.; Bäuerle, P. *Angew. Chem., Int. Ed.* **2007**, *46*, 1679−1683.
(25) Ma, C. Q.; Fonrodona, M.; Schikora, M. C.; Wienk, M. M.; Janssen, R. A. J.; Bäuerle, P. *Adv. Funct. Mater.* **2008**, *18*, 3323−3331.
(26) Schlüter, A. D.; Rabe., J. P. *Angew. Chem., Int. Ed.* **2000**, *39*, 864−883.
(27) Frauenrath, H. *Prog. Polym. Sci.* **2005**, *30*, 325−384.
(28) Zhuravel, M. A.; Davis, N. E.; Nguyen, S. T.; Koltover, I. *J. Am. Chem. Soc.* **2004**, *126*, 9882−9883.
(29) Gossl, I.; Shu, L.; Schluter, A. D.; Rabe, J. P. *J. Am. Chem. Soc.* **2002**, *124*, 6860−6865.
(30) Liang, C. O.; Helms, B.; Hawker, C. J.; Frechet, J. M. *J. Chem. Commun.* **2003**, *20*, 2524−2525.
(31) Li, C.; Bo, Z. *Polymer* **2010**, *51*, 4273−4294.
(32) Schlüter, A,D.; Loffler, M.; Enkelmann, V. *Macromolecules* **2000**, *33*, 2688−2694.
(33) Zhu, B.; Han, Y.; Sun, M.; Bo, Z. *Macromolecules* **2007**, *49*, 4494−4500.
(34) Fei, Z.; Han, Y.; Bo, Z. *J. Polym. Sci. A: Polym. Chem.* **2008**, *46*, 4030−4037.
(35) Kang, E.-H.; Lee, I. S.; Cho, T.-L. *J. Am. Chem. Soc.* **2011**, *133*, 11904−11907.
(36) Ponomarenko, S.; Kirchmeyer, S. *J. Mater. Chem.* **2003**, *13*, 197−202.
(37) Gelman, N. E.; Terenteva, E. A.; Shanina, T. M.; Kiparenko, L. M. *Identification of heteroatoms. Techniques of quantitative organic elemental analysis*; Chemistry: Moscow, 1987; p170.
(38) Tamao, K.; Kodama, S.; Nakajima, I.; Kumada, M.; Minato, A.; Suzuki, K. *Tetrahedron* **1982**, *38*, 3347−3354.
(39) Sheina, E. E.; Liu, J.; Iovu, M. C.; Laird, D. W.; McCullough, R. D. *Macromolecules* **2004**, *37*, 3526−3528.
(40) Wiesler, U. M.; Berresheim, A. J.; Morgenroth, F.; Lieser, G.; Müllen, K. *Macromolecules* **2001**, *34*, 187−199.
(41) (a) Sumi, N.; Nakanishi, H.; Ueno, S.; Takimiya, K.; Aso, Y.; Otsubo, T. *Bull. Chem. Soc. Jpn.* **2001**, *74*, 979−988. (b) Schumm, J. S.; Pearson, D. L.; Tour, J. M. *Angew. Chem., Int. Ed. Engl.* **1994**, *33*, 1360−1363.
(42) Tatarinova, E. A.; Voronina, N. V.; Bystrova, A. V.; Buzin, M. I.; Muzafarov, A. M. *Macromol. Symp.* **2009**, *278*, 14−23.
(43) (a) Bouachrine, M.; Lere-Porte, J.-P.; Moreau, J. J. E.; Sauvajol, J.-L.; Serein-Spirau, F.; Torreiles, C. *Synth. Met.* **1999**, *101*, 16−16. (b) Bokria, J. G.; Kumar, A.; Seshadri, V.; Tran, A.; Sotzing, G. A. *Adv. Mater.* **2008**, *20*, 1175−1178.
(44) Ponomarenko, S. A.; Kirchmeyer, S.; Elschner, A.; Alpatova, N. M.; Halik, M.; Klauk, H.; Zschieschang, U.; Schmid, G. *Chem. Mater.* **2006**, *18*, 579−586.

Macromolecules

Article

pubs.acs.org/Macromolecules

Multidimensional Analysis of the Complex Composition of Impact Polypropylene Copolymers: Combination of TREF, SEC-FTIR-HPer DSC, and High Temperature 2D-LC

Sadiqali Cheruthazhekatt,[†] Thijs F. J. Pijpers,[‡,§] Gareth W. Harding,[†] Vincent B. F. Mathot,[‡,§] and Harald Pasch*[,†]

[†]Department of Chemistry and Polymer Science, University of Stellenbosch, 7602 Matieland, South Africa

[‡]SciTe, Ridder Vosstraat 6, 6162 AX Geleen, The Netherlands

[§]Department of Chemistry, Katholieke Universiteit Leuven, Celestijnenlaan 200F, 3001 Heverlee, Belgium

ABSTRACT: A new multidimensional fractionation technique, temperature rising elution fractionation (TREF) combined with high temperature size exclusion chromatography FTIR (HT-SEC-FTIR), HT-SEC-DSC and high temperature two-dimensional liquid chromatography (HT-2D-LC) is used for the comprehensive analysis of a commercial impact polypropylene copolymer. HT-SEC-FTIR provides information regarding the chemical composition and crystallinity as a function of molar mass. Thermal analysis of selected SEC fractions yields the melting and crystallization behavior of these fractions which is related to the chemical heterogeneity of this complex copolymer. The thermal analysis of the fractions is conducted using a novel DSC method — high speed or high performance differential scanning calorimetry (HPer DSC) - that allows measuring of minute amounts of material down to micrograms. The most interesting and complex "midelution temperature" TREF fraction (80 °C) of this copolymer is a complex mixture of ethylene-propylene copolymers (EPC's) with varying ethylene and propylene contents and sequence length distributions, as well as iPP. High temperature solvent gradient HPLC has been used to show that there is a significant amount of PE homopolymer and EPC's containing long ethylene sequences in this TREF fraction. High temperature 2D-LC analysis reveals the complete separation of this TREF fraction according to the chemical composition of each component along with their molar mass distributions.

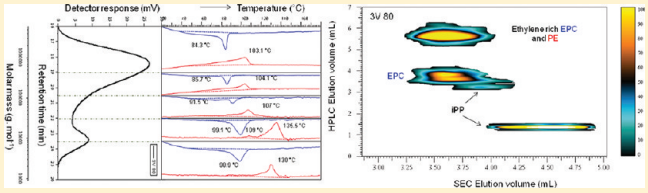

INTRODUCTION

Impact polypropylene copolymers (IPC) are a commercial grade of polypropylene (PP) which feature improved low temperature impact resistance. This class of polymers has seen growing demand in the thermoplastic market in recent times. The modified impact resistance of such heterophasic PP, together with the excellent properties of the polypropylene homopolymer such as rigidity and thermal and chemical resistance, makes the material highly useful in automotive and other applications.[1,2] Among the several methods reported for its production, the two-stage copolymerization process of propylene with ethylene is found to be the most effective and commercially adopted. The sequential multistage polymerization leads to the formation of highly complex materials consisting of many products, including amorphous, random, and segmented ethylene-propylene copolymers with different monomer sequence length distributions and molar mass distributions (MMD), as well as highly isotactic polypropylene and polyethylene homopolymers.[3−6] Preparative fractionation and subsequent analysis of the individual fractions is found to be an effective method for the complete characterization of such complex polymeric materials.[7−10] Offline coupling of SEC with FTIR is an established technique which has been used to characterize the chemical composition distribution (CCD) across the molar mass distribution.[11]

Despite the fact that SEC-FTIR can indicate the level of ethylene and propylene crystallinity across these bimodal molar mass distributions, it is necessary to study the thermal behavior and crystallinity of these fractions thoroughly.[12−15] It has been reported that it is possible to couple SEC fractionation with standard DSC,[16] and even better with HPer DSC in order to study the short chain branching distribution along the MMD.[17] This is important due to the effect of molecular structure on the crystallization behavior, and thereby the final properties of the materials.[18] HPer DSC has the ability to measure very small sample masses while scanning at higher heating rates (up to 500 °C/min) than traditional, standard DSC. Fast scanning rates help to separate or reduce reorganizational thermal behavior, such as cold crystallization, recrystallization and decomposition which may occur during heating. The improvement in fast scanning DSC technology also offers the opportunity to detect weak transitions, including glass transitions which could not be determined by standard DSC.[18]

Received: December 13, 2011
Revised: January 25, 2012
Published: February 8, 2012

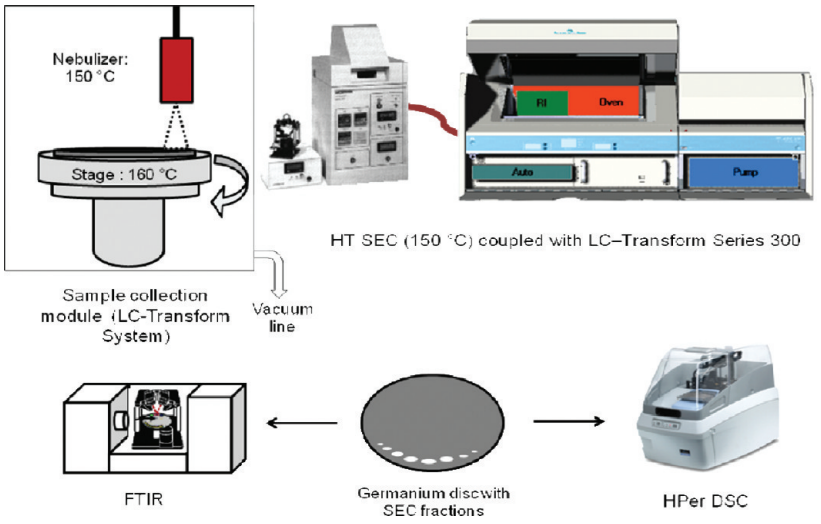

Figure 1. Polymer cross-fractionation techniques (SEC-FTIR and SEC-HPer DSC).

For many polymers, it has been proven that liquid chromatography is an efficient analytical technique for the fast separation of the polymer chains according to their chemical compositions.[19] However, the separation of polyolefins by high temperature liquid chromatography was only developed during the last couple of years by Pasch et al.[20] Initial work utilizing zeolites enabled the separation of polyolefins according to their chemical composition, however, the components could not be easily desorbed from the column packing.[21,22] Further development led to the separation of a blend of polypropylene and polyethylene based on the precipitation-redissolution mechanism on a modified silica gel column, using a solvent gradient of ethylene glycol monobutyl ether (EGMBE) (which is a good solvent for PP and not for PE) to 1,2,4-trichlorobenzene (TCB).[20,21] Most recently, research led to an HT-HPLC method capable of separating polypropylene according to tacticity in addition to the chemical composition separation of polyethylene from polypropylene.[23] This method is based on the adsorption−desorption mechanism and utilized the unique properties of the Hypercarb column.[24] To this date this is the only method for the swift and efficient separation of polyolefins and olefin copolymers according to their chemical compositions, where all components can be recovered from the column. The HPLC method separates polyolefin materials according to their chemical composition, although a slight molar mass influence on the retention volume has been observed for low molar masses. Despite this fact, the separation is governed mainly by the chemical composition or tacticity of samples; i.e., nearly baseline-separated peaks are obtained for all components. Several articles have been published based on the same separation methods for the analysis of polyolefins.[25−30] A new technique, high temperature thermal gradient interaction chromatography (HT-TGIC), has also been reported for the separation of olefin copolymers according to their comonomer content.[31] HT-HPLC allows one to estimate the chemical composition distribution (CCD) in such complex materials within a short period of time, which is a significant step forward for the characterization of these materials.

This study focuses on the molecular complexity of IPC and the analysis of different IPC components as separated by TREF and SEC using offline coupling with FTIR and HPer DSC, with emphasis on those TREF fractions exhibiting multimodal molar mass distributions. A single SEC separation and deposition is found to be sufficient for HPer DSC analysis. Melting and crystallization of an IPC sample and its 80 °C TREF fraction were studied. These investigations were complemented by fractionation and analysis using HT-HPLC and HT-2D-LC.

■ EXPERIMENTAL SECTION

A nonstabilized commercial IPC (designated as 3 V) was obtained from SASOL Polymers (Secunda, South Africa). The IPC sample has a comonomer (ethylene) content of 10.48 mol %, with a weight-average molar mass (M_w) and dispersity (D) of 228 kg·mol^{-1} and 3.5, respectively.

Size Exclusion Chromatography (SEC). Molar mass measurements for all samples were performed at 150 °C using a PL GPC 220 high temperature chromatograph (Polymer Laboratories, Church Stretton, U.K.) equipped with a differential refractive index (RI) detector. The column set used consisted of three 300 × 7.5 mm PLgel Olexis columns together with a 50 × 7.5 mm PLgel Olexis guard column (Polymer Laboratories, Church Stretton, UK). The eluent used was TCB at a flow rate of 1.0 mL/min with 0.0125% 2,6-ditert-butyl-4-methylphenol (BHT) added as a stabilizer. Samples were dissolved at 160 °C in TCB at a concentration of 1 mg/mL for 1- 2 h (depending on the sample type) and 200 μL of each sample was injected. Narrowly distributed polystyrene standards (Polymer Laboratories, Church Stretton, U.K.) were used for calibration.

Temperature Rising Elution Fractionation (TREF). Preparative TREF was carried out using an instrument developed and built in-house. Approximately 3.0 g of polymer and 2.0 w/w % Irganox 1010 (Ciba Specialty Chemicals, Switzerland) were dissolved in 300 mL of xylene at 130 °C in a glass reactor. The reactor was then transferred to a temperature-controlled oil bath and filled with sand (white quartz, Sigma-Aldrich, South Africa), used as a crystallization support. The oil bath and support were both preheated to 130 °C. The oil bath was then cooled at a controlled rate of 1 °C/h in order to facilitate the controlled crystallization of the polymer. The crystallized mixture was then packed into a stainless steel column which was inserted into a modified gas chromatography oven for the elution step. Xylene (preheated) was used as eluent in order to collect the fractions at predetermined intervals as the temperature of the oven was raised. The fractions were isolated by precipitation in acetone, followed by drying to a constant weight.

Deposition of SEC Fractions by the LC Transform Interface. An LC-Transform series model 300 (Lab Connections) was coupled to a PL GPC 220 (Polymer Laboratories, Church Stretton, England) in order to collect the SEC eluate. Samples were dissolved at 160 °C in TCB at a concentration of 2 mg/mL, with 200 μL of each sample being injected. The SEC column outlet was connected to the LC transform interface (see Figure 1) through a heated transfer line set at 150 °C.

dx.doi.org/10.1021/ma2026989 | Macromolecules 2012, 45, 2025−2034

The fractions were deposited by rotating a germanium disk (sample target in the LC-transform) at a speed of 20°/min. The disk stage and nozzle temperatures of the LC-transform were set to 160 and 150 °C, respectively. For HPer DSC sample preparation an aluminum foil was wrapped around the germanium disk in such a way as to ensure good contact with the disk, with the opaque side of the foil being used for collection of the polymer deposits. The surface roughness of the opaque side of the foil enables comparatively higher adhesion as compared to the glossy side of the Al foil.[32] The bulk sample was collected by deposition of the entire sample at a single point on the germanium disk (no rotation). All the samples for SEC-FTIR and SEC-HPer DSC were prepared under the same deposition and cooling conditions in order to ensure comparable sample and thermal histories.

FTIR Analyses of the Deposited Fractions. FTIR analyses of the deposited SEC fractions were performed on a Thermo Nicolet iS10 Spectrometer (Thermo Scientific, Waltham, MA), equipped with the LC-transform FTIR interface connected to a standard transmission baseplate. Spectra were recorded at a resolution of 8 cm^{-1} with 16 scans being recorded for each spectrum. Thermo Scientific OMNIC software (version 8.1) was used for data collection and processing.

Differential Scanning Calorimetry (DSC). Melting and crystallization behavior of the bulk material and 80 °C TREF fraction were measured on a TA Instruments Q100 DSC system, calibrated with indium metal according to standard procedures. A heating rate of 10 °C/min was applied across the temperature range of 0−180 °C. Data obtained during the second heating cycle were used for all thermal analysis calculations. Measurements were conducted in a nitrogen atmosphere at a purge gas flow rate of 50 mL/min.

High Performance Differential Scanning Calorimetry (HPer DSC). Thermal properties of the SEC LC-Transform deposits were investigated using a Perkin-Elmer DSC 8500 (situated at SciTe's laboratory, Katholieke Universiteit Leuven, Belgium). A single deposition on the aluminum foil delivers enough material (not weighed as yet) for measurement at 50 °C/min, in both cooling and heating regimes. The foil is cut between various rotation angles for sample analysis (see Figure 2). The sample on the foil is folded into a flat package for analysis. For each sample, the first heating, first cooling, and second heating curves have been measured and plotted (endo up, exo down). All transitions observed turn out to be either crystallization (during cooling) or melting (during heating), and possibly recrystallization.

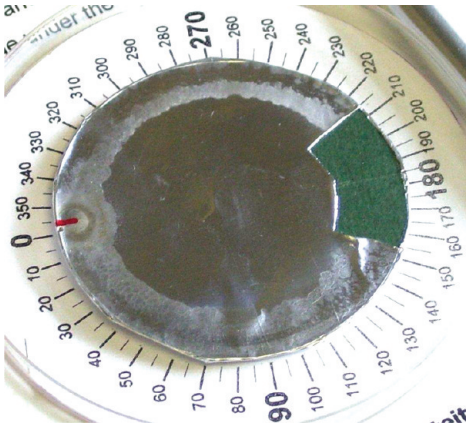

Figure 2. Example of an aluminum-covered disk after cutting out a sample for HPer DSC measurement. The portion of the aluminum foil removed is between 155° and 215°. This equates to the removal of the portion of the SEC eluate deposited between retention volumes of 20.75 to 24.75 mL.

Chromatographic System. All chromatographic experiments were performed using a new chromatographic system for high-temperature two-dimensional liquid chromatography constructed by Polymer Char (Valencia, Spain), comprising of an autosampler, two separate ovens, 2D switching valves and two pumps equipped with vacuum degassers (Agilent, Waldbronn, Germany). One oven was used for the HPLC column, while the second oven, where the injector and a switching valve were located, was used for the SEC column. The autosampler is a separate unit connected to the injector through a heated transfer line. A high-pressure binary gradient pump was used for HPLC in the first dimension and an isocratic pump was used for SEC in the second dimension. An evaporative light scattering detector (ELSD, model PL-ELS 1000, Polymer Laboratories, Church Stretton, England) was used with the following parameters: A gas flow rate of 1.5 L/min, a nebulizer temperature of 160 °C, and an evaporator temperature of 270 °C.

High Temperature HPLC. HT-HPLC was carried out using a Hypercarb column (Hypercarb, Thermo Scientific, Dreieich, Germany) with the following parameters: 100 × 4.6 mm i.d., packed with porous graphite particles with a particle diameter of 5 μm, a surface area of 120 m^2/g, and a pore size of 250 Å. The flow rate of the mobile phase was 0.5 mL/min. The column was placed in the column oven maintained at 160 °C. The HPLC separations were accomplished by applying a linear gradient from 1-decanol to TCB. The volume fraction of TCB was linearly increased to 100% within 10 min after the sample injection and then held constant for 20 min. Finally, the initial chromatographic conditions were re-established with 100% 1-decanol. Samples were injected at a concentration of 1−1.2 mg/mL, with 20 μL of each sample being injected.

High Temperature Two-Dimensional Liquid Chromatography (HT-2D-LC). The coupling of HT-HPLC and HT-SEC was achieved by using an electronically controlled eight-port valve system (VICI Valco instruments, Houston, TX) equipped with two 100 μL sample loops. A 110 μL sample loop was used for injection into the first dimension. The flow rate for the first dimension was 0.05 mL/min, using the same gradient as for one-dimensional analysis, adjusted for the longer analysis time. TCB was used as the mobile phase for the second dimension at a flow rate of 2.75 mL/min. The second dimension column used was a PL Rapide H (Polymer Laboratories, Church Stretton, U.K.) 100 × 10 mm i.d. column with a 6 μm particle diameter. The column was placed in the top heated oven, maintained at 160 °C. Detection was performed with an ELSD using the same settings as for the one-dimensional (HPLC) separation.

RESULTS AND DISCUSSION

This study explores the combination of selective fractionation with highly sensitive thermal analysis to investigate the correlation between molecular properties (chemical composition and molar mass) and thermal behavior. In a first step the bulk IPC sample has been investigated followed by TREF fractionation and the analysis of the most complex part of the sample, the midtemperature (80 °C) TREF fraction (3 V 80). Up to now the investigation of such complex polyolefins by SEC-HPer DSC cross-fractionation is at a preliminary stage.

Analysis of the Bulk Sample. When HT-SEC is coupled to FTIR, information about the chemical composition as a function of molar mass can be obtained. Using the LC-transform approach, a polymer concentration profile similar to the response from the conventional RI detector of the SEC instrument is obtained by integrating the spectral peak area over the 2800−3200 cm^{-1} range of the FTIR spectrum.[33,34] This time-based representation of the total IR absorbance over this range during elution as a function of the total amount of the polymer sample is termed the Gram-Schmidt (GS) plot. The composition distribution can be determined from the deposition on the disk by analyzing the characteristic fingerprint region for particular functional groups. The propylene content was quantified by the ratio of the areas of the CH_3 and CH_2 bending bands at 1376 and 1462 cm^{-1}, respectively. The ethylene content was quantified by the area ratio of the bands

dx.doi.org/10.1021/ma2026989 | Macromolecules 2012, 45, 2025−2034

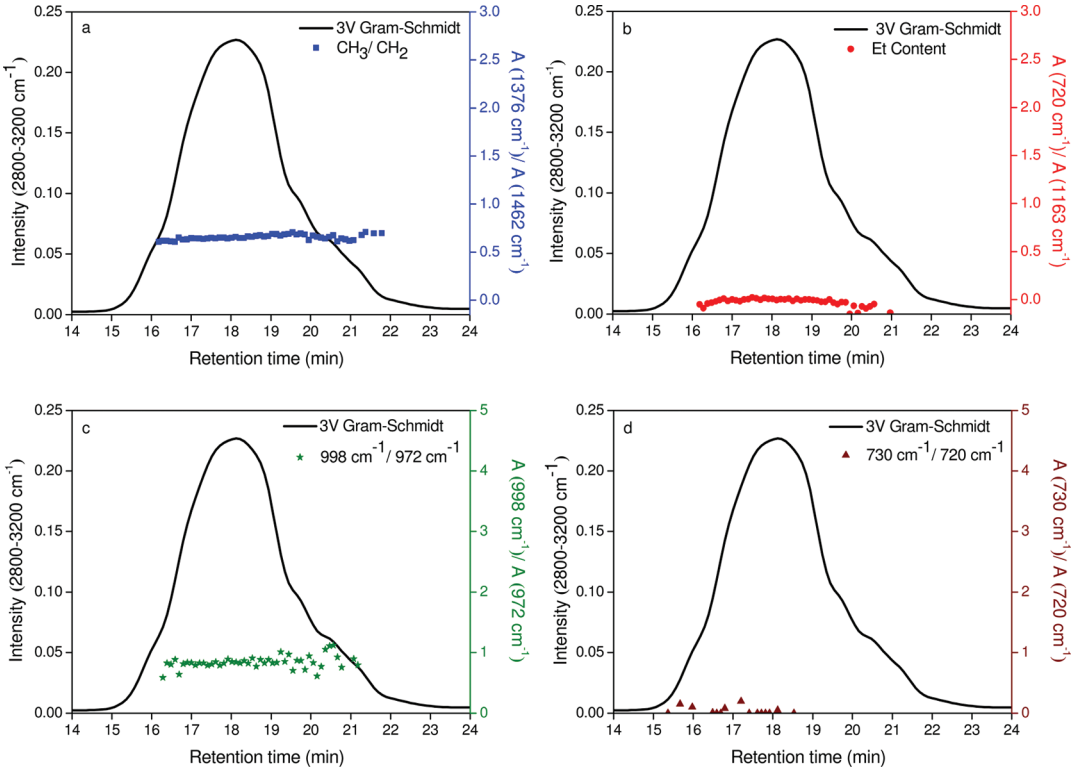

Figure 3. SEC-FTIR analysis of the bulk sample (3 V) illustrating (a) the propylene (CH_3/CH_2) and (b) the ethylene (Et content) distributions as well as their crystallinity distributions (c and d), respectively.

at 720 and 1163 cm^{-1}, which is used to determine the comonomer composition within EP block copolymers.[11,35,36]

Figure 3 illustrates the SEC-FTIR results for the bulk sample (3 V). A uniform propylene concentration and its crystallinity distribution (Figure 3a and 3c) were observed across the GS curve for the bulk sample. The ethylene content and its crystallinity distribution (Figure 3b and 3d) have a lower value across the GS plot. This means that either the methylene (CH_2) sequence lengths are short or that the number of methylene chain units is few, due to the relatively low ethylene content in the bulk copolymer sample.

It is possible to construct a crystalline distribution of ethylene and propylene (crystalline parts of PE and PP) across the GS. The two absorptions at 998 and 730 cm^{-1} are the result of molecular vibrations from crystalline PP and PE regions, respectively. The absorption bands at 998 and 841 cm^{-1} are known to originate from long repeating monomer units in the crystalline 3-fold helical structure of iPP. The band at 972 cm^{-1} is associated with short helix segments from the amorphous region of PP. The relative intensity of the two bands at 998 and 972 cm^{-1} can be used to estimate the level of PP crystallinity in the sample.[37−41] Similar to the propylene content distribution, a uniform propylene crystallinity distribution is observed across the GS plot. Because of the presence of crystalline ethylene sequences, the peak at 720 cm^{-1} splits and an additional peak appears at 730 cm^{-1}.[33,42] The relative ethylene crystallinity can be determined from the ratio of the absorbance at 730 cm^{-1} to 720 cm^{-1}. In the present sample the value of 730 cm^{-1}/720 cm^{-1} ratios across the GS curve was found to be zero, which indicates that either the sample does not contain any long crystallizable ethylene sequences or that the relative amount of long ethylene sequences in the sample is too low to be detected by SEC-FTIR of the bulk material.

The coupling of SEC with FTIR provides information on the propylene distribution and its crystallinity distribution across the molar mass distribution for this copolymer sample. On the other hand, it is difficult to determine the ethylene distribution and its crystallinity distribution for the bulk sample by using this technique. Since the amount of ethylene within this copolymer is small (10.5 mol %), it is difficult to differentiate it from the major component of the material which is isotactic polypropylene.

The DSC result for the bulk sample is displayed in Figure 4a showing a single distinct peak maximum for melting at 159 °C. This can be related to the melting process of the iPP matrix, since this melting endotherm is also observed in a pure iPP homopolymer sample and shows a similar melting temperature.[43,44] DSC on the bulk sample does not reveal any melting or crystallization events corresponding to the IPC components such as EPR, EPC, or PE homopolymers.

HPer DSC analysis of the bulk sample revealed that at 50 °C/min cooling and heating the peak maximum temperatures for crystallization and melting are approximately 100 and 159 °C, respectively, see Figure 4b. Compared to the standard DSC scan rate of 10 °C/min the crystallization temperature has shifted by 10 °C toward the lower temperature side with increasing the cooling rate from 10 °C/min to 50 °C/min. However, the peak maximum temperature of melting does not change, probably reflecting reorganization during heating, not nullified by heating at 50 °C/min because it would ask for a much higher heating rate. As is seen from Figure 4b, the cooling curve is broadened at 50 °C/min compared to the cooling curve at 10 °C/min, Figure 4a, the reason being that—when the sample mass is kept constant like in Figure 4 because the same sample packed in aluminum was used in both cases—the lowest scan rates induce the narrowest DSC peaks, while increasing the

dx.doi.org/10.1021/ma2026989 | Macromolecules 2012, 45, 2025−2034

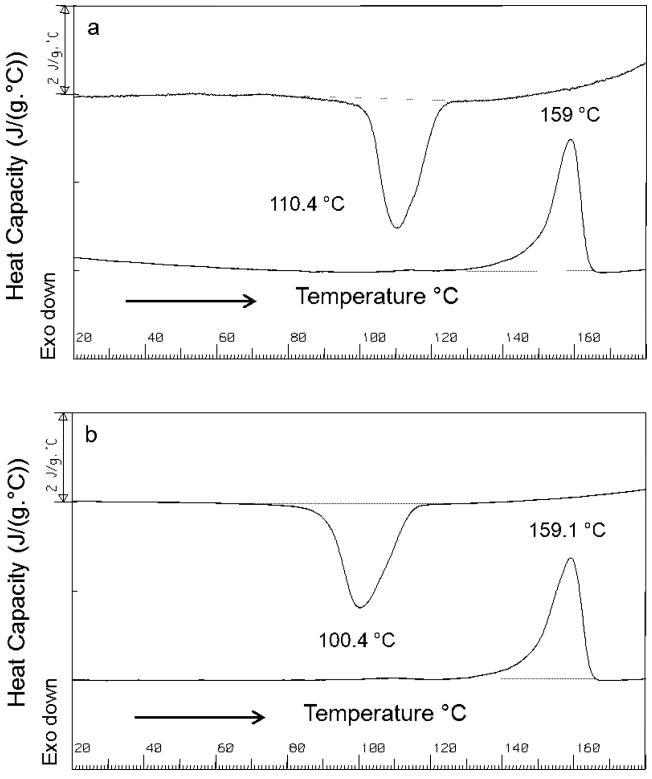

Figure 4. HPer DSC results for the bulk sample, (a) DSC 1st cooling and 2nd heating curves at 10 and 50 °C/min, respectively, and (b) 1st cooling and 2nd heating curves, both obtained at a scan rate of 50 °C/min.

scan rate will broaden these peaks,[18] as is the case here for the cooling curves.

A chemical composition separation of the sample can be achieved by HT-HPLC where elution takes place regarding the E/P content. Figure 5 indicates that the bulk sample elutes in

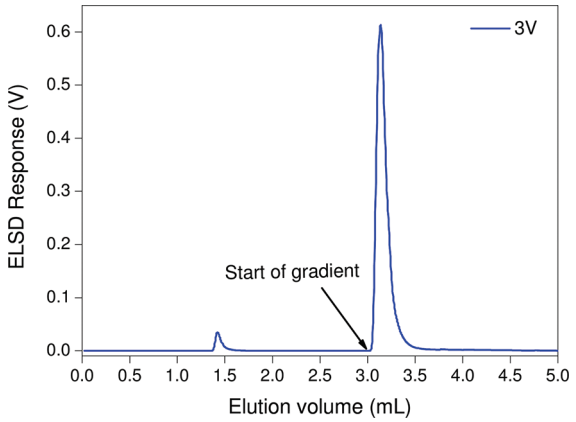

Figure 5. HT-HPLC chromatogram obtained after isocratic and gradient elution for the bulk IPC copolymer sample (3 V).

two regions, the first elutes in 1-decanol while the second elutes after the start of the gradient elution. All iPP standards, with the exception of the very low molar mass standards, elute in these two zones meaning that the PP chains are partially retained on the Hypercarb column from 1-decanol, being desorbed in the gradient from 1-decanol to TCB.[45] No peaks corresponding to EPR, EPC, or PE homopolymer were observed in the chromatogram for the bulk sample due to the low concentration of these components.

A first information on the thermal properties as a function of molar mass can be obtained by combining HT-SEC and HPer DSC. As is shown in the Experimental Section, different molar mass fractions are collected using the LC Transform system. The SEC depositions (approximately 0.4 mg of total weight), forming a continuous film on the aluminum foil, were divided into five separate SEC fractions. These fractions are subsequently subjected to HPer DSC measurements providing well resolved melting and crystallization curves.

The capability of measuring minute amounts of material from fractionations stems from the fact that by increasing the scan rate the sensitivity of the DSC is increased. However, the thermal lag also increases and, thus, smaller samples are to be taken in order to keep the thermal lag acceptable, meaning at the same level as is accepted for standard DSC. In practice, for HPer DSC, milligrams down to micrograms of material are being used, and the present, limited amounts available from the fractionations pose no problem for the HPer DSC.

Figure 6 combines the results from the first cooling and second heating HPer DSC curves for the SEC fractions of 3 V. The HPer DSC curves for each SEC fraction range are compared to the overall SEC chromatogram in terms of retention time as well as its calibrated molar mass distribution.

Figure 7 illustrates the molar mass dependence on the melting peak temperatures. The peak melting temperatures increase within the temperature range 145−165 °C, indicating the presence of crystalline iPP. The fractions eluting from 20.5 min onward show some broadening. This could indicate compositional heterogeneity in addition to the well-known stronger dependence of the crystallization and melting temperatures on molar mass in the lower mass range. A simple SEC separation is not able to reveal such subtleties, especially not for a bulk sample with relatively low comonomer content. SEC fractionation followed by HPer DSC analysis is a promising combination to provide important information regarding the chemical composition of the bulk sample.

As has been shown in these first and preliminary experiments, traditional bulk sample analysis even using the highly sophisticated HT-HPLC method cannot provide sufficient information regarding the different components in these complex copolymers. New analytical approaches are needed to obtain more detailed information about the different components, in particular when they are present in small concentrations. It is clear that for thorough characterization of such materials, the components with vastly differing chemical composition must be separated so that these components can be analyzed separately in higher concentrations. In principle, preparative TREF can be considered as a suitable method for the separation, isolation, and complete analysis of the individual components in the copolymer system, as one expects these would show different fractionation behavior based on the components' different crystallizabilities from solution.[7,10,11]

As has been shown previously by us and others, IPC can be separated into three major fractions, namely the highly crystalline iPP, the amorphous EP rubber and a "midtemperature" fraction that is speculated to contain segmented EP copolymers. This fraction elutes in the temperature range of 60−80 °C and amounts only to about 5 wt % of the total sample. It is assumed to be the most complex fraction, at the same time being very important for the phase formation in these multiphase copolymers. In the following section, this

dx.doi.org/10.1021/ma2026989 | Macromolecules 2012, 45, 2025−2034

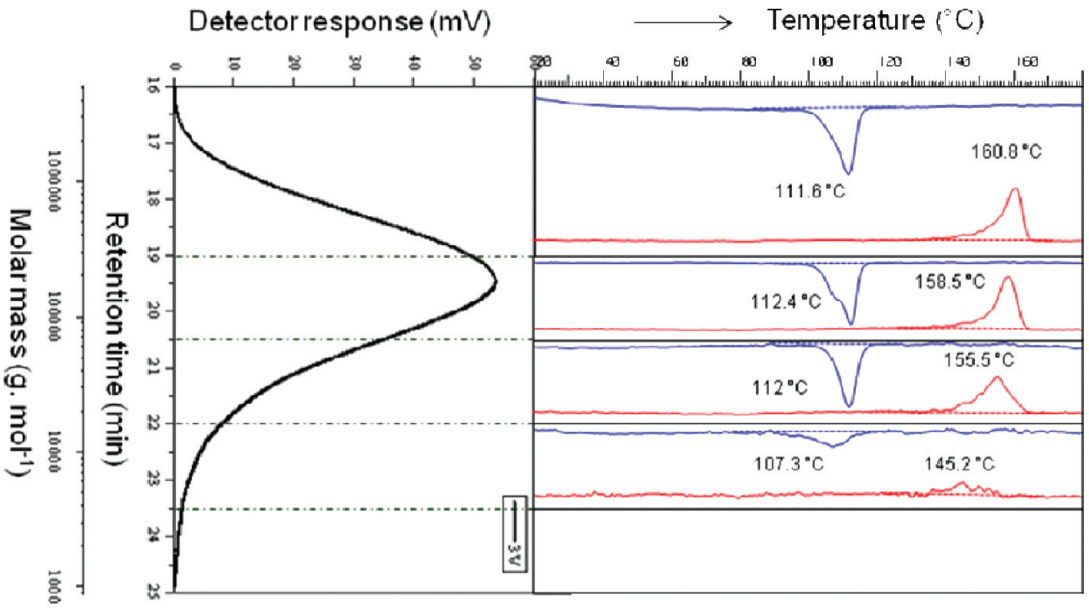

Figure 6. HPer DSC 1st cooling and 2nd heating curves for the SEC fractions of the bulk sample (3 V) at scan rates of 50 °C/min, along with the overall SEC elution profile. The left half of the figure depicts the molar mass distribution as recorded by the RI detector, while the right half of the figure depicts the individual HPer DSC results from each fraction as cut out from the aluminum foil at the specific retention time windows.

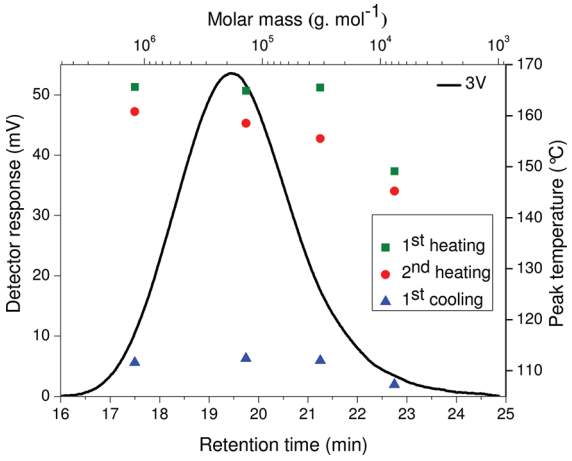

Figure 7. SEC curve of the bulk product 3 V showing the retention time axis and molar mass axis, indicating the peak maximum temperatures of the HPer DSC cooling and heating curves of the SEC fractions at 50 °C/min.

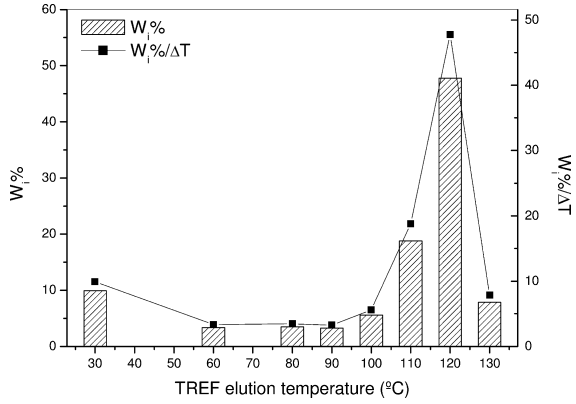

Figure 8. Mass distribution and mass fraction per temperature increment for the TREF fractions of copolymer 3 V.[11]

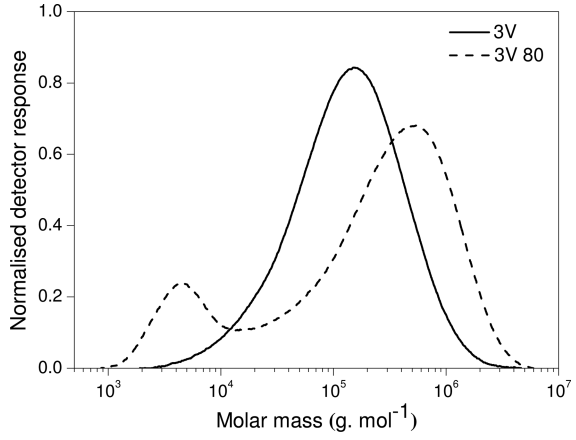

Figure 9. SEC curves for the bulk sample (3 V) and its 80 °C TREF fraction (3 V 80).

fraction shall be studied in detail to reveal its compositional complexity.

Analysis of the 80 °C TREF Fraction (3 V 80). The TREF fractionation of the bulk sample is presented in Figure 8. As has been discussed previously, the 30 °C TREF fraction contains mainly the EP rubber while the 100−130 °C TREF fractions contain mainly iPP.[11]

The molar mass distributions for the bulk sample 3 V and its 80 °C TREF fraction are compared in Figure 9. The 80 °C fraction shows a clear bimodality in MMD, which indicates compositional heterogeneity due to the coelution (from TREF) of nonidentical components. Multimodal distributions are often observed for these midelution temperature TREF fractions due to the coelution of semicrystalline EPCs and PP homopolymers, due to the tacticity distribution of PP.[11] The PP homopolymer does not elute entirely at temperatures >100 °C due to the fact that chains of lower tacticity become soluble at the same lower temperatures as the EPC phase of similar solubility.

dx.doi.org/10.1021/ma2026989 | Macromolecules 2012, 45, 2025−2034

TREF-SEC does not supply information on the chemical composition of these TREF fraction. It is clear that even the knowledge of MMD available from SEC analysis for the 80 °C TREF fraction is not sufficient to define the compositional heterogeneity, since SEC separates polymers according to the hydrodynamic volume of the molecules. It is important to understand the exact nature of the molecular species in this important fraction since they affect thermal, mechanical, and optical properties by the way they constitute the various phases present after cooling, like crystalline, amorphous, and possible rigid amorphous phases etc. In addition, on the molecular level, with respect to mechanical properties, the crystallites and their connections play an important role; such organization strongly depends on the way of crystallization as determined by the molecular architecture and the cooling conditions.

Two melt endotherms were observed for the 80 °C TREF fraction by standard DSC analysis, see Figure 10, which

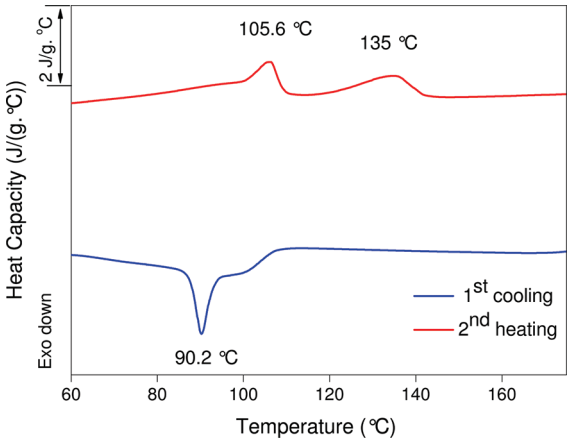

Figure 10. Two DSC melt endotherms present in the 80 °C TREF fraction (3 V 80). Heating and cooling rates were 10 °C/min.

indicates the compositional heterogeneity in the midtemperature eluting fraction. It is impossible to assign the melting endotherms from the standard DSC technique, for this specific complex TREF fraction, to a chain structure, since a single peak could result from one component overruling others, as is seen in the case of the bulk material. Possibly, one of the melting endotherms is due to the propylene rich segments of the EPC, while the other is due to the melting of the ethylene rich segments, crystallized in their respective crystal structures. However, due to variations in the tacticity of polypropylene, as well as comonomer content for the copolymers, it is possible that either monomer type could melt at both the observed temperatures. A more in-depth analysis is needed in order to assign the crystallization and melting transitions to particular chain types.

SEC-FTIR (Figure 11), has been used for the determination of the chemical composition and crystallinity distributions across the molar mass distribution for fraction 3 V 80. The fraction exhibits a gradual increase in the CH_3/CH_2 ratio (Figure 11a) across the bimodal molar mass distribution, indicating higher propylene content within the low molar mass component. The 720 cm^{-1}/1162 cm^{-1} area ratio (Figure 11b) of this fraction indicates the presence of ethylene within the higher molar mass component only. The 998 cm^{-1}/972 cm^{-1} ratio (Figure 11c) is essentially zero for low retention volumes and increases only at higher retention volumes where the low molar mass component of the fraction elutes which is revealed to be mostly polypropylene. Ethylene crystallinity (Figure 11d) is only observed at low elution volumes. It is concluded that the lower molar mass component of the bimodal distributions consists principally of propylene homopolymer only; whereas EPC's with different monomer distributions and longer crystallizable ethylene sequences are present within the higher molar mass component.

TREF-(SEC-HPer DSC) turns out to be an excellent tool for probing the crystallization and melting effects observed for complex polymer mixtures. What is difficult to realize with standard DSC is relatively easily revealed by the HPer DSC analysis of the TREF-SEC fractions as seen in Figure 12. All of the first three (high molar mass) SEC fractions have broad melting endotherms, indicating that these fractions probably contain a complex mixture of ethylene-propylene copolymers, possibly ethylene-rich copolymers and/or segmented EP copolymers; possible branched to almost linear, semicrystalline polyethylene, and finally, possibly low tacticity polypropylene homopolymer. This is in agreement with the SEC-FTIR results (Figure 11), which show that the copolymers which are richest in ethylene elute at low retention times (higher molar mass) and that there is a gradual increase in the propylene concentration with increasing retention time (decreasing molar mass). Crystalline polypropylene is found within the low molar mass fraction while crystalline polyethylene or PE segments of segmented EP copolymers are found in the higher molar mass fraction.

SEC fractions (Figures 12 and 13) at retention times of 16 to 22 min show a melting peak in the range of 103 to 107 °C (lower than T_m of HDPE and T_m of iPP). This suggests that there are insufficiently long iPP or PE segments to form highly stable crystallites of appreciable dimensions and perfection dissolving at 80 °C during TREF and eluting in this specific molar mass region of the TREF fraction.[46] SEC-FTIR results indicate that this fraction contains ethylene−propylene copolymers to a significant extent, with mainly longer ethylene sequences. Increasing melting temperature with retention time is observed even for late eluting fractions. SEC fractions eluting between 22 and 26.5 min show melting endotherms at 135 and 130 °C, respectively. The SEC-FTIR data (Figure 11) indicate the presence of high amounts of propylene in these fractions, with little or no ethylene present. These SEC fractions contain mostly propylene-rich copolymers or polypropylene homopolymers with lower tacticity and molar mass, which probably results in the formation of crystallites with reduced lamellar thickness and lower perfection as compared to highly crystalline iPP.[47−49] The lower tacticity and by that lower crystallizability is quite obvious if one compares the maximum peak temperatures of melting in this range of e.g. a molar mass fraction of 10000 g/mol (approximately 135 °C for the present case) with the one for the bulk sample 3 V 0 h (approximately 150 °C).

Finally, it has to be pointed out that the data as obtained by SEC-FTIR in principle have to be compared with the results obtained from the first heating experiment of the DSC, because then the thermal and sample histories by deposition on the disk are the same. For the present qualitative discussion, however, using the results from the second heating curves is acceptable because these are qualitatively analogous to the first heating curves; see Figures 7 and 13.

It is evident from the TREF-(SEC-FTIR) and TREF-(SEC-HPer DSC) results that there is an overlapping of EPC with

dx.doi.org/10.1021/ma2026989 | Macromolecules 2012, 45, 2025−2034

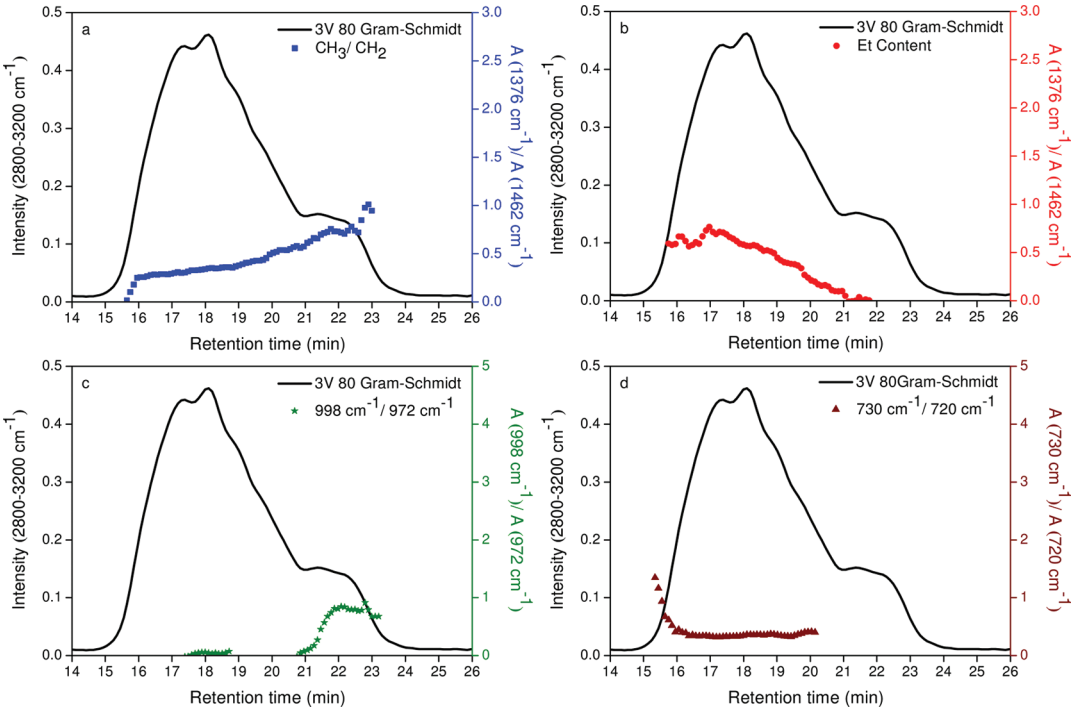

Figure 11. SEC-FTIR analysis of fraction 3 V 80, illustrating (a) the propylene (CH_3/CH_2) and (b) the ethylene (Et content) distributions as well as their crystallinity distributions (c and d), respectively.

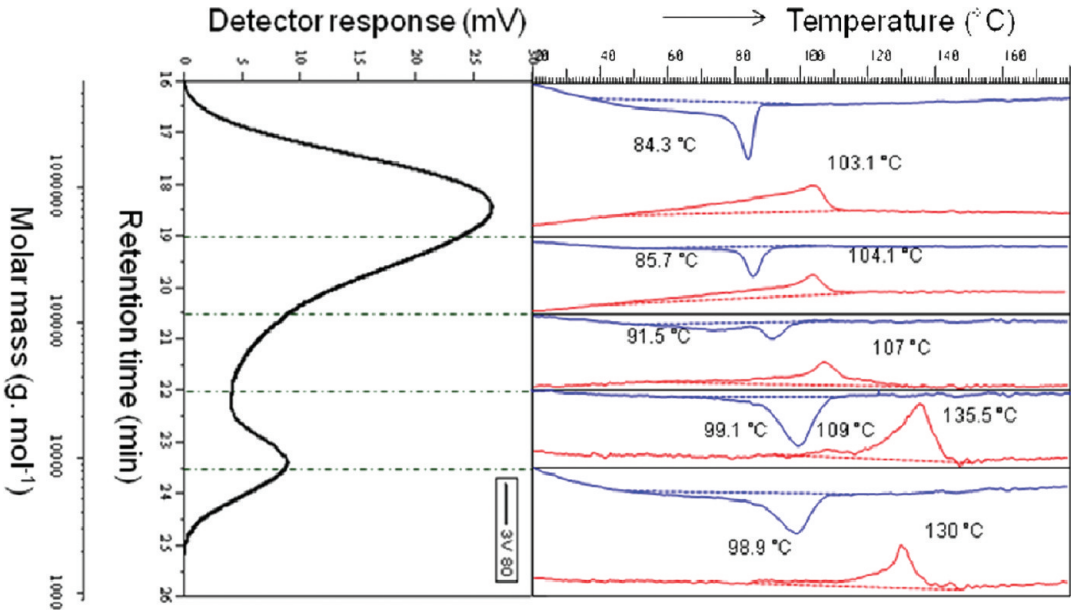

Figure 12. SEC curve of fraction 3 V 80 showing the retention time axis and molar mass axis, as well as the HPer DSC cooling and heating curves for the SEC fractions as "retention time boxes". HPer DSC scan rates were 50 °C/min.

iPP due to the tacticity distribution for this midelution temperature fraction (3 V 80). A complete separation of these components according to the chemical composition by using TREF is not possible, undoubtedly also due to cocrystallization of the components at the same temperature. Separation of blends of polyolefins containing iPP, sPP, aPP, and PE on a Hypercarb stationary phase with a gradient from 1-decanol to TCB has been previously reported.[23,50] In order to further investigate the 80 °C TREF fraction and confirm the results obtained from HPer DSC we separated the components in this fraction of an IPC sample using the same method reported for the blend. The results of this separation are given in Figure 14.

The low molar mass isotactic PP elutes in 100% 1-decanol at approximately 1.5 mL, followed by the retained iPP components that are desorbed by the gradient. Although the chemical composition is the primary parameter and governs the separation, the molar mass of the components also plays a role, especially for low molar masses. The EPC and linear PE are also fully retained due to their selective adsorption on the column packing, being only eluted in the gradient. It can be seen that the Hypercarb column is very selective with respect to

dx.doi.org/10.1021/ma2026989 | Macromolecules 2012, 45, 2025−2034

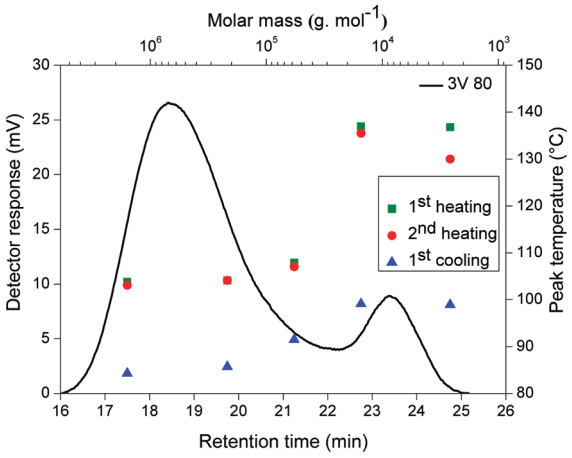

Figure 13. SEC curve of fraction 3 V 80 showing the retention time axis and molar mass axis, indicating the peak maximum temperatures of the HPer DSC cooling and heating curves for the SEC fractions at 50 °C/min.

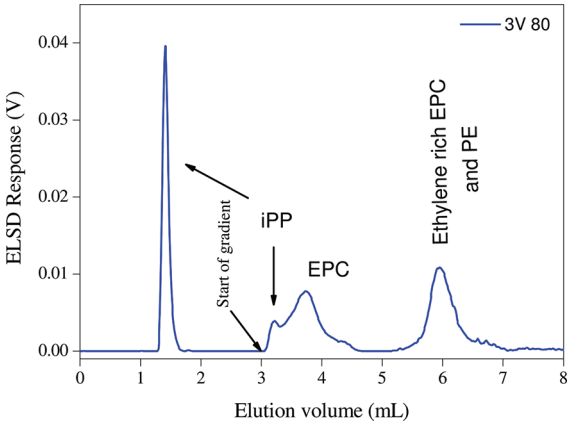

Figure 14. Chromatogram obtained after isocratic and gradient elution for fraction 3 V 80.

the chemical composition of the polymers, differentiating even with respect to their microstructure.

In order to study the influence of the molar mass of the components on the elution volume in HPLC, the fraction 3 V 80 was analyzed by HT-2D-LC. The corresponding contour plot is presented in Figure 15.

All components of fraction 3 V 80 are well separated from each other by both chemical composition and molar mass. It can be seen that the iPP has a lower molar mass component which elutes in pure 1-decanol and a second slightly higher molar mass component eluting in the gradient.[44] While EPC with different ethylene and propylene sequences as well as PE homopolymer having similar molar masses eluted according to their interaction on the Hypercarb column. There is a clear separation between the iPP and EPC copolymers. EPC dominated by longer propylene sequences elute closer to iPP while those dominated by longer ethylene sequences elute together with PE homopolymer (eluting at approximately 6.0 mL). As a result the HT-2D-LC represents a complete characterization of this TREF fraction in terms of both molar mass and chemical composition, accomplished within a relatively short analysis time.

The ethylene−propylene random/segmented copolymers (which constitute the bulk of the midelution TREF fractions)

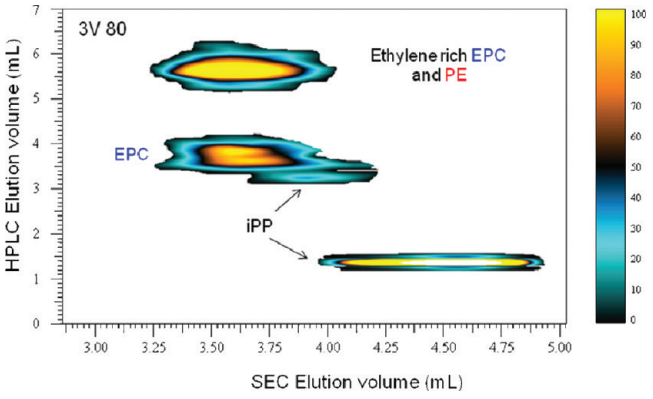

Figure 15. HT-2D-LC contour plot for the fraction 3 V 80.

improve the adhesion between the EPR phase and the iPP matrix by acting as a compatibiliser between the phases. Therefore, the role of such fractions is very important for the overall properties of impact copolymers. From an analytical point of view, SEC-HPer DSC yields further insight into the thermal and mechanical properties of such complex materials, while HT-HPLC can completely separate the components in the midelution temperature fractions according to their chemical composition. Thus, these techniques are found to be very important for the industrial, as well as academic fields.

CONCLUSIONS

The molecular characteristics (molar mass, chemical composition, and tacticity distributions) and thermal behavior (melting and crystallization) of a commercial impact polypropylene and its midelution temperature TREF fraction were investigated using various multidimensional analytical techniques such as SEC-FTIR, SEC-HPer DSC, and high temperature two-dimensional liquid chromatography. Analysis of the bulk sample by the above-mentioned techniques does not provide any in-depth information regarding the chemical composition and thermal behavior of the various components in this complex polymer system. For this reason, fractionation of the bulk sample and a more detailed study on one of the midelution temperature TREF fractions has been carried out in order to identify the complex components in the total polymer system and evaluate their effect on the thermal properties.

SEC-FTIR results indicate the presence of EPC copolymer and iPP homopolymer as the main constituents of the 80 °C TREF fraction. The crystallinity distribution of ethylene and propylene across the MMD by this technique indicates the presence of crystallizable ethylene sequences in the high molar mass component, with highly crystalline PP being found in the low molar mass component. Thermal analysis of the SEC fractions by HPer DSC provides information on the thermal properties of the different molar mass fractions, and, thereby, the compositional heterogeneity of the components. SEC-HPer DSC results also confirm the presence of EPC copolymers with crystalline sequences of ethylene and propylene with varying sequence lengths as well as ethylene homopolymers in the high molar mass SEC fractions, while crystalline PP homopolymer is found in the low molar mass SEC fractions. The ability to measure the thermal behavior of very small sample masses (SEC fractions) with HPer DSC enables the investigation of the thermal properties across the MMD of this complex midelution temperature TREF fraction. The combination of the two cross-fractionation techniques is found to be highly useful

dx.doi.org/10.1021/ma2026989 | Macromolecules 2012, 45, 2025−2034

for the mapping of the CCD across the molar mass slices for these complex TREF fractions.

The presence of PE homopolymer and EPCs containing long ethylene sequences in the 80 °C TREF fraction was proven by HT-HPLC. This is the first time that individual components in the midelution temperature TREF fraction of an IPC were separated according to their chemical composition using high temperature solvent gradient HPLC, which is based on the selective adsorption and desorption of the polymer molecules on a Hypercarb stationary phase at 160 °C. Finally, a complete separation of each component according to their chemical composition and molar mass was achieved through HT-2D-LC. The overall results demonstrate that these multidimensional techniques are found to be excellent analytical tools, necessary for a proper understanding of the molecular characteristics and thermal behavior of complex polymer fractions.

AUTHOR INFORMATION

Corresponding Author

*E-mail: hpasch@sun.ac.za.

Notes

The authors declare no competing financial interest.

ACKNOWLEDGMENTS

The involvement of PerkinElmer UK/USA is much appreciated by T.P. and V.M. Also the support for SciTe from the EU-FP7-NaPolyNet/Coordination Support Action NMP-2007-2.1-3/ Characterization of nanostructured materials, see http://www.napolynet.eu, is highly valued.

REFERENCES

(1) Maier, C.; Calafut, T. Polypropylene, The Definitive User's Guide and Databook. In *Polypropylene*; Plastics Design Library; Elsevier Inc.: Amsterdam, 1998; pp 11−25.

(2) Galli, P.; Haylock, J. C.; Simonazzi, T. Manufacturing and Properties of Polypropylene Copolymers. In *Polypropylene: Structure Blends and Composites*, Karger-Kocsis, J., Ed.; Chapman & Hall: London, 1995; Vol. 2, p 1.

(3) Tortorella, N.; Beatty, C. L. *Polym. Eng. Sci.* **2008**, *48*, 1476−148.

(4) Fan, Z. Q.; Zhang, Y. Q.; Xu, J. T.; Wang, H. T.; Feng, L. X. *Polymer* **2001**, *42*, 5559−5566.

(5) Tan, H.; Li, L.; Chen, Z.; Song, Y.; Zheng, Q. *Polymer* **2005**, *46*, 3522−3527.

(6) Hongjun, C.; Xiaolie, L.; Dezhu, M.; Jianmin, W.; Hongsheng, T. *J. Appl. Polym. Sci.* **1999**, *71*, 93−101.

(7) Francis, M.; Mirabella Jr. *Polymer* **1993**, *34*, 1729−1735.

(8) Xue, Y.; Fan, Y.; Shuqin, B.; Xiangling, J. *Eur. Polym. J.* **2011**, *47*, 1646−1653.

(9) Zacur, R.; Goizueta, G.; Capiati, N. *Polym. Eng. Sci.* **1999**, *39*, 921−929.

(10) Rafael, A.; García, B. C.; María-Teresa, E.; Inmaculada, S.; Almudena, F.; Caveda, S. *Macromol. Res.* **2011**, *19*, 778−788.

(11) de Goede, E.; Mallon, P.; Pasch, H. *Macromol. Mater. Eng.* **2010**, *295*, 366−373.

(12) Karger, K. J.; Kallo, A.; Szafner, A.; Bodor, G. *Polymer* **1979**, *20*, 37−43.

(13) Zhisheng, F.; Junting, X.; Yanzhong, Z.; Zhiqiang, F. *J. Appl. Polym. Sci.* **2005**, *97*, 640−647.

(14) Hongjun, L. C.; Xiaolie, M. D.; Jianmin, W.; Hongsheng, T. *J. Appl. Polym. Sci.* **1999**, *71*, 103−113.

(15) Luruli, N.; Pijpers, T.; Brüll, R.; Grumel, V.; Pasch, H.; Mathot, V. *J. Polym. Sci., Part B: Polym. Phys.* **2007**, *45*, 2956−2965.

(16) Mathot, V. B. F.: The Crystallization and Melting Region. In *Calorimetry and Thermal Analysis of Polymers*: Mathot, V. B. F., Ed.; Hanser Publishers: Munich/Vienna/New York, 1994; Chapter 9, pp 231−299.

(17) Krumme, A.; Basiura, M.; Pijpers, T.; Poel, G. V.; Heinz, L. C.; Brüll, R.; Mathot, V. B. F. *Mater. Sci.* **2011**, *17* (3), 260−265.

(18) Poel, G. V.; Mathot, V. B. F. *Thermochim. Acta* **2007**, *461*, 107−121.

(19) Pasch, H.; Trathnigg, B. *HPLC of Polymers*, 1st ed.; Springer: Berlin, 1998.

(20) Heinz, L. C.; Pasch, H. *Polymer* **2005**, *46*, 12040−12045.

(21) Macko, T.; Pasch, H.; Brüll, R. *J. Chromatogr. A* **2006**, *111*, 81−87.

(22) Macko, T.; Denayer, J. F.; Pasch, H.; Baron, G. V. *J. Sep. Sci.* **2003**, *26*, 1569−1574.

(23) Macko, T.; Pasch, H. *Macromolecules* **2009**, *42*, 6063−6067.

(24) Pereira, L. *J. Liq. Chromatogr. Related Technol.* **2008**, *31*, 1687−1731.

(25) Albrecht, A.; Heinz, L. C.; Dieter, L.; Pasch, H. *Macromol. Symp.* **2007**, *257*, 46−55.

(26) Macko, T.; Brüll, R.; Alamo, G.; Thomann, Y.; Grumel, V. *Polymer* **2009**, *50*, 5443−5448.

(27) Macko, T.; Cutillo, F.; Busico, V.; Brüll, R. *Macromol. Symp.* **2010**, *298*, 182−190.

(28) Dolle, V.; Albrecht, A.; Brüll, R.; Macko, T. *Macromol. Chem. Phys.* **2011**, *212*, 959−970.

(29) Chitta, R.; Macko, T.; Brüll, R.; Doremaele, G. V.; Heinz, L. C. *J. Polym. Sci., Part A: Polym. Chem.* **2011**, *49*, 1840−1846.

(30) Macko, T.; R. Brüll, R.; Alamo, R. G.; Stadler, F. J.; Losio, S. *Anal. Bioanal. Chem.* **2011**, *399*, 1547−1556.

(31) Cong, R.; deGroot, W.; Parrott, Al.; Yau, W.; Hazlitt, L.; Brown, R.; Miller, M.; Zhou, Z. *Macromolecules* **2011**, *44*, 3062−3072.

(32) Zhu, W. W.; Allaway, J. R. *J. Chromatogr. A* **2004**, *1055*, 191−196.

(33) Noel, L. V.; Baldo, L.; Bremmers, S. *Polymer* **2001**, *42*, 5523−5529.

(34) Liu, M. X.; Dwyer, J. L. *Appl. Spectrosc.* **1996**, *50*, 349−356.

(35) DesLauriers, P. J.; Rohlfing, D. C.; Hsieh, E. T. *Polymer* **2002**, *43*, 159−170.

(36) Tso, C. C.; DesLauriers, P. J. *Polymer* **2004**, *45*, 2657−2663.

(37) Liang, C. Y.; Pearson, F. G. *J. Mol. Spectrosc.* **1960**, *6*, 290−306.

(38) Luongo, J. P. *J. Appl. Polym. Sci.* **1960**, *3*, 302.

(39) Andreassen, E. Infrared and Raman Spectroscopy of Polypropylene. In *Polypropylene: An A-Z reference*; Karger- Kocsis, J., Ed.; Kluwer Publishers: Dordrecht, The Netherlands, 1999; p 320.

(40) Painter, P. C.; Watzek, M.; Koenig, J. L. *Polymer* **1977**, *18*, 1169.

(41) Monasse, B.; Haudin, J. M. Molecular Structure of Polypropylene Homo- and Copolymers. In *Polypropylene: Structure, Blends and Composites*; Karger-Kocsis, J., Ed.; Chapman & Hall: London, 1995; p 3.

(42) Cossar, M.; Teh, J.; Kivisto, A.; Mackenzie, J. *Appl. Spectrosc.* **2005**, *59*, 300−304.

(43) Schick, C. *Anal. Bioanal. Chem.* **2009**, *395*, 1589−1611.

(44) Burfield, D. R. *Macromolecules* **1983**, *16*, 702−704.

(45) Ginzburg, A.; Macko, T.; Dolle, V.; Brüll, R. *Eur. Polym. J.* **2011**, *47*, 319−329.

(46) Zhang, C.; Shangguan, Y.; Chen, R.; Zheng, Q. *J. Appl. Polym. Sci.* **2011**, *119*, 1560−1566.

(47) Mahdavi, H.; Nook, M. E. *Polym. Int.* **2010**, *59*, 1701−1708.

(48) Zhang, C.; Shangguan, Y.; Chen, R.; Wu, Y.; Chen, F.; Zheng, Q.; Hu, G. *Polymer* **2010**, *51*, 4969−4977.

(49) Tan, H.; Li, L.; Chen, Z.; Songa, Y.; Zheng, Q. *Polymer* **2005**, *46*, 3522−3527.

(50) Macko, T.; Brüll, R.; Zhu, Y.; Wang, Y. *J. Sep. Sci.* **2010**, *33*, 3446−3454.

Macromolecules

Article

pubs.acs.org/Macromolecules

Composition and Long-Range Density Fluctuations in PEO/PMMA Polymer Blends: A Result of Asymmetric Component Mobility

Dietmar Schwahn,*[,†] Vitaliy Pipich,[‡] and Dieter Richter[†]

[†]Jülich Centre for Neutron Science JCNS and Institute for Complex Systems ICS, Forschungszentrum Jülich GmbH, D-52425 Jülich, Germany

[‡]Jülich Centre for Neutron Science JCNS-FRM II, Forschungszentrum Jülich GmbH, Outstation at FRM II, Lichtenbergstraße 1, D-85747 Garching, Germany

ABSTRACT: Fluctuations of density and composition were observed in the disordered regime of a symmetric poly(ethylene oxide) (PEO) and a poly(methyl methacrylate) (PMMA) polymer blend. This blend is of particular interest as the glass transition (T_G) of both polymers happens at very different temperatures thereby inducing a dynamic asymmetry in the molecular dynamics. Small-angle neutron scattering and oscillatory shear rheology were the principle experimental tools. Composition fluctuations determined the Flory–Huggins parameter as well as glass and gelation temperature (T_A). The density fluctuations are of long-range and show a mass fractal dimension whose strength enlarges below the glass transition. A fairly constant T_A about 40 K above T_G separates two regions of distinctively different fluctuation behavior. A comparison of viscoelastic plateau modulus and high frequency modulus determined from rheology and SANS show that the relaxation modes in the regime between T_G and T_A are determined by the freezing segmental modes of PMMA.

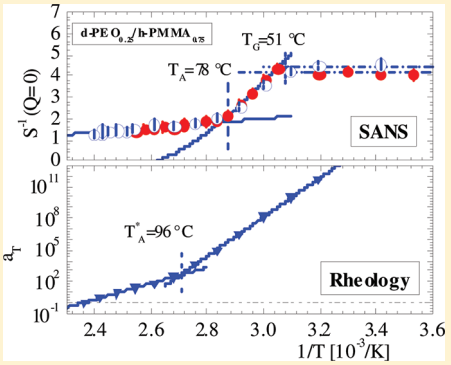

INTRODUCTION

The phase behavior of homopolymer blends is fairly well described by the Flory–Huggins theory. This mean-field theory is characterized by the Flory–Huggins (FH) interaction parameter, the molar volume and concentration of the polymer chains. Only in the near neighborhood of the critical point of phase decomposition, depending on the Ginzburg number, deviations from the mean-field approach become relevant.[1−3] The FH parameter is derived from the degree of thermal composition fluctuations in the miscible regime using scattering techniques such as small angle neutron scattering (SANS). The random phase approximation (RPA) represents a theoretical basis to interpret the SANS data in terms of the Flory–Huggins theory.[1−3]

Here we present a SANS study on the binary polymer blend poly(ethylene oxide) (PEO) and poly(methyl methacrylate) (PMMA). The particular interest of this blend stems from the large difference of the glass transition temperatures T_G of the two components that are about +121 and −57 °C for the PMMA and PEO polymer melt, respectively.[4] There are several studies of T_G in PEO/PMMA mainly determined with differential scanning calorimetry (DSC). Fernandes et al. published T_G data and a phase diagram of a 300 kDa PEO and 130 kDa PMMA blend showing miscibility at low temperatures with indication of phase decomposition at high temperatures, e.g., a lower critical solution temperature (LCST) phase diagram with a critical temperature at about 230 °C and 60% PEO concentration.[5] The phase boundary was determined by cloud point analysis. Polymer blends in the mixed state usually show a single T_G which usually agrees with the interpolated single component values via the Fox–Flory equation (p 243 in ref 6). Later differential DSC, however, showed two calorimetric glass transition temperatures in spite of macroscopic miscibility, an upper T_G between 121 and 30 °C depending on PEO concentration in the regime of $0 < \Phi_{PEO} < 0.40$ and a nearly constant T_G at about −57 °C.[4,7] The two glass transition temperatures are consistent with deuterium NMR experiments[8] observing a PEO segmental dynamics which only weakly depends on PEO concentration and is several orders of magnitude faster than the PMMA segments, thereby suggesting a decoupling of the PEO segmental motion from the PMMA matrix even below the upper T_G. This implies that the PEO component is still mobile when passing the upper T_G and freezes when passing the lower T_G at −57 °C. The terminal dynamics of the PEO chains in PMMA was explored with forced Rayleigh scattering[9] and was found to differ from the PEO segmental dynamics, and appeared to be coupled with the PMMA matrix. The dynamics of PEO in PMMA was also explored with neutron spectroscopy as reported by Colmenero and Arbe[10] and by Niedzwiedz et al.[11] In particular neutron spin echo (NSE) experiments determined the mobility of the PEO segments in a seemingly frozen PMMA matrix.[11] The mobility of the PEO segments was interpreted by a random

Received: August 22, 2011
Revised: January 24, 2012
Published: February 7, 2012

mobility rather than by random obstacles imposed by the PMMA.

So far thermal composition fluctuations and thereby the FH parameter of PEO/PMMA were explored by two groups using SANS. Hopkinson et al. extracted the FH interaction parameter of a 100 kDa PEO/PMMA blend in a temperature range of 150−200 °C from which they proposed phase separation below 77 °C thereby predicting an upper critical solution temperature (UCST).[12] Another study by Ito et al. on a 100 kDa PEO/PMMA blend of varying PEO concentration was performed at fixed temperature of 80 °C.[13] These authors found a small but negative FH parameter indicating blend miscibility, whereas a decision of LCST or UCST behavior was not possible because of missing a temperature dependent FH parameter. Both SANS experiments were performed at temperatures too far above the glass transition line to become sensitive to the phenomenon of "dynamical asymmetry".

Near the glass transition the phenomenon of "dynamical asymmetry" strongly influences the phase behavior as the stress field caused by the freezing component strongly couples to the order parameter fluctuations. A theory on dynamical asymmetry has been worked out by Doi and Onuki.[14,15] Experimentally the effect of dynamical asymmetry was observed on a polystyrene/poly(vinyl methyl ether (PS/PVME) blend that also exhibits a large difference of the glass transition temperature T_G and is of the LCST type. A strong suppression of thermal composition fluctuations happens if T_G is approached from above.[16−18] Another phenomenon is the observation of "dynamical heterogeneities". In PS/PVME heterogeneities of size less than 50 Å have been reported from ^{1}H and ^{13}C NMR experiments[19] whereas for PEO/PMMA similar heterogeneous regions of length between 20 and 500 Å were reported from experiments of ^{13}C and ^{129}Xe NMR.[20] Those heterogeneous regions are characterized by molecules of different mobility in comparison with the surrounding area whose origin with respect to a structural relationship is not clear.[21]

In this work we display a detailed SANS study on a symmetric PEO/PMMA blend of 25 kDa molar weight, with PEO concentrations between 10 and 25% and temperatures between 10 and 150 °C that was completed by oscillatory shear experiments on two selected samples. Our studies undoubtedly confirm the miscibility of the PEO/PMMA blend and show that this system belongs to the class of LCST blends. The phase boundary of the present Φ_{PEO} = 0.25 blend was estimated roughly at 400 °C. At PEO concentrations larger than 30% the blend crystallizes below 57 °C. This concentration regime is not covered as the process of crystallization is not part of the present study. We also found an isotope effect on the upper glass transition temperature; h-PEO/d-PMMA shows a lower T_G by about 25 K than the d-PEO/h-PMMA blend. Such isotope effect was not observed for the single PMMA component.

Above the upper glass temperature T_G a region of dynamical asymmetry is found that is characterized by an enhanced reduction of thermal composition fluctuations below a gelation temperature T_A. This temperature is nearly independent of PEO concentration in spite of the strong decrease of T_G with PEO concentration. Below the T_G-line the composition fluctuations are frozen even though the PEO is still mobile. A similar entering temperature to the region of "dynamical asymmetry" was identified from dynamical mechanical spectroscopy separating relaxation regimes of very different activation energy.

Independent from thermal composition fluctuations we also observed long-range fluctuations. These fluctuations were identified as density fluctuations in a particularly prepared sample of large averaged scattering length density and zero scattering contrast for thermal composition fluctuations. Regions of slight mass density or polymer packing variation between 600 and 700 Å of radius of gyration were observed over the whole temperature regime above T_G giving rise to an intensity which is orders of magnitude larger than estimated from compressibility. These structures start to grow when entering the glass regime. So far, cluster of similar scattering characteristics were observed in glass forming single polymer melts by the group of Fischer[22] and theoretically interpreted by several authors.[23−26] We have here the situation of two phenomena in the same system whose interrelations might illuminate some aspects of the phenomenon of glass transition.

This manuscript is organized as follows. First, we give a short description of the underlying theoretical models as the scattering functions that connect the thermodynamic parameters of the FH theory with the conformation of the participating polymer chains. Then the relevant expressions for the FH parameter when dynamical asymmetry becomes effective are displayed. The theoretical section is followed by presentation and analysis of the experimental data.

THEORETICAL BACKGROUND

Scattering Functions. This manuscript reports the exploration of thermal composition fluctuations as well as long-range density fluctuations and the conformation of both chains in the PEO/PMMA blend using the technique of small angle neutron scattering (SANS). A study of these phenomena requires blends of appropriate scattering contrast that have to be prepared by mixing polymer components of the proper hydrogen (H) and deuterium (D) contents. Table 2 (Appendix) compiles the relevant parameters, in particular, the coherent scattering length density of the polymer components. The two-component h-PEO/d-PMMA (h-protonated; d-deuterated) and d-PEO/h-PMMA blends were chosen to explore thermal composition fluctuations and for example the three-component h-PEO/d-PEO/h-PMMA blend to determine the conformation of the PEO component as well as density fluctuations in this blend (Table 3 in Appendix). We analyzed the scattering, i.e. the macroscopic cross-section $d\Sigma/d\Omega(Q)$ from thermal composition fluctuations with the expression

$$\frac{d\Sigma}{d\Omega}(Q) = [1/S^0_{PEO}(Q) + 1/S^0_{PMMA}(Q) - 2\Gamma]^{-1}\Delta\rho_{comp}{}^2/N_A + c(1-c)S_i^0(Q)\Delta\rho_i{}^2/N_A \quad (1)$$

Equation 1 is derived on the basis of the random phase approximation (RPA) for binary polymer blends with one component consisting of deuterated and protonated chains (i.e., a three component system) and assuming incompressibility (see section 3 of ref 27), which is the appropriate expression for samples S3−S6 (Table 3). $d\Sigma/d\Omega(Q)$ is a function of the magnitude of the wave vector $\mathbf{Q}$, which according to $Q = (4\pi/\lambda)\sin(\theta/2)$ is proportional to the scattering angle θ and inversely proportional to the neutron wavelength λ. The first term describes thermal composition fluctuations in terms of the RPA which should be a realistic

description as thermal composition fluctuations are small for the present system.[3] The second term describes scattering of the form factor of the PEO or PMMA chains (i = PEO or PMMA). The form factor of the PEO and PMMA chains $S^0_{PEO}(Q)$ and $S^0_{PMMA}(Q)$ is determined according to $S^0_i(Q) = \Phi_i V_i P_i(QR^i_g)$ by the chain volume fraction Φ_i, the molar volume V_i, the Debye form factor $P_i(Q)$. Parameter c in the second term of eq 1 describes the relative fraction of the protonated or deuterated chains. Thereby it is assumed that the chains follow Gaussian chain statistics, whose size is determined by the corresponding radius of gyration R_g. The interaction parameter Γ represents the Flory–Huggins interaction parameter χ normalized with the reference monomer volume $\Omega_0 = (\Omega_{PEO}\,\Omega_{PMMA})^{1/2}$ according to $\Gamma = \chi/\Omega_0$. The square of the parameters $\Delta\rho_{comp} = \overline{\rho}_{PEO} - \overline{\rho}_{PMMA}$ and $\Delta\rho = (\rho_{d-i} - \rho_{h-i})$, respectively, represent the scattering contrast of thermal composition fluctuations and of the single chain form factor; N_A is the Avogadro number.

The first term of eq 1 describes thermal composition fluctuations of the blend. The scattering contrast is determined by the mean coherent scattering length density of the deuterated and protonated component i according to $\overline{\rho}_i = c\rho_{h-i} + (1 - c)\rho_{d-i}$. In case of $c = 0$ or 1, i.e., of purely protonated or deuterated components such as h-PEO/d-PMMA or d-PEO/h-PMMA, one measures the well-known structure function of binary blends

$$S^{-1}(Q) = 1/S^0_{PEO}(Q) + 1/S^0_{PMMA}(Q) - 2\Gamma \tag{2}$$

This expression was fitted to the scattering patterns of the PEO/PMMA blends with Γ as fit parameters. It has to be mentioned that according to the fluctuation–dissipation theorem the inverse susceptibility $S^{-1}(0)$ is related to the second derivative of the Gibbs free energy of mixing with respect to the order parameter $\Phi = \Phi_{PEO}$ $\{\partial_\Phi{}^2(\Delta G/RT)\}$, thereby connecting the mean-field Flory–Huggins theory with the scattering experiment.[1] The second term in eq 1 represents the form factor of either the PEO or PMMA chain, which in the range of $Q \leq 1/R_g$ can be simplified by the Zimm approximation

$$1/S^0_i(Q) = (\Phi_i\overline{V}_i)^{-1}[1 + (R^i_g Q)^2/3] \tag{3}$$

From the extrapolated scattering to $Q = 0$ the chain molar volume ($\overline{V}_i = V_{h-i}\,V_{d-i}/(cV_{h-i} + (1-c)V_{d-i})$) and total volume fraction, (i.e., protonated plus deuterated chain) is derived whereas the Q dependence gives the radius of gyration.

Scattering from compressibility is induced by density fluctuations and described at $Q = 0$ according to:

$$\frac{d\Sigma}{d\Omega}(Q = 0) = k_B T \beta_T \langle\rho\rangle^2 \tag{4}$$

with the sample averaged coherent scattering length density $\langle\rho\rangle = \Phi_{PEO}\,\overline{\rho}_{PEO} + (1 - \Phi_{PEO})\,\overline{\rho}_{PMMA}$, the isothermal compressibility $\beta_T = -\partial[\ln V]/\partial P|_T$ (V sample volume), and the Boltzmann constant k_B (eq 7.13 of ref 28). The expression $k_B T\beta_T = \langle\Delta V^2\rangle/V$ is related to the mean squared variation of volume per volume. The compressibility of the PEO/PMMA blend is found in literature.[29] For $\Phi_{PEO} = 0.25$ one finds a linear temperature dependence according to β_T [1/GPa] = {(0.153 ± 0.008) + (2.93 ± 0.08) × $10^{-3}T$ [°C]}, which, in case of a fully deuterated PEO/PMMA blend of $\Phi_{PEO} = 0.25$ ($\langle\rho\rangle$ last column in Table 3 delivers a scattering of 3.5 × 10^{-3} cm^{-1} and 1.45 × 10^{-2} cm^{-1} at 10 and 140 °C, respectively). In our experiments we observed surprisingly large scattering (4 to 6 order of magnitude larger) from density fluctuations which we analyzed with a scattering function that combines Guiniers' and power law scattering at low and large Q, respectively

$$\frac{d\Sigma}{d\Omega}(Q) = \frac{d\Sigma}{d\Omega}(0)\exp(-u^2/3) + P_\alpha[(\mathrm{erf}(u/\sqrt{6}))^3/Q]^\alpha \tag{5}$$

with $u = R_g Q$, scaling exponent α and corresponding amplitude P_α. The erf(u) accounts for the validity of the underlying approximations within their Q ranges.[30] Equation 5 describes the scattering of sample S3 which by the choice of scattering contrast is only sensitive to density fluctuations.

Summing up, we describe the scattering from composition and density fluctuations as independent phenomena. This procedure is supported by basic consideration of the scattering at $Q = 0$ finding a decoupling of density and composition fluctuations, i.e., the additivity of the scattering from compressibility and composition fluctuations (chapter 7.2 of ref 28). The scattering function from density and composition fluctuations in polymer blends are also considered within the RPA avoiding the restriction of incompressibility. The obtained expressions as in ref 31 (eqs 27 and 28a) look rather complicated and deliver a Flory–Huggins parameter, which does not represent a thermodynamic number, in conflict with the fluctuation–dissipation theorem.

Thermodynamics of Blends and Viscoelastic Coupling. PEO/PMMA shows a strong asymmetry with respect to their self-diffusion coefficients leading to a viscoelastic coupling between stress and diffusion as mainly worked out by Onuki.[14,15] An asymmetry parameter $\varepsilon = (N_A D_A - N_B D_B)/(\Phi_B N_A D_A + \Phi_A N_B D_B)$ is defined from the self-diffusion constants $D_i = k_B T/(\Omega_i \zeta_{0i} N_i)$ and $D_i = k_B T N_e/(\Omega_i \zeta_{0i} N_i^2)$for Rouse and reptation model, respectively.[32] The diffusion constants are proportional to $k_B T$ and inversely proportional to friction coefficient ζ_{0i}, degree of polymerization N_i, and molar monomer volume Ω_i. N_e is the characteristic degree of polymerization between entanglements. The asymmetry parameter can be approximated as $\varepsilon \cong 1/\Phi_{PMMA}$ because of $N_{PEO} \cong N_{PMMA}$ and $\zeta_{0,PMMA} \gg \zeta_{0,PEO}$ ($D_{PMMA} \ll D_{PEO}$). In those systems a "dynamically coupling" situation between diffusion and stress field comes into existence. A stress field built up in a network of entangled polymers by means of their frictions acts differently on the two components with the result of relative motion between them. PEO/PMMA is special insofar as the stress field mainly acts on the PMMA component because of its large dynamical asymmetry. This means that the stress field is only build up by the weakly entangled PMMA chains in a similar way as in polymer solutions. The constitutive equation then relates according to $\sigma_{ij}(t) = \int_{-\infty}^{t} dt'\, G(t - t')\kappa^P_{ij}(t')$ the network stress field tensor $\sigma_{ij}(t)$ with the velocity gradient tensor $\kappa^P_{ij}(t)$ of the PMMA chains and the modulus $G(t)$. This linear relationship is valid for small network deformations on spatial scale larger than the radius of gyration.

A characteristic temperature, the gelation temperature T_A, is defined when the relaxation rate of thermal composition fluctuations, R_Q, and of the stress fields of entangled polymer network, $1/\tau_R$, become similar: i.e., below T_A the equilibration of thermal composition fluctuation becomes faster than the relaxation process of the network stress field. The relaxation rate of thermal composition fluctuations $R_Q = \Lambda(Q)Q^2S^{-1}(Q)$ is determined by the structure factor $S^{-1}(Q) = S^{-1}(0) + AQ^2$ (eq 2) and the kinetic Onsager coefficient $\Lambda(Q)$ ($\Lambda(Q)$ for

dx.doi.org/10.1021/ma2019123 | Macromolecules 2012, 45, 2035–2049

polymer blends see ref 2). Considering the extreme case of $R_Q \ll 1/\tau_R$, i.e., stress relaxation much faster than equilibration of thermal composition fluctuations, one has the relaxation rate

$$R_{eff}(Q) = \Lambda(Q)Q^2S^{-1}(Q)/(1 + \xi_{VE}{}^2Q^2) \quad (6)$$

with the viscoelastic length $\xi_{VE} = ((4/3)\Lambda(Q=0)\varepsilon^2\eta)^{1/2}$ ($\omega \ll 1/\tau_R$ delivers zero-shear viscosity $\eta^*(\omega) \cong \eta$) thereby renormalizing the Onsager coefficient but do not change $S(Q)$. In case the equilibration rate of thermal composition fluctuations is much faster than the stress relaxation, i.e., $R_Q \gg 1/\tau_R$, we get the relaxation rate of a gel ($\omega \gg 1/\tau_R$ delivers $\eta^*(\omega) \cong G/i\omega$),

$$R_{Gel}(Q) = \Lambda(Q)Q^2\{[S^{-1}(0) + (4/3)\varepsilon^2G] + AQ^2\} \quad (7)$$

with a revised structure factor $S^{-1}(Q) = [S^{-1}(0) + (4/3)\varepsilon^2G] + AQ^2$ and the modulus G for frequencies $\omega \gg 1/\tau_R$ (a detailed derivation of eqs 6 and 7 is found in section 7.1.6 of ref 15 and reviewed in refs 33 and17). The corresponding FH parameter with the FH parameters Γ from above T_A can be written as

$$\Gamma^* = \Gamma - 2\varepsilon^2(G/RT)/3. \quad (8)$$

Glass Transition of Dynamical Asymmetrical Polymer Blends. The glass transition temperature of a polymer blend is usually analyzed in terms of the Fox equation, interpolating the T_G's of the components.[34] Various relationships of T_G in blends were developed considering the FH interaction parameter and addressing the glass transition as a second order phase transition.[35−39] Painter et al. discussed the effects of strong specific interactions such as hydrogen bonds on T_G,[39] but this mode of interaction apparently does not play a role in PEO/PMMA as there are no proton donors present and IR-spectroscopy measurements in our laboratory also excluded this kind of interaction. The phase behavior of PEO/PMMA is governed by interactions of polar type (see p85 in ref 40). An analysis of the theory by Couchman and Karasz resultet in (eq 3 in ref 36)

$$\ln T_{G,CK} = \frac{w_{PEO} \ln T_{G,PEO} + kw_{PMMA} \ln T_{G,PMMA}}{w_{PEO} + kw_{PMMA}} \quad (9)$$

Equation 9 is solely based on the component parameters such as the T_G's, their concentration by weight w, and the parameter k, representing the ratio of the isobaric heat capacity increments, $k = \Delta c_{p,PMMA}/\Delta c_{p,PEO}$, at the corresponding T_G's. For atactic PMMA we found $\Delta c_{p,PMMA} = 0.29$ J/(g K), and for PEO $\Delta c_{p,PEO} = 2.28$ J/(g K), in ref 41 and Table 5.2 and 5.3 of ref 42, respectively, and determined $k = 0.13$. The resulting glass transition temperature is plotted as black dashed-point line in Figure 11, which is part of a later section. A similar expression as eq 9 was derived by Gordon and Taylor[37] with T_G instead of ln T_G in eq 9. $T_{G,CK}$ generally underestimates the experimental T_G's and of course cannot be sensitive to specific component interactions. Pinal[38] considered the configurational entropy of mixing, ΔS^C_{mix}, of an ideal mixture (FH parameter equal zero) when entering the glass regime, and derived the following expression

$$T_{G,m} = T_{G,CK} \exp(-\Delta S^C_{mix}/\Delta C_{p,m}) \quad (10)$$

with $T_{G,CK}$ from eq 9 and the heat capacity increment of the blend $\Delta C_{p,m} = w_1\Delta C_{p,PEO} + w_2\Delta C_{p,PMMA}$. The entropy ΔS^C_{mix} depends on the cooling rate and is smaller than $\Delta S^C_{mix}|_\infty$ one would obtain for an infinite slow cooling rate. Mixing two polymer species with finite FH parameter in a constant pressure field the entropy of mixing becomes $\Delta S^C_{mix} = \Delta H_{mix}/T + \delta S_{mix}$; it is determined by the enthalpy of mixing, ΔH_{mix}, plus an entropic term, δS_{mix}, describing the irreversible process. In case of an isobaric quasistatic (reversible) process, one gets $\Delta S_{mix} = \Delta H_{mix}/T$ as $\delta S_{mix} = 0$ (for more details, see ref 38). For a better comparison with our SANS data we expressed ΔS^C_{mix} by an enthalpic and entropic term of the FH parameter according to $\Delta S^C_{mix} = \Phi(1-\Phi)R/d \times [\Gamma^{mix}_h/T_{G;CK} + \delta\Gamma^{mix}_\sigma]$ (d mass density, R gas constant). For the choice of temperature, see eq 10 in ref 38). Equation 10 finally becomes

$$T_{G,m} = T_{G,CK} \exp\{-\Phi(1-\Phi)R/(d\Delta C_{p,m}) \times [\Gamma^{mix}_h/T_{G;CK} + \delta\Gamma^{mix}_\sigma]\} \quad (11)$$

with the enthalpic and (irreversible) entropic terms, Γ^{mix}_h and $\delta\Gamma^{mix}_\sigma$, as the fit parameters.

EXPERIMENTAL SECTION

Sample Preparation and Parameters. Deuterated poly(methyl methacrylate) (d-PMMA) was prepared by anionic polymerization at −78 °C in tetrahydrofuran (THF). Deuterated MMA monomer was purchased from CIL, Andover, Massachusetts. The monomer was carefully degassed, stirred over CaH_2 for one night, and treated with trioctylaluminum for 3 h prior to the polymerization. The initiator was (1,1-diphenyl-3,3-dimethyl) butyllithium prepared from 1,1-diphenylethylene and *tert*-butyllithium. Tetrahydrofuran was purified by drying over CaH_2, and potassium/benzophenone. The polymerization was accomplished in 1 h and subsequently terminated with degassed methanol. The d-PMMA was precipitated in methanol and dried under vacuum. The polymer was characterized by size exclusion chromatography (SEC) in THF relative to polystyrene standards and NMR determining the molecular weight and a syndiotactic microstructure larger than 79%, respectively.

The poly(ethylene oxide) polymers, h-PEO and d-PEO, were prepared by anionic polymerization in purified THF at 50 °C for 4 days under high vacuum conditions. h_4EO and d_4EO (CDN-isotopes, Quebec, CD, 99.8% D), were purified twice with CaH_2. As initiator potassium tert-butoxylate was used for d_4EO and potassium *n*-hexoxylate for h_4EO. The polymerization was terminated with acetic acid. The polymers were precipitated in cyclohexane and dried under vacuum. They were characterized by SEC with THF/dimethylacetamide, 90/10 vol/vol, as eluant, relative to PEO standards. The molar masses and polydispersities of all polymers are compiled in Table 2.

The PEO and PMMA chains were dissolved in toluene with a total polymer fraction less than 10%. Subsequently the toluene was slowly evaporated in an argon atmosphere at 40 °C and dried further in vacuum for at least 20 h at room temperature. The blend was then molded into a disk of 12 mm diameter and 1 mm thickness and stored in an airtight cell for SANS measurements with quartz glass windows for the neutrons to pass.

Neutron Scattering Experiments. The neutron experiments were carried out at the SANS diffractometers KWS-1 and 2 of the Jülich Centre of Neutron Science (JCNS) at the FRM II in Garching, Germany.[43] The experiments were performed with neutrons of wavelength of 4.75 (7) Å with 10 (20) % half-width of maximum and at sample-to-detector distances between 20 to 2 m in order to adjust the Q interval properly. The scattering data obtained were corrected for background scattering, detection sensitivity of the individual detector channels, and finally evaluated in absolute scale from calibration with a secondary standard. The transmission describing the decrease of nonscattered neutrons by the sample was automatically measured for all spectra with a separate monitor in front of the beam stop for the nonscattered neutron beam.

dx.doi.org/10.1021/ma2019123 | *Macromolecules* 2012, 45, 2035−2049

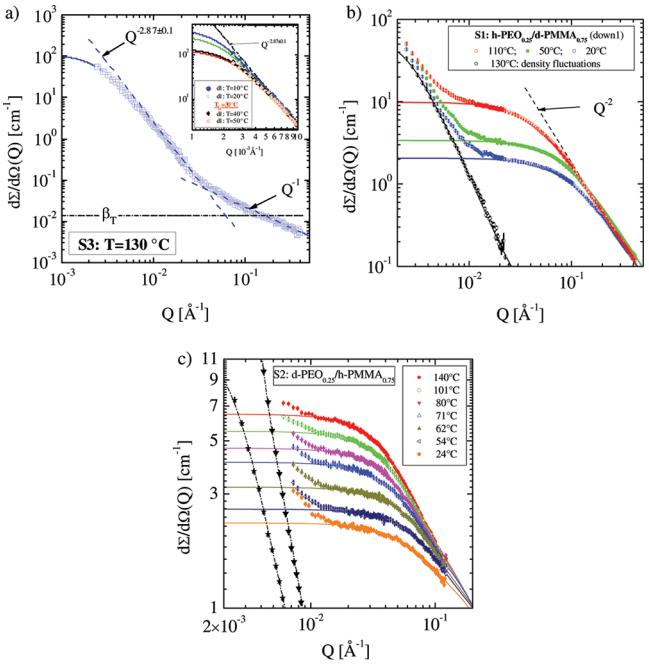

Figure 1. Scattering profiles of three symmetric 25 kDa $PEO_{0.25}$/$PMMA_{0.75}$ blends of different scattering contrast. (a) Sample S3: Long-range density fluctuations and small linear objects at 130 °C. (b and c) Samples S1 and S2: At larger Q scattering from composition fluctuations between 0 and 143 °C. The increase of intensity with temperature is characteristic for LCST blends. The curves with black symbols represent density fluctuations determined in S3 (a) after correction the correct $\langle\rho\rangle$ (eq 4; Table 3). A comparison of the small Q data leads to the interpretation of long-range density fluctuations also for samples S1 and S2.

Shear Experiments. Dynamic mechanical spectroscopy was used in order to determine the viscoelastic properties of both Φ_{PEO} = 0.25 d-PEO/h-PMMA and h-PEO/d-PMMA blends in a temperature interval from 155 to 25 °C in steps of 10 K. The measurements were performed with the strain controlled Rheometric Sci. ARES system operating in the dynamic mode. The temperature stability was about 0.5 K, the sample thickness of about 1 mm was varied with temperature keeping the normal force measurement constant. The frequency regime was between ω = 100−0.1 rad/s and the strain amplitude chosen to 1% in order to ensure the linear response approximation.

EXPERIMENTAL RESULTS AND ANALYSIS

We prepared samples of different scattering contrasts (see eq 1 and subsequent explanations) in order to explore thermal composition fluctuations, possible deviation from density homogeneity, as well as the chain conformation of both components. The parameters of the polymer components are compiled in Tables 2 and 3. Figure 1 depicts a selection of scattering patterns from Φ_{PEO} = 0.25 samples of different scattering contrast. Figure 1a shows the scattering pattern of sample S3 measured at 130 °C. Sample S3 has a large average scattering length density ($\langle\rho\rangle$), a large $\Delta\rho_{PEO}$ for the PEO form factor but a zero scattering contrast ($\Delta\rho_{crit} \cong 0$) for thermal composition fluctuations. Scattering from the PEO chain is negligible because of the small, i.e. 1.7 × 10^{-3}, h-PEO concentration, which means that the scattering of this sample is dominated by variations of the polymer density or by polymer packing changes. For this sample we observe a surprisingly large scattering much larger than expected from the compressibility β_T of the blend shown by the dashed-dotted line. The scattering from compressibility and PEO was subtracted from the scattering patterns. For all temperatures the low Q data follow a Guinier behavior below 0.004 Å^{-1} and a power law behavior at the larger Q with an average exponent of 2.87 ± 0.1 (see inset). The intensity increases (see inset) when passing the glass transition temperature and entering the glass regime. At large Q, we observe a transition to a Q^{-1} scattering which will be discussed below.

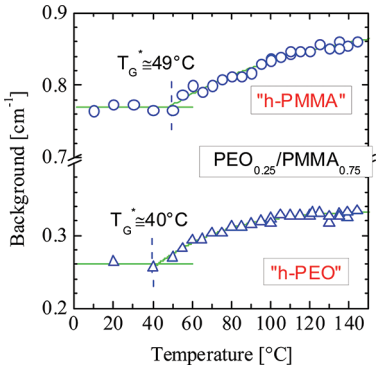

Figure 2. Constant scattering at large Q versus temperature of the two Φ = 0.25 blends S1: h-PEO/d-PMMA (T_G = 34 °C) and S2: d-PEO/h-PMMA (T_G = 49 °C). Because of inelastic scattering a change of intensity with temperature is observed above T_G. Even for "h-PEO" a constant intensity is measured below 40 °C even though PEO freezes at much lower temperatures.

The scattering in Figure 1, parts b and c, is dominated by thermal composition fluctuations as one component is deuterated and the other one protonated (samples S1 and S2 in Table 3). Heating the samples leads to a strong increase of scattering, i.e., to enhanced thermal composition fluctuations. These data show that PEO/PMMA is miscible at the explored temperatures and that the phase behavior is of "lower critical solution temperature" (LCST). At large Q, the scattering follows a Q^{-2} scaling as expected from the Ornstein−Zernike law. However, both samples are also sensitive to density fluctuations; sample S2 is less sensitive than S1 because of its larger amount of protonated polymer (h-PMMA). In both samples we observe an upturn of scattering at Q less than 0.02 Å^{-1}. The scattering curves represented by the black symbols display the scattering pattern of sample S3 (Figure 1a) after correction with respect to the mean scattering length density $\langle\rho\rangle$ of the samples. The scattering patterns of S3 had to be multiplied with, respectively, 0.6 and 0.13 in order to obtain a correct comparison with the low Q scattering of sample S1 and S2. The multiplication factors were calculated from the ratio of the corresponding scattering contrast $K_{si} = (\langle\rho\rangle_{Si}/\langle\rho\rangle_{S3})^2$ of samples S1 and S2 with respect to sample S3 (see the corresponding values in Table 3). A comparison shows that scattering from density fluctuations becomes relevant in the small Q regime of both S1 and S2 samples. In Figure 1c we also plotted the renormalized scattering pattern of S3 at 20 °C during first heating ("up1") run which is appreciably larger because of aging the sample for several days below T_G as will become clear later.

Another example of scattering data is shown in Figure 2. The background from constant incoherent and coherent scattering of sample S1 and 2 measured at large Q is plotted versus temperature. The interesting observation is that a constant intensity is measured at low temperatures within the glass

dx.doi.org/10.1021/ma2019123 | Macromolecules 2012, 45, 2035−2049

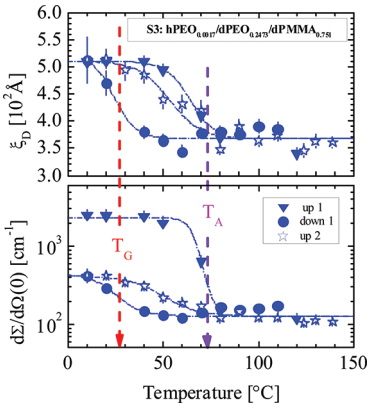

Figure 3. Correlation length ξ_D and extrapolated scattering at $Q = 0$ of the long-range density fluctuations in Sample S3 (Figure 1a). Long-range heterogeneities were found for all temperatures up to more than 100 K above T_G. Below T_A strong hysteresis with respect to size and intensity is observed indicating a nonequilibrium state.

regime, whereas at large temperatures an increase of scattering is observed. The degree of scattering of both samples is different by about a factor of 3 in consistence with the amount of protonated polymer.

Long-Range Density Fluctuations. Sample S3 (Table 3 and Figure 1a) represent a $PEO_{0.25}/PMMA_{0.75}$ blend with nearly zero $\Delta\rho_{comp} = \bar{\rho}_{PEO} - \bar{\rho}_{PMMA}$ contrast for composition fluctuations (eq 1) but with a large sample averaged coherent scattering length density $\langle\rho\rangle$ (Table 3 and eq 1). Scattering from single PEO chain is very weak because of the low concentration of the h-PEO content. Therefore, scattering can only be caused from mass density fluctuations. Sample S3 was investigated over a Q regime from 2×10^{-3} to 0.5 $Å^{-1}$ with a temperature program of heating and cooling between 10 and 140 °C (annealing time for each temperature was between 0.5 and 3 h). The scattering pattern in Figure 1a shows data at 130 °C during a cooling run. The solid line represents a fit of eq 5 assuming scattering from large fractal cluster and small linear objects. In Figure 3 the extrapolated scattering at $Q = 0$ and the

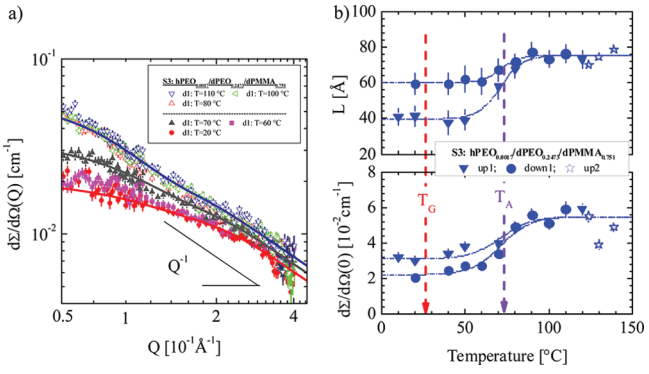

Figure 4. (a) Scattering profile (down 1) of S3 at large Q showing a Q^{-1} power law. The scattering was corrected from the density large size contribution. (b) Length L and I_0 of the small 1D-particles versus temperature of the "up1" and "down 1" temperature paths.

correlation length ξ_D from the large cluster are plotted versus temperature of the first heating run "up1", the first cooling run "down1", and the second heating run "up2". Before the first heating run ("up1") the sample was kept for at least 2 days at room temperature. The scattering is remarkably strong even for all temperatures above T_G. A relatively constant ξ_D of 370 ± 30 Å is measured in the viscous regime which strongly enhances to values of 510 ± 40 Å when entering the glass regime below T_G. The scattering at $Q = 0$ being slightly above 100 cm^{-1} increases to 400 cm^{-1} when passing T_G during the first cooling run "down1". Heating up the sample the first time ("up1") an even larger intensity of about 2000 cm^{-1} is measured at low temperatures clearly indicating the effect of aging within the glass regime. It has to be mentioned that the quantitative accuracy of the large cluster parameters suffers from low Q limitation of the data; an extension of the experiments to Q less than 10^{-3} $Å^{-1}$ would have improved the accuracy of the parameters very much. So the fit gave us a lower value estimation of the data. But despite of this experimental deficiency the data clearly show strong scattering from density fluctuations of large size up to 100 K above the glass transition, an enlargement of size below T_G, a strong hysteresis of the parameters from "up" and "down" heating runs between T_G and a temperature T_A whose relevance will become clear later. A relative change of the molecular packing by 4×10^{-3} between different domains has been estimated for all temperatures of the cooling process "down1" from $(d\Sigma/d\Omega(0))/\langle\rho\rangle^2 = \langle\Delta V^2\rangle/V$ (eq 4) and the parameters in Figure 3. The sample annealed at RT ("up1") showed a ~5 times enlargement of intensity but no change of the domain size (ξ_D). This corresponds to a molecular packing difference in the order of 1%.

The scattering of sample S3 is between four to 5 orders of magnitude larger than estimated from compressibility and beyond the Guinier regime it follows a power law with an exponent of 2.87 ± 0.10 thereby representing a fractal object. The dimensionality is very near the mass fractal dimensionality of three. At Q above 0.03 $Å^{-1}$ the scattering changes to a power law of dimensionality one (Figure 1a). Scaling behavior of Q^{-1} means diffraction at one-dimensional rod-like objects with a rod diameter $d < 1/Q$.[30,44] These objects might be identical with the microscopic elements of the large objects. Figure 4a displays scattering and the corresponding fitted curves in the high Q region. As already mentioned in context with Figure 1a, we corrected these data from contributions of incoherent (between 0.11 and 0.08 cm^{-1}), compressibility, and PEO single coil scattering. For a better visualization we further subtracted the scattering from the large objects which, as displayed in Figure 1a, follows a common power law at large Q according to $d\Sigma/d\Omega$ $(Q > 10^{-2}$ $Å^{-1}) = 4.58 \times 10^{-6} \times Q^{-2.87}$ cm^{-1}. In Figure 4b the length L as well as the $Q = 0$ scattering of the linear objects are displayed. A length of thin rods of about 80 Å above T_A and between 40 and 60 Å below T_A was determined from the radius of gyration according to $L = (12)^{1/2}R_g$ [,[44] page 159]. It is interesting to note that the gelation temperature T_A appears as a relevant temperature for these small linear objects as they become shorter below T_A. The change of L corresponds to changes of $d\Sigma/d\Omega(0)$.

Scattering from Thermal Composition Fluctuations. Thermal composition fluctuations were explored in symmetric 25 kDa PEO/PMMA blends of different H/D isotope labeling according to h-PEO/d-PMMA and d-PEO/h-PMMA (Table 3 and Figure 1, parts b and c). The blend h-PEO/d-PMMA was also explored over a larger composition regime between Φ_{PEO} = 0.1 and 0.75, whereas the d-PEO/h-PMMA blend was only studied at Φ_{PEO} = 0.25 but in some cases the d-PEO component was mixed with 4 and 100% of 1 kDa molar weight d-PEO. In Figure 5a–d, the inverse susceptibilities of the Φ_{PEO} = 0.25 samples are plotted versus $1/T$. According to

dx.doi.org/10.1021/ma2019123 | Macromolecules 2012, 45, 2035–2049

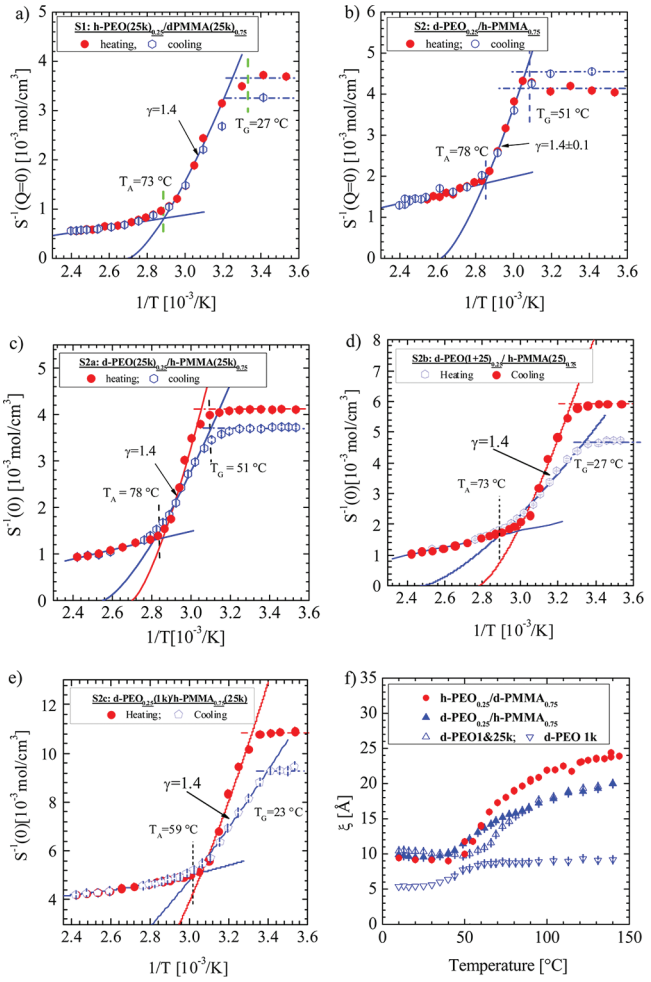

Figure 5. Susceptibility and correlation length versus inverse temperature of the symmetric 25 kDa PEO/PMMA blends of Φ_{PEO} = 0.25 composition. Two characteristic temperatures become apparent: At T_G the fluctuation modes of composition become frozen and no further change of $S(0)$ and ξ is observed below T_G. About 30 to 40 K above T_G a so-called gelation temperature T_A is observed. T_A separates the "usual" high temperature regime described by a negative FH parameter from a regime which shows an enhanced decrease of susceptibility, e.g. a further enhanced average number of PEO−PMMA contacts. In parts c−e, a hysteresis between heating and cooling path is observed below T_A; equilibration was not achieved because of the relatively fast measurements (see text). (f) Solid symbols show the correlation length of composition fluctuations ξ from cooling for the symmetric 25 kDa blends, whereas the open symbols blends symbolize samples with addition of 1 kDa d-PEO (corresponding S(0) in parts d and e).

RPA (eq 2) the susceptibility is determined by the difference of the FH parameter at the spinodal and the experimental temperature according to $S^{-1}(0) = 2[\Gamma_S - \Gamma]$. Γ_S is the FH parameter at the spinodal and is calculated according to $2\Gamma_S = 1/S^0_{PEO}(0) + 1/S^0_{PMMA}(0)$ (see eqs 2 and 3) by the molar volume and composition of the polymer components (Γ_S of the blends in Figure 5 is the same within small limits: $\Gamma_S \cong 1.4 \times 10^{-4}$ mol/cm^3). Because of $\Gamma = \Gamma_h/T - \Gamma_\sigma$ with Γ_h and Γ_σ the enthalpic and entropic terms of Γ, one derives the well-known mean-field scaling law $S^{-1}(0) = C_{MF}\tau^\gamma$ with the critical amplitude $C_{MF} = 2\Gamma_h/T_S$, reduced temperature $\tau = (T - T_S)/T$, and the critical exponent $\gamma = 1$.

Three characteristic regions are distinguished from $S^{-1}(0)$. At high temperature above T_A, $S^{-1}(0)$ follows a straight line in accordance with $\gamma = 1$ and a small slope determined by Γ_h. Below T_G, no change of S(0) occurs as the composition fluctuations are frozen. From DSC measurements, we know that the PMMA component freezes at T_G whereas the PEO component is still mobile at this temperature.[4] So the extremely slow PMMA chains strongly prevent the relaxation to the equilibration state of composition fluctuations. In most samples we measured a smaller $S(0)$ after annealing the samples for several (about two) days at room temperature (see solid and open points) known as "aging" in the glassy state. The range between T_G and T_A is characterized by a strong change of $S(0)$ with temperature; there appears a slight curvature in $S^{1-}(0)$ which can be fitted by a scaling form of $S^{-1}(0) \propto \tau^\gamma$ with

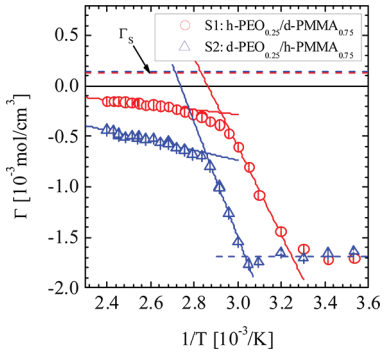

Figure 6. FH parameter of two Φ_{PEO} = 0.25 PEO/PMMA blends differing only in their isotope labeling. A smaller Γ but larger T_A and T_G are observed for the blend with h-PMMA.

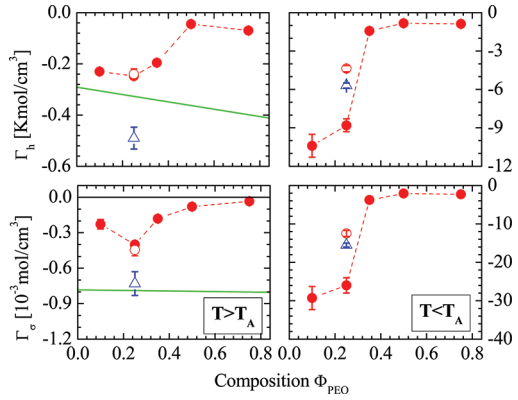

Figure 7. Enthalpic and entropic terms of the FH parameter Γ versus PEO concentration above and below the gelation temperature T_A. Red solid circles display Γ of h-PEO/d-PMMA: For PEO concentration at 40% and above the FH parameter approaches zero; i.e., the blend becomes an "ideal" solution. This implies that the immiscibility of PEO/PMMA is limited to the smaller PEO concentration. The open symbols were derived from the data in Figure 5, parts a and b. The blue open triangular and red open circular symbols represent the FH parameter of h-PEO/d-PMMA and d-PEO/h-PMMA in Figure 5, parts a and b, respectively. The green line displays the FH parameter of d-PS/PVME.[45] The isotope effect of Γ is more pronounced at high temperatures. The solid (red) spheres represent an earlier measurement. Their low T data stronger deviate from equilibrium.

$\gamma = 1.4$. This result should be considered as tentative since this regime is limited to a small interval between T_G and T_A with an insufficient number of experimental points for a more precise quantitative fit. The corresponding correlation length ξ of the

dx.doi.org/10.1021/ma2019123 | Macromolecules 2012, 45, 2035−2049

Φ_{PEO} = 0.25 samples obtained from cooling are plotted in Figure 5f versus temperature; the constant ξ within the glass regime and the enhancement with temperature is the expected behavior. Depending on the sample the correlation length of the thermal fluctuation is between 5 and 25 Å and thereby much smaller than the size of density fluctuations. The correlation length is determined from $\xi = (A \times S(0))^{1/2}$ with the susceptibility S(0) and the coefficient A of the Q^2 term in the Zimm approximation according to $S^{-1}(Q) = S^{-1}(0) + AQ^2$. In RPA the parameter A is determined as $A = [\sigma_{PEO}^2/\Phi_{PEO}\,\Omega_{PEO} + \sigma_{PMMA}^2/\Phi_{PMMA}\,\Omega_{PMMA}]/18$ assuming a Gaussian coil. The radius of gyration, $R_g^2 = \sigma^2 V/6\Omega_{Mon}$, of such polymer is determined by the statistical segment length σ and the molar monomer volume Ω_{Mon}. From the parameters compiled in Table 2, we evaluate A = 0.22 Å^2 mol/cm^3 for the Φ_{PEO} = 0.25 samples. For temperatures below T_G, we find a correlation length between 5 and 9 Å in very good agreement with Figure 5f.

The samples S2a–c in Figure 5c–e show a pronounced hysteresis below T_A. The scattering is weaker during the first heating run which was performed after annealing the samples at room temperature. On the other hand, samples S1 and S2 in Figure 5, parts a and b, show no hysteresis in the gelation regime. Samples S1 and S2 were annealed between 0.5 and 3 h before the start of measurements as they were measured in parallel with sample S3 (Figure 3) at three sample-to-detector distances of 20, 3.66, and 1.16 m with the corresponding collimator distances of 20 and 4 m. This time of annealing was sufficient to equilibrate the sample in the viscous regime above T_G. On the other hand the samples in Figure 5c,d, showing strong hysteresis, were also measured in parallel but at only one sample-to-detector position and therefore much faster with annealing times between 10 and 20 min. This time was sufficient for equilibration above T_A but not so below the gelation temperature.

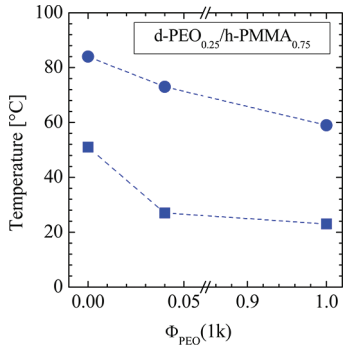

Figure 8. Glass and gelation temperature of Φ_{PEO} = 0.25 blends versus the concentration of 1 kDa PEO component. A strong decrease of both characteristic temperatures already occurs at low concentration.

The Flory–Huggins (FH–) parameter Γ was derived from the susceptibility $S(0)$ and Γ_S as already outlined in this section and is depicted in Figures 6 and 7. In all cases a negative FH interaction parameter was obtained indicating a miscibility of both components and a preference of PEO–PMMA neighboring contacts. The FH parameter versus $1/T$ are displayed in Figure 6 of the two Φ_{PEO} = 0.25 PEO/PMMA blends differing in their isotope labeling and whose susceptibilities are plotted in Figure 5, parts a and b. The negative Γ versus $1/T$ shows a negative slope; i.e. the absolute value of Γ_h strongly enhances when passing the gelation temperature T_A. There is also an appreciable isotope effect; Γ is lower for the d-PEO/h-PMMA blend but shows a larger T_A and T_G in comparison with the combination of d-PMMA. The enthalpic and entropic terms, Γ_h and Γ_σ, of Γ derived for $T > T_A$ (left) and $T < T_A$ (right) are shown in Figure 7 versus PEO composition. Both terms of the FH parameter are always negative, and between 1 and 2 orders of magnitude larger in amplitude below T_A. The red dots represent Γ of h-PEO/d-PMMA which for PEO concentration of 40% and above approach nearly zero; e.g., the blend becomes more an "ideal" solution, implying that LCST immiscibility in PEO/PMMA is limited to PEO concentrations of less than 40%. The FH parameter of the d-PEO/h-PMMA blend was measured only for Φ_{PEO} = 0.25 as depicted by the blue triangular symbols. The H/D exchange has a large effect on the FH parameter above T_A; the absolute values are nearly twice as large for the d-PEO/h-PMMA mixture. The green line represents the FH parameter of the d-PS/PVME blend.[45] It shows a more smooth dependence with respect to PVME

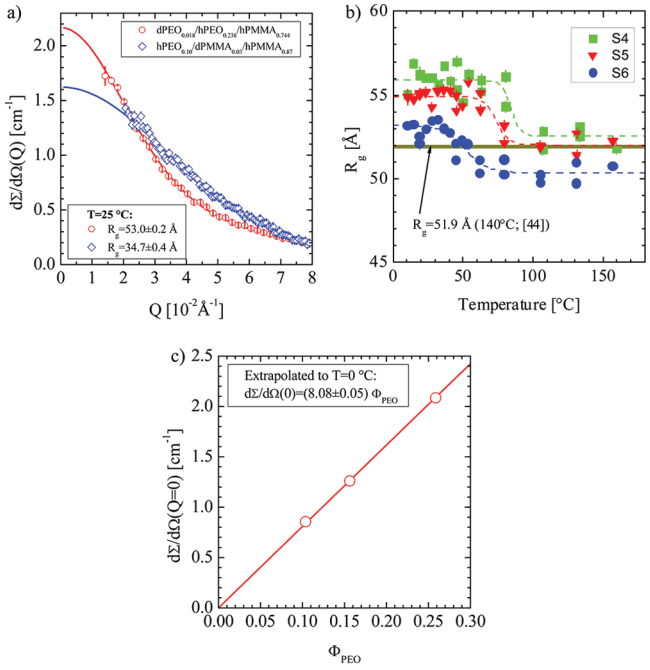

Figure 9. Form factor of PEO and PMMA chains in the blend (samples S4–6 in Table 3). (a) PMMA chain R_g increases about 2% when heating up the sample from RT to 200 °C. (b) R_g of PEO shows a 6% upturn at lower temperatures depending of the PEO content. The temperatures of upturn are depicted below in Figure 11 as triangles and are identified as the glass transition temperature. (c) PEO scattering at Q = 0 is linearly proportional with Φ_{PEO} and consistent with theory.

concentration and has a lower ratio of Γ_h/Γ_σ. This ratio determines the so-called compensation temperature T_{comp} which is defined as the temperature when $\Gamma = 0$ ($\Gamma_h/T_{comp} - \Gamma_\sigma = 0$). T_{comp} is calculated to 140 and 260 (395) °C for d-PS/PVME and h-PEO/d-PMMA (d-PEO/h-PMMA). The spinodal is defined for a positive Γ=Γ_S ($\Gamma_S \cong 1.4 \times 10^{-4}$ mol/cm^3 for both blends) which becomes identical to the line of T_{comp} in the limit of infinite molar weight with Γ_S = 0.[45] So the larger ratio of Γ_h/Γ_σ in PEO/PMMA explains its extended miscibility

dx.doi.org/10.1021/ma2019123 | Macromolecules 2012, 45, 2035–2049

which is reasonable because Γ_σ is the driving force for phase separation in LCST blends.

We also studied $\Phi_{PEO} = 0.25$ blends with a 25 kDa h-PMMA component mixed with different d-PEO molar weight combinations of 25 kDa and 1 kDa molar weight. In Figure 8 the temperatures T_A and T_G are plotted versus the concentration of 1 kDa d-PEO. Already a small addition of 1 kDa PEO leads to a strong decrease of T_A and T_G thereby working as a plasticizer. The plasticizer effect on T_G will be discussed below in context with the T_G's of the blend.

As already mentioned, in absolute value a larger Γ is derived for $T < T_A$ (Figure 6). This holds also for the enthalpic and entropic terms (Figure 7). Such a drastic change of Γ is expected for blends such as PEO/PMMA with a large dynamical asymmetry of the polymer components and has been formulated in eq 8. This theory interprets T_A as a gelation temperature. At this point the relaxation rate of thermal composition fluctuations, R_Q, and of the stress fields of entangled polymer network, $1/\tau_R$, becomes similar. Following eq 8 we evaluated from our SANS data (Figure 5a and b) for the h-PEO/d-PMMA and d-PEO/h-PMMA blends a shear modulus of $G = 2.9$ and 3.6 in units of 10^7 Pa, respectively. These values reasonably agree with rheological experiments on these blends presented below but are 2 orders of magnitude larger than the plateau modulus of PMMA ($G_N^0 \cong 3.1 \times 10^5$ Pa[46]). Whether the experimental FH parameter Γ^* represents an equilibrium value has to be carefully considered. The annealing time of 0.5 to 3 h for each temperature as applied for samples S1–3 (Figure 5a,b and Figure 3) was apparently sufficiently long as no hysteresis was observed for these samples below T_A.

PEO and PMMA Chain Conformation. In a further step the PEO and PMMA chain conformation in the blend was determined. Figure 9a shows the scattering patterns and Guiniers' law fits of the PEO and PMMA single chain form factor at 25 °C. The radius of gyration of the PEO chain of three samples of type d-PEO$_x$/h-PEO$_y$/h-PMMA$_{(1-x-y)}$ with zero scattering contrast for concentration fluctuations and $\Phi_{PEO} = (x + y) = 0.1$, 0.15, and 0.25 (samples S4–S6 in Table 3) are displayed in Figure 9b versus temperature. In those blends the second term of eq 1, representing the PEO form factor, contributes to scattering whereas scattering from density fluctuation is negligible small, e.g. 2% of the scattering of sample S2 which is less than 0.002 cm^{-1} within the Q regime of Figure 9a. In Figure 9c, the scattering extrapolated to $Q = 0$ and $T = 0$ °C is shown for all samples versus total PEO composition. The experimental points follow a straight line intersecting zero at $\Phi_{PEO} = 0$ according to $d\Sigma/d\Omega(0) = (8.08 \pm 0.05) \times \Phi_{PEO}$ with a slope 2.5% larger than evaluated from $S^0_{PEO}(0) = \Phi_{PEO} \times V_{PEO}$ in eq 1 and the parameters in Table 3. At temperatures between 80 and 40 °C, the radius of gyration of the PEO chain enhances by about 6%. The temperature of change corresponds to the respective glass transition temperatures as displayed below in the phase diagram (Figure 11). The R_g-values at high T are consistent with the data from ref 46 as indicated by the solid line and are about 10% less than determined in ref 47. The agreement of the PEO and PMMA chain dimensions determined from the blend and the corresponding pure homopolymer melts gives us confidence in the predictions of eq 1 and the sample preparation.

A similar conformational change at T_G was not observed for the PMMA chains; within the temperature interval of RT and 200 °C (not shown) the radii of gyration (average $\langle R_g \rangle = 32.1 \pm 0.45$ Å)

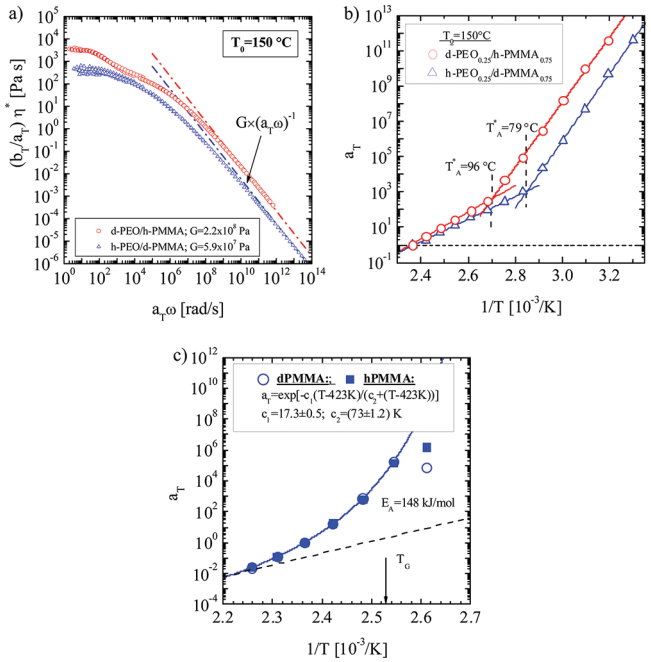

Figure 10. (a) Modulus of dynamic shear viscosity of the two $\Phi_{PEO} = 0.25$ PEO/PMMA blends after application the time–temperature superposition principle. (b) Frequency shift factors a_T show an Arrhenius behavior at high and low temperatures. The transition temperature T^*_A might be identified as a gelation temperature similarly to T_A in Figure 5. The averaged activation energy of both samples is 360 and 130 in units of kJ/mol at low and high temperatures, respectively. (c) Shift factor a_T of the PMMA melt is not sensitive to isotope labeling and show WLF behavior.

are constant within 2%. The statistical segment length $\sigma = 5.71 \pm 0.04$ Å is about 14% smaller than given in literature (Table 1 in ref 46). Seemingly, we have the situation that the PEO chain is slightly stretched by the freezing PMMA structure.

Shear Experiments. After finishing the SANS experiments on the $\Phi_{PEO} = 0.25$ samples S1 and S2, oscillatory shear experiments were performed in a temperature interval between 155 and 25 °C starting from high temperatures. At each temperature the samples were annealed for about 6.5 min before starting the measurements which took slightly more than 6 min. The time–temperature superposition principle according to $\eta^*(\omega,T) = (b_T/a_T) \times \eta^*(a_T\omega,T_0)$ with the reference temperature $T_0 = 150$ °C was applied. The resulting master curves for each sample are depicted in Figure 10a that presents the complex shear viscosity $\eta^*(\omega) = G^*(\omega)/i\omega = \int_0^\infty dt\, G(t)e^{-i\omega t}$ versus frequency (ω). In the limits of, respectively, $\omega\tau_R \ll 1$ and $\omega\tau_R \gg 1$ $\eta^*(\omega)$ assumes $\eta^*(\omega) \cong \eta$ and $\eta^*(\omega) \cong G(\omega)/i\omega$ where η is the zero-shear viscosity and $G=\eta/\tau$ the shear modulus (see page 327 of ref 15). A modulus of $G = 21.9$ (d-PEO/h-PMMA) and 5.89 (h-PEO/d-PMMA) in units of 10^7 Pa is obtained in the limit of large ω. These moduli lead to an increment of the enthalpic FH parameter of $\Delta\Gamma_h^* = -31.2$ (d-PEO/h-PMMA) and −8.4 (h-PEO/d-PMMA) in units of K mol/cm^3 ($\Delta\Gamma_h^* \triangleq (\Gamma_h^* - \Gamma_h) = -2\varepsilon^2(G/R)/3$ derived from eq 6 when cooling the samples below T_A and which are a factor of 6 and 2 larger in amplitude than the corresponding values shown as open symbols in Figure 7. The moduli from rheology as well as from SANS are 100 to 700 times larger than the PMMA plateau modulus. This means that the relaxation

dx.doi.org/10.1021/ma2019123 | Macromolecules 2012, 45, 2035–2049

process below T_A cannot be identified with the viscoelastic shear modulus of the system.

The shift factor a_T of both samples is plotted in Figure 10b versus 1/T (Arrhenius representation). Two temperature regimes, each described by an Arrhenius behavior ($\propto \exp[-E_A/RT]$), are found above and below T^*_A = 79 and 96 °C, respectively, for the h-PEO/d-PMMA and d-PEO/h-PMMA blends, whereas the shift factor b_T was nearly one (not shown). The corresponding activation energies (E_A) are 350 ± 45 kJ/mol for both blends at low temperatures and 142 ± 2 kJ/mol (132 ± 2 kJ/mol) for the d-PEO/h-PMMA (h-PEO/d-PMMA) at temperatures beyond T^*_A. Figure 10c shows a_T from pure h-PMMA and d-PMMA. Both polymer melts show the same shift factors that follow the WLF equation.[48] This finding implies that the time−temperature superposition principle is fulfilled for the PMMA single homopolymer melt with the same shift factors for the h- and d-materials. For the PEO/PMMA blend two temperature regimes for the viscous and gelation phases exist that indicate different underlying relaxation processes. A failure of the time−temperature superposition principle even within the high temperature regime was reported for PEO/PMMA in ref.[49] The parameters of this blend were Φ_{PEO} = 0.21 and about an order of magnitude larger molar weight than our sample. Four experimental temperatures were chosen between 120 and 174 °C, which are apparently above the gelation temperature.

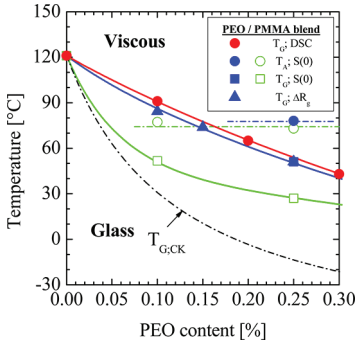

Figure 11. Diagram of a symmetric PEO/PMMA blend showing glass transitions. The red symbols represent the glass transition as determined by DSC for h-PEO/h-PMMA.[4] The open symbols stand for blends with d-PMMA while the closed symbols describe the result from h-PMMA blends. Circles denote T_A; squares depict T_G determined from the forward scattering $S(0)$. The triangles display T_G values from the R_g step of the PEO chain. The solid lines are fits with eq 11, the dashed dotted one represents eq 9.

The two regions of different rheological activation energy are reminiscent of the two regimes above T_G separated by the gelation temperature T_A; the corresponding temperatures T^*_A from shear experiment show the same isotope effect and are larger by about 20 K than those from SANS. Apparently, T^*_A is equivalent to the gelation temperature T_A from the susceptibility of thermal composition fluctuations.[15] The larger T^*_A might relate to a mechanical relaxation spectroscopy that leaves the system less time for aging.

Two remarks will finish this section. The first remark considers the equilibration of the samples during the shear experiments. The equilibrium state should always have been achieved at high temperatures but probably not at temperatures below T^*_A. This statement can be made from a comparison with the SANS data in Figure 5c−e, which show that an annealing time of 10 to 20 min is sufficiently long at $T > T_A$ but too short to prevent a hysteresis below the gelation temperature T_A when heating and cooling the samples. The second remark is related to a classification of glass forming systems into strong and fragile liquids according to their temperature depending viscosity following, respectively, an Arrhenius or Vogel−Fulcher−Tammann (VTF) behavior.[50] As expressed by the shift factors in Figure 10, parts b and c, PMMA appears as a fragile glass which apparently changes to a strong glass after mixing with PEO.

Glass Transition and FH Parameter. The phase diagram in Figure 11 displays the temperatures of gelation, T_A, and of glass transition, T_G, as determined from DSC and SANS experiments. PEO/PMMA is miscible at these temperatures and phase separation is expected at temperatures higher than 400 °C. The red dots represent the glass transition from the protonated blend h-PEO/h-PMMA determined from differential scanning calorimetry (DSC),[4] whereas the triangles and squares of blue and green color were determined from our SANS experiments. These symbols represent T_A and T_G from the two blends, d-PEO/h-PMMA and h-PEO/d-PMMA. The solid triangles were derived from the stepwise increase of the PEO radius of gyration R_g (Figure 9b); their agreement with the caloric glass transition (red dots) and $S(0)$ from SANS at Φ_{PEO} = 0.25 (blue square) shows the glass transition as the reason for the PEO chain stretching. DSC on the pure PMMA component showed no isotope effect as depicted by the red dot.

The observation of an isotope effect on the blend with respect to the position of T_G and T_A seems surprising. A possible explanation of the isotope effect might be obtained from the relationships in eq 10 and 11 that address the glass transition as a second order phase transition thereby naturally consider the FH interaction parameter of the polymer blend with the enthalpic and (irreversible) entropic terms, Γ_h^{mix} and $\delta\Gamma_\sigma^{mix}$, respectively. Equation 11 describes the glass temperature of the different samples very well as shown by the solid lines in Figure 11. The two variables Γ_h^{mix} and $\delta\Gamma_\sigma^{mix}$ from the fit together with the corresponding FH parameter from SANS and rheology are collected in Table 1 and the $T < T_A$ values are displayed in Figure 12 in the various columns. The "TG" enthalpic and entropic terms Γ_h^{mix} and $\delta\Gamma_\sigma^{mix}$ both show a large isotope effect, which in particular for h-PEO/d-PMMA seems to be unrealistic 15 times larger in absolute value if compared with the SANS data. In this respect it also might be interesting to consider $\Delta\Gamma^*_h$ (eq 6) from rheological measurements in Figure 10a which was determined as −31.2 and −8.4 in units of Kmol/cm^3 for, respectively d-PEO/h-PMMA and h-PEO/d-PMMA, and which have to be compared with the corresponding SANS values of −5.7 and −4.4 (Figure 7). Both theoretical expressions for shear viscosity (eq 8) and $T_{G,m}$ (eq 11) predict appreciably larger absolute FH parameters for PEO/PMMA in comparison with the SANS data from composition fluctuation. So we have to note from the data in Table 1 and Figure 12 that unfortunately the theoretical approaches of eqs 8 and 11 do not even qualitatively agree with the experimental findings and we must state a failure in rationalization of the observed anomalous isotope effect of T_G in the blends.

Reference 38 also discusses the effect of a plasticizer on T_G we observe in Figure 8, when adding a small amount of 1 kDa PEO.

dx.doi.org/10.1021/ma2019123 | Macromolecules 2012, 45, 2035−2049

Table 1. Flory-Huggins Parameter from SANS, T_G, and rheology

method	T_G [°C]	T_A [°C]		Γ_h [K mol/cm^3]	Γ_σ [mol/cm^3]
			SANS		
d-PEO/h-PMMA	51	78	$T > T_A$	-0.49 ± 0.04	$-(7.30 \pm 1) \times 10^{-4}$
			$T < T_A$	-5.7 ± 0.2	$-(1.55 \pm 0.05) \times 10^{-2}$
h-PEO/d-PMMA	33	75	$T > T_A$	-0.24 ± 0.02	$-(4.45 \pm 0.5) \times 10^{-4}$
			$T < T_A$	-4.38 ± 0.25	$-(1.25 \pm 0.08) \times 10^{-2}$
			Rheology: G [Pa] and Equation 8		
d-PEO/h-PMMA	–	96	$T < T_A$	−31.2	–
h-PEO/d-PMMA	–	79	$T < T_A$	−8.4	–
			$T_{G,m}$ and Equation 11		
d-PEO/h-PMMA	–	–	$T < T_A$	-2.37 ± 3.35	-0.112 ± 0.012
h-PEO/d-PMMA	–	–	$T < T_A$	-64.5 ± 4.5	0.167 ± 0.016
h-PEO/h-PMMA	–	–	$T < T_A$	7.86 ± 1.2	-0.157 ± 0.005

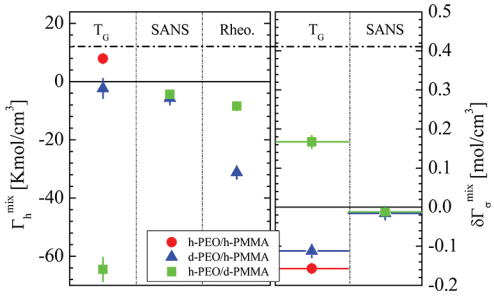

Figure 12. Fit parameters of eqs 7 and 12 giving rise to $T_{G,m}$ in Figure 11. The right figure shows the irreversible entropy from the fit as well as the SANS results. The left figure displays the enthalpic FH parameter term from the fit of $T_{G,m}$ and from rheology (eq 6 and Figure 10a) as well as from SANS (Figure 7) below T_A.

Addition of plasticizer increases the configurational entropy ΔS^C_{mix} and thereby according to eq 12

$$T^*_G = T_G \exp(-\Delta S^C_{mix}/\Delta C_{p,m}) \quad (12)$$

lowers the glass transition from T_G to T^*_G. We find a decrease from 51 °C (324 K) to 27 °C (300 K) thereby a $\Delta S^C_{mix}/\Delta C_{p,m} = 0.077$ or $\Delta S^C_{mix} = 0.057$ J/(g K) ($\Delta C_{p,m} = 0.74$ J/(g K)), which corresponds to an entropic FH parameter of $\Gamma^*_\sigma = 4.24 \times 10^{-2}$ mol/cm^3.

It has to be stressed that the "liquid-accessible or consumed configurational entropy of mixing", ΔS^C_{mix}, does not represent an equilibrium value but depends on the speed of cooling when approaching T_G. Only in the limit of an infinitely slow approach to T_G does one expect the maximum possible (equilibrium) $\Delta S^C_{mix}|_\infty$ and a T_G representing the Kauzmann temperature.[51] The nonachievement of equilibrium in some samples below the gelation temperature T_A is seen from the hysteresis of the susceptibility of thermal composition fluctuations in Figure 5 and of the long-range density cluster in Figures 3 and 4.

SUMMARY AND DISCUSSION

In this study we present small-angle neutron scattering (SANS) experiments on a symmetric 25 kDa PEO/PMMA polymer blend whose phase diagram for PEO concentrations smaller than 30% is displayed in Figure 11. We also performed dynamic mechanical spectroscopy on four selected samples. The SANS experiments confirmed that PEO/PMMA is of LCST type and miscible on macroscopic scale at temperatures below 400 °C. Two characteristic temperatures are found, namely the gel and glass transition temperatures T_A and T_G, respectively. The glass transition temperature separates the viscous and glass regimes at high and low temperatures, respectively. The other relevant boarder line T_A separates the regimes of the common "high temperature" disordered viscous phase from a gel-like regime.

The H/D Isotope Labeling has the well-known effect on the FH interaction parameter but also a remarkable influence on the position of the boarder lines between the viscous and gel-like (T_A) as well as gel-like and glass (T_G) regimes of the mixture, whereas T_G is the same for protonated and deuterated PMMA as proved by DSC (red point). The difference of FH parameters with respect to the choice of H/D isotope in the $\Phi_{PEO} = 0.25$ blend becomes particularly visible in Figure 6 and 7. An origin of the H/D isotope effect on the FH parameter is discussed in refs 52 and 53 and was derived from a combined effect of zero-point motion and interatomic potential anharmonicity, whereas the effect of interaction parameter and thereby the isotope effect on the glass transition might be explained by a Flory–Huggins interaction parameter as visualized in Figures 12. As discussed in ref 38, the "liquid-accessible entropy of mixing" determines the glass transition of the blend in accordance with eqs 10 and 11 and depends on the speed T_G is approached. The enthalpic and entropic terms show a large isotope effect, which in particular for h-PEO/d-PMMA has unrealistic large values. The high frequency shear viscosity also shows a large isotope effect for the enthalpic term (the entropic term is not determined from theory) but in a different direction, i.e. a larger absolute value for the d-PEO/h-PMMA blend. The FH parameter determined from thermal composition fluctuations are shown in Figure 7. The FH parameter below T_A seems the relevant parameter here and is plotted in Figure 12 for better comparison. It is between one and two order of absolute magnitude larger than the corresponding high temperature values and do not show a distinct change from the isotope difference. The discrepancy of the FH parameter from the different experimental methods in Figure 12 unfolds shortcomings in the theoretical approach of eqs 8 and 11 but also a possible underestimation of the FH parameter as the susceptibility of thermal composition between T_A and T_G does not follow a mean-field approach as the critical exponent is $\gamma = 1.4$ and not $\gamma = 1$. The deviation from mean-field approximation is shortly discussed below.

Two Fluctuation Phenomena. These are observed in PEO/PMMA, namely thermal composition and mass density fluctuations. The regions of mass density fluctuation have a fractal structure and are of long-range character. The identification of density fluctuations was possible in sample S3, which was designed to provide a selective sensitivity of

dx.doi.org/10.1021/ma2019123 | Macromolecules 2012, 45, 2035–2049

Table 2. Polymer Chain Parameter[a]

polymer	h-PEO	d-PEO		h-PMMA	d-PMMA
chemical structure	C_2H_4O	C_2D_4O		$C_5H_8O_2$	$C_5D_8O_2$
b_{Mon} [10^{-12} cm]	0.4133	4.578		1.491	9.82
ρ [10^{10} cm^{-2}]*	0.604	6.693		1.018	6.703
$d\Sigma/d\Omega_{inc}$ [cm^{-1}]	0.373	9.56×10^{-3}		0.349	8.95×10^{-3}
M_W [kDa] (M_W/M_N)	23.2 (1.02)	21.7 (1.02)	1.9 (1.12)	27.5 (1.10)	19.8 (1.13)
V_W [10^3 cm^3/mol]	21.0	17.7	1.55	23.6	15.7

parameter	PEO	PMMA
Ω_{Mon} [cm^3/mol]*	41.2	88.1
T_g [°C]	−57	121
σ [Å]	5.98 ± 0.04 (5.95;[67] 6.66[47])	5.71 ± 0.04 (6.49[67])
d [g/cm^3][b]	1.069	1.135

[a]Polymer components: poly(ethylene oxide) (PEO) and poly(methyl methacrylate) >79% syndiotactic (PMMA: $(C_5O_2H_8)_n$). Molar weights determined with GPC against PC standard. [b]Evaluated for 130 °C from mass densities: $d_{PEO} = -5.398 \times 10^{-4}T$ [K] + 1.287 and $d_{PMMA} = -4.643 \times 10^{-4}T$ [K] + 1.3218.

Table 3. Sample Parameters[a]

polymer	h-PEO	d-PEO	h-PMMA	d-PMMA
M_W [kDa] (M_W/M_N)	23.15 (1.02)	21.7(1.02)	27.5 (1.10)	19.8 (1.13)
V_W [10^3 cm^3/mol]	21.0	17.7	23.6	15.7

sample	C(h-PEO)	C(d-PEO)	Φ(PEO)	Φ(h-PMMA)	Φ(d-PMMA)
S1	1	–	0.249	–	0.751
S2[b]	–	1	0.25	0.75	–
S3	7×10^{-3}	0.993	0.249	–	0.751
S4	0.9307	6.93×10^{-2}	0.1038	0.8962	–
S5	0.9311	6.89×10^{-2}	0.1568	0.8432	–
S6	0.9309	6.91×10^{-2}	0.2562	0.7438	–
S7	1	-	0.25	0.72	0.03

sample[c]	$\Delta\rho_{com}$ [10^{10} cm^{-2}]	$\Delta\rho_{PEO}$ [10^{10} cm^{-2}]	$\Delta\rho_{PMMA}$ [10^{10} cm^{-2}]	$\langle\rho\rangle$ [10^{10} cm^{-2}]
S1	5.675	0	0	2.437
S2	6.099	0	0	5.184
S3	0.057	6.089	0	6.69
S4–S6	0	6.089	0	1.018
S7	0.641	0	5.685	1.085

[a]Scattering length densities: $\overline{\rho}_{PEO} = c\rho_{h-PEO} + (1-c)\rho_{d-PEO}$; $\Delta\rho_{comp} = |\rho_{PMMA} - \overline{\rho}_{PEO}|$; $\Delta\rho_{PEO} = \rho_{d-PEO} - \rho_{h-PEO}$). [b]Three samples of this type with different concentrations of 25 kDa and 1 kDa molar weight d-PEO were measured: (a) d-PEO(25k); (b) d-PEO(4% 1 kDa and 96% 25K); (c) d-PEO(1 kDa). [c]Values at T = 130 °C.

neutron scattering to density fluctuations by the choice of PEO and PMMA isotope chains (Table 3) whereas samples S1 and S2 were sensitive to both order parameter fluctuations as demonstrated in Figure 1, parts b and c.

Large-Scale Density Fluctuations with fractal dimensionality of slightly below 3 were observed for all temperatures (Figure 1a). At large Q above 0.03 Å^{-1} a transition to a Q^{-1} power law is observed which accounts for linear domains. Scattering from normal compressibility related density fluctuations is too small to explain the observed scattering. An estimation on the basis of PEO/PMMA compressibility leads to a scattering intensity of 10^{-2} cm^{-1} at 140 °C which is about 4 orders of magnitude smaller than the scattering in Figure 1a.[29] Because of a dimensionality of slightly less than D≅3 the large domains represent a mass fractal built up of aggregated objects of overall dimension less than $1/Q$, too small for destructive neutron interference. The transition above $Q \cong 0.03$ Å^{-1} to a Q^{-1} power law indicates linear objects (Figure 4) of length between 40 and 80 Å, which might represent the building units of the fractal domains and their number density might be defined as an order parameter. The parameters of the large and small domains are plotted in Figures 3 and 4 versus temperature. The temperatures T_A and T_G are indicated as arrows and was determined from thermal composition fluctuations in sample S1 (Figure 5a). The large domains above T_A are of same size of ξ_D = 370 ± 30 Å independent from thermal history and thereby might represent an equilibrium stage. Cooling the sample below T_G leads to an increase of the domain size which, when heated up, equilibrates above T_A and displays a hysteresis between T_G and T_A. Annealing the sample for several days (see heating history "up1") below T_G at room temperature a ξ_D and $d\Sigma/d\Omega(0)$ of 510 ± 40 Å and 2000 cm^{-1} is found which strongly decreases when heating the sample above T_G and after equilibration above T_A. The heating path ("up2") followed after the "down1" heating run displays a much smaller hysteresis. The evolution of the domain size shows that the time constant of density fluctuations is comparable with the SANS experimental time. The corresponding change of molecular packing of the domains was estimated as 1% and 0.4% for the sample after annealing at RT and heat treatment above T_A, respectively. Whereas both temperatures T_A and T_G seem to have an impact for the large scale density fluctuations the temperature T_A appears only relevant for the smaller linear structures; above T_A one determines a length of the order of 80 Å which gradually shortened when lowering the temperature below T_A and even further shortened to roughly half of this length during annealing at room temperature.

Heterogeneities in Glass Forming Systems are widely discussed in literature, however, in most cases as regions of different molecular mobility.[21,54−56] Regions of different molecular mobility support a strong non-Arrhenius temperature dependence characteristic for the transport coefficients such as viscosity in "fragile" liquids when approaching T_G. Experimentally, heterogeneous regions of "fast" and "slow" molecular motion were derived from NMR experiments;[19,20] heterogeneities of 35 ± 15 Å size were estimated in 50% PS/PMVE blend at 47 °C.[19] Other ^{13}C NMR measurements report heterogeneities between 20 and 500 Å in amorphous PEO/PMMA (Φ_{PEO} = 0.10) within the glass regime at 300 K.[20] The origin of heterogeneous regions of different molecular mobility is not yet understood and possible correlations with respect to structural heterogeneities are broadly discussed.[21,54]

Heterogeneities due to density fluctuations showing very similar scattering characteristics as our PEO/PMMA were reported in glass forming single component system by the group of Fischer (see ref 22 and references therein) from combined light (LS) and small-angle X-ray scattering (SAXS) experiments. This group also found long-range density fluctuations in a PMMA melt.[57] Other studies reported low Q enhanced scattering in solutions of atactic PS[58] and of syndiotactic PMMA.[59] Reference 58 proposed the formation of microcrystals involving chain segments and solvent molecules.

In particular the results by the Fischer group stimulated several theoretical approaches.[23−26,60] All these theories postulate small defects of a "locally favored structure of frustration limited cluster"[60] or species of solid-like and fluid-like short-range order.[23] In ref 26, a local atomic packing of regular tetrahedrons is assumed as the most stable configuration. As a compact structure of regular tetrahedron units is not possible in 3D space linear defects such as disclinations have to be introduced which avoid the formation of long-range ordering (frustration). Such theoretical approaches consider the glass transition as a phase transition of topological defects, defining their local density as an order parameter. According to the analysis in ref 26 the glass transition appears as a "hierarchical" phase transition of successive transitions starting with the formation of long-range correlated density fluctuations at a temperature T_0 and ending at T_G. An estimate gave $\xi \cong 3000$ Å and $|T_0 - T_G| \cong 100$ K in a size and temperature range consistent with our SANS data. The change of atomic density close to disclinations leads to a scattering contrast similar to those of the smaller linear structures shown in Figure 4b and whose observation might support the idea of linear defects in this glass-forming two-component system.

Thermal Composition Fluctuations represent the other order parameter of PEO/PMMA and are measured by the susceptibility $S(0)$ and correlation length ξ as displayed in Figure 5. The positive slope of $S^{-1}(0)$ within the 1/T representation indicates a miscible blend of LCST type with an expected two-phase regime at high temperatures - the spinodal temperature is roughly estimated to 400 °C for the $\Phi_{PEO} = 0.25$ blend. Three regimes of glass, gelation and viscous phases are clearly distinguished. The forth region of immiscibility lies outside achievable temperatures. The correlation length is between 10 and 25 Å as the spinodal phase transition line is far above the experimental temperatures and is much shorter than that of the density fluctuations. Below gelation (T_A) and glass (T_G) temperatures an enhanced suppression and freezing of the degree of thermal composition fluctuations took place, respectively.

Thermal composition fluctuations were interpreted in terms of a theory developed by Onuki.[14,15] Applying Onukis' theory in gel phase from our SANS data we evaluated a modulus of $G = 2.6$ and 3.7 in units of 10^7 Pa for samples S1 and S2, respectively which broadly agree with results from high frequency oscillatory shear experiments on these blends. In Figure 10, the complex shear viscosity of the two samples S1 and S2 is presented as 5.9 and 22 in units of 10^7 Pa. These values, however, are by more than 2 orders of magnitude larger than the PMMA viscoelastic plateau modulus (0.31 MPa). The retardation of composition fluctuations seems to rather relate to a glassy slow down of the PMMA segmental motions than to viscoelastic effects.

The corresponding *frequency shift factor* a_T follows an Arrhenius behavior with different activation energies above and below a temperature lightly above (20 K) the gelation temperature T_A thereby showing as SANS sensitivity to gelation. The shift factor a_T of the shear viscosity in Figure 10b is described by two Arrhenius functions above and below a temperature T^*_A, thereby belonging to the class of "strong" glasses in contrast to the PMMA melt belonging to the class of "fragile" glasses.[50] Fitting procedures of viscosity versus temperature are lengthily discussed for a variety of glass-forming systems in ref 61. Again their analysis shows a high and low temperature regime similarly to our findings for a_T. These authors consider both ranges of temperature as two separate regimes. At higher temperature the molecules are the unit of the liquid whereas at lower temperatures frustration limited domains determine the collective behavior. Such interpretation of microscopic units at low temperature is also related to an Arrhenius type behavior supporting a single "dominant structural" relaxation process.[61] This interpretation is consistent with our findings of density fluctuations and the linear defects as displayed in Figure 4 and may also be supported by the observed large discrepancy of the plateau shear modulus from entangled PMMA network and the much larger shear modulus from high frequency ($\omega\tau \gg 1$) rheological measurements as well as from SANS below T_A.

Frustration Limited Domains. These as the unit of collective behavior below T_A seem to have qualitatively the same effect as the process of gelation formulated by Onuki,[15] and that qualitatively describes thermal composition fluctuations of PEO/PMMA as well as of PS/PVME.[17] According to Onuki, the gelation temperature T_A is the temperature where the rheological and thermal composition fluctuation rate are of equal magnitude ($R_Q\tau_R \cong 1$). Below T_A we observe a strong decrease of the susceptibility $S(0)$. According to Onuki[15] this strong decrease of $S(0)$ below T_A is determined by the shear viscosity $\eta^*(\omega) \cong G/i\omega$ in the limit of $\omega\tau_R \gg 1$ (Figure 5). We note again that for our system the experimental G from SANS and mechanical spectroscopy are within the same order of magnitude but much larger than the viscoelastic PMMA plateau modulus. This discrepancy leads us to believe that the behavior of thermal composition fluctuations as well as the rheology below T_A (T^*_A) is controlled by glassy dynamics that might originate from frustration limited domains.

A remark is now made with respect to the scaling behavior of $S^{1-}(0)$ at temperatures in the intermediate regime between T_A and T_G that seems to be consistent with a critical exponent of $\gamma = 1.4$ larger than expected from the 3D-Ising case. Such unusual scaling behavior is reported in literature also for other polymer blends and polymer blend solutions[3,62] and is attributed to density fluctuations of impurities or solvent molecules, respectively.[63] The corresponding critical exponent of the susceptibility is determined according to $\gamma^* = \gamma/(1 - \alpha) = 1.39$ from the 3D-Ising critical exponents of susceptibility $\gamma = 1.24$ and heat capacity $\alpha = 0.11$ and represents the so-called renormalized 3D-Ising behavior.[63] In order to describe this effect the Gibbs free energy of mixing $\Delta G(T,P,\Phi)$ is extended by an additional term, namely the product of solvent or defect concentration Φ_S and its conjugate chemical potential $\mu_S = \partial_{\Phi_S}\Delta G|_{T,P,\Phi}$. The concentration Φ_S represents an additional order parameter. In polymer blends such an order parameter could also appear and be represented by the concentration of impurities or of those defects as discussed in context with Figure 3 and 4. According to the "isomorphism" approach by Anisimov et al.[64] μ_S and Φ_S are considered as "hidden" variables, i.e. the scaling form of the ΔG "fluctuation" part is as

usual a function of the two relevant parameter fields, namely, the temperature and the order parameter Φ (in our case Φ_{PEO}). Both are a function of pressure and the solvent chemical potential μ_S. One observes Ising critical exponents when the pressure and solvent chemical potential are constant during an isochoric approach to T_C. Such an approach, however, is experimentally not possible as it can only be realized at constant solvent concentration or in our case at constant linear defects, and therefore leads to a crossover to another class of critical universality with the renormalized critical exponents introduced above. The sketched theoretical background for the observed scaling of the susceptibility between T_A and T_G appears as a further support for a second order parameter related to the observed density fluctuations in Figures 3 and 4 and their effect on the thermodynamic behavior of the PEO/PMMA blend near the glass transition.

Qualitatively similar results on thermal composition fluctuations were obtained from SANS experiments in the LCST blend d-PS/PVME by Koizumi.[17,18] This blend obeys a similar "dynamical asymmetry" because of the different glass transition temperatures of PS and PVME at 100 and −22 °C, respectively and thereby the two components have a large difference in mobility. In ref 17, a quantitative comparison between plateau modulus of PS and modulus from SANS (eq 8) was not made but an analysis of their d-PS/PVME with Φ_{PS} = 0.80 deliver a G of about 4 MPa which is of the order of magnitude larger than the viscoelastic PS plateau modulus (0.2 MPa[46]). This does mean that below T_A the relaxation behavior of both blends is consistently determined by a glassy dynamics.

In ref 18, excess scattering at small Q is observed in qualitative agreement with our data in Figure 1b and 1c. The author interprets this result in terms of phase separated PEO and PMMA rich domains predicted from stress-diffusion coupling.[15] However, the interpretation of the latter SANS results is questionable as the scattering contrast of the PS/PVME blend is both sensitive to heterogeneities of composition and of density. On the other hand in our sample S3 the scattering contrast with respect to composition fluctuations was matched, i.e. $\Delta\rho_{comp}$ = 0. Therefore, the scattering results necessarily origin from strong long-range density fluctuations that contribute significantly to the scattering from samples S1 and S2 (see data in Figure 1). Furthermore, those SANS experiments on PS/PVME were also limited to Q larger than 6×10^{-3} Å^{-1}, which made an analysis of size and dimensionality of the larger objects impossible. A further argument against the interpretation of large composition precipitates in ref 18 is the dominance of glassy relaxation below the gel temperature.

The Conformation of the Polymer Components is fairly consistent with the conformation of the chains in their respective homopolymer melts and seems not much influenced by the long-range density fluctuations (Table 3). Only the PEO components stretches to a 6% larger radius of gyration when entering the glass regime (Figure 9b) and the phase diagram (solid triangles in Figure 11). It appears that in an increasingly solidifying PMMA, chain extension of the PEO chains occurs. This elongation points toward the existence of internal stresses that cannot relax in approaching T_G.

Density Fluctuations. These appear to not be affected by thermal composition fluctuations. This might be concluded from their large size and their slow relaxation behavior. Within the characteristic time of SANS experiments we observe a relaxation of the large objects when cooling below T_G and during equilibration above T_A. On the other hand, it appears obvious that the thermal composition fluctuations are correlated with these long-range density fluctuations. This becomes particularly apparent from the same characteristic temperatures T_A and T_G in Figures 3 and 4 as well as in Figure 5a for both blends with the d-PMMA component, and, similarly, from the renormalized 3D-Ising behavior below T_A (Figure 5). A correlation of the dynamic shear viscosity and density fluctuations, as indicated by T^*_A separating two regimes of activation energy of the shift factor a_T in Figure 10b, seems plausible, too. So, the clustering behavior of the linear defects shown by the density fluctuations appears a basic phenomenon of the present study.

Another possible explanation of long-range density fluctuations is given for stereoisometric homopolymers by Semenov.[65] Atactic polymer chains such as PS and PMMA might exhibit some longer stereoregular fragments of isotactic or syndiotactic units which aggregate to stable micellar cluster of lamellar crystalline structure. In our experiments, the deuterated as well as protonated PMMA shows a syndiotactic rich microstructure of larger than 79% which might differently behave as atactic PMMA. So, future experiments in particular with SANS may improve our understanding of long-range density fluctuations. (i) The spatial dimension of density fluctuations has to be determined more precisely from $d\Sigma/d\Omega$ at lower Q which is feasible down to 10^{-4} Å^{-1} and less.[66] (ii) The stability of density fluctuations has to be investigated over a larger temperature regime. (iii) It is of particular relevance to more systematically determine the time evolution, e.g., the relaxation rate of density fluctuations. This should be feasible on the basis of our present experiments. Furthermore, (iv) a change of PMMA tacticity and (v) the addition of small molecular PEO chains might be of interest with respect to structure and relaxation rate of the density fluctuations as the addition of 1 kDa PEO has strong influence on T_A and T_G.

APPENDIX

This appendix gives the characteristic sample parameters in Tables 2 and 3.

AUTHOR INFORMATION

Notes

The authors declare no competing financial interest.

ACKNOWLEDGMENTS

We thank Drs. Lutz Willner and Jürgen Allgaier for providing the polymers and in particular Drs. Wim Pyckhout and Andreas Wischnewski, all from our group, for performing the shear experiment and for illuminating discussions.

REFERENCES

(1) deGennes, P. G. *Scaling Concepts in Polymer Physics*: Cornell University: Ithaca, NY, 1979.
(2) Binder, K. *J. Chem. Phys.* **1983**, *79*, 6387−6409.
(3) Schwahn, D. *Adv. Polym. Sci.* **2005**, *183*, 1−61.
(4) Silva, G. G.; Machado, J. C.; Song, M.; Hourston, D. J. *J. Appl. Polym. Sci.* **2000**, *77*, 2034−2043.
(5) Fernandes, A. C.; Barlow, J. W.; Paul, D. R. *J. Appl. Polym. Sci.* **1986**, *32*, 5481−5508.
(6) Strobl, G. *The Physics of Polymers*; Springer-Verlag: Berlin Heidelberg, 1996.
(7) Lodge, T. P.; Wood, E. R.; Haley, J. C. *J. Polym. Sci.: Part B: Polym. Phys.* **2006**, *44*, 756−763.

(8) Lutz, T. R.; He, Y.; Edinger, M. D. *Macromolecules* **2003**, *36*, 1724−1730. He, Y.; Lutz, T. R.; Edinger, M. D. *J. Chem. Phys.* **2003**, *119*, 9956−9965.
(9) Haley, J. C.; Lodge, T. P. *J. Chem. Phys.* **2005**, *122*, 234914.
(10) Colmenero, J.; Arbe, A. *Soft Matter* **2007**, *3*, 1474−1485.
(11) Niedzwiedz, K.; et al. *Phys. Rev. Lett.* **2007**, *98*, 168301−168304.
(12) Hopkinson, I.; Kiff, F. T.; Richards, R. W.; King, S. M.; Farren, T. *Polymer* **1995**, *36*, 3523−3531.
(13) Ito, H.; Russell, T. P.; Wignall, G. D. *Macromolecules* **1987**, *20*, 2213−2220.
(14) Doi, M.; Onuki, A. *J. Phys. II (Fr.)* **1992**, *2*, 1631−1656.
(15) Onuki, A. *Phase Transition Dynamics*; Cambridge University Press: Cambridge, U.K., 2002.
(16) Takeno, H.; Koizumi, S.; Hasegawa, H.; Hashimoto, T. *Macromolecules* **1996**, *29*, 2440−2448.
(17) Koizumi, S. *J. Polym. Sci. Part B* **2004**, *42*, 3148−3164.
(18) Koizumi, S. *Soft Matter* **2011**, *7*, 3984−3992.
(19) Schmidt-Rohr, K.; Clauss, J.; Spiess, H. W. *Macromolecules* **1992**, *25*, 3273−3277.
(20) Schantz, S. *Macromolecules* **1997**, *30*, 1419−1425. Schantz, S.; Veeman, W. S. *J. Polym. Sci., Part B: Polym. Phys.* **1997**, *35*, 2681−2688.
(21) Sillescu, H. *J. Non-Cryst. Solids* **1999**, *243*, 81−108.
(22) Fischer, E. W. *Physica A* **1993**, *201*, 183−206.
(23) Kawasaki, K. *Physica* **1995**, *A217*, 124−139.
(24) Tanaka, H. *J. Chem. Phys.* **1999**, *111*, 3163−3174.
(25) Bakai, A. S. *J. Non-Cryst. Solids* **2002**, *307−310*, 623−629.
(26) Vasin, M. G.; Lad'yanov, V. I. *J. Phys.: Condens. Matter* **2005**, *17*, S1287−S1292.
(27) Warner, M.; Higgins, J. S.; Carter, A. J. *Macromolecules* **1983**, *16*, 1931−1935.
(28) Higgins, J. S.; Benoît, H. C. *Polymers and Neutron Scattering*; Clarendon Press: Oxford, U.K., 1994.
(29) Schmidt, M.; Maurer, F. H. J. *J. Polym. Sci., Part B: Polym. Phys.* **1998**, *36*, 1061−1080.
(30) Beaucage, G. *J. Appl. Crystallogr.* **1995**, *28*, 717−728.
(31) Bidkar, U. R.; Sanchez, I. C. *Macromolecules* **1975**, *28*, 3963−3972.
(32) Doi, M.; Edwards, S. F. *The Theory of Polymer Dynamics*; Oxford University Press: New York, 1989.
(33) Hashimoto, T. *J. Polym. Sci. Part B* **2004**, *42*, 3027−3062.
(34) Fox, T. G. *Bull. Am. Phys. Soc.* **1956**, *1*, 123.
(35) Lu, X.; Weiss, R. A. *Macromolecules* **1992**, *25*, 3242−3246.
(36) Couchman, P. R.; Karasz, F. E. *Macromolecules* **1978**, *11*, 117−119.
(37) Gordon, M.; Taylor, J. S. *J. Appl. Chem.* **1952**, *2*, 493−500.
(38) Pinal, R. *Entropy* **2008**, *10*, 207−223.
(39) Painter, P. C.; Graf, J. F.; Coleman, M. M. *Macromolecules* **1991**, *24*, 5630−5638.
(40) Coleman, M. M.; Graf, J. F.; Painter, P. C. *Specific Interactions and the Miscibility of Polymer Blends*; Technomic Publishing Company: Lancaster, PA, 1991.
(41) Roe, R. J.; Tonelli, A. E. *Macromolecules* **1979**, *12*, 878−883.
(42) van Kevelen, D. W.; Hoftyzer, P. J. *Properties of Polymers*: Elsevier Scientific Publishing Company: Amsterdam, 1976.
(43) SANS instruments at JCNS: (http://www.jcns.info/jcns_kws2/).
(44) Roe, R. J. *Methods of X-Ray and Neutron Scattering in Polymer Science*: University Press: Oxford, U.K., 2000.
(45) Schwahn, D.; Mortensen, K.; Springer, T.; Yee-Madeira, H.; Thomas, R. *J. Chem. Phys.* **1987**, *87* (10), 6078−6087. Schwahn, D.; Janssen, S.; Springer, T. *J. Chem. Phys.* **1992**, *97* (11), 8775−8788.
(46) Fetters, L. J.; Lohse, D. J.; Richter, D.; Witten, T. A.; Zirkel, A. *Macromolecules* **1994**, *27*, 4639−4641. Krishnamoorti, R.; Graessley, W. W.; Zirkel, A.; Richter, D.; Hadjichristidis, N.; Fetters, L. J.; Lohse, D. J. *J. Polym. Sci.: Part B: Polym. Phys.* **2002**, *40*, 1768−1776.
(47) Kugler, J.; Fischer, E. W. *Makromol. Chem.* **1983**, *184*, 2325−2334.
(48) Ferry, J. D. *Viscoelastic Properties of Polymers*; Wiley: New York, 1980.
(49) Colby, R. H. *Polymer* **1989**, *30*, 1275−1278.
(50) Debenedetti, P. G.; Stillinger, F. H. *Nature* **2001**, *410*, 259−267.
(51) Kauzmann, W. *Chem. Rev.* **1948**, *43*, 219−256.
(52) Bates, F. S.; Fetters, L. J.; Wignall, G. D. *Macromolecules* **1988**, *21*, 1086−1094.
(53) Schwahn, D.; Willner, L. *Macromolecules* **2002**, *35*, 239−247.
(54) Ediger, M. D. *Annu. Rev. Phys. Chem.* **2000**, *51*, 99−128.
(55) Ediger, M. D.; Angell, C. A.; Nagel, S. R. *J. Phys. Chem.* **1996**, *100*, 13200−13212.
(56) Tanaka, H.; Kawasaki, T.; Shintani, H.; Watanabe, K. *Nat. Mater.* **2010**, *9*, 324−331.
(57) Fischer, E. W.; Dettenmaier, M. *J. Non-Cryst. Solids* **1978**, *31*, 181−205.
(58) Gan, J. Y. S.; Francois, J.; Guenet, J.-M. *Macromolecules* **1986**, *19*, 173−178.
(59) Kusuyama, H.; Takase, M.; Higashihata, Y.; Tseng, H.-T.; Chatani, Y.; Tadokoro, H. *Polymer* **1982**, *23*, 1256−1258.
(60) Kivelson, D.; Kivelson, S. A.; Zhao, X.; Nussinov, Z.; Tarjus, G. *Physica A* **1995**, *219*, 27−38.
(61) Kivelson, D.; Tarjus, G.; Zhao, X.; Kivelson, S. A. *Phys. Rev. E* **1996**, *53*, 751−758. See also Comments and Reply: Cummins, H. Z. *Phys Rev. E* **1996**, *54*, 5870−5874.
(62) Nose, T.; Miyashita, N. *Critical Behaviour in Polymer Blend Solutions. in Scattering in Polymeric and Colloidal Systems*; Brown, W., Mortensen, K., Eds.; Gordon and Breach Science Publishers: London, 2000.
(63) Fisher, M. E. *Phys. Rev.* **1968**, *176*, 257.
(64) Anisimov, M. A.; Voronel, A. V.; Gorodetskii, E. E. *Sov. Phys. JETP* **1971**, *33*, 605. Anisimov, M. A.; Sengers, J. V. *Phys. Lett. A* **1992**, *172*, 114−118.
(65) Semenov, A. N. *Macromolecules* **2009**, *42*, 6761−6776.
(66) Frielinghaus, H.; Pipich, V.; Radulescu, A.; Heiderich, M.; Hanslik, R.; Dahlhoff, K.; Iwase, H.; S. Koizumi, S.; Schwahn, D. *J. Appl. Cryt* **2009**, *42*, 681−690.
(67) Fetters, L. J.; Lohse, D. J.; Richter, D.; Witten, T. A.; Zirkel, A. *Macromolecules* **1994**, *27*, 4639−4641. Krishnamoorti, R.; Graessley, W. W.; Zirkel, A.; Richter, D.; Hadjichristidis, N.; Fetters, L. J.; Lohse, D. J. *J. Polym. Sci.: Part B: Polym. Phys.* **2002**, *40*, 1768−1776.

Macromolecules

Article

pubs.acs.org/Macromolecules

Influence of the Electrolyte Film Thickness on Charge Dynamics of Ionic Liquids in Ionic Electroactive Devices

Jun-Hong Lin,[†,‡] Yang Liu,[‡,§] and Q. M. Zhang*[,†,‡,§]

[†]Department of Materials Science and Engineering, [‡]Materials Research Institute, and [§]Department of Electrical Engineering, The Pennsylvania State University, University Park, Pennsylvania 16802, United States

Supporting Information

ABSTRACT: Developing advanced ionic electroactive devices such as ionic actuators and supercapacitors requires the understanding of ionic diffusion and drifting processes, which depend on the distances over which the ions travel, in these systems. The charge dynamics of $[C_4mim][PF_6]$ ionic liquid films and Aquivion membranes with 40 wt % $[C_2mim][TfO]$ were investigated over a broad film thickness (d) range. It was found that the double layer charging time τ_{DL} follows the classic model $\tau_{DL} = \lambda_D d/(2D)$ very well, where D is the diffusion coefficient and λ_D the Debye length. In the longer time regimes ($t \gg \tau_{DL}$) where diffusion dominates, the charge dynamics become voltage dependent. For low applied voltage, the later stage charge process seems to follow the d^2 dependence. However, at high voltages (>0.5 V) in which significant device responses occur, the charging process does not show d^2 dependence so that $\tau_{diff} = d^2/(4D)$, corresponding to the ion diffusion from the bulk region, was not observed.

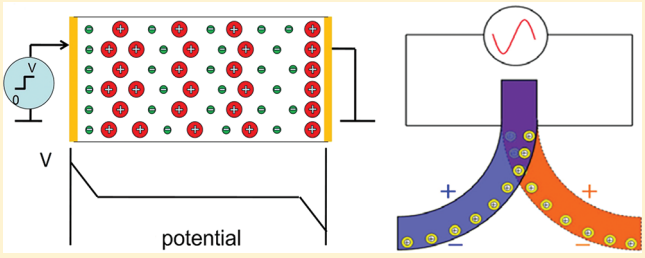

I. INTRODUCTION

Ion transport and storage in electrolyte containing films are of great interest for ionic electroactive devices, such as actuators, sensors, energy harvesting devices, and supercapacitors.[1−5] In general, charge transport is a result of drift and diffusion, described by the ion mobility μ, diffusion coefficient D, and mobile ion concentration n, e.g., the Nernst−Planck equation $\psi_{\pm} = \pm\mu n_{\pm}E - D(\partial n_{\pm}/\partial x)$, where ψ_+ and ψ_- are the fluxes of positive and negative charges. The first term on the right-hand side of the equation is the drift current and the second term describes the diffusion current. In dilute systems μ and D are related through the Einstein equation, $D = \mu kT/q$, where k is Boltzmann's constant, T is temperature, and q is the charge ions carry.[6−10] During charging, ions in the electrolyte moves toward electrodes of opposite polarity due to the electric field created by applied potential between charged electrodes which leads to the screening of the voltage and a potential drop at the two electrodes as illustrated in Figure 1a. For the metal−ionic conductor−metal (MIM) system of Figure 1a under a step voltage (from 0 at $t < 0$ to V volts at $t > 0$), the initial transient current follows the charging of electric double layer capacitors C_D in series with a bulk resistor R_{bulk} (see Figure 1b)[6−9]

$$I(t) = I_0 \exp(-t/\tau_{DL}) \quad (1)$$

where $\tau_{DL} = d\varepsilon\varepsilon_0/(2\lambda_D\sigma) = RC_D/2$ describes the typical charging time for the electric double layer which has a thickness λ_D, the Debye length

$$\lambda_D = (\varepsilon\varepsilon_0 kT/Z^2e^2n)^{1/2} \quad (2)$$

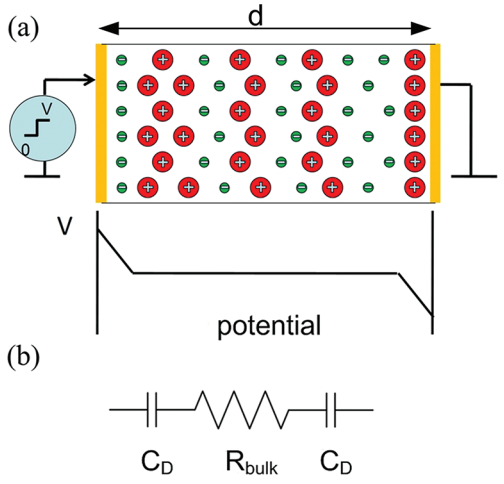

Figure 1. (a) Schematics of an electrolyte containing film sandwiched between metal electrodes under an applied voltage. The schematic of the voltage drop across the film after it is charged, illustrating that most voltage drop occurs near the blocking electrodes where the mobile ions screen the charges in the metal electrodes. (b) The equivalent circuit of ionic film metal system where R_{bulk} is the bulk resistance of the film, and C_D is the electrical double layer capacitance.

where $Ze = q$ is the mobile ion charge ($Z = 1$ for the ionic liquids investigated in this paper), e is the electron charge, ε is

Received: September 26, 2011
Revised: February 2, 2012
Published: February 10, 2012

the relative dielectric permittivity, and ε_0 is the vacuum permittivity ($\varepsilon_0 = 8.854 \times 10^{-12}$ F m^{-1}). $I_0 = \sigma VS/d$, where σ ($= qn\mu$) is the conductivity, d is the electrolyte film thickness, and S is the electrode area. For the ionic systems investigated in this paper, the Debye layer thickness λ_D is ~1 nm and $\tau_{DL} \ll 10^{-2}$ s. It should be pointed out that τ_{DL} here is the same as the electrode polarization time constant τ_{EP} in the MacDonald/Coelho model, treating electrode polarization as a simple Debye relation.[11−13] It is also noted that our recent study reveals that for the ionic systems investigated here this model (Figure 1b and eq 1) is valid up to 1 V in these highly concentrated electrolyte systems.[14]

For ionic electroactive devices, experimental results show that the device response time is much longer than τ_{DL}, and hence it is crucial to develop an understanding of the charge dynamics at longer time scale compared to τ_{DL}. Several theoretical models have been advanced for the ionic systems of Figure 1a to analyze the charge dynamics at longer time scales and modeling results suggest that following the initial charging process ($t \sim \tau_{DL}$, which is <10^{-2} s for the films studied here), there is a later charging process, dominated by diffusion from the bulk of the films.[8,9] In other words, the later stage charging process should scale with the time constant $\tau_{diff} = d^2/(4D)$. $\tau_{diff} \gg \tau_{DL}$ since $d \gg \lambda_D$, and for the ionic systems studied in this paper, τ_{diff} ranges from subseconds to tens of seconds.[7−9,15] For most ionic electroactive devices such as the ionic electroactive polymer (EAP) actuators and supercapacitors, the response time is in the same time range as τ_{diff} and is much longer than τ_{DL}. For example, for ionic membrane actuators, substantial actuation occurs during this later stage charging process. Hence, one interesting question is whether by reducing the ionic containing film thickness d a much faster device response can be achieved if τ_{diff} is proportional to d^2.

This paper investigates two ionic systems, a pure IL and an ionomer membrane containing ionic liquid (IL), focusing on the influence of the electrode separation d on the later stage (time > τ_{DL}) ion transport and storage processes. Ionic liquids (ILs), which are a class of salt in liquid form that contain both ions and neutral molecules, are used here as electrolytes because of many interesting properties that make them very attractive for ionic electroactive polymer (EAP) devices.[16−18] For example, the vapor pressure of ionic liquids is negligibly low, and as a result they will not evaporate out of the EAP devices when operated in ambient conditions. It has been demonstrated that compared with water the use of ILs as solvent for EAP actuators can dramatically increase the lifetime of the transducer.[19−21] Their high mobility leads to the potentially fast response of EAP devices while the wide electrochemical window (~4 V) allows it for higher applied voltages.[1−3,16−18] Two ILs, [C_4mim][PF_6] and [C_2mim] [TfO], were examined as electrolytes, where 1-butyl-3-methylimidazolium ([C_4mim]$^+$) and 1-ethyl-3-methylimidazolium ([C_2mim]$^+$) served as the cations and hexafluorophosphate ([PF_6]$^-$) and trifluoromethanesulfonate ([TfO]$^-$) served as the anions. Both cations and anions are present in ionic liquids. Because of high concentration of these ions in ILs compared with that of the side-chain SO_3^-, it is these cations and anions in ILs contribute to the ion transport here.[14] Moreover, the interaction among these cations and anions would cause the mobile charges to form clusters which consist of cation and anion binding together dynamically as described in recent publications.[10,22,23] For the study here it is assumed $n_+ = n_-$ and $\mu_+ = \mu_-$ (the subscripts + and − indicate positive and negative charges).

The experimental results reveal that over a broad thickness range and voltage range (<4 V) the initial charge dynamics can be well described by the *RC* circuit model (Figure 1b) where the resistance R is determined by the bulk conductivity of the ionic conductors and C_D is determined by the Debye length, which does not change with the membrane thickness d. On the other hand, the later stage charge responses display both voltage dependence and thickness d dependence. By analyzing the data with a reduced time constant t/τ_{diff} ($\tau_{diff} = d^2/(4D)$), it was found that the later stage charging process becomes progressively faster with increased voltage. That is, for voltage ~0.1 V, the charging process seems to follow d^2 dependence. However, for higher voltages (>0.5 V), the later stage charging time becomes much shorter than τ_{diff} ($= d^2/(4D)$), suggesting that the ion diffusion distance is shorter than $d/2$ for thick films.

II. EXPERIMENTAL SECTION

The charge dynamics of a pure IL, 1-butyl-3-methylimidazolium hexafluorophosphate ([C_4mim][PF_6]), at different thicknesses sandwiched between the electrodes was studied. Pure ILs provide an attractive ionic system in which to study charge dynamics with different electrode gap thicknesses as many electrolytes are investigated in supercapacitors.[24,25] [C_4mim][PF_6] is chosen for the pure IL study due to its relatively low conductivity and proper viscosity (1.4×10^{-3} S/cm and 450 cP at room temperature), which makes sample preparation and electrical characterization easier. A very high conductivity will cause high currents and very short τ_{DL} in thin MIM cells which can be beyond the measurement range of the experiment's setup. It was also found that it was necessary to carry out the experiment at −20 °C to further lower the conductivity to ($\sim 3 \times 10^{-5}$ S/cm) so that τ_{DL} for thin MIM cells is larger than the time resolution (~1 μs) of the experiment's setup.

The ionomer of Aquivion with 40 wt % uptake of 1-ethyl-3-methylimidazolium trifluoromethanesulfonat ([C_2mim][TfO]) is chosen for the ionomer system to investigate the influence of the ionomer matrix and more specifically the membrane thickness d on the charge dynamic of the IL electrolyte. This MIM material system has also been investigated for the ionic electroactive polymer actuators. Aquivion (Hyflon) is chosen for the ionomer membrane since it is known in the literature as a short side chain ionomer that may be more desirable than the normally used Nafion (indicated as a long side chain ionomer) for ionic EAP actuators.[14,20,21,26−29] These perfluorosulfonate ionomers consist of a polytetrafluoroethylene (PTFE) backbone and ether-linked tetrafluoroethylene side chains terminating in a sulfonic acid group as illustrated in Figure 2. [C_2mim][TfO] is chosen

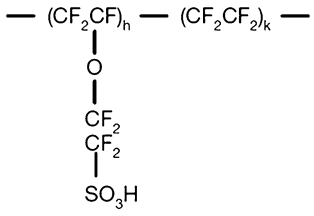

Figure 2. Molecular structure of short side chain Aquivion ionomer (EW830).

because of its high conductivity (8.6×10^{-3} S/cm) which ensures that the membrane with ILs has a high enough conductivity to be characterized, low viscosity (45 cP at 298 K), and a large electrochemical window (4.1 V). [C_2mim][TfO] is one of the commonly used ionic liquids in ionic EAP actuators.[14,19,21,26,30,31] Our earlier studies have shown that 40 wt % [C_2mim][TfO] uptake is above the critical IL uptake where the ionomer/IL membrane exhibits much higher conductivity (~9×10^{-6} S/cm) than that of the pure

dx.doi.org/10.1021/ma202165n | Macromolecules 2012, 45, 2050−2056

ionomer.[14,32,33] It should also be noted that the Aquivion membrane without ILs exhibits very low ionic conductivity which makes it unsuitable for studying the charge dynamics here.

Aquivion (EW830) solution, 1-butyl-3-methylimidazolium hexafluorophosphate ($[C_4mim][PF_6]$) and 1-ethyl-3-methylimidazolium trifluoromethanesulfonate ($[C_2mim][TfO]$), were purchased from Solvay Solexis and Aldrich, respectively. Both ionic liquids were dried in a vacuum at 80 °C to remove moisture before processing and characterization. Pure ionic liquid was sandwiched between two Si/Ti/Au electrodes with a 1 mm^2 electrode surface area to form metal−ionic conductor−metal sample systems. 3 μm Mylar and 20, 60 μm thick Kapton films are employed as the spacers for different thicknesses of the ionic conductors. The distance between electrodes was calibrated by measuring the capacitance $C = \varepsilon_0 S/d$, where S is the surface area of electrode and vacuum permittivity $\varepsilon_0 = 8.854 \times 10^{-12}$ F m^{-1}. The measured thickness of the gap is 4, 23, and 64 μm for the MIM systems with these spacers. To infiltrate the ionic liquid into the gap between the two electrodes, $[C_4mim][PF_6]$ was dropped on the gap and heated at 90 °C in a vacuum overnight. The capillary force drives the $[C_4mim][PF_6]$ from one end to the other to fill the whole gap between the electrodes.

Aquivion solution blended with 40 wt % uptake of $[C_2mim][TfO]$ was prepared and then diluted by *N*-methyl-2-pyrrolidone (NMP) solvent with a ratio of 1:3 for thicker films (11 and 20 μm thick) and 1:8 for thinner films (0.8 and 1.9 μm thick). Films were solution-casted on metalized Si substrates. In this study, Si/Ti/Au substrate is prepared by e-beam evaporator with an electrode area of 1 mm^2. Film thickness is controlled by the amount of mixture cast on the substrate. After drying at 96 °C for 10 h, the film is annealed at 150 °C for 2 h following. To form a metal−ionic conductor−metal (MIM) sample system, a 30 nm thick gold film is deposited as the top electrode.

The electrical measurement was carried out in a sealed metal box with desiccant inside to prevent the absorption of moisture. The box was equipped with a thermocouple to monitor the temperature during the measurement. The impedance spectroscopy was measured by a potentiostat Princeton 2237. The dc conductivity was calculated from the impedance data by $\sigma = d/RS$, where R is determined from the Nyquist plot (see Figure 3a).[14,26] To obtain the dielectric constant of the membranes, the samples were cooled in an environment chamber (Versa Tenn III) to reduce the conductivity of the MIM system so that the dielectric constant can be measured within the frequency window of the setup (which is below 1 MHz) before the screening of the applied field occurs, at frequencies $\gg 1/\tau_{DL}$. In contrast to the conductivity which decreases with temperature the dielectric constant of the ionomers is only very weakly temperature dependent, and the value thus acquired can be used for room temperature.[34−36] The transient current vs time was acquired by a potentiostat (Princeton 2237) whose output was connected to a high sampling rate oscilloscope (<1 μs) in order to capture the charge response during the fast charging process. The accumulation of blocked charges on membrane electrodes and the charge imbalance in the membrane may affect the electrical measurement. Therefore, several cycles of cyclic voltammetry (CV) scan with a low voltage (<1 V) and high scan rate were performed to help clean the electrode surface. The samples were shorted for at least 30 min to ensure that the charges redistributed to the equilibrium state as possible.[37]

By fitting the experimental transient current $I(t)$ under a step voltage with eq 1, as illustrated in Figure 3b, and using the ε of the ionomer membrane (with ILs) or pure IL acquired from the impedance measurement, σ, μ, and n can be obtained by eqs 3a−3c, respectively.[6,7,38] All the time domain data presented in the figures of the paper are acquired directly experimently using the fast oscilloscope interfaced with the potentiostat.

$$\sigma = \frac{I_0 d}{VS} \tag{3a}$$

$$\mu = \frac{qVS\varepsilon\varepsilon_0 d}{4kT\tau_{DL}{}^2 I_0} \tag{3b}$$

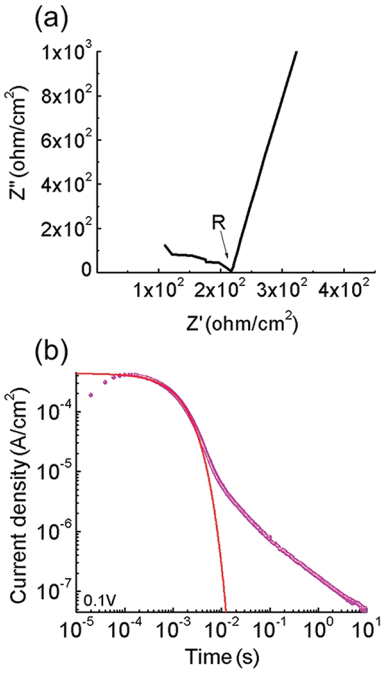

Figure 3. (a) Nyquist plot used to determine the membrane resistance R and (b) the current density (dots) and fitting (solid curve) to eq 1 of the 20 μm thick Aquivion membrane with 40 wt % uptake of $[C_2mim][TfO]$ under 0.1 V step voltage.

$$n = \frac{4kTI_0{}^2\tau_{DL}{}^2}{\varepsilon\varepsilon_0 q^2 V^2 S^2} \tag{3c}$$

Besides the time domain study, impedance spectroscope (frequency domain study) is also employed to study the capacitance and resistance changes with thickness d.

III. RESULTS AND DISCUSSION

3.1. Charge Dynamics of Pure Ionic Liquid of $[C_4mim][PF_6]$ at Different Thicknesses between Electrodes. ILs provide a convenient system to study the thickness dependence of charge dynamics of MIM systems. For a MIM system with pure IL of $[C_4mim][PF_6]$, the thinnest d for which we can fabricate the MIM cell is 4 μm. By fitting the transient current data for various gap thickness samples as illustrated in Figure 3, σ, μ, τ_{DL}, and λ_D are deduced for charging data under voltages <1 V (see Table 1). The charge response under a step voltage of 0.1 V for various gap thicknesses d is presented in Figure 4. For $[C_4mim][PF_6]$, there is no obvious change of σ and μ with thickness and within the experimental error the data obtained from 4 μm thick IL is the same as that from 64 μm thick IL. The charge response time τ_{DL} (which was obtained by

Table 1. Summary of σ, μ, λ_D, τ_{DL}, and τ_{diff} for Pure $[C_4mim][PF_6]$ Ionic Liquid Films with Different Thicknesses (d) under 0.1 V Step Voltage at −20 °C

electrodes distance (d)	64 μm	23 μm	4 μm
conductivity σ (S/cm)	3.01×10^{-5}	3.15×10^{-5}	3.34×10^{-5}
mobility μ (cm^2 V^{-1} s^{-1})	2.31×10^{-5}	2.52×10^{-5}	2.48×10^{-5}
Debye length λ_D (nm)	1.28	1.32	0.825
double layer τ_{DL} (s)	8.09×10^{-4}	2.73×10^{-4}	7.05×10^{-5}
diffusion τ_{diff} (s)	20.22	2.41	0.17

dx.doi.org/10.1021/ma202165n | *Macromolecules* 2012, 45, 2050−2056

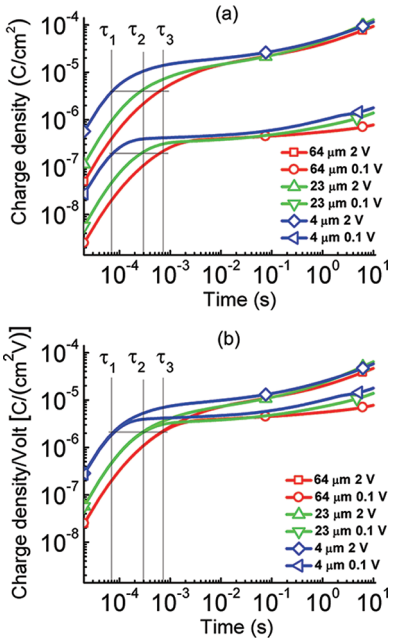

Figure 4. (a) Charge density as a function of time for the ionic liquid $[C_4mim][PF_6]$ under 0.1 and 2 V at the membrane thickness of d = 4, 23, and 64 μm. The data error is indicated by the size of the symbols at each data curve. τ_1, τ_2, and τ_3 are τ_{DL} for 4, 23, and 64 μm thick ionic systems. As indicated by eq 1, the charge density at $t = \tau_{DL}$ does not change with thickness d. (b) Charge density/voltage as a function of time for the data in (a) to show nonlinear capacitance response in these ionic systems. The error bar is indicated by the size of the symbols in the figure (the error bar is the same as the symbol size).

fitting the transient current with eq 1) for films of 4, 23, and 64 μm thick is also indicated in the figure and are presented in Figure 4 as τ_1 (7.05×10^{-5} s), τ_2 (2.73×10^{-4} s), and, τ_3 (8.09×10^{-4} s), respectively. These data indicate that the charge dynamics at a short time scale are controlled by the charging of the electrical double layer. Figure 4b presents the capacitance (charge density/voltage) under the stepped voltage vs time. The data reveals that the double layer capacitances (at $t = \tau_{DL}$) do not change with voltage. However, the capacitance corresponding to the later stage charging process increases with voltage, which is consistent with earlier studies.[14,20]

The impedance data (frequency domain data) for this MIM system are presented in Figure 5. In Figure 5a, the capacitance C of the complex impedance $Z = C \exp(j\delta)$, where δ is the phase angle is presented which shows that capacitance at $f_i = 1/\tau_{DL}$ does not change with the gap thickness d between the electrodes, which is consistent with the data observed from the time domain responses in Figure 4. Here the frequency $f_1 = 1/\tau_1$, $f_2 = 1/\tau_2$, and $f_3 = 1/\tau_3$. The result is also consistent with the commonly used electrode polarization model where the electrode polarization time constant is $\tau_{EP} = 1/f_i$.[11] Table 1 lists σ, μ, λ_D, τ_{DL}, and τ_{diff} ($= d^2/4D$) deduced for films with different thickness d. The Einstein equation, which is valid for dilute ionic systems, is used as an estimation to deduce D and hence τ_{diff}. Because of high ion concentration and hence strong interaction, the D values deduced here might be higher than that measured directly from NMR.[10,17] Nevertheless, the results show that τ_{diff} is much larger than τ_{DL} and electrical response of the electroactive devices is mainly controlled by this later stage ion diffusion process.

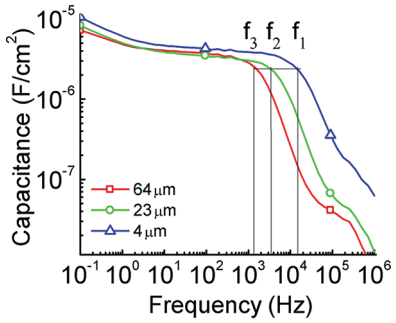

Figure 5. Capacitance as a function of frequency for ionic liquid $[C_4mim][PF_6]$ at the electrodes distance of d = 4, 23, and 64 μm under 0.1 V step voltage. The capacitance C at the characteristic frequency $f_i = 1/\tau_{DL}$ for electrodes distance of 4, 23, and 64 μm thick is also indicated in the figure, as f_1 (1.4×10^4 Hz for 4 μm), f_2 (3.66×10^3 Hz for 23 μm), and f_3 (1.23×10^3 Hz for 64 μm), respectively. The data show that the C at f_i does not change with electrodes distance d. The error bar is indicated by the size of the symbols in the figure.

As revealed in Figure 4, the charge responses at longer times beyond τ_{DL} (between 10^{-1} and 10 s, for example) under 2 V do not show significant changes with thickness that is different from that at 0.1 V. To further illustrate this difference, Figure 6

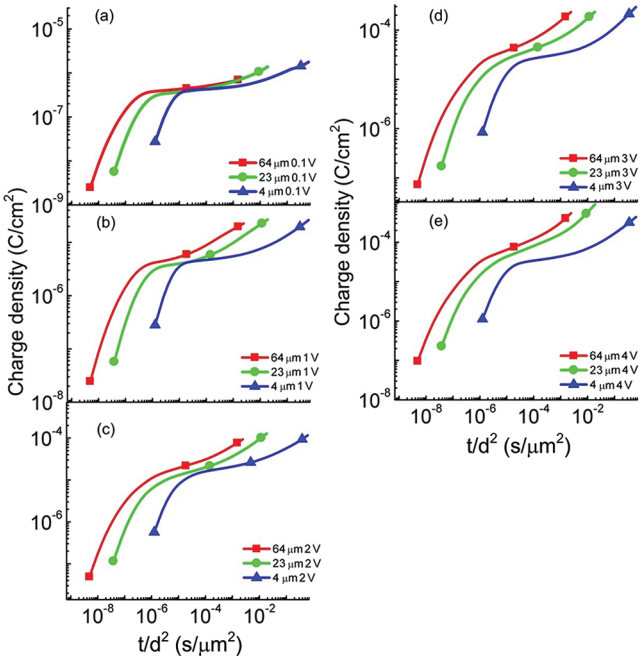

Figure 6. Charge density as a function of t/d^2 for the ionic liquid $[C_4mim][PF_6]$ under (a) 0.1, (b) 1, (c) 2, (d) 3, and (e) 4 V step voltages at the film thicknesses d = 4, 23, and 64 μm. The error bar is indicated by the size of the symbols in the figure. The unit for the reduced time axis (x-axis, t/d^2) is s/μm^2.

presents the charge response data versus the reduced time t/d^2. The charging time obtained under 0.1 V seems to follow approximately d^2 thickness dependence at reduced time interval between 10^{-5} and 10^{-2} s/μm^2, showing approximately the same charging responses. For higher voltages (>0.5 V), the deviation of the charging time from the d^2 dependence becomes progressively stronger. In fact, for data under 2 V or higher applied voltage, the later stage charging process seems not to

dx.doi.org/10.1021/ma202165n | Macromolecules 2012, 45, 2050–2056

show much change with thickness (see Figure 4). As shown in Figure 6, the charging response of 64 and 23 μm films show a much higher charge density than that of the 4 μm sample at the reduced time interval between 10^{-5} and 10^{-2} s/μm^2, implying that at high voltages the charge diffusion distance for the MIM systems studied here is mainly from the regions near the electrodes ($<d/2$) rather than from the bulk of the films.

3.2. Charge Dynamics of Aquivion Membranes with 40 wt % [C_2mim][TfO] Uptake at Different Membrane Thicknesses. The current responses of Aquivion with 40 wt % [C_2mim][TfO] uptake under various step voltages (from 0.1 to 4 V) were characterized for membranes of 0.8, 1.9, 11, and 20 μm thick to investigate the influence of the membrane thickness d on the charge dynamics of this MIM system. Figure 7

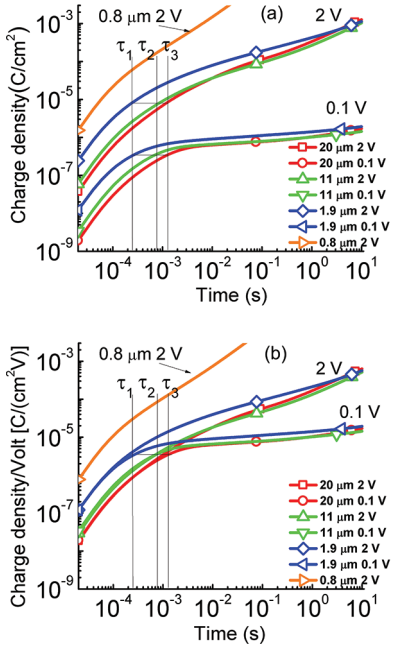

Figure 7. (a) Charge density as a function of time for the Aquivion film with 40 wt % uptake of [C_2mim][TfO] under 0.1 and 2 V at the membrane thickness of d = 0.8, 1.9, 11, and 20 μm. The abnormal high charge response of 0.8 μm sample may be a result of the high conduction current due to the reduction of the bulk thickness. τ_1, τ_2, and τ_3 are τ_{DL} for membranes of 1.9, 11, and 20 μm. As indicated by eq 1, the charge density at $t = \tau_{DL}$ does not change with thickness d. (b) Charge density/voltage as a function of time for the data in (a) to show nonlinear capacitance in these ionic systems. The error bar is indicated by the size of the symbols in the figure.

presents the charge density with time acquired under a 0.1 V step voltage for membranes of different thicknesses. Fitting of the transient current data (as illustrated in Figure 3) yields σ, μ, λ_D, and τ_{DL} for this MIM system (summarized in Table 2 for data acquired under 0.1 V). The charge response time τ_{DL} (see eq 1) for films of 1.9, 11, and 20 μm thick is also indicated in the Figure 7 and is labeled as τ_1 (2.49×10^{-4} s for 1.9 μm), τ_2 (7.25×10^{-4} s for 11 μm), and τ_3 (1.29×10^{-3} s for 20 μm), respectively. The data show that the charge dynamic at a short time scale is controlled by the charging of the electrical double layer, and C_D does not change with film thickness and voltage studied here.

The data for the 0.8 μm thick membranes displays a very different behavior where the current becomes much larger than that in other films. It is likely that there is a significant conduction current (where the current cannot be blocked by

Table 2. Summary of σ, μ, λ_D, τ_{DL}, and τ_{diff} for the Aquivion Membranes with 40 wt % [C_2mim][TfO] with Different Thicknesses (d) under 0.1 V Step Voltage at 25 °C

membrane thickness (d)	20 μm	11 μm	1.9 μm
conductivity σ (S/cm)	9.1×10^{-6}	9.0×10^{-6}	8.6×10^{-6}
mobility μ (cm^2 V^{-1} s^{-1})	2.45×10^{-6}	2.37×10^{-6}	2.23×10^{-6}
Debye length λ_D (nm)	0.82	0.81	0.79
double layer τ_{DL} (s)	1.29×10^{-3}	7.25×10^{-4}	2.49×10^{-4}
diffusion τ_{diff} (s)	15.60	4.86	0.15

the electrodes) in such a thin film, which superimposes on the regular diffusion and drifting currents. As illustrated in Figure 1a, due to the electric double layer, most voltage drop occurs within the Debye length near the electrodes, which is about 1 nm for the MIM systems studied here. Hence, the field level in the interface region can reach ~1 GV/m, which could induce strong charge injection from the electrodes. For thick membranes, the bulk resistance limits the current flow, resulting in low conduction current (the current flow is bulk limited). For thin membranes, this bulk resistance becomes small (the currents due to diffusion and drifting in the bulk region also become large), and consequently the current flow is interface limited, causing high conduction current as observed. The high conduction current in 0.8 μm thick membranes makes it difficult to perform quantitative data analysis and to deduce μ, τ_{DL}, λ_D, etc.

The impedance data ($Z = C \exp(j\delta)$), measured under 0.1 V, for the membranes with various thicknesses as a function of frequency are shown in Figure 8. As can be seen, the capacitance C at the frequencies below that for the charging of the Debye layer ($f_i = 1/\tau_{DL}$) are nearly the same for membranes of 1.9, 11, and 20 μm, which is consistent with the transient current data in Figure 7. At low frequencies ($<f_i$), C_D dominates the capacitance C, while at higher frequencies ($>f_i$), the contribution from R_{bulk} (see Figure 1b) to C becomes dominating, causing observed change of C with film thickness d since R_{bulk} is directly proportional to d. For membranes of 0.8 μm thick, the high conduction current causes a very large apparent capacitance which increases with reduced frequency and is typical for the capacitance due to the space charge effect. Figure 8b presents the data in Figure 8a in terms of the dielectric permittivity $\varepsilon^* = \varepsilon' - j\varepsilon''$.

We now examine the current and charge responses at a longer time beyond τ_{DL} which is the time domain for most practical ionic electroactive devices to display large responses.[14,19,20,30,31] As revealed in Figure 7, in contrast to the strong thickness dependence observed for τ_{DL}, the later stage charge responses do not seem to exhibit significant change with the membrane thickness when the membrane thickness d is reduced from 20 to 1.9 μm (except for the membranes of 0.8 μm thick). In Table 2, $\tau_{diff} = d^2/(4D)$ is also listed which is 0.15 s for 1.9 μm thick film and increases to 15.6 s for 20 μm thick film. In order to display data more clearly and compare them with τ_{diff} directly, the charge density of these films is plotted against t/d^2 as presented in Figure 9. The data show that under 0.1 V the later stage charging process seems not to deviate significantly from the d^2 dependence at the reduced time interval between 10^{-4} and 10^{-1} t/d^2, which is similar to that observed in the pure IL MIM system as presented in the preceding section. However, for higher voltages, the data deviate from the d^2 dependence markedly. At applied voltage >1 V, the data show that the charging time for films of 11 and

dx.doi.org/10.1021/ma202165n | Macromolecules 2012, 45, 2050–2056

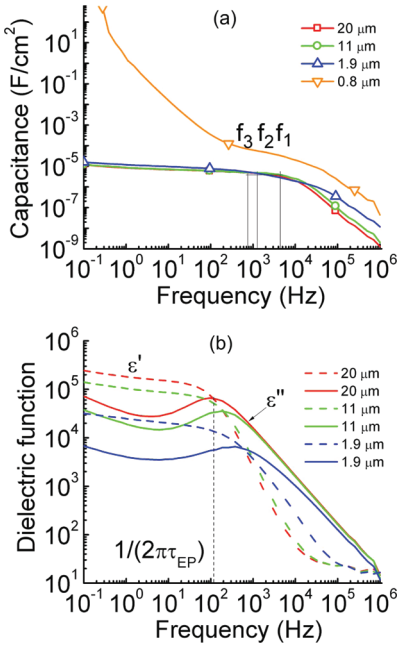

Figure 8. (a) Capacitance and (b) dielectric permittivity (ε', dashed line; ε'', solid line) as a function of frequency for the Aquivion film with 40 wt % uptake of [C_2mim][TfO] under 0.1 V ac voltage. The capacitance C at the characteristic frequency $f_i = 1/\tau_{DL}$ for films of 1.9, 11, and 20 μm thick is labeled at f_1 (4.03×10^3 Hz), f_2 (1.37×10^3 Hz), and f_3 (7.75×10^2 Hz), respectively. The data reveal that the C at f_i does not change with film thickness d for 1.9, 11, and 20 μm thick films. The observed abnormal high capacitance response of the 0.8 μm sample may be attributed to its high conduction current. The error bar is indicated by the size of the symbols in the figure.

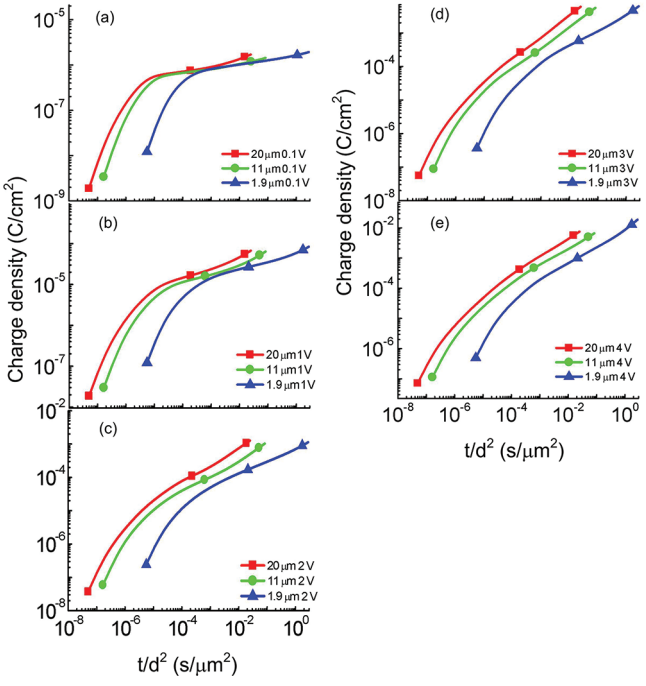

Figure 9. Charge density as a function of t/d^2 for the Aquivion film with 40 wt % uptake of [C_2mim][TfO] under (a) 0.1, (b) 1, (c) 2, (d) 3, and (e) 4 V at the membrane thickness of d = 1.9, 11, and 20 μm. The error bar is indicated by the size of the symbols in the figure.

20 μm becomes much shorter than the d^2 dependence compared with films with a 1.9 μm thick membrane.

IV. CONCLUSION

We investigated the influence of the gap thickness d between the electrodes on the charge dynamics of a pure IL, [C_4mim][PF_6], when d is varied from 4 to 63 μm. The experimental results indicate that for all the thicknesses studied the charge dynamics at the initial time follow the charging of interfacial capacitors C_D in series with a bulk resistor. For the charge dynamics at times $\gg \tau_{DL}$, the charge dynamics display both applied voltage and thickness d dependence. That is, for the data obtained under 0.1 V, the later stage charging process that is dominated by ion diffusion process seems not to deviate markedly from the d^2 dependence. For voltages >0.5 V, this later stage charging response does not show d^2 thickness dependence as the gap between the electrodes varies from 4 to 63 μm. Instead, the films with large d can be charged much faster than that predicted from $\tau_{diff} = d^2/(4D)$ compared with 4 μm thick films.

The influence of the ionic liquid containing film thickness on the ionic charge dynamics of the Aquivion/[C_2mim][TfO] with Au electrodes was also investigated. The results of initial charge response (at a short time) are very similar to that observed in the pure IL films. For charging responses at times $\gg \tau_{DL}$ which are the time domains where most electrical and electromechanical actions occur for ionic electroactive devices, experimental data reveal that charge dynamics depend on the applied voltage and film thicknesses, very similar to that observed in the pure IL films. These results also indicate that the IL containing ionomer membranes and pure IL films exhibit similar charge dynamics, when considering the influence of the voltage and film thickness dependence on ion transport and storage in these MIM systems.

The observed nonlinear charge dynamics with an applied voltage is likely caused by the very high electric fields near the blocking electrode regions. The electric field generated by an ion in a medium with dielectric constant of 10 is ~100 MV/m when 1 nm away from the ion. In contrast, for an electric double layer of 1 nm thick, 1 V applied will generate an electric field ~1 GV/m, which is much higher than the field generated from ions and will generate nonlinear effect (for example, capacitance changes with applied voltage) as observed in the paper.

■ ASSOCIATED CONTENT

Supporting Information

Time domain measurement setup, charge, and capacitance responses under step voltage and differential capacitance as a function of time. This material is available free of charge via the Internet at http://pubs.acs.org.

■ AUTHOR INFORMATION

Notes

The authors declare no competing financial interest.

■ ACKNOWLEDGMENTS

The material is based upon work supported in part by the U.S. Army Research Office under Grant W911NF-07-1-0452 IonicLiquids in Electro-Active Devices (ILEAD) MURI, NIH under Grant R01-EY018387-02, and NSF under Grant CMMI 0709333. The authors thank Ralph Colby and Shih-Wa Wang for many stimulating discussions regarding the research works reported here.

REFERENCES

(1) Lu, W.; Fadeev, A. G.; Qi, B. H.; Smela, E.; Mattes, B. R.; Ding, J.; Spinks, G. M.; Mazurkiewicz, J.; Zhou, D. Z.; Wallace, G. G.; MacFarlane, D. R.; Forsyth, S. A.; Forsyth, M. *Science* **2002**, *297* (5583), 983−987.

(2) McEwen, A. B.; Ngo, H. L.; LeCompte, K.; Goldman, J. L. *J. Electrochem. Soc.* **1999**, *146* (5), 1687−1695.

(3) Ue, M.; Takeda, M.; Toriumi, A.; Kominato, A.; Hagiwara, R.; Ito, Y. *J. Electrochem. Soc.* **2003**, *150* (4), A499−A502.

(4) Duncan, A. J.; Leo, D. J.; Long, T. E. *Macromolecules* **2008**, *41* (21), 7765−7775.

(5) Chen, L.; Hallinan, D. T.; Elabd, Y. A.; Hillmyer, M. A. *Macromolecules* **2009**, *42* (16), 6075−6085.

(6) Beunis, F.; Strubbe, F.; Marescaux, M.; Beeckman, J.; Neyts, K.; Verschueren, A. R. M. *Phys. Rev. E* **2008**, *78* (1), 011502−1−011502−15.

(7) Beunis, F.; Strubbe, F.; Marescaux, M.; Neyts, K.; Verschueren, A. R. M. *Appl. Phys. Lett.* **2007**, *91* (18), 182911−1−182911−3.

(8) Marescaux, M.; Beunis, F.; Strubbe, F.; Verboven, B.; Neyts, K. *Phys. Rev. E* **2009**, *79* (1), 011502−1−011502−4.

(9) Bazant, M. Z.; Thornton, K.; Ajdari, A. *Phys. Rev. E* **2004**, *70*, 2.

(10) Hou, J. B.; Zhang, Z. Y.; Madsen, L. A. *J. Phys. Chem. B* **2011**, *115* (16), 4576−4582.

(11) Klein, R. J.; Zhang, S. H.; Dou, S.; Jones, B. H.; Colby, R. H.; Runt, J. *J. Chem. Phys.* **2006**, *124*, 14.

(12) Macdonald, J. R. *Phys. Rev.* **1953**, *92* (1), 4−17.

(13) Coelho, R. *Rev. Phys. Appl.* **1983**, *18* (3), 137−146.

(14) Lin, J. H.; Liu, Y.; Zhang, Q. M. *Polymer* **2011**, *52* (2), 540−546.

(15) Kilic, M. S.; Bazant, M. Z.; Ajdari, A. *Phys. Rev. E* **2007**, *75* (2), 021502−021514.

(16) Fukumoto, K.; Yoshizawa, M.; Ohno, H. *J. Am. Chem. Soc.* **2005**, *127* (8), 2398−2399.

(17) Huddleston, J. G.; Visser, A. E.; Reichert, W. M.; Willauer, H. D.; Broker, G. A.; Rogers, R. D. *Green Chem.* **2001**, *3* (4), 156−164.

(18) Tokuda, H.; Hayamizu, K.; Ishii, K.; Abu Bin Hasan Susan, M.; Watanabe, M. *J. Phys. Chem. B* **2004**, *108* (42), 16593−16600.

(19) Liu, Y.; Liu, S.; Lin, J. H.; Wang, D.; Jain, V.; Montazami, R.; Heflin, J. R.; Li, J.; Madsen, L.; Zhang, Q. M. *Appl. Phys. Lett.* **2010**, *96* (22), 223503−1−223503−3.

(20) Liu, S.; Liu, W. J.; Liu, Y.; Lin, J. H.; Zhou, X.; Janik, M. J.; Colby, R. H.; Zhang, Q. M. *Polym. Int.* **2010**, *59* (3), 321−328.

(21) Bennett, M. D.; Leo, D. J. *Sens. Actuators, A* **2004**, *115* (1), 79−90.

(22) Kornyshev, A. A. *J. Phys. Chem. B* **2007**, *111* (20), 5545−5557.

(23) Liu, Y.; Liu, S.; Lin, J. H.; Wang, D.; Jain, V.; Montazami, R.; Heflin, J. R.; Li, J.; Madsen, L.; Zhang, Q. M. *Appl. Phys. Lett.* **2010**, *96*, 22.

(24) Balducci, A.; Bardi, U.; Caporali, S.; Mastragostino, M.; Soavi, F. *Electrochem. Commun.* **2004**, *6* (6), 566−570.

(25) Garcia, B.; Lavallee, S.; Perron, G.; Michot, C.; Armand, M. *Electrochim. Acta* **2004**, *49* (26), 4583−4588.

(26) Bennett, M. D.; Leo, D. J.; Wilkes, G. L.; Beyer, F. L.; Pechar, T. W. *Polymer* **2006**, *47* (19), 6782−6796.

(27) Hsu, W. Y.; Gierke, T. D. *J. Membr. Sci.* **1983**, *13* (3), 307−326.

(28) Ghielmi, A.; Vaccarono, P.; Troglia, C.; Arcella, V. *J. Power Sources* **2005**, *145* (2), 108−115.

(29) Kreuer, K. D.; Schuster, M.; Obliers, B.; Diat, O.; Traub, U.; Fuchs, A.; Klock, U.; Paddison, S. J.; Maier, J. *J. Power Sources* **2008**, *178* (2), 499−509.

(30) Liu, S.; Liu, Y.; Cebeci, H.; de Villoria, R. G.; Lin, J. H.; Wardle, B. L.; Zhang, Q. M. *Adv. Funct. Mater.* **2010**, *20* (19), 3266−3271.

(31) Liu, S.; Montazami, R.; Liu, Y.; Jain, V.; Lin, M. R.; Heflin, J. R.; Zhang, Q. M. *Appl. Phys. Lett.* **2009**, *95* (2), 023505−1−023505−3.

(32) Weber, R. L.; Ye, Y. S.; Schmitt, A. L.; Banik, S. M.; Elabd, Y. A.; Mahanthappa, M. K. *Macromolecules* **2011**, *44* (14), 5727−5735.

(33) Hallinan, D. T.; De Angelis, M. G.; Baschetti, M. G.; Sarti, G. C.; Elabd, Y. A. *Macromolecules* **2010**, *43* (10), 4667−4678.

(34) Serghei, A.; Tress, M.; Sangoro, J. R.; Kremer, F. *Phys. Rev. B* **2009**, *80* (18), 184301−1−184301−5.

(35) Krause, C.; Sangoro, J. R.; Iacob, C.; Kremer, F. *J. Phys. Chem. B* **2010**, *114* (1), 382−386.

(36) Wakai, C.; Oleinikova, A.; Ott, M.; Weingartner, H. *J. Phys. Chem. B* **2005**, *109* (36), 17028−17030.

(37) Lockett, V.; Sedev, R.; Ralston, J.; Horne, M.; Rodopoulos, T. *J. Phys. Chem. C* **2008**, *112* (19), 7486−7495.

(38) Strubbe, F.; Verschueren, A. R. M.; Schlangen, L. J. M.; Beunis, F.; Neyts, K. *J. Colloid Interface Sci.* **2006**, *300* (1), 396−403.

Macromolecules

Article

pubs.acs.org/Macromolecules

Comparison of Molecular Structure and Rheological Properties of Electron-Beam- and Gamma-Irradiated Polypropylene

Dietmar Auhl,[†,‡] Florian J. Stadler,[†,§] and Helmut Münstedt*,[†]

[†]Institute of Polymer Materials, University Erlangen-Nürnberg, Martensstr. 7, D-91058 Erlangen, Germany

[‡]Bio- and Soft Matter, Institute of Condensed Matter and Nanosciences,Université catholique de Louvain, Croix du Sud, 1, B-1348 Louvain-la-Neuve, Belgium

[§]School of Chemical Engineering, Chonbuk National University, Baekjero 567, Deokjin-gu, Jeonju, 561-756, Jeonbuk, Korea

ABSTRACT: Polypropylene (PP) irradiated with electrons or electromagnetic waves (gamma-rays) undergoes chain scission, and the macroradicals generated form branched molecules as shown by size-exclusion chromatography coupled with laser scattering. Information on the irradiation modification of the molecular structure of PP is still limited in the literature, especially with respect to the controlled generation of long-chain branches (LCB). This paper examines the branching structure of an electron-beam- and gamma-irradiated polypropylene. In general, appropriate irradiation conditions lead to the formation of LCB, which were analyzed in detail by rheological means. At smaller doses, the zero shear-rate viscosities η_0 of the electron-beam-irradiated PP lie above the values for the unmodified PP with the same M_w but are distinctly lower than the linear reference at higher doses. This result can be interpreted by the change from a starlike to a treelike branching topography. The gamma-irradiation leads to η_0 values smaller than those of the linear reference, giving rise to the assumption of the generation of treelike molecules. The measurements of the elongational viscosities support this molecular picture. An explanation of these findings is given along the line that the electron irradiation conducted at dose rates higher than the gamma-irradiation creates a larger concentration of short-living radicals, which will partially annihilate each other, but favor the growth of some long branches, which get branched themselves at higher doses. The structure of the gamma-irradiated samples is postulated to consist of a blend of linear and treelike molecules.

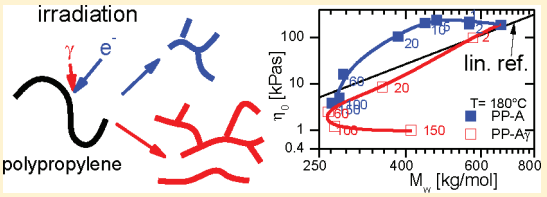

INTRODUCTION

The high interest in modifications of the molecular structure of thermoplastic materials with long-chain branching is due to its strong influence on processing as well as on some end-useproperties. Long-chain branched polypropylenes, for example, can be generated by electron-beam irradiation.[1,2] In the literature, the influence of different doses on the molecular structure[3−6] and rheological properties of a commercial polypropylene[6] has been investigated in detail. Classical size-exclusion chromatography coupled with multiangle laser light scattering (SEC-MALLS) indicated that the molecular weight decreased with increasing irradiation dose and the number of long-chain branches (LCB) got larger, whereas the polydispersity remained nearly unchanged.[3,6−9] Measurements of the zero shear-rate viscosity η_0 as a function of the absolute weight-average molecular weight M_w and the determination of the elongational viscosity as a function of time at various elongation rates demonstrated that these rheological quantities are much more sensitive to the generation of LCB than the classical characterization methods.[6] Moreover, some conclusions with respect to the architecture of the long-chain branches could be drawn from the rheological experiments.[6]

According to the literature,[8,9] for gamma-irradiation polypropylene undergoes also simultaneous chain scission and growth comparable to electron-beam irradiation, especially in the presence of oxygen. The crystalline morphology, irradiation conditions, and the comonomer content are the main factors influencing the result of the irradiation.[7,10] A higher dose rate, i.e., the irradiation energy applied per time, leads to a stronger effect on the viscosity, which can be explained by an effect molecular weight and the LCB structure, as well.[11]

These results pose the question of how different kinds of irradiation, such as electrons or gamma-rays, affect the molecular structure of polypropylenes. In addition to fundamental concerns, the findings of such investigations may offer some insights into the molecular modification of polypropylenes with respect to their applications. As well as the effects on rheology, the end-use properties are also affected, which is due to the influence of irradiation on the crystallization kinetics.[12]

Therefore, the aim of this paper is to compare the change of the molecular structure and its reflection with respect to rheological properties by irradiating the same basic polypropylene with various doses of gamma-rays or electrons, respectively. The results of the electron-beam-irradiated samples were already published in Auhl et al.[6] and are used in this paper for comparison with the gamma-irradiated specimens.

Received: October 9, 2011
Revised: January 1, 2012
Published: February 3, 2012

Table 1. Molecular Data of the Electron-Beam-Irradiated Samples[a]

	d [kGy]	n [kGy]	M_w [kg/mol]	M_z [kg/mol]	M_w/M_n	$\bar{\lambda}_{LCB}$ [LCB/1000 monomer]	$\bar{M}_S$ [kg/mol]	$\bar{M}_S/M_e$
PP	0	0	669	1654	4.2	n.d.		
PP1	1	1 × 1	604	1445	3.8	n.d.		
PP2	2	1 × 2	565	1369	3.6	n.d.		
PP5	5	1 × 5	473	1135	3.8	0.05	354	59
PP10	10	1 × 10	444	1145	3.6	0.07	232	38.7
PP20	20	2 × 10	384	916	3.5	0.12	158	26.3
PP60	60	6 × 10	285	874	3.4	0.30	71	11.8
PP100	100	10 × 10	279	921	3.4	0.58	39	65
PP150	150	15 × 10	268	1240	3.5	0.82	22	3.7
PP300*	300	30 × 10	339	1808	3.8			
PP100b	100	100 × 1	189		3.9	n.a.	n.a.	n.a.

[a]n: number and doses of irradiation steps, n.d.: not detectable; *: partially cross-linked; n.a.: data not available.

Table 2. Molecular Data of the Gamma-Irradiated Samples

	d [kGy]	M_w [kg/mol]	M_z [kg/mol]	M_w/M_n	$\bar{\lambda}_{LCB}$ [LCB/1000 monomer]	$\bar{M}_S$ [kg/mol]
PP	0	669	1654	4.2		
PP2γ	2.2	575	1219	4.1	0.04	357
PP20γ	21	352	1064	3.5	0.34	62
PP60γ	63	263	1014	3.1	0.75	29
PP100γ	108	272	1067	4.1	1.03	21
PP150γ	155	411	4804	6.1	1.45	15

MATERIALS AND METHODS

Sample Preparation. The commercial product Novolen PPH 2150 from Lyondell-Basell was used in this study. It is an isotactic polypropylene homopolymer (iPP) with a density at room temperature of 0.90 g/cm^3.

The granules were electron-beam-irradiated under a nitrogen atmosphere at atmospheric pressure and ambient temperature in a special vessel with 1.5 MeV electrons and with different total doses d up to 300 kGy using an accelerator of the type ELV-2 (Budker Institute of Nuclear Physics, Russia).[6,13,14] The doses higher than 10 kGy were usually applied in n of steps on 10 kGy (c.f. Tab. 1) in order to minimize the temperature increase resulting from the irradiation and to avoid variations in the molecular structure by a heating effect.[15] For the sample PP100b, a dose of 100 kGy was applied in 100 steps of 1 kGy in order to assess the effect of irradiation dose rate.

After the irradiation process, the samples were first annealed for 30 min at 80 °C to allow for a sufficient migration of chain fragments to free radicals in order to form chain branches and, finally, for 60 min at 130 °C to deactivate the residual radicals. Both annealing steps were also carried out directly in the vessel under a nitrogen atmosphere. The samples are listed in Table 1, the numbers denominate the irradiation doses in kGy. The results of the electron-beam-irradiated samples have been partially published before elsewhere[6] and are used as a reference in this article.

For gamma-irradiation, the virgin material was irradiated with a ^{60}Co gamma-ray source under a nitrogen atmosphere at doses between about 2 and 150 kGy. Pellets were filled into 500 mL glass tubes on a turntable in a panorama unit with 12 sample tubes, orientated at angles of 30° each. After the irradiation, the material was annealed at 80 °C for 1 h and then for 2 h at 130 °C. The applied dose rate was measured by chlorobenzene vessels and determined to be 1.26 kGy/h, which was 1 order of magnitude below the electron-beam irradiation rate of around 100 kGy/h. The samples are listed in Table 2, and the total irradiation doses applied are indicated by their numbers.

After irradiation the surface of the polypropylene pellets was powdered with a mixture of two sterically hindered phenolic antioxidants (0.2% Irganox 1010 and 0.2% Irganox 245) and one organophosphite stabilizer (0.2% Irgafos 38). These heat stabilizers were applied in order to prevent the samples from thermo-oxidative degradation during sample preparation and rheological measurements.

Molecular Characterization. The molecular characterization was performed according to the procedure already described in Auhl et al.[6] For the matter of completeness it is sketched once more in the following. Briefly, the molecular data were measured by high-temperature SEC (Waters GPC 150) coupled with a MALLS device from DAWN EOS, Wyatt Technology, and a refractive index (RI) combined with an infrared (IR) detector. Further experimental details have been published elsewhere.[6,16] By coupling SEC with MALLS, the absolute molecular weight M_{LS} and the mean-square radius of gyration $\langle r^2\rangle^{1/2}$ of every fraction can be determined directly. The ratio of the mean-square radius of gyration of a branched polymer $\langle r^2\rangle_{br}$ to that of a linear polymer $\langle r^2\rangle_{lin}$ is the so-called Zimm−Stockmayer branching parameter g.[17]

$$g = \frac{\langle r^2\rangle_{br}}{\langle r^2\rangle_{lin}} \tag{1}$$

For a trifunctional randomly branched polymer of approximately equal lengths of the branches, g can be related to the number of branching points m along the molecule by[17]

$$g = \left[\left(1 + \frac{m}{7}\right)^{0.5} + \frac{4m}{9\pi}\right]^{-0.5} \tag{2}$$

The Zimm−Stockmayer theory has not yet been verified experimentally for multifunctional randomly branched polymers, and it is debatable whether the branching structures of the irradiated polypropylene discussed in this paper fulfill the assumptions of the theory. Nevertheless, it allows some kind of numerical description of the branching architecture and comparison between the different samples. From the number of branching points m, the number of LCB per 1000 monomer units λ_{LCB} can be determined for each fraction as

$$\bar{\lambda}_{LCB} = \frac{m}{M}\cdot 1000\cdot M_M \tag{3}$$

with M_M being the molecular weight of the monomer unit and M the molecular weight of the branched polymer. The number of LCB per molecule also allows for calculating the segmental molecular weight $\bar{M}_S$ under the assumption that the branching is uniform for each fraction, i.e., that two or more differently branched species are not present and that they are statistically distributed. $\bar{M}_S$ can be determined from the

number of LCB per chain. As each molecule containing m branching points has $2m + 1$ segments, $\bar{M}_S$ followsas

$$\bar{M}_S(M) = \frac{M}{2m + 1} \quad (4)$$

Because of the mathematical nature of the determination of $\bar{M}_S$, it is not possible to calculate a molecular weight independent value of this quantity. Instead, a slight decrease with increasing molecular weight is found, which is stronger at low long-chain branching levels. Therefore, the average values $\bar{M}_S$ are used in this paper, which were determined for the high molecular weight range available from light scattering and correspond to the values of $\bar{M}_S$ at a molecular weight of about the z-average molecular weight M_z. However, there are more LCB in a statistically branched sample at higher molecular weights; it is sensible to analyze these highest molecular weights, for which the characteristic quantity is M_z.

Rheological Characterization. The elongational experiments were carried out with a uniaxial extensional rheometer as has been described in detail elsewhere.[6] Stressing experiments at 180 °C were conducted at different constant elongational rates $\dot{\varepsilon}_0$. The rheological measurements in shear were performed at 180 °C under a nitrogen atmosphere using a rotational rheometer.

The zero-shear viscosity η_0 was determined from creep experiments conducted with a constant stress rheometer (Gemini, Malvern Instruments). The applied constant shear stresses τ_0 were in the order of 10 Pa, i.e., in the linear range of deformation. In the steady state of deformation, the creep compliance $J(t)$ and η_0 are related as follows:

$$\lim_{\substack{t\to\infty \\ \tau_0\to 0}} \frac{t}{J(t)} = \eta_0 \quad (5)$$

i.e., η_0 can be determined in the linear range at sufficiently long creep times, when the spontaneous compliance and the viscoelastic part of deformation become very small compared to t/η_0.[18]

The thermal stability of the samples was tested by measuring the time dependence of the storage modulus $G'(t)$ at low angular frequencies. The time at which the storage modulus had changed by 5% was used as the criterion for the thermal stability. This time was sufficient for the different experiments performed.

RESULTS AND DISCUSSION

Molecular Characterization. Figure 1 shows the molar mass distributions of the electron-beam- and gamma-irradiated PP samples, which were modified with the identical doses of 20, 100, and 150 kGy in comparison with the neat PP.

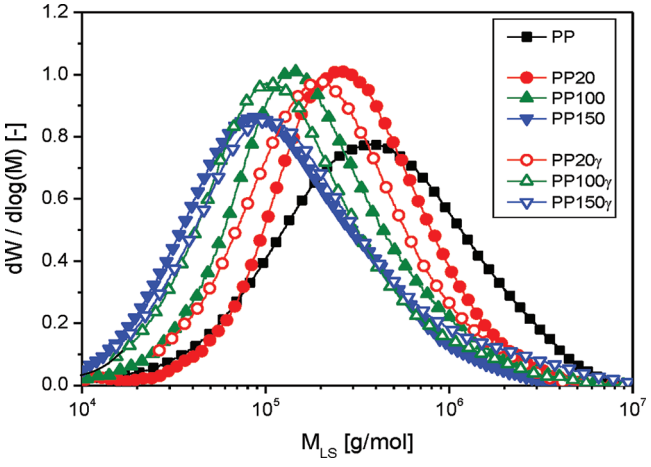

Figure 1. Differential molar mass distributions dW/d log M for the PP precursor and the irradiated samples.

M_w and the polydispersity index M_w/M_n are listed in Tables 1 and 2. M_w changes as a function of the dose for both methods of irradiation in a similar way. M_w/M_n decreases at already small doses for both irradiation methods but remains nearly constant at medium doses. The gamma-irradiation distinctly increases M_w/M_n at 100 and 150 kGy due to the pronounced high molecular weight tails (cf. Figure 1).

Figure 2 presents the radius of gyration $\langle r^2\rangle^{0.5}$ as a function of molecular weight M_{LS} in a double-logarithmic plot. The linear

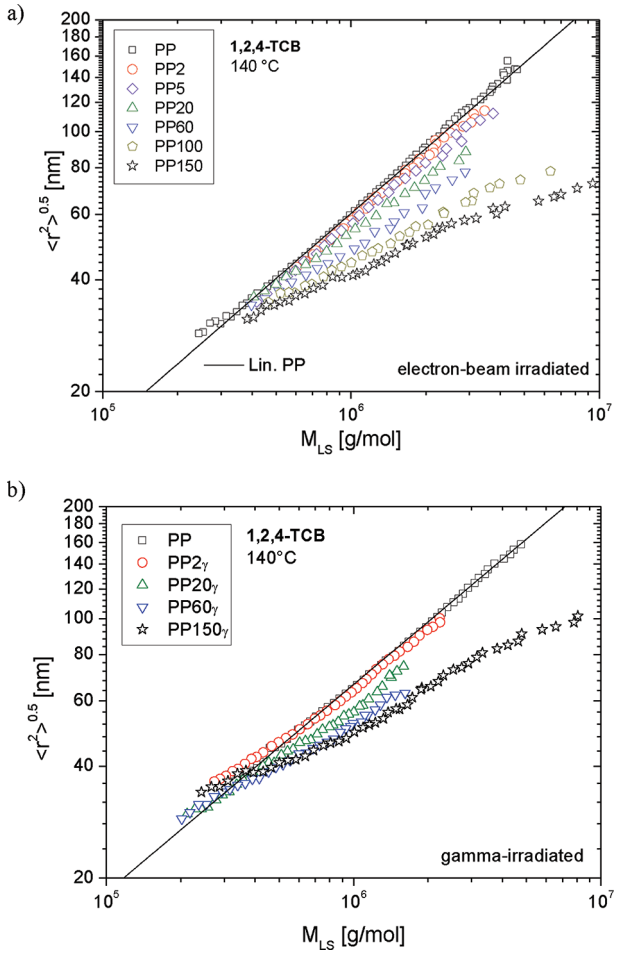

Figure 2. Mean radius of gyration $\langle r^2\rangle^{1/2}$ as a function of molar mass M_{LS} for the linear precursor and the irradiated samples: (a) electron-irradiated PP; (b) gamma-irradiated PPγ.

PP exhibits a linear relation with a slope of 0.58, which is in good agreement with the literature. The deviations of the irradiated samples from this line indicate a coil contraction that is related to long-chain branching. The deviation increases with growing irradiation dose and molecular weight. At the lowest dose of 2 kGy, the measured data lie within the scatter of the linear PP.

The dependences of the radius of gyration on the molecular weight for the electron-beam- and gamma-irradiated products of PP indicates a significant coil contraction for molecular weights larger than 5×10^5 g/mol. This result implies the preferential presence of LCB for larger molecules (Figure 2).

On the basis of the coil contraction, the concentration of long-chain branches per 1000 monomer units λ_{LCB} was determined according to eq 3. As these data showed a relatively large scatter, the average values, $\bar{\lambda}_{LCB}$, are discussed. They are

dx.doi.org/10.1021/ma202265w | Macromolecules 2012, 45, 2057–2065

represented in Table 1 and 2. The gamma-irradiated PP has a branching level $\bar{\lambda}_{LCB}$ that is significantly higher (about twice as high) than that of the electron-irradiated PP, if compared at the same doses. In Figure 3, the data are plotted for a direct

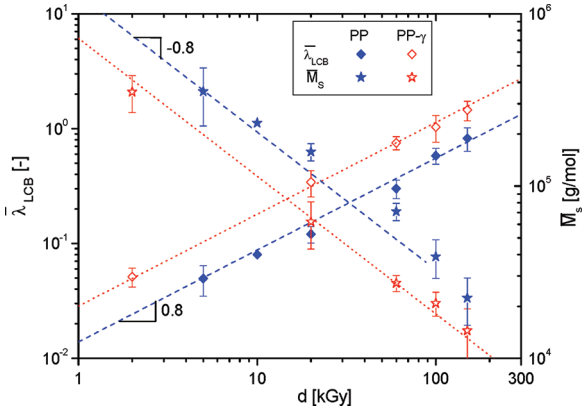

Figure 3. Average degree of long-chain branching $\bar{\lambda}_{LCB}$ and molecular weight of segments $\bar{M}_S$ as a function of dose for the differently irradiated PP.

comparison. The clearly apparent differences reveal a stronger dose dependency of $\bar{\lambda}_{LCB}$ in the case of gamma-irradiation. An increase of $\bar{\lambda}_{LCB}$ with an exponent of about 0.8 is found for the electron-beam as well as for the gamma-irradiated series.

Rheological Properties. *Linear-Viscoelastic Properties in Shear.* Rheological functions are not only an indicator of the flow properties of a polymer melt; they can also be used as a very sensitive means of assessing the molecular structure of polymers, especially with respect to long-chain branching.[19−21] Because of the high sensitivity of the linear-viscoelastic properties on the molecular structure, these quantities are preferably taken into consideration. Several correlations between molecular and rheological quantities can be applied for a molecular analysis.[22−31]

Molecular Weight Dependence of the Zero Shear-Rate Viscosity. One of the important correlations for analyzing the branching structure is the relation between the zero shear-rate viscosity η_0 and the weight-average molecular weight M_w.[16,22,32−34] For linear[15,16,22,27,33,35,36] and to some degree also for short-chain branched polymers,[18,37,38] the following correlation holds:

$$\eta_0 = KM_w{}^a \tag{6}$$

For polymers with M_w below a critical molecular weight M_c which is about 2−3 times the entanglement molecular weight $M_e \approx 6$ kg/mol for isotactic PP,[38,39] the exponent a is found to be around 1, whereas above M_c it is about 3.4−3.6.[40] Auhl et al.[6] found a = 3.54 and log K = −15.4 at 180 °C for isotactic PP, which is in good agreement with other findings in the literature.[18,37] As the initial PP is one of these linear polymers, this relationship is used in this paper as a reference. Unlike most other structure−rheology correlations, eq 6 is found to be independent of the molecular weight distribution within the experimental accuracy.[16,27,41−45]

For star-shaped polymers with only one branching point per molecule, the following relationship between the arm length M_a normalized by the entanglement molecular weight M is proposed:[46,47]

$$\eta_0 \propto \left(\frac{M_a}{M_e}\right)^{\kappa} \exp\left(\upsilon\frac{M_a}{M_e}\right) \tag{7}$$

where ν and κ are parameters in the order of 1. Although it seems counterintuitive, η_0 is hardly influenced by the number of arms but predominantly by their length. The validity of eq 7 has been proven for several different polymers (polystyrene, polybutadiene, hydrogenated polybutadiene, polyisoprene) over a wide range of molecular weights.[48−51] For comblike polymers different and more complicated relations are found that depend on several parameters.[52]

Because the zero shear-rate viscosity as a function of M_w is a very sensitive quantity to be used to detect even low amounts of long-chain branching, this relationship is used to analyze the irradiated polypropylenes. In Figure 4, the zero-shear viscosities

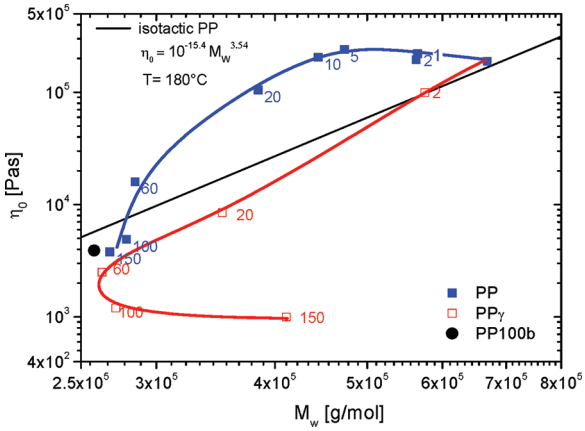

Figure 4. Dependence of the zero shear-rate viscosity η_0 at 180 °C on M_w (M_w determined from SEC-MALLS). The numbers at the data points refer to the irradiation dose in kGy.

of the irradiated samples are plotted as a function of the weight-average molecular weights. As expected from the branching analysis using SEC-MALLS (cf. Figure 3), the electron-beam-irradiated PP samples does not fulfill the η_0−M_w correlation for linear iPP. The η_0 values are higher than the zero-shear viscosity $\eta_0{}^{lin}$ expected for linear iPP of corresponding M_w. For irradiation doses up to about 10 kGy, the deviation from the η_0−M_w relation of linear polymers increases with increasing dose. The zero-shear viscosity increase factor $\eta_0/\eta_0{}^{lin}$ is clearly larger than 1 for small irradiation doses, which indicates the existence of long-chain branches.[6,53] For doses of about 60 kGy, the zero shear-rate viscosity η_0 agrees approximately to the relation for linear samples, while for higher irradiation doses, η_0 decreases below the linear relation.

The gamma-irradiated samples exhibited a totally different behavior (cf. Figure 4). PP2γ comes to lie on the line for the linear PP, indicating that the influence of the irradiation is negligible. All the other data points are below the relationship for the linear PP. The two highest irradiation doses are particularly surprising. Because of the increasing M_w, but still decreasing η_0 with higher irradiation doses, $\eta_0(M_w)$ bends off. Such a behavior has not been reported in the literature before. Since the dose rate was different for the two series, data are added for another electron-beam-irradiated PP sample with 100 kGy (PP100b), but at a dose rate similar to that of the gamma-

dx.doi.org/10.1021/ma202265w | Macromolecules 2012, 45, 2057−2065

irradiation. A comparison shows that for the two electron-beam-irradiated PP-100 samples the molecular weight as well as $\eta_0(M_w)$ are quite similar, which indicates that the dose rate may not be the decisive factor for the branching structure. This indicates that the type of irradiation induces chain growth and simultaneously enhances the branching efficacy.

The different effects of electron-beam and gamma-irradiation on η_0 are once more revealed from the plot of η_0/η_0^{lin} as a function of the irradiation dose d in Figure 5. The viscosity

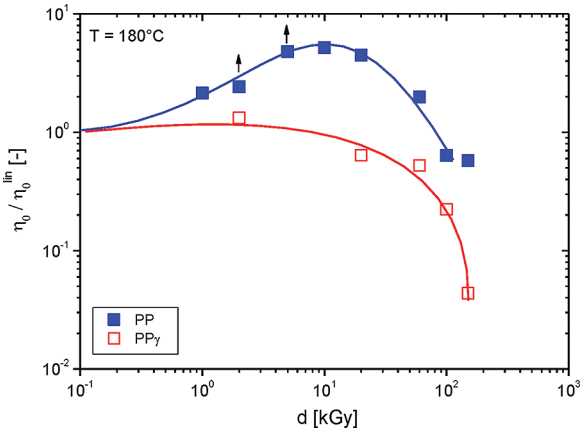

Figure 5. Zero shear-rate viscosity increase factor η_0/η_0^{lin} as a function of irradiation dose d.

ratio of the electron-beam-irradiated PP exhibits a maximum of "η_0/η_{0lin}" around 5 at around 10 kGy. However, no maximum of η_0/η_0^{lin} occurred for the gamma-irradiation, but $\eta_0/\eta_0^{lin}(d)$ decreases monotonously to ~0.04 at 150 kGy, compared to about 0.6 for the electron-beam-irradiated PP. This result gives further evidence that the type of irradiation distinctly influences the dose dependency of the zero shear-rate viscosity enhancement factor $\eta_0/\eta_0^{lin}(d)$. The dependence of this factor on the architecture of LCB implies that the two irradiation methods applied lead to different molecular structures. This conclusion is instructive insofar as the classical molecular analysis, the results of which are presented in Tables 1 and 2, does only show slight distinctions between the electron-beam and gamma-irradiation and gives no hint of any differences of the branching structure, except for a higher branching density for the gamma-irradiated series.

From a comparison with results on polyethylenes with a branching structure known from the polymerization conditions, more detailed predictions of the structure of the irradiated polypropylenes can be obtained. For long-chain branched polyethylenes it was shown that slightly long-chain branched PE with a starlike structure lie above the line of linear PE, whereas a position beneath the line indicates a treelike topography.[27,54−56] This anomaly was explained by the exponential dependence of η_0 on the ratio of M_a/M_e (cf. eq 7). Taking these findings into account, a treelike topography is likely for the electron-beam-irradiated samples with doses above 60 kGy and for the gamma-irradiated specimen already above 2 kGy.[6]

Some more detailed conclusions can be drawn from a comparison with the molecular analysis. The results of Figure 2 clearly showed the virtual absence of any LCB at small irradiation doses, but according to Figure 4, the η_0-M_w relation for linear PP was not obeyed. This finding further demonstrates that a small amount of long-chain branching not detectable by *SEC*-MALLS can have a profound impact on the rheological behavior.[54] From Tables 1 and 2 it can be concluded that only a minor fraction of the molecules of the samples irradiated with 20 kGy or less was actually long-chain branched. For PP20 for example, each chain of $M = M_w$ contains an average of 1.1 LCB. Hence, the samples with lower irradiation doses can be regarded as a mixture of linear and starlike chains of higher molecular weight. The molecules of higher molar mass contain more than one branching point. A growing irradiation dose increases the branched species at the cost of the linear ones. At around 60 kGy, corresponding to a number of 0.3 LCB per 1000 monomers (cf. Table 1), the effect of an increase of η_0 was diminished. This number was already reached for the gamma-irradiation at a dose of 20 kGy, in accordance with the findings that η_0 of this sample clearly comes to lie below the line of the linear PP.

To investigate the influence of the length of the branches on the zero shear-rate viscosity η_0, the data obtained from different irradiation doses and methods were compared to results from the literature. Because the exact molecular structure (position and distribution of the long-chain branches) is unknown in statistically branched polymers and cannot be assessed properly with analytical methods, the distribution is assumed to be uniform. Hence, the segmental molecular weight—assuming that a molecule with m long-chain branches contains $2m + 1$ molecular segments with a molecular weight $\bar{M}_S$—is used for the analysis. This assumption means that the introduction of LCB leads to shorter molecular segments if the molecular weight is constant. Furthermore, it is assumed that the number and lengths of long-chain branches per molecule is identical for all chains of the same molecular weight.

The electron-beam irradiation increased η_0/η_0^{lin} up to doses of 20 kGy due to the increase in the number of branched molecules (cf. Table 1). Despite a further increase in the concentration of branched molecules with increasing irradiation dose, η_0/η_0^{lin} decreases to less than 1. This finding can be explained by the assumption that the increase of the LCB concentration is accompanied by a decrease in the LCB length. Measurements and molecular models, e.g., on combs[52,57,58] or stars,[47,49,59] have shown exactly this effect for model architectures. For irradiation doses below 20 kGy, on average less than 1 LCB was present per molecule, which indicated the presence of a mixture of linear and predominantly star-branched chains. This conclusion is in agreement with the findings on various metallocene-synthesized LCB-mPE, which show the highest η_0/η_0^{lin} for mixtures of linear and star-branched chains.[25,31,34,60]

All samples with an irradiation dose of 20 kGy or less (except PP20γ) show $m(M_w)$ below about 1 (see Tables 1 and 2), which revealed the presence of at least some linear chains in all of these samples. The maximum in $\eta_0/\eta_0^{lin}(d)$ for the electron-beam-irradiated samples can be attributed to the nature of the following two opposing effects: an increasing concentration of branched chains and their decreasing arm length. The first effect increases η_0 due to the increase of the fraction of branched chains, whereas the second effect decreases it (cf. eq. 7).

The kind of irradiation, however, significantly affects η_0/η_0^{lin}, as revealed by the difference between the electron-beam- and gamma-irradiated PP, as the gamma-irradiation predominantly leading to $\eta_0/\eta_0^{lin} < 1$ (Figure 5). This finding indicated that the gamma-irradiation generated different branching structures compared to the electron-beam irradiation.

dx.doi.org/10.1021/ma202265w | *Macromolecules* 2012, 45, 2057−2065

Stange et al.[61] investigated blends of highly branched PP and linear PP, which also showed $\eta_0/\eta_0^{lin} < 1$ despite a low degree of long-chain branching. Hence, the average degree of long-chain branching alone cannot determine whether η_0/η_0^{lin} will be larger or smaller than 1 as Bersted[56] suggested. Stange et al.'s findings[61] show many similarities to the PPγ series, which supports the conclusion that the gamma-irradiation leads to the introduction of long-chain branches by forming a few highly branched molecules within a rather linear matrix. Such a structure has to be distinguished from the existence of some few star-shaped molecules surrounded by linear ones.

Uniaxial Elongational Flow. As it was shown in the literature, long-chain branching can significantly affect the elongational properties of polymer melts.[62−68] Particularly, the branching structure is reflected by the elongational behavior. Therefore, stressing experiments at different constant elongational rates were performed on the differently irradiated polypropylenes. The results are presented in Figure 6a,b.

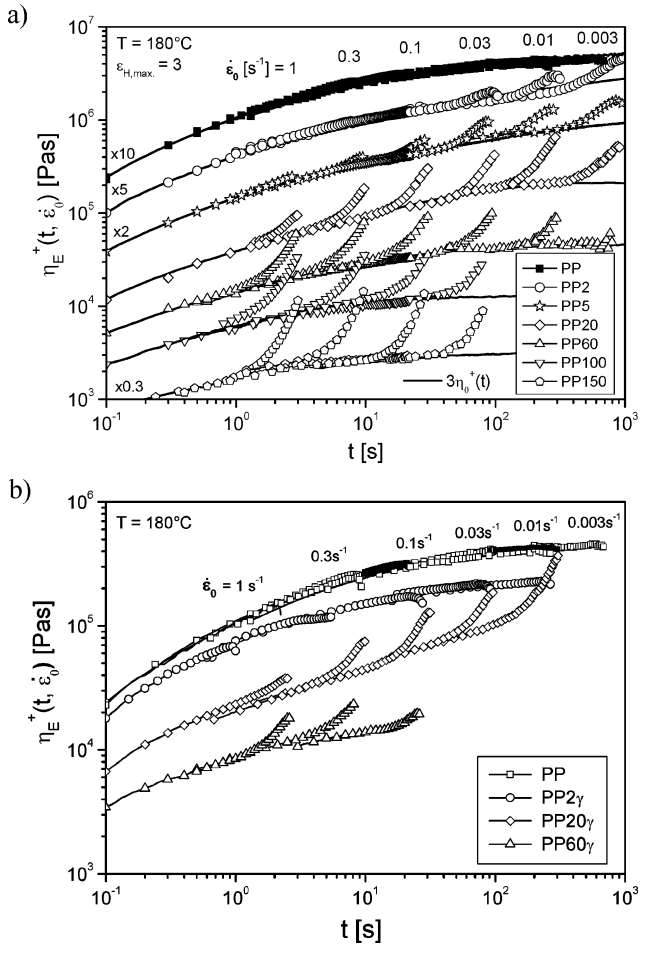

Figure 6. Transient elongational viscosity $\eta_E^+(t)$ as a function of time t at different Hencky strain rates $\dot{\varepsilon}_0$ for (a) electron-beam-irradiated PP and (b) the gamma-irradiated samples PP2γ to PP60γ.

For each irradiation dose, the respective curves superpose on the linear viscoelastic start-up curve at all strain rates up to a Hencky strain of about 0.7. Trouton's relation[69] $\eta_E^+(t) = 3\eta_S^+(t)$, which relates the transient shear and elongational viscosity in the linear range of uniaxial flow, is fulfilled for deformations ε_H smaller than 0.7 for all samples and evidence the reliability of the experiments. We have previously published some of the elongational data for the electron-beam-irradiated PP.[6]

The time-dependent functions of the elongational viscosity $\eta_E^+(t,\dot{\varepsilon}_0)$ did not show any strain-hardening for PP2γ within the experimental accuracy, while PP20γ and PP60γ exhibited a distinct deviation from the linear curve. For elongations ε_H higher than 0.7, the samples are strain hardening.

Strain hardening is very sensitive to the molecular structure. The so-called strain-hardening coefficient χ_E is defined by

$$\chi_E(t) = \frac{\eta_E^+(t, \dot{\varepsilon}_0)}{3\eta_0^+(t)} \quad (8)$$

with $\eta_0^+(t)$ being the time-dependent shear viscosity in the linear range of deformation. χ is presented in Figure 7 as a

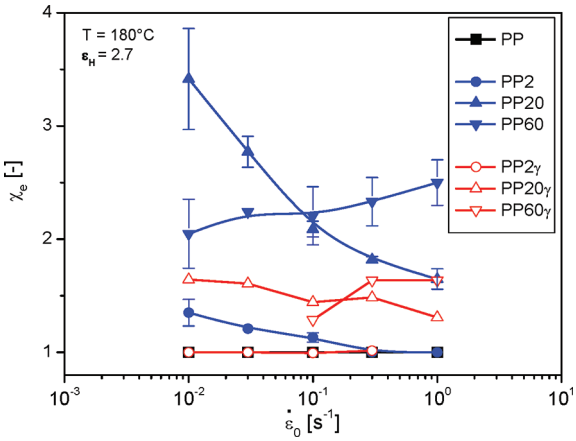

Figure 7. Strain-hardening factor χ_E as a function of strain-rate $\dot{\varepsilon}_0$ for electron-beam- and gamma-irradiated samples at a Hencky strain of 2.7.

function of the elongational rate. For the linear polypropylene PP, no strain hardening was observed at Hencky strains ε_H at least up to 2.7. This is the usual finding for linear samples with a unimodal molecular weight distribution.[67] In contrast, most of the irradiated samples showed strain hardening of increasing severity with increasing irradiation doses. The exception was PP2γ, and the absence of any strain hardening indicated a very low branching efficiency. This observation is in agreement with the zero-shear viscosity as a function of M_w which lies on the curve for the linear polypropylenes (cf. Figure 4).

PP100γ and PP150γ could not be characterized in elongation because their viscosities were too low. For the samples irradiated with 20 kGy, the strain hardening decreases with increasing strain rate. This effect was more pronounced for the electron-beam-irradiated sample than for the gamma-irradiated one. For the samples subjected to 60 kGy, the strain hardening increased with increasing strain rate. A decreased in strain hardening with increasing strain rate is usually associated with low degrees of long-chain branching of a starlike topography, while the opposite behavior is typical of a high degree of branching with a treelike topography.[6,62,64,67,70−75]

The polydispersity or, specifically, high molecular weight components can principally influence the elongational viscosity.[76,77] However, the molecular weight distributions of the irradiated samples are not so different that a significant effect on the strain hardening has to be taken into account. Furthermore, the SEC measurements showed that the polydispersity of the samples characterized in elongation is

dx.doi.org/10.1021/ma202265w | *Macromolecules* 2012, 45, 2057−2065

slightly decreased with irradiation and no bimodal molecular weight components were found. Hence, the results of the elongation behavior for the irradiated polypropylenes can be directly related to the branching structure

The general trend of the strain-rate dependence of the strain-hardening coefficient, χ_e, is comparable for electron- and gamma-irradiated PP, but the level of strain hardening for the gamma-irradiated products is lower and the dependence on the elongational rate weaker. Considering that the branching level $\overline{\lambda}_{LCB}$ of PP60 is almost the same as that of PP20γ, the strain-hardening coefficient as a function of strain rate $\chi_e(\dot{\varepsilon})$ could be expected to be comparable, if the LCB-structures were the same. However, PP60 shows the typical characteristic of a highly branched sample with $\chi_e(\dot{\varepsilon})$ increasing, while PP20γ exhibits the characteristic of a slightly branched sample with $\chi_e(\dot{\varepsilon})$ decreasing. This difference confirms the different branching structures of these two samples. Furthermore, it is obvious that PP20 shows a χ_E at $\varepsilon_H = 2.7$ distinctly decreasing with decreasing $\dot{\varepsilon}$, while the strain-hardening coefficient for PP20γ is rather constant.

Figure 7 clearly demonstrates that the strain-hardening coefficient decreases with increasing strain rates for the samples electron-beam-irradiated with 2−20 kGy.[6,62,64,67,70−75] In contrast to the weakly irradiated samples, the strain hardening of PP-60 increases with increasing strain rate. Such a behavior is found for low-density polyethylene (LDPE) with a high amount of long-chain branching and a treelike molecular structure.[67,71,72,75] Therefore, the differences of the strain-rate dependence of χ_E *at* $\varepsilon_H = 2.7$ support the conclusion that the branching structure changes with the irradiation dose.

CONCLUSIONS

The irradiation of PP under different conditions, i.e., electrons and gamma-rays, exhibits two general consequences: the molecular weight is reduced, and the number of long-chain branches was increased with increasing irradiation dose. The branching structure of the samples investigated is assumed as random, since the length of the branches and their position along the polymer backbone are of a statistical nature due to the irradiation process. The reduction of the molecular weight and, particularly, the long-chain branching significantly affected the viscoelastic properties of the melts. The generation of LCB was detected by usual molecular characterization methods. The shear and elongational properties were also strongly indicative of LCB of different amounts and topographies, which depend on the irradiation parameters. The various results are discussed below.

Shear Rheology. The η_0 values of the electron-beam-irradiated polypropylenes were significantly increased compared to those of the untreated PP samples of the corresponding weight-average molecular weights. At small irradiation doses, i.e., at comparably low amounts of LCB the ratio of the viscosity of the branched sample to that of the linear one, η_0/η_0^{lin}, reached a maximum, but approached unity again at higher LCB contents. This increase is explained by small amounts of long-chain branches with relatively high molecular weight of the arms M_a and, hence, a high ratio of M_a/M_e, which affects η_0 exponentially. The decrease of η_0/η_0^{lin} at higher doses can formally be related to a decline of the molecular weight M_a of the branches. Two mechanism are postulated to explain this change. First, the molecular weight decreases with increasing irradiation dose, which shortens the length of the molecules attached to the backbone. Second, it is not unrealistic to assume that a change of architecture from starlike to treelike branches takes place with increased irradiation. A treelike structure is characterized by branches randomly distributed along the chains, resulting in a higher number of chains with values of M_a smaller than in the case of a molecule with few long-chain branches.

The gamma-irradiation decreased M_w and η_0 up to doses of 100 kGy. The difference with respect to the electron-beam-irradiated series lies in the fact that $\eta_0/\eta_0^{lin}(d)$ monotonously decreased with no peak. In conjunction with the LDPE results, these findings can be interpreted as revealing that the samples contained long-chain branches in a treelike architecture.

Elongational Rheology. The irradiated samples show a distinct strain hardening in elongational flow with different strain-rate dependences. Two conclusions can be drawn from the results. First, the strong effect of branching is clearly demonstrated. This conclusion is supported by the finding that strain hardening increased for the more strongly irradiated samples, despite the significant decrease in the molecular weight. The results from SEC-MALLS that the polydispersities of the polymers remained nearly constant after irradiation with various doses and that a high-molecular-weight component was not detectable demonstrate that the elongational viscosity can be used as a reliable indicator of the generation of long-chain branching in polypropylene by electron irradiation. Second, the rate dependence of strain hardening supports a conclusion with respect to the topography of the polypropylene molecules, if the well-established results on polyethylenes are taken into account. The decreasing strain hardening with increasing strain rate, as exhibited by the low irradiated samples, is indicative of a small degree of branching with high molecular weights of the branches. The increase in strain hardening with increasing strain rate indicates a high degree of branching with smaller arm molecular weights M_a as it is typical of LDPE. These conclusions concerning the topography of the long-chain branches in electron-beam-irradiated polypropylenes form an experimental basis for a comparison of models on radical reactions initiated by irradiation.

Influence of the Type of Irradiation. The comparison of PP irradiated by the same doses of electrons or gamma-rays show a somewhat larger molecular weight reduction, but a higher degree of long-chain branching for the gamma-irradiation. The rheological properties differ significantly as the gamma-irradiated samples exhibit a lower zero shear-rate viscosity than the samples irradiated by electrons, when compared at the same molecular weight. While for the electron-beam-irradiated samples the viscosities lies above the reference line for the linear samples, i.e., η_0/η_0^{lin} is larger than 1, η_0 lay below this line for all the gamma-irradiated samples, i.e., η_0/η_0^{lin} is larger 1. The elongational behavior of the electron-beam- and gamma-irradiated samples exhibited the same basic characteristics, namely strain hardening, but there were clear differences with respect to its level, which was higher for the electron irradiation at the same dose. These findings confirm that gamma- and electron-beam irradiation did not yield the same molecular structure. A possible explanation lies in the much lower dose rate of the gamma-irradiation, which leaves the radicals more time to react compared to the electron-beam irradiation.

From Figure 4 and a comparison with literature results on polyethylenes, electron-beam-irradiated PP20 can be regarded as being roughly comparable to a long-chain branched mPE,[28,60,67,78] i.e., with an architecture predominantly consist-

ing of star-shaped and linear molecules, while PP20γ is rather comparable to an LDPE, if $\eta_0(M_w)$ is regarded. The branching structure has to be assumed somewhat different (less star-like and more linear and highly branched chains), however, as the strain-hardening patterns of PP20γ and LDPE differ significantly.

The differences found in the rheological behavior may go back to the different irradiation rates. Two reasons for these findings may be discussed. First, the type of irradiation causes different molecular reactions, and second, the different dose rates are responsible for the behavior observed. Spadaro and Valenza[79] showed that increasing the dose and dose rate leads to a higher number of radicals in PP. The smaller irradiation dose rate and hence the lower concentration of radicals mean that the elimination of two radicals by recombination is reduced; i.e., the radicals have a longer lifetime and can cause a higher number of scission and re-formation reactions, which eventually leads to a treelike structure of long-chain branching.

The strain hardening increasing with decreasing strain rate even at the highest doses are not in contrast to this assumption as the elongational viscosities of blends of a linear and a long-chain branched PP demonstrate.[61] For the components investigated by Stange et al.[61] up to a content of 50% LCB-PP a strain-hardening behavior similar to that of the gamma-irradiated PP is found. Therefore, the results on the gamma-irradiated PP can be interpreted in the way that it consists of a blend of linear and treelike chains.

However, as only a low dose rate of 1.26 kGy/h was applied during gamma-irradiation and usually high dose rates of about 100 kGy/h for the electron-beam irradiation (while the total doses are the same for both sample series) in the present study, the extent to which the effects described in this article are due to the irradiation type or to the dose rate could not finally be determined.

Structure–Property Relationships. The results of this work show that the rheological quantities in shear and elongational reacted more sensitively to the presence of long-chain branches than the quantities measured by the classical size-exclusion chromatography. Especially, the zero shear-rate viscosity η_0 was sufficiently sensitive to detect even low amounts of LCB and to provide a deeper insight into changes of the molecular structure.

To summarize, the results support the conclusion that the irradiated polypropylenes investigated consist of molecular structures with long-chain branches, the number of which increases with increasing irradiation doses. Strong evidence is presented that this increase leads to a change of branching architectures from starlike to treelike structures. The conclusions are drawn taking the findings on long-chain branched polyethylenes into account; i.e., the lightly electron-beam-irradiated samples are similar to metallocene-catalyzed sparsely long-chain branched polyethylene, while the highly irradiated ones resemble highly branched LDPE. The results presented on the irradiated PP-samples broaden the experimental base of the relationship between rheological properties of polymer melts and their molecular structure, which can be exploited in two ways. First, the results strengthen the role of rheological measurements as an analytical tool, and second, they offer some suggestions for the method by which polypropylene can be modified by irradiation. These insights will be particularly valuable for tailoring polypropylene for special applications.

■ SUMMARY

This work has compared the effects of electron-beam and gamma-irradiation on molecular and rheological properties of a polypropylene. While the differences between the two irradiation methods with respect to molecular properties measured by SEC-MALLS are rather small (gamma-irradiation led to higher degrees of long-chain branching and a high molecular weight tail), they are more pronounced regarding the rheological behavior. The gamma-irradiation leads to a much smaller zero shear-rate viscosity η_0 than the electron-beam irradiation at comparable doses, although the differences of the weight-average molecular weights are not very pronounced. This behavior indicates the generation of different branching architectures by the two irradiation methods. Considering results on branched polyethylenes and blends of linear and long-chain branched polypropylenes, it can be concluded that the gamma-irradiation led to a branching structure, which may be similar to that of a slightly branched LDPE, while electron-beam irradiation led to branched molecules, which carry fewer but probably longer long-chain branches of a starlike structure at smaller irradiation doses and seem to approach a treelike structure with higher doses. This conclusion can be drawn from the findings that η_0/η_0^{lin} becomes smaller than 1 for doses larger than 100 kGy (Figure 4) and that the strain hardening behavior resembles that of LDPE (cf. Figure 6a).

Although details of the branching structures generated have to be left open, the main conclusion is, therefore, that electron-beam and gamma-irradiation effects in polypropylene do not follow the same reaction kinetics and, thus, generate different structures of long-chain branching.

■ AUTHOR INFORMATION

Corresponding Author

*E-mail: fjstadler@jbnu.ac.kr (F.J.S.); helmut.muenstedt@ww.uni-erlangen.de (H.M.).

■ ACKNOWLEDGMENTS

The authors thank the German Research Foundation (DFG) for financial support of this work. D.A. and F.J.S. would like to thank the EU Framework 7 program for the "SupraDyn" Marie-Curie fellowship and "Human Resource Development (201040100660)" of the Korea Institute of Energy Technology Evaluation and Planning (KETEP), respectively. The contributions and useful discussions with J. Kaschta, J. Stange, I. Herzer (University Erlangen-Nuremberg), and S. Henning (MLU Halle-Wittenberg in Merseburg) are gratefully acknowledged. The work would not have been possible without the supply of irradiated PP samples by B. Krause, U. Lappan, and K. Lunkwitz (electron-beam irradiation, Leibniz-Institute of Polymer Research Dresden) as well as R. Godehard and G. Michler (gamma-irradiation, Martin-Luther University Halle-Wittenberg).

■ REFERENCES

(1) DeNicola, A. J. Process for making a propylene polymer with free-end long chain branching and use thereof. Europ. Patent 0,351,866, 1989.

(2) Scheve, B. J.; Mayfield, J. W.; DeNicola, A. J. High melt strength, propylene polymer, process for making it, and use thereof. U. S. Patent 4,916,198, 1990.

(3) Schnabel, W.; Dole, M. *J. Phys. Chem.* **1963**, *67*, 295–299.

(4) Henglein, A.; Schnabel, W.; Wendenburg, J. *Einführung in die Strahlenchemie*; Akademie Verlag: Berlin, 1969.

(5) Rizzo, G.; Spadaro, G.; Acierno, D.; Calderaros, E. *Radiat. Phys. Chem.* **1983**, *21* (4), 349−353.
(6) Auhl, D.; Stange, J.; Münstedt, H.; Krause, B.; Voigt, D.; Lederer, A.; Lappan, U.; Lunkwitz, K. *Macromolecules* **2004**, *37* (25), 9465−9472.
(7) Sarcinelli, L.; Valenza, A.; Spadaro, G. *Polymer* **1997**, *38* (10), 2307−2313.
(8) Nishimoto, S.; Kagiya, T. Radiation degradation of polypropylene. In *Handbook of Polymer Degradation*; Hamid, S. H., Amin, M. B., Maadhah, A. G., Eds.; Marcel Dekker: New York, 1992.
(9) Carlsson, D.; Chmela, S. *Mechanisms of Polymer Degradation and Stabilisation*; Elsevier: London, 1990.
(10) Valenza, A.; Piccarolo, S.; Spadaro, G. *Polymer* **1999**, *40* (4), 835−841.
(11) Shamshad, A.; Basfar, A. A. *Radiat. Phys. Chem.* **2000**, *57* (3−6), 447−450.
(12) Alariqi, S. A. S.; Kumar, A. P.; Rao, B. S. M.; Singh, R. P. *Polym. Degrad. Stab.* **2009**, *94* (2), 272−277.
(13) Dorschner, H.; Jenschke, W.; Lunkwitz, K. *Nucl. Instrum. Methods Phys. Res., Sect. B* **2000**, *161* (163), 1154−1158.
(14) Körber, H.; Lappan, U.; Geissler, U.; Lunkwitz, K.; Hanke, R. 2001, German Patent 19 930 742.
(15) Krause, B.; Voigt, D.; Haussler, L.; Auhl, D.; Münstedt, H. *J. Appl. Polym. Sci.* **2006**, *100* (4), 2770−2780.
(16) Stadler, F. J.; Piel, C.; Kaschta, J.; Rulhoff, S.; Kaminsky, W.; Münstedt, H. *Rheol. Acta* **2006**, *45* (5), 755−764.
(17) Zimm, B. H. M.; Stockmayer, W. H. *J. Chem. Phys.* **1949**, *17* (12), 1301−1314.
(18) Ferry, J. D. *Viscoelastic Properties of Polymers*; John Wiley and Sons: New York, 1980.
(19) Piau, J.-M.; Agassant, J. F. *Rheology for Polymer Melt Processing*; Elsevier Science: Amsterdam, 1996.
(20) Münstedt, H.; Steffl, T.; Malmberg, A. *Rheol. Acta* **2005**, *45* (1), 14−22.
(21) Münstedt, H. *Soft Matter* **2011**, *7* (6), 2273−2283.
(22) Dealy, J.; Larson, R. G. *Structure and Rheology of Molten Polymers - From Structure to Flow Behavior and Back Again*; Hanser: Munich, 2006.
(23) Piel, C.; Stadler, F. J.; Kaschta, J.; Rulhoff, S.; Münstedt, H.; Kaminsky, W. *Macromol. Chem. Phys.* **2006**, *207* (1), 26−38.
(24) Stadler, F. J.; Piel, C.; Kaminsky, W.; Münstedt, H. *Macromol. Symp.* **2006**, *236* (1), 209−218.
(25) Stadler, F. J.; Piel, C.; Klimke, K.; Kaschta, J.; Parkinson, M.; Wilhelm, M.; Kaminsky, W.; Münstedt, H. *Macromolecules* **2006**, *39* (4), 1474−1482.
(26) van Ruymbeke, E.; Stéphenne, V.; Daoust, D.; Godard, P.; Keunings, R.; Bailly, C. *J. Rheol.* **2005**, *49* (6), 1503−1520.
(27) Gabriel, C.; Münstedt, H. *Rheol. Acta* **2002**, *41* (3), 232−244.
(28) Gabriel, C.; Kokko, E.; Löfgren, B.; Seppälä, J.; Münstedt, H. *Polymer* **2002**, *43* (24), 6383−6390.
(29) Stadler, F. J.; Gabriel, C.; Münstedt, H. *Macromol. Chem. Phys.* **2007**, *208* (22), 2449−2454.
(30) Resch, J. A.; Stadler, F. J.; Kaschta, J.; Münstedt, H. *Macromolecules* **2009**, *42* (15), 5676−5683.
(31) Stadler, F. J.; Kaschta, J.; Münstedt, H. *Macromolecules* **2008**, *41* (4), 1328−1333.
(32) Stadler, F. J.; Münstedt, H. *Macromol. Mater. Eng.* **2009**, *294* (1), 25−34.
(33) Janzen, J.; Colby, R. H. *J. Mol. Struct.* **1999**, *485*, 569−584.
(34) Wood-Adams, P. M. *J. Rheol.* **2001**, *45* (1), 203−210.
(35) Graessley, W. W. *Polymer* **1977**, *10*, 332−339.
(36) Auhl, D.; Ramirez, J.; Likhtman, A. E.; McLeish, T. C. B.; Chambon, P.; Fernyhough, C. M. *J. Rheol.* **2008**, *52* (3), 801−835.
(37) Berry, G. C.; Fox, T. G. *Adv. Polym. Sci.* **1968**, *5*, 261−357.
(38) Stadler, F. J.; Münstedt, H. *J. Rheol.* **2008**, *52* (3), 697−712.
(39) Chen, X.; Stadler, F. J.; Münstedt, H.; Larson, R. G. *J. Rheol.* **2010**, *54* (2), 393.
(40) Fetters, L. J.; Lohse, D. J.; Milner, S. T.; Graessley, W. W. *Macromolecules* **1999**, *32* (20), 6847−6851.
(41) Gahleitner, M. *Prog. Polym. Sci.* **2001**, *26*, 895−944.
(42) Fujiyama, M.; Inata, H. *J. Appl. Polym. Sci.* **2002**, *84* (12), 2157−2170.
(43) Masuda, T.; Kitagawa, K.; Inoue, T.; Onogi, S. *Macromolecules* **1970**, *3* (2), 116−125.
(44) Struglinski, M. J.; Graessley, W. W. *Macromolecules* **1985**, *18* (12), 2630−2643.
(45) Fleissner, M. *Macromol. Symp.* **1992**, *61*, 324−341.
(46) Ball, R. C.; McLeish, T. C. B. *Macromolecules* **1989**, *22*, 1911−1913.
(47) Pearson, D. S.; Helfand, E. *Macromolecules* **1984**, *17* (4), 888−895.
(48) Kraus, G.; Gruver, J. T. *J. Polym. Sci., Part A: Gen. Pap.* **1965**, *3* (1), 105−122.
(49) Graessley, W. W.; Roovers, J. *Macromolecules* **1979**, *12* (5), 959−965.
(50) Rochefort, W. E.; Smith, G. G.; Rachcpudy, H.; Raju, V. R.; Graessley, W. W. *Polymer* **1979**, *17*, 1197−1210.
(51) Fetters, L. J.; Kiss, A. D.; Pearcon, D. S.; Quack, G. F.; Vitus, F. J. *Macromolecules* **1993**, *26* (4), 647−654.
(52) Inkson, N. J.; Graham, R. S.; McLeish, T. C. B.; Groves, D. J.; Fernyhough, C. M. *Macromolecules* **2006**, *39* (12), 4217−4227.
(53) Münstedt, H. Polymerschmelzen. In *Fliessverhalten von Stoffen und Stoffgemischen*; Kulicke, W., Ed.; Hüthig&Wepf-Verlag: Basel, 1986; pp 238−279.
(54) Wood-Adams, P. M.; Dealy, J. M.; deGroot, A. W.; Redwine, O. D. *Macromolecules* **2000**, *33* (20), 7489−7499.
(55) Bersted, B. H.; Slee, J. D.; Richter, C. A. *J. Appl. Polym. Sci.* **1981**, *26*, 1001−1014.
(56) Bersted, B. H. *J. Appl. Polym. Sci.* **1985**, *30*, 3751−3765.
(57) Kapnistos, M.; Vlassopoulos, D.; Roovers, J.; Leal, L. G. *Macromolecules* **2005**, *38* (18), 7852−7862.
(58) Das, C.; Inkson, N. J.; Read, D. J.; Kelmanson, M. A.; McLeish, T. C. B. *J. Rheol.* **2006**, *50* (2), 207−235.
(59) Raju, V. R.; Rachapudy, H.; Graessley, W. W. *J. Polym. Sci., Part B: Polym. Phys.* **1979**, *17* (7), 1223−1235.
(60) Stadler, F. J.; Karimkhani, V. *Macromolecules* **2011**, *44* (13), 5401−5413.
(61) Stange, J.; Uhl, C.; Münstedt, H. *J. Rheol.* **2005**, *49* (5), 1059−1079.
(62) Meissner, J. *Rheol. Acta* **1969**, *8* (1), 78−88.
(63) Laun, H. M. *Rheol. Acta* **1978**, *17*, 415−425.
(64) Münstedt, H. *Rheol. Acta* **1979**, *18*, 492−504.
(65) Münstedt, H.; Laun, H. M. *Rheol. Acta* **1981**, *20* (3), 211−221.
(66) Schweizer, T. *XIIIth Int. Congr. Rheol* **2000**, *1*, 219−221.
(67) Gabriel, C.; Münstedt, H. *J. Rheol.* **2003**, *47* (3), 619−630.
(68) Münstedt, H.; Gabriel, C.; Auhl, D. *Abstr. Pap. Am. Chem. Soc.* **2003**, *226*, U382−U382.
(69) Trouton, F. T. *Proc. R. Soc. London* **1906**, *77*, 426.
(70) Stadler, F. J.; Kaschta, J.; Münstedt, H.; Becker, F.; Buback, M. *Rheol. Acta* **2009**, *48* (5), 479−490.
(71) Hepperle, J.; Münstedt, H. *Rheol. Acta* **2006**, *45* (5), 717−727.
(72) Malmberg, A.; Gabriel, C.; Steffl, T.; Münstedt, H.; Lofgren, B. *Macromolecules* **2002**, *35* (3), 1038−1048.
(73) Mitsoulis, E. *J. Non-Newtonian Fluid Mech.* **1998**, *76*, 327−350.
(74) Laun, H. M.; Münstedt, H. *Rheol. Acta* **1978**, *17*, 415−425.
(75) Wolff, F.; Resch, J. A.; Kaschta, J.; Münstedt, H. *Rheol. Acta* **2010**, *49* (1), 95−103.
(76) Münstedt, H. *J. Rheol.* **1980**, *24* (6), 847−67.
(77) Auhl, D.; Chambon, P.; McLeish, T. C. B.; Read, D. J. *Phys. Rev. Lett.* **2009**, *103* (13), 136001.
(78) Stadler, F. J.; Nishioka, A.; Stange, J.; Koyama, K.; Münstedt, H. *Rheol. Acta* **2007**, *46* (7), 1003−1012.
(79) Spadaro, G.; Valenza, A. *Polym. Degrad. Stab.* **2000**, *67*, 449−454.

Macromolecules

Article

pubs.acs.org/Macromolecules

Prefracture Instabilities Govern Generation of Self-Affine Surfaces in Tearing of Soft Viscoelastic Elastomeric Sheets

Sandip Patil, Amit Ranjan,† and Ashutosh Sharma*

Department of Chemical Engineering and DST Unit on Nanosciences, Indian Institute of Technology, Kanpur, India

Supporting Information

ABSTRACT: We present an experimental study on fracture behavior of soft viscoelastic network solid films of polydimethylsiloxane (PDMS) and morphology of the fracture-generated surfaces. The most interesting behavior is the generation of fractal patterns when the storage and loss moduli are comparable. We find the formation of isolated defects and cracks ahead of the fracture-front. The observed morphology of the torn surfaces is correlated to the prefracture behavior by studying the crack propagation and coalescence. Tearing of PDMS containing 2% cross-linking agent with a terminal elastic modulus, G', of 10 kPa, shows distinct crack patterns at different tearing speeds. Slower tearing leads to the formation of dendritic patterns of propagating fingers, whereas at the higher deformation-rates, more frequent nucleation of bubble like defects occurs. The propagating fingers develop undulations along its sides. The effects of tearing speed on the length scale of the undulations and the bubbles are studied. The formation of undulations can be explained as a result of Saffman−Taylor instability with a modified *effective* surface tension which accounts for the dissipative energy loss. We also study the rate of formation of the defects, which is shown to be an activated process in that they form beyond a threshold value of the local stress.

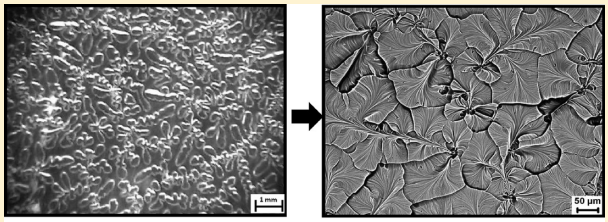

INTRODUCTION

Materials undergo cohesive failure by crack formation and propagation under excessive stress. Study of precrack events and morphology of cracks provides vital clues regarding the nature of the texture generated on the surfaces formed by the fracture and can also be a diagnostic tool for characterizing the failure mechanisms and the properties of the failed material. Materials with different mechanical properties exhibit different morphologies on their fractured surfaces. Ductile fracture in metals[1−3] is accompanied by plastic deformation prior to the fracture where the microvoids coalesce leading to a dimpled, irregular, and rough morphology commonly known as the cup-and-cone morphology. Brittle fracture in metals involves cleavage along crystallographic planes resulting into relatively smoother or faceted surfaces.[4,5] Fracture in polymeric materials has particularly drawn considerable scientific interest because of the complexity of the phenomena and richness of the resulting morphologies. In elastomers such as vulcanized polybutadiene,[6−8] vertical steps separating smooth regions form the characteristic features, whereas in the glassy polymers such as polystyrene, poly(methyl methacrylate), and polycarbonate, periodic micro/nano structured gratings are formed on the fractured surfaces.[9] Spatiotemporal patterns have been observed in peeling of adhesive tapes.[10] While adhesive interfacial failure of elastomeric surfaces have been extensively studied,[11−14] patterns formed by tearing of elastomeric sheets have not been explored. Previous studies on interfacial debonding have shown both bulk and interfacial fingering instabilities and cavitation during separation.[11,12,15,16] Interfacial debonding of both elastic[13] and viscoelastic adhesive layers[13,14] generate intricate surface structures including fractally rough surfaces during peeling.[14] Analysis of rough surfaces formed in fractured hydrogels has revealed interesting physics.[17,18] Surface instabilities without fracture, such as wrinkling by release of stresses, have also been studied.[19,20]

Here we explore the process and morphology of cohesive fracture in tearing of soft thin viscoelastic polydimethylsiloxane (PDMS) layers and the morphology of the torn surfaces thus generated. In particular, we focus on the chain of events starting from the generation of defects in the prefracture phase, their modifications during the crack propagation and the roles of these processes in determining the eventual surface morphology of completely torn surfaces. In order to assess the role of viscoelasticity, the fracture events and the resulting surface morphologies are studied at different tearing velocity. The morphology of the torn surfaces show novel patterns possessing different features at different length scales which also depend upon the tearing rate. The viscoelastic nature of the material strongly influences the generation and propagation of cracks which ultimately coalesce to cause fracture and form a particular surface morphology. Further, we show that the most interesting patterns in the form of self-affine fractal surfaces are observed only in a narrow range of elastic modulus ($G' \sim 1$ KPa to 10 KPa) of the elastomer. The structure of this paper is as follows: First, we

Received: October 19, 2011
Revised: December 28, 2011
Published: February 6, 2012

describe the details of the experimental setup, methodology, and the materials used. Subsequently our results are presented in two parts. In the first part, we discuss the morphology of the fracture generated surfaces resulting from the cohesive fracture of the elastomeric thin films. In the second part, we analyze the crack formation and propagation in the films while they are being fractured. On the basis of the crack behavior observed before the fracture and the final morphology of the fractured surface, we finally propose a simple physical model correlating the two.

MATERIALS AND METHODS

Sylgard-184 (a two part thermoset silicone elastomer; Dow Chemicals, USA) consisting of oligomer and cross-linking agent was used to prepare Polydimethylsiloxane (PDMS) in this study. The elastomer and cross-linking agent were mixed in the ratio of 100:2 by weight in order to make 2% cross-linked elastomer.[21,22] The solution was prepared in a 25 mL clean glass beaker and degassed under vacuum in order to remove trapped air from the solution. The prepared solutions were cast between two clean glass plates (Figure 1a) with predetermined gap controlled by inserting spacers of known heights between the plates. After casting, prepared solutions were cured at 85 °C for 48 h giving PDMS films of desired thickness. The elastic modulus, G' and loss modulus, G'' for the 2% cross-linked PDMS samples were separately measured at various temperatures by the oscillatory parallel plate method (Anton Paar MCR-501) as functions of frequency. Time−temperature superposition was used to construct the plot for the rheological response (Figure 5a).

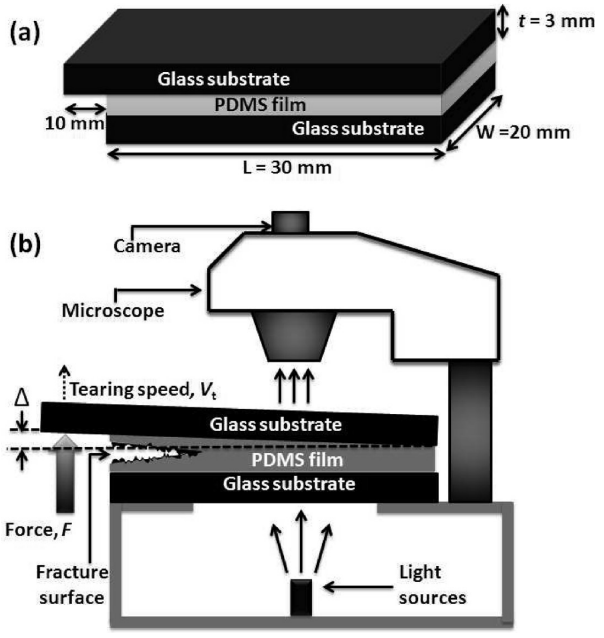

Figure 1. (a) PDMS film cast and bonded between the two glass plates. Typical dimensions of the glass plates are shown. (b) Experimental setup for tearing of PDMS film. The bottom glass plate is strongly attached to a rigid platform and the top plate is lifted from its hanging edge. Force F is applied by a micromanipulator causing a vertical displacement Δ and cohesive fracture in the film.

Figure 1b shows the tearing process in which the film sandwiched between the glass substrates was torn by lifting the hanging edge of one of the glass plates by a micromanipulator with controlled tearing speed, V_t, by applying a force, F on the edge. Application of F causes the point of application to move vertically by a distance Δ. The applied force was recorded using a load cell interfaced with a computer through a data acquisition card. During separation, the adhesive force between the film and glass substrate is much stronger than the cohesive force in the film, thus allowing cohesive fracture during separation. As shown in Figure 2, the most interesting cellular fractal morphologies were found only in the PDMS layers with the cross-linker concentration close to 2% (w/w), which produced a soft elastomeric solid of comparable storage and loss moduli at the time scales (frequencies) involved in the fracture. The rheology of these layers marks the border between transition from the liquid-like to solid-like behavior.[23,24] At relatively low cross-linker concentration of 0.5−1.5%, cracks propagated as the smooth Rayleigh fingers characteristic of cohesion failure in liquids. Beyond 2.5% cross-linker, fracture of elastic layers produced only disjointed craters on the surface.

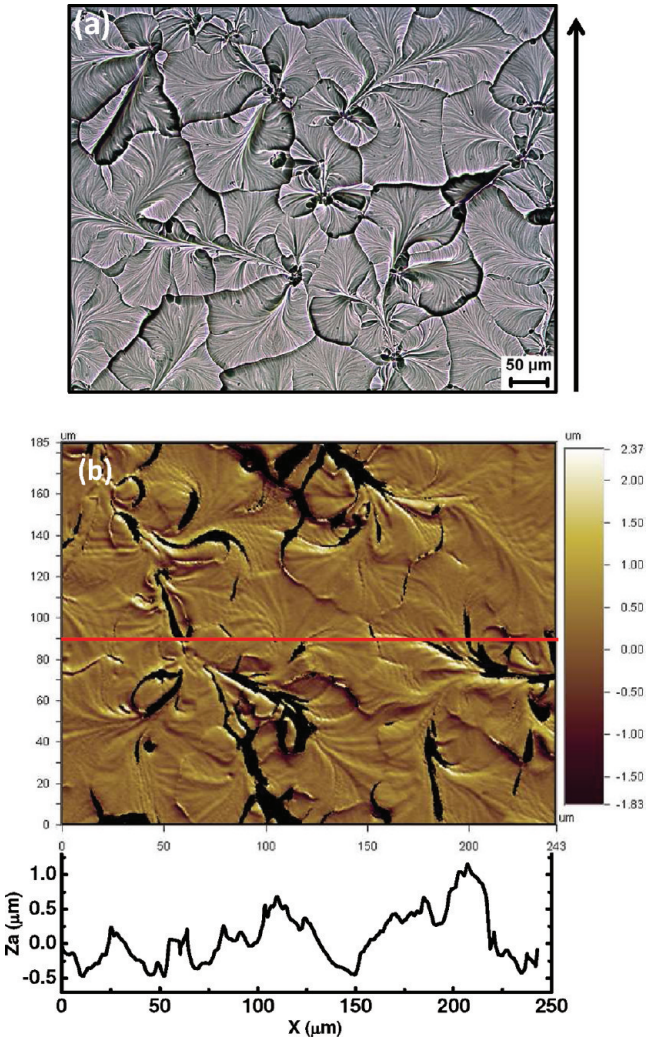

Figure 2. (a) Typical optical micrograph of the torn surface of a soft viscoelastic PDMS layer. The right side arrow signifies the direction of tearing. (b) Optical profilometry micrograph showing surface topography of the torn film of thickness $h \approx 20$ μm (roughly half of the total thickness) and tearing speed =100 μm/s.

RESULTS AND DISCUSSION

Morphology of Fracture-Generated Surfaces in Viscoelastic PDMS Layers. We first present the surface morphology of cohesive-fractured or torn viscoelastic PDMS films. The fracture was induced by tearing of homogeneous PDMS films bonded with two confining glass substrates. Fractured surfaces show novel fractal morphologies with cellular micropatterns on the torn surface of PDMS in which

dx.doi.org/10.1021/ma202339y | Macromolecules 2012, 45, 2066−2073

the ridged domains are separated as cells. One such typical morphology of torn surface is shown Figure 2a. The overall appearance of the domains on this scale is akin to leaves or petals. The surface profile was analyzed by surface topography analysis using optical profilometry (Wyko NT-1100) (a cross-section is shown in Figure 2b). The area of examination under microscope was 182 × 142 μm^2. The topographical surface characteristics such as the root-mean-square (RMS) roughness as well as fractal dimension were obtained to characterize these surfaces at different tearing rates. The surface roughness defined by the following relation was found to be 0.5 μm at a tearing speed of 100 μm/s:

$$R_q = \sqrt{\frac{1}{N}\sum_{i=0}^{N}(Z_i - Z_a)^2} \quad (1)$$

Here, Z_a is the average of the Z (height) values within the given area Z_i is the Z value at a given point, and N is the number of sampled points within the given area.

Figure 3 also shows a typical power spectral density curve of the fractured surface which gives the fractal dimension of the surface by the following relation:[25]

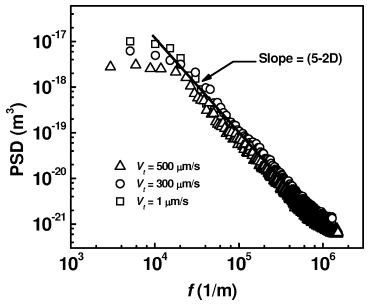

Figure 3. Power spectral density curves for V_t = 1, 300, and 500 μm/s for thickness h = 20 μm (half of the total thickness). The slope gives a value for the fractal dimension of the morphology close to 1.5.

$$S(f) = \frac{c}{f^{(5-2D)}} \quad (2)$$

Here f is the wavenumber, $S(f)$ is the power spectral density, C is a scaling constant, and D is the fractal dimension. The low f limit corresponds to the sample-size and the high f limit corresponds to the Nyquist frequency corresponding to the resolution limit of the analysis. The fractal dimension, D, can be obtained by extracting the slope of the power spectral density (PSD) function on a log−log plot as suggested by eq 2. The fractal dimension of the surface was found close to 1.5 independent of the tearing speed in the range of 1−500 μm/s. This value of the fractal dimension signifies that the height variation follows a Wiener process.[26,27] Interestingly, although the tearing speed altered the characteristic length scales of the pattern, it did not change its characteristic fractal dimension. The effect of layer thickness was more interesting. Increase in thickness increased the petal-leaf size without changing the overall apearance of the pattern as shown in Figure 4.

Prefracture Events in Soft Viscoelastic Elastomers. Fracture in viscoelastic elastomers is a complex and poorly understood phenomenon. According to the current understanding,[28,29] a processing zone lies in the immediate proximity to a blunted crack tip where energy is primarily dissipated through plastic deformation, chain-breakage and flow. An elastic zone lies further away from the crack tip where the energy is stored in an elastically strained material. Owing to the viscoelastic nature of the elastomer used, the behavior of crack propagation can be influenced by the crack speed. There are several theoretical and experimental studies on the instabilities in adhesive or interfacial failure seen in the peel experiments,[13,30−34] but a petal-leaf morphology shown here in the cohesive rupture has not been reported.

In what follows, we present the development of precrack morphologies within the still intact layer away from the crack line that tears the layer in two. The results are discussed for the 2% cross-linker containing PDMS films, which invariably yielded fractal morphologies upon completion of fracture. In order to gain an understanding of the processes involved in morphological development, rheological characterization of the

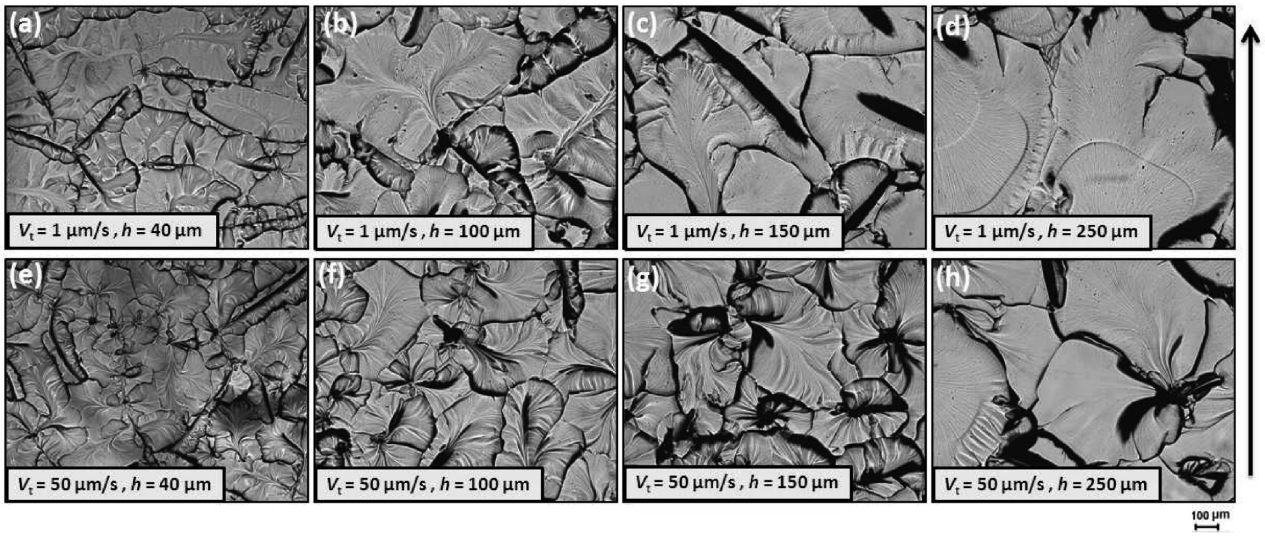

Figure 4. Optical micrographs of fractured surfaces of 2% cross-linked PDMS films with different thickness and tearing speed. Right side arrow indicates tearing direction of the film.

dx.doi.org/10.1021/ma202339y | Macromolecules 2012, 45, 2066−2073

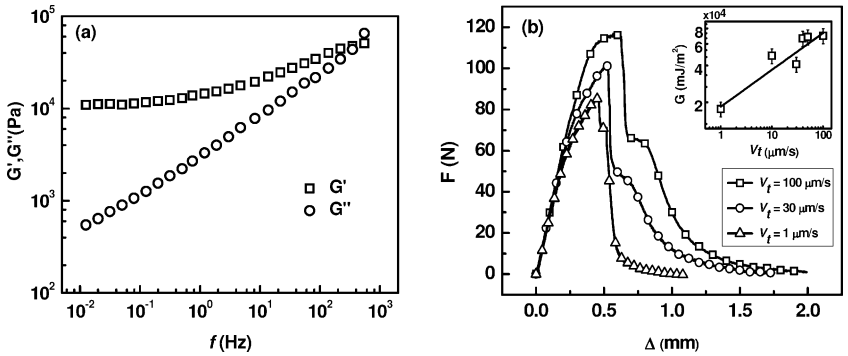

Figure 5. (a) Oscillatory response of 2% PDMS showing storage (squares) and loss (circles) modulus obtained using time−temperature superposition. (b) Force-displacement curves generated while tearing at three different tearing velocities. Inset shows the energy as a function of tearing speed curve for 40 μm thickness following a power law behavior with an exponent of 1/3.

PDMS networks was first performed. The oscillatory response of a 2% cross-linked PDMS sample obtained by time−temperature superposition is shown in Figure 5a. Rheology data confirms that the material is a soft viscoelastic solid made of an imperfect network.[34] In our study, the vertical tearing speed, V_t, of the plate lift-off ranged from 1 to 100 μm/s, which resulted in about 2 orders of magnitude variation also in the crack propagation speed, $V_c \sim 100\ V_t$ ($V_c \sim 100-10000\ \mu$m/s).

For a film with the thickness $h = 40\ \mu$m, the range of crack propagation speed corresponds to the frequency f (or the deformation rate, $f = V_c/h$) ranging from around 2 to 300 Hz. This range of frequency relevant to our experiments is close to the "transition region" in the frequency sweep rheological measurement of 2% cross-linked PDMS films. A characteristic of this regime is that both storage and loss moduli are comparable and increase with frequency. Therefore, both storage and dissipation of energy are about equally important in our experiments, although the terminal behavior of the material is that of a solid.

We first present the force vs. separation behavior for 2% cross-link films of 40 μm thickness. The force-separation curves at three different speed of tearing are shown in Figure 5b. The shapes of these curves are typical of pressure-sensitive adhesives. The initial linear rise in the force is caused by the stored elastic energy. The film starts to rupture beyond a critical stress and the energy is now released leading to a drop in the stress. The work done is now distributed between the dissipative loss and the energy of formation of new surfaces as the precrack structures form, reorganize as cracks and propagate in the material leading to fracture. The storage and loss are strongly dependent on crack propagation velocity which determines the effective shear rate of the system given by $f = V_c/h$, where f is the frequency, V_c is the crack propagation velocity, and h is the thickness of the film. The energy released can be calculated from the area under the force−distance curve beyond the critical stress where the force undergoes a sharp drop due to crack initiation. A plot of energy released per unit area as a function of fracture speed in the inset of Figure 5b shows a power law dependence with an exponent of 1/3. This exponent has been predicted by Persson and Brener.[28] Their model, essentially applicable to relatively high velocities such that the material lies in the 'transition regime' of frequency, accounts for the dissipative losses occurring near the crack tip. From the rheological data in Figure 5a, the onset of transition regime in our samples is expected for $f > 10$ Hz, and hence for crack propagation velocities larger than 400 μm/s. Since crack-propagation velocity ranges from 100 μm/s to 10000 μm/s, samples in most of our cases lie in the "transition regime" of rheological behavior. Thus, the data presented in Figure 5b confirms the prediction of Persson and Brener and underlines the importance of dissipative loss in the energetics of the tearing process.

We now examine the dynamics and morphology of the precrack patterns that form in the still intact layer beyond the propagating fracture front. As the upper plate was lifted, accumulated elastic stresses begun to relax by the formation of bubbles/cavities and fingers as shown in Figure 6. These formations are important for the understanding of the observed postfracture cellular micropatterns. The length scale and morphology of these precrack patterns shows dependence on the speed of tearing. Snapshots of the crack patterns in the layers fractured at different tearing speeds are presented in Figure 6. At low tearing speeds, (Figure 6a−c) long fingers or crack lines which develop side undulations dominate the pattern, whereas at high tearing speeds (Figure 6d−f) both bubbles as well as shorter and less well-defined crack-lines appear. These features lead to a pattern dominated by the long dendritic lines at low velocity, and a more uniform cellular pattern at high tearing velocities. In the case of low tearing velocity, the fine stems of the postfracture leaf pattern shown in Figure 2 correspond to the crack lines witnessed in Figure 6c. Nucleation of isolated bubbles or cavities is not witnessed at low tearing speeds, indicating more viscous behavior. The less defined crack-lines or fingers and a greater proportion of elongated bubbles are characteristic of more elastic behavior at higher tearing speeds. Indeed, propensity for the formation of fingers without bubbles in a viscoelastic liquid layer of 0.5% cross-linked PDMS corresponding to a viscous dominated behavior is clearly seen in Figure 6g. However, an elastic 4% cross-linked layer only forms bubbles instead of fingers as shown in Figure 6h. The side branches or waviness of the crack lines or fingers in Figure 6a, b, c were found to disappear on removal of tearing stress or by reversing the direction of tearing arm leading to crack closing (see Supporting Material). However, the main crack-lines were irreversible and remained after the removal of stress. This confirms that the side undulations originate from liquid-like Saffman−Taylor fingering instabilities. However, the long fine crack lines and the bubbles/cavities once formed persisted even after the removal of stress. Therefore, the fully formed crack lines/bubbles are characteristic of solid-like rupture caused by chain breakage and irreversible plastic deformations. These images suggest two length scales of interest: (i) λ_f, the length

dx.doi.org/10.1021/ma202339y | Macromolecules 2012, 45, 2066−2073

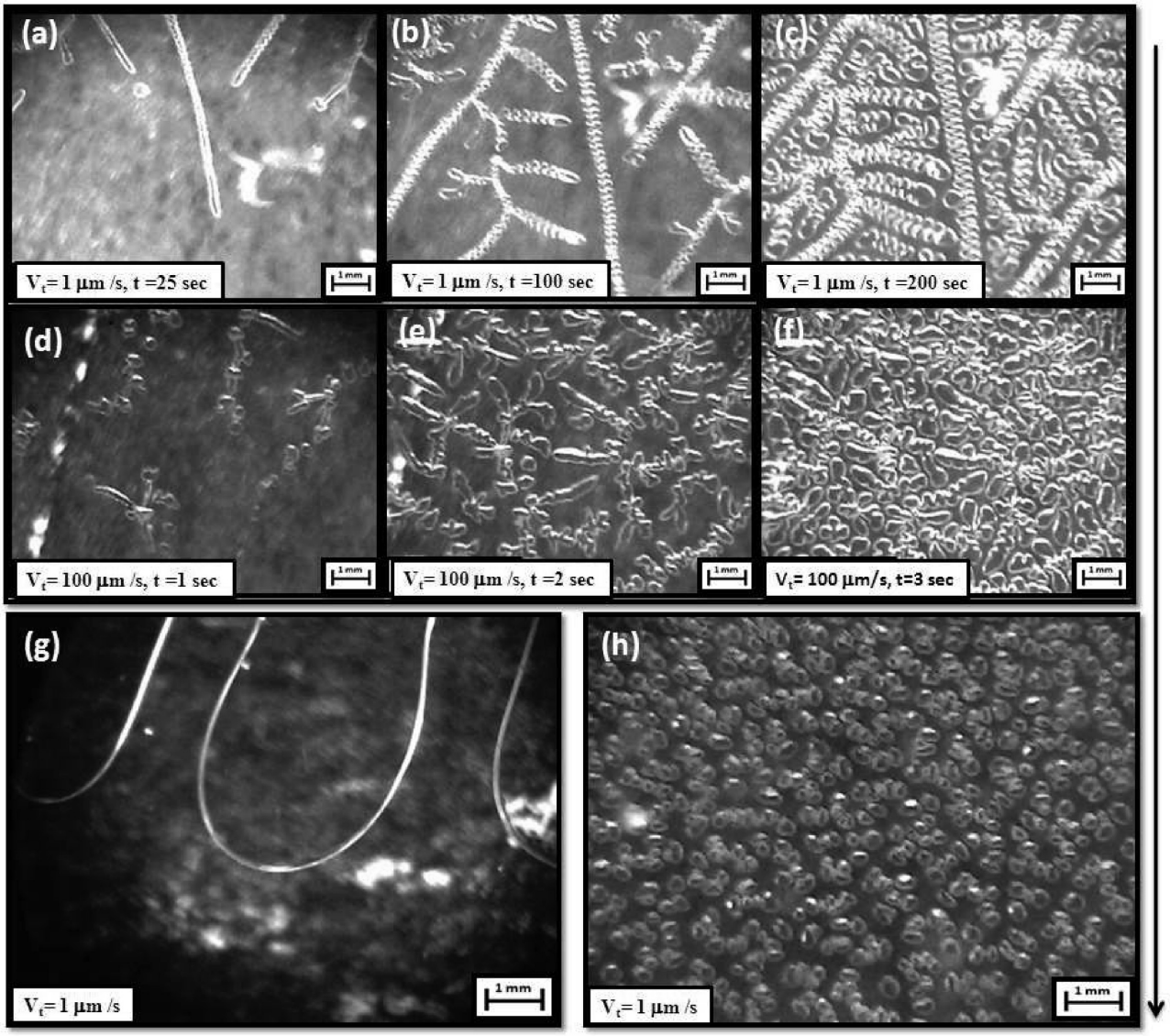

Figure 6. (a) Real time optical micrographs of precracks in 2% cross-linked 40 μm thick PDMS layers at different tearing speeds. First (a, b, c) and second (d, e, f) rows correspond respectively to V_t = 1 and 100 μm/s. Snapshots at three different times are presented for each tearing speed. (g, h) Real time optical micrographs of 0.5% and 4% cross-linker containing PDMS layers at tearing speed of V_t = 1 μm/s. Arrow on the right side of the figure shows direction of the crack propagation.

scale of the undulations appearing along the lateral boundaries of the linear fingers, and (ii) λ_b, the average distance between two crack-features (bubble or fingers). The former length scale is independent of time and as mentioned before, is found to depend on the liquid-like nature of the films. The latter which originates from the solid-like behavior of the film, depends on density of nucleated cracks and is therefore time dependent. We first address λ_f which shows a very weak but systematic variation with speed. We propose that the undulations in the finger like structures is due to a Saffman−Taylor like instability that arises along the interface of two liquids when a less viscous liquid is driven against a more viscous one in Hele−Shaw kind of geometry.[35] This effect has already been studied in adhesive failures occurring in viscoelastic materials using probe-tack experiments.[23] However, our studies gain a further understanding into the phenomena and establish the importance of viscous dissipation prevalent in the crack processing zone. We show that the dissipative energy loss plays an important role in determining the length scales of these modulations.

Variation of λ_f with V_t, the tearing speed, is presented in Figure 7 It is observed to systematically increase with speed and have a weak power-law dependence. This weak variation can be explained by combining the idea of Saffman−Taylor instability in liquid interfaces and Persson and Brener's result.[28] Saffman−Taylor instability arising in the interface between two liquids of unequal viscosity when the one with lower viscosity is driven against the other, results into surface undulations with a characteristic wavelength given by the following formula:[23]

$$\lambda_f \approx \frac{\pi h \sqrt{\gamma}}{\sqrt{\eta V_c}} \tag{3}$$

where λ_f is the wavelength of the instability appearing along the sides of the fingers, h is the film thickness, γ is the surface energy per unit area, and η is the viscosity of the medium.

dx.doi.org/10.1021/ma202339y | *Macromolecules* 2012, 45, 2066−2073

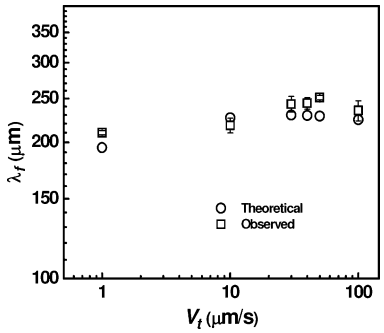

Figure 7. Wavelength variation with tearing speed with a constant thickness (h = 40 μm). Squares represent the experimentally observed values, and circles represent the theoretically calculated values that account for interfacial instability and viscous dissipation.

The viscosity, η can be estimated from the oscillatory rheology data by $\eta = ((G'^2) + (G''^2))^{1/2}/f$ where G' is the storage modulus and G'' is the loss modulus. Nase et al.[23] studied the finger formation in PDMS networks at different velocities using probe-tack test and found that λ_f decreases with velocity. These authors were able to fit their feature wavelengths to the above expression applicable to interfacial instability caused by the Saffman−Taylor like mechanism. However, in our case, we observe a systematic increase in λ_f with velocity although the dependence is very weak. Our data suggests, as argued in the next paragraph, that the origin of this weak dependence lies in the dissipative dynamics operating in the crack's vicinity. Persson and Brener calculated γ_{eff}, an effective surface energy per unit area by accounting for the dissipation in the surrounding region of the propagating cracks, and defining the γ_{eff} as follows:

$$\gamma_{eff} = 2G \tag{4}$$

Here G is the energy released per unit area at any given V_c, the crack tip velocity, and is given by the following expression:

$$G = G_o(1 + f(V_c)) \tag{5}$$

Here G_o is the energy released in the static limit, and $f(V_c)$ is the correction due to velocity dependent dissipation. Their result for γ_{eff} as a function of crack tip velocity is summarized by the following relation:

$$\gamma_{eff} = \gamma_o\left(\frac{V_c}{V_o}\right)^{1/3} \tag{6}$$

Equation 6 was obtained for the Rouse like relaxation of the chains which predicts that G'' scales as $f^{1/2}$. As seen in the rheological response in Figure 5a, our samples also show a scaling exponent close to 0.5, which justifies the use of eq 6. Where γ_o is the surface tension of the material in the low velocity limit, and $V_o \approx a_o/\tau$ where a_o is the size of the core region having a value close to atomic dimension and τ is the relaxation time of the network, which in our case is around 0.003 s (Figure 5a). Substituting γ_{eff} for γ, the surface energy, in Saffman−Taylor expression of eq 3, we obtain a final expression for a wavelength resulting from a Saffman−Taylor instability that also accounts for the dissipative losses. The experimental data and the theoretically predicted dependency of the wavelength on velocity are presented in Figure 7 and show an excellent agreement. Therefore, we argue that this weak dependence can originate from the dissipative dynamics and flow predominantly occurring in the immediate vicinity of the fingers.

Next we turn our attention to the phenomena of nucleation of cracks at different tearing speeds. At higher tearing speeds, formation of new voids that elongate into finger like patterns and branching of pre-existing fingers become more frequent. In quantification of defect density, every disjointed feature such as voids and the side-branch features were counted as defects. Our data show, as we argue next, that nucleation of these defects is an activated process. To this end we calculate dN/dt, the number of such defects formed per unit time, for the 40 μm thick film in a reference area at a distance of 10 mm from the edge of the film and 20 mm from the point of application of tearing force. dN/dt is measured by counting the number of defects, $N(t)$ in the reference area. For an activated process, the rate of nucleation is given by $dN/dt \propto e^{(-E_b/kT)}$ where E_b is the energy barrier.[36] We propose that the local elastic energy in a reference volume V, has to surmount a threshold energy ε, to activate the nucleation process. Here V and ε are unknown constants. If σ is the local stress, and μ is the bulk modulus, then local elastic energy in the reference volume is given by σ^2V/μ, such that the local energy barrier is $E_b = \varepsilon - (\sigma^2V/\mu)$. Therefore, the rate of nucleation is given by the following equation:

$$\frac{dN}{dt} \propto e^{[(1/kT)\{(\sigma^2V/\mu)-\varepsilon\}]} \tag{7}$$

Therefore, at constant temperature, the rate of nucleation at any point in the sample is proportional to $e^{((\sigma^2V)/(kT\mu))}$. For a crack propagating at a speed V_c, the local stress at a point located at a distance x_o from the edge of the plate at any time t is given by the following function:[1]

$$\sigma \approx \frac{K}{\sqrt{x_o - V_c t}} \tag{8}$$

where K is the stress intensity factor. The term under square-root in the denominator is the distance of the concerned point from the crack edge. A combination of eqs 7 and 8 predicts that logarithm of dN/dt should vary linearly with $1/(x_o - V_c t)$, which we indeed observe as shown in Figure 8. Thus, our results suggest

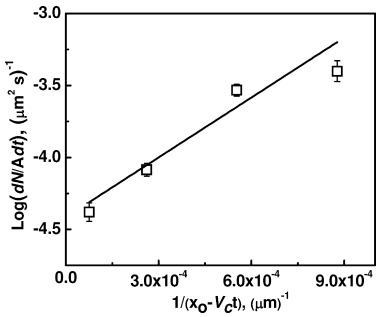

Figure 8. Dependency of the logarithm of nucleation rate per unit area with $1/(x_O - V_C t)$.The linear best fit line suggests that generation of the cracks is an activated process.

that the formation of cracks is an activated process where the activation energy keeps decreasing as the stress level increases with time, thereby leading to more frequent formation of cracks.

Another interesting observation in our experiments is that the fingers that otherwise keep elongating with time, tend to

dx.doi.org/10.1021/ma202339y | Macromolecules 2012, 45, 2066−2073

stop as soon as they are met at their tip with another pre-existing finger, that is, the fingers avoid intersecting each other. Majumder et al.[37] have also observed that propagating fingers formed as a result of peeling an adhesive slows down as they meet a microchannel running perpendicular to their direction of propagation. This phenomena can be explained by noting that as the tip of a finger of a later generation (secondary) approaches a pre-existing finger (primary) from sideways, the region lying ahead of the tip of the secondary finger where the elastic energy of the secondary finger gets released, can be assumed to be a composite of PDMS medium and air present inside the primary finger.

Thus, the effective modulus of this region is significantly reduced because of the presence of a pre-existing air-filled void. This effective modulus keeps becoming smaller as the secondary tip approaches the primary finger since the volume fraction of the neighboring region of the tip is increasingly dominated by air. As a result, the propagation of the secondary fingers is impeded because their further advancement does not lead to a significant release in stored elastic energy at the expense of exposing new surface. Another explanation of this observation could be that once finger-boundaries come very close, the stress is concentrated in the region between the fingers which leads to elongation of the material along the applied stress direction leading to fibril like formation, and consequently, further propagation of the fingers is not observed.

After the dynamic behavior of the propagating cracks, we next describe the correlation between the observed features in fracture generated surfaces and the coalesced crack pattern immediately before fracture. At larger separation speeds, the resulting surfaces invariably form cellular areas patterned with ridge-like formations. The cellular domains appearing in the postfracture images essentially are those surfaces which get exposed at the time of formation of the nascent cracks/bubbles.

Spans of these cellular domains correspond to the defects that coalesce immediately before fracture. The distance between the coalesced cells in the crack pattern observed right before fracture compares favorably with the typical size of the cells observed in the fracture generated surfaces. The points of rupture define the boundary of these cellular domains as well as the vertical protrusions in the surface of the films predominantly responsible for the rms roughness measured in the profilometry experiments. A schematic model correlating prefracture processes and the observed crack patterns as well as the finally observed surface morphology in the fractured surface is shown in Figure 9.

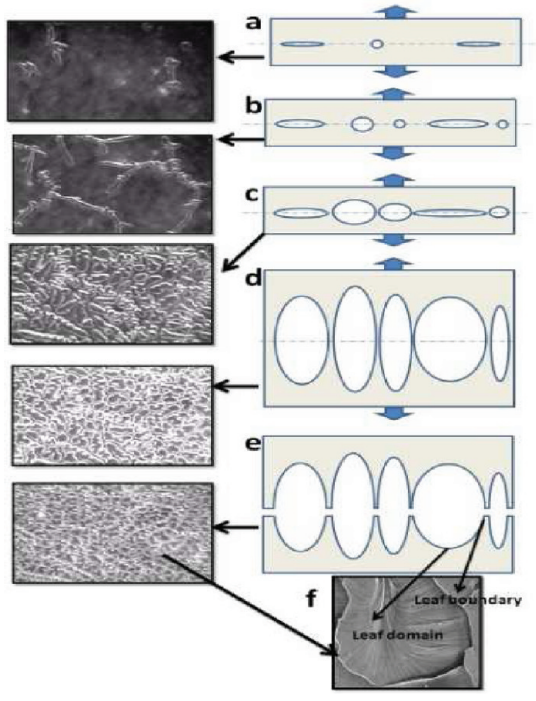

Figure 9. Proposed schematic model correlating prefracture processes, observed crack patterns, and the final surface morphology.

CONCLUSIONS

In summary, we have studied the tearing velocity dependence of crack formation in those soft viscoelastic films which form self-affine cellular micropatterns on fracture, and showed that during fracture, the nucleation of cracks is affected by the solid-like properties of the films. Fingers or bubbles nucleate after a sufficient accumulation of local stress. Exceeding the critical stress causes random breaking of the bonds resulting into rupture and thereby nucleation of cracks. During the course of fracture, the liquid-like instability in the medium generates undulations along the sides of the propagating cracks. In particular, two phenomena of (i) Saffman−Taylor instability of the interface and (ii) the dissipative loss in the vicinity of the propagating cracks govern the length scale of these undulations. Finally a correlation of the observed surface structure to the crack pattern formed right before fracture is established.

ASSOCIATED CONTENT

Supporting Information

Crack opening and closing videos. This material is available free of charge via the Internet at http://pubs.acs.org/.

AUTHOR INFORMATION

Corresponding Author

*E-mail: ashutos@iitk.ac.in. Telephone: +91-512-2597026. Fax: +91-512-2590104.

Present Address

[†]Department of Chemical Engineering, Rajiv Gandhi Institute of Petroleum Technology, Raebareli, India

ACKNOWLEDGMENTS

This work was supported by the DST, New Delhi, by its Unit on Soft Nanfabrication and by an IRHPA grant.

REFERENCES

(1) Dieter, G. E. *Mechanical Metallurgy*; McGraw-Hill: London, 1988.
(2) Wilsdrof, H. G. F. *Mater. Sci. Eng.* **1983**, *59*, 1−39.
(3) Thomason, P. F. *Acta. Mater.* **1999**, *47*, 3633−3646.
(4) Pugh, S. F. *Br. J. Appl. Phys.* **1967**, *18*, 129−162.
(5) Ravi-Chandar, K.; Yang, B. *J. Mech. Phys. Solids.* **1997**, *45*, 535−563.
(6) Gent, A. N.; Pulford, C. T. R. *J. Mater. Sci.* **1984**, *19*, 3612−3619.
(7) Cam, J.-B.; Le; Toussaint, E. *Macromolecules* **2010**, *43*, 4708−4714.
(8) Mathew, A. *Eur. Polym. J.* **2001**, *37*, 1921−1934.
(9) Pease, L. F.; Deshpande, P.; Wang, Y.; Russel, W. B.; Chou, S. Y. *Nat. Nanotechnol.* **2007**, *2*, 545−548.
(10) Yamazaki, Y.; Toda, A. *J. Phys. Soc. Jpn.* **2004**, *73*, 2342−2346.
(11) Crosby, A. J.; Shull, K. R.; Lakrout, H.; Creton, C. *J. Appl. Phys.* **2000**, *88*, 2956−2966.
(12) Shull, K.; Flanigan, C.; Crosby, A. *Phys. Rev. Lett.* **2000**, *84*, 3057−3060.
(13) Ghatak, A.; Chaudhury, M. K. *Langmuir* **2003**, *19*, 2621−2631.
(14) Persson, B. N. J.; Kovalev, A.; Wasem, M.; Gnecco, E.; Gorb, S. N. *Europhys. Lett.* **2010**, *92*, 46001−p4.

(15) Yamaguchi, T.; Koike, K.; Doi, M. *Europhys. Lett.* **2007**, *77*, 64002−p5.
(16) Nase, J.; Creton, C.; Ramos, O.; Sonnenberg, L.; Yamaguchi, T.; Lindner, A. *Soft Matter* **2010**, *6*, 2685−2691.
(17) Tanaka, Y.; Fukao, K.; Miyamoto, Y. *Eur. J. Phys. E* **2000**, *401*, 395−401.
(18) Baumberger, T.; Caroli, C.; Martina, D.; Ronsin, O. *Phys. Rev. Lett.* **2008**, *100*, 178303−4.
(19) Yang, S.; Khare, K.; Lin, P.-C. *Adv. Funct. Mater.* **2010**, *20*, 2550−2564.
(20) Lin, P.-C.; Yang, S. *Soft Matter* **2009**, *5*, 1011−1018.
(21) Mukherjee, R.; Pangule, R. C.; Sharma, A.; Banerjee, I. *J. Chem. Phys.* **2007**, *127*, 064703−6.
(22) Gonuguntla, M.; Sharma, A.; Mukherjee, R.; Subramanian, S. A. *Langmuir* **2006**, *22*, 7066−7071.
(23) Nase, J.; Lindner, A.; Creton, C. *Phys. Rev. Lett.* **2008**, *101*, 074503−4.
(24) Arun, N.; Sharma, A.; Pattader, P.; Banerjee, I.; Dixit, H.; Narayan, K. *Physi. Rev. Lett.* **2009**, *102*, 254502−4.
(25) Berry, M. V.; Lewis, Z. V. *Proc. R. Soc. London A* **1980**, *370*, 459−484.
(26) Majumdar, A.; Bhushan, B. *J. Tribol.* **1990**, *112*, 205−216.
(27) Barabási, A.-L.; Vicsek, T. *Phys. Rev. A.* **1991**, *44*, 2730−2733.
(28) Persson, B.; Brener, E. *Phys. Rev. E.* **2005**, *71*, 036123−8.
(29) Derks, D.; Lindner, A.; Creton, C.; Bonn, D. *J. Appl. Phys.* **2003**, *93*, 1557−1566.
(30) Ghatak, A.; Chaudhury, M. K.; Shenoy, V.; Sharma, A. *Phys. Rev. Lett.* **2000**, *85*, 4329−4332.
(31) Creton, C.; Leibler, L. *J. Polym. Sci., Polym. Phys.* **1996**, *34*, 545−554.
(32) Ghatak, A.; Mahadevan, L.; Chung, J. Y.; Chaudhury, M. K.; Shenoy, V. *Proc. R. Soc. London A* **2004**, *460*, 2725−2735.
(33) Ghatak, A.; Mahadevan, L.; Chaudhury, M. K. *Langmuir* **2005**, *21*, 1277−1281.
(34) Rubinstein, M.; Colby, R. H. *Polymer Physics*; Oxford University Press: London, 2003.
(35) Saffman, P. G.; Taylor, G. *Proc. R. Soc. London A* **1958**, *245*, 312−329.
(36) Krausz, A. S.; Krausz, K. *Fracture Kinetics of Crack Growth*: Kluwer Academic publisher: Dordrecht, The Netherlands, 1988.
(37) Majumder, A.; Ghatak, A.; Sharma, A. *Science* **2007**, *318*, 258−261.

Macromolecules

Article

pubs.acs.org/Macromolecules

Hierarchically Nanostructured Polyisobutylene-Based Ionic Liquids

Parvin Zare,[†,§] Anja Stojanovic,[†,§] Florian Herbst,[†] Johanna Akbarzadeh,[‡] Herwig Peterlik,[‡] and Wolfgang H. Binder*[,†]

[†]Institute of Chemistry, Chair of Macromolecular Chemistry, Faculty of Natural Sciences II (Chemistry, Physics and Mathematics), Martin-Luther-University Halle-Wittenberg, Von-Danckelmann-Platz 4, Halle 06120, Germany

[‡]Faculty of Physics, Dynamics of Condensed Systems, University of Vienna, Strudlhofgasse 4, 1090 Vienna, Austria

Supporting Information

ABSTRACT: A new type of highly temperature stable ionic liquid (IL) with strongly temperature dependent nanostructures is reported. The molecular design relies on the use of a liquid polymer with an ionic liquid headgroup, introducing liquid properties by both the polymeric and the ionic liquid (IL) headgroup. The IL polymers (poly(isobutylene)s) **3a**−**3c** (PIB-ILs) were prepared by a combination of living carbocationic polymerization (LCCP) and subsequent "click" chemistry for attachment of methylimidazolium (**3a**), pyrrolidinium (**3b**), and triethylammonium cations (**3c**). All three investigated PIB-ILs exhibited pronounced nanostructural organization at room temperature depending strongly on the nature of the anchored cation. Whereas the morphology of the imidazolium-based PIB-IL **3a** shows high thermal stability up to the decomposition temperature, order−order (OOT) and lattice disorder−order transitions (LDOT) characteristic for common ionomers could be observed in the case of pyrrolidinium **3b** and ammonium-based **3c** PIB-ILs. Control of flow behavior as well as adjustable relaxation times from the liquid to the viscoelastic regime can be adjusted by choice of the appropriate IL headgroup.

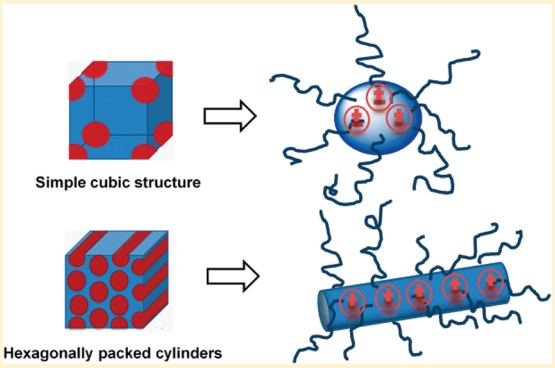

INTRODUCTION

Recently, polymeric ionic liquids (POILs),[1−6] carrying constrained cationic and anionic components of ionic liquids (ILs)[7−10] within the monomer units, have been developed as a new class of polymeric materials with widespread importance in science and technology. In contrast to (low molecular weight) ionic liquids (ILs), which are salts with arbitrary defined melting points below 100 °C, POILs are usually solids at room temperature, combining the unique properties of ILs with increased mechanical stability,[5] improved processability,[6,11] and more complex self-assembling ability of polymeric materials.[4,12,13] Similar to ILs, POILs generally consist of bulky nonsymmetrical organic cations (such as an imidazolium,[14] pyridinium,[15] ammonium,[16] or phosphonium cation[17]) together with various organic or inorganic anions, displaying unique properties such as extremely low vapor pressure, nonflammability, high polarity, high thermal stability, favorable electrochemical properties, and unorthodox and tunable miscibility behavior.[7,9] Therefore, POILs find widespread use, e.g., as polymer electrolytes for electrochemical devices,[5,18,19] sensors,[2] supports for catalysts,[20] polymeric dispersants,[21] CO_2 absorbing resins,[22] microwave absorbing materials,[23] or self-healing materials.[24] The latter application specifically requires detailed control over molecular relaxation and reorganization within POILs, as both their structure and dynamics can be controlled by the corresponding internal nanostructure.

Because of their self-assembling behavior,[25] both monomeric ILs as well as POILs display a subtle micro- and nanostructural organization resulting from the separate aggregation of apolar and ionic regions.[26,27] Since the pioneering work of Canongia Lopes and Pádua[26] numerous studies have confirmed the nanostructural organization of monomeric ILs.[27−29] Investigated ILs show first sharp diffraction peaks (FSDPs)[30] in X-ray[25,29] or neutron diffraction structure functions,[27a,31] which indicates the presence of intermediate range order (~5−10 Å). On the one hand, such intermediate range order can originate from either charge ordering (similar to the classical molten salts[30]) or, on the other hand, from the interdigitation of "bilayered" alkyl chains. Because of their nanostructural organization and hence their extraordinary miscibility behavior, ILs can be used as entropic drivers (the "IL effect") for the preparation of well-defined nanoscale structures with extended order, either in the bulk phase or at the gas/vacuum interface.[32] Because of their structural similarity to classical ionomers, POILs may form ionic aggregates, so-called "multiplets". Such ionic clustering and self-aggregation of POILs can lead to an increase of ionic conductivity of POILs, making them suitable for applications as valuable polyelectrolytes.[5] Furthermore,

Received: December 19, 2011
Revised: January 21, 2012
Published: February 6, 2012

several investigators have reported that POILs containing monomers with mesogen character tend to self-assemble into various liquid-crystalline phases with different organization.[4−6,33] Thus, a pronounced case of liquid-crystalline order was achieved by Ohno et al.,[34] who synthesized mesogen POIL containing tris(alkoxy)phenyl groups attached to acryloyl groups. Structural changes of IL monomer led to the formation of columnar phases which produced oriented one-dimensional ion conductive channels; thus, subsequent photopolymerization of ionic liquid film resulted in a well-ordered, highly conductive, liquid-crystalline POILs. The same working group further increased the conductivity of POIL materials via design of thermotropic bicontinuous cubic liquid-crystalline POILs based on a polymerizable ammonium moiety complexed with a lithium salt and thus obtained lithium ion-conductive solid polymeric films having 3D interconnected ionic channels.[35] A different approach for increasing the conductivity of POIL electrolytes is the specific design of ionic liquid block copolymers.[12,36,37] Thus, the use of microphase separating block copolymers displays numerous advantages such as a higher level of ionic conductivity by lowering the glass transition temperatures (T_g) or the increase of mechanical properties by selective cross-linking of ionic liquid monomers in one phase of an POIL.[12] Weber et al.[37] have shown that microphase separation of ionic liquid block copolymers strongly influences their conductivity. Well-structured lamellar microphase morphology of styrene−ionic liquid copolymers led to a 10-fold increase in conductivity as compared to copolymers with poorly organized hexagonal morphologies. Thus, control of the nanostructural organization of POILs is the key point in their application in many of the aforementioned uses, particularly when relaxation and flow behavior dominate major structural properties.

In this paper we for the first time report on a nanostructured IL with new features based on the high fluidity of a polymeric backbone in addition to the presence of ionic moiety similar to ionic liquids (ILs). The basic idea is the use of a polymer with an extremely low glass transition temperature (T_g) so as to introduce liquid properties already into the native polymer of the POIL. Additionally, the extremely large difference between the hydrophobic polymer and the attached IL end groups (affixed to one end group of the polymer) can induce significant nanostructural order within the then polymeric ionic liquid. Until now predominantly ionic liquid cations have been incorporated into polymer backbones obtained from vinyl,[1,38] styrenic,[22a] methacrylic,[39] ethylene glycol,[40] vinyl ether,[41] and norbornene monomers.[22c,39,42] As only few polymers display such liquid properties in themselves we have chosen poly(isobutylene) as polymer with such highly liquid properties. The use of poly(isobutylene) as biocompatible polymer with high hydrophobicity and chain mobility (as exemplified by its low glass transition temperature, T_g = −80 °C) has found increased use in fields of supramolecular polymer science,[43,44] amphiphilic conetworks,[14,45] and self-healing materials.[46] In contrast to the previously predominantly used radical polymerization, we have applied living carbocationic polymerization (LCCP) for the preparation of POILs, thus allowing for chain-length control and therefore control of the nanostructure's dimension.[47] The projected PIB-ILs were prepared by combining LCCP with a microwave-assisted azide/alkyne "click" reaction between an azido telechelic PIB and the corresponding alkyne containing IL headgroup. As significant phase separation effects were expected, detailed small-angle X-ray scattering (SAXS) investigations as well as rheology studies have been conducted to reveal structure and relaxation behavior of the prepared POILs.

EXPERIMENTAL SECTION

Materials. All materials were obtained from Sigma-Aldrich and used without further purification if not mentioned otherwise. 1-Methylimidazole, 1-methylpyrrolidine, and *N,N,N*-triethylamine was distilled over CaH_2 prior to use. Dichloromethane and toluene were predried over $CaCl_2$ and freshly distilled over CaH_2, sodium, and benzophenone.

Instrumentation. *^1H NMR and ^{13}C NMR spectra* were recorded on a Varian Gemini 2000 FT-NMR spectrometer (400 MHz) and a Varian Unity Inova 500 (500 MHz). MestRec-C software (version 4.9.9.6) was used for data interpretation. Deuterated chloroform ($CDCl_3$) and dimethyl sulfoxide (DMSO-d_6) were used as solvents. All chemical shifts (δ) are reported in parts per million (ppm) relative to tetramethylsilane (TMS) and referenced to the significant solvent signals. Coupling constants (J) are given in hertz (Hz).
Gel permeation chromatography (GPC) analysis was performed on a Viscotek GPCmax VE2001 system combined with a Viscotek TDA302 (triple detector array) using polyisobutylene standards and THF as solvent. PIB standards with a molecular weight of 340, 1650, 7970, 26 300, 61 800, and 87 600 g/mol were used for calibration. Data were analyzed with the OmniSec (4.5.6) software. The polystyrene−divinylbenzene-based column set consists of a H_{HR}-HGuard-17,369 precolumn followed by a GMH_{HR}-N-Mixed Bed 18055 (1000 to 4 × 10^5 Da) and a G2500H_{HR}-17,354 (100 to 2 × 10^4 Da) column. Both the detector and the column temperature was set to 35 °C, with flow rate of 1 mL min^{-1}, and injection volume of 100 μL.
Matrix-assisted laser desorption/ionization time-of-flight mass spectrometry (MALDI-TOF-MS) experiments were performed on a Bruker Autoflex III system operating in reflection and linear modes. The data evaluation was carried out on flexAnalysis software (version 3.0). Ions were formed by laser desorption (smart beam laser at 355, 532, 808, and 1064 ± 6.5 nm; 3 ns pulse width; up to 2500 Hz repetition rate), accelerated by a voltage of 20 kV, and detected as positive ions. The matrix solution was prepared by dissolving 1,8,9-anthracenetriol (dithranol) in THF at a concentration of 20 mg mL^{-1}. Polymers were dissolved in THF at a concentration of 10 mg mL^{-1}; salts sodium trifluoroacetate (NaTFA) and potassium chloride (KCl) were dissolved at a concentration of 10 mg mL^{-1} in THF. Solutions of the matrix, the polymer, and the salt were mixed in a volume ratio of 100:10:1, and 1 mL of each mixture was spotted on the MALDI-target plate. Baseline subtraction and smoothing of the recorded spectra were performed using a three point Savitzky−Golay algorithm. The instrument was externally calibrated with poly(ethylene glycol) standards (M_w = 2000 and 4200 g mol^{-1}) applying a quadratic calibration method with an error of 1−2 ppm.
Thermogravimetric analysis (TGA) was conducted on a Mettler Toledo (DSC-H22) instrument. The sample was heated in a Pt pan, under a nitrogen atmosphere, over a temperature range 25−800 °C, with a heating rate of 10 °C min^{-1}.
Differential scanning calorimetry (DSC) was conducted on Perkin-Elmer Pyris Diamond instrument. The glass transition temperatures were determined by cooling the samples at −90 °C and then heating up to 150 °C, both at rate 10 °C min^{-1}. The glass transition temperature is taken as a midpoint of a small heat capacity change upon heating from amorphous glass state to a liquid state.
Small-angle X-ray scattering (SAXS) experiments were carried out under vacuum with a rotating copper-anode X-ray generator (Nanostar, Bruker AXS), Cu Kα radiation (wavelength 0.1542 nm) monochromatized and collimated from crossed Goebel mirrors, and a 2-D position sensitive detector (Vantec 2000). For the *in situ* SAXS measurement a specially designed X-ray transparent furnace was developed, which allows stepwise heating of the samples from room temperature to 550 °C with an accuracy of ±0.5 °C. The samples were placed either in a quartz glass capillary with a diameter of 1.5 mm and a wall thickness of 10 μm (from Hilgenberg, Germany) or between

dx.doi.org/10.1021/ma202736g | Macromolecules 2012, 45, 2074−2084

Scheme 1. Synthetic Route toward Nonsymmetric Ionic Liquid-Functionalized PIBs 3a−3c[a]

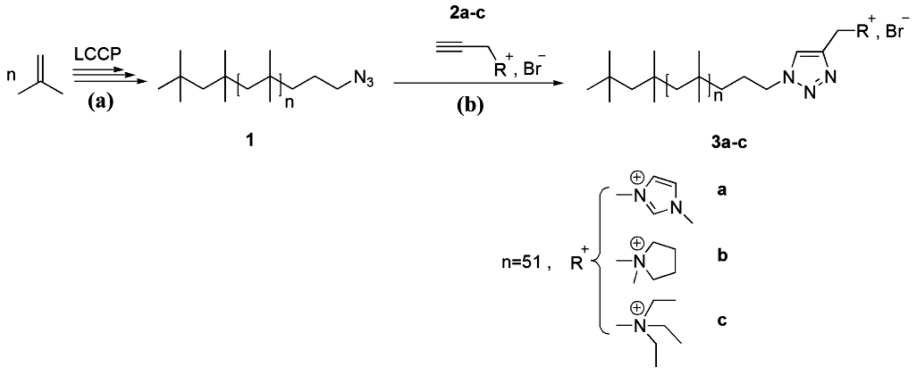

[a](a) Living carbocationic polymerization (LCCP):[47c] (i) synthesis of allyl-functionalized PIB; (ii) synthesis of hydroxyl-functionalized PIB; (iii) synthesis of bromide functionalized PIB; (iv) synthesis of azide functionalized PIB (**1**).[48] (b) Azide/alkyne "click" reaction. Reaction conditions are given in the Experimental Section.

commercial aluminum foils. The samples were heated up to the desired temperature, kept at this temperature for 5 min to ensure thermal equilibrium, and measured for 15−30 min depending on the scattering intensity of the respective samples. With a sample-to-detector distance of 108 cm an accessible q-range from 0.1 to 2.8 nm^{-1} was obtained. The SAXS patterns were radially averaged in order to obtain the scattering intensities $I(q)$, where $q = (4\pi/\lambda) \sin \theta$ is the scattering vector and 2θ the scattering angle. The d_{100} peak (the strongest Bragg reflection) was fitted with a Lorentzian function. This results in numerical values for the peak position (corresponding to the distance of the crystalline units in real space) and the peak breadth (proportional to the domain size).

Rheological measurements were performed on an Anton Paar MCR 101-DSO rheometer using parallel plates (diameter 8 mm). The sample temperature was regulated by thermoelectric cooling/heating in a Peltier chamber under a dry oxygen atmosphere. Frequency sweep measurements were performed within the LVE (if not mentioned otherwise). Temperature sweep measurements were performed with a heating rate of 1 °C/min at ω = 10 rad/s. Before each measurement the sample was annealed for 30 min.

Synthesis. Allyl telechelic PIB was synthesized via living carbocationic polymerization (LCCP) based on procedure known from the literature.[47c] Isobutylene was polymerized via LCCP in the presence of 2-chloro-2,4,4-trimethylpentane (TMPCl) and $TiCl_4$ as initiator and co-initiator (for details see Supporting Information S2). Quenching of the polymerization with allyltrimethylsilane (ATMS) resulted in allyl-functionalized PIB. Azido telechelic PIB (M_n = 2920 g/mol; M_w/M_n= 1.14) was synthesized via further modification of allyl telechelic PIB following procedure described by Binder et al.[48] The allyl moiety was converted into the hydroxyl group by hydroboration of the double bond using 9-borabicyclo[3.3.1]nonane (9-BBN) and subsequent oxidation with *m*-chloroperoxybenzoic acid (*m*-CPBA). Bromination of the obtained PIB was accomplished in the presence of carbon tetrabromide and triphenylphosphine with a yield of 99%. Bromo-functionalized PIB was converted to the azide using tetrabutylammonium fluoride (TBAF) and azidotrimethylsilane (TMSA) with a yield of 89%. The pure product PIB (**1**) was characterized using NMR and GPC (see Supporting Information, S2−S4).

General Procedure for the Synthesis of Compounds 2a−2c. To a solution of propargyl bromide (1 equiv) in dry toluene corresponding amine (1.2 equiv) was added dropwise. The reaction mixture was stirred at 50 °C. Then, the solvent was removed from reaction mixture under reduced pressure, and the obtained crude product was washed with ethyl acetate.

*1-Propargyl-3-methylimidazolium Bromide (**2a**).* 1-Methylimidazole (1.02 g, 12.43 mmol) was added dropwise to a solution of propargyl bromide (1.23 g, 10.36 mmol) in dry toluene (25 mL). After stirring the reaction mixture for 20 h, the obtained product was purified by washing with ethyl acetate. Yield of (**2a**): 84% (1.74 g, 8.70 mmol), as a brownish powder. ^{1}H NMR (400 MHz, DMSO-d_6) δ (ppm): 9.29 (s, 1H), 7.81 (t, J = 1.8, ^{1}H), 7.78 (t, J = 1.8, 1H), 5.24 (d, J = 2.56, 2H), 3.89 (s, 3H), 3.84 (t, J = 2.6, 1H). ^{13}C NMR (100.6 MHz, $CDCl_3$) δ (ppm): 136.2, 123.7, 121.8, 78.8, 75.9, 38.4, 35.8.

*1-Propargyl-1-methylpyrrolidinium Bromide (**2b**).* After addition of 1-methylpyrrolidine (1.06 g, 12.43 mmol) to a solution of propargyl bromide (1.23 g, 10.36 mmol) in dry toluene (25 mL), the reaction mixture was stirred for 24 h. After purification the product was obtained as slightly yellow solid with yield of 88% (1.69 g, 8.28 mmol). ^{1}H NMR (400 MHz, DMSO-d_6) δ (ppm): 4.50 (d, J = 2.5, 1H), 4.01 (dt, J = 2.45, 0.74, 2H), 3.63−3.49 (m, 4H), 3.15 (s, 3H), 2.18−2.05 (m, 4H). ^{13}C NMR (100.6 MHz, $CDCl_3$) δ (ppm): 81.6, 72.9, 63.0, 52.3, 48.7, 21.4.

*N-Propargyl-N,N,N-triethylammonium Bromide (**2c**).* According to the general procedure *N,N,N*-triethylamine (1.25 g, 12.72 mmol) was added to a solution of propargyl bromide (1.23 g, 10.36 mmol) in dry toluene (20 mL), and it was stirred for 16 h. The purification of the product resulted in a white solid with 82% (1.87 g, 8.49 mmol) yield. ^{1}H NMR (400 MHz, $CDCl_3$) δ (ppm): 4.34 (d, J = 2.56, 2H), 4.01 (t, J = 2.53, 1H), 3.30 (q, J = 7.2, 6H), 1.23 (t, J = 7.2, 9H). ^{13}C NMR (100.6 MHz, $CDCl_3$) δ (ppm): 82.1, 71.9, 52.9, 30.5, 7.3.

General Procedure for the Synthesis of PIBs Containing an Ionic Moiety via "Click" Reaction (3a−3c). Azido telechelic PIB (**1**, 1 equiv, M_n = 2920 g/mol; M_w/M_n = 1.14) and the corresponding ionic liquid containing alkyne (2 equiv) were dissolved in a solvent mixture of toluene/water/isopropanol (2:1:1) and placed in a microwave vial. After addition of *N,N*-diisopropylethylamine (DIPEA) (10 equiv), the vial was closed with a septum and the solution was purged with nitrogen for 30 min. Then copper(I) iodide (CuI) (0.2 equiv) was added to the mixture, and the solution was again purged with nitrogen for more than 30 min. Subsequently, the vial was sealed, placed in a microwave reactor, and irradiated under 70−80 W for several hours. After termination of the irradiation, the organic phase was separated and washed with water (3 times). The crude product which was obtained after removal of the solvents was purified by column chromatography (stationary phase: SiO_2; eluent: chloroform) to eliminate the unreacted azido-telechelic PIB. Then the eluent was changed to chloroform/methanol (15:1), and the fraction with R_f = 0.2 was collected. After evaporating of the solvent, the residue was dissolved in a small amount of chloroform and precipitated into methanol. The precipitate was collected and dried under high vacuum.

*3-Methyl-1-imidazolium Telechelic PIB (**3a**).* 3-Propargyl-1-methylimidazolium bromide (**2a**, 12.09 mg, 0.06 mmol), azido-telechelic PIB (100 mg, 0.03 mmol), CuI (10 mg); irradiation conditions: 80 W, 85−90 °C, 17 h. Yield of **3a**: 58% (67 mg). ^{1}H NMR (400 MHz, $CDCl_3$) δ (ppm): 10.70 (s, 1H) 8.47 (s, 1H), 7.63 (s, 1H), 7.09 (s, 1H), 5.86 (s, 2H), 4.29 (t, 2H, J = 7.5), 3.98 (s, 3H), 1.94−1.83 (m,

dx.doi.org/10.1021/ma202736g | *Macromolecules* 2012, 45, 2074−2084

Table 1. Reaction Conditions, Molecular Weight Data, Decomposition ($T_{d,onset}$), and Glass Transition Temperature (T_g) of the PIB Ionic Liquids 3a−3c

entry	POIL	catalyst	reaction condition[a]	conv[b] (%)	yield (%)	$M_{n(NMR)}$ (g/mol)	$M_{n(GPC)}$ (g/mol)	PDI	$T_{d,onset}$ (°C)	T_g (°C)
1	**3a**	CuI (0.03 mmol)	75 W/75 °C/16 h	86	58	3256	3241	1.2	310	−70.6
2	**3b**	CuI (0.03 mmol)	75 W/75 °C/16 h	81	52	3259	3207	1.2	398	−71.4
3	**3c**	CuI (0.03 mmol)	70 W/75 °C/16 h	74	48	3334	4700	1.2	352	−70.9

[a]Reaction condition is reported based on irradiation power (W), reaction temperature (°C), and duration (h). [b]Conversions were determined by ^{1}H NMR, comparing integration ratio of cationic moiety signals to the rest of the polymer chain, especially unreacted $-CH_2-N_3$.

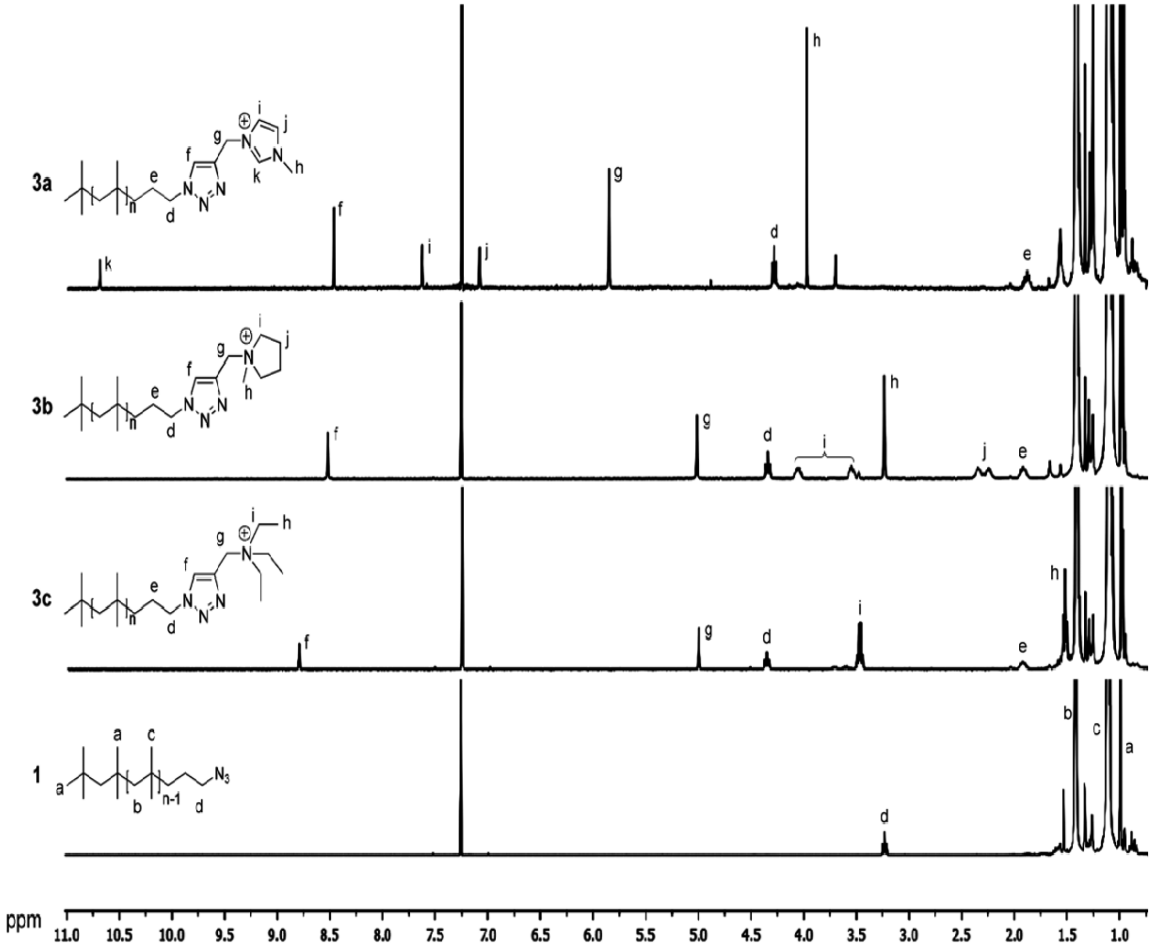

Figure 1. ^{1}H NMR spectra of the PIB-ILs (**3a−3c**) and the starting material (azido-telechelic PIB (**1**)).

2H), 1.47−1.36 (m, 104H), 1.16−1.05 (m, 312H), 1.00−0.97 (m, 15H). ^{13}C NMR (100.6 MHz, $CDCl_3$) δ (ppm): 139.8, 137.8, 125.2, 122.7, 122.5, 59.5, 58.8, 58.2, 55.9, 51.5, 44.4, 42.2, 38.1, 36.6, 34.8, 32.6, 32.5, 31.2, 30.8, 29.1, 25.5.

*1-Methylpyrrolidinum Telechelic PIB (**3b**).* 1-Propargyl-1-methylpyrrolidinum bromide (**2b**, 12.24 mg, 0.06), azido-telechelic PIB (100 mg, 0.03 mmol), CuI (8 mg); irradiation conditions: 80 W, 85−90 °C, 17 h. Yield of **3b**: 52% (56 mg). ^{1}H NMR (400 MHz, $CDCl_3$) δ (ppm): 8.52 (s, 1H), 5.02 (s, 2H), 4.34 (t, 2H, J = 7.5), 4.11−4.00 (m, 2H), 3.60- 3.50 (m, 2H), 3.24 (s, 3H), 2.40−2.18 (m, 4H), 1.98−1.81 (m, 2H), 1.47−1.36 (m, 104H), 1.16−1.05 (m, 312H), 1.00−0.97 (m, 15H). ^{13}C NMR (100.6 MHz, $CDCl_3$) δ (ppm): 128.4, 63.9, 59.5, 58.8, 58.2, 57.6, 55.9, 51.6, 49.4, 42.2, 38.2, 37.8, 34.8, 32.6, 32.4, 31.2, 30.8, 29.2, 25.5, 21.9.

*N,N,N-Triethylammonium Telechelic PIB (**3c**).* *N*-Propargyl-*N,N,N*-triethylammonium (**2c**, 13.20, 0.06 mmol), azido-telechelic PIB (100 mg, 0.03 mmol), CuI (10 mg); irradiation conditions: 80 W, 85−90 °C, 17 h. Yield of **3c**: 48% (51 mg). ^{1}H NMR (400 MHz, $CDCl_3$) δ (ppm): 8.81 (s, 1H), 5.01 (s, 2H), 4.36 (t, 2H, J = 7.5), 3.48 (q, 6H, J = 7.3), 1.98−1.88 (m, 2H), 1.52 (t, 9H, J = 7.2), 1.45−1.36 (m, 102H), 1.15−1.05 (m, 306H), 0.99−0.95 (m, 15H). ^{13}C NMR (100.6 MHz, $CDCl_3$) δ (ppm): 135.1, 128.4, 59.5, 58.8, 58.2, 55.9, 53.5, 51.9, 51.5, 42.1, 38.2, 37.9, 37.8, 34.8, 32.6, 32.4, 31.2, 30.8, 29.1, 25.4, 7.8.

RESULTS AND DISCUSSION

Synthesis of Polyisobutylene-Based Ionic Liquids (PIB-ILs). In general, POILs can be prepared either via direct polymerization of IL monomers or via chemical modification of existing polymers. Both strategies often involve polymerization techniques such as conventional[6] and living radical polymerization (ATRP[49] and RAFT[41,50]), ring-opening metathesis polymerization,[51] or chemical and electrochemical oxidative polymerization.[52] Our synthetic route for the preparation of polyisobutylene-based ionic liquids (PIB-ILs) follows the use of living carbocationic polymerization (LCCP) as presented in Scheme 1. It should be noted that for end-group modification of polyisobutylene with strongly polar moieties (as the IL groups are), only a few qualitatively useful reactions are

dx.doi.org/10.1021/ma202736g | Macromolecules 2012, 45, 2074−2084

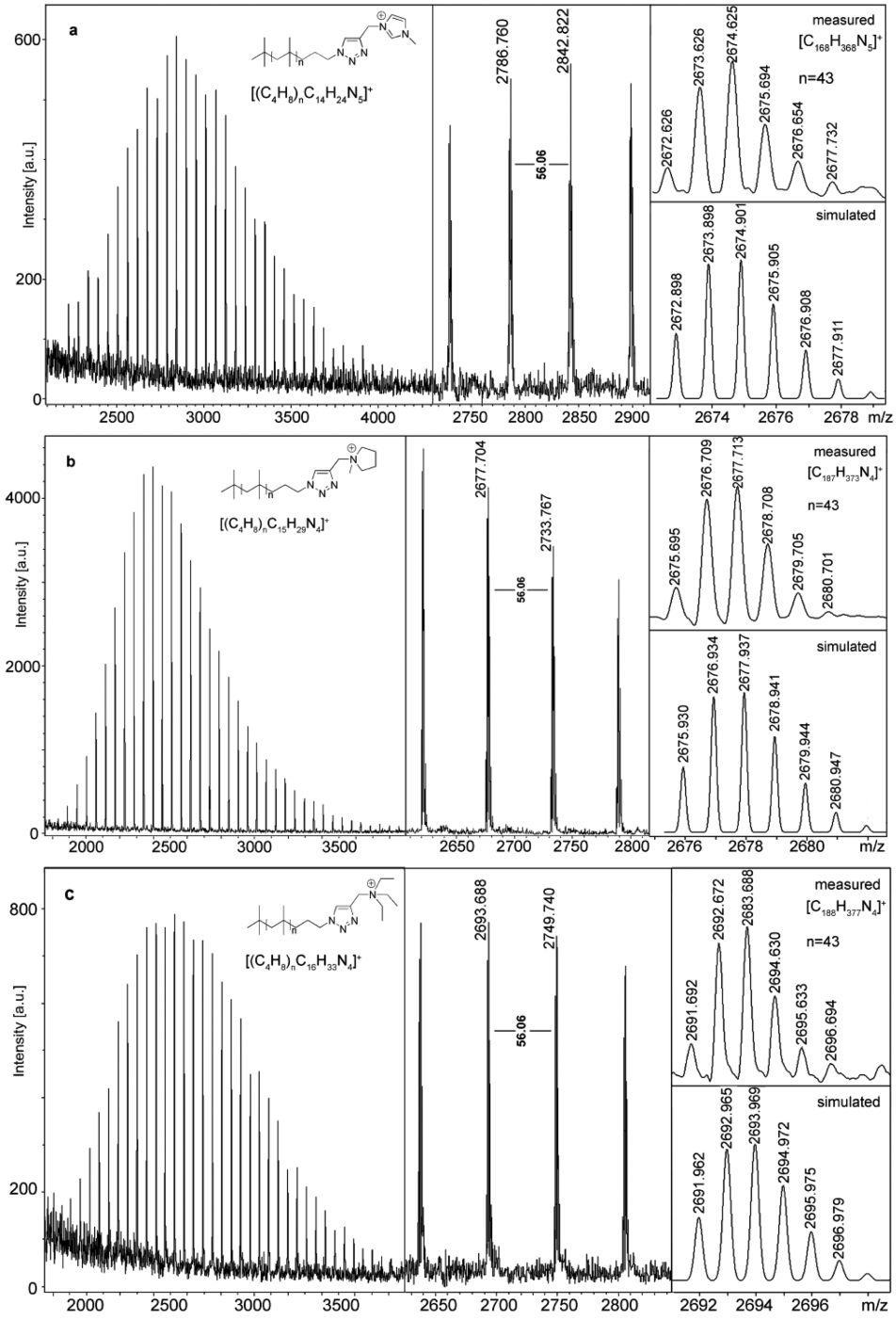

Figure 2. MALDI-TOF mass spectra of the PIB-ILs (**3a**–**3c**): (a) Compound **3a**, inset: simulation for $[C_{186}H_{368}N_5]^+$ with 43 units of isobutylene. (b) Compound **3b**, inset: simulation for $[C_{187}H_{373}N_4]^+$ with 43 units of isobutylene. (c) Compound **3c**, inset: simulation for $[C_{188}H_{377}N_4]^+$ with 43 units of isobutylene.

known.[47c,e,f,53] The azide/alkyne "click" reaction to attach these highly polar moieties therefore represents the best method to achieve this goal.

Allyl-functionalized telechelic PIB was synthesized via living carbocationic polymerization (LCCP) using 2-chloro-2,4,4-trimethylpentane (TMPCl) as described elsewere.[47c] Transformation of the allyl-functionalized PIB to the azido-telechelic PIB (**1**) was conducted according to the method developed earlier by us,[48] yielding PIB_n-N_3 (M_n = 2920 g/mol; M_w/M_n = 1.14) in 90% overall yield. Subsequent microwave-assisted azide/alkyne "click" reaction between PIB_n-N_3 (**1**) and the alkyne containing ILs (**2a**–**2c**) with a copper(I) catalyst resulted in the desired ionic-liquid-functionalized PIB. Upon testing different Cu(I) catalysts (Cu(I) iodide, Cu(I) bromide and tris(triphenylphosphine)copper(I) bromide, [Cu-$(PPh_3)_3Br$]), only [$Cu(PPh_3)_3Br$] and CuI proved conversions between 30 and 86% (see Table 1 and Supporting Information, Table S1). Best results were achieved using copper(I) iodide under microwave irradiation conditions, with a strong influence of the microwave-irradiation power on the obtained yields. Although the increase of irradiation power often leads to higher conversions, the formation of side products via Hofmann

dx.doi.org/10.1021/ma202736g | *Macromolecules* 2012, 45, 2074–2084

elimination could be observed. Lowering of the irradiation power also resulted in a decline of conversion. Therefore, optimization of microwave irradiation conditions for all three compounds led to a good conversion of the azide (conversions 74−86%, see Table 1).

Characterization of the PIB-ILs. The structure of the prepared PIB- ionic liquids (**3a**−**3c**) was confirmed via ^{1}H and ^{13}C NMR spectroscopy (see Figure 1 and Supporting Information, S8−S10) as well as MALDI-TOF-MS measurements (see Figure 2). Chromatographic and NMR spectroscopic data are shown in Table 1, revealing a good agreement between the $M_{n(GPC)}$ and $M_{n(NMR)}$ data and hence indicating a complete end-group functionalization. After purification by column chromatography it was possible to obtain pure compounds **3a**−**3c**, thus removing eventually present impurities or incompletely functionalized polymers.

All compounds showed the expected resonances in NMR spectroscopy as well as the expected absolute molecular weights in the respective mass spectra. The successful "click" reaction was confirmed by the proton shift of the terminal CH_2− group of poly(isobutylene) chain (triplet d in Figure 1) from 3.21 ppm for azido telechelic PIB (**1**) to 4.29−4.36 ppm in the case of PIB-ILs **3a**−**3c** and the appearance of a resonance of the triazole ring in the range between 8.47 and 8.81 ppm (signal f in Figure 1). Furthermore, no signals originating from the unreacted azido-telechelic PIB could be observed in ^{1}H NMR spectra of the PIB-ILs **3a**−**3c** (see Figure 1). MALDI-TOF-MS spectra of synthesized polymeric ionic liquids are shown in Figure 2. All three spectra show one main series with 56 Da differences which corresponds to the mass of one repeating unit. The observed signals in all three cases can be simply assigned to PIB containing cationic moiety. According to Figure 2a, the signal appearing at 2672.626 Da can be assigned to PIB containing imidazolium cation with chemical formula of $[C_{186}H_{368}N_5]^+$ with n = 43 units of isobutylene. In Figure 2b, the signal at 2675.695 Da can be represented by $[C_{187}H_{373}N_4]^+$, and the PIB-containing ammonium moiety can be identified by its signal at 2691.692 Da, which is assigned for $[C_{188}H_{377}N_4]^+$ (Figure 2c). The simulated isotopic pattern of the synthesized polymeric ionic liquids for repeating unit of n = 43 shows an excellent match with the pattern of the observed signals in MALDI spectra which confirms the formation of expected structures.

All three investigated PIB-ILs exhibit glass transition temperatures in the range −70.6 to −71.4 °C (see Table 1), indicating the increase of T_g compared to the PIB (−80 °C) due to the presence of the ionic moieties.

As thermal stability is an important selection criterion for a high-temperature use, thermogravimetric analysis of the PIB-ILs was performed (see Figure 3), indicating only one decomposition step with the onset decomposition temperature in the range between 310 and 398 °C (see Table 1). As expected, the thermal stability of the presented PIB-ILs **3a**−**3c** is higher compared to the classical monomeric ionic liquids[54] and lies in the range of other previously investigated POILs.[5]

SAXS Measurements of PIB Ionic Liquids. As already reported in the literature, the morphology of some POILs exhibits a behavior similar to those described for ionomers.[4,5,12] As the structure of prepared polyisobutylene-based POILs shows distinct resemblance to the structure of classical ionomers, composed of a polymeric tail and ionic groups at the end positions, similar microphase separation may be expected. According to the multiplet-cluster model for the

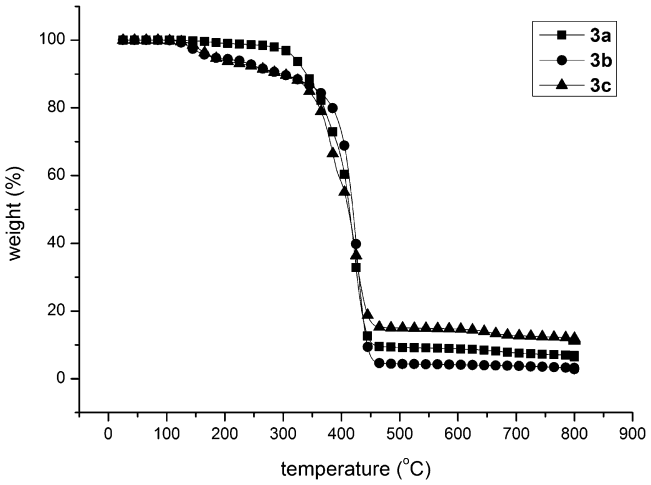

Figure 3. Thermogravimetric analysis (TGA) of the PIB-ILs (**3a**−**3c**) at a heating rate of 10 °C min^{-1} under a nitrogen atmosphere.

description of morphology of random ionomers postulated by Eisenberg et al.,[55,56] ion pairs aggregate to structures named "multiplets". Electrostatic interactions between "multiplets" favor their agglomeration to form phase-separated regions (clusters), whereas the elastic forces of free polymer chains are opposing cluster formation. Additionally, the mobility of the polymer chain in the immediate vicinity of the "multiplets" is strongly restricted, resulting in a region of restricted mobility surrounding each multiplet. As the ion content increases the average distance between "multiplets" decreases, resulting in overlap of regions with restricted mobility of polymer chains. After a certain critical ion concentration is reached cluster formation becomes more energetically favorable, therefore resulting in the formation of aggregates. As a consequence, the presence of clusters leads to the existence of large regions of material with restricted mobility. Since the stability of microphase separation is strongly temperature dependent, a loss of the internal structure at higher temperature due to the weakening of electrostatic interactions is expected. However, after cooling and distinct relaxation time re-establishment of the internal structure can be observed, indicative of the self-healing properties of such ionomers.[24c,56,57]

In order to investigate the morphologies of prepared PIB-ILs, SAXS measurements were conducted (see Figures 4−6 and Supporting Information, S11−S12).

The observed Bragg reflections in the SAXS patterns can be interpreted as the formation of ordered clusters in POILs, predominantly representing intracluster spacings. Both **3a** and **3b** show five reflections, which could be attributed to a simple cubic lattice with a d-spacing (the distance of the units) of 7.6 and 6.9 nm for **3a** and **3b**, respectively. The ammonium-containing compound (**3c**) exhibits four reflections, clearly indicating an arrangement in the form of 2-D hexagonally packed cylinders with a d-spacing of 7.95 nm (see also Supporting Information, S11−S12). Thus, it can be assumed that PIB-ILs **3a** and **3b** form "multiplets" clustered in a micellar fashion at room temperature, while **3c** assembles as a cylindrical phase (see Figure 4).

In the next step, PIB-IL samples were also subjected to variable-temperature *in situ* SAXS to identify any disorder−order or order−order transition in the range 25−300 °C and to further understand the relaxation of structural changes. As can be seen in Figure 5b, compound **3b** shows a lattice disorder−

dx.doi.org/10.1021/ma202736g | *Macromolecules* 2012, 45, 2074−2084

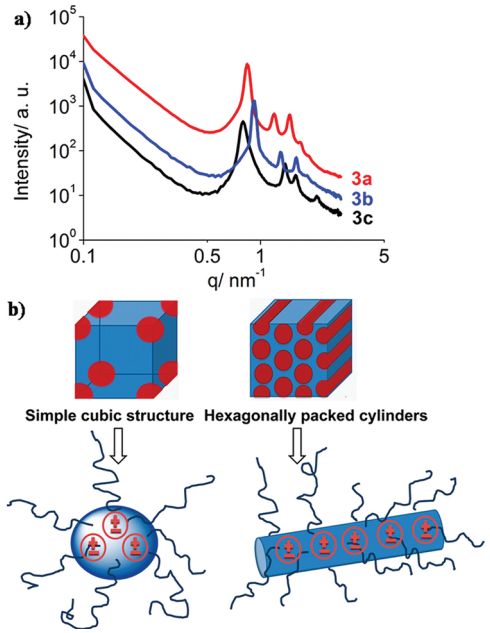

Figure 4. (a) SAXS profiles of PIB-based ILs (**3a**–**3c**) at room temperature. Each curve is shifted in the intensity axis (*y*-axis) for clarity. (b) Schematic illustration of simple cubic and hexagonally packed cylindrical nanostructure formed by PIB-ILs. The "multiplets" are representing the inner phase of the structures.

order transition (LDOT) at 80 °C, indicated by the broadening of the first and the gradual disappearance of higher order peaks. This resembles the phase disordering process of micelles during heating, which was distinguished by Han et al.[58] from the demicellation/micellation transition (DMT) at still higher temperatures. The increase of temperature leads to a gradual weakening of the electrostatic forces between ionic clusters. After reaching the transition temperature, loss of the internal structure due to the electrostatic interaction can be observed (loss of all four higher order scattering maxima). Breaking of the ionic clusters between "multiplets" subsequently leads to an increase in mobility of polymer chains, resulting in a shift and broadness of the main peak. After cooling to room temperature and waiting for a relaxation time of 132 h a clear re-establishment of the nanostructure can be observed (see Figure 5b). The relaxation time of **3b** is comparable with the results obtained by Varley et al.[24c] for classical ionomers with relaxations times up to 7 days.

Additionally, the obtained data were fitted with Lorentzian function, and the variation of the main peak position as well as its half-width at half-maximum (hwhm) with temperature are plotted. The variation of the main peak position with temperature and after relaxation is presented in Figure 6 (see also Supporting Information, S13–S14), indicating a continuous shift of the main peak to larger q values with increasing temperature, which corresponds to the formation of smaller structures. After a relaxation time of 132 h the original nanostructure is almost completely restored, which is in accordance with the observations of Eisenberg[56,57d] and others[57] regarding the thermal behavior of classical ionomers. Therefore, the investigated ionic liquid **3b** exhibits self-healing characteristic for ionomers.

However, a markedly different behavior was observed in the case of PIB-IL **3a** (see Figure 5a). The internal cubic nanostructure of the imidazolium-based IL **3a** is stable even at higher temperatures. Only a partial loss of the nanostructure can be observed at 275 °C (loss of the smallest two peaks). The strong electrostatic interactions between imidazolium cations, probably combined with pronounced π–π stacking between adjacent imidazolium rings, lead to the significantly stable internal structure. In the range between 275 and 300 °C the order–disorder transition can be observed, followed by the extreme broadening of the main peak. However, this loss of internal structure is probably due to the thermal decomposition of the compound, rather than due to the thermal transition of nanostructural organization. Furthermore, even after 1 week no structural relaxation could be observed, suggesting the irreversible thermal decomposition of the starting compound at 300 °C, which is in accordance with the thermal stability data obtained with TGA (see Figure 3).

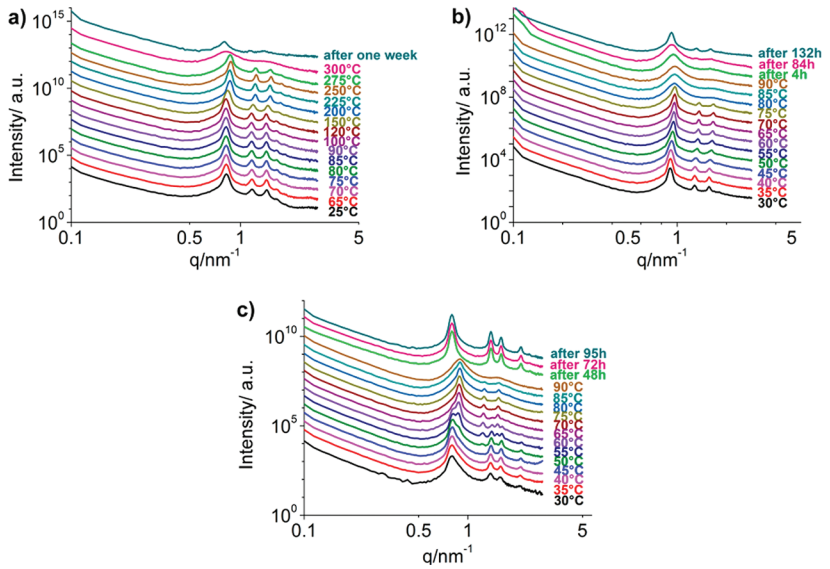

Figure 5. SAXS profiles of the prepared PIB-containing ionic liquids at different temperatures and after relaxation: (a) **3a**; (b) **3b**; (c) **3c**. Each curve is shifted in the intensity axis (*y*-axis) for clarity.

dx.doi.org/10.1021/ma202736g | *Macromolecules* 2012, 45, 2074–2084

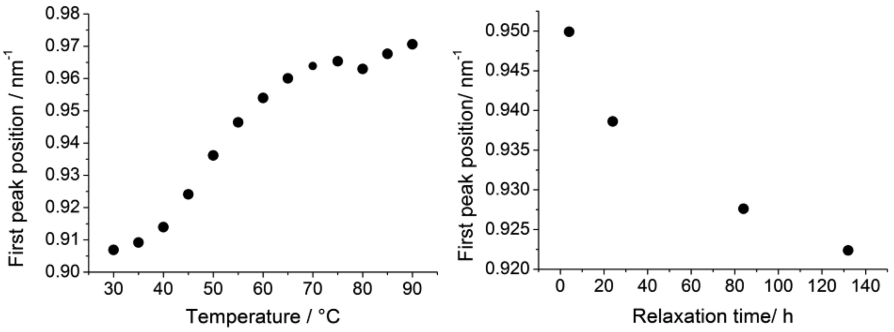

Figure 6. Variation of the main peak position with temperature (left), after heating to 90 °C, and relaxation at room temperature (right) obtained for **3b** via temperature-dependent SAXS measurements.

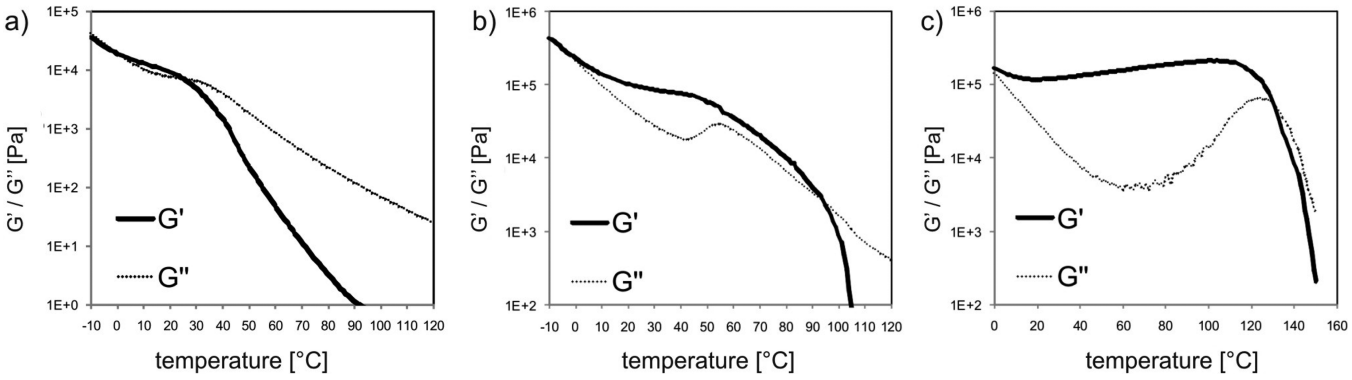

Figure 7. Temperature-sweep measurements for PIB-ILs: (a) for sample **3b**, (b) for sample **3c**, and (c) for sample **3a**. The heating rate was 1 °C/min at ω = 10 rad/s.

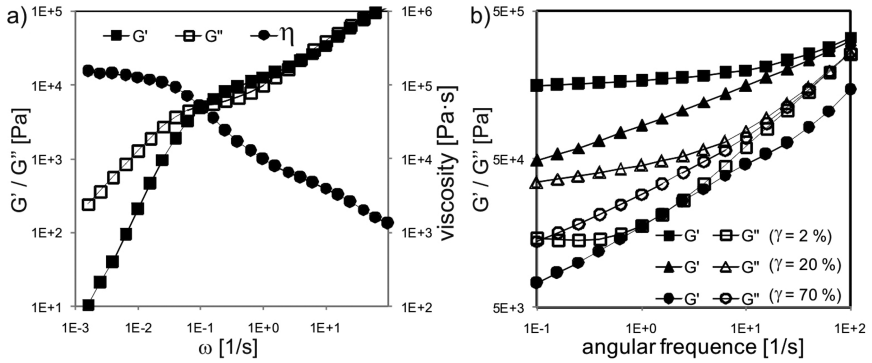

Figure 8. (a) Frequency-sweep measurement of **3b** at 20 °C (γ = 2%). (b) Frequency-sweep measurements of **3c** with different strains at 20 °C.

Whereas in the case of the compounds **3a** and **3b** no order−order transition (OOT) could be observed at any temperature, this is clearly the case for compound **3c** (see Figure 5c). Starting from the hexagonally packed cylindrical morphology at room temperature, the first OOT can be observed at 50 °C where the coexistence of hexagonally packed cylindrical and simple cubic morphology is clearly visible (see also Supporting Information, S11−S12). At 65 °C a second OOT can be observed, indicating the loss of the hexagonally packed cylindrical morphology. Finally, at 90 °C the loss of the cubic morphology and hence the order−disorder transition can be observed. Corresponding to the much more flexible structure of the cation in compound **3c**, significantly shorter relaxation times were observed compared to PIB-IL **3b** (see Figure 5c). After cooling to room temperature and only 48 h relaxation time the hexagonally packed cylindrical morphology of **3c** was almost completely re-established. Our results clearly indicate that the self-assembly and the stability of the microphase morphology of the presented POILs strongly depends on the nature of the cation anchored on the polymeric chain.[36]

Rheology Measurements of PIB Ionic Liquids. A closer look on the order/order and order/disorder transitions was achieved by melt rheology,[59] as in our samples the relaxation behavior expectedly stems from two different contributions. On the one hand, microphase separation should influence the viscous behavior similar to conventionally microphase-separated block copolymers above the T_g, whereas the ionic multiplets should strongly tend to retain the (cubic) structure due to their high stability even at high temperatures.[60] As shown in Figure 7, the samples exhibited strongly different rheological behavior, depending on the nature of the cation anchored onto the polymeric chain. At low temperatures only the PIB-IL **3b** shows terminal flow, as exemplified by the

dx.doi.org/10.1021/ma202736g | *Macromolecules* 2012, 45, 2074−2084

dependency of $G' \sim \omega^2$; $G'' \sim \omega^1$ at $\omega\tau \ll 1$, indicative of a viscoelastic fluid.

This behavior can be explained by the internal cubic structure of the PIB-IL, which consists of (spherical) ionic multiplets. These multiplets slide over each other similar to the model described by Antonietti et al.[61] for spherical microgels. Therefore, a small (rubbery) plateau can be observed, which fits into the model of viscous flow via cooperative movements of the ionic multiplets upon shear. Depending on the size of the multiplets (**3b** (6.9 nm); **3c** (7.24 nm); **3a** (7.6 nm) as determined via SAXS), flow is then achieved at increasing temperatures 40, 105, and 140 °C, respectively (see frequency-sweep measurement at ω = 10 rad/s in Figure 7). As our polymers are below the entanglement limit, the formation of a plateau by entangled chains can be definitely ruled out. However, in accordance with the work of Hadjichristidis,[59] a deaggregation of the ionic clusters at lower frequencies cannot be excluded. In contrast to the other PIB-ILs (**3a**, **3b**), PIB-IL **3c** shows a significant transition around T = 50 °C, which matches with the order/order-transition from cubic to hexagonal as observed in SAXS. Thus, a strongly shear-dependent behavior of G' and G'' at low strain (γ = 2−70%) was observed (see Figure 8b and Supporting Information, S15−19), similar to the behavior of nanotubes, dispersed in a IL matrix.[62] The tubular structures can form a transient network, which can then be broken by the applied forces with increasing strain. However, the obtained results may also indicate the alignment of the aggregates of the ionic groups under the applied strain.[63] As those two possibilites can hardly be discriminated, and the SAXS data point to the former behavior of cluster retainment, we tend to the first hypothesis. In general, the observed data clearly demonstrate an entirely different behavior than expected for conventional block copolymers, which are introduced by the ionic liquid head groups. Clearly fascinating is this strong change by the presence of only one small ionic headgroup within the comparable long polymer chain.

CONCLUSIONS

A new IL with a strongly temperature-dependent nanostructure is reported in this paper, relying on the synthesis of a liquid polymer with a IL headgroup, thus introducing liquid properties by both the polymer and via the IL headgroup. Thus, the poly(isobutylene)s containing polymeric ionic liquids **3a**−**3c** were prepared, and their temperature-dependent self-assembly behavior was investigated by SAXS. The synthetic approach combined living cationic polymerization with azide/alkyne "click" chemistry and enabled a full end-group transformation to the final polymeric ionic liquids, modified with either imidazolium, pyrrolidinium, or triethylammonium end groups.

SAXS measurements at different temperatures revealed a similar behavior of prepared PIB-ILs to classical ionomers. All three investigated PIB-ILs exhibited pronounced nanostructural organization at room temperature. However, the thermal stability of the nanophasic separation shows strong dependence on the nature of an anchored cation. Whereas the nanostructural morphology of the imidazolium-based PIB-IL **3a** shows high thermal stability up to the decomposition temperature, order−order and lattice disorder−order transitions characteristic for common ionomers could be observed in the case of pyrrolidinium **3b** and ammonium-based **3c** PIB-ILs. Furthermore, also the relaxation time and thus the re-establishment of the nanostructural organization after cooling at room temperature are strongly dependent on the nature of ionic group, with the relaxation time of compound **3c** being significantly shorter as compared to the **3b** with the rigid, cyclic pyrrolidinium cation. The reported PIB-ILs represent new types of ionic liquids, where both the polymeric part and the IL headgroup can be used to tune both the nanostructure and the rheological properties. Because of their additional high thermal stability, the so-identified ILs therefore are important candidates for strongly shear- and wear-resistant fluids in science and technology, in particular aiming at self-healing polymers, where the relaxation time can now be engineered by the IL end group, together with the strong shear- and temperature-dependent flow behavior.

ASSOCIATED CONTENT

Supporting Information

Optimization of reaction conditions, synthetical procedure for the compound **1**, NMR spectra of the compounds **1**, **2a**−**2c**, and **3a**−**3c**, GPC of the compound **1**, SAXS (including fitted Lorentzian curves), and rheology data of compounds **3a**−**3c**. This material is available free of charge via the Internet at http://pubs.acs.org.

AUTHOR INFORMATION

Corresponding Author

*E-mail wolfgang.binder@chemie.uni-halle.de; Fax (+49) 345 55 27392.

Author Contributions

§P.Z. and A.S. contributed equally to this work.

Notes

The authors declare no competing financial interest.

ACKNOWLEDGMENTS

We acknowledge the financial support from the research training network MINILUBES (FP-7 Marie Curie Action) (P.Z., A.S.), grants DFG BI 1337/7-1 (F.H.), DFG BI 1337/8-1 (within the SPP 1568 ("Design and Generic Principles of Self-Healing Materials")), DFG INST 271/249-1, INST 271/247-1, INST 271/248-1 (W.H.B.), and the Austrian science funds FWF proj. nr. I449 (J.A., H.P.).

REFERENCES

(1) Marcilla, R.; Alberto Blazquez, J.; Rodriguez, J.; Pomposo, J. A.; Mecerreyes, D. *J. Polym. Sci., Polym. Chem.* **2004**, *42*, 208−212.
(2) Marcilla, R.; Sanchez-Paniagua, M.; Lopez-Ruiz, B.; Lopez-Cabarcos, E.; Ochoteco, E.; Grande, H.; Mecerreyes, D. *J. Polym. Sci., Polym. Chem.* **2006**, *44*, 3958−3965.
(3) Nakajima, H.; Ohno, H. *Polymer* **2005**, *46*, 11499−11504.
(4) Firestone, M. A.; Green, O.; Grubjesic, S.; Lee, S. W. *Polym. Rev.* **2009**, *49*, 339−360.
(5) Mecerreyes, D. *Prog. Polym. Sci.* **2011**, DOI: 10.1016/j.progpolymsci.2011.05.007.
(6) Yuan, J.; Antonietti, M. *Polymer* **2011**, *52*, 1469−1482.
(7) Hallett, J. P.; Welton, T. *Chem. Rev.* **2011**, *111*, 3508−3576.
(8) Plechkova, N. V.; Seddon, K. R. *Chem. Soc. Rev.* **2008**, *37*, 123−150.
(9) Wasserscheid, P.; Welton, T., *Ionic Liquids in Synthesis*, 2nd ed.; Wiley-VCH: Weinheim, 2008; 724 pp.
(10) Werner, S.; Haumann, M.; Wasserscheid, P. *Annu. Rev. Chem. Biomol. Eng.* **2010**, *1*, 203−230.
(11) Marcilla, R.; Mecerreyes, D.; Winroth, G.; Brovelli, S.; Yebra, M. d. M. R.; Cacialli, F. *Appl. Phys. Lett.* **2010**, *96*, 043308−3.
(12) Elabd, Y. A.; Chen, H.; Choi, J. H.; Salas-de La Cruz, D.; Winey, K. I. *Macromolecules* **2009**, *42*, 4809−4816.

(13) Gnanou, Y.; Vijayakrishna, K.; Mecerreyes, D.; Taton, D. *Macromolecules* **2009**, *42*, 5167−5174.
(14) Domján, A.; Erdödi, G.; Wilhelm, M.; Neidhöfer, M.; Landfester, K.; Iván, B.; Spiess, H. W. *Macromolecules* **2003**, *36*, 9107−9114.
(15) Freire, M. G.; Neves, C. M. S. S.; Shimizu, K.; Bernardes, C. E. S.; Marrucho, I. M.; Coutinho, J. o. A. P.; Lopes, J. N. C.; Rebelo, L. s. P. N. *J. Phys. Chem. B* **2010**, *114*, 15925−15934.
(16) Stojanovic, A.; Kogelnig, D.; Fischer, L.; Hann, S.; Galanski, M.; Groessl, M.; Krachler, R.; Keppler, B. K. *Aust. J. Chem.* **2010**, *63*, 511−524.
(17) MacFarlane, D. R.; Fraser, K. J. *Aust. J. Chem.* **2009**, *62*, 309−321.
(18) Cornelius, C. J.; Hibbs, M. R.; Hickner, M. A.; Alam, T. M.; McIntyre, S. K.; Fujimoto, C. H. *Chem. Mater.* **2008**, *20*, 2566−2573.
(19) Hickner, M. A. *Mater. Today* **2010**, *13*, 34−41.
(20) Muldoon, M. J.; Gordon, C. M. *J. Polym. Sci., Polym. Chem.* **2004**, *42*, 3865−3869.
(21) Texter, J.; Yan, F. *Chem. Commun.* **2006**, 2696−2698.
(22) (a) Bara, J. E.; Lessmann, S.; Gabriel, C. J.; Hatakeyama, E. S.; Noble, R. D.; Gin, D. L. *Ind. Eng. Chem. Res.* **2007**, *46*, 5397−5404. (b) Mineo, P. G.; Livoti, L.; Giannetto, M.; Gulino, A.; Lo Schiavo, S.; Cardiano, P. *J. Mater. Chem.* **2009**, *19*, 8861−8870. (c) Tang, J.; Tang, H.; Sun, W.; Radosz, M.; Shen, Y. *J. Polym. Sci., Polym. Chem.* **2005**, *43*, 5477−5489.
(23) Tang, J.; Radosz, M.; Shen, Y. *Macromolecules* **2007**, *41*, 493−496.
(24) (a) Varley, R. J.; Shen, S.; van der Zwaag, S. *Polymer* **2010**, *51*, 679−686. (b) Varley, R. J.; van der Zwaag, S. *Polym. Test.* **2008**, *27*, 11−19. (c) Varley, R. J.; van der Zwaag, S. *Acta Mater.* **2008**, *56*, 5737−5750.
(25) (a) Sanmartín Pensado, A.; Malfreyt, P.; Pádua, A. A. H. *J. Phys. Chem. B* **2009**, *113*, 14708−14718. (b) Triolo, A.; Russina, O.; Bleif, H. J.; Di Cola, E. *J. Phys. Chem. B* **2007**, *111*, 4641−4644.
(26) Canongia Lopes, J. N. A.; Pádua, A. A. H. *J. Phys. Chem. B* **2006**, *110*, 3330−3335.
(27) (a) Deetlefs, M.; Hardacre, C.; Nieuwenhuyzen, M.; Padua, A. A.; Sheppard, O.; Soper, A. K. *J. Phys. Chem. B* **2006**, *110*, 12055−12061. (b) Migowski, P.; Zanchet, D.; Machado, G.; Gelesky, M. A.; Teixeira, S. R.; Dupont, J. *Phys. Chem. Chem. Phys.* **2010**, *12*, 6826−6833. (c) Wang, Y.; Voth, G. A. *J. Am. Chem. Soc.* **2005**, *127*, 12192−12193.
(28) (a) Bodo, E.; Gontrani, L.; Caminiti, R.; Plechkova, N. V.; Seddon, K. R.; Triolo, A. *J. Phys. Chem. B* **2010**, *114*, 16398−16407. (b) Santos, C. S.; Murthy, N. S.; Baker, G. A.; Castner, J. E. W. *J. Chem. Phys.* **2011**, *134*, 121101.
(29) Triolo, A.; Russina, O.; Fazio, B.; Triolo, R.; Di Cola, E. *Chem. Phys. Lett.* **2008**, *457*, 362−365.
(30) Wilson, M.; Madden, P. A. *Phys. Rev. Lett.* **1994**, *72*, 3033.
(31) FitzGerald, P. A.; Chatjaroenporn, K.; Zhang, X. L.; Warr, G. G. *Langmuir* **2011**, *27*, 11852−11859.
(32) Dupont, J. *Acc. Chem. Res.* **2011**, DOI: 10.1021/ar2000937.
(33) Hoshino, K.; Yoshio, M.; Mukai, T.; Kishimoto, K.; Ohno, H.; Kato, T. *J. Polym. Sci., Polym. Chem.* **2003**, *41*, 3486−3492.
(34) Yoshio, M.; Kagata, T.; Hoshino, K.; Mukai, T.; Ohno, H.; Kato, T. *J. Am. Chem. Soc.* **2006**, *128*, 5570−5577.
(35) Kato, T.; Ichikawa, T.; Yoshio, M.; Hamasaki, A.; Kagimoto, J.; Ohno, H. *J. Am. Chem. Soc.* **2011**, *133*, 2163−2169.
(36) Garcia, I.; Carrasco, P. M.; de Luzuriaga, A. R.; Constantinou, M.; Georgopanos, P.; Rangou, S.; Avgeropoulos, A.; Zafeiropoulos, N. E.; Grande, H. J.; Cabanero, G.; Mecerreyes, D. *Macromolecules* **2011**, *44*, 4936−4941.
(37) Weber, R. L.; Ye, Y.; Schmitt, A. L.; Banik, S. M.; Elabd, Y. A.; Mahanthappa, M. K. *Macromolecules* **2011**, *44*, 5727−5735.
(38) Ohno, H.; Ito, K. *Chem. Lett.* **1998**, *27*, 751−752.
(39) Ding, S. J.; Tang, H. D.; Radosz, M.; Shen, Y. Q. *J. Polym. Sci., Polym. Chem.* **2004**, *42*, 5794−5801.
(40) Ganapatibhotla, L. V. N. R.; Zheng, J.; Roy, D.; Krishnan, S. *Chem. Mater.* **2010**, *22*, 6347−6360.
(41) Vijayakrishna, K.; Jewrajka, S. K.; Ruiz, A.; Marcilla, R.; Pomposo, J. A.; Mecerreyes, D.; Taton, D.; Gnanou, Y. *Macromolecules* **2008**, *41*, 6299−6308.
(42) He, X.; Yang, W.; Pei, X. *Macromolecules* **2008**, *41*, 4615−4621.
(43) Binder, W.; Zirbs, R. Supramolecular Polymers and Networks with Hydrogen Bonds in the Main- and Side-Chain. In *Hydrogen Bonded Polymers*; Binder, W., Ed.; Springer: Berlin, 2007; Vol. *207*, pp 1−78.
(44) Herbst, F.; Schultz, M.; Binder, W. H. *Nachr. Chem.* **2010**, *58*, 734−739.
(45) (a) Erdödi, G.; Iván, B. *Chem. Mater.* **2004**, *16*, 959−962. (b) Süvegh, K.; Domján, A.; Vankó, G.; Iván, B.; Vértes, A. *Macromolecules* **1998**, *31*, 7770−7775.
(46) Gragert, M.; Schunack, M.; Binder, W. H. *Macromol. Rapid Commun.* **2011**, *32*, 419−425.
(47) (a) Adekunle, O.; Herbst, F.; Hackethal, K.; Binder, W. H. *J. Polym. Sci., Polym. Chem.* **2011**, *49*, 2931−2940. (b) Breland, L. K.; Storey, R. F. *Polymer* **2008**, *49*, 1154−1163. (c) Kennedy, J. P.; Ivan, B. *Designed Polymers by Carbocationic Macromolecular Engineering: Theory and Practice*; Hanser Publishers: Munich, NY, 1992. (d) Kwon, Y.; Faust, R. Synthesis of Polyisobutylene-Based Block Copolymers with Precisely Controlled Architecture by Living Cationic Polymerization. In *New Synthetic Methods*; Springer: Berlin, 2004; Vol. *167*, pp 247−255. (e) Puskas, J. E.; Brister, L. B.; Michel, A. J.; Lanzendörfer, M. G.; Jamieson, D.; Pattern, W. G. *J. Polym. Sci., Polym. Chem.* **2000**, *38*, 444−452. (f) Puskas, J. E.; Chen, Y.; Tomkins, M. *Eur. Polym. J.* **2003**, *39*, 2147−2153.
(48) (a) Binder, W. H.; Kunz, M. J.; Kluger, C.; Hayn, G.; Saf, R. *Macromolecules* **2004**, *37*, 1749−1759. (b) Binder, W. H.; Petraru, L.; Roth, T.; Groh, P. W.; Pálfi, V.; Keki, S.; Ivan, B. *Adv. Funct. Mater.* **2007**, *17*, 1317−1326.
(49) Tang, H. D.; Tang, J. B.; Ding, S. J.; Radosz, M.; Shen, Y. Q. *J. Polym. Sci., Polym. Chem.* **2005**, *43*, 1432−1443.
(50) Mori, H.; Yahagi, M.; Endo, T. *Macromolecules* **2009**, *42*, 8082−8092.
(51) Vygodskii, Y. S.; Shaplov, A. S.; Lozinskaya, E. I.; Lyssenko, K. A.; Golovanov, D. G.; Malyshkina, I. A.; Gavrilova, N. D.; Buchmeiser, M. R. *Macromol. Chem. Phys.* **2008**, *209*, 40−51.
(52) (a) Burns, C. T.; Lee, S.; Seifert, S.; Firestone, M. A. *Polym. Adv. Technol.* **2008**, *19*, 1369−1382. (b) Lee, S.; Becht, G. A.; Lee, B.; Burns, C. T.; Firestone, M. A. *Adv. Funct. Mater.* **2010**, *20*, 2063−2070.
(53) (a) Iván, B.; Kennedy, J. P. *J. Polym. Sci., Polym. Chem.* **1990**, *28*, 89−104. (b) Iván, B.; Kennedy, J. P.; Chang, V. S. C. *J. Polym. Sci., Polym. Chem.* **1980**, *18*, 3177−3191.
(54) (a) Del Sesto, R. E.; McCleskey, T. M.; Macomber, C.; Ott, K. C.; Koppisch, A. T.; Baker, G. A.; Burrell, A. K. *Thermochim. Acta* **2009**, *491*, 118−120. (b) Livi, S.; Duchet-Rumeau, J.; Pham, T. N.; Gérard, J.-F. *J. Colloid Interface Sci.* **2011**, *354*, 555−562. (c) Poole, C. F.; Poole, S. K. *J. Sep. Sci.* **2011**, *34*, 888−900.
(55) Eisenberg, A. *Macromolecules* **1971**, *4*, 125.
(56) Eisenberg, A.; Hird, B.; Moore, R. B. *Macromolecules* **1990**, *23*, 4098−4107.
(57) (a) Fang, Z.; Kennedy, J. P. *J. Polym. Sci., Polym. Chem.* **2002**, *40*, 3662−3678. (b) Fang, Z.; Kennedy, J. P. *J. Polym. Sci., Polym. Chem.* **2002**, *40*, 3679−3691. (c) Fang, Z.; Wang, S.; Wang, S. Q.; Kennedy, J. P. *J. Appl. Polym. Sci.* **2003**, *88*, 1516−1525. (d) Moore, R. B.; Bittencourt, D.; Gauthier, M.; Williams, C. E.; Eisenberg, A. *Macromolecules* **1991**, *24*, 1376−1382.
(58) Han, C. D.; Vaidya, N. Y.; Kim, D.; Shin, G.; Yamaguchi, D.; Hashimoto, T. *Macromolecules* **2000**, *33*, 3767−3780.
(59) van Ruymbeke, E.; Vlassopoulos, D.; Mierzwa, M.; Pakula, T.; Charalabidis, D.; Pitsikalis, M.; Hadjichristidis, N. *Macromolecules* **2010**, *43*, 4401−4411.
(60) Schädler, V.; Kniese, V.; Thurn-Albrecht, T.; Wiesner, U.; Spiess, H. W. *Macromolecules* **1998**, *31*, 4828−4837.
(61) Antonietti, M.; Pakula, T.; Bremser, W. *Macromolecules* **1995**, *28*, 4227−4233.
(62) Aida, T.; Fukushima, T.; Kosaka, A.; Ishimura, Y.; Yamamoto, T.; Takigawa, T.; Ishii, N. *Science* **2003**, *300*, 2072−2074.

(63) (a) Hamley, I. W.; Koppi, K. A.; Rosedale, J. H.; Bates, F. S. *Macromolecules* **1993**, *26*, 5959−5970. (b) Winey, K. I.; Patel, S. S.; Larson, R. G. *Macromolecules* **1993**, *26*, 2542−2549. (c) Hamley, I. W. *J. Phys.: Condens. Matter* **2001**, *13*, R643−R671.

Macromolecules

Article

pubs.acs.org/Macromolecules

Effective Value of the Dynamic Dilution Exponent in Bidisperse Linear Polymers: From 1 to 4/3

E. van Ruymbeke,*[,†,‡] Y. Masubuchi,[§] and H. Watanabe[§]

[†]Bio and Soft Matter, Institute on Condensed Matter and Nano-science, Université Catholique de Louvain, Louvain-la-Neuve, Belgium

[‡]Institute of Electronic Structure & Laser, FORTH, Heraklion, Crete, Greece

[§]Institute for Chemical Research, Kyoto University, Gokasyo, Uji, Kyoto 611-0011, Japan

Supporting Information

ABSTRACT: We revisit previously published dielectric and viscoelastic data of binary blends of linear *cis*-polyisoprene [Watanabe, H.; Ishida, S.; Matsumiya, Y.; Inoue, T. *Macromolecules* **2004**, *37*, 6619] in order to test the validity of the dynamic tube dilution (DTD) picture and to determine the most appropriate value of the dilution exponent α. We conclude that the DTD picture with $\alpha = 1$ is more appropriate at short times, while at longer time, a larger exponent of $\alpha = 4/3$ gives a better description of the experiments. Furthermore, between these two time regions, a broad crossover zone is found, going from an effective $\alpha = 1$ to an effective $\alpha = 4/3$. On the basis of this result, we propose to consider a new relaxation process, which is combined with the classical DTD picture with $\alpha = 1$ to give the experimentally observed effective $\alpha = 4/3$ at long times. This extra relaxation process results from the tension equilibration along the long chains, which takes place thanks to the blinking feature of release/reformation of the long−short entanglements and leads to a partial disorientation of the primitive path itself within the dilated tube. We have formulated the relaxation function considering this tension equilibration and demonstrated its validity for description of the experiments in the entire range of time.

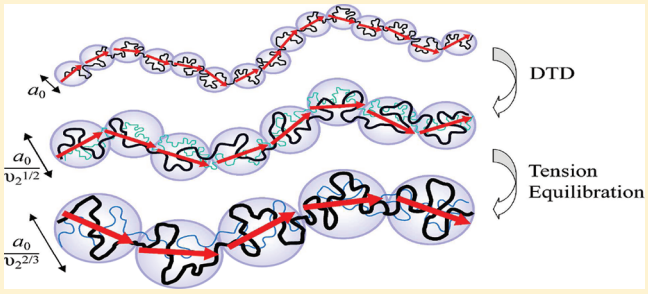

1. INTRODUCTION

Tube-based models represent a powerful tool for describing the dynamics of linear polymer melts.[1−5] Introduced by de Gennes[1] and Doi and Edwards,[2] the initial concept, which mainly takes into account reptation and contour length fluctuation (CLF) mechanisms, has been more and more refined in order to include the influence of the molecular environment on the relaxation of the focused chain. Therefore, concepts such as "double reptation",[6,7] "constraint release" (CR), "dynamic tube dilution" (DTD),[8] or "constraint release Rouse motion" (CRR)[9,10] were proposed in order to allow the long, unrelaxed chains to take advantage of the fast relaxation of the short chains and relax faster than in their monodisperse environment. Based on the DTD picture, which was first proposed by Marrucci[8] for describing the relaxation of linear polymers and later extended to branched polymers by Ball and McLeish,[11] tube models have been considerably improved, reaching nearly quantitative agreement with the experimental viscoelastic data for a large variety of model polymers.[4,12−16] According to the DTD picture, once a fraction of the polymer is relaxed, its diluting effect is taken into account by considering that the remaining chains are moving in an effectively dilated tube. The relaxation function of an entangled polymer, which is described—according to the tube picture—by the factorization of the survival fraction of the initial tube and of its constraint release term, is therefore, expressed as[8]

$$\mu(t) \equiv \frac{G(t)}{G_N^0} = (\varphi'(t))^{1+\alpha} \tag{1}$$

where G_N^0 is the plateau modulus, $\varphi'(t)$ is the survival fraction of the initial tube (defined with respect to a dilated diameter at time t), and α is the dilution exponent.

By now, despite many attempts, there is no consensus about the exact value of the dilution exponent α.[17] Varying between 1 and 4/3, its value depends on the model which is used as well as the architecture of the samples analyzed.[14,17−19] Many experimental studies have shown that α is close 4/3 (a value in solutions).[20−22] The same conclusion was drawn by Colby and Rubinstein,[23] by considering that an entanglement is created from a fixed number of binary contacts between the chains, and by determining the scaling of the diameter of the "blob" needed in order to contain this fixed number of contacts, knowing that the density of contacts varies with the square of the concentration: if there is one entanglement in a "blob" of volume a_0^3 in the melt state, dilution to a polymeric concentration of υ_2 gives

Received: September 26, 2011
Revised: January 17, 2012
Published: February 3, 2012

v_2^2 entanglements per "blob" of volume a_0^3 or, equivalently, one entanglement per a larger "blob" of size a^3. From this statement, one can indeed conclude that a is proportional to $1/v_2^{2/3}$ and thus $\alpha = 4/3$ *in a fully equilibrated state.* Milner extended this picture proposed for polymer solutions, to polymer melts,[24] linking the work of Lin and Noolandi[25] to the work of Colby and Rubinstein.[26]

However, by confronting predictions based on tube theory and experimental viscoelastic data of different polymer melts, several papers reported better agreement for $\alpha = 1$ rather than for $\alpha = 4/3$.[14,15,18] On the other hand, when looking at the level of the low-frequency second plateau of the storage modulus of complex architectures, which relax the stress hierarchically with the outer generation of branches expected to behave as a solvent for the relaxation of the inner generation, no clear conclusion could be derived, the data being scattered between the φ'^2 and $\varphi'^{7/3}$ dependence.[16,21,22,27,28] These results show the difficulty in discriminating the dilution exponents of $\alpha = 1$ and $\alpha = 4/3$ experimentally.

In order to investigate this issue for polymer melts, binary blends of linear chains are the ideal system; the short chains therein act as a solvent for the long chains in long time scales. Several studies have already been conducted in this direction. In particular, Watanabe et al. have demonstrated that $\alpha = 1.3$ ($\cong 4/3$) must be used in order to correctly match the reduced moduli $v_2^{-(\alpha+1)}G'$ and $v_2^{-(\alpha+1)}G''$ (v_2 being the volume fraction of the long chains) of binary blends having well-separated component molecular weights with the solution data at low frequencies.[22,27] Furthermore, for most of the blends, they showed that a full-DTD picture with $\alpha = 1.3$ overestimates the dilution effect at intermediate times. A model based on a partial-DTD picture explicitly incorporating the CRR process was proposed in order to correctly describe the experimental data.[22] However, while the set of data for the PI blends obtained in that work indicates that the experimentally determined α for those blends must be close to 4/3, Park and Larson found a better agreement between the same set of data and their tube-based predictions based on $\alpha = 1$[18] as well as for other sets of data for a variety of binary blends of linear chains. Facing this difficulty of fixing the value of α for bidisperse samples, slip-link simulations (NAPLES) on binary linear blends have been performed[29,30] to show that the terminal relaxation modulus of binary blends scales as $v_2^{7/3}$, even though the relationship $a = a_0/v_2^{1/2}$ (i.e., $\alpha = 1$) was intrinsically utilized in the simulation. This result, which starts with the basic assumption of the binary nature of the entanglement (and thus utilizes $\alpha = 1$),[8] shows once more the difficulty to define a unified picture for explaining the CR effect in polymer melts.

The objective of this paper is to revisit the experimental data presented in refs 22 and 27, starting from another point of view: rather than considering a partial-DTD picture and utilizing $\alpha = 4/3$, we start with the full-DTD picture combined with $\alpha = 1$. Furthermore, in order to account for the dilution effect of the short chains more significant than for the case of $\alpha = 1$, we introduce a new relaxation process, which allows the polymer blend to behave *as if* the dilution exponent in the full-DTD picture were larger than 1. This leads us to define an effective value of α, which corresponds to the value determined from the level of the low-frequency plateau of the storage modulus. This effective value can vary between 1 and 4/3 with time, while its real theoretical value is fixed at 1 (which corresponds to the binary nature of the entanglement). In other words, the effective α value in the blends can exhibit a crossover from $\alpha = 1$ at short times, where the long chains have not fully equilibrated their conformations after the relaxation of the short chains (and thus just the binary nature determines α), to $\alpha = 4/3$ at long times where this equilibration is completed, and the situation considered by Colby and Rubinstein is recovered.

This crossover of the α value does not seem to be properly addressed in the available theories (although a semiempirical approach of partial-DTD results in this crossover[22]). One of the aims of this paper is the explicit formulation of this crossover behavior. The formulation requires us to specify the unrelaxed fraction (survival fraction) of the dilated tube, $\varphi'(t)$ (cf. eq 1), but the time evolution of $\varphi'(t)$ is determined by coupling of the reptation, CLF, and CR mechanisms. In this work, we adopted an approach utilizing experimental data, rather than to challenge full specification of this coupling. As proposed in refs 27, 31, and 32, in order to only focus on the global effect of the DTD picture, we use the data of the dielectric relaxation function for determining $\varphi'(t)$. This approach allows us to skip detailed analysis for the influence of dilution on the reptation and contour length fluctuation processes and, therefore, to extract the clearest information about the α exponent.

This paper is organized as follows: In section 2, after a short presentation of the samples and experimental techniques used in this work, we present the DTD picture and confront the predictions of this picture with $\alpha = 1$ and/or $\alpha = 4/3$ to experimental viscoelastic data. In section 3, we mathematically formulate a previously discussed relaxation mechanism[33] in order to explain the experimental results, coming from the CR-activated tension equilibration along the chains, which takes place as soon as the chains start moving in their dilated tube. Conclusions are summarized in section 4.

2. TEST OF THE DTD MOLECULAR PICTURE ON BINARY BLENDS OF LINEAR CHAINS

2.1. Experimental Section. The samples used in this work are previously synthesized/characterized linear *cis*-polyisoprene (PI) samples.[22,27,34,35] Their molecular characteristics are summarized in Table 1, with the sample code number indicating their molar mass in kg/mol. The systems subjected to viscoelastic and dielectric measurements are blends of high-M and low-M PI samples (L308 + L94, and L308 + L21) having various values of the L308 volume fraction v_2. As detailed in refs 22 and 27, the blends were prepared by dissolving prescribed masses of L308 and L94 in benzene at 5 wt % and then allowing benzene to thoroughly evaporate. Dynamic viscoelastic measurements were conducted at several temperatures between −20 and 80 °C with a laboratory rheometer (ARES; Rheometrics), using parallel plate fixture of a diameter of 25 mm, while dielectric measurements were conducted for the blends charged in a guarded parallel-plate dielectric cell with a transformer bridge (1620A, QuadTech) and a homemade absorption current circuit, at temperatures between 10 and 80 °C.[35] The time−temperature superposition held excellently for both viscoelastic and dielectric data.[22,27]

Table 1. Characteristics of Linear PI Samples

code	$10^{-3}M_w$	M_w/M_n
L308	308	1.08
L94	94.0	1.05
L21	21.4	1.04

2.2. Full-DTD Molecular Picture. The full-DTD molecular picture considers that the relaxed portion of polymer acts as a solvent for the polymer relaxation at a certain time t (in the entanglement relaxation zone).[8]

An illustration of the full-DTD picture is shown in Figure 1 (considering $\alpha = 1$), for a long chain in a binary blend

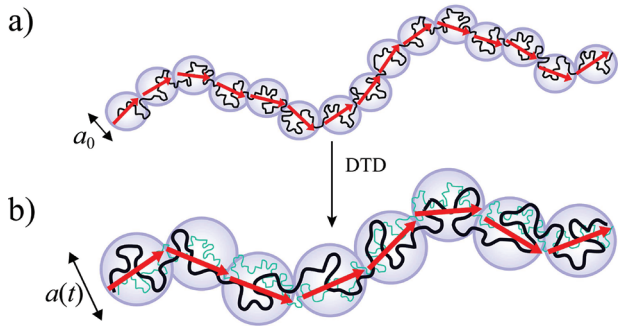

Figure 1. Full-DTD picture applied to a long chain in a bidisperse blend of short and long chains. (a) A long chain in its initial tube, before the short chain relaxation (i.e., at $t < \tau_{rel,1}$). (b) A long chain in its effective tube dilated due to the relaxed short chains (at $\tau_{rel,1} < t < \tau_{rept,2}$). In the specific case illustrated here, the volume fraction of long chains is $\upsilon_2 = 1/3$.

composed of well-entangled short and long chains. As shown in Figure 1a, at times t shorter than the relaxation time $\tau_{rel,1}$ of the short chains (component 1), all entanglements play an active role in the confinement of the long chain (component 2) in its tube. ($\tau_{rel,1}$ is essentially determined by reptation and CLF of the short chain, with the CR mechanism for this chain being suppressed by the long chain.) The monomers between two entanglements are coarse-grained into an "entanglement segment" (circles in Figure 1a) of a diameter a_0, and this diameter corresponds to a length scale that the monomers can explore before the entanglement relaxation occurs. The primitive path of the long chain, represented by the arrows, has an equilibrated average length of $L_{eq,0} = Z_0 a_0$, with Z_0 being the number of initial entanglement segments along the chain.[2]

At a time longer than the relaxation time of the short chains but shorter than the reptation time of the long chains ($\tau_{rel,1} < t < \tau_{rept,2}$), the short chains can move and therefore do not confine the long chain anymore in its initial tube (see Figure 1b). Consequently, the short chains are acting as a solvent for the long chain, and all entanglements involving the short chains must be ignored. This process is taken into account in tube models by considering that the chains are moving in a dilated tube characterized by an effective tube diameter, $a(t)$, which accounts for this dynamic tube dilation (DTD). To this effective tube diameter, correspond an effective molecular weight between two entanglements, $M_e(t)$, and an effective equilibrium length, $L_{eq}(t)$. As described by Marrucci,[8] these effective values are defined in relation to their initial values, a_0, $M_{e,0}$, and $L_{eq,0}$, as

$$a(t) = a_0(\varphi'(t))^{-\alpha/2} \tag{2}$$

$$L_{eq}(t) = L_{eq,0}(\varphi'(t))^{\alpha/2} \tag{3}$$

$$M_e(t) = M_{e0}(\varphi'(t))^{-\alpha} \tag{4}$$

In the specific case of binary blends of linear chains just after the relaxation of the short chains, the survival fraction of the dilated tube, $\varphi'(t)$, is (approximately) equal to the volume fraction of the long chains, υ_2, and each long−long entanglement segment is considered to behave as a relaxed Gaussian subchain. With this picture, the orientation of the whole primitive path stays strongly correlated with its initial orientation (see Figure 1b).

With the aid of the rescaled $M_e(t)$ given by eq 4, the effective plateau modulus during the DTD process is expressed as $\rho RT/M_e(t)$. Since a fraction $\varphi'(t)$ of the dilated entanglement segments (with the molecular weight $M_e(t)$) preserves the initial orientational anisotropy, $G(t)$ is given by $\varphi'(t)\rho RT/M_e(t) = G_N^0(\varphi'(t))^{1+\alpha}$ (cf. eq 4). Therefore, eq 1 is obtained.[8]

2.3. Localized Constraint Release Rouse (CRR) between Long−Long Entanglements. Despite its simple and clear physics, the above molecular picture of full-DTD has some limitations when confronted to experimental results. In particular, several studies revealed that the full-DTD picture fails for binary blends of linear chains[9,18,22,36] in the time zone just after the relaxation of the short chains. Indeed, the full-DTD picture assumes that long chains immediately explore all local conformations within the dilated tube, taking advantage of the short chain motion. However, this transition from the thin to dilated tube takes a certain time, which is not taken into account in the full-DTD picture.

Several different ways have been proposed in order to correct this issue. The simplest but reasonable solution is to consider a fact that the tube cannot dilate faster than described by the constraint release Rouse (CRR) mechanism. Most of the current tube-based models—see, for example, refs 10 (eq 12), 13 (eq 23), 18b (eq 10), or 43—incorporate this CRR-limited dilation of the tube and assume that the CRR motion in bidisperse blends is *localized between successive long−long entanglements* (not occurring along the whole backbone of the long chain). This extra condition can be cast in a condition specifying the effective tube diameter $a(t)$ at a time t:[10,15,18]

$$a(t) = a_0\{\phi(t)\}^{-\alpha/2} \tag{5a}$$

with

$$\phi(t) = \max\left\{\varphi'(t),\ \phi(t')\left[\frac{t'}{t}\right]^{1/2\alpha}\right\} \tag{5b}$$

In eq 5a, $\phi(t)$ is an effective fraction of the initial constraints that survive at time t: This $\phi(t)$ is defined a way that the number of entanglement segments in an effectively dilated segment at time t is expressed as $\{\phi(t)\}^{-\alpha}$.

In eq 5b, t' represents an (almost) arbitrarily chosen time prior to t, as explained below in more detail. *If* the CRR mechanism dominates the relaxation at all times $t' < t$, eq 5b analytically gives $\phi(t) = \phi(t')[t'/t]^{1/2\alpha}$ (which coincides with the Rouse function (cf. Appendix A) for the case of $\alpha = 1$, the theoretical value concluded in this study). Correspondingly, *irrespective of the* α *value*, the normalized viscoelastic relaxation function of the long chain, $\mu_2(t)$, is expressed in the Rouse form, $\mu_2(t) = \mu_2(t')[t'/t]^{1/2} \propto t^{-1/2}$ (see Appendix B1). However, if the actual survival fraction of the dilated tube, $\varphi'(t)$, is larger than $\phi(t')[t'/t]^{1/2\alpha}$, this CRR dominance vanishes and $\phi(t)$ does not decay to $\phi(t')[t'/t]^{1/2\alpha}$ but only to $\varphi'(t)$. Thus, ϕ at time t is determined by ϕ and φ' at the past times t'. Equation 5b specifies this condition in a form similar to the recurrence formula.

Here, we fully specify the arbitrariness of t' mentioned above. First of all, the survival fractions satisfy the initial condition,

dx.doi.org/10.1021/ma202167q | *Macromolecules* 2012, 45, 2085−2098

$\phi(\tau_e) = \varphi'(\tau_e) = 1$ (not $\phi(0) = \varphi'(0) = 1$), where τ_e is the relaxation time within the entanglement segment that serves as the *shortest unit time* for the entanglement relaxation. Thus, for a given t ($>\tau_e$), t' should be in a range between τ_e and $t - \tau_e$, and eq 5b should hold for t' *arbitrarily chosen in this range*. Consequently, eq 5b can be rewritten as an equation considering the minimum possible difference, $t - t' = \tau_e$:[37]

$$\phi(t) = \max\left\{\varphi'(t),\ \phi(t-\tau_e)\left[\frac{t-\tau_e}{t}\right]^{1/2\alpha}\right\}$$
$$\text{with } \phi(\tau_e) = \varphi'(\tau_e) = 1 \tag{5c}$$

(Note that eq 5b is automatically deduced if eq 5c is satisfied.)

As explained above, the time evolution of $\phi(t)$ is determined not only by $\phi(t)$ but also by the actual survival fraction of the dilated tube $\varphi'(t)$ defined earlier. In the full theoretical approach, we need to have the time evolution equation for $\varphi'(t)$ in addition to eq 5c to calculate $a(t)$ (cf. eq 5a). However, in the approach in this paper, we utilize the dielectric data to evaluate $\varphi'(t)$. The $\varphi'(t)$ thus obtained[22,27] was utilized in eq 5c, so that we were able to calculate $\phi(t)$ with no ambiguity.[37] An example of this unambiguous recurrence calculation of $\phi(t)$ on the basis of eq 5c is shown in Appendix B1. (The time step of this recurrence calculation was (and is to be) taken to be the unit time for the entanglement relaxation, τ_e. However, the calculation with a smaller time step gave the same result.)

For bidisperse blends, the function $\phi(t)$ is equal to $\varphi'(t)$ at short and long times (cf. Appendix B1). However, at intermediate times after the short chain relaxation, a subchain between successive long−long entanglements needs a time to explore all local conformations within the dilated tube. Therefore, the subchain exhibits the constraint release Rouse (CRR) motion in a supertube,[25] and the corresponding $\phi(t)$ should scale as $1/\sqrt{t}$ as long as $\phi(t)$ stays larger than the $\varphi'(t)$. This CRR feature at intermediate times is well described by eq 5c with $\alpha = 1$ (theoretical value concluded in this study) (cf. Appendix B1). In order to account for this extra condition in the determination of the viscoelastic relaxation function $\mu(t)$, we replace eq 1 by

$$\mu(t) \equiv \frac{G(t)}{G_N^0} = \varphi'(t)\left(\frac{a(t)}{a_0}\right)^{-2} \tag{6}$$

($a(t)$ is related to $\phi(t)$ and $\varphi'(t)$ through eqs 5a and 5c.) The CRR condition for the DTD relaxation of $\mu(t)$, eq 6 combined with eqs 5a and 5c, is especially important when a large proportion of chains relaxes at the same time, leading to a sudden decrease of the tube survival fraction $\varphi'(t)$, as in the case of bidisperse blends.[3,19] If this CRR condition is not active (i.e., if $a(t)$ is always given by $a_0(\varphi'(t))^{-\alpha/2}$), eqs 1 and 6 are equivalent to each other.

We should note that the CRR condition introduced above does not depend on the molecular weight of the chain of our focus, contrary to the much stronger CRR condition proposed in the molecular picture of partial-DTD.[22] Indeed, eqs 5a and 5c result in the localized Rouse-type CR relaxation of the entanglement segments just between successive long−long entanglements, not the global CR relaxation that occurs throughout the whole chain backbone in this dilated tube.[9]

This localization of CRR can be most easily realized if we focus on a plateau zone of $\phi(t)$ where the long−short entanglements have fully relaxed but the long−long entanglements remain unrelaxed. (This zone emerges when the short and long chains have widely separated molecular weights.) In the plateau zone, $\phi(t)$ is equal to the volume fraction of the long chain, v_2. The CRR relaxation of $\phi(t)$ starts at $t \sim \tau_{rel,1}$ (relaxation time of the short chains), and thus $\phi(t)$ in the CRR zone can be expressed as $\phi(t) = \phi(\tau_{rel,1})\{\tau_{rel,1}/t\}^{1/2\alpha}$ for $t \geq \tau_{rel,1}$ (cf. Appendix B1). This CRR relaxation is completed when $\phi(t)$ decreases to its plateau value, v_2, and a characteristic time for this completion is expressed as $\tau^* = \{\phi(\tau_{rel,1})\}^{2\alpha}\tau_{rel,1}\{v_2\}^{-2\alpha}$. The factor $\{\phi(\tau_{rel,1})\}^{2\alpha}\tau_{rel,1}$ in this expression can be regarded as the local CR hopping time, so that the factor $\{v_2\}^{-\alpha}$ is equivalent to the maximum number of entanglement segments involved in the CRR relaxation considered here. This number, $\{v_2\}^{-\alpha}$, is equal to the number of the entanglement segments per fully dilated segment of the size $a = a_0\{v_2\}^{-\alpha/2}$ (cf. eq 5a). Thus, the CRR relaxation formulated by eqs 5a, 5c, and 6 is localized between the long−long entanglements. In this respect, the CRR-DTD picture explained above differs from the partial-DTD picture, the latter considering the global equilibration of all long−short entanglements instead of the localized equilibration between the long−long entanglements.

2.4. Reptation and Contour Length Fluctuations Times. As noted from the $(a(t)/a_0)^{-2}$ factor in eq 6, DTD itself results in a decrease of the viscoelastic relaxation function $\mu(t)$. In addition to this effect, DTD can hasten the reptation process of the chains along the axis of the dilated tube.[8] Most of the tube models proposed in the literature take this effect into account.[13−16] However, several pieces of work in the literature have shown that considering reptation in a thin or in a dilated tube is not a trivial question, depending on the Struglinsky−Graessley parameter.[3,9,18,19] In the present work, in order to avoid any approximation related to the description of these processes, the disorientation of the chains by reptation or contour length fluctuations is experimentally determined from the dielectric relaxation function of the blends, following ref 22. Indeed, while a dielectric relaxation of PI chain having the type A dipoles parallel along its backbone is induced by fluctuations of the end-to-end vector, no dielectric relaxation is activated by the DTD mechanism itself, except a minor contribution from the chain motion at the dilated tube edge.[35] Therefore, from data of the dielectric relaxation function (of PI), the corresponding survival fraction of the initial tube, $\varphi'(t)$, is easily determined without any detailed dynamic model, by simply accounting for this tube edge fluctuation effect.

2.5. Test of Molecular Picture of Localized CRR-DTD for Binary Blends of Linear *cis*-PI. The molecular picture of localized CRR-DTD explained in the previous section is first tested for bidisperse linear samples with short L21 and long L308 chains of well-separated molecular weights (see Table 1). To do so, the viscoelastic relaxation function $\mu(t)$ determined from the dilated tube survival fraction $\varphi'(t)$ (evaluated from the dielectric data) with the aid of eqs 5 and 6 is confronted to the experimental viscoelastic relaxation function, while considering the value for the dilution exponent α equals to 1 or 4/3. Results are presented in Figure 2 for two different volume fractions of long chains, $v_2 = 0.1$ and 0.5.

While the viscoelastic relaxation function $\mu(t)$ predicted for $\alpha = 1$ correctly captures the experimental behavior at short times, it is not appropriate to describe the relaxation at longer times. On the contrary, while the dilution exponent $\alpha = 4/3$ correctly describes $\mu(t)$ at short and long times, it underestimates $\mu(t)$ at intermediate times. Furthermore, the smooth decrease observed in the experimental $\mu(t)$ between $t = 10^{-2}$ s and $t = 10^{-1}$ s (Figure 2a) is reproduced by *neither* $\alpha = 1$ *nor* $\alpha = 4/3$ and cannot be explained from polydispersity argument (see Table 1). Note that, in both cases, the local CRR limitation (see eq 5) is taken into account. This extra condition combined

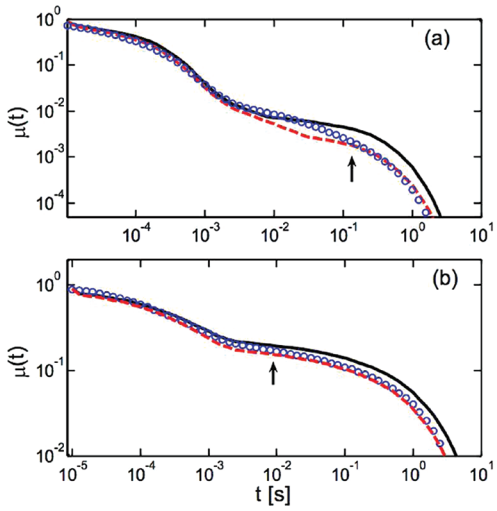

Figure 2. Viscoelastic relaxation function: experimental (○) versus predicted $\mu(t)$ (curves). Predictions are obtained from eqs 5 and 6 with $\alpha = 1$ (black —) or 4/3 (red - - -) for two different blends: (a) 10% L308−90% L21 and (b) 50% L308−50% L21. Arrows indicate the end of the crossover from $\alpha = 1$ to $\alpha = 4/3$.

with $\alpha = 4/3$ is thus not enough to describe the observed relaxation behavior of the long chains, in particular in bidisperse blends with small υ_2. (A reviewer for this paper was skeptical about the failure of the molecular picture of localized CRR-DTD explained above. However, this failure was unequivocally confirmed on the basis of the data of the CRR time for dilute long chains entangled only with the short chains that were combined with rigorous Rouse model (with the minimum model assumption), as explained in the Supporting Information.)

These first comparisons suggest that there is a slow crossover (transition) from $\alpha = 1$ to $\alpha = 4/3$. Since this crossover takes place after the relaxation of the short chains, it is unequivocally due to a reorganization of the long chains. Furthermore, since the crossover is seen at times between the terminal relaxation times of the short and long chains, its importance should depend on how widely separated these relaxation times are. This is indeed verified in Figure 3, which compares the predicted and

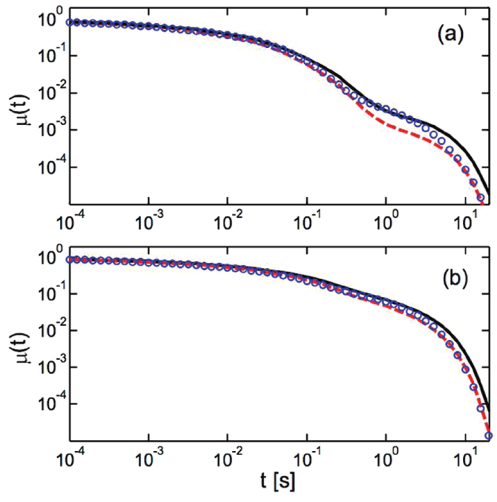

Figure 3. Viscoelastic relaxation function: experimental (○) versus predicted $\mu(t)$ (curves). Predictions are obtained from eqs 5 and 6 with $\alpha = 1$ (black —) or 4/3 (red - - -) for two different blends: (a) 10% L308−90% L94 and (b) 50% L308−50% L94.

experimental viscoelastic functions for the binary blends containing higher-M short chains L94 (see Table 1): predictions obtained with a dilution exponent $\alpha = 1$ are in good agreement in a wider range of time, and the crossover of the effective α value prevails at longer times. The importance of the crossover also depends on the volume fraction of long chains, as can be clearly noted from comparison of Figure 2a,b.

3. CR-ACTIVATED TENSION EQUILIBRATION

3.1. Tension Imbalance and Equilibration in Asymmetric Systems. In order to explain the crossover between the viscoelastic behavior described by the classical DTD picture with $\alpha = 1$ and with $\alpha = 4/3$, we revisit a relaxation process previously considered by Watanabe et al.,[33] called CR-activated tension balance or tension equilibration, and formulate this process quantitatively (which was not done previously). This mechanism works once the short chains have relaxed, i.e., when all entanglements involving the short chains become ineffective for confining the long chain in its tube. At that moment (see Figure 1b), a sequence of the segments of the long chain between successive long−long entanglements has a length of $a_2 = a_0\upsilon_2^{-1/2}$ on average and behaves as a Gaussian subchain. Correspondingly, the viscoelastic relaxation function $\mu(t)$ is equal to $G(t) = G_N^0\upsilon_2^2$. We thus start from the assumption of the tube models, according to which entanglements are binary events and *α must be equal to 1*.

By imposing $\alpha = 1$, a relaxation modulus $G(t)$ smaller than $G_N^0\upsilon_2^2$ can therefore be obtained only if some initial long−long entanglements are lost. This loss of long−long entanglements, which does not require the reptation or fluctuations of the long chains, is explained here by the conformation adjustment of the long chain in their dilated tube. A key point of this relaxation process is the blinking (loose-and-grip) feature of release/reformation of the long−short entanglements. As explained below, this local CR blinking allows the *whole backbone* of the long chain to move within the dilated tube, which leads to a partial disorientation (i.e., partial relaxation) of the primitive path at time t and reduces its correlation with the primitive path at time 0. In other words, the local CR blinking results in the global CRR relaxation, which is quite different from the localized CRR-DTD mechanism (eqs 5 and 6) discussed in the previous section.

For clear understanding of this process, we start with the long chain being fixed at its ends and entangled with the other end-fixed long chain as well as the free matrix chains and then switch to the system of our main interest, the blend of long and short chains having no fixed ends. For convenience of this understanding, the conformational changes of the long chain (with/without the fixed ends) activated by the local CR process are illustrated in Figure 4.

3.1.1. Tension Equilibration for Network Strand. Here, we consider an end-fixed long chain entangled with the other end-fixed long chains as well as the free matrix chains. These long chains are equivalent to strands of a cross-linked network exhibiting no fluctuation of the cross-linking points. Before relaxation of the matrix chains, a given strand is constrained by the matrix chains as well as the other strands to be effectively confined in a skinny tube, as illustrated in Figure 4a. On the release of a strand-matrix entanglement due to the matrix chain motion, the strand begins to explore, through its intrinsic Rouse dynamics, a conformation that is local but still goes beyond the skinny tube (see the change from Figure 4a to Figure 4b). After some waiting time, the strand-matrix entanglement is reformed isotropically (see Figure 4c). This isotropic reformation itself does not directly change the stress of the strand (because the

dx.doi.org/10.1021/ma202167q | Macromolecules 2012, 45, 2085−2098

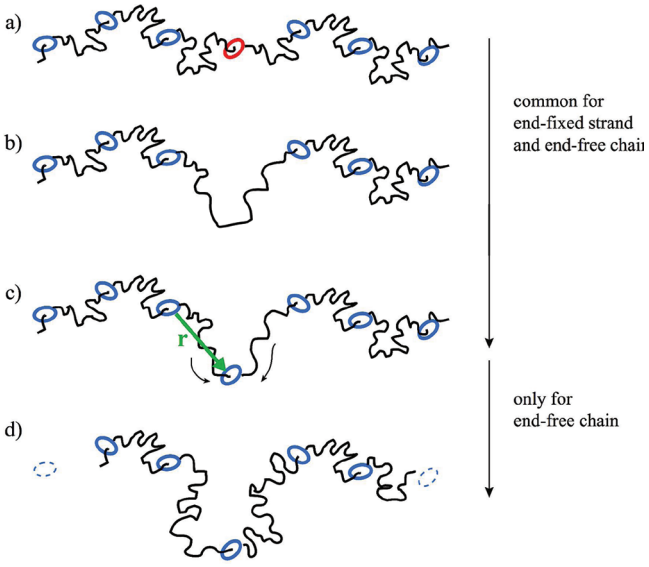

Figure 4. Illustration of the tension equilibration process along a long chain. (a) A long chain (or strand) constrained by the other long chains and short (matrix) chains. (b) The long chain starts exploring its dilated tube on local CR due to the short chain motion. (c) A long−short (strand-matrix) entanglement is transiently reformed isotropically, which leads to tension imbalance along the long chain, thereby activating the tension equilibration through the monomer transfer (sucking-in of monomers for the illustration here). (d) For end-free long chain, the tension equilibration results in some loss of initial long−long entanglements.

stress reflects the anisotropy of the strand orientation) but constrains the chain conformation thereby influencing the stress indirectly: The strand-matrix entanglement should be reformed in a way that the end-to-end vector **r** for the resulting entanglement segment shown in Figure 4c has a Gaussian distribution having the average $\langle \mathbf{r}^2 \rangle^{1/2}$ identical to the skinny tube diameter, a_0. This does not mean that $|\mathbf{r}|$ is always equal to a_0. Instead, $|\mathbf{r}|$ is different from a_0 for most cases, as can be easily noted for the Gaussian distribution. The configuration shown in Figure 4c depicts the case of $|\mathbf{r}| > a_0$. For this case, the tension is higher in the reformed entanglement segment than in the neighboring entanglement segments so that the former segment should suck in the monomers, through its intrinsic longitudinal Rouse mode, from the latter to balance the tension. (In the other case of $|\mathbf{r}| < a_0$ not shown here, the reformed entanglement segment transfers its monomers to the neighboring entanglement segments.) The conformational changes from Figure 4a to 4c are repeated *with a tempo of strand-matrix entanglement release, i.e., with the local CR time,* τ_{CR}*. Thus, a local event, the release/reformation of the stand-matrix entanglement, activates the tension equilibration and the conformational adjustment/stress decay of the whole strand with the tempo of τ_{CR}*. (τ_{CR}* is essentially proportional to the relaxation time of the matrix chain.)

The corresponding longest relaxation time of the strand, τ_{strand}, is expected to be given by $\tau_{CR}{}^* N'^2$ (as considered also in the partial-DTD picture[22]), with N' being the equilibrium number of the strand-matrix entanglements for the whole strand. (Note that the tension equilibration completes through accumulation of the local CR processes occurring at N' strand-matrix entanglements, and thus τ_{strand} is proportional to N'^2.) This expectation can be confirmed from the slip-link simulation (NAPLES) widely applied to entangled polymers. Details of this simulation have been described elsewhere,[29,30] and a summary is given in Appendix C. We made the simulation for the simplest model cases: (1) an end-fixed strand forming no strand−strand entanglement but Z_0 entanglements with the free matrix chains and (2) an end-fixed strand forming one permanent entanglement with the other strand and $Z_0 - 1$ entanglements with the free matrix chains. Each matrix chain also has Z_0 entanglements (either with the other matrix chains or with the strand). Details of this simulation are explained in Appendix C, and the results for $Z_0 = 4$ and 10 are shown in Figure 5. For both cases 1 and 2, the relaxation modulus of the

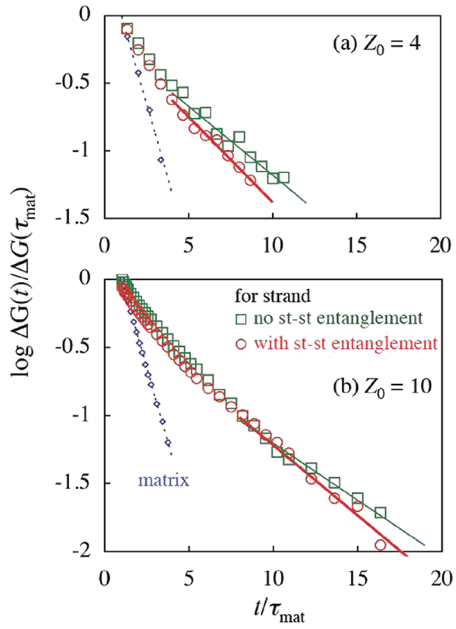

Figure 5. Normalized modulus decay of an end-fixed strand without and with strand−strand (st−st) entanglement (large symbols) obtained from NAPLES simulation for the cases of (a) $Z_0 = 4$ and (b) $Z_0 = 10$. Thin solid lines attached to the squares show the terminal behavior in the absence of the st−st entanglement, $\Delta G(t)/\Delta G(\tau_{mat}) \sim \exp(-t/\tau_{strand}^{case\ 1})$, and the thick solid lines attached to the circles, the behavior in the presence of this entanglement, $\Delta G(t)/\Delta G(\tau_{mat}) \sim \exp(-t/\tau_{strand}^{case\ 2})$ with $\tau_{strand}^{case\ 2} = \{(Z_0 - 1)/Z_0\}^2 \tau_{strand}^{case\ 1}$. For comparison, the modulus decay behavior is shown also for the matrix chain (small diamonds).

strand had an equilibrium plateau (G_e) and was expressed as $G(t) = \Delta G(t) + G_e$, where $\Delta G(t)$ is the relaxational part of the strand modulus reflecting the release/reformation of the strand-matrix entanglements (CR effect due to the matrix chain motion).

In Figure 5, the relaxational part of the strand modulus normalized by that at the matrix relaxation time τ_{mat}, $\Delta G(t)/\Delta G(\tau_{mat})$, is semilogarithmically plotted against the normalized time, t/τ_{mat}. For comparison, the normalized $\Delta G(t)/\Delta G(\tau_{mat})$ is shown also for the matrix chain. In a naive molecular picture considering no tension equilibration and no global conformational adjustment of the strand, the two sections of the strand separated by the permanent strand−strand entanglement relax independently (through the localized CRR mechanism discussed in section 2.3) so that the relaxation time $\tau_{strand}^{case\ 2}$ of $\Delta G(t)/\Delta G(0)$ for case 2 is expected to be smaller, by a factor of $Q = \{(Z_0-1)/2\}^2/Z_0^2$, compared to $\tau_{strand}^{case\ 1}$ for case 1. (Each section contains, on average, $(Z_0 - 1)/2$ strand-matrix entanglements, which gives this Q factor.) In contrast, in a sophisticated picture considering the global tension equilibration that completes through accumulation of the local CR events occurring at

dx.doi.org/10.1021/ma202167q | *Macromolecules* 2012, 45, 2085−2098

$Z_0 - 1$ strand-matrix entanglements, $\tau_{strand}^{case\ 2}$ for case 2 is smaller, by a factor of $\{(Z_0 - 1)/Z_0\}^2 = 0.81$ and 0.563 for $Z_0 = 10$ and 4, compared to $\tau_{strand}^{case\ 1}$ for case 1. (These factors are numerically very close to the factors calculated from the rigorous eigenvalues of the discrete Rouse model, $\sin^{-2}\{\pi/2(Z_0 - 1)\}/\sin^{-2}\{\pi/2Z_0\} = 0.811$ and 0.586 for $Z_0 = 10$ and 4.) The terminal relaxation behavior expected for this global tension equilibration process is shown with the solid lines attached to the circles in Figure 5. We note that $\tau_{strand}^{case\ 2}$ is indeed close to $\{(Z_0 - 1)/Z_0\}^2\tau_{strand}^{case\ 1}$ and much longer, by a factor of 4, than $Q\tau_{strand}^{case\ 1}$ expected for the localized CCR. This result demonstrates the importance of the CR-activated tension equilibration throughout the strand backbone that results in the global conformational adjustment of the strand. (For $Z_0 \to \infty$, the difference between the relaxation times (= equivalent to the tension equilibration times) for cases 1 and 2, $\tau_{strand}^{case\ 1}$ and $\tau_{strand}^{case\ 2} = \{(Z_0 - 1)/Z_0\}^2\tau_{strand}^{case\ 1}$, vanishes and the effect of nonlocalization of CRR would be observed more prominently compared to the cases for $Z_0 \leq 10$ examined in Figure 5.)

3.1.2. Tension Equilibration for Long Chain in Binary Blends. Now, we switch to the blend of the long and short chains, the system of our main interest. The short chain is equivalent to the matrix chain in the network system explained above and the long chain, to the network strand but without fixed ends. The changes of the conformation illustrated in Figure 4a–c are common for the network strand and the long chain. However, the long chain has the free ends so that the CR-activated tension equilibration also results in the motion of the chain ends. In an example illustrated in Figure 4d (for the case of $|\mathbf{r}| > a_0$), the tension is larger for the reformed entanglement segment, so that the monomers are sucked in this segment. Then, some entanglements near the chain ends, which include the long–long entanglements, are released (see the change from Figure 4c to Figure 4d). The release of the long–long entanglement results in a decrease of the stress to a level lower than that for the end-fixed network strand. For the other cases of $|\mathbf{r}| > a_0$ not illustrated here, the chain backbone is pushed out from the reformed entanglement to create a new entanglement nearby the chain ends, but this new entanglement should be created isotropically and lead to no increase of the stress. Thus, the local CR blinking (release/reformation of the long–short entanglements) activates the global motion of the long chain to decrease the stress through the tension equilibration. Completion of this equilibration, which results in some loss of initial long–long entanglements, allows the long chain in the blend to behave similarly to that in a solution having the entanglement plateau height $G_N = G_N^0\upsilon_2^{1+\alpha}$ with $\alpha = 4/3$.

It should be emphasized that the tension equilibration is activated by the local CR process common for the end-fixed strand and end-free chain and is totally different from the classical contour length fluctuation (CLF) due only to the intrinsic longitudinal Rouse mode (in the fixed tube). In fact, the stress relaxation of the end-fixed strand, being free from the end motion due to the CLF mechanism but activated by the tension equilibration, occurs at the characteristic global CR time $\tau_{CR}{*}N'^2$ for the whole sequence of N' long–short entanglements ($N' = Z_0 - 1$ in Figure 5), not at the intrinsic Rouse–CLF time ($\ll\tau_{CR}{*}N'^2$). It should be also noted that the tension equilibration leads to partial disorientation occurring almost uniformly for all primitive path segments, while CLF results in the disorientation mostly for the segments near the chain ends.

We also note that the end motion is reflected in the dielectric data, but the tube survival fraction $\varphi'(t)$ was evaluated from the dielectric data through the full-DTD/partial-DTD analysis of the data considering the end motion (and the motion at the dilated tube edge).[27] The $\varphi'(t)$ thus obtained represents exclusively the survival fraction of the initial tube defined with respect to the dilated diameter at time t (without a disturbance from the end motion).

As evidenced from the above argument, the initial dilation with $\alpha = 1$ is followed by the CR-activated tension equilibration (adjustment of the chain conformation) that results in an effective dilation described by $\alpha = 4/3$. This equilibration is absolutely necessary for the long chain in the blend to behave similarly to that in solutions[20−24] and recover the theoretical exponent of $\alpha = 4/3$ in the fully equilibrated solutions deduced by Colby and Rubinstein.[23] Thus, from an experimental point of view comparing the blend and solution behavior at long times, the dilation exponent should be $\alpha = 4/3$ (as demonstrated by Watanabe et al.[22,27]). However, from a theoretical point of view considering the binary nature of the entanglements, we should start with $\alpha = 1$ at short times and still find the effective dilution exponent of 4/3 after the tension equilibration explained above. This equilibration certainly occurs before the relaxation of the long–long entanglements if the relaxation times of the long and short chains are widely separated. The crossover of the α value due to this equilibration, ending up with the Colby–Rubinstein value of α at long times, is a novel process addressed in this work.

In Figure 6, this tension equilibration process is illustrated within the context of the molecular picture of tube: while

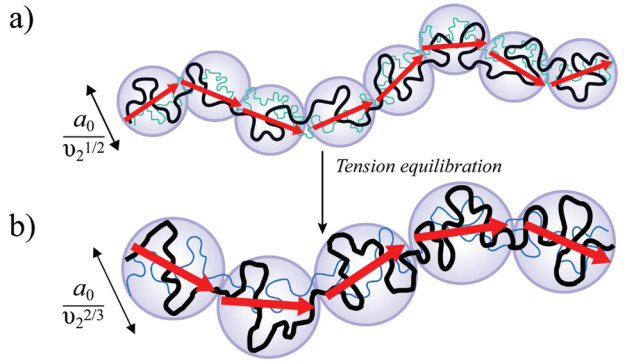

Figure 6. Tube-based picture of the tension equilibration. (a) After the relaxation of the short chains, the long chain starts to explore its dilated tube. (b) The same long chain, after its tension equilibration.

Figure 6a represents a long chain exploring its dilated tube after the relaxation of the short chains (see also Figures 1b and 4b), Figure 6b represents the same chain after its tension equilibration. In both cases, the long–long entanglement segments behave as Gaussian subchains. However, after the tension equilibration, the tube diameter has evolved from $a_0/\upsilon_2^{1/2}$ to $a_0/\upsilon_2^{2/3}$, and the average length of the primitive path has decreased from $\langle R^2\rangle/\{a_0/\upsilon_2^{1/2}\}$ to $\langle R^2\rangle/\{a_0/\upsilon_2^{2/3}\}$, while keeping the mean-square end-to-end distance $\langle R^2\rangle$ unchanged. Indeed, during the tension equilibration process, the primitive path explores new configurations within the dilated tube and partially disorients itself (and reduces the correlation with the initial primitive path), and some initial long–long entanglements are lost (due to the blinking of the local CR, see Figure 4d). Thus, the long chains relax more than expected by the classical DTD picture (with $\alpha = 1$) considering only local CR-equilibration between successive long–long entanglements. This explains why

dx.doi.org/10.1021/ma202167q | *Macromolecules* 2012, 45, 2085–2098

the viscoelastic relaxation function (cf. eq 6) scales as $\{\varphi'(t)\}\}^{7/3}$, not as $\{\varphi'(t)\}^2$, at long t after the tension equilibration completes.

This tension equilibration, activated by local CR, differs from the classical CLF, as emphasized earlier: The blinking of the long−short entanglements allows the chain to explore all local conformations (while keeping $\langle R^2\rangle$ unchanged; cf. Figure 6) and equilibrate the tension at a rate essentially determined by the motion of the short chains, not at the intrinsic Rouse rate associated with CLF.

It should be also noted that the tension equilibration, which requires the CRR motion of the whole backbone of the long chain, is slow compared to the localized CRR process (eq 5). This corresponds to the slow crossover from $\mu(t) = \{\varphi'(t)\}^2$ to $\mu(t) = \{\varphi'(t)\}^{7/3}$, as observed in Figures 2 and 3. Indeed, this interpretation is consistent with the results of the slip-link simulation (NAPLES) for bidisperse blends,[30] in which the relationship $a = a_0/\upsilon_2^{1/2}$ (i.e., with $\alpha = 1$) is used but the terminal relaxation intensity is found to scale as $\upsilon_2^{7/3}$ because of the conformational adjustment (and tension equilibration) of the long chain activated by removal/reformation of long−short slip-links.

3.3. Including the Tension Equilibration Process in the Viscoelastic Relaxation Function. It is desired to formulate the relaxation function for the tension equilibration process explained above. This process is expected to be well approximated by a Rouse process activated by the short chain motion (although a delicate deviation from the Rouse process may also exist[22]). In order to account for the tension equilibration in the viscoelastic relaxation function (eq 6), the time necessary for this conformational rearrangement, τ_{TE}, must be defined. Since it is a CR-Rouse time, which corresponds to the global CR motion of $\upsilon_1 Z_{2,0}$ long−short entanglements segments (with υ_1 = volume fraction of the short chains), determined by the rhythm imposed by the motion of the short chains—thus depending on $\tau_{rel,1}(M_1)$—we may safely approximate it as

$$\tau_{TE}(M_1, M_2, \upsilon_2) \approx \tau_{rel,1}(M_1)\{\upsilon_1 Z_{2,0}\}^2 \tag{7}$$

Equation 7 is similar to the empirically introduced expression of the equilibration time for the partial-DTD picture[22] and is consistent with the results seen in Figure 5, the relaxation time being proportional to square of the number of the long−short entanglements per long chain. The υ_1 dependence of τ_{TE} shown in eq 7 is also consistent with the observation in Figure 2 that the time for the crossover from the classical DTD (with $\alpha = 1$) to the dilation with the effective $\alpha = 4/3$ becomes longer with increasing υ_1. Namely, the more the tube is dilated (*for larger* υ_1), the larger becomes the number of conformations that the long chains have to explore in order to take advantage of the diluting effect from the short chains. On the other hand, whatever the proportion of long chains, this process seems to start just after the relaxation of the short chains, which is in harmony with the tension equilibration activated by the motion of the short chains.

Knowing the tension equilibration time τ_{TE}, we can modify the viscoelastic relaxation function of a bidisperse blend in order to account for this crossover from the classical DTD picture to the picture of DTD combined with the tension equilibration, both being characterized with $\alpha = 1$ but the latter including the effect of the primitive path disorientation. To this end, we consider the probability $p_{TE}(t)$ for a long chain not to relax by this tension equilibration. This $p_{TE}(t)$, giving the crossover, should relax through the CR-Rouse modes of all $\upsilon_1 Z_{2,0}$ long−short entanglements segments (per the long chain), with the longest relaxation time being identical to τ_{TE}. In fact, previous dielectric studies[21,22] showed that the crossover is satisfactorily described with the CR-Rouse modes. (These modes have been incorporated in the partial-DTD picture[22]). Thus, $p_{TE}(t)$ can be cast in a form

$$p_{TE}(t) \approx \frac{1}{\upsilon_1 Z_{2,0}} \sum_{p=1}^{\upsilon_1 Z_{2,0}} \exp\left(\frac{-p^2 t}{\tau_{TE}(M_1, M_2, \upsilon_2)}\right) \tag{8}$$

The CR-Rouse modes shown in eq 8 correspond to the global tension equilibration along the whole chain backbone as well as to the localized tension equilibration between two long−long entanglements. Since the number of long−short entanglements between the long−long entanglements is given by $\sim\upsilon_1 Z_{2,0}/\upsilon_2 Z_{2,0} = \upsilon_1/\upsilon_2$ on average, the fastest υ_1/υ_2 modes can be assigned to the localized equilibration (occurring in the time scale of localized CRR explained in section 2.3), and the remaining slower $\upsilon_1 Z_{2,0} - \upsilon_1/\upsilon_2$ modes, to the global equilibration.

In the crossover region explained above, the long chain should not significantly contribute to the dilation of its own tube. Thus, for the effective survival fraction of the initial constraint ϕ determining the dilated $a(t)$ (cf. eq 5a), the bare effect of the tension equilibration itself can be represented as a decay by a factor of $\upsilon_2^{1/3}$ (which corresponds to a decrease of the low-frequency plateau modulus from $G_N^0\upsilon_2^2$ to $G_N^0\upsilon_2^{7/3}$). Thus, $\phi_{TE,2}(t)$ just representing this effect can be expressed as

$$\phi_{TE,2}(t) = \{\upsilon_2 + \upsilon_1 p_{TE}(t)\}^{1/3} \tag{9}$$

Note that the exponent 1/3 has been fixed in eq 9 to ensure that the effective α value at long times is 4/3, consistent with a large set of experimental data in the literature for polymer solutions[20−24] and to the work of Colby and Rubinstein.[23] This effective exponent, 4/3, is attained only after the relaxation of $p_{TE}(t)$ that occurs through the tension equilibration and conformational adjustment of the long chain activated by many short chains (forming $\upsilon_1 Z_{2,0}$ long−short entanglements; cf. eq 7), not by a single short chain. In this sense, this effective exponent reflects the multichain feature of the entanglement in bidisperse blends in long time scales.

The relaxation of $\phi_{TE}(t)$ corresponds to the stress decay due to the tension equilibration and conformational adjustment, the latter including partial removal of the long−long entanglements. In bidisperse blends with $M_2 \gg M_1$, the short chains should behave as a solvent in the time scale of the terminal relaxation of the long chains, and thus $\tau_{rel,2}$ of the long chains is proportional to $M_2^{3.4}$. This $\tau_{rel,2}$ is much longer than the relaxation time of $p_{TE}(t)$, $\tau_{TE}(M_1,M_2,\upsilon_2) \approx \tau_{rel,1}(M_1)\{\upsilon_1 Z_{2,0}\}^2 \propto M_1^{3.4}M_2^2$ (eq 7), given that $M_2 \gg M_1$. For this extreme case, the number long−long entanglements per long chain, $N_{long-long}$, decreases from $\upsilon_2 Z_{2,0}$ (at short $t \ll \tau_{rel,1}$) to $\upsilon_2^{4/3}Z_{2,0}$ at $t \approx \tau_{TE}$, and the terminal relaxation of the long chain occurs from the corresponding low-frequency plateau modulus, $G_N^0\upsilon_2^{7/3}$. However, if M_2 is not sufficiently longer than M_1 (if $\tau_{rel,2}$ is shorter than τ_{TE}), this decrease of $N_{long-long}$ cannot be completed before the terminal relaxation of the long chain. For this case, $N_{long-long}$ would just partially decrease to $\{\upsilon_2 + \upsilon_1 p_{TE}(\tau_{rel,2})\}^{1/3}\upsilon_2 Z_{2,0}$ at $t \cong \tau_{rel,2}$, which corresponds to the effective low-frequency plateau modulus of $G_N^0\upsilon_2^2\{\upsilon_2 + \upsilon_1 p_{TE}(\tau_{rel,2})\}^{1/3}$ ($>G_N^0\upsilon_2^{7/3}$).

The above result also indicates that the role played by $\phi_{TE,2}(t)$ in the viscoelastic relaxation function depends on

dx.doi.org/10.1021/ma202167q | Macromolecules 2012, 45, 2085−2098

several parameters such as the length and the volume fraction of the long chains and the relaxation time of the short chains. This could explain the difficulty of fixing the α value through the data fitting with the models so far proposed.

Taking the relaxation by tension equilibration into account in the viscoelastic relaxation function, we can modify eq 6 (with a factorization approximation) as

$$\mu(t) = \varphi'(t)\phi(t)\phi_{TE,2}(t) \tag{10}$$

Note that the $(a(t)/a_0)^{-2}$ term in eq 6 is replaced by $\phi(t)\phi_{TE,2}(t)$ in eq 10. The functions $\phi(t)$ and $\phi_{TE,2}(t)$ appearing in eq 10 are specified by eq 5c (or 5b) and eqs 8 and 9, respectively, and the tension equilibration time τ_{TE} for $\phi_{TE,2}(t)$ is evaluated from the $\tau_{rel,1}(M_1)$ data (cf. eq 7). The other quantity appearing in eq 10, the dilated tube survival fraction $\varphi'(t)$, is experimentally determined from the dielectric data, as mentioned earlier. Thus, eq 10 enables us to calculate $\mu(t)$ just from experimental quantities.

It is informative to examine the contributions of $\phi(t)$, $\phi_{TE,2}(t)$, and $\varphi'(t)$ to the relaxation of $\mu(t)$ calculated from eq 10. As a representative example, Figure 7 shows these contributions for the

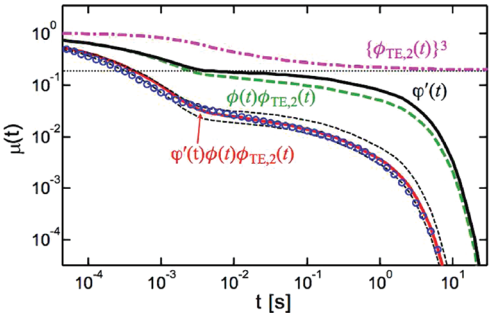

Figure 7. Experimental (○) and predicted (red, thick —) viscoelastic relaxation functions of the blend L308-L21, with υ_2 = 20%. The functions $\{\varphi'(t)\}^2$ and $\{\varphi'(t)\}^{7/3}$ are represented by the black, thin dashed curves (below and above the experimental data, respectively), while the function $\varphi'(t)$ is represented by the black, thick solid curve. The functions $\{\phi_{TE,2}(t)\}^3$ (pink —·—) and $\phi(t)\phi_{TE,2}(t)$ (green - - -) are also shown. The horizontal dotted line represents υ_2.

bidisperse blend L308-L21 containing 20% of long chains. The calculated $\mu(t)$ (thick red curve) agrees well with the data (circles) and exhibits the crossover from $\{\varphi'(t)\}^2$ to $\{\varphi'(t)\}^{7/3}$ at intermediate times (see two thin dotted curves). This crossover reflects decay of $\phi_{TE,2}(t)$ (cf. thick dash-dotted curve) that becomes significant at $t > 2 \times 10^{-3}$ s. The CR-Rouse modes determines this decay of $\phi_{TE,2}(t)$ (of $p_{TE}(t)$; cf. eq 9), and the fastest υ_1/υ_2 modes are assigned to the localized tension equilibration between the long–long entanglements, as explained earlier. For the blend examined here, υ_1/υ_2 (=4) is much smaller than the number of the modes for the global tension equilibration, $\upsilon_1 Z_{2,0} - \upsilon_1/\upsilon_2 = 58$. Thus, $\phi_{TE,2}(t)$ decays dominantly through the global tension equilibration in a time scale for global CRR (much longer than that for the localized CRR).

In Figure 8, we compare $\mu(t)$ calculated from eq 10 with the experimental data for the different bidisperse blends L308-L21 and L308-L94. The calculated $\mu(t)$ agrees with the data very well, which offers a new direction for linking the different values of α proposed in the literature, not only for blends of linear polymers but, more importantly, for branched polymers.

Here, a few comments is to be made for similarity/difference between the molecular picture formulated in this work (eq 10) and the previously reported partial-DTD picture.[22] In the

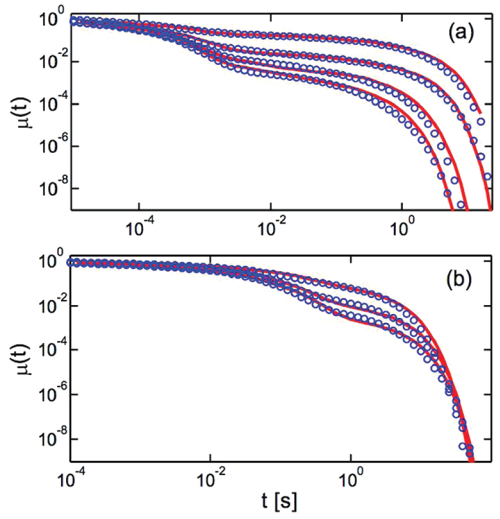

Figure 8. Experimental (○) and predicted (—) viscoelastic relaxation functions of (a) the blends L308-L21, with υ_2 = 5%, 10%, 20%, and 50%, and (b) the blends L308-L94, with υ_2 = 10%, 20%, and 50%.

partial-DTD picture, the exponent α = 1.3 (≅4/3) is adopted in the entire range of t, and the validity of the full-DTD process for this α value is examined through comparison of the number β of entanglement segments per dilated segments, $\beta_{full\text{-}DTD}(t) = \{\varphi'(t)\}^{-\alpha}$ assumed in the full-DTD picture and $\beta_{CR}(t) = 1/\psi_{CR}(t)$ allowed by the CRR mechanism, where $\psi_{CR}(t)$ is the full CRR function for all entanglements of our focus (= all long–short entanglements for the long chain) obtained from the empirically determined CR time. (This $\psi_{CR}(t)$ automatically incorporates the tension equilibration in the relaxation process.) Specifically, the partial-DTD picture considers that the tube is dilated to the maximum possible level consistent with the CRR mechanism to express the viscoelastic relaxation function as $\mu(t) = \varphi'(t)/\beta^*(t)$ with $\beta^*(t) = \min\{\beta_{full\text{-}DTD}(t), \beta_{CR}(t)\}$. This expression is similar to that in eq 5b (or eq 5c) in a sense that competition between the full-DTD and CRR is considered. However, we also note an important difference: The expression of $\beta^*(t)$ for the partial-DTD picture considers the competition between the global CRR and full-DTD, while eq 5b focuses on the competition between the localized CRR and full-DTD. In the formulation in this study, the effect of the global CRR is extracted as the tension equilibration and cast in $\phi_{TE,2}(t)$ (eq 9). This treatment allows explicit examination of the crossover of the effective dilation exponent, from α = 1 to α = 4/3. This crossover, not addressed in the partial-DTD picture, is the novel result demonstrated in this study.

3.3. Confronting the Tension Equilibration Concept to Other Bidisperse Linear Polymers. On the basis of the concept of extra dilation (from α = 1 to α = 4/3) due to the tension equilibration, it is interesting to revisit the results obtained in the literature, where experimental storage and loss moduli for bidisperse linear blends are compared to the ones predicted with tube-based models. In particular, in the studies of Park and Larson[38] and Khaliullin and Schieber,[39] different series of binary blends are presented and compared to the predictions obtained with the tube model developed by Larson et al., by considering the dilution exponent α = 1. This α value has been chosen based on previous works of Park and Larson,[18] who have shown that a better agreement between theoretical calculation and experimental data was obtained for most of the blends with this value of α. In the same way, we note in these two papers that a good agreement is obtained (at least for the low-frequency plateau modulus) between the tube model

dx.doi.org/10.1021/ma202167q | Macromolecules 2012, 45, 2085–2098

predictions and data for all the polystyrene (PS) blends where the molecular weights M_1 and M_2 of the short and long components are not too much separated; for example, $(10^{-3}M_1, 10^{-3}M_2)$ = (160, 670), (60, 177), (102, 390K), and (191, 670).[38,39] This is consistent with the picture proposed in this study, according to which the effective α is equal to 1 if the long chain relaxes before having explored all conformations in its dilated tube, i.e., when the relaxation times of short and long chains are rather close to each other.

However, for some of the binary blends, a larger discrepancy is observed between the data and the predictions with $\alpha = 1$, for example, in refs 38 and 39 for blends of two linear PS with $(10^{-3}M_1, 10^{-3}M_2)$ = (36, 294) and (39, 427), respectively: even by considering the reptation of the long chains in a dilated tube,[38] the predicted relaxation time of the long chain in these blends is too long and the predicted low-frequency plateau modulus too large *if* the value of α is fixed to 1. Park and Larson attributed this failure to lack of sufficient entanglement of the short chains ($Z < 3$). Another way to explain this discrepancy is found in the idea of tension equilibration: In Figure 9, we

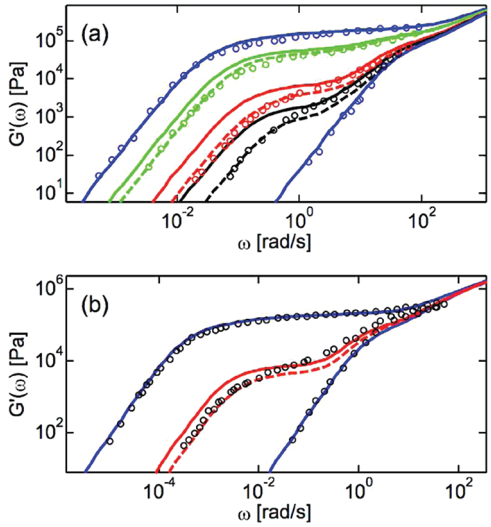

Figure 9. Experimental (○) and predicted storage modulus by considering $\alpha = 1$ (—) or $\alpha = 1.3$ (- - -) for (a) blends of PS-36 kg/mol and PS-294 kg/mol (T = 160 °C) with υ_2 = 0%, 10%, 20%, 60%, and 100% (data from Watanabe et al.[40]) and (b) the monodisperse linear PS-39 kg/mol and PS-427 kg/mol (T = 143 °C) and their blend with υ_2 = 20% (data from Watanabe et al.[41]).

compare the storage moduli of those PS blends (with various υ_2) and the moduli calculated from the tube model developed by van Ruymbeke et al.[15] The model parameters were G_N^0 = 220 kPa, M_e = 14 000 g/mol, and $\tau_e = 4.3 \times 10^{-3}$ s (at 160 °C) or 0.1 s (at 143 °C), respectively. As similar to the results by Park and Larson, the low-frequency plateau modulus is overestimated by the model with $\alpha = 1$, and we note a crossover from $\alpha = 1$ to $\alpha = 4/3$ with decreasing frequency (as seen for the PI blends examined in section 3.3). Moreover, this crossover occurs at lower frequencies for larger υ_1 (Figure 9a), again being in harmony with the tension equilibration concept.

Figure 10 shows another example for two series of polybutadiene (PB) blends measured by Wang et al.[42] and analyzed by Park and Larson.[38] Predictions shown therein were obtained with the model of van Ruymbeke et al.[15] with G_N^0 = 1.2 MPa, M_e = 1650 g/mol, and $\tau_e = 1.6 \times 10^{-7}$ s. (For a better prediction for the blends examined in Figure 10b, slightly different values of τ_e between 0.9×10^{-7} and 1.7×10^{-7} s were used,

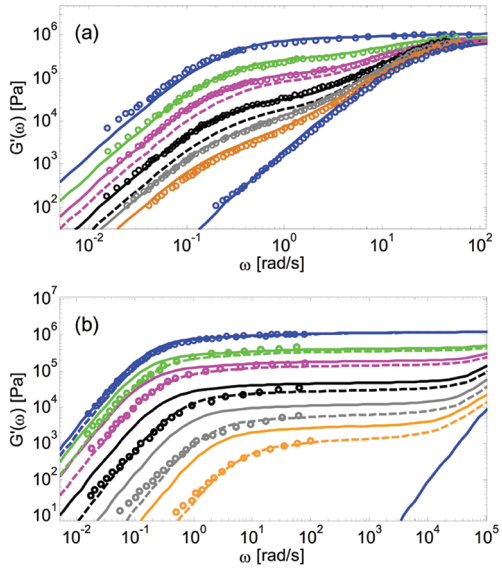

Figure 10. Experimental (○) and predicted storage modulus by considering $\alpha = 1$ (—) or $\alpha = 1.3$ (- - -) for (a) blends of PBD-100 kg/mol and PBD-410 kg/mol with υ_2 = 0%, 5%, 10%, 20%, 40%, 60%, and 100% (data from Wang et al.[42]). Predictions obtained by using $\alpha = 4/3$ are only shown for the blends with υ_2 = 10% and 20%. (b) Blends of PBD-3.9 kg/mol and PBD-410 kg/mol with υ_2 = 0%, 5%, 10%, 20%, 40%, 60%, and 100% (data from Wang et al.[42]).

depending on the blend composition. However, the τ_e value does not influence the low-frequency plateau modulus, and the α value can be still discussed for the predictions shown here.)

As seen in Figure 10a, the storage moduli of the PB blends with $(10^{-3}M_1, 10^{-3}M_2)$ = (100, 410) are reasonably well predicted by considering the dilution exponent $\alpha = 1$. On the other hand, when the same long chains are blended with much shorter chains ($10^{-3}M_1 = 3.9$), the model with $\alpha = 1$ (without the tension equilibration) clearly overestimates the low-frequency plateau modulus, while the model with $\alpha = 4/3$ correctly describes this modulus level. Again, these results are in agreement with the molecular picture of tension equilibration discussed in this study.

4. CONCLUSIONS

The viscoelastic relaxation function of binary blends of linear polymers has been investigated in order to test the validity of the dynamic tube dilution (DTD) ansatz and to properly determine the value of the dynamic dilution exponent α. Starting from the survival fraction of the dilated tube, $\varphi'(t)$, which was determined from experimental dielectric relaxation function in the previous work,[22,27] we could focus on the tube dilation effect, without having to analyze the reptation and contour length fluctuations mechanisms.[35] Comparing experimental and predicted viscoelastic relaxation functions, we first concluded that the classical DTD picture with $\alpha = 1$ is more appropriate at short times, while at longer time, the DTD picture with $\alpha = 4/3$ leads to a better agreement between experiments and predictions. Furthermore, at intermediate times, the α value exhibited a gradual crossover from 1 to 4/3, the latter being the theoretical α value deduced for fully equilibrated solutions. This crossover is a novel feature found in this study.

For explanation of this crossover behavior, we proposed a new relaxation process, which takes place in addition to the classical DTD with $\alpha = 1$ and which allows observing, after a certain time, a stronger dilution effect induced by the relaxation of the short chains, *as if α in the classical DTD picture were larger than 1*. With this relaxation, the assumption behind tube models

dx.doi.org/10.1021/ma202167q | *Macromolecules* 2012, 45, 2085−2098

according to which an entanglement is a binary event ($\alpha = 1$) is kept, while leading to an effective dilation exponent of $\alpha = 4/3$ for blends at long times, consistent with the experimental data from the literature. Then, this extra relaxation process was related to the tension equilibration along the long chains, which takes place after the relaxation of short chains thanks to the blinking feature of release/reformation of the long−short entanglements.[33] This CR-activated tension equilibration can be modeled as slow Rouse relaxation, which requires the motion of the whole contour of the long chain and which leads to a partial disorientation of its primitive path. Taking this process into account for describing the viscoelastic relaxation function, very good agreement was found between experimental and predicted viscoelastic relaxation function.

These results suggest that the effective value of α, i.e., the value experimentally determined from the low-frequency plateau modulus, can vary from system to system, depending on the contribution of the tension equilibration process that changes with the length, composition, and the architecture of the component chains. As a perspective, the viscoelastic data of several complex, branched polymers, in melt or in solution, are desired to be analyzed on the basis of this picture, in order to further validate it.

Finally, we should point out that the problem of the α value addressed in this study is intrinsic to the molecular picture of tube dilation that is based on the consistent coarse-graining of the length and time scales. This problem does not show up in the non-coarse-grained molecular picture that just considers the skinny tube (of the diameter a_0) moving through the CR dynamics. Nevertheless, the tension equilibration process discussed in this study can be still important in this non-coarse-grained view. The slip-link and atomistic models, being efficient for determining the primitive paths of the chains as well as their evolution through time,[30,39,42−49] adopt this view. It is an interesting subject of future work to examine the tension equilibration and coarse-graining (DTD) processes discussed in this study within the context of those non-coarse-grained models.

APPENDIX A. TIME EVOLUTION OF $\phi(T)$ FOR ROUSE RELAXATION

For the Rouse chain composed of N submolecules (segments), the time evolution of the normalized orientation function following an affine shear strain γ at time 0 is given by (for the case of $N \gg 1$)

$$S(n,t) \equiv \frac{\langle u_x(n,t)u_y(n,t)\rangle}{\langle \mathbf{u}^2\rangle_{eq}} = \frac{2\gamma}{3N}\sum_{p=1}^{N}\sin^2\left(\frac{p\pi n}{N}\right)\exp\left(-\frac{p^2 t}{\tau_R}\right) \quad (\text{for } N \gg 1) \tag{A1}$$

Here, $u_x(n,t)$ and $u_y(n,t)$ respectively indicate the components of the bond vector $\mathbf{u}(n,t)$ of nth submolecule at time t in the x and y directions (shear and shear gradient directions), $\langle ... \rangle$ denotes the ensemble average, and $\langle \mathbf{u}^2\rangle_{eq}$ is the ensemble average of $\mathbf{u}^2$ at equilibrium. τ_R is the longest viscoelastic relaxation time of the Rouse process. The corresponding normalized stress relaxation function is given by

$$\frac{G(t)}{G(0)} = \phi_R(t) = \frac{\int_0^N S(n,t)\,dn}{\int_0^N S(n,0)\,dn} = \frac{1}{N}\sum_{p=1}^{N}\exp\left(-\frac{p^2 t}{\tau_R}\right) \tag{A2}$$

This $\phi_R(t)$ for the Rouse process ($\phi_R(t) \to 1$ for $t < \tau_R/N^2$) can be satisfactorily approximated as

$$\phi_R(t) = 1 \quad \text{for } t < \tau_R/N^2 \tag{A3a}$$

$$\phi_R(t) = N^{-1}\{\tau_R/t\}^{1/2} \quad \text{for } \tau_R/N^2 \ll t \ll \tau_R \tag{A3b}$$

$$\phi_R(t) = N^{-1}\exp(-t/\tau_R) \quad \text{for } t > \tau_R \tag{A3c}$$

(Note that the shortest Rouse time is given by τ_R/N^2.) Thus, for two times t and t' ($<t$) chosen in the interval between τ_R/N^2 and τ_R, we find a relationship, $\phi_R(t)/\phi_R(t') = (t'/t)^{1/2}$. This Rouse relationship is utilized in eq 5b to describe the change of $\phi(t)$ due to the Rouse process (that includes the constraint release Rouse process).

In relation to the above result, we should note that the time evolution of $\phi_R(t)$ specified by eqs A3a−A3c results from the time evolution of the orientation function $S(n,t)$ given by eq A1. In the time zone for eq A3b, $\tau_R/N^2 \ll t \ll \tau_R$, $S(n,t)$ given by eq A1 is essentially independent of n (except in the vicinity of the chain ends, $n = 0$ and N) and can be approximated as $S(n,t) \cong \gamma\phi_R(t)/3$. Thus, the Rouse relationship, $\phi_R(t)/\phi_R(t') = (t'/t)^{1/2}$, can be safely utilized to describe the change of ϕ due to the Rouse mechanism in the interval from t' to t *if* $S(n,t')$ is (almost) independent of n, even for a case that a competing non-Rouse mechanism contributes to the time evolution of S at times $<t'$. At short times, the reptation and CLF mechanisms enhance the orientational relaxation nearby chain ends and do not significantly affect the relaxation at around the chain center. Thus, the Rouse relationship, $\phi_R(t)/\phi_R(t') = (t'/t)^{1/2}$, can be safely utilized in eq 5b as the first approximation for the case of competition of the Rouse (CRR) and reptation/CLF mechanisms.

APPENDIX B. $\phi(t)$ FOR LOCALIZED CRR-DTD

B.1. Calculation of $\phi(t)$

It would be informative to demonstrate how the effective survival fraction of the initial constraint, $\phi(t)$, for the localized CRR-DTD molecular picture (section 2.3) is calculated from eq 5c. To this end, Figure 11 shows an example of this calculation with $\alpha = 1$ for a simple model system having the

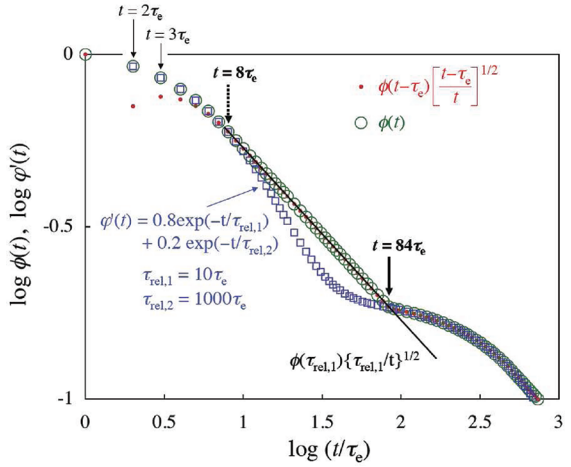

Figure 11. An example of calculation of $\phi(t)$ (large unfilled circles) for a model system having the dilated tube survival fraction $\varphi'(t)$ (squares). Comparison of $\varphi'(t)$ and $\phi(t-\tau_e)[(t-\tau_e)/t]^{1/2\alpha}$ (small filled circles; $\alpha = 1$ for the calculation shown here) allows us to unequivocally determine $\phi(t)$ with the aid of eq 5c. For further details, see Appendix B1.

dx.doi.org/10.1021/ma202167q | Macromolecules 2012, 45, 2085−2098

survival fraction of the dilated tube

$$\phi'(t) = 0.8\exp(-t/\tau_{rel,1}) + 0.2\exp(-t/\tau_{rel,2}) \quad \text{(B1)}$$

with

$$\tau_{rel,1} = 10\tau_e, \quad \tau_{rel,2} = 1000\tau_e \quad \text{(B2)}$$

(τ_e is the relaxation time within the entanglement segment.) This model system mimics the behavior of short and long chains having the volume fractions, $v_1 = 0.8$ and $v_2 = 0.2$, and the relaxation time ratio, $\tau_{rel,1}/\tau_{rel,2} = 1/100$.

According to eq 5c with $\alpha = 1$, we compare $\varphi'(t)$ (shown with the squares in Figure 11) and $\phi(t - \tau_e)[(t - \tau_e)/t]^{1/2}$ (small filled circles), the latter representing the CRR decay of ϕ, and adopt the larger of these as $\phi(t)$ at the time t (large unfilled circles). Starting from the initial condition, $\varphi'(\tau_e) = \phi(\tau_e) = 1$, we first compare $\varphi'(2\tau_e)$ and $\phi(\tau_e)[1/2]^{1/2}$ ($t = 2\tau_e$) to find that $\varphi'(2\tau_e) > \phi(\tau_e)[1/2]^{1/2}$ (see Figure 11). Thus, we obtain $\phi(2\tau_e) = \varphi'(2\tau_e)$. Then, we compare $\varphi'(3\tau_e)$ and $\phi(2\tau_e)[2/3]^{1/2}$ ($t = 3\tau_e$) to obtain $\phi(3\tau_e) = \varphi'(3\tau_e)$ ($>\phi(2\tau_e)[2/3]^{1/2}$). Repeating this process, we find $\phi(t) = \varphi'(t)$ (full-DTD behavior) in a range of $t \leq 7\tau_e$ for the model system examined here. However, for $t = 8\tau_e$, we note $\varphi'(8\tau_e) < \phi(7\tau_e)[7/8]^{1/2}$ and thus $\phi(8\tau_e) = \phi(7\tau_e)[7/8]^{1/2}$. This CRR behavior, prevailing because CRR is not fact enough to allow the tube to fully dilate to the diameter $a = a_0\varphi^{-1/2}$, is observed in a range of time, $8\tau_e \leq t \leq 83\tau_e$. At longer $t \geq 84\tau_e$, the full-DTD behavior ($\phi(t) = \varphi'(t) > \phi(t - \tau_e)[(t - \tau_e)/t]^{1/2}$) again prevails. (The calculation for the case of $\alpha = 4/3$ is made similarly.) Thus, eq 5c allows us to unequivocally determine $\phi(t)$ at each time. The behavior of actual bidisperse blends of PI was analyzed in the same way with the aid of the dielectrically determined $\varphi'(t)$, and the results have been shown in Figures 2 and 3.

As noted from the above results, eq 5c describes the crossover from the full-DTD behavior at short t (until the short chains fully relax) to the CRR behavior at intermediate t and further to the full-DTD behavior at long t (where the long–long entanglements begin to relax). The CRR behavior deduced from eq 5c corresponds to the CR equilibration of the long chains localized between successive long–long entanglements, as explained in section 2.3. This localized CRR process is described by the relationship, $\phi(t) = \phi(\tau_{rel,1})\{\tau_{rel,1}/t\}^{1/2\alpha}$ (for $t > \tau_{rel,1}$); see thick solid line in Figure 11 (for the case of $\alpha = 1$). In fact, this relationship is analytically obtained from eq 5c under the CRR condition, $\phi(t) = \phi(t - \tau_e)[(t - \tau_e)/t]^{1/2\alpha}$.

Here, a comment needs to be made for the normalized viscoelastic relaxation function $\mu_2(t)$ of the long chain in the localized CRR regime where CRR occurs just between successive long–long entanglements. As explained above, $\phi(t) = \phi(\tau_{rel,1})\{\tau_{rel,1}/t\}^{1/2\alpha}$ in this regime. $\mu_2(t)$ is given by $\varphi_2'(t)\{a(t)/a_0\}^{-2}$ (cf. eq 6), with $\varphi_2'(t)$ being the dilated tube survival fraction defined for the long chain. Dielectric data of bidisperse PI blends[22,27] showed that $\varphi_2'(t)$ remains very close to unity in the localized CRR regime just after the relaxation of the short chains. (This is the case also for the model system examined above; $\varphi_2'(t) = 0.2\exp(-t/\tau_{rel,2})$ remains very close to unity in the localized CRR regime at $8\tau_e \leq t \leq 83\tau_e$.) Thus, in this regime, we can safely utilize a relationship $\mu_2(t) = \{a(t)/a_0\}^{-2} = \{\varphi(t)\}^{\alpha}$ (cf. eq 5a) combined with $\phi(t) = \phi(\tau_{rel,1})\{\tau_{rel,1}/t\}^{1/2\alpha}$ to find $\mu_2(t) = \mu_2(\tau_{rel,1})\{\tau_{rel,1}/t\}^{1/2} \propto t^{-1/2}$ (with $\mu_2(\tau_{rel,1}) = \{\phi(\tau_{rel,1})\}^{\alpha}$). Namely, the Rouse expression of $\mu_2(t)$ is confirmed in the localized CRR regime irrespective of the α value.

In the presence of the tension equilibration, we start with $a(t)/a_0 = \{\phi(t)\phi_{TE}(t)\}^{-1/2}$ for the case of $\alpha = 1$ (as explained for eq 10) to find $\mu_2(t) = \phi(t)\phi_{TE,2}(t)$. $\phi_{TE,2}(t)$ (eq 9) relaxes slightly in the localized CRR regime, but this relaxation is much less significant compared to the relaxation of $\phi(t)$ ($\sim 1/t^{1/2}$): Namely, the number of the CR-Rouse modes corresponding to the localized tension equilibration between long–long entanglements is usually much smaller than the mode number corresponding to the global tension equilibration, as explained for Figure 7, so that the dominant decay of $\phi_{TE,2}(t)$ occurs only after completion of the localized CRR process. Thus, $\mu_2(t) = \phi(t)\phi_{TE,2}(t)$ in the localized CRR regime is not exactly but almost identical to $\phi(t) = \phi(\tau_{rel,1})\{\tau_{rel,1}/t\}^{1/2}$ (for the case of $\alpha = 1$), again confirming the Rouse-type viscoelastic relaxation of the long chain in this regime.

B.2. Continuous Expression of $\phi(t)$

Equation 5c allows us to unequivocally determine $\phi(t)$, as explained above. This $\phi(t)$ is determined at discretized times $t = p\tau_e$ ($p = 2, 3, \ldots$) because τ_e is the shortest unit time for the entanglement relaxation. Nevertheless, a continuous form of $\phi(t)$ can be obtained (if necessary) by introducing an extended initial condition,[37] $\phi(t) = \varphi'(t)$ for $\tau_e \leq t \leq 2\tau_e$.

One may also argue that the time evolution equation of $\phi(t)$ is to be expressed in a continuous form (instead of discretized eq 5c). For this purpose, we can take the limit of $\tau_e \to dt \to 0$ in eq 5c to find a continuous expression of $d\phi(t)/dt$. Specifically, we can utilize an approximation

$$\phi_R(t, \tau_e) = \phi(t - \tau_e)\left[\frac{t - \tau_e}{t}\right]^{1/2} \cong \left\{\phi(t) - \tau_e\frac{d\phi(t)}{dt}\right\}\left\{1 - \frac{\tau_e}{2t}\right\} \quad \text{(B3)}$$

(Here, the factor τ_e multiplied to $d\phi(t)/dt$ or divided by $2t$ should not be replaced by dt so as to enable the comparison between $\varphi'(t)$ and $\phi_R(t,\tau_e)$, the latter evolving only through the Rouse mechanism.) Then, $d\phi(t)/dt$ (for $t > \tau_e$) can be expressed as

$$\frac{d\phi(t)}{dt} = \frac{d\varphi'(t)}{dt} \quad \text{if } \varphi'(t) \geq \phi_R(t, \tau_e) \quad \text{(B4a)}$$

$$\frac{d\phi(t)}{dt} = -\frac{1}{2}\frac{\phi(t)}{t} \quad \text{if } \varphi'(t) < \phi_R(t, \tau_e) \quad \text{(B4b)}$$

The initial condition is $\phi(\tau_e) = 1$ (and $\varphi'(\tau_e) = 1$). Combining eq B4 with $\varphi'(t)$ obtained from the dielectric data, we may calculate $\phi(t)$ in a continuous sense. However, the actual calculation was (and is to be) made with the discretized eq 5c because τ_e is the unit time for the entanglement relaxation and the time evolution in a shorter time scale is irrelevant to the entanglement relaxation.

APPENDIX C. NAPLES SIMULATION

Summary of NAPLES

In the multichain simulation referred to as NAPLES,[29,30] sliplinks distributed on a polymer chain divide the chain into subchains (entanglement segment), and each sliplink bounds two chains (following the binary assumption of entanglement). The sliplink is allowed to move in space according to the balance of forces acting on it (see eq C1). The polymer chain

dx.doi.org/10.1021/ma202167q | Macromolecules 2012, 45, 2085–2098

also moves (i.e., slides) through the sliplinks according to the force balance along the chain (see eq C2). Furthermore, when the chain end passes a sliplink, this sliplink is removed. On the contrary, if a certain amount of the monomers slides out from the sliplink at the chain end, a sliplink is newly created to hook one of surrounding chains. Dynamics of the system is ruled by the motion of sliplinks, the monomer transfer *via* the chain sliding through the sliplinks, and the creation/removal of the sliplinks at chain ends.

At equilibrium, the motion of a sliplink is described by the Langevin equation for the position $\mathbf{R}$ of the sliplink[29,30]

$$\zeta \frac{\partial \mathbf{R}}{\partial t} = \mathbf{F}_B + \mathbf{F}_f + \sum_i^4 \mathbf{F}_i \tag{C1}$$

Here, ζ is the friction coefficient of the sliplink: $\zeta = 2n_0\zeta_m$ with ζ_m and n_0 being the monomeric friction coefficient and equilibrium number of monomers in the subchain, respectively. Among the forces appearing in eq C1, $\mathbf{F}_B$ is the thermal force modeled as a white noise characterized by[29] $\langle \mathbf{F}_B(t)\mathbf{F}_B(t')\rangle = 2k_BT\zeta\delta(t - t')\mathbf{I}$ (with k_BT = thermal energy and $\mathbf{I}$ = unit tensor). $\mathbf{F}_f$ is the osmotic force favoring uniform distribution of the sliplinks: $\mathbf{F}_f = -\nabla\mu$ with the chemical potential μ being obtained as a derivative of the free energy, $A = \varepsilon(\delta\tilde{\varphi})^2$ (for $\delta\tilde{\varphi} > 0$), where $\delta\tilde{\varphi}$ is the fluctuation of a normalized segment concentration $\tilde{\varphi}$ and ε (=0.5)[29] is an intensity parameter. Finally, $\mathbf{F}_i$ is the elastic force from the ith subchain: $\mathbf{F}_i = \{3k_BT/n_ib^2\}\mathbf{r}_i$, where $\mathbf{r}_i$ and n_i are the end-to-end vector and the monomer number of this subchain, respectively, and b is the monomer step length.

The time evolution of n_i is described by the Langevin equation[29,30]

$$\frac{\zeta_s}{\rho}\frac{\partial n_i}{\partial t} = (F_i - F_{i-1}) + f_B + f_f \tag{C2}$$

where ρ is average linear density of monomers between the $(i - 1)$th and the ith subchains and ζ_s is the friction coefficient given by $\zeta_s = n_0\zeta_m$.[29,30] F_i appearing in eq C2 is the elastic force due to the ith subchain ($F_i = |\mathbf{F}_i|$), and f_f is the field force along the chain calculated from the chemical potential defined with respect to subchain density.[20] Finally, f_B is the 1D Brownian force characterized by $\langle f_B(t)f_B(t')\rangle = 2k_BT\zeta_s\delta(t - t')$.

Simulation Condition

In this study, the simulation was conducted for an end-fixed network strand at equilibrium for the two cases: (1) for the strand forming no strand−strand entanglement but Z_0 entanglements with the free matrix chains and (2) for the strand forming one permanent entanglement with the other strand and $Z_0 - 1$ entanglements with the free matrix chains. The matrix chain forms Z_0 entanglements with the other matrix chains and/or strand. For both strand and matrix chains, eqs C1 and C2 were solved numerically to trace the time evolution of $\mathbf{R}$ and n. The strand ends were fixed in space, and the strand−strand sliplink (entanglement) in case 2 was allowed to move in space according to the force balance but never allowed to disappear. For the matrix chains, the end sliplink was removed and created when its end segment number became smaller than $0.5n_0$ and larger than $1.5n_0$, respectively.

The actual simulation was conducted in a simulation box with a dimension of $8 \times 8 \times 8$ (in length units of $b(n_0)^{1/2}$) containing one and two strands for the above cases 1 and 2. The two strands for case 2 were entangled through one sliplink. The remaining space in the simulation box was occupied by the matrix chains. The initial configuration in the simulation box was equilibrated by running the simulation for a sufficiently long time. Then, the relaxation modulus $G(t)$ was separately evaluated for the strand and matrix chain with the aid of the Green−Kubo formula, $G(t) \propto k_BT\langle r_x(t + t')r_y(t + t')r_x(t')r_y(t')\rangle_{eq,t'}$ where r_j $(j = x, y)$ is the j-component of the subchain bond vector. The average $\langle ...\rangle_{eq,t'}$ was taken for 10 runs at equilibrium starting from independent initial configuration, and the averaging of the origin of the time, t', was made in each run conducted for a time span of $100\tau_{mat}$ (with τ_{mat} being the relaxation time of the matrix chains). The results thus obtained for the cases of $Z_0 = 4$ and 10 are shown in Figure 5 where the relaxational part of the modulus, $\Delta G(t)$, is normalized by $\Delta G(\tau_{mat})$ and plotted against the normalized time, t/τ_{mat}.

■ ASSOCIATED CONTENT

Ⓢ Supporting Information

Analysis showing the failure of the molecular picture of localized CRR on the basis of the experimental data of the CRR time for dilute long chains entangled only with the short chains combined with rigorous Rouse calculation. This material is available free of charge via the Internet at http://pubs.acs.org.

■ AUTHOR INFORMATION

Notes

The authors declare no competing financial interest.

■ ACKNOWLEDGMENTS

We are very grateful to D. Vlassopoulos for his constant help and support along this work. We thank R. Larson, C. Bailly, and R. Keunings for helpful discussions. This work was supported by the EU (NoE Softcomp, grant NMP3-CT-2004-502235, Marie-Curie ITN DYNACOP), the Fonds National de la Recherche Scientifique (EVR, as chargé de recherche), and the Grant-in-Aid for Scientific Research (B) (grant # 21350063) from MEXT, Japan.

■ REFERENCES

(1) de Gennes, P. G. *J. Chem. Phys.* **1971**, *55*, 527.
(2) Doi, M.; Edwards, S. F. *The Theory of Polymer Dynamics*; Oxford University Press: New York, 1986.
(3) Watanabe, H. *Prog. Polym. Sci.* **1999**, *24*, 1253.
(4) McLeish, T. C. B. *Adv. Phys.* **2002**, *51*, 1379.
(5) Dealy, J. M.; Larson, R. G. *Structure and Rheology of Molten Polymers*; Hanser Verlag: Munich, 2006.
(6) (a) Tsenoglou, C. *ACS Polym. Prepr.* **1987**, *28*, 185. (b) Tsenoglou, C. *Macromolecules* **1991**, *24*, 1762.
(7) des Cloizeaux, J. *J. Europhys. Lett.* **1988**, *5*, 437.
(8) Marrucci, G. *J. Polym. Sci., Polym. Phys. Ed.* **1985**, *23*, 159.
(9) Struglinski, M. J.; Graessley, W. W. *Macromolecules* **1985**, *18*, 2630.
(10) Milner, S. T.; McLeish, T. C. B.; Young, R. N.; Johnson, J.; Hakiki, A. *Macromolecules* **1998**, *31*, 9345.
(11) Ball, R. C.; McLeish, T. C. B. *Macromolecules* **1989**, *22*, 1911.
(12) Milner, S. T.; McLeish, T. C. B. *Macromolecules* **1997**, *30*, 2159.
(13) Das, C.; Inkson, N. J.; Read, D. J.; Kelmanson, M. A.; McLeish, T. C. B. *J. Rheol.* **2006**, *50*, 207.
(14) (a) Larson, R. G. *Macromolecules* **2001**, *34*, 4556. (b) Wang, Z.; Chen, X.; Larson, R. G. *J. Rheol.* **2010**, *54*, 223.
(15) (a) van Ruymbeke, E.; Bailly, C.; Keunings, R.; Vlassopoulos, D. *Macromolecules* **2006**, *39*, 6248. (b) van Ruymbeke, E.; Orfanou, K.; Kapnistos, M.; Iatrou, H.; Pitsikalis, M.; Hadjichristidis, N.; Lohse, D. J.; Vlassopoulos, D. *Macromolecules* **2007**, *40*, 5941. (c) van Ruymbeke, E.; Muliawan, E. B.; Hatzikiriakos, S. G.; Watanabe, H.;

Hirao, A.; Vlassopoulos, D. *J. Rheol.* **2010**, *54*, 643. (d) van Ruymbeke, E.; Kapnistos, M.; Vlassopoulos, D.; Liu, C. Y.; Bailly, C. *Macromolecules* **2010**, *43*, 525.
(16) Kapnistos, M.; Vlassopoulos, D.; Roovers, J.; Leal, L. G. *Macromolecules* **2005**, *38*, 7852.
(17) Graessley, W. W. *Polymeric Liquids & Networks: Dynamics and Rheology*; Taylor & Francis: New York, 2008.
(18) (a) Park, S. J.; Larson, R. G. *J. Rheol.* **2003**, *47*, 199. (b) Park, S. J.; Larson, R. G. *Macromolecules* **2004**, *37*, 597. (c) Park, S. J.; Shanbhag, S.; Larson, R. G. *Rheol. Acta* **2005**, *44*, 319.
(19) van Ruymbeke, E.; Liu, C. Y.; Bailly, C. Quantitative Tube Model Predictions for the Linear Viscoelasticity of Linear Polymers. in *Rheology Reviews*; Binding, D. M., Hudson, N. E., Keunings, R., Eds.; The British Society of Rheology: Swansea, UK, 2007; pp 53−134.
(20) Raju, V. R.; Menezes, E. V.; Marin., G.; Graessley, W. W. *Macromolecules* **1981**, *14*, 1668.
(21) Auhl, D.; Chambon, P.; McLeish, T. C. B.; Read, D. *Phys. Rev. Lett.* **2009**, *103*, 136001.
(22) Watanabe, H.; Ishida, S.; Matsumiya, Y.; Inoue, T. *Macromolecules* **2004**, *37*, 6619.
(23) (a) Rubinstein, M.; Colby, R. H. *Polymer Physics*; Oxford University Press: New York, 2003. (b) Colby, R. H.; Rubinstein, M. *Macromolecules* **1990**, *23*, 2753.
(24) Milner, S. T. *Macromolecules* **2005**, *38*, 4929.
(25) Wang, Z.; Chen, X.; Larson, R. G. *J. Rheol.* **2010**, *54*, 223.
(26) Larson, R.; Wang, Z. *Dynamics of Entangled Polymers*, in press.
(27) Watanabe, H.; Ishida, S.; Matsumiya, Y.; Inoue, T. *Macromolecules* **2004**, *37*, 1937.
(28) (a) Kapnistos, M.; Koutalas, G.; Hadjichristidis, N.; Roovers, J.; Lohse, D. L.; Vlassopoulos, D. *Rheol. Acta* **2006**, *46*, 273. (b) Kirkwood, K. M.; Leal, L. G.; Vlassopoulos, D.; Driva, P.; Hadjichristidis, N. *Macromolecules* **2009**, *42*, 9592.
(29) Masubuchi, Y.; Takimoto, J.-I.; Koyama, K.; Ianniruberto, G.; Marrucci, G.; Greco, F. *J. Chem. Phys.* **2001**, *115*, 4387.
(30) Masubuchi, Y.; Watanabe, H.; Ianniruberto, G.; Greco, F.; Marrucci, G. *Macromolecules* **2008**, *41*, 8275.
(31) Watanabe, H.; Sawada, T.; Matsumiya, Y. *Macromolecules* **2006**, *39*, 2553.
(32) Watanabe, H.; Matsumiya, Y.; van Ruymbeke, E.; Vlassopoulos, D.; Hadjichristidis, N. *Macromolecules* **2008**, *41*, 6110.
(33) Watanabe, H.; Urakawa, O.; Kotaka, T. *Macromolecules* **1994**, *27*, 3525.
(34) Matsumiya, Y.; Watanabe, H.; Osaki, K. *Macromolecules* **2000**, *33*, 499.
(35) (a) Watanabe, H.; Ishida, S.; Matsumiya, Y. *Macromolecules* **2002**, *35*, 8802. (b) Watanabe, H.; Matsumiya, Y.; Inoue, T. *Macromolecules* **2002**, *35*, 2339.
(36) Wang, S.; Wang, S. Q.; Halasa, A.; Hsu, W. L. *Macromolecules* **2003**, *36*, 5355.
(37) Note that eq 5c is defined for the time t scaled with the shortest unit time τ_e, i.e., for $t = p\tau_e$ (p = 1, 2, ...), and thus eq 5c is still a discretized equation that determines the value of ϕ at the time t from the value of φ' at t and the value of ϕ at the past time $t - \tau_e$, as similar to a recurrence formula. In a formal sense, we may obtain the corresponding continuous expression of $d\phi(t)/dt$ by taking the limit of $\tau_e \to 0$, as explained in Appendix B2. However, the actual calculation was (and is to) made for the discretized form, eq 5c, because τ_e is the shortest unit time having the physical meaning for the entanglement relaxation. Concerning this point, one might argue that eq 5c is not well-defined because it gives the ϕ value only at a series of discretized times with the separation of τ_e. However, this is not the case. The CRR mechanism is activated negligibly at a time scale shorter than the relaxation time of the short chains $\tau_{rel,1}$ ($\gg \tau_e$), so that we can introduce an extended initial condition, $\phi(t) = \varphi'(t)$ for $\tau_e \le t \le 2\tau_e$. Then, eq 5c allows us to calculate $\phi(t)$ in a continuous sense, i.e., for *arbitrary* $t > 2\tau_e$, because $\varphi'(t)$ is dielectrically known in the entire range of t. In fact, eq 5c with this extended initial condition gave $\phi(t) = \varphi'(t)$ at t up to $\tau_{rel,1}$ of the short chain (well above $2\tau_e$), which lends support to this condition.
(38) Park, S. J.; Larson, R. G. *J. Rheol.* **2006**, *50*, 21.
(39) Khaliullin, R. N.; Schieber, J. D. *Macromolecules* **2010**, *43*, 6202.
(40) Watanabe, H.; Sakamoto, T.; Kotaka, T. *Macromolecules* **1985**, *18*, 1436.
(41) Watanabe, H.; Kotaka, T. *Macromolecules* **1984**, *17*, 2316.
(42) Wang, S.; Wang, S.; Halasa, A.; Hsu, W. L. *Macromolecules* **2003**, *36*, 5355.
(43) (a) Zhou, Q.; Larson, R. G. *Macromolecules* **2005**, *38*, 5761. (b) Zhou, Q.; Larson, R. G. *Macromolecules* **2006**, *39*, 6737.
(44) Foteinopoulou, K.; Karayiannis, N. C.; Mavrantzas, V. G.; Kröger, M. *Macromolecules* **2006**, *39*, 4207.
(45) Tzoumanekas, C.; Theodorou, D. N. *Macromolecules* **2006**, *39*, 4592.
(46) Hoy, R. S.; Robbins, M. O. *Phys. Rev. E* **2005**, *72*, 061802.
(47) Shanbhag, S.; Larson, R. G. *Phys. Rev. Lett.* **2005**, *94*, 076001.
(48) Stephanou, P. S.; Baig, C.; Tsolou, G.; Mavrantzas, V. G.; Kröger, M. *J. Chem. Phys.* **2010**, *132*, 124904.
(49) Kröger, M.; Ramírez, J.; Öttinger, H. C. *Polymer* **2002**, *43*, 477.

Macromolecules

Article

pubs.acs.org/Macromolecules

Nanoparticle Geometrical Effect on Structure, Dynamics and Anisotropic Viscosity of Polyethylene Nanocomposites

Ying Li,[†] Martin Kröger,[‡] and Wing Kam Liu*[,†,§]

[†]Department of Mechanical Engineering, Northwestern University, 2145 Sheridan Road, Evanston, Illinois 60208-0311, United States

[‡]Department of Materials, Polymer Physics, ETH Zurich, CH-8093 Zurich, Switzerland

[§]Visiting Distinguished Chair Professor, School of Mechanical Engineering, World Class University (WCU) Program in Sungkyunkwan University, Korea

ABSTRACT: Addition of nanoparticles into a polymer matrix can significantly alter its structure, dynamics as well as viscosity. In this paper, we study the structural, dynamical and viscous behaviors of polyethylene (PE) matrices under the influence of five differently shaped nanoparticles: buckyball, graphene, nanodiamond (ND), X-shaped and Y-shaped junctions, at fixed volume fraction (4 vol %). These nanoparticles have different surface-area-to-volume ratios, arranged as graphene, X-shaped junction, Y-shaped junction, buckyball, and ND, from the largest to the smallest. In turn, different interaction energies between nanoparticles and PE matrices are enabled according to their surface-area-to-volume ratios. The graphene sheet is expected to have the strongest interaction with the PE matrix in accord with its largest surface-area-to-volume ratio. The interaction between NDs and their PE matrix is the smallest, due to their truncated octahedron shapes and the smallest surface-area-to-volume ratio. However, the graphene sheets tend to aggregate at the PE melting temperature (450 K), lowering their interactions with the PE matrix. Because of this interplay, the interactions between nanoparticles and polymer matrices can be tailored through the shapes (also surface-area-to-volume ratios) of nanoparticles as well as their dispersions. The polymer chains are found to be densely packed around these nanoparticles in the range of 2 nm, except NDs, due to their strong interactions with PE matrices. Thus, these nanoparticles are found to be able to nucleate polymer entanglements around their surfaces and to increase the underlying entanglement densities of PE matrices. Both the polymer chain relaxation and anisotropic viscosity of PE nanocomposites are shown to be greatly affected by oriented nanoparticles. Our simulation results indicate that the surface-area-to-volume ratio of nanoparticles plays the dominated role in the structural, dynamical and viscous properties of PE nanocomposites.

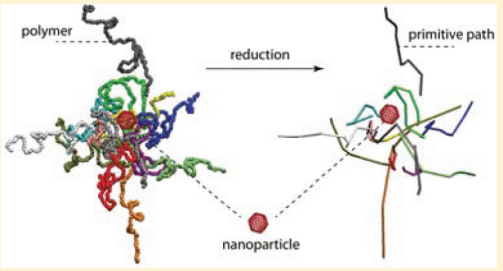

1. INTRODUCTION

The viscoelastic properties of polymers originate from their chain dynamics. For low molecular weight polymers, the viscosity is mainly induced by the monomer−monomer friction between different polymer chains (Rouse relaxation).[1] However, above the entanglement molecular weight M_e, the different polymer chains can mutually interpenetrate each other and self-entangle, driven by entropy. Since polymer chains cannot cross each other as they move, the dynamics of polymer chains is constrained (chain connectivity and uncrossability). Entanglements are commonly assumed to severely restrict the lateral motion of individual polymer chains into a tube-like region. The lateral motion of individual polymer chains is confined to the length scale of the tube diameter. Therefore, a polymer chain tends to move only back and forth, i.e. reptate, along the central axis of the tube, also denoted as primitive path (PP). The PP is considered as the shortest path remaining when one holds chain ends fixed, while continuously reducing (shrinking) a chain's contour without violating topological constrains (entanglements). Relaxation of a polymer chain is achieved by completely diffusing out of its original tube and forming another new tube. Such a conceptual framework, the tube model, developed by de Gennes[2] and later on generalized by Doi and Edwards,[3] has incorporated such a principle for studying the dynamics of polymer chains. The viscoelastic properties of polymers are described by the tube model within a mean-field approach[3] as the reptation is considered as a one-dimensional diffusion along the PP. Although the tube model can be used to capture the essential part of the entanglements dynamics, there are two refinements which have been incorporated to deal with PP contour length fluctuations (CLF)[4,5] and many-body effects. The latter, known as constraint release (CR),[4,6] considers the lateral softening of the confined tube, as both the chain and its virtual tube are equally moving under melt.

Fillers with dimensions on the micrometer scale are added into polymers in conventional polymer composites, as to enhance their mechanical properties. Such properties are highly related to volume fraction, shape and size of these fillers. If the size of fillers is on the nanometer scale, their mixtures with a

Received: October 12, 2011
Revised: January 23, 2012
Published: February 7, 2012

   dx.doi.org/10.1021/ma202289a | *Macromolecules* 2012, 45, 2099−2112

polymer matrix lead to so-called *polymer nanocomposites* (PNC). Compared to traditional polymer composites, the physical and mechanical properties of PNC can be remarkably enhanced by the addition of only a small volume fraction of nanoparticles. Therefore, PNC has attracted much interest both in industry and academia. The enhancement of mechanical performance of PNC, is mainly due to the nanoscale of fillers (because of extremely high surface-area-to-volume ratio), and to the strong polymer−nanoparticle interactions that can affect the loading transfer effectiveness between nanoparticles and polymer matrix. Since the motion of polymer chains is mainly constrained by entanglements for pure polymers, it is not hard to see that additional geometrical constraints are added into the pure polymers when the nanoparticles are infused. Therefore, the underlying PP network of polymers may also be affected by the presence of nanoparticles.

Several decades ago, Bueche assumed that entanglements nucleate at the surface of fillers, and effectively modify the underlying PP network of the polymer matrix.[7] Thus, the amount of surface area plays the major role in the reinforcement effect of nanoparticles.[7] More recently, Schneider et al[8] studied the dynamics of entangled polymer chains in PNC by neutron spin echo (NSE) experiments. They found that the basic Rouse relaxation rate was unaffected by the high volume fraction of nanoparticles.[8] However, the lateral confinement of polymer chains or tube diameter decreased with the increment of nanoparticle concentration, as a crossover from "polymer entanglements" to "nanoparticle entanglements" (chain motion is hindered by the fixed obstacles) occurs due to the geometrical confinement effect of these nanoparticles.[8] Our focus in this paper is then to investigate the microscopic origin of the observed behavior, as we study microscopic details such as entanglements, and orientations of polymer chains around nanoparticles, etc.

In recent years, computer simulations have successfully captured the PP network of polymers.[9−19] These simulation methods have been widely used for analyzing the PPs of polymer melts under both static and shear flow conditions.[9,10,12,13,17,20] The obtained results are useful for predicting and understanding viscoelastic properties of pure polymers.[21] Using these approaches, de Pablo and co-workers have done the pioneering works to study the PP network of entangled polymer matrix influenced by the spherical or rod-like nanoparticles.[20,22] They found that nanoparticles had significant impact on the entanglement network of the polymer matrix, served as entanglement attractors, especially at large deformations, which shed light on how the nanoparticles influence the viscoelastic properties of PNCs.[22] However, due to the limitation of computer power, many simulations have been limited to PNC with polymer chain lengths well below the entanglement molecular weight.[23−25] For the study of high molecular weight polymers, Monte Carlo (MC) methods are usually invoked, but they do not supply information about polymer chain dynamics. To overcome these shortcomings, we used the latest processor generation and performed long-time molecular dynamics (MD) simulations on polyethylene (PE) nanocomposites under the melt conditions. There are several aspects where this paper differs from past works. First, we simulate truly entangled PE nanocomposites at equilibrated conditions with differently shaped nanoparticles. The size of these nanoparticles is comparable with the size of polymer chains, which has great impact on the motion of PE polymer chains. Second, the effect of differently shaped nanoparticles on the structure and dynamical relaxation of PE matrix will be considered, which is directly related to the nanoparticle−polymer interactions. The dispersion/clustering effect of nanoparticles is also considered in this work. Third, the underlying PP networks of PE matrices with different nanoparticles are extracted by modified Z1 code,[15] as well as the underlying entanglement distributions, which can help us to understand how the viscoelastic properties of PNC will be affected by different nanoparticles. In short, we will study the effects of nanoparticle shape and their dispersion/clustering on the structure, dynamics, PP network and anisotropic viscosity of PE matrices, having in mind targeting a rational design of PNCs with optimal structural and mechanical properties.

2. MODEL AND METHODOLOGY

Carbon-based nanoparticles, i.e., singled-walled carbon nanotubes (SWNTs), are well-known for their extremely high mechanical properties (Young's modulus is around 1−5TPa and tensile strength is 100−150 GPa).[26,27] They have attracted much interest as reinforcing nanoparticles in PNC. In this paper, five different shapes of carbon components, i.e., buckyball, graphene, nanodiamond (ND), X-shaped SWNT junction and Y-shaped SWNT junction as shown in Figure 1,

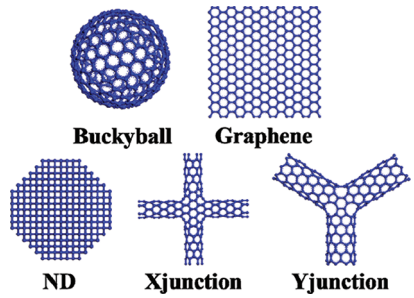

Figure 1. Models of buckyball, graphene, nanodiamond (ND), Xjunction and Yjunction used in PE nanocomposites. All these carbon nanoparticles have sp^2 bonds, except the ND (sp^3 bonds), which are indicated by the dots around covalent bonds. The shape of the ND is a truncated octahedron.

are used to generate different PE nanocomposites. The specifications of all these nanoparticles are summarized in Table 1. Here the graphene sheet was cut along armchair and

Table 1. Geometrical Details for Carbon Nanoparticles Used in This Work

	buckyball	graphene	ND	Xjunction	Yjunction
size (Å)	diameter 16.15	length 29	diameter 21.0	diameter 4.70	diameter 6.26
		width 29.8		length 14.66	length 14.82
carbon atoms	320	336	813	332	332

zigzag directions, where length and width were along zigzag and armchair directions, respectively. The shape of ND is round-like, i.e., a truncated octahedron. A (6,0) SWNT with length 14.66 Å was utilized for the construction of the X-shaped SWNT junction. However, the Y-shaped SWNT junction was built from a (8,0) SWNT with length 14.82 Å. The details for constructing X-shaped and Y-shaped SWNT junctions can be found in refs 28−30. All the covalent bonds in these carbon

nanoparticles are sp^2 bonds, except for the ND, which has sp^3 bonds. Although the surface of ND can form some sp^2 bonds, we do not consider these sp^2 bonds and simplify them into sp^3 bonds in our simulations. The pure PE polymer and PE matrices were represented by united atom $-CH_2-$ units, which were connected to form a straight, linear PE polymer chain. In order to study entangled and high-molecular-weight polymers, we considered PE polymers with N = 240 monomers per chain in the current work with molecular weight M_w = 3362 g/mol. The entanglement length, N_e, defined as the ratio between the number of monomers and the mean number of entanglements per chain, is about 56−86 at 463 K, according to different experimental and simulations results.[12,13,21] The PE polymer studied in the current work is truly entangled as N/N_e = 2.79−4.28.

The molecular model for pure PE was generated with the Amorphous Cell Module in Materials Studio[31] using the self-avoiding random walk technique.[32] The initial molecular structures of PE nanocomposites were obtained through positioning the center of each nanoparticle coincident with the center of its cubic simulation box, while symmetric planes of the nanoparticle were parallel to the facets of the simulation box. Then, PE polymer chains were randomly generated around nanoparticles and used for filling the simulation box based on the self-avoiding random walk technique.[32] These nanoparticles were added into PE matrices at approximately 4 vol %. After initial configurations were generated, all these models were repeated once along x, y and z directions of the simulation box to obtain the initial systems with large enough samples (polymer chains). Therefore, each PE nanocomposite has 8 nanoparticles, which are initially arranged into a cubic crystal-like structure. The number of polymer chains and geometry size for the initial pure PE and PE nanocomposite models are listed in Table 2. In order to simplify notations, the terms PE/Bucky, PE/Graphene, PE/ND, PE/Xjunction and PE/Yjunction are used for PE/buckyball, PE/graphene, PE/ND, PE/X-shaped junction and PE/Y-shaped junction nanocomposites, respectively. The pure PE polymer is also abbreviated as PE. Once the initial molecular structures are obtained, the corresponding force field should be assigned for future MD simulations. The PE polymer chain was described by appropriate bond, angle and dihedral, as well as nonbonded van der Waals (vdW) interactions. The united-atom representation for PE is adopted in this work as carbon atoms along with their bonded hydrogen atoms are lumped into single interacting sites. The methylene (CH_2) and methyl (CH_3) groups are treated as equivalent sites for all bonded interactions, but, not for vdW interactions. Such a united-atom model has been widely used and verified for studying diffusion and melting behaviors of PE polymers.[9,13,17,18,33−38] In order to explore the nanoparticle shape effect on PE matrices, all these carbon nanoparticles were modeled as nondeformable rigid bodies.[39] The bond length for these nanoparticles with sp^2 and sp^3 bonds was fixed to be 1.42 and 1.54 Å, respectively. The interactions between different nanoparticles are also modeled by vdW potentials. The potential forms with corresponding parameters are summarized in Table 3. The vdW interactions between PE monomers and carbon atoms of nanoparticles were obtained through the Lorentz−Berthelot rules of the 12−6 Lennard-Jones potentials between their vdW potential parameters. All the MD simulations were performed using the LAMMPS package supplied by Sandia National Laboratory.[40] Periodic boundary conditions were used as the simulation box was considered to be a representative volume element (RVE). The time step for MD simulations was 1.0 fs. All the simulations have been done at 450 K.

Table 2. Initial Simulation Box Size at Melt Temperature (450 K) and Polymer Chain Numbers of Pure PE Polymer and Its Nanocomposites[a]

	PE	PE/ Bucky	PE/ Graphene	PE/ ND	PE/ Xjunc-tion	PE/ Yjunction
side length (Å)	97.0	95.4	84.2	104.6	87.3	95.3
polymer chain number	112	104	72	136	80	104

[a]The volume fractions of nanoparticles are fixed to be 4 vol %.

Table 3. Functional Forms and Parameters for the Force Fields of PE and Carbon Nanoparticles Used in This Paper

interaction type (potential type)	functional form	parameters
bond (harmonic)	$U(r) = k_r(r - r_0)^2$	k_r = 419.518 kcal/mol/Å^2, r_0 = 1.54 Å
angle (harmonic)	$U(\theta) = k_\theta(\theta - \theta_0)^2$	k_θ = 62.09 kcal/mol/deg^2, θ_0 = 114°
dihedral (multiharmonic)	$U(\phi) = \sum_{i=0,3} a_i \cos^i(\phi)$	a_0 = 1.736 kcal/mol, a_1 = 4.500 kcal/mol
		a_2 = 0.764 kcal/mol, a_3 = −7.000 kcal/mol
nonbonded (Lennard-Jones)	$U(r) = 4\varepsilon[(\sigma/r)^{12} - (\sigma/r)^6]$	ε_{CH_3} = 0.227 kcal/mol, σ_{CH_3} = 4.01 Å
		ε_{CH_2} = 0.093 kcal/mol, σ_{CH_2} = 4.01 Å
		ε_C = 0.105 kcal/mol, σ_C = 3.367 Å

3. SELF-ASSEMBLY BEHAVIOR OF NANOPARTICLES

As the initial arrangement of the carbon nanoparticles is cubic crystal-like, we have carried out long MD simulations for all these PE nanocomposites to reach their equilibrium states. The simulations have been done under the NPT ensemble (p = 1 atm and T = 450K) at a time step 1 fs for a duration of 200 ns. The shapes of nanoparticles are fixed through "rigid body" constraints.[39] The pair distribution functions $g(r)$ between different nanoparticles and their interaction energies have been monitored during the relaxation process. Interestingly, we find that nanoparticles tend to self-assemble, $g(r)$ systematically increases with time at short distances within the first 100 ns (Figures 2a−e). Accordingly, the interaction energies between nanoparticles increase with time and finally reach a constant value (Figure 2f). After 100 ns, the aggregated nanoparticle structure has been established. Figure 3 shows the equilibrated structures of pure PE and PE nanocomposites. We clearly see that all the nanoparticles in PE nanocomposites are clustered together. Starr et al. have studied the underlying clustering mechanisms of nanoparticles inside nanocomposites and obtained corresponding phase diagrams.[23] They found that the crossover from the dispersed to the clustered state of nanoparticles is in good agreement with predictions from equilibrium particles association or equilibrium polymerization, but, not the first-order phase separation model.[23] The critical volume fraction φ for nanoparticle self-aggregation is related to

dx.doi.org/10.1021/ma202289a | Macromolecules 2012, 45, 2099−2112

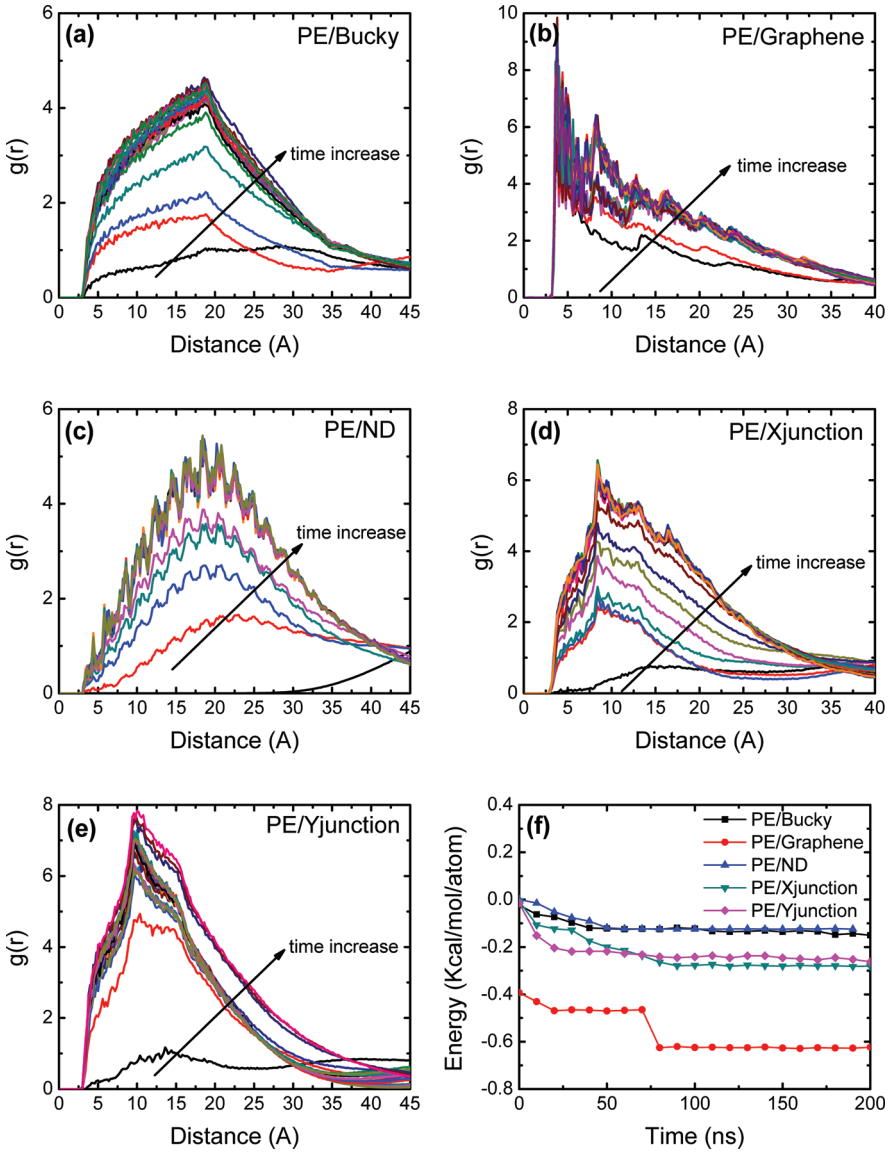

Figure 2. Evolution of pair distributions $g(r)$ between nanoparticles during the relaxation process for (a) PE/Bucky, (b) PE/Graphene, (c) PE/ND, (d) PE/Xjunction, and (e) PE/Yjunction at 450 K. The interaction energy between different nanoparticles is shown in part f.

the processing temperature as $\phi \sim \exp(-E_1^*/T^*)$, where E_1^* and T^* denote the thermal activation energy, $E_1^* = 6.9$, and system temperature in reduced LJ units, respectively.[23] As we know, the reduced temperature $T^* = 1$ corresponds to $T =$ 443Kfor pure PE.[41] Therefore, the critical volume fraction for nanoparticle clustering is only about 0.1 vol % in PE nanocomposites at 443 K, a value small compared to the 4 vol % employed here. To study well dispersed nanoparticles at 4 vol % in PE nanocomposites, the processing temperature should be set to 207 K. This is one of the reasons why the solid-state shear pulverization (SSSP) process can produce the well dispersed particles in PNCs as the processing is always under low temperature.[42]

As the nanoparticles tend to cluster, we consider two situations to explore the nanoparticle dispersion/clustering effect. One is an artificial, uniform nanoparticle distribution, denoted by 'U' (cubic crystal-like arrangement) as given in the initial conditions. The other is the fully equilibrated, more random distribution so-called 'R' as shown in Figure 3. The PE nanocomposites with uniformly dispersed nanoparticles are also equilibrated under the NPT ensemble (p = 1 atm and T = 450 K) for 100 ns, while all the motions of nanoparticles are frozen in this process to keep their arrangement fixed. The vdW surfaces and volumes of the 8 nanoparticles under both situations are listed in Table 4. The vdW radius of each carbon atom of a nanoparticle is considered as 3.4 Å (Table 3). These nanoparticles can be arranged as graphene, Xjunction, Yjunction, buckyball, and ND, according to their aspect ratios from the largest to the smallest. Such an order will be directly related to the structural, dynamical and viscous properties of PE nanocomposites, which we will discuss later. We can also see that both the vdW surfaces and volumes of the carbon nanoparticles reduce after the clustering, and that this effect is especially pronounced for graphene. Prior to self-aggregation, the graphene nanoparticles have the largest surface over volume aspect ratio as 0.731 $Å^{-1}$. This value drops to 0.551 $Å^{-1}$ after the clustering occurred. This phenomenon is directly related to the interactions between nanoparticles and PE matrices, which can help us to understand their viscous behaviors, to be discussed in the following parts.

dx.doi.org/10.1021/ma202289a | *Macromolecules* 2012, 45, 2099–2112

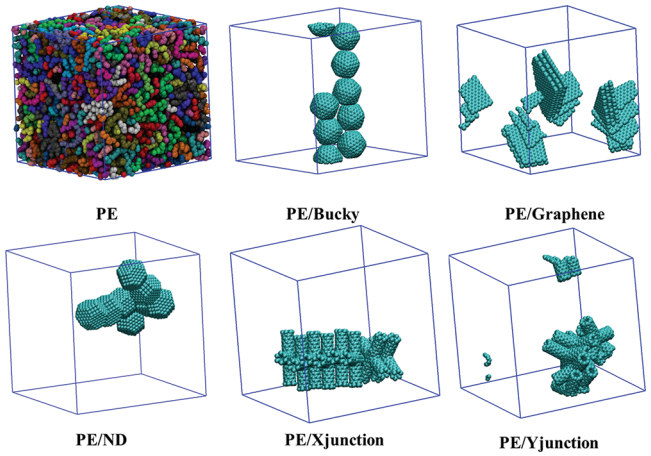

Figure 3. Equilibrated configurations for pure PE, PE/Bucky, PE/Graphene, PE/ND, PE/Xjunction, and PE/Yjunction at 450 K. All the nanoparticles are self-assembled together in the equilibration process. The simulation boxes are represented by blue lines. The different polymer chains are colored differently (randomly) in PE. In PE nanocomposites, all the polymer chains are made invisible for clarity of carbon nanoparticles. The volume fractions of all these carbon nanoparticles are fixed to be 4 vol %.

4. POLYMER CHAIN DYNAMICS

By using the well-equilibrated initial configurations of pure PE and PE nanocomposites (with both uniformly dispersed and clustered nanoparticles), all these models are further relaxed by NPT simulations (p = 1 atm and T = 450 K) for another 100 ns with time step 1.0 fs. In this process, all the motions of nanoparticles are frozen to keep their positions fixed. Both the end-to-end unit vector autocorrelation function $\langle \mathbf{u}(t)\cdot\mathbf{u}(0)\rangle$ and the mean-squared displacement (MSD) of PE polymer chains have been recorded to study the polymer chain dynamics. Figure 4 shows $\langle \mathbf{u}(t)\cdot\mathbf{u}(0)\rangle$ of PE chains exponentially decreasing with increasing time. For both uniformly dispersed and clustered nanoparticles, the dynamics of corresponding PE chains are slowed down in the presence of nanoparticles. We have fitted the $\langle \mathbf{u}(t)\cdot\mathbf{u}(0)\rangle$ curves with the function $\exp(-(t/\tau_e)^{\beta})$, where τ_e and β represent two fitting parameters. Ideally, β equals unity for Rouse chains and τ_e is the corresponding relaxation time. As the molecular weight of PE chains in this work is well above the entanglement molecular weight M_e, the dynamics of PE chains will be further constrained by entanglements and $\beta < 1$. We can see that the larger the relaxation time τ_e is, or the smaller β is, the slower the polymer chain relaxation is. The obtained values for τ_e and β are given in Table 5. The relaxation time of PE nanocomposites is always larger than that of the pure PE. Therefore, the dynamics of the PE polymer chains is crucially affected by the carbon nanoparticles. From $\langle \mathbf{u}(t)\cdot\mathbf{u}(0)\rangle$ curves of uniformly dispersed PE nanocomposites (Figure 4a), we can see that theses curved can be classified into three categories. The first one is pure PE, which has the fastest relaxation. The second one contains PE/buckyball, PE/ND and PE/Yjunction. The third one includes PE/graphene and PE/Xjunction, which have the slowest relaxation. These visual observations are in good agreement with the estimated relaxation times τ_e shown in Table 5. As qualitatively expected from the theory of ellipsoids of revolution,[43] the relaxation time τ_e follows a similar trend as the surface-area-to-volume ratio shown in Table 4: the larger the surface-area-to-volume ratio, the longer the relaxation time. Compared with the uniformly dispersed nanoparticles, the equilibrated PE nanocomposites with clustered nanoparticles exhibit faster relaxation, a point to be discussed in the following part. The MSD curves of these pure PE and PE nanocomposites show a similar trend (results not shown).

There are two important factors influencing the dynamical behavior of polymer chains in PNCs: first, the geometrical constraints or "particle entanglements" imposed by these nanoparticles, mainly characterized by the interactions between polymer matrix and nanoparticles, and second, the underlying topological change of the polymer matrix, i.e., entanglement density. Obviously, it is hard to distinguish between the two factors as they tend to be correlated. In this work, we will investigate these two effects qualitatively by studying the interaction energy between nanoparticles and polymer matrix, and the entanglement distribution through a PP network analysis. The nanoparticle−monomer pair correlation function $g_{12}(r)$ is determined to characterize local packing density of polymer chains around the nanoparticles as well as their interactions (Figure 5). We recall that the atomistic motions of nanoparticles are frozen in the underlying MD simulations. The $g_{12}(r)$ curve for PE/Bucky is basically identical with the one presented earlier by Adnan.[34] We observe that $g_{12}(r)$ vanishes between 0 and 3.4 Å for all these PE nanocomposites, and hereafter gradually increases with radial distance. The depleted region reflects the vdW wall thickness, which is identical for all these PE nanocomposites.[34] The intensity of $g_{12}(r)$ for all nanocomposites reaches a first peak at ≈5.0 Å, except for PE/ND, which does not exhibit any peak at this radial distance. The relative distribution of PE monomers as indicated by $g_{12}(r)$ is affected by the shape of nanoparticles. Apparently, more PE monomers tend to aggregate around the PE/Graphene interface compared with the other nanocomposites. There is also a sharper second peak in $g_{12}(r)$ for these nanocomposites at a radial distance smaller than 1.5 nm, except for PE/Bucky and PE/ND, presumably due to the low geometric symmetry of these nanoparticles. The interaction energies between nanoparticles and PE matrices are listed in Table 5. It can be seen that PE/Graphene has the largest interaction energy, while, PE/ND has the smallest. From the largest to the smallest interaction energy, these PE nanocomposites can be arranged

Table 4. Van der Waals Surface, S_{vdW}, and Volume, V_{vdW}, for Carbon Nanoparticles before and after Self-Assembling[a]

nanoparticles	S^U_{vdW} (Å^2)	V^U_{vdW} (Å^3)	S^U_{vdW}/V^U_{vdW} (Å^{-1})	S^R_{vdW} (Å^2)	V^R_{vdW} (Å^3)	S^R_{vdW}/V^R_{vdW} (Å^{-1})
PE/Bucky	9846	30 325	0.325	9301	29 144	0.319
PE/Graphene	18 355	25 093	0.731	12 859	23 350	0.551
PE/ND	14 448	45 588	0.317	12 821	45 608	0.281
PE/Xjunction	13 603	24 184	0.562	12 604	24 059	0.524
PE/Yjunction	12 356	25 028	0.494	11 466	25 173	0.455

[a]The superscripts "U" and "R" denote the uniformly dispersed and clustered nanoparticles, respectively.

dx.doi.org/10.1021/ma202289a | Macromolecules 2012, 45, 2099−2112

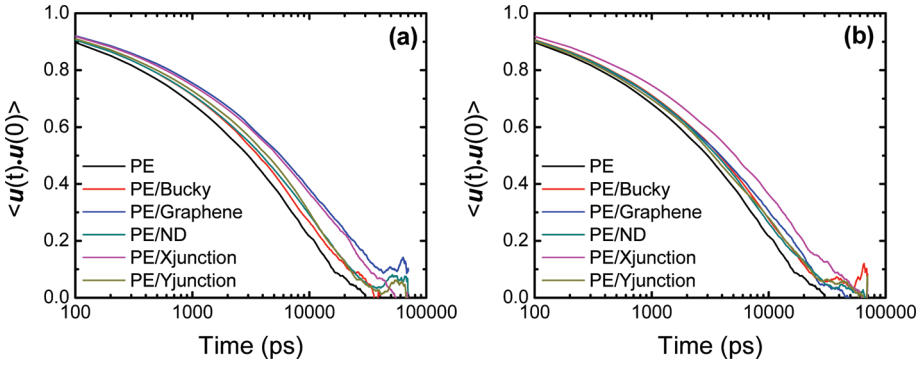

Figure 4. End-to-end unit vector autocorrelation function $\langle \mathbf{u}(t)\cdot\mathbf{u}(0)\rangle$ for PE polymer chains with (a) uniformly dispersed and (b) clustered nanoparticles at 450 K, respectively.

Table 5. Fitted Relaxation Time τ_e and Parameter β for End-to-End Unit Vector Autocorrelation Function $\langle \mathbf{u}(t)\cdot\mathbf{u}(0)\rangle = \exp(-(t/\tau_e)^{\beta})$, Nanoparticle−Polymer Interaction Energy per Atom E_{PE_Carbon}, Root of the Mean-Squared End-to-End Distance $\langle R_{ee}^2\rangle^{1/2}$ and Radius of Gyration $\langle R_g^2\rangle^{1/2}$ for PE Polymer Chains as Well as Their Shear Viscosities (Shear Strain Rate 10^9/s) at 450 K[a]

	τ_e (ns)	β	E_{PE_Carbon} (kcal/mol/atom)	$\langle R_{ee}^2\rangle^{1/2}$ (Å)	$\langle R_g^2\rangle^{1/2}$ (Å)	shear viscosity (cP)
PE	5.08	0.662	0	51.1 ± 1.7	20.7 ± 0.4	3.96 ± 0.45
PE/Bucky	6.30 (U)	0.633 (U)	−0.73 (U)	50.6 ± 1.8(U)	20.2 ± 0.3(U)	5.03 ± 0.63 (I)
	6.58 (R)	0.626 (R)	−0.60 (R)	53.4 ± 1.2(R)	20.9 ± 0.4(R)	5.10 ± 0.54(O)
PE/Graphene	10.68 (U)	0.554 (U)	−1.14 (U)	50.2 ± 2.1(U)	20.0 ± 0.3(U)	3.21 ± 1.03 (I)
	7.19 (R)	0.571 (R)	−0.79 (R)	50.5 ± 3.0(R)	20.5 ± 0.4(R)	14.0 ± 3.17(O)
PE/ND	6.89 (U)	0.615 (U)	−0.38 (U)	51.8 ± 1.4(U)	21.8 ± 0.3(U)	4.11 ± 0.47 (I)
	6.27 (R)	0.620 (R)	−0.31 (R)	53.2 ± 1.2(R)	21.9 ± 0.2(R)	4.50 ± 0.42(O)
PE/Xjunction	9.91 (U)	0.562 (U)	−0.81 (U)	54.2 ± 2.5(U)	21.2 ± 0.3(U)	4.95 ± 0.82 (I)
	9.46 (R)	0.578 (R)	−0.58 (R)	52.2 ± 1.9(R)	20.7 ± 0.5(R)	8.98 ± 1.24(O)
PE/Yjunction	7.25 (U)	0.652 (U)	−0.79 (U)	54.3 ± 1.3(U)	21.1 ± 0.4(U)	5.16 ± 0.68(I)
	6.30 (R)	0.583 (R)	−0.55 (R)	51.9 ± 1.4(R)	20.4 ± 0.3(R)	6.52 ± 0.88(O)

[a]"U" and "R" represent the uniformly dispersed and clustered nanoparticle systems, respectively. "I" and "O" denote the in-plane and out-of-plane directions of the PE nanocomposites with uniformly dispersed nanoparticles.

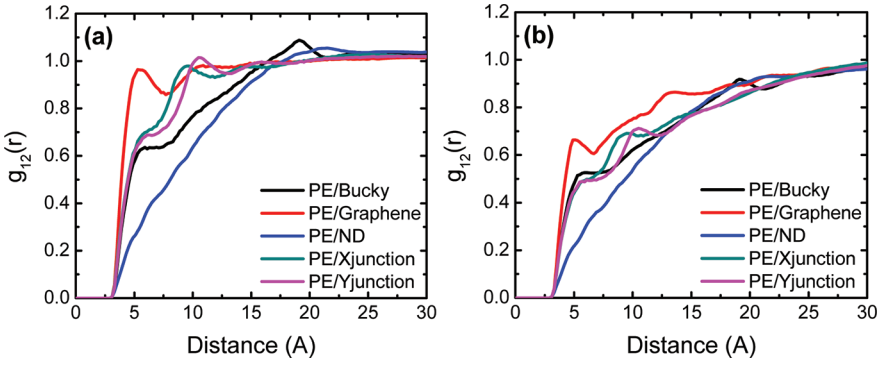

Figure 5. Nanoparticle−monomer pair distribution function $g_{12}(r)$ for PE nanocomposites with (a) uniformly dispersed and (b) clustered nanoparticles at 450 K.

as PE/Graphene, PE/Xjunction, PE/Yjunction, PE/Bucky, and PE/ND, which agrees reasonably well with their surface-area-to-volume ratios (Table 4). Such an order is also in good agreement with our $g_{12}(r)$ calculations (Figure 5a) and polymer chain relaxation (Figure 4a and Table 5). It is clearly shown that the stronger the nanoparticle-monomer interaction, the denser the packing of polymer chains around nanoparticles, and the slower polymer chains dynamics. When these nanoparticles are clustering together, the packing density of polymer chains around nanoparticles reduces (Figure 5b) as their vdW surface amount decreases (Table 4), leading to a reduction of the interaction energies between nanoparticles and PE matrices (Table 5). For uniformly dispersed carbon nanoparticles, their interaction energy with the PE matrices is about 0.16−0.19 (kcal/mol)/Å^2. When these nanoparticles aggregate, this energy lowers further, down to 0.12−0.17 (kcal/mol)/Å^2. Recent experiments reported interaction energy between carbon black and styrene butadiene/silica rubber of only about 0.038 (kcal/mol)/Å^2.[44] Since carbon blacks are highly aggregated, it is important to make them well dispersed in the polymer matrices to improve their mechanical properties.

After the interaction energies between nanoparticles and PE matrices are known, it is interesting to explore how the global polymer chain conformation is affected by nanoparticles as a

dx.doi.org/10.1021/ma202289a | Macromolecules 2012, 45, 2099−2112

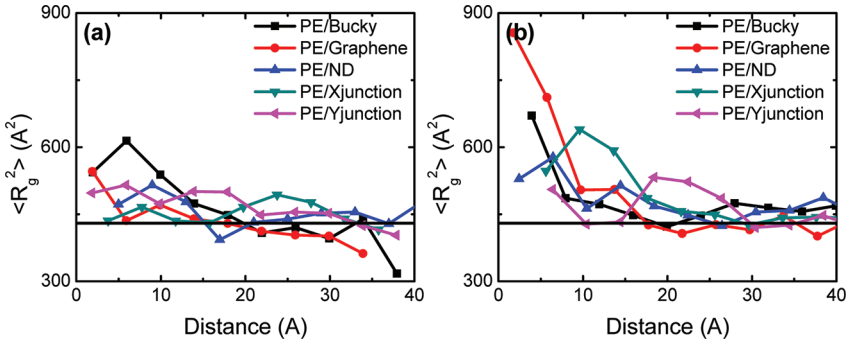

Figure 6. Mean-squared radius of gyration $\langle R_g^2 \rangle$ of PE polymer chains at 450 K around (a) uniformly dispersed and (b) clustered nanoparticles as a function of their centers of mass from the center of the carbon nanoparticle. The horizontal line indicates the mean-squared radius of gyration of pure PE (~430 Å^2) in the bulk.

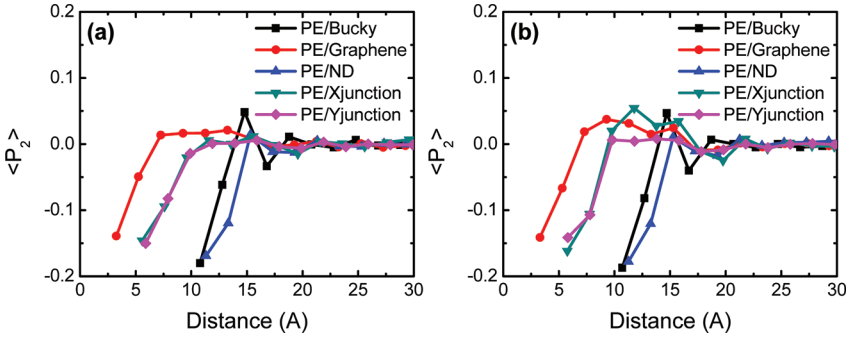

Figure 7. Mean second Legendre polynomial $\langle P_2 \rangle$ between the vector from the center of the nanoparticle to the monomer i and the vector between i and the next monomer in the same PE polymer chain $i + 1$ with (a) uniformly dispersed and (b) clustered nanoparticles. The distance is from the centers of mass of these nanoparticles to the monomer i. A preferential alignment of the polymer chains parallel to the surface of the nanoparticle is observed.

function of the distance from the surface of nanoparticles to the centers of masses of the polymer chains. Since the surfaces of carbon nanoparticles studied by us are very irregular, except for buckyball and ND, we instead monitor the distance from the center of nanoparticles to the center of mass of each polymer chain. As we have 8 nanoparticles in each PE nanocomposite, the distance from the center of each nanoparticle to the center of mass of a single polymer chain is calculated first. The minimum value of these distances is the closest distance between a given polymer and a nanoparticle. The mean-squared radius of gyration $\langle R_g^2 \rangle$ of this polymer is recorded at the same time. Figure 6 shows the $\langle R_g^2 \rangle$ of polymer chains as a function of their distance from the center of the nearest nanoparticle for PE nanocomposites with both uniform and random dispersed nanoparticles. The conformation profiles of the PE polymer chains are slightly affected by the different shapes of nanoparticles. When the polymer chains are very close (<1 nm) to a nanoparticle in a system of well dispersed nanoparticles, they tend to be stretched as their $\langle R_g^2 \rangle$ values are about 1.1−1.4 times of the $\langle R_g^2 \rangle$ value of pure PE in its bulk state. Such a behavior is also observed by Starr et al.[45] and Ndoro et al.[46] The reference value 430 Å^2 is obtained from the pure PE system. At distances larger than 2 nm, the $\langle R_g^2 \rangle$ approaches the bulk behavior of PE. Therefore, if the interphase thickness is considered responsible for peculiarities concerning chain extension, it should be also in this range. After the nanoparticles are clustered together, the $\langle R_g^2 \rangle$ profiles are greatly changed (Figure 6b). Polymer chains close to these clustered nanoparticles are highly stretched as the $\langle R_g^2 \rangle$ value is about 1.2−2.0 times the bulk value. As the clustered nanoparticles become very close to each other, they can be easily bridged by the polymer chains.[44] In this state, a polymer chain can be highly stretched and its $\langle R_g^2 \rangle$ value is greatly increased. Such a bridging behavior is related to the nonlinear viscoelastic properties of PNCs, i.e., Payne effect.[44,47] The averaged values of end-to-end distance $\langle R_{ee}^2 \rangle^{1/2}$ and $\langle R_g^2 \rangle^{1/2}$ for PE chains are listed in Table 5. $\langle R_{ee}^2 \rangle \approx 6 \langle R_g^2 \rangle$ for pure PE indicates that it behaves as Gaussian coils. Interestingly, all the PE polymer chains have similar values of $\langle R_{ee}^2 \rangle^{1/2}$ and $\langle R_g^2 \rangle^{1/2}$.

Since the polymer chains are stretched near the surface of nanoparticles, their orientation might also be affected. To this end we calculate the second Legendre polynomial $P_2 = (3 \cos^2\theta - 1)/2$, where θ is the angle formed between the vector connecting the center of the nanoparticle and monomer i, and the vector between i and the next monomer in the same PE polymer chain $i + 1$. The average orientation of the polymer chains is defined by taking the ensemble average $\langle P_2 \rangle$. Here $\langle P_2 \rangle = 0$ indicates a random orientation and $\langle P_2 \rangle = -0.5$ for perfect tangential alignment.[48] Figure 7 shows the $\langle P_2 \rangle$ as a function of distance from the center of nanoparticles to the center of mass of a polymer chain. When polymer chains are very close to the surface of nanoparticles, they are preferentially aligned tangentially to the surface of these nanoparticles as $\langle P_2 \rangle = -0.2$ to -0.15. Moving away from the nanoparticle surface to the bulk polymer, $\langle P_2 \rangle$ values gradually increase to zero, indicating they are randomly packed. Similar observations have been reported by Ndoro et al.[46] They found that the averaged orientational angle $\langle \theta \rangle$ was around 85° ($\langle P_2 \rangle = -0.49$, if all angles are identical) when the polymer chains were near the spherical particle surfaces.[46] As the distance increases, $\langle \theta \rangle$

dx.doi.org/10.1021/ma202289a | Macromolecules 2012, 45, 2099−2112

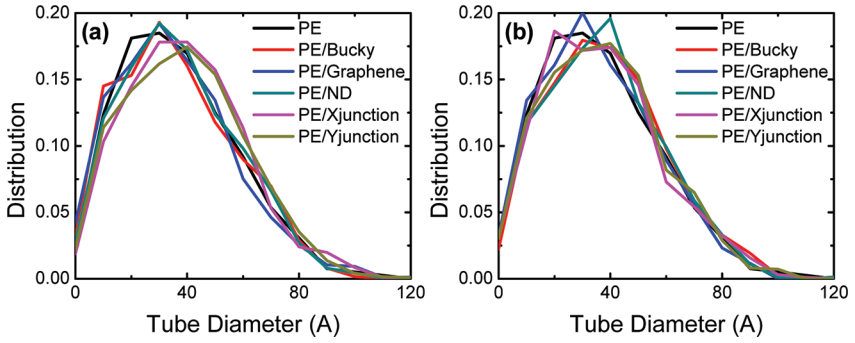

Figure 8. Distribution of tube diameter a_{pp} of pure PE and PE matrices with (a) uniformly dispersed and (b) clustered nanoparticles (see Appendix for details).

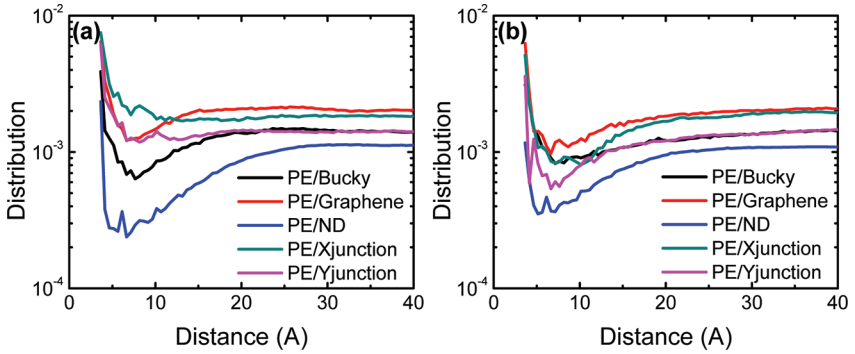

Figure 9. Nanoparticle-entanglement pair distributions of PE matrices with (a) uniformly dispersed and (b) clustered nanoparticles (see Appendix for details).

steadily decreases to approach its expected bulk value 57.3° ($\langle P_2\rangle = -0.06$).[46] Obviously, the local orientational order only persists to a very short distance from the center of nanoparticles, i.e., 2 nm, small compared with the polymer chain extension measured by the root mean-square radius of gyration (Figure 6). Within view of Figure 6, the clustering effect of nanoparticles on the $\langle P_2\rangle$ profiles is quite small as shown in Figure 7, and can even be ignored. In summary, the nanoparticles dispersion affects mainly the conformation of polymer chains, but not their orientations.

5. PRIMITIVE PATH ANALYSIS ON PE NANOCOMPOSITES

As the motion of polymer chains and their viscosity are known to be determined by their PP networks, the original Z1 code[14,15] and its modified version, able to deal with nanoparticles, have been applied to pure PE polymer and PE nanocomposites to extract and study their PP networks (see Appendix for details). The obtained contour length of PP for pure PE is $\langle L_{pp}\rangle$=67.22 ± 2.88 Å, which agrees reasonably well with existing simulation results.[12] Also, from $\langle R_{ee}^2\rangle$ and$\langle L_{pp}\rangle$, we can calculate the corresponding tube diameter of pure PE as $\langle a_{pp}\rangle = \langle R_{ee}^2\rangle/\langle L_{pp}\rangle$ =38.69 Å, which is again in good agreement with both experimental ($\langle a_{pp}\rangle$ = 32.8 Å with unknown M_w at 413 K[49]) and simulation ($\langle a_{pp}\rangle$ = 37 Å with M_w = 3.36 kg/mol at 450 K[12]) results. The average number of entanglements per chain $\langle Z\rangle$ for pure PE with M_w = 3.36 kg/mol studied in the current work is about 2.00 ± 0.11. Therefore, we obtain an entanglement molecular weight $M_e = M_w/\langle Z\rangle$=1.68 kg/mol, in agreement with both experimental and computational works (M_e = 0.79−1.2 kg/mol).[21] Since the lateral motion of polymer chains is confined in the range of the tube diameter a_{pp}, it is interesting to see the distribution of a_{pp} for each polymer chain under the influence of the nanoparticles. Figure 8 shows the distribution of a_{pp} for pure PE and PE nanocomposites with both uniformly dispersed and clustered nanoparticles. Interestingly, all these distributions follow the same trend, as the most favorable value for a_{pp} is about 10−60 Å (with probability >0.1). The distribution is well characterized by a beta function.[12] The peaks for the a_{pp}distributions of PE nanocomposites are slightly shifted to higher values, as well as their mean values ($\langle a_{pp}\rangle$ = 40−43 Å). Such an observation also agrees reasonably well with recent experimental results.[8] Schneider et al. found that the polymer chains in PNCs gradually disentangle as the volume fraction of nanoparticles increases, due to the transformation from "polymer entanglements" to "nanoparticles entanglements".[8] Therefore, the corresponding tube diameter $\langle a_{pp}\rangle$ of polymer matrices will also be gradually increased due to disentanglement, furthermore supported by mean-field theory.[8] The predicted critical volume fraction is 35 vol %.[8] When the volume fraction of nanoparticles is above 35 vol %, the polymer chain is expected to be completely disentangled and its motion is dominated by the geometrical constraints due to the nanoparticles.[8] Similar to the distribution of tube diameter a_{pp}, the distributions of contour length of PP, L_{pp}, and the number of entanglements per chain, Z, for PE matrices are similar to that of pure PE polymer (Gaussian distributions, results not shown here). The dispersion/clustering effect of nanoparticles on the PP networks of PE matrices is negligible as shown in Figure 8. Since our nanoparticle concentration is only 4 vol %, we also do not expect to observe huge changes of the PP network of PE matrices, compared with pure PE. The PP network of PNCs

dx.doi.org/10.1021/ma202289a | Macromolecules 2012, 45, 2099−2112

with highly loaded nanoparticles will be studied in our future work.

After the PP networks of PE matrices are extracted, we have access to the spatial distribution of entanglements. Figure 9 shows the pair distributions of nanoparticles to the entanglements of PE matrices. It is interesting to see that there are highly condensed entanglements near the nanoparticles surfaces, which is about 5−6 times of their bulk states. However, moving away from these nanoparticles surfaces to bulk polymer, the entanglement density rapidly drops, reaches a global minimum, and then gradually increases to a constant value. Because of the different nanoparticle shapes, the global minimum and bulk state—at a given concentration—of entanglement density are also changed. For the higher interaction energies, PE/Graphene and PE/Xjunction have larger bulk states of entanglement density than others. Also, PE/ND has the smallest global minimum and bulk state of entanglement densities, as the interaction between ND and PE matrix is very small (Table 5). Since polymer dynamics are constrained by entanglements as well as their densities, the geometrical confinement effect of nanoparticles on polymer chain entanglements is expected to affect the dynamics of these polymer chains. This picture is supported by the relaxation behavior of polymer chains in PE/Graphene and PE/Xjunction where it is significantly slowed down, compared to other PE nanocomposites and pure PE (Figure 4 and Table 5). Because of the dispersion/clustering effect, the bulk state of entanglement densities are also slightly decreased, as the interaction energies between nanoparticles and PE matrices are reduced (Table 5). The length scale for the variation of entanglement densities is around 2 nm, which is already present in the $\langle R_g^2 \rangle$ and $\langle P_2 \rangle$ profiles. Therefore, it is reasonable to suggest that the thickness of the interphase between carbon nanoparticles and PE matrices is around 2 nm.

By using the wall boundary model, Okuda et al. studied PP networks near the wall boundaries.[50] They made two assumptions: (1) polymer chains are not stuck, but randomly reflected by the wall boundaries and (2) the subchains below entanglement length behave like those in bulk state even though they are near the wall boundaries.[50] They found that the number of entanglements is increased near the wall boundaries due to the hooking process of their PP network models.[50] This finding is in good agreement with our current simulation results. However, we did not make any assumptions in our MD simulations and the PP networks are extracted based on our original PE matrices (real polymer chains). Papon et al. measured the local polymer chain dynamics near the surfaces of nanoparticles by low-field NMR.[51] They found that at least three different kinds of polymer mobility existed in the filled elastomers, which are also in agreement with gradient T_g around the surfaces of nanoparticles (which cannot be described by a simple core−shell approximation).[51] From our local entanglement distributions shown in Figure 9, we clearly see that the distribution profiles of entanglements are at least classified into three zones: high density (4−5 Å), low density (5−20 Å), and bulk density (20−40 Å), as the distance moving from the nanoparticle surfaces to the bulk polymer. Therefore, our PP network analysis as well as the distribution of entanglement density can be used to understand these local dynamical behaviors of polymer chains near nanoparticles surfaces from first principles.

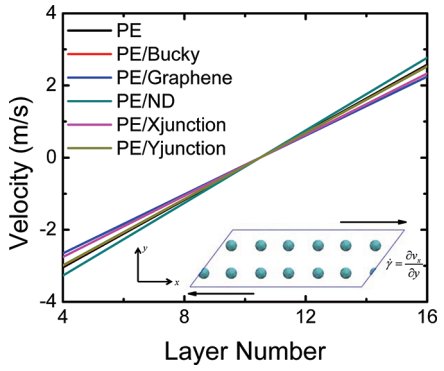

Figure 10. Velocity v_x profile in the simulation box along y direction for pure PE and PE nanocomposites with uniformly dispersed nanoparticles at 450 K, under the shear strain rate 10^9/s. The simulation box is divided into 20 layers along y direction and only 4−16 layers are shown here (see Appendix for details). The layer thicknesses are 4.68 Å, 4.61 Å, 4.08 Å, 5.03 Å, 4.24 Å, and 4.60 Å, respectively, for PE, PE/Bucky, PE/Graphene, PE/ND, PE/Xjunction, and PE/Yjunction. The inset shows the simulation box of PE/Bucky under NEMD simulation. For clarity, the surrounding PE polymer chains are made invisible.

6. ANISOTROPIC VISCOSITY OF PE NANOCOMPOSITES

Employing the nonequilibrium molecular-dynamics (NEMD) method, we obtain the velocity v_x profile along the along y direction of the simulation boxes for pure PE polymer and PE nanocomposites with uniformly dispersed nanoparticles of fixed orientation, under a high shear strain rate 10^9/s (see Appendix for details). Obviously, the velocity gradient $\partial v_x/\partial y$ is uniform throughout all these systems, which indicates that these systems reached a steady-state shear flow. The shear viscosities of pure PE and PE nanocomposites with uniformly dispersed nanoparticles are obtained by $\eta = -\langle P_{xy} \rangle/\dot{\gamma}$, where $\langle P_{xy} \rangle$ is the time average over the xy-component of the pressure tensor and $\dot{\gamma}$ is the shear rate. The obtained value for pure PE (M_w = 3.36 kg/mol) is 3.96 ± 0.45 cP at 450 K. Pearson et al. found that at low molecular weight, $M_w < M_c \approx 5$ kg/mol, the zero-rate shear viscosity η_0 of PE is well described by the power law, $\eta_0 = 2.1 \times 10^{-5} M_w^{1.8}$ (cP) at 450 K.[52] Obviously, our simulation result on pure PE is far away from the experimental result (46.78 cP), due to the shear thinning effect under high strain rate.[9] Baig et al. have performed NEMD simulations on PE (M_w = 5.60 kg/mol) over a broad range of different shear strain rates, under the melt condition (T = 450 K).[9] Under the strain rate 10^9/s, the viscosity of PE (M_w = 5.60 kg/mol) is estimated to be around 9 cP[9], which is very well comparable with our simulation result (3.96 ± 0.45 cP for M_w = 3.36 kg/mol). The obtained viscosities of PE nanocomposites with uniformly dispersed nanoparticles are listed in Table 5. As the carbon nanoparticles considered in the current work have different symmetries, we calculate the viscosities of PE nanocomposites along in-plane (x) and out-of-plane (z) directions. It is interesting to see that the PE nanocomposites have different viscosities in different directions, especially for PE/Graphene and PE/Xjunction. For PE/Bucky, PE/ND, and PE/Yjunction, they have the similar viscosities both in x and z directions, due to their highly symmetrical structures. Also, the viscosities along the out-of-plane direction of PE nanocomposites are mainly determined by the interaction energy between nanoparticles and polymer matrix (or surface-area-to-volume ratio of

dx.doi.org/10.1021/ma202289a | Macromolecules 2012, 45, 2099−2112

nanoparticles), which is in good agreement with our expectation.

The graphene and Xjunction nanoparticles are highly anisotropic. Therefore, the effective volumes occupied by these nanoparticles perpendicular to the flow direction are also anisotropic, especially for uniformly dispersed nanoparticles. To characterize the effective volume of a nanoparticle we use the gyration tensor, or moment of inertia tensor, $\mathbf{R} = n^{-1}\sum_{k=1}^{n} \mathbf{r}^k \mathbf{r}^k$ in its frame of principal axes, which corresponds to the orientation of the nanoparticles in their initial "U" states. Here $\mathbf{r}^k$ is the position vector of the kth particle from the center of mass of the system to its atomistic position, and n is the total number of atoms in a nanoparticle. Therefore, we can calculate the gyration tensor $\mathbf{R}$ for each single nanoparticle studied in the current work:

$$\mathbf{R} = \begin{bmatrix} 22.10 & 0 & 0 \\ 0 & 22.10 & 0 \\ 0 & 0 & 22.10 \end{bmatrix} (\text{Å}^2) \text{ for buckyball}$$

$$\mathbf{R} = \begin{bmatrix} 73.85 & 0 & 0 \\ 0 & 72.46 & 0 \\ 0 & 0 & 0 \end{bmatrix} (\text{Å}^2) \text{ for graphene}$$

$$\mathbf{R} = \begin{bmatrix} 22.10 & 0 & 0 \\ 0 & 22.10 & 0 \\ 0 & 0 & 22.10 \end{bmatrix} (\text{Å}^2) \text{ for ND}$$

$$\mathbf{R} = \begin{bmatrix} 49.63 & 0 & 0 \\ 0 & 47.59 & 0 \\ 0 & 0 & 2.88 \end{bmatrix} (\text{Å}^2) \text{ for Xjunction}$$

$$\mathbf{R} = \begin{bmatrix} 50.85 & 0.40 & -1.02 \\ 0.40 & 62.88 & -1.10 \\ -1.02 & -1.10 & 6.13 \end{bmatrix} (\text{Å}^2) \text{ for Yjunction}$$

For the buckyball and ND, the principle diagonal elements of their gyration tensors are very close to each other, due to their spherical shapes. However, for the graphene sheet, due to its single-atom layer structure, its $\mathbf{R}$ has a zero in its principle diagonal elements. From the wall boundary model study, the polymer chains perpendicular to the wall boundaries are greatly confined with increased entanglements, while the polymer chains parallel to these wall boundaries will be stretched and disentangled.[50] Therefore, for the PE/Graphene, the polymer chain dynamics will be accelerated by the graphene nanoparticles, when the shear flow is applied along its in-plane (x) direction. That is why we obtain a smaller viscosity value of PE/Graphene along its in-plane direction, compared with the bulk PE polymer. Because of the strong interactions between graphene nanoparticles and their PE matrix, the viscosity of PE/Graphene along its out-of-plane direction is almost four times that of pure PE. Similarly, the viscosity of PE/Xjunction along its out-of-plane direction is almost two times its viscosity along in-plane direction, due to the smaller diameter of its SWNT (also smaller R_{zz} value of its gyration tensor). However, for PE/Yjunction, this phenomenon is diminished, as the R_{zz} value of its gyration tensor is increased. From above discussions on interaction energies between nanoparticles and PE matrices as well as the PP analysis results, the PE/Graphene and PE/Xjunction with uniformly dispersed nanoparticles have larger viscosities (along their out-of-plane directions), due to their stronger interaction energies and higher entanglement densities. Among all the PE nanocomposites with uniformly dispersed nanoparticles, PE/ND has the smallest viscosity in the out-of-plane direction, since the interaction energy between ND nanoparticles and their PE matrix is the weakest.

Knauert et al. studied the nanoparticle shape effect on PNC rheology via NEMD simulation.[53] Icosahedron, rod, and sheet-shaped nanoparticles were considered with very short, unentangled polymer chains (10−40 monomers per chain). They found that there was a relatively weak enhancement of the viscosity of PNCs by using the sheet nanoparticles.[53] However, in their studies, the nanoparticles tend to cluster together, thus greatly reducing the interaction energy between nanoparticles and polymer matrix, cf. Table 5. Thus, the viscosity enhancement induced by sheet nanoparticles can also be greatly reduced by nanoparticle clustering. We observe a similar effect in our NEMD simulations on PE nanocomposites with randomly dispersed nanoparticles. The viscosity of PE/Graphene is only slightly larger than that of PE/Bucky and PE/ND, due to nanoparticle aggregation (results not shown). Grest et al. studied the shear rheology of nanoparticle suspensions with differently shaped nanoparticles, i.e., jacks, rods, plates, and spheres.[54,55] They found that the viscosity of the suspension was greatly increased by using jacks (with the arm length to diameter aspect ratio 21), due to their highly aggregated structures and large effective volumes.[54,55] However, the arm length to diameter aspect ratios of X junction and Y junction studied in current works are only 3.1 and 2.4, respectively. Thus, the interaction energy between nanoparticles and polymer matrix, as well as the gyration tensor $\mathbf{R}$ of clustered nanoparticles in the laboratory frame can be greatly changed. That is the reason we see that both graphene and X junction have comparable enhancement effects on the viscosity of PE nanocomposites.

7. CONCLUSIONS

To understand how the nanoparticle shapes affect structural, dynamical and viscous properties of their polymer nanocomposites, we performed extensive MD simulations on PE nanocomposites with five different nanoparticles: buckyball, graphene, ND, Xjunction, and Yjunction. We have revealed several key issues by analyzing the MD trajectories.

First, the nanoparticles tend to aggregate together under the conditions employed in our study, in agreement with theoretical considerations. Under the melting temperature (450 K), all the carbon nanoparticles surrounded by PE polymer chains self-assemble during the first 100 ns and form stable clusters. Compared with uniformly dispersed nanoparticles (cubic crystal-like distribution), the vdW surfaces and volumes of the nanoparticles are reduced upon clustering. Especially for graphene sheets, whose ratio of vdW surface area to volume is reduced from 0.731 to 0.551 Å^{-1}.

Second, the surface-area-to-volume ratio (shape) of nanoparticles greatly influences the interactions between nanoparticles and their polymer matrices, as well as the packing behaviors of their surrounding polymer chains. The nanoparticles considered in this paper can be arranged as graphene, Xjunction, Yjunction, buckyball, and ND, from the largest to the smallest of their surface-area-to-volume ratios. Both the interaction energy and polymer chain packing follow the same trend. Because of the strongest interactions between graphene sheets and their PE matrix, the PE polymer chains are highly

packed around graphene sheets at 5 Å (from the surface of graphene sheets to polymer chains). However, we do not find evidence for highly packed polymer chains around ND nanoparticles, in accord with their weak interactions with the PE matrix. During the clustering of nanoparticles, their interaction with the polymer matrices weaken as their vdW surfaces decrease. In turn, the polymer chain densities surrounding these nanoparticles are reduced. In short, the stronger the interaction between nanoparticles and the polymer matrix, the denser the polymer chains surround the nanoparticles. While this is expected, we have provided a detailed quantitative analysis.

Third, the relaxation behavior of polymer chains is also affected by the surface-area-to-volume ratio (shape) of the nanoparticle, as a result of both the interaction between nanoparticle and polymer chains, as well as the nanoparticle-induced topological changes of polymer chains surrounding the nanoparticles. The interaction between graphene sheets and their PE matrix is the strongest among all the nanoparticles considered in current work; correspondingly, the relaxation time of their PE chains is the longest. On the contrary, the relaxation time of PE chains in PE/ND is the shortest, since the ND nanoparticles have the weakest interactions with their PE matrix. Similar to the packing behaviors of polymer chains around nanoparticles, the relaxation of polymer chains is found to be accelerated after these nanoparticles clustered together, as the interactions between nanoparticles and their polymer matrices are weakened during this process. From the PP network analysis on the PE nanocomposites, the pair distributions between nanoparticles and entanglements of polymers are also available. A large entanglement density is found at the surfaces of the nanoparticles. Moving away from the nanoparticle surfaces to bulk, the entanglement density rapidly decreases, reaches its global minimum state at 6.4 Å (away from the nanoparticle surface), and gradually increases to its bulk state. The PE/Graphene and PE/Xjunction are found to have the largest bulk entanglement density, while PE/ND has the smallest. Therefore, the relaxation of polymer chains in PE/Graphene, PE/Xjunction, and PE/ND are the slowest and the fastest, respectively. However, the overall PP networks of PE matrices are very similar to that of pure PE, since the volume fraction of nanoparticles is very low (only 4 vol %) and these systems are still "polymer entanglements" dominated, as we discussed in detail.

Fourth, the polymer chains close to nanoparticles are highly stretched and they are preferentially aligned parallel to the surfaces of nanoparticles. From the profiles of radius of gyration $\langle R_g^2 \rangle$ and the second Legendre polynomial $\langle P_2 \rangle$, polymer chains close to nanoparticle surfaces (around 2 nm from the nanoparticles surfaces) are affected. From the pair distributions between nanoparticles and the polymers entanglements, the entanglement densities are greatly changed in the range of 2 nm from the nanoparticles surfaces. Therefore, the interphase thickness of PE polymers with carbon nanoparticles is determined to be in the same range.

Fifth, the anisotropic viscosities of PE nanocomposites are greatly affected by the surface-area-to-volume ratios (shapes) of nanoparticles and their moment of inertia tensors. From our NEMD simulations, both in-plane and out-of-plane viscosities of PE nanocomposites are obtained. Because of the highly anisotropic structures of graphene and X junction, their out-of-plane viscosities are much larger than their in-plane viscosities. From their gyration tensors, we find that their R_{zz} components are very small, compared with other elements in the principle diagonal directions. Therefore, the shear flows along the out-of-plane directions of PE/Graphene and PE/Xjunction are also greatly constrained by their in-plane effective volumes and their strong nanoparticle−polymer interactions (large surface-area-to-volume ratios), which in turn increase their out-of-plane viscosities. Because of the weak interactions between buckyballs/NDs and PE matrices (small surface-area-to-volume ratios), PE/Bucky and PE/ND have comparable viscosities with pure PE polymer, which indicates that the polymer chains in PE/Bucky and PE/ND are not greatly constrained by these nanoparticles.

From our current study, the surface-area-to-volume ratio of nanoparticles plays an important role in the mechanical properties of PNCs. Both the static and dynamical properties of polymer matrices are strongly affected by the surface-area-to-volume ratios of nanoparticles (nanoparticle−polymer interactions). Since the surface-area-to-volume ratios of nanoparticles can be easily tailored through the shapes of nanoparticles or their dispersion/clustering, we expect some motivations for experimental works to be performed. It is important to stress that the nanoparticle−polymer interaction considered in this work is mainly of physical nature, i.e., vdW interaction. As the surfaces of carbon nanoparticles can be chemically modified and bonded to polymer chains (chemical bonding or hydrogen bonding), it will be important to explore how these interactions will affect the dynamical and viscous properties of PNCs.

APPENDIX

A. PP Network Analysis on PE Nanocomposites. The original Z1 code[12−15,56] constructs the PP network of a polymeric system by fixing the ends of all polymer chains. Hereafter, each polymer chain is replaced by a sequence of infinitesimally thin, impenetrable and tensionless straight lines. The length of these multiple disconnected paths is monotonically reduced, subject to chain-uncrossability. Upon iterating the geometrical procedure, each multiple disconnected path converges to a final state, the shortest disconnected path, i.e., an individual PP for each chain. The convergence of the Z1 code is achieved

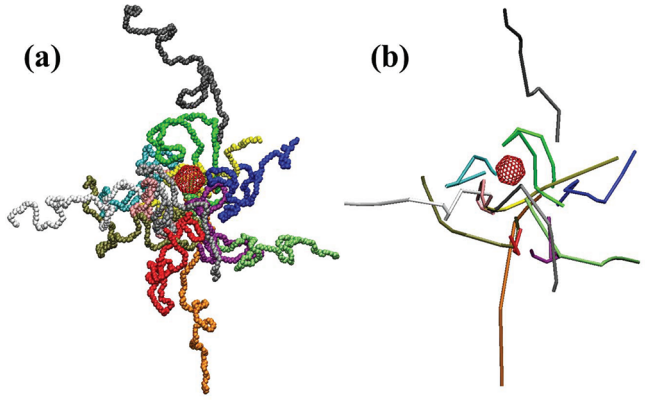

Figure 11. (a) Original molecular model of PE nanocomposites with a single buckyball and (b) its corresponding PP network under "frozen particle limit". In part a, the different colored particles represent different polymer chains. In part b, the PPs are different colored straight lines and the buckyball is fixed in the space in the topological analysis (Z1 code analysis). The kinks along straight lines represent the polymer chain entanglements.

dx.doi.org/10.1021/ma202289a | *Macromolecules* 2012, 45, 2099−2112

once the difference between two successive iterations is smaller than a preset numerical tolerance. In short, the PP can be considered as the shortest path remaining when one holds chain ends fixed, while continuously reducing (shrinking) a chain's contours without violating topological constrains (polymer chain uncrossability).[57] A single PP is often characterized by its conformational properties such as PP length L_{pp}, number of interior kinks (or entanglements) Z, and the end-to-end distance R_{ee}. More details on the implementation and application of Z1 code in PP study of polymers can be found in refs 12−16, 56. In order to calculate the PP network of PE matrix, we consider two modes for the PP network analysis of PE nanocomposites. One is the so called "phantom particle limit".[20] The nanoparticles in PNCs are ignored as we assume that the motion of the polymer chains is not constrained by these nanoparticles on the time scale of reptation dynamics. In that case, the nanoparticles are removed from the PNCs before the Z1 code[15,16] is applied on the PE matrix to extract its corresponding PP network. In this situation, the effect of nanoparticles on the PP network can only appear as they may change the underlying topology of the PE matrix. In the other direction, the nanoparticles may behave as the "particle entanglements", which behave as anchors to polymer chains and attach them together, then greatly restrict the motion of polymer chains. The other mode, i.e., "frozen particle limit" is also considered.[20] In the "frozen particle limit", all the nanoparticles are fixed in the space, then the Z1 code is applied to extract the corresponding PP network. All the nanoparticles are treated in the same manner as the PE matrix, based on the same geometrical criteria. Basically, the nanoparticles surfaces are meshed by using artificial rodlike chains (N = 2 polymers), and we use the original Z1 code to find the shortest path. Since a dumbbell does not move (fixed ends), the chain length of such a single-segment rodlike chain is also irreducible. Within the analysis of the final shortest path, the nanoparticles have of course to be ignored, and they do not move during the minimization procedure. When the Z1 code is applied on PE nanocomposites with nanoparticles, we can calculate their corresponding PP network as shown in Figure 11. Since the size of the nanoparticles considered in the current work is comparable to the size of PE polymer chains, which can greatly restrict the dynamics of polymer chains, we only consider the "frozen particle limit" case for PP analysis.

B. Viscosity Calculation on PE Nanocomposites. The viscosities of pure PE and PE nanocomposites are obtained through NEMD simulations, based on the GSLLOD algorithm,[58] with appropriate boundary conditions for shear deformation, e.g., Lees−Edwards boundary conditions.[59] The GSLLOD algorithm[58] is derived from rigorous statistical-mechanics principles, and usually coupled with a Nose−Hoover thermostat[60,61] for simulations at constant temperature so that the canonical ensemble is generated with following form:[58]

$$\dot{\mathbf{q}}_i = \frac{\mathbf{p}_i}{m_i} + \mathbf{q}_i \cdot \nabla \mathbf{u},$$

$$\dot{\mathbf{p}}_i = \mathbf{F}_i - \mathbf{p}_i \cdot \nabla \mathbf{u} - m_i \mathbf{q}_i \cdot \nabla \mathbf{u} \cdot \nabla \mathbf{u} - \frac{p_\xi}{Q}\mathbf{p}_i,$$

$$\dot{\xi} = \frac{p_\xi}{Q},$$

$$\dot{p}_\xi = \sum_{i=1}^{N} \frac{\mathbf{p}_i^2}{m_i} - dNk_B T \tag{A1}$$

In above equation, $\mathbf{q}_i$, $\mathbf{p}_i$, m_i, and $\mathbf{F}_i$ are the position vector, momentum vector, mass, and force vector of each atom in molecule i, respectively, d = 3 is the space dimensionality, N is the total number of atoms in the system, ξ and p_ξ are the coordinate- and momentum-like variables, respectively, of the Nose-Hoover thermostat controlling the temperature of the system at desired level, $Q = dNk_BT\tau^2$ is the thermostat mass parameter. The relaxation time τ is set to be 0.4 ps in all simulations with a time step of 1 fs. In the NEMD approach, a shear velocity profile is applied to the system and the corresponding response via an off-diagonal component of the stress tensor is measured, which is proportional to the momentum flux. If we apply the Couette flow along the x-axis and the gradient of the flow is along the y-axis, the flow rate dependent shear viscosity can be obtained by

$$\eta = -\frac{\langle P_{xy} \rangle}{\dot{\gamma}} \tag{A2}$$

where $\langle P_{xy} \rangle$ is the time average of xy- component of the pressure tensor and $\dot{\gamma}$ is the shear rate. In the current work, we had to limit our simulations to a very high strain rate, 10^9/s.The motions of nanoparticles are frozen in the co-moving triclinic system (simulation box) to keep the distribution of nanoparticles and their orientations fixed. Thus, the nanoparticle centers are convected affinely with the shear flow, as shown in the inset of Figure 10. In the laboratory frame, these nanoparticles change distances all the time, and they behave as infinitely massed particles. The atom crossing a periodic boundary will have a delta added to its velocity equal to the difference in prescribed macroscopic velocities between the lower and higher boundaries. This velocity difference can include tilt components, e.g., a delta in the x velocity when an atom crosses the y periodic boundary, when the shear flow is applied along the x direction. Thus, such a boundary condition is equivalent to the Lees−Edwards boundary condition.[59] The total simulation time is about 10−20 ns to make sure that the system achieves the steady-state shear flow condition. The shear velocity v_x profile was also monitored by dividing the simulation box into 20 slabs along its y direction (Figure 10), when the flow is along the x-axis and the gradient of the flow is along the y-axis. A typical snapshot for the simulation box of PE/Bucky is also shown in the inset of Figure 10, with surrounding polymer chains made invisible. Under the high shear strain rates, the polymer chains in the simulation box tend to orient along with the shear flow. Therefore, in order to minimize finite system size effects, all the simulation cells have been increased three times along the flow direction. The side

dx.doi.org/10.1021/ma202289a | *Macromolecules* 2012, 45, 2099−2112

lengths along the flow direction for PE, PE/Bucky, PE/Graphene, PE/ND, PE/Xjunction, and PE/Yjunction are 374.4, 368.5, 326.8, 402.6, 339.2, and 367.6 Å, respectively. The side lengths for other directions are 93.6, 92.1, 81.7, 100.7, 84.8, and 91.9 Å, respectively, for PE, PE/Bucky, PE/Graphene, PE/ND, PE/Xjunction, and PE/Yjunction. Fully equilibrated initial configurations (at all length scales) were used in the NEMD simulations. Since the orientational motions of nanoparticles are frozen, the obtained viscosities of PE nanocomposites are different along different directions, especially for PE/Graphene, PE/Xjunction, and PE/Yjunction. These anisotropic viscosities are only relevant for a system where these nanoparticles have a fixed orientation in space. This could be realized by magnetic nanoparticles in the presence of a strong external field. To this end, we are essentially studying the limit of strong magnetization by fixing the alignment of these nanoparticles, to explore their geometrical effects on the viscosity, which is typically done in the field of liquid crystals. The anisotropic viscosities are so called Miesowicz viscosities.[62] In short, we study the effect of nanoparticle shape of perfectly aligned nanoparticles on the anisotropic viscosities within the necessarily non-Newtonian regime of the PE matrix, due to the limitation of computational power. These results allow us to get an impression about the maximum anisotropy one can expect to find in a system of oriented nanoparticles. The viscosity ultimately becomes isotropic but remains nanoparticle geometry-dependent if the nanoparticles are dispersed and convected non-affinely with the shear flow.

AUTHOR INFORMATION

Corresponding Author

*E-mail: w-liu@northwestern.edu (W.K.L.). Fax: 847-491-3915.

Notes

The authors declare no competing financial interest.

ACKNOWLEDGMENTS

We are grateful to the helpful discussions with Brendan Abberton, John Moore and Dr. Sinan Keten. This work is supported by NSF CMMI Grants 0823327, 0928320, and NSF IDR CMM Grant I 1130948. Y.L. acknowledges the partial financial support from Ryan Fellowship at Northwestern University. M.K. acknowledges support by SNSF grant IZ73Z0-128169. W.K.L. was also partially supported by the World Class University Program through the National Research Foundation of Korea (NRF) funded by the Ministry of Education, Science and Technology (R33-10079). This research used resources of the QUEST cluster at Northwestern University and the Argonne Leadership Computing Facility at Argonne National Laboratory, which is supported by the Office of Science of the U.S. Department of Energy under contract DE-AC02-06CH11357.

REFERENCES

(1) Rouse, P. E. *J. Chem. Phys.* **1953**, *21*, 1272−1280.
(2) de Gennes, P.-G. *J. Chem. Phys.* **1971**, *55*, 572.
(3) Doi, M.; Edwards, S. F., *The theory of polymer dynamics*. Clarendon Press: Oxford, U.K., 1986.
(4) Likhtman, A. E.; McLeish, T. C. B. *Macromolecules* **2002**, *35*, 6332−6343.
(5) Wischnewski, A.; Monkenbusch, M.; Willner, L.; Richter, D.; Likhtman, A. E.; McLeish, T. C. B.; Farago, B. *Phys. Rev. Lett.* **2002**, *88*, 058301.
(6) McLeish, T. C. B. *Adv. Phys.* **2002**, *51*, 1379−1527.
(7) Bueche, F. *Reinforcement of elastomers*; Interscience Publishers: New York, 1965.
(8) Schneider, G. J.; Nusser, K.; Willner, L.; Falus, P.; Richter, D. *Macromolecules* **2011**, *44*, 5857−5860.
(9) Baig, C.; Mavrantzas, V. G.; Kröger, M. *Macromolecules* **2010**, *43*, 6886−6902.
(10) Baig, C.; Stephanou, P. S.; Tsolou, G.; Mavrantzas, V. G.; Kröger, M. *Macromolecules* **2010**, *43*, 8239−8250.
(11) Everaers, R.; Sukumaran, S. K.; Grest, G. S.; Svaneborg, C.; Sivasubramanian, A.; Kremer, K. *Science* **2004**, *303*, 823−826.
(12) Foteinopoulou, K.; Karayiannis, N. C.; Laso, M.; Kröger, M. *J. Phys. Chem. B* **2009**, *113*, 442−455.
(13) Hoy, R. S.; Foteinopoulou, K.; Kröger, M. *Phys Rev E* **2009**, *80*, 031803.
(14) Karayiannis, N. C.; Kröger, M. *Int. J. Mol. Sci.* **2009**, *10*, 5054−5089.
(15) Kröger, M. *Comput. Phys. Commun.* **2005**, *168*, 209−232.
(16) Shanbhag, S.; Kröger, M. *Macromolecules* **2007**, *40*, 2897−2903.
(17) Stephanou, P. S.; Baig, C.; Tsolou, G.; Mavrantzas, V. G.; Kröger, M. *J. Chem. Phys.* **2010**, *132*, 124904.
(18) Tzoumanekas, C.; Theodorou, D. N. *Macromolecules* **2006**, *39*, 4592−4604.
(19) Li, Y.; Kröger, M.; Liu, W. K. *Polymer* **2011**, *52*, 5867−5878.
(20) Toepperwein, G. N.; Karayiannis, N. C.; Riggleman, R. A.; Kröger, M.; de Pablo, J. J. *Macromolecules* **2011**, *44*, 1034−1045.
(21) Ramos, J.; Vega, J. F.; Theodorou, D. N.; Martinez-Salazar, J. *Macromolecules* **2008**, *41*, 2959−2962.
(22) Riggleman, R. A.; Toepperwein, G.; Papakonstantopoulos, G. J.; Barrat, J. L.; de Pablo, J. J. *J. Chem. Phys.* **2009**, *130*, 244903.
(23) Starr, F. W.; Douglas, J. F.; Glotzer, S. C. *J. Chem. Phys.* **2003**, *119*, 1777−1788.
(24) Starr, F. W.; Knauert, S. T.; Douglas, J. F. *J. Polym. Sci., Polym. Phys.* **2007**, *45*, 1882−1897.
(25) Starr, F. W.; Douglas, J. F. *Phys. Rev. Lett.* **2011**, *106*, 115702.
(26) Ramanathan, T.; Abdala, A. A.; Stankovich, S.; Dikin, D. A.; Herrera-Alonso, M.; Piner, R. D.; Adamson, D. H.; Schniepp, H. C.; Chen, X.; Ruoff, R. S.; Nguyen, S. T.; Aksay, I. A.; Prud'homme, R. K.; Brinson, L. C. *Nat. Nanotechnol.* **2008**, *3*, 327−331.
(27) Potts, J. R.; Dreyer, D. R.; Bielawski, C. W.; Ruoff, R. S. *Polymer* **2011**, *52*, 5−25.
(28) Li, Y.; Qiu, X. M.; Wang, M.; Yin, Y. J.; Yang, F.; Fan, Q. S. *EPL-Europhys Lett* **2009**, *88*, 26006.
(29) Li, Y.; Qiu, X. M.; Yang, F.; Yin, Y. J.; Fan, Q. S. *Carbon* **2009**, *47*, 812−819.
(30) Zsoldos, I.; Kakuk, G.; Reti, T.; Szasz, A. *Model. Simulat. Mater. Sci. Eng.* **2004**, *12*, 1251−1266.
(31) http://accelrys.com/products/materials-studio/
(32) Flory, P. J. *Statistical Mechanics of Chain Molecules*. Oxford University Press: NewYork, 1988.
(33) Mondello, M.; Grest, G. S.; Webb, E. B.; Peczak, P. *J. Chem. Phys.* **1998**, *109*, 798−805.
(34) Adnan, A.; Sun, C. T.; Mahfuz, H. *Compos. Sci. Technol.* **2007**, *67*, 348−356.
(35) Hossain, D.; Tschopp, M. A.; Ward, D. K.; Bouvard, J. L.; Wang, P.; Horstemeyer, M. F. *Polymer* **2010**, *51*, 6071−6083.
(36) Capaldi, F. M.; Boyce, M. C.; Rutledge, G. C. *Polymer* **2004**, *45*, 1391−1399.
(37) Chen, I. W. P.; Liang, Z. Y.; Wang, B.; Zhang, C. *Carbon* **2010**, *48*, 1064−1069.
(38) Li, Y. *Polymer* **2011**, *52*, 2310−2318.
(39) Sun, X. Q.; Lin, T.; Gezelter, J. D. *J. Chem. Phys.* 2008, *128*.
(40) Plimpton, S. *J. Comput. Phys.* **1995**, *117*, 1−19.
(41) Kröger, M.; Hess, S. *Phys. Rev. Lett.* **2000**, *85*, 1128−1131.
(42) Lebovitz, A. H.; Khait, K.; Torkelson, J. M. *Macromolecules* **2002**, *35*, 8672−8675.
(43) Kröger, M.; Ilg, P. *J. Chem. Phys.* **2007**, *127*, 034903.
(44) Stockelhuber, K. W.; Svistkov, A. S.; Pelevin, A. G.; Heinrich, G. *Macromolecules* **2011**, *44*, 4366−4381.

(45) Starr, F. W.; Schroder, T. B.; Glotzer, S. C. *Macromolecules* **2002**, *35*, 4481−4492.
(46) Ndoro, T. V. M.; Voyiatzis, E.; Ghanbari, A.; Theodorou, D. N.; Bohm, M. C.; Muller-Plathe, F. *Macromolecules* **2011**, *44*, 2316−2327.
(47) Raos, G.; Moreno, M.; Elli, S. *Macromolecules* **2006**, *39*, 6744−6751.
(48) Papakonstantopoulos, G. J.; Doxastakis, M.; Nealey, P. F.; Barrat, J. L.; de Pablo, J. J. *Phys. Rev. E* **2007**, *75*, 031803.
(49) Fetters, L. J.; Lohse, D. J.; Richter, D.; Witten, T. A.; Zirkel, A. *Macromolecules* **1994**, *27*, 4639−4647.
(50) Okuda, S.; Inoue, Y.; Masubuchi, Y.; Uneyama, T.; Hojo, M. *J. Chem. Phys.* **2009**, *130*, 214907.
(51) Papon, A.; Saalwachter, K.; Schaler, K.; Guy, L.; Lequeux, F.; Montes, H. *Macromolecules* **2011**, *44*, 913−922.
(52) Pearson, D. S.; Strate, G. V.; Vonmeerwall, E.; Schilling, F. C. *Macromolecules* **1987**, *20*, 1133−1141.
(53) Knauert, S. T.; Douglas, J. F.; Starr, F. W. *J. Polym. Sci., Polym. Phys.* **2007**, *45*, 1882−1897.
(54) Heine, D. R.; Petersen, M. K.; Grest, G. S. *J. Chem. Phys.* **2010**, *132*, 184509.
(55) Petersen, M. K.; Lane, J. M. D.; Grest, G. S. *Phys. Rev. E* **2010**, *82*, 010201(R).
(56) Foteinopoulou, K.; Karayiannis, N. C.; Mavrantzas, V. G.; Kröger, M. *Macromolecules* **2006**, *39*, 4207−4216.
(57) Tzoumanekas, C.; Theodorou, D. N. *Curr. Opin. Solid State Mater. Sci.* **2006**, *10*, 61−72.
(58) Tuckerman, M. E.; Mundy, C. J.; Balasubramanian, S.; Klein, M. L. *J. Chem. Phys.* **1997**, *106*, 5615−5621.
(59) Lees, A. W.; Edwards, S. F. *J. Phys., Part C Solid* **1972**, *5*, 1921−1929.
(60) Nose, S. *Mol. Phys.* **1984**, *52*, 255−268.
(61) Hoover, W. G. *Phys. Rev. A* **1985**, *31*, 1695−1697.
(62) Kröger, M.; Sellers, H. S. *J. Chem. Phys.* **1995**, *103*, 807−817.

Macromolecules

Article

pubs.acs.org/Macromolecules

Numerical Study of Linear and Circular Model DNA Chains Confined in a Slit: Metric and Topological Properties

Cristian Micheletti*

SISSA—Scuola Internazionale Superiore di Studi Avanzati and CNR-IOM Democritos, Via Bonomea 265, 34136 Trieste, Italy

Enzo Orlandini*

Dipartimento di Fisica e Astronomia and Sezione INFN, Università di Padova, Via Marzolo 8, 35131 Padova, Italy

ABSTRACT: Advanced Monte Carlo simulations are used to study the effect of nanoslit confinement on metric and topological properties of model DNA chains. We consider both linear and circularized chains with contour lengths in the 1.2−4.8 μm range and slits widths spanning continuously the 50−1250 nm range. The metric scaling predicted by de Gennes' blob model is shown to hold for both linear and circularized DNA up to the strongest levels of confinement. More notably, the topological properties of the circularized DNA molecules have two major differences compared to three-dimensional confinement. First, the overall knotting probability is nonmonotonic for increasing confinement and can be largely enhanced or suppressed compared to the bulk case by simply varying the slit width. Second, the knot population consists of knots that are far simpler than for three-dimensional confinement. The results suggest that nanoslits could be used in nanofluidic setups to produce DNA rings having simple topologies (including the unknot) or to separate heterogeneous ensembles of DNA rings by knot type.

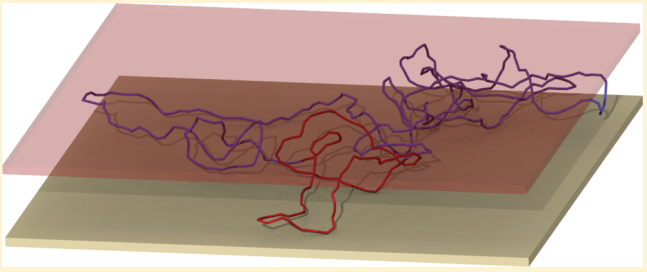

I. INTRODUCTION

Nanodevices are increasingly used to investigate the impact of spatial restraints on the statics and dynamics of polymers and biopolymers. DNA is ideally suited for such studies both for its applicative potential (nanoconfinement can be used to sort, sieve and sequence DNA[1−4]) and because its elastic properties can be exploited to elucidate issues of primary interest in polymer science.[5−11] In fact, the width of presently available confining nanodevices (a channel, a slit, a pit etc.) can be set to compete with one or more of the characteristic lengths of a DNA molecule and hence allow for probing different physical regimes.[8,11−18]

A classic example is offered by the one-dimensional (channel) confinement of linear DNA molecules whose elongation follows two different scaling laws, named after de Gennes[12] and Odijk,[19] according to whether the channel width is larger or smaller than l_p.[20] A second notable instance is offered by DNA molecules confined in three-dimensions, as inside a viral capsid. In the latter case, the interplay of the genome length and capsid size, can profoundly affect the entanglement of the packaged DNA.[21−24] Both aspects are aptly revealed by the abundance and complexity of knots that are trapped in DNA filaments that circularize inside viral capsids.[11,17,25−30]

Compared to the above one- and three-dimensional cases, two-dimensional polymer confinement is much less characterized both for the metric and topological properties. To the best of our knowledge there exist only a limited number of experimental and numerical studied of the size and shape of DNA molecules in nanoslits.[8,18,31−33] These seminal studies have addressed the interesting issue of whether multiple scaling regimes exist in *linear* DNA filaments inside slits. It appears that the same question has not been posed for circularized DNA molecules where, unlike the linear case, entanglement is trapped in the form of topological constraints (knots) which affect the physical behavior and biological functionality.[34−41] The impact of slit confinement on the topology of circularized polymers has been previously addressed by early simulations of lattice polymer models[42] so that its implications for slit-confined DNA are virtually unexplored.

As a step toward clarifying the above-mentioned aspects we carry out a systematic numerical study of linear and circularized chains in nanoslits whose salient physical properties, namely the thickness and bending rigidity are set to match those of dsDNA. Specifically, we use advan.ced Monte Carlo techniques to characterize the shape, orientation and entanglement of linear and circularized chains of contour lengths in the 1.20−4.8 μm range and confined in nanoslits of width from 50 to 1250 nm.

The computational scheme is first used to characterize the metric scaling by varying independently the chain contour length

Received: November 14, 2011
Revised: January 16, 2012
Published: February 7, 2012

   dx.doi.org/10.1021/ma202503k | *Macromolecules* 2012, 45, 2113−2121

and the slit width. The metric scaling predicted by de Gennes' blob model is found to hold, up to the strongest levels of confinement, for both linear and circular chains.

Next, we show that two-dimensional confinement affects the ring topology in a qualitatively different way from three-dimensional confinement. In fact, for increasing three-dimensional confinement both the incidence and complexity of knots grows monotonically.[23,24] In the two-dimensional case, instead, the knotting probability is nonmonotonic and the knot spectrum mostly consist of the simplest knot types. The fraction of knotted molecules is maximum, and exceeds by several times the bulk (unconstrained) value, when the slit width is a fraction of the average extension of the unconstrained chains. A reduction of the width below this value, causes the knotting probability to decrease rapidly.

This fact offers the opportunity to use the setup of two-dimensional confinement in nanoslits as an effective method to produce DNA rings with an *a priori* control on their topology and that can be tuned to yield a proportion of knotted molecules that is much higher or much lower than the bulk one. In addition, the sensitive dependence of the conformational entropy of knotted molecules with different topology on the size of the confining region, suggests that width-modulated slits could be profitably used in nanofluidic setups to sort circular DNAs by knot type.

II. METHODS

A. The Model. For this study, dsDNA is modeled as a semiflexible chain of cylinders. This coarse-grained model captures appropriately the metric and topological properties of DNA both when it is unconstrained[43,44] and when it is packed at moderate densities, that is for interstrand separations larger than ≈5 nm.[45] In such conditions, which are met in our study, dehydration effects and cholesteric interactions can be neglected.[11,17,28,46,47] It is further assumed that DNA is in a concentrated buffer of monovalent counterions so that the screened electrostatic repulsion can also be neglected. The cylinder diameter is accordingly set equal to the dsDNA hydration diameter, d = 2.5 nm. Notice that no potential energy term is introduced to account for the DNA torsional rigidity. Its interplay with bending rigidity can, *a priori* impact the relevant conformational space of densely packed DNA, as argued in ref 48 for closed DNA chains. However, recent independent simulations of three-dimensionally confined DNA with free ends have shown that torsional effects are negligible even at packing densities higher than considered here.[49] We shall therefore work under the hypothesis that the slit-confined DNA chains are torsionally relaxed both in the linear and in the circularized form. For the latter case it is assumed that DNA circularization occurs via noncovalent annealing of the DNA sticky ends so that all torsional stress can still be released.

We consider open and closed chains of contour length equal to L_c ranging from 1.2 to 4.8 μm and describe them as chains of cylinders with N = 120...480 vertices, respectively, as shown in Table 1. This discretization level corresponds to a long axis of the cylinder, b, approximately equal to 10 nm which is a fraction of the DNA persistence length, l_p = 50 nm.

The potential energy of a chain configuration, Γ, consists of two terms, $E_\Gamma = E_{excl-vol}(\Gamma) + E_b(\Gamma)$. The first term is the excluded volume interaction which enforces the chain self-avoidance. $E_{excl-vol}$ is set equal to "infinity" if two nonconsecutive cylinders overlap, otherwise is set equal to zero. The second term, E_b is the bending potential energy

$$E_b = -K_bT\frac{l_p}{b}\sum_i \vec{t}_i\cdot\vec{t}_{i+1} \tag{1}$$

where $\vec{t}_i$ is the orientation of the axis of the ith cylinder and the temperature T is set to 300 K. For linear chains, i runs from 1 to N. For circular ones, instead, i runs from 1 to N + 1 with the proviso that $\vec{t}_{N+1} \equiv \vec{t}_1$.

Table 1. Parameters of the Simulated Linear and Circular DNA Molecules[a]

N	bp	L_c [nm]	linear R_g^0 [nm]	circular $2R_g^0$ [nm]
120	3534	1201	128 ± 3	94 ± 3
240	7068	2403	190 ± 5	136 ± 5
320	9426	3204	222 ± 6	159 ± 6
360	10 602	3604	236 ± 6	169 ± 6
400	11 782	4006	251 ± 6	179 ± 6
480	14 136	4806	276 ± 7	198 ± 7

[a] N is number of cylinders of the model chains, bp is the total number of base-pairs and L_c is the corresponding contour length. The last two columns provide the bulk values of the root mean square radius of gyration, R_g^0 of the linear and circular chains.

DNA confinement in nanoslit is modeled by setting an upper bound, D, to the calliper size of the chains along one direction, conventionally taken as the z axis of the system Cartesian coordinate, see Figure 1. Because the z direction is perpendicular to the two impenetrable planes delimiting the slit, all observables measured along this direction will be indicated with the $\perp$ subscript, while those measured parallel to the slit plane will be denoted with the $\|$ subscript.

B. Advanced Sampling Techniques. An advanced Monte Carlo sampling technique is used to compute the equilibrium metric and topological observables of open and closed chains subject to slit confinement. The technique is described in detail in a recent review article[11] and therefore we shall describe it only concisely.

The method consists of using a standard set of crankshaft and pivot moves to evolve the chains but the canonical weights used for the Metropolis acceptance criterion are generalized to ensure that configurations are sampled according to the following (non-normalized) statistical weight

$$\exp\left\{-\frac{E_{excl-vol}(\Gamma) + E_b(\Gamma) - \mu\Delta_\perp(\Gamma)}{K_bT}\right\} \tag{2}$$

where $\Delta_\perp(\Gamma)$, is the configuration calliper size measured along the confining, z direction. The non-negative quantity μ can be viewed as an anisotropic pressure promoting the confinement along z. In fact, by increasing μ one can reduce the average calliper size of the generated configurations. By using a multiple Markov chain scheme, consisting of several parallel Monte Carlo simulations each at a different value of μ,[23,50] it is possible to sample very effectively configurations covering a wide range of calliper size, $\Delta_\perp(\Gamma)$. Finally, a thermodynamic reweighting technique analogous to the one used in ref 23 is used to combine the observables computed for configurations generated at various values of μ. This procedure gives an estimate of the equilibrium properties of chains that can be accommodated inside slits of width, D, in the 50−1250 nm range.

C. Metric Properties. The average size, shape anisotropy, and orientation of a given ring are characterized by means of the eigenvalues and eigenvectors of its gyration tensor, **Q**. The entries of this 3 × 3 symmetric matrix are given by

$$Q_{\alpha,\beta} = \frac{1}{N}\sum_{i=1}^{N}(\mathbf{r}_{i,\alpha} - \bar{\mathbf{r}}_\alpha)(\mathbf{r}_{i,\beta} - \bar{\mathbf{r}}_\beta) \tag{3}$$

where $\mathbf{r}_i$ is the position of the ith vertex of the chain, α and β run over the three Cartesian components and $\bar{\mathbf{r}} = \Sigma_i\mathbf{r}_i/N$ is the average vertex position in the chain. The non-negative eigenvalues of **Q**, ranked for decreasing magnitude, are indicated as Λ_1, Λ_2 and Λ_3 and their associated (normalized) eigenvectors are indicated as $\vec{e}_1$, $\vec{e}_2$ and $\vec{e}_3$.

The sum of the eigenvalues provides the square radius of gyration of the chain:

$$R_g^2 = \Lambda_1 + \Lambda_2 + \Lambda_3 \tag{4}$$

while the adimensional ratios Λ_1/Λ_3 and Λ_2/Λ_3 are used to characterize the chain shape anisotropy.

dx.doi.org/10.1021/ma202503k | Macromolecules 2012, 45, 2113−2121

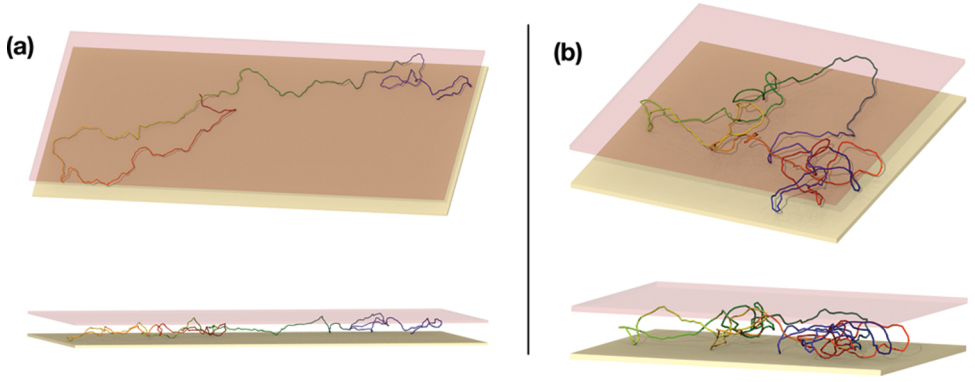

Figure 1. Two views of a confined semiflexible linear (panel a) and circular (panel b) chains of 480 cylinders, equivalent to a contour length L_c = 0.48 μm. In both cases the slit width is D = 70 nm.

The chain orientation inside the slit is conveniently described by the angle α formed by each principal gyration axis and the slit plane:

$$\cos \alpha_i = \sqrt{1 - |\vec{e}_i \cdot \hat{\mathbf{z}}|^2} \tag{5}$$

where $\hat{z}$ is the unit vector in the z direction.

To parallel the quantities that are customarily measured in nanoslit experiments, for each chain configuration we compute its mean square size projected in and out of the slit plane which are, respectively:

$$R_{||}^{\,2} = \sum_{i=1,2,3} \Lambda_i \cos^2 \alpha_i \tag{6}$$

$$R_{\perp}^{\,2} = R_g^{\,2} - R_{||}^{\,2} = \sum_{i=1,2,3} \Lambda_i (1 - \cos^2 \alpha_i) \tag{7}$$

D. Scaling Properties and the deGennes Regime. The de Gennes' blob theory provides a powerful reference framework for characterizing spatially constrained chains.[12] The theory, originally formulated to improve on standard mean-field theories for semidilute polymer solutions and,[51,52] has proved useful to understand the behavior of polymers confined in regions with transverse size larger than the molecule's persistence length

When such condition is met, the theory of de Gennes proposes to describe the self-avoiding chain, formed by N monomers of size b, as a sequence of "blobs", with each blob consisting of g monomers and having linear size about equal to the slit width, D, see Figure 2. Within each blob,

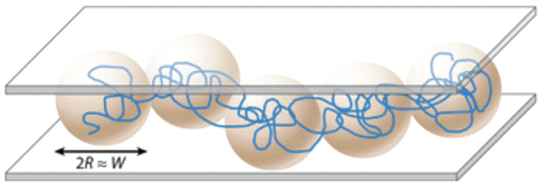

Figure 2. Pictorial representation of a confined polymer as a string of de Gennes' blobs.

the chain does not experience the confining constraints and hence it behaves as an unconstrained self-avoiding walk: $D \sim g^{\nu_{3D}}$, where $\nu_{3D} \sim 0.588$ is the three-dimensional self-avoiding walk scaling exponent.[53] At the same time, the string of blobs can be viewed as being a two-dimensional self-avoiding walk, with the blobs being the effective monomeric units of the walk. Accordingly, the in-plane size of the chain expectedly scales as $R_{||} \sim (N/g)^{\nu_{2D}} D$ where $\nu_{2D} = 3/4$ is the self-avoiding exponent in two dimensions.

This relationship can be recasted as $R_{||} \sim (N/g)^{\nu_{2D}} D \sim N^{\nu_{2D}} D^{-\nu_{2D}/\nu_{3D}} D$ or, equivalently,

$$\frac{R_{||}}{R_{||}^0} \sim \left(\frac{D}{R_g^0}\right)^{1-\nu_{2D}/\nu_{3D}} \sim \left(\frac{D}{R_g^0}\right)^{-0.276} \tag{8}$$

where we have exploited the proportionality of R_g^0 and $R_{||}^0$, which are respectively the root-mean-square values of the radius of gyration and the in-plane projected size of unconstrained chains. It is worth pointing out that the prefactor entering the scaling relationship of eq 8 changes according to whether the blobs are isometric or not.[13,20] This condition depends, in turn, on whether the slit width D is larger or smaller than $l_p^{\,2}/d$. For our case, the latter quantity is equal to 1 μm and therefore is always larger than the widths of the slits considered. The blobs are therefore expected to be anisometric (extended de Gennes regime).[20]

E. Topological Properties. The characterization of the entanglement of circular configurations is completed by establishing their knotted state. It should be noted, in fact, that the crankshaft moves employed for the MC evolution preserve the ring connectivity but not necessarily its topology.[54] In fact, even if the initial and final state of a crankshaft move are self-avoiding, the virtual crankshaft movement that bridges them can entail several bond crossings and hence can change the ring knotted state.

The topology of a ring is established using the same methodology of refs 23 and 45, which is articulated over the following steps. First, the ring geometry is simplified by topology preserving moves.[11,23,55,56] These moves consist of ring deformations involving no bond crossing and promote the collinearity of triplets of ring vertices that are nearby in sequence. After the chain simplification, a two-dimensional projection of the resulting configuration is next taken, encoded as a digital Dowker code, simplified algebraically and finally compared against a lookup table of prime knots with up to 16 crossings. If a match is found for all the prime component of a knot, then the ring knotted topology is unambigously established otherwise it is labeled as "unknown".

Notice that the "unknown" states may correspond to complicated knots with prime components having more than 16 crossings, or may be a simple knot that could not be simplified enough to positively identify it.

Further insights on the interplay between the topological properties of circular DNAs and the degree of confinement may be obtained by considering the average length of the knotted region in the ring. Locating the knotted portions in closed chains is a challenging problem, that presents the same conceptual difficulties as establishing the knotted state of a geometrically entangled open chain.[11,54] Although the application of topological concepts to open chains is *a priori* ambiguous, it has been recently verified that very different methods for locating knots in linear chains yield remarkably consistent results.[57] Among them we mention those based on the statistical closure scheme[58] and the minimally interfering one,[57] which is used here for its robustness and numerical efficiency.

III. LINEAR DNA IN NANO-SLITS

A. Effect of Confinement on Chain Orientation and Shape. The effect of slit confinement on the chain orientation is illustrated in Figure 3a.

dx.doi.org/10.1021/ma202503k | *Macromolecules* 2012, 45, 2113–2121

The data reflect the in-plane and out-of-plane orientations, see eq 5, of the three axes of inertia of open chains of contour length, L_c = 3604 nm. The bulk root-mean-square radius of gyration of these chains is R_g^0 = 236 nm (see Table 1) and its location in the plots of Figure 3 is depicted by the vertical dot-dashed line. For slit widths much larger than the chain bulk size the three mean square cosines are all close to the value 1/3, as expected in case of isotropic orientation of the chain in space.

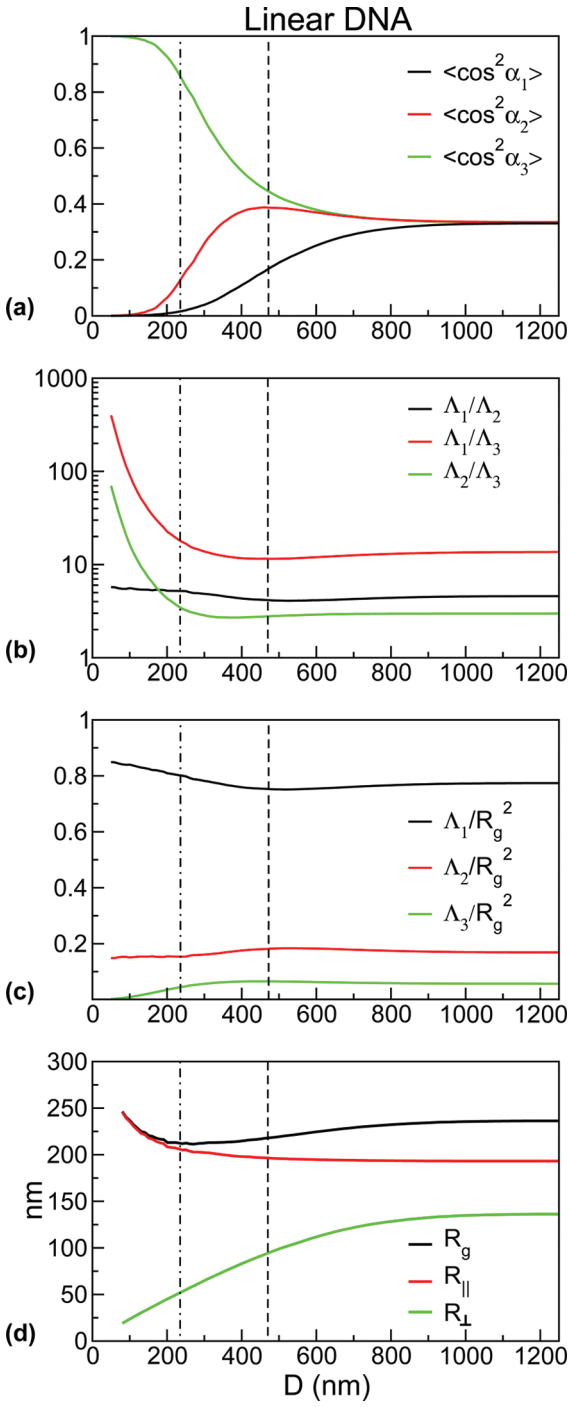

Figure 3. Metric properties of a linear chain L_c = 3604 nm inside a slit of width D. The orientation, shape and size of the gyration ellipsoid of the confined chain are shown in panels (a–c). The root-mean-square values of the chain radius of gyration, and its in- and out-of-plane projections are shown in panel (d). The range and scale of the x axis (representing the slit width, D) is common to all panels. The two vertical lines mark the reference slit widths R_g^0 (dot-dashed) and $2R_g^0$ (dashed).

The orientation of the longest axis of inertia begins to be noticeably nonisotropic when the slit width is about 700 nm, which exceeds three times the bulk radius of gyration. This is consistent with the strong shape anisotropy of unconstrained chains (Λ_1/Λ_3 = 13.8 and Λ_2/Λ_3 = 3.05) which implies that the longest axis of gyration cannot be freely accommodated inside the slit already when the width D is several times larger than R_g^0. The second longest axis of gyration is oriented isotropically, and maintains its bulk value, down to slit widths $D \approx 2R_g^0$ = 472 nm (shown in the panels of Figure 3 as a dashed vertical line). The value of Λ_2 reduces appreciably when D is decreased down to about R_g^0 and remains approximately constant for smaller slit widths. Analogous properties are found for the other chain lengths considered in this study.

For D < R_g^0, both the first and the second axes of inertia are mostly confined in the slit plane, while the third is oriented perpendicularly to it.

The progressive in-plane orientation of the two principal axes of inertia is paralleled by the flattening of the chain in the slit plane, see Figure 3b. From Figure 3c, it is noticed that for $D < 2R_g^0$ the progressive in-plane orientation of the second axis of inertia is accompanied by a decrease of its eigenvalue Λ_2 to a limiting value that is smaller than in the unconstrained, bulk case. The opposite is true for Λ_1. As a result, strongly confined open chains tend to have an elongated shape, as in the example of Figure 1a.

The adimensional data in Figure 3b,c compares favorably with available numerical and experimental results for the limiting cases of no- and strong two-dimensional confinement. In particular, Haber et al.[59] report the aspect ratios $(\Lambda_1/\Lambda_3)^{1/2}$ = 4.1 and $(\Lambda_1/\Lambda_2)^{1/2}$ = 2.3 for *fully flexible* unconstrained polymers, which are close to the corresponding values 3.7 and 2.1 found here. Finally, Maier et al., in their study of λ-phage DNA adsorbed on a flat bilayer lipid membrane,[60] found Λ_2/R_g^2 = 0.84 and Λ_2/R_g^2 = 0.14 which is in accord with the values Λ_1/R_g^2 = 0.84 ± 0.02 and Λ_2/R_g^2 = 0.148 ± 0.008 found here for the strongest two-dimensional confinement.

B. Effect of Confinement on Chain Size. The global, in-plane and transverse size of the chain at various levels of confinement are shown in Figure 3d.

The transverse size, $R_\perp$ and the parallel one, $R_\parallel$, have opposite monotonic dependence on D which result in a nonmonotonic behavior of R_g as a function of D. From Figure 3d, it is seen that R_g is minimum for D about equal to the bulk radius of gyration of the chain, R_g^0. This property is found consistently across chains of all considered lengths, as shown in Figure 4a.

To test the validity of the de Gennes' blob regime we analyzed the D dependence of $R_\parallel$. The result is shown in Figure 4b which reveals a remarkable collapse of data points from curves of lengths L_c between 2.4 and 4.8 μm. As shown in the figure, for high confinement $R_\parallel$ has a power law dependence on D, with exponent equal to −0.27 ± 0.05. This exponent, estimated by fitting the most asymptotic data, i.e., $L_c \geq$ 3604 nm, is well compatible with the −0.276 value predicted by the de Gennes' theory. Notice that, at all considered lengths no deviation from the de Gennes' theory is observed, consistently with the recent experiments of Doyle et al.[18] on longer DNA filaments.

IV. CIRCULAR DNA IN NANO-SLITS

We consider DNA rings with the same contour length as the previously discussed open chains, see Table 1, and for the same range of confining slit widths. The properties of rings are first characterized at the metric level and then at the topological one.

dx.doi.org/10.1021/ma202503k | Macromolecules 2012, 45, 2113–2121

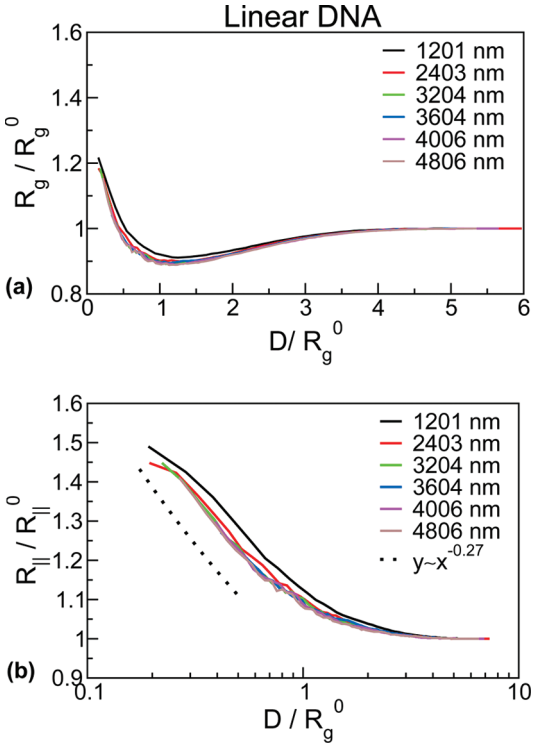

Figure 4. (a) Minimum three-dimensional size of the chain is achieved when the slit width is about equal to the average radius of gyration of the unconstrained chain. (b) Below such slit width the relationship between the average in-plane size, $R_{||}$, chain contour length, N, and slit width, D, is well accounted for by the de Gennes blob theory.

We shall particularly focus on the type, abundance and size of the various knots that are trapped in confined model DNA molecules that are circularized in equilibrium. These aspects are known to affect significantly the static and dynamics of polymers both in dilute[61,62] and dense solutions[63] or tightly packed in small volumes[17,24,25,27,28,57] or pulled through narrow channels[27,28] and are hence expected to be important for two-dimensional confinement too.

A. Effect of Confinement on Ring Orientation and Size. The dependence of a ring size and orientation on the confining slit width is illustrated in Figure 5. The data pertains to rings of length L_c = 3604 nm and therefore can be directly compared with those in Figure 3 for an equally long open chain.

The comparison of panels b and c in the two figures indicates that the shape of closed chains is significantly more spherical than open ones at all levels of confinement. The effect is aptly illustrated by the typical open and closed chains shown in Figure 1.

Notwithstanding the different shape, it is found that the changes in the ring orientation and size occur for values of the normalized slit width, D/R_g^0 that are similar to the linear case. In particular, the data in panel a show that the in-plane orientation of the ring principal axis of gyration sets in for $D \approx 2R_g^0$ while for the second one occurs at $D \approx R_g^0$. Furthermore, the average ring size, R_g, shown in panel d has a nonmonotonic dependence on D and its minimum value (again given by the opposite trends of $R_{||}$ and $R_\perp$) occurs for $D \approx R_g^0$, as for the linear case.

B. Scaling Properties and the de Gennes Regime. Because the bulk metric scaling exponents ν_{2D} and ν_{3D} are the same for open and closed chains, it is expected that the de Gennes scaling regime, originally based on the blob argument for linear chains, ought to hold for circular ones too.

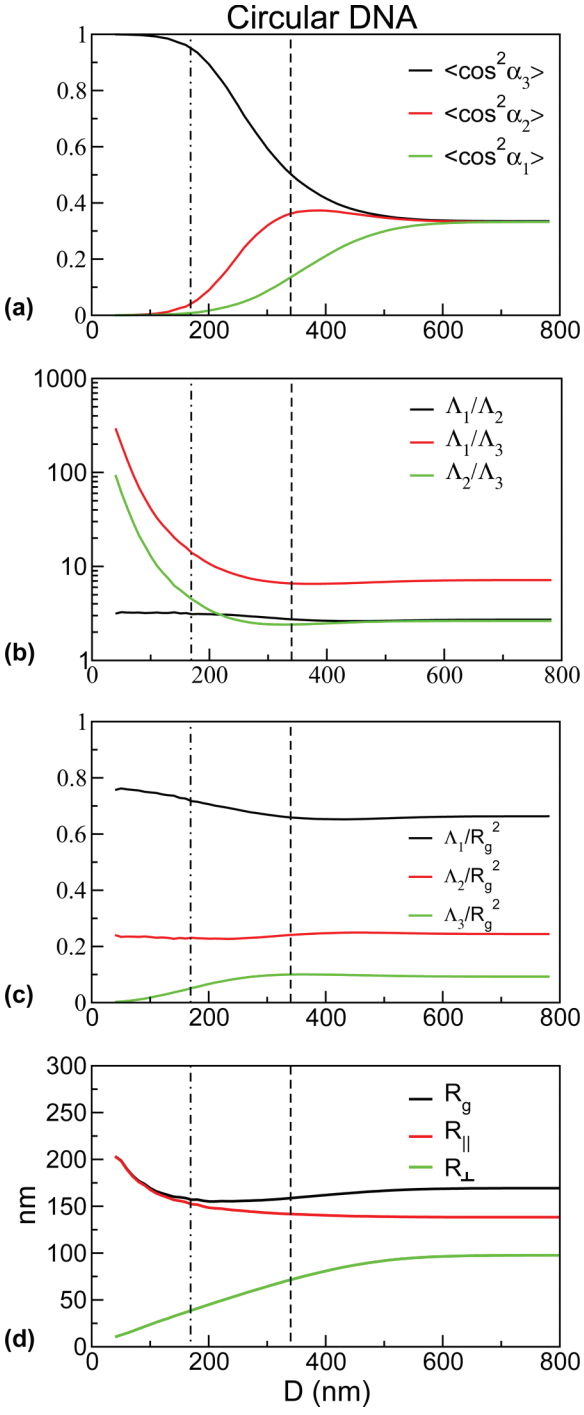

Figure 5. Metric properties of a circular chain L_c = 3604 nm inside a slit of width D. The orientation, shape and size of the gyration ellipsoid of the confined ring are shown in panels a–c. The root-mean-square values of the ring radius of gyration, and its in- and out-of-plane projections are shown in panel d. The range and scale of the x axis (representing the slit width, D) is common to all panels. The two vertical lines mark the reference slit widths R_g^0 (dot-dashed) and $2R_g^0$ (dashed).

However, the closed character of the rings introduces correlations in the orientation in pairs of bonds at a large chemical (contour) distance that have no analogue in linear chains[64,65]

To clarify the effect we show in Figure 6 the same observables reported in Figure 4 to analyze the de Gennes regime for confined linear chains.

dx.doi.org/10.1021/ma202503k | Macromolecules 2012, 45, 2113–2121

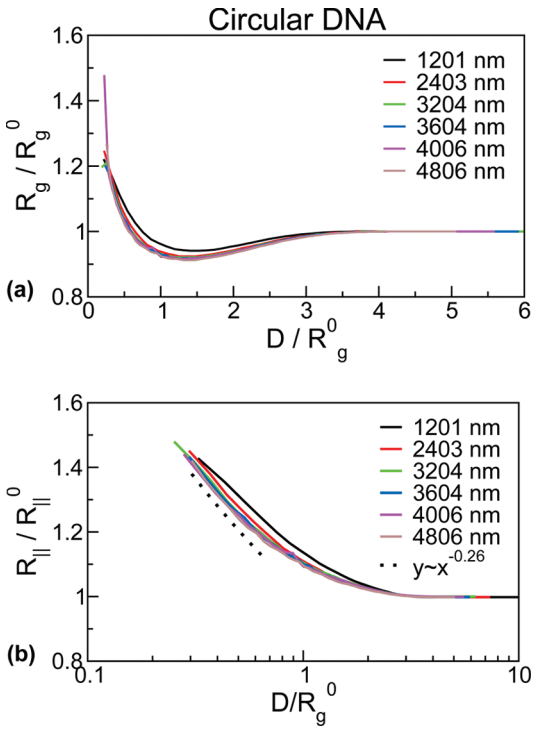

Figure 6. (a) Minimum three-dimensional size of the ring is achieved when the slit width is about equal to the average radius of gyration of the unconstrained ring. (b) Below such slit width the relationship between the average in-plane size, $R_{||}$, ring contour length, N, and slit width, D, is well accounted for by the de Gennes' blob theory.

Panel a shows that, except for the data at the smallest ring contour length, there is a good overlap of the rescaled ring size versus width curves. In particular, for all considered chain lengths the minimum overall ring size is obtained for $D \approx R_g^0$, consistently with the open chain case

For $D < R_g^0$ the mean in-plane size shows a behavior that is compatible with the de Gennes scaling regime, as illustrated in panel (b). The power-law fit of the asymptotic data in the figure, i.e., $L_c \geq 3604$ nm and $D/R_g^0 < 1$, yields the scaling exponent -0.26 ± 0.04. This value is compatible with the -0.276 value predicted by the de Gennes theory, consistently with what found for the linear case.

C. Topological Entanglement. *1. Knotting Probability.* The Monte Carlo strategy employed here and in other previous studies provides the means to characterize the occurrence of nontrivial knots in rings that are circularized in equilibrium. The knotting probability of unconstrained rings depends on several length scales such as the molecule's persistence length, its contour length and thickness.[66,67] Accordingly, the topological complexity of the circularized molecules can be tuned, to some extent, by varying these lengths, for example by intervening of the solution ionic strength.[43,68]

Spatial confinement introduces a further length scale in the problem, the width of the confining region, which can affect dramatically the molecule's entanglement. The effect has been addressed by several studies of isotropic three-dimensional confinement[17,23,25,45] which established that progressive reduction of the volume resulted in an ever-increasing fraction of knotted molecules and of their geometrical and topological complexity.[24]

By comparison, the case of two-dimensional confinement is virtually unexplored, except for lattice polymer models.[42,69,70] Making progress in this problem is not only important to fill a conceptual gap but is especially so in view of the dramatic qualitative differences that are expected *a priori* compared to the isotropic, three-dimensional, confinement.

In fact, it should be considered that for extreme two-dimensional confinement, i.e., for slit width only slightly larger than the chain intrinsic thickness, over/under-crossings of the chain are impossible and knots cannot be formed. Therefore, unlike the isotropic case, progressive slit confinement cannot result in an ever increasing complexity of the ring topology and geometry.

To clarify this aspect we investigated the dependence of the knotting probability on D. The results are shown in Figure 7a

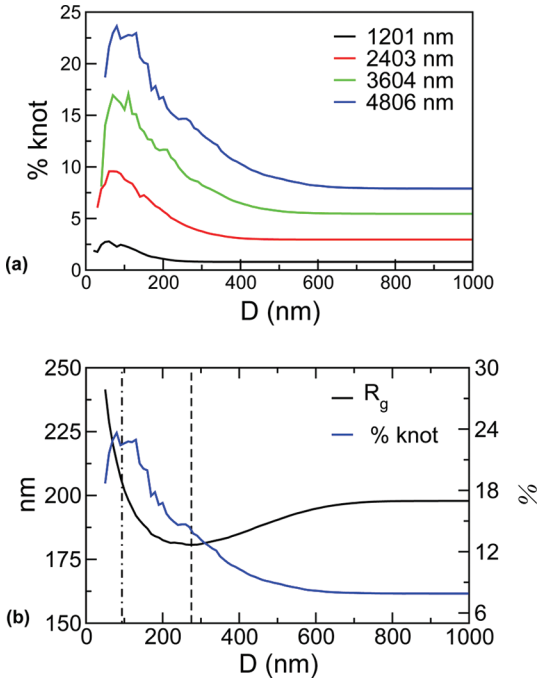

Figure 7. (a) Knotting probability of equilibrated rings of different contour length. (b) Dependence on the slit width, D, of the average radius of gyration and knotting probability for a circular DNA ring of L_c = 4806 nm. The vertical dashed line marks the slit width, D^*, corresponding to the minimum three-dimensional size of the ring. The dot-dashed line marks the maximum of the knotting probability.

and indicate that the ring knotting probability is nonmonotonic and for a certain slit width, D_e reaches a maximum enhancement compared to the bulk case. Notice that the peak value exceeds the bulk knotting probability by several factors. The figure indicates that the limiting value of zero knotting probability is rapidly reached for $D < D_e$.

It could be intuitively expected that the maximum knotting enhancement occurs for the same slit width, D^*, associated with the maximum chain density (minimum R_g).[42] This is, however, not the case. In fact, in the example of Figure 7b the peak of the probability distribution occurs when the slit width is $D_e \approx 90$ nm, which is about one-third of D^*. As a matter of fact, over the considered range of contour lengths, D_e is consistently equal to about half the bulk ring size.

2. Knot Spectrum. It is most interesting to examine how the various, topologically inequivalent knot types, contribute to the nonmonotonic trend of the overall knotting probability.

The results are shown in Figure 8a,b which portrays the probability of occurrence of various knot types (including the

dx.doi.org/10.1021/ma202503k | *Macromolecules* 2012, 45, 2113–2121

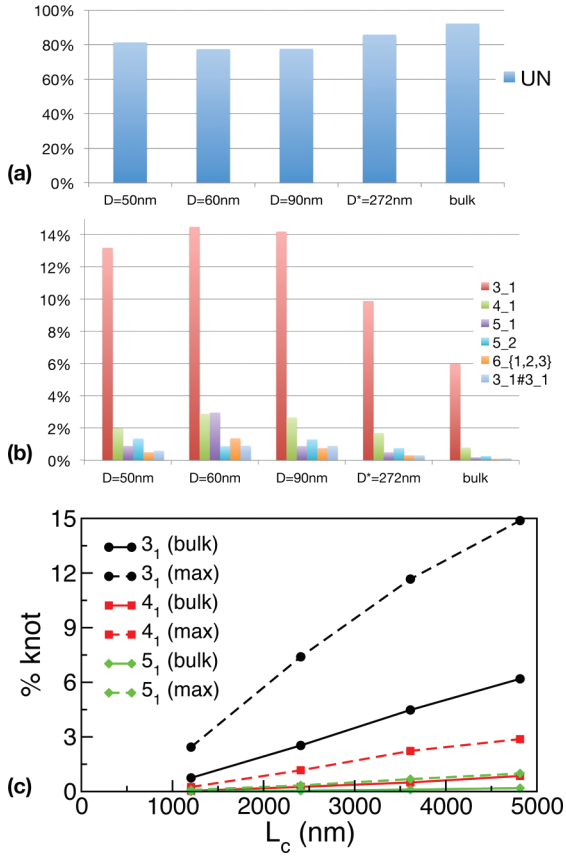

Figure 8. (a, b) Slit-width dependence of the knot spectrum of confined circular DNA with L_c = 4806 nm. D^* is the slit width at which the mean 3D extension of the rings reaches its minimum value. (c) Maximum probability of occurrence for knot types 3_1, 4_1, and 5_1 as a function of the contour length L_c (dashed curves). Solid curves refer to the corresponding case of unconstrained circular DNAs.

unknot) for four different slit widths and L_c = 4.8 μm. It is seen that, at all level of confinement, the knot population consists of very simple knots, and is dominated by the simplest of all, the trefoil or 3_1 knot, whose peak abundance is ~14%.

The result is notable in several respects. First, the knot spectrum of Figure 8a is qualitatively very different from the one of an equivalent model of circular DNA subject to isotropic, spherical confinement.[45]

In fact, even for moderate three-dimensional confinement in a sphere of diameter equal to 180 nm, the knot spectrum of molecules of L_c = 3.4 μm is largely constituted by highly complex knots: trefoils are less than 10% of the nontrivial knots (which, in turn are 55% of the ring population). Conversely, for slit confinement, at all considered values of L_c and D, complex knots are virtually absent and the population of simple knot types, such as the trefoil, reaches values that cannot be matched by rings of the same or longer contour lengths subject to any degree of isotropic confinement.[23]

We finally turn to the dependence of the peak of the probability of occurrence of simple knots as a function of chain length. The data in Figure 8c indicate a monotonic increase of the peak probability with L_c. Therefore, the population of simple knots can be further increased compared to the values in panel b by suitably confining rings with L_c > 5 μm. At the same time, it is noticed that the derivative of the peak probability curves decreases with L_c so that, by analogy with the bulk probability case, one can envisage that the curves will eventually decrease for sufficiently large values of L_c. This is an interesting point that would deserve to be addressed in future studies.

3. Knot Length. We conclude the topological characterization by reporting on the degree of localization (in space and along the chain) of the knots formed in the confined rings. The knot location along the ring was established using the bottom-up search of the smallest arc(s) that, after closure, has the same topology of the whole ring;[57,71] see the example in Figure 9.

The average contour length spanned by the knots (all nontrivial topologies) as a function of D is shown in Figure 10

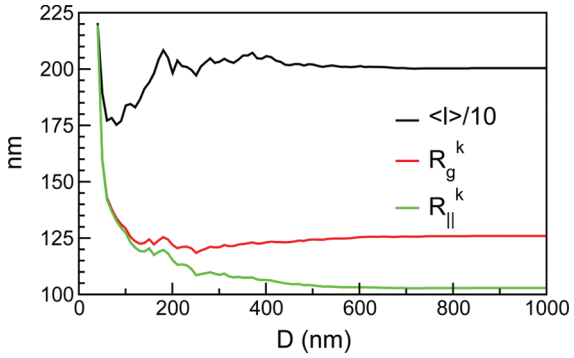

Figure 10. Three-dimensional and parallel mean estension of the knotted portion of circular trefoil knots with L_c = 4806 nm. Circles refer to the average knot size expressed in unit of cylinders.

for rings of length L_c = 4.8 μm. It is seen that up to the point where the average ring size is minimum, the length of the knotted region is about constant, and drops significantly at smaller slit widths.

The same figure also shows the average in-plane and overall size of the knotted region, which is indicated with R_g^k and $R_{||}^k$, respectively. It is apparent that the drop in knot length occurs when the slit width is about equal to the bulk value of the overall knot size, $D \approx$ 125 nm. These results suggest that for

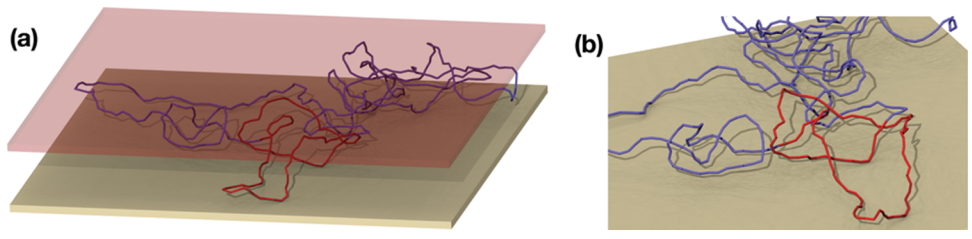

Figure 9. (a) Trefoil-knotted ring confined in a nanoslit. The configuration is the same as the one shown in Figure 1c,d. The ring contour length is 0.48 μm and the slit width is 70 nm. The shortest knotted portion of the ring is highlighted in red. (b) Close-up of the knotted portion. For graphical clarity the slit top is not shown.

dx.doi.org/10.1021/ma202503k | *Macromolecules* 2012, 45, 2113–2121

knotted polymer rings confined into slits the typical size of the knotted region introduces an additional length scale into the problem that could play a relevant role in understanding the metric and mechanical properties of these confined molecules at equilibrium.[70,72]

V. CONCLUSIONS

The equilibrium properties of linear and circularized model DNA molecules confined in nanoslits were studied by numerical methods. By using thermodynamic reweighting techniques the properties of these systems were systematically profiled as a function of the molecules' contour length and nanoslit width. The analysis proceeded by first considering the molecules' geometrical properties and next the topological ones. The former included the size, shape and spatial orientation of the molecules in the slit, while the latter consisted of the knotting probability and knot spectrum.

We found that the scaling of the metric properties was described very well by de Gennes' blob theory for both linear and circular molecules of all considered lengths and down to the highest confinement. To the best of our knowledge, it is the first time that the applicability of the blob theory is discussed (and shown to hold) for equilibrated ring polymers. In addition, even for linear molecules, the fact that the de Gennes' scaling is investigated upon varying *both* the molecules' contour length and the slit width represents a significant broadening of the scope of previous investigations. Our results are consistent with the conclusions of recent experiments of nanoslit confinement of linear λ-DNA which found no indications of deviations from de Gennes' blob theory.[18]

Finally, and most importantly, we characterized the topological entanglement that is trapped in molecules that circularize in equilibrium inside nanoslits. For both applicative purposes and for fundamental polymer science, the characterization of the physical properties of DNA molecules with various topologies (linear, circular planar, circular knotted) has attracted much interest in the past decades. Our contribution represents a step forward in the characterization of such systems in the presence of confinement: while the three-dimensional confinement has been heavily investigated,[23,25,26,28,45] the two-dimensional one by means of slits is still largely unexplored. Our study has pointed out a remarkable feature that has no parallel with three-dimensional confinement, namely the nonmonotonicity of the knotting probability for increasing confinement. Specifically, it is seen that, among the rings resulting from equilibrium circularization (studied without enforcing topology conservation) the fraction of knotted rings has a maximum at a length-dependent slit width, D_e. The peak knotting probability exceeds by several factors the one in the bulk. Upon decreasing D below D_e, the knotting probability decreases very rapidly to zero.

The above result shows that nanoslit confinement ought to be profitably used in contexts where an *a priori* control of the knotted topology of DNA rings is desired. In particular, the nonmonotonic dependence of the knotting probability as a function of confinement, makes it possible to conceive experiments where the slit width is tuned so that the knotting probability is either significantly enhanced or largely depressed with respect to the bulk case.

The natural extensions of the present study are 2-fold. On the one hand it would be interesting to consider much longer chain lengths and establish the detailed length-dependence of D_e and the associated maximum knotting probability. On the other hand, it would be most interesting to repeat the present investigation to the one-dimensional confinement case (i.e., nanochannels) and analyze how the expected consecutive onsets of the de Gennes and Odijk regimes impact both the geometrical and the topological properties of confined rings.

AUTHOR INFORMATION

Corresponding Author

*E-mail: (C.M.) michelet@sissa.it; (E.O.) orlandini@pd.infn.it.

Notes

The authors declare no competing financial interest.

ACKNOWLEDGMENTS

We acknowledge support from the Italian Ministry of Education. We thank A. Rosa for useful discussions.

REFERENCES

(1) Han, J.; Craighead, G. *Science* **2000**, *288*, 1026.
(2) Jo, K.; et al. *Proc. Natl. Acad. Sci. U.S.A.* **2007**, *104*, 2673.
(3) Zwolak, M.; Di Ventra, M. *Rev. Mod. Phys.* **2008**, *80*, 141.
(4) Fu, J.; Yoo, J.; Han, J. *Phys. Rev. Lett.* **2006**, *97*, 018103.
(5) Schoch, R. B.; Han, J.; Renaud, P. *Rev. Mod. Phys.* **2008**, *80*, 839.
(6) Maier, B.; Radler, J. O. *Phys. Rev. Lett.* **1999**, *82*, 1911.
(7) Drube, F.; Alim, K.; Witz, G.; Dietler, G.; Frey, E. *Nano Lett.* **2010**, *10*, 1445.
(8) Bonthuis, D. J.; Meyer, C.; Stein, D.; Dekker, C. *Phys. Rev. Lett.* **2008**, *101*, 108303.
(9) Lin, P.-K.; Fu, C.-C.; Chen, Y.-L.; Chen, Y.-R.; Wei, P.-K.; Kuan, C. H.; Fann, W. S. *Phys. Rev. E* **2007**, *76*, 011806.
(10) Krishnan, M.; Monch, I.; Schwille, P. *Nano Lett.* **2007**, *7*, 170.
(11) Micheletti, C.; Marenduzzo, D.; Orlandini, E. *Physics Reports* **2011**, *504*, 1.
(12) de Gennes, P.-G. *Scaling Concepts in Polymer Physics*; Cornell University Press: Ithaca, NY, 1979.
(13) Odijk, T. *Phys. Rev. E* **2008**, *77*, 060901.
(14) Valle, F.; Favre, M.; De Los Rios, P.; Rosa, A.; Dietler, G. *Phys. Rev. Lett.* **2005**, *95*, 158105.
(15) Reisner, W.; Morton, K. J.; Riehn, R.; Wang, Y. M.; Yu, Z.; Rosen, M.; Sturm, J. C.; Chou, S. Y.; Frey, E.; Austin, R. H. *Phys. Rev. Lett.* **2005**, *94*, 196101.
(16) Ercolini, E.; Valle, F.; Adamcik, J.; Witz, G.; Metzler, R.; Rios, P. D. L.; Roca, J.; Dietler, G. *Phys. Rev. Lett.* **2007**, *98*, 058102.
(17) Marenduzzo, D.; Micheletti, C.; Orlandini, E. *J. Phys.: Condens. Matter* **2010**, *22*, 283102.
(18) Tang, J.; Levy, S. L.; Trahan, D. W.; Jones, J. J.; Craighead, H. G.; Doyle, P. S. *Macromolecules* **2010**, *43*, 7368.
(19) Odijk, T. *Macromolecules* **1983**, *16*, 1340.
(20) Wang, Y.; Tree, D.; Dorfman, K. *Macromolecules* **2011**, *44*, 6594.
(21) Michels, J. P. J.; Wiegel, F. W. *J. Phys. A: Math. Gen.* **1989**, *22*, 2393.
(22) Tesi, M. C.; Janse Van Rensburg, E. J.; Orlandini, E.; Whittington, S. G. Topology and geometry in polymer science. In *IMA Volumes in Mathematics and Its Application*; Whittington, S. G., Sumners, D. W., Lodge, T., Eds.; *103*, 135 (1998).
(23) Micheletti, C.; Marenduzzo, D.; Orlandini, E.; Sumners, D. W. *J. Chem. Phys.* **2006**, *124*, 064903.
(24) Tubiana, L.; Orlandini, E.; Micheletti, C. *Phys. Rev. Lett.* **2011**, *107*, 188302.
(25) Arsuaga, J.; Vázquez, M.; Trigueros, S.; Sumners, D. W.; Roca, J. *Proc. Natl. Acad. Sci. U.S.A.* **2002**, *99*, 5373.
(26) Arsuaga, J.; Vázquez, M.; McGuirk, P.; Trigueros, S.; Sumners, D. W.; Roca, J. *Proc. Natl. Acad. Sci. U.S.A.* **2005**, *102*, 9165.
(27) Matthews, R.; Louis, A. A.; Yeomans, J. M. *Phys. Rev. Lett.* **2009**, *102*, 088101.
(28) Marenduzzo, D.; Orlandini, E.; Stasiak, A.; Sumners, d. W.; Tubiana, L.; Micheletti, C. *Proc. Natl. Acad. Sci. U.S.A.* **2009**, *106*, 22269.
(29) Gelbart, W. M.; Knobler, C. M. *Science* **2009**, *323*, 1682.
(30) Leforestier, A.; Siber, A.; Livolant, F.; Podgornik, R. *Biophys. J.* **2011**, *100*, 2209.

(31) Chen, J. Z. Y.; Sullivan, D. E. *Macromolecules* **2006**, *39*, 7769.
(32) Dimitrov, D. I.; Milchev, A.; Binder, K.; Klushin, L. I.; Skvortsov, A. M. *J. Chem. Phys.* **2008**, *128*, 234902.
(33) Atapour, M.; Soteros, C.; Whittington, S. G. *J. Phys. A: Math. Theor.* **2009**, *42*, 322002.
(34) Grosberg, A. Y. *Phys. Rev. Lett.* **2000**, *85*, 3858.
(35) Moore, N. T.; Lua, R. C.; Grosberg, A. Y. *Proc. Natl. Acad. Sci. U.S.A.* **2004**, *101*, 13431.
(36) Schvartman, J. B.; Stasiak, A. *EMBO Rep.* **2004**, *5*, 256.
(37) Virnau, P.; Mallam, A.; Jackson, S. *J. Phys.: Condens. Matter* **2011**, *23*, 033101.
(38) Virnau, P.; Kantor, Y.; Kardar, M. *J. Am. Chem. Soc.* **2005**, *127*, 15102.
(39) Sumners, D. W.; Ernst, C.; Spengler, S. J.; Cozzarelli, N. R. *Q. Rev. Biophys.* **1995**, *28*, 253.
(40) Liu, Z.; Mann, J. K.; Zechiedrich, E. L.; Chan HS, H. S. *J. Mol. Biol.* **2006**, *361*, 268.
(41) Liu, Z.; Zechiedrich, L.; Chan, H. S. *J. Mol. Biol.* **2010**, *400*, 963.
(42) Tesi, M. C.; Janse Van Rensburg, E. J.; Orlandini, E.; Whittington, S. G. *J. Phys. A: Math. Gen.* **1994**, *27*, 347.
(43) Rybenkov, V. V.; Cozzarelli, N. R.; Vologodskii, A. V. *Proc. Natl. Acad. Sci. U.S.A.* **1993**, *90*, 5307.
(44) Shimamura, M. K.; Deguchi, T. *Phys. Lett. A* **2000**, *274*, 184.
(45) Micheletti, C.; Marenduzzo, D.; Orlandini, E.; Sumners, D. W. *Biophys. J.* **2008**, *95*, 3591.
(46) Strey, H. H.; Podgornik, R.; Rau, D. C.; Parsegian, V. A. *Curr. Opin. Struct. Biol.* **1998**, *8*, 309.
(47) Leforestier, A.; Livolant, F. *Proc. Natl. Acad. Sci. U.S.A.* **2009**, *106*, 9157.
(48) Grosberg, A.; Zhestkov, A. *J. Biomol. Struct. Dyn.* **1985**, *3*, 515.
(49) Rollins, G. C.; Petrov, A. S.; Harvey, S. C. *Biophys. J.* **2008**, *94*, 38.
(50) Tesi, M. C.; Janse Van Rensburg, E. J.; Orlandini, E.; Whittington, S. G. *J. Stat. Phys.* **1996**, *82*, 155.
(51) De Gennes, P. *Isr. J. Chem.* **1975**, *14*, 154.
(52) Daoud, M.; Cotton, J. P.; Farnoux, B.; Jannink, G.; Sarma, G.; Benoit, H.; Duplessix, C.; Picot, C.; de Gennes, P. G. *Macromolecules* **1975**, *8*, 804.
(53) Clisby, N. *Phys. Rev. Lett.* **2010**, *104*, 055702.
(54) Orlandini, E.; Whittington, S. G. *Rev. Mod. Phys.* **2007**, *79*, 611.
(55) Taylor, W. R. *Nature* **2000**, *406*, 916.
(56) Koniaris, K.; Muthukumar, M. *Phys. Rev. Lett.* **1991**, *66*, 2211.
(57) Tubiana, L.; Orlandini, E.; Micheletti, C. *Prog. Theor. Phys.* **2011**, *191*, 192.
(58) Millett, K.; Dobay, A.; Stasiak, A. *Macromolecules* **2005**, *38*, 601.
(59) Haber, C.; Ruiz, S. A.; Wirtz, D. *Proc. Natl. Acad. Sci. U.S.A.* **2000**, *97*, 10792.
(60) Maier, B.; Rädler, J. O. *Macromolecules* **2001**, *34*, 5723.
(61) Rawdon, E.; Dobay, A.; Kern, J. C.; Millett, K. C.; Piatek, M.; Plunkett, P.; Stasiak, A. *Macromolecules* **2008**, *41*, 4444.
(62) Rawdon, E. J.; Kern, J. C.; Piatek, M.; Plunkett, P.; Stasiak, A.; Millett, K. C. *Macromolecules* **2008**, *41*, 8281.
(63) Rosa, A.; Orlandini, E.; Tubiana, L.; Micheletti, C. *Macromolecules* **2011**, *44*, 8668.
(64) Witz, G.; Rechendorff, K.; Adamcik, J.; Dietler, G. *Phys. Rev. Lett.* **2008**, *101*, 148103.
(65) Witz, G.; Rechendorff, K.; Adamcik, J.; Dietler, G. *Phys. Rev. Lett.* **2011**, *106*, 248301.
(66) Frank-Kamenetskii, M. D.; Lukashin, A. V.; Vologodskii, A. V.; V., A. *Nature* **1975**, *258*, 398.
(67) Deguchi, T.; Tsurusaki, K. *Phys. Rev. E* **1997**, *55*, 6245.
(68) Toan, N. M.; Micheletti, C. *J. Phys.: Condens. Matter* **2006**, *18*, S269.
(69) Soteros, C.; Whittington, S. G. *Israel J. Chem.* **1991**, *31*, 127.
(70) Janse van Rensburg, E. J. *J. Stat. Mech.* **2007**, P03001.
(71) Marcone, B.; Orlandini, E.; Stella, A. L.; Zonta, F. *J. Phys. A: Math. Gen.* **2005**, *38*, L15.
(72) Matthews, R.; Louis, A. A.; Yeomans, J. M. *Mol. Phys.* **2011**, *109*, 1289.

Macromolecules

Article

pubs.acs.org/Macromolecules

Diffusion Resonance of Nanoconfined Polymers

Alexander R. Klotz,* Hugo B. Brandão, and Walter W. Reisner

Department of Physics, McGill University, Montreal, Quebec, Canada H3A 2T8

ABSTRACT: We examine the diffusive behavior of single polymers under spatially varying entropic confinement. A nanofluidic slit embedded with a lattice of pits was used to constrain single DNA molecules to discrete conformational states. Diffusion was characterized by dwelling in specific conformations followed by transitions to neighboring states. In contrast to studies involving simple 2D (nanoslit) and 1D (nanochannel) geometries, the diffusivity showed nonmonotonic dependence with respect to the parameters of confinement. In particular, the nanopit array allows us to fine-tune the diffusivity of a single polymer to a local resonance minimum. Moreover, we show that energetically favorable states dominate over higher energy states and that a single state can be stable over a wide range of parameter space. These stable states correspond to resonances in the diffusion.

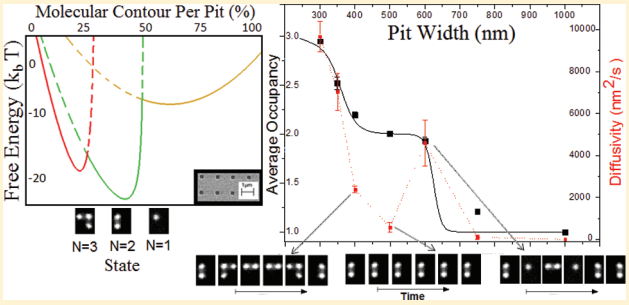

INTRODUCTION

Over the past decade workers at the interface of polymer physics, nanoscience, and biotechnology have developed the field of DNA nanoconfinement, focused on using nanoconfined geometries to modulate DNA conformation on-chip. The bulk of work in the field has been focused on simple confinement, e.g., two-dimensional nanoslits and one-dimensional nanochannels.[1] In simple geometries, the confinement alters the DNA conformation, leading to either a pancake-like conformation (nanoslit) or an extended cigar-like conformation (nanochannel). Highly parallel nanochannel arrays can be used to extend many DNA molecules in parallel and forms the basis of new type of single-molecule mapping technology.[2,3] There has been significant work investigating the diffusion and equilibrium conformation of DNA confined in nanoslits and nanochannels.[4−9] In these simple devices polymer dynamic and static properties are observed to scale monotonically with confinement (although controversy still exists regarding the details of the scaling exponents[10,11]).

Nanoslit and nanochannel geometries allow only for a uniform expansion of the polymer coil, either along the axis of the nanochannel or perpendicular to the confining lid of a nanoslit device. Recently, Reisner et al.[12] proposed a new type of complex nanodevice consisting of an open nanoslit with embedded nanotopography. By spatially varying confinement, it is possible to create a user-defined free energy landscape for controlling polymer conformation. Polymers will have greater conformational freedom in locally less confined regions of the device, leading to a locally increased entropy. A higher local entropy corresponds to a free energy minimum, acting as a potential trap for molecule contour. In particular, if the confinement is varied over scales comparable to the molecular gyration radius, it is possible to directly "sculpt" the conformation of a single DNA molecule. In the initial study of Reisner et al.,[12] the embedded nanotopography consisted of a square lattice of nanopits. The pit depth, pit-to-pit separation, and slit height could be adjusted via the fabrication process. This device demonstrated enhanced control over local polymer conformation, in particular the ability to direct self-organization of DNA into complex conformations linking multiple nanopits, demonstrating simultaneous stretching and trapping of DNA. This system provides an ideal platform for dictating polymer self-organization in a solid-state device, and the templated self-assembly that it facilitates may reduce the need for highly specific surface chemistry.

We show here that the nanopit arrays can be used to control dynamic properties such as single-molecule diffusion, in addition to static equilibrium conformation. We explore a wide enough range of parameter space to deduce the detailed dependence of diffusion and static conformation on device geometry. We show that, in contrast to simple geometries, where the diffusion depends upon confinement in a purely monotonic way, the diffusion has a complex nonmonotonic dependence, undergoing a resonance effect as a function of the nanopit width.

The original work of Reisner et al.[12] focused purely on static properties of DNA molecules in the nanopit lattices. Reisner et al.,[12] in particular, did not demonstrate the existence of stable conformational states over a range of device parameters (as predicted by their model): the four lattice spacings investigated were not sufficient to demonstrate the existence of stable conformations (corresponding to plateaus in the pit occupancy versus lattice spacing). Subsequent work examined the mobility of DNA in linear nanopit arrays, both experimentally[13] and theoretically.[14] Again, these authors did not explore a wide-enough range of parameter space to make quantitative

Received: December 2, 2011
Revised: February 7, 2012
Published: February 15, 2012

   dx.doi.org/10.1021/ma202596j | *Macromolecules* 2012, 45, 2122−2127

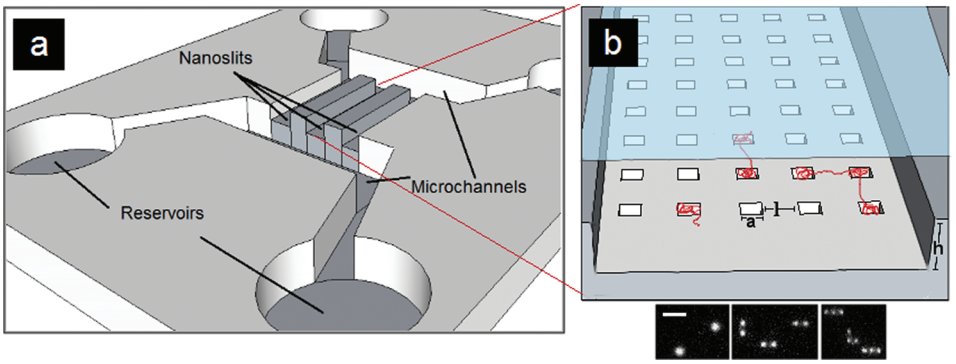

Figure 1. (a) Schematic of the overall design of the device. (b) Schematic of the nanoslit and embedded nanopit lattice with DNA and fluorescence images of molecules in the device. Scale bar is 2 μm. Typical dimensions: slit height (h): 100 nm; pit width (a): 500 nm; pit separation (l): 1000 nm.

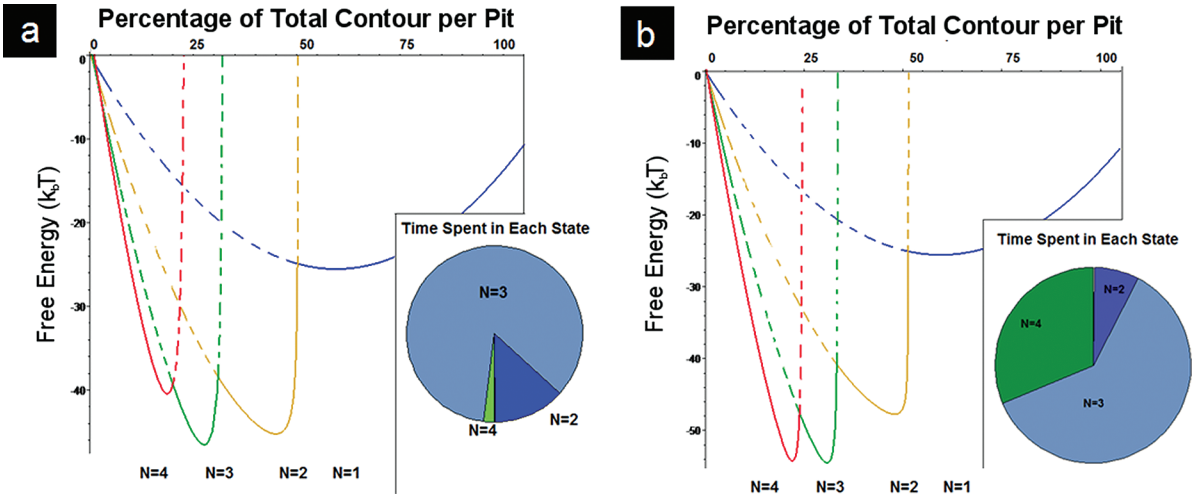

Figure 2. Free energy landscapes as a function of contour partitioned per pit. Each curve, corresponding to a given occupancy state on the lattice (with N occupied pits), gives the free energy as a function of the contour partitioned per pit (expressed as a percentage of the total molecule contour). The curve minima correspond to the equilibrium values of contour partitioned per pit. When the free energy differences between the curve minima are much greater than k_bT, the molecules will be found in a single state. When the free energy differences are on the order of k_bT, multiple occupancy states will be accessed in equilibrium. In (a), the N=3 state dominates, but transitions are also possible to N=2 and N=4 states (although of low probability). In (b), the N=3 state still dominates but the N=4 and N=2 states are more probable.

predictions for the dependence of mobility on device parameters. Moreover, the two-dimensional lattice behavior discussed here offers a richer experimental landscape than the one-dimensional arrays. Additional work by Mikkelson et al.[15] is similar to that of DelBonis-O'Donnell,[13] in that the mechanisms of trapping and escape under external driving are examined, but the effects of varying confinement dimensions and equilibrium behavior are left unexplored. Finally, our system differs from classic work on entropic trapping of DNA, such as that of Han and Craighead[16] or Nykypanchuk et al.,[17] in that it involves strong lateral confinement as well as vertical confinement, leading to the ability to fine-tune local DNA conformation.

EXPERIMENT

These experiments took place in a nanofluidic lab-on-a-chip device (Figure 1), first described by Reisner et al. in 2008.[12] A nanoslit, on the order of 100 nm in height and smaller than the radius of gyration of the polymer, constrained the dynamics of the polymer to two dimensions. The nanoslit was embedded with a square lattice of square pits with double the depth of the slit, on the order of a few hundred nanometers to a micrometer in width with separations on the order of a micrometer. Because of the greater conformational degeneracy within the pits, the square pits acted as entropic traps.

The devices were fabricated using standard clean-room techniques. The nanopits were patterned onto a fused silica wafer in zep520A resist using electron beam lithography and etched using CF_4:CHF_3 reactive ion etching. The nanoslit and microchannels were patterned in S1813 resist using UV lithography and etched similarly. The individual wafers were bonded to coverslips to seal the slits and channels.

λ-DNA was used as a model polymer in these experiments. After being stained with YOYO-1 fluorescent dye with a 10:1 intercalation ratio, it had a total contour length of ~19 μm and a persistence length of ~52 nm.[18] The stained DNA was loaded into a 50 mM TRIS buffer (pH 8.0) with 2% β-mercaptoethanol to prevent photobleaching. The DNA was pipetted into the reservoirs of the chip, and the chip was fastened to a chuck and attached to a Nikon Eclipse TI inverted microscope. A Nikon Plan Apo VC 100× lens was used to focus on the system. By applying pneumatic pressure externally to the reservoirs, DNA could be driven from the microfluidic channels into the nanoslit. When the driving pressure was turned off, the molecules quickly self-assembled into the configurations dictated by the nanopits and a time series was recorded using a cooled Andor iXon EM-CCD camera. The images were analyzed by tracking the position of each occupied pit over time.

THEORY

In this network of pits, entropy is maximized when the entire polymer occupies a single pit, but self-exclusion interactions—

dx.doi.org/10.1021/ma202596j | Macromolecules 2012, 45, 2122–2127

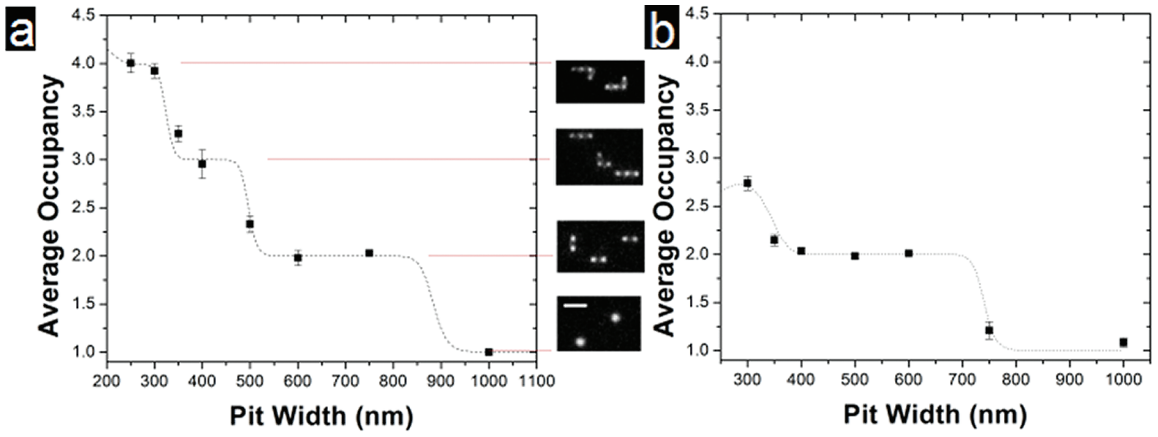

Figure 3. Static behavior of DNA molecules in this system: (a) A plot of average occupancy as a function of pit size in a 50 nm slit, with theoretical fit. Occupancy decreases with increasing pit size. Fluorescence micrographs show the corresponding configurational states. Scale bar is 2 μm. (b) A plot of average occupancy as a function of pit size in a 70 nm slit, with theoretical fit. A plateau is apparent for the dimer state. Error bars represent variation between molecules, and may be absent if all molecules were observed in a single state.

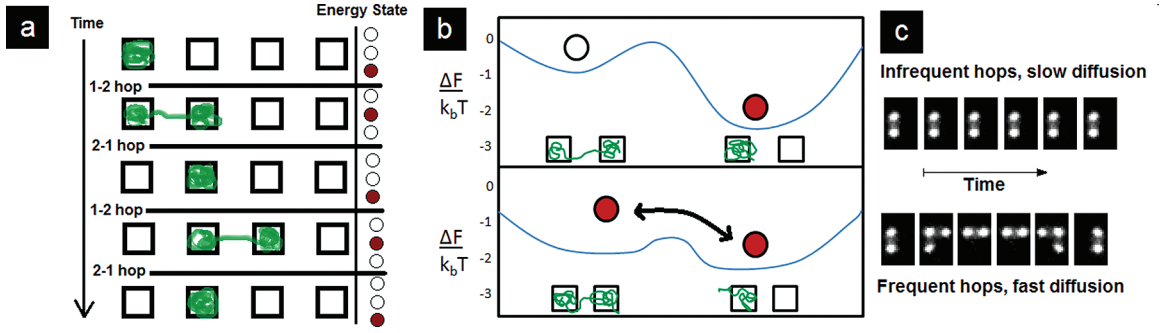

Figure 4. Dynamic behavior of molecules in this system. (a) The mechanism of diffusion, involving discrete hops between energy states that displace the center of mass. (b) Two model free energy landscapes demonstrating that diffusion can be fast or slow depending on the stability of each state. (c) Time series of a DNA molecule demonstrating slow and fast diffusion.

arising from binary chain collisions in the restricted pit volume—limit the contour that can be stored in a single pit. Thus, a single polymer may occupy multiple pits. These competing interactions dictate a free energy landscape, with the amount of contour in each pit acting as the independent variable (Figure 2).

At equilibrium, the Helmholtz free energy of the polymer is determined entirely by the number of occupied pits. The absolute free energy of each state can be tuned by varying geometric parameters such as the height of the nanoslit or spacing of the pits, but ultimately the molecule is in a system of energetically discrete configurations where the number of occupied pits is the only dynamical variable. The simplification of the system to one variable simplifies it greatly, both experimentally and theoretically. The free energy for a molecule occupying N pits is

$$\frac{\Delta F(N)}{k_bT} = N(-AL_p + BL_p{}^2) + (N-1)F_s$$

This model is derived by Reisner et al.[12] and elaborated upon by Klotz.[19] L_p represents the amount of contour in the pit, determined by minimizing the free energy. F_s represents the free energy of the spring linker spanning adjacent pits.[20] A and B are prefactors that represent the strength of the entropic and excluded volume interactions, respectively. B is inversely proportional to the volume of each pit. They may be defined based on geometric definitions assuming certain free energy scaling laws or fit to experimental results. This theory is used to calculate the probability of each occupancy state N for a given set of device parameters. The theory predicts a decreasing mean occupancy for increasing pit size. It also predicts plateaus, regions of parameter space over which a single state dominates (Figure 3).

The dynamics of a polymer in a fluid under equilibrium are described by diffusion. Single polymer diffusion is characterized by Rouse−Zimm dynamics in free solution and by reptation in a highly disordered medium.[21] In a nanoslit, polymer diffusion is described by a chain of "blobs", where chain segments within each blob behave as if free. Hydrodynamic interactions between blobs are screened,[5] leading to a − 2/3 power scaling law of diffusion with respect to slit height.

Numerical simulations from Hickey and Slater[22] show a nonmonotonic dependence on diffusion between the Rouse and reptation disorder extremes. Experiments by Nykypanchuk et al.[17] suggest that entropic trapping leads to a distinct polymer diffusion mechanism. This entropic trapping regime is characterized by a polymer dwelling in the trap and escaping in discrete steps, analogous to the diffusion mechanism investigated here.

The mechanism of diffusion in this system is as follows: a DNA molecule occupies N pits. The molecule becomes thermally activated or relaxes and transitions to another state and now occupies $N - 1$ or $N + 1$ pits (Figure 4), leading to a displacement of the molecule center of mass. Typically, a

dx.doi.org/10.1021/ma202596j | Macromolecules 2012, 45, 2122−2127

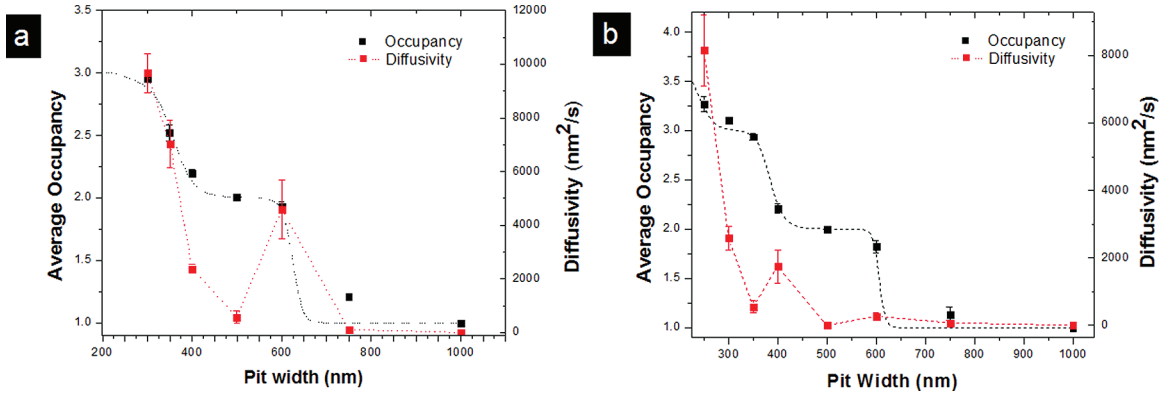

Figure 5. Measurements of diffusion with respect to pit width for two systems, alongside occupancy measurements. (a) Diffusion and occupancy as a function of pit width in a 100 nm nanoslit. A local minimum in diffusion corresponds to a stable dimer state. (b) Diffusion and occupancy as a function of pit width in a 70 nm nanoslit. Two local minima in diffusion corresponds to stable dimer and trimer states.

molecule will tend to be found in its lowest energy ground state. It becomes thermally activated to the first excited state, where it decays to its ground state. Over longer periods of time, a molecule will diffuse throughout its environment by hopping between different occupancy states. The lifetime of a ground of order several minutes, while a higher energy state may last tens of seconds; the lifetimes of states are orders of magnitude greater than the Rouse relaxation time of polymers in the pit.[21]

The characteristics of this mechanism can be examined with a toy model: a polymer on a one-dimensional array with two accessible states (a single pit state and a two pit state; Figure 4). Assuming a certain rate R_{12} for the transition from the one to two pit state and a rate R_{21} for the backward transition, it can be shown that the effective rate for motion of the molecule center-of-mass one position over on the lattice is $R = R_{12}R_{21}/(R_{12} + R_{21})$. The net rate is maximized when $R_{12} = R_{21}$, corresponding to a system in which each state is of equal probability (e.g., via detailed balance). If the molecule spends a long time in either the one pit or two-pit state, corresponding to a system in which one state is of much lower energy than the other, the net rate will be strongly diminished. If only one state is accessible, motion is not possible. However, a more complex model is needed when a diffusing molecule can access multiple occupancy states on a square lattice. In this case there is no analytic expression for the diffusion constant as a function of the transition rates.

STATICS

The diffusion of polymers in this system is best discussed in the context of their static behavior. As the size of the pits was varied, the equilibrium state tended to change, as seen in Figure 3. In systems with the largest pits the molecules occupied only a single pit: the monomer state. As the pits decreased in width, the molecule tended to occupy two (dimer) and then three and four pits. Increasing confinement leads to stronger excluded volume effects, forcing the molecule to occupy more pits, while decreasing confinement allows entropic effects to dominate.

By measuring the mean occupancy of an ensemble of polymers as a function of pit width for a single slit depth and lattice spacing, the behavior of the system with respect to pit size was observed (Figure 3). The behavior with respect to lattice spacing was discussed by Reisner et al.[12] As described qualitatively, the mean occupancy tended to decrease with increasing pit size. Theory predicts regions of parameter space over which a single state dominates, termed plateaus. Within a system that exists on a plateau, the molecules are expected to be found predominately in a single state, suggested by a near-integer mean occupancy. In addition, relatively few transitions to higher or lower states are expected, corresponding to the aforementioned diffusion resonances. Plateaus were observed in several devices corresponding to a stable $N = 2$ state. The experimental observation of the plateaus suggests that the nanopit−nanoslit system can be used to create stable conformations at equilibrium.

DYNAMICS

While it is known that slit confinement affects the diffusivity of a polymer,[5] these experiments show that an additional level fine-tuning can be achieved with embedded nanotopography. In weakly bound systems where the free energy difference between states is relatively small, there is a monotonic decrease in diffusivity when the pit size is increased: in a 200 nm nanoslit with 1 μm pit spacing, the diffusion coefficient in a system with 1 μm pits was a factor of 90 smaller than that in a system of 350 nm pits. This allows an additional degree of freedom in the fine-tuning of the diffusivity of a single polymer, beyond confinement due to slit height.

In systems with greater energy separation of their states, the diffusion shows nonmonotonic behavior. Diffusion resonances were observed, as a function of nanopit width, in devices with a slit height $h = 70$ and 100 nm and lattice spacing $l = 1000$ nm (Figure 5). Both systems showed a diffusivity minimum for an occupancy $N = 2$ state and a corresponding diffusion maxima at occupancy values between 1 and 2. In particular, for the 70 nm system, multiple occupancy minima were observed (at $N = 2$ and $N = 3$ states, with corresponding maxima between occupancy values of 1 and 2 and 2 and 3). Local minima exist when the molecule is strongly bound to a certain state because there are fewer thermal transitions to higher or lower states. These local minima occur at integer values of the mean occupancy (because only one occupancy state is accessible for these parameter ranges). Such a resonance can be seen in Figure 5, where local minima in diffusion correspond to integer values of mean occupancy.

The requirement for diffusion minima is that the ground state is much lower in energy compared to the first and second excited states (Figure 4). In systems with higher occupancy ground states, for example those with smaller pits, the excited states tend to be closer together in energy. Thus, it is difficult to observe diffusion minima at, for example, the $N = 4$ state. This

dx.doi.org/10.1021/ma202596j | Macromolecules 2012, 45, 2122−2127

can be overcome by placing the system in a narrower slit, which increases the energy difference between states. Unfortunately, it is experimentally difficult to observe diffusion in these systems because the occupancy times of the stable states can last over an hour.

Molecules of the same size are expected to have the same dynamics, but a dispersity in sizes would lead to molecules with different equilibrium behavior and different diffusion coefficients. λ-DNA is known to cleave near its midpoint due to an AT-rich block;[2] analyzing the intensity and average occupancy of each molecule allowed us to remove fragmented DNA from the analysis. If a small pressure imbalance exists in the microchannels, a net hydrodynamic flow will exist and the dynamics would not be purely diffusive. Data in which the direction of diffusion was clearly biased in one direction along the nanochannel were excluded.

One final issue can lead to systematic errors in the measurements: it is critical to ensure that the distribution of pit states sampled actually reflects the equilibrium distribution. In particular, metastable states can exist at certain parameter values:[12] these are long-lived states that are not accessible from equilibrium states. Metastable states are formed initially when the molecules are introduced into the nanopit arrays. Including metastable states in the analysis will lead to an overestimation of the average occupancy and also the diffusion constant (i.e., a decay from a metastable to equilibrium state could be confused with a single diffusive lattice step). Metastable states can be identified experimentally if transitions between occupancy states proceed almost completely in one direction. In our data, metastability is a problem for only one parameter value (in Figure 5a): the point taken for a 750 nm pit width. In particular, the dimer state for a 750 nm width is metastable: decays to single-pit states are observed with very few backward transitions (10 times as many decays from a two-pit to single pit state versus the one-to-two transition). Average occupancy in this case was estimated by detailed balance. The relative abundances of observed transitions was used to estimate the ratio of the state probabilities $P_2/P_1 = R_{12}/R_{21}$. The normalization condition $P_1 + P_2 = 1$ could then be used to extract the absolute state occupation probability (once the ratio was determined). The diffusion constant for the 750 nm data point was calculated using only the molecules that were in the $N = 1$ state at $t = 0$.

DISCUSSION

The vanishing diffusion in the $N = 1$ state is important as it indicates that the nanopit devices can be used to localize polymers. From the point of view of our model, this result follows simply because in the limit of large pit separations only one occupancy state is accessible. In this sense, single pits can trap molecules for tens of minutes, and molecules can also be held in higher occupancy states for similar time scales. Electrostatic trapping in nanoscale pits is an alternative to optical tweezers,[23] and entropic trapping in a single pit could be used as a method of studying biomolecules, as evidenced by the long occupation times of the monomer state in these experiments. Entropic trapping has benefits over double-layer electrostatic trapping, in that it has much more flexibility in terms of the dielectric properties of the trapped particle, as well as the range of salt concentrations that are necessary to achieve efficient trapping.

We also observed dimer states persisting for over half an hour without transition, suggesting such a system can be used to trap a biomolecule in a partitioned state. A device consisting of an array of nanopits (termed nanowells) in a gold surface has been used as a biosensor,[24] an application that is also possible with the nanofluidic devices in these experiments. While we have mainly focused on the effect of varying geometry using λ-DNA, it is also possible to use a fixed geometry with varying sized molecules. In that scenario, molecules whose lengths are resonant to that particular geometry will become trapped and will diffuse much more slowly, so that the nanopit structures will act as a passive trap for molecules of specific lengths.

A similar system was described by Nykypanchuk et al. in a 2002 paper.[17] DNA was observed in a two-dimensional network of hollow spheres of submicrometer diameter connected by holes on the order of 100 nm in diameter. Some of the features of DNA in a network of traps are observed in both the nanofluidic and spherical systems: stable occupation of multiple traps and constrained diffusion due to discrete hopping between traps. In a subsequent thesis,[25] a nonmonotonic behavior of diffusivity was reported but not understood. In addition to the nonmonotonic diffusivity dependence on geometry, stable higher-occupancy states were observed, with a free energy minimum corresponding to the dimer state. Both these effects, while unexplained by Nykypanchuk and colleagues, serve to demonstrate the main point of this paper: that diffusion is minimized when a polymer is entropically trapped in a stable state.

In conclusion, the experiments presented in this paper indicate that a nanopit−nanoslit system can be use to fine-tune the diffusivity of a single polymer to a resonance minimum or maximum. The positions of the diffusion minima correspond to plateaus in the occupancy (where only a single state is accessible). The positions of the diffusion maxima correspond to parameter combinations where a number of occupancy states are accessible, allowing the DNA molecules to diffuse via successive transitions between different occupancy states. We hope to explore several questions in additional work. In particular, one issue highly relevant to understanding how longer molecules (occupying many pits) would behave in the nanopit arrays is whether pit-to-pit transitions that occur at the end of a molecule follow a different mechanism than transitions which occur via herniation from the molecule midsection. Such a question could be explored by experiments with circular DNA (following the example of previous work[26]). Finally, it would be interesting to probe thermal fluctuations of contour between the pits and linkers via stroboscopic imaging with a pulsed laser. While this study has focused on diffusion, it should be possible to extend the concept of diffusion resonance to transport under constant driving forces (such as hydrodynamic flow[13,15] or electrophoresis). The dynamic mechanism discussed here—motion mediated via transitions between neighboring occupancy states—should apply as well if the dynamics are driven by a constant force, and the force is weak enough (or the vertical confinement strong enough) so that molecules remain assembled in the pits during the motion. In this case, molecular transport would be maximized at the same parameter values that give rise to a diffusion resonance. We predict that the nanopit structures would in effect be "transparent" to molecules only in a certain size range (blocking passage of molecules in other ranges), creating a molecular "band-gap" effect.

AUTHOR INFORMATION

Corresponding Author

*E-mail: klotza@physics.mcgill.ca.

Notes

The authors declare no competing financial interest.

■ ACKNOWLEDGMENTS

This work was funded through the Natural Sciences and Engineering Research Council of Canada (NSERC) discovery grants program (RGPIN 386212). We thank Henrik Flyvbjerg for illuminating discussions and Philippe Fortin Simard for his assistance. We also gratefully acknowledge use of the DANCHIP fabrication facility (at the Technical University of Denmark), the Nanotools fabrication facility (McGill University), and the Laboratoire de Micro et Nanofabrication (at l'institute nationale de recherche scientifique-INRS, Varennes Quebec).

■ REFERENCES

(1) Tegenfeldt, J. O.; Prinz, C.; Cao, H.; Chou, S.; Reisner, W. W.; Riehn, R.; Wang, Y. M.; Cox, E. C.; Sturm, J. C.; Silberzan, P.; Austin, R. H. *Proc. Natl. Acad. Sci. U. S. A.* **2004**, *101*, 10979−10983.
(2) Reisner, W.; Larsen, N. B.; Silahtaroglu, A.; Kristensen, A.; Tommerup, N.; Tegenfeldt, J. O.; Flyvbjerg, H. *Proc. Natl. Acad. Sci. U. S. A.* **2010**, *107*, 13294−13299.
(3) Fang Lim, S.; Karpusenko, A.; Sakon, J.; Hook, J.; Lamar, T.; Riehn, R. *Biomicrofluidics* **2011**, *5*, 34106−341068.
(4) Wang, Y.; Tree, D. R.; Dorfman, K. D. *Macromolecules* **2011**, *44*, 6594−6604.
(5) Balducci, A.; Mao, P.; Han, J.; Doyle, P. S. *Macromolecules* **2006**, *39*, 6273−6281.
(6) Krishnan, M.; Mönch, I.; Schwille, P. *Nano Lett.* **2007**, *7*, 1270−1275.
(7) Strychalski, E. A.; Levy, S. L.; Craighead, H. G. *Macromolecules* **2008**, *41*, 7716−7721.
(8) Lin, P.-K.; Fu, C.-C.; Chen, Y.-L.; Chen, Y.-R.; Wei, P.-K.; Kuan, C. H.; Fann, W. S. *Phys. Rev. E* **2007**, *76*, 011806.
(9) Hsieh, C.-C.; Balducci, A.; Doyle, P. S. *Macromolecules* **2007**, *40*, 5196−5205.
(10) Harden, J. L.; Doi, M. *J. Phys. Chem.* **1992**, *96*, 4046−4052.
(11) Mathé, J.; Meglio, J.-M. D.; Tinland, B. *J. Colloid Interface Sci.* **2008**, *322*, 315−320.
(12) Reisner, W.; Larsen, N. B.; Flyvbjerg, H.; Tegenfeldt, J. O.; Kristensen, A. *Proc. Natl. Acad. Sci. U. S. A.* **2009**, *106*, 79−84.
(13) DelBonis-O'Donnell, J. T.; Reisner, W.; Stein, D. *New J. Phys.* **2009**, *11*, 075032.
(14) Zhang, Y.; de Pablo, J. J.; Graham, M. D. *J. Chem. Phys.* **2012**, *136*, 014901.
(15) Mikkelsen, M. B.; Reisner, W.; Flyvbjerg, H.; Kristensen, A. *Nano Lett.* **2011**, *11*, 1598−1602.
(16) Han, J.; Craighead, H. G. *Science* **2000**, *288*, 1026−1029.
(17) Nykypanchuk, D.; Strey, H. H.; Hoagland, D. A. *Science* **2002**, *297*, 987−990.
(18) Reisner, W.; Larsen, N. B.; Flyvbjerg, H.; Tegenfeldt, J. O.; Kristensen, A. *Nucleic Acids Res.* **2010**, *38*, 6526−6532.
(19) Klotz, A. McGill University Thesis, 2011.
(20) Bustamante, C.; Marko, J. F.; Siggia, E. D.; Smith, S. *Science* **1994**, *265*, 1599−1600.
(21) Larson, R. *The Structure and Rheology of Complex Fluids*; Oxford University Press: New York, 1999.
(22) Hickey, O. A.; Slater, G. W. *Phys. Lett. A* **2007**, *364*, 448−452.
(23) Krishnan, M.; Mojarad, N.; Kukura, P.; Sandoghdar, V. *Nature* **2010**, *467*, 692−695.
(24) Lee, H.; Park, J.; Kim, J.; Jung, H.; Kawai, T. 2006, *89*, 113901.
(25) Nykypanchuk, D. University of Massacheusits Doctoral Thesis, 2005.
(26) Nykypanchuk, D.; Hoagland, D. A.; Strey, H. H. *ChemPhysChem* **2009**, *10*, 2847−2851.

Macromolecules

Article

pubs.acs.org/Macromolecules

Computer Simulation of Concurrent Bulk- and Surface-Initiated Living Polymerization

Salomon Turgman-Cohen† and Jan Genzer*

Department of Chemical & Biomolecular Engineering, North Carolina State University, Raleigh, North Carolina 27695-7905, United States

Supporting Information

ABSTRACT: We use Monte Carlo simulation implementing the bond fluctuation model formalism in the canonical (NVT) ensemble to study living polymerization initiated concurrently in bulk and on flat substrates. Our results reveal that the molecular weights and molecular weight distributions of both classes of polymers depend on the grafting density of the surface-bound polymers (σ) and the fraction of polymers on the surface (η) relative to that in bulk. In general, polymer grafts on the surface possess lower molecular weight and higher polydispersity index compared to their bulk counterparts. The difference between the molecular weight of the two populations of polymers decreases with decreasing σ and increasing η. Our work provides evidence that the common practice of using the molecular weight of bulk-initiated polymers in estimating the grafting density of polymeric anchors on flat substrates is not generally valid.

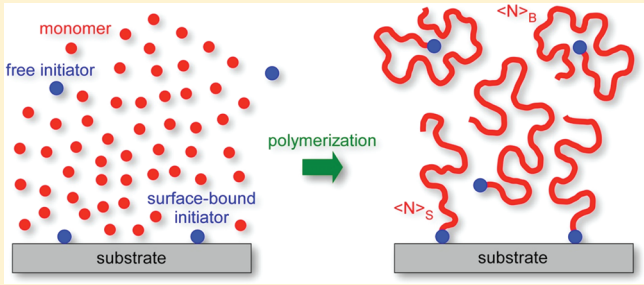

INTRODUCTION

Decorating material surfaces with polymeric grafts has become a routine method for generating functional materials for various applications, including, friction, biocompatibility, self-assembly, responsive materials, and many others.[1−7] The parameters that govern the performance of macromolecular tethers are the polymer chemical composition, topology (i.e., linear or branched), grafting density, and molecular weight. The past decade witnessed enormous progress in generating and probing the physicochemical characteristics of such surface-anchored polymer assemblies. Two general classes of methods have been developed for the preparation of polymeric tethers on material surfaces.[8−10] In the "grafting onto" technique, polymers are synthesized in bulk and grafted (chemically or physically) to the substrate of interest. This method benefits from knowing a priori the characteristics of the polymers, i.e., chemical composition, molecular weight (M_n), and molecular weight distribution (MWD), before they get grafted to the substrate. However, entropic constrains during chain grafting limit the grafting density (σ) of polymeric tethers to moderate values. This limitation of the "grafting onto" method can be technically eliminated by synthesizing grafted polymers directly from surfaces by the so-called "grafting from" methodology. Here, the surfaces are decorated with polymerization initiators and polymers grow from these active centers upon exposure to a solution of monomer, catalyst, and/or solvent. While the "grafting from" technique can in principle yield grafted systems with higher σ than the "grafting onto" process, it is not without flaws. Specifically, the structure of the brush near the surface, its molecular weight, and MWD are not known a priori and have to be established after brush formation.

A typical method for determining the molecular weight of surface-grown polymers ($M_{n,S}$) and their MWD involves cleaving the chains from the substrate by some chemical treatment, collecting them, and testing them with size exclusion chromatography (SEC).[11−13] While for grafted polymers grown from convex (i.e., particle) or concave (i.e., pore) substrates with high surface areas this methodology is feasible, it is generally not applicable for grafts polymerized from flat substrates because the amount of material cleaved from the surface is not sufficient for SEC analysis. Hence, most papers describing the growth of polymeric grafts from flat substrates report the properties of brushes in terms of their dry thickness (h). These data alone, however, do not provide direct means of determining the $M_{n,S}$ of the grown polymer (nor does it say anything about the MWD) unless information about σ is available. Unfortunately, this is not the case in most situation because determining σ is even more challenging than measuring M_n. To solve this dilemma, one typically conducts simultaneous polymerization initiated both on the surface and in the bulk and assumes that both bulk- and surface-initiated polymers grow at

Received: December 10, 2011
Revised: January 29, 2012
Published: February 8, 2012

similar rates. By assuming that $M_{n,S} \approx M_{n,B}$, one can calculate σ from

$$\sigma = \frac{h\rho N_a}{M_{n,S}} \quad (1)$$

In eq 1, which can be derived simply by conservation of mass arguments, ρ is the density of the polymer and N_a is Avogadro's number. The objective of this work is to determine the validity of the $M_{n,S} \approx M_{n,B}$ assumption and to compare the MWDs of the two classes of macromolecules.

The synthesis of surface-grafted polymers is often accomplished by controlled radical polymerization (CRP) methods.[1,11,14,15] Within this class of reactions, atom transfer radical polymerization (ATRP) is a widely employed reaction scheme[1,16] due to its compatibility with an extensive library of monomers, the living character of the reaction (allowing the creation of block copolymers), insensitivity to impurities (compared to free radical or ionic polymerization techniques), the ability to control the average molecular weight, and to obtain polymers with low PDI in bulk. In the context of ATRP, the presence of free initiators in solution can have an effect on the intrinsic growth kinetics of the surface polymers. Surface reactions, especially those from planar substrates, produce very small amounts of the deactivating species (i.e., CuX_2 in ATRP where X = Cl or Br) leading to loss of control due to excessive terminations at the early stages of the polymerization. Sacrificial (free) initiators added to the bulk solution increase the concentration of the deactivating species, thus restoring control to the reaction.[1,17−19] A second way in which free initiators may affect polymerization from surface-bound initiators involves competing with the surface-bound polymers for the available monomers. It is possible for surface- and bulk-grown polymers to exhibit different polymerization rates leading to dissimilar molecular weights and PDIs for these two populations of polymers. Such a difference invalidates the application of eq 1 for the characterization of the grafted polymer layers because the assumption that $M_{n,S} \approx M_{n,B}$ becomes unfounded.

This study focuses on investigating the competition between polymerization initiated in bulk and concurrently on flat impenetrable surfaces. Initial findings pertaining to this goal have been presented recently.[20] Here we elaborate on the system parameters that affect the characteristics of polymers grown simultaneously from surfaces and in bulk. Specifically, we plan to address how the molecular weight and the MWD of both classes of macromolecules (i.e., bulk- and surface-initiated) depend on the initiator grafting density (σ), fraction of polymers on the surface (η) relative to the total number of polymers grown, and the initial number of free monomers in the simulation box (M_0). We neglect any effects that the presence of bulk initiators may have on the activation/deactivation and on the buildup of deactivating species since we incorporate these processes in our simulations implicitly. This is to say that the polymerizations studied herein remain living (i.e., without termination or chain transfer) and controlled, and the value of η has no effect on the intrinsic kinetics of the polymerization process. In addition, we assume that bulk and surface polymers possess equal probabilities of undergoing activation and deactivation reactions and of reacting with nearby monomers.

SIMULATION MODEL AND ALGORITHM

We employ the Monte Carlo (MC) algorithm in the canonical (NVT) ensemble described in our earlier work[20−22] and the bond fluctuation model (BFM)[23,24] under good solvent conditions to investigate the effects of M_0, η, and σ on the simultaneous polymerization of bulk- and surface-initiated polymers. Briefly, in every MC step either a reaction or a motion depends on a preselected reaction probability, P_r (chosen 0.01 for this study). If motion is selected, a typical BFM single monomer move is attempted. In the case of reaction, a reaction is attempted between a randomly selected polymer and one of its nearest-neighbor free monomers. The randomly selected polymer may only react if it is active at a given time. Similar to the ATRP mechanism, in which only a certain fraction of polymers is "living" for a certain period of time, we specify the lifetime of active polymers (LT) and fraction of living polymers (FLP) that can undergo reaction (i.e., initiation or propagation in our case). In the current simulations every polymer has equal probability of initiating or reacting regardless of it being a bulk- or a surface-initiated polymer. Additional details of the simulation can be found in our previous publications.[20−22]

The initial number of total initiators (combined bulk and surface) remains constant (I_0 = 400). By choosing η, we therefore vary the number of bulk and surface polymers (i.e., for η = 0 only bulk polymerization takes place while η = 1 polymerization occurs only on the substrate). In order to vary σ and η independently, we alter the dimensions of the lattice in the lateral ($L_X = L_Y$) and vertical (L_Z) dimensions independently while keeping the total volume of the lattice at $\approx 5 \times 10^5$ cubic lattice units. In order to vary σ, we employ the procedure for resizing the lattice described in our previous publications.[20,22] Additional variations in the lattice sizes are needed when keeping σ constant while varying η. We resize the lateral dimensions of the lattice as the number of polymers on the surface varies to maintain a constant σ. We also vary M_0 in order to explore the effects of free monomer density on polymerization. Varying M_0 should reveal any possible effects associated with diffusion limitation during the course of the polymerization reaction. The surfaces of lattices corresponding to various σ and η investigated and the positions of the initiator sites (i.e., the $X-Y$ plane at L_Z = 0) are depicted in Figure S1 of the Supporting Information. Some of the lattices investigated possess large aspect ratios (L_Z/L_X = 62.7 for η = 6% and σ = 0.25), which might confine the polymers and affect the polymerizations. To verify that the large lattice aspect ratio does not affect the properties of the growing polymers, we compared the PDIs of bulk polymers (η = 0%) grown in lattices with low (L_Z/L_X = 1) and high (L_Z/L_X = 62.7) aspect ratios as a function of conversion and number-average molecular weight. Our results (not shown here) determined that the molecular weights and PDIs were equivalent for all lattice aspect ratios tested.

The living nature of polymerizations described by our algorithm is achieved by omitting reactions that lead to chain termination or chain transfer. Hence, we only consider the initiation and propagation steps. To test the effect that diffusion and the scarcity of monomers may have in our results, we perform simulations at varying values of M_0, which requires adjustments to the parameters affecting the reaction kinetics (cf. Table 1). The parameters requiring adjustment are P_r and LT. If we increase the initial number of free monomers in the

Table 1. Parameters Adjusted in Order To Change M_0 Correctly

M_0	beads	P_r	LT
6 250	7 050	0.0187	535
12 500	13 300	0.0100	1000
25 000	25 800	0.0052	1930

simulation while keeping P_r constant, there will be, on average, a lower fraction of total beads attempting to move between attempted reaction steps. This is equivalent to a change in the relative rates of reaction and motion, an undesirable consequence of a simple increase in M_0. We therefore adjust P_r depending on the value of M_0 in order to keep the relative rates of reactions and motions constant. For instance, if M_0 equals 12 500 and P_r = 0.01, there will be on average 99 attempted motions for every attempted reaction, which corresponds to 0.74% of the beads attempting a move. In contrast, for P_r = 0.01 and M_0 = 25 000, 0.38% of the beads would undergo attempted motion. To take this effect into account, we use the M_0 = 12 500 and P_r = 0.01 simulations as a benchmark, and for other values of M_0, we adjust P_r to maintain the fraction of beads attempting a move between attempted reactions equal to 0.74% of the total beads (cf. Table 1). The value of LT also affects the kinetics of the polymerization reaction in our simulations. If P_r adjustments are needed to account for the varying number of beads, then LT corrections are necessary to account for the unintended consequences of varying P_r. As P_r is adjusted, the average number of reactions occurring within a living polymer cycle varies proportionally. For instance, if P_r equals 0.01 or 0.10 and LT = 1000, there will be on average 10 or 100 attempted reactions, respectively, every living cycle. Kinetic theories of CRP reactions have shown that the number of propagations per living cycle is an important parameter in the CRP scheme and that it can have significant effects on the molecular weight distribution of the resulting polymers.[25] Adjustments in P_r and LT are therefore needed to compare systems with different M_0. In the MC simulations described here, we use the values of P_r and LT listed in Table 1.

The initial configurations comprise equidistant arrays of initiators on the flat surface (cf. Figure S1 in Supporting Information). The bulk initiators and free monomers are distributed regularly throughout the lattice. Each initiator corresponds to two BFM monomers, of which one can undergo initiation if approached by a free monomer. For surface bound initiators, the noninitiating site is grafted firmly to the surface and is not allowed to move during the simulation. We pre-equilibrate the configurations thus constructed for at least 1×10^5 attempted MC moves per bead (MCPB), yielding a random spatial distribution of free initiators and monomers on the lattice. The randomly distributed configurations serve as an input to the reactive simulations. As mentioned earlier, we model "living" polymerization conditions by disabling termination and chain transfer reactions. We obtain averages of the number-average molecular weight and the PDI by repeating each simulation five times and sampling the system at regular values of the free monomer conversion (X_m). Prior to the initialization of the reactive MC algorithm, we perform a final short equilibration consisting of 1×10^6 attempted MC moves. The reactive MC scheme described earlier[16] then begins and continues until either 80% of the free monomer is exhausted (i.e., polymerized) or a predetermined maximum number (1×10^9) of MCS elapses. For some of the lattices in Table 1 the distance between the substrate and the opposing impenetrable wall (L_Z) is very small. To prevent interaction of the tethered polymers with the opposite wall, it is necessary to truncate some of the data sets (Table SI, Supporting Information). Because the weight of the monomers is unity, we express the molecular weights of the bulk- and surface-grown polymers in terms of the average number of monomers in the respective polymers, i.e., $\langle N \rangle_B$ and $\langle N \rangle_S$.

RESULTS AND DISCUSSION

To elucidate the effects of η and σ, we monitor the average molecular weight as a function of X_m at M_0 = 25 000 independently for bulk- and surface-based polymers and compare them to the η = 0 or 100% (cf. Figure 1). Note that pure bulk or surface polymers exhibit identical average molecular weights as a function of conversion, as expected

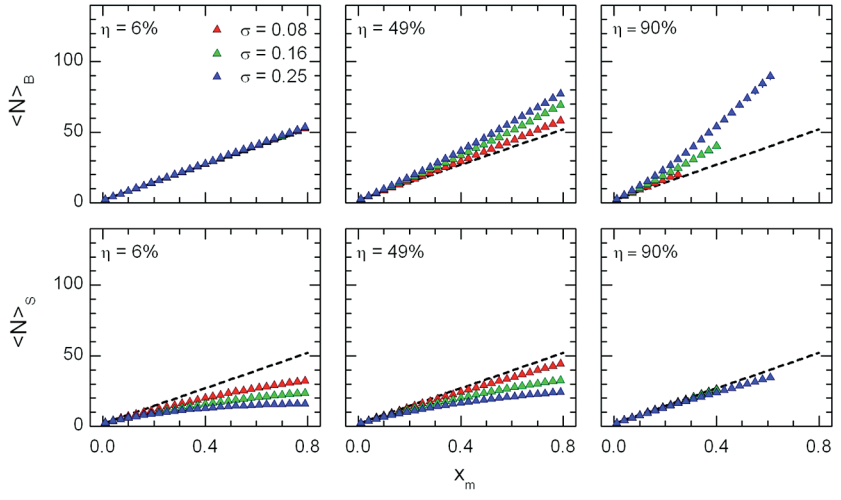

Figure 1. Average molecular weight for bulk (top row) and surface (bottom row) polymers as a function of monomer conversion with initial number of monomers (M_0) of 25 000; percentages of surface polymers (η): 6% (left column), 49% (middle column), and 90% (right column); grafting densities of initiators (σ): 0.08 (red), 0.16 (green), and 0.25 (blue). The black dashed lines represent the conditions corresponding to η = 0% (top) and 100% (bottom). The η = 90% data are truncated because the brush starts interacting with the opposite impenetrable surface.

dx.doi.org/10.1021/ma202679r | Macromolecules 2012, 45, 2128–2137

(dashed lines). The average molecular weight of bulk-grown macromolecules increases linearly at η = 6%, as one would expect from polymerizations in which only bulk polymers are grown (η = 0%, black dashed lines). With η increasing from 6% to 90%, $\langle N\rangle_B$ deviates from the dashed line and becomes larger than expected. The deviation for σ = 0.08 is small, indicating that polymers growing sparsely from surfaces propagate at a similar pace to their bulk counterparts. The magnitude of the deviation depends on σ, however, indicating that the surface-bound initiators affect the properties of the bulk-grown polymers under these conditions. Namely, increasing the density of surface-bound initiators increases the molecular weight of the bulk-grown polymers. The surface-initiated polymers exhibit the opposite trend. Specifically, the data lie below the black line indicating that shorter polymers are produced relative to η = 100% case (i.e., polymerization is initiated only from the surface). While for the surface-grown polymers the deviation between the η = 90% and the dashed line is very small, the deviation becomes larger as η decreases from 90% to 6%, indicating that at low η the polymers initiating from the surface grow at a slower pace than the bulk-initiated macromolecules. Increasing σ tends to enlarge the deviation from the η = 100% line, suggesting that the larger the σ, the slower the rate of surface-initiated polymerization. Furthermore, at η = 6% and σ = 0.25, $\langle N\rangle_S$ reaches a plateau at approximately X_m = 0.6, indicating that depending on σ and η the presence of the bulk polymers might cap the growth of the surface-bound layer. This observation is consistent with many experimental studies, in which the thickness of the polymer layer reaches a plateau value at long polymerization times.[26] The presence of this plateau has typically been attributed to excessive terminations during the polymerization, thus decreasing the density of the propagating radicals on the surface. This explanation alone, however, cannot hold true in our simulations due to the lack of termination reactions. We thus suggest that in addition to termination (and possible chain transfer) the plateau in $\langle N\rangle_S$ can be associated (at least in part) with (1) the competition for free monomers between the bulk- and surface-initiated macroinitiaitors (i.e., growing chains) and (2) the slower polymerization rate from the surface-initiated sites that, in turn, depends on the degree of confinement of the surface-grown macromolecule. Comparing $\langle N\rangle_B$ and $\langle N\rangle_S$ reveals the principal finding of this study, namely, that at a particular monomer conversion$\langle N\rangle_B - \langle N\rangle_S = \delta > 0$. The magnitude of δ depends on the combination of σ and η. Generally, δ decreases with decreasing σ and increasing η. These observations, on which we will elaborate more in the following sections, suggest that the common practice of associating the properties of surface-grown polymers with those polymerized in the bulk is of limited validity.

To understand the growth rate of both sets of polymers, we plot $\langle N\rangle_B$ (η = 0%, left column) and $\langle N\rangle_S$ (η = 100%, right column) as a function of MC step per bead (cf. Figure 2). The top row shows the raw data. As expected, increases in M_0 lead to higher rates of polymerization (initial slopes of the plots) and polymer molecular weights. The rate of polymerization of surface-grown polymers also depends on σ; it decreases with increasing σ. Furthermore, the rate of polymerization for surface-initiated polymers at low σ is similar to that of the bulk-initiated chains. This reinforces the claim that at low σ and X_m low chain crowding on the surfaces results in similar growth for bulk- and surface-initiated polymers. Classical polymerization kinetics suggests that the rate of polymerization is proportional

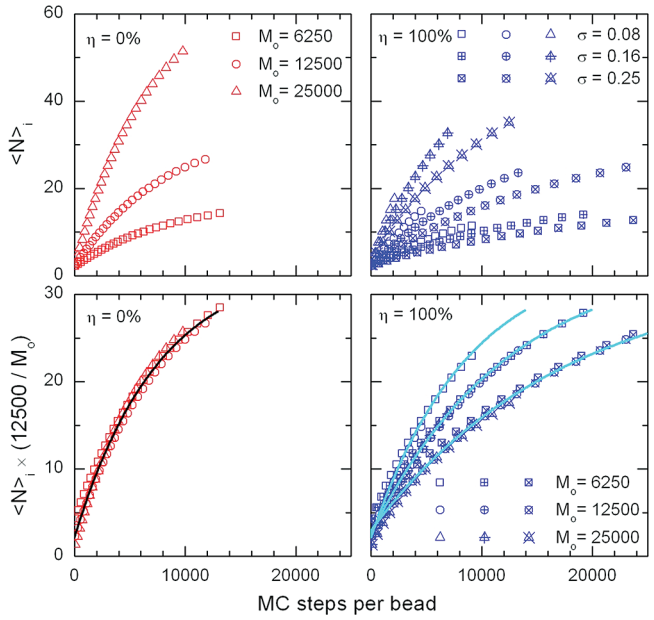

Figure 2. Number-average molecular weight (top row) and the same quantity scaled (bottom row) for bulk (left column, red, η = 0%) and surface (right column, blue, η = 100%) polymers as a function of Monte Carlo steps per bead for initial number of monomers (M_0): 6250 (squares), 12 500 (circles), and 25 000 (triangles); grafting density of initiators (σ): 0.08 (hollow), 0.16 (cross), and 0.25 (ex). The black and cyan lines are guides to the eye for the bulk- and surface-initiated data, respectively.

to the concentration of free monomers. To verify this, we use the M_0 = 12 500 case as a benchmark and scale the data by multiplying by 12 500/M_0 (bottom row in Figure 2). All bulk data and surface data for a given value of σ overlap visually, confirming the rate dependence on M_0 and validate the choices of P_r and LT discussed earlier. Figure 3 shows the scaled data for various combinations of η, σ, and M_0. A few trends can be identified by exploring the data in Figure 3. First, at σ = 0.08, the η = 0% (i.e., only bulk-initiated polymerization, black line) and η = 100% (i.e., only surface-initiated polymerization, cyan line) cases exhibit essentially the same growth rates. As σ increases and the surface chains start to crowd, we observe differences between the η = 0% and η = 100% cases; the surface growth rate slows down while the bulk growth rate remains fairly constant. Second, at low values of η, $\langle N\rangle_B$ traces perfectly the η = 0% line while $\langle N\rangle_S$ lies below the η = 100% line. At large values of η the opposite trend occurs; namely, $\langle N\rangle_S$ traces the η = 100% line closely (except at large monomer conversions) while $\langle N\rangle_B$ lies above the η = 0% line. The initial polymerization rates obtained by fitting a first-order exponential to the data (X_m < 0.2) and evaluating the derivative at X_m = 0 are plotted in Figure 4. We observe a dependence of the initial rate of polymerization on M_0, indicating that not all of the rate variation is accounted for by scaling the data by M_0. Two additional and somewhat related factors that may affect the rate of polymerization include (1) monomer diffusion limitation and (2) the percentage of accepted attempted moves. Diffusion limitation can arise if the monomer concentration decreases close to the surface or in proximity to the polymer chain ends. This effect results in lower polymerization rates as M_0 decreases. The move acceptance rate may affect the initial polymerization rates by perturbing the time unit in the simulation. Increasing M_0, for example, results in an increase

dx.doi.org/10.1021/ma202679r | Macromolecules 2012, 45, 2128–2137

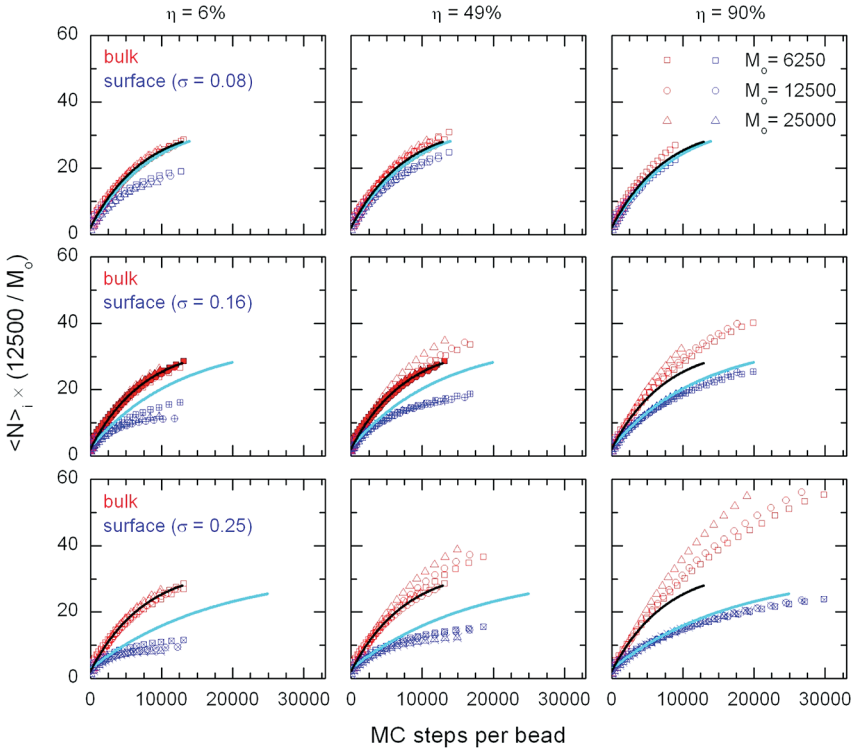

Figure 3. Scaled number-average molecular weight as a function of Monte Carlo step per bead for bulk (red) and surface (blue) polymers with fraction of surface polymers (η, left to right columns): 6%, 49%, and 90%; initiator grafting densities (σ, top to bottom rows): 0.08, 0.16, and 0.25; initial number of monomers (M_0): 6250 (squares), 12 500 (circles), and 25 000 (triangles). The solid lines correspond to η = 0% (black) and η = 100% (cyan).

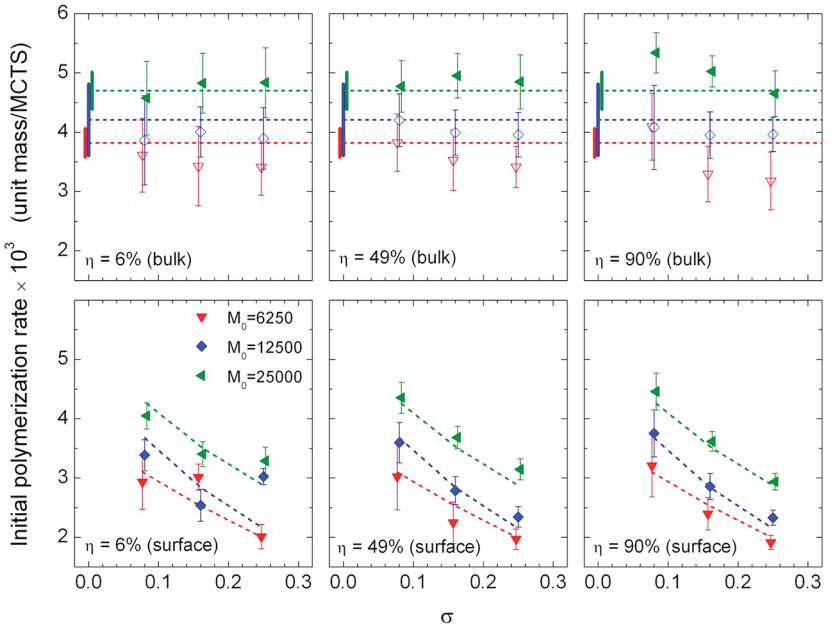

Figure 4. Initial polymerization rate as a function of σ for bulk (open symbols, top row) and surface (close symbols, bottom row) for η equal to 6% (left column), 49% (middle column), and 90% (right column) and M_0 equal to 6250 (red down triangle), 12 500 (blue diamond), and 25 000 (green left triangle). For clarity, the data for M_0 = 6250 and M_0 = 25 000 have been shifted horizontally by a small arbitrary increment to the left and right, respectively. The dotted lines in the top and bottom rows represent η = 0% (bulk-only polymerization) and 100% (surface-only polymerization), respectively. The solid vertical lines in the top row at σ = 0 denote the range of the η = 0% data.

of the lattice occupancy and therefore the probability of an attempted move to an already occupied lattice site. This would lead to a higher fraction of attempted moves being rejected resulting in slower motion. This effect would result in slower polymerization rates for M_0 = 25 000 than for the systems with lower M_0. Barring other factors, it appears that diffusion limitation may play a role in our simulations, although its effect on the rate of polymerization is small compared to that of the

dx.doi.org/10.1021/ma202679r | *Macromolecules* 2012, 45, 2128–2137

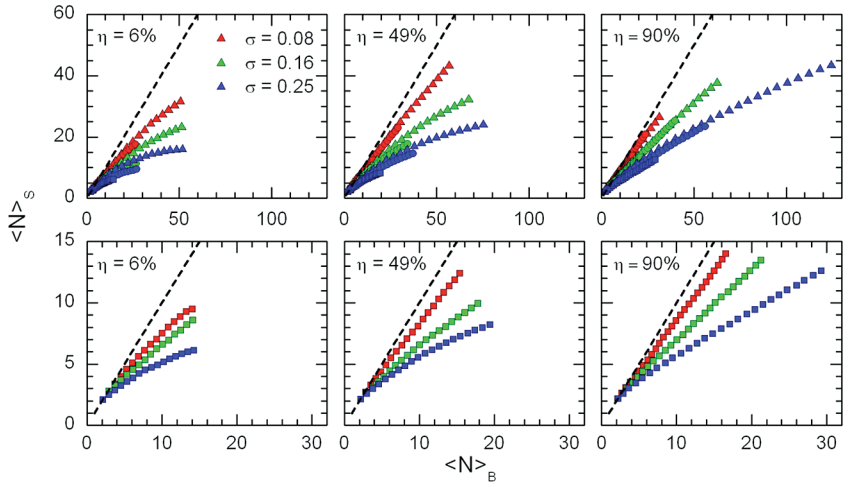

Figure 5. Number-average molecular weight of surface polymers as a function of number-average molecular weight of bulk polymers for the three values of M_0 (top row) and for M_0 = 6250 (bottom row). Percentage of surface polymers (η): 6% (left column), 49% (middle column), and 90% (right column); initial number of free monomers (M_0): 6250 (squares), 12 500 (circles), and 25 000 (triangles); grafting density of initiators (σ): 0.08 (red), 0.16 (green), and 0.25 (blue). The black dashed line represents $\langle N\rangle_S = \langle N\rangle_B$.

monomer concentration, M_0. Figure 4 also depicts the dependence of the initial polymerization rate on σ for bulk- and surface-grown polymers. In most cases the rate of bulk polymerization is independent of σ (the sole exception being the η = 90% and M_0 = 25 000 case). The bulk polymers, at least at the beginning of the reaction, are unaffected by the presence of the surface-growing polymers or by their grafting density. The surface-initiated polymers, however, do exhibit a polymerization rate dependence on σ as would be expected from the findings reported in our earlier publication.[22] As σ increases, the rate of polymerization decreases consistently likely due to chain crowding at the surface.

To better discern the relation between the molecular weights of surface- and bulk-grown polymers at a particular instant of the polymerization reaction, in Figure 5 (top row) we plot the number-average molar weight of the surface grown polymers ($\langle N\rangle_S$) as a function of the number-average molar weight of the bulk polymers ($\langle N\rangle_B$). The black dashed lines correspond to $\langle N\rangle_B = \langle N\rangle_S$. For all combinations of σ, η, and M_0, the data lie below the diagonals, indicating that $\langle N\rangle_S < \langle N\rangle_B$ at all conversions. An important characteristic of these systems is the competition for free monomers between the bulk- and surface-grown polymers and the higher growth rate of the bulk polymers relative to the surface ones. This is a clear indication that confining the initiators on the flat impenetrable surface reduces the rate of polymerization. As the density and confinement of the initiators on the surface increases, the difference between the growth rates of the surface and bulk polymers widens yielding shorter surface-bound macromolecules relative to free chains initiated in bulk. The data in Figure 5 suggest that in the limit of low σ and high η the $\langle N\rangle_B = \langle N\rangle_S$ assumption is valid. Unfortunately, most experiments employing simultaneous bulk and surface initiators operate at low values of η instead.

By inspecting the top row of Figure 5, we observe that the data lie closer to the diagonal on going from η = 6% to η = 90% (from left to right). This observation is counterintuitive since we invoke confinement and crowding as the reasons for the difference between $\langle N\rangle_B$ and $\langle N\rangle_S$. As explained before, the confinement on the surface for all values of η is identical as long as σ remains constant. One would expect that an increase in η would have no effect in the deviation of the data from the diagonal. We explain this behavior by the presence (or lack thereof) of the fast growing polymers in the bulk. At η = 6% most of the polymers in the simulation are fast-growing bulk polymers. Increasing the amount of these fast growing polymers, relative to the polymers attached to the surface, results in larger differences between $\langle N\rangle_B$ and $\langle N\rangle_S$. At high η, the slow-growing surface polymers outnumber the bulk polymers. Although the bulk polymers possess a faster growing rate per chain, as a group they add fewer monomers than the surface-based chains. This then results in the observed shift of the trends toward the diagonal and the better match between $\langle N\rangle_B$ and $\langle N\rangle_S$ at large values of η.

An interesting trend to note from Figure 5 is the behavior of the final values of $\langle N\rangle_B$ and $\langle N\rangle_S$ at X_m = 0.80 as a function of σ and η for the M_o = 6250 case (bottom row). At η = 6%, $\langle N\rangle_B$ (X_m = 0.80) remains nearly constant at a value of ≈12 with increasing σ. However, as σ increases, $\langle N\rangle_S$ decreases from ≈10 to ≈7. At η = 90% $\langle N\rangle_B$ is more sensitive to increasing σ than $\langle N\rangle_S$; $\langle N\rangle_S$ decreases from ≈14 to ≈13, and $\langle N\rangle_B$ increases from ≈17 to ≈30. The latter observation is intriguing because one would not expect σ, which is a property of the surface, to have such a large effect on $\langle N\rangle_B$ (X_m = 0.80). To explain this behavior, we have to take into consideration three factors: (1) the effect of crowding/confinement on the rate of surface polymerization, (2) the relative rates of surface and bulk growth, and (3) the ratio of bulk polymers to free monomers. The slight variation in $\langle N\rangle_B$ with σ at η = 6% is explained by noting that the surface in this system constitutes a small perturbation and therefore cannot inflict a large effect on the bulk-based polymers. The differences in $\langle N\rangle_S$ are due to the crowding and slowing down of the surface-initiated reaction at higher σ.[22] For η = 90%, the decrease in $\langle N\rangle_S$ is still explained by the effects of surface confinement. The large increase in $\langle N\rangle_B$, however, is interesting and more complex to explain. In this system, the surface plays a very significant role because this is where most of the polymers are located. As σ increases, the rate of polymerization of the surface-initiated polymers slows down and because surface-initiated polymers represent the majority component; the overall rate of polymerization decreases as well. In contrast to η = 6%, at η = 90% the bulk

dx.doi.org/10.1021/ma202679r | Macromolecules 2012, 45, 2128–2137

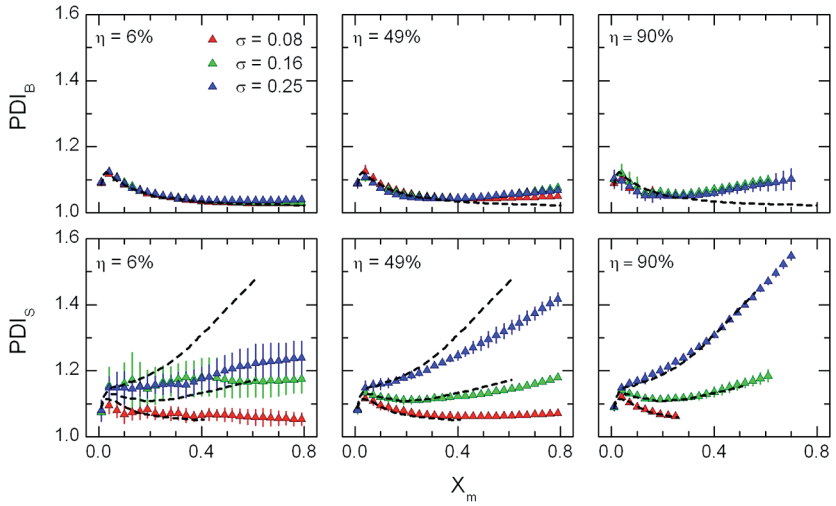

Figure 6. Polydispersity index for bulk (top row) and surface (bottom row) polymers as a function of monomer conversion with initial number of monomers (M_0) of 25 000; percentages of surface polymers (η): 6% (left column), 49% (middle column), and 90% (right column); grafting densities of initiators (σ): 0.08 (red), 0.16 (green), and 0.25 (blue). The black dashed lines represent the η = 0% (top row) and η = 100% (bottom row), M_0 = 25 000 and σ = 0.08, 0.16, and 0.25 conditions.

polymers only compete with the slow-growing surface-based polymers. The same trends are expected for higher values of M_0 although they cannot be observed here due to the aforementioned truncation of the data sets at η = 90% (cf. Table SI).

As mentioned above, our aim is to explore the consequences of these findings on the common experimental practice that assumes similar properties between polymers grown simultaneously in bulk and on the surface and using the molecular weight of the bulk-based macromolecules to estimate σ. The typical approach involves measuring the dry thickness of the polymer layer by means of optical ellipsometry or neutron/X-ray reflectivity and employing eq 1, in which $M_{n,S}$ (= $\langle N\rangle_S$) is determined by SEC. As can be seen in Figure 5, the only situation in which this assumption is approximately valid is for small values of σ on flat substrates and for small fraction of bulk-initiated polymers. At high σ, the differences between $\langle N\rangle_B$ and $\langle N\rangle_S$ are likely to be larger than the error of the SEC measurement, resulting in inaccurate estimates of σ. These results highlight the need for continued development of direct measurement experimental techniques of either $\langle N\rangle_S$ or σ.

Simultaneous polymerization of bulk-based and surface-anchored initiators also influences the broadness of the molecular weight distributions of both populations of polymers. In Figure 6 we plot the PDI of bulk (PDI_B, top) and surface (PDI_S, bottom) polymers as a function of X_m, η, and σ for M_0 = 25 000. At low η, the PDI_B resembles very closely the situation corresponding to the η = 0% case for all values of σ. As η increases, the PDI deviates above the η = 0% line at approximately X_m = 0.3. This provides an additional indication that when the surface polymers constitute the majority component in the simulation they can affect the properties of the bulk-initiated polymers. The surface polymers exhibit the opposite trend; namely, that at η = 90%, their PDI values are nearly identical to those corresponding to the polymerization at η = 100%, and as η decreases, the PDI_S values for σ equal to 0.16 and 0.25 decrease below the η = 100% line. This is difficult to see in the η = 6% case because the error in the PDI of a small number of polymers is significant. At a particular conversion and for η = 6% and 49%, the presence of bulk polymers imparts a lower PDI to the surface-grown polymers. Although this observation is intriguing, it is misleading, as we will explain below (Figure 8).

The data in Figure 7 show the evolution of the PDI of the bulk and surface polymers as a function of monomer

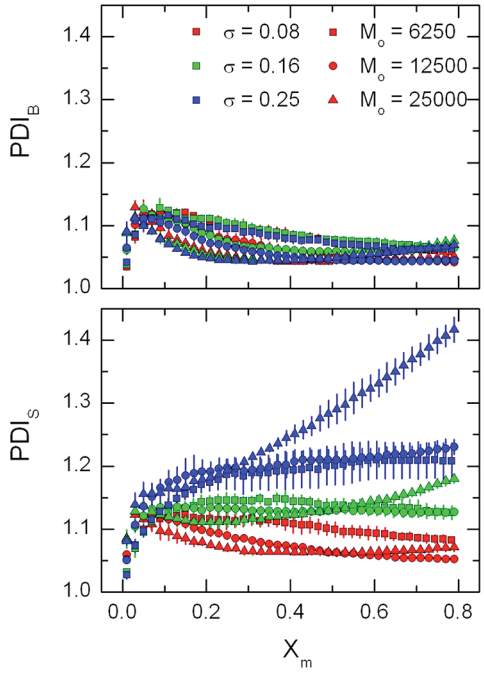

Figure 7. PDIs of bulk (top) and surface (bottom) polymers as a function of the monomer conversion for η = 49%. Initiator grafting densities (σ): 0.08 (red), 0.16 (green), and 0.25 (blue); initial number of free monomers (M_0): 6250 (squares), 12 500 (circles), and 25 000 (triangles).

conversion for η = 49% and M_0 equal to 6250, 12 500, and 25 000. When plotted against X_m, one can see how the results of a hypothetical SEC experiment would depict the broadness of the distributions at any time during the polymerization reaction. At σ = 0.08, the assumption that the PDI obtained for

dx.doi.org/10.1021/ma202679r | Macromolecules 2012, 45, 2128–2137

the bulk polymers is similar to that of polymers initiated from the surface is reasonable. However, as σ increases to 0.25, this assumption ceases to be valid and PDI_S becomes much larger than PDI_B for all values of M_0. At $X_m = 0.8$ and $M_0 = 25\,000$ the difference in the PDI of the surfaces from that of the bulk is ~0.3. A change of this magnitude in the PDI will most certainly alter the properties of the surface-grown polymer layers[27] (thickness, density, etc.) and therefore their performance in practical applications that rely on monodisperse polymer chains[28] (i.e., antifouling coatings). These observations suggest that in order to assume that the simultaneously grown bulk and surface polymers possess similar properties it is necessary to know the value of σ precisely. As described above, estimation of σ requires that the properties between bulk and surface polymers be similar, resulting in a circular problem. The differences between the molecular weight distributions are evident when plotted as PDI_S vs PDI_B (cf. Figure S2 in Supporting Information).

One motivation to explore polymerizations with different values of M_0 is the possibility that $\langle N\rangle_S$ has an effect on the growth rate and PDI of polymers grown from flat surfaces. For instance, at the beginning of the polymerization process when $\langle N\rangle_S$ is low, the surface-based polymers grow with little or no crowding. With increasing polymerization time, the molecular weight of the macromolecular grafts increases and neighboring chains approach one another. At some point, excluded volume interactions will cause chain stretching away from the surface. In addition, chain crowding among neighbors may hinder the delivery of monomers to the chains with conformations in which the chain ends reside inside the polymer layer. Whereas plotting the PDIs as a function of X_m elucidates the differences between bulk and surface polymers at a particular instant during the polymerization, this plot masks the dependence that the PDI may have on the average molecular weights. A plot of the PDI as a function of the average molecular weight of the polymers can document this type of dependency effectively (cf. Figure 8). When plotted against $\langle N\rangle_B$ and $\langle N\rangle_S$, the PDI_B and PDI_S are independent of M_0 because for a given value of $\langle N\rangle_B$ or $\langle N\rangle_S$ we consider the same number of beads in the bulk- or surface-based polymer, respectively, regardless of the solution conditions. The bulk polymers also prove to be insensitive to σ, indicating that no matter what the characteristic of the surface are, the bulk polymers that grow to a particular molecular weight possess similar PDIs. The surface-grown polymers, however, do exhibit a dependence on σ as should be expected from our earlier study.[22] As σ increases, the PDI_S increases due to chain crowding resulting in the uneven delivery of monomers to the short and long chains. This insensitivity of the PDI to the value of M_0 can explain the observed decrease in PDI_S when most of the growing polymers are in the bulk ($\eta = 6$ and 49%, Figure 6) relative to the case rich in surface polymers. This is in fact due to the fast growing polymers leading to lower $\langle N\rangle_S$ at a particular conversion and therefore a lower level of confinement and observed PDI_S.

In this work, we have established that η and σ have a strong effect on the MWDs of bulk- and surface-grown polymers and that knowing these parameters is essential for the validation of the $\langle N\rangle_B \approx \langle N\rangle_S$ assumption. We now draw parallels between the range of σ and η studied here and those found in the experimental literature. Experiments where the initiation of surface polymerization occurs from a planar substrate operate often at very low values of η (or $\eta = 0\%$, i.e., no sacrificial initiator) due primarily to the low surface area of the planar

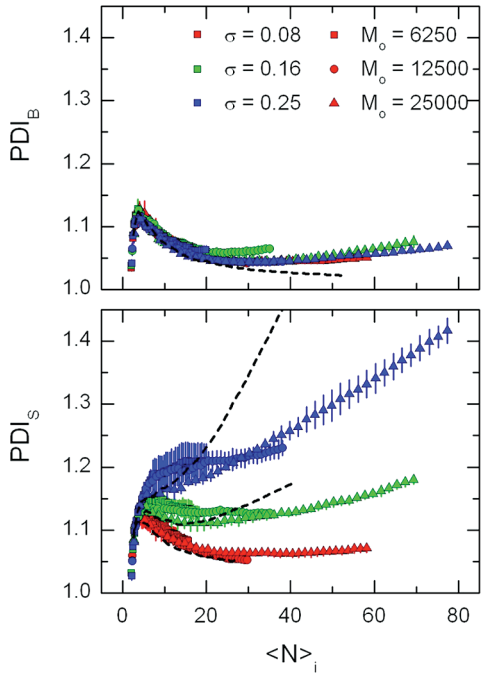

Figure 8. PDIs of bulk (top) and surface (bottom) polymers as a function of the average molar mass of bulk and surface polymers, respectively, for $\eta = 49\%$. Initiator grafting densities (σ): 0.08 (red), 0.16 (green), and 0.25 (blue); initial number of free monomers (M_0): 6250 (squares), 12 500 (circles), and 25 000 (triangles). The black dashed lines represent the $\eta = 0\%$ (top) and $\eta = 100\%$ (bottom), $M_0 =$ 25 000 and $\sigma = 0.08$, 0.16, and 0.25 conditions.

sample. Thus, the determination of σ encounters problems outlined in this paper. For example, Husseman et al.[18] and Koylu and Carter[29] performed their experiments at $\eta \ll$ 0.0001% and 0.01%, respectively. The values of σ calculated by the authors in these studies ranged from 0.5 to 1.4 chains/nm^2. Koylu and Carter concluded that the assumption of equal bulk and surface average molecular weights is not universally valid based on their SEC measurements of the grafted and solution chains. Specifically, Koylu and Carter reported a lower molecular weight of polymers grown in solution relative to those polymerized from the substrate, which is opposite to the trend described here. Based on their computed values of σ ($\approx$ 1.0 chain/nm^2), the estimated value of η cited above, and the data in Figure 3, one would expect the average molecular weight on the surface to be substantially smaller than that in the bulk. The discrepancy may lie in the nature of the substrate in the work of Koylu and Carter. Instead of an impenetrable surface confining the initiators to a two-dimensional plane, the initiators were bound to a three-dimensional photopolymer film. Husseman and co-workers did not measure the molecular weight of polymer brushes grown from planar substrates. Instead, their results showed similar molecular weights and PDIs between polymer cleaved from silica gel particles and those free in solution. The positive convex curvature of the substrate may have contributed to a relatively low PDI of the surface-initiated polymers due to lower chain crowding relative to that seen in flat substrate geometries. A comparison to polymers grown from the substrate is thus not appropriate unless one works with very low values of σ or very small curvatures. Jeyaprakash et al. compared ATRP polymerizations with added deactivators ($\eta = 100\%$) and with sacrificial initiators (η unknown) and showed that polymerizations in the

dx.doi.org/10.1021/ma202679r | Macromolecules 2012, 45, 2128–2137

presence of deactivators produce thicker grafted layers than those carried out in the presence of free initiators.[26] The explanation Jeyaprakash and co-workers put forth is consistent with our observations; i.e., η affects the rate of polymerization of the surface-initiated polymers and can therefore lead to polymers with $\langle N\rangle_S \neq \langle N\rangle_B$.

Silica-based mesoporous materials can also serve as supports for surface initiated CRP studies. In this case, it is possible to cleave sufficient amount of polymeric material from the substrate for subsequent SEC analysis. However, the negative curvature of the initiator-covered surfaces and the diffusion of monomer to the pores may accentuate the effects observed in this study. Kruk et al.[30] performed such polymerizations at η = 0% and noted that the polymerization was controlled and the PDI remained as small as in solution based ATRP (<1.1). Pasetto[31] and co-workers, however, carried out polymerizations from similar mesoporous materials over a whole range of η and noted higher PDIs and lower molecular weights for the surface-bound polymers. Similar conclusions have been reached in the study of Gorman and co-workers although simultaneous bulk polymerizations were not carried out.[32] This inconsistency of observations for both planar substrates and mesoporous materials highlights the need for continued research in the area and for a systematic investigation of the effects of η and σ in the controlled growth of polymer chains. The simulations performed here can serve as a guide to the proper design of such investigation.

CONCLUSIONS

The computer simulations implemented herein provide insight into the competitive growth of macromolecules initiated simultaneously in the bulk and on flat surfaces. We observe that the common assumption invoked in the literature of equality between the molecular weights of the bulk ($\langle N\rangle_B$)- and surface ($\langle N\rangle_S$)-based polymers is generally invalid. We find that in most instances $\langle N\rangle_B > \langle N\rangle_S$. Furthermore, the broadness of the molecular weight distribution of surface-grown polymers is highly dependent on their grafting density (σ), suggesting that claims, often found in the literature, of narrowly distributed surface-grown polymers polymerized by means of living polymerization are not generally valid.

We confirm that σ has an important effect on the growth rate and polydispersity of surface-grown polymers. Depending on the percentage of polymers on the surface (η), the properties of the bulk polymers are also affected by σ, which is a surface property. When η is large, the surface represents a strong perturbation to the growth of bulk polymers; as a consequence, the molecular weights of the bulk polymers at a monomer conversion of 0.8 increase with increasing σ. This behavior is attributed to the fact that at low η the bulk polymers compete with each other (they are the majority component) while at high η they compete primarily with the slow-growing surface-initiated polymers. By performing simulations at various initial numbers of free monomers (M_0), we confirm that the initial rate of polymerization is proportional to M_0. However, diffusion limitation likely affects the polymerization; this effect becomes less important with increasing M_0. The initial rates of polymerization also depend on σ. Increasing σ results in decreases in the rate of polymerization, confirming the results presented earlier.[16]

In the present work we utilized the canonical (NVT) ensemble. A more realistic model would require implementing the grand canonical ensemble that would describe a situation involving a constant chemical potential of the free monomers in solution. The latter is encountered in a typical experimental setup. We note, however, that the general conclusions reached here should still be valid even in the grand canonical ensemble. Namely, the molecular weight of bulk-initiated polymers should be higher than that of polymer brushes grown from surfaces. In fact, given the constant large excess of monomers in the reservoir, the differences between $\langle N\rangle_S$ and $\langle N\rangle_B$ and the corresponding PDI of both families of polymers will likely be higher than those reported herein.

ASSOCIATED CONTENT

Supporting Information

Description of the lattice employed in MC BFM simulations for various values of σ and η, plots of PDI_S vs PDI_B, and details of the data truncation. This material is available free of charge via the Internet at http://pubs.acs.org.

AUTHOR INFORMATION

Corresponding Author

*E-mail Jan_Genzer@ncsu.edu, Tel +1-919-515-2069.

Present Address

[†]School of Chemical & Biomoleculer Engineering, Cornell University, Ithaca, NY 14853-5201.

Notes

The authors declare no competing financial interest.

ACKNOWLEDGMENTS

We thank the National Science Foundation for supporting this work through Grant DMR-0906572.

REFERENCES

(1) Barbey, R.; Lavanant, L.; Paripovic, D.; Schüwer, N.; Sugnaux, C.; Tugulu, S.; Klok, H.-A. *Chem. Rev.* **2009**, *109*, 5437−527.
(2) Jones, D. M.; Smith, J. R.; Huck, W. T. S. *Adv. Mater.* **2002**, 1130−1134.
(3) Jones, D. M.; Huck, W. T. S. *Adv. Mater.* **2001**, *13*, 1256.
(4) Matyjaszewski, K.; Dong, H.; Jakubowski, W.; Pietrasik, J.; Kusumo, A. *Langmuir* **2007**, *23*, 4528−4531.
(5) Gautrot, J. E.; Trappmann, B.; Oceguera-Yanez, F.; Connelly, J.; He, X.; Watt, F. M.; Huck, W. T. S. *Biomaterials* **2010**, *31*, 5030−41.
(6) Moglianetti, M.; Webster, J. R. P.; Edmondson, S.; Armes, S. P.; Titmuss, S. *Langmuir* **2010**, *26*, 12684−9.
(7) Takahashi, H.; Nakayama, M.; Yamato, M.; Okano, T. *Biomacromolecules* **2010**, *11*, 1991−9.
(8) Advincula, R. C. In *Polymer Brushes*; Advincula, R. C., Brittain, W. J., Caster, K. C., Rühe, J., Eds.; Wiley-VCH Verlag GmbH & Co. KGaA: Weinheim, 2004; p 501.
(9) Zhao, B.; Brittain, W. . *Prog. Polym. Sci.* **2000**, *25*, 677−710.
(10) Brittain, W. J.; Minko, S. *J. Polym. Sci., Part A: Polym. Chem.* **2007**, *45*, 3505−3512.
(11) Jones, D. M.; Brown, A.; Huck, W. *Langmuir* **2002**, *18*, 1265−1269.
(12) Baum, M.; Brittain, W. J. *Macromolecules* **2002**, *35*, 610−615.
(13) Kim, J.-B.; Huang, W.; Bruening, M. L.; Baker, G. L. *Macromolecules* **2002**, *35*, 5410−5416.
(14) Brinks, M. K.; Studer, A. *Macromol. Rapid Commun.* **2009**, *30*, 1043−1057.
(15) Ye, Q.; Wang, X.; Li, S.; Zhou, F. *Macromolecules* **2010**, *43*, 5554−5560.
(16) Matyjaszewski, K.; Xia, J. *Chem. Rev.* **2001**, *101*, 2921−2990.
(17) Pyun, J.; Kowalewski, T.; Matyjaszewski, K. *Macromol. Rapid Commun.* **2003**, *24*, 1043−1059.

(18) Husseman, M.; Malmström, E. E.; McNamara, M.; Mate, M.; Mecerreyes, D.; Benoit, D. G.; Hedrick, J. L.; Mansky, P.; Huang, E.; Russell, T. P.; Hawker, C. J. *Macromolecules* **1999**, *32*, 1424−1431.
(19) Tomlinson, M. R.; Efimenko, K.; Genzer, J. *Macromolecules* **2006**, *39*, 9049−9056.
(20) Turgman-Cohen, S.; Genzer, J. *J. Am. Chem. Soc.* **2011**, *133*, 17567−17569.
(21) Genzer, J. *Macromolecules* **2006**, *39*, 7157−7169.
(22) Turgman-Cohen, S.; Genzer, J. *Macromolecules* **2010**, 101022125807042.
(23) Carmesin, I.; Kremer, K. *Macromolecules* **1988**, *21*, 2819−2823.
(24) Deutsch, H.; Binder, K. *J. Chem. Phys.* **1991**, *94*, 2294−2304.
(25) Goto, A.; Fukuda, T. *Prog. Polym. Sci.* **2004**, *29*, 329−385.
(26) Jeyaprakash, J. D.; Samuel, S.; Dhamodharan, R.; Rühe, J. *Macromol. Rapid Commun.* **2002**, *23*, 277−281.
(27) de Vos, W. M.; Leermakers, F. A. M. *Polymer* **2009**, *50*, 305−316.
(28) de Vos, W. M.; Leermakers, F. A. M.; de Keizer, A.; Kleijn, J. M.; Cohen Stuart, M. A. *Macromolecules* **2009**, *42*, 5881−5891.
(29) Koylu, D.; Carter, K. R. *Macromolecules* **2009**, *42*, 8655−8660.
(30) Kruk, M.; Dufour, B.; Celer, E. B.; Kowalewski, T.; Jaroniec, M.; Matyjaszewski, K. *Macromolecules* **2008**, *41*, 8584−8591.
(31) Pasetto, P.; Blas, H.; Audouin, F.; Boissière, C.; Sanchez, C.; Save, M.; Charleux, B. *Macromolecules* **2009**, *42*, 5983−5995.
(32) Gorman, C. B.; Petrie, R. J.; Genzer, J. *Macromolecules* **2008**, *41*, 4856−4865.

Macromolecules

Article

pubs.acs.org/Macromolecules

Interfacial and Annealing Effects on Primary α-Relaxation of Ultrathin Polymer Films Investigated at Nanoscale

Hung K. Nguyen,*[,†] Massimiliano Labardi,[‡] Simone Capaccioli,[†,‡] Mauro Lucchesi,[†,‡] Pierangelo Rolla,[†,‡] and Daniele Prevosto[‡]

[†]Dipartimento di Fisica "Enrico Fermi", Università di Pisa, Largo Pontecorvo 3, 56127 Pisa, Italy

[‡]CNR-IPCF, Consiglio Nazionale delle Ricerche, Istituto per i Processi Chimico-Fisici, c/o Dip. Fisica Largo Pontecorvo 3, 56127 Pisa, Italy

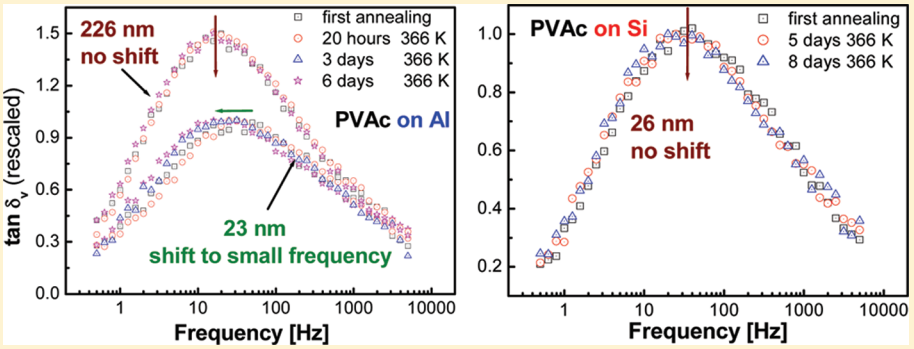

ABSTRACT: The influence of interfacial interactions and annealing time on dynamics of the α-relaxation in ultrathin poly(vinyl acetate) films deposited on different substrates has been studied using local dielectric spectroscopy at ambient pressure and controlled humidity. After annealing at 323 K for about 3 days, for polymer films supported on gold and aluminum substrates, an increase of the relaxation rate with decreasing film thickness below 30−35 nm was observed, whereas for films deposited on silicon substrates a thickness-independent dynamics was found for films as thin as 12 nm. The difference in size effect on dynamics of the films could reasonably be related to the difference in interfacial energy between polymer films and substrates, even though a criterion simply based on interfacial energy cannot be used to explain all the results. In fact, further annealing at a higher temperature evidenced an annealing-dependent dynamics in films prepared on aluminum substrates consistent with the presence of long-living metastable states at the polymer/substrate interface. The lifetime of such metastable states seems related to the nature of the substrate as well as to the molecular weight of the polymer.

1. INTRODUCTION

Effects of interfacial interactions on relaxation dynamics of polymeric materials under confinement are considered as a key factor for understanding the deviation of relaxation properties and glass transition temperature, T_g, from the bulk behavior.[1−3] It is suggested that at the free surface of a polymer film a layer of few nanometers of thickness exists,[1,2,4] in which chain motions are faster than in the bulk system. Moreover, depending on the degree of the polymer/substrate interaction, the mobility of polymer chains at the interface with the substrate can be increased, decreased, or remain the same as in the bulk.[3,5] The most used parameter to estimate the degree of interfacial interactions is the interfacial energy between the substrate and polymer, γ_{sp}. It is generally accepted that with increasing interfacial energy the segmental mobility of polymer chains in the regions close to the substrate slows down, leading to increase the T_g in such regions compared to that in the bulk.[6−9]

Recently, such a scenario has been strongly criticized by a series of works showing that polymer relaxation dynamics, and consequently the dynamic glass transition, is independent of the film thickness, even in the nanometer range, as well as on polymer/substrate interactions.[10−12] Variations ascribed to different sample preparation procedures were supposed to be the main factor leading to observed deviations of dynamics of ultrathin films from the bulk.[12] For example, thickness-independent dynamics has been found in poly(vinyl acetate) (PVAc) films as thin as 13 nm when subjected to an annealing procedure lasting for several tens of hours at a high temperature (366 K, i.e., $\sim T_g$(bulk) + 50 K).[11] Surprisingly, such annealing time is much longer than any conventional time scale used to determine physical processes of polymers, for example, the primary α-relaxation or reptation relaxation time at the annealing temperature. On the contrary, polymer films annealed at lower temperatures and/or for shorter time usually confirm the presence of the size-dependent dynamics, as reported by broadband dielectric spectroscopy (BDS) on capped and uncapped films[9,13−15] and by other techniques on supported films.[3,16,17]

Received: December 21, 2011
Revised: January 27, 2012
Published: February 13, 2012

Besides sample preparation issues, the need of annealing over a very long time has led some authors to hypothesize the presence of long-living metastable states in supported polymer films. In this respect, the existence of an interfacial polymer layer in contact with the supporting substrate was discussed several years ago[18] and recently measured in silicon-supported polystyrene (PS) films as a function of the annealing time.[19] Moreover, in a recent report Napolitano et al.[20] have evidenced the correlation between the annealing-dependent relaxation dynamics of ultrathin PS films deposited on aluminum substrates and the annealing-controlled growth of an irreversibly adsorbed polymer layer at the substrate surface. A dimensionless number given by the ratio between the time scale of the adsorption and the annealing time was introduced to describe the growth of the adsorbed layer and consequently the annealing-dependent dynamics observed in ultrathin polymer films.[20] The proposed mechanism seems to be suited to reconcile the results obtained on several Al-supported polymer films under different annealing conditions[11] and to explain on a physical basis the conclusions drawn by Erber et al.[12] about the importance of sample preparation procedures.

In recent years, a new method named local dielectric spectroscopy (LDS)[21] has been successfully applied to measure dielectric relaxation of supported polymer films. The LDS method was initially implemented to measure primary α-relaxation on thick PVAc films (thickness ~1 μm) with nanometer scale resolution under ultrahigh-vacuum conditions.[21] Soon afterward, the method has been developed to be applied on ultrathin films under ambient conditions and with controlled humidity.[17,22,23] A benefit of LDS method is that it can be used to measure dielectric relaxation on uncapped films, thus avoiding problems related to the evaporation of the capping electrode, such as shorts and metal particles diffusion inside the film. Moreover, by such technique dielectric properties of polymer films are measured with a lateral positioning resolution of tens of nanometers, releasing the need of continuous and uniform ultrathin polymer films over extended areas, also allowing LDS to be applied to detect inhomogeneities of dynamic behavior of the sample on the nanometer scale.[22,24]

In the current work, we apply LDS developed by using an improved frequency-modulated electrostatic force microscopy (FM-EFM) method to get access to a frequency interval up to four decades, to study with greater accuracy confinement effects on dynamics of uncapped ultrathin PVAc films deposited on different substrates, namely gold, aluminum, and silicon. By a systematic study of samples annealed in the same conditions, the annealing effects on the primary α-relaxation of the films are also addressed. In addition, interfacial energies between PVAc and supporting substrates are determined and correlated to the effects of nanoconfinement on the dynamics.

2. EXPERIMENTAL METHODS

2.1. Sample Preparation. Poly(vinyl acetate) (PVAc), with molecular weight M_w = 350 kg/mol, polydispersity index PDI = 2.80, and gyration radius R_g ~ 17 nm,[25] was purchased from Scientific Polymer Products, Inc. Ultrathin PVAc films were prepared by spin-coating solutions of PVAc in toluene onto gold, aluminum, and silicon substrates. Gold layers of 30 nm thickness were obtained by thermal evaporation on glass disks previously evaporated with a ~5 nm adhesion layer of chromium, whereas 50 nm thick aluminum layers were directly evaporated on glass disks. Silicon substrates were obtained from standard monocrystalline, doped Si(100) wafers for microelectronics use. The film thickness was controlled in the range from 8 to 233 nm by changing the concentration of polymer solutions as well as spinning speed.

Prior to dielectric measurements, all polymer films were annealed with a similar procedure at 323 K under vacuum for about 3 days. We would like to clarify that it is not our intent to propose a new criterion of annealing. Our choice is merely based on a previous experimental procedure,[17] used on PVAc films with M_w = 167 kg/mol, that was found sufficient to completely remove the residual solvent and moisture from our thickest film. After such common procedure some films used for studying annealing effects have been annealed at higher temperature, which will be detailed in section 3.

Before measurements, a scratch was made on each film by a steel cutter in order to uncover part of the conductive substrate beneath. Calibration spectra were taken on the conductive substrate and used as reference to obtain local dielectric spectra of the polymer. Moreover, AFM profiling of the scratch was used to determine the film thickness.

2.2. Interfacial Energy Calculation. In order to determine the interfacial energies, γ_{sp}, between PVAc and solid substrates, contact angles of three liquids, namely water, glycerol, and diiodomethane, on each substrate were measured using a CAM 200 optical contact angle meter (KSV) at room temperature. The values of the contact angles, φ, were obtained from averaging five measurements for each sample (Table 1).

Table 1. Measured Contact Angles of Water, Glycerol, and Diiodomethane on Solid Substrates and Calculated Interfacial Energies with PVAc

	contact angle φ [deg]			
substrate	water	glycerol	diiodomethane	interfacial energy with PVAc [mJ/m^2]
gold	89.2 ± 0.9	74.6 ± 1.5	33.4 ± 1.8	1.2 ± 0.2
aluminum	27.9 ± 1.3	39.2 ± 3.1	28.7 ± 0.8	1.6 ± 0.3
silicon	41.9 ± 2.4	32.2 ± 1.9	57.3 ± 1.3	3.4 ± 0.3

The dispersive component, γ^{LW}, the electron acceptor, γ^+, and the electron donor, γ^-, contributions to the surface energy of a liquid and a solid are related to the contact angle of a droplet of the liquid on the surface of the solid, through the Young–Dupre equation[26]

$$(1 + \cos\phi)\gamma_L = 2\left(\sqrt{\gamma_s^{LW}\gamma_L^{LW}} + \sqrt{\gamma_s^+\gamma_L^-} + \sqrt{\gamma_s^-\gamma_L^+}\right) \quad (1)$$

where "s" and "L" indicate the substrate and liquid, respectively. Using measured contact angles of three liquids and their previously determined surface tension parameters,[27] surface energies of the solids were calculated by eq 1.

Interfacial energies of PVAc film with the three substrates were estimated using the well-accepted Good–Girifalco–Fowkers combining rule[28]

$$\gamma_{sp} = \left(\sqrt{\gamma_s^{LW}} - \sqrt{\gamma_p^{LW}}\right)^2 + 2\left(\sqrt{\gamma_s^+\gamma_s^-} + \sqrt{\gamma_p^+\gamma_p^-} - \sqrt{\gamma_s^+\gamma_p^-} - \sqrt{\gamma_s^-\gamma_p^+}\right) \quad (2)$$

where "p" denotes the polymer. The three surface tension parameters of PVAc were determined from the literature.[29]

2.3. Local Dielectric Spectroscopy Technique. In this work, a Veeco Multimode atomic force microscope (AFM) (Nanoscope IIIa with ADC5 extension) was adapted to a frequency-modulated electrostatic force microscope (FM-EFM) and operated in lift mode as previously described.[22] FM-EFM with improved bandwidth was here implemented through a RHK Technology PLLProII phase-locked-loop (PLL) frequency detector, having a nominal response bandwidth of 4 kHz that could be extended to about 10 kHz by appropriate setting of internal filters and DAC sampling rates. In essence, such bandwidth indicates the limit frequency at which the PLL detector is able to follow a rapid change of the resonant frequency of the AFM cantilever. The latter frequency is made to shift by the effect of the

dx.doi.org/10.1021/ma202757q | Macromolecules 2012, 45, 2138–2144

electric force gradient induced by biasing of the tip. Such gradient is proportional to the term d^2C/dz^2, where C is the tip/sample capacitance.[17]

As demonstrated by the spectra herein reported, we were able to acquire spectra with electric excitation frequency as high as 5 kHz, thereby extending our previous bandwidth[17] by 2 decades and therefore up to 4 decades in total. This was possible while not giving up the high sensitivity and spatial resolution obtainable by frequency-modulation EFM[30] in comparison to different methods based on direct force measurement.[23]

For electric excitation and acquisition of dielectric spectra, an external dual-phase lock-in amplifier (SRS SR830DSP) was used, controlled through a GPIB interface by a homemade LabView routine. Doped silicon, Pt-coated AFM cantilevers (Nanosensors PPP-NCLPt) were used, with spring constant $k \sim 40$ N/m, resonant frequency $f_{res} \sim 165$ kHz, and nominal tip radius of around 25−30 nm. Oscillation amplitude was calibrated as customary by AFM tapping mode amplitude/distance curves. By this way, the distance between the AFM tip and the sample surface during the electric measurements was calculated by summing the average tip−sample distance on tapping mode with the set-lift height. For all dielectric measurements, the tip/sample distance was estimated around 20 nm.

Our microscope was operated in controlled humidity within a homemade enclosure and during measurements the relative humidity was about 3−4%. The sample temperature was controlled using a thermal application controller (TAC, Veeco). The actual temperature on the sample surface was calibrated using a PT100 sensor.

3. RESULTS AND DISCUSSION

3.1. Dielectric Measurements by LDS. In LDS, dielectric relaxation of polymer films is represented in terms of an electric phase shift angle, δ_v, the tangent of which is related to the tip/substrate capacitance by

$$\tan \delta_v = \frac{\partial^2 C''/\partial z^2}{\partial^2 C'/\partial z^2} \tag{3}$$

where z is the distance between the tip and the sample surface and C' and C'' are the real and imaginary parts of the tip/substrate capacitance. As described in previous reports,[22,23,31,32] in the distance range of the order of the tip radius, R, the tip/substrate capacitance can be conveniently expressed by approximated relations. We adopt the one proposed by Fumagalli et al.[31]

$$C(z, \omega) = 2\pi\varepsilon_0 R \ln\left\{1 + \frac{R(1 - \sin\theta)}{z + h/\varepsilon(\omega)}\right\} \tag{4}$$

where h and $\varepsilon(\omega)$ are the thickness and the relative dielectric permittivity of the polymer film, respectively, θ is the aperture half-angle of the tip shaft, assumed of conical shape, and ε_0 is the vacuum permittivity. Noticing that the capacitance (eq 4) is not linearly dependent on ε, thus the quantity $\tan \delta_v$ is dependent on the material properties as well as on the geometry of the capacitor. In other words, $\tan \delta_v$ is a different quantity from the tangent of the loss angle usually considered in conventional dielectric spectroscopy, even if their temperature and frequency dependencies are qualitatively very similar.

In Figure 1, the tangent of δ_v, in the following also called loss-tangent, obtained in a frequency range from 0.5 Hz to 5 kHz and at different temperatures for a 233 nm thick film deposited on aluminum substrate is presented. The spectra show the presence of a relaxation peak that moves toward higher frequencies with increasing temperature in a similar way of dielectric loss spectra obtained by BDS.[14] A measurement around the T_g value (~310 K) is also presented to show the background of the instrument. At T_g the secondary relaxation

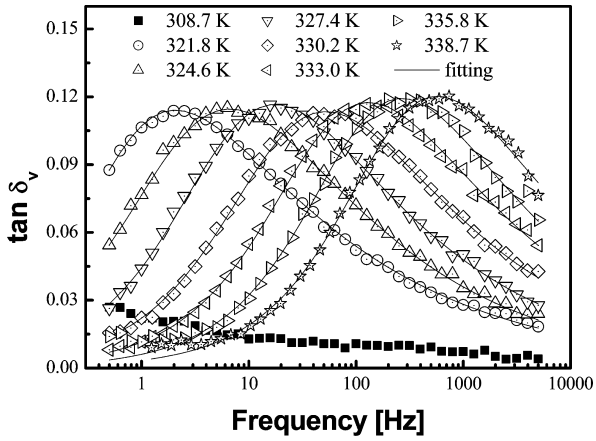

Figure 1. Loss-tangent spectra on a 233 nm thick PVAc film, deposited on aluminum, measured at different temperatures. Lines represent fitting with eqs 3, 4, and 5.

peak is at much higher frequency and the α-structural relaxation peak is at lower frequency than the measured interval, so that only its high-frequency tail is observable. By α-relaxation or structural relaxation we refer to the process associated with the glass transition and cooperative segmental dynamics. The solid curves represent a fitting performed by using analytical models describing the substrate/tip capacitance (eq 4), the phase shift of the tip resonant frequency modulation (eq 3), and the Havriliak−Negami relation, often used in the phenomenological description of the dielectric function of a polymer:

$$\varepsilon(\omega) = \varepsilon_\infty + \frac{\Delta\varepsilon}{[1 + (i\omega\tau_{HN})^{1-\alpha_{HN}}]^{\beta_{HN}}} \tag{5}$$

In our fitting procedure we fixed ε_∞ as constant as that obtained for bulk samples ($\varepsilon_\infty = 3.1$),[33] while the other parameters in eq 5 were adjusted to get the best fits that were evaluated by checking the residues between the experimental data and fitting curves. As shown in Figure 1, fitting curves interpolate well the measured data at all temperatures. We point out that the parameters obtained from the analysis describe the dielectric function $\varepsilon(\omega)$ of the material and consequently are comparable to the parameters obtained from conventional dielectric measurements.

The shape parameters of the dielectric function of eq 5 obtained by fitting are almost temperature-independent within the fitting uncertainties (data not shown), while the peak frequency of the α-structural relaxation process increases with increasing temperature as expected due to the enhancement of segmental mobility at higher temperatures. The data measured on the 233 nm thick film will be assumed as the bulk value. Indeed, in a previous study[17] we have found that the relaxation rate measured on PVAc film (with lower molecular weight than in the present paper) of 137 nm thickness by LDS is similar to that of the bulk PVAc sample with a similar molecular weight measured by BDS. Moreover, by using a similar technique, Schwartz et al.[23] have observed a thickness-independent dynamics (once corrected for the geometrical contribution to the spectra) on films with thicknesses from 250 to 1000 nm, confirming that the thickness-independent regime is already reached at 250 nm.

dx.doi.org/10.1021/ma202757q | Macromolecules 2012, 45, 2138−2144

The logarithm of maximum frequency of the dielectric loss, ε'', as a function of temperature, has been fitted by the Vogel–Fulcher–Tammann (VFT) equation (Figure 2):

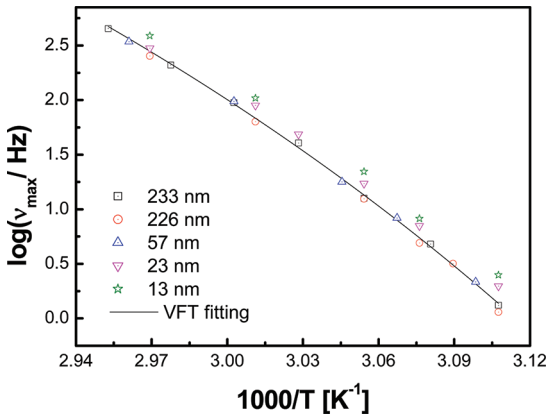

Figure 2. Logarithm of maximum frequency of the α-structural relaxation in PVAc films deposited on aluminum, as a function of reciprocal temperature. Solid line represents VFT fitting for the film of 233 nm thickness.

$$\log \nu_{max} = \log \nu_0 - \frac{DT_0}{T - T_0} \quad (6)$$

where ν_{max} is the frequency of the maximum dielectric loss, ν_0 is the relaxation frequency of the α-process at infinite temperature, D is a constant anticorrelated to the fragility parameter, and T_0 is the so-called Vogel temperature.[34] The VFT parameters resulting from fitting of such data, as well as the glass transition temperature, T_g, according to the definition $\nu_{max}(T_g) = 1/(200\pi)$ Hz, are listed in Table 2. The good agreement of

Table 2. VFT Fitting Parameters for the 233 nm Thick Film Supported on Aluminum in Comparison with Bulk Data on PVAc with M_w = 170 kg/mol

sample	log ν_0 [Hz]	D	T_0 [K]	T_g ($\nu_{max} = 1/200\pi$ Hz) [K]
233 nm	11.8 (fixed)	6.3 ± 0.1	261.1 ± 0.9	310.0 ± 1.1
bulk[35]	11.8 ± 0.1	6.3 ± 0.1	261.4 ± 1.0	310.4

such parameters with those obtained for the bulk samples of PVAc[35,36] using BDS supports the fact that the loss-tangent spectra obtained by LDS represent the α-structural relaxation of the polymer film, and the used models are working well at least in the present experimental conditions.

Finally, we mention that LDS technique has been proposed as a surface technique, but the estimation of the thickness of the surface layer to which it is sensitive is matter of debate.[21,37] According to our understanding based on previous investigation from us and others[17,23] in the thickness range here investigated, the data report information averaged over the entire thickness.

3.2. Effects of Film Thickness and Supporting Substrate. The size effect on the α-structural relaxation of Al-supported PVAc films is presented in Figure 2 where the logarithm of the frequency of the maximum of ε'' measured on films with thickness from 233 to 13 nm is reported as a function of reciprocal temperature. The relaxation rate is almost thickness-independent from 233 to 57 nm, but it increases on the film of 23 nm, and even more on the thinnest film of 13 nm. This result is quantitatively consistent with the findings reported in our previous study about the confinement effect on the α-structural relaxation of gold-supported PVAc films with lower molecular weight.[17]

As shown in a variety of reports, interactions at surfaces and interfaces play an important role in ruling the deviations of dynamics of confined polymers from the bulk behavior.[6,8] By changing the supporting substrates, the interplay between polymer/substrate interaction and size effects on α-structural relaxation of ultrathin films can be observed. In this study, three different substrates, namely gold, aluminum, and silicon, which are very commonly employed in the study of supported ultrathin polymer films, were used. Loss-tangent spectra obtained at the temperature of 327.4 K for PVAc films on gold and aluminum substrates and 328.2 K on silicon are reported in Figures 3a–c,

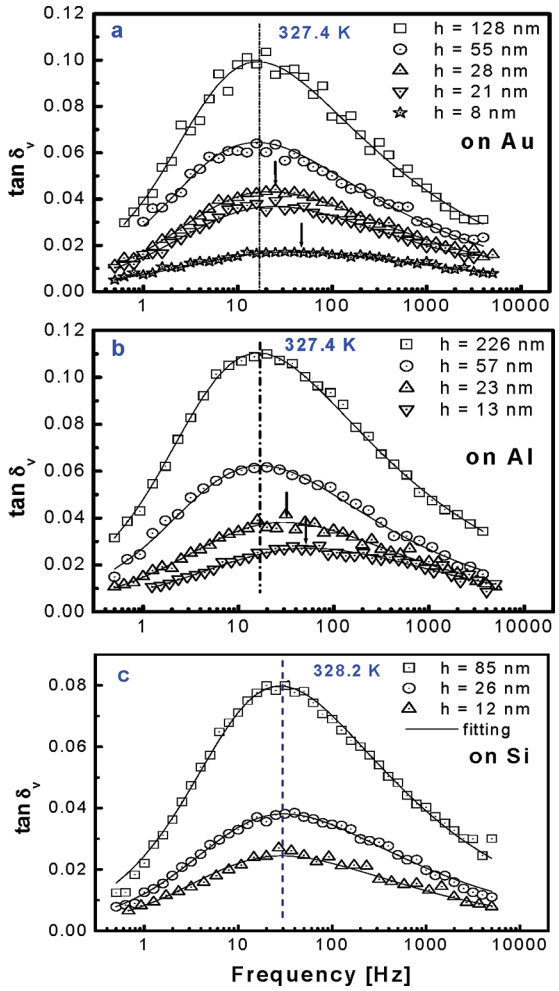

Figure 3. Isothermal loss-tangent spectra of PVAc films with different thicknesses deposited on (a) gold (measured at 327.4 K), (b) aluminum (measured at 327.4 K), and (c) silicon (measured at 328.2 K).

respectively. As clearly visible, a shift of the relaxation peak to higher values of frequency is observed on gold- and aluminum-supported PVAc films (Figures 3a,b). The shift becomes more pronounced on thinner films, and spectra seem also to become broader. In contrast, there is no significant change in the relaxation peak of all films deposited on silicon substrates with thickness from 85 nm down to 12 nm (Figure 3c).[38]

dx.doi.org/10.1021/ma202757q | Macromolecules 2012, 45, 2138–2144

The effects of film thickness and supporting substrate on the shape parameters of the relaxation peak were also analyzed, as shown in Figure 4. The values of α_{HN} and β_{HN} both slightly

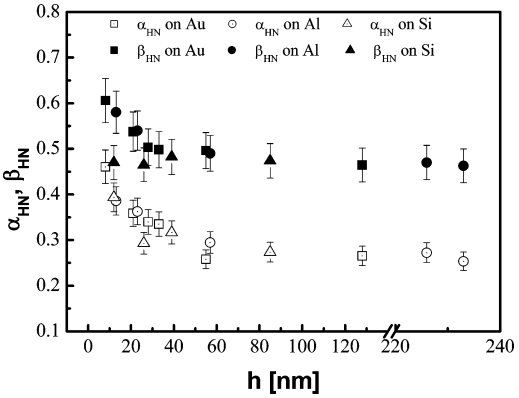

Figure 4. Shape parameters of the α-structural relaxation (eq 5) as a function of film thickness.

increase with decreasing thickness of films supported on gold and aluminum, meaning that the α-structural relaxation on such substrates becomes more symmetric and broader on decreasing the film thickness. However, for films deposited on silicon, only α_{HN} seems to increase with decreasing film thickness, while β_{HN} remains independent of the sample thickness. In principle, the observed broadening of the relaxation peak can be ascribed to a more heterogeneous dynamics, which is consistent with the presence of layers with different mobility. The observed increase of the symmetric broadening of the spectra in samples prepared on all substrates should be contrasting with the hypothesis of a selective suppression of slow modes.[14]

In Figure 5, the difference in the value of T_α—defined as the peak temperature of the α-structural relaxation process

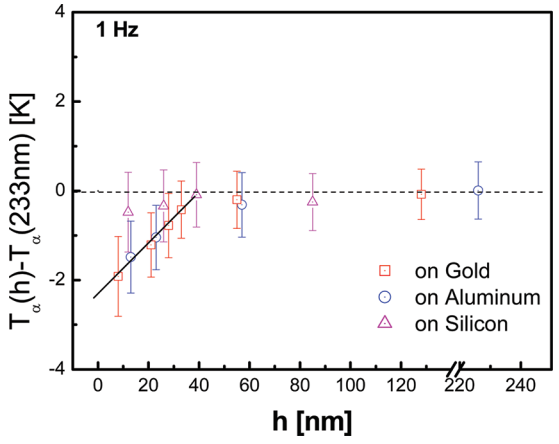

Figure 5. Thickness dependence of the difference in the T_α between ultrathin films and the 233 nm thick film. The dashed and solid lines are guides to the eye.

measured at 1 Hz—compared to the 233 nm thick film is plotted as a function of the film thickness. For films deposited on gold and aluminum substrates, there was almost no change in the T_α when the film thickness was decreased down to about 35 nm, while a systematic reduction of T_α was observed with further decreasing film thickness, and the T_α-reduction measured on films as thin as 10 nm was about 2−3 K. Even though the reduction of T_α obtained here is small, somehow comparable to the measurement uncertainties, such reduction occurs in a systematic way on both gold and aluminum substrates. Furthermore, a small change in dynamics of PVAc with decreasing film thickness was found in previous reports, also using different techniques, on samples with lower molecular weight and different procedures of sample preparation.[14,22,39] For example, using the microbubble inflation method to determine the creep compliance of freely standing PVAc films, O'Connell et al. found a reduction of the T_g from the bulk value of less than 1.5 K on the thinnest film of 23.7 nm.[39]

Films prepared on Si substrates did not show change of dynamics for film thicknesses down to 12 nm. This observation agrees with BDS results obtained with the air-gap capacitor geometry by Serghei et al.[10] Indeed, after annealing the samples well above the T_g in a pure nitrogen atmosphere for several hours until the reproducible measurements were reached, no shift of the relaxation rate respect to the bulk was found on several polymers studied in the uncapped geometry, among which ultrathin PVAc films supported on silicon. Interestingly, these results were apparently contrasting with the size effects on relaxation dynamics of capped PVAc films between two aluminum electrodes previously reported by the same authors using BDS.[14] Indeed, they found a reduction of the T_α, corresponding in this case to the frequency of 38 Hz, of about 2−3 K from the bulk value when the film thickness decreases down to about 10 nm, in agreement with our present observation on Au- and Al-supported films. Such results suggest that the discrepancy in refs 10 and 14 could not be due to the evaporated aluminum electrode or to a noneffective removal of solvent in the Al-supported films, but more probably to the difference in polymer/substrate interactions. Moreover, we can confirm that the confinement effects on PVAc relaxation dynamics are much weaker than those on other polymers such as PS[40] or poly(methyl methacrylate) (PMMA).[41] The difference might be the result of diverse macromolecular structures or arrangements of polymer chains close to the free surface or to the interface. A recent study by Kim et al.[42] addressed the importance of water content in PVAc when measuring in ambient conditions to the strength of the T_g reduction with decreasing film thickness. However, in our measurements at relative humidity of 3−4% this water content is very small, less than 0.5% as found by Miyagi et al.[43] for PVAc bulk. Therefore, we can deduce that the humidity-induced change of T_g or T_α herein is smaller than our experimental errors.

In order to understand how interfacial interactions impact the T_α reduction, the interfacial energy, γ_{sp}, between PVAc films and the three solid substrates was also obtained (Table 1). The results show a similarity in interfacial interactions of PVAc films with gold and aluminum surfaces, which are less than the critical value of about 2 mJ/m^2 estimated in Fryer's report[6] separating the energy region where a negative deviation of T_g in ultrathin films was observed (γ_{sp} < 2 mJ/m^2) from that of positive deviation (γ_{sp} > 2 mJ/m^2). Noteworthy, for Au- and Al-supported films the values of γ_{sp} are very similar to each other and they correspond to similar ΔT_α, whereas for Si-supported films we have larger values of γ_{sp} and smaller ΔT_α compared with the two other substrates (gold and aluminum) (Figure 5).

The value of γ_{sp} measured on the silicon substrate is much higher than the critical value, indicating a strong interaction between PVAc and silicon surface. Fryer et al.[6] have found an increase of the T_g on both PS and PMMA films with decreasing

film thickness compared to the bulk value when the polymer−substrate interfacial energy was higher than 2 mJ/m^2. However, in our case, instead of an increase of the T_α we observed no significant T_α shift for all films deposited on silicon. Therefore, we confirm that samples made of the same material, and annealed in the same way on different substrates, exhibit confinement effects that can be qualitatively related to the interfacial energy. Nevertheless, the comparison of our results with those from the literature evidence that γ_{sp} alone is not sufficient to explain the variation of T_g from the bulk with decreasing film thickness, as also mentioned elsewhere.[44] This result is not surprising as differences in molecular structure and chain stiffness are factors affecting polymer dynamics in the bulk and likely also the confinement effects on dynamics. This is evidenced for example by Priestley et al.,[8] who found that the change of T_g at the free surface and substrate interface of polymer films depends substantially on the structure of polymers. However, the mechanism behind the interaction between polymer and supporting substrate still awaits to be clarified in detail.

3.3. Annealing Effects. The dependence on annealing of the α-structural relaxation time and glass transition was evidenced on Al-capped PVAc films,[11] and it was inferred that such dependence might be due to the growth of an absorbed polymer layer at the polymer/substrate interface as for the case of the Al/PS system.[20,45] We considered interesting to investigate such aspect on PVAc films deposited on substrates with quite different interfacial energies. As a consequence, samples annealed at 323 K for 3 days (first annealing) were further annealed at 366 K for different times ranging from 20 h to 8 days. For the 226 nm thick PVAc film deposited on aluminum, the α-structural relaxation is found independent of further annealing; i.e., the loss-tangent spectra measured before and after annealing up to 6 days at 366 K are unchanged (Figure 6a). In contrast, the relaxation rate of the structural process on the 23 nm thick Al-supported PVAc film decreases slightly after 3 days of annealing and eventually decrease to that of the thick film after 6 days of annealing. These results demonstrate that further annealing seems to affect the dynamics of the ultrathin film only. As a simple hypothesis, it is suggested that the region of polymer located at the layers close to the free surface or polymer/substrate interface evolves through a series of metastable states characterized by different time scales. The latter possibility is in agreement with, and in case extends, the results obtained by Napolitano et al.,[20] evidencing that the influence of annealing on the dynamics of ultrathin polymer films is correlated to the growth of an irreversibly adsorbed layer at the substrate interface and to packing of macromolecules in such layer.

We have also observed that the time scale of the evolution of such metastable states in PVAc films during annealing is related to the molecular weight, as already found for PS.[20] The disappearance of dynamics enhancement in our sample of M_w = 350 kg/mol and thickness 23 nm was obtained with more than 3 days of annealing at 366 K (plus the first annealing at 323 K for 3 days), as seen in the inset of Figure 6a showing the time evolution of the relative maximum frequency of the α-process measured on 226 and 23 nm thick films at 327.4 K, where $n = \nu_{max}(t, \text{h})/\nu_{max}(0\ \text{s}, 226\ \text{nm})$. However, only 32 h was necessary for the 13 nm thick PVAc film with M_w of 157 kg/mol[11] to recover bulklike dynamics. The M_w dependence of the evolution time of metastable states is found more than linear, but it appears weaker than that observed on PS[20] in the same range of molecular weights. In fact, Napolitano et al.[20] found

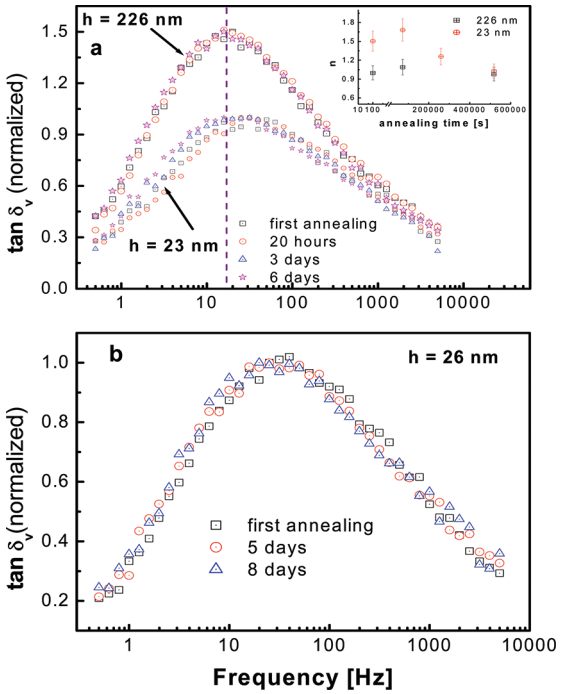

Figure 6. Loss-tangent spectra measured after different annealing times at 366 K of PVAc: (a) on Al measured at 327.4 K, the inset shows the evolution of the relative maximum frequency, n, upon annealing time on both thicknesses; (b) on Si measured at 328.2 K. The data have been normalized to the maximum and rescaled for clarity.

that increasing the molecular weight from 97 to 160 kg/mol (both larger than the critical value for entanglement) the characteristic time increase from less than 3 h to more than 6 weeks (more than a factor 100). In our case for an increase of a factor 2 of M_w the increase of the characteristic time is a bit larger than a factor 3.

In order to clarify whether the interfacial energy between the polymer and the supporting substrate has actually a role in the annealing effects observed above, a similar annealing procedure was performed on the 26 nm thick film deposited on the silicon substrate. As shown in Figure 6b, no difference in the peak position among loss-tangent spectra obtained at different annealing times could be observed, suggesting that annealing at 323 K for 3 days is sufficient to equilibrate polymer chains even at interfacial layers. This result also suggests that the adsorption time of PVAc onto substrates can depend on the polymer/substrate interactions as well as on substrate roughness. Further investigation is in progress to elucidate this point.

4. CONCLUSIONS

Confinement effects on the α-structural relaxation of supported ultrathin PVAc films on a frequency range of up to 4 decades were studied by means of an improved local dielectric spectroscopy approach. Relaxation dynamics was measured for PVAc films deposited on different substrates and subjected to different annealing conditions. After the first annealing step (at 323 K for 3 days), faster relaxation was observed on films supported on gold and aluminum substrates when film thickness decreased to below 30−35 nm. The maximum observed T_α reduction from the bulk value was 2−3 K for film with thickness of about 10 nm. In contrast, no thickness-dependent relaxation was found for all films deposited on silicon substrates with thickness

dx.doi.org/10.1021/ma202757q | Macromolecules 2012, 45, 2138−2144

from 85 nm down to 12 nm. Such difference can be reasonably related to the difference in interfacial energy between polymer films and substrates, which is larger for silicon than for gold and aluminum. However, a criterion simply based on interfacial energy cannot be used to explain all the results. In fact, by annealing at higher temperature (366 K) up to 8 days, no shift of loss-tangent spectra was observed for the 226 nm thick film on aluminum as well as on the 26 nm thick film on silicon. However, an effect was observed on the 23 nm thick film on aluminum; in particular, the bulk dynamics was recovered after 6 days of annealing. Our results are consistent with the presence of long-living metastable states of the polymer at the interfacial layer close to the substrate. We find that the characteristic time of such states may depend on the molecular weight of the polymer as well as on the nature of the substrate. These findings help to reconcile literature data obtained on supported and capped thin PVAc films[10,14] that appeared conflicting.

AUTHOR INFORMATION

Corresponding Author

*E-mail: nguyen@df.unipi.it.

Notes

The authors declare no competing financial interest.

ACKNOWLEDGMENTS

We thank Dr. P. Pingue and M. Cecchini (Scuola Normale Superiore, Pisa) for assistance in sample preparation and contact angle measurements and M. Bianucci (University of Pisa) for assistance in developing our LDS setup. We also thank Prof. K. Fukao (Ritsumeikan University) for information about R_g of PVAc. H.K.N. thanks the Galileo Galilei School of Graduate Studies at Pisa University for financial support.

REFERENCES

(1) Keddie, J. L.; Jones, R. A. L.; Cory, R. A. *Faraday Discuss.* **1994**, *98*, 291−230.
(2) DeMaggio, G. B.; Frieze, W. E.; Gidley, D. W.; Zhu, M.; Hristov, H. A.; Yee, A. F. *Phys. Rev. Lett.* **1997**, *78*, 1524.
(3) Alcoutlabi, M.; McKenna, G. B. *J. Phys.: Condens. Matter* **2005**, *17*, R461.
(4) Dinelli, F.; Ricci, A.; Sgrilli, T.; Baschieri, P.; Pingue, P.; Puttaswamy, M.; Kingshott, P. *Macromolecules* **2011**, *44*, 987−992.
(5) Forrest, J. A.; Mattsson, J. *Phys. Rev. E* **2000**, *61*, R53−56.
(6) Fryer, D. S.; Peters, R. D.; Kim, E. J.; Tomaszewski, J. E.; de Pablo, J. J.; Nealey, P. F.; White, C. C.; Wu, W. L. *Macromolecules* **2001**, *34*, 5627.
(7) Tate, R. S.; Fryer, D. S.; Pasqualini, S.; Montague, M. F.; de Pablo, J. J.; Nealey, P. F. *J. Chem. Phys.* **2001**, *115*, 9982.
(8) Priestley, R. D.; Mundra, M. K.; Barnett, N. J.; Broadbelt, L. J.; Torkelson, J. M. *Aust. J. Chem.* **2007**, *60*, 765.
(9) Napolitano, S.; Prevosto, D.; Lucchesi, M.; Pingue, P.; D'Acunto, M.; Rolla, P. *Langmuir* **2007**, *23*, 2103.
(10) Serghei, A.; Huth, H.; Schick, C.; Kremer, F. *Macromolecules* **2008**, *41*, 3636.
(11) Serghei, A.; Kremer, F. *Macromol. Chem. Phys.* **2008**, *209*, 810.
(12) Erber, M.; Tress, M.; Mapesa, E. U.; Serghei, A.; Eichhorn, K. J.; Voit, B.; Kremer, F. *Macromolecules* **2010**, *43*, 7729.
(13) Fukao, K.; Uno, S.; Miyamoto, Y.; Hoshino, A.; Miyaji, H. *Phys. Rev. E* **2001**, *64*, 051807.
(14) Serghei, A.; Tress, M.; Kremer, F. *Macromolecules* **2006**, *39*, 9385.
(15) Rotella, C.; Napolitano, S.; Wubbenhorst, M. *Macromolecules* **2009**, *42*, 1415.
(16) Ellison, C. J.; Mundra, M. K.; Torkelson, J. M. *Macromolecules* **2005**, *38*, 1767.
(17) Nguyen, H. K.; Prevosto, D.; Labardi, M.; Capaccioli, S.; Lucchesi, M.; Rolla, P. *Macromolecules* **2011**, *44*, 6588.
(18) Reiter, G.; de Gennes, P. G. *Eur. Phys. J. E* **2001**, *6*, 25−28.
(19) Fujii, Y.; Yang, Z.; Leach, J.; Atarashi, H.; Tanaka, K.; Tsui, O. K. C. *Macromolecules* **2009**, *42*, 7418.
(20) Napolitano, S.; Wübbenhorst, M. *Nature Commun.* **2011**, *2*, 260.
(21) Crider, P. S.; Majewski, M. R.; Zhang, J.; Oukris, H.; Israeloff, N. E. *Appl. Phys. Lett.* **2007**, *91*, 013102.
(22) Labardi, M.; Prevosto, D.; Nguyen, K. H.; Capaccioli, S.; Lucchesi, M.; Rolla, P. *J. Vac. Sci. Technol. B* **2010**, *28*, C4D11.
(23) Schwartz, G. A.; Riedel, C.; Arinero, R.; Tordjeman, P.; Alegría, A.; Colmenero, J. *Ultramicroscopy* **2011**, *111*, 1366.
(24) Riedel, C.; Sweeney, R.; Israeloff, N. E.; Arinero, R.; Schwartz, G. A.; Alegría, A.; Tordjeman, P.; Colmenero, J. *Appl. Phys. Lett.* **2010**, *96*, 213110.
(25) Mark, J. E. In *Physical Properties of Polymers Handbook*, 1st ed.; Fetters, L. J., Lohse, D. J., Colby, R. H., Eds.; AIP Press: New York, 1996; Chapter 24, p 338.
(26) Vanoss, C. J.; Chaudhury, M. K.; Good, R. J. *Chem. Rev.* **1988**, *88*, 927.
(27) Lee, L. H. *Langmuir* **1996**, *12*, 1681−1687.
(28) Good, R. J.; Girifalco, L. A. *J. Chem. Phys.* **1960**, *64*, 561−565.
(29) McCafferty, E.; Wightman, J. P. *J. Adhes. Sci. Technol.* **1999**, *13*, 1415.
(30) Colchero, J.; Gil, A.; Baró, A. M. *Phys. Rev. B* **2001**, *64*, 245403.
(31) Fumagalli, L.; Ferrari, G.; Sampietro, M.; Gomila, G. *Appl. Phys. Lett.* **2007**, *91*, 243110.
(32) Lucchesi, M.; Privitera, G.; Labardi, M.; Prevosto, D.; Capaccioli, S.; Pingue, P. *J. Appl. Phys.* **2009**, *105*, 054301.
(33) Negami, S.; Ruch, R. J.; Myers, R. R. *J. Colloid Interface Sci.* **1982**, *90*, 117.
(34) Böhmer, R.; Ngai, K. L.; Angell, C. A.; Plazek, D. J. *J. Chem. Phys.* **1993**, *99*, 4201.
(35) Dlubek, G.; Kilburn, D.; Alam, M. A. *Macromol. Chem. Phys.* **2005**, *206*, 818.
(36) Roland, C. M.; Casalini, R. *Macromolecules* **2003**, *36*, 1361.
(37) Fumagalli, L.; Gramse, G.; Esteban-Ferrer, D.; Edwards, M. A.; Gomila, G. *Appl. Phys. Lett.* **2010**, *96*, 183107.
(38) This finding evidences that the shift of the loss tangent peak that we obtain by LDS is not affected by contributions due to the experimental method used, as put forward in ref 23.
(39) O'Connell, P. A.; Hutcheson, S. A.; McKenna, G. B. *J. Polym. Sci., Part B: Polym. Phys.* **2008**, *46*, 1952.
(40) Fukao, K.; Miyamoto, Y. *Phys. Rev. E* **2000**, *61*, 1743.
(41) Wübbenhorst, M.; Murray, C. A.; Dutcher, J. R. *Eur. Phys. J. E* **2003**, *12*, s01.
(42) Kim, S.; Mundra, M. K.; Roth, C. B.; Torkelson, J. M. *Macromolecules* **2010**, *43*, 5158−5161.
(43) Miyagi, Z.; Tanaka, K. *Colloid Polym. Sci.* **1979**, *257*, 259.
(44) Tsui, O. K. C.; Zhang, H. F. *Macromolecules* **2001**, *34*, 9139.
(45) Reiter, G.; Napolitano, S. *J. Polym. Sci., Part B: Polym. Phys.* **2010**, *48*, 2544.

Macromolecules

Article

pubs.acs.org/Macromolecules

Collapse of Polyelectrolyte Star. Theory and Modeling

O. V. Rud,*[,†] A. A. Mercurieva,[‡] F. A. M. Leermakers,[§] and T. M. Birshtein[†]

[†]Institute of Macromolecular Compounds of the Russian Academy of Sciences, 199004, St. Petersburg, Russia

[‡]Physics Department, St. Petersburg State University, 199034 St. Petersburg, Russia

[§]Laboratory of Physical Chemistry and Colloid Science, Wageningen University, Wageningen, The Netherlands

ABSTRACT: The collapse of hydrophobic polyelectrolyte stars in aqueous solutions is studied using the Scheutjens–Fleer self-consistent field (SF-SCF) approach. The hydrophobic property of the segments tends to compact the stars, whereas the presence of charges has the opposite effect. As a result, star conformations can be switched from an extended, strongly hydrated, and swollen state to a collapsed state via semicollapsed, quasi-micellar state using control parameters such as the solvent quality, specified by the Flory–Huggins parameter, the pH value or the ionic strength. More specifically, there exists a range of parameters wherein the stars have an inhomogeneous radial structure with a collapsed region, referred to as the core, and a swollen region forming the corona. In such microphase segregated state the fraction of arms of the star that form the core, or alternatively escape into the swollen corona, can be controlled. The SF-SCF analysis is complemented with analytical models to rationalize the complex phase behavior.

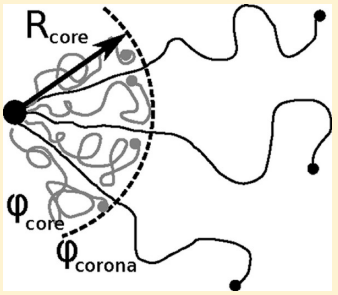

1. INTRODUCTION

Linear polyelectrolyte chains are prime examples of macromolecules that show interesting physical and chemical behavior that have relevance in numerous applications.[1,2] The list of potential applications can only grow when several polyelectrolyte chains are tethered to one common center, forming so-called polyelectrolyte stars. Typically, the center is a small colloidal particle, or some multifunctional chemical entity. To qualify as stars, the polyelectrolyte chains, often referred to as arms, must be much larger than the central grafting entity.

Moreover, there exists many examples of macromolecular association colloids. Our interest is in the situation when such macromolecular micelles, formed by an amphiphilic block copolymers, have a small compact core and a much larger swollen corona. For (kinetically) frozen core the number of chains in the star-like corona is constant and does not change with external conditions. Such macromolecular aggregates, can be considered as polymeric stars or, as *polyelectrolyte* ones if the corona chains carry their own charges. Star shaped polymer aggregates are thus key structures studied in soft matter physics, materials science and nanotechnology. A common feature is that they combine properties of linear polymers and of spherical soft colloids. The polymer corona makes them considerably more stiff than linear polymers, but much softer than hard colloidal spheres. Both, the polymer stars and the corona in macromolecular aggregates, are often regarded as a strongly curved polymer brushes.

The simplest among the star-shaped polymers is the homopolymeric noncharged star. These systems are understood in large detail due to intensive research in recent years.[3−9] Conformations of neutral stars are influenced by relatively few parameters, namely the functionality (number of arms) M, the degree of polymerization N of each arm, and the solvent quality. The structure of polyelectrolyte stars, on the other hand, is controlled by many more parameters. In this case, the degree of ionization, the salt concentration and the valency of counterions and co-ions as well as the temperature and pH of the solution also influence the properties. A few reviews on PE stars are available.[10−12]

The focus of this paper is on the theoretical description of *amphiphilic* polyelectrolyte stars. Such macromolecules show self-assembly properties, and therefore are often referred to as "smart" nano-objects, that respond in a dramatic way to small changes in the environment.[13]

Typically, amphiphilicity is caused by the presence in a molecule of two types of segments with differ affinities to the solvent. The amphiphilic polymeric star may be either com posed of two (or more) types of arms, (heteroarm star)[14−16] or composed of identical di- (or more) block copolymers.[17−20] Such molecules are reported to form single-molecule micelle-like core–corona structures: chains or chain-parts, for which the solvent is poor, are collected in a dense core, whereas chains or chain-parts, for which the solvent is good, form a corona providing the solubility (colloidal stability) of these stars. The popularity of polymeric micelles is explained by the expected relevance for, e.g., drug delivery applications.[20,21]

Our interest is in *homopolyelectrolyte* stars, of which the segments are amphiphilic. More specifically, we consider *annealed* polyelectrolyte stars whose monomers are either charged or not depending on the pH of the solution. As the charges like to be hydrated, monomers in the charged state are hydrophilic. Monomers in non charged state are assumed to be hydrophobic. This type of amphiphilicity is typical for many

Received: October 3, 2011
Revised: January 13, 2012
Published: February 3, 2012

polyelectrolytes, as these are, apart from the charged groups, often decorated by relatively long hydrophobic moieties linked as side-chains to the backbone. For example, as compared to poly(acrylic acid) , even the presence of one extra methyl group in polymethacrylic acid leads to a clustering of the uncharged chain segments (cf. ref 22).

Two opposing forces determine the conformation of such polyelectrolyte stars in aqueous solutions. The hydrophobicity makes the chain monomers stick together and avoid contact with the solvent molecules, leading to a compression (collapse) of the polymer arms. The electrostatic forces lead to swelling of the chains. The electrostatic swelling is caused by the osmotic pressure of counterions which are tend to locally compensate the charges of the polyelectrolyte chains. Swelling mediated by the osmotic pressure of counterions plays more important role than the direct electrostatic (Coulombic) repulsion between like-charged monomers since, the Debye length appears to be sufficiently low to consider charged monomers as screened by counterions.[23−26]

The hydrophobicity and electrostatics provide two different star structures. The presence of these two forces leads to the fact, that the collapsed and swollen states of amphiphilic polyelectrolyte system appear to be the different *phases*, separated by a phase transition, with a jump in polymer density.[27,28] The choice of equilibrium state is controlled by the characteristics of the solvent, namely proton concentration, given by the pH, and the concentration of mobile ions Φ^{ion}. In spatially inhomogeneous systems, such as polyelectrolyte brushes or stars all these characteristic turn out to have a local value and are functions of the local polyelectrolyte concentration. As a result, both phases may coexist in polyelectrolyte amphiphilic brush forming a dense and a swollen microphases.[29,30]

Such a dense core and swollen corona coexistence was established in star theoretically in,[31] and obtained using Monte Carlo simulation[32] and experimentally in the kinetically frozen multimolecular polystyrene-block-polymetacrylic acid micelles.[33] Collapsed part of the corona formed by an annealed polyelectrolyte is situated close to the hydrophobic core of the micelle. The similar picture was observed in micelles with the corona composed of quenched polyelectrolyte.[34]

The molecular dynamics (MD) simulation of collapse of the star with quenched polyelectrolyte arms has shown that depending on the solvent conditions one can find various partially collapsed states, including micelle-like (core−shell) structure[35] as well as the star-like one when the arms form pearl-necklace structures or interarm aggregates.[35,36] Note that the structures with the inter or intra chain compact formations are typical for quenched polyelectrolytes. While the solvent becomes poor, the individual chain, during its collapse, forms pearl-necklace conformation[37] and in the solution with finite concentration the microphase segregated structures appear.[38] This effect is due to the repulsion of electrostatic nature in the condensed phase. Core−shell structure in[35] was observed only in a narrow range of conditions, when the core is neutralized by the condensation of counterions. In this case the form of compact phase is defined by the minimization of interphase surface, i.e. lead to the spherical core.

In this paper we study the conformation of the *annealed* star. Monomer units in this case can be in a neutral deionized state. Moreover, as it will be shown, inside the compact phase they are always neutral. That is why we use the assumption about the spherical symmetry of the star conformations. The microphase segregated conformation might be only the core−shell one, with noncharged core.

The formation of the core−shell structure can be explained in the following discourse. In the vicinity of the star center, concentration of polymer segments is, essentially due to geometric reasons, higher than in the peripheral parts. In the case of annealed polyelectrolyte in low ionic strength conditions it is possible to show, and it is shown in this paper, that when the concentration of monomers becomes higher than a threshold value, it is advantageous for the polymer to drop the charge and become neutral. As the neutral polymer segments are hydrophobic, they expel water and form a compact core. For monomers in peripheral region where the monomer concentration is not high enough it is reasonable to be charged and hydrated. As a result, the star has a microphase segregated micelle-like or *quasi-micellar* structure with an uncharged condensed core and a charged swollen corona. We have shown in the article that not the star monomers suffer segregation but star arms do it as a whole, i.e., the core and corona are formed by almost uniformly collapsed and stretched arms. As in classical star-like micelles, the swollen corona is responsible for the colloidal stability of the phase-segregated star.

We use the numerical SCF method and specifically the algorithm developed by Scheutjens and Fleer for polymers at interface[39] and extended to the case of polyelectrolyte.[40−42] The computational efficiency of the method is the result of a local mean-field approximation. By making use of the symmetry of the system the method reduces the computations and solves for one gradient distributions, implementing a local averaging over two direction. It must be understood that in the averaging directions the fluctuations in density are ignored.

This paper is organized as follows. The next section, called Model and Methods, details the model we use in numerical "experiments" and the main features of the numerical scheme. The numerical SCF results are presented in the Results. In the section Theoretical Analysis, we elaborate on the basic system in a membrane equilibrium, which is used for our analytic estimation for the phase behavior of a single polyelectrolyte chain. This phase behavior is also used to rationalize results from the numeric SF−SCF calculations for a hydrophobic polyelectrolyte star. We propose a simple model of the star conformation in quasi-micellar state. As usual we conclude the paper with summing up our conclusions.

2. MODEL AND METHODS

Let us consider a homopolymer polyelectrolyte star immersed in aqueous salt solution. We assume that the star consists of M linear polyelectrolyte chains (arms), each composed of N identical spherically symmetric segments (monomers). Without loss of generality we assume that we are dealing with a polyacid, implying that the chain monomers can be either neutral or negatively charged. The chains are pinned by one of their ends to a sphere with radius R_0 (see Figure 1a,b). Each segment can be ionized depending on the local pH by a reaction with water

$$HA^0 + H_2O \overset{K}{\rightleftarrows} A^- + H_3O^+ \quad (1)$$

where K is ionization constant.

The solution, in which the star is immersed, is assumed to be an aqueous 1−1 electrolyte (e.g., NaCl). Properties of the solution are specified by several parameters which are the following.

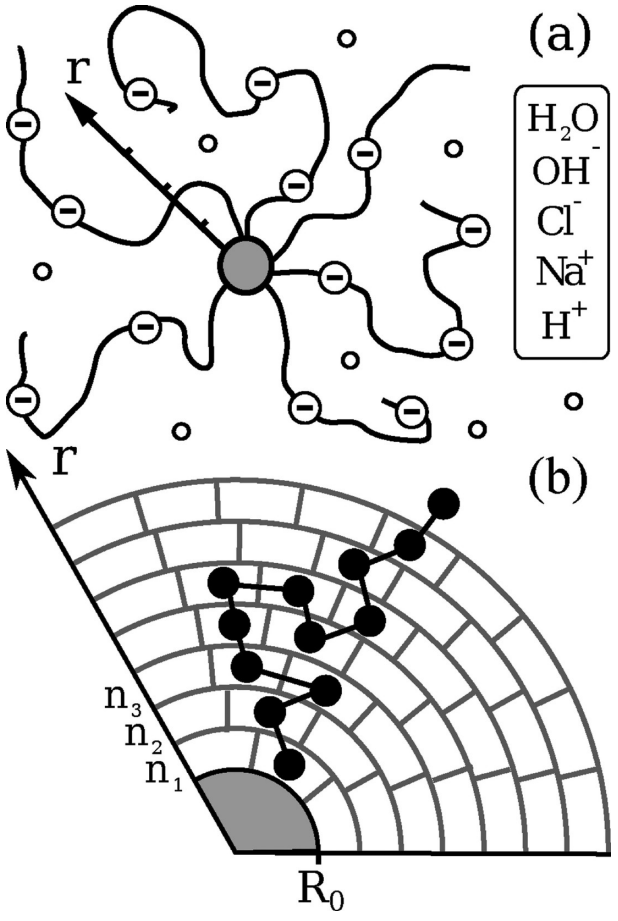

Figure 1. (a) Schematic presentation of the polyelectrolyte star in an aqueous salt solution. In this case six chains (arms) are grafted to a central particle. The radial coordinate r is indicated by the arrow. Small molecules that are present in the system are indicated in the box. (b) Star is in the spherically symmetric lattice with spherical lattice layers. One arm is given as an example. The central particle, to which arms are grafted, has radius R_0. The number of segments per layer n_r for layers r = 1, 2, 3 are indicated and these numbers are used to find the volume fractions $\phi(r) = n_r/L(r)$ that is, by normalizing with the number of sites per layer $L(r) \propto 4\pi r^2$.

The first one is the Flory–Huggins χ −parameter, which specifies the affinity of the monomers and solution (water) particles. A positive value implies repulsion and a negative value attraction. For simplicity, the same value of the χ parameter was chosen to specify interaction between polymer segments and all types of mobile particles, that is, χ value is the same for polymer contacts with water, positive (sodium, proton) or negative (chloride, hydroxyl) ions. Moreover, the χ parameter does not depend on whether the monomer is charged or not. Hence, the interaction of the polymer segment have an invariable contribution due to the solvent quality (χ) and this is augmented by an electrostatic contribution in case the monomer is ionized. As mentioned, our star is hydrophobic and therefore we choose a value that is larger than the theta-value $\chi > 0.5$.

The second parameter is the (dimensionless) salt concentration, which is represented by the total concentration of the mobile ions in bulk, that is, $\Phi^{ion}_{bulk} = [Cl]_{bulk} + [Na]_{bulk} + [OH]_{bulk} + [H_3O]_{bulk}$. As the bulk must remain electroneutral, the concentrations of the negative ions is invariably chosen equal to that of the positive ions: $[Cl^-]_{bulk} + [OH^-]_{bulk} = [Na^+]_{bulk} + [H_3O^+]$. Typically, in our systems it will be true that the salt concentration is much higher than the concentration of water ions H_3O^+ and OH^- and therefore it is possible to approximate Φ^{ion}_{bulk} as

$$\Phi^{ion}_{bulk} \cong 2[Cl^-]_{bulk} \quad (2)$$

Following the Scheutjens—Fleer ansatz, all the particles, namely, star monomers, the water molecules and the mobile ions are assumed to be of the same size that exactly fit a lattice site each (see Figure 1b). The size of the lattice site, which naturally has some "average" value, gives the conversion factor of dimensionless volume fractions to molar concentrations. We advice to estimate the size of the lattice site as follows. Starting with pure water (i.e., the most abundant species) with concentration C_w = 55.5 mol/L, one can estimate that the volume of one water molecule as $v_0 = 2.99 \times 10^{-29}$ m^3. This implies a unit of length $l_e = v_0^{1/3} \cong 3.1$ Å. With this choice the conversion factor to compute the molar concentration from the dimensionless salt concentration is 55.5.

The third parameter is the pH value, which is related with hydronium volume fraction $[H_3O^+]_{bulk}$ in the bulk $pH = -\log[H_3O^+]_{bulk}$. Hydroxyl and hydronium ions in solution are coupled according to the reaction

$$2H_2O \overset{K_w}{\rightleftarrows} H_3O^+ + OH^-$$

where K_w is water dissociation constant.

We shall measure the concentration in dimensionless volume fraction units and use the square brackets $[\cdots]$ notation. These units are the usual molar concentration C (measured in mol per liter) just normalized by $C_w = 55.5(mol)/(l)$. All quantities having the dimension of concentration should be normalized to C_w. If the bulk volume fraction of hydronium ions under neutral pH condition is $[H_3O^+]_{bulk} = C^{bulk}_{H_3O}/C_w$, i.e., neutral pH_n condition corresponds to volume fraction $[H_3O^+]_{bulk} = (10^{-7}$ mol/L)/(55.5 mol/L) $= 1.8 \times 10^{-9}$ and the dimensionless pH_n value is $pH_n = 7 + \log_{10} C_w = 8.74$. The number $\log_{10} C_w = 1.74$ should be added once to the pK_a and twice added to pK_w to make these quantities dimensionless. Everywhere in the paper, if it is not mentioned, $pK_a = 6$ and pH = 7 in usual units.

As all the monomeric species in our system are considered to be of the same size, namely the size of the lattice site, the transition to moles per liter cannot be fully accurate. Therefore, we advise that the results have comparative and qualitative character rather than a strict quantitative one.

Numerical Method. In our study we use the Scheutjens–Fleer self-consistent field (SF-SCF) approach. Here, we just describe the main features of the method that are of key importance to understand the premises. For more details we refer to the literature, e.g., to references.[39−42]

The polymer volume fractions are obtained through the evaluation of (sub) partition functions $G(r_s,s|r_{s'},s')$ for individual chains. These partition functions can be interpreted as the statistical weights of all step-weighted random walks from segment with ranking number s to segment with ranking number s' occurring at points r_s and $r_{s'}$, respectively. These sub partition functions are generated using a propagator formalism, which implements a freely jointed chain (FJC) on a lattice. The FJC has the property that the chains cannot be stretched further than their contour length. However, as long as the chains are not too strongly stretched the results are very similar to the Gaussian chain. In this limit, it can be shown that the propagator scheme is a discrete variant of the Edwards diffusion equation, which enumerates the partition functions of Gaussian

chains in an external potential field. Here our interest is in the chain partition functions $G(r,N|R_0,1)$ for the chain starting at the central grafting surface and ending with segment $s = N$ at a distance r from the center. Integrating over all coordinates gives the partition function of one arm, $q = \sum_r L(r)G(r,N|R_0,1)$, where the number of sites L in spherical coordinates is $L(r) \approx 4\pi r^2$. Here we shall number the coordinates $r = R_0 + 1$, $R_0 + 2$, ···, starting from the grafting surface. The partition function for the star is given by $Q = q^M/M!$. The propagator formalism not only gives access to the distribution of free ends, but also to that of middle segments, by implementing the so-called composition law, which combines two complementary sub partition functions $\phi(r,s) \propto G(r,s|R_0,1)G(r,s|N)$. In this equation $G(r,s|N)$ is the sub partition function for walks started with the unconstrained segment $s = N$ and ending at segment s in coordinate r. The overall volume fraction distribution is given by a summation over the segment ranking number, i.e., $\phi(r) = \sum_s \phi(r,s)$ and the normalization of the volume fractions is chosen such that each star contains exactly $N \times M$ segments.

Both in the Edwards equation and the propagator method, there is a segment potential $u(r)$, which implements excluded volume, nearest neighbor and electrostatic interactions.

The local volume fraction of segments ϕ presents a crowding contribution to the segment potentials. This contribution to the segment potential is related to the compressibility contribution. More explicitly, we implemented the incompressibility condition, which says that the volume fractions of the components in the system have to add-up to unity at all lattice coordinates. In good solvents, it can be shown that there is a contribution of $-\ln(1 - \varphi)$ to the segment potential (see refs 39 and 43).

The (short-range) interactions between the nearest neighbors X and Y in the lattice are specified by the Flory–Huggins parameter χ_{XY}, where X and Y are monomers, i.e., the segments of the star, the water molecules and any of the ions. The number of contacts are evaluated using the Bragg-Williams approximation. In this scheme the probability of pair interactions is given by the product of the volume fractions. By definition the FH parameters are nonzero for unlike contacts, that is $X \neq Y$.

The electrostatic term is given by $u_X^{(el)}(r) = q_X y(r)$, where q_X is the charge of segment X (in our case q_X is $-e$, zero, or e), and $y(r)$ is the (dimensionless) electrostatic potential determined via the solution of the Poisson–Boltzmann equation.

The SCF equations, including the Poisson–Boltzmann one, are solved by an iterative procedure. It assumes the consistent counting of the monomers distribution on the lattice by means of their potentials and counting the monomer potentials by means of the distribution in the system. A fixed point of the equations is known as the self-consistent solution. It can be shown that for this solution the (mean field) free energy of the system is optimized. The free energy as a function of both the volume fraction distribution and the corresponding segment potential distributions is straightforwardly evaluated.

Since the electrostatic interactions are not short-range, that is, they extend further than the size of a lattice cell, parameters such as the lattice constant, and temperature becomes relevant. As mentioned above, we have chosen the lattice constant $l_e \approx 3.1$ Å to normalize all linear lengths, we use room temperature (297.15 K) conditions and the dielectric constant in water $\varepsilon = 80$, thus the Bjerrum length $l_B \approx 7$ Å and $l_B/l_e \sim 1$. All the energies are normalized by k_BT.

3. RESULTS

The Star Size. Effect of Salinity. In parts a and b of Figure 2, we show results from the numerical SCF method for the radius of gyration R_g as a function of the salinity, $[Cl]_{bulk}$, for stars with $M = 50$ and $M = 10$ arms that have a length of $N = 250$ segments each. In both graphs there are six curves for specified FH parameters, namely $\chi = 0.5$, 1.0, 1.5, 2.0, 2.5, and 3.0. It is clearly seen that the radius of gyration of the stars is low at low salt concentration, first increases and then decreases with increasing ionic strength. This nonmonotonic behavior is found for both values of the number of arms per star and for (almost) all χ values. A similar nonmonotonic dependence was theoretically predicted for a flat weak polyelectrolyte brushes in a good solvent[25] and subsequently confirmed by numerical self-consistent field calculations.[44] In ref 45, this effect was shown by modeling a weak polyelectrolyte star under Θ-solvent conditions. Soon this effect was observed experimentally in the study of spherical micelles formed by polystyrene-block-poly(methacrylic acid). The size of the charged star-like polymethacrylic acid corona passes through a maximum at a monotonic variation of ionic strength.[33] Modeling of polyelectrolyte star using the molecular dynamics also proved the nonmonotonic

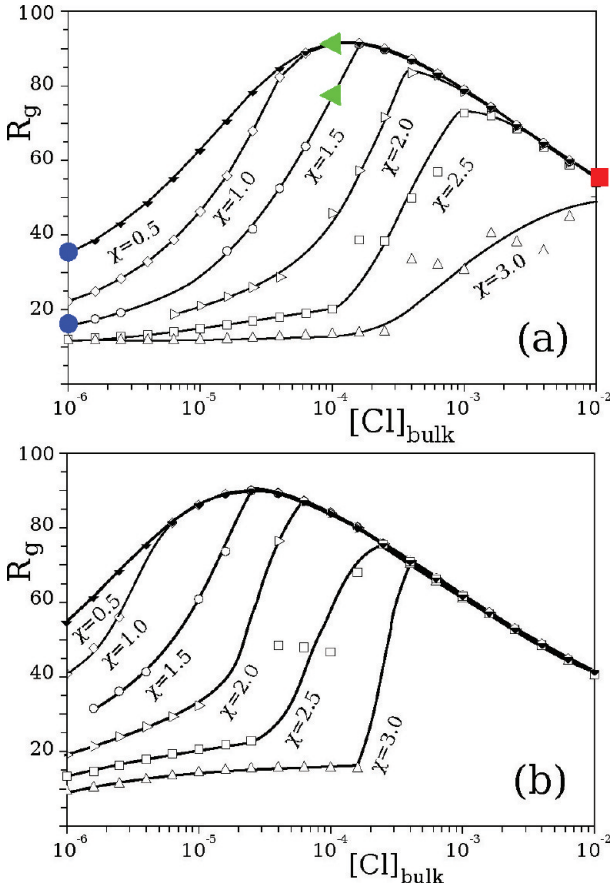

Figure 2. Radius of gyration as found by the numerical SCF method for a star with $M = 50$ arms (a) and $M = 10$ arms (b) each of length $N = 250$ monomers as a function of the ionic strength $[Cl]_{bulk}$, for different χ values as indicated. Each point marked on the $\chi = 1.5$ and $\chi = 0.5$ curves corresponds to one line in Figure 3a–c and Figure 5a–c. Colored marks at $\chi = 0.5$ and $\chi = 1.5$ match the colored curves in the respective figures. Curves in plots are guides for the eyes.

dx.doi.org/10.1021/ma202201m | Macromolecules 2012, 45, 2145–2160

dependence of the star radius of gyration on the strength of the electrostatic interactions.[35]

The nonmonotonic dependence of R_g at $\chi = 0.5$ can be understood from the fact that by increasing the salt concentration two competing effects have an impact on the swelling of the star.[25,45] At high ionic strength, the size of a polyelectrolyte star decreases with increasing ionic strength. This effect is known as electrostatic screening: the electrostatic repulsion between star monomers gets weaker with increasing ionic strength. The decrease in repulsion leads to a smaller size. This effect happens provided that the salt concentration outside the star is larger than the concentration of the star own charges inside the star, i.e., at high ionic strength. For low ionic strength it is found that the size of the *annealed* polyelectrolyte star increases with increasing ionic strength. Unique for annealed stars, it is known that the degree of ionization of the segments in the star is suppressed when the screening is low. With increasing salt concentration the suppression is diminished and this leads to increasing ionization of the star monomers and, therefore increased Coulombic interactions lead to an increase in the size. In more detail, we notice that H_3O^+ and OH^- ions do not only contribute to the ionic strength, but also participate in the dissociation equilibrium of the star segments and thus influence the charge of the polyelectrolyte. The degree of dissociation α is given by the following equation (see also eq 11 in next section)

$$\begin{cases} \dfrac{\alpha}{1-\alpha} \simeq \dfrac{K}{[H^+]_{bulk}} \dfrac{[Cl]_{bulk}}{\alpha\varphi}, & \alpha\varphi \gg [Cl]_{bulk} \\ \alpha \simeq \alpha_{bulk} \simeq \dfrac{K}{[H]_{bulk}}, & \alpha\varphi \ll [Cl]_{bulk} \end{cases} \quad (3)$$

At a not too high pH value, the addition of salt in the bulk results in a progressive substitution of H_3O^+ ions inside the star volume by Na^+ ions and, hence, in an additional ionization followed by an extension of the arms of the star. The latter effect is evident only at the low ionic strengths.

Parts a and b of Figure 2 show that, although the nonmonotonic dependence exists for all χ-values, the character of the dependence changes with increasing degree of hydrophobicity. At low $[Cl]_{bulk}$ a regime appears where R_g is small and independent of $[Cl]_{bulk}$. The region of this regime becomes larger with increasing hydrophobicity. After this regime there is a steep increase of R_g (the star "explodes" in size) after which all curves join together and show a common decrease of R_g with $[Cl]_{bulk}$.

Figure 2b is included to prove that this behavior is universal, that is, it does not depend on the composition of the star. A change in the number of arms only leads to a shift of the transition area, but the qualitative effect remains. For the current example the reduction of the number of arms by a factor of 5 needs significant fewer salt ions to substitute hydronium and to screen the charges of the star. In other words, the transitions shift to lower salt concentrations.

Note that in ref 35, a star composed of a strong polyelectrolyte chains (quenched polelectrolyte) was considered using molecular dynamics method. The Bjerrum length l_B was chosen as the parameter which control the strength of electrostatic interactions. There were shown that monotonic change of l_B leads to a nonmonotonic change of the dimension of the star. For small l_B values (which corresponds to the weak electrostatics) the star had a small size. The star were small also at large l_B, when the strong condensation of counterions led to the collapse of the star (cf. ref 36)

In the next two paragraphs we focus on the internal structure of the star for the conditions that correspond to the marked points in Figure 2a.

Quasi-Micellar Star Conformation. Parts a–c of Figure 3 show, in double logarithmic coordinates, the radial polymer segment density distribution, $\phi(r)$, the distribution of free ends, $\phi_{ends}(r)$, and the degree of ionization, $\alpha(r)$, respectively, at $\chi = 1.5$. Each curve refers to one point lying on the $\chi = 1.5$ curve in Figure 2a. The colored circle, triangle, and square in

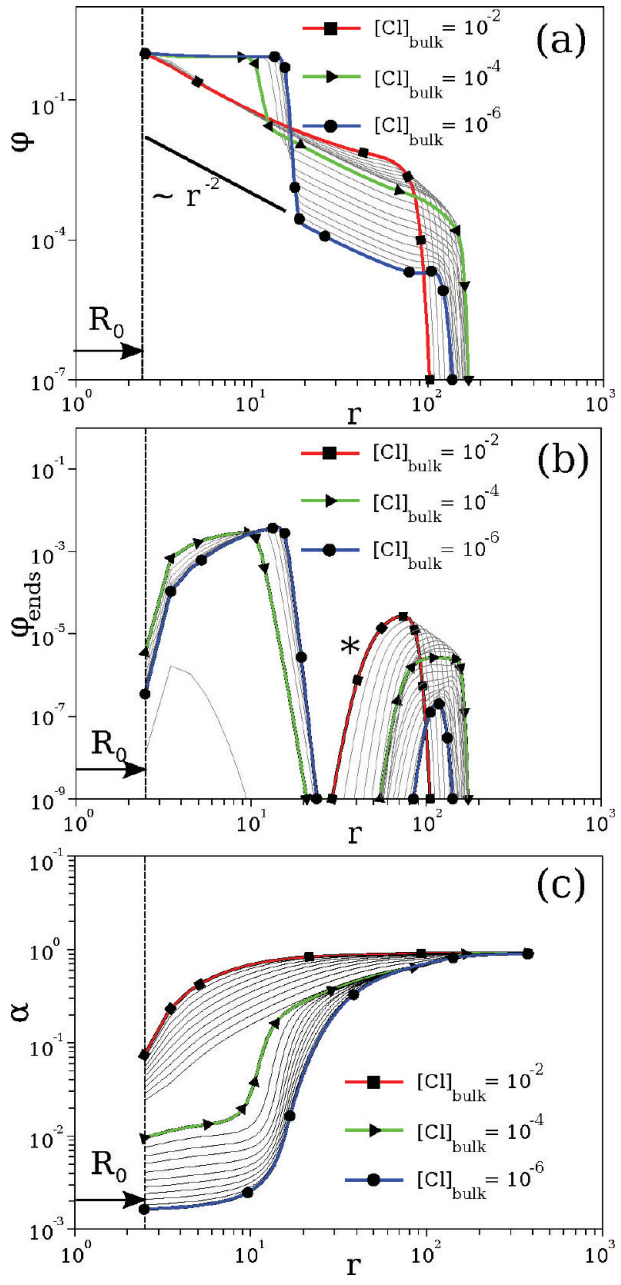

Figure 3. Double–logarithmic plot of the radial distribution of volume fraction, $\phi(r)$ (a), the corresponding distribution of the free end segments, $\phi_{ends}(r)$ (b), and the degree of dissociation, $\alpha(r)$ (c), of the polyelectrolyte star. These are given as functions of the distance from the center r for a set of $\chi = 1.5$ and various $[Cl]_{bulk}$ values. Each curve corresponds to one of the marks in Figure 2a and we refer to this figure for other characteristics.

dx.doi.org/10.1021/ma202201m | *Macromolecules* 2012, 45, 2145–2160

Figure 2a match the lines colored and marked the same in Figure 3a–c. This lines correspond to the ionic strength $[Cl]_{bulk} = 10^{-6}$, 10^{-4}, and 10^{-2}, respectively. The thin black lines are for intermediate $[Cl]_{bulk}$ values. For comparison, in Figure 5 we show similar dependencies, for the theta-conditions, i.e. $\chi = 0.5$.

The curves in Figure 3a–c split up into two types. One type represents a homogeneous swollen star and the other one indicates an inhomogeneous structure. More specifically, the inhomogeneous star has a plateau in polymer density at $\phi \sim 1$ near the star center and a region with much lower density for larger values of r. We refer to the inhomogeneous stars as quasi-micelles as these stars appears to be microphase segregated.

It is seen that somewhere between $[Cl]_{bulk} = 10^{-2}$ and 10^{-4} the transition takes place from the homogeneous star to the quasi-micelle. The size of the core decreases with increasing $[Cl]_{bulk}$ and above a certain ionic strength the core vanishes and the star becomes homogeneous.

In the quasi-micellar state the two regions differ greatly in all their properties. The monomers in the core are almost uncharged, while the corona monomers do carry a charge (see Figure 3c). The monomer density in the core is constant (near unity), and virtually independent of the ionic strength, $[Cl]_{bulk}$. At the core–corona interface the monomer density drops abruptly. With increasing $[Cl]_{bulk}$ the segment density of the corona near the interface increases: the jump changes from several orders of magnitude at $[Cl]_{bulk} = 10^{-6}$ to just one order at $[Cl]_{bulk} = 10^{-4}$. In the corona the segment density decay has a power-law dependence, $\phi \sim r^{-2}$ (Figure 3a). This decay corresponds to the scaling prediction for spherical polyelectrolyte stars at low salt concentration.[7,8]

The radial distribution of the terminal monomers is an interesting characteristic of the star structure, which can be obtained easily in the SCF calculations but not from analytical theory. As follows from Figure 3b, at low salinity this distribution is presented by two peaks with a pronounced wide zone between them, where no free ends occur (a dead zone). One peak is located in the depths of the star, in the core, whereas the other one lies in vicinity of the star interface. These two maxima indicate two populations of chains, which points to the choice a chain can make: it can either dissociate weakly and remain weakly extended, or it can dissociate substantially, resulting in strong electrostatic repulsion and significant stretching. Such a behavior, namely the separation of arms into two groups, have already been studied for stars and for brushes.[9,29,30,46]

To evaluate how many free ends are in the core and corona, respectively, we replotted the results in Figure 4a, wherein the radial distribution of the number of end segments $n_{ends}(r)$ is given as a function of the radial coordinate r,

$$n_{ends}(r) = L(r)\phi_{ends}(r) \approx 4\pi r^2 \phi_{ends}(r) \quad (4)$$

It is seen that the height of the external maximum increases monotonically with increase of $[Cl]_{bulk}$ while its radial position changes nonmonotonically. The terminal monomers move away from the center at low values of the salt concentration $[Cl]_{bulk} \in [10^{-6}, 10^{-4}]$ and then approaching to it with further increase in $[Cl]_{bulk}$.

At the lowest salt concentration used in calculations, $[Cl]_{bulk} = 10^{-6}$, almost all branches are in the core and only a few arms are strongly stretched, populating the charged corona.

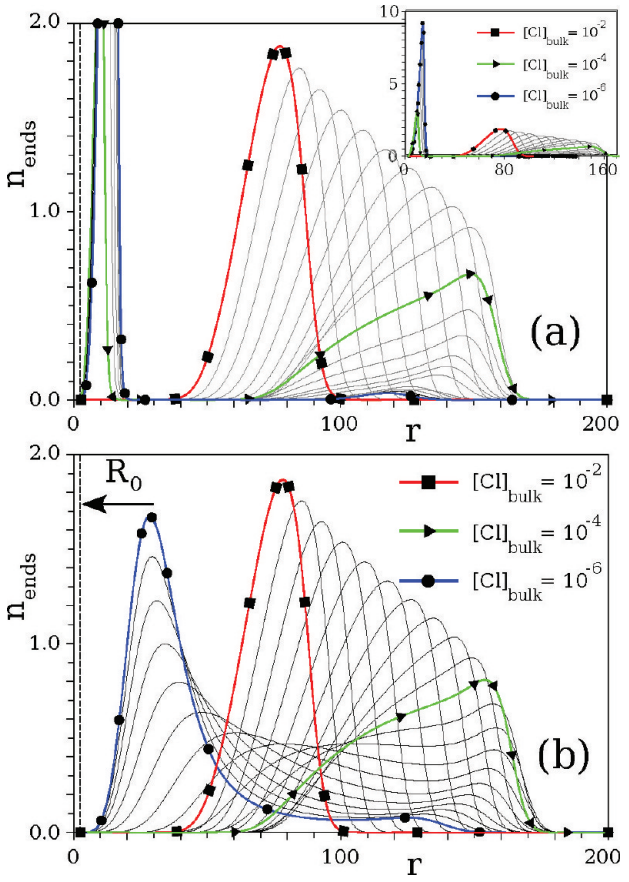

Figure 4. The radial distribution of the number of end segment, $n_{ends}(r)$, of a polyelectrolyte star. (a) Zoomed-in part of the end distribution is given in the main figure and the inset gives the overall distributions of the free ends for χ =1.5 and (b) $\chi = 0.5$. The lines are obtained for a series of salt concentration $[Cl]_{bulk}$ values as in Figure 3 and Figure 5. Parameters: $M = 50$ and $N = 250$.

With increasing ionic strength, gradually more and more chain ends leave the core until at $[Cl]_{bulk} = 10^{-4}$ the star is almost completely swollen. In the last case only 5 arms form the core. And thus, an evident increase in the value of R_g with ionic strength is observed (Figure 2a).

With a further increase in salinity the compact core disappears and the star structure becomes homogeneous. Both, the radial polymer density and the degree of ionization profile vary smoothly, without any jumps. The distribution of the end points is unimodal (see Figure 3b and Figure 4a). Inspection of Figure 2a reveals that the dependencies $R_g([Cl]_{bulk})$ for the swollen stars coincide for different χ values. In other words, the radius of gyration does not depend on χ in this range of $[Cl]_{bulk}$. The value of χ determines the lowest concentration $[Cl]_{bulk}$ at which R_g becomes independent of χ.

Swollen Star Conformation. For better understanding the structural transition at $\chi > 0.5$, we turn to the behavior of the star at Θ-conditions $\chi = 0.5$. This case has been studied extensively in ref 45. The star profiles are given in Figure 5a–c in the same manner as for $\chi = 1.5$, each curve matches one point lying on the $\chi = 0.5$ curve in Figure 2a. In this case for neutral star, the water appears to be the Θ-solvent, the volume interactions becomes repulsive; therefore, in this case for charged stars there is no interplay between steric and electrostatic forces, both of them is repulsive. Since there are no attractive forces the formation of a globular core is impossible.

dx.doi.org/10.1021/ma202201m | Macromolecules 2012, 45, 2145–2160

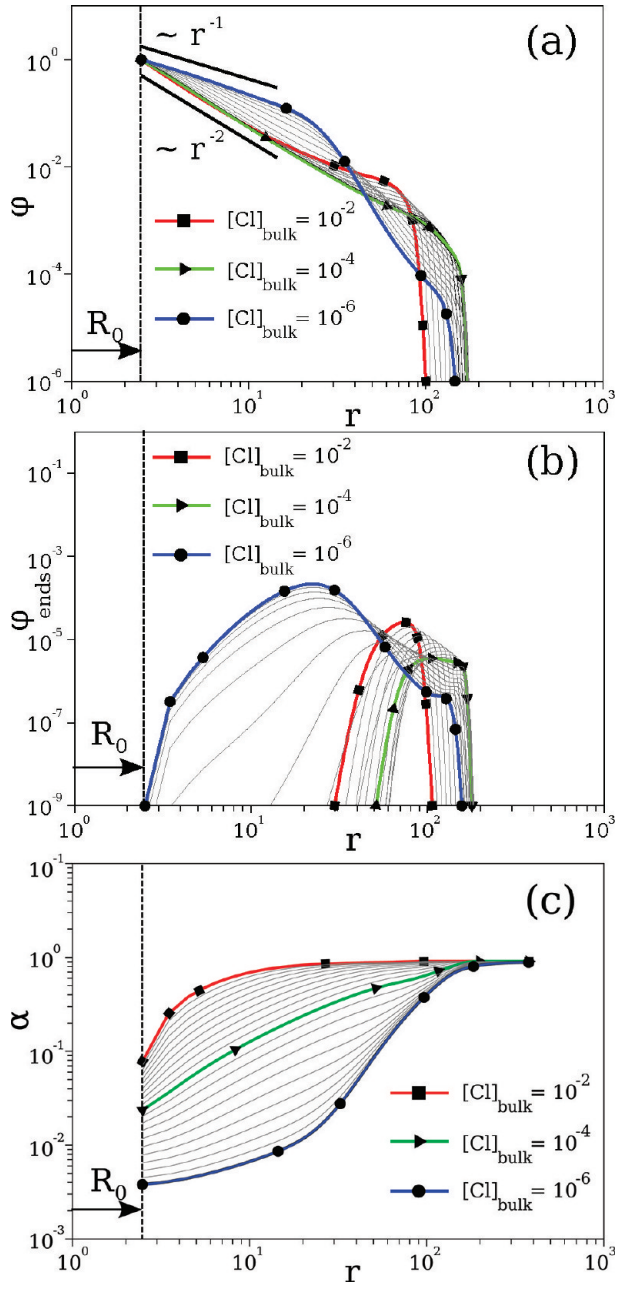

Figure 5. Double−logarithmic plot of the radial distribution of volume fraction, $\phi(r)$ (a), the corresponding distribution of the free end segments, $\phi_{ends}(r)$ (b) and the degree of dissociation, $\alpha(r)$, of the polyelectrolyte star (c). These characteristics are given as functions of the distance from the center r for $\chi = 0.5$ and various $[Cl]_{bulk}$ values. Each curve corresponds to one of the marks in Figure 2a, and we refer to this figure for other details.

Nevertheless, the general trend for the Θ-solvent case, i.e., Figure 5, is similar to the star in poor solvent (cf. Figure 3). Moreover, at high salt concentration, when the star is in the homogeneous swollen state, the characteristics are the same for both solvent strengths (see Figure 2a,b and Figure 3, Figure 5, Figure 4a,b, red lines marked with squares, $[Cl]_{bulk} = 10^{-2}$). Hence, not only the radius of gyration but also other characteristics of the swollen star are functions of the electrostatic interactions only. As in this regime the electrostatics dominate,[24,25] all star conformations respond in the same way on ionic strength and the χ values are not essential. This conclusion applies to the right-hand side of Figure 2a,b where the curves corresponding to various χ have merged together.

The decrease of the size of the star with increasing salt concentration, is typical for a polyelectrolyte brush in the salted brush regime[24,25,47] and is understood in terms of the electrostatic excluded volume, which depends on the Debye length. There are some intricacies. For example, it is seen that the decay of the polymer volume fraction $\phi(r)$ at $[Cl]_{bulk} = 10^{-2}$ (Figure 3, Figure 5) is less steep as $\phi \sim r^{-2}$ expected for fully extended arms and found, e.g., at $[Cl]_{bulk} = 10^{-4}$, but does not yet reach the theoretical profile $\phi \sim r^{-4/3}$ expected for chains with excluded volume.

For stars at lower salt concentrations, i.e. $[Cl]_{bulk} = 10^{-4}$ and poor solvents ($\chi = 1.5$), the compact core and the swollen corona are observed. For the $\chi = 0.5$ case, there is no singular behavior in the center and the star remains completely unfolded. As it is seen from Figure 3, Figure 5, and Figure 4a,b, the behavior of the corona of the star is the same in Θ- and in poor solvents. More specifically, the radial decrease of the polymer density follows a power-law $\phi \sim r^{-2}$ decay, which is specific for a polyelectrolyte star at low $[Cl]_{bulk}$.

Again, the conformation of the star turns out to be the most complicated at the lowest salt concentration, $[Cl]_{bulk} = 10^{-6}$. We recall that for poor solvents the polymer density profile has two regions with different scaling dependencies. For the Θ-condition case the radial decay near the center approximately goes as $\phi \sim r^{-1}$. Hence, most of the arms obey the law for Θ-conditions (ideal chains that have no charge) and reside not too far from the center of the star. The chain parts that escape from this Θ-region become charged, thus have polyelectrolyte behavior and the distribution of the free ends is very wide (Figure 5b, Figure 4b). As is seen from Figure 4b, approximately nine terminal monomers distribute almost uniformly throughout the outer region of the star.

In the Θ-solvent case, we do not see the microphase segregation. Figure 5 and Figure 2 indicate that all the star conformations respond gradually to changes of the salt concentration. The radius of gyration R_g is nonmonotonic but there is no jump in the density distribution. In the poor solvent case, as was shown above, there are two distinct regions in $R_g([Cl]_{bulk})$ dependence and the jump between them becomes more and more pronounced with increasing χ.

The ability to be in a microphase-segregated state is a key characteristic of the hydrophobic polyelectrolyte star. It is of interest to map out this ability in terms of a phase diagram.

Microphase Segregation. The phase diagram in Figure 6 presents the star state in the plane defined by the interaction parameters χ and the salt concentration $[Cl]_{bulk}$. In this phase diagram the darkness of an area corresponds to the number of free ends that have fallen into the core M_{core}. Hence, the white cells correspond to stars that are completely swollen and the black ones represent the fully collapsed stars. It is clearly seen that the transition boundary is smeared and the collapse of the star goes continuously through a spectrum of intermediate semicollapsed states, i.e., the quasi-micelles.

Figure 7 and Figure 8a,b detail the changes in the conformational characteristics of the star according to one vertical and two horizontal cross sections through the phase diagram Figure 6. In these Figures, the line marked with diamonds are the number of ends that have partitioned into the core $M_{core} = M\beta_M$, the lines marked with triangles correspond to the fraction of monomers in the core $N_{core}/N = M\beta_N$ where we introduced

dx.doi.org/10.1021/ma202201m | Macromolecules 2012, 45, 2145−2160

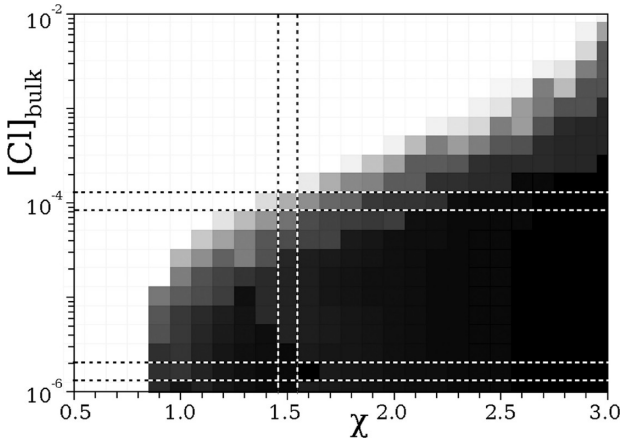

Figure 6. Phase diagram in $\chi - [Cl]_{bulk}$ coordinates illustrating the transition between stars that are swollen or are in the quasi-micellar state. The darkness of each cell corresponds to the number of the free ends that reside inside the core. This means that the black cells correspond to the fully collapsed star and the white cells are for the swollen stars. Dashed lines mark the cross sections which are shown in Figure 7 and Figure 8. Parameters: $M = 50$, $N = 250$.

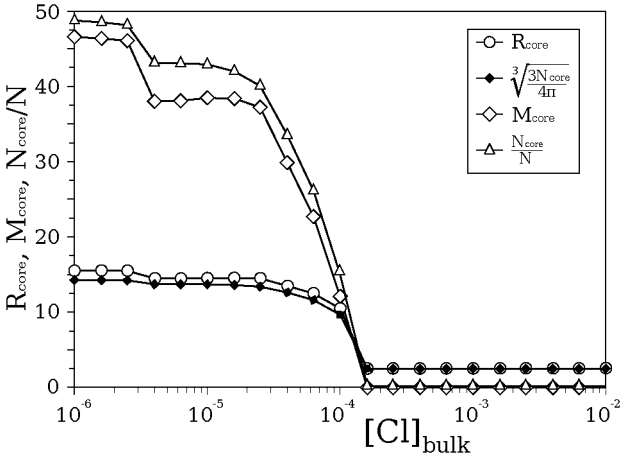

Figure 7. Vertical cross-section of the phase diagram corresponding to the $\chi = 1.5$. In this graph we plot various quantities as a function of the salt concentration: M_{core} is the number of free ends that have partitioned into the core, N_{core}/N is the fraction of monomers in the core and we have two measures for the size of the core R_{core}, as indicated. Parameters: $M = 50$, $N = 250$. Curves in plots are guides for eyes.

β_M and β_N as the fraction of the terminal groups and fraction of all monomers that are in the core. It is remarkable that there is a strong correlation between these quantities, which points to a model of the collapse of the star for which the core of the star consists of monomers of completely collapsed arms, augmented with monomers of passing-through arms (that form the corona). The presence of passing through arms explains why the values of M_{core} are a bit less than those of N_{core}/N.

Comparison of parts a and b of Figure 8 shows that at a moderate ionic strength, i.e., around $[Cl]_{bulk} = 10^{-4}$, the formation of the core goes gradually with changing χ. At a lower salinity $[Cl]_{bulk} = 2.5 \times 10^{-6}$ this process proceeds in a step-like manner: the core, which then contains the majority of arms appears suddenly. This fact is also noticed in the phase diagram Figure 6,

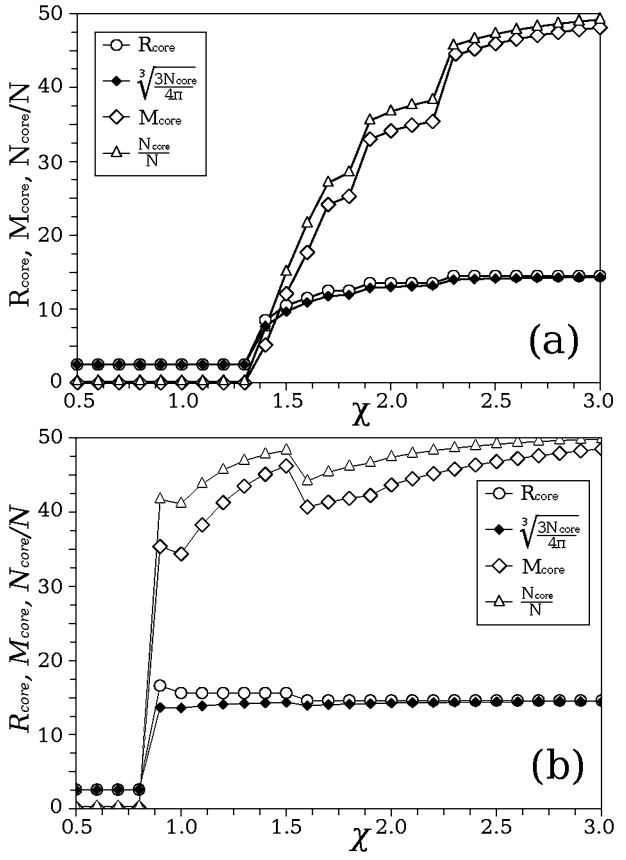

Figure 8. Horizontal cross sections through the phase diagram Figure 6. Plotted are: M_{core}, that is, the number of free ends that have partitioned into the core, N_{core}/N which represents the fraction of monomers in the core and two measures for the size of the core R_{core} as a function of the solvent quality χ. (a) For $[Cl]_{bulk} = 10^{-4}$ and (b) for $[Cl]_{bulk} = 2.5 \times 10^{-6}$. Parameters $M = 50$, $N = 250$. The non-monotonicity of the curves in part b are artifacts due to the use of the lattice. Curves in plots are guides for eyes.

wherefore at higher salt concentrations, $[Cl]_{bulk}$, the boundary is more blurred.

The lines marked with circles and filled diamonds in Figure 7 and Figure 8a,b give the core radius and a value of radius calculated on the assumption that the core density is equal to unity $((3/4\pi)N_{core})^{1/3}$, respectively. Both measures give very similar results proving that the density in the core is indeed close to unity. Note that R_{core} is non monotonic at low ionic strength, i.e., at $[Cl]_{bulk} = 2.5 \times 10^{-6}$ while is monotonic at $[Cl]_{bulk} = 10^{-4}$.

The collapse of the hydrophobic polyelectrolyte star obviously depends on the architectural parameters N (length of the arms) and M (number of arms). In Figure 9a, we present the fraction β_M of ends that have accumulated in the core versus the number of arms M, for different lengths of the arms $N = 100$, 250, and 500, at $\chi = 1.5$, and $[Cl]_{bulk} = 10^{-4}$. The larger the lengths of the arms, N, the less cooperative is the uptake of the arms in the core, i.e., the less the fraction β_M. At the same time, for given arm-length, the fraction of ends in the core increases with increasing M. For each N, β_M reaches a plateau at high M. The presence of a plateau explained by the fact that for large M/N fraction the star more and more resembles the planar brush. In the following section we shall consider this dependency in detail using the scaling arguments.

dx.doi.org/10.1021/ma202201m | Macromolecules 2012, 45, 2145–2160

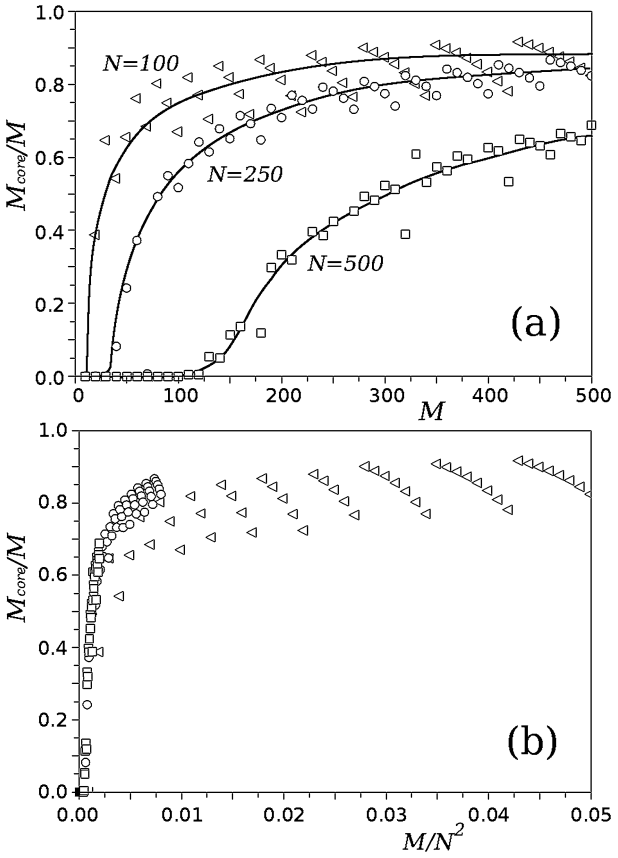

Figure 9. (a) Fraction of the end monomers in the core $\beta_M = M_{core}/M$ for hydrophobic polyelectrolyte stars as a function of the number of arms M, for various lengths of the arms N as indicated. Parameters: $\chi = 1.5$ and $[Cl]_{bulk} = 10^{-4}$. Curves in plot are just guides for eye . (b) The same data as in part a but plotted as a function of M/N^2. The same marks in both graphs correspond to the same N. It is seen that, in this case, all the curves are very close together.

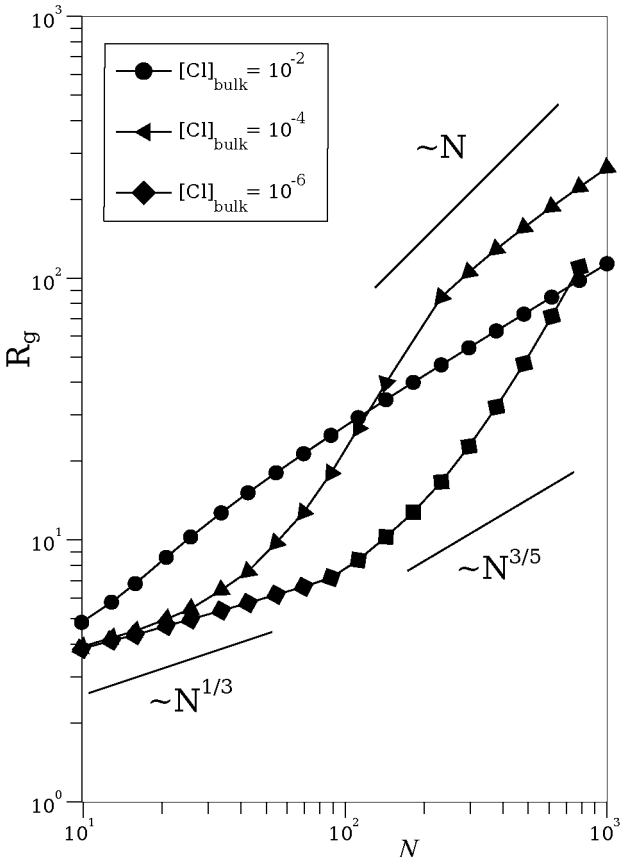

Figure 10. Radius of gyration as a function of the degree of polymerization of the arms in double logarithmic coordinates. The number of arms is set to $M = 25$, solvent quality $\chi = 1.5$ and the dependence is given for various values of the ionic strength $[Cl]_{bulk}$ as indicated. The various slopes that are discussed in the text are indicated.

In the Figure 10, the radius of gyration R_g as a function of the length of the arms N is depicted in double logarithmic coordinates for various salt concentrations $[Cl]_{bulk}$ and poor solvent conditions. For the highest salt concentration, $[Cl]_{bulk} = 10^{-2}$, we find that the radius of gyration scales as $R_g \sim N^{3/5}$, which is the same as for the star (or single chain) in good solvent conditions. The star show such behavior because its size is defined by electrostatic excluded volume. We have seen the same case in Figure 5 and Figure 3 where at high salinity the distribution of free ends has a bell-like shape.[8] When the salt concentration drops to moderately low values, $[Cl]_{bulk} = 10^{-4}$, it is found that $R_g(N)$ has two regimes: for sufficiently low degrees of polymerization N, the star is collapsed and $R_g \sim N^{1/3}$, whereas for very high degrees of polymerization the arms are fully stretched and $R_g \sim N$. Inbetween these regimes, that is, at intermediate lengths of the arm, the star is in a quasi-micellar states. At very low ionic strength, $[Cl]_{bulk} = 10^{-6}$, only the collapsed and the intermediate quasi-micellar state is found for the arm length range used in the calculations.

Note that from Figure 10, it follows that for the star with $M = 25$ arms the nonmonotonic dependence of $R_g([Cl]_{bulk})$ was observed only at $N > 200$. At lower N values this dependency is monotonic, i.e., $R_g([Cl]_{bulk} = 10^{-6}) < R_g([Cl]_{bulk} = 10^{-4}) < R_g([Cl]_{bulk} = 10^{-2})$.

4. THEORETICAL ANALYSIS

The Basic (Reference) System. It is well-known and discussed in various works, e.g., refs 9, 29, 30, and 48−50, that a basic understanding on how a brush structure depends on the physical properties of the system, in particular on the solvent composition, can be constructed on knowing the phase diagram of a simple reference system, implementing a membrane model. We follow this strategy and therefore consider a solution of polymer with $N \to \infty$ in a membrane equilibrium with the solvent, which will be referred to as *the basic system* and is illustrated in Figure 11. In such a system as in a polymer brush, the translation entropy of chains is absent. However unlike for a star (spherical brush) the basic system is homogeneous. To understand the nature of the microphase segregation in the polyelectrolyte star systems, we have to match the polymer properties and other physical chemical properties of the basic system with that of the polymer star.

Let us next specify the reservoir, which is separated from the polymer solution by a semipermeable membrane (see Figure 11). In the reservoir we find the solvent composed of water and monovalent ions Na^+ and Cl^- with so-called "*bulk*" conditions. In the system we thus have a solution of infinitely long polyelectrolyte chains. All values marked with an index "*bulk*" refer to the right-hand side and all values without an index refer to the left-hand side of the figure.

dx.doi.org/10.1021/ma202201m | *Macromolecules* 2012, 45, 2145−2160

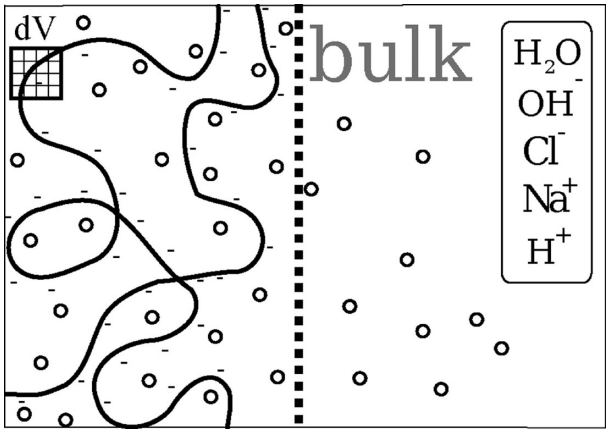

Figure 11. Schematic illustration of the solution of an infinitely long polyelectrolyte chain in a membrane equilibrium (the membrane is indicated by the vertical dashed line) with a low molecular weight (1:1) electrolyte solution.

The membrane inhibits the translation of the polymer, but does not hinder the translation of the small species. Hence these species can equilibrate between the system and the bulk. The solvent parameters pH = $-\log_{10}[H_3O]_{bulk}$ and ionic strength Φ^{ion}_{bulk}, are specified in the bulk.

Let the concentration of polymer in the left-hand side be given by φ. As usual the energy of polymer−solvent contacts is parametrized by the χ parameter, then the expression for the free energy density can be written as

$$f(\varphi) = (1-\varphi)\ln(1-\varphi) + \chi(1-\varphi)\varphi + \varphi\ln(1-\alpha(\varphi)) + \Delta\Pi_{osm}(\alpha\varphi) \quad (5)$$

Here the first term is the entropy of polymer and solvent mixing, the second is the energy of volume interactions. The last two terms account for the polyelectrolyte features, implementing the annealed charge character of the polymer segments. The third one is the entropy associated with the distribution of charged and uncharged segments along the polyelectrolyte chain. Here $\alpha(\varphi)$ is degree of dissociation (fraction of charged group on the chain). The fourth term is the osmotic pressure caused by the difference in ion concentrations between the right and left sides of the membrane.

A few notes are in place. In this Ansatz, we assume that the solvent is a single component and therefore, in the first contribution we do not take the entropy of mixing of the ions into account. Instead we have introduced the excess of the osmotic pressure. We further assumed (in line with the calculations) that the energies of contact between water and polymer and between polymer and ions are the same. We ignore Coulomb interactions, which is reasonable as long as the Debye length is sufficiently small.[9,23,44] The last two polyelectrolyte terms implements the so-called local electroneutrality approximation (LEA).

Ionization Degree of Weak Polyelectrolyte (Local Electroneutrality Approximation). As we said in the Model and Methods, we consider a polyelectrolyte as a polyacid, assuming that each polymer segment can be ionized

$$HA \overset{K}{\rightleftarrows} H^+ + A^- \quad (6)$$

Here we just rewrote the ionization eq 1 in a simplified form by replacing $[H_3O] \equiv [H]$. The dissociation constant K and the pH determine the degree of dissociation:

$$\frac{\alpha}{1-\alpha} = \frac{K}{[H]} = \frac{K}{[H]_{bulk}}\frac{[H]_{bulk}}{[H]} \quad (7)$$

The LEA concept assumes a complete compensation of all charges everywhere in solution. In other words, it dictates the equality of concentrations of all negatively and all positively charged ions at any point of the system. Hence, in the LEA we have for left-hand side of Figure 11

$$\alpha\varphi + [Cl^-] + [OH^-] = [H^+] + [Na^+] \quad (8)$$

The relation of co- and counter- ions in the right and left sides is determined by the Donnan rule. In the case of monovalent ions this rule gives

$$\frac{[Cl]}{[Cl]_{bulk}} = \frac{[OH]}{[OH]_{bulk}} = \frac{[Na]_{bulk}}{[Na]} = \frac{[H]_{bulk}}{[H]} \quad (9)$$

By the substitution the ion volume fractions expressed in terms of $[H]_{bulk}/[H]$, one arrives at a quadratic equation

$$\left(\frac{[H]_{bulk}}{[H]}\right)^2 + \frac{2\alpha\varphi}{\Phi^{ion}_{bulk}}\frac{[H]_{bulk}}{[H]} - 1 = 0 \quad (10)$$

where Φ^{ion}_{bulk} as mentioned above is concentration of all mobile ionic species, i.e. $\Phi^{ion}_{bulk} = [Cl]_{bulk} + [Na]_{bulk} + [OH]_{bulk} + [H]_{bulk}$. The solution leads to an expression for the degree of ionization $\alpha(\varphi)$ following from eq 7

$$\frac{\alpha}{1-\alpha} = \frac{K}{[H]_{bulk}}\left(\sqrt{1+\left(\frac{\alpha\varphi}{\Phi^{ion}_{bulk}}\right)^2} - \frac{\alpha\varphi}{\Phi^{ion}_{bulk}}\right) \quad (11)$$

In this expression K and $[H]_{bulk}$ are found only in the combination $[H]_{bulk}/K$. This means that all the polyelectrolyte properties depend on pH and pK only as this relation or as the difference pH − pK. Figure 12(a) gives the concentration dependence of the degree of ionization $\alpha(\varphi)$ for various values of the salt concentration Φ^{ion}_{bulk}. Here and below we use $[C1]_{bulk} \simeq \Phi^{ion}_{bulk}/2$ for the convenience of comparison with numerical results. The value α_{bulk} depicted in this figure is the degree of dissociation of the polymer in the limit of zero polymer concentration. It is seen that the degree of ionization decreases with the increasing polymer concentration and with decreasing salinity. The approximate equations are presented in eq 3.

The last term of eq 5 is connected with the excess osmotic pressure of the mobile ions. The value is evaluated by adding up concentrations assuming ideality (van't Hoffs law), $\Delta\Pi_{osm} = \sum_i[i]_{bulk} - \sum_i[i]$, where the summation is going over all types of mobile ions, i.e.

$$\Delta\Pi_{osm} = \Phi^{ion}_{bulk} - [Cl] - [OH] - [H] - [Na] = \Phi^{ion}_{bulk} - \frac{\Phi^{ion}_{bulk}}{2}\left(\frac{[H]_{bulk}}{[H]} + \frac{[H]}{[H]_{bulk}}\right)$$

dx.doi.org/10.1021/ma202201m | Macromolecules 2012, 45, 2145−2160

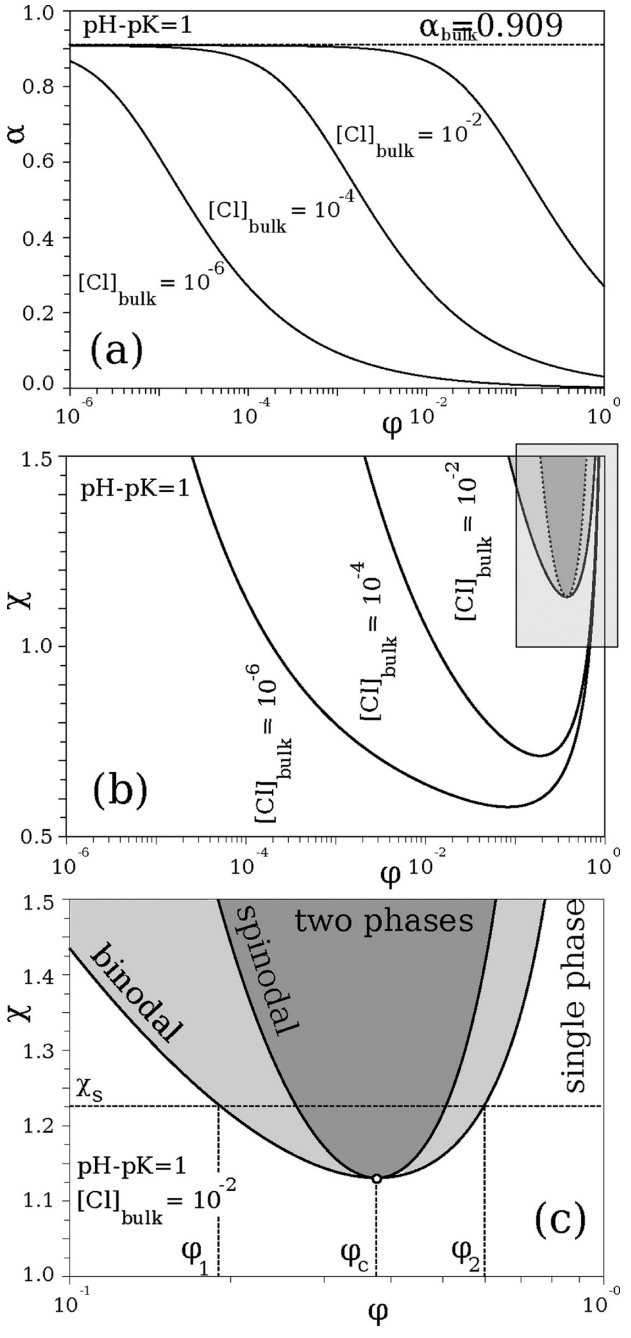

Figure 12. (a) Degree of ionization $\alpha(\varphi)$ as a function of the polymer concentration for various values of the salt concentration $[Cl_{bulk}]$. (b) Phase diagrams for the basic system in the $\chi - \varphi$ plane for the same set of $[Cl_{bulk}]$. The area bounded by rectangle is depicted in panel c. (c) Zoomed in part of panel b. The shaded regions are the "forbidden" compositions, where the system is in two-phases state. The dark gray region, within the spinodal is instable, the region between the binodal and spinodal (light gray) is metastable. At $\chi = \chi_S$ the system is in two-phases state with two polymer concentrations presented, namely φ_1 (dilute) and φ_2(concentrated). The critical density is indicated by φ_c. Parameters pH − pK = 1.

or

$$\Delta\Pi_{osm} = \Phi_{bulk}^{ion}\left(1 - \sqrt{1 + \left(\frac{\alpha\varphi}{\Phi_{bulk}^{ion}}\right)^2}\right) \quad (12)$$

Polyelectrolyte Phase Behavior. Now armed with the equations for the free energy, a dependence for the degree of dissociation of the segments and a formula for the excess osmotic pressure, we can evaluate the polyelectrolyte phase behavior. By neglecting the constant term Φ_{bulk}^{ion}, we can rewrite the expression 5

$$f(\varphi) = (1-\varphi)\ln(1-\varphi) + \chi(1-\varphi)\varphi + \varphi\ln(1-\alpha(\varphi)) - \Phi_{bulk}^{ion}\sqrt{1 + \left(\frac{\alpha\varphi}{\Phi_{bulk}^{ion}}\right)^2} \quad (13)$$

which must be analyzed in combination with eq 11

Using this pair of equations, we can evaluate the chemical potentials of the solvent and the polymer, $\mu_s(\varphi)$ and $\mu_p(\varphi)$

$$\mu_s(\varphi) = f - \varphi\frac{\partial f}{\partial\varphi} = \varphi + \chi\varphi^2 + \ln(1-\varphi) + + \frac{\varphi^2\alpha'_\varphi}{1-\alpha} - \frac{\Phi^2 - \varphi^3\alpha\alpha'_\varphi}{\sqrt{\Phi^2 + (\alpha\varphi)^2}}$$

$$\mu_p(\varphi) = f + (1-\varphi)\frac{\partial f}{\partial\varphi} = \varphi - 1 + \chi\varphi^2 + \ln(1-\alpha) - - \frac{(1-\varphi)\varphi\alpha'_\varphi}{1-\alpha} - \frac{\Phi^2 + \varphi^2(1-\varphi)\alpha\alpha'_\varphi + \alpha^2\varphi}{\sqrt{\Phi^2 + (\alpha\varphi)^2}}$$

Here, for simplicity, we have omitted the indices of the value of ionic strength, designating Φ_{bulk}^{ion} as Φ

Let the polymer volume fraction be φ^I in the phase (I) and φ^{II} in the phase (II). Coexistence between the two phases implies that the corresponding chemical potentials have to be equal to each other, namely

$$\begin{cases} \mu_s(\varphi^I) = \mu_s(\varphi^{II}) \\ \mu_p(\varphi^I) = \mu_p(\varphi^{II}) \end{cases}$$

In Figure 12b, a set of phase diagrams (coexistence curves or binodals) are given for different $[Cl]_{bulk}$. In Figure 12c, one of the phase diagrams, corresponding to $[Cl]_{bulk} = 10^{-2}$, is given in more detail for which not only the binodal, but also the spinodal is presented. The latter is given by the condition

$$(f(\varphi))''_\varphi = 0$$

The shaded regions, those are within the binodal, are "forbidden" zones and correspond to the phase separation or phase coexistence regions. The darkest region, that is within the spinodal, represents the region where one phase system is unstable. Between the binodal and spinodal (light gray) the one phase system is metastable. In the lowest point on the binodal, or where the binodal and spinodal tough, one finds the critical point.

As it is seen from Figure 12b,c, for given χ higher than the critical value, the binodal specifies the concentration of polymer in the two coexisting phases, namely one which is dilute in polymer (φ_1 on the left-hand side) and one (φ_2 on the right-hand side) which has a high polymer concentration. Combining this with Figure 12a, we see that in the solution with a low concentration polymer has a high degree of ionization, and in

dx.doi.org/10.1021/ma202201m | Macromolecules 2012, 45, 2145–2160

the concentrated solution has a vanishing low degree of ionization. At $[Cl]_{bulk} = 10^{-6}$ the size of two-phases region in Figure 12b is relatively large. With increasing ionic strength the two-phases region narrows and the critical point is shifting up and to the right, that is, to higher χ and φ values.

For comparison with numerical results (i.e., with Figure 6) Figure 13 shows the phase diagram in (χ, $[Cl]_{bulk}$) coordinates.

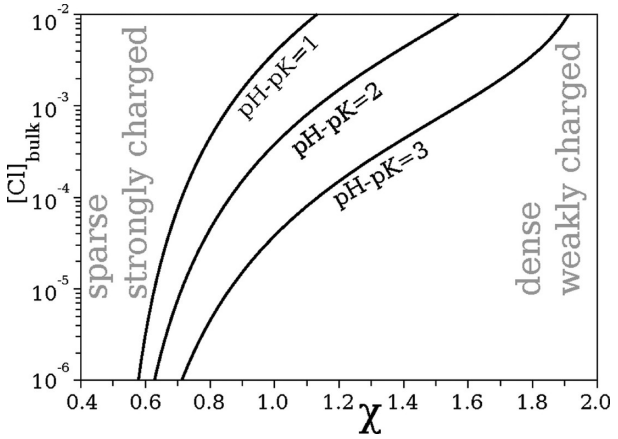

Figure 13. Phase diagram of the basic system in (χ, $[Cl]_{bulk}$) lin−log coordinates. Three lines for systems with different values of pH − pK are presented as indicated. To the left of the lines is the phase, where the polymers are strongly charged and have a low concentration. To the right the concentration is high and the polymers are weakly charged.

The lines in figure are presenting the ordinate of critical point (see Figure 12b,c) depending on $[Cl]_{bulk}$. It is seen that at given pH − pK the critical point shifts to higher value of $[Cl]_{bulk}$ with increasing of χ. Increase in the difference pH − pK, which leads to increase of α, shifts the phases coexistence curve (phase of the dilute polymer solution with high α and phase of highly concentrated solution with low α) to higher value of χ. This means that the increased hydrophilicity requires greater hydrophobicity to form the collapsed phase.

Basic System and Amphiphilic Polyelectrolyte Star. Let us now summarize the main conclusions that follow from the numerical SCF modeling.

1 Homopolymeric stars with ionizable and hydrophobic (in noncharged state) monomers in aqueous solutions are collapsed at extremely low salt concentration. The collapsed star unfolds with increasing salt concentration.
2 The transition from a compact collapsed star to a hydrated swollen star proceeds gradually through an intermediate quasi-micellar state. The quasi-micellar state is characterized by a compact and almost neutral core decorated by a swollen polyelectrolyte corona.
3 The polymer density in the corona near the core is higher at higher salinities.
4 The arms of a hydrophobic polyelectrolyte star choose between two distinct conformations: a fraction of the arms is completely included in the core, whereas the remaining arms pass through the core (leaving as few segments as possible behind) and form the corona.
5 The increase in the arm length N leads to the unfolding of the star, whereas the increase in number of arms M contributes to the collapsed state.

We can translate the results from the membrane-system to the case of a polymer star by the insight that the concentrations forbidden in the membrane system, must be avoided in the polymer star. Hence, states that are within the binodal in the basic system cannot be realized in a polymer brush.[29,30,48,50] In this context, it is natural that the hydrophobic polyelectrolyte star at χ value higher than the critical point in Figure 12b should be in a two phases coexistence. Or, for example, for a given χ, a reduction of the salt concentration will generate a more sparse corona, and therefore a larger core. Conversely, with increasing salt concentration the core size diminishes and at some point looses its stability.

These theoretical findings completely explain the behavior of a star obtained in the current study and specifically enumerated in items 1, 2, and 3. As follows from the phase diagrams in Figure 12b, the left branch of binodal is shifting to lower φ with the decrease in the salt concentration $[Cl]_{bulk}$. That is why the star coronas have to be sparser, the jump in polymer concentration at the core−corona interface broader, and the core larger at lower concentration $[Cl]_{bulk}$. Comparison of phase diagrams in Figure 6 and Figure 13 also shows a good qualitative agreement.

However, while there is good qualitative agreement there is also a marked quantitative discrepancy. Difference between numerical calculations and those given by basic system is shown in Figure 14. Here the binodals of the basic system given by

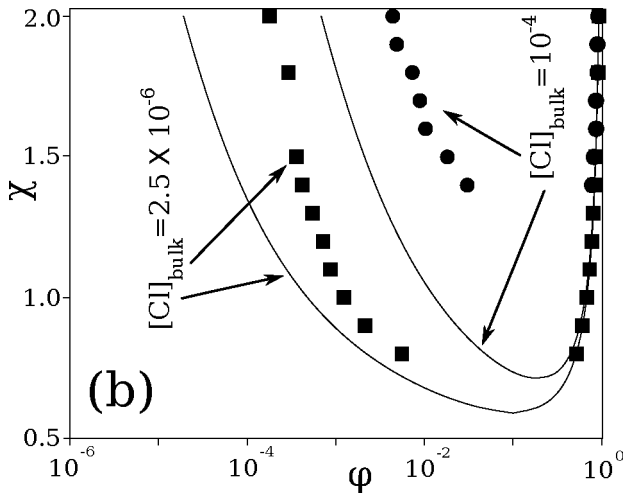

Figure 14. Phase diagrams in the χ−φ plane for two $[Cl_{bulk}]$ values as indicated. These phase diagrams (solid lines) are similar to those presented in Figure 12b, but in contrast here, for comparison, diagrams are also computed on the basis of the numerical method. Squares and circles in the picture matches the polymer density in core and corona near the core−corona interface at $[Cl]_{bulk} = 2.5 \times 10^{-6}$ and $[Cl]_{bulk} = 10^{-4}$ respectively (cf. Figure 3). All the star and the solvent parameters are chosen the same as in Figure 12.

Figure 12b are shown corresponding to two salinities, and are compared with those given by numerical experiment, i.e., with the values of polymer density $\varphi(r)$ taken in two nearest to the core−corona interface external and internal layers (roughly speaking that is $\varphi(R_{core} + 1)$ and $\varphi(R_{core} - 1)$, respectively) . It is seen that the polymer density values in the core fit well on the right branch of binodals, while in the corona these values are shifted to the higher φ. For a given value of $[Cl]_{bulk}$ binodal of the star appears to be within the binodal of the basic system. The star critical point, i.e., the conditions when the

dx.doi.org/10.1021/ma202201m | Macromolecules 2012, 45, 2145−2160

quasi-micelle is loosing stability and the star becomes swollen, lies higher than in basic system one (compare Figure 13 and Figure 6).

This quantitative discrepancy is not surprising. In contrast to the homogeneous basic system, considered star is essentially heterogeneous small nanosystem. Developing a rigorous theory of the conformational transformations is beyond the scope of this work. Let us restrict the discussion to two features of the star which are not taken into account in the basic system. The first is the significant role of the free energy penalty in the core−corona interface, which leads to destabilization of the compact core.[51−53] We believe that the upward shift of the critical point, obtained for a two-phases conformation of the star, relatively to that for the basic system, is mainly due to the contribution of interface energy.

The second feature is the fact that the corona in quasi-micelle (or the star in a swollen state) is a spherical brush and has all typical for brush properties. Peculiarities of the brushes thermodynamics lead to the features of the two-phases star structure presented in items 4 and 5.

Microphase Coexistence in Brushes. Let us show, that the separation of arms of the star in two populations, which has been observed in the numerical calculations, is caused by the properties of swollen polymer brush. In our case, this is the corona of the star. Indeed, regardless of the brush topology and the nature of the interactions in the brush, at a given molecular mass of grafted chain per unit of grafting surface, a free energy is always less for the sparse brush of long chains than for more dense brush of short chains.[29] Let us confirm this argument in the basis of simple scaling relations for free energy of different brush topologies. Let us begin from a planar brush.

Per unit area, the free energy of a flat brush of chains of length N, grafted with a density σ can be represented as[7]

$$F = AN\sigma^{\beta} = An\sigma^{\beta-1} \tag{14}$$

where $n = N\sigma$ is the effective length of the chains normalized per unit surface area. Parameters A and β depend on the interaction character according to Table 1a (cf. ref 7). As is seen from the table, at a given n the value of F in eq 14 is always increasing with σ, i.e.

$$\frac{\partial F}{\partial \sigma}(n = constant) > 0 \tag{15}$$

Table 1. (a) Values for the Free Energy Parameters A and β for Flat Polymer Brushes and (b) Values for the Free Energy Parameters A, β, and γ for Polymer Stars at the Indicated Conditions

(a) Flat Polymer Brushes	
$\beta = 2$, $A > 0$	uncharged brush in Θ-solvent
$\beta = 5/3$, $A > 0$	uncharged brush in good solvent, polyelectrolyte brush in high salinity solution (salt regime)
$\beta = 1/3$, $A < 0$	weak polyelectrolyte brush in low salinity solution
$\beta = 1$, $A = A_0 \log\sigma$, $A_0 > 0$	strong polyelectrolyte brush in low salinity solution
(b) Polymer Stars	
$\gamma = 0$, $\beta = 3/2$, $A > 0$	uncharged star in Θ-solvent
$\gamma = 1/5$, $\beta = 7/5$, $A > 0$	uncharged star in good solvent, polyelectrolyte star in high salinity solution (salt regime)
$\gamma = 5$, $\beta = -1$, $A < 0$	weak polyelectrolyte star in low salinity solution

So, the free energy of swollen brush always decreases with decreasing grafting density σ.

A similar free energy pattern presents itself for stars. In this case the number of arms M plays the role of the grafting density. Using the scaling expressions in a quasiplanar approximation[7,8] we have

$$F = AN^{\gamma}M^{\beta} = An^{\gamma}M^{\beta-\gamma} \tag{16}$$

Here, $n = MN$ and the terms A, γ and β are characteristic for the type of interactions the polymers experience, according to Table 1(b). Now, analogously to the flat brush case, we find that the magnitude of the free energy is increasing function of M.

$$\frac{\partial F}{\partial M}(n = constant) > 0 \tag{17}$$

The tendency to minimize M can only be realized in microphase segregated conditions, that is, when there is a second compact phase of which the thermodynamical characteristics are fully given by the number of monomers it contain: the thermodynamics of a swollen corona enforces that upon extraction of a chain from the corona it must enter the core as a whole. This result explains item 4 formulated in the beginning of this paragraph and assists the rationalization of item 5. More specifically, this generic argument explains why we do not need to consider arms that are partly in the core and partly in the corona.

As was shown, the formation of a core requires the transfer of branches from a swollen corona into the core. According to eq 16 and Table 1b, the free energy per branch of an annealed polyelectrolyte star in low salinity solution is given by

$$F_{\text{branch}} = \frac{F}{M} = -|A|N^5M^{-2} \tag{18}$$

and free energy per monomer

$$F_{\text{monomer}} = -|A|N^4M^{-2} \tag{19}$$

These equations show that the free energy per monomer strongly decreases with increasing arm length, N, and with decreasing number of branches M. At the same time, the monomer free energy in the core does not depend on these parameters

$$F_{\text{monomer in core}} = -|B| \tag{20}$$

That is why, at given solution conditions, the star is collapsed when N is small and swollen for large N and the growth in number of arms leads to a collapse. The fact that at fixed solution parameters the conformation of a star depends on M/N^2 is shown in Figure 9b, wherein it was shown that all the curves in Figure 9a more or less overlap when the fraction of monomers in the core is plotted as a function of M/N^2.

The results presented here also allow us to interpret the reason for the shift between left branches of the binodals plotted for the star and for the basic system (see Figure 14). As it is seen from eq 19 monomer free energy of a spherical brush (star corona) is smaller for a longer branch. That is not surprising. The spherical geometry gives more space to chain fragments that are further from the curvature center. Since for weak polyelectrolytes at low salt concentration, the degree of ionization α increases with decreasing concentration φ, the distant from the center monomers are ionized stronger, and their free energy is the smaller the further they are removed.

dx.doi.org/10.1021/ma202201m | Macromolecules 2012, 45, 2145−2160

In the core−corona equilibrium each branch is involved as a whole. So the determining parameter here is not the chemical potential of the monomer at the boundary with the corona, but the chemical potential of the monomers of the whole branch (or free energy per monomer) which is given by eq 19. This quantity is markedly less due to the contribution of distant from the phase boundary monomers, that leads to increased stability region to the left of the binodal and a shift of the binodal toward higher φ.

Polyelectrolyte Star Collapse Model. Now, using the argumentation given above, we may present a model that describes the formation of semicollapsed (quasi-micellar) star conformations. We consider a simple model schematically drawn in Figure 15a. Again, there are $M = 50$ arms in the star, each with length of $N = 250$ segments. The star is considered to be spherically symmetric as in the numerical model given in Figure 1b. In the Collapse Model, we consider the star in a quasi-micellar state with one part of the arms in the collapsed core (these chains are uncharged) and the remaining arms in the swollen corona.

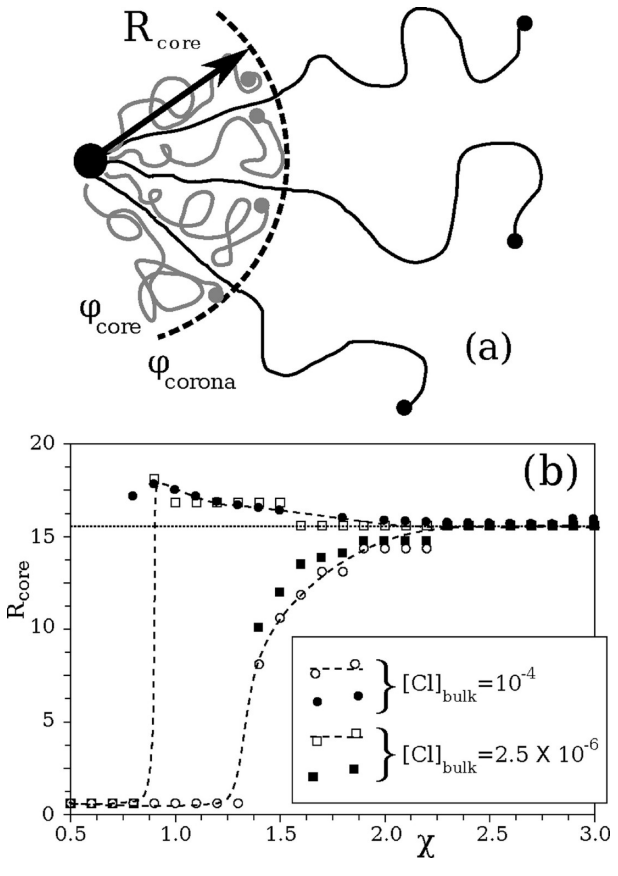

Figure 15. (a) Illustration of the Collapse Model. Here parameters of the model are specified: the size of the core R_{core}, the polymer volume fraction in the core φ_{core}, and in the corona near the core φ_{corona}. Dotted line shows the core−corona interface. (b) The size of the core $R_{core}(\chi)$ as a function of the solvent quality χ as found by the Collapse Model, for two values of the salt concentration as indicated (filled squares and circles). The horizontal dotted line represents the radius of the globule when all segments are collapsed in the core with unit density. Here also the R_{core} data computed in numerical section is plotted for comparison (opened squares and circles). The same points are plotted in Figure 8, parts a and b. The dashed lines are guides for the eye. Remaining parameters pH − pK = 1, M = 50, N = 250.

As follows from phase diagrams in Figure 12a,b and as is seen from the numerical calculations, the collapsed core is formed by uncharged (or at least weakly charged) arms of the star. Let us therefore assume in the model that the polymer density in the core is homogeneous and the branches in the corona are strongly stretched (for example due to the osmotic pressure of the counterions). The core consists of its own totally collapsed arms and passing parts of the corona arms which are almost completely stretched. Because of the force balance those parts of arms which are just near the core−corona interface are stretched uniformly on the both sides of this interface.

With the specified assumptions about the conformations of the arms, it is possible to estimate how the radius of the core depends on the solution and star parameters. Let us assume that the polymer density in the corona near the core is φ_{corona}, and the density in the core is φ_{core} and M_{core} is the number of arms that form the core, then

$$\begin{cases} \frac{4}{3}\pi {R_{core}}^3 \varphi_{core} = NM_{core} + (M - M_{core})R_{core} \\ M - M_{core} = 4\pi {R_{core}}^2 \varphi_{corona} \end{cases}$$

When φ_{corona} and φ_{core} are identified by the binodal concentration φ_1 and φ_2 given in Figure 11, we can extract a prediction for the core radius as a function of the solvent quality. But as we have discussed above, there can not and should not be a quantitative agreement between the results from the basic system and from the numeric frameworks. So here, just to show the wellness of the model, we shall not use the φ_{corona} and φ_{core} given by the basic system, but take these values from numeric calculations. In this case φ_{corona} and φ_{core} are the values of polymer density profile $\varphi(r)$ corresponding to the nearest to the core−corona interface layer, that is $\varphi(R_{core} + 1)$ and $\varphi(R_{core} - 1)$ respectively. This concentrations are given in Figure 14.

Figure 15b shows the $R_{core}(\chi)$ dependency for two values of the salt concentration namely $[Cl]_{bulk} = 2.5 \times 10^{-6}$ and $[Cl]_{bulk} = 10^{-4}$. For comparison, in this figure corresponding data from numerical calculation are given (see Figure 8a,b).

It is seen that the results are in good agreement: both dependencies marked with filled circles and filled squares has the beginning at $\chi = \chi_C$, which corresponds to a critical point in the phase diagram in Figure 14. The values of R_{core} computed in numerical section experience jump at this point, R changes from the radius of grafting sphere R_0 to R_{core}. At $[Cl]_{bulk} = 10^{-4}$, R_{core} monotonically increases with χ and reaches a limiting size in very poor solvent conditions. For very poor solvents, the core size, R_{core}, corresponds to densely packed core. The limiting core size is reached nonmonotonically at low salinity, $[Cl]_{bulk} = 2.5 \times 10^{-6}$. As has been discussed in the Results, at low salinity conditions the star collapse goes abruptly so that almost all branches retract into the core in a narrow χ range. Despite the fact that all the branches are collapsed and situated in the core, they are not packed compactly. That is why we see the nonmonotonic $R_{core}(\chi)$ dependency.

So here we see that properties of the quasi-micelle are consistent with properties of both corona and core phases, by means of our model. That makes it possible to calculate the size of the quasi-micelle core by knowing the concentrations in core and corona. Also, using the fact that right branches of both binodals, one corresponding to basic system and another to numerical experiment, fit well to each other (see Figure 14),

our model might help us to make vice versa the assumptions about φ_{corona} by knowing the R_{core} and φ_{core} from the basic system binodal.

5. CONCLUSIONS

We have investigated structural characteristics of an annealed polyelectrolyte (polyacid) star in water-salt solution. It is shown that the star radius of gyration appears to be a nonmonotonic function of the salt concentration in the solution. In the low ionic strength region, we found a dramatic transition from a swollen star to a compact globular one, under decreasing the salt concentration, deteriorating the solvent or reducing the pH. The key result of the work is that in between these extremes, the star can be found in a quasi-micellar state with a collapsed core composed of neutral arms and decorated by charged arms which are solvated. These micelle-like objects have properties that are very similar to those of the micelles composed of copolymers and may have similar applications.

We have studied this system using a numerical self-consistent field model, this numerical technique allows to take into account all the contributions to the free energy of the system, so we are not limited by necessity to count only the main one, which determines the scaling regime of system behavior. Calculation of the distribution of small ions was carried out by solving the Poisson−Boltzmann equation. Basing on the numerical results we have built a model of the collapse process using a membrane equilibrium approach and treating the polyelectrolyte corona as a spherical brush.

We argue that there are two populations of arms in the star: one population constitutes the core and another one forms the corona. Semicollapsed arms do not exist because such conformations do not optimize the free energy to its fullest. The arms in the core are uncharged and melt-like. The arms in the corona construct a star-like spherical brush, which at low salinity increases in size with the growth of the salt concentration, by means of the core−corona transition of arms up to the state when the whole star becomes swollen. With further increase of the salt concentration, in the high salinity region, the star size decreases, showing the usual polyelectrolyte behavior due to the screening effect. We found that the star size scales as $R_g \sim N^{1/3}$ when the star is collapsed, and as $R_g \sim N^1$ for the star with strongly stretched arms, and as $R_g \sim N^{3/5}$ for the star in the salted brush regime.

Our results are consistent with the experimental data,[33] Monte Carlo simulations,[32] and the molecular dynamics performed in ref 35. Even despite the fact that[35] deals with quenched polyelectrolyte (in our work it is annealed), system behaves similarly in many aspects. The strength of electrostatic interactions in ref35 was controlled by the Bjerrum length l_B. We assume that this parameter plays the same role as the salinity and pH for annealed polyelectrolytes. At large values of l_B, in the model[35] as well as at low salinity in our case, we obtain a noncharged core (due to counterions condensation at large l_B—at high electrostatic interaction). With decrease in l_B, the corona surrounding core appears and grows with further decrease in l_B up to the core disappearing. The size of the star goes through the maximum and decreases with further decrease in l_B. In such a case (salted star) there is a discrepancy in the conformations given by MD and numerical SCF. In the MD results, local binding within or between the star arms[35,36] is observed, whereas in our case such a structures are not seen. It should be mentioned that, on the one hand, we can not directly see these structures, as we include the assumption about the spherical symmetry in our model. However, on the other hand, we deal with annealed case, so we do not expect any non symmetrical conformations. We suppose that the question about similarities and differences in the behavior of amphiphilic annealed and quenched stars require further investigation.

AUTHOR INFORMATION

Corresponding Author

*E-mail: helvrud@gmail.com.

Notes

The authors declare no competing financial interest.

ACKNOWLEDGMENTS

This work was supported by the Russian Foundation for Basic Research (RFBR), Grant No. 11-03-00969-a, and by the Department of Chemistry and Material Science of Russian Academy of Sciences.

REFERENCES

(1) Nalwa, H. S. *Handbook of Polyelectrolytes and Their Applications*; Tripathy, S., Kumar, J., Eds.; American Scientific Publishers: Valencia, CA, 2002; Vols. *1, 2, and 3*.
(2) Dobrynin, A.; Rubinshtein, M. *Prog. Polym. Sci.* **2005**, *30*, 1049.
(3) Likos, C. N. *Soft Matter* **2006**, *2*, 478.
(4) Grest, G. S.; Fetters, L. J.; Huang, J. S.; Richter, D. Star Polymers: Experiment, Theory, and Simulation. In *Advances in Chemical Physics: Polymeric Systems*; Prigogine, I., Stuart, A. R., Ed.; John Wiley and Sons, Inc.: New York, 1996; Vol. *94*, p 67.
(5) Birshtein, T. M.; Zhulina, E. B. *Polymer* **1984**, *25*, 1453.
(6) Daoud, M.; Cotton, J. P. *J. Phys. (Paris)* **1982**, *43*, 531.
(7) Zhulina, E. B.; Birshtein, T. M.; Borisov, O. V. *Eur. Phys. J. E, Soft Matter* **2006**, *20*, 243−56.
(8) Birshtein, T. M.; Mercurieva, A. A.; Leermakers, F. A. M.; Rud, O. V. *Polym. Sci., Ser. A* **2008**, *50*, 992.
(9) Birshtein, T. M.; Amoskov, V. M. *Polym. Sci. C* **2000**, *42*, 172−207.
(10) Jusufi, A.; Likos, C. *Rev. Mod. Phys.* **2009**, *81*, 1753.
(11) Ballauff, M. *Prog. Polym. Sci.* **2007**, *32*, 1135.
(12) Borisov, O. V.; Zhulina, E. B.; Leermakers, F. A. M.; Ballauff, M.; Müller, A. H. E. *Adv. Polym. Sci.* **2011**, *241*, 1.
(13) Rodríguez-Hernández, J.; Chécot, F.; Gnanou, Y.; Lecommandoux, S. *Prog. Polym. Sci.* **2005**, *30*, 691.
(14) Theodorakis, P. E.; Wolfgang, P.; Binder, K. *Macromolecules* **2010**, *43*, 5137.
(15) Kyriazis, A.; Aubry, T.; Burchard, W.; Tsitsilianis, C. *Polymer* **2009**, *50*, 3204.
(16) Iatridi, Z.; Tsitsilianis, C. *Chem. Commun.* **2011**, *47*, 5560−2.
(17) Ying, L.; Xiaohui, L.; Zhongmin, D.; Baixiang, L.; Xuesi, C.; Yue-Sheng, L. *Biomacromolecules* **2008**, *9*, 2629−36.
(18) Kreutzer, G.; Ternat, C.; Nguyen, T. Q.; Plummer, C. J. G.; Manson, J.-A. E.; Castelletto, V.; Hamley, I. W.; Sun, F.; Sheiko, S. S.; Herrmann, A.; Ouali, L.; Sommer, H.; Fieber, W.; Velazco, M. I.; Klok, H.-A. *Macromolecules* **2006**, *39*, 4507.
(19) Xu, S.; Luo, Y.; Haag, R. *Macromol. Biosci.* **2007**, *7*, 968−74.
(20) Mercurieva, A. A.; Birshtein, T. M.; Leermakers, F. A. M. *Langmuir* **2009**, *25*, 11516−27.
(21) Ajun, W.; Yuxia, K. *J. Nanopart. Res.* **2008**, *10*, 437.
(22) Anufrieva, E. V.; Birshtein, T. M.; Nekrasova, T. N.; Ptitsyn, O. B.; Sheveleva, T. V. *J. Polym. Sci. C* **1968**, *16*, 3519−3531.
(23) Pincus, P. *Macromolecules* **1991**, *24*, 2912.
(24) Borisov, O. V.; Zhulina, E. B.; Birshtein, T. M. *Macromolecules* **1994**, *27*, 4795.
(25) Zhulina, E. B.; Birshtein, T. M.; Borisov, O. V. *Macromolecules* **1995**, *28*, 1491.
(26) Polotsky, A. A.; Zhulina, E. B.; Birshtein, T. M.; Borisov, O. V. *Macromol. Symp.* **2009**, *278*, 24.
(27) Borisov, O. V.; Birshtein, T. M.; Zhulina, E. B. *J. Phys. II* **1991**, *1*, 521.

(28) Zhulina, E. B.; Borisov, O. V.; Birshtein, T. M. *J. Phys. II* **1992**, *2*, 63.
(29) Klushin, L. I.; Birshtein, T. M.; Amoskov, V. M. *Macromolecules* **2001**, *34*, 9156.
(30) Amoskov, V. M.; Birshtein, T. M.; Mercurieva, A. A. *Macromol. Theory Simul.* **2006**, *15*, 46.
(31) Misra, S.; Mattice, W. L.; Napper, D. H. *Macromolecules* **1994**, *27*, 7090.
(32) Uhlík, F.; Limpouchová, Z.; Jelínek, K.; Procházka, K. *J. Chem. Phys.* **2004**, *121*, 2367−75.
(33) Matjíček, P.; Podhájecká, K.; Humpolíčková, J.; Uhlík, F.; Jelínek, K.; Limpouchová, Z.; Procházka, K.; Špírková, M. *Macromolecules* **2004**, *37*, 10141.
(34) Förster, S.; Hermsdorf, N.; Böttcher, C.; Lindner, P. *Macromolecules* **2002**, *35*, 4096.
(35) Sandberg, D. J.; Carrillo, J.-M. Y.; Dobrynin, A. V. *Langmuir* **2007**, *23*, 12716−12728.
(36) Košovan, P.; Kuldová, J.; Limpouchová, Z.; Procházka, K.; Zhulina, E. B.; Borisov, O. V. *Soft Matter* **2010**, *6*, 1872.
(37) Dobrynin, A. V.; Rubinstein, M.; Obukhov, S. P. *Macromolecules* **1996**, *29*, 2974.
(38) Boryu, V.Yu.; Erukhimovich, I.Ya. *Macromolecules* **1988**, *21*, 3240.
(39) Fleer, G. J.; Cohen Stuart, M. A. ; Scheutjens, J. M. H. M.; Cosgrove, T.; Vincent, B., *Polymers at Interfaces*; Chapman and Hall: London, 1993.
(40) van Male, J.; Leermakers, F. A. M.*"sfbox", A computer program* 2006.
(41) Klein Wolterink, J. Ph.D. thesis, 2003.
(42) Israels, R.; Leermakers, F. A. M.; Fleer, G. J.; Zhulina, E. B. *Macromolecules* **1994**, *27*, 3249.
(43) Flory, P. J. *Principles of polymer chemistry*; Cornell University Press: Ithaca, NY, 1953.
(44) Lyatskaya, Yu.V.; Leermakers, F. A. M.; Fleer, G. J.; Zhulina, E. B.; Birshtein, T. M. *Macromolecules* **1995**, *28*, 3562.
(45) Klein Wolterink, J.; van Male, J.; Cohen Stuart, M. A.; Koopal, L. K.; Zhulina, E. B.; Borisov, O. V. *Macromolecules* **2002**, *35*, 9176.
(46) Larin, S. V.; Darinskii, A. A.; Zhulina, E. B.; Borisov, O. V. *Langmuir* **2009**, *25*, 1915−8.
(47) Zhulina, E. B.; Klein Wolterink, J.; Borisov, O. V. *Macromolecules* **2000**, *33*, 4945.
(48) Pryamitsyn, V. A.; Leermakers, F. A. M.; Fleer, G. J.; Zhulina, E. B. *Macromolecules* **1996**, *29*, 8260.
(49) Amoskov, V. M.; Birshtein, T. M. *Polym. Sci. B* **2003**, *45*, 237−263.
(50) Amoskov, V. M.; Birshtein, T. M. *Macromol. Theory Simul.* **2009**, *18*, 453.
(51) Grosberg, A. Yu.; Khokhlov, A. R. *Statistical Physics of Macromolecules*; Springer: Berlin, 1994.
(52) Polotsky, A. A.; Charlaganov, M. I.; Leermakers, F. A. M.; Daoud, M.; Borisov, O. V.; Birshtein, T. M. *Macromolecules* **2009**, *42*, 5360.
(53) Polotsky, A. A.; Daoud, M.; Borisov, O. V.; Birshtein, T. M. *Macromolecules* **2010**, *43*, 1629.

Macromolecules

Article

pubs.acs.org/Macromolecules

Effect of Architecture on the Phase Behavior of AB-Type Block Copolymer Melts

M. W. Matsen*

School of Mathematical and Physical Sciences, University of Reading, Whiteknights, Reading RG6 6AX, United Kingdom

ABSTRACT: Equilibrium phase diagrams are calculated for a selection of two-component block copolymer architectures using self-consistent field theory (SCFT). The topology of the phase diagrams is relatively unaffected by differences in architecture, but the phase boundaries shift significantly in composition. The shifts are consistent with the decomposition of architectures into constituent units as proposed by Gido and co-workers, but there are significant quantitative deviations from this principle in the intermediate-segregation regime. Although the complex phase windows continue to be dominated by the gyroid (G) phase, the regions of the newly discovered *Fddd* (O^{70}) phase become appreciable for certain architectures and the perforated-lamellar (PL) phase becomes stable when the complex phase windows shift toward high compositional asymmetry.

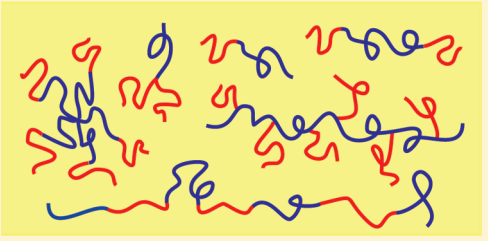

INTRODUCTION

The phase behavior of AB diblock copolymer melts has been well studied experimentally,[1] and self-consistent field theory (SCFT)[2] has been remarkably successful in explaining the equilibrium phase behavior.[3−5] Vavasour and Whitmore[6] produced the first SCFT phase diagram, but it was limited to the classical lamellar (L), cylindrical (C), and bcc spherical (S) phases. Matsen and Schick[7] then extended it to include complex phases, predicting the gyroid (G) phase to be more stable than the perforated-lamellar (PL) phase as confirmed later by experiment.[8] In a subsequent calculation by Matsen and Bates,[9] a narrow closed-packed spherical (S_{cp}) phase was predicted along the order−disorder transition (ODT), which has since been associated with a region of densely packed spherical micelles.[10,11] Most recently, the *Fddd* (O^{70}) phase was predicted by Tyler and Morse[12] and later observed in experiment.[13−15] Figure 1 shows the current up-to-date SCFT phase diagram for AB diblock copolymer melts.

The AB diblock is just the simplest block copolymer among an unlimited variety of different architectures. It is natural to ask how the phase behavior changes for other architectures, but this has proven to be a daunting task as soon as a third chemically distinct component is involved; in fact, even the simple linear ABC triblock exhibits so many morphologies that we might never catalogue them all.[16] Nevertheless, the phase behavior appears manageable for those architectures comprised of just two segment types. Among this class of architectures, the ABA triblock is the next most studied block copolymer,[17] mainly because of its commercial use as a thermoplastic elastomer. There were also a considerable number of early experiments on star block copolymers, formed by joining three or more diblocks together by their ends.[18−20] More recently, though, experiments have focused on miktoarm stars[21−26] and various graft architectures.[27−30] The theoretical work on AB-type architectures is starting to catchup with experiment; SCFT phase diagrams now exist for ABA triblocks,[31,32] linear ABAB... multiblocks,[33] diblock-arm stars,[34] triblock-arm stars,[35] various miktoarm stars,[35,36] branched diblocks,[37,38] and multigraft combs.[39]

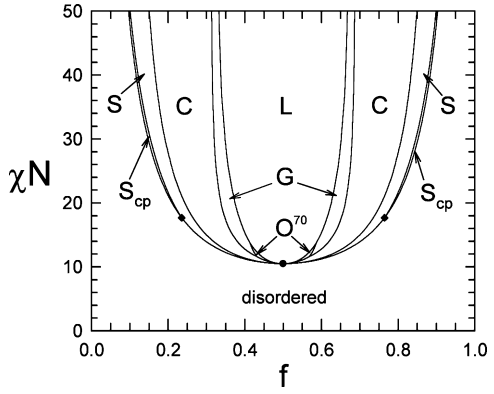

Figure 1. Phase diagram for melts of AB diblock copolymers, showing the stability regions of the ordered lamellar (L), cylindrical (C), bcc spherical (S), hcp spherical (S_{cp}), gyroid (G), and *Fddd* (O^{70}) morphologies. The dot denotes a mean-field critical point, and the diamonds mark a couple of the difficult to resolve triple points.

The general conclusion from these studies is that all AB-type architectures have similar phase diagrams, but with significantly shifted phase boundaries. The reason for the similarity is fairly well understood. Although mechanical properties are completely altered by snipping the middle B blocks of an ABA triblock melt in half, the free energy is relatively unaffected, and thus its equilibrium phase diagram remains much the same as that of an AB diblock copolymer melt.[31] The same rational applies to linear ABAB.. multiblocks, and likewise the phase

Received: December 23, 2011
Revised: January 27, 2012
Published: February 7, 2012

behavior of diblock-arm stars should be reasonably unaffected by uncoupling their arms. Gido and co-workers[27−29] have taken this idea one step further, decomposing multigraft block copolymers into constituent A_mB_n miktoarm stars and mapping them on to a phase diagram calculated by Milner[40] using the strong-stretching theory (SST) of Semenov,[41] which is the infinite-segregation limit of SCFT.[42] This has been successful in explaining the compositional shift in the phase boundaries.

The effect of architecture on complex phase behavior is less well understood. Experiments are far too time-consuming to thoroughly address this issue, while theoretical calculations have been computationally costly. Consequently, SCFT calculations for the complex phases have been restricted to relatively weak segregations, often with some of the potential phases omitted from consideration. The *Fddd* morphology has never been considered largely because it was not even discovered at the time of most calculations, and similarly many previous studies where not aware of alternatives to the bcc packing of spheres. We now know of other potential arrangements such as close-packed spheres (fcc or hcp) as well as an A15 packing predicted by Grason and Kamien[36] for AB_n miktoarm stars and later confirmed in experiment.[43] Fortunately, there have been a number of recent numerical advances[44−46] that allow the complex phases to be readily examined up to high segregations. Therefore, we now revisit the ABA triblock, linear ABAB... multiblock, diblock-arm star, and AB_2 miktoarm star architectures, updating their phase diagrams from all the known morphologies and mapping the complex phase windows to higher segregation. We also evaluate a new phase diagram for combs with a B-type backbone and A-type teeth, formed by stringing AB_2 stars together, so as to further test if the phase behavior of multigraft block copolymers is equivalent into that of their constituent units.

RESULTS

There are ample descriptions of the SCFT for complex architectures in the existing literature,[31−34,38,39] and so we forego any further repetition of the theory. It suffices to say that we perform standard calculations for incompressible melts using the standard Gaussian chain model with conformational symmetry between the A and B segments.[3] Our study considers five different architectures, where the constituent units are either the AB diblock or the AB_2 miktoarm star. The relevant parameters are the number of segments per constituent unit, N, the standard Flory−Huggins interaction parameter, χ, and the volume fraction of the A component, f.

After the AB diblock architecture, the symmetric ABA triblock, formed by joining two identical AB diblocks together by their B ends, is the most common block copolymer. Its phase diagram is shown in Figure 2, which extends the previous calculation[31] to show the gyroid (G) channel to much higher segregation and to include the *Fddd* (O^{70}) morphology. Since the triblock is formed by joining two diblocks together, the phase diagram is expected to be similar to Figure 1 when N is defined as the half of the total polymerization, and indeed it is. Nevertheless, the phase boundaries are shifted somewhat and the symmetry about $f = 0.5$ is now broken. Interestingly, the stability regions of the O^{70} phase are about half again as large as those of the diblock copolymer melt, but the regions of the close-packed spherical (S_{cp}) phase are somewhat narrower.

Naturally, we can create ever larger linear multiblocks by joining more diblocks together by their equivalent ends. As the number of blocks increases, the system reaches an asymptotic

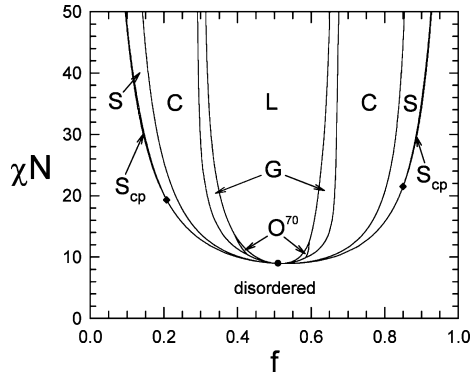

Figure 2. Phase diagram analogous to that of Figure 1, but for symmetric ABA triblock copolymers. Here N is the degree of polymerization of the diblocks formed by snipping the triblocks in half.

limit,[47] previously investigated by Matsen and Schick.[34] Figure 3 extends that calculation by plotting the complex phase

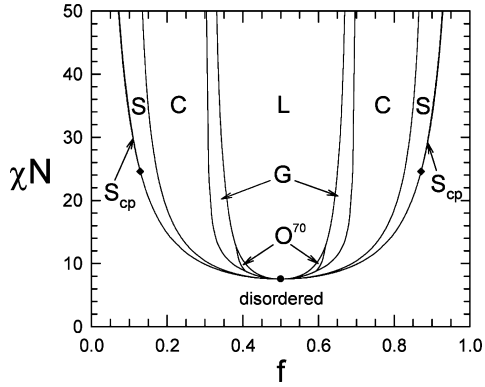

Figure 3. Phase diagram analogous to that of Figure 1, but for infinite linear ABAB... multiblock copolymers. Here N is the degree of polymerization of the diblocks formed by cutting all the blocks in the middle.

channel to far higher segregation and testing for the O^{70}, S_{cp}, and S_{A15} phases. As expected, the topology of the phase diagram remains equivalent to that of the diblock copolymer melt, since the multiblock architecture is just a string of diblocks joined together. In the limit of an infinite number of blocks, the phase diagram again becomes symmetric about $f = 0.5$. Continuing the trend from the diblock to the triblock, the multiblock architecture has slightly larger O^{70} regions and narrower S_{cp} regions.

Another way of joining diblocks together is by connecting, for example, the B-ends to form a diblock-arm star. This is evidently the first system for which experiments[18−20] observed a gyroid morphology, although it was mistakenly identified as a double-diamond morphology. This misassignment was corrected[48] shortly after SCFT calculations[34] predicted gyroid to be more stable than double-diamond. The SCFT calculations, however, only explored the complex phase channel at weak segregations and furthermore did not test for the O^{70}, S_{cp}, and S_{A15} phases. Figure 4 now provides a more complete phase diagram for 9-arm stars. Although the topology of the diagram remains equivalent to that of the diblock, there are particularly large shifts in the phase boundaries. Equally significant is the fact that the O^{70} regions are far bigger than those of the

dx.doi.org/10.1021/ma202782s | *Macromolecules* 2012, 45, 2161−2165

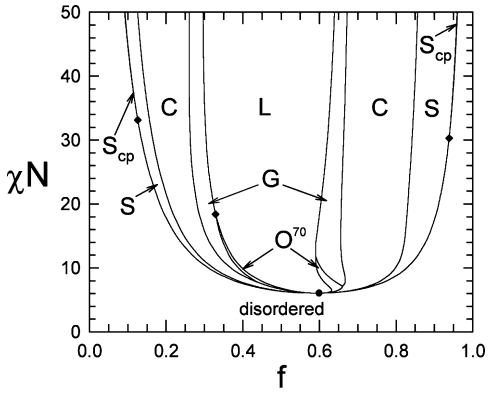

Figure 4. Phase diagram analogous to that of Figure 1, but for 9-arm star block copolymers where each molecule is formed by joining 9 diblocks together by their B-ends. Here N is the degree of polymerization of each diblock arm.

previous architectures, while the S_{cp} regions are particularly narrow.

In general, the constituent units of AB-type architectures are A_mB_n miktoarm stars, where m arms are entirely composed of A segments and n arms are made up of entirely B segments.[27−29] Grason and Kamien[36] have calculated phase diagrams for $m = 1$ with $n = 2$, 3, 4, and 5, but they did not consider the perforated-lamellar (PL) and *Fddd* (O^{70}) phases. Therefore, we redo the calculation for the AB_2 star, which is the simplest version beyond the trivial diblock where $m = n = 1$. The new phase diagram in Figure 5 exhibits a sizable O^{70} region on the large-f

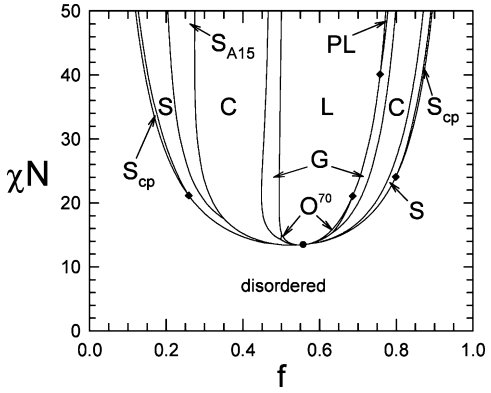

Figure 5. Phase diagram analogous to that of Figure 1, but for AB_2 star block copolymers where each molecule has one A-type arm and two identical B-type arms. The change in architecture results in additional stability regions for the ordered A15 spherical (S_{A15}) and perforated-lamellar (PL) morphologies. Here N is the degree of polymerization of the entire molecule.

side of the diagram, where the B-component forms the network and the A-component forms the matrix. More interestingly, however, is the emergence of a stable PL region on the same side of the phase diagram but at higher segregation. To the best of our knowledge, PL has only been previously predicted to be stable for diblock/homopolymer blends[49,50] and never for a neat block copolymer melt. It is also worth noting that the closed-packed spherical (S_{cp}) regions are substantially larger than for the other architectures.

By joining the AB_2 miktoarm stars together in a series by their B ends, one obtains a comb block copolymer with a B-type backbone and A-type teeth. As our last example, Figure 6

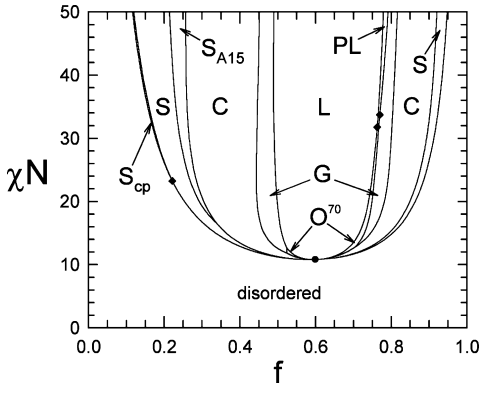

Figure 6. Phase diagram analogous to that of Figure 5, but for a comb architecture where the backbone is type B and the regularly spaced teeth are of type A. Here N is the degree of polymerization per tooth.

plots the phase diagram of the comb architecture in the limit where it has an infinite number of teeth. The phase diagram for a finite number of teeth will naturally be intermediate to Figures 5 and 6. For the most part, stringing the stars together to form a comb has little effect on the phase diagram, but it does cause a substantial increase in the size of the complex O^{70} and PL regions. There is also a significant narrowing of the S_{cp} regions, so much so that the one on the right vanishes for our range of segregations (i.e., $\chi N \leq 50$).

■ DISCUSSION

According to SST, the free energy of a strongly segregated block copolymer melt should be relatively unaffected by snipping in half those blocks that have both ends constrained to the internal A/B interfaces. This leads to the hypothesis that complex architectures can be decomposed into constituent units,[27−29] implying that Figures 2−4 should closely resemble the AB diblock phase diagram in Figure 1, while Figure 6 should approximately match the AB_2 star block phase diagram in Figure 5. This principle is vaguely accurate near $\chi N \approx 50$ and must become exact in the infinite-segregation limit (i.e., $\chi N \rightarrow \infty$).[42] Nevertheless, there are significant deviations in the intermediate-segregation regime, and there are also considerable shifts in the order−disorder transition (ODT). The latter occurs simply because architectures composed of fewer units result in more free ends per unit volume, and end segments are able to escape their domains more easily than middle segments which promotes the disordered state.

One might suspect that architecture could have a big effect on the complex phase behavior, since the free energy differences between the competing phases are relatively small. However, there is no dramatic change. The gyroid (G) phase continues to dominate the complex phase channel, and the newly discovered *Fddd* (O^{70}) phase remains stable extending down to the mean-field critical point just as it does for diblock copolymer melts.[51] In the diblock copolymer system, the predicted O^{70} regions are rather small and thus prone to the effect of fluctuations.[52] However, O^{70} does evidently survive fluctuations given the fact that it has been identified by experiments in diblock copolymer melts,[13−15] although this may have been aided by conformational asymmetry.[46] Nevertheless, we can expect the O^{70} phase to be a common feature of AB-type block copolymer melts, given that its predicted stability regions are significantly larger for all the other

dx.doi.org/10.1021/ma202782s | Macromolecules 2012, 45, 2161−2165

architectures we examined, particularly so for the star and comb block copolymers.

As expected from the decomposition principle, the A15 spherical (S_{A15}) phase occurs for combs (Figure 6) in the same place that Grason and Kemien[36] predicted it for AB_2 miktoarm stars (Figure 5). Likewise, the perforated-lamellar (PL) phase occurs in the same region of both phase diagrams. Not surprisingly, its occurrence between the L and G morphologies is precisely where it is most metastable in the diblock phase diagram. Even the preferred version of the PL phase, where perforated layers pack in an abcabc... sequence, is the same as in the diblock system.[46] We suspect that PL becomes stable for the star and comb architectures because the complex phase window has been shifted toward high asymmetries, where the majority-component layers are particularly thick. It has been shown that the PL phase is only metastable in diblock copolymers because of packing frustration in its majority-component layers.[53] This conclusion stems from the fact that PL can be stabilized with the addition of majority-component homopolymer.[49,50] Likewise, we attribute the stability of PL in Figures 5 and 6 to a reduction in packing frustration that results from the extra thickness of the majority-component layers.

Just as in the diblock system, all the phase diagrams have triple points (denoted by diamond symbols) along the ODT beyond which there are narrow regions of the close-pack spherical (S_{cp}) phase. Although it is missing from the right side of Figure 6 for the comb architecture, we expect that it does become stable at some point beyond the range of the plot. In all cases, the hcp symmetry was slightly more stable than the fcc packing of spheres as found earlier for the diblock architecture.[46] Although Grason et al.[37,38] predict fcc regions along the ODT for number of different architectures, this is evidently because they did not consider the hcp arrangement. Interestingly, we observe a narrowing of the S_{cp} regions for architectures with more units, which is relatively easy to explain. The S_{cp} phase occurs when the minority-component blocks start pulling out of the spherical domains and swelling the matrix, which relieves the packing frustration responsible for the usual bcc arrangement of spheres. This happens more readily when the minority-component blocks have free ends, and thus the smaller AB diblock and AB_2 star architectures have the larger S_{cp} regions.

Of course, there is still the possibility that a stable morphology is missing from our new phase diagrams. There are screening methods[54,55] that could be used to search for new phases, but it is unclear how effective they are at capturing all the stable phases. So far, the known phases for AB-type block copolymer melts have been found by experimental observation. Even the discovery of the *Fddd* phase in the diblock copolymer system, which was predicted by SCFT[12] two years before it was experimentally identified,[13] is ultimately accredited to experiment. It was only realized as a potential candidate structure after an analogous phase was experimentally identified in ABC triblock copolymer melts.[56] Similarly, the A15 spherical phase was observed in lyotropic liquid crystals,[57] before being considered as a candidate structure for block copolymers.

Our current calculations were made possible by recent numerical developments, whereby the spectral algorithm for evaluating the concentration profiles for given fields was combined with Anderson mixing for solving the self-consistent field equations.[46] We have previously[7,9,31−34] used a quasi-Newton−Raphson algorithm (specifically the Broyden algorithm) to solve the field equations, which requires the calculation of a Jacobian. This works exceptionally well when the morphology requires $\lesssim$100 generalized Fourier functions to accurately represent the composition profiles, and thus we still use it in these instances. However, far more Fourier terms are required for triply periodic phases at high segregation, and then the calculation of the Jacobian becomes prohibitive. Fortunately, Anderson mixing is capable of solving the field equations without a Jacobian, which permits calculations involving as many as 5000 basis functions with just a single computer processor. Even though our calculations were performed to high accuracy, we never needed more than 2000 basis functions.

Pseudospectral methods can also be combined with Anderson mixing to produce an efficient algorithm for calculating SCFT phase diagrams.[44] However, the full-spectral method is still generally faster apart from the upper part of the complex phase channel, where the morphologies require $\gtrsim$1000 basis functions. Furthermore, the spectral method is superior at handling some of the more complex architectures, such as the linear and comb multiblock copolymers in Figures 3 and 6, respectively. The real advantage of the spectral method though is that it only has one source of numerical inaccuracy to contend with, the truncation of the Fourier series. In contrast, the pseudospectral methods have two distinct sources, the finite spatial resolution and the finite step-size along the chain contour, making it far more of a chore to ensure sufficient numerical accuracy.

SUMMARY

We have presented complete phase diagrams for six different AB-type block copolymer melts obtained with self-consistent field theory (SCFT). The principle that complex architectures can be decomposed in constituent A_mB_n stars appears to be reasonably accurate at strong segregations, but significant deviations are evident in the intermediate-segregation regime. Nevertheless, the qualitative behavior is preserved. For instance, the ABA triblock, linear ABAB... multiblock and diblock-arm star have phase diagrams that are topologically equivalent to that of the simple AB diblock. In all cases, the gyroid (G) morphology dominates the complex phase channel while the new *Fddd* (O^{70}) microstructure remains stable in small regions extending down to the mean-field critical point. Similarly, the phase diagram for combs with A-type teeth and a B-type backbone has the same topology as that of AB_2 miktoarm stars. In particular, the comb exhibits a stable region of A15 spheres (S_{A15}) in the same place Grason and Kamien[36] predicted it for AB_2 stars, and furthermore both architectures exhibit a perforated-lamellar (PL) morphology with perforations in the B-rich lamellae, which is stable between the L and G phases for well-segregated conditions. The appearance of the PL phase occurs presumably because the complex phase window is shifted toward large f, which thickens the A-rich lamellae thereby relieving packing frustration.

The ability to use architecture to control the composition and size of the stability regions in the phase diagram is yet another useful means for designing block copolymer materials. However, investigating the effect of architecture by experiment alone would be extremely time-consuming and costly, and simple principles such as decomposing complex architectures into their constituent units are of limited application and accuracy. Fortunately, recent developments in numerical methods[44−46] allow high-precision SCFT calculations to be performed on even the most complex periodic morphologies

using very modest computational resources. Thus, SCFT will be a particularly valuable tool for navigating the immense variety of possible architectures.

AUTHOR INFORMATION

Corresponding Author

*E-mail: m.w.matsen@reading.ac.uk.

Notes

The authors declare no competing financial interest.

ACKNOWLEDGMENTS

This work was funded by the EPSRC (Grant EP/G026203/1).

REFERENCES

(1) Bates, F. S.; Schulz, M. F.; Khandpur, A. K.; Förster, S.; Rosedal, J. H.; Almdal, K.; Mortensen, K. *Faraday Discuss.* **1994**, *98*, 7−18.

(2) Helfand, E. *J. Chem. Phys.* **1975**, *62*, 999−1005.

(3) Matsen, M. W. *J. Phys.: Condens. Matter* **2002**, *14*, R21−R47.

(4) Matsen, M. W. In *Soft Matter: Polymer Melts and Mitures*; Gompper, G., Schick, M., Eds.; Wiley-VCH: Weinheim, Germany, 2006; Vol. *1*, Chapter 2.

(5) Fredrickson, G. H. *The Equilibrium Theory of Inhomogeneous Polymers*; Oxford University Press: New York, 2006.

(6) Vavasour, J. D.; Whitmore, M. D. *Macromolecules* **1992**, *25*, 5477−5486.

(7) Matsen, M. W.; Schick, M. *Phys. Rev. Lett.* **1994**, *27*, 2660−2663.

(8) Hajduk, D. A.; Takenouchi, H.; Hillmyer, M. A.; Bates, F. S.; Vigild, M. E.; Almdal, K. *Macromolecules* **1997**, *30*, 3788−3795.

(9) Matsen, M. W.; Bates, F. S. *Macromolecules* **1996**, *29*, 1091−1098.

(10) Schwab, M.; Stühn, B. *Colloid Polym. Sci.* **1997**, *275*, 341−351.

(11) Han, C. D.; Vaidya, N. Y.; Kim, D.; Shin, G.; Yamaguchi, D.; Hashimoto, T. *Macromolecules* **1998**, *33*, 3767−3780.

(12) Tyler, C. A.; Morse, D. C. *Phys. Rev. Lett.* **2005**, *94*, 208302.

(13) Takenaka, M.; Wakada, T.; Akasaka, S.; Nishitsuji, S.; Saijo, K.; Shimizu, H.; Kim, M. I.; Hasegawa, H. *Macromolecules* **2007**, *40*, 4399−4402.

(14) Kim, M. I.; Wakada, T.; Akasaka, S.; Nishitsuji, S.; Saijo, K.; Hasegawa, H.; Ito, K.; Takenaka, M. *Macromolecules* **2008**, *41*, 7667−7670.

(15) Kim, M. I.; Wakada, T.; Akasaka, S.; Nishitsuji, S.; Saijo, K.; Hasegawa, H.; Ito, K.; Takenaka, M. *Macromolecules* **2009**, *42*, 5266−5271.

(16) Bates, F. S.; Fredrickson, G. H. *Phys. Today* **1999**, *52*, 32−38.

(17) Mai, S.-M.; Mingvanish, W.; Turner, S. C.; Chaiundit, C.; Fairclough, J. P. A.; Heatley, F.; Matsen, M. W.; Ryan, A. J.; Booth, C. *Macromolecules* **2000**, *33*, 5124−5130.

(18) Thomas, E. L.; Alward, D. B.; Kinning, D. J.; Martin, D. C.; Handlin, D. L.; Fetters, L. J. *Macromolecules* **1986**, *19*, 2197−2202.

(19) Alward, D. B.; Kinning, D. J.; Thomas, E. L.; Fetters, L. J. *Macromolecules* **1986**, *19*, 215−224.

(20) Herman, D. S.; Kinning, D. J.; Thomas, E. L.; Fetters, L. J. *Macromolecules* **1987**, *20*, 2940−2942.

(21) Pochan, D. J.; Gido, S. P.; Pispas, S.; Mays, J. W.; Ryan, A. J.; Fairclough, P. A.; Hamley, I. W.; Terrill, N. J. *Macromolecules* **1996**, *29*, 5091−5098.

(22) Pochan, D. J.; Gido, S. P.; Pispas, S.; Mays, J. W. *Macromolecules* **1996**, *29*, 5099−5105.

(23) Gido, S. P.; Lee, C.; Pochan, D. J.; Pispas, S.; Mays, J. W.; Hadjichristidis, N. *Macromolecules* **1996**, *29*, 7022−7028.

(24) Beyer, F. L.; Gido, S. P.; Poulos, Y.; Avgeropoulos, A.; Hadjichristidis, N. *Macromolecules* **1997**, *30*, 2373−2376.

(25) Beyer, F. L.; Gido, S. P.; Uhrig, D.; Mays, J. W.; Bech Tan, N.; Trevino, S. F. *J. Polym. Sci., Part B* **1999**, *37*, 3392−3400.

(26) Yang, L.; Hong, S.; Gido, S. P.; Vellis, G.; Hadjichristidis, N. *Macromolecules* **2001**, *34*, 9069−9073.

(27) Xenidou, M.; Beyer, F. L.; Hadjichristidis, N.; Gido, S. P.; Beck Tan, N. *Macromolecules* **1998**, *31*, 7659−7667.

(28) Lee, C.; Gido, S. P.; Poulos, Y.; Hadjichristidis, N.; Bech Tan, N.; Trevino, S. F.; Mays, J. W. *Polymer* **1998**, *39*, 4631−4638.

(29) Beyer, F.; Gido, S. P.; Buschl, C.; Iatrou, H.; Uhrig, D.; Mays, J. W.; Chang, M.; Garetz, B. A.; Balsara, N.; Bech Tan, N.; Hadjichristidis, N. *Macromolecules* **2000**, *33*, 2039−2048.

(30) Zhu, Y.; Burgaz, E.; Gido, S. P.; Staudinger, U.; Weidisch, R.; Uhrig, D.; Mays, J. W. *Macromolecules* **2006**, *39*, 4428−4436.

(31) Matsen, M. W.; Thompson, R. B. *J. Chem. Phys.* **1999**, *111*, 7139−7146.

(32) Matsen, M. W. *J. Chem. Phys.* **2000**, *113*, 5539−5544.

(33) Matsen, M. W.; Schick, M. *Macromolecules* **1994**, *27*, 7157−7163.

(34) Matsen, M. W.; Schick, M. *Macromolecules* **1994**, *27*, 6761−6767.

(35) Lynd, N. A.; Oyerokun, F. T.; O'Donogue, D. L.; Handlin, D. L. Jr.; Fredrickson, G. H. *Macromolecules* **2010**, *43*, 3479−3486.

(36) Grason, G. M.; Kamien, R. D. *Macromolecules* **2004**, *37*, 7371−7380.

(37) Grason, G. M.; DiDonna, B. A.; Kamien, R. D. *Phys. Rev. Lett.* **2003**, *91*, 058304.

(38) Grason, G. M.; Kamien, R. D. *Phys. Rev. E* **2005**, *71*, 051801.

(39) Wang, L.; Zhang, L.; Lin, J. *J. Chem. Phys.* **2008**, *129*, 114905.

(40) Milner, S. T. *Macromolecules* **1994**, *27*, 2333−2335.

(41) Semenov, A. E. *Sov. Phys. JETP* **1985**, *85*, 733−742.

(42) Matsen, M. W. *Eur. Phys. J. E* **2010**, *33*, 297−306.

(43) Cho, B.-K.; Jain, A.; Gruner, S. M.; Wiesner, U. *Science* **2004**, *305*, 1598−1601.

(44) Stasiak, P.; Matsen, M. W. *Eur. Phys. J. E* **2011**, *34*, 110.

(45) Cochran, E. W.; Garcia-Cervera, C. J.; Fredrickson, G. H. *Macromolecules* **2006**, *39*, 2449−2451.

(46) Matsen, M. W. *Eur. Phys. J. E* **2009**, *30*, 361−369.

(47) Kavassalis, T. A.; Whitmore, M. D. *Macromolecules* **1991**, *24*, 5340−5345.

(48) Hajduk, D. A.; Harper, P. E.; Gruner, S. M.; Honeker, C. C.; Thomas, E. L.; Fetters, L. J. *Macromolecules* **1995**, *28*, 2570−2573.

(49) Matsen, M. W. *Phys. Rev. Lett.* **1995**, *74*, 4225−4228.

(50) Matsen, M. W. *Macromolecules* **1995**, *27*, 5765−5773.

(51) Ranjan, A.; Morse, D. C. *Phys. Rev. E* **2006**, *74*, 011803.

(52) Miao, B.; Wickham, R. A. *J. Chem. Phys.* **2008**, *128*, 054902.

(53) Matsen, M. W.; Bates, F. S. *Macromolecules* **1996**, *29*, 7641−7644.

(54) Drolet, F.; Fredrickson, G. H. *Phys. Rev. Lett.* **1999**, *83*, 4317−4320.

(55) Guo, Z. J.; Zhang, G. J.; Qiu, F.; Zhang, H. D.; Yang, Y. L.; Shi, A.-C. *Phys. Rev. Lett.* **2008**, *101*, 028301.

(56) Bailey, T. S.; Hardy, C. M.; Epps, T. H.; Bates, F. S. *Macromolecules* **2002**, *35*, 7007−7017.

(57) Sakya, P.; Seddon, J. M.; Templer, R. H.; Mirkin, R. J.; Tiddy, G. J. T. *Langmuir* **1997**, *13*, 3706−3714.

Macromolecules

Note

pubs.acs.org/Macromolecules

Structure–Photophysical Property Relationship of Conjugated Rod–Coil Block Copolymers in Solutions

Jui-Hsiang Hung

Institute of Polymer Science and Engineering, National Taiwan University, Taipei, Taiwan 106, R.O.C

Yung-Lung Lin and Yu-Jane Sheng*

Department of Chemical Engineering, National Taiwan University, Taipei, Taiwan 106, R.O.C

Heng-Kwong Tsao*

Department of Chemical and Materials Engineering, Department of Physics, National Central University, Jhongli, Taiwan 320, R.O.C

Supporting Information

The self-assembly of amphiphilic coil–coil block copolymers in a selective solvent has a wide range of potential applications, including formulations, pharmaceuticals, and separations, due to their unique physical and chemical properties. Lately, much attention has been focused on the aggregation behavior of the rod–coil copolymer, which is further complicated by the inflexible rodlike segments of these molecules. The rigid chain conformations come from π-conjugation along the polymer backbone (as in conjugated polymers),[1] helical secondary structures (as in biomolecules),[2] or mesogenic units (as in liquid crystals).[3] Photoresponsive rod–coil block polypeptides which can undergo a reversible aggregation–dissolution process are used as viable model systems for photoinduced drug release applications.[2e] As for the π-conjugation rod–coil copolymers, due to their distinct photoactive and electroactive properties, they have advanced applications in optoelectronic materials, including lasers,[4] photovoltaic cells,[5] and polymer light-emitting diodes for full-color displays,[6] to name a few.

It has been shown that the photophysical properties of π-conjugated rod–coil copolymers are highly correlated to their molecular structures and microscopic arrangements of rod blocks. The combination of the molecular amphiphilic nature and the preference of orientational ordering of rod blocks drives rod–coil block copolymers to self-assemble into a variety of intriguing morphologies such as structural sphere, inverted cylindrical vesicle, and segmented network.[7,8] These supramolecular morphologies often induce a significant variation in the optical or electronic properties of the π-conjugated segments. That is, different self-assembled patterns of conjugated rod blocks affect the electronic structure of the system and lead to different photophysical behaviors examined by UV–vis and photoluminescence spectroscopy. For example, the spectral shift is commonly observed as conjugated rod–coil copolymer systems proceed from the dispersed phase to the aggregated phase in solution or solid state.[9−11] Thus, a detailed investigation of the morphological structures and internal rod arrangements is of great importance in understanding the photophysical properties for future polymer technologies and optoelectronic applications.

According to the extensive studies on dye molecules which often assemble into large aggregates in a parallel way, the hypsochromic (blue) shift is attributed to the formation of H-aggregates while the bathochromic (red) shift is accounted for by the formation of J-aggregates.[12] Dyes are normally very large aromatic molecules consisting of many linked rings. The direction of spectral shifts, red or blue, is largely dictated by the angle of slippage (α) of successive conjugated planes.[12] As shown in Figure 1, the slippage angle is defined as the angle

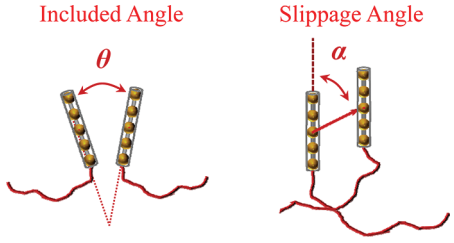

Figure 1. Schematic representations of the included angle (θ) and slippage angle (α) in rod–coil systems. Note that $0 \le \theta \le 90°$ and $0 \le \alpha \le 90°$.

between the line-of-centers of a column of molecules and the long axis of any one of the parallel molecules. It is believed that planes with slippage angle larger than a certain value leads to bathochromic shifts, while planes with slippage angle less than that value result in hypsochromic shifts. Note that the larger the slippage angle, the less the slippage extent (planar offset). Although dye molecules tend to be parallel to each other for both types of aggregates, the slippage extent is larger for J-aggregates and smaller for H-aggregates.

To demonstrate this principle applicable to rodlike molecules, the largest absorption wavelength (λ_{max}) of the π-conjugated molecule F3T8 which contains three fluorene units and eight thiophene units at different molecular arrangements

Received: January 6, 2012
Revised: February 5, 2012
Published: February 16, 2012

dx.doi.org/10.1021/ma300039d | *Macromolecules* 2012, 45, 2166–2170

is calculated by using the VAMP package[13] based on quantum semiempirical calculations. For the dispersed phase, $\lambda_{max} \approx 308$ nm. The variation of λ_{max} with α is illustrated in Figure 2. When

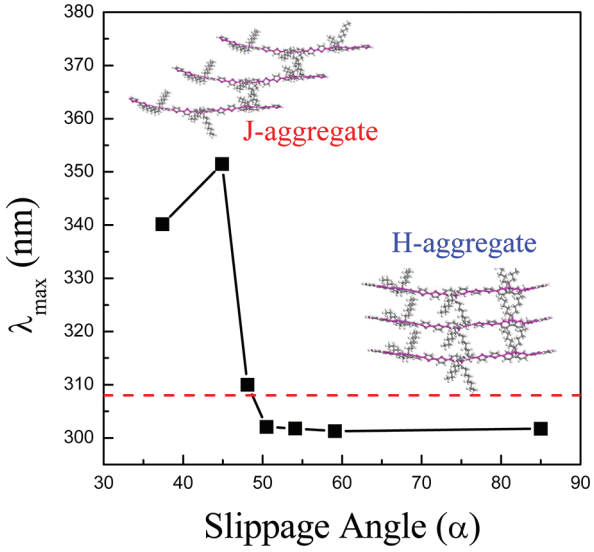

Figure 2. UV–vis absorption wavelength versus slippage angle of F3T8 using VAMP. The dashed line indicates the absorption wavelength of the dispersed state at 308 nm. The critical slippage angle for the direction of spectral shift is found around 50°.

the slippage angle of the parallel aggregate consisting of three F3T8 molecules is larger than a critical value (say 50°), λ_{max} of such H-aggregates becomes shorter. On the contrary, λ_{max} turns longer for J-aggregate with smaller slippage angle. Evidently, the spectral shift varies with the stacking pattern in the aggregate in terms of the slippage angle, which affects the electronic structure and thereby the photophysical behavior. However, the structural packing and the self-assembly morphology is generally determined by the molecular architecture.

Though considerable efforts have been dedicated to the knowledge of the self-assembly behaviors of conjugated rod–coils, there are no manifest and self-contained guidelines to date that can be used to account for the relationships between the fundamental molecular architectures as well as the morphologies and spectral behaviors associated with their self-assembly. To tackle this significant issue, in this Note we explore the self-assembly of conjugated rod–coil copolymers via the dissipative particle dynamics (DPD). Structural effects including molecular architectures, rod/coil block length, and strength of π–π interaction on the orientational order and self-assembled patterns are thoroughly investigated. Our study shows that the gaps between the molecular architectures and the aggregation patterns can be bridged by the classification of rod–coils with various architectures (multiple blocks, star, brush, dendron, etc.) into rod–coil diblocks (RC-type) or coil–rod–coil triblocks (CRC-type) structures. The former tends to have parallel arrangements of rod blocks with smaller slippage extent while the latter displays the stacking structure with larger slippage extent.

The DPD method is a coarse-grained particle based, mesoscopic simulation technique.[14] DPD beads with the mass m and diameter r_c are clusters of several atoms or molecules that have similar properties and they obey Newton's equation of motion. The interaction between any pair of DPD beads is soft and consists of three intrinsic pairwise-additive forces: conservative, dissipative, and random forces. The interaction parameters for the conservative forces are listed in Table 1. The

Table 1. Interaction Parameters (a_{ij}) for the Rod–Coil Block Copolymer Systems

	coil	rod	solvent
coil	25		
rod	35	25	
solvent	30	45	25

polymeric beads are bound together by spring forces to keep the neighboring beads at an equilibrium distance. The rigidity of the rod block is provided by additional spring forces.[7] Since conjugated rods have a tendency to orient parallel to one another due to the π–π interaction when situated in close proximity, an orientational potential is further employed, $U_o = -k(1 - r/r_c)\cos^2\theta$ as $r \le r_c$ and zero otherwise.[7] The strengths as well as the causes of the π–π interaction vary strongly. It is generally accepted that the π–π strength ranges between 0 and 50 kJ/mol.[7c] Therefore, the strength of the orientational force k, which essentially corresponds to the Maier–Saupe parameter, is adjusted between 0 and 10. Note that all the physical variables are scaled by m, r_c, and k_BT. The volume fraction of rod–coils is kept at 0.05.

In most rod–coil block copolymer solutions, the solvent is selective for the coil block, leading to the formation of aggregates with the soluble coils exposed to the solvent. The self-assembly morphology is influenced by the molecular structure, including architecture, rod length (y), coil length (x), and the π–π interaction. First, we consider the archetypical rod–coil systems, diblock copolymers with y:x. Though the aggregate morphology is quite complicated and intriguing, the optoelectronic property is closely related to the inner rod arrangement. Therefore, the internal structure of the rod domain is analyzed via both orientational and positional order. The extent of rod alignment can be reflected via the distribution of the included angle θ (as defined in Figure 1) between two neighboring rods, $P(\theta)$, and the local order parameter, $S = \langle(3\cos^2\theta - 1)/2\rangle$. Note that $\theta = 0$ indicates two neighboring rods being perfectly aligned in parallel and the value of S is on the order of 0.3–0.8 for a typical liquid crystal sample.

The effects of the rod length and π–π interaction on the alignment of rod blocks are illustrated in Figure 3. Consider $P(\theta)$ of rod–coil diblocks with y:x = 6:3. When the orientational force is absent (k = 0), the included angle is uniformly distributed, indicating an isotropic structure in the rod domain. However, once the orientational force is introduced, the rod blocks tend to align with each other and the distribution is highly skewed toward θ = 0. As k is further increased, the width of the included angle distribution gets narrower. In terms of the order parameter, S grows quickly from around zero to greater than 0.8 for $0 \le k \le 10$, as shown in the inset for rod length = 6. In addition to π–π interaction (k), the rod alignment can also be enhanced by increasing the rod length (y).[7a] As also can be seen in the inset of Figure 3, for k = 0, the rod domain for rod–coils with y = 3 is essentially isotropic and $S \simeq 0$. However, as the rod length is varied from 3 to 15, the order parameter rises due to entropy effect associated with excluded volume interactions, and the crossover from isotropy to alignment is observed at $y \approx 8$. The presence of the orientation force raises the orientational order furthermore and

dx.doi.org/10.1021/ma300039d | Macromolecules 2012, 45, 2166–2170

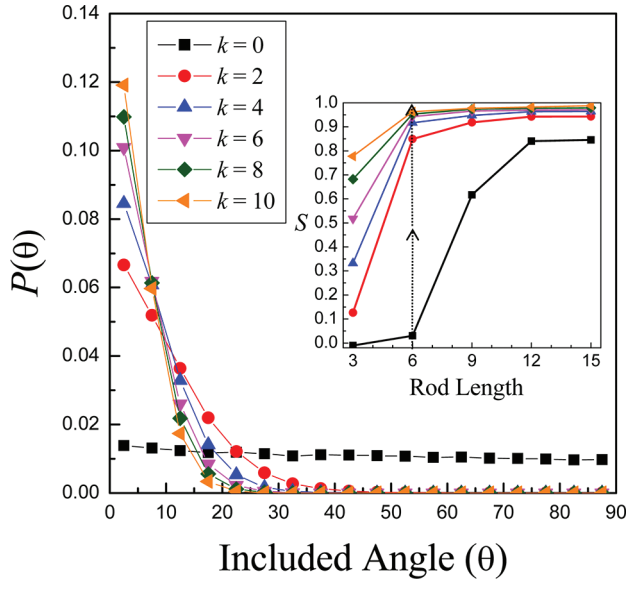

Figure 3. Distribution of the included angle for rod–coil diblocks (6–3) with k varying from 0 to 10. In the inset, the orientational order parameter is plotted against the rod length with the coil length fixed at 3.

one has $S > 0.3$ for short rods ($y = 3$) when $k > 4$. Note that in this case the coil length is fixed at 3 and an increase of the coil length hinders the tendency of rod alignment due to the bulky end, but such an effect is relatively weak.[7a,b]

The change of the spectral properties takes place in the rod domain with parallel arrangements and is dependent on the positional order, which can be realized through the slippage angle measurement. Without loss of generality, the arrangement with larger mean slippage angle, $\bar{\alpha} \geq 67.5°$, is defined as smectic A, of which the slippage angle distribution exhibits a peak at $\alpha = 90°$, as shown in Figure 4. In contrast, that with

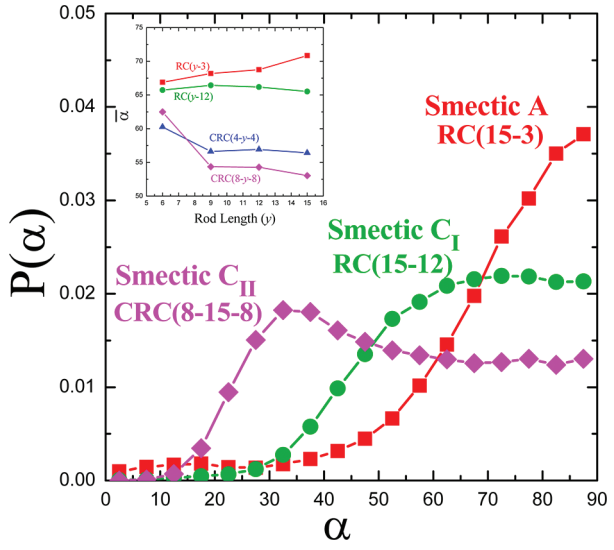

Figure 4. Slippage angle distribution for RC (15–3 and 15–12) and CRC (8–15–8). The inset shows the average slippage angle versus rod length for RC and CRC with varied coil lengths and $k = 10$.

smaller angle, $\bar{\alpha} < 67.5°$, is defined as smectic C, of which the peak occurs at $\alpha < 90°$. To further demonstrate the degree of the slippage between rods, the aggregate with $\bar{\alpha} = 60°–67.5°$ is denoted as smectic C_I and that with $\bar{\alpha} < 60°$ is depicted by smectic C_{II}. The former shows a wide distribution skewed toward $\alpha = 90°$ while the latter displays a peak significantly less than 60°. The distinct difference of the rod arrangement between RC and CRC can be demonstrated by the variation of the mean slippage angle with the rod length at a specified coil length, as shown in the inset of Figure 4. Although $\bar{\alpha}$ varies with the rod length, it is evident that the mean slippage angle of the RC is always significantly greater than that of the CRC. Their differences can also be manifested by the feature of the distributions of α, as illustrated in Figure 4. There exists a peak at lower values of α for the CRC while the maximum is skewed toward 90° for the RC. These characteristics associated with the slippage angle distribution are closely related to the morphology of the rod domain.

The photophysical phase diagram (coil length versus rod length) is shown in Figure 5a for rod–coil diblocks with strong

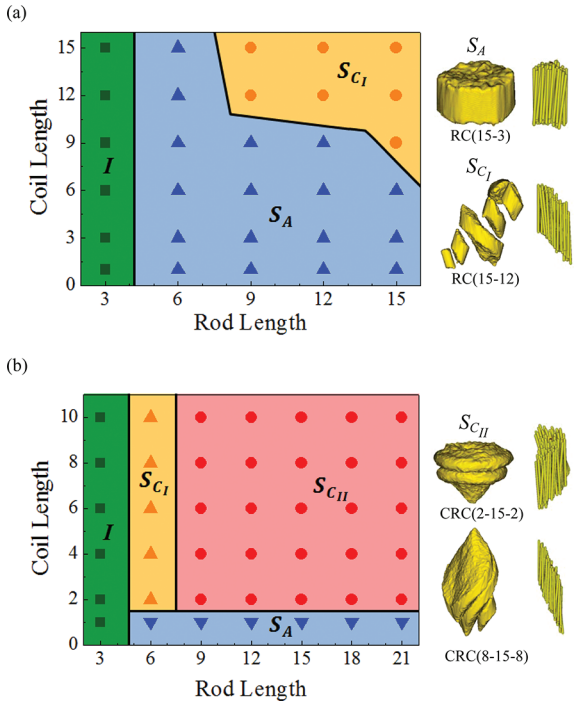

Figure 5. Phase diagram of the structure of the rod domain for RC (a) and CRC (b) with $k = 10$. I, S_A, and S_C represent the isotropic, smectic A, and smectic C arrangements of the rod domains. The corresponding morphologies are also shown.

enough π–π interaction ($k = 10$). When the rod length is small enough, i.e. $y = 3$, the isotropic arrangement in the rod domain is observed regardless of the coil length. Thereby, no spectral shift is expected. As the rod length is long enough, however, the smectic A aggregates are formed and the blue-shift behavior prevails. Note that at a given rod length the increment of the coil length leads to the decline of α, and thus the arrangement of rods tends to shift from smectic A to smectic C type. This consequence reveals that RC molecules tend to form H-aggregate with large slippage angles (small slippage extent) and thus exhibit blue-shift spectra. This is consistent with the majority of the experiment findings.[10,15,16]

Now let us consider coil–rod–coil triblocks (x:y:x). The diagram of the aggregation pattern is illustrated in Figure 5b through coil length against rod length and the π–π interaction

dx.doi.org/10.1021/ma300039d | Macromolecules 2012, 45, 2166–2170

k = 10. Similar to RC molecules, the isotropic arrangement is observed for short rod length y = 3, and the rod blocks prefer being parallel to each other at long rod length ($y \geq 6$). The smectic C_I structure is observed for y = 6 with $x \geq 2$, while the smectic A structure is seen for x = 1 with $y \geq 6$. Except the aforementioned triblock configurations, the rest of the CRC structure result in the smectic C_{II} aggregates. That is, CRC molecules tend to form J-aggregate with small slippage angles (large slippage extent) and thus exhibit red-shift spectra.[10,15,17] Note that the blue-shift behavior corresponding to smectic A can only be observed in a very narrow regime.[11] The rod domain of the RC displays a trunklike shape for smectic A phase and a slanted trunk for smectic C_I phase, as shown in Figure 5a. On the other hand, the morphology of the rod domain of the CRC is very interesting. The presence of the small slippage angle is accompanied by a leaf-like shape (8:15:8) or a funnel-like structure (2: 15: 2), as illustrated in Figure 5b. It is evident that the morphologies of the rod domain vary with both rod and coil lengths significantly.

DPD simulation results indicate that the rod−coil diblocks favor the formation of H-aggregates while the coil−rod−coil triblocks tend to form J-aggregates. What happens for rod−coils with complicated molecular architectures, such as multiblock, star, brush, and dendron? DPD simulations are also performed to explore the influence of molecular architecture, and similar phase diagrams are obtained. Their spectral behavior can be simply classified into two categories: RC type and CRC type. The schematic representations of the general RC-type and CRC-type structures are shown in Figure 6. For CRC-type copolymers, both ends of all rod blocks are connected with coil blocks, while for RC-type copolymers, only one end of some rod blocks is attached with coil blocks. This distinct difference plays the major role in determining the feature of the slippage angle distribution. Some simulation results of the slippage angle distributions (Figures S1−S6) are presented as Supporting Information. Figures S1−S3 demonstrate the typical slippage angle distributions of the RC-type copolymers: RCR, RC-star, and RC-graft block copolymers.

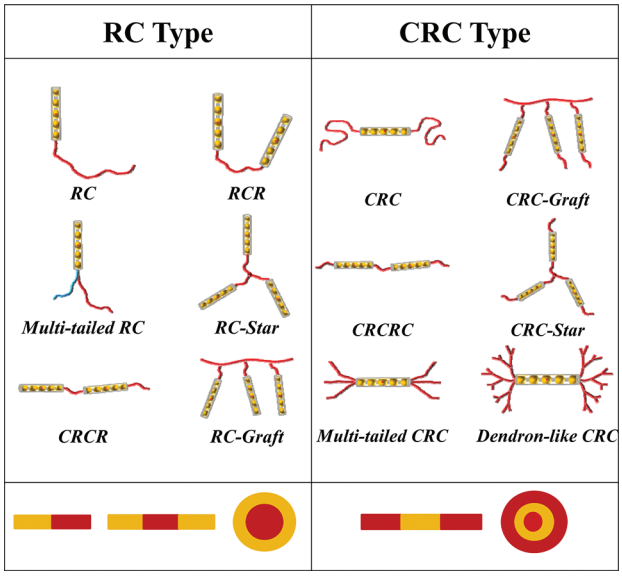

Figure 6. Classification of the spectral behavior of rod−coils with various architectures into the general RC-type and CRC-type structures with their schematic representations.

Figures S4−S6 show the typical slippage angle distributions of the CRC-type copolymers: CRCRC, CRC-star, and CRC-graft block copolymers. As one can clearly see, the RC-type copolymers tend to form H-aggregates with large slippage angles and CRC-type copolymers tend to form J-aggregates with small slippage angles.

In a single lamellar sheet, densely grafted coils are highly stretched. The preference of smectic A or smectic C phase in the rod domain depends on the competition between the deformation energy of coil stretching and the interfacial energy between rod and coil domains.[18] The coil stretching penalty can be lowered by the reduction of the apparent grafting density of coils. For RC-type copolymers, the interfacial energy is dominant and smectic A phase is favored. The apparent grafting density reduction is achieved by the head-to-tail arrangement, as in the puck micelle model, for rod−coil diblocks, multitailed RC, and CRCR or is attained by the common share of coils for RCR, RC-stars, and RC-graft. On the contrary, for CRC-type copolymers, the deformation energy becomes dominant and smectic C_{II} phase prevails. Since their apparent grafting density cannot be reduced by simply changing the rod orientation as in the RC-type, rod blocks of the CRC-type dislocate significantly at the expense of the increment of interfacial area to reduce the crowdedness among coils.

In CRC systems the crossover from smectic C_I to C_{II} phase occurs as the rod length increases. Different from the driving force for the transition from smectic A to C phase, the crossover between smectic C_I and C_{II} phases is due to the effect of $\pi-\pi$ interactions between two rods, which grow with the rod length. As a result, longer rods become more parallel-aligned. This result can be demonstrated through the included angle distribution $P(\theta)$, as shown in Figure S7. Evidently, longer rods possess higher probability of parallel alignment (θ = 0) and their distributions skew toward θ = 0. For CRC with short rods, the $\pi-\pi$ attraction is weak and the rods are less parallel-aligned. This conformation has more free space for the coils and the interfacial energy becomes more important than the coil stretching energy. The competition between the two energies results in small slips between rods. As a result, smectic C_I phase is formed. The schematic representation of smectic C_I phase is shown in Figure S8. For CRC with long rods, the $\pi-\pi$ attraction is strong and most of the rods in close proximity align in parallel formations. Large slips between rods are needed to prevent coils from stretching. Consequently, smectic C_{II} phase takes shape. The schematic representation of smectic C_{II} phase is also shown in Figure S8.

Conjugated rod−coil copolymers in a coil-selective solvent self-assemble into aggregates with parallel arrangements of rod blocks. The spectral properties of the aggregative polymers are significantly affected by their supramolecular morphologies, which in turn are greatly influenced by the molecular architectures of rod−coils. In this Note the relationship between spectral properties and molecular architecture is established based on DPD simulations, which incorporates large-scale molecular features while avoiding atomic scale details. It is found that rod−coil copolymers can be qualitatively classified into two types: RC-type and CRC-type. RC-type is generally with large slippage angle (smectic A), and blue-shift behavior prevails. CRC-type is normally with small slippage angle (smectic C_{II}) and thus exhibits red-shift spectra. The structural packing in the rod domain is the consequence of the competition between the deformation energy of coil stretching and the rod/coil interfacial energy. The interfacial energy is

dx.doi.org/10.1021/ma300039d | Macromolecules 2012, 45, 2166−2170

dominant in smectic A-aggregates while the deformation energy dominates in smectic C-aggregates. Our predictions of rod−coil diblocks exhibiting blue-shift spectra and coil−rod−coil triblocks showing red-shift spectra are consistent with experimental observations.

■ ASSOCIATED CONTENT

Ⓢ Supporting Information

Detailed simulation results of the slippage angle distributions of for some RC-type and CRC-type copolymers; typical slippage angle distributions of the RC-type copolymers CRCR, RC-star, and RC-graft (Figures S1−S3); typical slippage angle distributions of the CRC-type copolymers CRCRC, CRC-star, and CRC-graft (Figures S4−S6). Figure S7 shows the included angle distributions for CRC triblocks. Figure S8 are the schematic representations of the smectic C (I and II) phases. This material is available free of charge via the Internet at http://pubs.acs.org.

■ AUTHOR INFORMATION

Corresponding Author

*E-mail: yjsheng@ntu.edu.tw (Y.-J.S.); hktsao@cc.ncu.edu.tw (H.-K.T.).

Notes

The authors declare no competing financial interest.

■ ACKNOWLEDGMENTS

This research work is supported by National Science Council of Taiwan.

■ REFERENCES

(1) (a) Yesodha, S. K.; Pillai, C. K. S.; Tsutsumi, N. *Prog. Polym. Sci.* **2004**, *29*, 45. (b) Cho, M. J.; Choi, D. H.; Sullivan, P. A.; Akelaitis, A. J. P.; Dalton, L. R. *Prog. Polym. Sci.* **2008**, *33*, 1013. (c) Moliton, A. *Optoelectronics of Molecules and Polymers*; Springer: New York, 2005. (d) McCulloch, I.; Yoon, H. *J. Polym. Sci., Part A: Polym. Chem.* **1995**, *33*, 1177.

(2) (a) Cornelissen, J.; Fischer, M.; Sommerdijk, N.; Nolte, R. J. M. *Science* **1998**, *280*, 1427. (b) Klok, H. A.; Langenwalter, J. F.; Lecommandoux, S. *Macromolecules* **2000**, *33*, 7819. (c) Checot, F.; Lecommandoux, S.; Gnanou, Y.; Klok, H. A. *Angew. Chem., Int. Ed.* **2002**, *41*, 1339. (d) Rodriguez-Hernandez, J.; Lecommandoux, S. *J. Am. Chem. Soc.* **2005**, *127*, 2026. (e) Kotharangannagari, V. K.; Sánchez-Ferrer, A.; Ruokolainen, J.; Mezzenga, R. *Macromolecules* **2011**, *44*, 4569.

(3) (a) Lee, M.; Cho, B. K.; Ihn, K. J.; Lee, W. K.; Oh, N. K.; Zin, W. C. *J. Am. Chem. Soc.* **2001**, *123*, 4647. (b) Lee, M.; Cho, B. K.; Oh, N. K.; Zin, W. C. *Macromolecules* **2001**, *34*, 1987. (c) Braun, P. V.; Osenar, P.; Tohver, V.; Kennedy, S. B.; Stupp, S. I. *J. Am. Chem. Soc.* **1999**, *121*, 7302. (d) Stupp, S. I.; LeBonheur, V.; Walker, K.; Li, L. S.; Huggins, K. E.; Keser, M.; Amstutz, A. *Science* **1997**, *276*, 384.

(4) Tessler, N.; Denton, G.; Friend, R. *Nature* **1996**, *382*, 695.

(5) (a) Günes, S.; Neugebauer, H.; Sariciftci, N. S. *Chem. Rev.* **2007**, *107*, 1324. (b) Thompson, B. C.; Fréchet, J. M. J. *Angew. Chem., Int. Ed.* **2008**, *47*, 58. (c) Sariciftci, N. S.; Smilowitz, L.; Heeger, A. J.; Wudl, F. *Science* **1992**, *258*, 1474. (d) Campoy-Quiles, M.; Ferénczi, T.; Agostinelli, T.; Etchegoin, P. G.; Kim, Y.; Anthopoulos, T. D.; Stavrinou, P. N.; Bradley, D. C.; Nelson, J. *Nature Mater.* **2008**, *7*, 158. (e) Park, S. H.; Roy, A.; Beaupre, S.; Cho, S.; Coates, N.; Moon, J. S.; Moses, D.; Leclerc, M.; Lee, K.; Heeger, A. J. *Nature Photonics* **2009**, *3*, 297.

(6) (a) Burroughes, J.; Bradley, D.; Brown, A.; Marks, R.; Mackay, K.; Friend, R.; Burns, P.; Holmes, A. *Nature* **1990**, *347*, 539. (b) Rhee, J.; Wang, J.; Cha, S.; Chung, J.; Lee, D.; Hong, S.; Choi, B.; Goh, J.; Jung, K.; Kim, S. *J. Soc. Inf. Display* **2006**, *14*, 895. (c) Choi, M. C.; Kim, Y.; Ha, C. S. *Prog. Polym. Sci.* **2003**, *33*, 581. (d) Akcelrud, L. *Prog. Polym. Sci.* **2003**, *28*, 875.

(7) (a) Chou, S. H.; Tsao, H. K.; Sheng, Y. J. *J. Chem. Phys.* **2011**, *134*, 034904. (b) Chou, S. H.; Wu, D. T.; Tsao, H. K.; Sheng, Y. J. *Soft Matter* **2011**, *7*, 9119. (c) Steed, J.; Atwood, J. *Supramolecular Chemistry*; Wiley & Sons: Chichester, 2000.

(8) Chen, X. L.; Jenekhe, S. A. *Macromolecules* **2000**, *33*, 4610.

(9) (a) Jenekhe, S.; Chen, X. *Science* **1998**, *279*, 5358. (b) Rubatat, L.; Kong, X.; Jenekhe, S.; Ruokolainen, J.; Hojeij, M.; Mezzenga, R. *Macromolecules* **2008**, *41*, 1846.

(10) Huo, H.; Li, K.; Wang, Q.; Wu, C. *Macromolecules* **2007**, *40*, 6692.

(11) Bu, L.; Qu, Y.; Yan, D.; Geng, Y.; Wang, F. *Macromolecules* **2009**, *42*, 1580.

(12) (a) Harrison, W.; Mateer, D.; Tiddy, G. *J. Phys. Chem.* **1996**, *100*, 2310. (b) McRae, E.; Kasha, M. *J. Chem. Phys.* **1958**, *28*, 721. (c) Czikkely, V.; Forsterling, H.; Kuhn, H. *Chem. Phys. Lett.* **1970**, *6*, 11−14. (d) Norland, K.; Ames, A.; Taylor, T. *Phot. Sci. Eng* **1970**, *14*, 295−307.

(13) Accelrys Software Inc., Materials Studio Release Notes, Release 4.4, Accelrys Software Inc., San Diego, CA, 2008.

(14) (a) Hoogerbrugge, P. J.; Koelman, J. M. V. A. *Europhys. Lett.* **1992**, *19*, 155. (b) Español, P.; Warren, P. *Europhys. Lett.* **1995**, *30*, 191. (c) Groot, R. D.; Warren, P. B. *J. Chem. Phys.* **1997**, *107*, 4423.

(15) Lin, C.; Tung, Y.; Ruokolainen, J.; Mezzenga, R.; Chen, W. *Macromolecules* **2008**, *41*, 8759−8769.

(16) Tung, Y.; Wu, W.; Chen, W. *Macromol. Rapid Commun.* **2006**, *27*, 1838−1844.

(17) (a) Lee, M.; Kim, J.; Hwang, I.; Kim, Y.; Oh, N.; Zin, W. *Adv. Mater.* **2001**, *13*, 1363. (b) Cuendias, A. D.; Ibarboure, E.; Lecommandoux, S.; Cloutet, E.; Cramail, H. *J. Polym. Sci., Part A: Polym. Chem.* **2008**, *46*, 4602−4616. (c) Cuendias, A.; Hellaye, M.; Lecommandoux, S.; Cloutet, E.; Cramail, H. *J. Mater. Chem.* **2005**, *15*, 3264−3267.

(18) (a) Halperin, A. *Europhys. Lett.* **1989**, *10*, 549−553. (b) Halperin, A. *Macromolecules* **1990**, *23*, 2724−2731. (c) Semenov, A. *Mol. Cryst. Liq. Cryst.* **1991**, *209*, 191−199. (d) Williams, D.; Fredrickson, G. *Macromolecules* **1992**, *25*, 3561−3568. (e) Sary, N.; Mezzenga, R.; Brochon, C.; Hadziioannou, G.; Ruokolainen, J. *Macromolecules* **2007**, *40*, 3277.

Macromolecules

Note

pubs.acs.org/Macromolecules

Pressure Effects on Cononsolvency Behavior of Poly(*N*-isopropylacrylamide) in Water/DMSO Mixed Solvents

Noboru Osaka[†] and Mitsuhiro Shibayama*[,‡]

[†]Department of Organic and Polymer Materials Chemistry, Tokyo University of Agriculture and Technology, Koganei-shi, Tokyo 184-8588, Japan

[‡]Neutron Science Laboratory, Institute for Solid State Physics, The University of Tokyo, 106-1 Shirakata, Tokai, Ibaraki 319-1106, Japan

INTRODUCTION

Cononsolvency is defined as a phenomenon that a polymer, being soluble in two pure solvents, becomes insoluble in their mixture depending on the composition.[1−6] For solutions of poly(*N*-isopropylacrylamide) (PNIPA) in water/methanol (MeOH) mixtures,[1,2,7,8] the lower critical solution temperature (LCST) decreases upon addition of MeOH and then increases by further addition of MeOH. A theoretical investigation by Tanaka et al. showed that the origin of this phase behavior was the reentrant change of the total number of hydrogen bonding along the chain because of the competitive attachment and detachment of the two solvents.[9,10] On the other hand, in water/dimethyl sulfoxide (DMSO) mixtures, PNIPA shows an upper critical solution temperature (UCST) in the high DMSO mole fraction, φ_{DMSO}, in addition to the LCST in the low φ_{DMSO}.[3,4]

Hydrostatic pressure compresses the molecular volume and modulates the interaction between the solution components. Water-soluble polymers usually show an LCST phase behavior by heating due to breakage of hydrogen-bonding between the polymer and water molecules. The phase diagrams of these polymers are convex upward curves in the pressure−temperature ($P-T$) plane. The LCST increases in the low pressure region and then decreases with further increase in the pressure.[11−15] Nonaqueous polymers do not have the specific interactions, such as hydrogen bonding, and usually show a UCST phase behavior by cooling due to the positive contribution of the enthalpic term in the Flory−Huggins equation. Their phase diagrams are convex downward curves in the $P-T$ plane. The UCST decreases in the low pressure region and then increases with further increase in the pressure.[16−18]

To our knowledge, there have been few reports about the effects of pressure on polymers in mixed solutions of aqueous and nonaqueous solvents. When a nonaqueous solvent is added to an aqueous polymer solution, some of the nonaqueous solvent molecules may be preferentially adsorbed on the polymers in competition with the hydrating water molecules. In particular, for PNIPA in water/DMSO mixtures, the phase behavior can be controlled between LCST and UCST by tuning φ_{DMSO}, and hence, this is the possible model system to investigate the effect of pressure on the different phase behavior with one polymer. In this study, to investigate the pressure effects on the cononsolvency, we constructed the $P-T$ phase diagrams of PNIPA in water/DMSO mixtures with different φ_{DMSO} by using light transmission measurements. In addition, to elucidate the molecular origin of the pressure effect on the phase behavior, we used differential scanning calorimetry (DSC) at ambient pressure.

EXPERIMENTAL SECTION

PNIPA ($M_n = 3.9 \times 10^4$ and $M_w/M_n = 1.45$) purchased from Polymer Source Inc. was used without further purification. The polymer was dissolved in a mixture of hydrogenated water and DMSO, in which the mole fraction of DMSO was varied. Concentration of the polymer in the solutions was constant at 7 wt %.

A He−Ne laser (22 mW, λ = 6328 Å) and a FieldMaster-GS (COHERENT, Co. Ltd., Japan) were used to monitor beam intensity. Pressure dependent experiments were carried out with an inner-cell type pressure cell having a set of optical windows (PCI-400, Teramex, Co. Ltd., Kyoto, Japan).[19,20] DSC measurements were carried out with a DSC8230 (Rigaku Co. Ltd.) at ambient pressure. The polymer solution was crimped in a sealed pan, and DSC thermograms were taken with a heating rate of 3 °C/min. No noticeable change in the weight of the sample pan before and after a DSC run was observed, indicating that no water evaporation occurred during the DSC run.

RESULTS AND DISCUSSION

At ambient pressure, the solutions of PNIPA (7 wt %) in water/DMSO were transparent at low temperature with low mole fraction of DMSO ($0 < \varphi_{DMSO} < 0.1$). The transmission rapidly decreased at the lower critical solution temperature (T_{LCST}) by heating. T_{LCST} monotonically decreased as φ_{DMSO} increased. On the other hand, with high mole fraction of DMSO ($0.65 < \varphi_{DMSO} < 0.76$), the solutions were transparent at high temperature. The transmission decreased at the upper critical solution temperature (T_{UCST}) by cooling, and T_{UCST} monotonically but drastically decreased as φ_{DMSO} increased. The obtained phase diagram with both T_{LCST} and T_{UCST} is shown in Figure 1. On the basis of this phase diagram, we conducted the following measurements under hydrostatic pressure.

Figure 2 shows the $P-T$ phase diagram of PNIPA in water/DMSO obtained by *in situ* transmission measurement under (a) LCST conditions ($0 < \varphi_{DMSO} < 0.1$) and (b) UCST conditions ($0.65 < \varphi_{DMSO} < 0.76$). In Figure 2 (a), an upward-convexity of T_{LCST} with respect to the pressure is observed as reported for other water-soluble polymers.[11,13−15] It is noteworthy that the phase curve shifted toward higher temperature and pressure as φ_{DMSO} increased while T_{LCST} at ambient pressure monotonically decreased. Especially, a subtle addition of DMSO (φ_{DMSO}

Received: December 15, 2011
Revised: February 5, 2012
Published: February 10, 2012

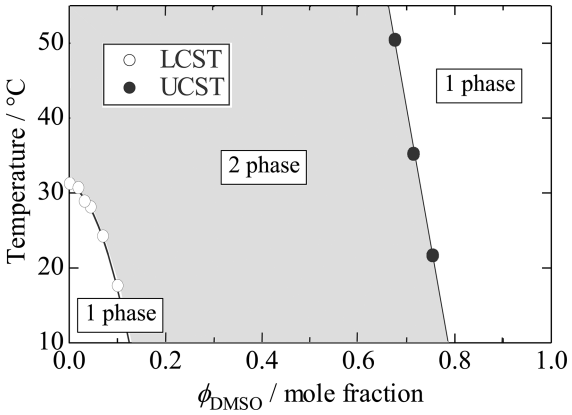

Figure 1. Phase diagram of PNIPA (7 wt %) in water/DMSO mixed solvents with various φ_{DMSO}'s at ambient pressure. Open circles indicate the LCST points ($\varphi_{DMSO} < 0.1$) and closed circles indicate the UCST points ($0.65 < \varphi_{DMSO} < 0.76$).

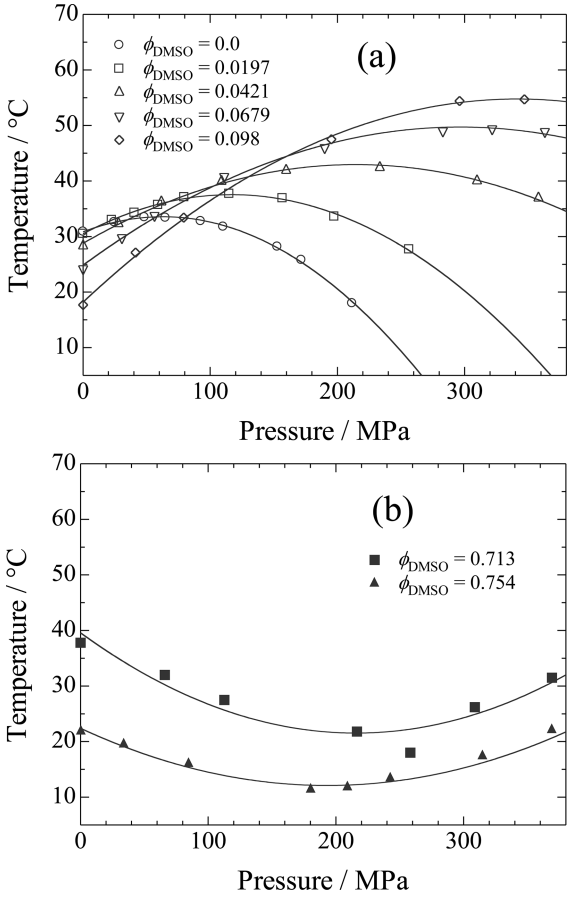

Figure 2. (a) Upward-convexity and (b) downward-convexity phase diagrams in the $P-T$ plane of PNIPA (7 wt %) in water/DMSO mixed solvents under the LCST ($\varphi_{DMSO} < 0.1$) and the UCST conditions ($0.65 < \varphi_{DMSO} < 0.76$), respectively. The solid lines at various φ_{DMSO}'s are fits by quadratic functions.

= 0.098) shifted the pressure at the maximum point, P_{max}, from 55 MPa (φ_{DMSO} = 0.00) to 340 MPa.

On the other hand, T_{UCST} first decreased in the low pressure region and then increased with further increase in the pressure (Figure 2b). In contrast with the behavior under LCST conditions, the downward-convexity of T_{UCST} with respect to the pressure is observed. The phase diagram shifted slightly toward lower temperature as φ_{DMSO} increased. The thermodynamic origin of the shift depending on φ_{DMSO} was investigated by DSC at ambient pressure.

Figure 3a shows the DSC results of PNIPA in water/DMSO with various φ_{DMSO}'s upon heating under the LCST conditions

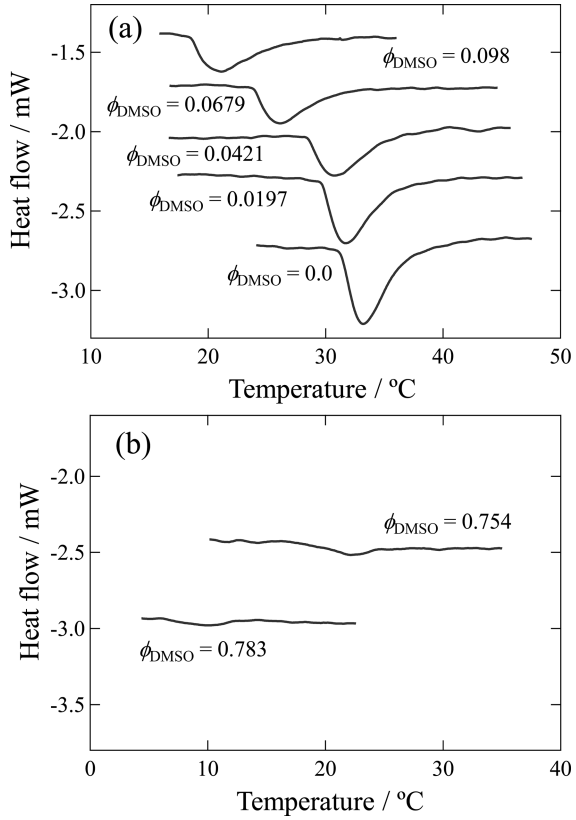

Figure 3. DSC measurements of PNPA (7 wt %) in water/DMSO mixed solvents by heating at a rate of 3 °C/min under the (a) LCST condition and (b) UCST condition at ambient pressure.

at ambient pressure. The endothermic peaks shifted toward lower temperature as φ_{DMSO} increased and the onset temperatures of the endotherm agreed with the T_{LCST} determined by transmission measurements. As φ_{DMSO} increased, the endothermic peak became smaller and the transition behavior became broader. The endothermic heat is required to break the hydrogen-bonding between the solvent and PNIPA. Addition of DMSO into the solutions reduced the total number of hydrogen bonding along the chain because of the competitive attachment and detachment of the two solvents.[9,10] Therefore, reduction of the number of hydrogen bonding and the resulting decrease in the cooperativity of the hydrating solvents were reflected in the reduced endothermic heat and the broader transition, respectively.

φ_{DMSO} dependence of molar endothermic heat, ΔH_m, obtained by the DSC measurements at ambient pressure is shown on the left in Figure 4. This data now allow an estimate of change in the molar volume of PNIPA with the hydrating solvents, ΔV_m, at ambient pressure under the LCST conditions by using the Clausius–Clapeyron equation,

$$\frac{dP}{dT} = \frac{\Delta H_m}{T_{LCST}\Delta V_m} \quad (1)$$

dx.doi.org/10.1021/ma2027116 | *Macromolecules* 2012, 45, 2171–2174

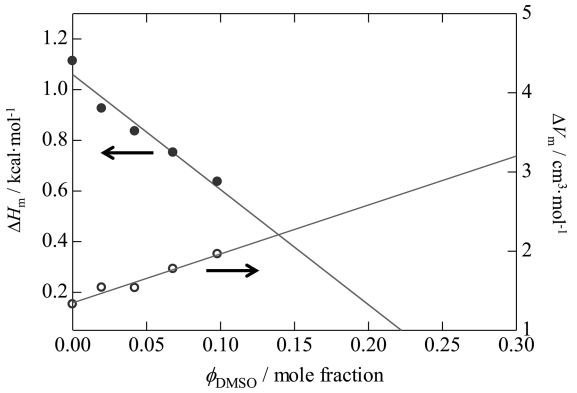

Figure 4. φ_{DMSO} dependence of molar endothermic heat in the left axis obtained by DSC measurements and change of molar volume in the right axis obtained by using eq 1.

where dP/dT is the inverse of the slope of the phase separation curve in the $P-T$ plane shown in Figure 2. Although this Clausius−Clapeyron equation is originally derived for the phase transition of the single component system,[21] this equation is often applied to many polymer solution systems. Especially, for PNIPA/water systems, the mixing molar volume estimated by the Clausius−Clapeyron equation showed good agreement with one obtained by the volumetric measurements at ambient pressure.[11,22] Furthermore, the solvent is a mixture and can be treated as a solvent because water and DMSO mixes at any compositions. Therefore, we assumed that this Clausius−Clapeyron equation is approximately applicable to our system to estimate the molar volume of PNIPA in the low mole fraction region of DMSO at ambient pressure. Monotonic increase of ΔV_m with φ_{DMSO} at ambient pressure obtained by using eq 1 is shown on the right in Figure 4. Since molar volume of DMSO (72 cm^3/mol) is larger than that of water (18 cm^3/mol), ΔV_m increases with φ_{DMSO} by attachment and detachment of more hydrating DMSO molecules from PNIPA. It should be noted that the maximum point in the P-T phase curve corresponds to $dT/dP = 0$ from eq 1, which leads to $\Delta V_m = 0$. In general, pressurizing a system decreases the volume. Since ΔV_m increases with φ_{DMSO}, higher pressure is needed to reduce the larger ΔV_m to zero. This may be the possible thermodynamic origin of the shift of the phase curve toward the higher pressure as φ_{DMSO} increases. In addition, as φ_{DMSO} increases, the total number of hydrogen bonding along the chain decreases and a hydrogen bonding between the C═O group of PNIPA and the methyl group of DMSO is weaker than one between the C═O group of PNIPA and the hydroxyl group of H_2O.[4] These facts suggest that the shift of the maximum point with φ_{DMSO} is determined by the change in the hydrating volume not by the interaction between polymer and the hydrating solvents. With respect to the shift of the maximum point toward higher temperature, T_{LCST} increases up to $\Delta V_m = 0$ in the low pressure region. The increased slope of the phase curve at ambient pressure and the shift of the maximum points toward the higher pressure with increase of φ_{DMSO} will shift the maximum point toward higher temperature.

On the other hand, under the UCST conditions, significant enthalpic heat was not obtained from the DSC measurements at ambient pressure (Figure 3b). This result suggests that the origin of the UCST phase behavior is not related to the hydrating solvents. UCST phase behavior is usually driven by the positive enthalpic term in the Flory−Huggins equation, such as van der Waals type interaction. At ambient pressure, a subtle addition of DMSO into the mixed solution decreased T_{UCST} by specifically modulating the nonspecific interaction.[3] However, the shape of the $P-T$ phase curve was almost the same irrespective of φ_{DMSO} except for the shift toward lower temperature. This suggests that the compression effect by the hydrostatic pressure did not significantly modulate the nonspecific interaction. In the future, the detailed mechanism for the shifts will be investigated using *in situ* scattering and spectroscopy measurements under high pressure.

■ CONCLUSIONS

In summary, the effect of pressure on the phase behavior of PNIPA (7 wt %) in water/DMSO was investigated using *in situ* transmission measurements under hydrostatic pressure and DSC measurements at ambient pressure. Under the LCST conditions with low φ_{DMSO}, the $P-T$ phase diagrams were convex upward curves and shifted drastically toward both higher pressure and temperature as φ_{DMSO} increased. By contrast, under the UCST conditions with high φ_{DMSO}, the $P-T$ phase diagrams were convex downward curves and shifted toward lower temperature as φ_{DMSO} increased. On the basis of the Clausius−Clapeyron equation, the drastic shift of the phase curve with φ_{DMSO} under the LCST conditions was attributed to the increased molar volume of PNIPA at ambient pressure. For the UCST phase behavior under pressure, addition of DMSO modulated the nonspecific interaction such as van der Waals interaction, and the hydrating solvents were not important.

■ AUTHOR INFORMATION

Corresponding Author

*E-mail: sibayama@issp.u-tokyo.ac.jp.

Notes

The authors declare no competing financial interest.

■ ACKNOWLEDGMENTS

This work was partially supported by the Ministry of Education, Science, Sports and Culture, Japan (Grant-in-Aid for Scientific Research (S), 2008−2012, No. 20221005).

■ REFERENCES

(1) Winnik, F. M.; Ringsdorf, H. *Macromolecules* **1990**, *23*, 2415−2416.
(2) Schild, H. G.; Muthukumar, M.; Tirrell, D. A. *Macromolecules* **1991**, *24*, 948−952.
(3) Costa, R. O. R.; Freitas, R. F. S. *Polymer* **2002**, *43*, 5879−5885.
(4) Yamauchi, H.; Maeda, Y. *J. Phys. Chem. B* **2007**, *111*, 12964−12968.
(5) Wang, H.; An, Y.; Huang, N.; Ma, R.; Shi, L. *J. Colloid Interface Sci.* **2008**, *317*, 637−642.
(6) Shankar, R.; Klossner, R. R.; Weaver, J. T.; Koga, T.; van Zanten, J. H.; Krause, W. E.; Colina, C. M.; Tanaka, F.; Spontak, R. J. *Soft Matter* **2009**, *5*, 304−307.
(7) Winnik, F. M.; Ottaviani, M. F.; Bossmann, S. H.; Garcia-Garibay, M.; Turo, N. J. *Macromolecules* **1992**, *25*, 6007−6017.
(8) Asano, M.; Winnik, F. M.; Yamashita, T.; Horie, K. *Macromolecules* **1995**, *28*, 5861−5866.
(9) Tanaka, F.; Koga, T. *Phys. Rev. Lett.* **2008**, *101*, 028302.
(10) Tanaka, F.; Koga, T.; Kojima, H.; Winnik, F. M. *Macromolecules* **2009**, *42*, 1321−1330.
(11) Otake, K.; Karaki, R.; Ebina, T.; Yokoyama, C.; Takahashi, S. *Macromolecules* **1993**, *26*, 2194−2197.

(12) Shibayama, M.; Isono, K.; Okabe, S.; Karino, T.; Nagao, M. *Macromolecules* **2004**, *37*, 2909−291.
(13) Nasimova, I. R.; Karino, T.; Okabe, S.; Nagao, M.; Shibayama, M. *Macromolecules* **2004**, *37*, 8721−8729.
(14) Osaka, N.; Shibayama, M. *Phys. Rev. Lett.* **2006**, *96*, 048303.
(15) Osaka, N.; Shibayama, M.; Kikuchi, T.; Yamamuro, O. *J. Phys. Chem. B* **2009**, *113*, 12870−12876.
(16) Janssen, S.; Schwahn, D.; Mortensen, K.; Springer, T. *Macromolecules* **1993**, *26*, 5587−5591.
(17) Schwahn, D.; Frielinghaus, H.; Mortensen, K.; Almdal, K. *Phys. Rev. Lett.* **1996**, *77*, 3153.
(18) Steinhoff, B.; Rullmann, M.; Wenzel, M.; Junker, M.; Alig, I.; Oser, R.; Stuhn, B.; Meier, G.; Diat, O.; Bosecke, P.; Stanley, H. B. *Macromolecules* **1998**, *31*, 36−40.
(19) Matsumoto, M.; Murakoshi, K.; Wada, Y.; Yanagida, S. *Chem. Lett.* **2000**, *29*, 938−939.
(20) Osaka, N.; Takata, S.; Suzuki, T.; Endo, H.; Shibayama, M. *Polymer* **2008**, *49*, 2957−2963.
(21) Loozen, E.; Nies, E.; Heremans, K.; Berghmans, H. *J. Phys. Chem. B* **2006**, *110*, 7793−7802.
(22) Kato, E. *J. Appl. Polym. Sci.* **2005**, *97*, 405−412.